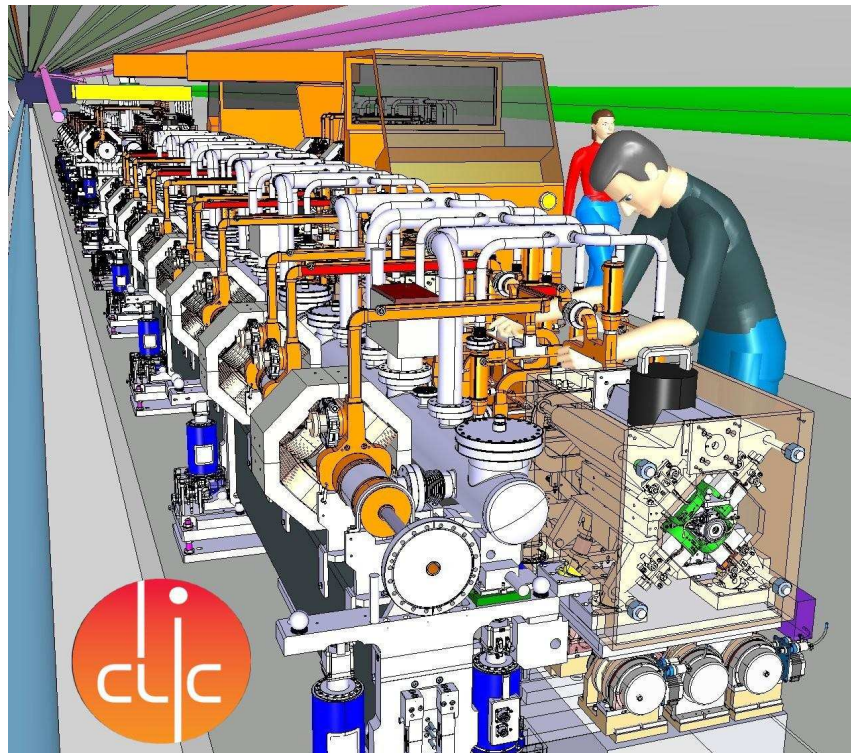


SLAC-R-985
KEK Report 2012-1
PSI-12-01
JAI-2012-001
CERN-2012-007
12 October 2012

ORGANISATION EUROPÉENNE POUR LA RECHERCHE NUCLÉAIRE
CERN EUROPEAN ORGANIZATION FOR NUCLEAR RESEARCH



A MULTI-TeV LINEAR COLLIDER BASED ON CLIC TECHNOLOGY


CLIC CONCEPTUAL DESIGN REPORT

GENEVA
2012

ISBN 978-92-9083-379-6

ISSN 0007-8328

Copyright © CERN, 2012

 Creative Commons Attribution 3.0

Knowledge transfer is an integral part of CERN's mission. CERN publishes this report Open Access under the Creative Commons Attribution 3.0 license

(<http://creativecommons.org/licenses/by/3.0/>) in order to permit its wide dissemination and use.

This report should be cited as:

A Multi-TeV linear collider based on CLIC technology: CLIC Conceptual Design Report,
edited by M. Aicheler, P. Burrows, M. Draper, T. Garvey, P. Lebrun, K. Peach, N. Phinney,
H. Schmickler, D. Schulte and N. Toge, CERN-2012-007

Abstract

This report describes the accelerator studies for a future multi-TeV e^+e^- collider based on the Compact Linear Collider (CLIC) technology. The CLIC concept as described in the report is based on high gradient normal-conducting accelerating structures where the RF power for the acceleration of the colliding beams is extracted from a high-current Drive Beam that runs parallel with the main linac. The focus of CLIC R&D over the last years has been on addressing a set of key feasibility issues that are essential for proving the fundamental validity of the CLIC concept. The status of these feasibility studies are described and summarized. The report also includes a technical description of the accelerator components and R&D to develop the most important parts and methods, as well as a description of the civil engineering and technical services associated with the installation. Several larger system tests have been performed to validate the two-beam scheme, and of particular importance are the results from the CLIC test facility at CERN (CTF3).

Both the machine and detector/physics studies for CLIC have primarily focused on the 3 TeV implementation of CLIC as a benchmark for the CLIC feasibility. This report also includes specific studies for an initial 500 GeV machine, and some discussion of possible intermediate energy stages. The performance and operation issues related to operation at reduced energy compared to the nominal, and considerations of a staged construction program are included in the final part of the report.

The CLIC accelerator study is organized as an international collaboration with 43 partners in 22 countries. An associated report describes the physics potential and experiments at CLIC and a shorter report in preparation will focus on the CLIC implementation strategy, together with a plan for the CLIC R&D studies 2012–2016. Critical and important implementation issues such as cost, power and schedule will be addressed there.

List of Signatories

Introductory Remarks

Starting in September 2011, an invitation has been addressed to the particle physics and accelerator community to sign up for a common signatories list for the CLIC Accelerator and Physics & Detectors CDR. In the invitation, the following text was used:

You are cordially invited to subscribe to the CDR Signatories List

- *If you have made contributions to the CLIC accelerator or the Linear Colliders Physics and Detector studies, or intend to contribute in the future,*

OR / AND

- *If you wish to express support to the physics case and the study of a multi-TeV Linear Collider based on the CLIC technology, and its detector concepts. (Note that signing the CDR does not imply an expression of exclusive support for CLIC versus other major collider options under development. Naturally the same disclaimer applies to the institutes with which the individual signatories are associated)*

A. Ioannisian

Yerevan Physics Institute, Yerevan, Armenia

M. Boland¹

Australian Synchrotron, Clayton, Australia

D. Kim

Monash University, Melbourne, Australia

R. Foot, A. Medina², R. Rassool³, B. von Harling, K. Wootton

University of Melbourne, Melbourne, Australia

T. Bergauer, M. Dragicevic, S. Frank, M. Krammer, W. Mitaroff, C. Schwanda, M. Valenta

Austrian Academy of Sciences, Vienna, Austria

S.D. Bass, P. Jussel

University of Innsbruck, Innsbruck, Austria

A. Hoang

University of Vienna, Vienna, Austria

J. van Hoorne⁴

Vienna University of Technology, Vienna, Austria

K. Afanaciev⁵

Belarusian State University, Minsk, Belarus

V. Gilevsky, A. Patapenka, A. Safronava, I. Zhuk

Joint Institute for Power and Nuclear Research - Sosny, Minsk, Belarus

A. Pankov, I. Serenkova⁶, A. Tsytrinov

P.O. Sukhoi State Technical University of Gomel, Gomel, Belarus
 M. Grunewald, M. Tytgat, E. Yazgan
Ghent University, Ghent, Belgium
 K. Mawatari
Vrije Universiteit Brussel, Brussels, Belgium
 A. Maciel
Centro Brasileiro de Pesquisas Físicas - CBPF, Rio de Janeiro, Brazil
 C. Lagana⁴, R. Rosenfeld
Universidade Estadual Paulista Júlio de Mesquita Filho, Sao Paulo, Brazil
 D. Stamenov, I. Tsakov
Institute for Nuclear Research and Nuclear Energy, Bulgarian Academy of Sciences, Sofia, Bulgaria
 A. Bellerive, F. Tarrade
Carleton University, Ottawa, Canada
 J. Cline, P. Scott
McGill University, Montreal, Canada
 N. Toro
Perimeter Institute for Theoretical Physics, Waterloo, Canada
 I. Trigger
TRIUMF, Vancouver, Canada
 M. Barbi
University of Regina, Regina, Canada
 R. Teuscher
University of Toronto, Toronto, Canada
 R. McPherson⁷
University of Victoria, Victoria Canada
 Q. Li
Beijing University, Beijing, China
 S.L. Chen
Central China Normal University, Wuhan, China
 G.L. Wang, T. Wang
Harbin Institute of Technology, Harbin, China
 G. Chen, J. Gao, W. Li, C.D. Lu, D. Wang, Y. Wang⁴, Z.Z. Xing, C. Xu⁸
Institute of High Energy Physics, Beijing, China
 Y. Gao, Y.P. Kuang, B. Li⁴, Y. Li
Tsinghua University, Beijing, China
 Y. Li
Yantai University, Yantai, China
 N. Bilic
Ruder Boskovic Institute, Zagreb, Croatia
 A. Ilakovac, I. Picek
University of Zagreb, Zagreb, Croatia

J. Chyla, P. Gallus, T. Jakoubek⁹, J. Kvasnicka, T. Lastovicka, M. Marcisovsky, M. Mikestikova,
I. Polak, J. Ridky, P. Sicho, P. Travnicek, V. Vrba⁹, J. Zalesak
Institute of Physics, Academy of Sciences, Prague, Czech Republic

J. Esberg⁴, U.I. Uggerhøj
Aarhus University, Aarhus, Denmark

E. Del Nobile, T. Hapola
CP3-Origins, University of Southern Denmark, Odense, Denmark

P. Damgaard, J.B. Hansen, J.D. Hansen⁴, P. Hansen¹⁰, M.D. Joergensen
Niels Bohr Institute, Copenhagen, Denmark

E. Gabrielli, M. Kadastik, A. Racioppi, M. Raidal
National Institute of Chemical Physics and Biophysics, Tallinn, Estonia

S. Groote¹¹
University of Tartu, Tartu, Estonia

E. Brücken, F. Djurabekova, P. Eerola¹², F. Garcia, J. Hahkala, K. Huitu, J. Huopana, V. Karimaki⁴,
S. Lehti, T. Niinikoski, K. Nordlund, R. Nousiainen¹³, K. Österberg¹², J. Paro¹³, S. Parviainen,
A. Pohjonen, R. Raatikainen, A. Ruzibaev, N.A. Törnqvist, J. Turunen⁴, J. Väinölä¹³
Helsinki Institute of Physics, Helsinki, Finland

S. Lavignac, G. Soyez
CEA, IPhT, Saclay, France

M.N. Bakirci¹⁴, M. Besancon, S. Choudhury, P. Colas, B. Dalena⁴, F. Deliot, W. Farabolini, P. Girardot,
Y. Guler¹⁴, C. Guy, P. Jarry, F. Kircher, E.C. Lancon, F. Peauger, C. Royon, I. Shreyber¹⁵, M. Titov
CEA, Irfu, Saclay, France

E. Aslanides, O. Leroy, G. Mancinelli, S. Muanza, M. Perrin-Terrin, L. Vacavant
*Centre de Physique des Particules de Marseille (CPPM), Aix-Marseille Université, CNRS/IN2P3,
Marseille, France*

R. Coquereaux⁴, M. Knecht
Centre de Physique Théorique (CPT), Aix-Marseille Université, CNRS/IN2P3, Marseille, France

D. Tapia Takaki
Institut de Physique Nucléaire d'Orsay (IPN), IN2P3/CNRS, Orsay, France

A. Arbey⁴, X. Artru, R. Chehab, M. Chevallier, A. Deandrea
Institut de Physique Nucléaire de Lyon (IPNL), IN2P3/CNRS, Villeurbanne, France

B. Fuks
Institut Pluridisciplinaire Hubert Curien (IPHC), IN2P3/CNRS, Strasbourg, France

C. Adloff, J. Allibe, G. Balik, J. Blaha, J.J. Blaising, L. Brunetti, M. Chefdeville, G. Coignet,
G. Deleglise, A. Espargilière, R. Gaglione, N. Geffroy, A. Jeremie, Y. Karyotakis, N. Massol,
J.M. Nappa, S. Rosier Lees, J. Tassan Viol, S. Vilalte, G. Vouters
*Laboratoire d'Annecy le Vieux de Physique des Particules (LAPP), Université de Savoie, IN2P3/CNRS,
Annecy, France*

P. Bambade, J. Brossard, S. Callier, I. Chaikovska, O. Dadoun, M. Davier, N. Dinu, F. Dulucq,
J.F. Grivaz, J. He, G. Martin-Chassard, F. Poirier, R. Roux, N. Seguin-Moreau, A. Variola
Laboratoire de l'Accélérateur Linéaire (LAL), Université de Paris-Sud XI, IN2P3/CNRS, Orsay, France

D.E. Boumediene, P. Gay, N. Ghodbane
Laboratoire de Physique Corpusculaire (LPC), IN2P3/CNRS, Clermont-Ferrand, France

W. Da Silva, S. de Cecco, F. Kapusta

Laboratoire de Physique Nucléaire et des Hautes Energies (LPNHE), IN2P3/CNRS, Paris, France

S. Kraml, G. Sajot

Laboratoire de Physique Subatomique et de Cosmologie (LPSC), Université Joseph Fourier Grenoble 1, IN2P3/CNRS, Grenoble, France

A. Djouadi, D. Guadagnoli, Y. Mambrini

Laboratoire de Physique Théorique d'Orsay (LPT), IN2P3/CNRS, Orsay, France

S. Rychkov

Laboratoire de Physique Théorique ENS, Paris, France

C. Clerc, M. Ruan, Y. Sirois, H. Videau, E. Guliyev

Laboratoire Leprince-Ringuet (LLR), Ecole Polytechnique, IN2P3/CNRS, Palaiseau, France

A. Badel, B. Caron

Laboratoire Systèmes et Matériaux pour la Mécatronique (SYMME)-Polytech Annecy Chambéry, Université de Savoie, Annecy, France

L. Basso, V. Bertone, O. Brein, M. Schumacher

Albert-Ludwigs-Universität Freiburg, Freiburg, Germany

G. Müller, S. Patariaia⁴, S. Weber, M. Worek

Bergische Universität Wuppertal, Wuppertal, Germany

S. Aplin, M. Beckmann¹⁶, M. Berggren, K. Buesser, S.S. Caiazza¹⁶, A. Cakir, M. Chera¹⁶, J. Dietrich, W. Ehrenfeld, G. Eigen¹⁷, B. Foster¹⁸, F. Gaede, E. Garutti¹⁶, A. Grohsjean, C. Günter, O. Hartbrich¹⁹, A. Hartin, B. Hermberg⁴, A. Ignatenko²⁰, S. Karstensen, A. Kaukher, J. List, S. Lu, B. Lutz, M. Medinnis, I. Melzer-Pellmann, V. Morgunov¹⁵, S. Morozov¹⁶, J. Reuter, A. Rosca, I. Rubinskiy²¹, S. Schreiber, F. Sefkow⁴, M. Stanitzki, N. Styles, M. Terwort, B. Vormwald, A. Weiler, P. Zerwas, *DESY, Hamburg, Germany*

I. Bloch, J. Bluemlein, C. Grah, H. Henschel, W. Lange⁴, W. Lohmann²², K. Mönig⁴, O. Novgorodova²², S. Riemann, T. Riemann, H.J. Schreiber, M. Stanescu Bellu

DESY, Zeuthen, Germany

O. Arnaez, V. Buescher, T. Hurth, H. Spiesberger, S. Tapprogge, S. Weinzierl

Johannes Gutenberg-Universität Mainz, Mainz, Germany

H. Stenzel

Justus Liebig Universität Giessen, Giessen, Germany

A. Bernhard, A.S. Brogna, S. Casalbuoni, M. Fitterer⁴, S. Gieseke, R. Grober, N. Hiller, V. Judin, A.S. Mueller, M. Mühlleitner, M. Nasse, U. Nierste, P. Peiffer, G. Quast, R. Rossmanith, F.P. Schilling, M. Schuh, M. Steinhauser, M. Weber

Karlsruhe Institute of Technology, Karlsruhe, Germany

G. Buchalla

Ludwig-Maximilians-Universität München, Munich, Germany

M. Schmelling, H. Zhang

Max Planck Institute for Nuclear Physics, Heidelberg, Germany

A. Caldwell, G. Grindhammer, K. Seidel²³, R. Settles⁴, F. Simon²³, C. Soldner²³, L. Weuste²³, S. Zhou²⁴

Max Planck Institute for Physics, Munich, Germany

W. Bernreuther, M. Czakon, M. Krämer, A. Kulesza, A. Meyer, A. Perieanu

RWTH Aachen University, Aachen, Germany

H. Henke

Technische Universität Berlin, Berlin, Germany

W.F. Mader, J.H. Park, G.M. Pruna, A. Straessner

Technische Universität Dresden, Dresden, Germany

M. Ratz, J. Torrado Cacho, R. Ziegler

Technische Universität Munich, Munich, Germany

Y. Bilevych²⁵, I. Brock, J. Conley, M. Cristinziani⁴, K. Desch, M. Drees, H. Dreiner, S. Hillert, J. Kaminski, M. Lupberger, C. Marinus²⁶, J. Tattersall, N. Vermes, P. Wienemann

Universität Bonn, Bonn, Germany

S. Albino, N. Feege²⁷, J. Kersten, B. Kniehl, G. Moortgat-Pick²⁷, S. Schuwalow⁵

Universität Hamburg, Hamburg, Germany

P. Eckert, I. Peric, H.C. Schultz-Coulon

Universität Heidelberg, Heidelberg, Germany

I. Fleck, C. Grupen, K. Ikematsu

Universität Siegen, Siegen, Germany

A. Denner, T. Ohl, W. Porod, R. Rückl

University of Würzburg, Würzburg, Germany

G.J. Gounaris, C. Petridou⁴, D. Sampsonidis

Aristotle University of Thessaloniki, Thessaloniki, Greece

P. Zisopoulos

National and Kapodistrian University of Athens, Athens, Greece

E. Gazis⁴, N. Gazis⁴, E. Ikarios⁴

National Technical University of Athens, Athens, Greece

N. Beni, Z. Szillasi

Institute of Nuclear Research of the Hungarian Academy of Sciences (ATOMKI), Debrecen, Hungary

G. Bencze, S. Czellar⁴, D. Horvath,

Wigner Research Centre for Physics, Hungarian Academy of Sciences, Budapest, Hungary

B. Ananthanarayan, S.K. Garg, R. Godbole, K. Mohan, M. Patra, R. Varma²⁸, S. Vempati

Centre for High Energy Physics, Indian Institute of Science, Bangalore, India

A. Nyffeler

Harish-Chandra Research Institute, Allahabad, India

D.K. Ghosh

Indian Association For The Cultivation Of Science, Calcutta, India

R. Singh

Indian Institute of Science Education and Research, Calcutta, India

K. Rao

Indian Institute of Technology, Bombay, India

S. Rakshit

Indian Institute of Technology, Indore, India

S. Gopalakrishna

Institute of Mathematical Sciences, Chennai, India

R. Gupta

Panjab University, Chandigarh, India

S. Rindani, P. Sharma

Physical Research Laboratory, Ahmedabad, India

P.D. Gupta, P. Shrivastava

Raja Ramanna Centre for Advanced Technology, DAE, Indore, India

S. Banerjee, G. Bhattacharyya, N. Majumdar, P. Mathews, S. Mukhopadhyay

Saha Institute of Nuclear Physics, Calcutta, India

G. Majumder

Tata Institute of Fundamental Research, Mumbai, India

A. Kundu

University of Calcutta, Calcutta, India

B. Choudhary, D. Choudhury, P. Saxena

University of Delhi, Delhi, India

S. Paktinat Mehdiabadi

Institute for Research in Fundamental Sciences, Tehran, Iran

H. Abramowicz²⁹, G. Alexander, G. Bella, S. Kananov, A. Levy, I. Sadeh, R. Schwartz

Tel Aviv University, Tel Aviv, Israel

E. Duchovni

Weizmann Institute of Science, Rehovot, Israel

M. Maggi, A. Ranieri

INFN, Bari, Italy

M. Caffo³⁰, D. Hatzifotiadou³⁰

INFN, Bologna, Italy

A. Tricomi

INFN, Catania, Italy

S. Catani³¹, S. de Curtis³¹, S. Paoletti, G. Sguazzoni⁴, G. Valenti

INFN, Florence, Italy

D. Alesini, M.E. Biagini, C. Biscari, A. Ghigo, G. Isidori⁴, F. Marcellini, G. Pancheri, P. Raimondi³²,

M. Serio, A. Stella

INFN, Frascati, Italy

C. Troncon³³

INFN, Milan, Italy

C. Gatto

INFN, Naples, Italy

O. Nicrosini, F. Piccinini

INFN, Pavia, Italy

O. Panella

INFN, Perugia, Italy

F. Bedeschi, T. Boccali³⁴, F. Palla, P. Spagnolo³⁴, R. Tenchini³⁴

INFN, Pisa, Italy

B. Mele, L. Silvestrini

INFN, Rome, Italy

A. Ballestrero, C. Mariotti⁴

INFN, Turin, Italy

M. Nemevsek

International Centre for Theoretical Physics, Trieste, Italy

K. Kannike, A. Lusiani³⁵

Scuola Normale Superiore, Pisa, Italy

D. Marzocca³⁶, M. Monaco, A. Romanino, M. Spinrath

SISSA, Trieste, Italy

R. Bonomi, A. Degiovanni³⁷, R. Kieffer, A. La Rana, S. Verdù-Andrès²⁶

TERA Foundation, Novara, Italy

M. Caccia³⁸

Università degli Studi dell'Insubria, Como, Italy

F.L. Navarria³⁹

Università degli Studi di Bologna, Bologna, Italy

I. Masina, M. Moretti

Università degli Studi di Ferrara, Ferrara, Italy

M. Calvetti, R. Casalbuoni⁴⁰, V. Ciulli⁴⁰, F. Coradeschi⁴⁰, D. Dominici⁴⁰

Università degli Studi di Firenze, Florence, Italy

C.M. Becchi⁴¹

Università degli Studi di Genova, Genoa, Italy

U. Amaldi⁴², C. Oleari

Università degli Studi di Milano-Bicocca, Milan, Italy

M. Levchenko⁴, F. Ragusa

Università degli Studi di Milano, Milan, Italy

G. Montagna

Università degli Studi di Pavia, Pavia, Italy

G. Bellettini⁴³, A. Strumia⁴⁴

Università degli Studi di Pisa, Pisa, Italy

R. Contino⁴⁵, S. Gentile⁴⁵, C. Luci⁴⁵, G. Organtini⁴⁵

Università degli Studi di Roma La Sapienza, Rome, Italy

L. Magnea⁴⁶, G. Passarino

Università degli Studi di Torino, Turin, Italy

G. Della Ricca³⁶, N. Paver³⁶, A. Schizzi³⁶

Università degli Studi di Trieste, Trieste, Italy

G. Blankenburg

Università degli Studi Roma Tre, Rome, Italy

T. Abe, A. Aryshev, K. Fujii, T. Higo, T. Kamitani, Y. Makida, T. Matsuda, A. Miyamoto, T. Shidara, T. Takatomi, Y. Takubo, T. Tauchi, N. Toge, K. Ueno, J. Urakawa, A. Yamamoto, M. Yamanaka

High Energy Accelerator Research Organization, KEK, Tsukuba, Japan

M. Kuriki¹⁰⁶, T. Takahashi

Hiroshima University, Higashi-Hiroshima City, Japan

T. Tanabe, S. Yamashita

International Center for Elementary Particle Physics, The University of Tokyo, Tokyo, Japan

M. Ishino

Kyoto University, Kyoto, Japan

K. Kawagoe, K.I. Okumura

Kyushu University, Fukuoka, Japan

J. Hisano

Nagoya University Nagoya, Japan

H. Ono

Nippon Dental University, Tokyo, Japan

K. Kotera, T. Takeshita

Shinshu University, Nagano, Japan

T. Nagamine, H. Yamamoto

Tohoku University, Sendai, Japan

S.Y. Choi, E.J. Kim

Chonbuk National University, Jeonju, Korea

P. Ko, S.C. Park⁴⁷

Korea Institute for Advanced Study, Seoul, Korea

A. Aranda

Universidad de Colima, Colima, Mexico

H. Beijers, S. Brandenburg

Kernfysisch Versneller Instituut, University of Groningen, Groningen, the Netherlands

S. Bentvelsen, P. de Jong, M. Merk, D.B. Ta, J. Timmermans²⁷, N. van Bakel, H. van der Graaf

Nikhef, Amsterdam, the Netherlands

S. Caron²⁵, N. de Groot²⁵, S. de Jong²⁵, F. Filthaut²⁵, W. Metzger²⁵

Radboud University of Nijmegen, Nijmegen, the Netherlands

P. Osland

University of Bergen, Bergen, Norway

E. Adli³², A. Raklev, K. Sjobak⁴, A. Strandlie

University of Oslo, Oslo, Norway

I. Ahmed

COMSATS Institute of Information Technology, Islamabad, Pakistan

R. Khalid

National University of Sciences and Technology, Islamabad, Pakistan

H. Hoorani

Quaid-i-Azam University, Islamabad, Pakistan

J. Aguilar, M. Idzik, S. Kulis

AGH University of Science and Technology, Krakow, Poland

T. Lesiak, B. Pawlik, M. Skrzypek, Z. Was⁴, W. Wierba²⁷, L. Zawiejski
Institute of Nuclear Physics PAN, Krakow, Poland

W. Placzek
Jagiellonian University, Krakow, Poland

J. Kalinowski, M. Krawczyk, M. Misiak, Z. Lalak
University of Warsaw, Warsaw, Poland

G.C. Branco, F. Joaquim, M.N. Rebelo, J. Romão
Instituto Superior Técnico, Lisbon, Portugal

A. David, J. Varela
Laboratório de Instrumentação e Física Experimental de Partículas, Lisbon, Portugal

C. Coca, M.O. Dima, O. Marius Ciprian, E. Teodorescu
Horia Hulubei National Institute of Physics and Nuclear Engineering, Bucharest, Romania

F. Elena, M. Marian, G. Mogildea, A.T. Neagu, P.M. Potlog, T. Preda, G. Veta
Institute of Space Science, Bucharest, Romania

A. Bragin, E. Levichev, P. Piminov, S. Sinyatkin, V.M. Strakhovenko, V. Telnov⁴⁸, K. Zolotarev
Budker Institute of Nuclear Physics, Novosibirsk, Russia

S. Grishin
Institute for High Energy Physics (IHEP), Protvino, Moscow Region, Russia

S. Gninenko
Institute for Nuclear Research, Moscow, Russia

M. Chadeeva, M. Danilov, O. Markin²⁷, E. Tarkovsky, M. Vysotsky
Institute for Theoretical and Experimental Physics, Moscow, Russia

M. Chizhov⁴⁹, M. Filippova, A. Gongadze⁵⁰, S. Grigoryan⁵¹, D. Gudkov⁴, A. Olyunin,
A. Samochkine⁴, V. Samoylov, A. Sapronov²⁷, V. Soldatov, A. Solodko, E. Solodko, I. Tyapkin,
V. Uzhinsky⁴, A. Vorozhtsov⁴
Joint Institute for Nuclear Research, Dubna, Russia

V. Grichine⁴
Lebedev Physical Institute of the Russian Academy of Sciences, Moscow, Russia

N. d'Ascenzo²⁷, V. Saveliev²⁷
National Research Nuclear University, Moscow, Russia

E. Boos, L. Gladilin, L. Smirnova
Skobeltsyn Institute of Nuclear Physics, Moscow State University, Moscow, Russia

P. Michael
The Institute of Applied Physics of the Russian Academy of Sciences, Nizhny Novgorod, Russia

A. Gurtu⁵²
King Abdulaziz University, Jeddah, Saudi Arabia

P. Adzic⁵³, I. Bozovic-Jelisavcic, S. Lukic, M. Pandurovic, I. Smiljanic
Vinca Institute of Nuclear Sciences, Belgrade, Serbia

J. Kamenik
J. Stefan Institute, Ljubljana, Slovenia

A. Hamilton

University of Cape Town, Cape Town, South Africa

M. Aguilar-Benitez, J. Alcaraz Maestre, F.M. de Aragón, L. Garcia-Tabares, D. Iglesias, C. Oliver, I. Podadera, E. Rodríguez García, L. Sanchez Garcia, F. Toral, C. Vazquez

CIEMAT, Madrid, Spain

S. Heikkinen

Fusion for Energy, The European Joint Undertaking for ITER and the Development of Fusion Energy, Barcelona, Spain

J.R. Espinosa

Institut de Física d'Altes Energies, Barcelona, Spain

C. Belver-Aguilar, C. Blanch Gutierrez, A. Celis, A. Faus-Golfe, J. Fuster⁵⁴, I. García García, J.J. Garcia-Garrigos, E. Higon Rodriguez⁴, C. Lacasta, A. Pich, J. Resta Lopez, J.W.F. Valle⁵⁵, M. Vos

Instituto de Física Corpuscular, Valencia, Spain

M.R. Celso, M. Felcini⁵⁶, C. Martinez Rivero, A. Ruiz Jimeno, I. Vila Alvarez

Instituto de Física de Cantabria, (CSIC-Univ. Cantabria), Santander, Spain

M. Grefe, M. Herrero, L. Ibanez, C. Munoz, R. Torre

Instituto de Física Teórica UAM/CSIC, Madrid, Spain

J.J. Fernandez-Melgarejo, E. Torrente-Lujan

TH-FISPAC Murcia University, Murcia, Spain

F. Cornet, O. Kittel

Universidad de Granada, Granada, Spain

N. Armesto, H. Lin

Universidade de Santiago de Compostela, Santiago de Compostela, Spain

A. Dieguez, S. Penaranda-Rivas⁵⁷, B. Pie Valls, J. Sola, J. Trenado

Universitat de Barcelona, Barcelona, Spain

R. Morón Ballester

Universitat Jaume I, Castelló de la Plana, Spain

Y. Kubyshin⁵⁸, E. Marin⁴, G. Montoro

Universitat Politècnica de Catalunya, BarcelonaTech, Barcelona, Spain

P. Christiansen, V. Hedberg, L. Jönsson, U. Mjörnmark, A. Oskarsson, L. Österman, T. Sjöstrand, E. Stenlund

Lund University, Lund, Sweden

C. Ohm, S. Zimmer

Stockholm University, Stockholm, Sweden

G. Angelova Hamberg, R. Brenner, T. Ekelöf, A. Ferrari, M. Jacewicz, T. Muranaka, A. Palaia, R. Ruber, R. Santiago Kern⁴, V. Ziemann

Uppsala University, Uppsala, Sweden

D. Abbaneo, A. Adiguzel, M. Aicheler⁵⁹, G. Altarelli⁶⁰, M. Anastasopoulos, A. Andersson, G. Anelli, I. Antoniadis, F. Antoniou⁶¹, J. Apostolakis, A. Apyan⁶², G. Arnau Izquierdo, K. Artoos, P. Aspell, R. Assmann, S. Atieh, E. Auffray, J. Baechler, R. Ballabriga, G. Ballesteros, D. Banfi, M.J. Barnes, J. Barranco Garcia, A. Bartalesi, A. Behrens, M. Benoit, A. Benot-Morell²⁶, L. Benucci, D. Bergesio⁴², S. Bettoni, G. Blanchot, B. Bolzon, J. Boyd, D. Bozzini, C. Bracco, J. Bremer, H. Breuker, M. Brugger, P. Buncic, H. Burkhardt, F. Butin, M. Buzio, S. Calatroni, E. Calvo, M. Campbell, T. Camporesi, G. Cancio, O. Capatina, N. Catalan Lasheras, A. Cattai, E. Chevallay, P. Chiggiato, J. Christiansen,

E. Ciapala, M. Cirilli, C. Collette⁶³, B. Constance, R. Corsini, G. Cosmo, B. Cure, D. D'Enterria, A. Dabrowski⁶⁴, A. Dallochio, D. Dannheim, M. De Gaspari, G. de Rijk, A. De Roeck, L. Deacon⁶⁵, S. Deghay, J.P. Delahaye, A. Descoeudres, B. Di Girolamo, T. Dobers, S. Doeber, A. Dotti, M. Draper, F. Duarte Ramos, A. Dubrovskiy, K. Elsener, M. Esposito, P. Fassnacht, V. Fedosseev, P. Fernandez Carmona, P. Ferracin, K. Foraz, T. Fowler, H. Franca⁶⁶, M. Frank, D. Froidevaux, J.F. Fuchs, C. Fuentes, E. Fullana⁶⁷, A. Gaddi, D. Gamba³³, G. Ganis, E. Garcia Garcia⁶⁸, H. Garcia Morales⁶⁹, J. Garcia Perez, C. Garion, M. Gastal, L. Gatignon, P. Gavillet, J.C. Gayde, A. Gerbershagen⁷⁰, M. Gersabeck, H. Gerwig, G. Geschonke, S. Gibson⁷⁰, M. Girone, G.F. Giudice, B. Goddard, M. Goulette⁷¹, S. Gowdy, C. Grefe⁷², S. Griffet, C. Grojean⁷³, J.F. Grosse-Oetringhaus, A. Grudiev, E. Gschwendtner, M. Guinchard, K. Hamilton, M. Hauschild, C. Hauviller, R. Hawkings, A. Hektor⁴⁴, A. Henriques, M. Herdzina, C. Hessler, J. Holma⁷⁴, E.B. Holzer, A. Honma, Y. Inntjore Levinsen⁷⁵, V. Ivanchenko, S. Janssens⁷⁶, B. Jeanneret, E. Jensen, J.M. Jimenez, M. Jones, O.R. Jones, M. Jonker, C. Joram, J.M. Jowett, M. Kaya⁷⁷, M. Keil, J. Kemppinen, K. Kershaw, V. Khan, M. Killenberg, W. Klempt, A. Kluge, J. Knobloch, R. Knoops⁷⁸, K. Koenke, O. Kononenko, A. Kosmicki, E. Koukovini Platia³⁷, J.W. Kovermann⁷⁹, A. Kuzmin, F. Lackner, T. Lagouri⁸⁰, C.B. Lam⁸¹, S. Langeslag⁸¹, A. Latina, J.M. Le Goff, P. Lebrun, P. Lecoq, H.M. Lee, T. Lefevre, A. Lenz, B. Lenzi, R. Leux, T. Lienart⁸², R.L. Lillestol⁷⁵, M. Limper, L. Linssen, A. Lipniacka¹⁷, X. Llopart Cudie, J.J. Lopez-Villarejo⁸³, C. Lopez, M. Losasso⁸⁴, R. Losito, A.I. Lucaci Timoce, D. Luckey, M. Ludwig, R. Maccaferri⁴², C. Maglioni, R. Mahbubani, F. Mahmoudi⁵¹, C.O. Maidana⁸⁵, H. Mainaud Durand, L. Malgeri, M. Mangano, D. Manglunki⁷⁶, M. Mannelli, C. Marrelli, Z. Marshall, P. Mato, G. Mavromanolakis, G. McMonagle, A. Mereghetti, D. Mergelkuhl, O. Mete, D. Missiaen, M. Modena, M. Moll, L. Moneta, A. Muennich, D. Muenstermann, M. Mulders, L. Musa, J. Nardulli, A. Naumann, A. Newborough, B. Nicquevert, D. Nisbet, M. Nonis, M. Nordberg, P. Nouvel⁸⁶, M. Olvegård⁸⁷, A. Onnela, T. Orimoto, J. Osborne, R. Ostojic, T. Otto, S. Palestini, Y. Papaphilippou, S. Pasinelli, C. Pasquino, G. Pasztor, M. Pepe Altarelli, A.T. Perez Fontenla⁸⁸, G. Perez, T. Persson, P. Petagna, C. Petrone, A. Pfeiffer, J. Pfingstner, S. Pittet, S. Poss, D. Prieur, M. Pullia, S. Pütz, L. Quertenmont, A. Raimondo, A.U. Rehman⁸⁹, Y. Renier, J.P. Revol, A. Ribon, E. Richards, G. Riddone, P. Riedler, L. Rinolfi, S. Roesler, J. Rojo, P. Roloff, L. Ropelewski, F. Rossi, G. Roy, V. Rude, G. Rumolo, S. Russenschuck, A. Sailer⁹⁰, G. Salam⁹¹, J. Salicio-Diez, E. Salvioni⁹², M. Sapinski, P. Schade²⁷, K.M. Schirm, D. Schlatter, H. Schmickler, B. Schmidt, D. Schoerling⁹³, D. Schulte, S. Sekmen, G. Servant⁷³, N. Siegrist, A. Sfyrila, S. Sgobba, S.H. Shaker⁹⁴, A. Sharma, J. Shi, P. Sievers, M. Silari, P. Skands, P. Skowronski, J. Snuverink, L. Soby, P. Speckmayer, P. Sphicas⁹⁵, J. Stafford-Haworth⁶⁴, S. Stapnes, J. Steinberger, G. Sterbini, J. Strube, M. Struik, F. Stulle, I. Syratheev, A. Sznajder, A. Tauro, F. Tecker, H. ten Kate, F. Teubert, A. Thamm³⁷, P.A. Thonet, L. Thorndahl, L. Timeo, H. Timko⁹⁶, R. Tomas Garcia, D. Tommasini, F. Tramontano⁹⁷, P. Tropea, J. Uythoven, P. Valerio⁹⁸, E. van der Kraaij, E. van Herwijnen, R. van Weelden, G. Vandoni, R. Veness, M. Vesterinen, H. Vincke, A. Vivoli⁸, V. Vlachoudis, J. Vollaie, C. Waaijer, R. Wegner, J.D. Wells⁹⁹, P.S. Wells, T. Wengler, P. Wertelaers, U.A. Wiedemann, H. Wilkens, I. Wilson, S. Worm¹⁰⁰, W. Wuensch, M. Zakaria, J. Zalieckas¹⁷, C. Zamantzas, T. Zickler, F. Zimmermann

CERN, Geneva, Switzerland

A. Bay, N. Charitonidis⁴, T. Montaruli⁷¹, D. Pappadopulo, R. Rattazzi

Ecole Polytechnique Fédérale de Lausanne, Lausanne, Switzerland

G. Dissertori, P. Le Coultre, F. Moortgat, L. Pape, F.J. Ronga, D. Treille⁴, R. Wallny

ETH Zurich, Zurich, Switzerland

H.H. Braun⁴, G. Chachamis, M. Csatari Divall⁴, G. De Michele³⁷, M. Dehler, T. Garvey⁴, T. Pieloni⁴, J.Y. Raguin, L. Rivkin³⁷, R. Zennaro

Paul Scherrer Institut, Villigen, Switzerland

H.P. Beck, G. Colangelo, A. Ereditato, C. Greub, P. Minkowski⁴, A. Oeftiger⁴

University of Bern, Bern, Switzerland

R. Durrer, D. Haas, M. Pohl

University of Geneva, Geneva, Switzerland

M. Grazzini⁴⁰, S. Pozzorini, E. Weihs

University of Zurich, Zurich, Switzerland

C.H. Lin

Academia Sinica, Taipei, Taiwan

G.W.S. Hou

National Taiwan University, Taipei, Taiwan

B. Tali

Adiyaman University, Adiyaman, Turkey

H. Aksakal¹⁰¹, A. Aksoy, V. Ari, O. Cakir, A.K. Ciftci, R. Ciftci, H. Duran Yildiz, S. Kuday, I. Turk Cakir⁴

Ankara University, Ankara, Turkey

B. Antmen, S. Cerci, Z.S. Demiroglu, I. Dumanoglu, E. Eskut, F.H. Geçit, E. Gurpinar, I. Hos, O. Kara, T. Karaman, A. Kayis Topaksu, G. Onengut, M. Özcan, K. Ozdemir, A. Polatoz, D. Sunar Cerci, H. Topakli, S. Türkçapar

Cukurova University, Adana, Turkey

N. Sonmez

Ege University, Izmir, Turkey

B. Belma Sirvanli

Gazi Universitesi Rektörlüğü, Ankara, Turkey

B. Demirköz, A.M. Guler

Middle East Technical University, Ankara, Turkey

S. Sultansoy

TOBB Economics and Technology University, Ankara, Turkey

E. Bulyak, A. Dovbnya

National Science Center, Kharkov Institute of Physics and Technology, Kharkov, Ukraine

L. Teodorescu

Brunel University, Uxbridge, United Kingdom

F. Krauss, A. Signer

Durham University, Durham, United Kingdom

P.D. Dauncey, K. Stelle, M. Vazquez Acosta

Imperial College, London, United Kingdom

J. Ellis⁴

King's College London, London, United Kingdom

P.K. Ambattu¹⁰², I. Bailey¹⁰², G. Burt¹⁰², A. Dexter¹⁰², B. Woolley¹⁰²

Lancaster University, Lancaster, United Kingdom

A. Bevan

Queen Mary, University of London, London, United Kingdom

T. Aumeyr, G. Blair, L.M. Bobb⁴, V. Boisvert, S. Boogert⁶⁵, G. Boorman, N. Joshi⁴, K. Lekomtsev, A. Lyapin, S. Molloy, W. Shields, P. Teixeira-Dias, S. West¹⁰⁰

Royal Holloway, University of London, Egham, United Kingdom
 J.A. Clarke¹⁰², N.A. Collomb, S.P. Jamison, B.J.A. Shepherd
STFC Daresbury Laboratory, Warrington, United Kingdom
 C. Damerell, K. Harder, S. Moretti¹⁰³, G.N. Patrick, F. Wilson
STFC Rutherford Appleton Laboratory, Didcot, United Kingdom
 G. Shore
Swansea University, Swansea, United Kingdom
 C. Welsch¹⁰⁴
The Cockcroft Institute, Daresbury, United Kingdom
 R. Apsimon, R. Bartolini, D. Bett, K. Peach⁷⁰, A. Reichold⁷⁰, A. Seryi
The John Adams Institute for Accelerator Science, Oxford University, Oxford, United Kingdom
 A. Bosco, F. Cullinan⁶⁴, P. Karataev
The John Adams Institute for Accelerator Science, Royal Holloway, University of London, Egham, United Kingdom
 F. Deppisch, T. Gonzalo Velasco, O. Grachov, D. Miller, M. Wing
University College London, London, United Kingdom
 C. Hawkes, T. Price¹¹⁶, N.K. Watson
University of Birmingham, Birmingham, United Kingdom
 J. Goldstein, D. Newbold¹⁰⁰, J. Velthuis
University of Bristol, Bristol, United Kingdom
 B. Allanach, F. Brochu, B. Gripaios⁴, C. Lester, J. Marshall, D.J. Munday, M.A. Parker, J. Stirling, M. Thomson, D. Ward
University of Cambridge, Cambridge, United Kingdom
 A. Gillespie
University of Dundee, Dundee, United Kingdom
 V.J. Martin, H. Tabassam¹⁰⁵
University of Edinburgh, Edinburgh, United Kingdom
 B. Colquhoun, A. Moraes, A. Robson
University of Glasgow, Glasgow, United Kingdom
 R. Barlow
University of Huddersfield, Huddersfield, United Kingdom
 M. Korostelev¹⁰², S. Mallows⁴, T. Teubner
University of Liverpool, Liverpool, United Kingdom
 R.B. Appleby¹⁰², J. Forshaw, C. Glasman¹⁰², R. Jones¹⁰², G. Lafferty, J. Masik, H. Owen¹⁰², C. Parkes, A. Pilaftsis, C. Schwanenberger, N. Shipman⁴, A. Siodmok⁴, G. Xia¹⁰², U.K. Yang
University of Manchester, Manchester, United Kingdom
 N. Blaskovic Kraljevic¹⁸, P. Burrows, G. Christian, L. Corner¹⁸, M. Davis, N. Harnew, C. Hays, B.T. Huffman, A. Nomerotski, S. Sarkar, C. Swinson¹⁰⁶, R. Walczak, T. Weidberg
University of Oxford, Oxford, United Kingdom
 E. Berger, B. Bilki¹⁰⁷, M. Demarteau, G. Drake, K. Francis, W. Gai, J. Gainer⁶², T. Le Compte, J. Repond, J.R. Smith¹⁰⁸, D. Trojand¹⁰⁹, H. Weerts, L. Xia, G. Yang, J. Zhang
Argonne National Laboratory, Argonne, USA

B. Ward
Baylor University, Waco, USA

J. Butler, A. Heister
Boston University, Boston, USA

C. Amelung
Brandeis University, Waltham, USA

M. Harrison, S. Mtingwa, M.-A. Pleier
Brookhaven National Laboratory, Upton, USA

B. Barish, J. Schwarz
California Institute of Technology, Pasadena, USA

M. Paulini
Carnegie Mellon University, Pittsburgh, USA

G. Brooijmans, E. Ponton
Columbia University, New York, USA

M. Blanke, J. Crittenden, A. Mikhailichenko, M. Palmer, M. Perelstein, D. Peterson, A. Ryd, J. Serra
Cornell University, Ithaca, USA

J. Alwall¹¹⁰, S. Cihangir, W. Cooper, L. Elementi, H.E. Fisk, D. Green, C.T. Hill, Y.K. Kim²,
A.S. Kronfeld, P. Levchenko⁴, A. Para, R. Roser, N. Shah, L. Taylor, M. Wendt, H. Wenzel
Fermi National Accelerator Laboratory, Batavia, USA

D. Krohn, M. Reece
Harvard University, Cambridge, USA

W. Hoelzl
IEEE, New York, USA

R. Dermisek, R. van Kooten
Indiana University, Bloomington, USA

J. Hauptman
Iowa State University, Ames, USA

J. Bagger, B. Barnett, B. Blumenfeld, A. Gritsan, K. Grizzard, M. Swartz, Y. Zhou
Johns Hopkins University, Baltimore, USA

Y. Maravin
Kansas State University, Manhattan, USA

S. Alioli, J.F. Arguin, S. Lidia
Lawrence Berkeley National Laboratory, Berkeley, USA

M. Graesser
Los Alamos National Laboratory, Los Alamos, USA

P. Fileviez Perez, G. Gabadadze
New York University, New York, USA

G. Blazey, D. Chakraborty, D. Hedin, G. Lima, S.P. Martin⁴³
Northern Illinois University, DeKalb, USA

M.M. Velasco
Northwestern University, Illinois, USA

C. Tully

Princeton University, Princeton, USA

D. Bortoletto, I. Shipsey

Purdue University, West Lafayette, USA

C. Adolphsen, K. Bane, T. Barklow, M. Breidenbach, S.J. Brodsky, R. Cassell, S. Dimopoulos⁴,
S. Gessner, N. Graf, J. Hewett, M.P. Le, T. Markiewicz, T. Maruyama, J. McCormick, K. Moffeit,
T. Nelson, D. Onoprienko, M. Oriunno, R. Partridge, N. Phinney, M. Pivi, T. Raubenheimer, T. Rizzo,
J.C. Sheppard, S. Smith⁴, S. Tantawi¹¹¹, F. Wang, J. Wang, F. Zhou

SLAC National Accelerator Laboratory, Menlo Park, USA

R. Rios

Southern Methodist University, Dallas, USA

D. Curtin, K. Dehmelt²⁷, M. Douglas, R. Essig, P. Grannis

Stony Brook University, New York, USA

Y. Pakhotin

Texas A&M University, College Station, USA

M. Poelker

Thomas Jefferson National Accelerator Facility (Jefferson Lab), Newport News, USA

K. Sliwa

Tufts University, Medford, USA

D. Wackerroth

University at Buffalo, The State University of New York, New York, USA

L. Clavelli, A. Das, N. Okada

University of Alabama, Tuscaloosa, USA

G. Chambers III

University of Arkansas at Little Rock, Little Rock, USA

J. Gunion

University of California at Davis, Davis, USA

Y. Nomura

University of California, Berkeley, USA

J.L. Feng

University of California, Irvine, USA

V. Andreev

University of California, Los Angeles, USA

B. Grinstein, D. Stone, P. Uttayarat

University of California, San Diego, La Jolla, USA

J. Incandela⁴

University of California, Santa Barbara, USA

T. Banks¹¹², M. Battaglia⁴, M. Dine, P. Draper, H. Haber, B. Schumm

University of California, Santa Cruz, USA

M. Oreglia, C. Wagner⁶⁷, L.T. Wang

University of Chicago, Chicago, USA

J. Zupan

University of Cincinnati, Cincinnati, USA
 S. de Alwis, U. Nauenberg, J.G. Smith, S. Wagner
University of Colorado, Boulder, USA
 S. Hussain
University of Delaware, Newark, USA
 D. Bourilkov
University of Florida, Gainesville, USA
 G. Varner
University of Hawaii, Manoa, USA
 Y.O. Günaydin¹¹³, G. Halladjian, U. Mallik, E. Norbeck, Y. Onel, S. Ozturk, R. Zaidan
University of Iowa, Iowa City, USA
 K.C. Kong, D. Marfatia, G. Wilson
University of Kansas, Lawrence, USA
 D. Brown
University of Louisville, Louisville, USA
 R. Franceschini, N. Hadley
University of Maryland, College Park, USA
 B. Brau, D. Ventura, S. Willocq
University of Massachusetts, Amherst, USA
 D. Feldman, D. Gerdes, S. Goldfarb, R.S. Gupta, K. Riles
University of Michigan, Ann Arbor, USA
 R. Kriske¹¹⁴
University of Minnesota, Minneapolis, USA
 S. Seidel
University of New Mexico, Albuquerque, USA
 Y.J. Ng
University of North Carolina at Chapel Hill, Chapel Hill, USA
 I. Bigi, A. Delgado, M. Hildreth, C. Kolda
University of Notre Dame, Notre Dame, USA
 J. Brau, R. Frey, G. Kribs, N. Sinev³², D.M. Strom, E. Torrence
University of Oregon, Eugene, USA
 C. Ainsley¹¹⁵
University of Pennsylvania, Philadelphia, USA
 T. Han, V. Savinov
University of Pittsburgh, Pittsburgh, USA
 I. Bars
University of Southern California, Los Angeles, USA
 C. Jackson, E. Sarkisyan-Grinbaum⁴, A. White, J. Yu
University of Texas at Arlington, Arlington, USA
 G. Watts
University of Washington, Seattle, USA

S. Dasu, A. Hervé, P. Huang, G. Shaughnessy

University of Wisconsin, Madison, USA

T. Weiler

Vanderbilt University, Nashville, USA

P. Karchin

Wayne State University, Detroit, USA

T. Appelquist, S. Dhawan, J. Shelton

Yale University, New Haven, USA

A. Font

Universidad Central de Venezuela, Caracas, Venezuela

¹*Melbourne University, Melbourne, Australia*

²*University of Chicago, Chicago, USA*

³*Australian Synchrotron, Clayton, Australia*

⁴*CERN, Geneva, Switzerland*

⁵*DESY, Zeuthen, Germany*

⁶*International Centre for Theoretical Physics, Trieste, Italy*

⁷*TRIUMF, Vancouver, Canada*

⁸*Laboratoire de l'Accélérateur Linéaire (LAL), Université de Paris-Sud XI, IN2P3/CNRS, Orsay, France*

⁹*Czech Technical University in Prague, Prague, Czech Republic*

¹⁰*University of Copenhagen, Copenhagen, Denmark*

¹¹*Johannes Gutenberg-Universität Mainz, Mainz, Germany*

¹²*University of Helsinki, Helsinki, Finland*

¹³*VTT Technical Research Centre of Finland, Finland*

¹⁴*Cukurova University, Adana, Turkey*

¹⁵*Institute for Theoretical and Experimental Physics, Moscow, Russia*

¹⁶*Universität Hamburg, Hamburg, Germany*

¹⁷*University of Bergen, Bergen, Norway*

¹⁸*The John Adams Institute for Accelerator Science, Oxford University, Oxford, United Kingdom*

¹⁹*Bergische Universität Wuppertal, Wuppertal, Germany*

²⁰*Belarusian State University, Minsk, Belarus*

²¹*National Research Nuclear University, Moscow, Russia*

²²*Brandenburgische Technische Universität, Cottbus, Germany*

²³*Excellence Cluster 'Universe', TU Munich, Garching, Germany*

²⁴*Institute of High Energy Physics, Beijing, China*

²⁵*Nikhef, Amsterdam, the Netherlands*

²⁶*Instituto de Física Corpuscular, Valencia, Spain*

²⁷*DESY, Hamburg, Germany*

²⁸*Indian Institute of Technology, Bombay, India*

²⁹*Max Planck Institute for Physics, Munich, Germany*

³⁰*Università degli Studi di Bologna, Bologna, Italy*

- ³¹*Università degli Studi di Firenze, Florence, Italy*
- ³²*SLAC National Accelerator Laboratory, Menlo Park, USA*
- ³³*Università degli Studi di Milano, Milan, Italy*
- ³⁴*Università degli Studi di Pisa, Pisa, Italy*
- ³⁵*INFN, Pisa, Italy*
- ³⁶*INFN, Trieste, Italy*
- ³⁷*Ecole Polytechnique Fédérale de Lausanne, Lausanne, Switzerland*
- ³⁸*INFN, Milan, Italy*
- ³⁹*INFN, Bologna, Italy*
- ⁴⁰*INFN, Florence, Italy*
- ⁴¹*INFN, Genoa, Italy*
- ⁴²*TERA Foundation, Novara, Italy*
- ⁴³*Fermi National Accelerator Laboratory, Batavia, USA*
- ⁴⁴*National Institute of Chemical Physics and Biophysics, Tallinn, Estonia*
- ⁴⁵*INFN, Rome, Italy*
- ⁴⁶*INFN, Turin, Italy*
- ⁴⁷*Chonnam National University, Gwangju, Korea*
- ⁴⁸*Novosibirsk State University, Novosibirsk, Russia*
- ⁴⁹*Sofia University, Sofia, Bulgaria*
- ⁵⁰*Andronikashvili Institute of Physics, Georgian Academy of Sciences, Tbilisi, Georgia*
- ⁵¹*Laboratoire de Physique Corpusculaire (LPC), IN2P3/CNRS, Clermont-Ferrand, France*
- ⁵²*University of Delhi, Delhi, India*
- ⁵³*University of Belgrade, Belgrade, Serbia*
- ⁵⁴*University of Valencia and CSIC, Valencia, Spain*
- ⁵⁵*Joint Institute of University of Valencia and Spanish Research Council (CSIC)*
- ⁵⁶*University of California, Los Angeles, USA*
- ⁵⁷*Universidad de Zaragoza, Zaragoza, Spain*
- ⁵⁸*Skobeltsyn Institute of Nuclear Physics, Moscow State University, Moscow, Russia*
- ⁵⁹*Ruhr-Universität Bochum, Bochum, Germany*
- ⁶⁰*Università degli Studi Roma Tre, Rome, Italy*
- ⁶¹*National Technical University of Athens, Athens, Greece*
- ⁶²*Northwestern University, Illinois, USA*
- ⁶³*University of Brussels, Brussels, Belgium*
- ⁶⁴*Royal Holloway, University of London, Egham, United Kingdom*
- ⁶⁵*The John Adams Institute for Accelerator Science, Royal Holloway, University of London, Egham, United Kingdom*
- ⁶⁶*Instituto Superior Técnico, Lisbon, Portugal*
- ⁶⁷*Argonne National Laboratory, Argonne, USA*
- ⁶⁸*Universitat Politècnica de València, Valencia, Spain*
- ⁶⁹*Universitat Politècnica de Catalunya, BarcelonaTech, Barcelona, Spain*
- ⁷⁰*University of Oxford, Oxford, United Kingdom*

- ⁷¹*University of Geneva, Geneva, Switzerland*
- ⁷²*Universität Bonn, Bonn, Germany*
- ⁷³*CEA, IPhT, Saclay, France*
- ⁷⁴*Aalto University School of Science and Technology, Espoo, Finland*
- ⁷⁵*University of Oslo, Oslo, Norway*
- ⁷⁶*Université Libre de Bruxelles, Brussels, Belgium*
- ⁷⁷*Bogazici University, Istanbul, Turkey*
- ⁷⁸*KU Leuven, Leuven, Belgium*
- ⁷⁹*RWTH Aachen University, Aachen, Germany*
- ⁸⁰*Yale University, New Haven, USA*
- ⁸¹*University of Twente, Enschede, the Netherlands*
- ⁸²*Université catholique de Louvain, Louvain-la-Neuve, Belgium*
- ⁸³*Universidad Autónoma de Madrid, Madrid, Spain*
- ⁸⁴*Fusion for Energy, The European Joint Undertaking for ITER and the Development of Fusion Energy, Barcelona, Spain*
- ⁸⁵*Idaho State University, Pocatello, USA*
- ⁸⁶*Université de Toulouse, Toulouse, France*
- ⁸⁷*Uppsala University, Uppsala, Sweden*
- ⁸⁸*Universidade de Vigo, Vigo, Spain*
- ⁸⁹*GSI Helmholtzzentrum für Schwerionenforschung, Darmstadt, Germany*
- ⁹⁰*Humboldt-Universität zu Berlin, Berlin, Germany*
- ⁹¹*Princeton University, Princeton, USA*
- ⁹²*Università degli Studi di Padova, Padua, Italy*
- ⁹³*Technische Universität Bergakademie Freiberg, Freiberg, Germany*
- ⁹⁴*Institute for Research in Fundamental Sciences, Tehran, Iran*
- ⁹⁵*National and Kapodistrian University of Athens, Athens, Greece*
- ⁹⁶*Helsinki Institute of Physics, Helsinki, Finland*
- ⁹⁷*Università degli Studi di Napoli Federico II, Naples, Italy*
- ⁹⁸*Università degli Studi di Roma La Sapienza, Rome, Italy*
- ⁹⁹*University of Michigan, Ann Arbor, USA*
- ¹⁰⁰*STFC Rutherford Appleton Laboratory, Didcot, United Kingdom*
- ¹⁰¹*Nigde University, Nigde, Turkey*
- ¹⁰²*The Cockcroft Institute, Daresbury, United Kingdom*
- ¹⁰³*University of Southampton, Southampton, United Kingdom*
- ¹⁰⁴*University of Liverpool, Liverpool, United Kingdom*
- ¹⁰⁵*Quaid-i-Azam University, Islamabad, Pakistan*
- ¹⁰⁶*High Energy Accelerator Research Organization, KEK, Tsukuba, Japan*
- ¹⁰⁷*University of Iowa, Iowa City, USA*
- ¹⁰⁸*University of Texas at Arlington, Arlington, USA*
- ¹⁰⁹*McGill University, Montreal, Canada*
- ¹¹⁰*National Taiwan University*

¹¹¹*Stanford University, Palo Alto, USA*

¹¹²*Rutgers, the State University of New Jersey, Piscataway, USA*

¹¹³*Kahramanmaras Sutcu Imam University, Kahramanmaras, Turkey*

¹¹⁴*California Institute of Technology, Pasadena, USA*

¹¹⁵*University of Cambridge, Cambridge, United Kingdom*

¹¹⁶*University of Edinburgh, Edinburgh, United Kingdom*

Contents

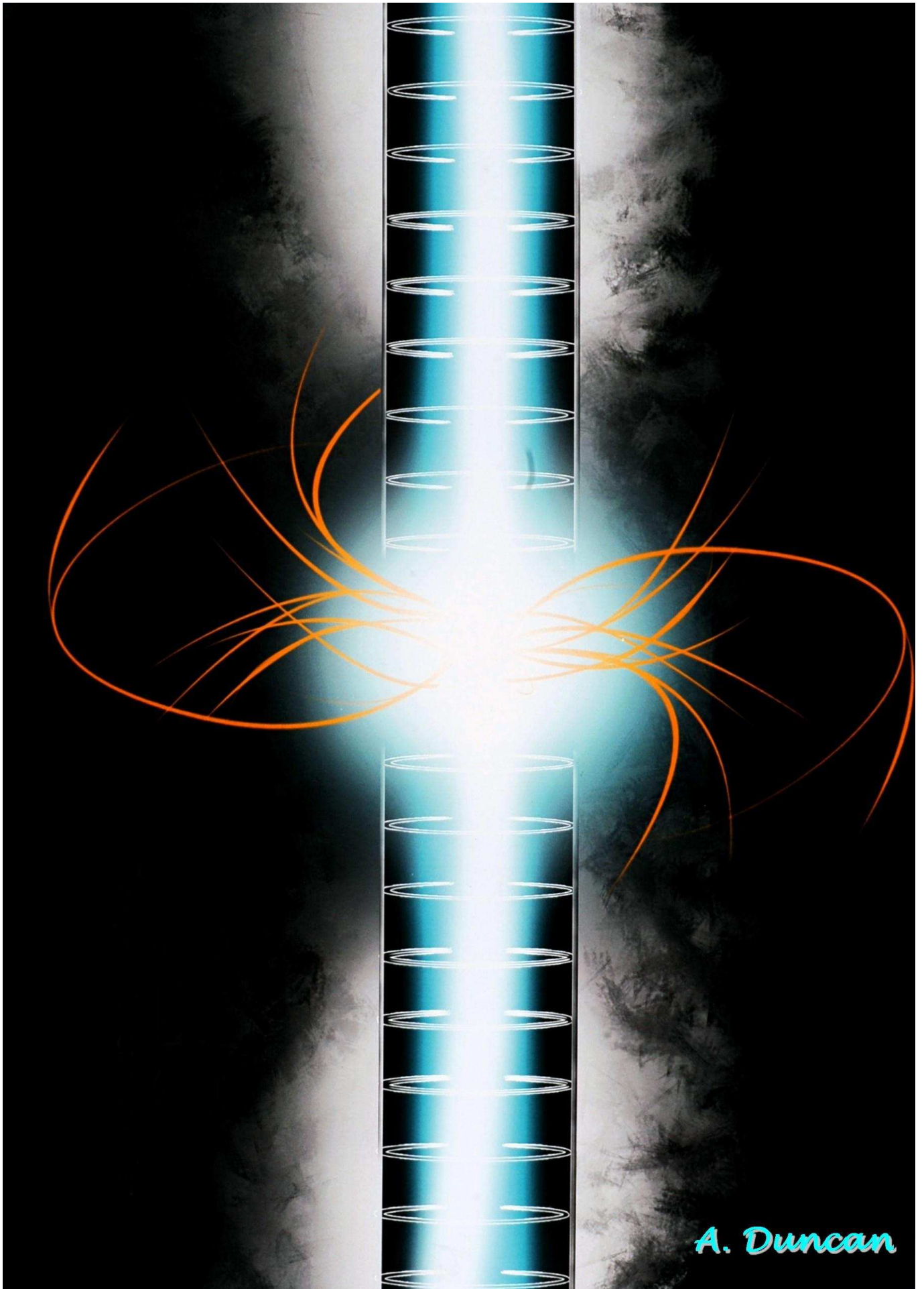
1	Introduction	1
	References	5
2	The CLIC concept: key issues and feasibility	7
2.1	CLIC scheme overview and parameter optimization	9
2.2	Key issues of the CLIC two-beam acceleration scheme	18
2.3	RF structures	21
2.4	The CLIC two-beam acceleration scheme	27
2.5	Drive Beam generation and Main Beam RF power production	34
2.6	Creation of ultra-low emittance beams	47
2.7	Preservation of ultra-low emittances	50
2.8	Machine protection	59
2.9	Total power consumption	61
2.10	Assessment of the CLIC feasibility	69
	References	90
3	Accelerator Physics description of the Main Beam complex	97
3.1	Injectors	99
3.2	The Damping Rings complex	107
3.3	Ring to main linac transport (RTML)	138
3.4	Main linacs	146
3.5	Beam delivery systems	153
3.6	Machine Detector Interface	163
3.7	Post-Collision Line	171
3.8	Integrated simulations on low emittance preservation	179
	References	205
4	Accelerator Physics description of the Drive Beam complex	219
4.1	Drive-Beam accelerators	221
4.2	Drive-Beam Recombination Complex	233
4.3	Beam transport	248
4.4	Decelerators	255
4.5	Dump lines	262
	References	269
5	Technical description of the accelerator	273
5.1	Sources	275
5.2	Normal-conducting and permanent magnets	284
5.3	Superconducting magnets	298
5.4	Radio Frequency systems	324

5.5	X-band RF system	345
5.6	Two-beam module	392
5.7	Vacuum system	418
5.8	Powering CLIC	434
5.9	Beam instrumentation	442
5.10	Beam transfer systems	502
5.11	Beam intercepting devices	528
5.12	Machine Detector Interface	539
5.13	Controls	559
5.14	Fine time generation and distribution	571
5.15	Real-time feedback equipment	579
5.16	Machine protection	593
5.17	Active pre-alignment systems	602
5.18	Main Beam quadrupole stabilization equipment	608
	References	627
6	Civil engineering and technical services	653
6.1	Overview	655
6.2	Civil engineering	655
6.3	Electricity supply	666
6.4	Cooling and ventilation	668
6.5	Transport and installation	679
6.6	Safety systems	685
6.7	Survey and alignment	700
	References	703
7	CLIC technologies demonstrated at CTF3	705
7.1	Objectives of CTF3	707
7.2	Achievements	709
	References	741
8	Energy Scanning	745
8.1	Overview: CLIC operation at low energies	747
8.2	Parameter choice	747
8.3	Baseline design and luminosity	750
8.4	Impact on accelerator systems	752
8.5	Alternative approach	757
8.6	Conclusion	758
	References	759
9	Staged construction	761
9.1	Motivation and possible scenarios for staged construction	763

9.2	Preliminary design of a 500 GeV accelerator	766
9.3	Parameter space for other intermediate energies	781
9.4	Power consumption with staged construction	784
9.5	Construction schedules	792
	References	800
	Appendices	801
	A CLIC parameters	803
	B Artwork in this CDR	809

Chapter 1

Introduction



A. Duncan

Research on particle interactions at the terascale is considered to hold the answers to many of the key open questions in particle physics. These range from the mechanism of electroweak symmetry breaking, to possible verification of new symmetries, to understanding Dark Matter, to searches for a wealth of other possible phenomena beyond the Standard Model. With the LHC, experimental access to Terascale physics is becoming reality. Future LHC energy and luminosity increases will make it possible to do detailed studies in order to seriously address these questions. The particle physics community worldwide, supported by ICFA [1, 2] has, in parallel, expressed a consensus that the results of the LHC will need to be complemented by experiments at a lepton collider in the tera-electron-volt (TeV) energy range. The required energy range and detailed physics requirements are expected to be defined from LHC results when substantial integrated luminosity has been accumulated at full LHC energy, tentatively by 2015–16.

The highest energy lepton collisions, 209 GeV, have been reached with electron and positron colliding beams in LEP at CERN. In spite of the 27 km circumference of LEP the beam energy was limited by synchrotron radiation losses, just compensated by a powerful superconducting RF system providing up to 3640 MV per revolution. Since synchrotron radiation is inversely proportional to the bending radius and proportional to the fourth power of the particle mass, two alternatives are being explored to overcome this limitation and build a Terascale lepton collider:

1. Use muons which have a mass 207 times larger than electrons. The feasibility of muon colliders is being studied [3] and critical challenges addressed; in particular the limited muon lifetime ($2\ \mu\text{s}$ in the laboratory frame) and their production in large emittance beams requiring novel cooling methods.
2. Avoid the bending of particle trajectories by using $e^+ e^-$ linear colliders where two opposing linear accelerators accelerate the particles to their final energy in one pass before focusing and colliding them in a central interaction point.

Following the successful development and operation of the 100 GeV SLAC Linear Collider (SLC) [4] about 25 years of R&D and technical progress have greatly improved the design of linear colliders and their potential performances. Global collaborations are currently developing two alternative technologies, with significantly different energy reach:

1. Following an ICFA recommendation [5] for a linear collider in the TeV energy range, the International Linear Collider (ILC), [6] aiming at colliding beam energy of 500 GeV, upgradeable to 1 TeV, is based on beam acceleration by superconducting RF structures. A Reference Design Report (RDR) [7] was published in 2007 and a Technical Design Report (TDR) is foreseen for 2012.
2. The Compact Linear Collider (CLIC) study is exploring the possibility of extending the energy range of linear colliders into the multi-TeV energy region by developing a novel technology of two-beam acceleration (TBA), providing colliding beams up to 3 TeV. Conceptional Design Reports covering the accelerator studies (this volume), detector and physics studies [8] (completed) and summary/outlook (in preparation) provide a complete documentation of this approach.

The ILC and CLIC studies are both contributing to the preparation for the most appropriate facility to complement the LHC. Taking advantages of the large number of synergies, a close and fruitful collaboration between CLIC and ILC has been launched.

A linear collider at the multi-TeV scale, such as CLIC, can offer a compelling and comprehensive physics program of discoveries and precision measurements, perfectly complementing the LHC. High gradients are critical in order to reach multi-TeV energies in a reasonable length collider. The CLIC two-beam concept proposed in 1986 provides a unique approach to reach multi-TeV energies with an $e^+ e^-$ collider. The CLIC concept continued to be studied and developed through the 1990s but was

given increased focus and importance in 2004 by the CERN Council's decision to produce a Conceptual Design Report (CDR) on the timescale of 2010. This date was chosen to match the expected first physics results from the LHC. Currently the LHC data-taking at initial energies of 7–8 TeV is expected to end in 2012 and full energy operation to resume in 2014–15.

The CLIC study is organized as an international collaboration with 44 partners in 22 countries, where each partner contributes to the work in ways similar to what is done in detector collaborations. The concept of organizing an accelerator project as a collaboration has proven very successful for CLIC, and has allowed both large and small accelerator groups to become fully integrated partners. The CLIC study is hosted by CERN and the CLIC test facility at CERN remains a central part of the project. However, there are also many other test facilities and R&D efforts around the world, many in close collaboration with ILC. These study key parameters of such a collider and provide experimental verification that they can be achieved.

Since 2008, the focus of CLIC R&D has been on addressing a set of key feasibility issues which are essential for proving the fundamental validity of the CLIC concept. These studies form the basis of this report. The aim of the accelerator CDR is hence to document:

- the feasibility results following about 25 years of R&D on critical issues of the CLIC scheme and technology,
- the concept of a linear collider in the multi-TeV energy range based on CLIC technology with a preliminary performance estimate,
- a description of its technical subsystems.

In parallel, physics and detector groups have started to design detectors for CLIC based on the ILC detector concepts [7], as well as mapping out the physics potential of the CLIC machine in more detail. The physics and detector studies are described in the volume *Physics and Detectors at CLIC - CLIC CDR* [8]. This work has been organized in close coordination with both the ILC physics and detector community and the CLIC accelerator collaboration. This allows both physics and detector groups to adopt an open approach and adapt to whatever collider design is eventually built.

Both the accelerator and detector/physics studies described in these two CDR volumes have primarily focused on the 3 TeV implementation of CLIC as a benchmark for CLIC feasibility. The reports also include specific studies for an initial 500 GeV machine, and some discussion of possible intermediate energy stages.

The implementation of CLIC will need to be optimized to address the physics that can be reached at various energy ranges. This must be based on our best knowledge of the physics landscape at the time of launching the project, relying on measurements at LHC and elsewhere. CLIC could be built in stages, starting at the lowest energy required by physics, with successive energy upgrades, in order to obtain a well-performing machine over a large energy range. A third volume of the CDR describes the development of such an implementation strategy, together with a plan for the post-CDR CLIC R&D studies 2012–2016. The third volume is also intended to provide input to the *European Strategy for Particle Physics* and to other similar roadmap processes. Critical and important implementation issues such as cost, power, and schedule are addressed in this volume.

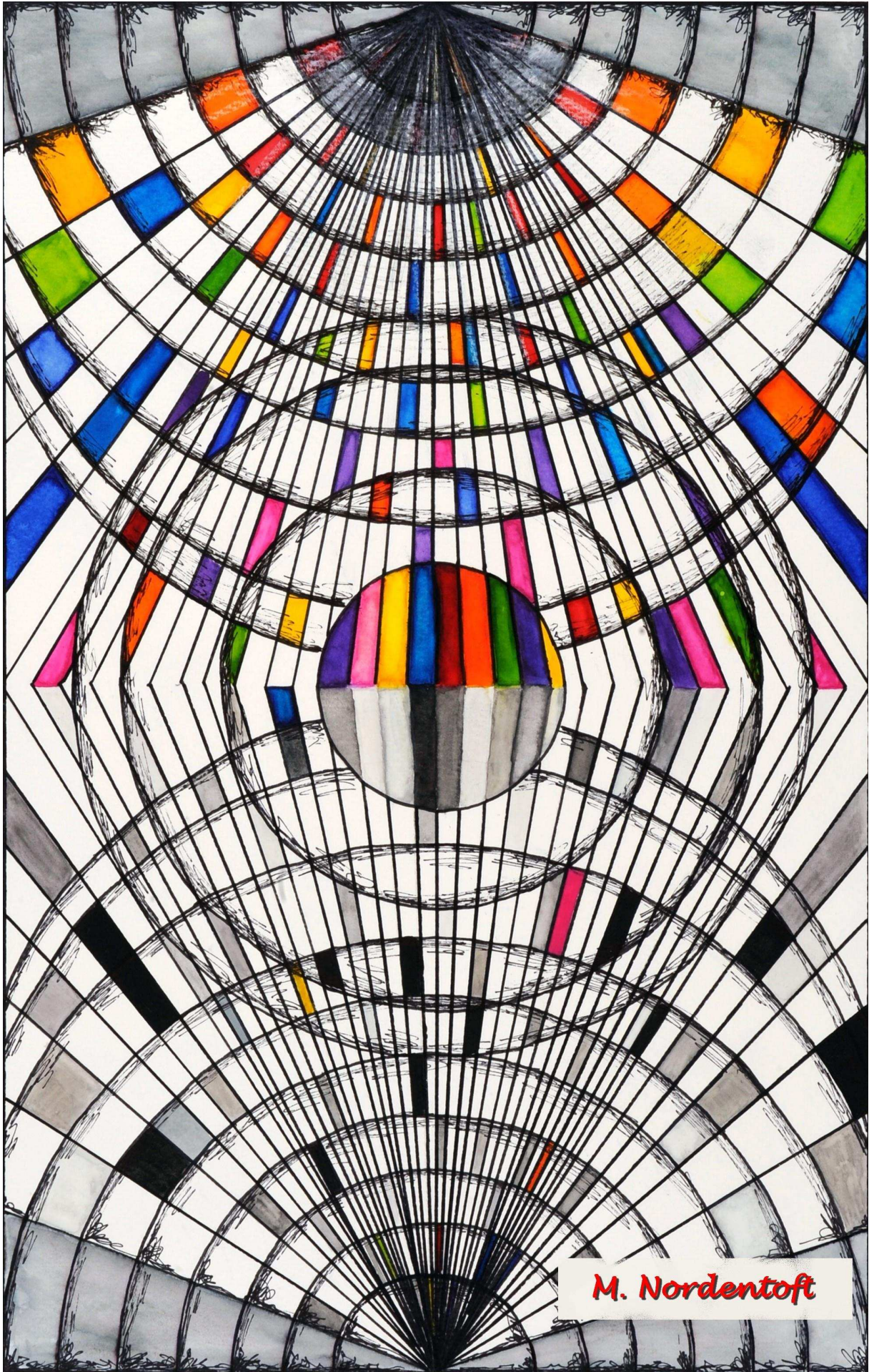
REFERENCES

References

1. *ICFA Statement on Linear Colliders* ICFA. <http://www.fnal.gov/directorate/icfa/icfa_LCstatement.html> (1999).
2. *Research and Development Towards TeV Linear $e+e-$ Colliders* ICFA. <http://www.fnal.gov/directorate/icfa/icfa_r&d.html> (1993).
3. Shiltsev, V. When will we know a muon collider is feasible? Status and directions of muon accelerator R&D. *Modern Phys. Lett. A* **25**, 567–577 (2010).
4. *SLAC Linear Collider (SLC)* <<http://www-sldnt.slac.stanford.edu/alr/slc.htm>>.
5. *ICFA Statement on Linear Colliders* ICFA. <http://www.fnal.gov/directorate/icfa/icfa_LCstatement0204.html> (2004).
6. *International Linear Collider* <<http://www.linearcollider.org/>>.
7. *ILC Reference Design Report* <<http://www.linearcollider.org/about/Publications/Reference-Design-Report>> (2007).
8. *The Compact Linear Collider Study. Collaborations* <<http://cllc-study.web.cern.ch/CLIC-Study/Collaborations.htm>>.

Chapter 2

The CLIC concept: key issues and feasibility



M. Nordentoft

2.1 CLIC SCHEME OVERVIEW AND PARAMETER OPTIMIZATION

Following a general introduction into the so-called ‘CLIC acceleration scheme’ the parameter optimization of the CLIC linear collider for a 3 TeV centre-of-mass collision energy is presented below. The optimization represents the best parameter choice for the highest luminosity at a high energy at the lowest possible cost. As a result the novel so-called ‘two-beam acceleration’ scheme is proposed.

This novel acceleration scheme is linked to several critical issues, cost and performance, overall power consumption, and the feasibility of key technologies. They are listed and described in §2.2 including the overall approach for R&D on these issues. The details are then treated in §2.3–§2.8. In §2.10 the present situation of the CLIC feasibility study is summarized including further R&D to be undertaken during the project preparation phase.

2.1 CLIC scheme overview and parameter optimization

2.1.1 Overview of the CLIC accelerator complex

Following preliminary physics studies based on an electron–positron collider in the multi-TeV energy range [1], [2], the CLIC study is focused on the design of a linear collider with a centre-of-mass collision energy of 3 TeV and a luminosity of $2 \times 10^{34} \text{ cm}^{-2} \text{ s}^{-1}$; these numbers being the extreme of the considered parameter space. Before describing the layout of the accelerator complex, the main design arguments and the choices that make up the so-called ‘CLIC technology’ are listed.

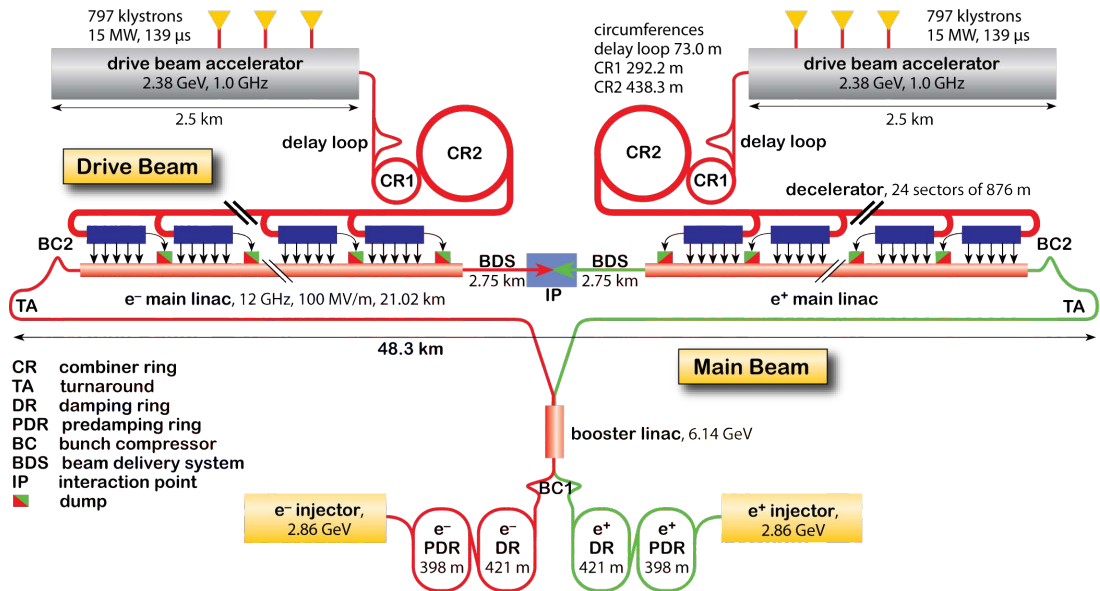


Fig. 2.1: CLIC layout at 3 TeV

The layout of the CLIC accelerator complex is shown in Fig. 2.1. The Main Beams are generated and pre-accelerated in the injector linacs and then enter the Damping Rings for emittance reduction (lower part of the figure). Target figures are 500 nm and 5 nm normalized beam emittances in the horizontal and vertical planes respectively at the exit of the injector complex. The small emittance beams are further accelerated in a common linac before being transported through the main tunnel to the turnarounds. After the turnarounds the acceleration of the Main Beam begins with an accelerating gradient of 100 MV/m. Using a classic approach the linacs for the acceleration of the Main Beams would be powered by klystrons. In this novel acceleration scheme the klystron powering is replaced by the generation of a second ‘Drive Beam’ and its compression and reversion into RF power close to the Main Beam accelerating structures.

The top part of the figure shows the Drive Beam generation in two Main Linacs and the successive time compression of the Drive Beam pulses in the Delay Loops and Combiner Rings (CR1 and CR2).

The time-compressed Drive Beam reaches a current of about 100 A at a beam energy of about 2.4 GeV. This compressed Drive Beam is transported through the Main Linac tunnel to 24 individual turnarounds. Each Drive Beam segment is directed by pulsed extraction elements, for the final RF power generation, into the accelerating structures of the Main Beams. Hence in the Main Linac tunnel we find four beam transport lines: the transport lines of the Main Beam and Drive Beam plus the acceleration line for the Main Beam and the deceleration line for the Drive Beam. The beams collide after a long Beam Delivery Section (BDS) (collimation, final focus) in one interaction point (IP) in the centre of the complex.

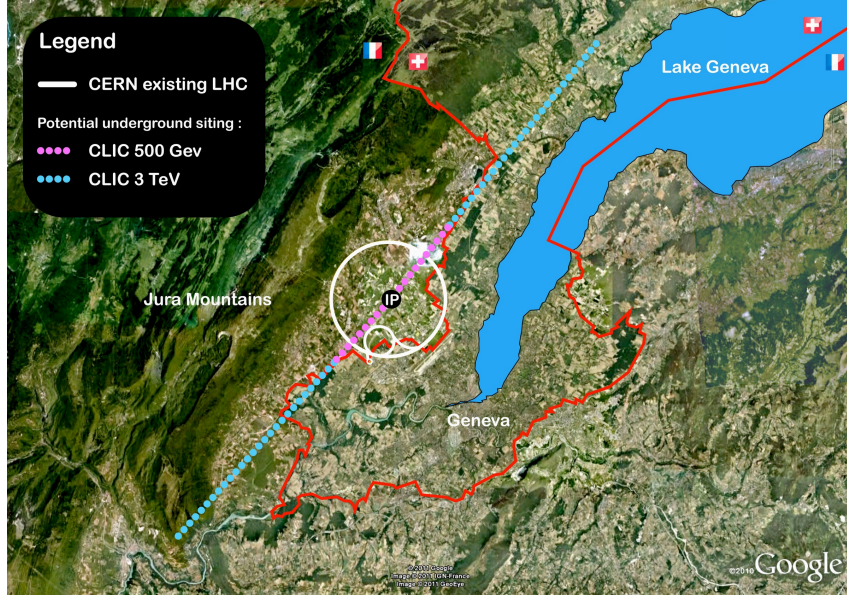


Fig. 2.2: Map showing a potential location for the CLIC accelerator complex

Figure 2.2 shows a possible implementation of this accelerator in the Geneva area. The proportions become more clear. The generation of the Main Beams, the Drive Beams, and the central collision point would fall into existing CERN territory, whereas the two 24 m long acceleration tunnels would extend into the local area as underground installations. The blue dots show the tunnel length needed for a collision energy of 3 TeV, whereas the pink dots indicate the size of the installation for 500 GeV.

2.1.2 Why two-beam acceleration?

In order not to confuse the arguments, no explicit references are given in this section. All important details are developed in the following sections of this chapter including references.

- The main objective is to build at reasonable cost and at a reasonable size a linear collider for the Multi-TeV range. This requires a very high acceleration gradient (100 MV/m), which can not be achieved with superconducting technology.
- For a given breakdown rate there is a very steep scaling between gradient and RF pulse length, hence the beam pulse has to be limited to about 150 ns. This short beam pulse is the fundamental design parameter, which has major consequences for the physics analysis of the events, for beam parameters to achieve the required luminosity, and for the RF power generation.
- In a circular accelerator the counter-rotating beams collide with a high repetition frequency, typically in the tens of kHz range. The repetition frequency of a linear collider by contrast is typically only 5–100 Hz. The luminosity necessary for the particle physics experiments has then to be reached with challenging parameters for bunch charge, beam emittance, and strength of the final focusing magnets. In the case of CLIC about 300 bunches at high bunch charge spaced by only 0.5 ns have to be accelerated.

2.1 CLIC SCHEME OVERVIEW AND PARAMETER OPTIMIZATION

- For the generation of very high RF power only klystrons are currently available as power sources. There are, however, no klystrons on the market which can generate the required power for the short RF pulses (some 200 ns, which accounts for the 150 ns beam pulse plus some filling time of the accelerating cavities). The available klystrons can only deliver power into pulses which are about one order of magnitude longer. Hence klystrons with subsequent pulse compression networks would have to be used. A klystron powered linear collider with 100 MV/m accelerating cavities would need about 35 000 high power klystrons (about 50 MW each) with each klystron having a factor of five pulse compression.
- The numbers presented for klystron powering are not feasible in terms of cost and maintenance; they might be reconsidered as an option in case of a collider with a very low centre-of-mass energy.
- The so-called CLIC scheme foresees the generation of the necessary RF power through the production of a second low-energy Drive Beam over a very long pulse (high-power klystrons are readily available) followed by a sophisticated compression scheme, in which the RF pulse is not time compressed, but the generated electron ‘Drive Beam’ itself is. The time-compressed Drive Beam then travels along with the Main Beam and generates the necessary RF power for acceleration by losing its energy in the ‘decelerator’ in special RF structures (PETS).

The following will give a more quantitative view of the parameter optimization for highest luminosity and high energy.

2.1.3 The luminosity challenge

The luminosity, \mathcal{L} , of a linear collider [3] can be written as

$$\mathcal{L} = H_D \frac{N^2}{\sigma_x \sigma_y} n_b f_r \quad (2.1)$$

or equivalently

$$\mathcal{L} = H_d \frac{N}{\sigma_x} \frac{1}{\sigma_y} \frac{P_b}{E_b} = H_D \frac{N}{\sigma_x} \frac{1}{\sigma_y} \eta \frac{P_{AC}}{E_b} \quad (2.2)$$

where:

E_b	is the beam energy
f_r	is the linac repetition rate
n_b	is the number of bunches per pulse
N	is the number of particles per bunch
$\sigma_{x,y}$	$= \sqrt{\frac{\epsilon_{x,y} \beta_{x,y}}{\gamma}}$ the horizontal (vertical) r.m.s. beam size at the collision point
γ	$= E_b/E_0$ the beam energy normalized to the rest electron energy, $E_0 = 511$ keV
H_D	is a correction factor representing the combined effect of ‘hour-glass’ (change of beta function in longitudinal direction over the collision region) and disruption enhancement (due to the attractive force that the two colliding bunches exert on each other)
$\epsilon_{x,y}$	is the normalized horizontal (vertical) emittance
$\beta_{x,y}$	is the horizontal (vertical) beta function at the collision point
P_b	$= f_r n_b N E_b = \eta P_{AC}$ the beam power where η stands for the wall-plug-power-to-beam-power conversion efficiency and P_{AC} the wall-plug power for beam acceleration

$\eta = \eta_{\text{RF}}^{\text{AC}} \eta_{\text{b}}^{\text{RF}}$ is the wall plug to beam conversion efficiency. It corresponds to the convolution of the AC-to-RF conversion efficiency, $\eta_{\text{RF}}^{\text{AC}}$, and the RF-to-beam transfer efficiency, $\eta_{\text{b}}^{\text{RF}}$

After collision, the beam spectrum and background, as well as the ratio of peak to total luminosity, which are all of primordial importance for physics and detector considerations, are highly dominated by the number of beamstrahlung photons emitted per electron (or positron), n_γ , with an average energy, E_γ , during the collision in the field of the opposing beam. The beamstrahlung is similar to synchrotron radiation and characterized by the ‘beamstrahlung parameter’ Υ given by

$$\Upsilon = \frac{N\gamma r_e}{(\sigma_x + \sigma_y)\sigma_z} \quad (2.3)$$

At lower beam energies one usually finds $\Upsilon \ll 1$; this is true for CLIC at 500 GeV, but for CLIC at 3 TeV, $\Upsilon \gg 1$. In the low-energy regime (500 GeV), where beamstrahlung radiation during collisions is not too large, the number of photons produced in the collision is given by

$$n_\gamma \propto \frac{N}{\sigma_x} \quad E_\gamma \propto \frac{N}{\sigma_x \sigma_z} \quad (2.4)$$

The luminosity then becomes

$$\mathcal{L} \propto H_D \frac{n_\gamma}{\sqrt{\beta_y \epsilon_y}} \frac{P_b}{E_b} \propto H_D n_\gamma \frac{1}{\sqrt{\beta_y \epsilon_y}} \eta \frac{P_{\text{AC}}}{E_b} \quad (2.5)$$

Two lower limits exist for β_y . In order to mitigate the luminosity reduction by the ‘hour-glass’ effect, one requires $\beta_y \geq \sigma_z$. The design of the beam delivery system will also yield a practical limit for β_y due to the optics. In the case of CLIC with its very short bunches we are more limited by the latter constraint. For a given design of the beam delivery system (i.e., for $\beta_y = \text{constant}$)

$$\mathcal{L} \propto H_D \frac{n_\gamma}{\sqrt{\epsilon_y}} \frac{P_b}{E_b} \propto H_D n_\gamma \frac{\eta}{\sqrt{\epsilon_y}} \frac{P_{\text{AC}}}{E_b} \quad (2.6)$$

In the high-energy regime (3 TeV), where beamstrahlung radiation during collisions is large, the luminosity becomes

$$\mathcal{L} \propto H_D \frac{n_\gamma^{3/2}}{\sqrt{\sigma_z} \sqrt{\beta_y \epsilon_y}} \frac{P_b}{E_b} \propto H_D \frac{n_\gamma^{3/2}}{\sqrt{\sigma_z}} \frac{\eta}{\sqrt{\beta_y \epsilon_y}} \frac{P_{\text{AC}}}{E_b} \quad (2.7)$$

Again the limit for β_y is given by the design of the beam delivery system ($\beta_y = \text{const}$):

$$\mathcal{L} \propto H_D \frac{n_\gamma^{3/2}}{\sqrt{\epsilon_y}} \frac{P_b}{E_b} \propto H_D \frac{n_\gamma^{3/2}}{\sqrt{\sigma_z}} \frac{1}{\sqrt{\epsilon_y}} \eta \frac{P_{\text{AC}}}{E_b} \quad (2.8)$$

The factor of merit, M , of a linear collider can be defined as the luminosity per wall-plug power for a given beam energy and number of photons n_γ emitted in the collision.

In the low-energy and beamstrahlung regime, the factor of merit, M , becomes

$$M = \frac{\mathcal{L}}{P_{\text{AC}}} \propto \eta \frac{1}{\sqrt{\epsilon_y}} \quad (2.9)$$

In the high-energy and beamstrahlung regime, the factor of merit, M , becomes

2.1 CLIC SCHEME OVERVIEW AND PARAMETER OPTIMIZATION

$$M = \frac{\mathcal{L}}{P_{AC}} \propto \eta \frac{1}{\sqrt{\sigma_z} \sqrt{\epsilon_y}} \quad (2.10)$$

Thus the luminosity depends on a very limited number of parameters, specifically:

- The beam power:
 - The wall-plug-to-beam-power efficiency is of primordial importance in order to limit the wall-plug power consumption and therefore the operational cost of the facility.
- The bunch length:
 - Beam acceleration by high-frequency RF structures with short wavelength is strongly favoured.
- The vertical beam emittance:
 - Small beam emittance generation and preservation during acceleration and focusing are extremely important.
- The beam energy:
 - Colliders at the energy and luminosity frontiers are extremely challenging especially when considering the required luminosity increasing with energy to compensate for the corresponding decrease of many physics cross-sections.

2.1.4 The energy challenge

The energy, E , of the colliding beams is given by the average loaded gradient in the structures, E_a , the length of each linac, L , and the fill factor, F — the fraction of the linac filled with structures — as

$$E = F E_a L \quad (2.11)$$

To minimize the linac length and cost the fill factor is maximized by tightly integrating the beamline components and by using high gradients. The choice of fill factor and gradient is dominated by efficiency considerations.

For a given structure, the efficiency $\eta_{RF \rightarrow beam}$ of transforming RF to beam power is proportional to the beam current I_{beam} , in the limit of small efficiencies. One therefore uses the highest possible current, the limit being given by single and multi-bunch beam break-up due to wakefield effects. The maximum stable current I_{max} depends on the average betatron-function $\langle \beta \rangle$ in the Main Linac as

$$I_{max} \propto \frac{1}{\langle \beta \rangle} \quad (2.12)$$

Hence more and longer (i.e., stronger) magnets increase the beam current and efficiency. We have chosen a lattice in which about 10% of the linac is filled with quadrupoles. Including unavoidable interconnections, this leads to a fill factor of approximately 80%.

The gradient that can be achieved in the accelerating structures is mainly a function of the aperture radius; for smaller apertures higher gradients can be reached. For any given structure and lattice design, the maximum single bunch charge N and length σ_z are limited by single bunch break-up due to short-range wakefields. Similarly the minimum distance between bunches is limited by beam break-up due to long-range wakefields. Small apertures increase the level of these wakefields. Hence the beam break-up will occur at lower currents, limiting the efficiency and luminosity. The optimum aperture has been found in a full optimization.

2.1.5 CLIC 3 TeV main parameters

The specific choice of parameters results from a trade-off between conflicting requirements:

As pointed out in §2.1.3 and in §2.1.4, high accelerating fields limit the extension of the facility but reduce the RF-to-beam transfer efficiency. Structures with high RF frequency are favoured for high RF-to-beam efficiency. They reduce the necessary RF power at the structure input for high-field acceleration of large beam current with short bunches and small intervals but they generate strong wakefields. The preservation of beam quality during acceleration in such a strong wakefield environment limits the beam current and imposes tight tolerances on alignment and stability.

- **Accelerating field:** $E_{\text{acc}} = 100 \text{ MV/m}$

In order to limit the overall extension of the facility and its corresponding cost, the CLIC scheme is based on beam acceleration with (beam loaded) electric fields of 100 MV/m which result from an overall performance and cost optimization (see §2.1.6). With a filling factor of 78.6% and taking into account overhead of 5 degrees off-crest acceleration to provide BNS damping, the length of each 1.5 TeV linac is 21 km.

- **RF frequency of the Main Linac accelerating structures:** $F_{\text{RF}} = 12 \text{ GHz}$

The main linacs are made of normal-conducting travelling-wave accelerating structures (§2.1.4) operating at an RF frequency of 12 GHz chosen for overall performance and cost optimization reasons (§5.5). Such structures not only allow a high accelerating field of 100 MV/m with a limited RF input power of 65 MW but also provide trains of bunches with a length of $44 \mu\text{m}$ and an interval of 0.5 ns between bunches; both of which are favourable to high luminosity [Eq. (2.7)].

- **RF power source: two-beam acceleration (TBA)**

In spite of the accelerating structures with high RF frequency, 12 GHz, and short length, 23 cm, the generation of the 100 MV/m accelerating field requires high peak RF power (typically 250 MW per metre of the 21 km linacs or about 10^4 GW in total). Klystrons are excluded due to the large number required (about 35 000 with a power capacity of 50 MW and equipped with RF pulse compression by a factor 5) and their low efficiency (about 40% when taking into account the RF pulse compression). For the sake of cost mitigation and power efficiency, a novel power source — an innovative two-beam acceleration scheme — in which the RF power is extracted from a low-energy but high-intensity Drive Beam, is developed in §2.4.

- **Charge per bunch:** $N = 3.7 \times 10^9 \text{ nC}$

A high charge-per-bunch is favoured in order to improve the RF-to-beam efficiency. It is limited to $N = 3.7 \times 10^9$ by short-range wakefields (§3.8 and §2.3).

- **Bunch interval:** $\Delta_b = 0.5 \text{ ns}$

A short interval between bunches is also favoured in order to improve the RF-to-beam efficiency. It is limited to 0.5 ns by long range wakefields. Such a short bunch interval makes the detector design particularly challenging.

- **Number of bunches per train:** $N_b = 312$

A large number of bunches per pulse is also favoured in order to improve the RF-to-beam efficiency. It is limited to $N_b = 312$ by an RF pulse length of 156 ns compatible with the scaling law between RF pulse length, accelerating field and break-down rates. (§2.3).

- **Beam power:** $P_b = 14 \text{ MW}$ **and wall-plug power:** $P_W = 582 \text{ MW}$

The above parameters result in a challenging beam power of 14 MW per 1.5 TeV beam. Generation, handling, and machine protection systems with such a high beam power are key issues. In order to limit the wall-plug consumption and the operating cost of the facility, power transfer efficiency at every stage of the RF power generation and beam acceleration is critical. Thanks to the two-beam acceleration (TBA) scheme and, despite the high accelerating field, a reasonable wall-plug-to-beam-transfer efficiency of 5% is obtained. Nevertheless, a large wall-plug power of 582 MW is necessary for a 3 TeV CLIC.

2.1 CLIC SCHEME OVERVIEW AND PARAMETER OPTIMIZATION

- **Normalized vertical emittance:** $\varepsilon_y = 2 \times 10^{-8}$ m
The luminosity is directly proportional to $1/\sqrt{\varepsilon_y}$ (Eq. 2.6). The target value of 2×10^{-8} mrad is challenging but consistent with the latest-generation of light sources. The bunch length will be reduced below the smallest-obtainable vertical beta function at the IP. In the case of 3 TeV, even further shortening is beneficial since the beamstrahlung is suppressed.
- **Vertical beam size at IP:** $\sigma_y = 0.9$ nm
The luminosity is directly proportional to $1/\sigma_y$. The small beam size is achieved by a combination of small emittance and beta function. A particular challenge is to keep the small beams in collision.
- **Vertical beta-function at IP:** $\beta_y = 68 \mu\text{m}$
The vertical beta function needs to be reduced as much as the Beam Delivery System design allows.
- **Horizontal emittance**
The horizontal emittance is a challenge for the Damping Ring, which is met by use of strong wigglers.
- **Horizontal beam size at IP**
The total luminosity is proportional to the $1/\sigma_x$ but the peak luminosity depends less on the horizontal beam size, since an increase in size leads to an improvement in the spectrum quality. The combination of bunch charge, length, and horizontal size has been chosen as to optimize the total peak luminosity. The horizontal beam size requires a limited beta-function and horizontal emittance.
- **Horizontal beta function at IP**
The horizontal beta function is important for the beam size. The challenge consists in achieving the horizontal beta function in combination with the small vertical beta function.

Main Beam and Main Linac parameters are summarized in Table 2.1 below. Detailed parameters can be found in Appendix A

Table 2.1: CLIC main parameters for 500 GeV and 3 TeV

Description [units]	500 GeV	3 TeV
Total (peak 1%) luminosity	$2.3 (1.4) \times 10^{34}$	$5.9 (2.0) \times 10^{34}$
Total site length [km]	13.0	48.4
Loaded accel. gradient [MV/m]	80	100
Main Linac RF frequency [GHz]		12
Beam power/beam [MW]	4.9	14
Bunch charge [10^9 e ⁺ /e ⁻]	6.8	3.72
Bunch separation [ns]		0.5
Bunch length [μm]	72	44
Beam pulse duration [ns]	177	156
Repetition rate [Hz]		50
Hor./vert. norm. emitt. [$10^{-6}/10^{-9}$ m]	2.4/25	0.66/20
Hor./vert. IP beam size [nm]	202/2.3	40/1
Beamstrahlung photons/electron	1.3	2.2
Hadronic events/crossing at IP	0.3	3.2
Coherent pairs at IP	200	6.8×10^8

The quest for beam performance beyond both current energy and luminosity frontiers at an affordable cost and power consumption imposes the development of an innovative two-beam acceleration scheme with parameters well beyond the present state-of-the-art, specifically:

- the generation and collision of electron and positron beams of 14 MW,
- their acceleration with high field and high wall-plug-to-beam efficiency,
- their focusing and collision with extremely small dimensions of 1 nm in the vertical plane,
- their alignment and stability in the sub-nanometre range.

Addressing their feasibility is key for the multi-TeV $e^+ e^-$ collider. A list of the critical key issues is presented in §2.2. Ambitious R&D has been launched to address their feasibility with results and prospects developed in Chapter 5.

Such a technology could be used for the staged development of the collider starting in the sub-TeV energy range with less challenging parameters and reduced cost as explained in Chapter 9 and summarized in Table 2.1.

2.1.6 Main Linac accelerating structure parameter optimization

As pointed out in §2.1.3, the Main Beam accelerating structure is the key component of the main linacs and is a major driver of the CLIC design and associated parameters.

An optimization procedure has been derived based on a systematic and iterative variation of the structure parameters, namely iris diameter, iris thickness, RF phase advance per cell, RF frequency, and average loaded accelerating gradient. For each structure, the bunch charge N is determined from the results of beam dynamics simulations which take into account the effect of short-range wakefields on emittance growth. The long-range wakefields of the lowest dipole mode are calculated based on interpolated parameters and an uncoupled model.

The closest bunch separation, Δ_b , in the number of RF cycles is limited by the acceptable value of the transverse wake envelope at the position of the second bunch, as provided by beam dynamics simulations [4]. Structures are selected which satisfy the following RF constraints:

1. Surface electric field [5]: $E_{\text{surf}}^{\text{max}} < 260 \text{ MV/m}$
2. Pulsed surface heating [6]: $\Delta T^{\text{max}} < 56 \text{ K}$
3. Power density [7]: $P_{\text{in}}/C\tau_p^{1/3} < 18 \text{ MW/mm ns}^{1/3}$

Here $E_{\text{surf}}^{\text{max}}$ and ΔT^{max} refer to maximum surface electric field and maximum pulsed surface heating temperature rise in the structure, respectively. Here P_{in} , C and τ_p denote input power, input iris circumference, and pulse length respectively. Since both $\Delta T^{\text{max}} \propto \sqrt{\tau_p}$ and $P_{\text{in}}/C\tau_p^{1/3}$ depend on pulse length (τ_p) conditions, constraints 2 and 3 can always be satisfied by reducing the number of bunches, n_b , in the train. This reduction is however limited because the shorter the pulse the lower the RF-to-beam efficiency given the incompressible fill time of the structure. Hence n_b is chosen to make the pulse as long as possible under pulsed surface heating and power constraints. Then, if the structure satisfies constraint 1 above, RF-to-beam efficiency and other pulse-length dependent parameters of the structure are scaled for this value of n_b .

Although a different choice of optimization criteria is possible, the main goal is to reach the design luminosity at a given energy in the most efficient way. Hence the optimum structure must provide the highest ratio of luminosity to Main Linac input power. In terms of the structure parameters this corresponds to maximizing the figure of merit, $\mathcal{L}_{\text{bx}} \cdot \eta/N$, where \mathcal{L}_{bx} denotes the luminosity per bunch crossing with an energy above 99% of the nominal centre-of-mass energy. This is obtained from beam dynamics simulations of the CLIC Main Linac and Beam Delivery System. Thus, the optimum structure is that which gives the maximum figure of merit for all structures satisfying conditions 1–3.

In addition, a parametric cost model [8] has been used for optimization. The optimization procedure has been performed for a range of RF frequencies from 10 GHz to 30 GHz and for a range of average loaded accelerating gradients from 90 MV/m to 150 MV/m. The average iris-radius-to-wavelength ratio

2.1 CLIC SCHEME OVERVIEW AND PARAMETER OPTIMIZATION

$\langle a \rangle / \lambda$ was varied from 0.9 to 0.21, the iris-thickness-to-wavelength ratio $\langle d \rangle / \lambda$ was varied from 0.025 to 0.1. More than 65 million structures have been analysed during the optimization procedure. The overall optimization results are presented in Fig. 2.3 and Fig. 2.4.

– **Accelerating gradient:** $E_a = 100$ MV/m

Within the range of the considered RF frequency, the optimum gradient depends on the optimization criterion. As far as performance is concerned, the lower the gradient, the higher the performance (Fig. 2.3). A minimum cost is obtained around 120 MV/m with a flat minimum (Fig. 2.4). An average accelerating gradient of 100 MV/m has finally been adopted as the best trade-off between performance and cost. The resulting optimum structure is presented in §2.3. Independent of the RF frequency, performance increases with lower accelerating field.

– **RF frequency:** $F_{RF} = 12$ GHz

Within the range of the considered accelerating gradient, the optimum RF frequency of the CLIC Main Linac is clearly in the X-band frequency range both for maximizing the performance Figure of Merit (FoM) and for minimizing the total cost. An RF frequency of 12 GHz has been selected as the closest to the NLC/GLC RF frequency of 11.4 GHz in order to take advantage of the successful developments performed over many years by SLAC and KEK and to benefit from the available expertise and test facilities.

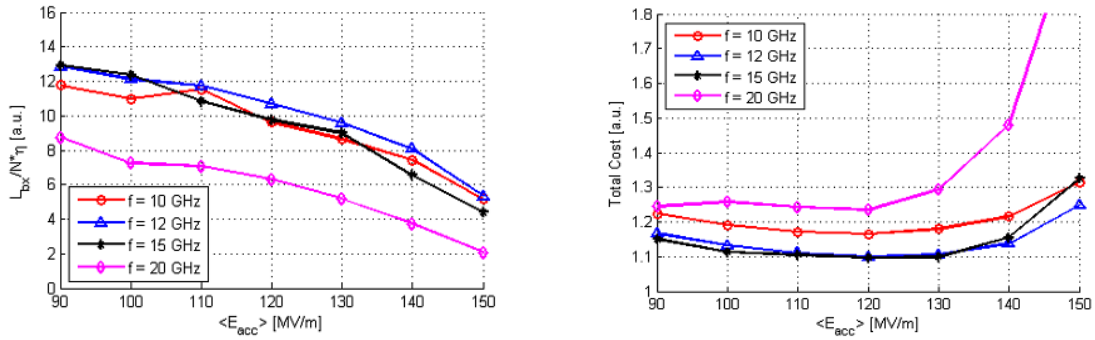


Fig. 2.3: Performance figure of merit (left) and relative cost (right) as a function of the average accelerating field

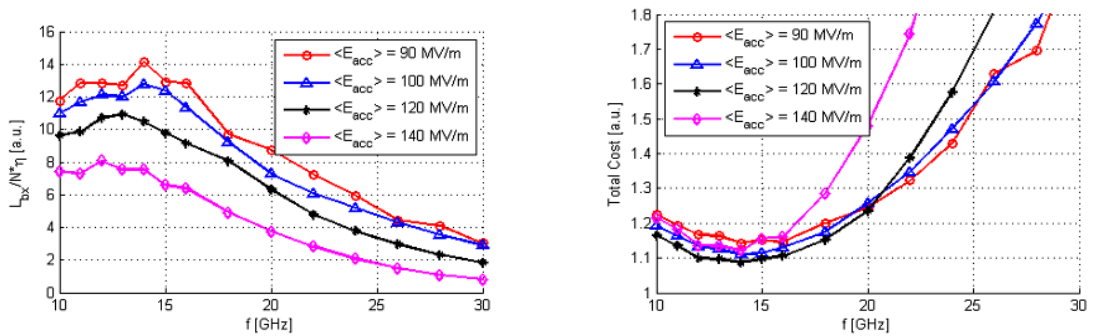


Fig. 2.4: Performance figure of merit (left) and relative cost (right) as a function of the accelerating structure RF frequency

2.2 Key issues of the CLIC two-beam acceleration scheme

2.2.1 Introduction

The CLIC innovative scheme with immensely challenging parameters, as described in §2.1, has a number of issues. In each case, when a parameter specification happens to be above present state-of-the-art, the corresponding item is classified as a ‘key issue of the CLIC technology’. A comprehensive list of CLIC key issues has been established [9]. In this list all items are classified into four categories:

1. Feasibility issues:
 - corresponding to a novel scheme which has never been done before;
 - corresponding to a parameter which, if the corresponding specification is not achieved, would render the scheme either unfeasible or feasible but with substantially degraded performance, or with the associated cost or power consumption substantially higher than expected from the baseline scenario.
2. Performance issues:
 - corresponding to a parameter which, if the corresponding specification is not achieved, would still allow the scheme to be feasible but with a performance lower than expected from the CLIC parameter list.
3. Cost issues:
 - corresponding to a parameter which, if the corresponding specification is not achieved, would still allow the scheme to be feasible and the performance achieved but with a cost higher than expected from the baseline scenario.
4. Power issues:
 - corresponding to a parameter which, if the corresponding specification is not achieved, would still allow the scheme to be feasible and the performance achieved but with a power consumption higher than expected from the baseline scenario.

Obviously any given issue can be part of one or more of the above categories. All issues have, in principle, to be addressed and demonstrated before the project can be reasonably proposed for approval. Only CLIC feasibility issues are fully addressed at the present Conceptual Design stage. Performance, cost and power issues, although already partially addressed, will be the subject of R&D in the next Project Preparation Phase.

2.2.2 Feasibility issues

Ten CLIC feasibility issues have been clearly identified by the CLIC team and the linear collider community following extensive discussions in working groups during dedicated workshops ([10], [11]) and after critical scrutiny by the CLIC Advisory Committee (ACE) [12]. They pertain to beam physics or technology considerations; comparing the requested parameters to the present state-of-the-art. A major target of the CLIC study has been to have demonstrated a solution for each feasibility item before the publication of this CDR.

2.2.2.1 Accelerating structures

An accelerating structure that allows high gradient and a stable beam is essential for a cost-effective design. This requires:

- an accelerating field of 100 MV/m (beam loaded) during a pulse of 156 ns. This is well above the present accelerating structures which have been developed as part of the NLC project ([10], [13]) and which have achieved accelerating fields of 50 MV/m over 400 ns;

2.2 KEY ISSUES OF THE CLIC TWO-BEAM ACCELERATION SCHEME

- RF breakdown rate of $<3 \times 10^{-7}$ per pulse per metre of structure. This is a factor two above the best performance achieved in NLC with an accelerating field a factor two lower, which is particularly challenging but includes some safety margin since the specification assumes that every beam affected by breakdown along the linac does not contribute to the luminosity;
- RF-to-beam efficiency as high as 28.5% for RF power and wall plug power mitigation which, although similar to the performance achieved by the NLC structure, is extremely challenging with an accelerating field twice higher.

2.2.2.2 *Two-beam acceleration*

The novel scheme of two-beam acceleration (TBA) as described in §2.4 is obviously a feasibility issue since such a scheme has never been built and operated. Major issues are related to the beam behaviour at high intensity and the tight stability and timing requirements. Their feasibility has to be addressed in a dedicated Test Facility with beam, specifically:

- the generation of a 100 A, 12 GHz Drive Beam and its acceleration, with an RF-to-beam-transfer efficiency as high as 97%, by accelerating structures operating in the unusual fully loaded mode;
- beam-driven RF power production:
 - novel Power Extraction and Transfer Structure (PETS) producing an RF pulse of 132 MW for 176.5 ns and equipped with an on/off mechanism in order to tune the power during operation or to allow conditioning of structures in parallel with the operation in case of problems;
 - up to 90% of power extraction from the Drive Beam with high beam stability in spite of the large momentum spread generated during power generation by a series of PETS in a 878 m long sector of the Drive Beam decelerator;
 - RF pulse shape generation with a precision better than 0.1% in order to allow adequate beam loading compensation in the accelerating structures.
- technical integration of the two-beam acceleration module:
 - compact integration with high filling factor of all components for beam-driven power generation and beam acceleration within a two-beam acceleration module as the basic block of the CLIC linacs, including RF structures, RF distribution, magnetic components, beam instrumentation, vacuum equipment, alignment and stabilisation;
 - independent alignment with minimum coupling of the two-beam accelerator and decelerator lines;
 - tight positional control and stability of the Drive and Main Beams with respect to each other in the sub-picosecond range for acceleration and collision efficiency.

2.2.2.3 *Ultra-low emittances and nanometre beam sizes*

Generation of ultra-low emittances and emittance preservation during bunch compression, acceleration and beam delivery are key feasibility issues in order to achieve high luminosity. They include:

- generation of normalized emittances of 500 nm and 5 nm respectively in the horizontal and vertical planes; significantly smaller than the best performance achieved in the latest-generation light sources. The present state-of-the-art is achieved in the CsrTA facility of Cornell [14] with emittances about a factor 20 larger in both planes and in the Swiss Light Source (SLS) of PSI [15] with a vertical emittance only a factor 2 larger but with a horizontal emittance a factor 50 larger.

- preservation of emittances with a limited blow-up during transfer from the Damping Ring to the Main Linac (RTML) and bunch compression in several stages. Acceleration in the Main Linac is particularly challenging due to the strong wakefield environment of the 21 km long main linac equipped with high-frequency RF structures. No experience is available for such a long linac. The present state-of-the-art has been achieved in the SLC [16] including a two-mile-long linac equipped with 3 GHz accelerating structures. After extensive developments, the blow-up has been limited to 15 000 nm and 5800 nm (in addition to the specific arc contribution), a factor 94 and 390 larger than the nominal CLIC specifications in the horizontal and vertical planes respectively.
- focusing to extremely small beam sizes of about 40 nm and 1 nm respectively in the horizontal and vertical planes, whereas the smallest sizes ever achieved are 70 nm in the Final Focus Test Beam (FFTB) at SLAC [17]. Such small beam sizes can only be achieved with strong final doublet quadrupoles producing detrimental effects on the beam quality; especially large chromaticities related to the ratio of β^*/L^* where β^* is the value of the beta-function at the Interaction Point (IP) and L^* the distance between the final doublet and the IP. Although the nominal CLIC effective $\beta^* = 0.1$ mm is similar to that achieved in the FFTB, the CLIC nominal L^* is larger by a factor 8 thus generating a chromaticity 8 times larger.
- Such performances can only be achieved with beam-based alignment of components pre-aligned to about 10 microns over a distance of several betatron wavelengths (200 m), an order of magnitude tighter than the present state-of-the-art.
- Active stabilization of the quadrupoles along the linac in the nanometre range is also required to preserve beam emittances about one order of magnitude lower than ground vibrations. This is particularly challenging in the two-beam modules when fully equipped with all systems and cooling. Stabilization of the final focusing doublet in the sub-nanometre range, to allow beam collision at high luminosity, is even more challenging in the very noisy environment of the detectors. This is a factor 10 above the state-of-the-art achieved in ACIS at SLAC [18].

2.2.2.4 Operation and Machine Protection

The unprecedented beam power of 72 MW of the 24 CLIC Drive Beams constitutes a major issue for the CLIC scheme; this is a factor 50 above the value achieved with protons in the SNS linac [19]. Although the beam power of the Main Beam, 14 MW, is substantially lower, the power density due to the extremely low beam emittance and spot sizes is very critical. Both issues have to be addressed with the machine protection system to allow safe and reliable operation.

2.3 RF structures

The two-beam RF system of the Drive Beam decelerator, the Main Beam accelerator, and the connecting RF network is described in this section. A general introduction is presented first, which includes a description of the two-beam scheme from the point of view of the RF system and a summary of the main issues which drive the design of the overall system and its components. The general introduction is included in this report because the clear identification of the critical issues has been an essential aspect of the design itself, particularly for a system like CLIC operating at performances well above those found elsewhere. Detailed descriptions of the main components, PETS and accelerating structures, and a summary of test results are presented in the subsequent sections.

2.3.1 The two-beam concept and the CLIC RF configuration

The peak RF power per unit length required to establish the fields necessary for acceleration of CLIC is approximately 200 MW/m, which is a direct consequence of the choice of the high, 100 MV/m, accelerating gradient. This extremely demanding peak-power requirement is met in CLIC by adopting two-beam acceleration. The basic concept behind two-beam acceleration is to transfer kinetic energy from a high-current and relatively low-energy Drive Beam (100 A and 2.5–0.25 GeV) to a (relatively) low-current and high-energy Main Beam (about 1 A and 9 GeV–1.5 TeV) using RF structures in a configuration which has a high voltage–transformer ratio. An early description of the scheme can be found in Ref. [20]. The two-beam concept is implemented in CLIC by using two distinct structures connected by a waveguide network. It consists of a low-impedance PETS (Power Extraction and Transfer Structure) which decelerates the Drive Beam and a high-impedance accelerating structure which accelerates the Main Beam. The high transformer ratio is given by the relative impedances of the two structures — low impedance for the PETS with large aperture and high group velocity and high impedance for the small aperture and low-group-velocity accelerating structures. The RF parameters of the PETS and accelerating structures are directly compared in Table 2.2. More complete parameter sets for the structures are presented in the specific sections which describe the structures in more detail.

Table 2.2: Two-beam structure parameters

	PETS	Accelerating structure
Aperture radius [mm]	11.5	3.15–2.35
R'/Q [k Ω /m]	2.2	15–18
v_g/c	0.49	0.0165–0.0083
Gradient [MV/m]	–6.3	+100

CLIC has transversely separated decelerating and accelerating beams and structures in contrast to the collinear configurations of plasma, and some forms of dielectric, wakefield acceleration schemes. The choice of using separated structures is driven by the demanding low-emittance requirements for the Main Beam. The separated beams allow optics to be adapted to the significantly different energies of the beams and also to the opposite change of energy with propagation — the Drive Beam energy decreases while the Main Beam energy increases along the length. Equally the separated structures minimize the transfer of instabilities of the Drive Beam — which is high-current, relatively high-emittance and has relatively high (order of 100 μ m) offsets and jitters especially at low energy — to the Main Beam via higher-order modes.

The two-beam acceleration configuration used in CLIC, in which a single PETS feeds two accelerating structures, is described in detail in §5.5.3.

2.3.2 Main performance issues

The main performance issues which drive the design of the CLIC two-beam system and its component structures are

- high-gradient and high-power performance
- RF-to-beam efficiency
- transverse wakefield suppression

The optimization procedure used to determine the parameters for components of the RF system is based on an iterative loop which also includes beam dynamics effects of both the Main and Drive Beams. The overall design is described in detail in §3.4 and only a synthesis of the main issues is presented here in order to identify those critical for the RF system and give them context. The initial discussion is focused primarily on the accelerating structures because they have more demanding performance requirements and, to a large extent, drive the parameters of the whole machine.

The 100 MV/m acceleration is a direct consequence of specifying a 3 TeV collision energy in CLIC while restricting the overall machine length to below approximately 50 km. The gradient is accompanied by two constraints — it must be achieved at the nominal pulse length and shape (156 ns flat-top, 240 ns full length) and with a breakdown rate below approximately 3×10^{-7} events/pulse.m. The interrelation between the three quantities, gradient E , pulse length τ , and breakdown rate BDR has been measured in many structures and closely follows the empirical scaling law [21]:

$$BDR \propto E^{30} \tau^5 \quad (2.13)$$

Breakdowns cause luminosity loss because they induce transverse kicks of the beam causing transverse displacements at the interaction point. There are two distinct origins for the transverse kicks. Firstly high currents, hundreds of amperes, are generated in a structure during breakdown, causing parasitic magnetic fields which deflect the beam. These currents are easily measured using Faraday cups during high-gradient experiments and the level of the current can also be estimated from the nearly complete absorption of the approximately 50 MW of structure input power. However, it has not yet been possible to measure the spatial distribution of the currents inside the structure — the structure apertures are small, less than 1 cm, and the events are random and fast. Consequently the resulting kick cannot be estimated with sufficient accuracy from simple experiments or, for the moment, simulations. Instead it is necessary to measure the kick on the beam directly. This has been done with 50 MV/m NLC/GLC structures in the NLCTA [22]. The kick was measured to be around 10 kV. This measurement will be repeated in the TBTS with CLIC structures operating at 100 MV/m. The second source of kick comes from the combination of missing acceleration during a breakdown and angular misalignment of accelerating structures. During normal operation, the beam alignment algorithms compensate for these kicks. The misalignment specification for a structure is of the order of $40 \mu\text{rad}$ corresponding to a transverse kick of about 1 kV. When a breakdown occurs, and acceleration is suppressed in a structure, there is then a net kick to the beam which corresponds to the negative of the missing transverse kick. A breakdown in the PETS, or in the connecting RF network, which suppresses power production, produces an equivalent effect. On the other hand, the missing energy gain for a single accelerating structure is not significant since it is of the order of 10^{-5} .

While waiting for data from further experiments, the conservative estimate is used in the current CLIC design which assumes that kicks due to breakdown will result in a full loss of luminosity of the pulse in which the breakdown occurs. CLIC parameters budget a 1% luminosity loss due to this effect. Since the active length of acceleration is 3×10^4 m the breakdown rate must be limited to $0.01 \text{ events/pulse} \times 3 \times 10^4 \text{ m} = 3 \times 10^{-7} \text{ events/pulse.m}$. If the experiments show that a significant portion of the kick distribution is well below the 10 kV measured in NLCTA, or that most breakdowns occur at the end of a pulse, then the breakdown rate specification could perhaps be relaxed.

2.3 RF STRUCTURES

The combination of gradient, pulse length, and breakdown rate results in a demanding high-gradient requirement for CLIC. Typical operational gradients of existing linacs lie in the range of 15 to 20 MV/m with pulses in the microsecond range but, since most linacs are quite short compared to that envisaged for a linear collider, breakdown rates are not generally specified. Gradients of around 50 MV/m were achieved with measured low, in the order of 10^{-7} , breakdown rate and 400 ns pulse length in the NLC/GLC program [23]. The CLIC study has given high priority to extending achievable performance to 100 MV/m.

Breakdown, arcing in regions of high electric field and power flow, is the main physical effect which limits gradient in accelerating structures. Breakdown is a complex phenomenon which is beginning to be relatively well understood and modelled. The description which follows is based on Refs. [24–35]. Breakdowns occur at sites on the structure surface which exhibit enhanced electron field emission. The current from an individual field emission site is typically in the pA to nA range. The upper limit on the site size of the order of nm^2 has been estimated from the fact that breakdowns can occur in less than the order of 100 ns, assuming that the origin of the breakdown is thermal. A combination of contaminants, geometric field enhancement features and crystal defects (which result in a locally lower work function) result in feature-enhanced local field emission. A certain amount of neutral-atom field evaporation accompanies field emission and a field emission site will evolve into a breakdown when the density of neutral atoms above the emitter exceeds a critical value. Field-emitted electrons collide with field-evaporated atoms, ionizing them and setting off an ionization cascade which forms a plasma locally above the breakdown site. The plasma expands transversely and forms a sheath where it contacts the metal surface. This extends the field emission area to the size of the plasma spot, which is typically 10 μm in diameter. The size is determined through both optical images and microscopic analysis of the craters formed by the breakdowns. Through the plasma formation processes the emitted current rises to the 100 A range in less than a few ns. This current is then accelerated by the incoming RF, absorbing it, and suppressing transmission through the structure. Nearly all of the incoming power, above 90%, can be absorbed by the incoming RF.

In DC high-voltage systems the breakdown probability is largely a function of the electric field on the cathode surface (stored energy of the system has some influence). In an RF cavity the situation is more complex and breakdown probability is a strong function of both surface electric and magnetic fields. For example it has been observed in a wide variety of structures that low group-velocity structures can tolerate higher surface electric fields than high group-velocity structures [36]. In order to quantify the high-power RF design procedure and to arrive at the highest gradient structure designs, the CLIC study has invested a significant effort into understanding the effect of geometry on achievable gradient. The result has been the development of high-gradient, high-power scaling laws [21]. The scaling laws are based on the idea that the evolution of an emission site to a breakdown requires power flow. Two scaling laws have been proposed, $P/\lambda C$ and S_c , which are based on global and local power flow respectively.

These quantitative laws quite accurately predict the relative performance of RF structures made according to the same fabrication procedure. For example, the scaling laws successfully predicted the increasing gradient observed from NLC/GLC structures to the CLIC test structures T18 and T24. These performance results are described in §5.5.1.3, and represent a strong indication of the validity of the scaling laws. And of course, the results from the T18 and T24 structures show that the 100 MV/m accelerating gradient which CLIC has adopted is indeed feasible.

The addition of higher-order-mode damping waveguides, described later, can reduce achievable gradient due to a concentration of surface currents in the outer cavity walls. The extent of this effect has now been measured in damped versions of the test structures referred to above. A summary of the high gradient test results is shown in Fig. 2.5. The results show that the gradient can be achieved in a fully featured CLIC structure, the so-called TD24, without beam loading. This represents a clear demonstration of one of the most important feasibility issues for CLIC. Efforts will now focus on improving statistics and running for longer periods. The effect of beam loading, which redistributes the field pattern around

the same average value, will be investigated in a dedicated test in CTF3.

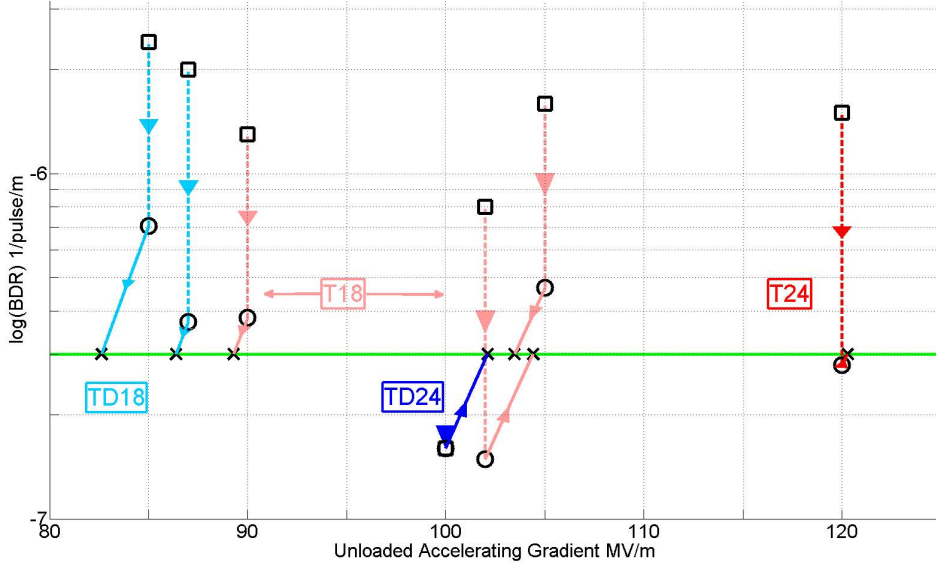


Fig. 2.5: A summary of the high-gradient testing results as of 5 April 2012. The TD24 is a test version of the CLIC accelerating structure (with damping waveguides, a mode launcher coupler but without silicon carbide absorbers). Experimental data, square points, taken under various conditions are scaled in pulse length (dotted lines) and gradient (angled lines) according to Eq.(2.13) to the CLIC breakdown rate specification of $3 \times 10^{-7} \text{ /m/pulse}$ in order to make a direct comparison amongst the structures.

The scaling laws have also been used in the design process of the PETS, which operates in a high-group velocity, high-power flow, regime. Because the aperture of the PETS is so large, 23 mm, surface electric and magnetic fields are very low: 56 MV/m surface electric field and 80 kA/m surface magnetic field for the nominal output power of 134 MW. Conservative values of $P/\lambda C$ and S_c are ensured by the condition that the PETS aperture radius be at least larger than the sum of the accelerating structure input-aperture radii it drives. This establishes that one PETS can be used to feed two accelerating structures. A klystron-driven test of the PETS has established the feasibility by showing operation at an output power of 147 MW for a pulse length of 266 ns and a breakdown rate less than $3 \times 10^{-7} \text{ events/pulse.m}$. The PETS are described in §5.5.2.

The second physical effect that is a major concern for high-gradient accelerating structures is pulsed surface heating [37–41]. The structure surfaces that carry surface currents are subject to cyclic, thermally-induced compressive stresses causing fatigue-induced damage, which limits the life-time of the accelerating structures. An operational lifetime of 10 years corresponds to approximately 10^{11} pulses. The pulsed surface heating parameters are limited to 50°C temperature rise with a corresponding compressive stress of 100 MPa. Recent high-power test results, however, indicate that pulsed surface heating above this value will also directly contribute to an enhanced breakdown rate although the physical explanation for this is not yet clear [42],[43]. Fortunately, safe values for the enhanced breakdown rate appear to be essentially the same as the safe values for lifetime, which have already been targeted. The peak value of surface magnetic field, and consequently pulsed surface heating, is strongly influenced by the cell geometry, especially by higher-order-mode damping features, described below. A crucial step in demonstrating feasibility of the accelerating structures is that such features be included in the test structures.

2.3 RF STRUCTURES

The accelerating structures exhibit another potentially damaging high-power effect which is dynamic vacuum. Residual gas in accelerating structures can lead to train instabilities caused by ionization of the gas by the beam (see §5.7). The accelerating structures will have a base vacuum pressure, as do all vacuum systems, however, this is accompanied by dynamic vacuum rises during the RF pulse. The mechanism is driven by field-emitted currents which are accelerated and then strike the cavity walls and induce electron-stimulated desorption. The specification for the dynamic vacuum is 10^{-9} mbar [44]. The vacuum level, both static and dynamic, is strongly dependent on the RF conditioning state of the accelerating structures; consequently a dedicated simulation and measurement program has been initiated. An early indication that the dynamic vacuum effect may not be too severe is that the diffusion distance in 240 ns, the RF pulse length, is only of the order of 1 mm. Desorbed gas molecules would consequently be concentrated near the cavity surface during the beam-on time. This subject is covered in more detail in §5.6.13.

A higher accelerating gradient results in a shorter facility, but this is not necessarily optimum for overall efficiency and cost — this is because increasing gradient results in a lower RF-to-beam efficiency and a higher peak-power requirement. The latter results in a higher power requirement in the Drive Beam injector complex. Reduced RF-to-beam efficiency at higher gradient occurs because acceleration is proportional to field level while ohmic wall losses scale as the square of the fields. The basic mechanism to maintain RF-to-beam efficiency in the range of 20–30% in high-gradient normal-conducting linear collider designs is to accelerate bunch trains. With trains of sufficiently high current, power is transferred to the beam ‘before’ it is lost to the cavity walls.

However, there are two main limitations to increasing the current and, consequently, the efficiency: lower average gradient due to beam loading and more sensitivity to beam instabilities driven by wakefields. For the first limitation, the compromise between maximizing accelerating gradient and maximizing efficiency found for the CLIC main linac results in a beam-loaded gradient about 20% lower than the unloaded gradient. The detailed optimization gives an RF-to-beam efficiency of about 28%. In contrast, the CLIC drive-beam accelerator, where accelerating gradient is not a crucial parameter, runs with full beam loading. There the loaded gradient is half the unloaded one and an RF-to-beam efficiency around 98% is achieved. The current level, and through it the beam loading, is determined by the bunch charge and bunch separation. The bunch-train characteristics which have been chosen for CLIC are a bunch charge of 0.6 nC and a separation of 0.5 ns, which corresponds to six fundamental cycles. The total train length is 312 bunches.

Emittance growth due to short-range transverse wakefields places strong constraints on the maximum single-bunch charge and the minimum iris aperture of the accelerating structures. Smaller aperture structures have a higher accelerating gradient limit which is both observed experimentally and is a consequence of $P/\lambda C$ and S_c limits. On the other hand, the lower limit on the aperture from beam dynamics constrains increasing gradient by modifying the structure geometry. Consequently one of the most crucial design compromises for the CLIC main linac is the choice of accelerating structure iris aperture. Understanding accurately the dependence of gradient on structure aperture becomes a high priority. Optimum structures are tapered around this average aperture value such that $P/\lambda C$ and S_c are kept nearly constant over the structure length. In this way the highest possible total gradient of the structure is obtained. Downstream apertures are reduced to compensate for the power lost to the cavity walls. The average iris aperture also influences short-range longitudinal wakefields which play a crucial role in stabilizing the beam.

The excitation of short-range transverse wakefields can be mitigated by maintaining tight transverse alignment tolerances, which are of the order of $10\text{ }\mu\text{m}$ for CLIC as described in §5.5.1.1. Such tight alignment tolerances are achieved in CLIC through a combination of micro-precision machining of the disks which make up the structures, precise assembly and fixing of the structures on support girders, and adoption of an active alignment system. The alignment tolerance requirement of mounting structures on the girders is eased by the use of wakefield monitors, described below.

The bunch trains are also susceptible to a bunch-to-bunch instability driven by long-range transverse wakefields. Relative offsets between beam and structure of the leading bunches in a train excite higher-order modes (HOMs) which then give transverse kicks to the following bunches. In order to counteract this effect the accelerating structures have two characteristics which suppress the effect of the long-range transverse wakefields: detuning and damping. HOM-suppressing structures have been developed by the NLC/GLC project, see, for example, Ref. [45]. The solution adopted for CLIC is heavily waveguide-damped structures with a moderate level of detuning. Alternative designs are also being pursued including an adaptation of the NLC/GLC DDS design [46] to 100 MV/m and choke-mode damping [47].

The damping features consist of four waveguides which are coupled to each cell. Such damping easily produces Q 's below 10 for the crucial dipole modes. However, it results in a strong magnetic field concentration in the outer cavity wall, which enhances pulsed surface heating. This effect can be mitigated, while maintaining the level of damping, by introducing a convex outer cavity wall between the waveguides. The presence of the damping waveguides also makes fabrication challenging since the disks from which the structures are made have a significant fraction of the surface which requires milling. Micron precision milling is now within the state of the art, and a number of suppliers have successfully made such parts. Assembly issues complicated by the damping waveguides are also being resolved. Structure manufacture is covered in §5.5.1.2.

The PETS also require significant long-range transverse wakefield damping. The large aperture and high group velocity result in the choice of longitudinal damping slots. This is the same damping mechanism as found in the CTF3 and drive-beam accelerating structures. The fundamental mode does not couple to the slots due to symmetry while the dipole modes couple strongly. The low surface fields of the PETS, combined with the large diameter of the structure allow the slots to be relatively wide, 2.2 mm, which is essential for maintaining high-gradient performance and maximizing the damping. Slotted-iris damping accelerating structures have been considered because they offer very high levels of damping with little impact on fundamental mode characteristics, especially enhanced pulse surface heating. However, initial tests of X-band slotted-iris accelerating structures have not been successful [48] although it is not certain that the reduced performance is due to the slots.

Dipole modes can be detuned through a geometrical variation in cell dimensions along the length of the structures. The resulting spread in synchronous dipole-mode frequencies results in a de-coherence in the wake at a distance from the driving bunch which is related to the inverse of the bandwidth of the detuning spectrum. In the CLIC design geometrical variation along the length of the structure which gives the detuning is driven by the high-gradient design as described above. The outcome of the high power optimization is a strongly tapered structure — the resulting detuning of higher order modes is sufficient when combined with the strong damping.

HOM damping features are also used to determine the relative position of individual accelerating structures on an alignment girder using the beam as a reference for a straight line. The offset information can then be used to position alignment girders so that the net offset of the accelerating structures, and consequently total wakefield, is reduced to tolerable values. HOM damping features equipped for read-out are referred to as wakefield monitors (see §5.5.1.1).

2.4 The CLIC two-beam acceleration scheme

2.4.1 Overview

This section explains in more detail the CLIC two-beam acceleration scheme. All technical systems are described in more detail elsewhere in this document; in the interest of readability there are no cross references to other sections.

The two main linear accelerators of CLIC accelerate electrons and positrons from 9 GeV to 1.5 TeV in one pass. The accelerating field must be as high as possible to limit the length of the machine. This leads to the choice of a room temperature system based on copper accelerating structures and rules out superconducting accelerating cavities because of their intrinsic maximum field limitation. The accelerating field is generated by feeding these structures with very high radio frequency power. A detailed optimization procedure taking into account the design luminosity, cost (tunnel length), RF breakdown and beam stability issues as well as power efficiency has led to the choice of parameters for the CLIC acceleration system: the accelerating gradient was chosen to be 100 MV/m and the RF frequency 12 GHz. This high accelerating field leads to an RF power of about 270 MW per metre of active structure length at the accelerating structure input. A total of about 9.2 TW of RF peak power is required for both linacs. Such high power levels cannot be maintained for very long, the bunch train to be accelerated is only 156 ns long, with a repetition frequency of 50 Hz. The RF pulse feeding the structure is longer, 244 ns, taking into account the filling time of the acceleration structures. A very crude estimate of a system based on individual RF power sources (klystrons), assuming a klystron unit power of 50 MW with a hypothetical pulse compression of a factor of 5 shows that about 35 000 such klystrons would be required together with their ancillary equipment, not taking into account the losses in the pulse compression system. This is clearly a rather unattractive, if not impossible solution. Instead, CLIC is based on a two-beam scheme,

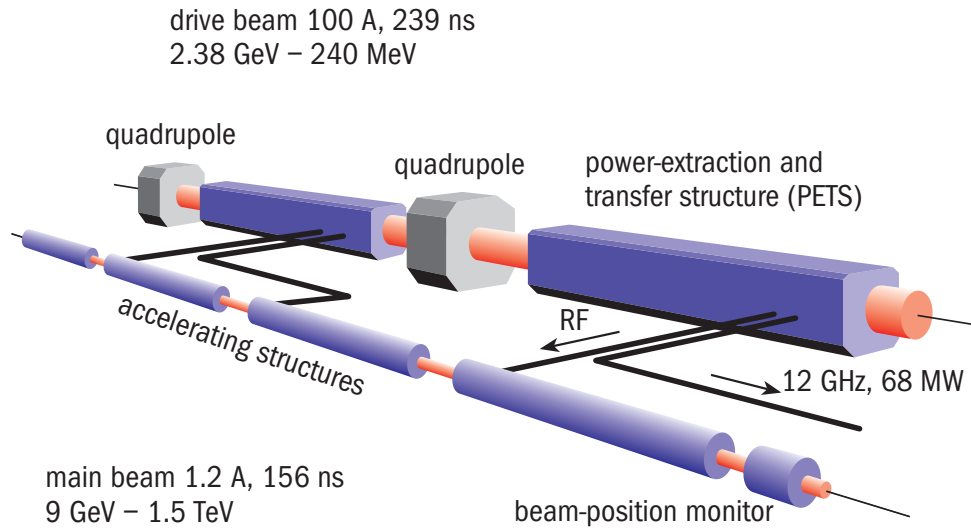


Fig. 2.6: Principle of the two-beam scheme: The beam power in the Drive Beam is converted to RF power in PETS, each feeding two accelerating structures in the Main Beam running parallel at a distance of 60 cm.

where the power for acceleration is transported to the accelerating structures by a second electron beam, the Drive Beam, which runs parallel to the Main Beam. Beam power is extracted from this beam and converted to RF power in special RF devices called PETS (Power Extraction and Transfer Structures) and is then transported to the accelerating structures in the Main Beam running at a distance of about

60 cm. One PETS provides RF power for two accelerating structures. This is illustrated in Fig. 2.6.

CLIC is divided into sectors on average 878 m long, each with about 3000 accelerating structures, accelerating the Main Beam by about 62 GeV. The Drive Beam consists of bunch trains, each train supplying one sector with RF power. These trains need relatively low energy, 2.4 GeV, but high peak current of about 100 A during the pulse. About 84% of their stored energy is converted to RF power, after which they are dumped at the end of the sector. At this point a new Drive Beam bunch train arrives to supply the following linac section. Each of the two main linacs consists of 24 such sections. Each

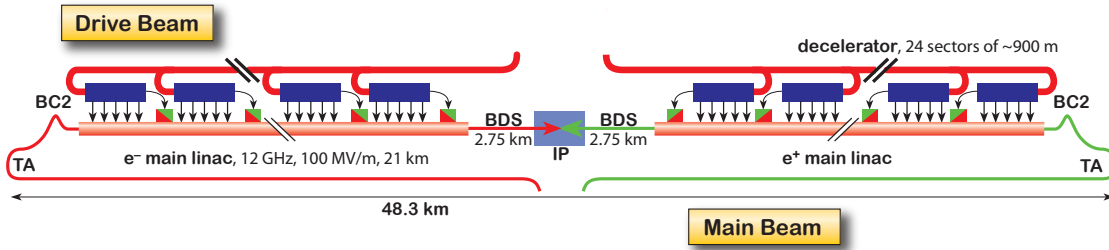


Fig. 2.7: Each Drive Beam pulse supplies RF power to 2984 accelerating structures in the Main Beam over the length of one sector. Each linac consists of 24 such sectors

fresh Drive Beam pulse train carries a peak power of about 240 GW. Sixteen per cent of this power is eventually dumped after the beam is decelerated. The RF power pulses are very short, 244 ns, and follow each other with a repetition frequency of 50 Hz; therefore the average beam power transported to each linac sector is only 2.9 MW.

The Drive Beam is generated at the central campus of the CLIC complex and is transported in counter flow to the Main Beam, after which turnaround loops make it run parallel with the Main Beam. The first bunch train runs all the way to the first sector at the low-energy end of the main linac, the following one is turned around already 878 m upstream; the next ones travel subsequently shorter distances to the next turnaround loops. The gradually reducing travel distances ensure proper timing of the arrival of the Drive Beam bunch trains in the decelerating sectors. CLIC has a single tunnel, which houses the main linac, the Drive Beam and the transfer lines. Therefore at each point the tunnel has four beam lines: the Drive and Main Beams of the high-energy linac as well as the Drive Beam and Main Beam transfer lines. Every 876 m turnaround loops bring the Drive Beam parallel to the Main Beam and after this distance beam dumps dispose of the decelerated Drive Beam bunch trains. This is shown in Fig. 2.7.

This two-beam acceleration scheme offers good power efficiency. The transport of power to the place where it is converted to RF is done by an electron beam, which is nearly lossless.

Figure 2.8 shows the full system needed to generate the Drive Beam with the required beam parameters. The following sections give an overview of the individual components.

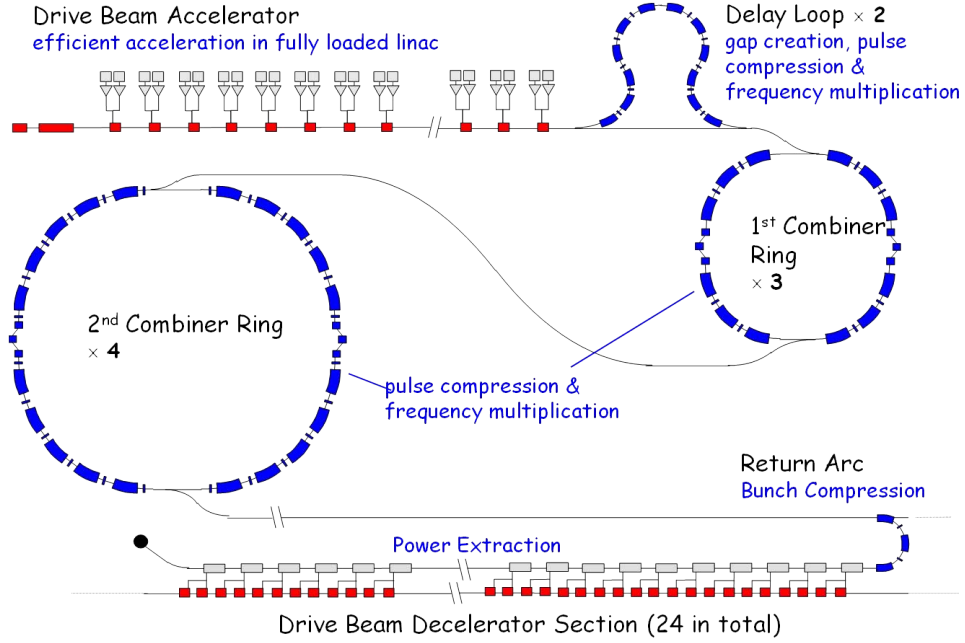


Fig. 2.8: Full Drive Beam complex (not to scale)

2.4.2 Drive Beam generation

The Drive Beam is generated in the centre of the complex and then sent via long transfer lines to the low-energy end of each main linac. The Drive Beam consists of 24 short bunch trains of 244 ns length, which follow each other at about 6 μ s intervals (see Fig. 2.12). Each train has about 3000 bunches (including some bunches at the beginning and the end of the pulse, that are not used for Main Beam acceleration) with a repetition frequency of 12 GHz — the acceleration frequency of the main linac — and an average current over the pulse of 101 A. The total length of the Drive Beam for one acceleration cycle is therefore 142 μ s. These cycles repeat with a frequency of 50 Hz. The bunch charge is 8.4 nC.

This beam, with very high peak beam power during short bursts and very high bunch repetition frequency, is generated from a bunch train with the length of the full cycle (142 μ s) and the nominal charge per bunch (8.4 nC) but large bunch spacing, thus low average power. The final time-structure of the beam is achieved by pulse compression using bunch funnelling and interleaving techniques with RF deflectors. This is described in detail below.

Each Drive Beam carries the total power required for acceleration of the Main Beam. This is, as was shown above, 24 trains of 2.9 MW each, i.e., 70 MW average per linac at 50 Hz operation. This power is put into the beam in the Drive Beam accelerator (DBA). The DBA accelerates long trains of bunches of 142 μ s length; it is a normal-conducting linac, with an acceleration frequency of about 1 GHz. At this frequency, high efficiency klystrons can be used as RF power sources.

The beam in the DBA is ‘phase-coded’. This means it consists of sub-trains of 244 ns length — the length of the final bunch train — and all together there are 576 such sub trains. Bunches follow each other with a repetition frequency $f_r = 0.5$ GHz, i.e., only every second bucket of the accelerator is occupied. After each sub-train the bunches are switched from odd to even buckets, subsequent sub-trains occupy odd or even buckets. This is illustrated in Fig. 2.10 in §2.4.3.

For the DBA acceleration system this represents constant beam loading, with negligible transients

during bucket-switching.

Considering the average power of 24 beam pulses of 2.9 MW each, i.e., 70 MW per Drive Beam, it is clear that power efficiency is of the utmost importance. For this reason the DBA is operated under full beam loading conditions. Figure 2.9 illustrates acceleration in a travelling-wave accelerating structure. Full beam loading means that no RF power leaves the structure and all RF power at the input is converted to beam power with the exception of wall current losses. This is possible for a certain combination of beam current, accelerating gradient and accelerating structure length. The price to pay is an energy transient at the beginning of the pulse and steady state is only reached after the filling time. This mode of operation also strongly couples beam current fluctuations to beam energy. CTF3 is routinely demonstrating the feasibility of this type of operation. Taking into account all losses, the transfer efficiency of RF power at the klystron output to beam power is 89%.

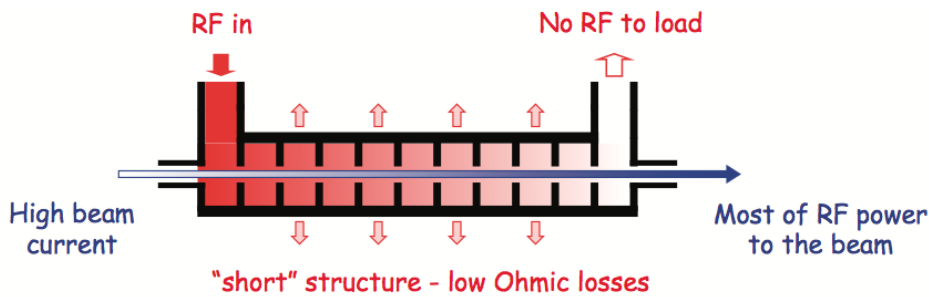


Fig. 2.9: Acceleration of a beam in a travelling wave structure. Under full beam loading operation no RF power is leaving the structure

Ideally the switching of bunches from even to odd buckets happens within the spacing separation between two bunches, i.e., 2 ns. Two possibilities exist for the generation of this phase-coded beam: a thermionic electron gun or a laser-driven photo-injector.

2.4.2.1 Thermionic electron gun

This is the present CLIC baseline design. The injector consists of a thermionic gun, followed by a bunching system.

The bunch charge of 8.4 nC does not present a particular difficulty for standard cathodes, however, the long train of 142 μ s requires some effort to guarantee energy stability.

The phase-coding is done via a sub-harmonic bunching system operating at half the acceleration frequency, 500 MHz. This system must have a large enough bandwidth to allow fast switching of its phase by 180 degrees every 244 ns. Real systems will have a limited bandwidth and there is a switching transient between buckets. In addition about 5% of the charge ends up in the wrong buckets, called satellite bunches. They have to be eliminated for reasons of efficiency and machine protection.

2.4.2.2 Laser-driven photo injector

A photo-cathode sits on the axis of an accelerating cavity where it sees the full RF field. An electric field of the order of 80 MV/m can be achieved, which has the potential of producing small-emittance beams. The bunches are generated by illuminating the cathode with a short laser beam. This system has the advantage that no bunching system is required. The bunch shape and time structure are achieved with the laser and its timing. The phase-coding of the beam can be done with the laser timing, no sub-harmonic

bunching system is required. No satellite bunches are produced and the switching between odd and even buckets can be done in between two bunches. Even though the photo-injector has very attractive features, questions still remain concerning the total bunch charge over the long pulse and laser performance and stability.

2.4.3 Frequency multiplication

The DBA accelerates long bunch trains ($140\ \mu\text{s}$) with a low bunch repetition frequency, f_r , of 500 MHz and an average beam current, i_b , of only 4.2 A. Finally the bunch repetition frequency has to be

$$f_r \times 24 = 12\ \text{GHz}$$

and the beam current

$$I_b \times 24 \approx 101\ \text{A over a series of short bursts.}$$

This is done with a system of several rings and beam lines.

2.4.3.1 Delay loop

As described in the previous section the beam is first phase-coded. An RF deflector operating at the bunch frequency f_r will deflect subsequent 244 ns long trains alternately into the loop or along the straight path. If the flight time of the electrons between the two paths exactly matches the length of the train, the bunches of the delayed train will be placed between the bunches of the following train using a second deflector. The combined train therefore has twice the bunch repetition frequency and twice the peak current. This is shown in Fig. 2.10. The circumference of the delay loop corresponds to one pulse train or L_D of about 72.2 m

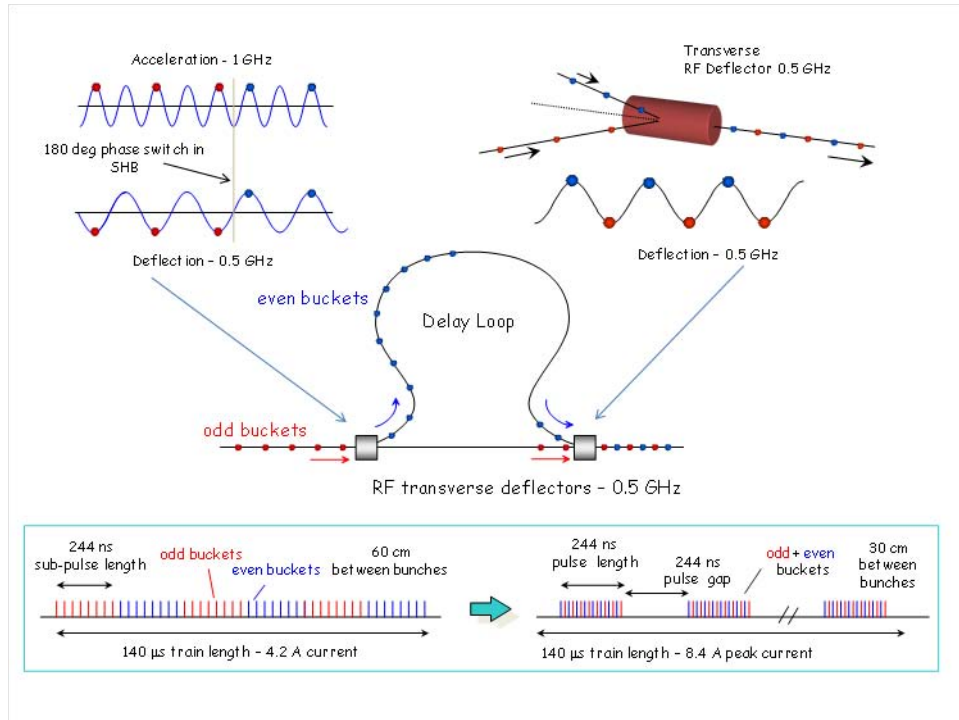


Fig. 2.10: Principle of bunch combination in the delay loop. The schematic top left shows the position of the phase-coded bunches relative to the RF in the DBA and in the RF deflector. Bunches in odd and even buckets in the DBA will therefore be injected into the delay loop or continue on the straight path. Top right shows the recombination of the two paths in the second deflector. The box at the bottom shows the time structure of the beam before and after the delay loop.

2.4.3.2 Combiner ring

These trains are then injected into the first combiner ring, which has, in its simplest form, a circumference of about twice the delay loop. A set of two RF deflectors, operating at a frequency $f_0 = 2 \times f_r = 1000$ MHz, creates a closed orbit bump for circulating particles. The second deflector compensates the transverse kick created by the first one. The beam is injected between the two deflectors, always at the maximum of the deflecting field. After one turn, the bunches of the newly arriving train are interleaved in between the already circulating bunches, the exact position depending on the length of the ring. For a combination factor of m , $m - 1$ bunches are placed between every two bunches of the first injected train at equal distances of λ_0/m . This principle is demonstrated in Fig. 2.11 for the case of a combination factor of four.

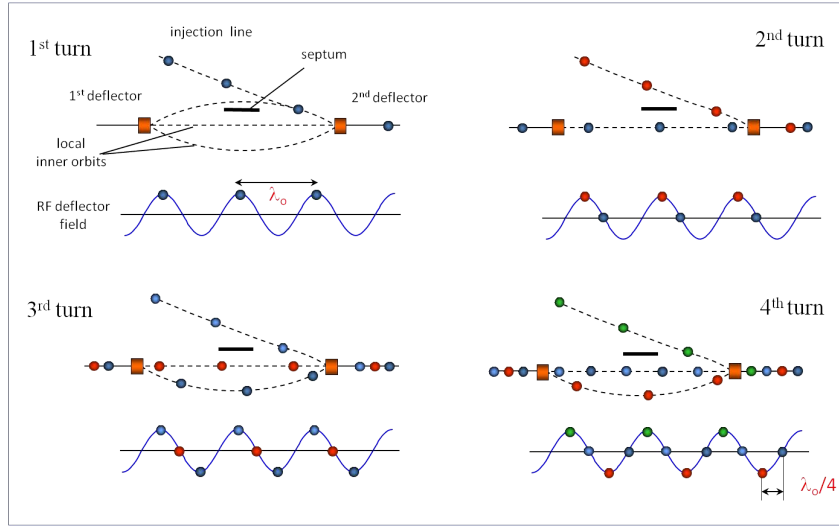


Fig. 2.11: Principle of bunch combination in the combiner ring for the example of a combination factor four

CLIC will have two combiner rings, the first one with a combination factor of three, the second one with a factor of four. For reasons of operational flexibility as explained in later sections, the first combiner ring will have about twice the minimum circumference, about 293 m, with the RF deflector operating at about 1 GHz. The second combiner ring will have a circumference of about 439 m and the RF deflector operating at about 3 GHz.

After the second combiner ring the Drive Beam has its final bunch structure as shown in Fig. 2.12. The bunch repetition frequency has been increased to 12 GHz, and the peak current has gone up by a factor of 24 to 101 A.

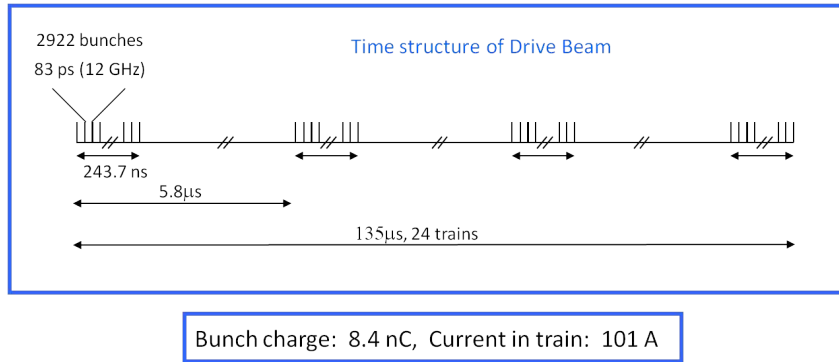


Fig. 2.12: Time structure of the Drive Beam after the second combiner ring

2.4 THE CLIC TWO-BEAM ACCELERATION SCHEME

The rings need very special optics, they have to be isochronous in order to avoid bunch lengthening and minimize effects due to the energy distribution over the bunches. In order to avoid beam energy loss due to emission of coherent synchrotron radiation, the bunch length is increased after the DBA from 1 mm to 2 mm. After the second ring the bunch length is reduced again to 1 mm, in order to achieve maximum energy extraction in the decelerators.

2.5 Drive Beam generation and Main Beam RF power production

2.5.1 Introduction

The principles of the CLIC Drive Beam production have been described in detail in the previous section. In this section technical details of the Drive Beam production, results from the CLIC Test Facility at CERN (CTF3) and details of the RF power production in the decelerators in the Power Extracting Structures (PETS) are described.

2.5.2 Phase Coding

The CLIC baseline design for Drive Beam production consists of a thermionic gun, followed by a sub-harmonic bunching system. A potential alternative scheme makes use of a photo-injector RF gun.

The bunch charge of 8.4 nC and the initial beam current of 4.2 A is well within the reach of standard cathodes. The phase-coding is done via a sub-harmonic bunching system operating at half the acceleration frequency, i.e., at 500 MHz. This system must have a large enough bandwidth to allow fast switching of its phase by 180° every 240 ns. Owing to the finite bandwidth a switching transient is present, during which the bunch phase and charge are ill defined. In order to limit the perturbation to the steady-state beam loading in the linac, the switching time must be lower than 10 ns. Currently in CTF3 about 5% of the gun current is captured in the wrong buckets. Such satellite bunches must be eliminated early enough to avoid inefficiencies and limit machine activation.

The requirements on transverse emittance and bunch length (see §4.1) can be met by using multiple sub-harmonic bunching cavities followed by a pre-buncher and a travelling-wave buncher operating at the fundamental frequency, and by a careful design of the solenoidal field used to focus the beam and control space-charge-induced emittance growth.

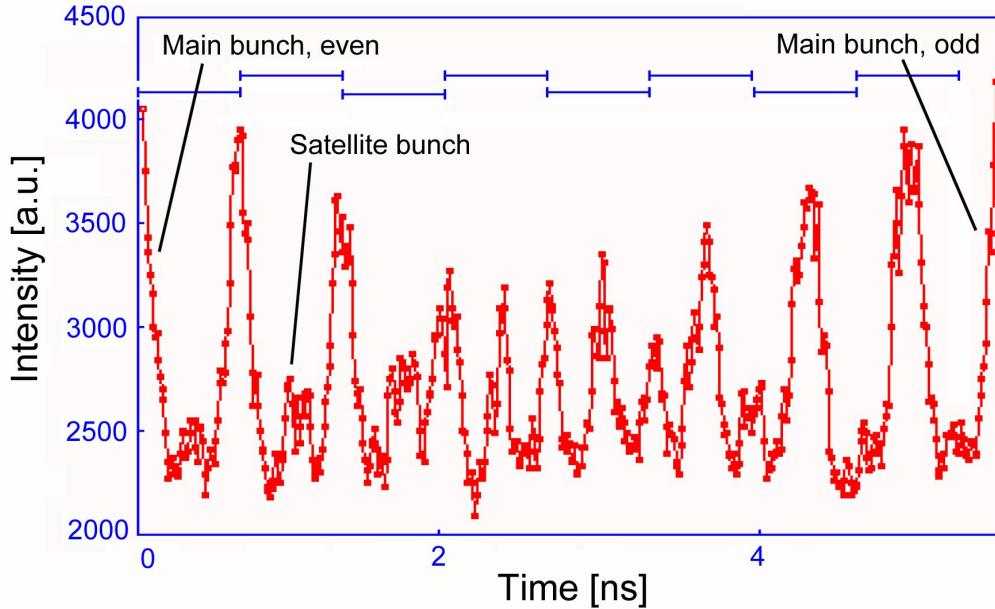


Fig. 2.13: Fast bunch phase switch, measured in CTF3 by a streak camera

The overall performance of the Drive Beam injector has been demonstrated fully in CTF3, with parameters very similar to the ones required in CLIC [49], including the feasibility of a fast (measured value equal to 6 ns) 180° phase switch in sub-harmonic bunching cavities. The measured performance of the CTF3 injector in terms of emittance, bunch length, and charge content of satellites, is in very good

agreement with predictions from the PARMELA simulation code, which was also used to design and optimize the CLIC injector (see Fig. 2.13). The current stability of the CTF3 Drive Beam injector is also well within the CLIC specifications [50].

The main remaining challenge is the operation at a pulse length 100 times longer than that of CTF3, and the handling of the correspondingly high average power. It should also be noted that, even though the CTF3 injector has been operated at 50 Hz for short periods of time, long-term operation was mainly done at a lower repetition rate (from 1 to 25 Hz) and the control of losses and activation in the CLIC case could be more problematic. However, the larger aperture should mitigate the issue. The full performance at the right CLIC parameters will be verified in a test facility currently under design and planned for construction and commissioning in 2012–2016.

The photo-injector option has not been established to the same level of confidence. Phase coding within one RF cycle was fully demonstrated and excellent beam quality for parameters close to the CLIC ones was obtained in the PHIN installation at CERN [51]. The needed laser parameters are at the edge of the present state of the art for pulse power and time structure, but appear to be feasible. The main remaining issues for the photo-injector option are the cathode lifetime (untested at the very high average current needed in CLIC), the beam current stability (probably within reach using a feed-back system on the laser, but yet unproven), and reliability concerns.

2.5.3 Fully loaded acceleration, linac transverse stability

An essential ingredient of the Drive Beam linac is full beam-loading operation (see also §2.4). The high pulse current of both CLIC and CTF3 (about 4 A in both cases), in conjunction with the use of short travelling-wave accelerating structures with relatively low gradient, results in an extremely high energy transfer efficiency to the beam. No RF power is transmitted to the load when the beam is present, and the resistive losses in the cavity walls are minimal. However, an energy transient is present at the beginning of the pulse, where the first bunches have twice the energy of the steady-state part reached after the filling time. This mode of operation also strongly couples beam current fluctuations to the beam energy.

The large average current also implies that transverse higher order modes (HOMs) must be damped in order to prevent transverse beam instability and control emittance growth to the desired level. Up to 10% emittance growth is allowed in the Drive Beam linac. (see §4.1 and §5.4). A Slotted Iris — Constant Aperture structure (SICA) has been designed to be used in the Drive Beam linac. Irises are radially slotted to guide dipole and quadrupole modes into SiC loads situated outside the cells. In this approach the selection of the damped modes is obtained through their field distribution, so that all dipole modes are strongly damped (Q typically below 20), while monopole modes are not influenced due to the symmetry. In addition to strong damping, SICA uses detuning of the dipole modes along the structure; this improves the suppression of HOMs and allows one to change group velocity along the structure, so providing the desired gradient profile. The HOM detuning is obtained by nose cones of variable geometry. The aperture can therefore be kept constant along the structure which helps in reducing the short-range wakefields.

Results of the study of transverse focusing in the Drive Beam linac have identified a FODO lattice as the best solution, giving transverse amplification and emittance growth well within the limits assuming realistic quadrupole and structure misalignments. The FODO lattice has the additional advantages of lower cost and easier operation compared to other solutions. In the study all elements were assumed to be scattered around a perfectly aligned trajectory with a normal distribution of $\sigma = 200 \mu\text{m}$ and $\sigma' = 200 \mu\text{rad}$. A combination of one-to-one correction and dispersion-free steering was applied. Figure 2.14 shows the simulated emittance growth along the linac for different lattices. The FODO lattice gives the best performance, with emittance growth well within the 10% limit.

The CTF3 linac [52] was the first to use the highly efficient full beam-loading regime and there were many concerns, both on possible drawbacks about this mode of operation and about transverse beam

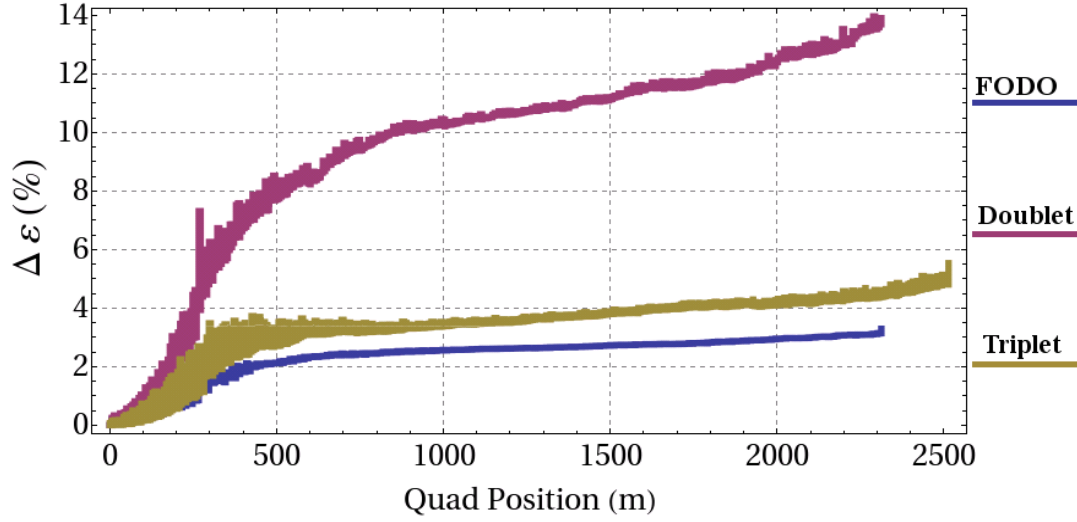


Fig. 2.14: Emittance growth along the beamline for FODO, doublet, and triplet lattices. The bunch compressor section is assumed to be perfectly aligned

stability. SICA structures operating at 3 GHz were built and used in CTF3. The operational experience has been successful since the very beginning. The CTF3 linac turned out to be very stable and easy to tune. The RF signals from the structure output (see Fig. 2.15), measuring the amount of beam loading, proved very useful in operation to tune and monitor the relative phase between the RF and the beam. Dedicated measurements were carried out to determine experimentally the RF-to-beam efficiency and compare it to expectations [53].

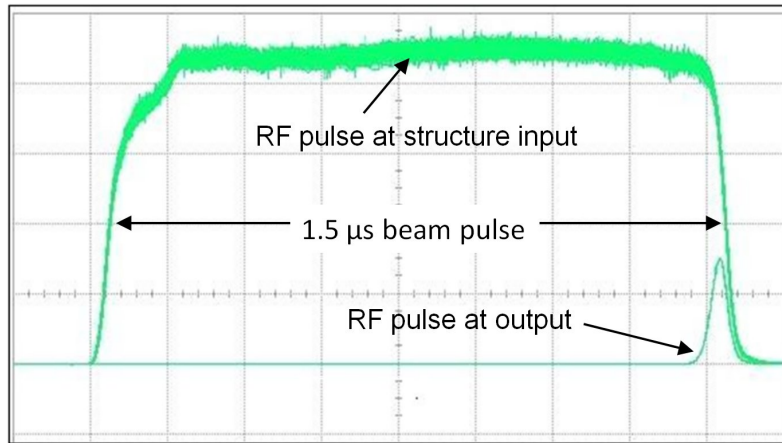


Fig. 2.15: RF power measured at the input and output of a CTF3 linac structure when operated in full beam-loading mode, showing how nearly all the power is taken out by the beam. RF-to-beam efficiency in CTF3 was measured to be 95%, in agreement with expectations.

Experiments were also performed to test the use of delayed filling techniques in order to minimize the momentum spread during the transient. The transient can thus be transported without losses to the end of the linac and disposed of after the delay loop, thus avoiding pulse erosion. Again, as for the injector, the issues not fully covered in CTF3 are linked to the handling of the correspondingly high

average power and beam loss management. In particular, non-intercepting diagnostic devices are needed for beam transverse-profile measurements.

2.5.4 Delay loops and Combiner Ring issues

The 140 μs Drive Beam pulse from the linac is first split and then compressed to obtain twenty-four 240 ns long pulses by using RF deflectors in a series of delay lines and rings.

The first RF deflector sends odd and even phase-coded sub-pulses in separate lines, whose length difference is equal to the sub-pulse length. Each couple of sub-pulses arrives simultaneously (bar half a wavelength distance) in a second RF deflector where their orbits are merged to obtain 240 ns long pulses with twice the current and half the bunch repetition frequency. The pulses are combined again in two rings, 3 and 4 times respectively. In each ring a pair of RF deflectors is employed to create a time-dependent closed bump at injection, which can be used to interleave the bunches. The whole system is designed to preserve transverse and longitudinal beam emittances during the combination process: isochronous lattices, smooth linear optics, low-impedance vacuum chambers and diagnostics, HOM-free RF active elements are all needed to accomplish this task.

One of the main requirements is to preserve the beam quality during the compression process and obtain in a stable way the correct timing both between trains and between individual bunches. In particular, bunch length and longitudinal phase-space distribution must be preserved and train-to-train, bunch-to-bunch fluctuations in phase and transverse position minimized. In the Drive Beam decelerator, the bunch length must be short compared to the 12 GHz wavelength in order to maximize the RF power production efficiency. The nominal value is 1 mm r.m.s. bunch length (in speed-of-light length equivalent), corresponding to 94% efficiency for 12 GHz power production (see §5.5.2). The transverse emittance growth through the complete system must also be kept below 20%.

Possible detrimental effects include non-isochronicity, coherent and incoherent synchrotron radiation emission, beam loading and wakefields in the RF deflectors and collective instabilities.

The isochronicity requirement is $|R_{56}| < \pm 1$ cm. All ring and turnaround arcs are based on the isochronous cell used in the CTF3 combiner ring: three dipoles, with two symmetric quadrupole triplets (see Fig. 2.16). The range of tunability of such a cell with three independent quadrupole families has been tested in CTF3 and fits the requirements well [54], [55]. The second-order term T_{566} must also be kept under control using sextupoles.

Energy spread can be a source of transverse emittance growth. Sextupoles used to zero T_{566} tend to increase the second-order terms relating the horizontal plane to the energy spread (T_{16n} , T_{26n} , $n = 1:6$), thus increasing the effective horizontal emittance. In turn, large amplitude transverse motion translates through the terms T_{51n} and T_{52n} ($n = 1:6$) in an effective loss of the isochronicity. The higher order terms of transverse and longitudinal chromaticity must then be corrected simultaneously [56] in order to ensure preservation of beam emittances in all planes (see Fig. 2.17).

Incoherent and coherent synchrotron radiation emission can both cause average energy loss and energy spread increase. Coherent synchrotron radiation (CSR) in particular can be a relevant issue when transporting short bunches. CSR-induced energy loss can lead to growth of longitudinal and transverse emittances. Bunches belonging to different trains make a different number of turns in the rings, therefore they will undergo different energy losses and develop different energy distributions. This may give rise to relative phase errors between bunches through residual non-isochronicity, while the energy spread within each bunch will lead to bunch lengthening and phase space distortion. The CSR emission can be minimized by using longer bunches in the loop and rings, and by reducing the height of the beam pipe in the bends, increasing the shielding effect by cut-off, but in this case a limit is imposed by the necessary beam ‘stay-clear’ distance. Short, high-charge bunches will also interact with any small discontinuity of the beam chamber (e.g., bellows, septa), leading to further energy loss, energy spread increase, and possibly transverse instabilities.

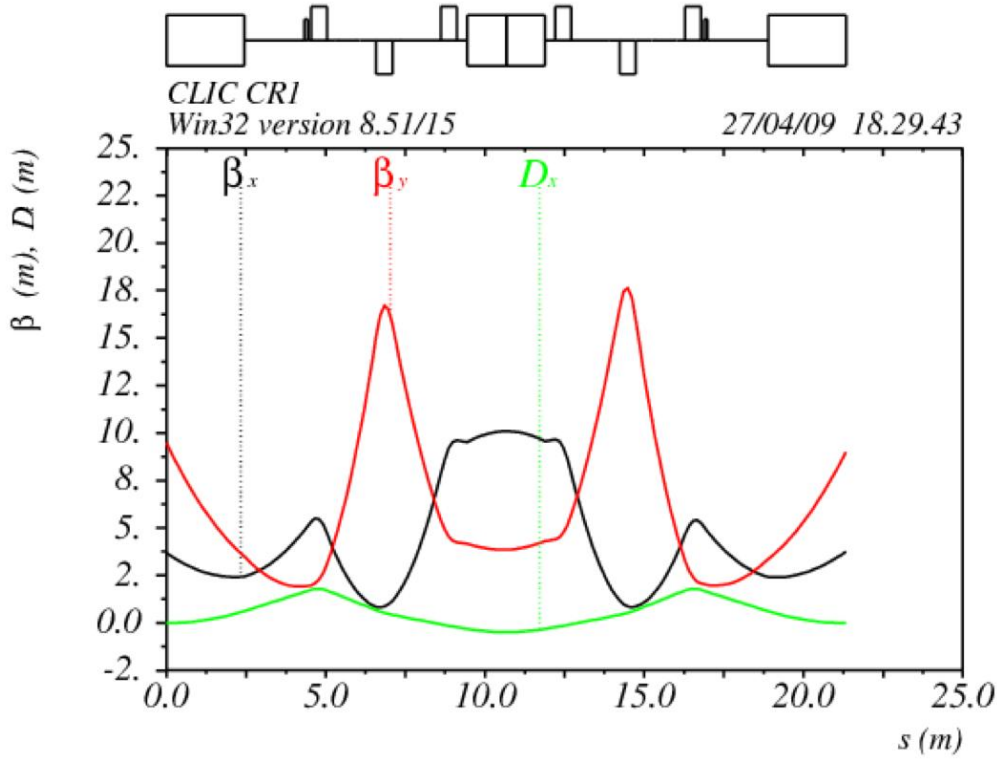


Fig. 2.16: Isochronous cell optical functions

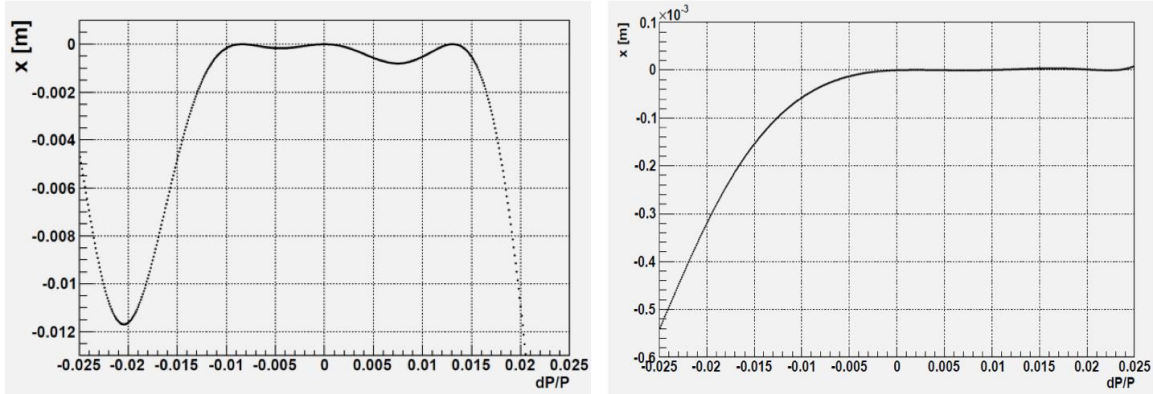


Fig. 2.17: Illustration of non-linear effects in the first combiner ring and effect of the correction using sextupoles. Final horizontal position as a function of initial energy deviation $\Delta p/p$ after tracking over three turns starting on the reference orbit. Left: no sextupoles. Right: with sextupoles.

It is therefore highly desirable to manipulate relatively long bunches in the bunch train compression system, and compress them just before injection into the Drive Beam decelerator sections. The Drive Beam bunches are kept in the whole bunch train compression system at 2 mm r.m.s. length. The upper limit to the bunch length in the combination system is given by the phase extension in the RF deflectors (to limit potential emittance growth). In order to get the final compression to 1 mm r.m.s., the intra-bunch energy/time correlation must be preserved all along the compression system. Therefore all

the distortions to the longitudinal phase space must be kept small. Consequently non-linear terms in the path length dependence on energy spread (like T_{566}) must also be considered, as previously mentioned. By choosing 2 mm r.m.s. bunch length, CSR emission is effectively suppressed, and non-coherent SR is dominant. While standard SR does not significantly deteriorate the beam quality, attention must be paid to its absorption, because of the high-peak power.

One particular problem in the delay loop and combiner rings is the potential Drive Beam transverse instability arising from beam resonant excitation of the electric field in the RF deflectors. The effect can be described in terms of beam loading on the fundamental mode. A bunch train passing through the structure couples to the mode through both the transverse and the longitudinal velocity. The transverse coupling in most practical cases is negligible, owing to the small value of the transverse velocity.

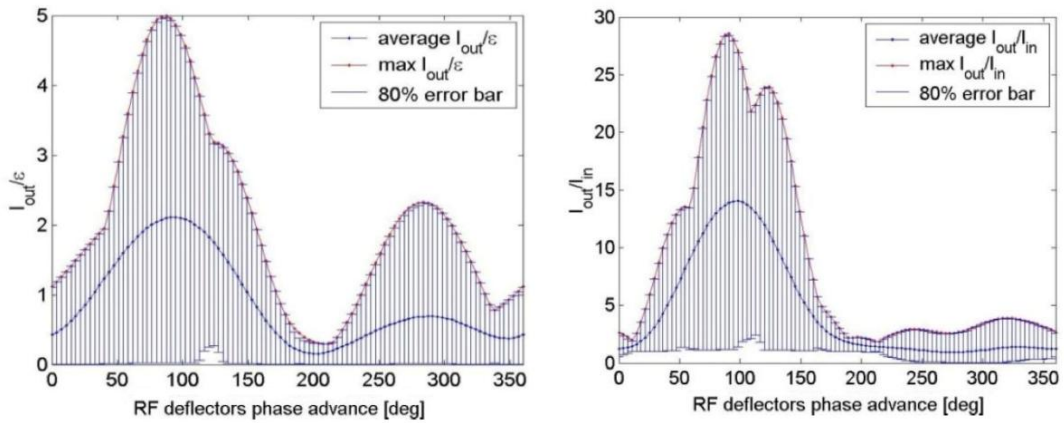


Fig. 2.18: Left: ratio between the output CS invariants of bunches and the nominal projected emittance for CR2 (systematic coupling) as a function of the betatron phase advance. Right: amplification factor for an initial error in position in CR2 as a function of the betatron phase advance. The stable region around a phase advance of $\sim 200^\circ$ is clearly visible. The effect in CR1 is similar but smaller, due mainly to the lower frequency of the RF deflectors.

Longitudinal coupling takes place when the train is displaced with respect to the deflector axis (where the longitudinal field component is zero). In the case of perfect injection, the beam offset inside the deflector is, in general, small, and the systematic longitudinal coupling is not harmful. However, if an injection error is present, it can induce a strong excitation of the fundamental mode (wakefield), in quadrature with the externally generated deflecting field. Since it is out of phase, such a component does not have a direct influence on the exciting train, but when the different trains are interleaved during combination, the bunch pattern is such that a mutual perturbation between trains can lead to an amplification of the injection errors.

It has been shown [57], [58] that a proper choice of the ring tune and of the β -function in the RF deflectors minimizes the effect of wakefields (see Fig. 2.18). This constitutes a main constraint on the delay loop and combiner ring optics design, as discussed in §4.2. Experience in CTF3 has confirmed the previous theoretical analysis, and has made clear that the effect in the vertical plane, which was previously neglected since it is non-resonant, can indeed also be harmful but can easily be kept under control by a combination of detuning and damping. [59]

The extraction system for both rings is also a critical item, the issues being the high repetition rate (particularly in the 1st ring), the impedance (particularly in the 2nd ring where the current is higher) and the kick stability and flatness. The current solution is based on the use of a fast kicker constituted by travelling TEM wave transmission line pairs.

2.5.5 Long transfer lines and turnarounds

Drive Beam trains are formed in the frequency multiplication system on the surface. After the system, a long turnaround loop (LTA), moves half of the trains towards the e^- main linac (see §4.2). The Drive Beams are then transported below the surface towards the beginning of the main tunnels by long transfer lines as shown in Fig. 2.19. Periodically, a Drive Beam pulse is extracted from the line and injected by dedicated turnarounds into each of the 24 + 24 decelerator sections.

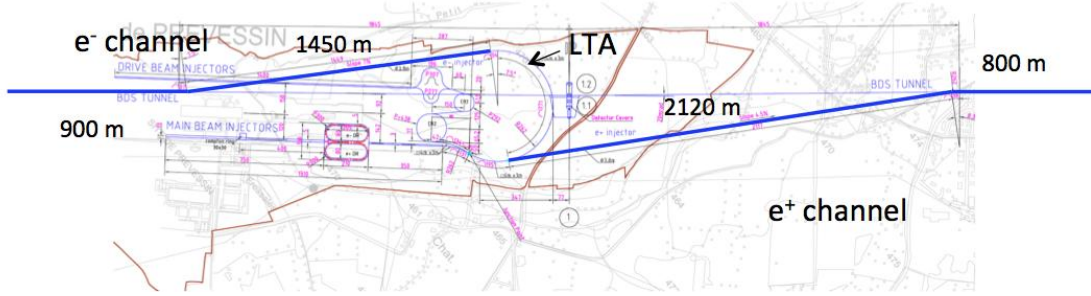


Fig. 2.19: The first part of the long transfer line, between the surface site and the end of the two main linac tunnels

The descent to the main tunnels and the transport over 21 km to the beginning of the main linacs is done through a simple FODO lattice. The FODO period is nearly identical all along. The total length is 23.4 km for the e^- main linac and 23.9 km for the e^+ one. The main issue with this long beamline is the emergence of parasitic dispersion induced by quadrupole misalignment. The use of a straight FODO structure made of long cells and weak quadrupoles guarantees an inherently low chromaticity and acceptably small parasitic dispersion.

The Drive-Beam trains which travel in the opposite direction with respect to the Main-Beam line are driven to their decelerator through a turnaround loop which makes an angle of 180° . The optics are similar to those of the first combiner, offering isochronicity and achromaticity in order to preserve the beam emittance in all planes. The loop is preceded by a longitudinal de-compression chicane and followed by a compression chicane (see §2.5.7).

The large value of the beam current (100 A) has strong implications for collective effect issues. In particular, the multi-bunch resistive wall effect and trapped-ion instability give stringent requirements on the beam pipe material and geometry and to the vacuum quality. Simulations have shown that a 20 cm beam pipe with an internal copper surface is needed in the long line to keep the resistive wall under control. A pressure of 10^{-10} Torr or lower is required in order to preserve good beam quality (see §4.3).

2.5.6 RF power production — decelerators

The decelerators run in parallel to the two Main Beam lines for the full length of the electron and positron main linacs. Each decelerator is divided into 24 sectors. In each sector the RF power for the main linacs is extracted from a 100 A Drive Beam pulse, 240 ns long, which is decelerated to convert its kinetic energy to 12 GHz RF power in resonant power extraction and transfer structures (PETS) [60]. Most of the beam energy is extracted from the Drive Beam, which makes the beam transport challenging. A detailed discussion of the beam physics of the CLIC decelerators is found in Ref. [61].

Beam dynamics studies have been used in order to define the requirements and guide PETS development, leading to the present design, in which the transverse wakes are sufficiently damped (see §5.5.2). In particular, in their final configuration, the PETS comprise of eight octants (bars), defining a 23 mm aperture and separated by the 2.2 mm wide damping slots (see Fig. 2.20). Each of the bars is

equipped with HOM damping loads.

A frequency-scaled PETS prototype at 11.4 GHz was high-power tested using a klystron in the ASTA test area at SLAC. The PETS was processed at the maximum available power level, and has demonstrated the nominal CLIC power, pulse length, and breakdown rate (135 MW, 240 ns, 10^{-7} pulse m^{-1}). A long 12 GHz prototype of the CLIC PETS was tested with beam in the Two-beam Test Stand (TBTS) of CTF3, where an external power recirculation circuit was installed to boost power production. RF power production, up to nominal CLIC parameters and beyond, has been measured with and without recirculation and compared with expectations from a detailed model, finding very good agreement [62],[63].

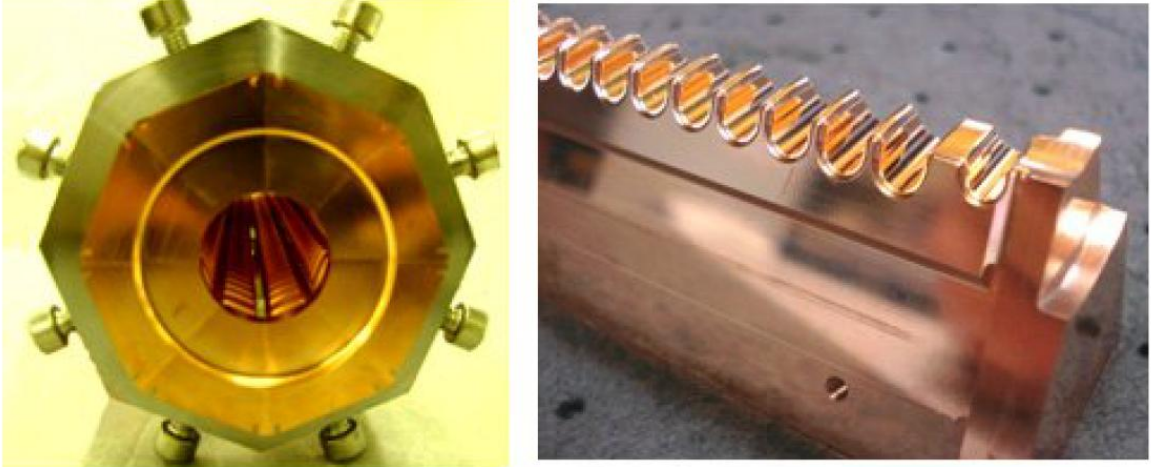


Fig. 2.20: The front view of the pre-assembled PETS (left) and a detail of one PETS bar

During normal machine operation, the main accelerating structure and/or the PETS will periodically experience breakdowns. In case of consecutive breakdowns, the RF power production from a PETS will need to be switched off locally. A gradual, controlled ramping up of the power to nominal conditions will be needed. A system has been developed based on an external high power variable RF reflector [64]. Normally operated at full transmission, when set to full reflection it will fully block the RF power transfer from the PETS to the accelerating structure.

The produced RF power is then returned to the PETS where a fixed internal RF reflector located at its upstream end establishes recirculation of the RF power inside the PETS itself. The round-trip length of the RF circuit is tuned to be at half an integer wavelength, such that destructive interference rapidly brings the power level inside the PETS to a steady-state value of about 1/4 of the nominal one, sufficient to avoid subsequent breakdown and allow, if needed, to perform the reconditioning procedure (obtained by gradually switching the variable RF deflector back to full transmission). The PETS on-off mechanism described here was tested at nominal power levels in CTF3 (see Chapter 7).

The beam current is determined by the power production requirement, while the initial energy is determined by requiring a maximum particle energy extraction of 90%. The length of the decelerator sectors varies from about 840 m to 1050 m in order to ensure the same power extraction efficiency in each sector, since the space needed for Main Beam focusing increases as the Main Beam energy increases. Two major challenges must be addressed in order to ensure a robust beam transport: the significant transverse wakes in the PETS (see Fig. 2.5.6) and the large energy spread induced by the power extraction process. The initial normalized emittance is assumed to be $\epsilon_{x,y} = 150 \pi \mu\text{m}$. The large energy extraction combined with significant transverse wakefields implies a need for strong focusing.

Simulations show that the beam energy spread induced by the deceleration implies that standard 1-to-1 correction might not ensure satisfactory Drive Beam transport. A correction scheme based on dispersion-free steering and on the exploitation of the structure beam loading has shown excellent per-

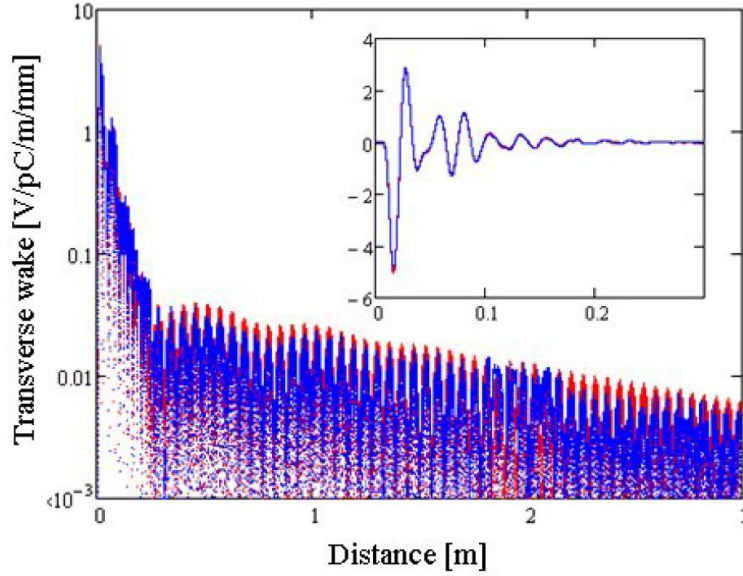


Fig. 2.21: The PETS transverse wakefield, showing its fast decay over more than two orders of magnitude, calculated using the program GDFIDL (blue) and the semi-analytical model used for beam dynamics simulation in PLACET (red)

formance, assuming a sufficient beam position monitor resolution. FODO focusing is used, with two quadrupoles per CLIC module (see §4.4). The initial maximal r.m.s. beam size is $\sigma_{x,y} = 0.3$ mm. As a metric for the decelerator beam envelope, the 3σ transverse beam envelope of the outermost slice of the beam is used. Using the specified tolerances (see §4.4), no single instability source or error source increases the beam envelope by more than 5% (see also Fig. 2.22). Successful demonstrations of similar orbit correction schemes have also been performed in the CTF3 linac [61].

The efficiency of transverse HOM damping in the PETS is being studied experimentally in the Test Beam Line (TBL) in CTF3, where 16 PETS will be installed and tested with 30 A Drive Beam. The latest results obtained in 2011, using a 20 A beam decelerated through 9 PETS, were in good agreement with simulations, producing a total peak power of more than 500 MW and demonstrating stable deceleration by 25% of the initial energy (see Chapter 7).

2.5.7 RF power production — phase and amplitude stability

The Main Beam should experience the correct RF phase and amplitude within tight tolerances in order to be efficiently accelerated. Phase and amplitude errors will result in energy errors, causing emittance blow-up and luminosity reduction. The stability of the Drive Beam used to produce the RF power is therefore of crucial importance, since the bunch charge and phase jitter contribute quadratically to the luminosity loss [65].

The main concern is that energy jitter generated in the Drive Beam accelerator would be transformed into beam-phase jitter during the final bunch compression. The tolerances are extremely tight: about 0.2% for the RF power and 0.05° for the RF phase are required in the Drive Beam accelerator, while a maximum variation of 0.1% for the Drive Beam bunch charge and 0.25° at 1 GHz for the Drive Beam bunch phase are allowed. Such tolerances are evaluated for a maximum contribution per parameter of 1% to the luminosity loss and assuming a feed-forward system (briefly described below, see §5.15 for a more complete description) capable of reducing the Drive Beam phase jitter by the factor of 10.

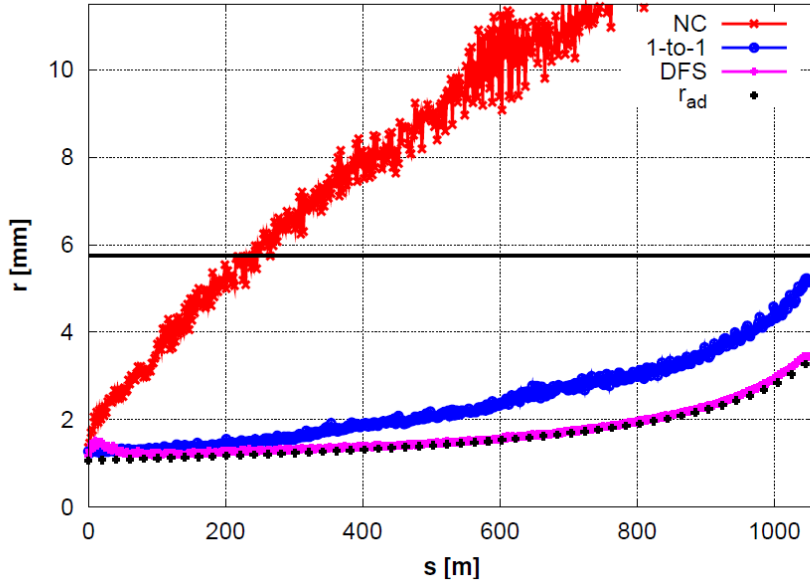


Fig. 2.22: The 3σ beam envelope (worst of 100 machine random samples) along the decelerator lattice in the cases of no correction (red), one-to-one correction (blue) and dispersion-free steering (magenta). The minimum achievable envelope due solely to adiabatic emittance undamping is plotted in black. We observe that the dispersion-free steering has taken out almost all residual envelope growth.

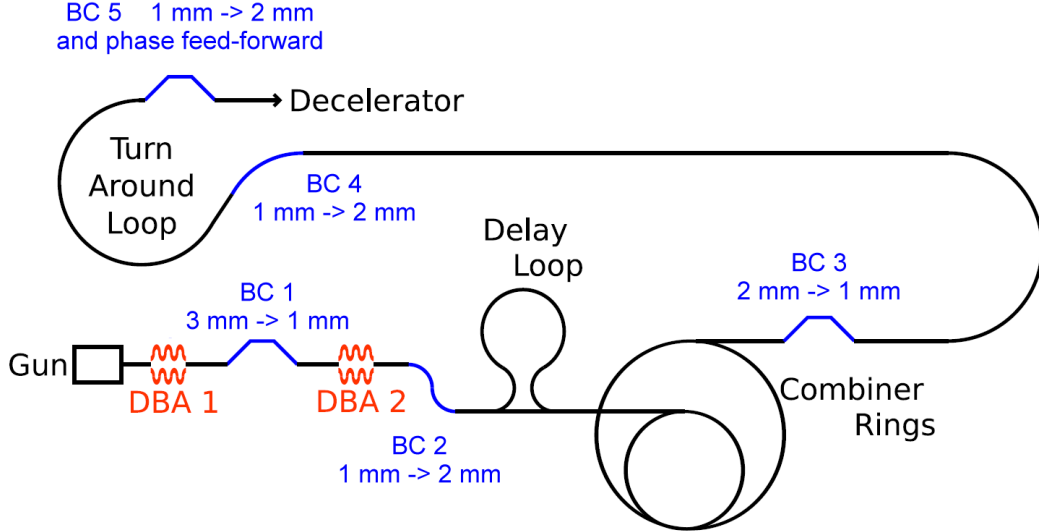


Fig. 2.23: Conceptual layout of the CLIC Drive Beam complex, showing the bunch length evolution and the location of the final phase feed-forward system. Only one of the $24 + 24$ turnaround loops required is shown.

In order to minimize the effects, and taking into account the different requirements on the bunch length in the different parts of the Drive Beam complex, a compression/decompression scenario has been developed (see Fig. 2.23). The bunches are compressed to a length of 1 mm after a first section of the Drive Beam linac, at an energy of 300 MeV, and then accelerated to their final energy of ~ 2.5 GeV, thus reducing the total energy spread. To avoid the impact of coherent synchrotron radiation and high-

frequency impedance, the bunches are de-compressed to 2 mm before they enter the delay loop and re-compressed behind the combiner rings.

It must be noted that after the initial compression, the global R_{56} is zero. Assuming a good control of nonlinear terms, this ensures that energy jitter after the first compression point is not translated to phase errors. Therefore the more stringent requirements on Drive Beam linac RF are valid only for DBA1.

In order to further reduce beam-phase jitter, it is foreseen to have a phase feed-forward system just in front of each decelerator section [66]. The beam phase is measured in front of the turnaround loop and is corrected afterwards. The path length is changed in a controlled manner using fast kickers inside a magnetic chicane. Based on this design we allow an incoming r.m.s. phase jitter of 2.5° which the feed-forward should reduce by a factor 10.

The tolerances discussed above are for pulse-to-pulse jitter, coherent over the 24 decelerators. The tolerances for uncorrelated and intra-pulse jitter are more relaxed. In particular, high-frequency intra-pulse variations are filtered out by the combination scheme and by the main linac accelerating structure filling time [67].

2.5.8 RF power production — beam loading compensation

A high beam loading is needed in the CLIC Main Beam accelerating structure in order to reach 28.5% efficiency in RF-to-beam transfer. Owing to the beam loading, the field profile along the structure changes as the beam train is accelerated, reaching a steady state after about one filling time. The transient effect must be compensated in order to keep the resulting energy variation along the Main Beam pulse within tolerance (3×10^{-4} for 1% luminosity loss). An appropriate ramp in the RF pulse during the initial filling time is needed so as to simulate the steady-state profile during the initial 88 ns of Main Beam pulse.

The shape of the RF pulse depends in turn on the beam current profile of the Drive Beam pulse. The chosen solution to synthesize the desired current profile is the modulation of the 180° phase switch timing from one sub-pulse to the next [68]. By such a method, pulses of different lengths are recombined in the delay loop and the rings, resulting in a current ramp created by changing the bunch density rather than the charge per bunch. The ‘missing’ bunches are appended to the Drive Beam pulse tail, which is not harmful, since it will enter the structure after the Main Beam pulse passage (see Fig. 2.24). This solution does not require any additional hardware.

An optimization of the timing distribution of the 23 available phase switches based on generic algorithms was done [69]. Such detailed calculations fully take into account the main linac structure RF properties, and show that the maximum difference in gradient seen by any two bunches can be reduced to around 8×10^{-4} while the r.m.s. energy spread is of the order of the 3×10^{-4} required, as shown in Fig. 2.24. The switch duration (< 10 ns) is not a problem, and can even improve the performance of the compensation scheme. Also, by using different switch patterns for consecutive Drive Beam sectors the performance can be further improved. Some preliminary tests have been done in CTF3, showing the possibility of precisely controlling the phase switch timing. A full test, including sampling of the acceleration by the probe beam, is planned for 2012 (see also Chapter 7).

2.5.9 Two-beam acceleration

Already during the 2009 run, the PETS produced over 170 MW peak in full RF re-circulation mode, well above the nominal 135 MW foreseen in CLIC, but in presence of pulse shortening. The performance was limited by this effect, linked to RF breakdown in recirculation components such as a high power splitter and phase shifter. These parts were repaired and improved for the 2010 run, when RF power levels in the 300 MW range were reached at the nominal pulse length. During the 2010 run the first two-beam acceleration of the probe beam was achieved.

The nominal CLIC accelerating gradient of 100 MV/m corresponds to a $\Delta E = 21.4$ MeV. The

2.5 DRIVE BEAM GENERATION AND MAIN BEAM RF POWER PRODUCTION

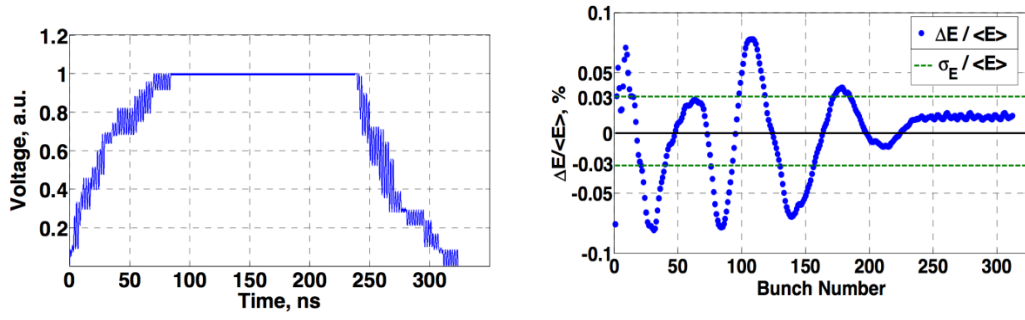


Fig. 2.24: Voltage profile for the CLIC optimized RF pulse (left) and corresponding relative energy spread along the bunch train (right)

acceleration measurements were done using the spectrometer screen while running the probe beam at twice the repetition rate of the Drive Beam. Thus accelerated and non-accelerated beam energies can be measured alternatively. Figure 2.25 shows an example 23 MeV probe beam acceleration measured with the spectrometer screen, corresponding to an accelerating gradient of 106 MV/m. Note that due to screen size limitations it is only possible to monitor the accelerated and non-accelerated beam simultaneously when the energy gain is not more than ~ 27 MeV.

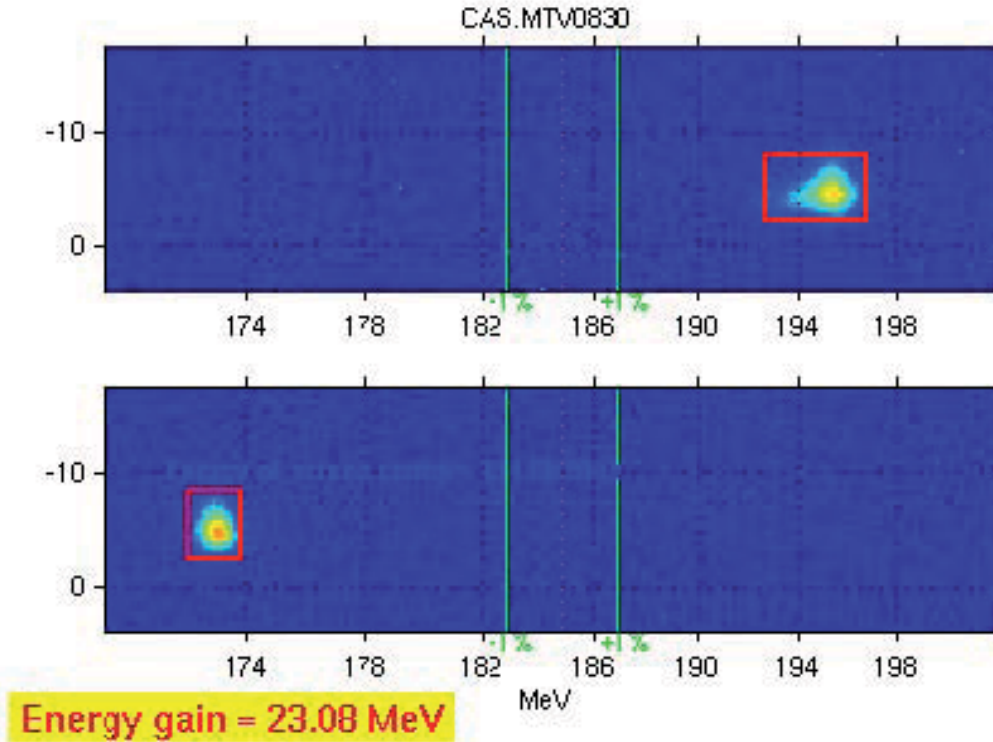


Fig. 2.25: Example probe beam acceleration in the TBTS with the 12 GHz RF power on (top) and off (bottom). The energy gain is 23.08 MeV which corresponds to a gradient of 106 MV/m in the accelerating structure.

2.5.10 Conclusions

Most feasibility issues linked to Drive Beam generation and Main Beam RF power production have already been experimentally covered in CTF3. The CTF3 experimental program has so far demonstrated

the feasibility of high-current beam generation and acceleration in a fully loaded linac, including fast phase switching for phase coding, and the subsequent recombination and bunch frequency multiplication using transverse RF deflectors in a delay loop and a combiner ring. In particular, stability measurements of the RF phase and the beam current in CTF3 have shown that CLIC requirements can be reached. Efficient 12 GHz power production in PETS and its use for two-beam high-gradient acceleration were also successfully tested. The operation, with beam and at high power, of a PETS with on-off capability was recently demonstrated.

The remaining issues are currently being addressed in CTF3. Preliminary tests in the Test Beam Line (TBL) have shown stable and lossless deceleration of the Drive Beam by 25% in a string of nine PETS. The experimental verification of the one-to-one and dispersion-free steering algorithms needed in the CLIC decelerators has also begun. We expect to consolidate these results next year, with up to 16 PETS installed and deceleration down to 50%, which should enable the extrapolation to CLIC requirements. Also planned for next year is an experiment on RF pulse-shape control to demonstrate experimentally the feasibility of the Main Beam loading compensation scheme (see Chapter 7 for more details).

All feasibility issues identified have been successfully addressed. In most cases the feasibility has been established and for the few remaining issues we expect decisive input in the near future. CTF3 will continue its experimental program over the next five years in order to give further indications on cost and performance issues, to act as a test bed for the CLIC technology, and to conduct beam experiments aimed at mitigating technological risks. It is also planned to build, in the next five years, a new test facility, the CLIC 0 front-end, to help the CLIC study advance towards a project implementation plan. Such a facility will consist of a 20–30 MeV Drive Beam injector and will be a first step towards the CLIC 0 facility [70], [71]. It will drive the technology development of modulators, klystrons, and accelerating structures for the CLIC Drive Beam linac at the correct CLIC parameters and will address the issues related to high average power and long-pulse beam handling.

2.6 Creation of ultra-low emittance beams

The high luminosity of a linear collider depends strongly on the generation of ultra-low emittance high-intensity bunches. Conventional electron sources and positron production schemes provide beams with emittances that are several orders of magnitude greater than those needed. Natural synchrotron radiation damping of the beam when circulating in rings is the damping mechanism enabling one to reach these small emittances.

Table 2.3: CLIC versus ILC and NLC parameters driving the damping ring design

Parameters [units]	ILC	NLC	CLIC
Bunch population [10^9]	20	7.5	4.1
Bunch spacing [ns]	369	1.4	0.5
Number of bunches/train	2625	192	312
Number of trains	1	3	1
Repetition rate [Hz]	5	120	50
Horizontal normalized emittance [nm]	4400	2400	500
Vertical normalized emittance [nm]	20	30	5
Longitudinal normalized emittance [keV.m]	38	11	6

The performance challenges of these damping rings (DRs) are driven by the key parameters of the collider and the requirements of the upstream and downstream systems, and principally the efficiency of the main linac RF. The parameters driving the design of ILC [72], NLC [73], and CLIC damping rings are presented in Table 2.3. The technological choice of superconducting over copper RF cavities for the main linacs clearly differentiates the designs, although a number of design issues and challenges still remain common. In one type of damping ring such as that for CLIC or NLC, the bunch trains are relatively short with even shorter bunch spacing and high repetition rate. The ILC bunch train is much longer, necessitating a much longer damping circumference where the train is compressed and uncompressed in a bunch-by-bunch beam transfer scheme. To get high luminosity in the ILC the bunch charge is much higher whereas CLIC targets orders of magnitude lower emittances in all three dimensions (500 nm horizontal, 5 nm vertical, and 6 keV.m longitudinal). Although these emittances are unprecedented, modern X-ray storage rings currently in operation or in the construction phase are rapidly approaching these regimes. In the case of vertical emittance, which requires challenging magnet alignment tolerances and stringent control of the optics and orbit, the electron storage rings hold the current record, at the level of 1–2 pm [74] and are rapidly reaching the CLIC DR target. Figure 2.26 presents the horizontal and vertical normalized emittance in a number of low-emittance rings, including test facilities, DRs, B-factories and synchrotron light sources, under operation (red) or in the design phase (blue).

A schematic layout of the CLIC damping ring complex is shown in Fig. 2.6 comprising two pre-damping rings, two damping rings, and a delay loop. The large input emittance and energy spread, especially coming from the positron source and the high repetition rate of 50 Hz, require that the beam damping be performed in two stages, with a pre-damping ring (PDR) for each particle species. A careful lattice design and non-linear dynamics optimization is necessary for providing a solid PDR design, with large dynamic and momentum aperture, enabling the efficient capture and transfer of the incoming bunch trains from the injector linacs [75].

The design challenges of the CLIC main DRs are driven by the extremely high bunch density, i.e., the ratio between bunch charge and the 3-dimensional beam volume, and the collective effects associated with it. In this respect, the CLIC DR parameters shown in Table 2.4 are carefully chosen and optimized in order to mitigate these effects. In addition, these parameters drive the technology of a number of components such as wigglers, RF system, kickers, vacuum, instrumentation and feedback.

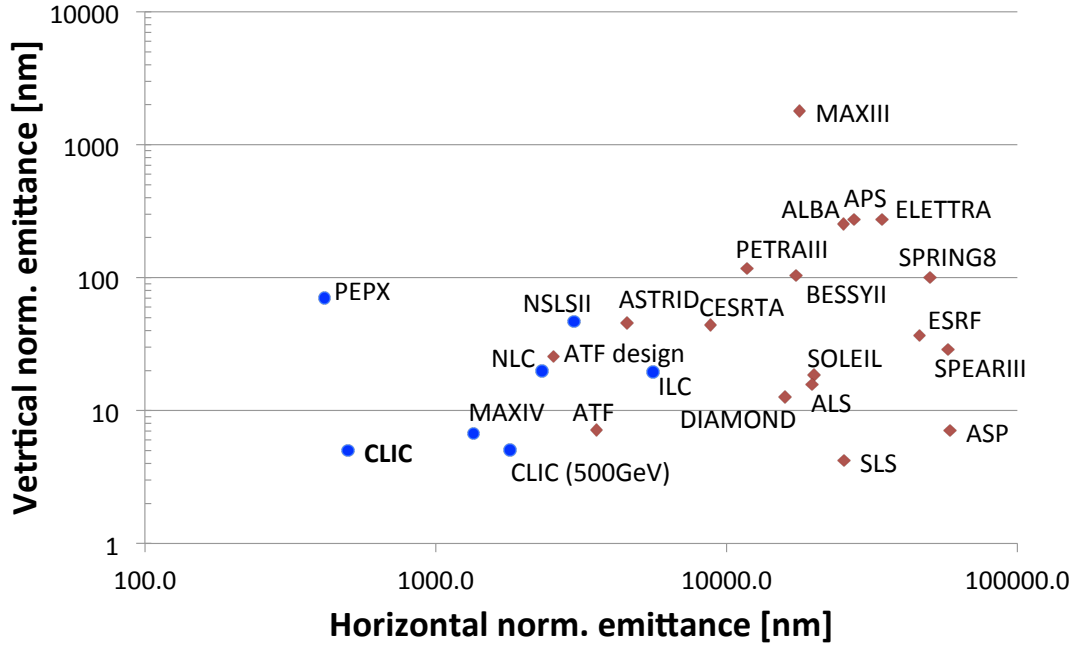


Fig. 2.26: Horizontal versus vertical normalized emittance for low-emittance rings in operation (red) and in the design phase (blue)

Table 2.4: CLIC DRs design parameters.

DR parameter [units]	Value
Energy [GeV]	2.86
Circumference [m]	427.5
Energy loss/turn [MeV]	4.0
RF voltage [MV]	5.1
Compaction factor	1.3×10^{-4}
Damping time transverse / longitudinal [ms]	2.0 / 1.0
Number of arc cells/wigglers	100 / 52
Dipole/wiggler field [T]	1.0 / 2.5

The steady-state emittance is dominated by intra-beam scattering (IBS) and the ring energy has to be chosen in a regime where the ratio between the IBS-dominated emittance and the ‘zero-current’ one is the lowest possible and within the required emittance tolerance [76]. On the other hand, the lattice based on a racetrack shape with Theoretical Minimum Emittance (TME) arc cells and long straight sections filled with wiggler FODO cells, has to be optimized in order to reduce the IBS growth rates [77].

Owing to the very small beam size, especially in the vertical plane, the space-charge tune shift is large, reaching a maximum when equilibrium has been reached. So that the tune shift is kept below 0.1, the ring has to be as compact as possible, and at the same time, the longitudinal beam characteristics (bunch length and energy spread) have to be increased [78] but remain within the requirements.

Producing the ultra-low horizontal emittance in a compact ring within the machine pulse of 20 ms necessitates the use of high-field damping wigglers with short period, which in the case of CLIC are superconducting (2.5 T with 50 mm period). Prototyping and measurements in storage rings are foreseen in order to qualify these technologies in the future.

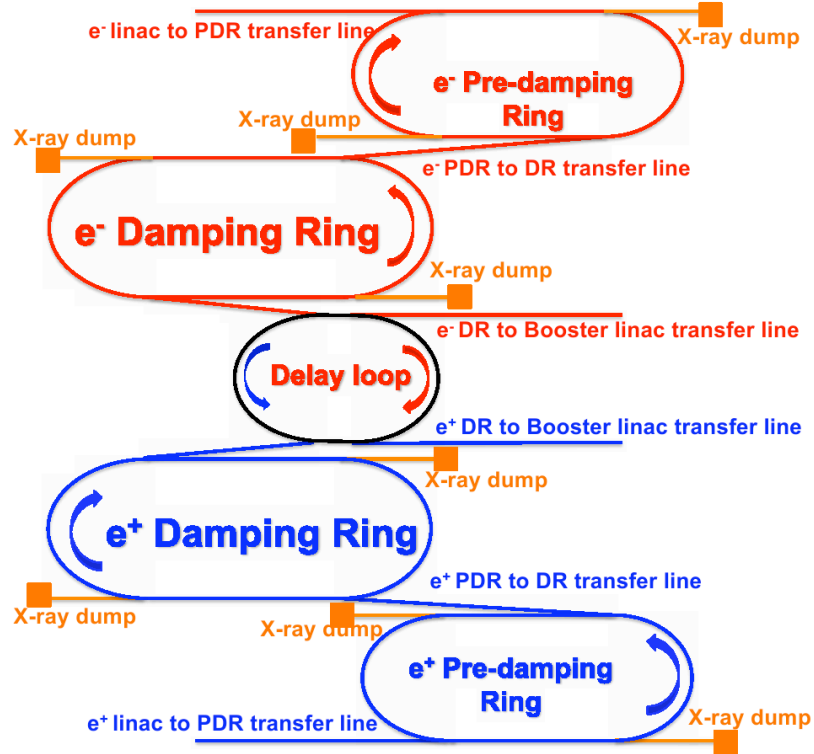


Fig. 2.27: The damping ring complex layout including two pre-damping rings, two damping rings and a single delay loop

High bunch density in combination with the short bunch spacing triggers two-stream instabilities. In the e^- ring, the fast ion instability can be avoided with ultra-low vacuum pressure of the order of 0.1 nTorr and/or partial filling of the rings and bunch-by-bunch transverse feedback [79]. In order for the electron cloud build up to be reduced and instability not to occur in the e^+ ring, it is necessary that the vacuum chambers present a secondary emission yield (SEY) below 1.2–1.3; the photo-emission yield should also be very low (around 0.1%) [79]. The low SEY can be achieved with special chamber coatings. In particular, a novel amorphous carbon coating pioneered at CERN SPS [80], has shown a big reduction of the electron cloud activity in coated chambers at CESR-TA [81]. The low photo-emission yield is indeed in the requirements and capabilities of the absorbers which have to protect the superconducting wigglers from quenching. The stringent beam stability requirement of typically 10% of the beam size imposes tight jitter tolerances for the damping ring extraction kicker (a few 10^{-4}). An ILC type beam extraction experiment using a prototype strip-line kicker has been carried out at KEK-ATF [82] with quite encouraging results, approaching the stability requirements of CLIC. The very high peak and average currents, corresponding to the full train of 312 bunches spaced by 0.5 ns, present a big challenge due to transient beam loading, especially for a 2 GHz RF system. It was decided to inject two bunch trains symmetrically spaced from each other in the DRs, with 1 ns bunch spacing. Apart from relaxing two-stream instabilities, this bunch structure significantly reduces the beam loading, the RF system with frequency of 1 GHz is more conventional, and an extrapolation from existing designs is possible. Nevertheless, the trains have to be recombined in a delay loop, downstream of the damping rings, with half the circumference. The recombination is achieved as in CTF3, with an RF deflector [83] pulsing at 2 GHz, and the transverse kick stability requirements are similar, as for the extraction kickers. A single delay loop is considered for both species, and the RTML size for electrons and positrons has to be adjusted by 1100 ns for synchronization purposes.

2.7 Preservation of ultra-low emittances

The generation of ultra-low-emittance beams has been addressed in the previous section. This section describes the designs and technical solutions in order to preserve this low emittance through the whole accelerator complex.

- The design of the relevant beam transport system from the damping ring to the interaction point, which is required to achieve the very small spot size at collision;
- The emittance degradation due to static imperfections in the main linac and beam delivery system, where the main issue is the accuracy of the pre-alignment of the beam line components;
- The luminosity loss due to dynamic imperfections in the main linac and beam delivery system. Important sources of imperfections are ground motion, which is mitigated using active stabilization of the magnets, and fluctuations of the Drive Beam intensity and phase.

A detailed description of the integrated design studies leading to the present parameter set is given in §3.8.

2.7.1 Transport lattice design and nanometre beam sizes

The different beam transport lines from the damping rings to the interaction point exist, particularly challenging is the beam delivery system design. Simulations show that in the absence of imperfections these designs would allow us to reach 250% of the CLIC luminosity goal.

2.7.2 Static imperfections and pre-alignment

The most important static imperfections are the misalignments of the beam position monitors (BPMs) and the accelerating structures. The beam position monitors will be used to define the beam trajectory. If it is not straight, beam particles with different energies will take slightly different paths, leading to an increase of the beam emittance. Similarly, offsets of the accelerating structures will lead to the generation of parasitic transverse fields, so-called wakefields, which kick the tails of the bunches, thus generating emittance growth.

To ensure excellent alignment of the main linac components, the BPMs are mounted on girders equipped with movers, which can be remotely controlled, and sensors, which measure their position with respect to a reference system of overlapping wires, similar to that used in the LHC insertions. A reference system has been developed and built for CLIC, the first prototype showing an r.m.s. accuracy of $14\ \mu\text{m}$, which is already very close to the target of $10\ \mu\text{m}$ and would lead to very little reduction of the luminosity. The other system components have been developed for the test module and will be tested soon in CTF3. This system will be used to pre-align the components after installation. Then orbit measurements with different energy beams will be used to measure and improve the effective alignment of the beam position monitors and magnets. Finally, the generation of wakefields in the accelerating structures is minimized by measuring the beam offset in the structures using novel wake monitors. Simulations show that with these procedures the emittance growths stay within specifications.

In the beam delivery a similar pre-alignment procedure is foreseen, with an accuracy of $10\ \mu\text{m}$ for all components. The beam-based alignment and tuning is somewhat more complex due to the sophisticated nature of the system design. However, simulations show that one can achieve the target luminosity, including the margins foreseen for dynamic effects, with a likelihood of 65% with no hardware intervention. With further improvements of the algorithms it is expected to further increase this probability. The beam-based tuning is currently being tested in ATF2.

2.7.3 Dynamic imperfections and stabilization

The Main Beam is very sensitive to magnet motions, in particular in the main linac and in the beam delivery system. An important source is ground motion, which is very site specific. Technical systems can

also induce vibrations, but those can be mitigated by the design of each technical component. Hence they will be addressed in the technical design phase. As a conservative benchmark, we use a ground motion model that is based on measurements on the floor of the CMS experimental hall, which is significantly more noisy than the LEP tunnel.

The main linac and BDS magnets are equipped with active stabilization systems, which use motion sensors and piezo-electric actuators controlled by a local feedback/feed-forward system. A prototype system has been developed and the transfer of the ground motion to the magnet has been measured and compared to simulations with reasonable agreement. Based on the results of the first simulation studies, an improved system concept has also been developed, which will be constructed in the future. The final quadrupoles, which are most sensitive to motion, are mounted on a pre-isolator, consisting of a large concrete block that is supported by air springs.

The expected impact on luminosity is calculated using a simulation code that models the ground motion, the transfer through the stabilization system, and the beam-based feedback. The nominal luminosity includes a 20% safety margin for dynamic imperfections in the main linac and BDS. With the existing prototype system 13% luminosity would be lost, using most of this margin. With the new system only 3% would be lost.

Fluctuations of the Drive Beam phase or current change the CLIC Main Beam acceleration and lead to luminosity loss since the energy bandwidth of the beam delivery system is limited. This places tight tolerances on the Drive Beam current stability (7×10^{-4}) and on the phase and power stability of the Drive Beam accelerator klystrons (0.05° and 0.2%) in order to limit the luminosity loss to 1%. Measurements in the CTF3 Drive Beam accelerator show that the beam current has a stability of 5×10^{-4} and a good klystron has a phase stability of 0.07° and a power stability of 0.21% , close to the CLIC requirements.

2.7.4 Technical solutions

As the most important technical systems needed to preserve low beam emittances and hence producing high luminosity we have identified:

- stability of quadrupole-fields against vibrations,
- high-precision mechanical pre-alignment of the main linacs,
- distribution of femto-second timing throughout the accelerator complex.

More details on these technical systems can be found in the corresponding sections of Chapter 5; a summary including some key results is given in the following paragraphs.

2.7.4.1 Stability of quadrupole fields

Requirements and technological solutions

In order to preserve the ultra-low transverse emittance during the beam transport from the damping rings to the collision point, the stability of the fields of all Main Beam Quadrupoles (MBQs) and the final-focus magnets (QD0 and QF0) is of fundamental importance. The stability of the magnetic fields is mainly impacted by vibrations of the quadrupole itself created by ground motion or by technical noise.

As observable we display the integrated r.m.s. $\sigma_x(f)$ of the spectral density of absolute displacements of the magnetic field centre of the quadrupoles, with $\Phi_x(f)$ being the power density of the displacements.

$$\sigma_x(f) = \sqrt{\int_f^\infty \Phi_x(v) dv} \quad (2.14)$$

As a first approximation we can formulate that $\sigma_x(f)$ shall stay below 1.5 nm above 1 Hz in the vertical direction (see §2.6) for all quadrupoles in the main linac. Similarly, it shall stay below 5 nm in the

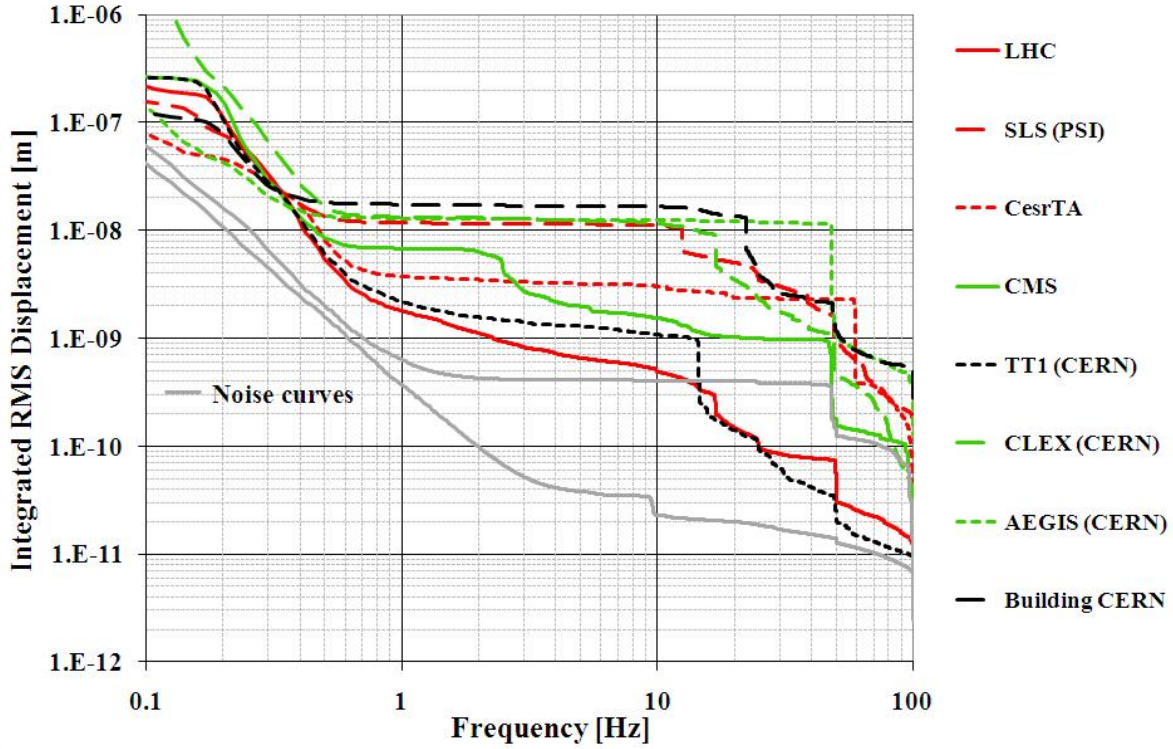


Fig. 2.28: Integrated vertical r.m.s. displacement at a variety of particle accelerators locations

horizontal direction. For the final focus quadrupoles the tolerances are even tighter (see §5.12). Several comparisons of measurements of the ground vibrations are available in the literature [84, 85]. The vibrations measured on the ground are composed of a seismic background superimposed with the technical or ‘cultural’ noise linked to human activities. The measurement of the seismic background was made in deep and remote locations, in geologically stable rock configurations. In such locations, integrated r.m.s. displacements of 0.5 nm at 1 Hz were measured. Models have been developed to represent this seismic background, like the ATL law [86] or the USGS Low-Noise Model [87]. Figure 2.28 shows measurements made by CERN in 2009 in various representative locations at night. The two light grey lines show measurements from very quiet places (only seismic vibrations), whereas the others show a variety of additional technical noise in accelerator locations.

Figure 2.29 shows as an example a recently obtained result in the laboratory, when a prototype quadrupole (type-1) was stabilized with an active feedback system. A gain of about 20 could be achieved bringing the residual quadrupole vibration within specifications of the CLIC project.

Assessment and outlook

The stabilization of structures at the nanometre scale is a concern in various fields of precision engineering such as interferometers, microscopes, or in the manufacturing of electronic components. The concept proposed to reach such a stability for the CLIC MBQ is a mechanical stabilization system under each quadrupole plus a very stringent requirement for low technical noise in the CLIC main tunnel. To a certain extent the active stabilization system will also counteract the technical noise of the tunnel installations, which, by design, will have to be kept to a very low value. Exact specifications will be obtained from the full-scale prototypes of the two-beam accelerator modules (see §5.6) currently being built. The basic setup comprises high-resolution motion sensors on the outer shell of the quadrupoles, piezo-based actuators in an arrangement to control five degrees of freedom of the quadrupoles, and a

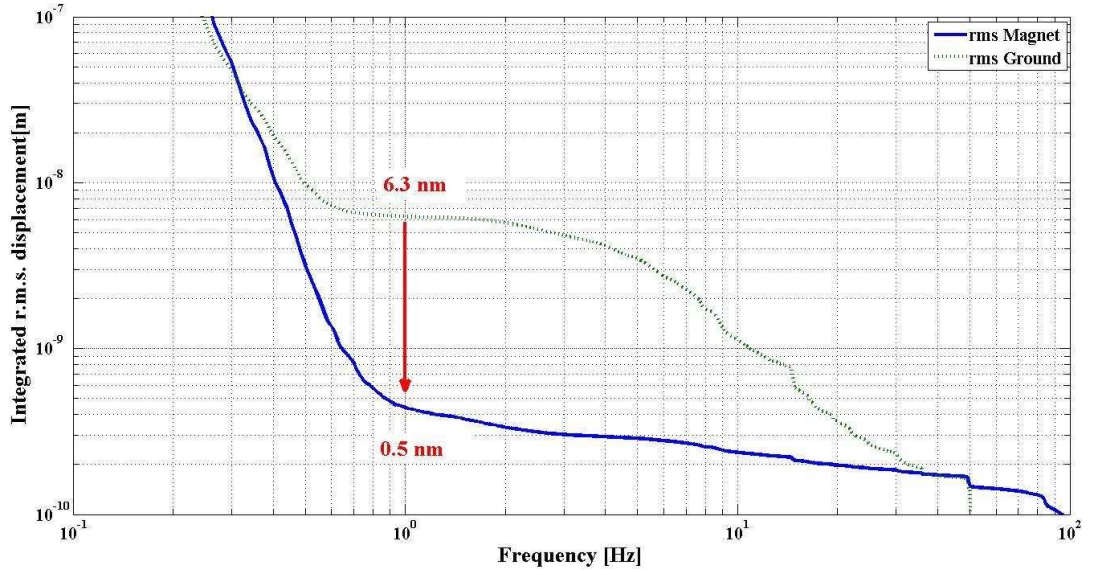


Fig. 2.29: Integrated vertical r.m.s. displacement measured under laboratory conditions at a Type-1 Main Beam quadrupole with feedback ‘on’ and ‘off’

real-time stabilizing feedback system.

From Fig. 2.28 it can be seen that the measured integrated r.m.s. displacements are one to two orders of magnitude larger than the specifications for the quadrupole stability in the Main Linac in the final focus system. The present assumption is that the stability of the magnetic centre can be achieved by stabilizing the position of the external magnet yoke in a feedback system, for which a closed loop gain of 10–100 seems feasible. Many more details on this subject are given in §5.18. The assumption that the stability of the magnetic-field axis can be achieved by stabilizing the outer shell of the quadrupoles will have to be verified with independent measurements (e.g., laser interferometry on the position of the pole tips or beam experiments measuring directly the deflection of the beams [88]). According to the present schedule, in 2013 three prototype two-beam acceleration modules will be installed in the CTF3 facility and there will be a first assessment of the technical noise levels for the CLIC Main Linac.

During the last few years of technology development the following additional requirements were identified, linked to the technical integration of the stabilization components into the complete linac.

- The stabilization system should be fully integrated in the module design. The combined height of alignment and stabilization systems should allow a beam height at 620 mm.
- The stabilization system should be compatible with the stringent alignment requirements.
- The stabilization system should be compatible with the accelerator environment, in particular with the expected radiation levels.

The problem of quadrupole stabilization seems to be solved in principle, but many technical design problems and choices will need to be addressed during the coming years.

2.7.4.2 High-precision mechanical pre-alignment of the Main Linacs

Requirements and technological solution

The pre-alignment of CLIC accelerator components will take place without beams in the linacs. In general a two-step approach is proposed:

1. A classical mechanical pre-alignment system yielding an accuracy of ± 0.1 mm r.m.s. with respect to the Metrological Reference Network (MRN). This system will use jacks for the adjustment and needs local intervention of technicians.
2. An active remotely controlled pre-alignment system. This active system will only be needed for the Main Linac (ML) and the Beam Delivery System (BDS), which have tighter tolerances on pre-alignment than the other parts of the accelerator. These tighter tolerances are formulated such that for a sliding window of 200 m, the standard deviations of the transverse position of each component with respect to a straight line fit must be less than a few micrometres. Since this system would be used over the whole linac typically every two weeks, only a fully remote-controlled system is feasible.

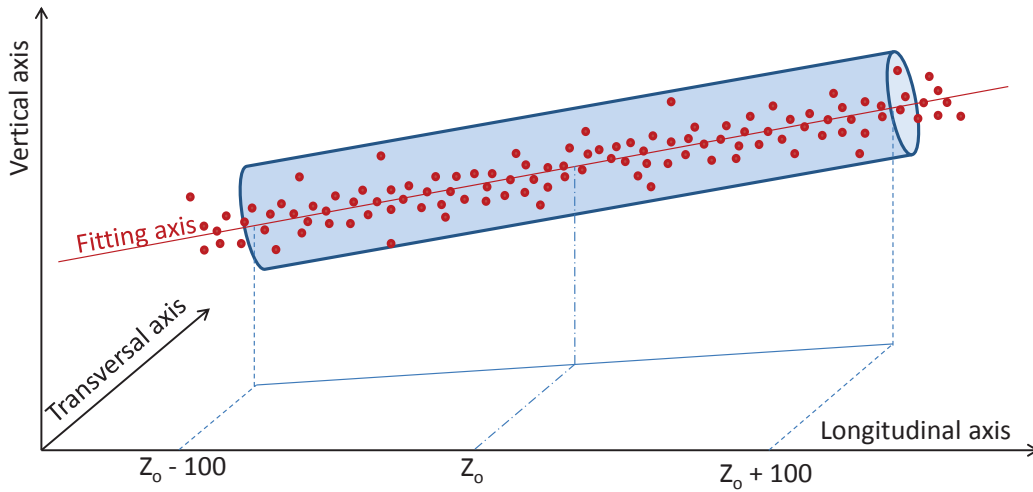


Fig. 2.30: Illustration of the alignment tolerance

The radius of the cylinder in Fig. 2.30 over a sliding window of 200 m describes well the total error budget allocated to the absolute positioning of the major accelerator components. Along the Main Beam (MB), it is equal to $14 \mu\text{m}$ r.m.s. for the RF structures and to $17 \mu\text{m}$ r.m.s. for the Main Beam Quadrupoles [89]. In the BDS, the total error budget is $10 \mu\text{m}$ r.m.s. for all components [90]. The sensitivity of the main linac to positioning errors is not the same for the different wavelengths in the distortion pattern, so future integrated simulations will allow a refinement, i.e., probably a small loosening of the above specifications. For the moment a first specification based on the r.m.s. if the positioning error is sufficient.

The active pre-alignment consists of two sequential actions: the determination of the actual position of each component and the re-adjustment of these components to their nominal position through the remote-controlled actuators.

The determination of the position of each component is carried out as follows: First, as it is not possible to implement a straight alignment reference line over the full length of the linac, overlapping references of at least 200 m will represent the straight reference [91]. This is the purpose of the primary network, called the Metrological Reference Network (MRN). The MRN propagates the accuracy of the alignment needed: a few micrometres over more than 200 m. A secondary network, the Support Pre-alignment Network (SPN), framed by the MRN network, associates sensors to each support structure to be aligned with an accuracy of a few micrometres over 10 m. A third step is required to link every support structure to the components to be aligned: this is the Alignment and Fiducialization of those

2.7 PRESERVATION OF ULTRA-LOW EMITTANCES

components on the supports (AFC).

The proposed technical solution consists of stretched wires with Wire Positioning Sensors (WPS). WPS sensors are biaxial ecartometers, based on a capacitive technology, measuring transverse offsets, in the sensors' frame of reference, with respect to a stretched wire. The resolution is sub-micrometre over a range of 10 mm [92].

Once the position of the components is known, the re-adjustment phase can take place. In order to simplify the re-adjustment, several components are pre-aligned on supports. Two types of supports are involved: girders for the RF components of the Main Beam and the Drive Beam, and interface plates for MB quadrupoles. DB and MB girders will be interlinked with their extremities, based on the cradles. This allows movement in the transverse girder interlink plane within three degrees of freedom (DOF), while the longitudinal direction is adjusted with micrometric mechanical guiding. The MB quadrupole is mounted on an interface plate allowing an adjustment along five DOF (the longitudinal axis will be blocked longitudinally after initial mechanical alignment) [93].

Assessment and outlook

The requirements of CLIC can be met with a further refinement of a stretched-wire-based alignment system. Such systems are a standard solution in most existing accelerators and the emphasis had been to improve these systems in order to match the requirements of a very long linac tunnel and the high demand of accuracy. The currently proposed solution has proven to be adequate, but it remains complicated and costly. Hence the emphasis of the next few years will be to search actively for an alternative, which more precisely means a system based on a 'laser wire'. Given the length of CLIC such an optical system has to operate under vacuum and the fundamental question will be how to intercept the laser beam with sensors without disturbing its straight propagation and also on how to translate the once measured reference position inside the vacuum to fiducials outside the vacuum tube. This new development together with studies of further cost reduction of the present wire system will be the focus of the next few years.

2.7.4.3 Distribution of femto-second timing throughout the accelerator complex

Requirements and proposed solutions

Most of the text in this section is taken from Ref. [94]. In CLIC there are three critical longitudinal tolerances that directly impact luminosity:

- the relative arrival time of the colliding bunches at the interaction point;
- the relative phasing of the two crab cavities;
- the relative phasing between Drive Beam and Main Beam in each sector of the two-beam accelerators.

Relative Main Beam arrival time

If the two beams do not arrive at the same time at the nominal collision point, they will collide before or after this point. Since the β -function increases around the collision point (so-called 'hourglass effect'), the beam sizes will then be larger than nominal, which leads to a luminosity reduction. The tolerance on the Main Beam to Main Beam timing jitter is 22 μm or 66 fs for 1% luminosity loss. There is a possibility to correct for some errors by dynamically changing the focusing of the final quadrupoles, or by accelerating the beam slightly just before them. This would ensure that the minimum beam-waists occur at the point of collision but would also move the collision point longitudinally within the detector as the relative timing of the two Main Beams varies. The resulting longitudinal jitter of the collision point seems to be acceptable for the physics analysis of the events.

Phasing of the crab cavities

Crab cavities are used in CLIC to rotate the bunches before the collision such that they collide with no crossing angle, see §5.5.4. A difference of the RF phases in the crab cavities on the electron and on the positron side leads to a horizontal offset of the two beams at the collision point. While the static difference can be corrected with the orbit feedback system, the dynamic difference needs to be limited. A relative phase stability of 0.01° is required to limit the luminosity loss to 1%.

Drive Beam phase and amplitude jitter

Jitter of the Drive Beam current, bunch length, or phase in the decelerators will lead to jitter of the amplitude or phase of the RF that accelerates the beam in the Main Linac. This will lead to energy errors of the Main Beam along the linac, which in turn can lead to luminosity loss via two main effects. Firstly, the energy bandwidth of the BDS is limited. Hence too large an energy jitter of the beam entering the BDS will lead to luminosity loss. Secondly, the beam energy error along the linac can lead to emittance growth.

Luminosity loss due to energy errors

The Main Beam is accelerated with an average RF phase of about 12° before crest. Consequently a phase jitter of $\Delta\phi = 0.1^\circ$ leads to an effective gradient error of 3.6×10^{-4} . The RF phase is not constant along the linac. Over the main part a phase typically smaller than 12° is used to provide a correlated energy spread in the beam for BNS damping. At the end of the linac a phase of 30° is used in order to compress the beam energy spread to the target r.m.s. value of 0.35%. Hence phase jitter in the end of the linac will impact the beam energy more than at the beginning.

A more detailed description of these effects can be found in §3.8.

Meeting these strict requirements to achieve high luminosity is one of the fundamental problems of the CLIC design. The solution to this is rather complex and will be achieved on several levels:

- by proper accelerator physics design of the accelerator subsystems in order to make them the least sensitive to known sources of jitter and imperfections.
- by proper technical design of the subsystems to achieve good stability. For example, special efforts have been made in recent years to achieve the required intensity, energy, and phase stability of the Drive Beam in CTF3. The results obtained look promising and are reported in Chapter 7.
- by designing real-time feed-forward systems acting on dynamic imperfections during each beam pulse. Good candidates for this are a feed-forward in the turnaround of the Main Beam before the long linac, by which the arrival time of one Main Beam can be slightly changed with respect to the other, and a feed-forward system in the turnarounds of the Drive Beam, in which the phase of the Drive Beam with respect to the Main Beam can be modified. Typically these feed-forward systems are designed to accommodate a factor 10 of control range between the required tolerances and the dynamic errors of the subsystems in question.
- by designing slow feedback loops correcting for quasi static imperfections based on measured averages of arrival times and relative beam phases.
- by modelling all these feedback loops and feed-forward systems and ensuring by the proper choice of parameters that they do not interact with one another.

Timing reference

There are many user devices in the CLIC accelerator complex demanding a clock reference in the femtosecond domain. The most stringent requirements come from the relative phasing of the crab cavities

2.7 PRESERVATION OF ULTRA-LOW EMITTANCES

(which will be solved by a common power source and a length-compensated wave-guide system) and the relative phasing of the Main Beam and Drive Beam as described above.

For example, in order to achieve the required phase stability of 46 fs of any Drive Beam with respect to the Main Beam, the measurement used for feed-forward correction must be better than 23 fs and the timing reference must be better than 10 fs. There are two distinct options for such a timing reference. The first uses local oscillators at all measurement/correction locations. They are synchronized with the outgoing Main Beam, which constitutes the global reference of the machine. The second option constructs a global timing reference distributed from a central generation point, i.e., a system similar to that presently proposed for the European X-FEL.

Beam-based timing

In the first strategy, the Main Beam is used as the timing reference for the phase jitter correction system. The Main Beam is picked up in the outgoing direction, and its timing relative to a stable local oscillator is established. This information is then stored until the arrival of the Drive Beam, up to 160 μ s later (corresponding to the return trip time for a 24km linac), and used in the final calculation of timing mismatch between the beams [95]. The required highly stable local oscillators exist, with a minimum integrated time jitter (<10 fs over 160 μ s) and two have been ordered for beam tests in CTF3. The phase monitors are being developed and will also be tested.

Central master clock and femtosecond timing distribution (XFEL type)

The second strategy has been explored to meet the challenging European X-FEL timing requirements. They have thus developed a centrally generated timing reference, distributed through stabilized optical fibres. Optical synchronization with <10 fs resolution has been demonstrated over \sim 300 m at DESY [96]; but the extension of the deployed technologies to long distances represents several technological challenges.

Stability of RF signal transmission:

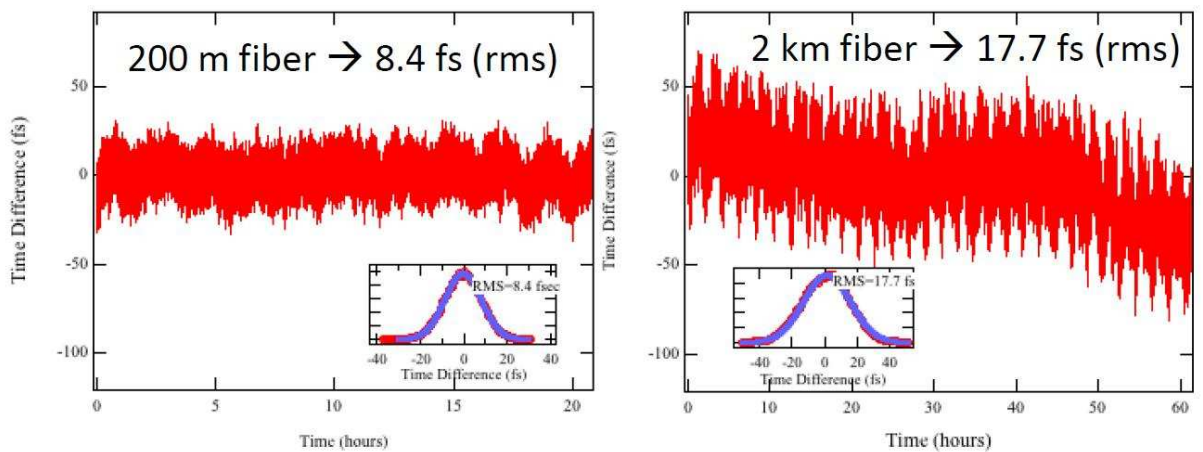


Fig. 2.31: Residual timing jitter for different transmission lengths

Figure 2.31 (taken from Ref. [97]) depicts the deterioration of jitter, when the fibre length is increased by an order of magnitude. More details can be found in §5.14.

Assessment and outlook

For the two different timing systems we find the following final beam–beam jitter at the interaction point:

$$\sigma_{\text{BB}} \approx \sqrt{2} \left(\sigma_{\text{MB}} \oplus \frac{6}{7} [\sigma_{\text{MB} \rightarrow \text{LO}} \oplus \sigma_{\text{LO} \rightarrow \text{RF}}] \right) \quad (2.15)$$

$$\sigma_{\text{BB}} \approx \sqrt{2} \left(\frac{1}{7} \sigma_{\text{MB}} \oplus \frac{6}{7} [\sigma_{\text{ref}} \oplus \sigma_{\text{ref} \rightarrow \text{RF}}] \right) \quad (2.16)$$

where the symbol \oplus describes the spectral convolution of the noise spectra, which in the case of no correlation corresponds to the root of the quadratic sums.

Equation (2.15) is valid when using the outgoing Main Beam as a reference, where σ_{MB} is the timing error of the outgoing Main Beam, $\sigma_{\text{MB} \rightarrow \text{LO}}$ the error of the local oscillator with respect to the Main Beam, and $\sigma_{\text{LO} \rightarrow \text{RF}}$ the error in correction of the RF phase. Equation (2.16) is valid for an X-FEL type timing system with σ_{ref} the error between the central timing reference and the one at the final turnaround, and $\sigma_{\text{ref} \rightarrow \text{RF}}$ the error in correction of the RF phase.

It can be clearly seen that the X-FEL-type timing system is less sensitive to errors in timing between the two Main Beams. The primary challenge is to scale up such a system to CLIC size while maintaining stability of the reference below 10 fs.

In case of beam-based timing, the problem of reference stability is already solved. But the system requires seven times tighter relative phasing tolerances for the two Main Beams after the RTML. This tolerance could be relaxed if this error is measured in the central complex before the Main Beams are sent to the linacs. In this case one could shift the position of the beam waists at collision longitudinally to reduce the luminosity loss. This can be achieved by a feed-forward that either uses fast quadrupoles or changes the beam energy slightly just before the final doublet.

As a CLIC-scale global timing reference seems, at the present time, to be far from implementation, the beam-based timing system remains attractive, in particular if one develops the ability to feed-forward on the Main-Beam to Main-Beam jitter, thus reducing the sensitivity to Main-Beam generation errors. But even if this solution is retained, an X-FEL type timing system would complement the beam-based timing system for diagnostics. It is hard to imagine how one could disentangle the performance of all phase detectors and feed-forward systems without a stable point of reference for comparative measurements.

2.8 Machine protection

2.8.1 Overview

The machine protection system for CLIC has to cope with a wide variety of failures, from real-time failures (RF breakdowns, kicker misfiring), to slow equipment failures, to beam instabilities caused by, for example, temperature drifts and ground motion.

Owing to the many different types of accelerator components and the beams of various characteristics throughout the complex, CLIC machine protection is an extensive subject. The machine protection system has the mission to protect the various machine components from damage caused by ill-controlled beams. The severity of the damage is given by the financial impact of the damage and the reduction in the operational availability of the facility. The risk equivalent is given by the product of the fault rate and the impact of the fault (i.e., in statistical terms risk is the expectation value of the fault impact).

The machine protection system should reduce the risk to a level where it becomes acceptable. An acceptable risk can be expressed by the notion that the total expected operational downtime from all risk terms should be smaller than a few per cent and likewise, that the total expected financial impact is also less than a few per cent of the operational cost.

2.8.2 Strategy

As there are various sources of failure, the machine protection for CLIC will deploy a wide spectrum of machine protection strategies. These strategies are summarized in Fig. 2.8.2 and are explained below.

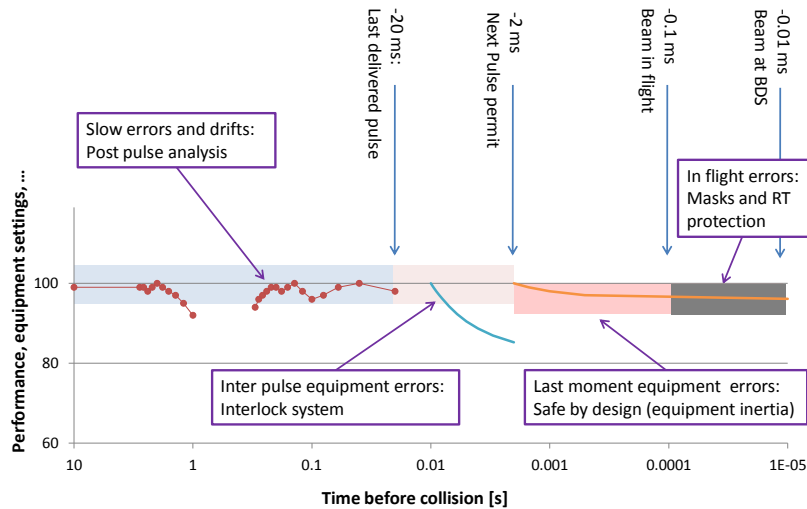


Fig. 2.32: The various failure classes and corresponding protection strategies given as a function of the time left to the next beam collisions

The very short pulse lengths (156 ns for the Main Beam and 244 ns for the Drive Beam) of CLIC, make it practically impossible to correct real-time (RT) or ‘in-flight’ errors, i.e., once a pulse has been committed, there is not much that can be done to safely intercept the Main Beam or Drive Beam in the event that beam losses are detected. For a small set of cases where a circulating beam can be dumped, real-time protection is a possibility. Examples are the combiner rings, the damping rings, the Main Beam and Drive Beam turnaround systems. Also the overall Drive Beam pulse length will allow some real-time protection.

For the remaining cases of ‘in-flight’ failures, the machine protection system has to rely on fixed protection. Most notably, a fixed protection (i.e., mask) is needed to protect the extraction and transfer channels that follow any fast extraction or injection element. The design of the mask will be a challenging task as the charge density of the extracted beam is high enough to damage the mask. Special attention has to be given to the design of these masks (i.e., reusable surfaces) and to the reliability of the kicker systems. An example of the implementation of a mixture of active and passive protection is the final Main Beam collimation system. The transverse collimation system can potentially be destroyed by a full beam pulse, but orbit changes due to magnet failures or power converter failures can be detected in advance.

A very large failure class is made up of equipment failures. All failures occurring during the inter-beam period will be intercepted by the interlock system. As the interlock system has a finite signal-handling time, the interlock system will only cope with errors that are detected up to 2 ms before the next pulse permit is given. This implies that all the equipment circuits must be designed such that there is enough inertia in the system for the settings to stay within the tolerance required for safe beam passage during 2 ms.

The last class of failures are those caused by slow drifts (e.g., temperature and ground motion) that are not sufficiently well tracked by the feedback systems (e.g., due to saturation). The strategy to catch such slow drifts is to have a rigorous post-pulse analysis following every cycle and to allow the next pulse only if the performance of the previous pulse was well understood and within the limits of tolerance for safe beam passage.

2.8.3 Intensity ramps

The post-pulse analysis will inhibit the next pulse when the machine is not safe. This of course poses a problem as a successful pulse is required to establish the next pulse permit. In order to ‘bootstrap’ the next pulse permit following an interruption in the beam operation, a controlled intensity ramp will ensure that the machine intensity is gradually increased in a safe manner. In a machine with a completely unknown behaviour, the bootstrap starts with a beam charge density that cannot cause structural damage to the accelerator components. Each time a few pulses have been delivered successfully, i.e., without showing any problem in the post-pulse analysis, the beam intensity control authorizes a safe increase in the intensity.

Because of the high repetition rate, the expected time to perform a full-intensity ramp will be of the order of seconds (including possible machine setting optimization) provided that there are no errors that need operator or system expert assistance.

The detection of ill-controlled beam conditions by the post-pulse analysis will also be paired with a number of false positives, i.e., unjustified decisions to inhibit the next pulse permit. To limit the down time, caused by the intensity ramp associated with these false positives, to a few per cent, the rate of false positives has to be less than one per ten minutes. With an intensity ramp time of 10 seconds a false positive rate of one per ten minutes contributes $10/600 = 1.7\%$ to the dead time.

The limit on the false-positive rate puts constraints on the performance of the post-pulse analysis, specifically on the beam loss monitoring system. This further implies that an RF breakdown (estimated to occur somewhere in the whole machine once per 100 pulses) should not normally lead to a next pulse inhibit, but be recovered transparently by the RF and beam control systems.

2.9 Total power consumption

2.9.1 Overview

The total electrical power consumption of CLIC at a centre-of-mass energy, E_{CM} , of 3 TeV and for a luminosity $\mathcal{L}_{1\%} = 2 \times 10^{34} \text{ cm}^{-2} \text{ s}^{-1}$ is $P_{\text{tot}} = 582 \text{ MW}$. This estimation is based on detailed studies developed all through this volume. A schematic view of the CLIC complex is shown in Fig. 2.33. The breakdown between major systems is given in Table 2.5 and Fig. 2.34. Each entry includes the basic power need to which cooling, ventilation, instrumentation, and control needs are added. A proportional fraction of the losses of the electrical network for transformation and distribution is also included. A more detailed breakdown is discussed in the following. The production of the Drive-Beam power is the major contributor. The principle of the two-beam acceleration system is discussed in §2.4. Together with their overhead contributions, the two Drive-Beam linacs need a total of 305 MW to produce the overall Drive-Beam power, P_{DB} , of 141 MW which is transported to the two-beam modules in the main tunnels. A power of $P_{\text{DB-FT}} = 88 \text{ MW}$ feeds the frequency multiplication systems, the transport to the tunnels and the return loops at the entrance of each decelerator. In parallel to the Drive-Beam production and distribution, a power of $P_{\text{MB-FT}} = 74 \text{ MW}$ is needed to produce and form the Main Beams. This splits into approximately three equal contributions, namely sources (So), damping rings (DR), and transport (Tr) to the main tunnel. The power consumption of the main linacs, $P_{\text{ML}} = 67 \text{ MW}$ is shared between the magnets of the two lines (TBM, $\sim 30\%$), the cooling of the Drive-Beam power, and the absorption of the residual spent beam after deceleration ($\sim 70\%$). Finally, the last item covers the beam delivery system and the dump lines (27 MW) together with one experiment and its area (20 MW). The method used to arrive at these values is discussed below.

Table 2.5: Electrical power consumption for major systems of CLIC at 3 TeV for a luminosity of $\mathcal{L}_{1\%} = 2 \times 10^{34} \text{ cm}^{-2} \text{ s}^{-1}$. The power is the sum of the intrinsic power of a system and the contribution from auxiliary systems (instrumentation, control, cooling, ventilation, and electrical network).

System	Sub-system	Power [MW]	Fractional power
Drive-Beam production	Linacs	305	52 %
	Frequency multiplication and transport	88	15 %
Main-Beam production	Sources	23	4 %
	Damping rings	29	5 %
	Transport	22	4 %
Main Linac (TBM)		67	12 %
Beam delivery & experiment		47	8 %
Total		582	

2.9.2 Detailed power estimates

The power map presented here is split into sub-systems and their main components in Table 2.9. These data are grouped by type of technical component in Table 2.9.2 and Fig. 2.35. The two main components, namely radio-frequency and magnets, are discussed in the next two sections. The cooling and ventilation system is the third big contributor to power consumption, amounting to 14 % of the total. This is worked out in detail in §6.4. The power need of the experiment is somewhat indicative and was derived from the known consumption of LHC experiments. The contributions of the instrumentation and control systems is based on the number of components and compared to the LHC systems. This approximate estimate is

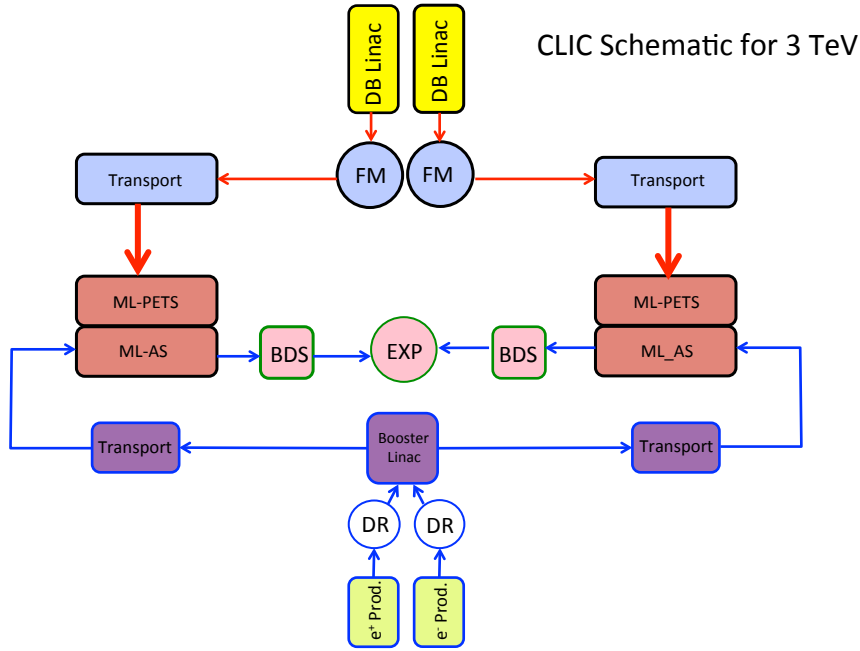


Fig. 2.33: The block diagram of the CLIC complex at 3 TeV. The Drive-Beam complex is made of two systems. Each of them consists of a source and a 1 GHz linac, followed by the frequency multiplication system (FM: delay loop and combiner rings) and the transport to the main tunnel down to each decelerator (PETS). The Main-Beam production is made up from two sources (electrons and positrons), each followed by a damping ring (DR), and a transport to the head of the Main Linac (ML). The Main Linac is made of two-beam modules, with PETS structures to decelerate the Drive Beam and feed the RF power to the Accelerating Structures (AS). The Beam Delivery System (BDS) prepares the Main Beam for high-luminosity collisions in the experimental area.

justified by the fact that these items contribute to only 3% of the total. The network contribution (5%) combines losses in voltage transformation and along distribution lines, see §6.3.

Table 2.6: The power map by technical components at 3 TeV for a luminosity of $\mathcal{L}_{1\%} = 2 \times 10^{34} \text{ cm}^{-2} \text{ s}^{-1}$. The total power is 582 MW.

Component	Power [MW]	Fractional power
RF (DB+MB)	289	50%
Magnets (DB+MB)	124	21%
Cooling & ventilation (CV)	93	16%
Network	28	5%
Beam instrumentation & controls (BIC)	17	3%
Detector & experimental area	31	5%

2.9.2.1 Drive Beam and Main Linac RF

The detailed power flow for the RF of the Drive-Beam production and main-linac acceleration is presented in Fig. 2.36. The data shown include RF items only, excluding the overhead of cooling, network, and auxiliary systems. The Frequency Multiplication system which is mostly made of magnets does not

2.9 TOTAL POWER CONSUMPTION

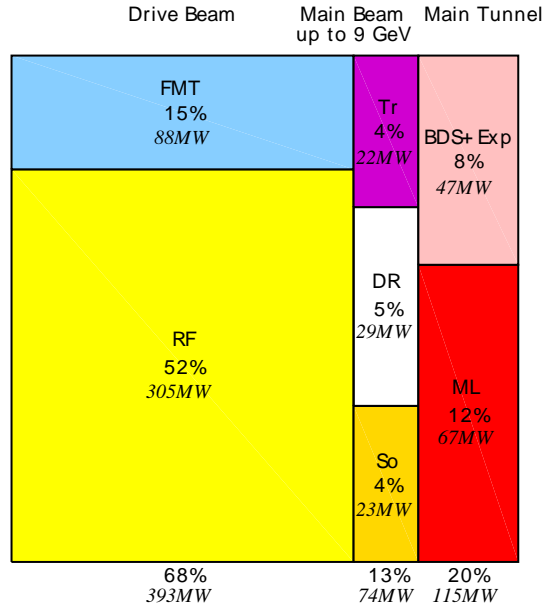


Fig. 2.34: The power consumption for CLIC at 3 TeV by main systems, see text and Table 2.5. The total power is 582 MW. The contribution of each system is made up of its own consumption to which a proportional fraction of contributions from cooling, ventilation, network losses, beam instrumentation and control is added. RF: power for the Drive-Beam Linac, FMT: frequency multiplication and transport. So: e^- and e^+ sources and acceleration up to 2.5 GeV, DR: damping rings, Tr: Booster Linac up to 9 GeV and transport. ML: Main Linac, BDS+Exp: beam delivery system, main dump, one experiment and its experimental area.

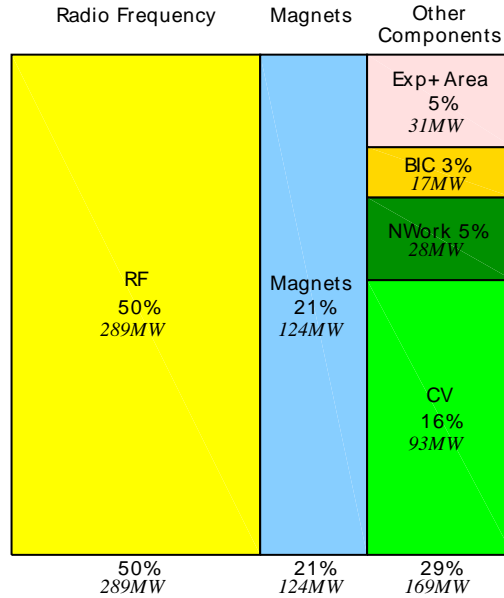


Fig. 2.35: The power consumption for CLIC at 3 TeV by technical components. The total power is 582 MW. All of the RF systems of either the Drive-Beam or the Main-Beam complexes are grouped under 'RF'. The magnet contribution of all systems is grouped under 'Magnets'. The contributions of auxiliary systems appear separately: Cooling and Ventilation (CV), Electrical Network Losses (NWork), and Beam Instrumentation and Control (BIC). The components of the experiment and its area are grouped into a single item (Exp+Area).

appear here in the figure. Every sub-system is optimized for best efficiency. Options under study for the modulators are discussed in §5.8.3. An efficiency $\eta_{\text{mod}} = 0.89$ is worked-out considering a flat-top yield of 0.95 combined with short rise and setting times (3 and 5 μs respectively). An R&D program is underway to meet these challenging parameters. The technology of klystrons is quite mature. The quoted yield $\eta_k = 0.7$ slightly exceeds the best achieved performance today (0.68) and so still requires some R&D. The overall yield of power transfer between the klystron and the Drive Beam is $\eta_{\text{rf}} = 0.89$. It combines the extraction from the klystrons, the wave-guide, the coupler, small ohmic losses in the structures, and slightly off-crest acceleration needed for beam stability. After frequency multiplication (from 1 GHz bunch spacing to 12 GHz) the 141 MW of Drive-Beam power is transported to the deceleration lines in the main linac. The fully loaded PETS structure has a nearly perfect yield of $\eta_{\text{pets}} = 0.98$ but the beam cannot be fully decelerated due to the adiabatic increase of beam size and the onset of instabilities. A relative residual beam power of 17% must be dumped at the exit of each decelerator. As a result, the effective yield of the system is $\eta_{\text{decel}} = 0.81$. Finally the yield $\eta_{\text{mb}} = 0.25$ of the Main Beam accelerating structures is the result of an optimization between the quest for a large accelerating gradient to contain the length of the linacs, good efficiency, and the minimization of detrimental wakefield effects to preserve the small emittance of the beams, see §2.3. The overall yield of the RF system, from the power input of the modulators, 255 MW, to the Main-Beam power, 28 MW, is $\eta = 0.11$.

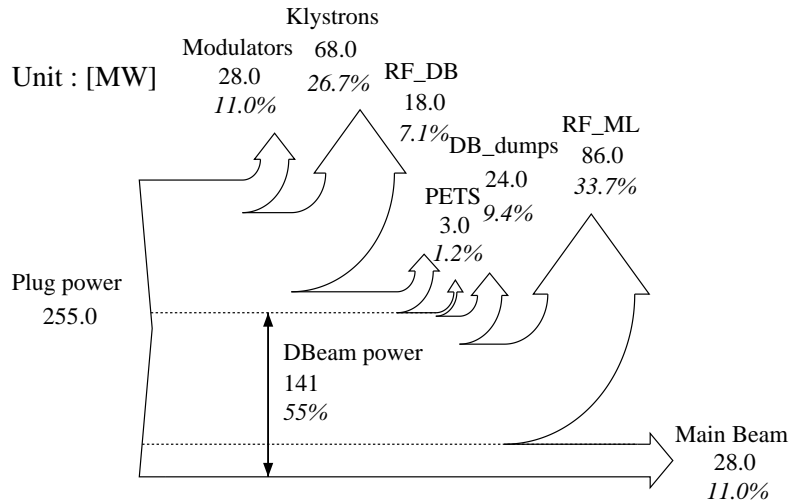


Fig. 2.36: The power flow for the main RF system of CLIC at 3 TeV. No overhead included for cooling, ventilation, or network. Arrows pointing upwards correspond to power losses at each stage of the system.

2.9.2.2 Other RF systems

Most of the other RF systems are used to produce the Main Beams (injectors, intense electron beam for positron production, damping rings, and booster linac). These systems are dominated by the constraints imposed by the production of ultra-low emittance beams. The margin left for power optimization is small and is not considered here.

2.9.2.3 Magnets

An optical layout exists for most of the beamlines. This allowed a detailed specification and basic design of the magnets. The use of normal-conducting magnets is the choice at this stage of the project, for

2.9 TOTAL POWER CONSUMPTION

their reliability, precision, and flexibility in operation. Design considerations can be found in §5.2. The optimization is made with classical cost considerations including capital and power consumption over the expected lifetime of the project. The powering is studied in detail for linacs where the gradient of every magnet is different. A clever proposal to strongly reduce the cabling and the power consumption in the main tunnel is discussed in §5.8. For the other beamlines, the powering technology is mature and cannot be significantly further optimized. The overall magnet power including cooling and network overhead is 156 MW, or 27 % of the total power of 582 MW. The use of alternative magnet technologies in order to reduce the power consumption is briefly discussed in §2.9.5.

2.9.3 Overall efficiency

An overall power flow is shown in Fig. 2.37. To the sole RF power map presented in §2.9.2.1 for Main-Beam acceleration, a fraction of the power of auxiliary systems (mainly cooling, ventilation and network losses) must be added. The two-beam scheme requires a Drive-Beam production at 1 GHz followed by a frequency multiplication to 12 GHz bunch spacing through combiner rings (items 9 to 12 in Table 2.9). Finally, the two lines of the main linac need 67 MW for the focusing magnets, the Drive-Beam dump lines and the cooling of the dissipated Drive-Beam power $P = P_{DB} - P_{MB} = 141 - 28 = 113$ MW which is not transferred to the Main Beam. Therefore, the overall yield of the Main-Beam acceleration up to the end of the main linac is 6.1%. Adding the production and the transport of the Main Beams at 9 GeV, the BDS and the experimental area (items 1–6, 16–18 in Table 2.9), the yield of plug-power to beam is 4.8%. A proportional fraction of auxiliary systems is added to every system. Data corresponds to those displayed in Fig. 2.34

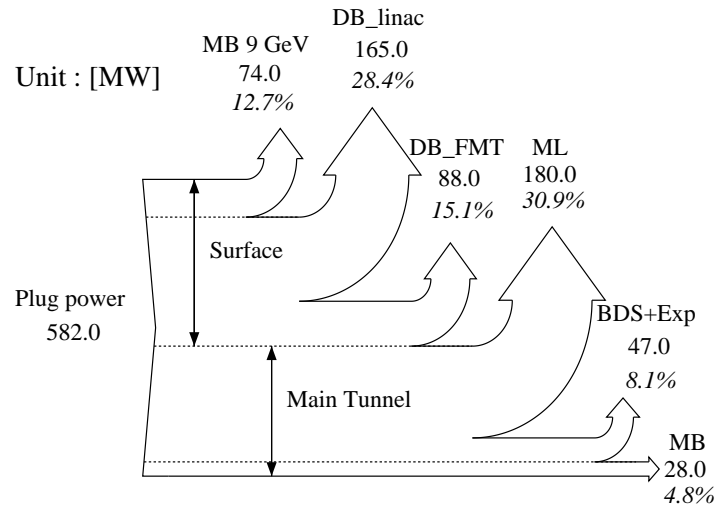


Fig. 2.37: The overall power flow for CLIC at 3 TeV. Arrows pointing upwards correspond to power losses at each stage of the system. Each item contains its contribution to cooling and ventilation, network losses, beam instrumentation, and control power needs.

2.9.4 Energy consumption

The total power $P = 582$ MW will be used in nominal beam conditions during a fraction of the year. The machine will be stopped for a long shutdown of approximately 90 days per year for scheduled maintenance. Considering a short technical stop of 2 days every two weeks (reset of non-critical faulty

equipment) and a longer one of 7 days every two months (maintenance), 54 days must be further subtracted. Therefore programmed stops amount to 144 days leaving 221 days for production. Additional stops associated with faults are estimated using LHC data, where 20% of beam time is lost. With ten times more active elements, CLIC cannot be expected to have better availability. With the same figure, an additional down-time of 44 days must be assumed, leaving 177 days of production at nominal power. During stops there is a minimal residual power consumption, mostly in order to maintain ventilation and cooling or heating in buildings and tunnels and some control systems. This is estimated to be $P = 60$ MW. The yearly energy consumption $E = 2.74$ TWh per year in Table 2.7 integrates both the days of operation and the stops.

Table 2.7: Yearly energy and power consumption for the nominal 3 TeV CLIC

	Power [MW]	Days	Energy [TWh]
Nominal operation mode	582	177	2.47
Fault-induced downtime	60	44	0.06
Programmed stops	60	144	0.21
Energy consumption per year			2.74

2.9.5 Potential for power and energy savings

2.9.5.1 Options for lower magnet consumption

Reducing the power consumption of the magnet systems requires the use of either permanent magnets or super-ferrie superconducting magnets. The latter option which allows one to reduce the consumption by a factor ~ 3 has not been considered explicitly but may be promising for lumped systems like the combiner rings or the return loops of the Drive-Beam trains in the tunnel (items 9 and 11 in Table 2.9). A preliminary study of mechanically tunable permanent quadrupoles for the decelerators (item 14 in Table 2.9) is discussed in §5.2. Permanent magnets cannot be considered in cases where the nominal field is too high or when heavy synchrotron radiation power impacts on their vacuum chamber. Overall, but subject to further studies, a decrease of power consumption by a factor 2 can be considered when using either alternative magnet technology in every system where applicable without loss of performance. The power budget for magnets might therefore go down from $P = 124$ MW (see Table 2.9.2) to $P \simeq 62$ MW. This is subject to further detailed studies in the next phase of the project.

2.9.5.2 Cooling and ventilation

The power consumption for cooling and ventilation $P = 93$ MW (see Table 2.9.2) is split between water cooling (33 MW) and ventilation (60 MW). For water cooling, little reduction can be expected. A large fraction is used in the main linac, where very tight mechanical tolerances prevent one from considering large ΔT operation. Ventilation is needed both for temperature regulation (cooling in summer, heating in winter) and air replacement (control of humidity and health requirements). The air flow is fixed by the more demanding of the two criteria. This varies from case to case (surface building or tunnel, size, etc.). A detailed study must be made for each element of the CLIC complex in order to optimize precisely the power consumption of the ventilation system. But considering several improvements (improved thermal insulation of surface buildings, natural ventilation, increased fraction of heat removal with water, use of heated water for air heating, etc.), an estimate for an economy of 30% , or 20 MW on this power can be considered. As for water, a reduction of 4 MW will come from the alleviated cooling duty for the magnets (see §2.9.5.1). The power budget would therefore decrease to $P = 93 - 24 = 69$ MW. This should be confirmed by further studies. A balance with investment costs must be worked out and the

2.9 TOTAL POWER CONSUMPTION

usual construction standards for industrial building must be considered for specific cases.

2.9.5.3 Other components

The main item of power consumption at CLIC is the normal-conducting RF (Drive-Beam production, RF only: 255 MW). The quoted efficiency is already rather optimized, and must still be partially demonstrated (modulators, klystrons, see §2.9.2.1) before considering further improvements. Recirculation schemes cannot be envisaged, because of the small residual Drive-Beam power $P = 25$ MW which is split between 48 decelerators and where the beam quality is poor.

2.9.5.4 Summary for savings

Considering the improvements discussed here, the total power need for nominal operation could be reduced by 86 MW (62 MW for magnets and 24 MW for CV), while the power consumption during stops becomes 40 MW. The reduced energy consumption per year is given in Table 2.8. Compared to the nominal case shown in Table 2.7, the yearly energy consumption is reduced by 16%. This can be obtained without considering big technological jumps, but associated additional investment costs remain to be evaluated.

Table 2.8: Yearly energy and power consumption with improved power management.

	Power [MW]	Days	Energy [TWh]
Improved nominal operation mode	496	177	2.11
Fault-induced down-time	40	44	0.04
Programmed stops	40	144	0.14
Energy consumption per year			2.29

2.9.5.5 Other considerations related to energy management

With RF systems and magnets operated at room temperature (nominal case), CLIC can be turned off quickly and down to a small residual power consumption. This can be conveniently exploited with respect to global network needs in two ways. The CLIC operation schedule can be optimized for network peak-power saving on diurnal and seasonal basis. Similarly, CLIC can be turned down to small power consumption at short notice in case of unexpected network overload.

2.9.5.6 Waste heat recovery

The large production of heat, in excess of 2 TWh per year, can be considered as a secondary source of energy, but with two difficulties. First, the temperature increase of the cooling water through either magnets and RF systems is of the order $\Delta T = 20$ K. Secondly, the power consumption over the year is not constant, with scheduled and unwanted stops. Only in limited cases such as the beam dumps, may the heat rejection temperature be increased to thermodynamically interesting values. In the other cases, the rather small ΔT can be increased by using heat pumps, but at additional cost. The need for warm water on the CLIC site for heating is limited and largely inferior to the potential production. Therefore, a use at larger scale must be considered (e.g., connection to an urban heating complex or industrial use of the heat). Warm water may also be used to provide cooling through absorption or adsorption cycles. Again, the needs of the CLIC site are relatively small and a wider approach must be considered with external users. An effective study requires an expert approach and can be only be envisaged in the technical design phase of the project.

Table 2.9: Detailed direct electrical power map at 3 TeV for a luminosity of $\mathcal{L}_{1\%} = 2 \times 10^{34} \text{ cm}^{-2} \text{ s}^{-1}$

Item no.	System	Power [MW]
1	MB injectors magnets	1.0
2	MB injectors RF	16.5
3	MB PDR+DR magnets	5.1
4	MB PDR+DR RF	17.2
5	MB transport	16.5
6	MB long transport line	0.5
7	DB injectors solenoid+magnets	6.8
8	DB injectors RF	255.2
9	DB FM	18.5
10	DB transport to tunnel	3.0
11	DB transport in tunnel	39.1
12	DB long delay line	0.0
13	TBM MB	4.9
14	TBM DB	13.3
15	DB post decelerator	10.6
16	BDS	1.6
17	Interaction area	16.3
18	MB dump line	3.3
19	Instrumentation main tunnel	10.0
20	Instrumentation (other)	4.0
21	Controls main tunnel	2.0
22	Controls (other)	1.0
23	Experiments	15.0
Sub-total		462.0
24	Cooling + ventilation	93.0
25	Network losses	28.0
Total [MW]		582.0
Total [MVA]		609.0

2.10 Assessment of the CLIC feasibility

Table 2.10 summarizes the present level of achievements in the CLIC feasibility studies as identified in §2.2. The individual issues have been described in detail in §2.4 to §2.7. The following text makes an assessment issue by issue.

Table 2.10 summarizes the present situation of the so-called ‘CLIC feasibility demonstration’.

Table 2.10: Critical parameters of CLIC feasibility issues

System	Item	Feasibility Issue	Unit	Nominal	Achieved CLIC	
				Value	Value	Where
Accelerating structures	Drive beam generation	Accelerating field (loaded/unloaded) for 176.5 ns flat top RF pulse duration and $<3 \times 10^{-7}$ /m RF breakdown rate	MV/m	100/120	~103	KEK,SLAC
		Fully loaded accel. effic.	%	97	95	CTF3
		Freq. & current multiplication factors	–	$2 \times 3 \times 4$	2×4	CTF3
		Combined beam current (12 GHz)	A	$4.2 \times 24 = 100$	$3.5 \times 8 = 28$	CTF3
		Combined pulse length (12 GHz)	ns	240	140	CTF3
		Intensity stability	10^{-3}	0.75	<0.54	CTF3
Two-beam acceleration	Beam-driven RF power generation	Drive Beam linac RF phase stability	Deg (1 GHz)	0.05	0.035	CTF3, XFEL
		PETS RF Power	MW	136	>140	CTF3/SLAC
		– with PETS flat top RF pulse duration	ns	176.5	–	–
		– and PETS breakdown rate	/m	$<1 \times 10^{-7}$	–	–
		PETS ON/OFF	–	–	–	CTF3(TBTS)
		Drive-Beam-to-RF efficiency	%	90%	26%	CTF3(TBL)
		RF pulse shape control	%	$<0.1\%$	–	CTF3(TBTS)
	Two-beam Acceleration	Power production and probe beam acceleration in two-beam module with nominal pulse duration	MV/m	100	145	CTF3(TBTS)
		Drive to Main Beam timing stability	ps	0.05	–	–
		Main to Main Beam timing stability	ps	0.07	–	–
Ultra-low emittance & beam sizes	Ultra-low Emittances	Norm. emittance generation	H/V (nm)	500/5	3800/15	ATF, NSLA/SLS
		Emittance preservation: blow-up	H/V (nm)	160/15	160/15	Simulation
	Nanometre beam sizes	Strong focusing: β^* eff/L* from IP	mm/m	0.1/3.5	2.0/1.0	ATF2
		Nanometre beam sizes at IP	H/V (nm)	40/1	70	FFTB, ATF2
	Alignment	Main Linac components	μm	14–17	–	Align. & mod. test bench
		Main Linac reference points	μm	10	14	–
		Beam Delivery System components	μm	10	–	–
	Vertical stabilization	Main Linac Quad.	nm > 1 Hz	1.5	0.5	Stabilization test bench
Operation and Machine Protection System		Final doublet (with feedback)	nm > 4 Hz	0.2	0.13	–
		Drive Beam power at 2.4 GeV	MW	72	–	–
		Main Beam power at 1.5 TeV	MW	14	–	–
						Simulations

A large part of the feasibility issues has been addressed in the purpose-built and commissioned CLIC Test Facility (CTF3) [98] described in Chapter 7. The other issues have been addressed in dedicated test benches or in important test facilities, especially NLCTA [99] and ASTA [100] at SLAC, Nextef [101], ATF [102] and ATF2 [103] at KEK and CesrTA [104] in Cornell.

2.10.1 Accelerating structures

Accelerating structures are the components of the main linacs with the most significant impact on the performance, cost, and overall extent of the CLIC complex. The target accelerating gradient, 100 MV/m, is very challenging and is roughly a factor two above the present state of the art. The gradient must also be achieved maintaining an RF-to-beam-transfer efficiency in the order of 30%.

An impressive R&D program on accelerating structures has been carried out over the past 20 years in close collaboration with SLAC and KEK and has taken advantage of the developments which have addressed similar issues in the framework of the NLC/GLC study. As described in §2.3, outstanding results have been achieved, although with low statistics, culminating with fully equipped structures demonstrating nominal performances of accelerating fields larger than 100 MV/m, with nominal pulses of 240 ns and extremely low breakdown rates (Fig. 2.38). Specifically:

1. The ‘first generation’ series of T18 structures, designed by the CLIC team and built and tested at SLAC and KEK achieved nominal performance with a remarkably high reproducibility. The design was made using newly-developed high-power scaling laws while fabrication was based on the well-established methods developed during the NLC/GLC program. The 20% reduced performance of the TD18 series, which are equipped with damping slots, is believed to be due to excessive pulsed surface heating.
2. An improved RF design: the T24 structure, with optimized surface fields and higher RF-to-beam efficiency, demonstrated excellent performance with an unloaded accelerating field of more than 120 MV/m; the input power for this gradient is the same as that required for a loaded gradient of 100 MV/m. So the structure fulfils the above specifications at the nominal CLIC RF pulse length and breakdown rate.
3. The CLIC baseline TD24 structure, equipped with damping slots, demonstrated an accelerating field of 100 MV/m during an RF pulse of 412 ns with a breakdown rate of $5 \times 10^{-5}/\text{m}$. This corresponds to an accelerating gradient of 97 MV/m after scaling to the nominal pulse length and breakdown rate, and is thus very close to the nominal field of 100 MV/m.

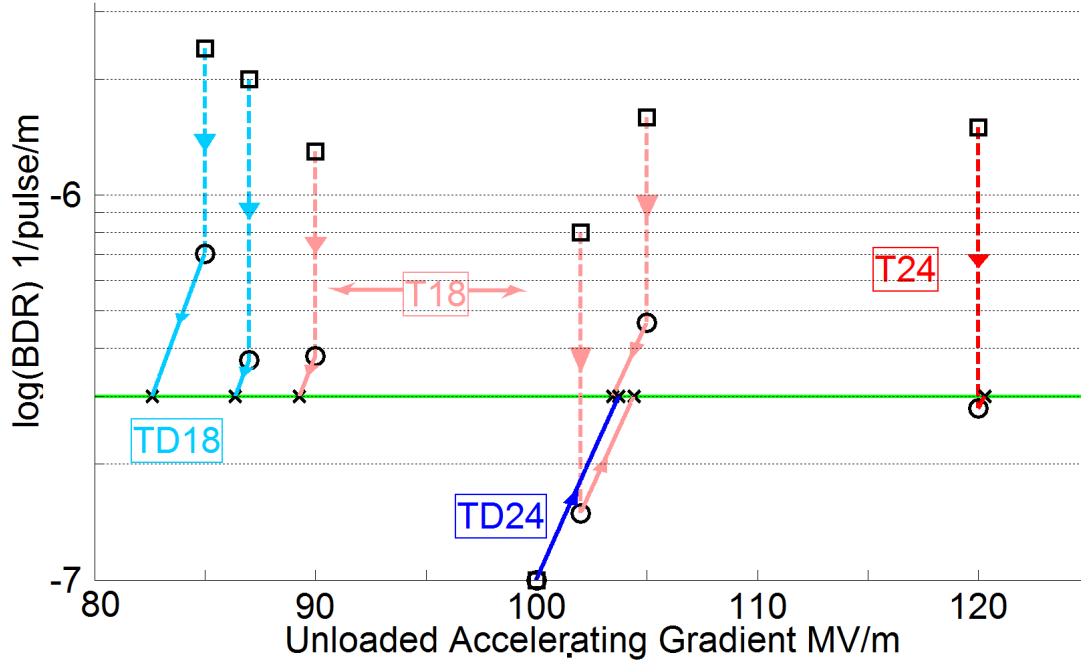


Fig. 2.38: Accelerating Structure performances scaled to CLIC nominal breakdown rate of various series. T18=inspired from NLC structure, TD18=same including damping, TD24=CLIC baseline structure, T24=same without damping.

The CLIC accelerating structure development programme has strongly benefited from the outstanding developments made during the NLC/GLC program and the continuing involvement of experts from SLAC and KEK. The beam-driven Two-Beam Test Stand (TBTS) and Test Beam Line (TBL) in CTF3 provide essential complementary information. They are, however, limited to a repetition rate which is too low to measure accelerating structures at nominal breakdown rates. The repetition rate limitation is due to limited shielding of the CTF3 building. Consequently a klystron/modulator-based 12 GHz test stand, like those at KEK and SLAC, is being built at CERN. It is based on a 12 GHz 50 MW klystron which has been successfully developed by SLAC but is only now available for tests. Therefore, all tests of structures presented here have relied on X-band Power Stations available at SLAC [99] and KEK [101] as a key contribution to the CLIC study. Unfortunately, the access to these facilities is restricted due to

other priorities. The progress on the development of the CLIC accelerating structures has therefore been primarily limited by the availability of X-band power sources. Such a limitation will have to be overcome for significant progress to be made in the next CLIC development phase, which will concentrate on improving performance and demonstrating the statistical and long-term behaviour of structures.

2.10.2 Drive Beam generation

The feasibility of the novel scheme of Drive Beam generation presented in §2.4 is fully demonstrated by the successful design, installation, commissioning and operation over several years of the CLIC Test Facility, CTF3, although with slightly different parameters, as summarized in Table 2.11 and outlined in Chapter 7.

Table 2.11: CLIC and CTF3 major Drive Beam parameters

Parameter [units]	CTF3	CLIC	Ratio CLIC/CTF3
Intensity & frequency multiplication factor	$2 \times 4 = 8$	$2 \times 3 \times 4 = 24$	3
Bunch charge [nC]	2.3	8.3	3.3
Bunch repetition frequency [GHz]	12	12	1
Beam current (linac) [A]	3.5	4.2	1.05
Beam current (combined beam) [A]	$3.5 \times 8 = 28$	$4.2 \times 24 = 100$	3.6
Intensity stability in linac [10^{-4}]	5.4	7.5	1.4
RF phase stability [$^\circ$]	0.07 (3GHz)	0.05 (1GHz)	0.7
RF power stability [10^{-3}]	2.1	2.0	0.95
Pulse length (1 sector/24 sectors) [ns]	140	240/5760	1.7/41
Beam energy [MeV/c]	120	2370	19.8
Pulse repetition rate [Hz]	0.8–5	50	10
Beam power (1sector/24sectors) [MW]	0.003	3/72	1000/24000

2.10.2.1 Source

The two options of Drive Beam generation, by either thermionic gun or photo-injectors, have been tested and are both feasible, each with their pros and cons. The present CLIC baseline relies on a thermionic gun. As an alternative, a photo-injector will be considered as soon as it has proven high enough performance, stability and reliability. CTF3 is based on a thermionic gun with similar nominal beam intensity of 3.5 A. The CTF3 injector reached up to 7 A.

2.10.2.2 Acceleration by Drive beam Acceleration (DBA)

A high beam intensity of 4 A is accelerated up to 120 MeV in a specially designed fully-loaded Drive Beam Accelerator (DBA) linac and has been operated routinely in CTF3 for several years with an RF-to-beam efficiency of 95% close to the CLIC nominal value of 97% (Fig. 2.39). A 3 GHz RF frequency, a factor three higher than the nominal CLIC DBA, has been adopted in CTF3 to reduce the cost since modulators and klystrons were available from the LEP Injector Linac (LIL). The extrapolation to the lower CLIC DBA RF frequency of 1 GHz with wakefields substantially smaller will make the beam even more stable in CLIC. Owing to limited RF power stations, the beam acceleration in CTF3 is limited to 120 MeV instead of the CLIC value of 2.4 GeV. CTF3 is a valid bench-mark since it covers the low-energy part of the CLIC DBA which is the most sensitive to instabilities and blow-up. The beam current provided by the CTF3 DBA is similar to the CLIC DBA but with a charge per bunch lower by a factor of 3.6. The beam stability, which is mainly driven by the beam current, is therefore fully demonstrated

given that beams of up to 7 A have been accelerated in the first half of the CTF3 linac for 30 GHz power production, with no sign of any instability. Limitations to the bunch charge for a given current could come from space charge effects in the injector, below 20 MeV. However, comparison between PARMELA simulation results for CTF3 and CLIC injectors shows no significant effects for transverse and longitudinal emittances.

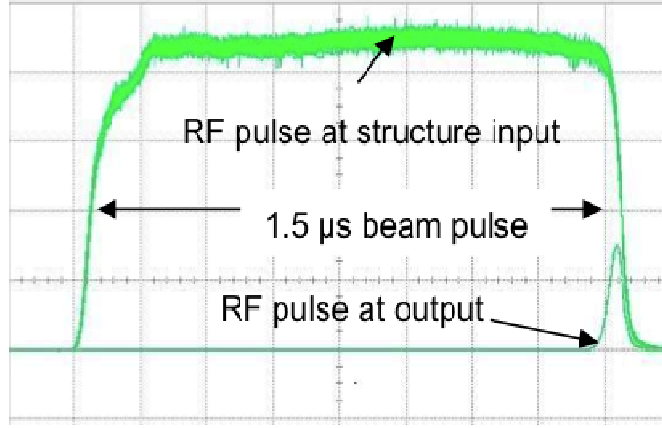


Fig. 2.39: Scope traces of RF pulse at a DBA structure input and output when accelerating a 1.5 ms Drive Beam pulse. All the RF energy is transmitted to the beam, except for a small transient at the trailing edge and resistive losses on the short cavity walls.

2.10.2.3 Intensity and frequency multiplication by beam combination

A beam combination with a multiplication factor 8 in intensity and bunch repetition frequency has been successfully demonstrated in CTF3, resulting in a beam intensity of 28 A and 12 GHz bunch repetition frequency (Fig. 2.40). As a consequence, the feasibility of the CLIC first stage combination by a factor 2 in a delay loop and by a factor 4 in a combiner ring with similar initial beam intensity is fully demonstrated. The additional multiplication by a factor 3 in a second multiplication stage, as foreseen in CLIC, is very similar and should not be problematic. The successful experiment with an operational energy of 150 MeV is very valid since beam simulations show a more stable beam at the nominal CLIC DBA energy of 2.4 GeV in spite of its 100 A intensity. The pulse length is limited by the ring geometry which was initially designed for 30 GHz operation. Longer-than-nominal beam pulses have also been demonstrated although with a smaller combination factor.

2.10.2.4 Intensity stability

The very challenging beam intensity stability of 7.5×10^{-4} , imposed for energy stability of the Drive Beam in the DBA and for the Main Beam in the main linac, has been achieved and measured at the output of the CTF3 linac. The stability for a Drive Beam that is either only combined in the combiner ring or only in the delay loop is between 1 and 2×10^{-3} , and for the fully combined beam is still at the per cent level. Further feedback improvement will be implemented in the future to provide a margin for safe and reliable operation.

2.10.2.5 RF phase and amplitude stability

The very challenging RF phase stability of 0.05° necessary in the DBA to limit Drive Beam bunch length errors in the final bunch compression, has also been achieved and measured in CTF3 (Fig. 2.41). The maximum pulse-to-pulse jitter of a 10 ns long piece of the bunch train is 0.07° , the jitter of the average phase of the train is 0.035° . The RF power stability requirement is 0.2%, which has almost been achieved

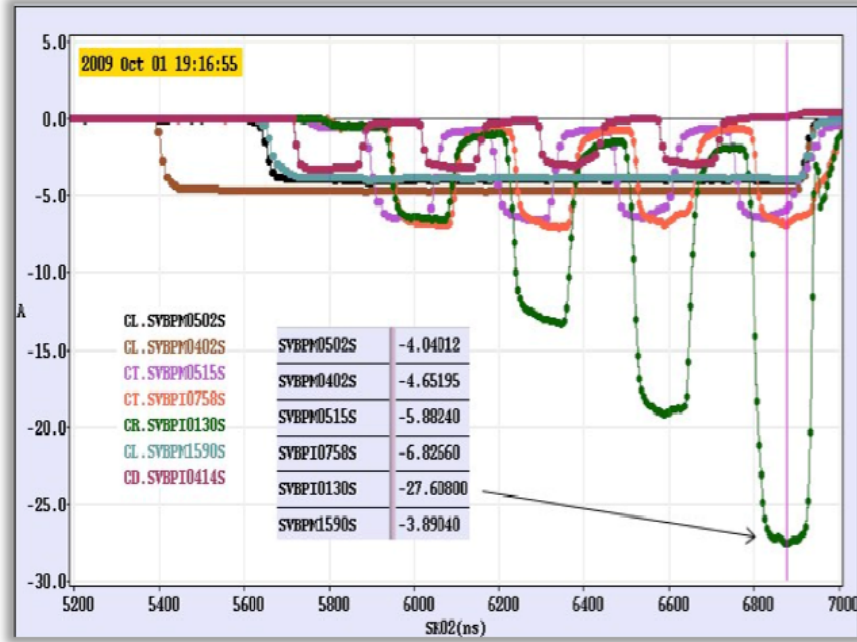


Fig. 2.40: DBA intensity and frequency multiplication by a factor 8 as measured in CTF3

in CTF3 with a jitter of 0.21%. A feedback loop is currently implemented in order to improve further the performance stability and provide a tuning tool.

2.10.2.6 Beam current and power

The Drive Beam current in CTF3 is lower than in CLIC by a factor of 3.6. The final beam energy is smaller by a factor of 20, hence the handling of the beam is more difficult in CTF3 in most respects and the beam current related issues are largely addressed. However, two Drive Beam parameters are not fully addressed in CTF3. These are the full beam pulse length, which is about two orders of magnitude larger in CLIC, and the average beam power, which is lower by more than four orders of magnitude with respect to the full CLIC Drive Beam which powers 24 sectors in 3 TeV operation. This is due to the shorter pulse duration, lower energy, and lower repetition rate in CTF3.

We expect that the issues related to the longer pulses and higher beam power can be handled. It is foreseen to test this in a more substantial facility, CLIC0, as a first part of the project implementation.

2.10.3 Beam-driven RF power generation

The feasibility of beam-driven RF power generation has been successfully demonstrated in two different ways:

1. The feasibility of the PETS operation at a peak RF power level $\sim 7\%$ higher and with RF pulses $\sim 10\%$ longer compared to the CLIC requirements has been successfully demonstrated in klystron driven experiments at SLAC (Fig. 2.42 (left)). The tests at a fixed power level were ended when the measured breakdown trip rate was close enough to the CLIC specification of 1×10^{-7} /pulse/m. In this test the PETS was operated for 80 hours without any breakdown ($BDR < 2.4 \times 10^{-7}$ /pulse/m), before it had to be removed from the test stand. The demonstration has been done in a more

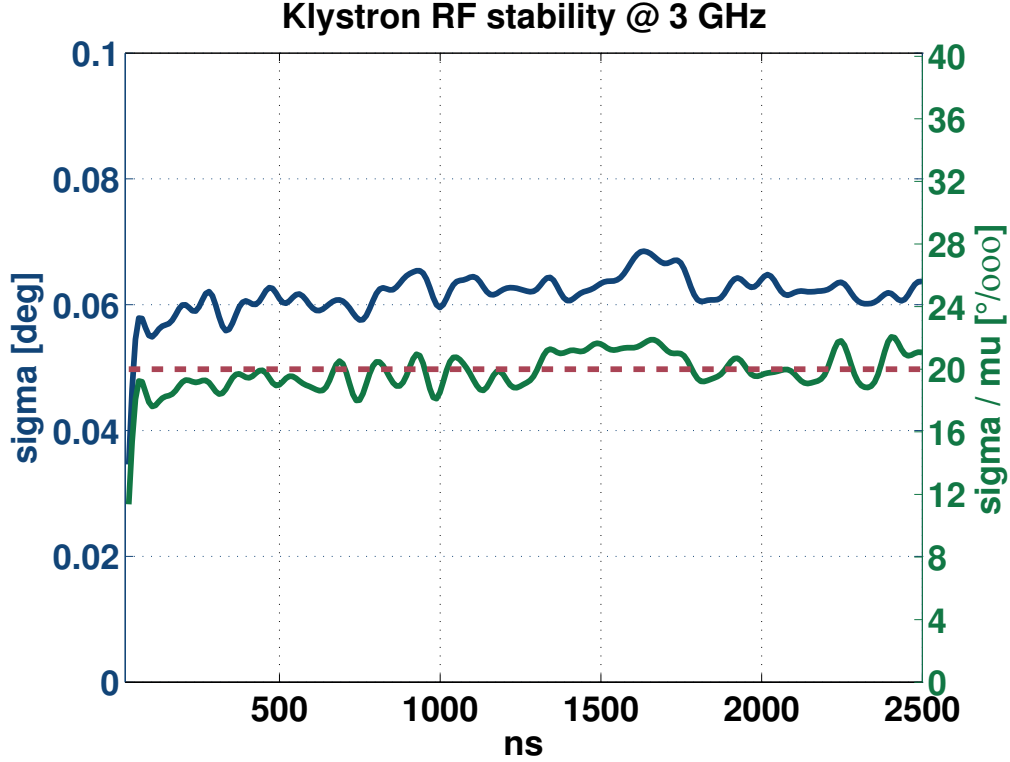


Fig. 2.41: Measured RF amplitude and phase stability

demanding environment than needed for CLIC with an extra input coupler and a uniform RF power distribution along the structure. The PETS was equipped with damping material.

2. In CTF3, the scaled 1 m long PETS was operated in beam-driven mode with external RF recirculation in order to compensate for the lack of Drive Beam current in CTF3 when operated with beam pulses as long as specified in CLIC. PETS routinely produces RF power with peak levels well above the CLIC specifications (Fig. 2.42 (right)). Firm conclusions about breakdown rates cannot be deduced from these experiments because of insufficient statistic (CTF3 operates at 1 Hz repetition rate). However, in most cases (>90%), the breakdowns occur in the waveguide recycling loop and not in the PETS itself.

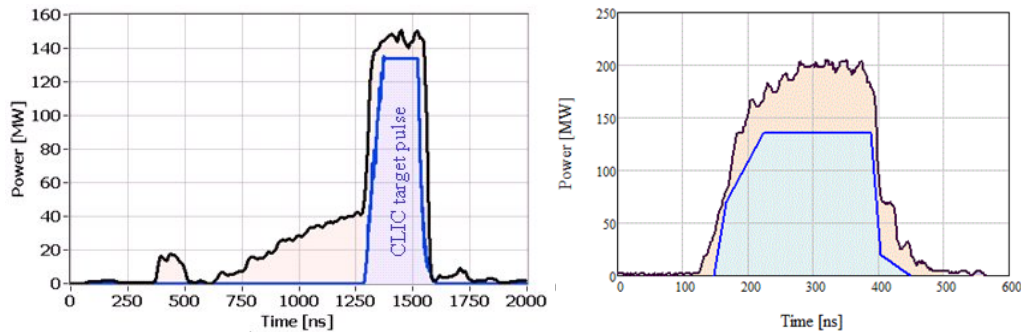


Fig. 2.42: Typical RF pulse shape in klystron driven (left) and beam driven (right) experiments. For reference the shape of the CLIC target pulse is plotted (blue).

An ON/OFF mechanism with a novel concept based on external commutation and internal anti-phase RF recirculation has been designed, built, and successfully tested with beam at power levels above

CLIC nominal (Fig. 2.43). In the OFF position, the RF power extracted from the Drive Beam in a steady state is reduced to 25% of its original value, which is enough to prevent, or to dramatically reduce the probability of RF breakdown in the PETS itself. At the same time, the RF power delivery to the accelerating structure is completely suppressed. In Fig. 2.43, the pulses for the two extreme positions (ON and OFF) are shown.

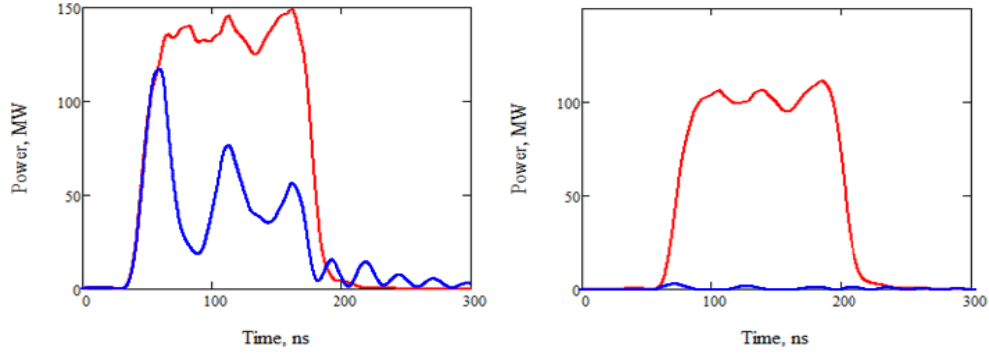


Fig. 2.43: RF pulses generated by PETS (left) and delivered to the accelerating structure (right). The pulses for ‘PETS ON’ are shown in red and the pulses for ‘PETS OFF’ in blue.

Finally, a test beam line (TBL) was installed in the CLEX building of CTF3 to study the CLIC decelerator beam dynamics and the 12 GHz power production by a series of PETS structures. The beam line consists of a FODO lattice with high-precision BPMs and quadrupoles on movers for precise beam alignment. A total of 16 PETS will be installed between the quadrupoles to extract 12 GHz power from the Drive Beam provided by CTF3. The fully combined Drive Beam with a bunch-train length of 140 ns, 12 GHz bunch repetition frequency, and an average current over the train of up to 28 A will be injected into the test beam line. Each PETS structure will produce 135 MW of 12 GHz power at nominal current corresponding to the nominal PETS output power in CLIC. The beam will have lost more than 50% of its initial energy of 150 MeV at the end of the beam line and will contain particles with a large spread of energies between 65 MeV and 150 MeV. Owing to the low initial energy of CTF3, a demonstration of 90% energy extraction from the CTF3 Drive Beam is not possible. Since most aspects of the transport of this beam in TBL are more challenging than for the CLIC case due to the lower initial energy, the CTF3 experiment is considered significant to demonstrate the CLIC decelerator.

So far, nine PETS have been installed. The maximum power produced in one PETS structure has been about 60 MW with a 21 A beam without any signs of breakdown. Up to 26% of the beam energy has been extracted. The measured power production is in agreement with the theoretical predictions using the measured RF output power from each PETS, the beam current and bunch form factor and as well with the decelerated energy profile of the beam at the end of the line (Fig. 2.44). A first measurement of the BPM resolution measuring the trajectory of the beam in three consecutive BPM to take out the effects of beam jitter has been performed. For a beam with 13 A average current, 9 mm resolution was measured which corresponds well to the specified resolution of 5 mm for the nominal beam current of 28 A.

2.10.4 Two-beam acceleration

The demonstration of the novel scheme of two-beam acceleration is critical for the credibility and feasibility of the CLIC scheme. As described in Chapter 7, two-beam acceleration has been successfully demonstrated with beam in the CTF3 Two-Beam Test Stand (TBTS) experiment. A larger than nom-

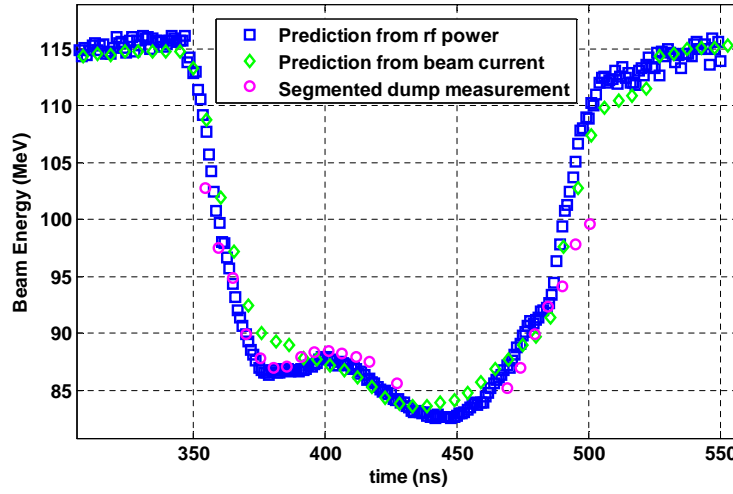


Fig. 2.44: Comparison between the measured time-resolved energy profile of the beam along the pulse with a segmented beam dump and the predictions from beam current and power production measurements. The prediction from the beam current uses a measured bunch form factor of 0.85. In this example a 20 A beam was decelerated by 31 MeV averaged over the pulse width corresponding to 26% energy extraction.

inal acceleration field of 145 MV/m has been achieved in a baseline CLIC accelerating structure, fed with RF power produced by a PETS equipped with recirculation, and driven by a high-intensity Drive Beam generated in CTF3. As a consistency check, it was used to accelerate a probe beam (Fig. 2.45). All parameters from the Drive Beam, from the produced RF power to the probe beam acceleration are consistent with the theoretical model of RF power production, transfer and beam acceleration.

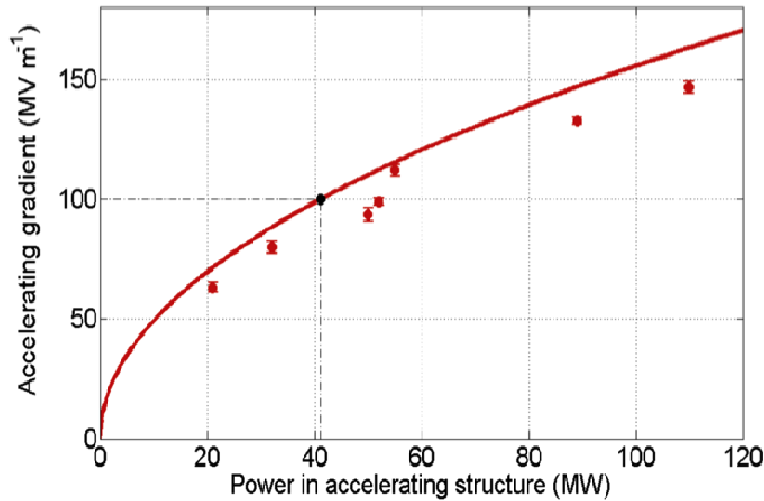


Fig. 2.45: RF power vs. measured accelerating gradient during two-beam tests in CTF3, using a nominal TD24 accelerating structure. The continuous line corresponds to the theoretical maximum expectation.

2.10.5 Two-beam-module integration

Two-beam modules (TBMs) constitute the building blocks of the 21 km long linacs which have 20 760 modules per linac. Their design, fabrication, and installation in large series is particularly critical for CLIC operation, performance, and cost. As described in §5.6, the five different types of modules have been designed with a compact integration of all components necessary for two-beam acceleration including RF structures and network, magnets, instrumentation, vacuum, pre-alignment, stabilization, cooling and supporting systems (Fig. 2.46). They are equipped with prototypes or mock-ups of the various components. Four modules have been built using various technological options, installed in a string test and tested in the laboratory, namely two modules of Type-0 (without any quadrupole), one Type-1 (with one short quadrupole), and one Type-4 (with one long quadrupole). The fabrication, installation and operation of the string test fully confirm the feasibility and operability of all types of TBMs with a nominal linac filling factor, thus preserving the effective accelerating field. The string test has been extremely fruitful for:

1. studying the integration, interference and compatibility of the various systems such as the coupling between the drive and main linacs or the alignment and stabilization perturbations by technical noise like cooling, ventilation, etc.
2. comparing measurements of various kinds of supporting systems with analytical models derived from thermo-structural analysis
3. measuring deformations and misalignment induced by transport.

A small module length of 2 m has been adopted for the sake of alignment and stability but this implies a large number of components and associated high cost.

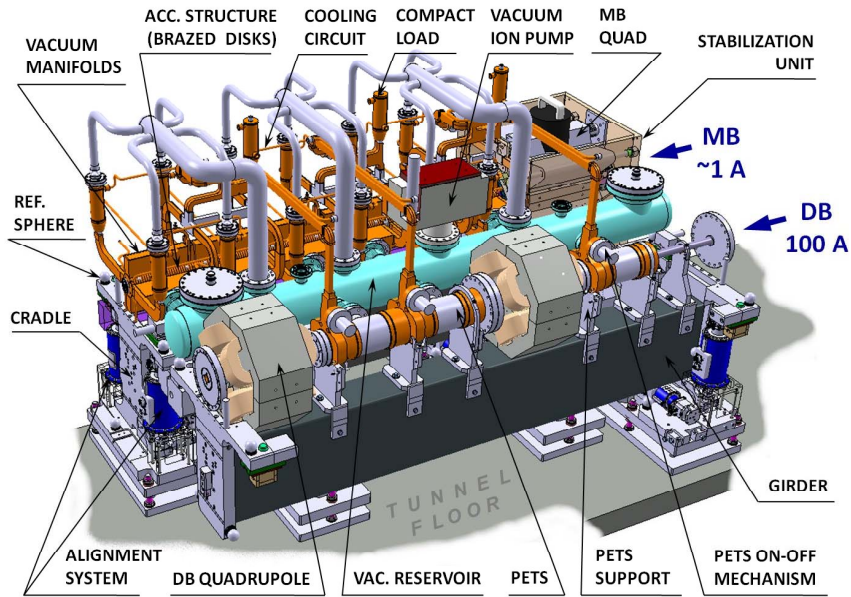


Fig. 2.46: 3D integration study of a two-beam module

A second generation of three additional modules, taking into account the lessons learnt during the string test study in the laboratory, is being prepared for future tests with beam in the CLEX area of CTF3.

Owing to their large number and the compact integration of many components, the two-beam modules have been clearly identified as a major CLIC cost driver. Even if demonstrated to be feasible, the adopted technological options, e.g., the module and structure lengths, will have to be critically reviewed during the next CLIC phase in order to

1. mitigate the number of components and thus the cost of each module
2. optimize their fabrication and installation in large numbers by industrialization.

2.10.6 Emittance generation

The beam emittances at collision at the Interaction Point (IP) are particularly critical for the CLIC luminosity. The ultra-low specified figures require generation of electron and positron beams with a minimum emittance and their tight preservation during acceleration and focusing.

As pointed out in §2.2, the specified normalized beam emittances of 500 nm and 5 nm at the exit of the injector complex are challenging with a factor 7 and 3 smaller than the present state of the art in the horizontal and vertical planes respectively (Fig. 2.47). They are generated by the Damping Rings for both electron and positron beams. As described in §2.6 and §3.2, a Damping Ring has been designed with performances better than the CLIC specifications of 500 nm and 5 nm in the horizontal and vertical planes respectively. The Damping Ring design relies on a race-track shape with arcs equipped with compact Theoretical Minimum Emittance (TME) cells and long straight sections housing a large number of super-conducting wigglers with high field and short period. Prototypes have been built and successfully tested.

All critical design issues have been addressed with convincing schemes as described in §3.2, specifically:

1. Large Intra beam Scattering (IBS) and space charge tune shifts mitigated by lattice design.
2. Ion beam instability due to high bunch density mitigated by Secondary Emission Yield (SEY) reduction with special coatings of the vacuum chamber.
3. High beam loading due to the large beam current in cavities with a RF frequency of 1 GHz mitigated by RF structure design and appropriate feedbacks.
4. High beam stability at extraction by special design of extraction kickers.

Prototypes of every critical component are being built and are foreseen to be tested with beam in existing facilities, especially the dedicated Test Facility, CesrTA in Cornell [102] for tests of fast ion instability and electron cloud activity in coated vacuum chambers with low Secondary Emission Yield (SEY).

The feasibility of small emittance generation is addressed experimentally by the purpose-built Accelerator Test facility (ATF) in KEK [103]. It has demonstrated emittances of:

1. 3000 nm and 12 nm in single bunches with low charge in the horizontal and vertical planes respectively therefore a factor 6 and 2.5 larger than the nominal CLIC specifications. Adding the emittance growth budgets until the end of the main linac, the emittance would be a factor 4.8 and ~ 1.6 larger than the target.
2. 3800 nm and 15 nm in single bunches with a charge similar to the one specified for CLIC @ 3 TeV in the horizontal and vertical planes respectively; therefore a factor 7.6 and 3 larger than the nominal CLIC specifications.

ATF already achieved, with single bunch, the CLIC geometrical vertical emittance of 1 pm (Fig. 2.48), although with a large spread between the various measurement methods.

The latest generation of light sources like the Swiss Light Source (SLS), Diamond, and the Australian Synchrotron storage ring have reported geometrical vertical emittances below 2 pm, with coupling coefficients of less than 0.1%. In particular, the Swiss Light Source storage ring [104], routinely delivers this emittance, corresponding to 18 nm normalized, at high intensity similar to the one envisaged in the CLIC Damping Ring.

2.10 ASSESSMENT OF THE CLIC FEASIBILITY

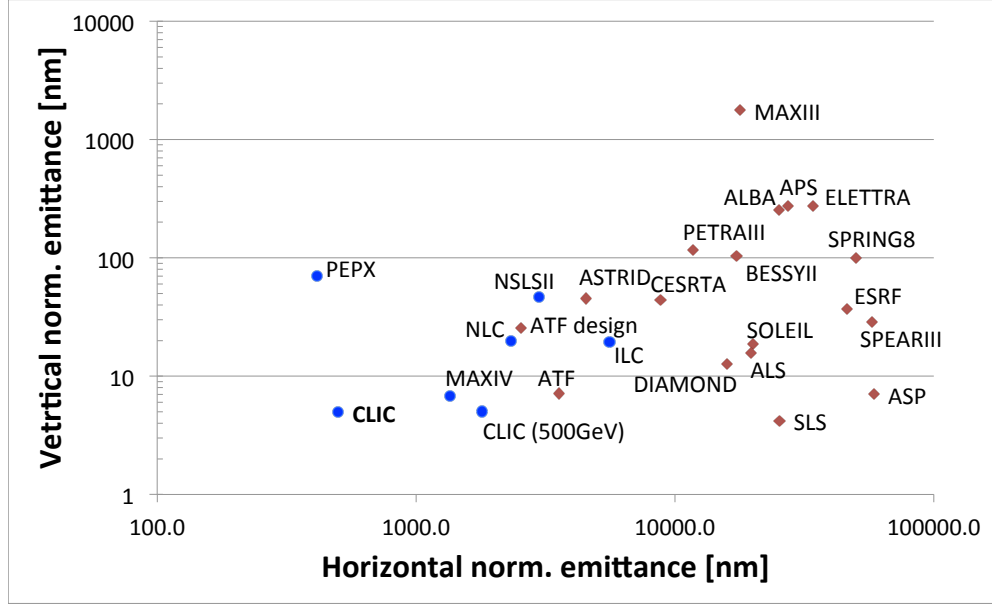


Fig. 2.47: Comparison of CLIC emittances generation with performances in existing (red) or planned (blue) facilities

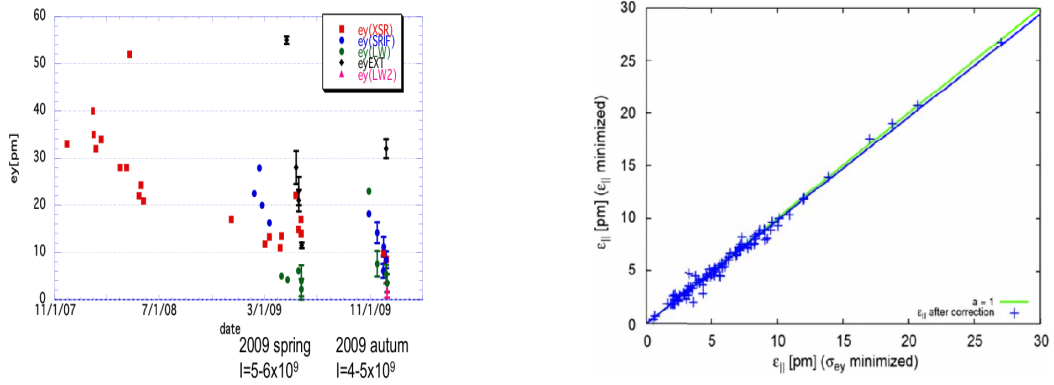


Fig. 2.48: Physical beam emittances achieved at ATF/KEK (right) and SLS (left)

The currently achieved performances are compared in Table 2.12 with the design emittances of the CLIC Damping Ring for the 500 GeV and the 3 TeV CLIC complexes. It clearly shows that emittances close to the CLIC design performances have already been demonstrated although with non-consistent beam parameters.

With the already achieved ATF performances, the CLIC peak luminosity at 3 TeV is expected to be reduced by a factor 3 with respect to the baseline performance such that the generation of the required small emittances can be considered feasible but still constitutes a performance issue, which will

have to be addressed in the next CLIC phase. With the development of ambitious light sources like NSLSII or MAXIV planned in the near future, substantial progress towards demonstration of nominal CLIC emittances can reasonably be expected within the next few years. At 500 GeV, the reduction factor would be about 1.5.

Table 2.12: Ultra-low emittances: achieved performances versus CLIC DR design

Parameter [units]	Achieved			CLIC design	
	ATF	CesrTA	SLS	500 GeV	3 TeV
Energy [GeV]	1.3	2.1	2.4	2.86	2.86
Horizontal normalized emittance [nm]	3800	11000	2700	1800	500
Vertical normalized emittance [nm]	15	84	10	5	5
Horizontal physical emittance [pm]	1500	2600	5600	320	89
Vertical physical emittance [pm]	5.9	20	2	0.9	0.9
Particles per bunch [10^9]	4	21	6	7.5	4.1
Number of bunches	1	45	400	312	312
Average beam intensity [mA]	3.5	60	400	265	145

2.10.7 Emittance preservation

As pointed out in §2.2, the specifications of the beam emittance preservation from the Damping Ring to the Interaction Point (IP) through the Ring-to-Main-Linac (RTML), the 21 km long linacs, and the Beam Delivery System (BDS) are extremely challenging with a beam blow-up limited to 160 nm and 15 nm in the horizontal and vertical planes up to the end of the linac and a luminosity loss in the BDS limited to 20%. The beam blow-up has three major causes: i) detrimental effects due to coherent and incoherent synchrotron radiation strongly related to the optics design; ii) static imperfections especially critical due to the strong wakefield environment generated in the linac by the large number of accelerating structures with high RF frequency and the strong focusing required to limit wakefield effects; iii) dynamic imperfections mainly caused by ground motion and technical noise. The blow-up budget is shared about half and half between static and dynamics effects.

As described in §3.8 and §3.4, simulations of the Main Beam taking into account all possible detrimental beam dynamics effects in the main linac and the BDS show that the beam blow-up and corresponding loss in luminosity can be controlled. This requires good quality-control during the construction followed by careful alignment during the installation, and finally stabilization of the most critical components with tight specifications as well as continuous beam-based feedbacks during operation. The specifications for all these steps have been demonstrated. The developed tools and simulation codes have been to some extent bench-marked during the SLC era and with experiments in CTF3. Start-to-end simulations allow one to characterize the overall emittance blow-up and the individual contributions of the various systems in the transfer lines and the main linac as well as the luminosity loss in the BDS with the computer codes PLACET and GUNIEA-PIG respectively. The design and specifications of the individual components are then deduced from a budget distributed between the various systems in order to keep the beam blow-up below the final overall target.

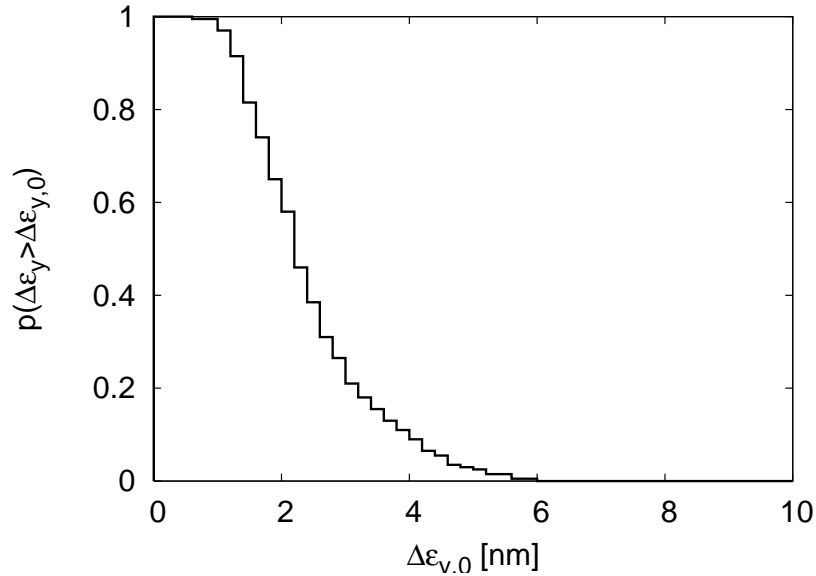
As far as static effects are concerned, the alignment budget and specifications of the major linac components are summarized in Table 2.13. The feasibility of the tight pre-alignment specifications is addressed in §5.17 and assessed below in §2.10.9.

The effects of the residual static imperfections corresponding to the above pre-alignment specifications are then mitigated by Beam Based Alignment (BBA) techniques. As shown in Fig. 2.49, the

Table 2.13: Alignment specifications of the main linac components and resulting emittance growth after application of the beam-based correction techniques

Imperfection	With respect to	Value	Emittance growth
BPM offset	Wire reference	$14\ \mu\text{m}$	0.367 nm
BPM resolution	–	$0.1\ \mu\text{m}$	0.04 nm
Accelerating structure offset	Girder axis	$10\ \mu\text{m}$	0.03 nm
Accelerating structure tilt	Girder axis	$140\ \mu\text{rad}$	0.38 nm
Articulation point offset	Wire reference	$10\ \mu\text{m}$	0.1 nm
Girder end point	Articulation point	$5\ \mu\text{m}$	0.02 nm
Wake monitor	Structure centre	$3.5\ \mu\text{m}$	0.54 nm
Quadrupole roll	Longitudinal axis	$100\ \mu\text{rad}$	0.12 nm
All			2.34 nm

emittance blow-up at the end of the main linac is limited well below the specified 5 nm, with a probability of more than 95%, using a BBA approach with three successive steps (one-to-one correction, dispersion-free steering, and alignment of structures to beam using wakefield monitors).

**Fig. 2.49:** Probability distribution of the emittance growth by static effects in the main linac

In order to preserve beam emittances and limit the luminosity reduction by dynamic effects, the beam jitter due to ground motion and technical noise integrated over the whole frequency range has to be maintained below 0.2 nm during collisions at the IP. This is obtained by the combined effects of

1. integrated beam-based orbit feedbacks
2. quadrupole strength r.m.s. stability of 0.5×10^{-4}
3. tight r.m.s. transverse stability of individual components by mechanical stabilization with maximum vibrations of the order of
 - (a) 5 nm and 1.5 nm in the frequency range above 1 Hz in the horizontal and vertical planes, respectively, for all 4000 quadrupoles of the main linac

- (b) 0.15 nm for the two quadrupoles of the final doublet (FD) in the frequency range above 4 Hz.

Some of the specifications above could be relaxed by about a factor of two using an intra-pulse feedback at the IP, although this is challenging due to the short time interval of 0.5 ns between bunches and the short beam pulse of 150 ns.

Integrated simulations using i) ground motion measured on the floor of the hall of the LHC CMS detector; ii) modelling of the tested stabilization system and iii) beam-based feedbacks yield 108% of the target luminosity. Up to 118% of the target luminosity has recently been reached using an improved concept of stabilization system described in §5.18. The stabilization systems for the quadrupoles of the main linac and of the FD quadrupoles are described in §5.18 and §5.12.2.2, respectively. Their feasibilities are assessed in §2.10.10.1.

2.10.8 Nanometre beam sizes

As pointed out in §2.2, the focusing to unprecedented small beam sizes at the Interaction Point is critical for the CLIC luminosity. The specified beam sizes are extremely challenging with about 40 nm and 1 nm in the horizontal and vertical planes respectively (Fig. 2.50), thus a factor 70 smaller than the present state-of-the-art corresponding to 70 nm demonstrated in the Final Focus Test Beam (FFTB) at SLAC.

As described in §3.5, a tuning procedure of the Beam Delivery System (BDS) including the Final Focus (FF) has been defined. It allows one to achieve at least 90% of the luminosity with a probability as high as 90% (Fig. 2.50) in the baseline configuration where the final doublet is integrated inside the detector with an effective distance to the IP of 3.5 m. This falls slightly short of the target, which is to achieve 110% of the nominal luminosity, to provide a budget for the luminosity loss due to dynamic effects in the BDS.

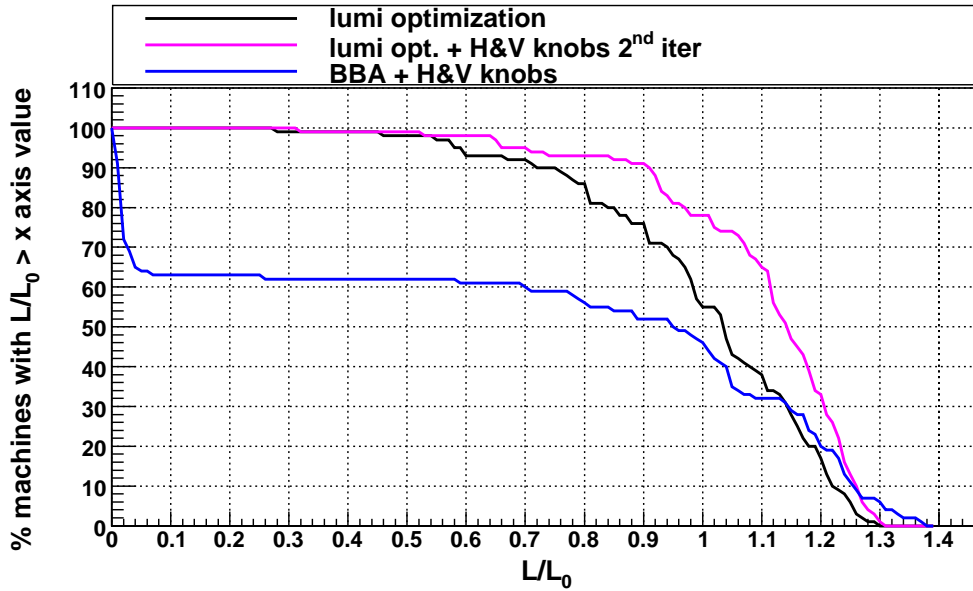


Fig. 2.50: Tuning performance of the CLIC Beam Delivery System: the black line shows the large improvement by the Simplex luminosity optimization of the initial performance (blue line) obtained by Beam Based Alignment (BBA) and orthogonal knobs. A second iteration of orthogonal knobs scanning allows then to reach a 90% success rate in reaching 90% luminosity.

The feasibility of small beam size generation has been addressed in the Final Focus Test Beam (FFTB) with a different BDS design and is currently being addressed for the same design by the specially built Accelerator Test facility (ATF2) in KEK [105]. It has demonstrated beam sizes of 300 nm (Fig. 2.51)

in agreement with the simulations, thus giving hope that the design of 37 nm can be achieved in the near future. An upgrade of ATF2 to a beam size of 20 nm has been approved and will allow us to demonstrate figures closer to the CLIC and ILC specifications. It should be noted that these beam sizes are limited by the small energy of the ATF2 beam. The difficulty of the design is mainly due to the ratio of the vertical beta-function to the distance between the final quadrupole and the interaction point, which is roughly the inverse of the chromaticity. This value is comparable between CLIC and ATF2 and will be the same in the final ATF2 phase.

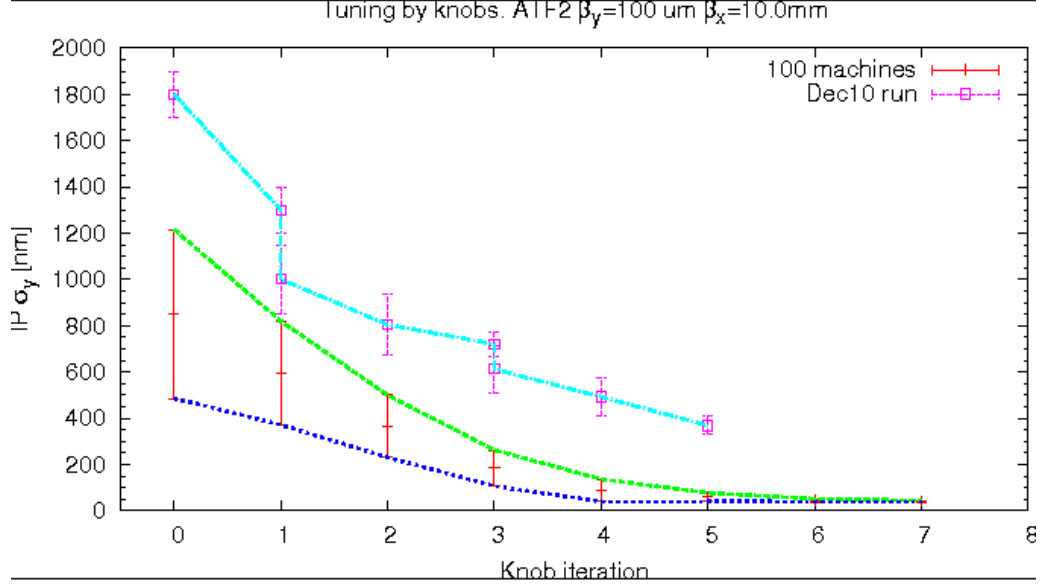


Fig. 2.51: ATF2 beam size evolution as measured during the December 2010 run compared to simulations with 100 statistical realizations of the ATF2 beam line. The horizontal axis shows the orthogonal knob iteration number.

Table 2.14: Chromaticity and IP parameters for the two CLIC energies and for the ultra-low β^* configuration of ATF2

Parameter [units]		CLIC 3 TeV	CLIC 500 GeV	ATF2
Beam size [nm]	σ_x/σ_y	40/1	202/2.3	20
Focusing [mm]	β_{eff}^*	4/0.07	8/0.1	0.025
FD to IP [m]	L^*	3.5	4.3	1.0
Chromaticity	ξ_y	63 000	54 000	76 000

Beam sizes lower than 20 nm as well as synchrotron radiations effects are out of reach of a reasonable sized test facility. Nevertheless, beam simulations extrapolating beam focusing to smaller beam dimensions show that beam sizes in the few nm range will be obtained after an acceptable beam commissioning time. As a consequence, the generation of the ultra-low beam sizes at a level providing acceptable performance is considered feasible. Nevertheless, it would still constitute a performance issue which will have to be addressed in the next CLIC phase and especially during beam commissioning of a real facility built in stages.

2.10.9 Pre-alignment

Pre-alignment is a key issue of beam emittance preservation. As outlined in §2.2, the pre-alignment specifications require a factor 10 improvement with respect to the present state of the art. More specifically,

the standard deviations of the radial and vertical positions with respect to the straight fitting line along a sliding window of 200 m have to be maintained below $14\text{ }\mu\text{m}$ for the Beam Position Monitors (BPMs), $17\text{ }\mu\text{m}$ for the Main Beam quadrupoles, and $10\text{ }\mu\text{m}$ for the components in the Beam Delivery System (BDS). A wire-based method has been developed to achieve the above specifications. It is described in §5.17. In the main linac, the system requires an accuracy of $10\text{ }\mu\text{m}$ for the reference points. Feasibility tests have been performed in pre-alignment test benches in the dedicated TT1 facility at CERN and demonstrated performances very close to the required specification with a precision of $2\text{ }\mu\text{m}$ r.m.s. and an r.m.s. scatter of $17\text{ }\mu\text{m}$ in radial and $11\text{ }\mu\text{m}$ in vertical (Fig. 2.52). A prototype version is integrated in the two-beam module string tests described in §5.6 in order to study their compatibility and interaction with the other components. In parallel, low-cost versions of the components built in large series are being developed for cost optimization in the next CLIC phase.

The alignment system will also generate errors of the reference system over long distances. Based on the expected errors, these deviations have been modelled and the luminosity loss has been simulated finding only a negligible effect.

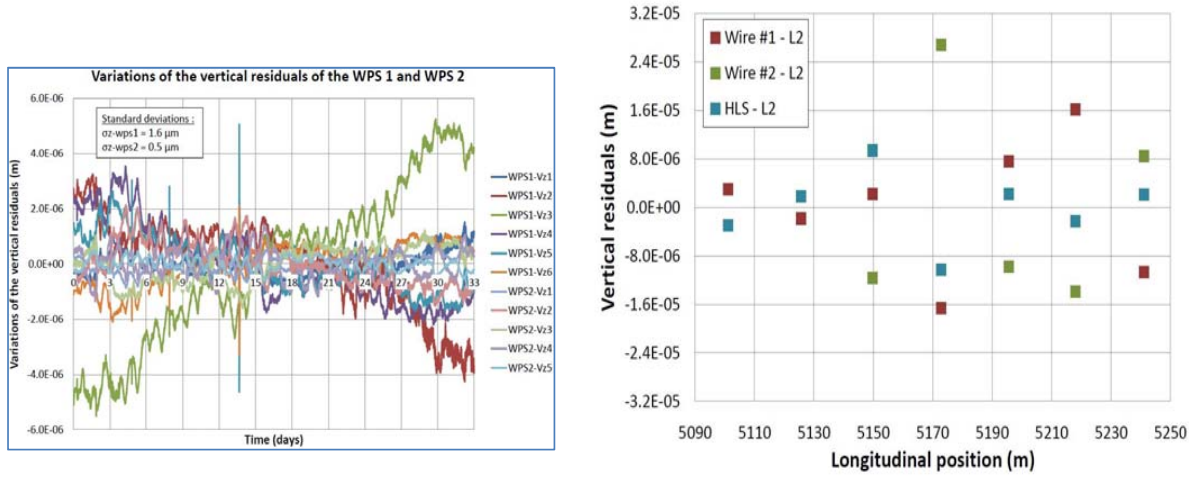


Fig. 2.52: Alignment precision (left) and accuracy (right) achieved after final adjustment of the TT1 facility

2.10.10 Stabilization

As pointed out in §3.8, the stabilization of the quadrupoles is a key issue for beam emittance preservation both along the main linac and in the Beam Delivery System (BDS).

2.10.10.1 Main linac quadrupoles

As outlined in §2.2, the stability specifications of the main linac quadrupoles are extremely challenging with an r.m.s. displacement integrated over the whole frequency range above 1 Hz lower than 5 nm and 1.5 nm in the horizontal and vertical planes, respectively. A method based on active isolation with a stiff actuating support and with combined feedback and feed-forward with reference masses mounted on the magnets (feedback) and on the ground (feed-forward) as described in §5.18, has been developed. It has been tested on a specific test bench using a type MB1 quadrupole mock-up with a mass of 100 kg mounted on a stabilization support. A factor 6 reduction of the background vibration and stability down to 0.5 nm at 1 Hz, better than specified in the frequency range of interest, has been demonstrated (Fig. 2.53). Both horizontal and vertical required stability is maintained with some margin from a technical background noise range on the floor representative of a deep underground CLIC machine; 2–5 nm integrated r.m.s. vertical displacement was measured in the LHC machine in operation (§5.18.2). A very stiff actuating support has been selected in order to limit the influence of direct acting forces such

2.10 ASSESSMENT OF THE CLIC FEASIBILITY

as water cooling and ventilation as shown in models. The method has still to be tested and confirmed by measurements with a 400 kg mass corresponding to a Type-4 MBQ quadrupole. It will also have to be made compatible with the pre-alignment system. At a later stage the radiation hardness of all components needs to be verified. The stabilization integration will be studied in the two-beam module test benches although the noisy location is not ideal for precise measurements.

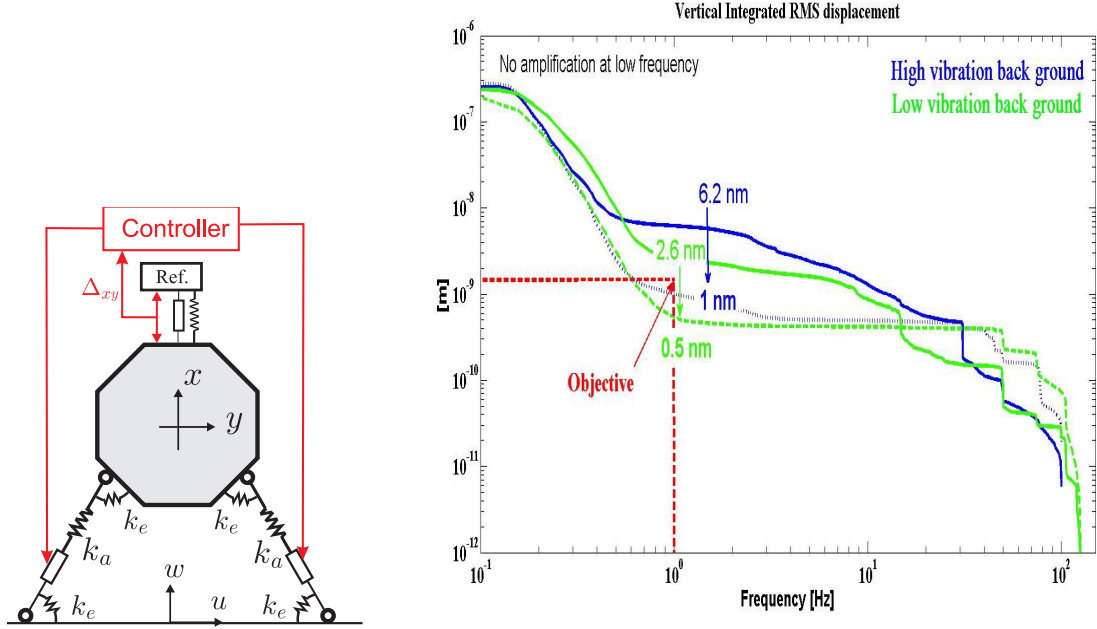


Fig. 2.53: Concept of the MBQ stabilization system and demonstration of its feasibility in the laboratory with performances of 0.5 nm above 1 Hz better than CLIC specifications

2.10.10.2 Final doublet (FD)

The specification of the Final Doublet stabilization is even more challenging with an r.m.s. displacement above 4 Hz lower than 0.15 nm in the vertical plane. The required Final Doublet stability is deduced from the necessary r.m.s. beam-beam stability of 0.20 nm integrated over the whole frequency range during collisions at the Interaction Point in order to preserve luminosity as described in §3.8. As pointed out in §5.12 on the Machine Detector Interface (MDI) such an extreme beam stability is achieved by a combination of the following measures.

A pre-isolator has been designed to support the magnets of the final doublet. It consists of a large mass of concrete supported by air springs directly supported from the tunnel. The final quadrupole that extends into the detector is supported by a cantilever mounted on this pre-isolator. The transfer of the ground motion through this system has been calculated and is used in the integrated simulations of the luminosity loss showing little luminosity loss, see below. In addition, a combined active and passive stabilization system is under development.

The ability to stabilize the final doublet magnets has been demonstrated using a simple model of a final quadrupole cantilevered from a support that is placed on a table combining passive and active isolation; isolating them from the ground motion with the addition of an extra feedback to compensate for the structure resonance. A stabilization of 0.13 nm r.m.s. in the frequency range above 4 Hz has been achieved in the laboratory at the extremity of a cantilever prototype (Fig. 2.54).

The Final Doublet stability would obviously greatly benefit from removal of the final doublet from inside the detector with a solid attachment to the main tunnel, thus avoiding the noisy environment of

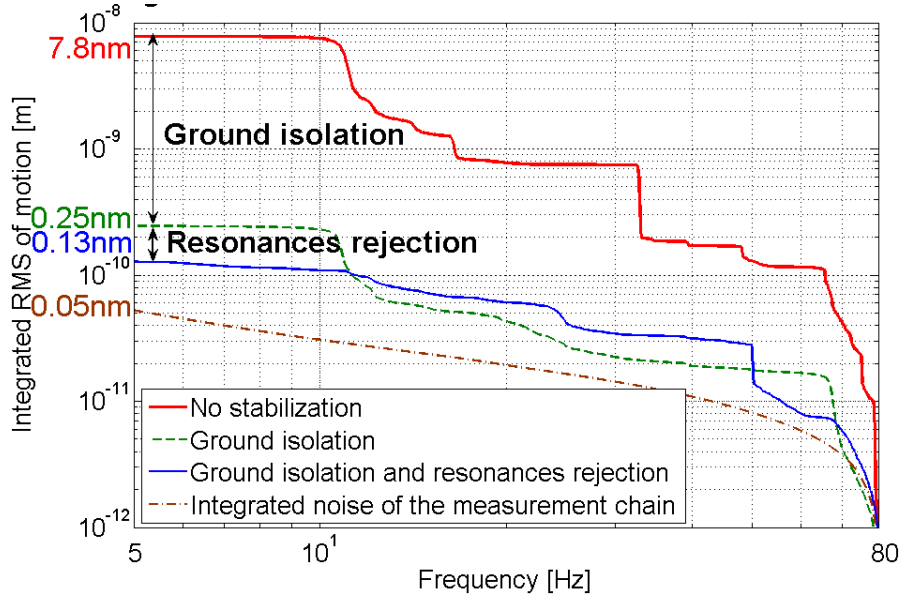


Fig. 2.54: Stabilization to 0.13 nm above 4 Hz of a QD0 prototype at the extremity of a cantilever prototype in the laboratory

the detector. Such a configuration would also ease the critical push–pull operation. It is considered an alternative to be adopted as soon as a tuning of the final focus has been demonstrated with a distance of 6 m distance the final doublet and the IP.

2.10.10.3 Luminosity loss due to ground motion

In order to estimate the potential luminosity loss due to ground motion, an extensive analysis has been performed. The ground motion has been measured in different locations, since it varies from one place to another. We assume a level of ground motion consistent with that of the floor of the CMS experimental hall and the floor of the laboratory at LAPP in Annecy. The stabilization hardware for the main linac and BDS magnets can be described by a transfer function, which captures the mechanical transfer of vibrations if the hardware feedback is working. The pre-isolator can be similarly described. These models have been integrated into a simulation together with a model of the machine and the beam-based feedback including the controller. This allows one to predict the luminosity loss for the given environment. For the tested prototype of the main linac magnet stabilization a marginally acceptable luminosity loss of 13% is found. An improved system is being designed that will reduce the loss to 3% or less.

In addition to the pulse-to-pulse beam-based feedback an intra-train feedback can be used at the interaction point, as described in §3.6.6. This feed-back is challenging due to the short train length of 150 ns, which requires a very short latency. Our luminosity estimates do not contain the impact of this feedback, which therefore provides an additional margin on the tolerances by up to a factor two.

2.10.11 Operation and machine protection system

As pointed out in §2.2, CLIC high luminosity at high energy necessitates unprecedented beam powers of 70 MW and 14 MW, a factor 50 and 10 above the present state of the art for the Drive Beam and the Main Beam respectively.

2.10 ASSESSMENT OF THE CLIC FEASIBILITY

In fact, as outlined in §5.16, the large damage capability of the CLIC facility is not so much caused by the large beam power as by the energy deposition density due to the small beam sizes, whilst the total damage potential is determined by the energy contained in the beam. The highest damage capability therefore occurs from the Main Beam focused to beam sizes in the nanometre range at high energy at the Interaction Point. The charge density and beam energy of the various CLIC beams are compared in Fig. 2.55 with those observed in operational facilities. The CLIC damage capability is therefore a major issue; 4 to 6 orders of magnitude above the damage threshold of copper and 2 to 3 orders of magnitude above the damage potential of facilities currently in operation.

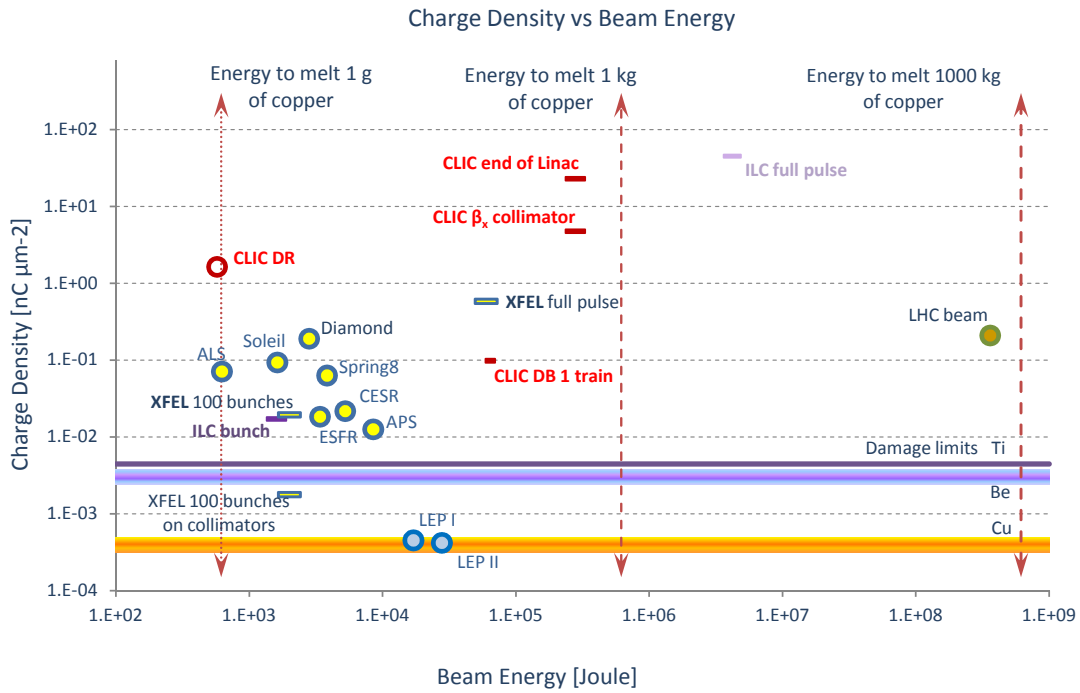


Fig. 2.55: Charge density and beam energy of the stored (circular) or pulsed (linear) beam for various existing and projected particle accelerators (circular or linear, collider or light-source, proton or lepton)

The vertical scale gives the transverse charge density of the beams. Beams with a charge density above the damage level for a given material have the capacity to cause structural damage in this material. (Note, these numbers do not take into account the time over which the charge density deposits energy in the material, which for long time durations may increase the effective heat spot due to thermal diffusion.)

The horizontal scale gives the total energy in the beam, which is a measure of the total destructive potential of the beam. Beams with a destructive potential up to the equivalent of a few grams of copper melted, will mainly cause limited local damage. Beams with an equivalent of several tenths of kilograms may cause substantial damage over an extended range of the accelerator.

The CLIC Main Beam, if badly controlled, has the potential to damage a very large fraction of the copper accelerator structures. Although the total damage impact of the extracted beam from the CLIC damping ring is small, the charge density of the beam is small enough that damage of a badly extracted beam will cause structural damage to the septum of the extraction channel.

After analysis of all possible failures and their classification, a protection strategy has been elaborated in §5.16 and summarized in Fig. 2.56. It is based on

1. passive protection with masks and spoilers,
2. real-time protection at each possible location, especially when the geometry of the complex provides opportunity for short-cut of the signal path like rings and turnarounds,

3. a beam interlock system inhibiting the next cycle for failures occurring more than 2 ms previously,
4. safe by design through components with large inertia in order to cover the 2 ms blind period before each cycle,
5. post-cycle analysis during the 10 ms following a cycle and next cycle permit when considered safe.

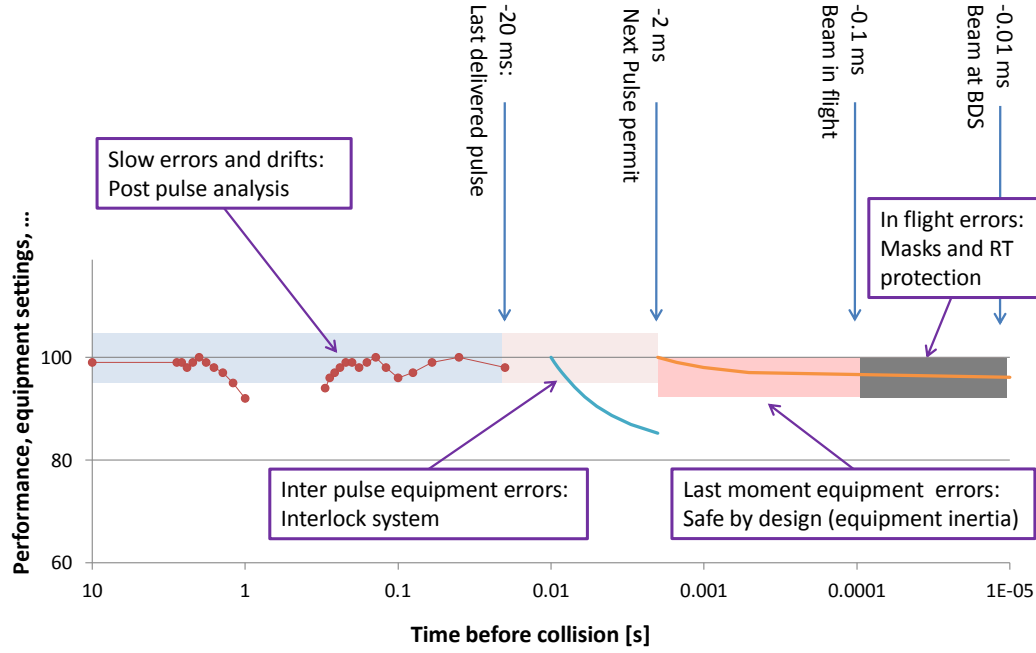


Fig. 2.56: The various failure classes and corresponding protection strategies as a function of the time left to the next beam collision

Ongoing simulations show that a CLIC facility, in spite of the unprecedented beam powers and beam densities, can be operated safely thanks to its advanced machine protection system. Specific issues will be tested with beam in the CLIC Test Facility, CTF3.

2.10.12 Conclusions

As summarized in Table 2.10 at the beginning of this section, the feasibility of the novel CLIC scheme and technology, although challenging, is demonstrated for a large number of the critical parameters. The remaining technical issues are being addressed with R&D from which results are expected during the project preparation phase. The CLIC scheme and technology is therefore available to extend the linear collider reach into the Multi-TeV range.

Nevertheless, a realistic proposal will certainly be limited by considerations like power consumption or overall project cost. A large amount of work has still to be completed before a multi-TeV linear collider based on the CLIC technology can be envisaged. Indeed, the present phase of the CLIC study has been focused on the feasibility issues of this novel scheme and technology. As pointed out several times above, some of the issues, although demonstrated to be feasible, must still be considered critical. Other issues related to performance, cost, and power as outlined in §2.2 still have to be addressed with more detailed optimization studies.

2.10 ASSESSMENT OF THE CLIC FEASIBILITY

These will be the major subjects for R&D in the next CLIC phase towards a Project Implementation Plan and a detailed Technical Design. During this phase a large enough number of systems for each of the relevant issues will have to be built and tested for a long enough time with a successful yield high enough to guarantee the performance, cost, power consumption, and reliability and to mitigate technological risks.

References

1. *Linear Collider Detector* CERN. <<http://lcd.web.cern.ch/LCD/>>.
2. Ellis, J. New physics with the Compact Linear Collider. *Nature* **409**, 431–435 (2001).
3. Delahaye, J.-P., Guignard, G., Raubenheimer, T. & Wilson, I. Scaling laws for e+/e- linear colliders. *Nucl. Instr. and Meth. A* **421**, 369–405 (1998).
4. Schulte, D. in *Proc. 8th European Particle Accelerator Conf., 3-7 June 2002, Paris, France* (2002), 59–61. <<http://accelconf.web.cern.ch/AccelConf/e02/PAPERS/MOZGB002.pdf>>.
5. Wuensch, W., Braun, H., Doeber, S., Syrathev, I. & Wilson, I. in *Proc. 20th IEEE Particle Accelerator Conf., 12-16 May 2003, Portland, Oregon, USA* (2003), 495–497. <<http://accelconf.web.cern.ch/accelconf/p03/PAPERS/ROAA011.PDF>>.
6. Heikkinen, S. T., Calatroni, S. & Neupert, H. in *Proc. 6th International congress on thermal stresses, 26-29 May 2005, Vienna, Austria* (2005). <<http://cdsweb.cern.ch/record/921679/files/open-2006-004.pdf>>.
7. Wuensch, W. in *Proc. 4th Asian Particle Accelerator Conf., 29 January - 2 February 2007, Indore, India* (2007), 544–546. <<http://epaper.kek.jp/a07/PAPERS/THYMA02.PDF>>.
8. Grudiev, A., Braun, H.-H., Schulte, D. & Wuensch, W. in *Proc. XXIV Linear Accelerator Conf., 29 September - 3 October 2008, Victoria, British Columbia, Canada* (2008), 527–529. <<http://accelconf.web.cern.ch/accelconf/LINAC08/papers/tup055.pdf>>.
9. Riddone, G. *CLIC List of critical/feasibility* CERN. <<https://edms.cern.ch/document/918791/11>> (2009).
10. International Linear Collider Technical Review Committee. *International Linear Collider Technical Review Committee. Second report 2003: prepared for the International Committee for Future Accelerators. ILCTRC/2003 SLAC-R-606* (SLAC, Stanford, CA, USA, 2003). <<http://cdsweb.cern.ch/record/314343>>.
11. *International Workshop on Linear Colliders (IWLC10)* <<https://espace.cern.ch/LC2010/default.aspx>>.
12. *CLIC Advisory Committee (ACE)* <<http://clic-study.org/structure/CLIC-AdvisoryCommittee.php>>.
13. Phinney, N. *The Next Linear Collider* SLAC-R-571 (SLAC, Stanford, CA, USA, 2001). <<http://www.slac.stanford.edu/pubs/slacreports/reports12/slac-r-571.pdf>>.
14. *CesrTA* <<http://www.docstoc.com/docs/15753542/CesrTA-Program-Overview-ILC-Damping-Rings-Electron-Cloud-Effort>>.
15. *Swiss Light Source - SLS* <<http://www.psi.ch/sls/>>.
16. Raimondi, P. *et al. SLC - The End Game* SLAC-PUB-9724 (SLAC, Stanford, CA, USA, 2003). <<http://www.slac.stanford.edu/cgi-wrap/getdoc/slac-pub-9724.pdf>>.
17. *FFTB* <<http://www2.slac.stanford.edu/vvc/experiments/fftb.html>>.
18. Bowden, G. *ACIS*
19. *SNS Instruments* Oak Ridge National Laboratory. <<http://www.sns.gov/instruments/SNS/>>.
20. Schnell, W. *A Two-Stage RF Linear Collider Using a Superconducting Drive Linac* (CERN, 1986). <<http://cdsweb.cern.ch/record/165833/files/cer-000077205.pdf>>.

REFERENCES

21. Grudiev, A., Calatroni, S. & Wuensch, W. New local field quantity describing the high gradient limit of accelerating structures. *Phys. Rev. ST Accel. Beams* **12**, 102001 (2009).
22. Adolphsen, C. in *Proc. 21st IEEE Particle Accelerator Conf., 16-20 May 2005, Knoxville, Tennessee, USA* (2005), 204–206. <<http://accelconf.web.cern.ch/accelconf/p05/PAPERS/TOPE002.PDF>>.
23. Doeber, S., Adolphsen, C., Bowden, G. B., Burke, D. L. & et al. in *Proc. 21st IEEE Particle Accelerator Conf., 16-20 May 2005, Knoxville, Tennessee, USA* (2005), 372–374. <<http://accelconf.web.cern.ch/accelconf/p05/PAPERS/ROAC004.PDF>>.
24. Descoeur, A., Djurabekova, F. & Nordlund, K. *DC Breakdown experiments with cobalt electrodes* CERN-OPEN-2011-029. CLIC-Note-875 (CERN, 2009). <<http://cdsweb.cern.ch/record/1355401/files/CERN-OPEN-2011-029.pdf>>.
25. Timko, H. *et al.* Mechanism of surface modification in the plasma-surface interaction in electrical arcs. *Phys. Rev. B* **81**, 184109 (2010).
26. Parviainen, S., Djurabekova, F., Pohjonen, A. & Nordlund, K. Molecular dynamics simulations of nanoscale metal tips under electric fields. *Nucl. Inst. and Meth. B* **269**, 1748–1751 (2011).
27. Pohjonen, A., Djurabekova, F., Kuronen, A., Nordlund, K. & Fitzgerald, S. Dislocation nucleation from near surface void under static tensile stress on surface in Cu. *J. Appl. Phys.* **110**, 023509 (2011).
28. Calatroni, S. *et al.* in *Proc. XXth Linear Accelerator Conf., 12-17 September 2010, Tsukuba, Japan* (2010), 217–219. <<http://accelconf.web.cern.ch/accelconf/LINAC2010/papers/mop070.pdf>>.
29. Djurabekova, F., Parviainen, S., Pohjonen, A. & Nordlund, K. Atomistic modeling of metal surfaces under electric fields: Direct coupling of electric fields to a molecular dynamics algorithm. *Phys. Rev. E* **83**, 026704 (2011).
30. Djurabekova, F. *et al.* Crater formation by single ions, cluster ions and ion showers. *Nucl. Inst. and Meth. B* **272**, 374–376 (2012).
31. Parviainen, S., Djurabekova, F., Timko, H. & Nordlund, K. Electronic processes in molecular dynamics simulations of nanoscale metal tips under electric fields. *Computational Materials Science* **50**, 2075–2079 (2011).
32. Timko, H. *et al.* A One-Dimensional Particle-in-Cell Model of Plasma Build-Up in Vacuum Arcs. *Contrib. Plasma Phys.* **51**, 5–21 (2011).
33. Timko, H. *2D Arc-PIC code description: methods and documentation* CERN-OPEN-2011-027. CLIC-Note-872 (CERN, Geneva, 2001). <<http://cdsweb.cern.ch/record/1354562/files/CERN-OPEN-2011-027.pdf>>.
34. Timko, H. *et al.* Energy Dependence of Processing and Breakdown Properties of Cu and Mo. *Phys. Rev. ST Accel. Beams* **14**, 101003 (2011).
35. Timko, H., Crozier, P. S., Hopkins, M. M., Matyash, K. & Schneider, R. *Why perform code-to-code comparisons: a vacuum arc discharge simulation case study* submitted for publication. 2011.
36. Adolphsen, C. in *Proc. 21st IEEE Particle Accelerator Conf., 16-20 May 2005, Knoxville, Tennessee, USA* (2005), 204–206. <<http://accelconf.web.cern.ch/accelconf/p05/PAPERS/TOPE002.PDF>>.
37. Wilson, H. I. *Surface heating of the CLIC main linac structure* CLIC-Note-52 (CERN, 1987). <<http://cdsweb.cern.ch/record/255087/files/CM-P00064739.pdf>>.
38. Pritzkau, D. P. & Siemann, R. H. Experimental study of rf pulsed heating on oxygen free electronic copper. *Phys. Rev. ST Accel. Beams* **5**, 112002 (2002).

39. Heikkinen, S. *Thermally Induced Ultra High Cycle Fatigue of Copper Alloys of the High Gradient Accelerating Structures* CERN-THESIS-2010-203. TKK-ME-DIS-10. CLIC-Note-859 (Helsinki U. of Tech., 2010). <<http://cdsweb.cern.ch/record/1333037/files/CERN-THESIS-2010-203.pdf>>.
40. Aicheler, M. *Surface phenomena associated with thermal cycling of copper and their impact on the service life of particle accelerator structures* CERN-THESIS-2010-189 (Ruhr University, Bochum, 2010). <<http://cdsweb.cern.ch/record/1326036/files/CERN-THESIS-2010-189.pdf>>.
41. Laurent, L. *et al.* Experimental study of RF pulsed heating. *Phys. Rev. ST Accel. Beams* **14**, 041001 (2011).
42. Dolgashev, V., Tantawi, S., Higashi, Y. & Higo, T. in *Proc. 11th European Particle Accelerator Conf., 23-27 June 2008, Genoa, Italy* (2008), 742–744. <<http://accelconf.web.cern.ch/accelconf/e08/papers/mopp083.pdf>>.
43. Higo, T. *et al.* in *Proc. 1st Int. Particle Accelerator Conf., 23-28 May 2010, Kyoto, Japan* (2010), 3702–3704. <<http://accelconf.web.cern.ch/accelconf/IPAC10/papers/thpea013.pdf>>.
44. Rumolo, G. *Vacuum System for the CLIC Two-Beam Modules. Parameter Specification* EDMS 992778 v.2 (CERN, 2010). <https://edms.cern.ch/file/992778/2/Vacuum_system_Main_Linac.doc>.
45. Jones, R. M., Adolphsen, C. E., Wang, J. W. & Li, Z. Wakefield damping in a pair of X-band accelerators for linear colliders. *Phys. Rev. ST Accel. Beams* **9**, 102001 (2006).
46. Khan, V. F. *et al.* in *Proc. 1st Int. Particle Accelerator Conf., 23-28 May 2010, Kyoto, Japan* (2010), 3425–3427. <<http://accelconf.web.cern.ch/accelconf/IPAC10/papers/wepe032.pdf>>.
47. Shi, J., Grudiev, A., Wuensch, W., Chen, H. & Huang, W. in *Proc. 2nd Int. Particle Accelerator Conf., 4-9 September 2011, San Sebastian, Spain* (2011), 113–115. <<http://accelconf.web.cern.ch/accelconf/IPAC2011/papers/mopc021.pdf>>.
48. Adolphsen, C. *et al.* in *Proc. 22nd Particle Accelerator Conf., 25-29 June 2007, Albuquerque, New Mexico, USA* (2007), 2191–2193. <<http://accelconf.web.cern.ch/accelconf/p07/PAPERS/WEPMN070.PDF>>.
49. Urschuetz, P. *et al.* in *Proc. 10th European Particle Accelerator Conf., 26-30 June 2006, Edinburgh, Scotland, UK* (2006), 795–797. <<http://accelconf.web.cern.ch/AccelConf/e06/PAPERS/MOPLS101.PDF>>.
50. Schulte, D. *et al.* in *Proc. XXV Linear Accelerator Conf., 12-17 September 2010, Tsukuba, Japan* (2010), 103–105. <<http://accelconf.web.cern.ch/accelconf/LINAC2010/papers/mop024.pdf>>.
51. Csatari Divall, M. *et al.* in *Proc. 2nd Int. Particle Accelerator Conf., 4-9 September 2011, San Sebastian, Spain* (2011), 430–432. <<http://accelconf.web.cern.ch/accelconf/IPAC2011/papers/mopc150.pdf>>.
52. Corsini, R. *et al.* in *Proc. 9th European Particle Accelerator Conf., 5-9 July 2004, Lucerne, Switzerland* (2004), 39–41. <<http://accelconf.web.cern.ch/accelconf/e04/PAPERS/MOCH02.PDF>>.
53. Braun, H. *et al.* in *Proc. 2006 Linear Accelerator Conf., 20-25 August 2006, Knoxville, Tennessee, USA* (2006), 31–33. <<http://accelconf.web.cern.ch/accelconf/l06/PAPERS/MOP002.PDF>>.

REFERENCES

54. Corsini, R., Ferrari, A., Rinolfi, L., Royer, P. & Tecker, F. Experimental results on electron beam combination and bunch frequency multiplication. *Phys. Rev. ST Accel. Beams* **7**, 040101 (2004).
55. Welsch, C. P. *et al.* Longitudinal beam profile measurements at CTF3 using a streak camera. *J. Instrum.* **1**, 09002 (2006).
56. Barranco Garcia, J., Skowronski, P., Tecker, F. & Biscari, C. in *Proc. 2nd Int. Particle Accelerator Conf., 4-9 September 2011, San Sebastian, Spain* (2011), 1045–1047. <<http://accelconf.web.cern.ch/accelconf/IPAC2011/papers/tupc022.pdf>>.
57. Gallo, A. *et al.* in *Proc. 7th European Particle Accelerator Conf., 26-30 June 2000, Vienna, Austria* (2000), 465–467. <<http://accelconf.web.cern.ch/accelconf/e00/PAPERS/THP6B09.pdf>>.
58. Corsini, R. & Schulte, D. in *Proc. XXI Int. Linear Accelerator Conf., 19-23 August 2002, Gyeongju, Korea* (2002), 112–114. <<http://accelconf.web.cern.ch/accelconf/102/PAPERS/MO434.PDF>>.
59. Corsini, R. *et al.* in *Proc. 11th European Particle Accelerator Conf., 23-27 June 2008, Genoa, Italy* (2008), 574–576. <<http://accelconf.web.cern.ch/accelconf/e08/papers/mopp011.pdf>>.
60. Syrathev, I. in *X-Band RF Structure and Beam Dynamics Workshop, 1-4 December 2008, Daresbury, UK* (2008). <<http://indico.cern.ch/getFile.py/access?contribId=24&sessionId=36&resId=1&materialId=slides&confId=39372>>.
61. Adli, E. *A Study of the Beam Physics in the CLIC Drive Beam Decelerator* (University of Oslo, 2009). <<http://cdsweb.cern.ch/record/1239173/files/CERN-THESIS-2010-024.pdf>>.
62. Syrathev, I. *et al.* in *Proc. 23rd IEEE Particle Accelerator Conf., 4-8 May 2009, Vancouver, British Columbia, Canada* (2009), 1873–1875. <<http://accelconf.web.cern.ch/accelconf/PAC2009/papers/we3rac02.pdf>>.
63. Adli, E. *et al.* X-band rf power production and deceleration in the two-beam test stand of the Compact Linear Collider test facility. *Phys. Rev. ST Accel. Beams* **14**, 081001 (2011).
64. Syrathev, I. & Cappelletti, A. in *Proc. 1st Int. Particle Accelerator Conf., 23-28 May 2010, Kyoto, Japan* (2010), 3407–3409. <<http://accelconf.web.cern.ch/accelconf/IPAC10/papers/wepe026.pdf>>.
65. Schulte, D. & Tomas, R. in *Proc. 23rd IEEE Particle Accelerator Conf., 4-8 May 2009, Vancouver, British Columbia, Canada* (2009), 3811–3813. <<http://accelconf.web.cern.ch/accelconf/PAC2009/papers/th6pfp046.pdf>>.
66. Schulte, D. *et al.* in *Proc. XXV Linear Accelerator Conf., 12-17 September 2010, Tsukuba, Japan* (2010), 103–105. <<http://accelconf.web.cern.ch/accelconf/LINAC2010/papers/mop024.pdf>>.
67. Gerbershagen, A., Schulte, D. & Burrows, P. in *Proc. 2nd Int. Particle Accelerator Conf., 4-9 September 2011, San Sebastian, Spain* (2011), 1018–1020. <<http://accelconf.web.cern.ch/accelconf/IPAC2011/papers/tupc013.pdf>>.
68. Schulte, D. & Syrathev, I. in *Proc. 20th International Linear Accelerator Conf., 21-25 Aug 2000, Monterey, CA, USA* (2000). <<http://accelconf.web.cern.ch/accelconf/100/papers/MOA04.pdf>>.
69. Grudiev, A., Cappelletti, A. & Kononenko, O. in *Proc. XXV Linear Accelerator Conf., 12-17 September 2010, Tsukuba, Japan* (2010), 94–96. <<http://accelconf.web.cern.ch/accelconf/LINAC2010/papers/mop021.pdf>>.

70. Braun, H. in *CLIC08 Workshop, 4-17 October 2008, CERN* (2008). <<http://indico.cern.ch/getFile.py/access?contribId=25&sessionId=0&resId=1&materialId=slides&confId=30383>>.
71. Corsini, R. in *CLIC09 Workshop, 12-16 October 2009, CERN* (2009). <<http://indico.cern.ch/getFile.py/access?contribId=34&sessionId=1&resId=1&materialId=slides&confId=45580>>.
72. Phinney, N., Toge, N. & Walker, N. *ILC Reference Design Report Vol. 3 - Accelerator* arXiv:0712.2361 (2007). <<http://arxiv.org/pdf/0712.2361.pdf>>.
73. NLC Design Group. *Next Linear Collider Zeroth-Order design report* LBNL-5424. SLAC-R-474. UC-414. UCRL-ID-124161 (SLAC, Stanford, CA, USA, 1996). <<http://www.slac.stanford.edu/accel/nlc/zdr/>>.
74. *Low Emittance Rings Workshop 2010* <<http://ler2010.web.cern.ch>>.
75. Antoniou, F. & Papaphilippou, Y. in *Proc. 23rd IEEE Particle Accelerator Conf., 4-8 May 2009, Vancouver, British Columbia, Canada* (2009), 2760–2762. <<http://accelconf.web.cern.ch/accelconf/PAC2009/papers/we6pfp107.pdf>>.
76. Papaphilippou, Y., Braun, H.-H. & Korostelev, M. in *Proc. 11th European Particle Accelerator Conf., 23-27 June 2008, Genoa, Italy* (2008), 679–681. <<http://accelconf.web.cern.ch/accelconf/e08/papers/mopp060.pdf>>.
77. Levichev, E. *et al.* in *Proc. 23rd IEEE Particle Accelerator Conf., 4-8 May 2009, Vancouver, British Columbia, Canada* (2009), 2757–2759. <<http://accelconf.web.cern.ch/accelconf/PAC2009/papers/we6pfp105.pdf>>.
78. Papaphilippou, Y., Antoniou, F., Barnes, M. J., Bettoni, S. & *et al.* in *Proc. 1st Int. Particle Accelerator Conf., 23-28 May 2010, Kyoto, Japan* (2010), 3554–3556. <<http://accelconf.web.cern.ch/accelconf/IPAC10/papers/wepe089.pdf>>.
79. Rumolo, G., Bruns, W. & Papaphilippou, Y. in *Proc. 11th European Particle Accelerator Conf., 23-27 June 2008, Genoa, Italy* (2008), 661–663. <<http://accelconf.web.cern.ch/accelconf/e08/papers/mopp050.pdf>>.
80. Shaposhnikova, E. N., Arduini, G., Axensalva, J., Benedetto, E. & *et al.* in *Proc. 23rd IEEE Particle Accelerator Conf., 4-8 May 2009, Vancouver, British Columbia, Canada* (2009), 366–368. <<http://accelconf.web.cern.ch/accelconf/PAC2009/papers/mo6rfp008.pdf>>.
81. Palmer, M. A., Alexander, J. P., Billing, M. G., Calvey, J. R. & *et al.* in *Proc. 1st Int. Particle Accelerator Conf., 23-28 May 2010, Kyoto, Japan* (2010), 1251–1255. <<http://accelconf.web.cern.ch/accelconf/IPAC10/papers/tuymh02.pdf>>.
82. Naito, T. *et al.* in *Proc. 1st Int. Particle Accelerator Conf., 23-28 May 2010, Kyoto, Japan* (2010), 2386–2388. <<http://accelconf.web.cern.ch/accelconf/IPAC10/papers/weobmh02.pdf>>.
83. Alesini, D. & Marcellini, F. RF deflector design of the CLIC test facility CTF3 delay loop and beam loading effect analysis. *Phys. Rev. ST Accel. Beams* **12**, 031301 (2009).
84. Amirikas, R., Bertolini, A., Bialowons, W. & Ehrlichmann, H. in *Proc. 36th ICFA Advanced Beam Dynamics Workshop, 17-21 October 2005, Kyoto, Japan* (2005). <http://vibration.desy.de/sites/site_ground-vibrations/content/e1454/e3974/e1475/infoboxContent1489/Nanobeam2005.pdf>.
85. Bolzon, B. *Etude des vibrations et de la stabilisation à l'échelle sous-nanométrique des doublets finaux d'un collisionneur linéaire* (University of Savoie, Annecy-le-Vieux, 2007). <<http://cdsweb.cern.ch/record/1100434/files/cer-002754217.pdf>>.

REFERENCES

86. Baklakov, B. A. *et al.* in *Proc. IEEE Particle Accelerator Conf.*, 6-9 May 1991, San Francisco, California, USA (1991), 3273–3275. <http://accelconf.web.cern.ch/accelconf/p91/PDF/PAC1991_3273.PDF>.
87. Peterson, J. *Observations and modeling of background seismic noise* 93-322 (U. S. Geological Survey, 1993). <<http://earthquake.usgs.gov/regional/asl/pubs/files/ofr93-322.pdf>>.
88. Schmickler, H. *et al.* in *Proc. 14th Beam Instrumentation Workshop*, 2-6 May 2010, Santa Fe, NM, USA (2010), 69–71. <<http://accelconf.web.cern.ch/accelconf/BIW2010/papers/tucnb01.pdf>>.
89. Schulte, D. in *Proc. 23rd IEEE Particle Accelerator Conf.*, 4-8 May 2009, Vancouver, British Columbia, Canada (2009), 4664–4666. <<http://accelconf.web.cern.ch/accelconf/PAC2009/papers/fr5rfp055.pdf>>.
90. Tomàs, R. *et al.* in *Proc. 1st Int. Particle Accelerator Conf.*, 23-28 May 2010, Kyoto, Japan (2010), 3419–3421. <<http://accelconf.web.cern.ch/accelconf/IPAC10/papers/wepe030.pdf>>.
91. Mainaud Durand, H., Touzé, T., Griffet, S., Kemppinen, J. & Lackner, F. in *Proc. 11th International Workshop on Accelerator Alignment*, 3-7 September 2010, DESY, Hamburg, Germany (2010). <http://iwaa2010.desy.de/e107506/e107507/e113203/e119271/IWAA2010_HMD_CLIC.pdf>.
92. Mainaud, H. *Une nouvelle approche metrologique: l'écartométrie biaxiale. Application à l'alignement des accélérateurs linéaires* (Université Louis Pasteur, Strasbourg, France, 1996).
93. Mainaud Durand, H. *The CLIC alignment studies: past, present and future* TS-Note 2005-028 (CERN, 2006). <[https://edms.cern.ch/file/590561/1/TS-Note-2005-028\(Mainaud\).pdf](https://edms.cern.ch/file/590561/1/TS-Note-2005-028(Mainaud).pdf)>.
94. Schulte, D. *et al.* in *Proc. XXV Linear Accelerator Conf.*, 12-17 September 2010, Tsukuba, Japan (2010), 103–105. <<http://accelconf.web.cern.ch/accelconf/LINAC2010/papers/mop024.pdf>>.
95. Andersson, A. & Sladen, J. *Final Report for the Timing and Phase Monitoring (TPMON) Task* EUROTeV-Report-2008-095 (EUROTeV, 2009). <http://www.eurotev.org/reports/_presentations/eurotev_reports/2008/e1543/EUROTEV-Report-2008-095.pdf>.
96. Loehl, F. *Optical Synchronization of a Free-Electron Laser with Femtosecond Precision* DESY-Thesis 2009-031. TESLA-FEL 2009-08 (DESY, 2009). <http://flash.desy.de/sites2009/site_vuvfel/content/e403/e1642/e2410/e2411/infoboxContent58704/TESLA-FEL_2009-08.pdf>.
97. Loehl, F. *Timing and Synchronization* Cornell University. <<http://cas.web.cern.ch/cas/Greece-2011/Lectures/Loehl.pdf>> (2001).
98. *CLIC Test Facility CTF3* <<http://ctf3.home.cern.ch/ctf3/CTFindex.htm>>.
99. *NLCTA facility* <https://slacportal.slac.stanford.edu/sites/ard_public/tfd/facilities/nlcta/Pages/Default.aspx>.
100. *ASTA facility* <https://slacportal.slac.stanford.edu/sites/ard_public/tfd/facilities/asta/Pages/Default.aspx>.
101. *KEK Nextef facility* <[http://www.pasj.jp/web_publish/pasj4_lam32/PASJ4-LAM32%20\(D\)/contents/PDF/TO/TO03.pdf](http://www.pasj.jp/web_publish/pasj4_lam32/PASJ4-LAM32%20(D)/contents/PDF/TO/TO03.pdf)>.

102. *CesrTA* <<http://www.docstoc.com/docs/15753542/CesrTA-Program-Overview-ILC-Damping-Rings-Electron-Cloud-Effort>>.
103. *KEK Accelerator Test Facility (ATF)* <<http://lcdev.kek.jp/ATF>>.
104. *Swiss Light Source - SLS* <<http://www.psi.ch/sls/>>.
105. *ATF2* <https://slacportal.slac.stanford.edu/sites/ard_public/tfd/facilities/atf2/Pages/Default.aspx>.

Chapter 3

Accelerator Physics description of the Main Beam complex



P. Tenconi

3.1 INJECTORS

3.1 Injectors

3.1.1 Overview

The CLIC Main Beam injectors consist of a polarized electron source and a positron source. Both particle species are pre-accelerated up to 200 MeV before they are injected into a common injector linac which brings the energy up to 2.86 GeV for the pre-damping and damping ring complex. The RF frequency chosen for the whole injector complex is 2 GHz, although the bunch spacing before the damping rings is only 1 GHz. This choice enables a higher accelerating gradient and the possibility to use the same RF system throughout the injector complex. This section describes the injectors up to the damping rings. The damping rings and the booster linac are described in separate sections. A schematic view of the injector complex can be seen in Fig. 3.1. The whole injector complex is situated in a central location close to the IP and oriented parallel to the Main Linac. The positron and electron beams are then transported after acceleration in the booster linac to both ends of the Main Linacs as described in §3.3.

The design and parameter choices for the Main Beam injectors up to the damping rings are considered to be conservative and conventional since reliability and operability is one of the most important goals. Therefore, the design is mostly inspired by existing facilities and proven hardware.

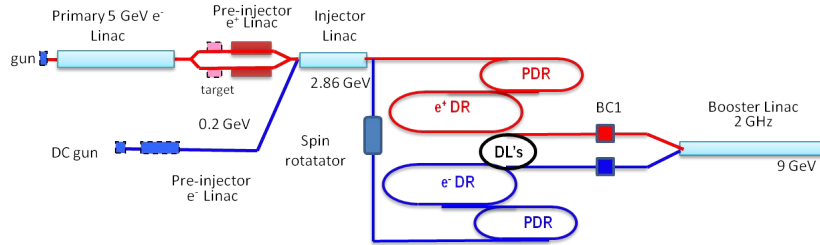


Fig. 3.1: Schematic layout of the Main Beam injector complex.

A polarized positron beam is not part of the baseline configuration for CLIC but an option for future upgrades and was therefore studied. A brief description of this study can be found in §3.1.4.

3.1.2 Beam parameters

The beam parameters at the entrance of the pre-damping rings for polarized electrons and for positrons are summarized in Table 3.1. The parameters for the positrons come from detailed simulations from the production target to the entrance of the pre-damping ring. The beam parameters for the electrons are considered as conventional up to the damping rings, so no detailed simulations have been done. The injectors have been designed to be capable of delivering 15% more charge per bunch to the entrance of the pre-damping rings than required at the entrance of the Main Linac.

Polarized electron and unpolarized positron beams are produced independently and accelerated up to 200 MeV before injection into the common injector linac. For the 3 TeV CLIC, the two trains follow each other with a delay of $2.3 \mu\text{s}$ in the injector linac. This distance respects the geometrical constraints of the layout and the requirements of the damping rings.

3.1.3 System description

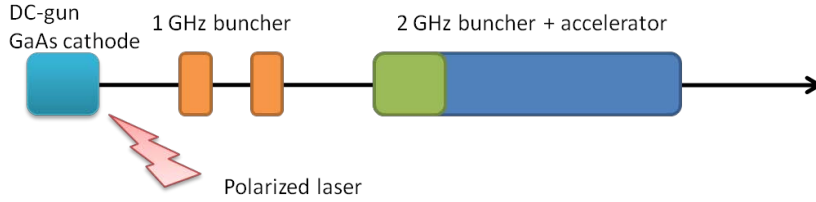
3.1.3.1 Polarized electron source

The CLIC polarized electron source consists of a DC-photo gun, a 1 GHz bunching system, and a 2 GHz accelerator. The electrons are accelerated up to 200 MeV before injection into the common injector linac. A spin-rotator in front of the pre-damping ring orients the spin vertically in the rings. A schematic of the

Table 3.1: Beam parameters at the entrance of the pre-damping ring for polarized electrons and for positrons at 2.86 GeV.

Parameter	Polarized electrons	Positrons
E [GeV]	2.86	2.86
N	4.3×10^9	7.7×10^9
n_b	312	312
Δt_b [ns]	1	1
t_{pulse} [ns]	312	312
$\varepsilon_{x,y}$ [μm]	< 100	7685, 8105
σ_z [mm]	< 4	5.4
σ_E [%]	< 1	4.5
Charge stability shot-to-shot [%]	0.1	0.1
Charge stability flatness on flat top [%]	0.1	0.1
f_{rep} [Hz]	50	50
P [kW]	29	29

source is shown in Fig. 3.2. A strained multilayer GaAs cathode is illuminated by a long pulse (900 ns) Q-switched laser. An efficient bunching system consisting of pre-bunchers and a tapered buncher followed by 2 GHz accelerating structures prepares the beam for injection into the linac.

**Fig. 3.2:** Schematic of the polarized electron source and bunching system.

The electron source produces spin-polarized electrons with a degree of polarization as high as 80%. It uses GaAs-type cathodes, such as strained GaAs layer or InGaAs–AlGaAs super-lattice. Such cathodes have been studied extensively around the world and are currently used at several accelerator laboratories [1–3]. They have demonstrated lifetimes of thousands of hours under similar conditions as those needed for CLIC.

The process for producing a polarized beam relies on two main physical mechanisms. Circularly polarized photons optically pump the valence band (VB) electron to the conduction band (CB) with selection of the electron helicity. Then, the Negative Electron Affinity (NEA) surface is activated to extract the polarized electron into vacuum.

The laser has the following requirements to produce the polarized electron beam. The wavelength has to match the band-gap of the chosen photo-cathode. For GaAs, this is ~ 800 nm. For a high degree of polarization ($> 80\%$) in the electron beam, the wavelength must be optimized (800 ± 25 nm) [4] for each cathode and the laser must have circular polarization ($> 99.8\%$). An additional constraint is that the laser be able to change the helicity of the beam quickly [5]. Several laser systems fulfilling this specification have been built and used successfully.

The cathode is placed in an ultra-high vacuum (UHV) electrostatic DC-gun equipped with a load-

3.1 INJECTORS

lock system for cathode transfer and activation. The high voltage is at least 120 kV. SLAC demonstrated the feasibility of such a source using their gun test facility. They produced a 160 ns macro-pulse of polarized electrons with 87% polarization, 0.3% quantum efficiency (QE), and charge up to 1400 nC from a InAlGaAs/AlGaAs photocathode [6]. The beamline used for the experiment includes an UHV electrostatic DC-gun, a load-lock chamber for the cathode transfer and activation, and a beam transport line. Downstream of the transport line, a Mott analyser was used to determine the beam polarization. The photoemission is triggered by a flash-lamp pumped Ti:Sa laser. The macro-pulse charge required by the CLIC Main Beam (300 nC) has been demonstrated. The laser pulse energy required for that charge on the cathode was $\sim 100 \mu\text{J}/\text{pulse}$ (see Fig. 3.3).

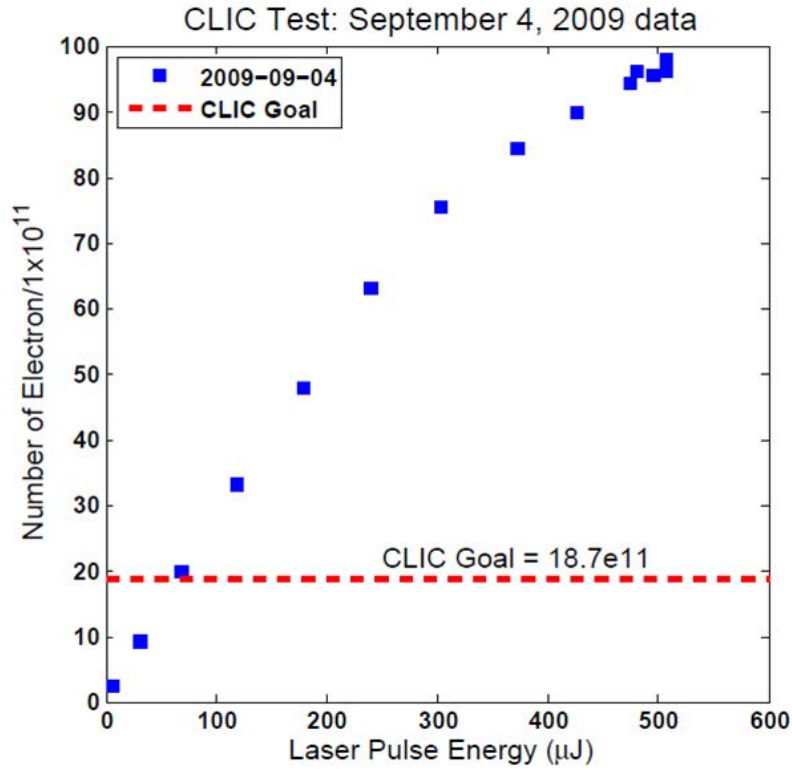


Fig. 3.3: Number of polarized electrons produced as a function of the laser energy during an experiment using the SLAC polarized gun test facility. The total charge was produced in a 156 ns long pulse using a 120 kV DC gun and a GaAs cathode.

The CLIC bunching system includes two sub-harmonic 1 GHz pre-bunchers, one 5-cell tapered- β buncher, and a 2 GHz accelerator, as shown in Fig. 3.1. The two pre-bunchers are used to modulate the macro bunch, then the 5-cell tapered- β travelling-wave 2 GHz structures compress the micro bunches down to 14 ps FWHM. The 2 GHz accelerator downstream of the buncher accelerates the beam to 200 MeV using a 2 GHz RF structure. Simulations indicate that a capture efficiency of 88% can be achieved [7].

The transfer line between the common 2.86 GeV injector linac and the electron pre-damping ring contains solenoids to adjust the spin orientation to the vertical at the entrance of the pre-damping ring. This spin-rotator uses the same design as one located after the damping rings described in §3.3.

An alternative option briefly studied is to use a laser based on a 1 GHz oscillator to produce directly the desired time structure. This option requires a laser pulse length on the cathode that is shorter than 200 ps which is very challenging in terms of the space charge. Also, surface charge limits have not yet

been demonstrated for this type of cathode. The whole polarized electron source and its subsystem are described in more technical detail in §5.1.

3.1.3.2 Positron source

The baseline design for the CLIC positron source provides only unpolarized positrons. The source consists of a conventional primary electron-beam linac with energy of 5 GeV, followed by hybrid targets (one thin crystal tungsten target plus one thick amorphous tungsten target), a positron capture section, and a pre-injector linac to accelerate the positrons to 200 MeV. The CLIC positron source will have two parallel target stations to enhance the reliability and operability of the system. For 3 TeV, one target is sufficient and only one is used at a time. The second target allows for continuous operation while one target is being exchanged. The 500 GeV version described in §9.2 requires a higher bunch charge and therefore uses two target stations in parallel.

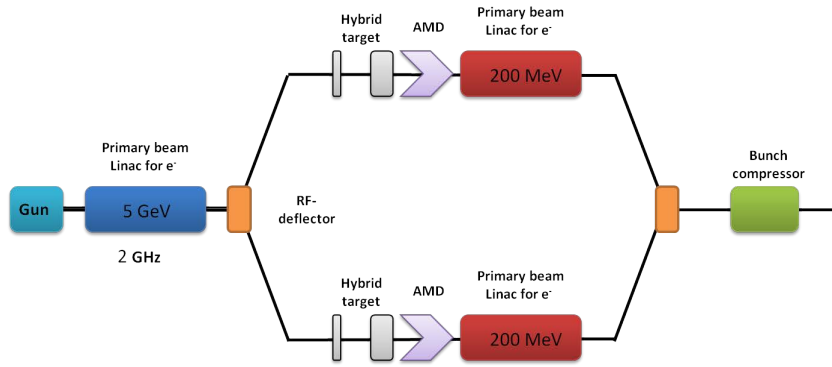


Fig. 3.4: Schematic layout of the CLIC positron source. A two-target system was chosen for reliability and for the higher charge requirements at 500 GeV.

Figure 3.4 shows the major elements of the positron source. A primary 5 GeV electron beam impinges on a thin tungsten crystal oriented on its $\langle 111 \rangle$ axis and generates a photon beam, which is largely soft photons. The characteristics of the electron beam impinging on the crystal target are summarized in Table 3.2. In order to limit the energy deposition in the amorphous target, the charged particles are swept away after the crystal with a dipole magnet. Only the photon beam impinges on the amorphous target located downstream from the crystal target. These photons produce positrons in an electromagnetic shower. Downstream of the amorphous target, there is a capture section based on an adiabatic matching device (AMD). This is followed by a 2 GHz pre-injector linac surrounded by a 0.5 T solenoid field. The positron beam is accelerated to an energy of 200 MeV.

The photons are generated in the crystal, mainly by axial channelling radiation, from relativistic electrons as they pass along the $\langle 111 \rangle$ axis. This axis is aligned with the direction of the 5 GeV incoming electron beam. An intense photon beam exits the crystal. The optimum value for the tungsten crystal thickness is 1.4 mm, equivalent to 0.4 radiation lengths [8]. The power deposited in the crystal has been investigated theoretically at different incident electron beam energies [9, 10]. At 5 GeV it is below 1% of the primary electron beam power. The distance between the crystal and the amorphous target allows the photon beam spot-size to increase, thereby decreasing the energy density on the amorphous target.

There has been a systematic study of positron production as a function of the amorphous target thickness, the distance between crystal and amorphous targets, for different incident electron beam energies [11]. The Peak Energy Deposition Density (PEDD) decreases with distance, but the number of captured positrons also decreases. The optimized parameters are an amorphous tungsten target with a 10 mm thickness corresponding to 3 radiation lengths and an optimized distance between the two targets

Table 3.2: Primary electron beam parameters

Parameter	Value
Energy [GeV]	5
Number of e^- / bunch	1.1×10^{10}
Charge per bunch [nC]	1.8
Bunches per pulse	312
Pulse repetition rate [Hz]	50
Beam radius (r.m.s.) [mm]	2.5
Bunch length (r.m.s.) [ps]	1
Beam power [kW]	140

of 2 m. The total power deposited on the amorphous target is ~ 11 kW and the PEDD is around ~ 30 J/g. At the target exit, the total positron yield is around $8 e^+/e^-$. At SLC, the first linear collider, it was found experimentally that such a target failed after about 1000 days of operation with a PEDD of 35 J/g.

The AMD captures a larger fraction of the produced positrons downstream of the target. In effect, the AMD transforms the positron phase space into larger transverse dimensions and smaller momentum spread which makes the beam easier to transport. It uses a magnetic field decreasing from 6 T immediately behind the target to 0.5 T after 20 cm. It provides a large energy acceptance that increases the number of accepted positrons. At the AMD exit, the positron yield is around $2.1 e^+/e^-$.

The pre-injector linac is downstream of the AMD and accelerates the e^+ beam (and e^- secondaries) up to an energy of 200 MeV. The positron yield at that point is $0.9 e^+/e^-$. An aperture of 20 mm radius and an accelerating gradient of 5 MV/m were used for these simulations. The yield of positrons at the end of this linac may increase with further studies. In particular, the positron capture in the linac can be improved by decelerating the beam in the first structure [12].

3.1.3.3 Common e^-/e^+ injector linac

The injector linac accelerates both positrons and electrons from 200 MeV to 2.86 GeV. Since the transport of the large phase-space positron beam presents the main challenge in the injector linac design, detailed beam dynamics simulations were performed only for positrons. The polarized electrons have a factor of 100 smaller emittance and transporting them without major losses is straightforward with the same optics.

Simulations [13, 14] indicated that a bunch compressor was needed between the e^+ pre-injector and the injector linac to reach the required final yield of e^+ injected in the PDR. The e^- beam does not need a bunch compressor. The e^+ bunch compression uses a 2 GHz RF structure to produce a chirp on the beam followed by a magnetic chicane. Transverse slits inserted between the inner bending magnets of the chicane also collimate the positron energy. These slits also absorb the secondary electrons captured in the pre-injector linac.

The injector linac consists of approximately 300 m of travelling-wave accelerating structures at a frequency of 2 GHz with a loaded gradient of 16 MV/m. Each structure is 1.5 m long and has a tapered aperture ranging from a radius of 20 mm down to 14 mm. The design of the accelerating structures used throughout the injector complex is described in more detail in §5.5. The beam optics for the injector linac uses quadrupole triplets in three different arrangements, adapted to the decreasing geometrical beam emittance. The spaces between the quadrupole triplets are filled with accelerating structures. The beam dynamics of the injector linac has been simulated for positrons using the expected phase space at the output of the 200 MeV pre-injector linac and bunch compressor. The final positron yield at the

entrance of the pre-damping ring is $0.7 e^+/e^-$. Only a fraction of these positrons will match into the acceptance of the pre-damping ring which reduces the yield to $0.39 e^+/e^-$. The beam parameters at the end of the linac are summarized in Table 3.1.

The positron bunch train trails the electron bunch train by 1100 ns at the entrance of the booster linac. This ensures the correct arrival time at the IP given the geometric layout. The electron injector has an additional 364-m-long transfer line for the electrons to reach their pre-damping ring. Therefore the distance between the two species is 2314 ns in the common injector linac. The two trains of each species with 1 GHz bunch spacing are separated by 717 ns corresponding to half the damping ring length. The compressed RF pulses feeding the accelerating structures are amplitude modulated in order to ensure the correct beam loading compensation for all trains. The total compressed RF pulse length used in the different injector linacs varies from linac to linac. More details can be found in §5.1.

3.1.4 Options for polarized positrons

Preliminary studies of two main options to produce polarized positrons are described briefly below. The first option uses Compton backscattering of a polarized laser from an electron beam to generate polarized gamma rays which can then be converted into polarized electron-positron pairs in a conversion target. The second option uses a helical undulator to produce directly polarized photons which are then converted into polarized positrons via a target. Neither option has yet had a feasibility demonstration.

3.1.4.1 Compton Backscattering

Three different Compton backscattering options for producing polarized positrons for CLIC have been studied. They differ in the way the electrons for the scattering process are produced. The three options are a 4 GeV linac-based source, a Compton storage ring, and an energy recovery linac. They all use a final conversion target with a capture section and a 200 MeV linac similar to the target stations described for the conventional positron source in this section.

One main advantage of the Compton scattering source is that it is completely independent from the Main Linacs. Other advantages are the relatively-low-energy beam needed to interact with the laser and the high polarization achievable, about 60%. In addition, such a source could be added to the CLIC injector complex at any time without disturbing operation. The drawback of the Compton scheme is that it has a relative low scattering cross-section. To generate the necessary positron charge per bunch requires electron bunch and laser pulse intensities that are not at present available with existing technology. It would be necessary to use a stacking process in the pre-damping ring to accumulate enough intensity for the collider.

The preferred option so far is the use of a Compton storage ring. A 1 GeV electron beam is stored in a ring and collides in a double-chicane scheme with a polarized laser. The resulting polarized gamma rays are subsequently converted into positrons in a target. This scheme would need stacking of several hundred pulses to accumulate the necessary charge in the pre-damping ring. Details can be found in Refs. [15–17].

A second option is to use an energy recovery linac (ERL), a continuous low-charge high-repetition-frequency electron linac. An ERL based e^+ source can provide a large number of low charge bunches. The ERL facilitates stacking if the repetition rate is large enough but would still require a stacking factor of around 2000. Additional storage rings for the accumulation process would also be needed to satisfy the CLIC parameters. The scheme is described in Refs. [18, 19]. Figure 3.5 shows a basic layout of the ERL scheme.

Finally, the electrons could be generated by a powerful 4 GeV linac feeding a chain of consecutive electron-photon interaction points [17, 20]. A powerful CO₂ laser would be needed and an electron bunch charge of 5 nC. The advantage of this option would be that no stacking is required to produce the necessary positron intensity.

3.1 INJECTORS

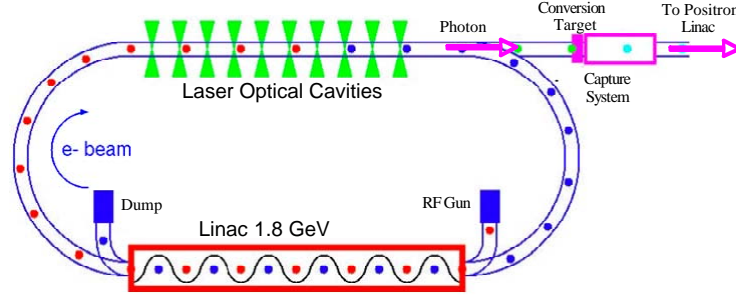


Fig. 3.5: Basic layout for an ERL scheme.

3.1.4.2 Undulator

A positron source scheme similar to the one chosen by ILC [21] would use circularly polarized gamma rays generated from the main 250 GeV electron beam. The beam passes through a helical superconducting undulator with a magnetic field of ~ 1 T and a period of 1.15 cm. The gamma rays produced in the undulator in the energy range between ~ 3 MeV and 100 MeV are directed to a titanium target and produce polarized positrons. The positrons are then captured, accelerated, and transported to the pre-damping ring. Effects on the 250 GeV Main Beam, including emittance growth and energy loss from the beam passing through the undulator seem acceptable [22]. A thesis has been written concerning the study of undulator configurations for CLIC [23]. One of the big issues is the e^+ transport from the main tunnel to the PDR over tens of kilometres. A drawback of the scheme is the coupling of the Main Beam and the positron production. It is also not easily implemented after initial construction as it would require major intervention in the Main Linac.

3.1.5 Accelerator physics issues

3.1.5.1 Polarized electron source

The baseline option to produce polarized electrons for CLIC has been demonstrated at SLAC. However, the source could benefit from further R&D and alternative solutions. A 1 GHz oscillator-based laser seems feasible and would produce the required time structure directly. However, cathode R&D would have to demonstrate that this implementation did not suffer from space charge and surface charge limitations. It would also require a higher voltage DC-gun in the range 200–300 kV. There is an ILC-funded R&D program at Jefferson Lab to evaluate the performance of such a gun.

3.1.5.2 Positron source

One of the main issues for the e^+ source is the beam power deposition and potential target failures. The intense Coulomb scattering of the shower components on the target materials may cause target degradation and damage.

In the crystal target, radiation damage occurs by elastic collisions of the incident electrons on the nuclei. If the recoil energy $T = Q^2/M$ (where Q is the momentum transfer and M the nucleus mass) is above some threshold E_d (about 25 eV for tungsten), the nucleus is dislodged from its lattice. For T

larger than $2E_d$, the primary nucleus can initiate a cascade of displacements of neighboring nuclei. An evaluation has been done for different crystals (W, Si, Ge, C(d)-diamond) [24]. The maximum tolerable flux was found to be between 10^{19} and 10^{21} particles/cm². An experiment with a thin W crystal was done at SLAC in 1996 at the SLC target and showed that a flux of 2×10^{20} e⁻/cm² did not affect the nominal mosaic spread [25, 26]. For CLIC, the flux is 4×10^{14} e⁻/cm²/sec for a 2.5 mm r.m.s. beam radius. At that flux, it would take 140 hours to reach the flux measured at SLAC. The critical flux might be higher, in which case the target would last longer. Annealing can be used to recover the crystal qualities.

Heating of the crystal increases the amplitude of thermal vibrations and affects the available potential on the axis. This potential has been parameterized [27] and simulations done for rather thick crystals [28]. As the temperature increases, the potential decreases and therefore the photon yield decreases as well. For CLIC, the energy deposited in the crystal is rather low (12.5 MeV/e⁻ for a 1.4 mm crystal with a 5 GeV beam). The total energy deposited is less than 0.25 kW and should not affect the yield. The instantaneous heating for tungsten must be less than 35 J/g to avoid inhomogeneous energy deposition and intolerable mechanical stresses [29]. For the parameters chosen, the PEDD in the crystal is less than 7 J/g, which is only 20% of the maximum limit.

However, in the amorphous target (10 mm thick) a large amount of power is deposited. This impacts the cooling system, which must be sufficient to remove the average heating, and causes instantaneous heating. The PEDD in the target has been calculated to be about 22 J/g, still below the expected limit. This is one of the main arguments for choosing the hybrid target as the baseline for the CLIC e⁺ source. However, all these issues related to beam power deposition and target breakdown remain to be verified experimentally.

A detailed technical design of the entire area close to the target is a significant engineering challenge because of the high radiation. A special accelerating structure with a larger aperture might improve the yield of the positron source. The transport of the large positron beam from the target to the damping ring requires careful and complex optimization. A feasible configuration has been found and described above but there is certainly room for improvement. This topic is probably the most challenging accelerator physics issue for the Main Beam injector complex.

3.1.6 Component specification

The injector complex for the Main Beam described here consists mostly of standard components which are commonly found in particle accelerators. The magnets for the different linacs are standard iron-yoke magnets with state-of-the-art tolerances for the field distribution and power supply stability. The RF system consists of 50 MW, 2 GHz klystrons with a pulse length of 8 μ s and a pulse compressor. The amplitude stability required for the accelerating fields is around 1% and a phase stability of 0.1° is sufficient. Beam diagnostic elements also have standard requirements. The most demanding specification for diagnostics is the sub per cent range resolution for beam current monitoring. The specification for the laser for the polarized electron source and its cathode is described in detail in §5.1. The most demanding area of the complex is the positron production target area. The requirements for the conversion targets are described above. The whole area will be a high radiation area requiring special care in the design and choice of materials for each component installed close to the targets. Remote handling techniques might be needed after some years of operation to replace a target or other components.

3.2 The Damping Rings complex

3.2.1 Overview and target parameters

The main purpose of the CLIC damping rings is to ‘cool’ the incoming electron and positron beams to the very small emittances needed for collisions. This goal is achieved with four rings, a pre-damping and a main damping ring for each particle species, schematically shown in Fig. 3.6. Two pre-damping rings (PDRs) are needed to damp the large input emittance, particularly the positrons, at the high repetition rate of 50 Hz.

At every machine cycle of 20 ms, two trains are injected into the damping rings separated by half the damping ring circumference. The bunches in the trains have twice the nominal bunch separation (1 vs 0.5 ns) in order to reduce the transient beam loading effects in the RF cavities. The heads of the two trains are damped simultaneously and then extracted in a single turn from the main damping rings. A delay and recombination loop, downstream of the main rings, provides a unique train with the required 2 GHz bunch structure.

Standard transport lines transfer the beam between the injector linac, the damping rings, the delay loop and the booster linac. The same recombination loop is used for both species and the downstream systems have different path lengths to compensate for the time delay between the e^+ and e^- trains.

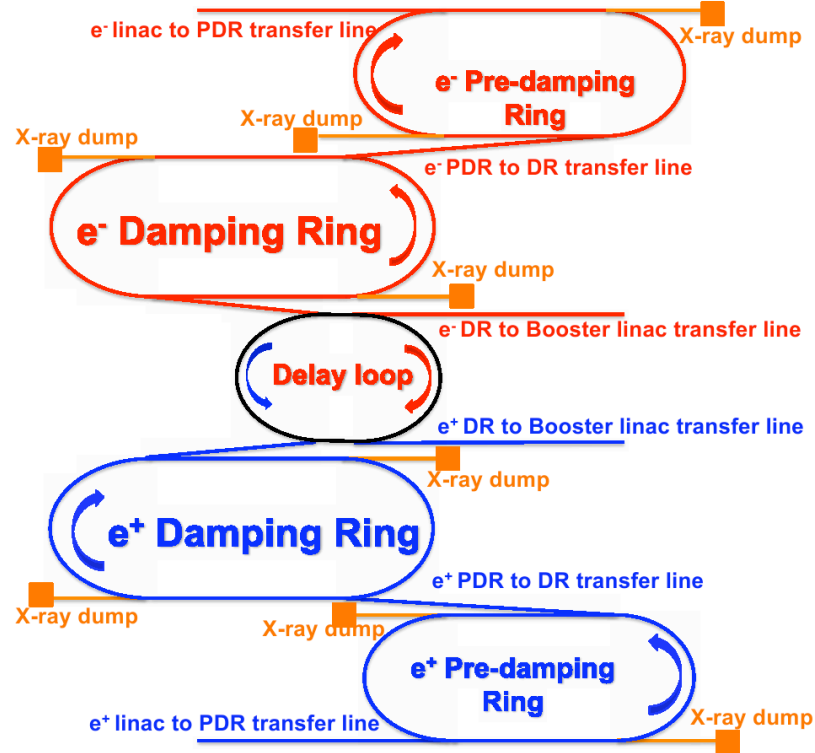


Fig. 3.6: A schematic view of the damping ring complex, with blue for positrons and red for electrons. A single delay and recombination loop (black) is used for both species

The damping ring designs must satisfy the main parameters of the collider and the requirements of the upstream and downstream systems, as summarized in Tables 3.3 and 3.4. The positron beam has a large energy spread which reduces the capture efficiency in the pre-damping ring and requires a much larger bunch population in the ring. The electrons are captured more efficiently and roughly a 10% overhead is adequate for ring and transfer losses. The transverse emittances for the two particle species also differ by almost three orders of magnitude. The huge positron emittance to be captured is a challenge for the pre-damping ring, necessitating large dynamic transverse and momentum acceptance.

The design optimization is discussed in §3.2.2.

The design of the main damping rings is described in §3.2.3, including optics, collective effects and related technology. Most of the parameter choices of the CLIC main DRs are driven by the requirement for unprecedented low emittance at their output, especially in the horizontal plane. In addition, the bunches have a very high charge density with an extremely small phase space volume in all three dimensions. This induces a number of collective effects, which have to be reduced either by a parameter optimization or with mitigation techniques and dedicated feedbacks. Finally, the design requirements drive the technology of a number of components, such as wigglers, RF systems, kickers, and vacuum.

Table 3.3: Parameters required at the exit of the low energy linac and before injection to the pre-damping rings

Injected parameters	e^-	e^+
Bunch population [10^9]	4.3	6.6
r.m.s. Bunch length [mm]	4	5.4
r.m.s. Energy spread [%]	1	4.5
Hor., Ver. Norm. emittance [nm]	100×10^3	7×10^6

Table 3.4: Parameters required at the extraction of the damping rings

Extracted parameters	e^-/e^+
Bunch population [10^9]	4.1
Bunch spacing [ns]	0.5
Number of bunches/train	312
Number of trains	1
Repetition rate [Hz]	50
Normalized horizontal emittance [nm]	500
Normalized vertical emittance [nm]	5
Normalized longitudinal emittance [keV.m]	6

3.2.2 Pre-damping rings

3.2.2.1 Challenges

The PDRs have to accommodate the large emittance bunches from the positron source [30], and damp them to emittances that are small enough to be injected in the DR without losses.

The required input and output parameters are given in Table 3.5 [31]. Both electron and positron PDRs are needed to damp the injected beams to the parameters required by the main DR. The injected positrons have a normalized emittance of 7 mm and an r.m.s. energy spread of around 4%. The injected electron emittance, although three orders of magnitude lower than positrons, is still two orders of magnitude too high in the vertical plane. Without the PDR, the electron beam injected directly into the DR would have too small a dynamic acceptance in the vertical plane.

The electron PDR is also required to provide adequate damping time. The injected electron emittance is five orders of magnitude higher than the 5 nm required at the exit of the DR. With a damping time of around 2 ms in the DR, at least 20 ms (i.e., ten damping times) is needed to reach equilibrium, which is equal to the beam cycle time. This is even without considering the effect of intra-beam scattering. If the injected electron emittance could be reduced by about a factor of ten, it may be possible to eliminate the electron PDR.

Unlike the main DR, the PDR lattice design is not driven by the emittance requirements. The target geometrical horizontal emittance of 10 nm is a value easily achieved by synchrotron light source

3.2 THE DAMPING RINGS COMPLEX

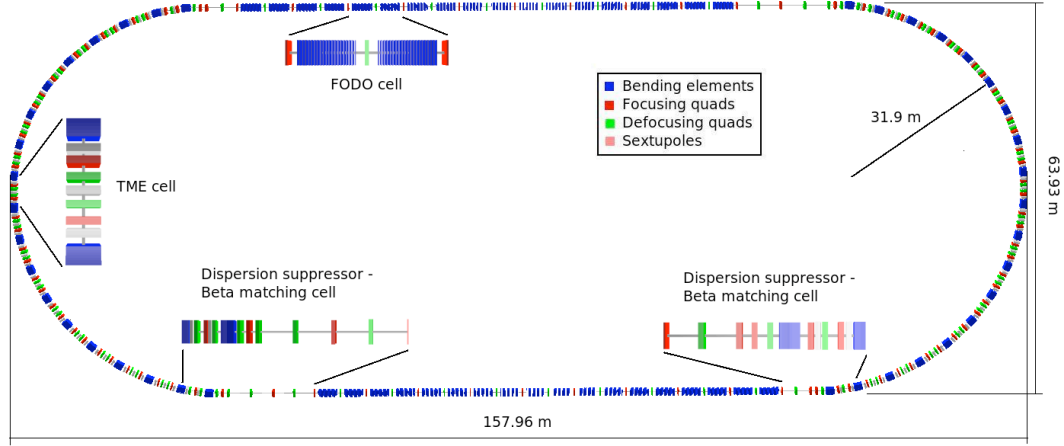


Fig. 3.7: Schematic layout of the CLIC Pre-damping rings.

storage rings at this energy. On the other hand, the large energy spread and the large beam size of the injected positron beam requires a ring with large momentum acceptance and dynamic aperture.

Table 3.5: CLIC PDR injected beam parameters (after injection and capture losses) [32] and required extracted parameters.

Parameters	Injected		Extracted
	e^-	e^+	
Bunch population [10^9]	4.3	4.3	4.3
r.m.s. bunch length [mm]	4	5.4	10
r.m.s. energy spread [%]	1	0.6	0.5
Long. emittance [keV.m]	114	93	143
Hor. Norm. emittance [μm]	100	7×10^3	63
Ver. Norm. emittance [μm]	100	7×10^3	1.5

3.2.2.2 Layout and design parameters

The PDRs have a racetrack configuration similar to the DR, as shown in the schematic layout of Fig. 3.7. The arc sections have dipoles surrounded by doublet quadrupoles forming Theoretical Minimum Emittance (TME) cells. The long straight sections (LSS) are composed of FODO cells filled with normal conducting damping wigglers. The optics between the arcs and the straight sections are matched with dispersion suppressor - beta matching sections. The total length of the rings is 389.15 m. The injection and extraction regions are in the dispersion free sections upstream of the wigglers, while the RF cavities are downstream of this long straight section. The radiation absorption system must protect sensitive equipment in these areas. The PDR design parameters are summarized in Table 3.6. The two columns correspond to the different parameters for the 2 and 1 GHz RF frequency options.

3.2.2.3 Optics design

Each arc is composed of 17 TME cells (16 plus 2 half cells at each edge) and two different dispersion suppressor and matching sections. This accommodates independently the requirements for beam transfer and RF. The target emittances of the PDRs are not extremely low and therefore the TME cells can be

Table 3.6: Design parameters for the PDRs

Parameter, Symbol [Unit]	2 GHz	1 GHz
Energy, E [GeV]	2.86	
Circumference, C [m]	389.15	
Bunch population, N [10^9]	4.3	
Basic cell type in the arc/LSS	TME/FODO	
Number of dipoles, N_d	38	
Dipole Field, B_0 [T]	1.2	
Horizontal and vertical tune, (Q_x, Q_y)	(16.39, 12.26)	
Horizontal and vertical chromaticity, (ξ_x, ξ_y)	(-19.0, -22.9)	
Number of wigglers, N_w	36	
Wiggler peak field, B_w [T]	1.9	
Wiggler length, L_w [m]	3	
Wiggler period, λ_w [cm]	30	
Norm. equil. horizontal emittance, $\gamma\epsilon_{x0}$ [μm]	54	
Hor., vert. and long. damping time, (τ_x, τ_y, τ_l) [ms]	(2.7, 2.7, 1.35)	
Momentum compaction factor, α_c [10^{-3}]	3.7	
Energy loss/turn, U [MeV]	2.8	
Equil. energy spread (r.m.s.), σ_δ [%]	0.1	
RF Voltage, V_{RF} [MV]	10	
Synchrotron tune, Q_s	0.071	0.051
Bunches per train, n_b	312	156
Bunch spacing, τ_b [ns]	0.5	1
RF acceptance, ϵ_{RF} [%]	1.2	1.7
Harmonic number, h	2596	1298
Equil. bunch length (r.m.s.), σ_s [mm]	3.2	4.6

strongly detuned from the absolute minimum emittance. The TME cells are chosen for their compactness, which reduces the overall size of the ring. The arc cell optics is optimized to give the large dynamic aperture (DA) and momentum acceptance required by the large incoming positron emittance and energy spread.

The DA of low emittance rings is dominated by the non-linear fields of the strong chromaticity sextupole magnets. To increase the DA, it is necessary to reduce the natural chromaticity of the cell while still achieving the target output emittance. To fully explore the parameter space, an analytical solution for the TME cell optics based on a thin lens approximation was developed [33]. Low horizontal chromaticity is achieved for horizontal phase advances smaller than π , but the corresponding detuning factor is above 10. To reduce the vertical chromaticity, the vertical phase advance should also be below π .

The choice of cell length, total number of cells and optics, are displayed in Fig. 3.8. The cell is 5.3 m long with horizontal and vertical phase advances of 0.294 and 0.176. A 1.2 T dipole 1.31 m-long is surrounded by two quadrupole doublets 0.28 m long. The bending field is high enough (1.2 T) to reduce the dipole length (1.31 m) and low enough to increase the bending radius and thus the damping time.

Four families of sextupoles provide chromaticity correction. Two sextupoles powered in series are located on either side of the focusing quadrupoles in each cell, and another sextupole is sandwiched between the two defocusing quadrupoles. Two additional families are placed in the dispersion suppression area for controlling higher order chromaticity and off-momentum optics beating.

The required damping is mainly achieved by the damping wigglers in the long straight sections. These are hybrid permanent magnet wigglers with 1.9 T peak field, 30 cm period and a gap of 41 mm.

3.2 THE DAMPING RINGS COMPLEX

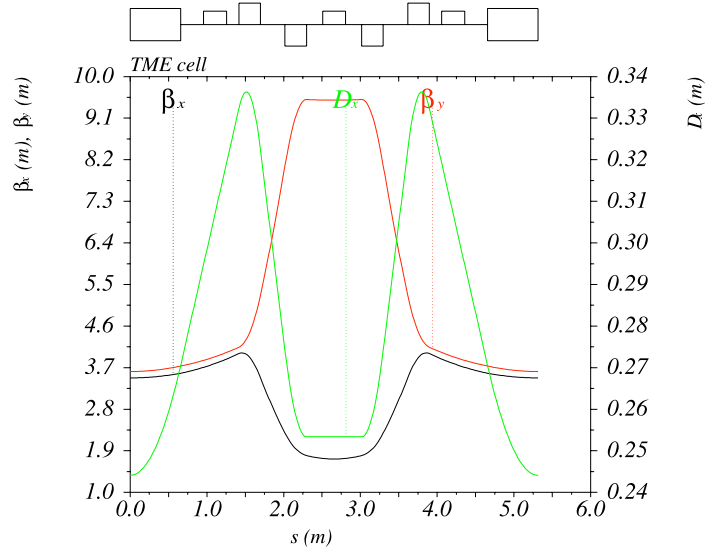


Fig. 3.8: Horizontal (black), vertical (red) beta functions and horizontal dispersion (green) of the TME arc cell of the PDR.

The wiggler parameters achieve the required damping with a gap which is large enough to fit the large beam. The peak magnetic field B_w on axis is related with the gap g and wiggler period λ_w according to the equation by Halbach [34]:

$$B_w = a \exp \left[b \frac{g}{\lambda_w} + c \left(\frac{g}{\lambda_w} \right)^2 \right] \quad (3.1)$$

where both B_w and a are expressed in units of Tesla and b and c are dimensionless. These parameters depend on the wiggler performance and the materials used in the magnet. The coefficients a , b , c have been computed using a 3D magnetostatic code [35].

Two 3 m-long wigglers are placed in each FODO cell with phase advance close to $\pi/2$. Each LSS consists of 13 FODO cells. The total number of wigglers is 52 with a total wiggler length of 108 m. The quadrupoles of the FODO cell are used to adjust the ring tune. The optical functions of the FODO cell is shown in Fig. 3.9.

The optical functions between the arcs and the straight sections are matched with the dispersion-suppressor - beta matching (DS-BM) sections. Two different DS-BM sections are used in the dispersion free regions upstream and downstream of each wiggler section. Space is reserved for the beam transfer elements upstream and the RF cavities downstream of the wiggler section. The optical functions of the two dispersion suppressors are shown in Fig. 3.10. The optics in the kicker areas will be further optimized during the project preparation phase, in conjunction with the design of the beam transfer-line optics, the beam transfer element parameters and the overall damping ring complex layout.

3.2.2.4 Main magnet parameters and physical aperture

Table 3.7 summarizes the magnet parameters of the PDR lattice. There are 38 main dipoles in one family, four of which are located in the DS-BM section for dispersion suppression. There are 198 quadrupoles of three different types (i.e., differing in length) for the arc, LSS and DS-BM sections. The pole-tip field is around 1 T. There are 110 sextupoles with a pole-tip field of 0.8 T. One hundred and two (two families) are located in the arcs and the remainder in the DS-BM section. All of the magnets except the dipoles and wigglers have a circular aperture with 30mm radius from the centre to the magnet pole. The main bending magnets and wigglers have an elliptical aperture with vertical gaps of 30 and 41 mm, respectively.

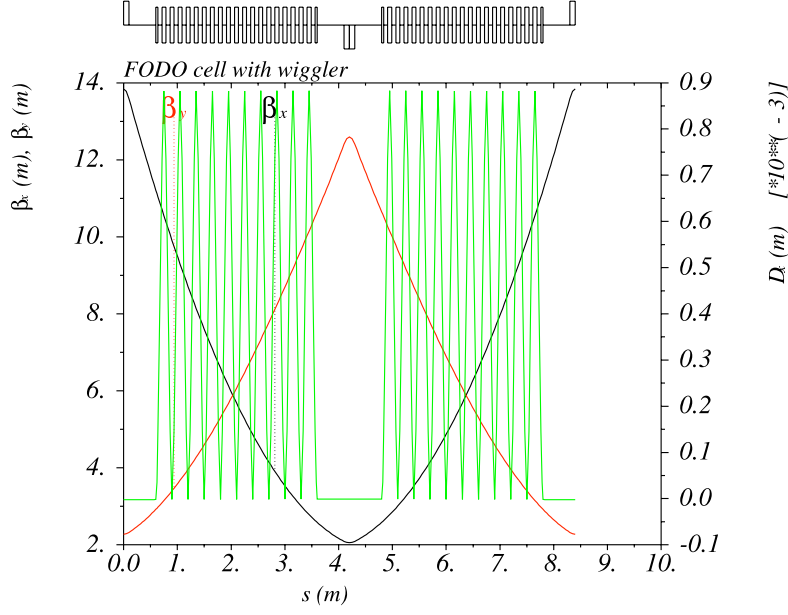


Fig. 3.9: Horizontal (black), vertical (red) beta functions and horizontal dispersion (green) of the FODO cell in the LSS of the PDRs the straight section.

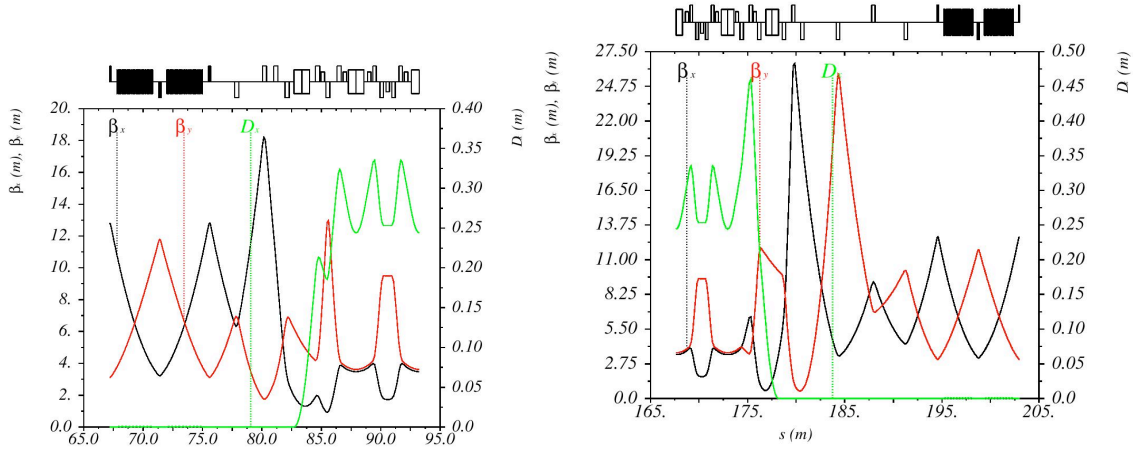


Fig. 3.10: Horizontal (black), vertical (red) beta functions and horizontal dispersion (green) of a TME cell, the two dispersion suppressor-beta matching sections and the FODO cell. Space is reserved for RF cavities (left) and injection/extraction elements (right)

The acceptance of the ring is defined as $R_{acc} = \sqrt{2\beta\epsilon_{edge} + \eta\delta}$, where η the dispersion, $\delta = 1.7\%$ the full momentum acceptance for positrons and $\epsilon_{edge} = 10\epsilon_{inj}$ is the edge emittance of the positron beam. The injected particle distribution is not really Gaussian and the injected emittance corresponds to 99% of this distribution. According to Fig. 3.11, the required acceptance for the straight sections is around 4.5 times the beam size in both planes due to the uniformity of the optical functions in the FODO cells. The required vertical acceptance remains the same in the arc, but the horizontal acceptance is less than twice the beam size, due to the smaller horizontal beta functions. As shown on the right part of Fig. 3.11, the required acceptance for both planes is everywhere less than 30 mm which is the minimum magnet half gap for all magnets except the vertical wiggler which is 20.5 mm. In that section, the vertical acceptance requirement is below 20 mm. The two PDRs are identical even though the required acceptance for the electron PDR is smaller, which would allow smaller magnet apertures and reduced cost and power consumption.

3.2 THE DAMPING RINGS COMPLEX

Table 3.7: List of magnetic parameters for the CLIC PDRs.

Type	Location	Length [m]	Number	Families	Pole tip field [T]	Full aperture H/V [mm]
Dipoles	Arc DS-BM	1.31	34 4	1	1.2	60/30
Quadrupoles	Arc	0.28	128	2	1.0	60/60
	LSS	0.20	36	2		
	DS-BM	0.35	32	16		
Sextupoles	Arc	0.30	68 + 34	2	0.5	60/60
	DS-BM		8	2		
Wigglers	LSS	3.00	36	1	1.9	60/41

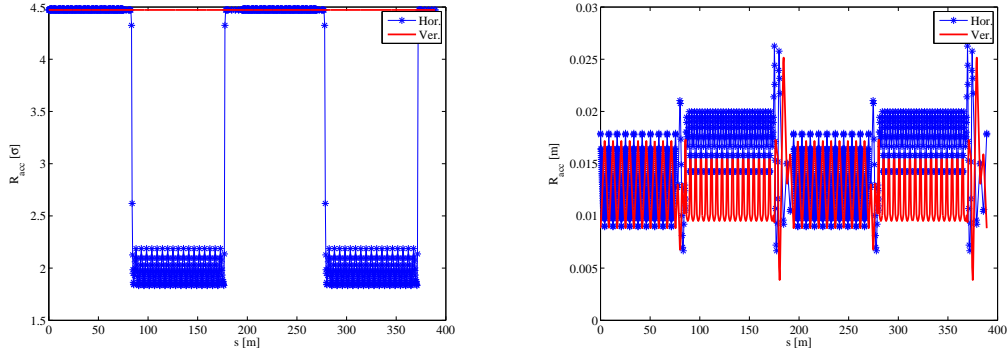


Fig. 3.11: The required acceptance around the PDR in order to fit the positron beam in units of beam sizes (left) and in metres (right).

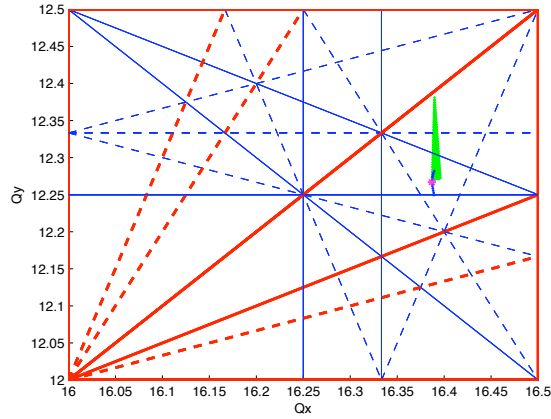


Fig. 3.12: Tune-space of the CLIC PDR around the on-momentum working point of (16.39, 12.27), with the analytical first order tune shift with amplitude up to 6σ (green) and the chromatic tune-shift for momentum deviations from -1.2% to 1.2% (blue).

3.2.2.5 Longitudinal and RF parameters

The large momentum acceptance needed for the positron injection efficiency can be achieved with either a small momentum compaction factor and/or a high total RF voltage. A small momentum compaction

would require cell optics with small emittance detuning and this reduces the DA dramatically. A moderate momentum compaction combined with a high RF voltage (total of 10 MV) is a better solution. This increases the total RF system length but makes the beam loading compensation easier through the reduction of the RF stationary phase (see §5.4.2.3). The RF acceptance is higher at 1 GHz ($\pm 1.7\%$ versus $\pm 1.2\%$) due to the reduction of the harmonic number. At 2 GHz, twice the RF voltage is required to achieve the same momentum acceptance. This significantly impacts the RF system length and cost. The baseline design has the same RF voltage for both frequencies. Further lattice optimization will be required with the 2 GHz frequency. Even with low momentum acceptance, the e^+/e^- yield is 0.453 which is acceptable, given the target survivability of the positron source [32]. Four 3 m long RF cavities located in the dispersion free region downstream of the wiggler sections provide the 10 MV voltage (see §5.4.2.3).

3.2.2.6 Non-linear optimisation and Dynamic Aperture

The nonlinear lattice optimization was based on the analytical parameterization of the TME cells [33] and the resonance free lattice concept [36]. The analytical analysis indicated that a large detuning factor and low phase advance per cell are required to keep chromaticity low. To avoid resonances, the proper choice of cell phase advance is crucial to cancel the large number of resonance driving terms. The optimal number of cells per arc was chosen to be 17 (16 TME arc cells plus 2 half TME cells in the dispersion suppressors) and the phase advance per cell are 5/17 horizontally and 3/17 vertically. This provides the required output emittance as well as cancelling resonance driving terms. Even if the chosen phase advances provide the required equilibrium emittance, the tune-spread is non-negligible and mostly dominates the DA. Figure 3.12 shows the working point in tune space (blue curve) for momentum deviations $\delta p/p$ varying from -1.2% to 1.2% and the analytical first order tune shift with amplitude (green) up to $6\sigma_{x,y}$. The on momentum working point is located at (16.39, 12.27), in order for the tune-spread to be confined to an area where low order systematic resonances (red lines) are not present. As noted above, the tune-shift with amplitude is quite large especially in the vertical plane. Future study should explore additional sextupole families or octupoles to reduce this tune-shift.

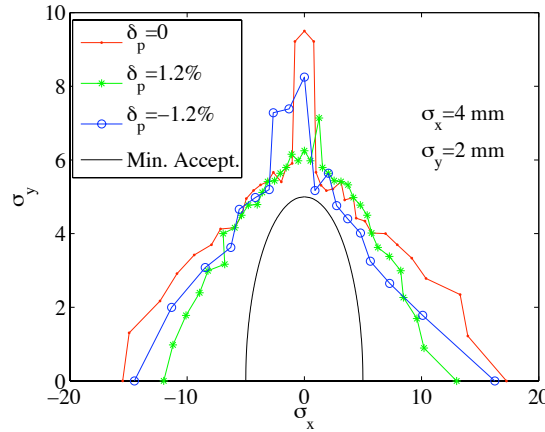


Fig. 3.13: The 5D, 1000-turns, Dynamic Aperture of the PDR, for particles with momentum deviations of zero (red), +1.2% (green) and -1.2% (blue), as compared to the physical ring acceptance (black)

The DA has to be larger than the maximum ring acceptance, which is around 5σ in both planes, as shown in Fig. 3.11. The DA of the ring was computed for particles tracked in 5D, over 1000 turns with the PTC module of MADX [37], for three momentum spreads of $\delta p/p = 0$ and $\pm 1.2\%$ representing 70% (or the full) bucket size for the 1 GHz (or 2 GHz) RF parameters. The model takes into account the magnet fringe fields and the main sextupoles which are tuned to cancel chromaticity. No further magnet

3.2 THE DAMPING RINGS COMPLEX

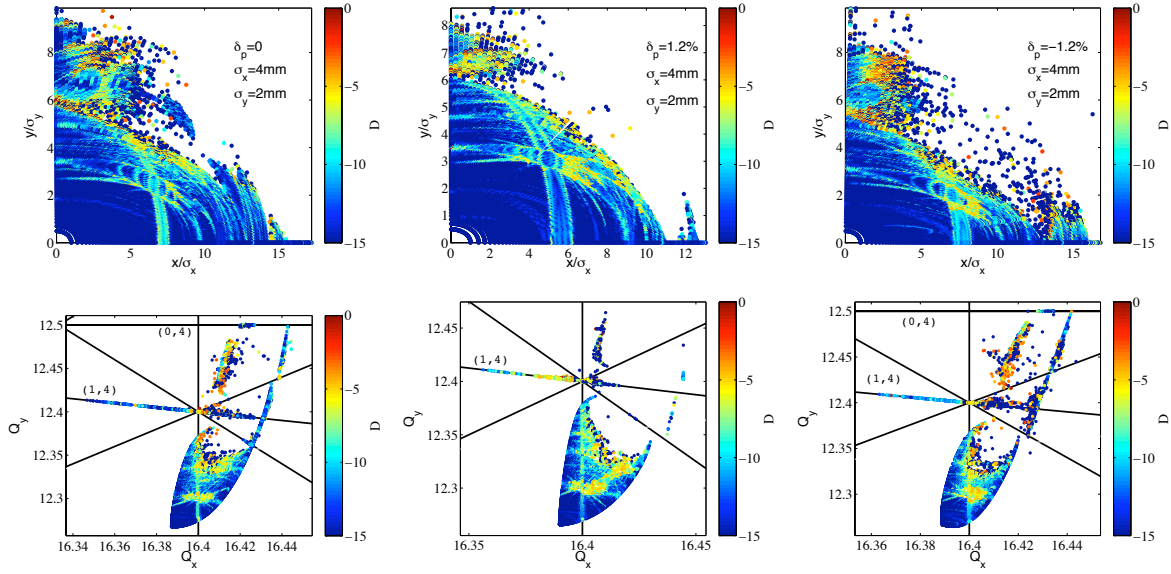


Fig. 3.14: Frequency (bottom) and diffusion (top) maps, for momentum deviations of zero (left), $+1.2\%$ (centre) and -1.2% (right). The different colours correspond to tune diffusion coefficients.

misalignments or multi-pole errors have been considered yet. The results are displayed in Fig. 3.13, including a continuous black curve indicating the physical aperture. The on-momentum DA (red curve) is comfortable, especially in the horizontal plane. There is some reduction of the DA for off-momentum particles but the DA is still larger than the physical acceptance.

In order to further understand the limitations of the DA, frequency (bottom) and diffusion (top) maps are plotted in Fig. 3.14, for $\delta p/p = 0$ (left), $\pm 1.2\%$ (centre and right), colour coded with the frequency diffusion coefficient D , a measure of the computed tune-variation over two consecutive time spans of 500 turns. Blue colour indicates very small tune diffusion whereas red colour indicates fast diffusion which is associated with resonances. The empty areas in the plots are for particles which are lost before reaching 1000 turns and show the DA. For large amplitudes, the tune crosses a node of normal 5^{th} order resonance lines. In particular, the $(1,4)$ resonance appears to be the main limitation for the DA. Indeed, this resonance cannot be eliminated for this choice of phase advance. This is an additional indication of the need to further control the tune-shift with amplitude in order to move high-amplitude particles away from this resonance.

3.2.2.7 Collective effects

Collective effects are not expected to present serious limitations in PDRs as compared to the main DRs. The bunch population is moderately higher but the transverse emittance and bunch length are much larger, so space charge effects are negligible and cause only a very small vertical tune shift of around 2×10^{-4} . Intra-beam scattering is also negligible causing an emittance growth of less than 0.1% . The longer bunches and the larger vacuum chamber aperture increases significantly the thresholds for broadband and resistive wall impedance. The growth rates for coupled bunch instabilities are also much larger than the damping times. The ion instabilities in the electron PDR are not a problem due to the larger beam sizes and can be mitigated by moderately low vacuum pressure. The only issue which depends primarily on bunch current and bunch spacing and not on transverse emittance is the electron cloud instability. This needs to be mitigated with special coatings for reducing the secondary electron yield, similar to the ones used in the main DRs.

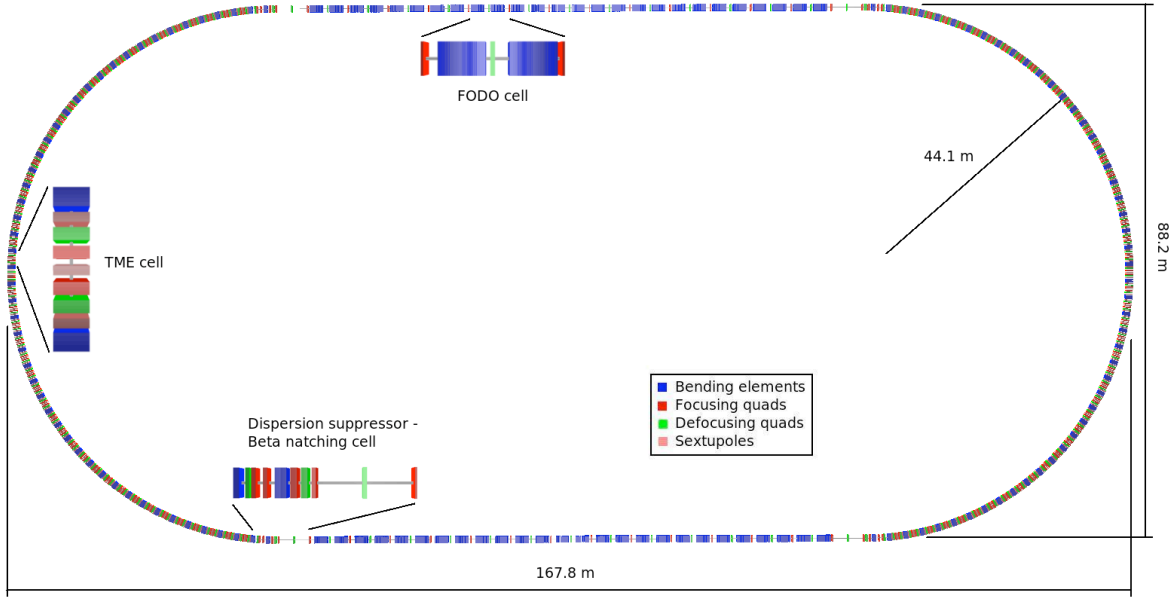


Fig. 3.15: Schematic layout of the CLIC main Damping Rings.

3.2.3 Main Damping Rings

3.2.3.1 Challenges

The role of the main damping rings is to provide the final stage of damping to the required low emittance at a fast repetition rate. The parameter requirements are summarized in Table 3.4. The bunch population is 4.1×10^9 particles which allows a 10% margin for losses in the downstream systems between the DR and the IP. The emittance requirements are extremely low, 500 nm and 5 nm horizontal and vertical normalized to the beam energy, in spite of the high bunch intensity. These low emittances, although unprecedented, are approached by modern light sources either in operation or under construction phase [38, 39]. The main difference compared with the light sources is the very small longitudinal normalized emittance of 6 keV·m, which is required for the bunch compression in the RTML [40]. The high beam density triggers a number of single bunch collective effects including Intrabeam Scattering (IBS), Space-Charge (SC), Coherent Synchrotron Radiation (CSR) and Transverse Mode Coupling Instabilities (TMCI). Two-stream phenomena such as ions or electron cloud build up are amplified by the short bunch spacing of only 0.5 ns, making the vacuum technology and the photon absorption quite demanding. The short bunch spacing also creates a high peak current as seen by the RF system, where low level RF system to cope with the beam loading transients is very challenging. In addition, a high frequency (2 GHz) pulsed RF power source is not currently available. Finally, the small emittance has to be extracted in a very stable and reproducible way imposing tight tolerances in the kicker system stability.

3.2.3.2 Layout and design parameter choice

The main DRs have a racetrack configuration, as shown in the schematic layout of Fig. 3.15. The arc sections are filled with TME cells, whose dipoles have a small defocusing gradient. The long straight sections (LSS) are composed of FODO cells containing 52 superconducting damping wigglers. The optics between the arcs and the straight sections are matched with dispersion suppressor sections. The dispersion free sections in the LSS contain beam transfer and RF. The total length of the rings is 427.5 m. The DR design parameters are summarized in Table 3.8. The two columns correspond to the different parameters for the 2 and 1 GHz RF frequency options.

3.2 THE DAMPING RINGS COMPLEX

Due to the very high bunch charge and small size in all three beam dimensions, the steady-state emittances are dominated by Intra-beam scattering (IBS) [41]. After the latest change in main linac RF system parameters, the damping ring design had to be modified to reduce the emittance blow-up due to IBS [31]. The ring energy was increased and the optics changed to mitigate the IBS effect. In particular, the left side of Fig. 3.16 shows the scaling of the ratio between the steady state and zero current emittances with energy. The IBS effect is reduced at higher energy. The right side of Fig. 3.16 shows the dependence of the steady state emittances on the energy. There is a broad minimum in the horizontal and vertical emittances around 2.0 GeV, where the IBS becomes weaker. At higher energies collective effects are reduced but the zero current emittance increases due to stronger quantum excitation. An energy of 2.86 GeV has been chosen even if the expected emittance is slightly larger than at lower energy because the contribution from IBS is smaller. This reduces the risk associated with any uncertainty of the IBS effect. [42].

Table 3.8: Design parameters for the main DRs.

Parameters, Symbol [Unit]	2 GHz	1 GHz
Energy, E [GeV]		2.86
Circumference, C [m]		427.5
Bunch population, N [10^9]		4.1
Basic cell type in the arc/LSS		TME/FODO
Number of dipoles, N_d		100
Dipole Field, B_0 [T]		1.0
Norm. gradient in dipole [m^{-2}]		-1.1
Horizontal and vertical tune, (Q_x, Q_y)	(48.35, 10.40)	
Horizontal and vertical chromaticity, (ξ_x, ξ_y)	(-115, -85)	
Number of wigglers, N_w		52
Wiggler peak field, B_w [T]		2.5
Wiggler length, L_w [m]		2
Wiggler period, λ_w [cm]		5
Hor., vert. and long. damping time, (τ_x, τ_y, τ_l) [ms]	(2.0, 2.0, 1.0)	
Momentum compaction factor, α_c [10^{-4}]		1.3
Energy loss/turn, U [MeV]		4.0
Norm. horizontal emittance, $\gamma\epsilon_x$ [μm]	472	456
Norm. vertical emittance, $\gamma\epsilon_y$ [μm]	4.8	4.8
Energy spread (r.m.s.), σ_δ [%]	0.1	0.1
Bunch length (r.m.s.), σ_s [mm]	1.6	1.8
Longitudinal emittance, ϵ_l [keV m]	5.3	6.0
IBS growth factors hor./ver./long.	1.5/1.1/1.2	1.5/1.1/1.2
RF Voltage, V_{RF} [MV]	4.5	5.1
Stationary phase [$^\circ$]	62	51
Synchrotron tune, Q_s	0.0065	0.0057
Bunches per train, n_b	312	156
Bunch spacing, τ_b [ns]	0.5	1
RF acceptance, ϵ_{RF} [%]	1.0	2.4
Harmonic number, h	2851	1425

The demand for low emittance at repetition rate of 50 Hz sets tight constraints on the lattice including the number of cells, the bending magnet characteristics, the wiggler field and period. In particular, the wiggler peak fields require super-conducting materials. The vertical emittance at ‘zero current’ is dominated by vertical dispersion rather than coupling, requiring tight alignment tolerances and excellent

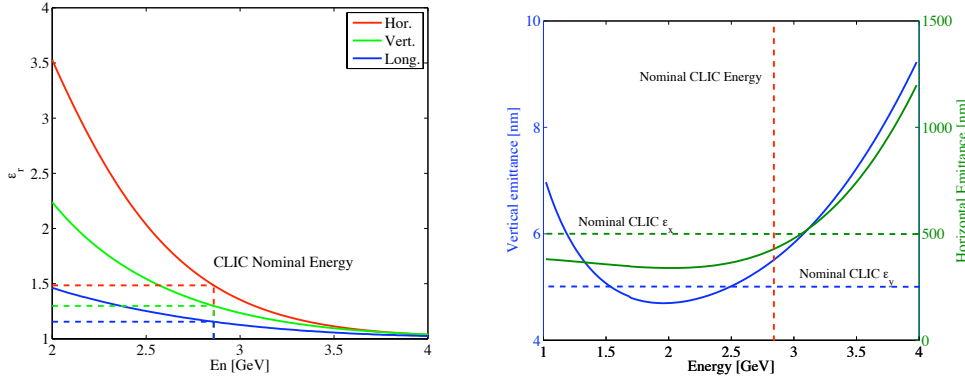


Fig. 3.16: Dependence of the IBS growth factor, i.e., ratio between steady-state and equilibrium emittances (left) and steady state emittances (right) with energy. The different curves represent horizontal, vertical and longitudinal emittance and the dashed lines correspond

correction and control of the orbit. The geometrical target emittance of less than 1 pm is equal to the present record achieved in synchrotron light source storage rings for similar energies and bunch currents [43].

The space charge tune-shift is significant because of the very small beam size especially in the vertical plane. To minimize the impact, the ring circumference is as short as possible and the TME cell is tuned to increase the momentum compaction factor and make the bunch length as long as can be accepted by the RTML.

The beam loading transients in the RF cavities are reduced by halving the RF frequency, which then requires that there be two trains which are subsequently recombined in a delay loop.

Two stream instabilities are an issue with the high bunch density and short bunch spacing. In the electron ring, the fast ion instability is avoided with ultra-low vacuum pressure. The vacuum chambers are coated with getters like NEG for increasing pumping and vacuum conditioning. To mitigate electron cloud build up in the positron ring, the vacuum chambers have a low secondary electron and photo-emission yield (SEY and PEY). The low SEY is achieved with special chamber coatings, whereas the absorption efficiency required to reduce the heat deposition in the super-conducting magnets already guarantees a low PEY. In addition, the longer bunch spacing with the two trains also relaxes these requirements.

3.2.3.3 Optics design

Optics functions for the TME arc cells, long straight FODO sections and dispersion suppressors have been calculated. Each arc is filled with 48 TME cells and 2 half cells at either side for dispersion suppression. The original compact TME cell [41] was re-optimized for space and magnet strength constraints and to reduce the effect of IBS [44]. The major contribution of IBS is at the locations where the beam sizes, i.e., beta functions and dispersions, reach their minima. In the standard TME cell, both horizontal and vertical beam sizes become minimum at the centre of the arc cells and it is exactly at this location where IBS growth rates are maximum. This can be alleviated by adding a defocusing gradient in the dipoles. This further reduces the emittance and also reduces the IBS growth rate by reversing the behaviour of the vertical beta at the centre of the dipole.

Figure 3.17 shows the emittance dependence on the gradient in the bending magnet. The gradient is limited by the iron core saturation and the maximum available value of magnetic field in the good field region. For a dipole field of 1.5 T in the horizontal mid-plane ± 3 cm, the gradient cannot exceed 8.6 T/m (or 1.1 m^{-2} normalized). Figure 3.18 shows the IBS increments for a nominal TME cell (left) and a

3.2 THE DAMPING RINGS COMPLEX

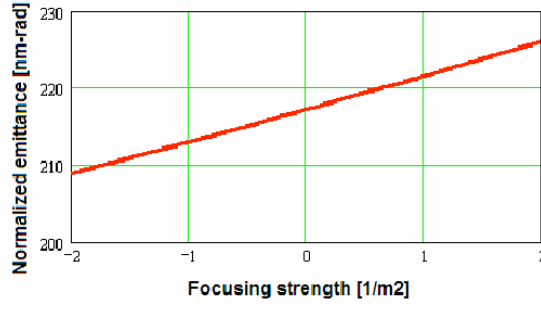


Fig. 3.17: Normalized TME emittance vs. gradient of the dipole magnet.

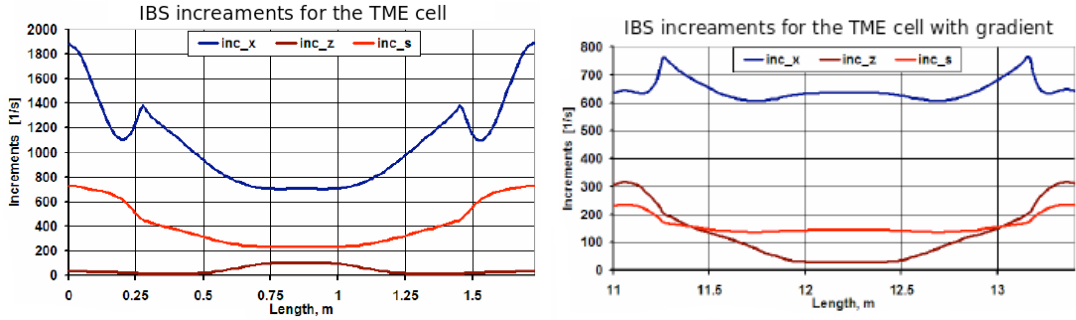


Fig. 3.18: The IBS increments for the original TME cell (left) and the modified cell with vertical gradient. in the dipole (right).

modified TME cell with vertical gradient (right). The IBS growth is reduced with the added gradient, while the output emittance is almost unchanged [44].

Since the damping wigglers in the straight sections further reduce the final emittance and provide fast damping, the TME cell used is detuned for added flexibility, ease of implementation and lower chromaticity. The horizontal and vertical phase advances are $\mu_x=0.408$ and $\mu_y=0.005$. This choice of horizontal phase advance increases the momentum compaction factor, while maintaining the final emittance. The vertical phase advance is the smallest possible in order to increase the vertical beta functions and reduce IBS kicks while keeping the beam acceptance large enough. The bending radius of the dipole (field of 1 T and length of 0.58 m) minimizes the energy loss per turn while increasing the bunch length.

The long straight sections (LSS) contain FODO cells and the damping wigglers. There are 13 FODO cells per straight section with two wigglers per cell. The lattice functions in the wiggler are set to minimize the emittance [45]. For a FODO cell, the minimum emittance is reached with the horizontal phase advance $\mu_x \sim 0.31$ and with the vertical near zero. The vertical phase advance is set as low as possible ($\mu_y \sim 0.12$) in order to minimize the chromaticity. Another possible choice is $\mu_y \sim 0.25$ corresponding to minimum vertical betas and thus, maximum vertical acceptance.

The lattice functions between the arcs and the straight sections are matched with the dispersion suppressors and matching sections. The first part is a half TME cell, with different quadrupole strengths. These two quads are used as knobs in order to minimize the length of the suppressor. A dipole is then used for the suppression of the dispersion and four more quads as knobs for matching of all the optics functions at the entrance of the LSS. Space is reserved in the dispersion free region for injection/extraction and RF cavities.

3.2.3.4 Magnet parameters

Table 3.9 summarizes the main magnet parameters of the DRs. There are 100 main dipoles in one family, four of which are located in the DS-BM section for the dispersion suppression. There are 458 quadrupoles of two different types (0.2 and 0.31 m long). Their pole-tip field is around 1 T. There are 282 0.15 m-long sextupoles in two families with a pole-tip field of 0.8 T. Finally, there are 52 2 m-long super-conducting wigglers. All the magnets except the dipoles and wigglers have a circular aperture of 20 mm diameter. The main bending magnets and wigglers have an elliptical aperture with vertical gaps of 20 and 13 mm, respectively. The geometrical acceptance of the whole ring is quite comfortable since the injected beam emittances are quite small, especially in the vertical plane.

Table 3.9: A list of the DR main magnets including CLIC DRs

Type	Location	Length [m]	Number	Families	Pole tip field [T]	Full aperture H/V [mm]
Dipoles	Arc DS-BM	0.58	96 4	1	0.97	80/20
Quadrupoles	Arc	0.20	376	2	1.0	20/20
	LSS	0.20	28 + 26	2		
	DS-BM	0.20	24	12		
	DS-BM	0.31	4	2		
Sextupoles	Arc	0.15	188 + 94	2	0.5	20/20
Wigglers	LSS	2.00	52	1	2.5	80/13

3.2.3.5 Wiggler specifications and performance

Damping wigglers are required to produce the ultra-low horizontal emittance in a compact ring within the machine pulse of 20 ms. They have high field and relatively short period in order to reach the target emittances [46]. Pure permanent magnets cannot reach the required field (the maximum is around 1.2 T for $\text{Sm}_2\text{Co}_{17}$). This could be increased with pole concentrators (e.g., vanadium permendur). Figure 3.19 shows the simulated peak field reached in a hybrid permanent magnet wiggler as a function of the period length, for a fixed 14 mm magnetic gap. The behaviour is almost linear and shows that only 1.1 T is reached for 40 mm period, up to 1.8 T for 100 mm period, and a maximum of 2.3 T for 140 mm period. Unfortunately, the longer period would more than double the horizontal emittance, which could only be recovered by doubling the number of wigglers and increasing the ring circumference by 40%. Superconducting damping wigglers are required to obtain very small emittances in a compact ring.

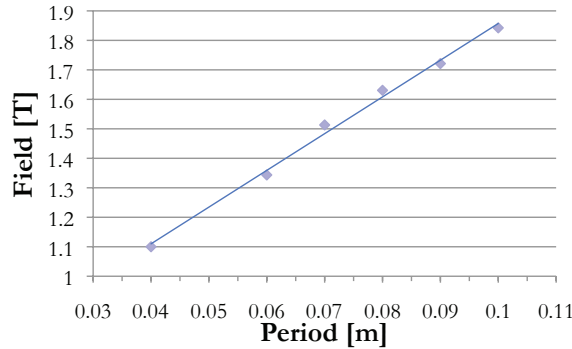


Fig. 3.19: Simulated dependence of a hybrid permanent magnet wiggler peak field with the period length.

3.2 THE DAMPING RINGS COMPLEX

There are 52 wigglers in each DR with peak field $B_w = 2.5$ T and 50 mm period, based on NbTi technology. A short prototype with these characteristics was developed and measured at Budker Institute and achieved the field requirements. Another mock-up with more challenging design (2.8 T field, with 40 mm period) wound with Nb₃Sn wire is also under test at CERN [47].

For a ring with energy E and average beam current \bar{I} , the total radiation power emitted by each wiggler is given by $P = \frac{2c^2 r_e}{3m_0^3} E^2 B_w^2 \bar{I}$, where r_e the electron classical radius and m_0 the electron rest mass. Around 9 kW of total power is produced by each wiggler. An absorption system is critical to protect machine components and wigglers against quench, and also to lower the photo emission yield to limit the e-cloud buildup in the positron ring. The power limit is between 1 and 10 W/m, depending on the superconductor technology and the vacuum chamber cooling. A series of horizontal and vertical absorbers are placed downstream of the wigglers as shown in Fig. 3.20. A terminal absorber at the end of the long straight section absorbs the remaining 100 kW of photon power.

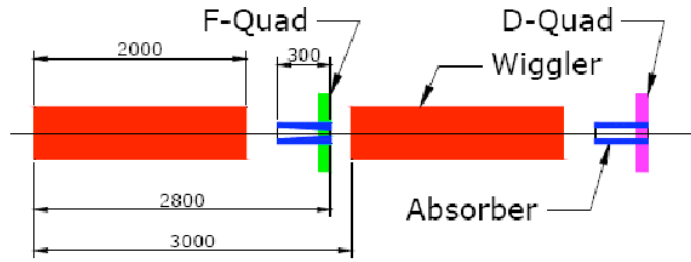


Fig. 3.20: Schematic view of the absorbers in the wiggler section.

Full wiggler prototypes with similar magnetic characteristics will be built at BINP and installed in a straight section of the ANKA synchrotron for tests under beam conditions in an electron storage ring. This will validate the cooling design and the resistance of the wiggler to heat load under real beam conditions.

3.2.3.6 Longitudinal and RF parameters

Parameters relevant to the design of the DR RF system are given in Table 3.10. The transient beam loading would be very challenging with the very high peak and average current of a full train of 312 bunches spaced by 0.5 ns, especially for a 2 GHz RF system. The two bunch trains with 1 ns bunch spacing reduce significantly the beam loading, however the trains have to be recombined in a delay loop downstream of the DRs with an RF deflector.

Table 3.10: CLIC DR parameters relevant to RF

Parameter	DR @ 1 GHz	DR @ 2 GHz
Circumference [m]	427.5	
Energy [GeV]	2.86	
Mom. compaction factor	1.3×10^{-4}	
Energy loss per turn [MeV]	3.98	
Energy spread (r.m.s.) [%]	0.1	0.1
Bunch length (r.m.s.) [mm]	1.6	1.8
Longitudinal emittance [keVm]	5.3	6.0
RF voltage [MV]	5.1	4.5
RF stationary phase [°]	62	51
Peak/Average current [A]	0.66/0.15	1.3/0.15
Peak/Average power [MW]	2.8/0.6	5.5/0.6

The two train configuration relaxes requirements in both the PDRs and the main DRs. By doubling the bunch spacing, the harmonic number is halved and this increases the momentum acceptance. There is less time available for the extraction kicker rise time but it is still long enough (560 ns), although it may no longer be possible to use IGBT switches. The 2-train structure may require two separate extraction kicker systems or one kicker with a longer flat top (1 μ s). The beam loading is significantly reduced, as the longer bunch spacing reduces peak current and power by a factor of two. Several beam dynamics issues are also eased due to the doubled bunch spacing. The e-cloud production and instability is reduced. The fast ion instability is also reduced because the critical mass above which particles get trapped increases by a factor of two. With fewer bunches per train, the central ion density and the induced tune-shift decrease and the rise time of the instability is doubled. This relaxes the feedback system requirements. Finally, 1 GHz is a more conventional frequency for a bunch-by-bunch feedback system than 2 GHz.

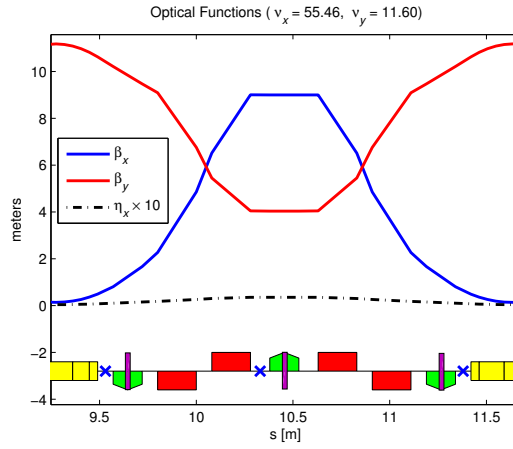


Fig. 3.21: BPMs and correctors considered for TME arc cell. Steering correctors are shown in purple as additional windings on sextupoles, and BPMs indicated as blue crosses.

3.2.3.7 Low emittance tuning

The DRs have a very low normalized horizontal emittance, in addition to a vertical emittance of 5 nm. The zero-population equilibrium vertical emittance is $\gamma\epsilon_y = 3.7$ nm to allow for growth due to IBS [46, 48].

The formalism for estimation of flat-beam vertical emittance follows closely the work of Raubenheimer [49]. The main sources of vertical emittance growth are dispersion introduced by vertical quadrupole offsets and main dipole rolls, and coupling of horizontal dispersion or betatron motion introduced by quadrupole rolls and sextupole vertical offsets. The impact of these misalignments on the vertical emittance have been estimated by simulations [50].

The present lattice design has significantly looser alignment tolerances than initially estimated [51]. There are horizontal and vertical orbit correctors on each arc sextupole (three per TME cell), alternating horizontal and vertical steering correctors adjacent to the wiggler straight quadrupoles (two per FODO cell), and additional steering correctors in the matching sections. There are beam position monitors (BPMs) capable of measuring both transverse planes in the arc cells at points of alternating high and low dispersion, as well as high and low beta functions. In total, there are 358 BPMs and 340 horizontal and vertical correctors. The corrector and BPM pattern for the arc cells is shown in Fig. 3.21. Additional windings on the sextupole assemblies provide skew quadrupole correction. This configuration of steering and skew quadrupole correctors allows complete orbit correction without adjusting the main sextupole field.

3.2 THE DAMPING RINGS COMPLEX

For these simulations, the orbit correction was implemented in MADX-PTC using singular value decomposition (SVD). There were global corrections of tunes, chromaticity and energy but beta-beating was uncorrected.

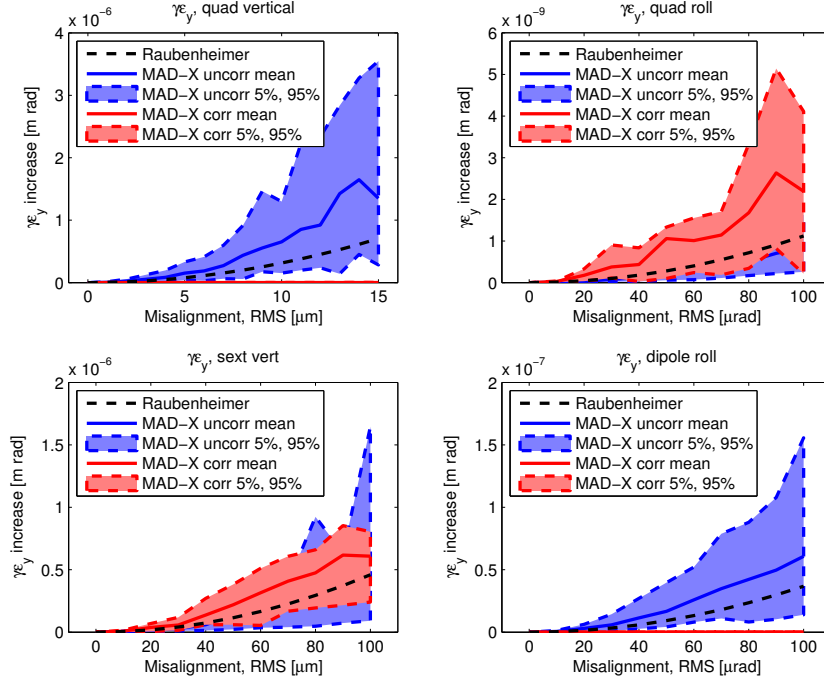


Fig. 3.22: Normalized vertical emittance under random vertical quadrupole offsets (top left), quadrupole rolls (top right), sextupole vertical offsets (bottom left) and dipole rolls (bottom right). Emittances of uncorrected orbits shown in blue, corrected in red, black curve shows analytical estimate of uncorrected emittance.

The equilibrium vertical emittance is summarized in Fig. 3.22. Orbit correction reduces the emittance contribution from quadrupole vertical offsets and main dipole rolls to acceptable levels. In the absence of a skew quadrupole corrector scheme, the sextupole vertical misalignment would have to be better than $6 \mu\text{m}$ to achieve the nominal vertical emittance. The skew quadrupole correctors relax this alignment tolerance to approximately $50 \mu\text{m}$. Large misalignments from dipole and quadrupole rolls of $100 \mu\text{m}$ are tolerable, and quadrupole misalignment of $50 \mu\text{m}$ acceptable.

3.2.3.8 Non-linear optimization and dynamic aperture

In order to evaluate and understand the limitations of the DA, frequency and diffusion maps were produced [52] for a DR lattice including chromatic sextupoles tuned for zero chromaticity, hard-edge fringe-fields and misalignments as given above.

The wigglers are modelled as a sequence of bends with alternating polarity. The working point of the DR is tuned to $\nu_x = 48.35$ and $\nu_y = 10.40$. The synchrotron motion is neglected and 5D tracking is performed with fixed momentum off-sets. The maps are produced by launching a large number of individual particles with different transverse offsets and tracking them with MADX-PTC [37] for 1056 turns or until lost. If a particle has survived up to the last turn, the tunes are evaluated by analysing the tracking data with Laskar's NAFF algorithm [53], and displayed on Fig. 3.23. The frequency diffusion rate is the difference of the tune vector estimated in two consecutive time spans and the points are colour-coded using this coefficient, on the frequency and initial conditions space.

The large tune shift of 0.3 for around $6\sigma_x$ transverse beam offset in the horizontal plane, is due

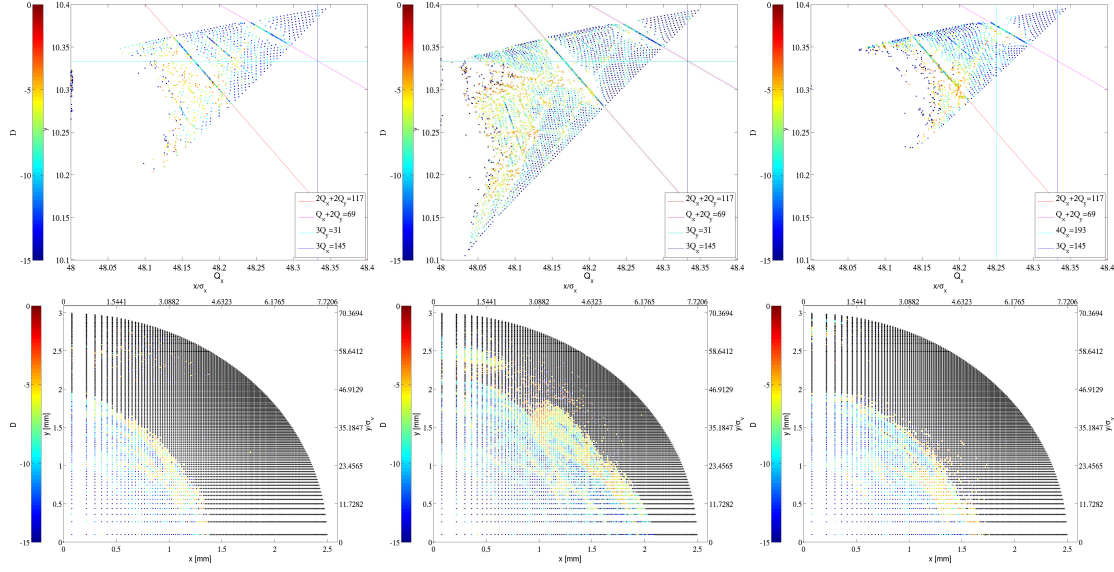


Fig. 3.23: Frequency map (top) and diffusion maps (bottom) of the ideal CLIC DR with, from left to right, a momentum deviation of respectively -0.5%, 0 and 0.5%. The colour code follows the tune diffusion coefficient from stable particles (blue) to highly chaotic (red). Black markers are for lost particles. Some relevant resonance lines are shown in the frequency maps.

to the strong sextupoles needed for chromaticity correction. In the horizontal plane, the tune approaches very close to the integer resonance $Q_x = 48$, which is the main limitation on the dynamic aperture, at least for the on-momentum optics. Two more resonances are clearly excited but do not seem to cause beam loss, at least from the single particle dynamics point of view. The closest to the working point (pink line) is the normal third order resonance $Q_x + 2Q_y = 69$, which can be directly excited at first order by the chromaticity sextupoles and dipole fringe fields. The second (purple line) is the 4th order normal resonances $2Q_x + 2Q_y = 117$, which can be excited by the quadrupole fringe-fields at leading order or by the sextupoles at higher order.

For off-momentum particles with momentum spread of 0.5%, there is a 25% reduction of the DA. The same major resonance lines are visible, but the loss is observed earlier, probably due to the overlapping of a large number of resonances near the horizontal integer line. For the vertical plane, where the beam entering the DR has an emittance which is 50 times lower than the horizontal one, the DA is still comfortable. This is visible in the right and top axes labels of the diffusion marks, where the number of beam sizes are quoted instead of the real size in mm (bottom and left axes labels). However, for the horizontal plane, the dynamic aperture becomes really tight and equal to around $4.5\sigma_x$. This shows how critical is the performance of the PDRs in order to produce the lowest possible horizontal emittance without compromising dynamic aperture of the DRs. In addition, it is important to find sextupole settings that reduce the tune-shift with amplitude, without exciting other resonances, as with this large tune-shift there is no hope in finding a working point, with a much larger dynamic aperture.

Magnet errors and misalignments can drastically change the optical properties of the DR, breaking symmetries of the lattice. To obtain more realistic frequency and diffusion maps, errors on magnetic fields and misalignments have been introduced similar to the ones used for the low emittance tuning.

The high quality fields for quadrupoles can be obtained as the beam is pre-damped and so the beam pipe can be small (around 2cm diameter). No higher order multi-poles above the sextupole term are considered. In addition, there are no multi-pole errors included in the dipoles. The values for the integral of the magnetic field errors in the wigglers are obtained as the third of the maximal values given by the specifications [47].

3.2 THE DAMPING RINGS COMPLEX

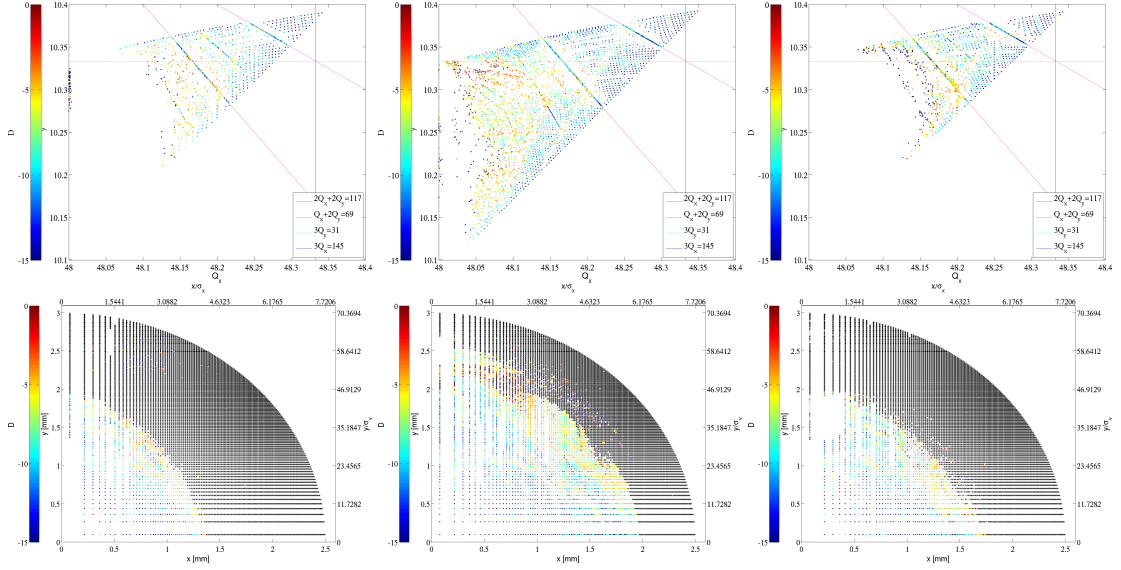


Fig. 3.24: Frequency map (top) and diffusion maps (bottom) for CLIC DR after correction with, from left to right, a momentum deviation of respectively -0.5%, 0 and 0.5%. The colour code follows the tune diffusion coefficient from stable particles (blue) to highly chaotic (red). Black markers are for lost particles. Some relevant resonance lines are shown in the frequency maps.

Once these errors are introduced, the orbit and Twiss functions are greatly perturbed, resulting in emittance blowup, large tune shifts and an inadequate dynamic aperture. A series of corrections are required to restore the optics, similar to the low emittance tuning process [50].

The diffusion and frequency map with errors and after corrections are shown in Fig. 3.24, for on (centre) and off-momentum (left and right) particles. The frequency maps are very similar to the lattice without magnet errors for all three momentum deviations. The same resonances are observed as in the perfect lattice. The diffusion seems to be slightly increased in the area where the beam survives the short term tracking, probably because the errors break the symmetry of the lattice and drive resonances. On the other hand, the correction has completely restored the dynamics and the dynamic aperture is almost identical.

Further studies should focus in the elimination of the large tune-shift, either with other sextupole families or with octupoles, but without exciting additional resonances. Although the vertical dynamic aperture is very large due to the very small emittance coming from the PDRs, it may become an issue if modern electron sources and linacs can reach the horizontal emittance performance of the PDRs (around $60\mu\text{m}$), and eliminate the need for the electron PDR.

3.2.3.9 Collective effects

Intrabeam scattering

One of the main limitations of the CLIC DRs is the effect of intrabeam scattering (IBS) which increases the output emittances in all three dimensions. IBS is a small angle multiple Coulomb scattering effect which depends on the lattice characteristics and the beam dimensions. The IBS theory for accelerators was first introduced by Piwinski [54] and extended by Martini [55]. This formulation is called the standard Piwinski method. An alternate approach is that by Bjorken and Mtingwa (BM) [56]. There is also the high energy approximation by Bane [57], which is valid under some conditions depending on the optics of the ring and other beam characteristics. In order to have a reference point, the results of the three theories are first compared to the results of the multi-particle tracking code SIRE [48], developed at CERN for evaluating the IBS effect on the emittance, including damping and quantum excitation.

Growth rate and geometrical emittance calculations were performed for each point of the lattice for one turn, starting from the zero current (equilibrium) emittance values, where the effect of IBS is strong. As SIRE is a Monte-Carlo code, the tracking simulations were performed for 20 different seeds and error-bars for one standard deviation are also shown Fig. 3.25. The three plots correspond to the behaviour of the horizontal and vertical emittance and the energy spread squared, over one turn of the ring. In all three plots the results from SIRE simulations are shown in dark blue, the results from BM theory in red, the results from Piwinski theory in green and the ones from Bane approximation in black. The results seem to be in very good agreement with the Piwinski theory for all three planes, while the B-M theory and Bane's approximation seem to overestimate the effect. Given that the trend of the emittance evolution is similar for all theories, and that the simulations are quite lengthy, it is convenient to use an analytical approach for understanding and minimizing the IBS effect. The Piwinski theory was chosen, as it seems to be the closest to the simulation results [46].

There is an open question about the final shape of the steady-state distribution due to IBS. The SIRE simulations show that tails get depopulated due to the strong damping, but this may be a simulation artifact, as there are no additional non-linear diffusion mechanism apart from the IBS kicks included in the particle tracking.

Measurements at CESR-TA and SLS have been used to evaluate IBS effects and benchmark theories and simulation codes.

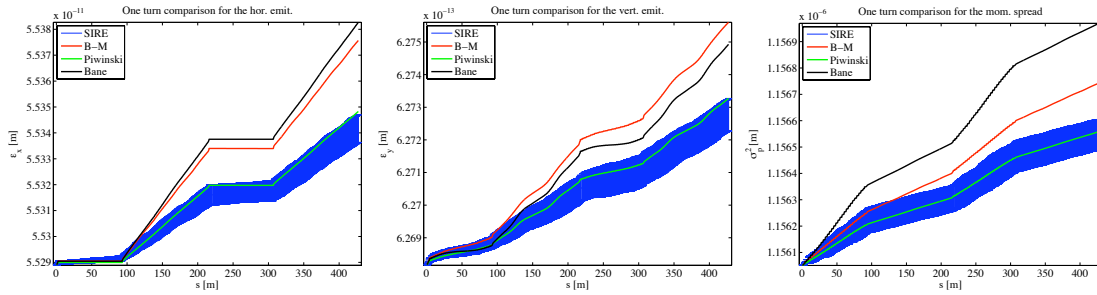


Fig. 3.25: The one turn behaviour of the horizontal emittance (left), vertical emittance (center) and energy spread (right), starting from the zero current values, as they are computed by SIRE (dark blue) and BM (red), modified Piwinski (green) and Bane (light blue) formalisms. In the case of SIRE, error-bars corresponding to one standard are also shown.

Space charge

Due to the very small beam size especially in the vertical plane, the space charge tune-shift, given by

$$\delta\nu_{x,y} = -\frac{N_b r_e}{(2\pi)^{3/2} \gamma^3 \sigma_z} \oint \frac{\beta_{x,y}}{\sigma_{x,y}(\sigma_x + \sigma_y)} ds \quad (3.2)$$

can be quite large. Although simulations in a previous version of the lattice, with vertical space charge tune-shift of around 0.2 have shown that the emittance growth is small [58], an effort was made to reduce the vertical tune-shift to around 0.1. The bunch charge N_b and the beam sizes cannot be changed without compromising luminosity and the DR energy was optimized to reduce the relative impact of IBS, while reaching the required steady-state emittances. Consequently, in order to reduce the space charge, the ring has to become as compact as possible, so the optics integral in the right hand side of (3.2) becomes smaller. At the same time, the bunch length σ_z has to be increased without affecting the performance of the downstream bunch compressors [40]. This was achieved by increasing the equilibrium bunch length

$\sigma_{z0} = \sigma_{z0} C \sqrt{\frac{\alpha_p E}{2\pi h \sqrt{V_0^2 - U_0^2}}}$ through a combination of shorter circumference C (removing wiggler cells), lower harmonic number h by reducing the RF frequency and higher momentum compaction α_p . The

3.2 THE DAMPING RINGS COMPLEX

space charge tune-shift grows to its final large value during the first few ms of damping to the steady-state emittance thus forcing the beam core to traverse resonances. Fast pulsing quadrupoles may be necessary, in order to control the coherent tune-shift in order to avoid emittance growth or beam loss.

Electron cloud effect and mitigation

The short bunch spacing in the positron DR can induce electron cloud growth. The positron beam emits synchrotron radiation photons, which create a large number of photoelectrons at the inner chamber wall surface. Antechambers are used to absorb a large percentage of the synchrotron radiation and thus reduce the number of photoelectrons, but there is still a considerable number of photoelectrons scattered inside the vacuum chamber and they can multiply through secondary emission. This causes electrons to be accumulated in the chamber in large amounts with a possible destabilizing effect on the circulating beam.

The electron cloud build up was simulated with the Faktor2 code [58]. Primary generation of electrons can come both from residual gas ionization and from photoemission. Then the electrons are tracked in the beam field (or in field-free region between bunches) and in their own space charge field and, when they hit the beam pipe inner wall, they can cause secondary emission or be elastically reflected. In the Faktor2 model the beam is rigid and does not feel the effect of the electron or ion cloud. The beam pipes were modeled as elliptical.

In the dipoles, the electron cloud formation as simulated by the Faktor2 code appears to be largely dominated by photoemission up to maximum secondary emission yields of $\delta = 1.8$. Electron cloud central densities in the range of 10^{11} to 10^{13} m^{-3} can be reached.

In the wigglers, the situation is more critical because of the smaller beam pipe radius. The electron cloud build up is dominated by secondary emission for maximum SEYs around 1.5. Fig. 3.26 shows the electron central densities (i.e., within a region of $5\sigma_x \times 5\sigma_y$ around the beam centre) for three different values of photoemission yield of 90, 99% or 99.9% and maximum SEY of 1.3, 1.5 and 1.8. These studies show that, independently of the initial seed of photoelectrons, extremely high central densities of electrons can be reached for $\delta = 1.8$, in the order of 10^{13} m^{-3} . For $\delta = 1.3$, the electron central density would still be very high (10^{12} to 10^{13}) if the antechamber absorbs less than 99.9% of the emitted synchrotron radiation. Therefore, even for maximum SEY below 1.3, there can still be a large number of photoelectrons in the wiggler beam pipe if the antechamber does not absorb a sufficiently high fraction of the emitted radiation.

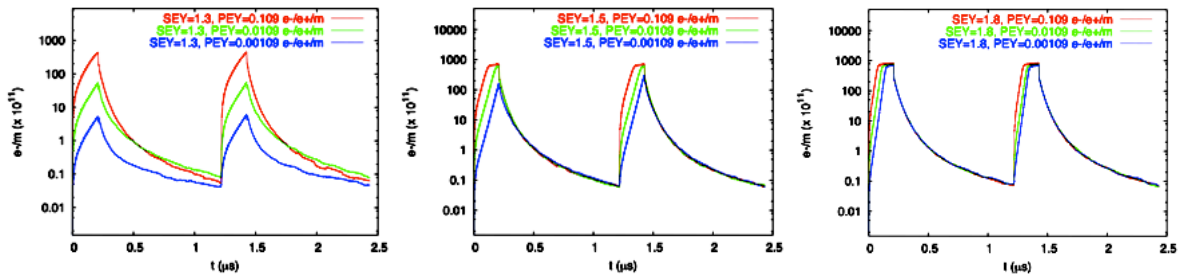


Fig. 3.26: Electron central densities in the wiggler chamber of the CLIC DRs for photoemission yields of 90 (red), 99 (green) or 99.9% (blue) and secondary electron yield of 1.3 (left), 1.5 (center) and 1.8 (right).

The single bunch electron cloud instability has been studied by means of HEADTAIL [59]. The results for electron densities of a few 10^{11} m^{-3} for the dipoles and few 10^{13} m^{-3} for the wigglers are plotted in Fig. 3.27. These densities can result from a combination of low maximum SEY and high photoemission or higher maximum SEY and lower photoemission. In both cases, they make the bunch unstable. Simulations showed that the threshold value for the e-cloud density lies at about $5 \times 10^{13} \text{ m}^{-3}$ in the wigglers, independent of the electron density in the dipoles. This means that countermeasures are

needed to prevent electron accumulation in the wigglers, because the electron cloud very quickly reaches the critical level to cause beam instability.

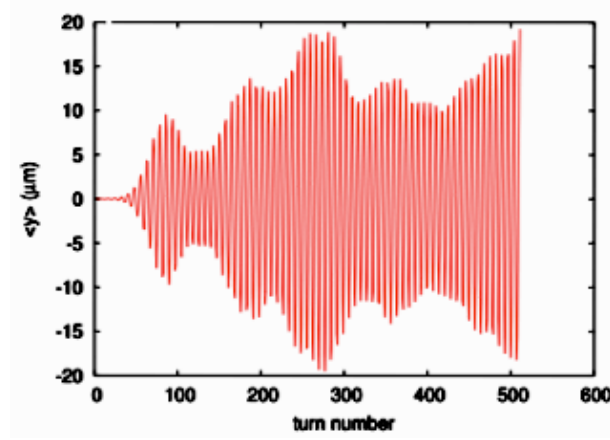


Fig. 3.27: Bunch centroid motion with an electron cloud of $3 \times 10^{11} \text{ m}^{-3}$ in the dipoles and $2 \times 10^{13} \text{ m}^{-3}$ in the wigglers.

Conventional feedback systems cannot damp the e-cloud instability, as a very wide band is needed. Several mitigation techniques are presently under study [38, 39], including low impedance clearing electrodes, solenoids (only usable in field free regions), low SEY surfaces, grooved surfaces, and coatings with NEG and TiN. In particular, an amorphous carbon coating has been extensively tested at the SPS [60] and later at CESR-TA [61], with very promising results. In Fig. 3.28, the SEY of an amorphous carbon surface is shown as a function of the primary electron energy. The different curves correspond to different exposure times, from 2 h to a few days. The maximum SEY starts from below 1 and gradually grows to only around 1.1 after 23 days of air exposure. The peak of the SEY moves to lower energy.

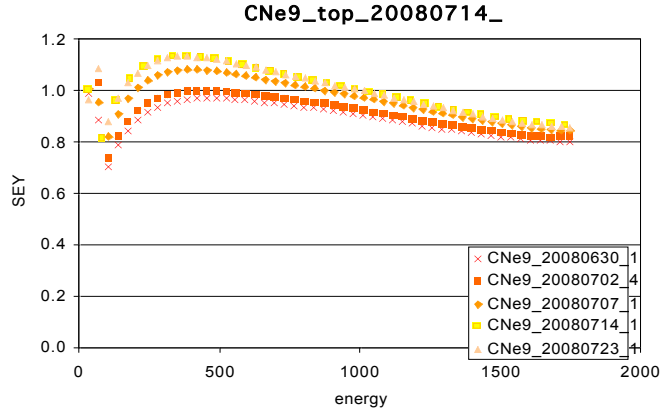


Fig. 3.28: Secondary electron yield measured in the laboratory, as a function of the primary electron energy, for time exposures of 2 hours (red crosses), 3 (dark squares), 8 (diamonds), 15 (light squares) and 23 (triangles) days.

The photo-electron yield of an amorphous carbon coated surface was measured in CESR-TA for a positron beam at 5 GeV. Fig. 3.29 shows a comparison between amorphous carbon and an aluminium chamber, as a function of the bunch intensity for different bunch spacing (14 versus 28ns) and train lengths (45 and 75 bunches). The electron flux for the amorphous carbon is four times less than for aluminium. There is another factor of two difference in the number of photoelectrons in the two chamber locations.

3.2 THE DAMPING RINGS COMPLEX

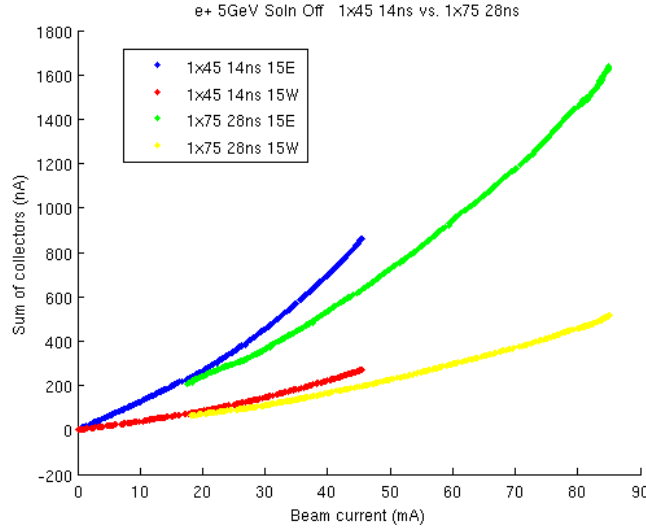


Fig. 3.29: Photo-electron yield as a function of the total current at CESRTA for 14ns (blue and red) and 28ns (green and yellow) bunch spacing for a carbon coated chamber (red and yellow) and an aluminium chamber (blue and green).

Some techniques such as surface coatings, non smooth surfaces or clearing electrodes to fight electron cloud do not come for free and can be serious sources of high frequency impedance. In order to study resistive wall phenomena in much higher frequency regimes, where coatings become important, a new analytical method was used [62] to compute the impedance and wake functions of axisymmetric structures with multiple layers. This was applied to the DR parameters [38]. These computations provide the necessary input for studying instabilities in more detail using multi-particle codes like HEADTAIL [59].

Ion effects

In the electron DR, the ion oscillation frequency inside the bunch train during stored beam is in the range of 300 MHz (horizontal plane) to about 1 GHz (vertical plane). This must be divided by the the square root of the mass number of the ion \sqrt{A} . However, not all ion types are trapped in the bunch train, and the critical mass for trapping of a singly charged ion is:

$$A_{\text{crit}} = \frac{N_b \Delta T c r_e}{2 \sigma_y (\sigma_x + \sigma_y)} \quad (3.3)$$

The ions trapped around the beam are those having a mass number above a critical value, which depends on the location in the ring (due to the different beam sizes) as shown in Fig. 3.30.

Molecules like N_2 , CO can be trapped almost along the full ring (1 and 2 GHz) and accumulate around the electron beam, potentially becoming a source of fast ion instability. For the 1 GHz option the critical masses for trapping are twice as large, reducing the fraction of the ring over which ions like H_2O can be trapped. The induced tune shift at the end of the train due to the ion cloud is given by

$$\Delta Q_{\text{ion}} = \frac{N_b n_b C r_e}{\pi \gamma \sqrt{\epsilon_x \epsilon_y}} \frac{\sigma_{\text{ion}} p}{k_B T} \quad (3.4)$$

With a pressure of 10 –9 mbar and assuming an ionisation cross-section of 2 Mbarn, the tune shift is moderate (0.008 and 0.02 for 1 and 2GHz, respectively). The exponential rise time of the fast ion instability is:

$$\tau_{\text{inst}} \approx \frac{0.1 \gamma \sigma_x \sigma_y}{N_b n_b c r_e \beta_y \sigma_{\text{ion}}} \frac{k_B T}{p} \sqrt{\frac{8}{\pi}} \quad (3.5)$$

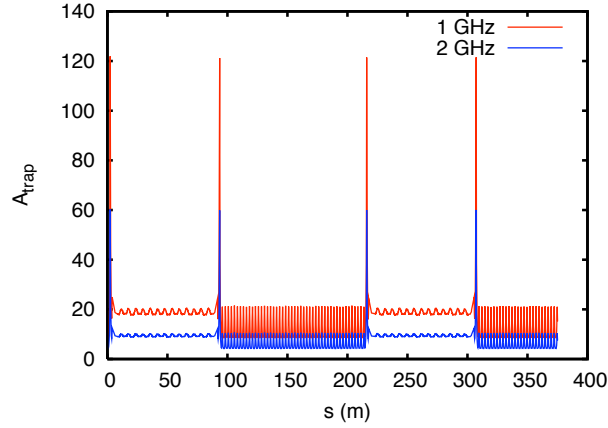


Fig. 3.30: Critical mass of ions trapped around the CLIC electron DR for the 1 (red) and 2 (blue) GHz bunch structure.

This is quite large and equal to a few turns for both options. To control it would require a very demanding multi-bunch feedback system and/or an even lower vacuum pressure through coatings with getters (NEG) or conditioning. The train gaps also provide a natural cleaning mechanism for the trapped ions.

Instabilities and impedance budget

The total impedance of the full ring is modelled with three main components: resistive wall, several narrow-band resonators, and one broad-band resonator. The narrow-band resonator models cavity-like objects. Its wakefield is long range and mainly affects many bunches, therefore, it is responsible for multi-bunch instabilities. A broad-band resonator models the global effect of all discontinuities in the beam pipe and replaces the effect of the actual impedance consisting of many small short range contributions. It is responsible for single bunch instabilities.

The broad-band model is used as a first approximation to model the whole ring in order to scan over different impedance values and define the instability threshold and the impedance budget. In these models, the impedance source is assumed to be identical in the horizontal and vertical planes.

In the transverse plane, a strong head-tail instability or Transverse Mode Coupling Instability (TMCI) can occur and cause rapid beam loss. In the case of a round beam and axisymmetric geometry for a short bunch there is a criterion to find the threshold of TMCI [63]:

$$\frac{R_T [k\Omega/m] f_r^2 [GHz]}{Q} \leq 0.6 \frac{E [GeV] Q_s}{\langle \beta_y \rangle [m] Q_b [C] \sigma_t [ps]}, \quad (3.6)$$

where R_T is the transverse impedance in $k\Omega/m$, $f_r = \omega_r/2\pi$ represents the resonant frequency in GHz where ω_r is the resonant angular frequency of the resonator and is assumed to be the cut off frequency of the beam pipe, Q the quality factor, $\langle \beta_y \rangle$ the average beta value in the y-plane in m, $Q_b = Ne$ the bunch charge in Coulomb and $\sigma_t = \sigma_z/\beta c$ represents the r.m.s. bunch length in ps. Since the CLIC DR bunch is short, compared to the wavelength of electromagnetic waves propagating in the beam pipe, Eq. (3.6) can be used to predict a TMCI threshold of around $10.7 M\Omega/m$ for the transverse broad-band resonator in the vertical plane for $Q = 1$ and $f_r = 5$ GHz.

The HEADTAIL code gives the evolution of the bunch centroid over several turns for different impedance values. By applying a frequency analysis [53] on the coherent bunch motion, the spectrum of the bunch modes can be obtained. The relative tune shift $(Q - Q_x)/Q_s$ with respect to the zero-current tune Q_x is normalized to the synchrotron tune Q_s to identify each of the azimuthal modes. The mode

3.2 THE DAMPING RINGS COMPLEX

spectrum represents the natural coherent oscillation frequencies of the bunch. The tune shift is plotted, for the case of zero chromaticity, as a function of impedance in Fig. 3.31. Modes 0 and -1 are observed to move and couple for impedance values of 18 M Ω /m and 7 M Ω /m in the horizontal and vertical plane respectively, causing a TMCI. The value, in the vertical plane, is about 34% lower than that calculated with the analytical formula given in Eq. 3.6. The difference in the impedance thresholds in the two planes is explained by the difference in the average beta values over the DR used in this simulation for the broad-band resonator, where $\langle\beta_x\rangle = 3.5$ m and $\langle\beta_y\rangle = 9.2$ m. Therefore in the vertical plane, the impedance has a factor of 2.7 higher impact than in the horizontal plane and the TMCI threshold is smaller by almost the same fraction.

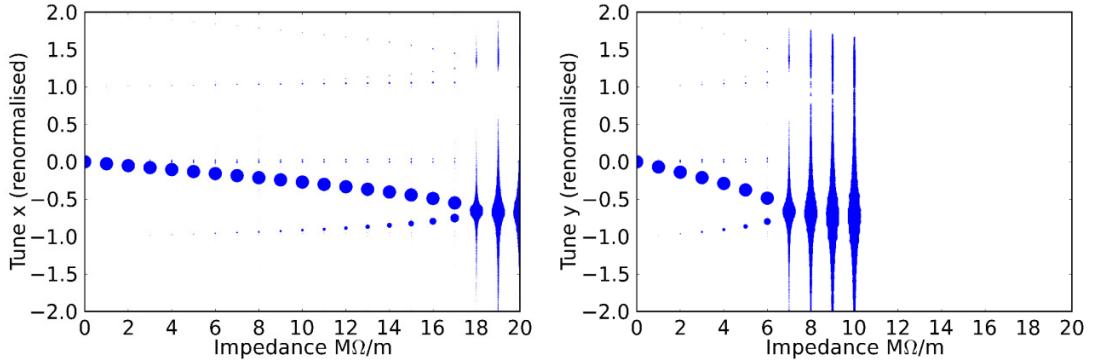


Fig. 3.31: Mode spectrum of the horizontal (left) and vertical (right) coherent motion for zero chromaticity, as a function of impedance. A TMCI is observed at 18 M Ω /m and 7 M Ω /m in x and y plane respectively.

Chromaticity raises the TMCI threshold because it causes tune spread and locks the coherent modes to their low intensity values, making mode merging weaker. For this reason, a simulation was done for different positive and negative values of chromaticity. For positive chromaticity, the dipole mode $m = 0$ is damped whereas for negative chromaticity it becomes unstable.

As expected, the presence of chromaticity causes the modes to move less and not to merge. As a consequence, it avoids a TMCI, but another type of instability occurs, the head-tail instability. In Fig. 3.32, in the case of positive chromaticity, higher order modes get excited whereas $m = 0$ is damped, showing that while a TMCI can be avoided, a head-tail instability develops on a single mode. The TMCI quickly becomes very fast above the threshold for the onset, but the rise time of the head-tail instability can be slower and comparable with the damping time in the DR. In Fig. 3.33, the damping time of 2 ms defines an instability threshold at 6.5 M Ω /m and 6 M Ω /m in the horizontal and vertical plane respectively.

Table 3.11: Impedance thresholds in M Ω /m for slightly positive and negative chromaticity

Chromaticity ξ_x/ξ_y	Threshold in x (M Ω /m)	Threshold in y (M Ω /m)
0.018/ 0.019	6.5	6
0.055/ 0.057	4	4
0.093/ 0.096	5	3
-0.018/ -0.019	4	5
-0.055/ -0.057	2	2
-0.093/ -0.096	2	2

The results from Table 3.11 show that the instability thresholds are even lower for the case of

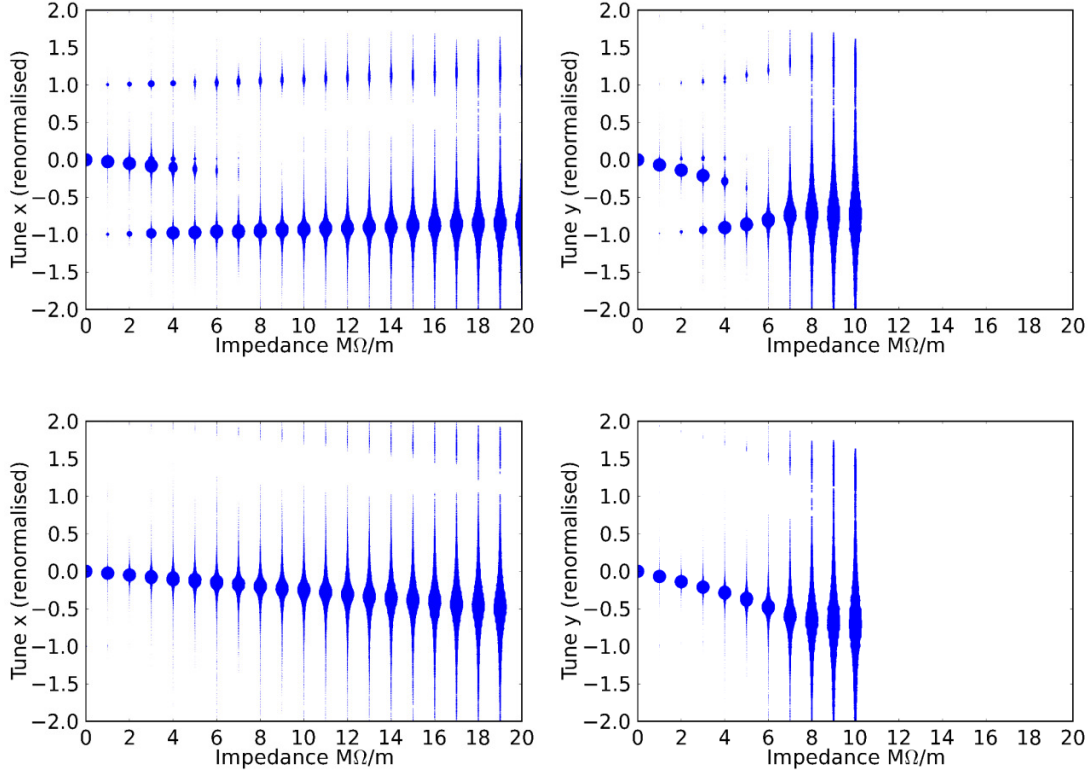


Fig. 3.32: Mode spectrum of the horizontal (left) and vertical (right) coherent motion as a function of impedance, for positive 0.018 and 0.019 (top pictures) and negative chromaticity -0.018 and -0.019 (bottom pictures) in x and y plane respectively.

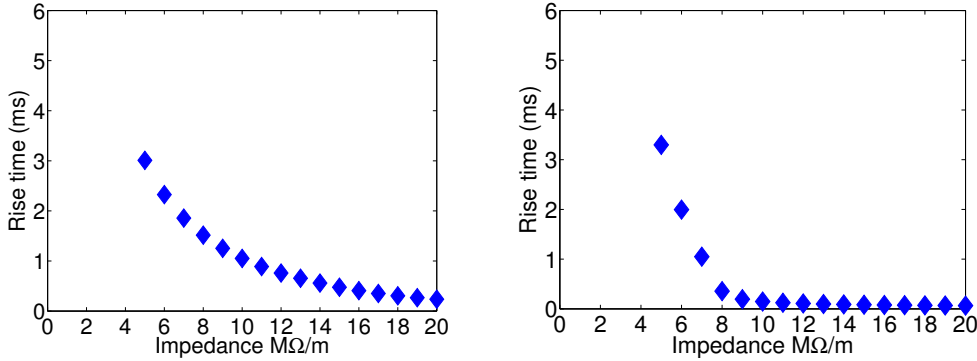


Fig. 3.33: Rise time in the horizontal (left) and vertical (right) plane for positive 0.018 and 0.019 chromaticity in horizontal and vertical plane respectively. Damping time is 2 ms in the two planes, therefore the instability threshold is at 6.5 MΩ/m and 6 MΩ/m in the horizontal and vertical plane respectively.

positive or negative chromaticity than the zero chromaticity values of 18 MΩ/m and 7 MΩ/m in the horizontal and vertical plane respectively. Lower instability thresholds translate into a lower impedance budget for the DR. The impedance budget is larger with zero chromaticity, but since the chromaticity value is set slightly positive, the impedance budget is taken to be 4 MΩ/m.

The wiggler sections have a vertical half aperture of 6 mm compared to 9 mm for other parts of

3.2 THE DAMPING RINGS COMPLEX

the ring, so the resistive wall contribution from the wigglers takes a significant fraction of the available impedance budget. Moreover, layers of coating materials, which are necessary for e-cloud mitigation or good vacuum, significantly increase the resistive wall impedance especially in the high frequency regime. To check whether operation is possible at nominal intensity, simulations were performed with stainless steel (ss) and copper for the pipe of the wigglers, which is assumed to be flat. Copper has a conductivity of $5.9 \times 10^7 \Omega^{-1}m^{-1}$ and stainless steel of $1.3 \times 10^6 \Omega^{-1}m^{-1}$. Coating materials were amorphous carbon (aC), used for e-cloud mitigation, and non-evaporated getter (NEG), used for good vacuum. Different material and coating combinations were tried, in order to study the effect of coating on the threshold. The beam intensity ranged from 1×10^9 to 29×10^9 . The average beta values for the wigglers were $\langle\beta_x\rangle = 4.2$ m and $\langle\beta_y\rangle = 9.8$ m.

Table 3.12: Intensity threshold in the y-plane for non-coated and coated wigglers. The thickness of the coating layers, amorphous carbon (aC) and non-evaporated getter (NEG), is given in mm.

Stainless Steel (SS)	21×10^9
aC on SS (0.0005 mm)	19×10^9
aC on SS (0.001 mm)	17×10^9
NEG on SS (0.001 mm)	20×10^9
NEG on SS (0.002 mm)	19×10^9
Copper	$> 29 \times 10^9$
aC on copper (0.0005 mm)	$> 29 \times 10^9$
aC on copper (0.001 mm)	$> 29 \times 10^9$
NEG on copper (0.001 mm)	$> 29 \times 10^9$
NEG on copper (0.002 mm)	26×10^9

Table 3.12 shows that the thresholds are higher for copper than for stainless steel and well above the beam intensity for most cases. This makes copper a better choice in terms of instabilities but it is also a more expensive material. In addition, adding a layer of coating material on the beam pipe reduces the intensity thresholds and in fact the thicker the coating is, the more the threshold is reduced. However, the instability thresholds are still within the range of tolerance and much higher than the nominal intensity. In the worst case where the instability threshold is 17×10^9 , this would correspond with an impedance of ~ 1 M Ω /m scaled from the nominal intensity 4.1×10^9 which corresponds to 4 M Ω /m for the broad-band model. This then reduces by 25% the total impedance budget.

In conclusion, the DR impedance requirements from the broad-band resonator model are 18 M Ω /m and 7 M Ω /m in the horizontal and vertical plane respectively.

The rise time of the coupled bunch modes caused by resistive wall are calculated from the imaginary part of the formula:

$$\Delta\omega_{x,y} = -i\Gamma(m+1/2) \frac{N_b r_0 c^2 \langle\beta_{x,y}\rangle}{\gamma C \sigma_z} \frac{\sum_{p=-\infty}^{\infty} Z_{x,y}(\omega_p) h_m(\omega_p - \omega_{\xi_{x,y}})}{\sum_{p=-\infty}^{\infty} h_m(\omega_p - \omega_{\xi_{x,y}})} \quad (3.7)$$

with

$$h_m(\omega) = \left(\frac{\omega \sigma_z}{c}\right)^{2m} \exp\left(\frac{\omega^2 \sigma_z^2}{c^2}\right) \quad (3.8)$$

$$\omega_p = (pM + \mu + Q_{x,y} + m\nu_s)\omega_0 \quad (3.9)$$

$$\mu = 0, 1, \dots, M-1 \quad (3.10)$$

$$m = 0, \pm 1, \pm 2, \dots \quad (3.11)$$

The resistive wall impedance is inversely proportional to the square root of the conductivity and to the third power of the beam radius. M is assumed to be the harmonic number of the radiofrequency. The numbers obtained are pessimistic because the wigglers only cover half of the ring, therefore the fastest growth time is a factor of two larger. In addition, the formula assumes a ring fully filled with bunches, so the real growth rate of the instability is scaled by another factor of n_b/M . The growth rates for $m = 0$ and the parameters corresponding to the 1 and 2 GHz RF system are plotted in Fig. 3.34. The minimum growth time of 0.3 ms for 1 GHz corresponds to about 210 turns and can be damped with a transverse feedback. This time is a factor of two smaller for 2 GHz.

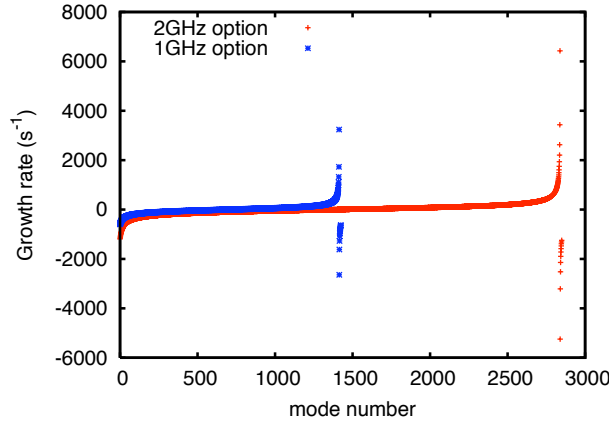


Fig. 3.34: Growth/damping times of the $m = 0$ coherent modes as a function of the μ mode number for a coupled bunch resistive wall instability in the DRs.

HEADTAIL simulations were done using a bunch train made of disk-like macro-particle sets tracked through one or more interaction points around the ring. All particles in bunches subsequent to the first feel a transverse kick at each point from the sum of the resistive wall contributions of all the preceding bunches (integrated over the distance L between points). The simulations were done for the 2 GHz parameters, which have the fastest growth rate. The evolution of the horizontal and vertical beam centroid is plotted in Fig. 3.35. The centroid motion of the train has an exponential growth in both the horizontal (slow) and vertical (fast) planes. The rise time is larger than the analytical calculation by about a factor 5-10, as the simulation takes into account the real wiggler and the train length.

3.2.3.10 Injection/Extraction

The injection and extraction process is quite simple with only one pulse stored in the damping ring per cycle. This pulse contains two trains of 156 bunches with 1 GHz structure. Each train is symmetrically spaced in the DR, and covers only 11% of the circumference. The injection and extraction systems are located at symmetric locations, at the end of the arc, after the dispersion suppressor and upstream of the super-conducting wigglers to avoid damage from synchrotron radiation. The kickers are located at a maximum of the horizontal beta function to minimize the deflection angle. For the same reason, the phase advance between injection (extraction) septa and kickers is around $\pi/2$. Additional space is provided to allow for possibly longer elements with reduced voltage and to accommodate protection systems.

Any ripple on the extraction kicker pulse produces beam size jitter which is propagated up to the collider IP. On the other hand, jitter on the injection kicker reduces the beam stay clear during the injection process. Both kickers have a tolerance of 10% of the beam size, although the injection jitter

3.2 THE DAMPING RINGS COMPLEX

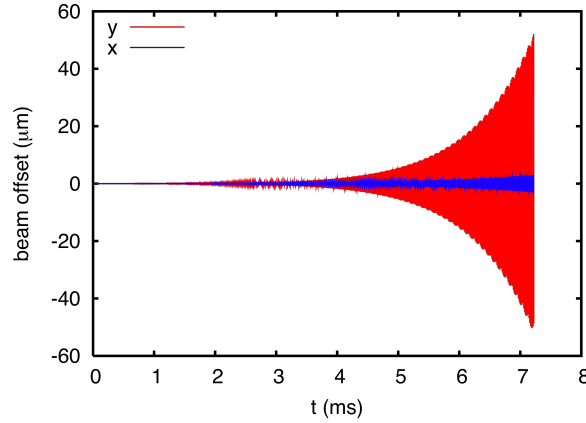


Fig. 3.35: Evolution of the horizontal (blue) and vertical (red) beam centroid motion of the train due to resistive wall.

could be larger (e.g., 20–30%). The relative deflection stability requirement is

$$\delta\theta/\theta \leq \frac{\sigma_{jit}}{x_{sep}} = \frac{0.1\sigma_x}{x_{sep}},$$

with σ_x the beam size at extraction and x_{sep} the position of the beam with respect to the septum, which must be larger than injected beam size plus the septum thickness. Assuming a septum thickness of 3 mm, an available aperture of 7 injected beam sizes plus 4.5 mm for closed orbit distortion, the position of the beam at the septum is around 9 mm. Taking into account that the extracted beam size for the required normalized emittance of 500 nm corresponds to a few tens of microns, the kicker stability tolerance is of the order of 10^{-4} .

There is a similar tolerance for the kicker roll, which induces vertical beam size jitter. The extracted vertical beam size is of the order of a few μm and to keep the distortion to the order of a few hundred nm, the kicker alignment should be better than a few tens of μrad . Future refinement in the lattice of the damping rings will not change significantly the kicker specifications, especially the stringent required stability.

This very tight requirement can be relaxed by installing a 2nd identical kicker powered by the same pulser in the extraction line, at a phase advance of π for jitter compensation. This was already proposed for the NLC damping rings [64] and the ILC collaboration is currently developing kickers with much faster rise and fall times but similar stability requirements. There is also a double strip-line kicker system under development at ATF with similar stability requirements but shorter rise/fall times and flat top [65]. The DR kicker specifications for the damping rings are given in Table 3.13. The flat top corresponds to the length of the two bunch trains plus the train separation. The effective length can be increased by up to 2 m, reducing the field needed to give the required kick of 1.5 mrad. The aperture of the kicker is the same as the downstream quads. The kicker stability refers to field uniformity and pulse-to-pulse stability, including any drop or ripple of the flattop.

Strip-lines are required for low longitudinal coupling impedance. Initial predictions using 3D simulations, for both un-tapered and tapered strip-lines, compare well with analytical equations and give a maximum impedance value of 60Ω [66]. The kicker systems are technologically challenging and significant R&D is needed for PFL (or alternative), switch, transmission cable, feed-throughs, strip-line and terminator. A strip-line is currently being prototyped under the Spanish Program ‘Industry for Science’ and there is a collaboration with ALBA and ATF for beam tests.

Table 3.13: Damping ring kicker specifications

Parameter	CLIC DR @ 1 GHz
Total kick deflection angle [mrad]	1.5
Deflection	Horizontal
Aperture [mm]	20
Beam pipe range [mm]	20–30
Effective length [m]	1.7
Field rise/fall time [ns]	560
Pulse flat top duration [ns]	900
Flat top reproducibility [ns]	$\pm 1 \times 10^{-4}$
Injection stability (per system)	$\pm 2 \times 10^{-3}$
Extraction stability (per system)	$\pm 2 \times 10^{-4}$
Injection field homogeneity @ 3 mm [%]	± 0.1
Extraction field inhomogeneity @ 1 mm [%]	± 0.01
Repetition rate [Hz]	50
Pulse voltage per stripline [kV]	± 12.5

3.2.3.11 Diagnostics and instrumentation

The DR has around 300 BPMs with turn-by-turn readout and a precision of $10\mu\text{m}$. For orbit measurements, the precision averaged over a few turns is around $2\mu\text{m}$. This is required to measure the vertical dispersion of below 1 mm, coupling correction and orbit feedback. Wide band pick-ups with bunch-by-bunch and turn-by-turn position monitoring provide high precision ($\sim 2\mu\text{m}$) for injection trajectory control, and bunch by bunch transverse feed-back. Standard pick-ups provide extraction orbit control and feed-forward.

The tune monitors and fast tune feed-back have a precision of 10^{-4} to resolve instabilities, i.e., synchrotron side-bands, ions, etc.

Turn-by-turn and bunch-by-bunch transverse profile monitors using X-ray or visible light follow the beam emittance evolution during the machine cycle of 20 ms. The dynamic range is very wide as the beam size varies from a few hundreds to tens of microns in the horizontal plane and from tens down to 1 micron in the vertical plane. These monitors must be capable of resolving tails, in order to understand the influence of IBS in the beam distribution and they are the most challenging instrumentation.

Longitudinal profile monitors measure the energy spread from 0.5% to 0.1% and bunch length from 10 to 1 mm. Note that the dispersion around the ring is extremely small with maximum values not exceeding a few cm. Finally, diagnostics for fast beam loss monitoring and bunch-by-bunch current measurements include e-cloud and ion diagnostics.

3.2.3.12 Delay loop

The two trains of the CLIC DR are recombined in a single delay loop for both species, using RF deflectors. The loop is a unique α -shape loop, as in CTF3, with a circumference of 263 m, i.e., half of the damping rings. The optics is based on TME cells and has high-order isochronicity. The emittance growth due to synchrotron radiation is negligible due to the low energy and relatively short length of the loop. The path length correction is critical and a wiggler, orbit correctors or a chicane are required to control the length to a few mm. The systematic energy loss is roughly half that of the DR and can be corrected with RF cavities of a few hundred kV. The beam stability requirement is quite tight (10% of the beam size), and this imposes tight jitter tolerances on the RF deflector (10^{-3}). This tolerance is within the capability of modern klystrons but should be demonstrated by measurements in CTF3 which

3.2 THE DAMPING RINGS COMPLEX

has similar RF deflectors for the Drive Beam recombination and frequency multiplication [67]. Some further simulations for refining the tolerances are necessary for the project preparation phase, especially regarding the phase error.

3.3 Ring to main linac transport (RTML)

3.3.1 Overview

The ring to main linac transport (RTML) connects the damping rings and the main linacs. It also matches beam properties like bunch length and energy from the values delivered by the damping rings to the values required by the main linacs. The RTML consists of beam lines for the transport of the beams from the central injector site, which is close to the surface, to the outer ends of the main linac, which is about 100 m underground. It includes sections for longitudinal bunch compression, acceleration and spin rotation. There is provision for collimation, if needed, to prevent beam halo from entering the main linac. Extensive diagnostics are required along the entire RTML and several commissioning dumps are included to allow staged commissioning of the beamline.

The two RTMLs for electrons and positrons each have a total length of approximately 27 km. Their lattices are very similar but there are small differences due to geometric constraints and to the fact that positron polarization is not included in the CLIC baseline (see §3.1). The layout of the RTML is shown in Fig. 3.36. The same RTML lattice is suitable for all different stages of CLIC, regardless of final energy or detailed parameter choices. The only change is that the long transfer lines at 500 GeV are shorter because of the shorter site length.

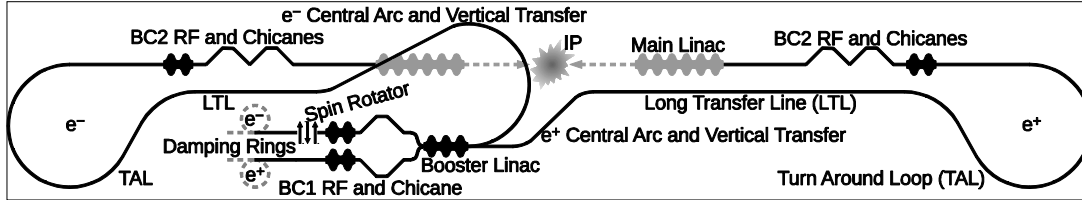


Fig. 3.36: Sketch of the RTML.

3.3.2 Beam parameters

Table 3.14 gives the beam parameters at the entrance of the RTML as delivered by the damping rings. Table 3.15 shows beam parameters at the end of the RTML as required by the main linac. These are identical for conservative and nominal CLIC running scenarios except for the larger emittances in the conservative case.

Table 3.14: Beam properties at the start of the RTML.

Property [units]		Value	Value
		3 TeV	500 GeV
Particle energy [GeV]	E_0	2.86	2.86
Bunch charge [nC]	q_0	0.65	1.2
r.m.s. bunch length [μm]	σ_s	1800	1800
r.m.s. energy spread [%]	σ_E	0.12	0.12
Normalized emittance [nm rad]	$\varepsilon_{n,x}$	500	1800
	$\varepsilon_{n,y}$	5	5

3.3.3 System description

The RTML consists of distinct subsystems, which are described below in order from the damping ring to the linac. They are connected by short optics matching sections. The central arcs and transfers lines are slightly different for the electron and positron RTMLs because of civil engineering constraints. There

3.3 RING TO MAIN LINAC TRANSPORT (RTML)

Table 3.15: Beam properties at the end of the RTML.

Property [units]		Value 3 TeV	Value 500 GeV
Particle energy [GeV]	E_0	9	9
Bunch charge [nC]	q_0	> 0.6	> 1.1
r.m.s. bunch length [μm]	σ_s	44	70
r.m.s. energy spread [%]	σ_E	< 1.7	< 1.7
Normalized emittance [nm]	$\epsilon_{n,x}$	< 600	< 2200
	$\epsilon_{n,y}$	< 10	< 10

is also no positron spin rotator in the baseline, but the required space has been reserved. There are diagnostic sections after the two bunch compression stages, BC1 and BC2 to characterize the beam properties as completely as possible. They include diagnostics to measure emittances, transverse and longitudinal profiles, energy and energy spread. There are additional diagnostics along the entire RTML to support commissioning and operation (see §5.9).

3.3.3.1 e^- Spin rotator

The electron spin rotator is located at the start of the RTML. There is a pair of solenoids, followed by an arc and another pair of solenoids. Between each solenoid pair is a reflector beam line with the transfer matrix, $\begin{pmatrix} I_2 & 0 \\ 0 & -I_2 \end{pmatrix}$ to correct coupling. The arc bends by an angle corresponding to 90° spin rotation. This configuration allows the spin vector to be oriented in any direction by appropriate settings of the solenoid strengths [68].

The layout of the 134 m long electron spin rotator is described in Ref. [69]. The 1.3 m long solenoids provide a maximum field of 6 T. The arc bend is 13.9° to achieve the necessary spin rotation. The momentum compaction factor of the arc is small, only 5.9 cm, to limit the bunch lengthening to $2 \mu\text{m}$, taking into account the small energy spread of 0.13%.

To simplify the civil engineering layout, the 13.9° bend of the arc is compensated by an arc in front of the spin rotator with an equivalent bend in the opposite direction. It is also possible to introduce an angle into the extraction of the beams from the delay loop which follows the damping rings (see §3.2). Either option has negligible impact on performance.

3.3.3.2 Bunch compressor 1

The first stage of bunch compression (BC1) compresses the initially 1.8 mm long bunches to a length of $300 \mu\text{m}$. The RF consists of twenty 2 GHz cavities embedded in a FODO lattice identical to that for the booster linac. Each cavity has a length of 1.5 m and an average gradient of 13.3 MV/m. The cavities are described in §5.5.

The beam passes through the cavities at a phase of 90° off-crest, i.e., at zero crossing, so there is on average no acceleration but trailing particles gain a little energy while particles at the head lose energy. This leads to an almost linear energy chirp of $u_{BC1} = \frac{1}{E_0} \frac{dE}{ds} = -5.9 \text{ m}^{-1}$ which is required to compress the bunches to $300 \mu\text{m}$ in the chicane that follows which has an $R_{56} = -14.5 \text{ m}$. The 30 m long chicane contains four equal dipoles, where the outer two bend by 4.4° and the inner two by -4.4° .

The setup of BC1 and BC2 (see below) is the result of an optimization process that takes into account effects like coherent synchrotron radiation (CSR) and incoherent synchrotron radiation (ISR) [70], the energy acceptance of the downstream arcs, beam phase stability and RF properties [71, 72].

A possible alternate design would be based on 4 GHz cavities. The BC1 RF would benefit from

the higher gradient of the 4 GHz cavities and from the twice-as-large slope at zero crossing and the low voltage required makes wakefields unimportant. In this version of the design, the frequency choice of the BC1 RF is coupled to the frequency of the booster linac cavities for cost reasons (see §3.3.3.3 below).

3.3.3.3 *Booster linac*

The booster linac accelerates the beam to the main linac injection energy of 9 GeV. The same linac is shared by electrons and positrons. The two incoming bunch trains are shifted in time (see below). The booster linac has the same type of 2 GHz cavities as BC1. There are a total of 276 cavities at an average gradient of 14.9 MV/m. They are embedded into a FODO lattice using 8 cavities per cell with an average beta function of 16 m. The total length of the booster linac is 538 m.

Dispersion-free steering can reduce the vertical emittance growth due to short-range wakefields to 1 nm.rad (90th percentile). The simulations assumed an RMS misalignment of the cavities and quadrupoles by $100\ \mu\text{m}$ and $100\ \mu\text{rad}$. The BPMs need a resolution of $1\ \mu\text{m}$. Simulations including the effect of long-range wakefields gave double the vertical emittance growth. The equations derived in [73] were used to analytically study the impact of long-range wakefields for a perfectly aligned booster linac in the presence of incoming beam position jitter. To safely avoid amplification of such jitter, the higher-order modes in the cavities need to be damped to Q factors below 30.

An alternate design with 4 GHz cavities has also been proposed for the booster linac. The higher gradient would shorten the booster linac length, but the higher wakefields would affect beam dynamics. Simulations of the 4 GHz booster linac including short-range wakefields in Ref. [74] showed the vertical emittance growth could be limited to about 2 nm. Detailed studies, especially of the impact of long-range wakefields, would be required before selecting such a design.

Electron and positron beam lines need to be merged before and split after the booster linac. Due to the opposite charge of the particles, this requires only constant-field dipoles. The layout of the merging beam line depends on the horizontal distance between the incoming electron and positron beam lines. The layout of the splitting beam line depends on the exact location of the split. Consequently, the final civil engineering design has a strong impact on the layout of both beam lines.

Bunch train timing and beam loading compensation

Both electron and positron pulse trains pass through the same booster linac separated by a short time. The minimum possible timing offset between the beginning of the trains is given by the maximum pulse length of 568 ns, which is required at 1 TeV centre-of-mass energy (see §8.1), plus an additional offset required for the RF beam-loading compensation.

The distance between the first bunches of the two trains is 1100 ns, which allows to independently perform beam loading compensation for each train. This corresponds to a path length difference to the beginning of the linacs of 330 m.

The optimum solution for RF operation and train timing would be to power the booster linac with two separate RF pulses for electrons and positrons. This would require the two trains to be separated by $3.6\ \mu\text{s}$. It would increase the RF efficiency, simplify the beam loading compensation [75] and improve the train combination. The only drawback is that the path length difference would increase to 1200 m, a value that cannot easily be incorporated into the current civil engineering layout.

3.3.3.4 *Central arc and transfer to tunnel*

The central arcs transport the beams from the booster linac both horizontally and down 100 m vertically to the main linac tunnels. The beam lines also compensate for the timing offset between electrons and positrons.

The electrons are bent by 180° in the central arc to send them towards the end of their linac. The

3.3 RING TO MAIN LINAC TRANSPORT (RTML)

arc has an average radius of 305 m. The lattice is copied from the lattice of the turn-around loops (see below). It is achromatic, almost isochronous, and optimized for acceptable emittance growth due to incoherent synchrotron radiation (ISR). A dog-leg follows this arc to correct the horizontal offset. The vertical transfer to the tunnel takes place in the straight section of the dog-leg. Two vertical arcs are connected by a simple periodic lattice. To limit the slope of the beamline, the straight section is about 1400 m long. Horizontal and vertical bends are separated to simplify the lattices and to avoid coupling of the planes. The total length of electron arc and transfer is 2400 m.

The positron beam is already pointed in the right direction, so the central arc is just a dog-leg with the vertical transfer to the tunnel embedded as for the electrons. To correct the bunch train timing, the path length for the positrons needs to be shorter compared to the electron path length. The current baseline in the civil engineering layout has a difference of 221.8 m. The total length of positron dog-leg and transfer is 2180 m which does not influence the beam dynamics. The lattices of the arcs are similar to those for electrons.

3.3.3.5 Long transfer line

Long 21 km transfer lines transport the beams to the far ends of the main linacs. They have a FODO lattice with very weak quadrupoles, $k_1 = 0.0097 \text{ m}^{-2}$, resulting in a cell length of 438 m and an average beta function of 620 m. The phase advance is 45° . A beam pipe radius of 6 cm reduces resistive wall wakefields [76, 77] which could otherwise cause a multi-bunch instability. To suppress the fast beam-ion instability, the vacuum must be below 10^{-10} mbar [77].

Studies of emittance preservation show that an rms quadrupole alignment of $100 \mu\text{m}$ r.m.s. is adequate even when only correcting with one-to-one steering [78]. On the other hand, studies show that there are very tight tolerances on the allowed dynamic variation of stray magnetic fields. Periodic stray fields with a wavelength equal to the betatron wavelength must be below 10 nT with a variation of 0.1 nT [79],[71]. The turn around loop that follows the long transfer line has a large acceptance so the limit on stray fields is set by the acceptable beam deflection at the entrance of the main linac. A feed-forward system (described below) will loosen these requirements by about a factor ten.

3.3.3.6 Turn around loop

The turn around loop directs the outgoing beam towards the interaction point (IP). The beams are bent by 180° and the resulting horizontal offsets are corrected by dog-legs. The choice of two 60° arcs per dog-leg is a compromise between limiting ISR and lattice length. The arcs of each dog-leg are connected by a simple 354 m long periodic lattice. The average radius of the arc is 305 m and the total loop length is 1944 m. Both turn-around loops contain 50 arc cells.

Since the loops must be achromatic, almost isochronous and minimize ISR emittance growth, the lattice is rather complex, based on Ref. [80]. Each 31.9 m long cell produces a 6° bend, with five dipoles, seven quadrupoles and four sextupoles. The phase advance is 432° in the horizontal plane and 144° in the vertical plane. Beta functions β_x , β_y , dispersion R_{16} and momentum compaction R_{56} along a single cell are plotted in Fig. 3.37. ISR emittance growth is minimized by small beta functions and small dispersion in the dipoles.

The turn-around loops must be isochronous to avoid bunch lengthening. Otherwise, bunch compressor 2 would need to be stronger to compensate and that would produce more synchrotron radiation. First results from error tolerance studies indicate that the bends and quadrupoles must be aligned to $100 \mu\text{m}$ and $100 \mu\text{rad}$ RMS, assuming a BPM resolution of $1 \mu\text{m}$. The sextupole's alignment tolerance is even tighter, but coupling and dispersion correction will help to alleviate the alignment tolerances.

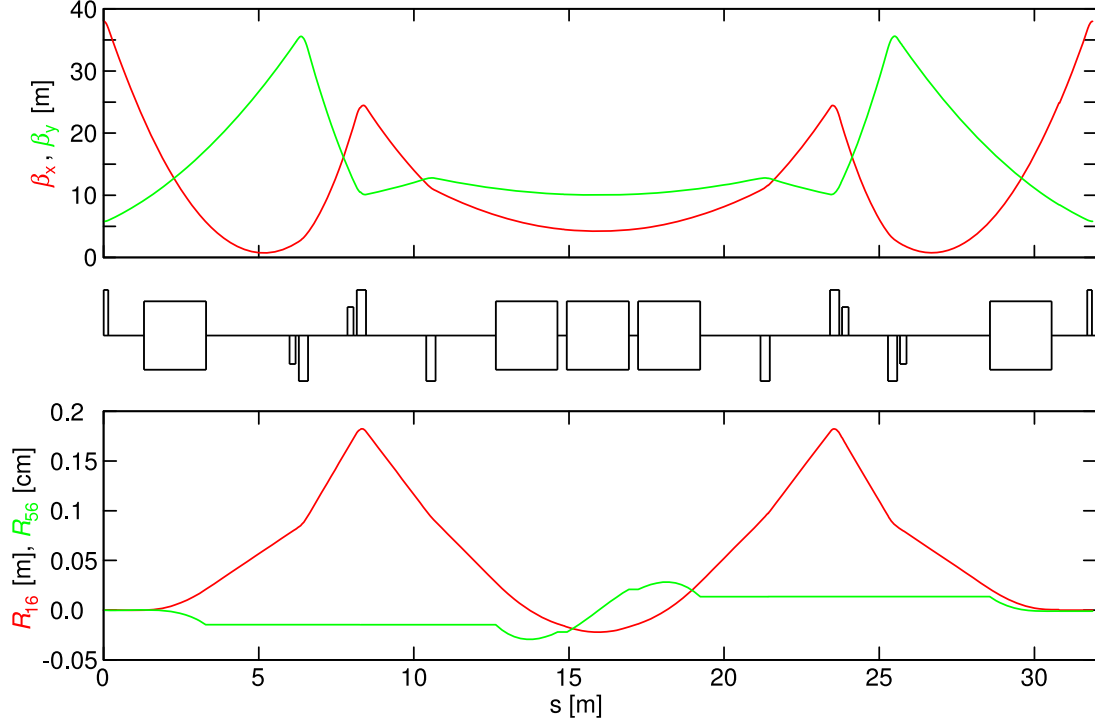


Fig. 3.37: Beta functions (top), dispersion and momentum compaction (bottom) along an arc cell.

3.3.3.7 Feed-forward system

Feed-forward systems are installed around the turn-around loops to correct for beam errors that have accumulated in upstream beamlines. A critical prerequisite is that the acceptance of the turn around is large enough so that these errors, e.g., beam offsets, do not dilute emittance. The beam is measured upstream of the turn around and corrections applied after it. The feed-forward systems will correct beam orbit, energy and perhaps phase if it turns out that external phase references are being used (see §3.8). The feed-forward systems should reduce beam errors by up to a factor of ten. Since most errors will influence a full bunch train, diagnostics and correctors do not have to be very fast.

3.3.3.8 Coupling and dispersion correction

Since emittances are extremely small and their aspect ratio ϵ_x/ϵ_y is large, even the slightest residual dispersion or coupling can lead to significant emittance growth in the vertical plane. Because of their complexity, the turnarounds can be a major source of such aberrations, so they are followed by coupling correction sections containing skew quadrupoles. Dispersion correction is integrated into the last arcs of the turnarounds.

3.3.3.9 Bunch compressor 2

The second bunch compression stage (BC2) compresses the bunches to their final length of $44 \mu\text{m}$, i.e., by a factor of seven. It contains an RF section with 78 12 GHz cavities which are 0.23 m long and run 90° off-crest at an average gradient of 94 MV/m. These cavities are of the same type as the main linac cavities at 500 GeV (see §5.5). The high gradient is possible since on average no energy is extracted by the beam. The gradient is sufficient to compensate for the impact of short-range wake fields, which tend to lower the induced energy chirp. To ensure that short-range wakefields do not degrade beam quality, the lattice of the BC2 RF is the same as at the start of the nominal main linac.

An energy chirp of $u_{\text{BC2}} = \frac{1}{E_0} \frac{dE}{ds} = -49.5 \text{ m}^{-1}$ is required to fully compress the bunches in the two

3.3 RING TO MAIN LINAC TRANSPORT (RTML)

BC2 chicanes with $R_{56,1} = -1.38$ cm and $R_{56,2} = -0.60$ cm. Full bunch compression, i.e., compression until the longitudinal phase-space ellipse is fully upright, provides stability in the main linac. Two chicanes, each with four dipoles, are needed to reduce CSR for very short bunches. They each have a length of 30 m and are made of the same 1.5 m long dipoles. Another advantage of using two independent chicanes is flexibility, for example to adapt the system to the parameters at 500 GeV (see §9.2).

3.3.3.10 *Emittance measurement*

The beam emittances in both transverse planes are measured just before the main linac. The beam size measurements are made with four laser-wire beam profile monitors (see §5.9.8). The measurement section consists of four FODO cells with a phase advance of 45° in both planes with the laser wires placed just after the horizontally defocussing quadrupoles [81]. Each monitor has two orthogonal laser beams to measure the micron-scale horizontal and vertical beam sizes with a precision of 10%. The projected emittances can also be reconstructed with a precision of 10%. The Compton-scattered photons are detected either by a Cherenkov detector or a calorimeter. A weak dog-leg with an offset of 10 cm separates the particles from the photons behind the last monitor. The total length of the section is 82 m, beta functions at its entrance are $\beta_x = 40$ m and $\beta_y = 18$ m.

A similar station is also installed at the beginning of the RTML. Since the beam energy is smaller, beam sizes are slightly larger and the measurement is simpler, but the same technology is used.

3.3.3.11 *Commissioning dumps and spectrometers*

To facilitate commissioning and machine studies, beam dumps are provided at various points along the RTML, including just after the damping rings, at the entrance and exit of the booster linac, at the entrance of the turn-around loops and just before the main linacs. The average beam power is 30 kW entering the booster linac, i.e., at a beam energy of 2.86 GeV, and 90 kW after the booster linac, i.e., at a beam energy of 9 GeV, so the dumps are rather small (see §5.9.4.7). The beam lines leading to the dumps are also used as spectrometers for precise energy and energy spread measurements.

3.3.4 Accelerator physics issues

The RTML includes a large variety of subsystems and there are numerous accelerator physics issues. The most important ones are described here.

3.3.4.1 *Incoherent synchrotron radiation*

Incoherent synchrotron radiation (ISR) is emitted whenever the beam changes direction. While the energy loss is a static effect, which can be easily compensated, the induced emittance growth poses a serious challenge. The emittance growth depends strongly on particle energy and bend angle [82],

$$\Delta\epsilon \propto E_0^5 \frac{\theta^5}{l_{\text{arc}}} . \quad (3.12)$$

so the arcs after the booster linac have long, weak bends. The ISR emittance growth is also reduced by optics where the beam size and dispersion is small at the bend locations. In spite of these considerations, the RTML turn-around loops are still the largest source of emittance growth in the horizontal plane.

3.3.4.2 *Coherent synchrotron radiation*

Coherent synchrotron radiation (CSR) is an issue in strong bends [83]. Like a wakefield, the longitudinal component of CSR induces a non-uniform energy loss along the bunch. If the CSR occurs in a dispersive section, e.g., a bunch compressor chicane, the dispersion cannot be compensated for all particles. Some particles experience a transverse shift in the bend plane and the resulting projection of the beam profile

increases, much like emittance growth, even though the slice emittance remains unchanged. The transverse phase-space distribution is largely unaffected by CSR.

CSR emitted in the chicanes of the bunch compressors is a major contribution to horizontal emittance growth while CSR emitted in the arcs and turnarounds is small. The shielding effect of the conducting chamber walls [84] can lower the CSR to acceptable levels [70] but only when the vertical aperture of the vacuum chambers in the bunch compressor chicanes is less than about 2 cm.

3.3.4.3 *Cavity wakefields*

A particle beam traversing an RF cavity will be affected by both longitudinal and transverse wakefields which depend on the geometry of the cavity. If the cavity axis and beam trajectory are perfectly aligned with respect to each other, the wakefield is entirely longitudinal. This wakefield is a significant effect in BC2 and it changes the energy distribution along the bunch.

In the BC2 RF cavities, the longitudinal wakefields induce an energy chirp opposite to the one required for bunch compression. This is compensated by increasing the integrated cavity voltage by 72 MV compared to the value obtained by simplified first-order calculations. In the BC1 RF and in the booster linac the effects are very small.

If the beam passes off-axis through the cavity, either due to cavity misalignments or due to jitter of the incoming beam position, the whole beam receives a transverse deflection. There is also a transverse wakefield which deflects either particles within the same bunch (short-range wakefields) or even trailing bunches (long-range wakefields). These kicks lead to a growth of either single bunch emittance or projected emittance of the full bunch train.

The cavities must be designed to reduce wakefields, e.g., by enlarging irises and by including higher order mode (HOM) damping (see §5.5). Tight cavity alignment and stable control of the beam trajectory is also mandatory. Strong focusing of the lattice in the RF sections also reduces wakefield effects.

3.3.4.4 *Magnetic stray fields*

Magnetic stray fields are produced by external sources, i.e. by sources which are not part of the beamline lattice, in contrast to magnetic field errors, which are errors of the magnets within a beam line. The stray fields may be caused by technical equipment of the accelerator itself, e.g., vacuum pumps, technical equipment near the accelerator, e.g., power lines, or even geophysical conditions of the accelerator site, e.g., fluctuations in the earth's magnetic field.

Stray fields are primarily a concern in the long transfer lines, not only because of their length, but also because of their weak focusing. The beams can experience an accumulation of kicks from the stray fields which change the trajectory downstream and may even dilute the emittance. Simulations [79] showed the strongest effect from periodic stray fields along the entire transfer line with a wavelength equal to the betatron wavelength. In reality, such a long uniform array of periodic stray fields is unlikely, and the feed-forward system is intended to compensate any beam deflections.

3.3.4.5 *Multi-bunch resistive wall instability*

The electromagnetic fields from the particle bunches interact with the walls of the vacuum chamber. If the bunch is not well aligned with the chamber, it will be affected by transverse resistive wall wakefields. Depending on radius and resistivity of the chamber, these fields may persist long enough for the following bunch to feel a transverse kick, which can drive an instability along the bunch train [77]. To limit this effect, the copper beam pipes are wide aperture with a radius of 6 cm.

3.3 RING TO MAIN LINAC TRANSPORT (RTML)

3.3.4.6 Fast beam-ion instability

Particles of the residual gas in the vacuum chambers can be ionized by the beams. The electron beam repels the electrons of the ionized gas and traps the ions, whereas the positron beam repels the ions and traps the electrons. Since the ions have low mobility, they accumulate during the passage of the electron bunch train and start to defocus or transversely kick the beam particles, possibly triggering an instability. Onset and growth rate of this effect depend on charge density within the bunch, bunch repetition rate, vacuum pressure, i.e., number of gas particles, and gas species. In the long transfer line for the electrons, a vacuum pressure must be less than 10^{-10} mbar to safely avoid the fast beam-ion instability [77]. Electrons are less likely to be trapped by the positron beam because of their higher mobility, so the vacuum pressure could be higher. The current baseline is to have the same pressure for both lines.

3.3.4.7 Polarization

The RTML contains a spin rotator after the damping ring for the electron beam to turn the spin from vertical to longitudinal. The design of the turn-arounds and dog-legs after the booster linac are made to have zero integral bending angle. Therefore the total spin precession is zero and the beam energy spread will cause no depolarization.

3.3.5 Component specifications

The RTML includes a large variety of subsystems with differing components. The number of magnets and cavities is summarized in Table 3.16 and magnet details are given in §5.2. The number of steering magnets is assumed to be equal to the number of quadrupoles and sextupoles. Additional magnets will be required for the diagnostic beamlines and the beamlines for the commissioning dumps. These are not yet specified.

The 12 GHz cavities of the BC2 RF are the same as those for the main linac at 500 GeV. The 2 GHz cavities of the BC1 RF and booster linac are the same as those in the Main Beam injector complex. They are described in §5.5.

Studies [72] have specified the tolerances on the RF phases and RF amplitudes required to limit beam phase jitter at the main linac entrance to 0.2° (12 GHz) and bunch energy jitter to 0.2%. The feed-forward system relaxes these tolerances but has not yet been included in the calculations. The magnetic field error of the bunch compressor dipoles should not exceed a few 10^{-4} . The amplitude of the bunch compressor RF must be stable to less than 2% to reduce bunch length jitter to less than 1%. The booster linac amplitude has to be stable to less than 0.1%. The phase jitter of the booster linac cavities has to be less than 2° (2 GHz), and the BC1 RF phase jitter must be less than 0.08° (2 GHz). The BC2 RF phase jitter must be less than 0.2° (12 GHz). Final design specifications are based on these values.

Other requirements have not yet been fully evaluated. In general magnet stability at the 10^{-5} – 10^{-4} level seems to be sufficient.

Table 3.16: Total number of magnets and cavities in the electron and positron RTML not including steering magnets.

Type	Number
Dipoles	710
Quadrupoles	1744
Sextupoles	541
Solenoids	4
Cavities (2 GHz)	314
Cavities (12 GHz)	96

3.4 Main linacs

3.4.1 Overview

The two main linacs, one for positrons and one for electrons, accelerate the beams from an initial energy of 9 GeV to the final value of 1.5 TeV using normal conducting accelerating structures with an RF frequency of 12 GHz and a gradient of 100 MV/m. This choice of frequency and gradient is based on an optimisation of the total accelerator cost. The linac design is identical for electrons and positrons and the linacs are each about 21 km long. This includes a total energy overhead of 10% to allow for different operational margins. A key design goal is the preservation of the ultra-low transverse emittances during beam transport. This goal is achieved by a combination of careful lattice design, precise pre-alignment of the beam line components, stabilisation of the beam guiding quadrupoles against vibrations and use of beam-based correction methods. The main linac tunnel and the beam line are laser straight. This avoids the complications that would result from a linac that follows the curvature of the earth [85].

3.4.2 Beam Parameters

Table 3.17 shows the key beam parameters for the main linacs. In the linac the bunch length remains constant, while the transverse emittances increase due to machine imperfections. The beam is accelerated at an average RF phase of 12° in order to limit the final energy spread; this results in an effective gradient reduction of about 2 %.

Table 3.17: Key beam parameters in the CLIC main linac.

Particles per bunch	3.7×10^9	bunches per pulse	312
bunch spacing	15 cm	bunch length	44 μm
initial r.m.s. energy spread	$\leq 2\%$	final r.m.s. energy spread	0.35 %
initial horizontal emittance	$\leq 600 \text{ nm}$	final horizontal emittance	$\leq 660 \text{ nm}$
initial vertical emittance	$\leq 10 \text{ nm}$	final vertical emittance	$\leq 20 \text{ nm}$

3.4.3 System description

The RF power to accelerate the Main Beam is provided by 24 drive-beam decelerators which run parallel to the main linac. In order to facilitate the geometric matching between Drive Beam decelerator and main linac, both systems are built using a chain of 2.01 m-long two-beam modules.

3.4.3.1 Two-beam modules

Because the quadrupole spacing changes with energy, five types of module are needed, four of which contain a quadrupole. The most frequently used module consists of a girder that supports eight 0.23 m-long accelerating structures. The RF power for each pair of these structures is provided by one PETS, see Fig. 3.38.

The linac design uses quadrupoles of four different lengths. Each quadrupole is preceded by a beam position monitor and both are mounted on a single support that is equipped with movers. The quadrupole with its support is integrated into a two-beam module, replacing between two and eight of the accelerating structures. The four different module configurations corresponding to the four different quadrupole lengths are shown in Fig. 3.39. The quadrupole supports allow for the quadrupole/BPM assemblies to be moved independently of the two-beam modules. The quadrupoles are equipped with corrector windings that allow adjustment of the magnetic centre in the vertical and horizontal planes. The quadrupoles are also equipped with a stabilisation system that suppresses transverse vibrations caused by ground motion and technical noise. This system is described in detail in §5.18.

3.4 MAIN LINACS

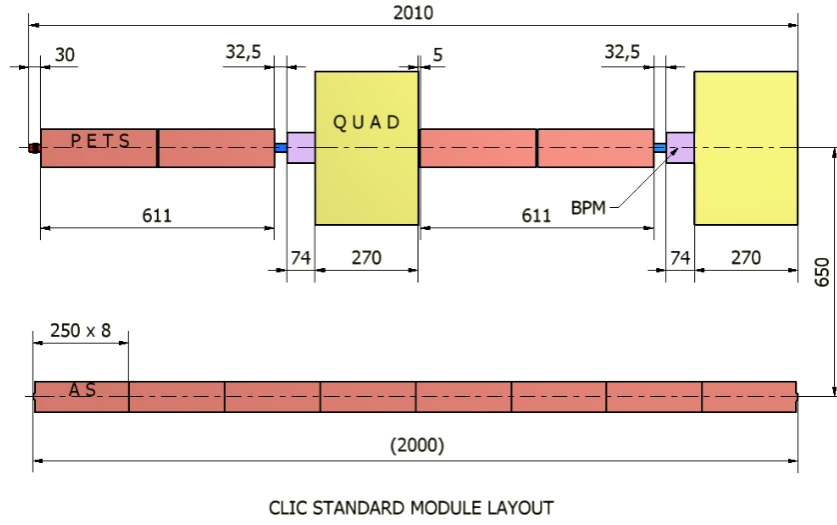


Fig. 3.38: Schematic layout of a two-beam module.

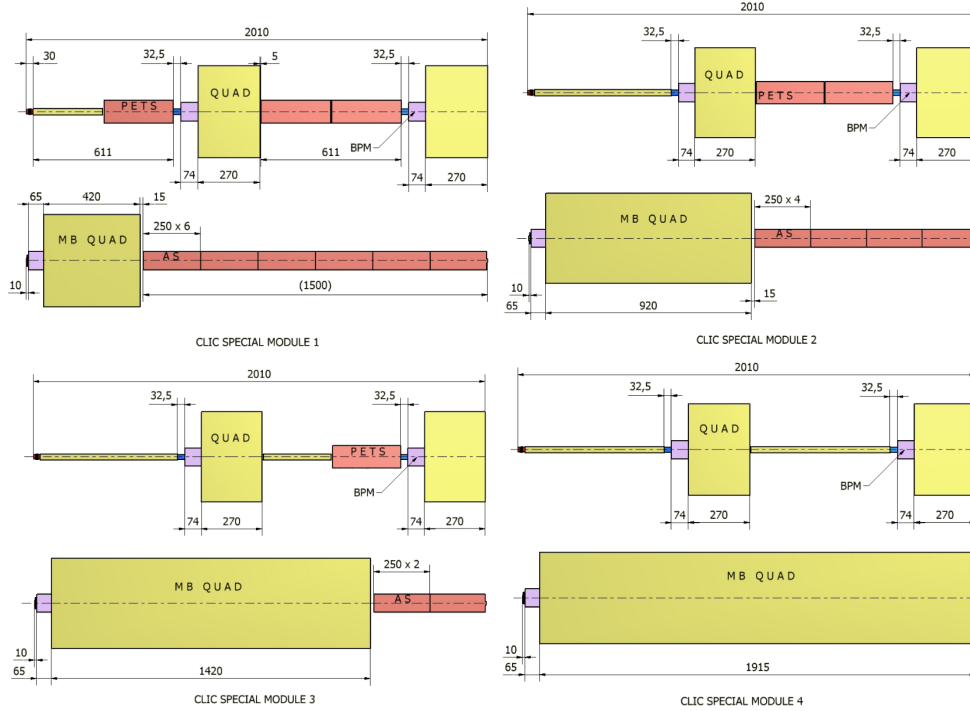


Fig. 3.39: Schematic layouts of the modules that contain quadrupoles.

3.4.3.2 Linac Layout and Optics

Each linac is divided into 24 drive-beam decelerator sectors, each of which is powered by a different mini-pulse train within the Drive Beam pulse. Each sector powers 2986 accelerating structures. The length of a sector is about 900 m but it varies depending on the number and length of the quadrupoles. The length of each sector can be derived from the number of accelerating modules per sector listed in Table 3.18. At the end of each sector about 8 m of space is needed to switch from one mini-pulse train to the next. The space is achieved by four consecutive modules without accelerating structures.

The main linac lattice choice is important for emittance preservation. A strong focusing lattice will reduce the impact of transverse wakefields but increases dispersive effects and vice versa. In order to

Table 3.18: The number of the accelerating modules per Drive Beam sector

sector	modules	sector	modules	sector	modules	sector	modules
1	523	2	467	3	445	4	432
5	454	6	441	7	441	8	428
9	429	10	432	11	438	12	439
13	438	14	430	15	429	16	429
17	428	18	422	19	422	20	423
21	423	22	418	23	418	24	413

best balance these effects, the lattice strength is varied along the main linac as a function of beam energy. The design focal strength is thus the result of careful optimisation of the overall linac performance.

The main linac optics consist of twelve lattice sectors each using a FODO optics [86]. The phase advance is about 72° per cell throughout the main linac. The quadrupole spacing is constant in any particular sector but varies from sector to sector following an approximate scaling with \sqrt{E} , see Table 3.19. There is a quadrupole on every module in the first sector (2.01 m spacing). The quadrupole spacing increases along the linac until there is one quadrupole for every ten acceleration modules in the last sector (20.1 m spacing). This quadrupole spacing balances the contributions to emittance growth from dispersive and wakefield effects along the linac. The total length of quadrupoles is roughly the same in every sector resulting in an almost constant fill factor (the ratio of the length of the accelerating structures to the total length.) The lattice functions between sectors are matched using the last four quadrupoles of the lower energy sector and first three quadrupoles of the higher energy sector.

Table 3.19: The main parameters of the different lattice sectors

sector number	1	2	3	4	5	6
quadrupole number	154	68	234	212	124	82
quadrupole length [m]	0.35	0.85	0.85	0.85	0.85	1.35
quadrupole spacing [m]	2.01	2.01	4.02	6.03	8.04	8.04
sector number	7	8	9	10	11	12
quadrupole number	208	192	214	200	198	124
quadrupole length [m]	1.35	1.35	1.85	1.85	1.85	1.85
quadrupole spacing [m]	10.05	12.06	14.07	16.08	18.09	20.10

3.4.3.3 Pre-alignment System

The beam line elements, in particular the BPMs, need to be aligned with high accuracy to prevent excessive emittance growth. To this end each linac is equipped with a sophisticated pre-alignment system. This system's reference line is established using a sequence of overlapping wires that run along the whole linac. The positions of the acceleration modules and quadrupoles with respect to these wires are measured using sensors that are attached to one end of each module and to both ends of each quadrupole support.

The pre-alignment and installation procedure is described in detail in §5.17 and consists of the following four steps:

3.4 MAIN LINACS

- the wire system is installed in the tunnel
- the movers for the acceleration modules are installed using the wire system as a reference
- the acceleration modules, which have been pre-assembled at ground level, are placed on the mover system
- using the wire system as a reference each module is precisely aligned using the manual actuators and then adjacent modules are connected. Each module is equipped with an additional sensor to help with the pre-alignment later removed after installation

When all the modules are installed, the system can be further aligned using the movers and the signals from the sensors. During operation, beam signals will be used to further optimise the alignment of the linac components.

3.4.4 Accelerator Physics Issues

3.4.4.1 Single bunch beam break-up and RF phases

If a beam passes off axis through an accelerating structure, the transverse wakefields can distort the bunch and lead to single bunch beam break-up. This instability is suppressed by the use of BNS damping [87]. In this scheme, a correlated energy spread is introduced along the bunch such that the tail has a lower energy than the head. This energy spread is naturally produced by the longitudinal short-range wakefields. For most of the main linac, the beam is accelerated at a small RF phase Φ_1 , which leads to little compensation of the longitudinal wakefield resulting in a significant correlated energy spread, see Fig. 3.40. In the last part of the linac, a larger RF phase $\Phi_2 = 30^\circ$ is used to reduce the energy spread. The length of this last part is adjusted to provide an RMS energy spread of 0.35%, which is acceptable for the beam delivery system. Smaller values of Φ_1 (larger energy spread in most of the linac) leads to better stability but larger emittance growth due to dispersive effects and vice versa. For the present bunch parameters, a nominal value of $\Phi_1 = 8^\circ$ has been chosen, as it provides a good compromise. Figure 3.40 shows the energy spread along the linac for different RF configurations.

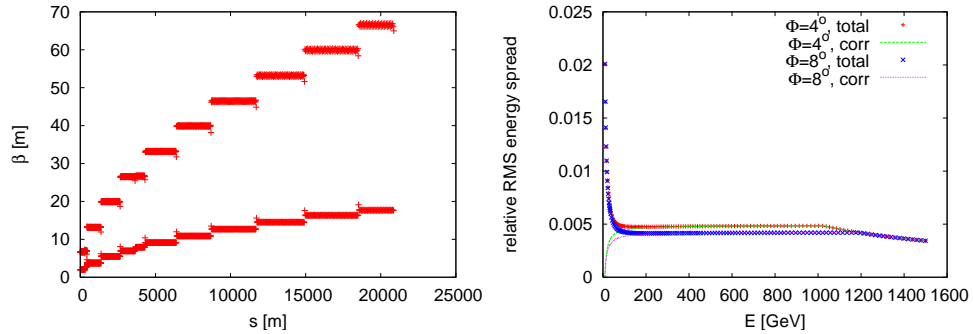


Fig. 3.40: Left: Main linac lattice functions and energy spread. Right: The energy spread along the linac for two different RF configurations. Both, the total r.m.s. energy spread and the correlated part are shown.

3.4.4.2 Static Imperfections and Beam-Based Alignment

Beam based alignment techniques are used to minimize the emittance growth due to residual misalignment of beam line elements after the initial pre-alignment. First, simple one-to-one steering is used to make the beam pass through the linac without significant beam loss. Then dispersion free steering is used to optimise the position of the beam position monitors and quadrupoles [88–91]. This can also be done with ballistic alignment [92]. Next, the offsets of the accelerating structures relative to the beam are determined using the wakefield monitors and minimized using the movers on which the acceleration modules are installed [93]. Finally, emittance tuning knobs are used to further reduce the emittance growth [94].

These knobs cancel the wakefield effects globally by moving accelerating structures at various locations until the emittance measured at the end of the linac is minimized.

Dispersion free steering is implemented by varying the beam energy. The bunch compressor phase is used to vary the energy at the entrance of the main linac. Within the main linac, the energy can be varied by changing the Drive Beam current, either pulse to pulse or within a pulse. The preferred solution is to vary the energy within a single pulse such that the first and last part of the pulse have different energies. This allows the same RF setup for each pulse, rather than switching back and forth between different RF settings. It also allows measurement of the trajectory difference within a single pulse. This avoids the complication that ground motion between pulses can introduce spurious trajectory differences. In-between the two subpulses of different energy, there is a transition period, which has a length corresponding to the fill time of the main linac accelerating structures. The beam position monitors must be able to measure the beam orbit for two short samples of the same beam pulse.

3.4.4.3 *Dynamic imperfections and feedback*

Feedback systems are used to suppress orbit jitter and drift [95, 96]. The mechanical alignment of quadrupoles in the linac is stabilized using a mechanical feedback based on accelerometers and piezo-electric actuators. A beam-based pulse-to-pulse trajectory feedback system is also used to keep beam well centered in the linac. This system consists of 41 measurement stations with eight BPMs each and pairs of dipole correctors between these stations to steer the beam.

Jitter of the main linac RF phase and amplitude can also lead to luminosity loss [97–100], as it changes the beam energy at the end of the main linac. The beam delivery system has limited energy acceptance, so energy changes lead to an increased spot size at the interaction point.

3.4.4.4 *Other Issues*

Long-range geometric transverse wakefields in the accelerating structures can lead to multi-bunch beam break-up. In the CLIC main linac structures these wakefields are suppressed by strong damping and by detuning the frequencies of the relevant modes from cell to cell. The main wakefield kick of a bunch is on the second bunch. The requirement for the long-range wakefield is that the sum of the amplitudes at the following bunches is $\sum_{i=1}^n |W_{\perp}(z_i)| \leq 6.6 \text{ kV} / (\text{pCm}^2)$. Simulations of the linac design show that the long-range wakefield effects are small and do not lead to beam break-up or to a significant impact on the beam emittance [101].

Resistive wall wakefields can also lead to emittance growth, in particular the wakefields due to the beam pipes in the quadrupoles. This effect is suppressed by the use of a relatively large beam pipe radius (4 mm), copper coating of the inside of the beam pipe and accurate alignment. The quadrupole beam pipes need to be aligned to the beam with an accuracy of $40 \mu\text{m}$. To achieve this tolerance, the beam pipe is designed as an integral part of the quadrupole and is accurately aligned to the magnetic centre of the quadrupole during assembly. Simulations show that dispersion-free steering can then automatically align the beam to the magnetic field centre, and hence the beam pipe centre, with the required precision [102].

Fast beam-ion instability can lead to beam break-up or large emittance growth in the electron linac [103–105]. Molecules from the residual gas in the beam pipe are ionized by the beam. Depending on the beam parameters, these ions can interact with the electrons in the beam. The leading bunch in the train applies a small kick to the ions which in turn apply small kicks to the trailing bunches. This can lead to beam break-up in a similar way to that from transverse long-range wakefields. Simulations of the CLIC main electron linac show that if the vacuum levels are below a partial pressure of less than 10^{-9} mbar for CO and N_2 ion effects will not significantly degrade the beam.

Beam loading in the structures needs to be compensated in order to avoid accelerating different bunches to different energies. Beam loading compensation is achieved by shaping the RF pulse using the delayed switching technique [106–108], see §2.5, to ensure that all beam bunches see the same accelerating

3.4 MAIN LINACS

gradient regardless of the bunch position within the pulse train. This method achieves local energy gain stability of better than 1% and reduces the overall energy difference between bunches to less than 0.1% at the end of the linac.

Ground motion and vibrations of beam line components lead to emittance growth in the beam. Here the emittance growth is defined with respect to the average beam trajectory, i.e., integrated over a number of consecutive pulses. As can be seen in Table 3.20, the quadrupole jitter tolerance for 1% luminosity loss is extremely tight, about 1 nm. However, it is consistent with the expected performance that can be achieved using the quadrupole stabilisation scheme mentioned above. An alternative solution is to only measure the quadrupole motion in between beam pulses and compensate their impact on the beam using dipole correctors.

Table 3.20: r.m.s. jitter tolerances for the different beamline components that each lead to 1% luminosity loss

Error	Horizontal tolerance	Vertical tolerance
quadrupole position	10 nm	1.6 nm
Accelerating structure position	8 μm	1.4 μm
Accelerating structure angle	6 μrad	1.1 μrad

3.4.5 Main Linac components

Table 3.21 shows a summary of the total numbers of components in both the electron and positron main linacs.

Table 3.21: Number of components for both linacs

Modules	20 924
BPMs	4020
Quadrupoles, 35 cm-long	308
Quadrupoles, 85 cm-long	1276
Quadrupoles, 135 cm-long	964
Quadrupoles, 185 cm-long	1472
Accelerating structures	142 812

3.4.5.1 Quadrupoles

Four different quadrupole types are used in the main linac with different active lengths, see Table 3.20. The field gradient is up to 200 T/m and the beam pipe radius 4 mm. The quadrupoles are stabilized against vibrations with a mechanical feedback system. They can be moved in steps of 1 μm using stepping motors. Finer corrections with a step size of a few nm can be made using the mechanical stabilisation system. Each quadrupole is also equipped with a beam position monitor and a corrector dipole. The dipole correctors as well as the quadrupole stabilisation system each allow a correction within a range of $\pm 5 \mu\text{m}$.

3.4.5.2 BPMs

The beam position monitors have an accuracy of 5 μm and a resolution of 50 nm. The pre-alignment system establishes an r.m.s. accuracy of 10 μm between the position of the BPM centre and the reference

line. In order to be able to use dispersion-free steering, the BPMs must measure the distance between the trajectories of two short samples of a single pulse to an accuracy of $0.1\ \mu\text{m}$, as explained above. The bunch length of the samples varies between $44\ \mu\text{m}$ and $75\ \mu\text{m}$.

3.4.5.3 Accelerating Structures

The accelerating structures have an active length of 23 cm and a gradient of 100 MV/m; their iris radius a varies from 2.35 mm to 3.15 mm with an average of $\langle a \rangle = 2.75\ \text{mm}$. A hardware unit (super-structure) consists of two accelerating structures. Each of these units is equipped with a wakefield monitor, which can determine the beam offset with an accuracy of $3.5\ \mu\text{m}$. The wakefield monitor is located close to the beginning of the second structure. The longitudinal position of the monitor is not important for detecting overall transverse offsets but the central location minimizes the impact of transverse tilts. If the entire superstructure is tilted with respect to the beam direction, the wakefield kick in the first half is cancelled by a kick in the opposite direction in the second half. The girders that support the structures are equipped with movers that can be used to align the structures to the beam. The information from the wakefield monitors indicates the girder motions needed in order to minimize the impact of the wakefields.

3.4.5.4 Vacuum System

In order to reliably suppress the fast beam-ion instability in the electron linac a dynamic vacuum pressure of less than 10^{-9} mbar is required, see §2.6.

3.5 Beam delivery systems

3.5.1 Overview

The CLIC Beam Delivery System (BDS) transports the e^+/e^- beams from the exit of the high energy linacs, focusing them to the sizes required to meet the CLIC luminosity goals ($\sigma_x = 45$ nm, $\sigma_y = 1$ nm in the nominal parameters) and bringing them into collision. In addition, the BDS performs several critical functions:

1. Measure the linac beam and match it into the final focus.
2. Protect the beamline and detector against mis-steered beams from the main linacs.
3. Remove any large amplitude or off-energy particles (beam-halo) from the linac to minimize background in the detectors.
4. Measure and monitor the key physics parameters such as energy and polarization.

Functions 2 and 3 are accomplished by the collimators. Therefore, the first collimator needs to survive the impact of any mis-steered CLIC bunch train. This condition requires large beam sizes at the first collimator, and drives the length of the system. The BDS provides sufficient instrumentation, diagnostics and feedback systems to achieve these goals. All the CLIC BDS lattices can be found in [109].

3.5.2 Beam parameters

Table 3.22 shows the key BDS parameters for the nominal configuration at 3 TeV.

Table 3.22: Key parameters of the BDS.

Parameter	Units	Value
Length (linac exit to IP distance)/side	m	2750
Maximum energy/beam	TeV	1.5
Distance from IP to first quad, L^*	m	3.5
Crossing angle at the IP	mrad	20
Nominal core beam size at IP, σ^* , x/y	nm	45/1
Nominal beam divergence at IP, θ^* , x/y	μ rad	7.7/10.3
Nominal beta-function at IP, β^* , x/y	mm	10/0.07
Nominal bunch length, σ_z	μ m	44
Nominal disruption parameters, x/y		0.15/8.4
Nominal bunch population, N		3.7×10^9
Beam power in each beam	MW	14
Preferred entrance train to train jitter	σ	< 0.2
Preferred entrance bunch to bunch jitter	σ	< 0.05
Typical nominal collimation aperture, x/y	σ_x/σ_y	15/55
Vacuum pressure level, near/far from IP	10^{-9} mbar	1000/1

3.5.3 Subsystems

The main subsystems of the beam delivery starting from the exit of the main linacs are the diagnostics region, the energy and betatron collimation and the final focus. The layout of the beam delivery system is shown in Fig. 3.41.

There is a single collision point with a 20 mrad crossing angle. The 20 mrad geometry provides space to separate the spent beam lines and requires crab cavities to rotate the bunches in the horizontal

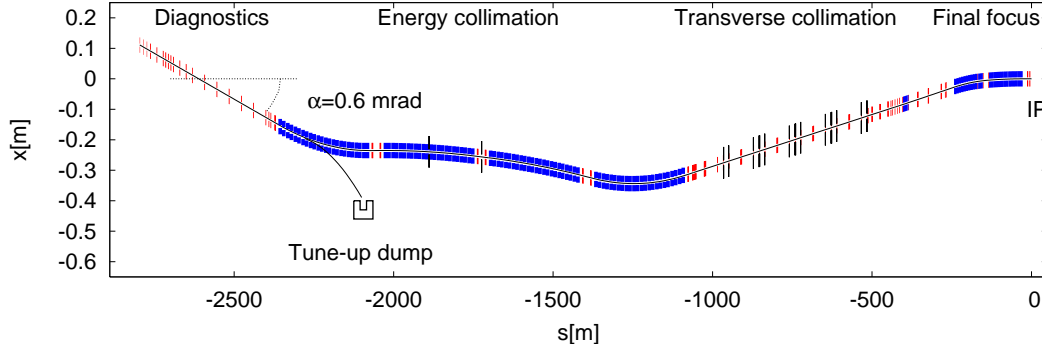


Fig. 3.41: CLIC 3 TeV layout. Dipoles, quadrupoles and collimators are shown in blue, red and black, respectively. The tune-up dump and its extraction line are also displayed.

plane for head-on collisions. There are two detectors in a common IR cavern complex (plus two garage caverns) which alternately occupy the single collision point, in a so-called ‘push-pull’ configuration, see §5.12.4 for more details.

3.5.3.1 Diagnostics

The initial part of the BDS, from the end of the main linac to the start of the collimation system, is where the properties of the beam are measured and corrected before it enters the Collimation and Final Focus system. The optics and the layout of the diagnostics section is shown in Fig. 3.42. Starting at the exit of the main linac, the system includes a skew correction section, emittance diagnostic section and beta matching section. The skew correction section contains 4 orthonormal skew quadrupoles which provide complete and independent control of the 4 betatron coupling parameters. This layout allows correction of any arbitrary linearized coupled beam.

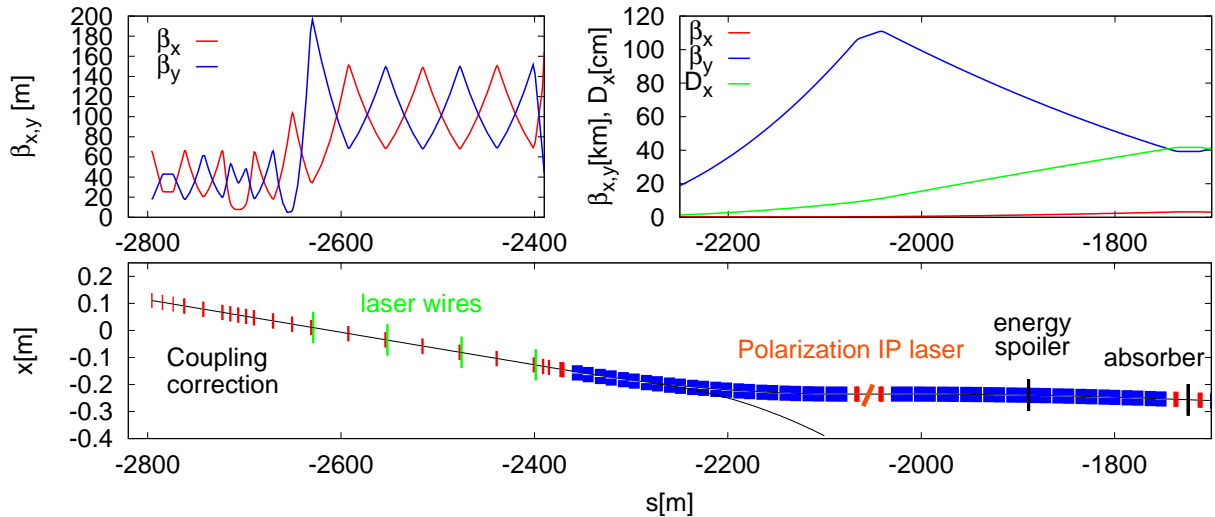


Fig. 3.42: Optics (top) and layout (bottom) of the CLIC diagnostics and energy collimation sections

The emittance diagnostic section contains four laser wires which are capable of measuring horizontal and vertical r.m.s. beam sizes down to $1 \mu\text{m}$. The wire scanners are separated by 45° in betatron

phase to allow a complete measurement of the 2D transverse phase space and determination of the projected horizontal and vertical emittances.

The energy measurement has been designed to minimize the required space due to the tight constraints on the CLIC total length. The deflection of the first dipole in the energy collimation section together with high precision BPM pairs before and after the dipole provides the most compact energy measurement. The integrated magnetic field is assumed to have a calibration error of 0.01% and the BPM resolution must be 100 nm or better. This setup provides a relative energy resolution better than 0.04%. Reference trajectories are regularly established by zeroing the magnetic field and safely disposing of the beam in the tuneup dump.

The BDS has a polarization measurement station [110] integrated into the energy collimation section. Figure 3.42 shows the location of the polarization laser IP. At this location, the beam travels parallel to the beam direction at the e^-/e^+ IP and there is enough free space for the polarization laser. The backscattered electrons (or positrons) deviate from the Main Beam trajectory in the bending dipoles. These lower energy particles are collected in a detector right before the energy spoiler. Particles losing about 95% of the energy are deflected on the order of 100 mm. With current existing laser technology, the polarization measurement achieves a resolution better than 0.1% when averaging over 60 seconds. The systematic errors of the setup will be analysed during the technical design phase.

3.5.3.2 *Tune-up extraction lines & dumps*

During the commissioning of the main linacs, the beam must be dumped before the collimation, final focus, or IR areas. There is an extraction line before the energy collimation where the beam can be diverted to a water-filled dump capable of absorbing the full beam power.

3.5.3.3 *Collimation*

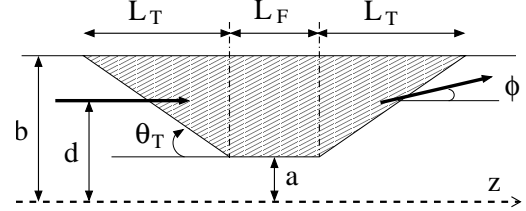
The CLIC collimation section has two critical functions; it protects the downstream beamline and detector against mis-steered beams from the main linac and it removes the beam halo. The most likely scenario for having mis-steered beams in the BDS is the failure of some component of the accelerating RF in the 20 km linac, resulting in a lower beam energy. Therefore, placing the energy collimation before the betatron collimation guarantees the most efficient absorption of the errant beams. The energy spoiler is designed to survive the impact of a full bunch train, however, recent simulations indicate that a solid energy spoiler may be damaged by some impacts [111]. This can be avoided by use of a hollow spoiler that provides the same thickness in radiation length at any impact parameter. This requires further investigation during the technical phase, particularly a detailed study of failure scenarios.

The transverse collimators, made of Ti, are sacrificial or consumable. A collimator absorber is placed downstream of the spoiler as shown in Fig. 3.43 to stop the particles scattered at the spoiler. The full description of the BDS spoilers and absorbers is given in Table 3.23.

Particles in the beam halo produce backgrounds in the detector and must be removed in the BDS collimation system. One of the design requirements for the CLIC BDS is that no particles are lost in the last several hundred metres of beamline before the IP. Another requirement is that all synchrotron radiation passes cleanly through the IP to the extraction line. The BDS collimation must remove any particles in the beam halo which do not satisfy these criteria. These requirements define a system where the collimators have very narrow gaps and the system is designed to address the resulting machine protection, survivability and beam emittance dilution issues. The betatron collimation system has four spoiler/absorber x/y pairs located as displayed in Fig. 3.43. These provide collimation at each of the final doublet (FD) and IP betatron phases. All spoilers and absorbers have adjustable gaps.

There is a small probability (of the order of some 10^{-4}) that high-energy secondary muons are produced in the collimation of the halo particles which may reach the experimental cavern and detector. This was studied by detailed tracking using PLACET [112] with HTGEN [113] for the halo modeling

Table 3.23: Geometry of the BDS spoilers and absorbers. The radiation lengths for Be and Ti are $X_0 = 0.353$ m and $X_0 = 0.036$ m, respectively. The material (Ti-Cu) of the transverse spoilers (YSP and XSP) is Ti with a Cu coating.



Name	a_x [mm]	a_y [mm]	θ_T [mrad]	L_F [X_0]	L_T [mm]	Mat.
ESP	3.51	8	50	0.05	90	Be
EAB	5.41	8	100	18	27	Ti
the following $\times 4$						
YSP	8	0.1	88	0.2	90	Ti-Cu
XSP	0.12	8	88	0.2	90	Ti-Cu
XAB	1	1	250	18	27	Ti
YAB	1	1	250	18	27	Ti

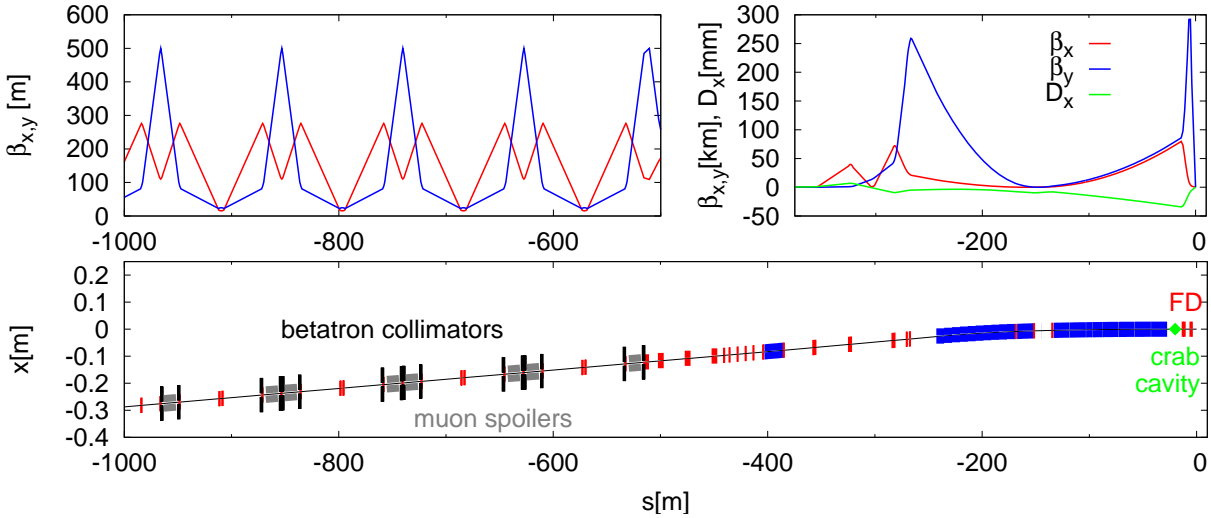


Fig. 3.43: Optics (top) and layout (bottom) of the CLIC betatron collimation and final focus sections

and BDSIM [114] for the study of muon production and tracking towards the detector.

The muon tracks generated have been used as input to detector simulations. These simulations indicate that the background muon rates from the machine must be kept to a low level, of not more than five muons per bunch crossing on average, integrated for both beams and over the cross-section of the detector [115].

The simulations of halo particles are based on beam-gas scattering as the primary halo source, assuming design vacuum conditions with residual gas pressure at the 10^{-9} mbar level both in the LINAC and the BDS. With these vacuum levels, only on the order of 10^{-5} of the beam particles are lost at the collimators. This results in a muon flux that is well below one muon per bunch crossing.

3.5.3.4 Muon suppression

The actual distribution of halo particles in a realistic machine with imperfections could be much higher than simulated by beam-gas scattering for the ideal machine. For more conservative estimates, the collimation system would be hit by a fraction of 10^{-3} of the beam particles resulting in one to two orders of magnitude higher muon rates [116] than desirable.

One possibility to reduce the muon flux into the detector region is to use cylindrical magnetized iron shielding with an outer radius of 55 cm around the beampipe located about 100 m downstream of the spoilers. Based on current tracking studies using BDSIM, a factor of ten reduction of the muon flux would require 80 m long shielding. More detailed simulations are ongoing. Space must be reserved in the BDS for the muon shielding as shown in Fig. 3.43. The muon shielding could be installed in stages, as required by the actual beam conditions.

3.5.3.5 Final Focus

The role of the Final Focus System (FFS) is to demagnify the beam to the required size ($\sigma_x = 45$ nm and $\sigma_y = 1$ nm) at the IP. The FFS optics creates a large and almost parallel beam at the entrance to the Final Doublet (FD) of strong quadrupoles. Since particles of different energies have different focal points, even a relatively small energy spread of 0.1% significantly dilutes the beam size, unless adequate corrections are applied. The design of the FFS is thus mainly driven by the need to cancel the chromaticity of the FD. The CLIC FFS baseline has local chromaticity correction [117] with sextupoles next to the final doublets. A bend upstream generates dispersion across the FD, which is required for the sextupoles and non-linear elements to cancel the chromaticity. The dispersion at the IP is zero and the angular dispersion is about 1.4 mrad, i.e., small enough that it does not significantly increase the beam divergence. Half of the total horizontal chromaticity of the final focus is generated upstream of the bend in order for the sextupoles to simultaneously cancel the chromaticity and the second-order dispersion. The horizontal and the vertical sextupoles are interleaved in this design, so they generate third-order geometric aberrations. Additional sextupoles upstream and at the proper phase with respect to the FD sextupoles partially cancel these third order aberrations. The residual higher order aberrations are further minimized with octupoles and decapoles [118]. The final focus optics is shown in Fig. 3.43.

3.5.3.6 Crab Cavity

With a 20 mrad crossing angle, crab cavities are required to rotate the bunches so they collide head on. They apply a z-dependent horizontal deflection to the bunch that zeroes at the center of the bunch. The crab cavity is located prior to the FD as shown in Fig. 3.43 but sufficiently close to be at 90° degrees phase advance from the IP.

3.5.3.7 Alternative L^*

In the nominal configuration with $L^* = 3.5$ m the last quadrupole of the FD, QD0, sits inside the detector, see §3.6.3.1 for detailed illustrations. As a possible fallback solution to alleviate engineering and stabilization issues, another option is to move QD0 from the detector to the tunnel, increasing L^* . A collection of FF systems with L^* values between 3.5 m and 8 m have been studied for CLIC. The performance of these FFS is shown in Table 3.24. Both the total luminosity and the luminosity in the energy peak degrade as the L^* increases. Only the cases with L^* of 3.5 m and 4.3 m meet the CLIC requirements with a 20% margin for static and dynamic imperfections. The shortest L^* that would remove QD0 from the detector is 6 m. The FFS with $L^* = 6$ m meets the CLIC requirements with a tight margin of 5% for imperfections [119]. The last case with $L^* = 8$ m does not meet the CLIC requirements.

Table 3.24: Total luminosity and luminosity in the 1% energy peak for the various L^* under consideration.

L^* [m]	Total luminosity [$10^{34}\text{cm}^{-2}\text{s}^{-1}$]	Peak luminosity [$10^{34}\text{cm}^{-2}\text{s}^{-1}$]
3.5	6.9	2.5
4.3	6.4	2.4
6	5.0	2.1
8	4.0	1.7

3.5.4 Accelerator physics issues

3.5.4.1 Synchrotron radiation and the detector solenoid

Synchrotron radiation from all of the BDS magnets causes a 22% luminosity loss [120]. About 10% comes from the FFS bending magnets and another 10% from the FD quadrupoles. The CLIC vertical IP beta function is slightly smaller than the theoretical beta function that minimizes the Oide effect [121, 122]. These numbers do not yet take into account the effect of the detector solenoid as this strongly depends on the detailed final configuration of the IR. Simulations in Ref. [123] show that the luminosity loss due to the solenoid ranges between 3% and 25%. This luminosity loss can be minimized by optimizing the length of the antisolenoid, the L^* , the detector solenoid field and the crossing angle.

3.5.4.2 Crab Cavity effects

Use of a crab cavity increases the luminosity to 95% of the head-on case [124]. The remaining difference is due to a traveling waist introduced by sextupoles downstream of the crab cavity. With no crab crossing the luminosity would be reduced to a fraction. Various solutions to avoid this luminosity loss have been suggested [125]: (i) compensation with an extra crab cavity [126], (ii) changing the location of the crab cavity, (iii) reversing the beam crossing direction with opposite crab cavity voltage.

3.5.4.3 Beam pipe aperture

The aperture of the CLIC BDS beampipe must be large enough to contain the beam ($14\sigma_x$ and $55\sigma_y$) and to avoid the effects of resistive wall wakefields [127]. It must also be small enough so that the BDS magnets are feasible. A reference beampipe radius of 8 mm is acceptable in terms of resistive wall effects [127]. A larger aperture is used where the beam requires more space and a smaller aperture is used where the magnet feasibility allows it. A round aperture is assumed throughout the BDS, see Fig. 3.44.

3.5.4.4 Collimators wakefields

Betatron spoilers are the main source of emittance growth due to wakefields in the BDS. The effects of the collimator wakefields on the luminosity have been evaluated for the design transverse collimation apertures $15\sigma_x$ and $55\sigma_y$ and the materials as given in Table 3.23. Figure 3.45 compares the relative luminosity degradation as a function of initial vertical position offsets at the entrance of the BDS with and without collimator wakefields. This calculation includes the effect of all the BDS collimators. A beam offset of $\pm 0.4\sigma_y$, leads to 20% luminosity reduction with with collimator wakes, and 10% without. This implies a reduction of the jitter tolerance by 30%.

3.5.4.5 FFS tuning

The biggest challenge for the BDS is to achieve the required performance assuming realistic static and dynamic imperfections. The diagnostics and the collimation sections have been shown to be robust

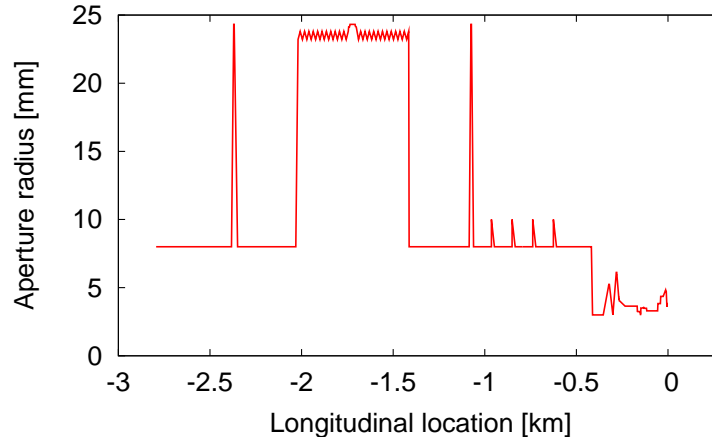


Fig. 3.44: Beam pipe aperture radius along the BDS

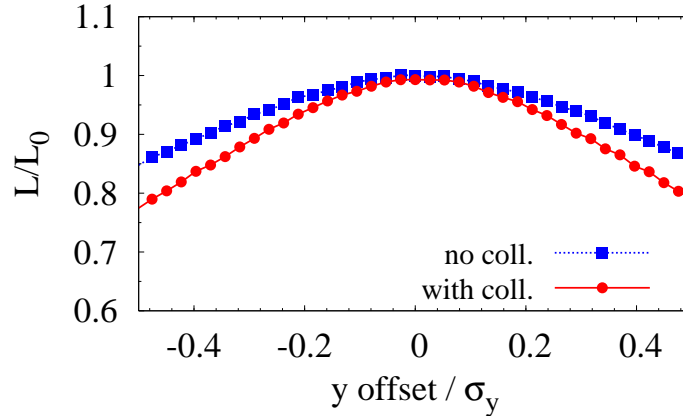


Fig. 3.45: Relative CLIC luminosity versus initial beam offsets for the cases with and without collimator wakefield effects

against misalignments (prealignment of $10\ \mu\text{m}$ over 500 m as discussed in §3.5.5.4). Standard orbit correction techniques, such as dispersion free steering, guarantee the beam transport without blow-up in these regions, but these techniques are not applicable in the FFS. The CLIC FFS is a very non-linear system with a β_y^* as small as 0.07 mm. Many different approaches have been investigated to tune the FFS in the presence of realistic misalignments. Currently the two most successful approaches follow:

- **Luminosity optimization:** Maximize the luminosity using all the available parameters in the FFS applying the Simplex algorithm.
- **Orthogonal knobs:** Maximize the luminosity by scanning pre-computed arrangements of sextupole displacements (knobs) which target the IP beam correlations in an orthogonal fashion.

These approaches have been simulated for the CLIC FFS with 100 statistical misalignment seeds. The final luminosity distribution and the number of iterations for these two approaches are shown in Fig. 3.46 in black and blue. The number of iterations corresponds to the number of luminosity measurements. A random error of up to 3% has been assumed for the luminosity measurement. Neither the Simplex approach, nor the orthogonal knobs reach a satisfactory result in terms of luminosity. However, the orthogonal knob procedure is much faster, and it can be applied after the Simplex approach. This is shown in the magenta curves in Fig. 3.46. With both procedures, there is a 90% probability of reaching 90% of the design luminosity after a maximum of 18 000 iterations. The luminosity performance is ade-

quate since new approaches may further improve the final luminosity, e.g., non-linear knobs. This number of iterations would be prohibitive using conventional luminosity measurements which take between 7–70 minutes [128]. Fortunately, different combinations of beamstrahlung signals [129] and hadronic events [130] can give faster luminosity estimates. Studies suggest that less than ten bunch crossings should be enough to obtain accurate signals for tuning. With these signals, 18 000 iterations would take about an hour, which is reasonable for tuning the BDS.

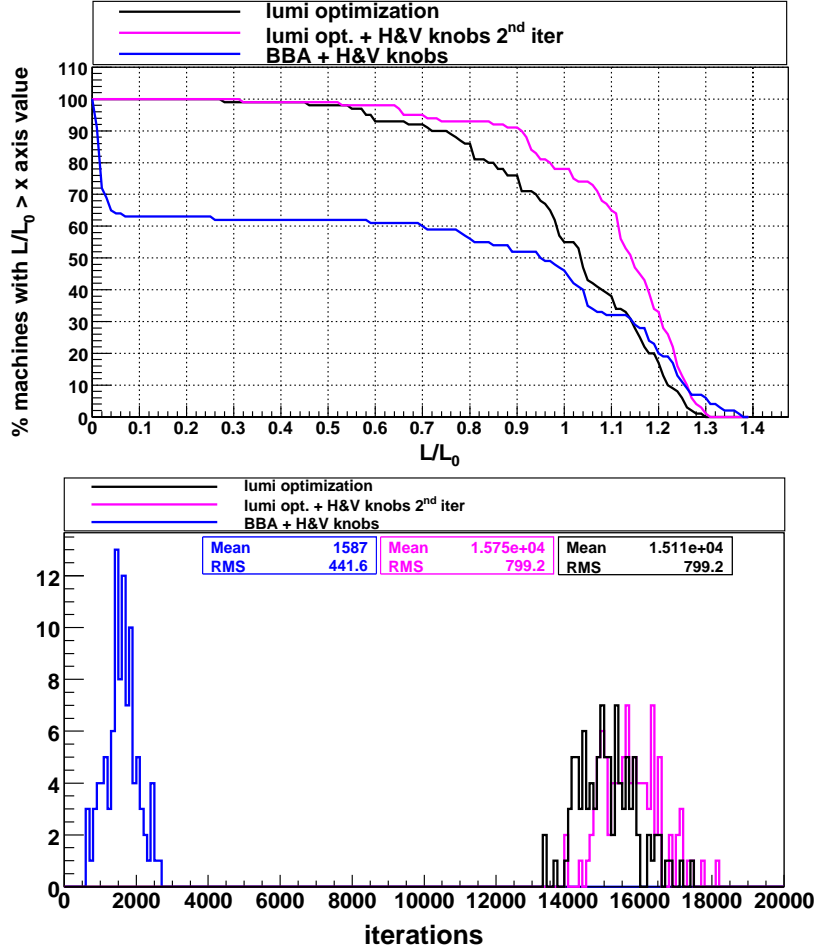


Fig. 3.46: Top: Luminosity performance for 100 statistical realizations of the CLIC FFS after tuning using three different approaches. Bottom: Required number of luminosity measurements for the three different approaches.

During the CLIC project preparation phase, improved tuning algorithms should be developed taking into account realistic errors in all BDS elements (e.g., the solenoid and the crab cavity were excluded in this study). The e^- and e^+ BDS lines should be optimized simultaneously and more robust FFS designs considered.

3.5.5 Component specifications

3.5.5.1 Magnets

The CLIC BDS contains 206 dipoles with a total length of 1.3 km, 70 quadrupoles with a total length of 190 m, and 18 sextupoles with a length of 34 m. At the moment there are not detailed engineering designs for all of the BDS magnets, but no technical obstacles have been identified. Detailed magnet designs will be part of the CLIC project preparation phase.

The dipoles have magnetic fields between 20–120 Gauss with a relative field precision and jitter

3.5 BEAM DELIVERY SYSTEMS

better than 10^{-4} . The relative sextupole field error in the dipoles at 10 mm must be below 6×10^{-4} . The CLIC baseline is to use normal conducting dipoles, however superconducting dipoles have the advantage of naturally shielding stray fields.

The most challenging quadrupole in the BDS is the final quadrupole QD0. Its specifications are given for the different L^* FFS options in Table 3.25. The technical description of QD0 is given in §3.6.3.1.

Table 3.25: Specifications of the FD QD0 quadrupole for the different L^* cases.

Parameter [units]	L^* [m]			
	3.5	4.3	6.0	8.0
Gradient [T/m]	575	382	200	211
Length [m]	2.7	3.3	4.7	4.2
Beam aperture [mm]	3.8	6.7	8	8.5
Jitter tolerance [nm]	0.15	0.15	0.2	0.18
Gradient tolerance [10^{-6}]	5	5	–	3
Octupolar error [10^{-4} @1 mm]	7	7	–	3
Prealignment [μ m]	10	10	8	2

An antisolenoid is required to shield QD0 from the magnetic field of the detector solenoid [131] and also to avoid the blowup of the beam emittance. A more detailed view of the antisolenoid is given in §3.6.4.1.

3.5.5.1.1 Instrumentation

There are about 100 BPMs per BDS line (total of 200). Most of these BPMs need between 20 and 50 nm resolution. The BPMs in the FD require 3 nm resolution in order to monitor and feedback the orbit.

There are four horizontal and four vertical beam size laser wires per BDS line, see Fig. 3.42. The vertical laser wires must resolve a 1μ m beam with 1% resolution.

The polarization laser collides with the beam with a 10 mrad angle. It has a wavelength of 532 nm and an IP spot size of 50μ m to achieve a resolution of 0.1%.

Other required instrumentation such as beam loss monitors, beam profile monitors, etc., will be specified during the technical design phase.

3.5.5.2 Crab cavities

The baseline crab cavities operate at 12 GHz and require a phase stability of 0.02° and an amplitude stability of 2% for a luminosity loss of 2%. Crab cavities also need strong high order mode damping. Figure 3.47 shows the current design of the crab cavity [132].

3.5.5.3 Vacuum

The vacuum system for the BDS can be separated into four main types of systems, linked by common interfaces and requirements.

There are 206 dipole magnet chambers with 24 mm internal radius and 70 quadrupole magnet chambers with 8 mm inner radius where the dimensions are constrained by the surrounding magnetic elements. These are separated by drift sections where dimensions and materials are optimized for vacuum and mechanics. Finally there are a number of special vacuum sections containing collimators and crab cavities which have special requirements.

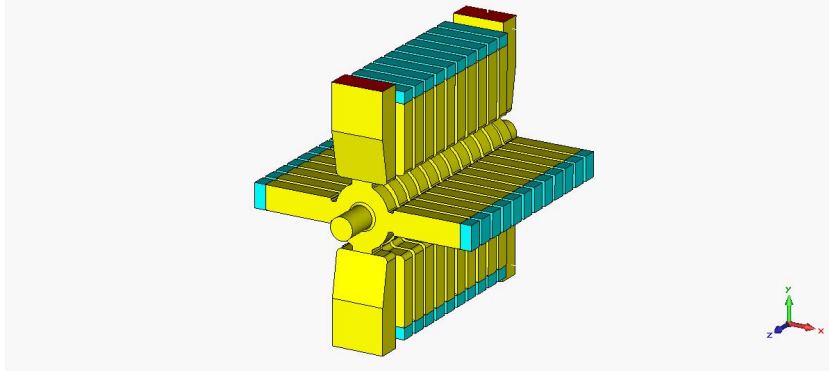


Fig. 3.47: 12 cell crab cavity design including wakefield dampers (length ~ 300 mm).

The requirements from the accelerator physics side are for an average pressure better than 10^{-9} mbar [133]. From the point of view of vacuum and surface physics, the pressure and surfaces must be designed to prevent pressure instabilities in the positron line. Additional requirements for the special vacuum sectors remain to be determined.

Preliminary pressure analysis indicates that the dipole chambers can be un-baked, with lumped ion pumps at both extremities. The small conductance of the quadrupole chambers means that a distributed pumping system along the chamber length is required. This could use the same concept as for the main LINAC module chambers, i.e., ante-chambers with NEG pumping strips connected to the beam aperture [134].

3.5.5.4 Alignment

All elements in the CLIC BDS are pre-aligned to $10\ \mu\text{m}$ transversely over a distance of 500 m. The longitudinal pre-alignment of the elements in the FFS is determined within $\pm 25\ \mu\text{m}$. The determination of the transverse position of each element follows the same strategy as for the main linac (see §5.17). It uses two different networks [135]:

- A Metrological Reference Network (MRN), consisting of overlapping wires with a length of 500 m, linked by biaxial Wire Positioning Sensors (WPS) installed and measured on a common metrological plate. This network propagates the precision of a few microns over 500 m.
- A Support Pre-alignment Network (SPN), framed by the MRN network, that associates sensors to each support to be aligned. This provides a few microns precision and accuracy over more than 10 m. A third step is required to link the support to the element to be aligned. This uses a 3D Coordinate Measurement Machine (CMM), with a measurement uncertainty of $0.3\ \mu\text{m} + 1\ \text{ppm}$.

The longitudinal monitoring of the elements in the Final Focus relies on capacitive sensors coupled to each component. These sensors measure with respect to targets located at the extremities of a carbon bar, independent from the components.

High precision and remote adjustment uses eccentric cam movers, similar to those for the Main Beam quadrupoles (see §5.17.2). The only difference is that in the final focus, the longitudinal axis can also be adjusted remotely. A stepper motor acting on the blocking longitudinal point provides this adjustment.

3.6 Machine Detector Interface

3.6.1 Overview

The Machine Detector Interface (MDI) is the region within the detector cavern where the beamlines of the accelerator overlap with the physics detector. Key issues are support of the final beamline components within the detector, luminosity monitoring and feedback, background suppression, and radiation shielding. The final-focusing quadrupoles, QD0, extend into the detector and have very stringent alignment and stabilization requirements. Luminosity monitoring is integrated with the detector. The spent beams have a power of 14 MW each and must be transported away cleanly through the experiment onto two beam dumps, via the post-collision lines. Collimators and masking must suppress backgrounds from the incoming beams, from the beam-beam interaction and from the beam dumps. The cavern layout and shielding must minimize the exposure of equipment and personnel to radiation.

The experimental hall has two detectors in a push-pull configuration with each detector assembled on a platform in its garage position. One detector at a time is moved into the beamline. The QD0 magnets move with the detector and are supported by the detector during the move. Access to the inner detector is possible only with the detector in the garage position where the QD0 magnets can be removed to allow a full opening.

The detectors are based on the ILC detectors SiD [136] and ILD [137], adapted to the CLIC parameters. The distance, L^* , between the exit of the last quadrupole, QD0, and the interaction point (IP) is 3.5 m for CLIC_SiD and 4.34 m for CLIC_ILD. The shorter L^* allows higher luminosity, but it is more difficult to satisfy all design constraints. This report concentrates primarily on the more difficult layout. More detailed studies of the two different L^* values will be addressed for the Technical Design Report.

A particular challenge is the support and stabilization of the QD0 quadrupole which focuses the beam to a 1 nm r.m.s. vertical beam size. Any vertical motion of this quadrupole translates into an equivalent displacement of the beam at the interaction point. To maintain the beams in collision, the vertical position of the quadrupole must be stabilized to 0.15 nm at frequencies above 4 Hz. Measurements on and near the CMS detector [138] indicate that ground motion and technical noise are much larger on the detector (as much as 80 nm on top of the yoke) than at the ends of the tunnel (few nanometres). For this reason, the QD0 magnet is mounted on a very stiff support attached to the tunnel floor via a high-mass pre-isolation system with a very low natural vibration frequency. The quadrupole is then actively stabilized by a system of piezo-actuators.

Beam-based feedback and feed-forward systems in the linacs and beam delivery systems compensate for lower-frequency motion. An intra-pulse feedback also corrects the beam position within the 156 ns pulse train. Vibrations at frequencies close to the machine frequency of 50 Hz and its higher harmonics have less impact on the machine performance.

A simplified view of the Machine Detector Interface is shown in Fig. 3.48. Technical details are described in §5.12.

3.6.2 Beam parameters

Table 3.26 lists nominal values of the beam parameters relevant for the Machine Detector Interface. Particularly important are the vertical beam-spot size at the interaction point and the length of the bunch train.

3.6.3 System description

3.6.3.1 QD0 and support

Figure 3.48 shows the tight integration of the QD0 quadrupole with the vacuum pipe of the incoming beam (smaller diameter) and the vacuum pipe of the outgoing beam (larger diameter). The incoming and outgoing beam-lines cross at an angle of 20 mrad and the outgoing (post-collision) vacuum pipe has a

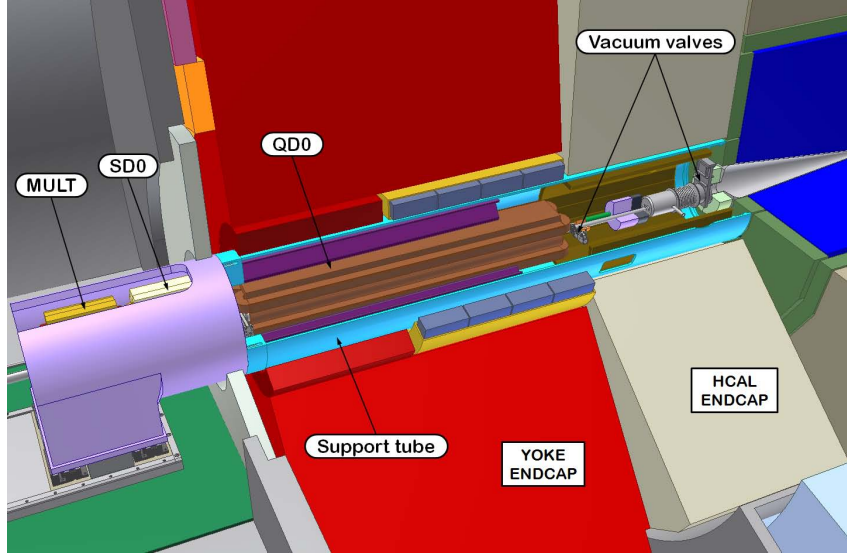


Fig. 3.48: Simplified MDI layout view showing a representation of part of the final-focus quadrupole, QD0, integrated into the CLIC_SiD detector

Table 3.26: Beam parameters of interest to the MDI region

Beam parameter	Value
Centre-of-mass energy	3 TeV
Total luminosity	$5.9 \times 10^{34} \text{ cm}^{-2} \text{ s}^{-1}$
Luminosity L_{99} (within 1% of energy)	$2 \times 10^{34} \text{ cm}^{-2} \text{ s}^{-1}$
Linac repetition rate	50 Hz
Number of bunches per train	312
Number of particles per bunch	3.72×10^9
Bunch separation	0.5 ns
Bunch-train length	156 ns
Beam power per beam	14 MW
Nominal horizontal IP β function	6.9 mm
Nominal vertical IP β function	0.068 mm
Horizontal IP beam size	45 nm
Vertical IP beam size	1 nm
Bunch length	44 μm

conical shape with a half opening angle of 10 mrad.

A major consequence of this geometry is that the post-collision vacuum pipe is inside the QD0 envelope and subsequent magnets until the point where the separation of the two vacuum pipes is sufficient to allow the post-collision line to run alongside the magnets.

QD0 main parameters

The design parameters for the QD0 quadrupole [139] are defined by the Beam Delivery System (BDS) and listed in Table 3.27:

Rather than using a superconducting magnet, the QD0 is a compact ‘hybrid’ magnet with permanent magnet (PM) inserts and classical electro-magnetic (EM) coils (see §5.12.2.1 for details of the magnet design). This choice was motivated by the following considerations:

Table 3.27: QD0 main parameters

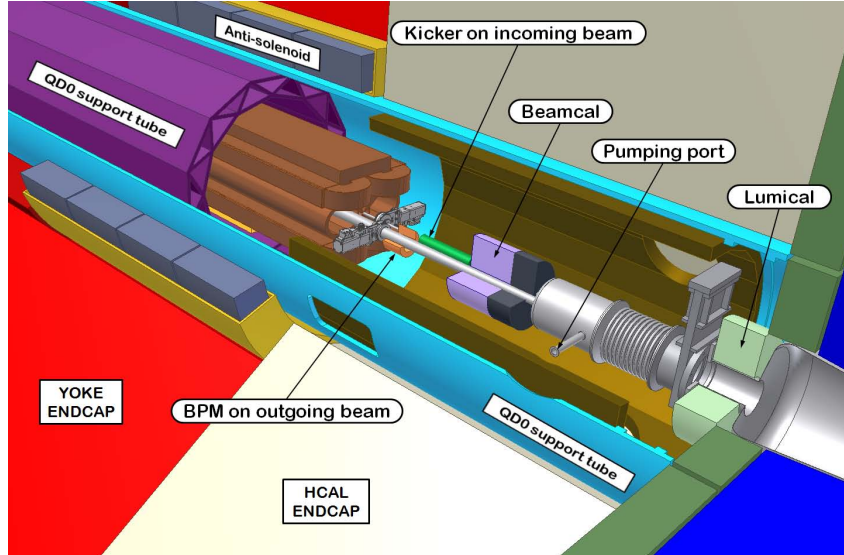
Parameter	Value
Magnet aperture (diameter)	8.00 mm
Nominal gradient	575 T/m
Effective length (magnetic)	2.73 m
Required tunability of the gradient	80–100 %

- the space available for the magnet is extremely limited and cannot easily accommodate a cryostat with all its ancillary systems;
- the magnet aperture is too small to be wound with superconducting cables using standard techniques, particularly given the large electromagnetic forces on such a small radius;
- the complex assembly of a superconducting magnet with different layers of coils, collars or other force-bearing structures, thermal insulation, thin supports, cryostat, etc. is difficult to align and stabilize at the sub-nanometer level;
- the integration of a conical post-collision line is difficult for a cryostat assembly.

For CLIC a permanent-magnet-based QD0 quadrupole satisfies all requirements.

3.6.4 QD0 support

Figure 3.49 shows the conceptual layout of the MDI region with several elements (QD0, BeamCal, LumiCal and the feedback kicker) supported by two tubes cantilevered from the cavern wall. Details of this removable support tube, which is a key element of the ‘push–pull’, stabilization and alignment systems, are presented in §5.12.

**Fig. 3.49:** Support tube concept in the MDI region

3.6.4.1 Anti-solenoid

Because the beam enters the detector solenoid with a crossing angle, the magnetic field of the solenoid has a component perpendicular to the incoming beam direction. This causes several distortions of the beam at the IP as described in Ref. [139]. With the short L^* , the most severe effects come from the fact

that the main solenoid and QD0 fields [140–143] overlap. In addition, since the QD0 uses permendur and permanent magnet material, the QD0 must be shielded from external fields. In order to both shield the QD0 magnet and reduce the beam distortions, an anti-solenoid is required [144]. Preliminary designs of such an anti-solenoid consist of bucking coils surrounding the QD0 support tube and connected to the detector end-caps. The current of each bucking coil is adjusted in order to minimize the detector solenoid flux density along the beam trajectory. Beam dynamics simulations show that the anti-solenoid can cancel more than 90% of the beam distortions at the IP [142]. The simulated field map is shown in Fig. 3.50 for CLIC_SiD.

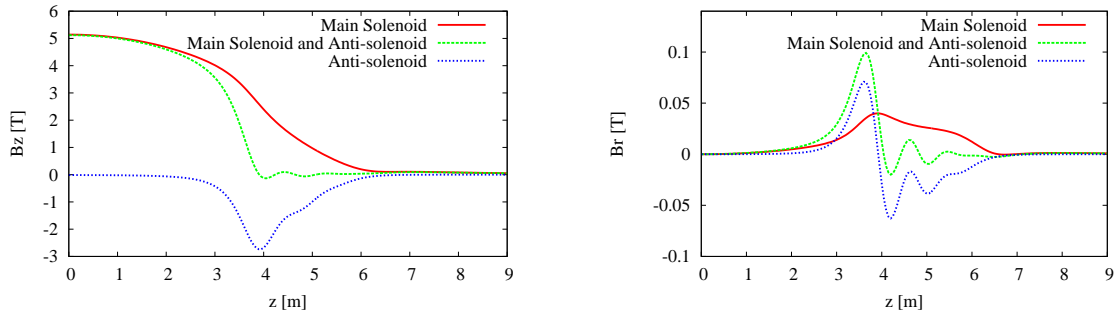


Fig. 3.50: The longitudinal field after compensation, B_z , with the anti-solenoid (top plot), the radial field, B_r , (bottom plot), for the CLIC_SiD layout

The anti-solenoid also reduces the impact of the main solenoid on the luminosity, such that the remaining luminosity reduction is only half of the total Beam Delivery System (BDS) budget for luminosity loss.

In the $L^* = 6$ m option (a backup solution where the QD0 is mounted outside the detector, in the tunnel, but with reduced luminosity) the anti-solenoid is simpler: the bucking coils have a smaller radius and just surround the QD0 magnet and the post-collision line. Further optimization of the bucking coils design and the overall integration of the anti-solenoid within the MDI region will be studied during the project preparation phase.

3.6.5 Forward region design

Figures 3.48 and 3.49 show the forward region for the CLIC_SiD detector. Two forward detectors complete the coverage at small angles: a luminosity calorimeter (LumiCal) [145] for precision luminosity measurements and an instrumented absorber for beam–beam background pairs (BeamCal) that can also tag high-energy electrons. Together they provide angular coverage down to a polar angle of 11 mrad. Since the BeamCal is located closest to the beams, it also acts as a mask against particles back-scattering from the beam dump.

The LumiCal is an electromagnetic sandwich calorimeter consisting of 40 layers of 3.5 mm tungsten absorbers with silicon sensors, covering an angular region from 40 to 110 mrad. It counts Bhabha events to provide a slow but precise measurement of the luminosity. The luminosity precision is 1% for an integrated luminosity of 100 fb^{-1} . The lower acceptance angle of the LumiCal is just outside the cone of incoherent scattering products to avoid degradation of its energy resolution.

The BeamCal is another electromagnetic sandwich calorimeter, consisting of 40 layers of 3.5 mm tungsten absorbers and silicon sensors. A 10 cm thick graphite disk on the IP-facing side reduces back-scattering from the surface of the BeamCal. The BeamCal must survive a radiation dose of up to several

MGray per year, so a radiation-hard sensor material must be used. The BeamCal extends the angular coverage down to 11 mrad and is therefore the primary absorber of background pairs that might otherwise damage the final-focus quadrupole or the equipment of the intra-train feedback system. At the ILC, the BeamCal tags high-energy electrons, and the distribution of deposited energy from the background pairs can also be used for beam diagnostics [146]. It remains to be confirmed whether this is also possible at CLIC.

3.6.6 Intra-train feedback system

A fast beam-based intra-train feedback (FB) system corrects for the relative vertical displacement of the colliding beams at the IP by steering them back into collision. This FB system is the last line of defense against relative beam–beam offsets, and relaxes the tight vibration tolerance of the QD0 quadrupoles. At CLIC, intra-train FB is especially challenging due to the extremely small bunch separation of 0.5 ns and bunch train length of 156 ns. With current technology, one cannot apply a bunch-to-bunch correction, but can only make a few correction iterations per train by using an all-analogue FB system. Owing to latency time constraints, there is no intra-train angle FB system in the current design.

The key components of the intra-train FB are a stripline beam-position monitor (BPM) for measuring the position (and hence deflection angle) of the outgoing beam; a front-end signal processor and feedback circuit; an amplifier to provide the required output drive signals; and a kicker for applying an angular correction to the opposite incoming beam. The BPM and kicker locations are shown in Fig. 3.49.

Two such systems, one on each side of the IP, provide backup. Details of prototype components and system tests with real beams are given in Ref. [147, 148]. For this layout, the total latency due to beam time of flight and hardware delays can be kept to 37 ns or less [149]. This allows for approximately three luminosity correction cycles during the bunch train duration, as shown in Fig. 3.51. The simulation shown assumes a perfect linac and a single random seed of (very noisy) ground motion for the element misalignments in the BDS. A detailed description of the potential luminosity recovery performance is given in Ref. [149].

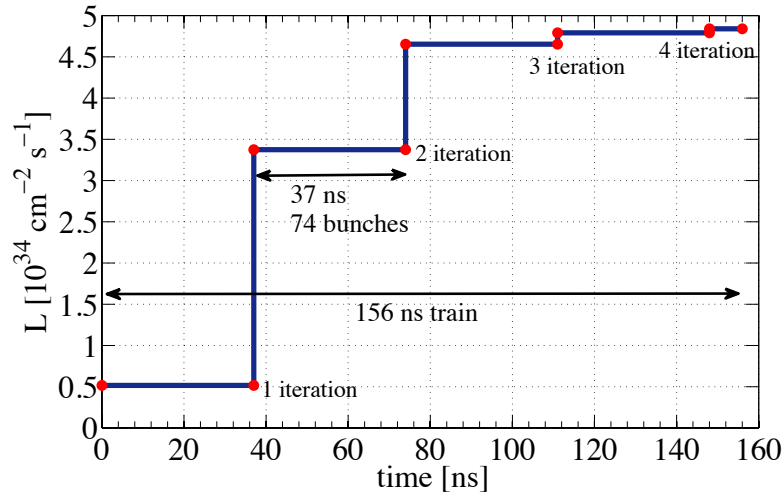


Fig. 3.51: Simulated luminosity versus bunch number for nominal CLIC 3 TeV parameters assuming a noisy site (for the ground motion)

3.6.7 Vacuum system

Conceptually the MDI vacuum system is composed of three physically connected sectors (QD0, experimental and post-collision lines) with different requirements.

The QD0 sector consists of an incoming beam chamber inside the magnet and a post-collision chamber passing through the magnet structure. CLIC uses room-temperature QD0 magnets as opposed to the superconducting QD0 planned for the ILC. This means that the CLIC QD0 does not have the high-capacity cryo-pumping available within a magnet cold bore. However, simulations for CLIC [150] and ILC [151] show that incoherent instabilities and beam gas background are acceptable in this region up to pressures of 10^{-4} mbar and 10^{-6} mbar respectively. These relatively relaxed pressure requirements would allow a vacuum design with local lumped pumping from the extremities of the magnet. However, to avoid beam size increase due to multiple scattering 10^{-9} mbar is preferred.

An additional constraint is imposed by the detector ‘push–pull’ concept, which implies by definition that the beam vacuum must be separated in order to switch detectors. The system must therefore be capable of reaching the required operating pressure within ~ 24 hours of reconnecting the ‘push–pull’ sector.

The IP vacuum system is constrained by both the BDS vacuum requirements and the needs of the detectors. The beam pipe inside the detectors consists of a cylindrical section inside the vertex detector with symmetric cones on either side. The vacuum system design (chambers, supports, instrumentation) within each detector is optimized to minimize the radiation length of material within the detector acceptance. Low- Z materials such as beryllium and aluminium also have high secondary emission yields. Optimizing the vacuum chamber for physics therefore requires coatings and/or *in situ* heating of the chamber to achieve the required vacuum.

The post-collision line vacuum has less demanding pressure requirements in the medium vacuum range, allowing for a conventional unbaked system design.

3.6.8 Accelerator physics issues

Two key issues for the design of the detector and the MDI are the luminosity spectrum and the accelerator backgrounds. The main background sources are those coming from the beam interactions before and after the collision point, the so-called machine background, and those arising from beam–beam interactions, the so-called beam–beam background.

3.6.8.1 Luminosity spectrum

Figure 3.52 shows the total luminosity spectrum and the luminosity in the peak for the CLIC nominal beam parameters listed in Table 3.26. The high energy and small transverse dimensions of the beams at the collision point cause them to interact strongly. These beam–beam interactions, primarily beamstrahlung, degrade the luminosity spectrum, even though the single-bunch energy spread has been optimized to minimize these interactions as much as possible. Coherent processes (see §3.6.8.2) also contribute to luminosity ($\sim 4\%$) and increase the low-energy tail of the spectrum. This includes collisions where an electron, from a coherent pair produced in the positron beam, collides with the electron beam (and vice versa). The contribution of these collisions to the luminosity spectrum ($\sim 1\%$) is shown in red in Fig. 3.52.

3.6.8.2 Beam–Beam background

The high-energy and high-charge-density electron and positron bunches produce strong electromagnetic fields which can deflect or focus the particles in the colliding bunch. The strong focusing causes a luminosity enhancement, but the strong bending of the particle trajectories causes them to emit high-energy photons, so-called beamstrahlung. There are also other QED and QCD processes that produce backgrounds, such as coherent pair production, incoherent pair production, and $\gamma\gamma \rightarrow$ hadrons events. At multi-TeV energies, higher order coherent processes also have a significant production rate, the so-called tridents [152]. A detailed description of the production processes and typical cross-sections can be

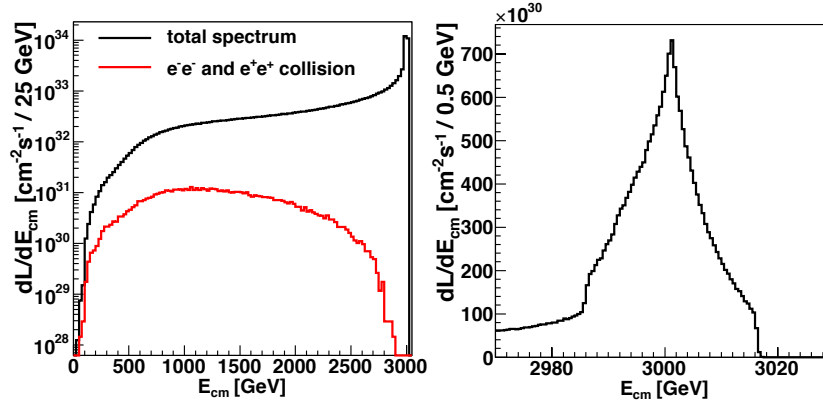


Fig. 3.52: Total luminosity spectrum (left) and zoomed view of the luminosity in the peak (right)

found in Ref. [153]. The expected rates per bunch crossing for the nominal CLIC parameters are given in Table 3.28.

If operational conditions produce smaller than nominal emittance, the luminosity may be higher but the background levels can increase by up to 40%. Even if imperfections reduce the luminosity somewhat, the ratio of background to luminosity may nevertheless increase [154].

Table 3.28: Expected background rates for the CLIC nominal beam parameters

Background	Rate per bunch crossing
Beamstrahlung photons	2.1 per primary particle
Incoherent pairs	3.3×10^5 particles
Coherent pairs	6.8×10^8 particles
$\gamma\gamma \rightarrow \text{hadrons}$ ($W_{\gamma\gamma} > 2\text{ GeV}$)	3.2 events

3.6.8.3 Machine background

The most important machine-related backgrounds come from muons produced in the upstream collimation system, from backscattered particles produced by the outgoing beam, and from synchrotron radiation emitted in the last magnets upstream of the IP.

Beam halo particles stopped by the collimators of the beam delivery system (BDS) produce secondary muons that can reach the detector. The absolute muon flux depends on the number of halo particles hitting the collimators, which in turn depends on the collimator settings and on details of the lattice, including imperfections and misalignment. Considering only halo particles generated by beam-gas scattering, and assuming a perfect BDS lattice, a fraction of 7×10^{-8} of the beam hits the spoilers, producing a flux of $\mathcal{O}(10)$ muons/train at 10 m from the interaction point within a 6 m radius around the beam line [155]. Muon suppression methods are discussed in §3.5.3.4.

The disrupted beams after the collision and the pairs produced during the interaction are transported to the main dump with minimal losses. Nevertheless, particles striking the carbon magnet protection absorbers, the intermediate dump and the main dump [156] generate backscattered photons and neutrons that can reach the detector. The flux from the intermediate dump through a $2 \times 2\text{ m}^2$ plane at 0.0 m is calculated as 8.4 ± 2.8 photons per cm^2 per bunch crossing, with an average energy of $162 \pm 4\text{ keV}$. Further details as well as the estimated neutron flux can be found in §3.7.

Typical synchrotron radiation fans from the final doublet (QF1 and QD0) to the interaction region are depicted in Fig. 3.53, for an envelope covering 15 standard deviations in x and 55 in y. At the IP the

photon cone is inside a cylinder of radius of 5 mm and thus within the beam pipe radius. Therefore, they do not cause significant backgrounds in the detectors.

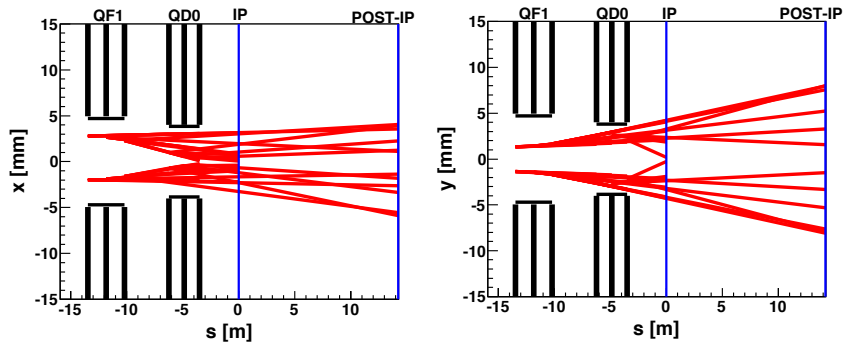


Fig. 3.53: Synchrotron radiation fans at 3 TeV centre-of-mass energy

3.6.9 Component specifications

The main components and their required specifications are listed in Table 3.29.

Table 3.29: Specifications for the main components in the Machine Detector Interface region

Component	Quantity	Requirements
QD0 magnet	4	Gradient 575 T/m, length 2.73 m, aperture radius 3.8 mm
QD0 stabilization system	2	r.m.s. movements <0.15 nm above 4 Hz, in combination with diverse feedback systems
QD0 prealignment system	2	Alignment precision 10 μ m
Vacuum system	–	10^{-6} mbar in MDI region
IP feedback system	4	37 ns latency (1/4 of train length)
Anti-solenoid	4	Solenoid cancellation to below 0.2 T

3.7 Post-Collision Line

3.7.1 Overview

To reach the required luminosity, the 1.5 TeV electron/positron CLIC beams, with a total power of 14 MW per beam, must be focused to nanometre spot sizes in the interaction point (IP). The resulting strong beam–beam effects lead to a large emittance growth for the outgoing beam as well as to the production of bremsstrahlung photons and e^+e^- pairs. If the beams do not collide, these processes do not occur and the outgoing beam has very different characteristics. The post-collision line from the IP to the Main Beam dump must transport both the un-collided beam as well as the collided beam (disrupted beam, coherent e^+e^- pairs, and beamstrahlung photons) with its increased momentum spread and angular divergence [157]. The post-collision line is also optimized to produce minimal losses, and thus minimal background contributions to the detector at the IP. It must also guarantee sufficient divergence of the beams to avoid damage to the vacuum exit and dump entrance windows. The post-collision line also contains a luminosity monitoring system for fast feedback to the beam steering. In addition, for a staged construction of CLIC, the post-collision line must handle an initial operation at lower centre-of-mass energy, e.g., 500 GeV and with a slightly different crossing angle.

3.7.2 Beam parameters of relevance for the post-collision line

Nominal values of beam parameters of interest for the post-collision line are listed in Table 3.30.

Table 3.30: CLIC beam parameters of interest for the post-collision line

Bunch train frequency [Hz]	50
Bunch spacing [ns]	0.5
Particles per bunch	3.72×10^9
Bunches per train	312
Bunch train length [ns]	156
Beam power per beam [MW]	14
Crossing angle [mrad]	20
Core beam size at IP horiz./vert. $\sigma_{x/y}^*$ [nm]	45 / 1
Beamstrahlung energy loss	28%
Number of photons per beam particle	2.1
Number of coherent pairs per bunch-crossing	6.8×10^8

3.7.3 System description

3.7.3.1 Transport line

The baseline layout of the post-collision beam line is shown in Fig. 3.54. The extraction line provides an early separation of the outgoing charged beam from the lower energy products of the strong beam–beam interaction (photons, coherent pairs). Therefore, the line has a large acceptance for emittance and energy spread. In the following, the post-collision line is described in the beam direction from the interaction point to the main dump. The post-collision line on the other side of the IP is identical.

Starting at the IP, the spent beam leaves the detector region through 27.5 m of drift space before traversing five vertically bending magnets which provide separation between electrons, positrons and beamstrahlung photons. To protect these magnets, carbon-based absorbers are installed upstream of each magnet. At 67 m from the IP, lower energy particles strike the intermediate dump, which stops a fraction of the electron/positron pairs. Particles that pass through the aperture of the intermediate dump

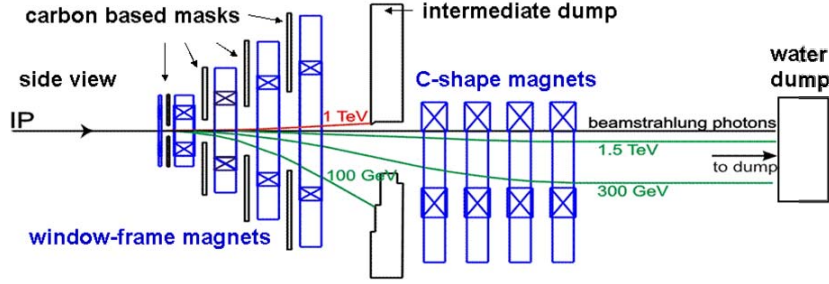


Fig. 3.54: Schematic layout of the CLIC post-collision line.

traverse four vertically bending C-type magnets, that reduce the derivative of the dispersion to zero. At this point, both the electrons/positrons and beamstrahlung photons are transported in parallel towards the main dump. Due to the vertical magnetic chicane the beamstrahlung photons hit the Main Beam dump vertically separated by about 12 cm from the disrupted Main Beam and the same-sign coherent pairs. Figure 3.55 shows the vertical distribution of the beams at the front face of the Main Beam dump. The main dump is located at a distance of 315 m from the IP.

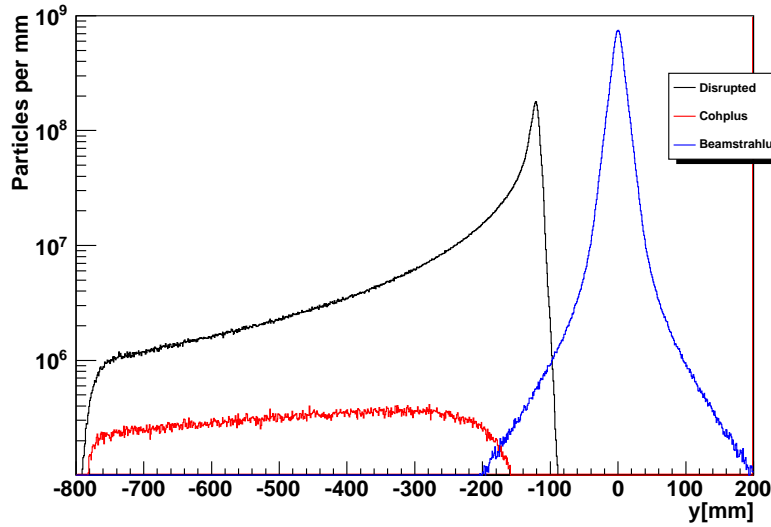


Fig. 3.55: Vertical distribution of the beamstrahlung photons (blue), the disrupted beam (black) and the same-sign coherent pairs (red) at the front face of the Main Beam dump.

Magnets

There are strong geometrical constraints on the post-collision line beam layout due to the presence of the opposite incoming beam. The first magnets in the post-collision line are located upstream of the intermediate dump; these are five rectangular window frame warm dipole magnets with a magnetic strength of 0.8 T. The aperture of the magnets needs to increase along the beamline as the separation between particles of different momenta increases in order to avoid excessive losses (see Table 3.31). The

3.7 POST-COLLISION LINE

biggest of these magnets is Mag4, with a full aperture of 0.444 m horizontally and 1.531 m vertically. The outer dimensions are 1.344 m horizontally and 2.84 m vertically. A cross-section of the ‘Mag4’ dipole and a list of its main parameters are shown in §5.2.5.1.

The deflection provided by the window frame magnets must be followed by a bend in the opposite direction at the exit of the intermediate dump, in order to transport the beam and photons in parallel to the Main Beam dump. Four C-type magnets are used, each of them with a magnetic strength of 0.8 T and a magnetic length of 4 m.

Table 3.31 summarizes the properties of the required magnets. Details of the magnet design criteria and the parameter lists for all magnets can be found in [158].

Table 3.31: List of magnets for the CLIC post-collision line.

Name	Quantity	Magnetic Length	Full magnet aperture H/V	Good field region H/V	Tuning Range	Rel. Field Accuracy	Higher Harmonics bn/b1
		[m]	[m]		[m]	[%]	
Mag1a	2×2	2	0.222/0.577*	0.2/0.44	10	10 ⁻²	<10%
Mag1b							
Mag2	1×2	4	0.296/0.839*	0.27/0.702	10	10 ⁻²	<10%
Mag3	1×2	4	0.37/1.157*	0.34/1.02	10	10 ⁻²	<10%
Mag4	1×2	4	0.444/1.531*	0.41/1.394	10	10 ⁻²	<10%
Mag C-type	4×2	4	0.45/0.75**	0.428/0.74	10	10 ⁻²	<10%

Magnet protection absorbers and intermediate dump

A set of four pairs of carbon absorbers in the upstream part of the post-collision line protect the vertical bending magnets from the low energy tail of the coherent e^+e^- pairs (see Fig. 3.54). The latest simulations show that a denser material such as iron is required in order to stop the particles. Iron absorbers significantly increase the predicted lifetime of the magnet coils [159]. The lifetime could be further increased by using radiation hardened materials. The absorbers are mounted in fixed positions outside the post-collision line vacuum. The collimator between Mag3 and Mag4 absorbs the most energy, 10.7 ± 0.4 kW. Further studies and modifications to the magnet shielding design will be part of the project preparation phase.

The intermediate dump is located 67 m from the interaction point and vertically offset with respect to the post-collision line. The dump consists of a carbon-based absorber with water-cooled aluminum plates and an iron jacket. The minimum vertical half-aperture is 5 cm for the upper aperture and 49 cm for the lower aperture, centred on the beamstrahlung photon axis. This asymmetric aperture allows all coherently produced electrons/positrons of the opposite charge to be absorbed. Beamstrahlung photons pass through the aperture, as well as all electrons/positrons of the same charge as the Main Beam that have at least 14% of the nominal beam energy. Electrons/positrons below this energy threshold are stopped in the lower half of the dump. The total power deposition in the intermediate dump is 527 ± 8 kW.

While a dump with a few-100 kW continuous power deposition is non-trivial, examples of possible designs exist. For example, the dumps in neutrino experiments (water-cooled with a graphite core and copper/iron mantle) have to withstand up to 4 MW proton beams [160].

Beam Instrumentation

An overview of the beam instrumentation foreseen for each post-collision line is presented Table 3.32.

Four beam position monitors (BPMs) measure the Main Beam through the post-collision line: one at the entrance of the line, one each upstream and downstream of the intermediate dump, and the last

Table 3.32: Beam instrumentation in one post-collision line.

Type of instrument	Accuracy/ Resolution	Time Resolution	Quantity	Proposed Technology
Beam Position Monitor	1 mm/100 μm	10 ns	4	Button/Strip line
Beam Intensity Monitor	10^{-2} / 10^{-3}	10 ns	4	Fast transformer/Wall current monitor
Transverse Profile Monitor	1 mm	–	3	OTR/Scintillating Screen
Type of instrument	Dyn. Range/ Sensitivity [Gy/pulse]	Time Resolution	Quantity	Proposed Technology
Beam Loss Monitor	10^6 / 10^{-7}	<8 ms	28	Ionization chambers

monitor upstream of the Main Beam dump. The expected accuracy and resolution of the BPMs is very modest compared to other regions of CLIC. Measuring beam size and profile for beams as large as those in the post-collision line appears feasible. However, the fact that both electrons and positrons are in the same BPM (pick-up) at the same time needs careful study. A general discussion on the design of CLIC beam position monitors is given in §5.9.2.

Intensity monitors are also located close to the beam position monitors. They measure the number of particles impinging on the absorbers and the intermediate dump. In addition, there are 28 beam loss monitors (BLM) along the post-collision line: four per window frame magnet, four at the intermediate dump (due to the asymmetric losses on the dump), one for each C-shaped magnet and four at the main dump. The exact location of the BLMs may change as better information about the expected loss distribution becomes available. Details on the design and performance of CLIC beam loss monitors can be found in §5.9.7.

Finally, a set of three beam imaging systems measure the beam spot size and are used to tune the steering of the line. For setting up the beam line, the first two ‘screens’ are motorized in order to move them in or out of the beam position inside the vacuum chamber. The last transverse profile monitor is installed in a permanent position very close to the entrance window of the Main Beam dump; it monitors the beam dilution and ensures that the beamstrahlung photons are well separated from the primary particles. The total diameter of this final ‘screen’ is 30 cm, since typical beam sizes up to several centimetres in the vertical direction are expected with colliding beams. A technical discussion on the choice of beam profile monitors for the post-collision line is given in §5.9.4.

A key diagnostic of the CLIC performance is the measurement of luminosity related signals by using the beam-beam products either in the interaction region or in the post-collision line. These diagnostics are described below in §3.7.4.2.

Vacuum

The post-collision line consists of a series of stainless steel vacuum chambers in stepped or conical forms inside the magnets and absorbers. As the absorbers are outside the vacuum chambers, the chambers have windows upstream of the absorbers and intermediate dump and an exit window separating the collider vacuum system from the main dump body.

The vacuum pressure required is in the medium range, allowing for a conventional un-baked system. However, the system requires a high pumping speed due to the large surface area combined with beam-induced outgassing from windows. A combination of sputter-ion, turbo-molecular and mechanical pumps are used.

The post-collision line is separated from the collider beam line by a sector valve to allow independent interventions to the two sectors. A fast shutter is installed on each post-collision line to prevent

3.7 POST-COLLISION LINE

contamination of the experimental sector due to incidents in the post collision line. The sector requires a self-contained system of pumps and vacuum instruments for measurement of pressure and to interlock the sector valve.

3.7.3.2 *Main Beam dump*

The Main Beam dump is installed at the end of the post-collision line, 315 m from the interaction point. It absorbs a power of 14 MW coming from either the collided or the un-collided beam. For the colliding beam, the main issue is the beam size (order of 1 m diameter), while for non-colliding beams, the concern is the small beam spot (some mm²) which deposits a high power density on a small point of impact on the dump window and the dump itself.

The CLIC main dump is based on the ILC water beam dump, where a beam power of 18 MW must be absorbed [161, 162]. A dump with pressurized water was first proposed and realized at SLAC for SLC and then adapted for the NLC, TESLA and ILC design studies.

The water dump consists of a 1.8 m diameter and 10 m long cylindrical titanium vessel with a wall thickness of 15 mm. The water is pressurized at 10 bar to prevent boiling. The water is continuously circulated through an external heat exchanger in order to remove the dissipated heat from particle interactions. The front window of the water vessel is made of a Titanium Alloy. The main difference for the CLIC dump is the large number of coherent pairs with a wide spectrum of energies. This could require a larger diameter for the entrance window (and possibly for the dump itself). In the ILC reference design, this window has a diameter of 30 cm and a thickness of 1 mm. Details of the energy-depositions and thermo-mechanical studies of the dump are shown in Ref. [163].

3.7.4 Accelerator physics issues and background studies

3.7.4.1 *Background from the post-collision line to the Interaction Region*

The magnet protection absorbers, the intermediate dump and the Main Beam dump in the post-collision line generate backscattered photons and neutrons that can trigger background hits in the detector. This background has been estimated using BDSIM [164], a GEANT4 toolkit [165]. Three datasets of simulations results have been produced: background photons originating from the disrupted beam, from same-sign and from opposite-sign coherent pair particles.

The bremsstrahlung photons do not interact in the absorbers and intermediate dump but are fully absorbed in the Main Beam dump. Therefore their background contribution is negligible. Similarly, other background contributions from the Main Beam dump can be neglected.

On the contrary, the backgrounds from the intermediate dump are significant. In earlier beam-loss estimates [157], the so-called ‘hard-edge’ collimation model (assuming total absorption of any particle lost) predicted negligible losses on the C-type magnets downstream of the intermediate dump. However, the more complete GEANT4 model, taking into account secondary particles and showers in more detail, reveals appreciable losses in these magnets. These losses are from photons leaving the downstream face of the intermediate dump in the direction of the C-type magnets (73 m from the IP).

Figure 3.56 shows the low energy photon density at the intermediate dump exit side with momenta downstream in direction of the C-type magnets. The disrupted beam and same-sign coherent particles produce photons on the lower section of the aperture, which is where they are lost on the lower internal surface. Opposite-sign coherent particles are lost in the upper part of the dump, and thus photons from these showers have a higher density in this region.

Eigthy nine % of opposite-sign coherent particle energy flux is lost in the intermediate dump and the resulting backscattered photon flux is considerable. Figure 3.57 shows the backscattered photon density at the intermediate dump entrance (67 m from the IP).

The intermediate dump has an asymmetric aperture to capture the entire opposite-charge beam, as

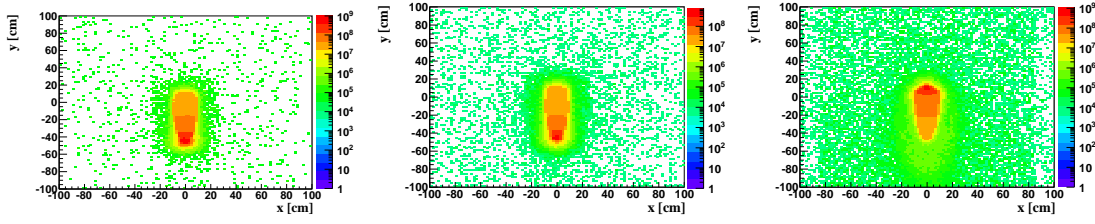


Fig. 3.56: Forward-moving photon density in particles per cm^2 per bunch crossing from the intermediate dump exit for the disrupted, same-sign and opposite-sign coherent pairs

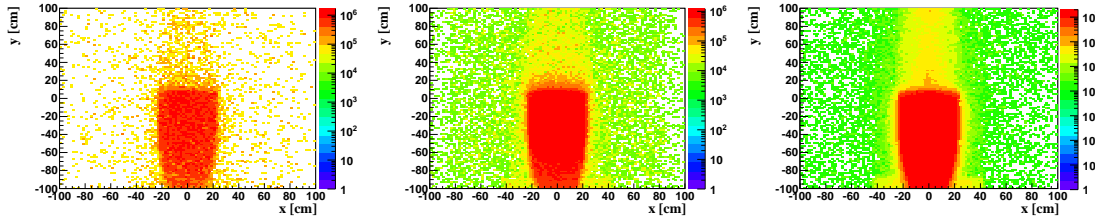


Fig. 3.57: Backscattered photon density in photons per cm^2 per bunch crossing from the intermediate dump entrance for the disrupted, same-sign and opposite-sign coherent pairs

well as the same-sign beam particles with less than 14% of the nominal energy. Due to the self-shielding effect of the absorber material, a low photon density is observed in the region of the absorber itself. The majority of the backscattered photons are found in the vacuum pipe region where there is no such self-shielding.

In order to have a well defined interface with the CLIC detector simulations, the photon flux is quoted through a $2\text{ m} \times 2\text{ m}$ plane at 3.35 m from the IP. All of the silicon detectors that might be vulnerable to background photons are contained within this cross-sectional area. The total photon flux originating from the post-collision line is found to be 72^{+46}_{-18} photons per bunch crossing per cm^2 , i.e., $1.1^{+0.72}_{-0.28} \times 10^6 \text{ s}^{-1} \text{ cm}^{-2}$, per beam [159]. However, the photons do not all arrive within the bunch train. With a 156 ns long bunch train and 12.4 m long detector, only particles backscattered from less than 26.5 m from the IP reach the detector face within the time of one bunch train. First studies indicate that the number of such photons is negligible.

In addition to photons, low energy neutrons are abundantly produced in the post-collision line. The principal source of neutrons is the main dump. First studies have shown, however, that the number of neutrons backscattered into the experiment at the IP is $3.9^{+1.6}_{-1.1}$ per cm^2 per bunch crossing, averaged across the entire detector face [159]. The neutrons have kinetic energies of a few hundred keV and therefore arrive at the detector long after the end of a bunch train. Space is available along the post-collision line to install dedicated shielding against neutrons, should this be found to be necessary in future more detailed studies.

3.7.4.2 Luminosity monitoring using beamstrahlung photons

The luminosity can be optimized measuring the beamstrahlung photons using detectors placed at several locations downstream of the interaction point [166]. The number and distribution of the beamstrahlung photons can potentially provide information about the spatial and angular distribution of the colliding beams [167, 168]. A luminosity monitoring system in the Main Beam dump area detects high-energy

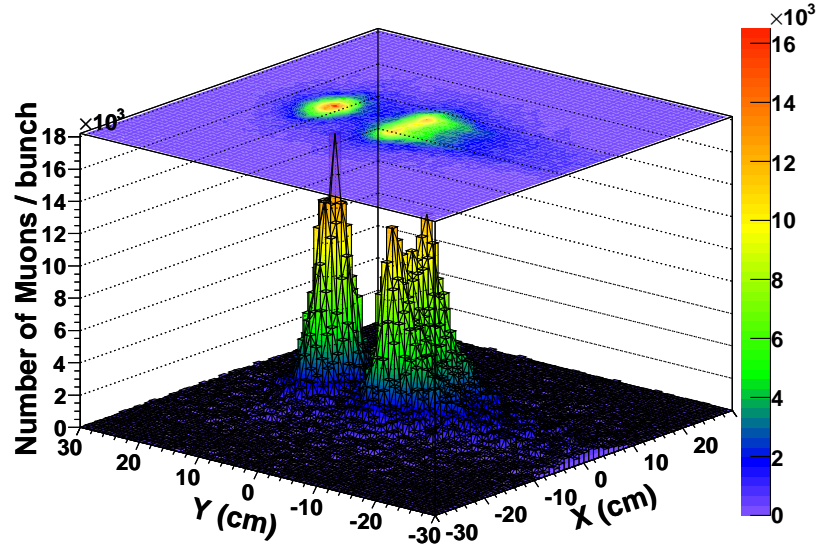


Fig. 3.58: Muon distribution with energies above 13 GeV downstream the Main Beam dump. The left peak originates from beamstrahlung photons, the right double peak from the disrupted beam.

muons resulting from beamstrahlung photon conversion into muon pairs [169]. This monitor is installed downstream of the Main Beam dump after a few metres of concrete shielding. The muon detectors are threshold Cherenkov counters.

Beamstrahlung photons impinging the water dump predominantly produce electron-positron pairs. However, a significant fraction of these high energy photons also produce muon pairs. While the electromagnetic shower is fully absorbed in the dump, the high energy muons exit the dump. The main background to these photon induced muons comes mainly from the high energy muons that are produced by the intense disrupted beam and by the coherent pairs. Fortunately the magnetic chicane design of the post-collision line separates the peaks of the muon distributions vertically (see Fig. 3.55).

GUINEA-PIG [170] was used to simulate the particles and photons after collision; these particles were tracked with BDSIM through the post-collision line to the entrance face of the beam dump. GEANT4 simulations were performed for the production of the muons inside the water and its steel container, and for transporting the muons through the beam dump and concrete blocks. Figure 3.58 shows the muon distribution with energies above 13 GeV downstream of the beam dump and originating from the beamstrahlung photons (left peak) and from the disrupted beam (right double peaks) for perfect head-on collisions.

The distribution and number of photons, and thus the spatial distribution of muons downstream of the dump, is sensitive to the offset of the beam at collision. Therefore the studies were done for several beam offsets in the vertical and horizontal direction at the interaction point. Figure 3.59 summarizes the simulation results for the number of muons measured in a detector with 156 mm diameter, placed downstream of the beam dump. The detector is located horizontally centred and vertically at +10 cm from the nominal beamstrahlung photon beam axis. The results are shown for two possible muon energy thresholds. The number of muons strongly depends on the colliding beam offset, which indicates the potential of such a muon monitor for luminosity monitoring.

The luminosity might also be monitored by directly detecting the beamstrahlung photons. As for the dump-based monitoring, the rate and x–y distribution of these detected photons is correlated to the beam offsets at the IP. The location and signal of such detectors, which are not currently part of the

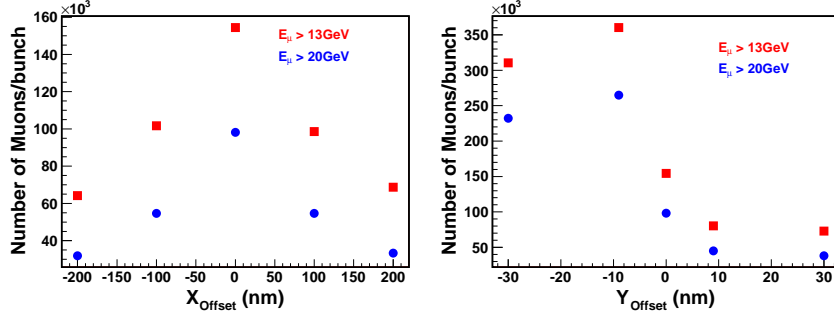


Fig. 3.59: Left plot (right plot): Number of muons/bunch measured downstream of the Main-Beam dump and concrete shielding for various horizontal (vertical) misalignments scenarios in the interaction point of the colliding beams. Red squares: muons with energy $> 13\text{GeV}$, blue circles: muons with energy $> 20\text{GeV}$.

base-line conceptual design, is studied in [169].

3.7.4.3 500 GeV scenario

While the CLIC baseline is designed for 3 TeV and 20 mrad total beam crossing angle, the 500 GeV option requires a crossing angle of 18.6 mrad. It is assumed that the positions of the IP, the intermediate and main dumps and the nine magnets are fixed. For 500 GeV operation, the current in the vertical dipoles is lowered and horizontal dipoles are added to steer the beam to a fixed position at the dump. The beamstrahlung photon spot shifts by 22.05 cm at the dump window and is reduced in size, due to the reduced beam-beam interaction. This offset is within the aperture of the dump window as designed. In summary, there is minimal impact of 500 GeV operation on the post-collision line.

3.7.5 Component specifications

In Table 3.33 specifications for the main components in the post-collision line and dumps region are given.

Table 3.33: Specification of the main components in the post-collision line region.

Component	Number	Requirements
Window-frame magnets	2 x 4	Different sizes
C-frame magnets	2 x 4	
Vacuum system	2 x 1	Medium pressure range
Beam instrumentation	2 x 39	Different types
Luminosity monitors	2 arrays	Cerenkov
Magnet protection absorbers	2 x 8	Different sizes
Intermediate dump	2 x 1	a few 100 kW
Main beam dump	1 x 2	14 MW

3.8 Integrated simulations on low emittance preservation

3.8.1 Overview

The CLIC luminosity target is $\mathcal{L}_{0.01} = 2 \times 10^{34} \text{ cm}^{-2}\text{s}^{-1}$. To achieve this goal very small beam emittances are required. The damping rings will deliver emittances of $\varepsilon_x = 500 \text{ nm}$ horizontally and $\varepsilon_y = 5 \text{ nm}$ vertically. During the transport of the beam from the damping rings to the beam delivery system (BDS), the emittances increase due to:

- effects from the lattice design, e.g., incoherent and coherent synchrotron radiation in the RTML;
- effects from static imperfections, e.g., misalignment of the BPMs;
- effects from dynamic imperfections, e.g., quadrupole jitter.

In order to limit the emittance to $\varepsilon_x \leq 660 \text{ nm}$ and $\varepsilon_y \leq 20 \text{ nm}$ at the entrance of the BDS, emittance growth budgets have been defined, see Table 3.34. The ‘design’ emittance growth, intrinsic to the lattice, is known, whereas the emittance growth due to static imperfections varies from case to case, and drifts in time when one considers dynamic effects. It is required that the machine remains below the static emittance growth budgets with a probability of 90%. The ‘dynamic budgets’ correspond to the emittance growth due to dynamic effects averaged over time.

The goal for the BDS is to achieve at least 110% of the nominal luminosity if all emittance budgets are fully used and only static imperfections are present in the BDS. The additional 10% are the budget for dynamic imperfections in the BDS.

Table 3.34: Emittance growth budgets for CLIC

	RTML			Main linac		
	Design	Static	Dynamic	Design	Static	Dynamic
$\Delta\varepsilon_x \text{ [nm]}$	60	20	20	0	30	30
$\Delta\varepsilon_y \text{ [nm]}$	1	2	2	0	5	5

In the following, the lattice design issues are discussed first, followed by the static imperfections and the dynamic imperfections. These sections are limited to single bunch effects, which are most critical. Finally the multi-bunch effects are detailed.

3.8.2 System Design

3.8.2.1 Damping Rings to Main Linac

The RTML transports the beam from the damping rings to the main linac and transforms beam properties like energy and bunch length to match the main linac requirements.

The effect causing the largest emittance growth is the emission of incoherent synchrotron radiation (ISR) in the bends. ISR absorbs about 40 nm of the horizontal emittance budget for the electron beam, and about 25 nm for the positron beam (which does not require a central arc). In the vertical plane, where only weak arcs are required for the transfer tunnels, ISR emittance growth is less than 1 nm.rad. The second largest contribution to the emittance growth is the emission of coherent synchrotron radiation (CSR) in the bunch compressor chicanes. CSR absorbs 20 nm of the total budget in the horizontal plane. CSR can be reduced by shielding the conducting walls of the vacuum chambers. It has been calculated that, for the shielding to be effective, the vertical aperture must be smaller than about 2 cm.

In conclusion, the design emittance budgets can be fulfilled.

3.8.2.2 Main Linac

In the main linac a strong focusing lattice has been chosen to balance the impact of transverse wakefields in the accelerating cavities. The lattice strength is varied with the beam energy to have an almost constant fill factor. The twiss parameters of the baseline lattice are as shown in Fig. 3.60. To compensate for the defocussing effect of the short-range wakefields, BNS damping is used. BNS damping consists in accelerating the particles slightly off-phase with respect to the rf cavities, so that the bunch tail is slightly less accelerated than the head and experiences a stronger quadrupole focusing [171]. The RF phase offset chosen is 8° at the beginning and 30° at the end of the linac. Details on the Main Linac lattice optimisation can be found in Ref. [172]. The total emittance growth in a Main Linac without imperfections is about zero.

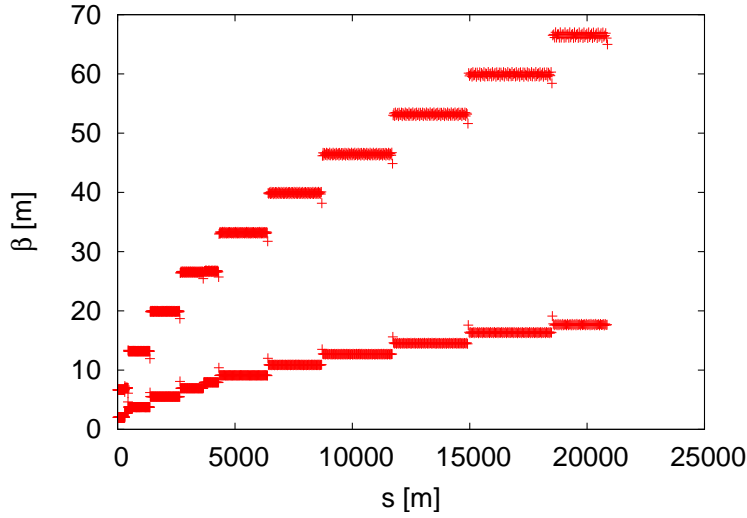


Fig. 3.60: Twiss parameters for the main linac. The minima and the maxima of the β -functions for the 12 sectors are clearly visible.

3.8.2.3 Beam Delivery System

The beam delivery system (BDS) transports the main beam from the linac end to the IP. See §3.5 for details concerning the design. The BDS uses the dispersion generated by horizontal bending dipoles to collimate low-energy particles and to correct the chromaticity with the sextupoles in the Final Focus (FF). This design requirement is an intrinsic source of emittance dilution due to two effects: synchrotron radiation emission and higher-order transport aberrations.

Incoherent synchrotron radiation is responsible for 20% loss of luminosity. The bending dipoles and the final doublet are also responsible for an equivalent luminosity loss. The IP vertical beta function is designed to operate slightly below the theoretical optimum given by the Oide effect [173]. Coherent synchrotron radiation has negligible effects on emittance dilution.

Higher order aberrations have been carefully minimized by adding multipolar corrector magnets to the lattice [174]. The residual higher-order aberrations increase the vertical beam size by 15%. Assuming an ideal transport without aberrations and neglecting synchrotron radiation, luminosity would increase by about 40%. Thus design aberrations and synchrotron radiation approximately share the luminosity loss in equal parts.

3.8.2.4 Start-to-end simulation

Start-to-end simulations of low emittance transport throughout the entire machine have been performed. An electron bunch has been tracked from the damping rings to the interaction point using the tracking code PLACET [175]. Figure 3.61 shows the resulting phase space at the interaction point. The luminosity has been calculated using GUINEA-PIG [176]. The results are shown in Table 3.35.

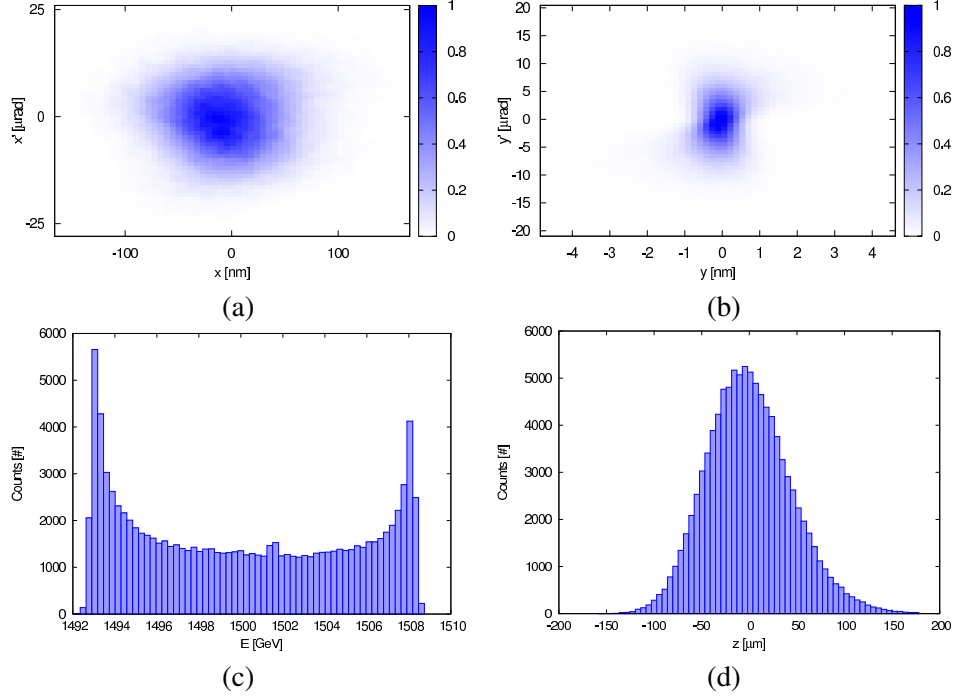


Fig. 3.61: Final phase space after full tracking for an electron bunch

Table 3.35: Luminosity achieved after a complete tracking through the CLIC RTML, ML and BDS. The luminosity is 2.5 times larger than nominal because no imperfections were considered.

Luminosity	Symbol	Value	Unit
Peak	L_{peak}	5.0	$10^{34} \text{ cm}^{-2} \text{ s}^{-1}$
Total	L_{total}	1.5	$10^{35} \text{ cm}^{-2} \text{ s}^{-1}$

3.8.3 Static Imperfections

3.8.3.1 Damping Rings To Main Linac

Studies of static imperfections in the RTML are still underway, because the priority was given to the main linac and the beam delivery system which are more critical.

The static misalignment of the booster linac was studied for a linac made of 4 GHz cavities including single-bunch wakefields. It was found that an r.m.s. misalignment of $100 \mu\text{m}$ of the cavities, quadrupoles, and BPMs would lead to an acceptable dilution of the vertical emittance of $2 \text{ nm} \cdot \text{rad}$ after applying dispersion-free steering. A BPM resolution of $10 \mu\text{m}$ was assumed. In the baseline booster linac with 2 GHz cavities the impact of wakefields should be even smaller.

Misalignment studies of the long transfer line showed that BPM misalignments of up to $100 \mu\text{m}$ should lead to less than $\Delta\epsilon_y = 1 \text{ nm} \cdot \text{rad}$ when applying one-to-one steering. Dispersion-free steering

should result in even lower emittance dilution. The turn-around loop is currently being studied. First results show that misalignment tolerances are tight. A large contribution to the vertical emittance was found to stem from coupling and residual dispersion. Since it is planned in any case to have coupling and dispersion correction sections at the end or after the turn around loop these contributions should be correctable. Another improvement is expected from dispersion-free steering.

Fully integrated studies are planned. The experience gained from the ILC RTML emittance preservation let us think that these studies will not present any major problem.

3.8.3.2 Main Linac

The major sources of emittance growth in the main linacs are the dispersive effects due to misaligned quadrupoles and BPMs, and to the strong wakefields in the accelerating cavities. Table 3.36 summarises the individual contributions to the emittance growth for the major imperfections. Target of the beam-based alignment procedures is to limit the total emittance growth to less than 5 nm in the vertical plane. Considering that the emittance growth can vary significantly from case to case, the global performance of the system is evaluated averaging the result of hundreds of different random configurations (seeds). The requirement is that 90% of the simulated random seeds meet this target. Fig. 3.62 shows that this requirement is achieved, as 90% of the simulated machines have less than 2 nm emittance growth.

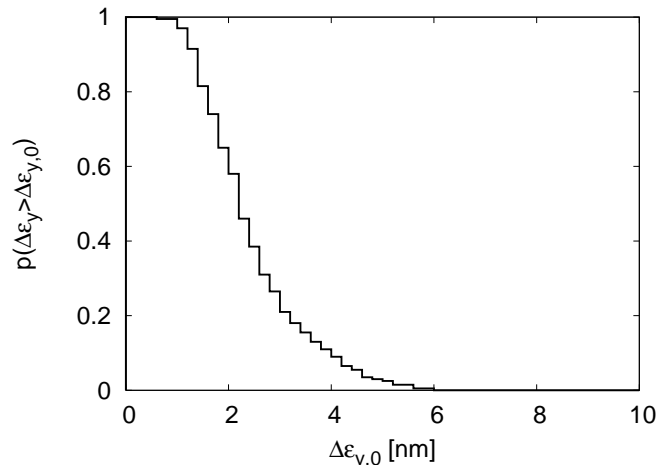


Fig. 3.62: Probability distribution of the final emittance growth if all imperfections are included, except for the wire system.

Beam-Based Alignment Procedure

The correction of the static imperfections is performed applying beam-based alignment techniques. In the CLIC main linac, the quadrupoles, as well as all other components, are mounted on movable girders. Most girders support eight accelerating structures, but the first structures of some girders are replaced by a beam position monitor (BPM) and a quadrupole, which are mounted on a common support. Each quadrupole is equipped with a dipole corrector that is used to align its magnetic centre to the beam. The support for the BPM/quadrupole/corrector unit can also be moved using motors, with a step size of about 1 μm . The quadrupoles are held transversely stable to the nanometer level by piezo-electro movers, that can be used to move the quadrupoles up to about $\pm 10 \mu\text{m}$. The complete beam-based alignment procedure foreseen for the main linac consists of three stages [177]:

1. The beam is steered through the centres of each BPMs to ensure that it will pass the linac without losses (one-to-one correction);

2. Dispersion-Free Steering (DFS) is applied. DFS is a technique that measures the dispersion along the linac, using off-energy test beams, and corrects it to zero. The required correction is calculated to minimize the following figure of merit

$$\chi^2 = \sum_{i=1}^N \left(\omega_i (x_{i,1})^2 + \sum_{j=2}^m \omega_{i,j} (x_{i,1} - x_{i,j})^2 \right)$$

where the index i identifies the test beam and the index j the BPM.

For the CLIC main linac, the optimal performance has been found for $\omega_i = 1$ and $\omega_{i,j} = 1000$. The chosen test beam has an initial energy that is lower than the nominal beam and is accelerated using lower gradients. The initial lower energy is obtained by changing the RF phase in the bunch compressor (which in turn changes also the bunch length). The lower gradient is achieved by modifying the drive-beam current in the whole linac [178, 179];

3. As the accelerating structures are equipped with a wakefield monitor to measure the beam position, the supporting girders are moved to centre the beam with respect to such monitors and therefore minimize the creation of wakefields. Starting from the first girder the downstream articulation point of each girder is moved to minimize the average offset of the beam in the structures.

After this alignment procedure, emittance and luminosity can further be improved using specific tuning procedures. Different designs can be thought for such tuning knobs, as it has been explained in detail in [180]. Dispersion-free steering could be replaced by alternative methods, such as Ballistic Alignment and Kick Minimisation [181, 182]. All the results presented in the following are based on simulations with the PLACET tracking code [175].

Local Pre-Alignment

For the local imperfections it is assumed that the reference line is perfectly straight over the whole machine. The misalignment is modeled starting from a perfect machine and applying successively the imperfections in Table 3.36. All values for the imperfections are drawn from a Gaussian distribution.

- Each quadrupole is transversely offset and rolled around the longitudinal axis.
- Each BPM is misaligned, the value used in the simulation is a combination of the wire-reference to external BPM error and the internal BPM error.
- The wakefield monitor in each structure is misaligned with respect to the structure.
- The structure is misaligned and tilted with respect to the supporting girder.
- The endpoints of the girders are misaligned with respect to the articulation points; all structures on the girders are moved accordingly.
- The articulation point between the girders are misaligned.

The simulations have been performed for each of the different imperfections individually. This allows to estimate the impact of each error source; it scales with the square of the error size. The results are listed in Table 3.36. An important imperfection is the accuracy of the BPM position with respect to the reference line. This error is dominated by the misalignment of the BPM by the pre-alignment system and the internal BPM accuracy. In the table the two contributions are grouped into a single value. All imperfections are important along the whole linac with the exception of the structure tilt, which is dominated by the very first part of the linac. It may be possible to fix this problem by modifying the alignment method at this location, e.g., by locally optimising the weight, differently from the rest of the machine.

The misalignment of the articulation points leads to an emittance growth which is acceptable, yet noticeable given the assumed pre-alignment performance. This is a result of the specific implementation of the procedure to align the structures to the beam. All girders are aligned in sequence starting with

the upstream one. For each girder only the downstream end is adjusted until the mean structure offset is zero. Moving the upstream and the downstream end of the girder would in principle allow to completely recover from any misalignment of the articulation points. But it makes the alignment procedure more complex since a common solution has to be found for all the girders in the main linac. An additional articulation point after each quadrupole would allow to simplify the method, as only the girders between two quadrupoles would need to be aligned simultaneously.

Table 3.36: List of individual imperfections and resulting emittance growth. The accelerating structure tilt is dominated by the internal error of the accelerating structure not by the mechanical alignment of the structure on the girder.

Imperfection	With respect to	Value	Emittance growth
BPM offset	wire reference	14 μm	0.367 nm
BPM resolution		0.1 μm	0.04 nm
Accelerating structure offset	girder axis	10 μm	0.03 nm
Accelerating structure tilt	girder axis	140 μradian	0.38 nm
Articulation point offset	wire reference	10 μm	0.1 nm
Girder end point	articulation point	5 μm	0.02 nm
Wake monitor	structure centre	3.5 μm	0.54 nm
Quadrupole roll	longitudinal axis	100 μradian	0.12 nm
All			2.34 nm

Wire Reference System

The reference line is defined by a system of overlapping wires. All wires have the same length and the overlap is half the wire length (see 5.17.3). This system has been simulated [183] and the end-points of the wires have been determined in real space for a number of random seeds. This data has been used as the basis for the present pre-alignment simulations. An example of the linac misalignments can be seen in Fig. 3.63.

It is assumed that each wire is perfectly straight. The end points of each girder are aligned using one of the wires. After half a wire length we switch from using one wire to using the newly starting parallel wire. The position of the end points is not interpolated using the information of two wires. In principle, this would allow to obtain a smoother alignment but it would be more costly as two sensors would be required for each point. At the points where one switches from one wire to the next this leads to a very rapid change in the position of the elements.

Simulations show that the accuracy of the wire sensors is relevant. But even a relatively bad accuracy of 20 μm leads to an additional emittance growth of only 0.1 nm, which is still acceptable. For a good wire sensor resolution of 5 μm the emittance growth is only 0.01 nm and does not depend significantly on the number of pits used. In conclusion, the wire sensor accuracy is an important parameter with an impact on the emittance growth while the number of external reference points does not impact the results significantly. Further studies should assess the impact of the wire length and other imperfections, in particular errors of the assumed wire sag.

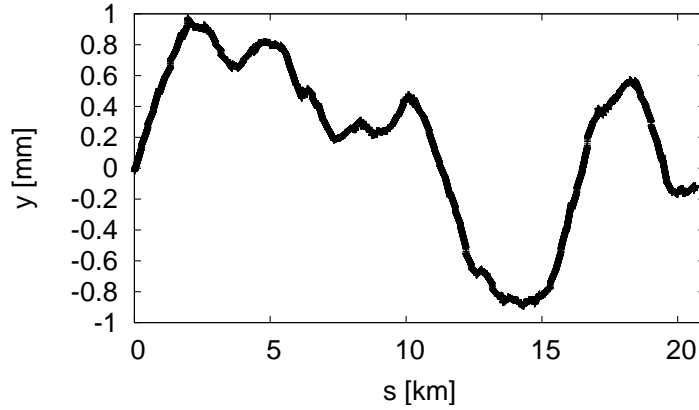


Fig. 3.63: An example of the simulated misalignment of the main linac elements due to the wire reference system.

3.8.3.3 Beam Delivery System

Beam-Based Alignment

Also in the BDS sophisticated beam-based alignment procedures are used to preserve the emittance during the transport from the damping rings to the interaction point.

The static beam-based alignment and the tuning of the beam delivery system are somehow more complicated than those of the main linac. This is due to two reasons: the strongly non-linear behavior of the system due to multipolar magnets (sextupoles, octupoles), and the significant emission of incoherent synchrotron radiation from the bends and the strong quadrupoles in the lattice. To align the beam delivery system, two procedures have been studied and compared: the simplex minimisation of the beam sizes at the interaction point, and the beam-based alignment followed by luminosity-tuning bumps. The first method, the simplex minimisation, tries to minimize the beam sizes at the IP by moving both vertically and horizontally all quadrupoles and all higher-order magnets in the lattice, using the Neadler and Mead algorithm [184]. This method has the great advantages to minimize the beam sizes without requiring any prior knowledge of the system and to always converge toward a minimum (although this is not guaranteed to be the global minimum), but has the great disadvantage of a very slow convergence time. The second method, described in details in the following text, is much faster in spite of a smaller success rate with the current setup. It has been estimated that the simplex minimisation would require about 17000 luminosity measurements to converge, whereas the beam-based alignment and tuning knobs would require only 400.

The beam-based alignment (BBA) algorithm consists of steering the measured orbit to its nominal value using correctors and knowing the response matrix of the system. The orbit is measured using Beam Position Monitors (BPMs) located at each magnet exit. The correction is performed using dipole kickers located at each quadrupole entrance. The option of moving the quadrupoles to steer the orbit, instead of using dipole kickers, is also being considered. The simulations showed that usually the orbit correction is not sufficient to recover the luminosity and it needs to be followed by a luminosity tuning procedure, in which the luminosity is maximized moving the sextupole magnets appropriately (tuning knobs). The direct measurement of the luminosity is still an open issue. Studies to identify suitable luminosity signals from the beam-beam background are being carried out [185].

In the simulations of both cases, the luminosity calculation is performed using GUINEA-PIG [176] on symmetric beams. That is, the bunch is collided with itself, as if coming from a beamline with misalignments symmetric to the one simulated, with respect to the interaction point. This assumption speeds up the simulations significantly, as it avoids to simulate the additional feedback loops that should bring the beams into collision. Despite being a simplification, this approach has been demonstrated to be acceptable also for the ILC [186]. The simulation is performed assuming that the RTML and the the ML use the full emittance-growth budgets. The goal of the procedure is to recover 110% of the nominal

luminosity with 90% of the randomly misaligned machines. The alignment of each such machine is performed in the conservative scenario that the beam initial emittance accounts for the entire budget allowed in the main linac (see Table 3.34). The complete alignment and tuning procedure is summarized in the following four steps:

1. In the first phase of the correction, when the beam trajectory is supposedly very far from the ideal orbit, the beam delivery system is run with the multipolar magnets switched off. This allows to avoid complicated non-linear behavior in the beam dynamics and strong radiation in the multipoles. In this phase, a step of 1-to-1 correction and a step of dispersion-free steering are applied (as the nominal dispersion is not zero in the horizontal plane, this is more a target-dispersion steering than a proper dispersion-free steering);
2. The second phase consists of switching on the multipolar magnets and performing a tuning of appropriate multipolar knobs. These knobs are generated off-line using a perfect machine to study the impact of linear combinations of multipoles on the beam phase-space covariance matrix. During the alignment procedure, these calculated knobs are individually tuned to maximize the luminosity;
3. The third phase is a non-linear target-dispersion steering plus orbit correction, running with all multipolar magnets on;
4. The fourth phase of the alignment procedure is another run of multipolar knobs to maximize the luminosity.

Table 3.37 summarizes the procedure. It has been seen that reiterating the steps 3 and 4 can progressively improve the correction. Figure 3.64 shows the luminosity obtained for 100 random misalignments after the various steps of correction, for both methods. The goal is to achieve 110% of the target luminosity for at least 90% of the simulated random machines. The current result is that 70% of the simulated seeds meet this requirement when the simplex minimisation is used, whereas only 40% of the machines meet the requirement in case of BBA plus tuning knobs. As this result is not fully satisfactory, several studies are still on-going to improve it: optics redesign optimized for tuning, increased L^* ; non-linear beam-based alignment procedures and tuning knobs.

Table 3.37: The four phases of the alignment procedure

Step	Multipoles	Alignment technique
I	Off	Orbit correction followed by dispersion correction
II	On	Multipole-knobs
III	On	Simultaneous orbit and dispersion correction
IV	On	Multipole-knobs

3.8.4 Dynamic Imperfections

This section will give an overview of the dynamic imperfections in the Main Linac (ML) and Beam Delivery System (BDS), in particular ground motion, and its mitigation techniques. Mitigation techniques include the mechanical stabilisation system for the quadrupoles and for the final doublet, the beam-based orbit feedback and the interaction point (IP) feedback.

Simulations incorporating the dynamic imperfections and mitigation techniques have been performed, where the ML and the BDS are treated as one integrated system and are simulated together.

First, the relevant dynamic imperfections and the mitigation techniques are described and modeled. Then the beam-based orbit feedback design is presented. Finally, the transverse feedback performance including all the imperfection and mitigation techniques is shown.

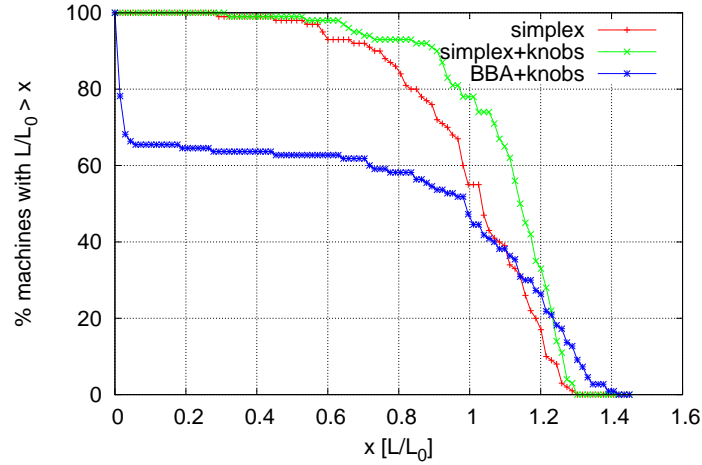


Fig. 3.64: Luminosity distribution for 110 random misalignments after the various steps of the alignment procedure.

It is shown that with the current design the tight luminosity budget for dynamic imperfections, and in particular ground motion, is fulfilled for all studied ground motion models. Dependent on the ground motion different mitigation techniques may be required.

In the final part the relevant longitudinal imperfections are described and requirements for the longitudinal tolerances are given.

3.8.4.1 Modeling of mechanical vibrations and dynamic imperfections

Ground motion

Given the tight tolerances on the quadrupole positions, the dominant luminosity degradation by dynamic imperfections is caused by ground motion [187]. The luminosity is reduced by two effects: an offset of the beams with respect to each other at the interaction point (IP) due to the movement of the magnets close to the IP and an emittance growth along the beamline due to offsets of the ML quadrupoles.

The ground motion can be divided in two frequency regimes, one for lower frequencies, which impacts the emittance preservation, and one for higher frequencies, which has most impact on the beam-beam offset at the IP. Phenomenological models for the ground motion have been developed [188] and an extensive review of the current state has been given in [189, 190]. Analogous to the regime division, two models are used in the ground model simulations, one for short time scales, and one for longer time scales ('ATL-law'). Both models include correlations in time (frequency) and space. Ground motion is very site-dependent and for several sites measurements have been performed to fit the model parameters, see Fig. 3.65, where the power spectral density is shown. Three different sites have been considered in these studies. Model A is based on measurements in the empty LEP tunnel, which is a very quiet site. Model B is based on measurements on the Fermilab site. The third model considered is model B10, which is model B with additional peaks to match measurements from LAPP (Annecy) and the technical noise level that was measured in the CMS hall. Other sites that have even more ground motion, like model C, are not considered as it is believed that CLIC is not able to maintain a stable luminosity at such noisy sites.

To counteract the impact of the ground motion several mitigation techniques are deployed in CLIC are summarized in the next sections. Since the repetition rate of CLIC is 50 Hz, beam-based feedback is less effective for 'high' frequencies (i.e., ≥ 1 Hz). For these 'high' frequencies other systems have to be

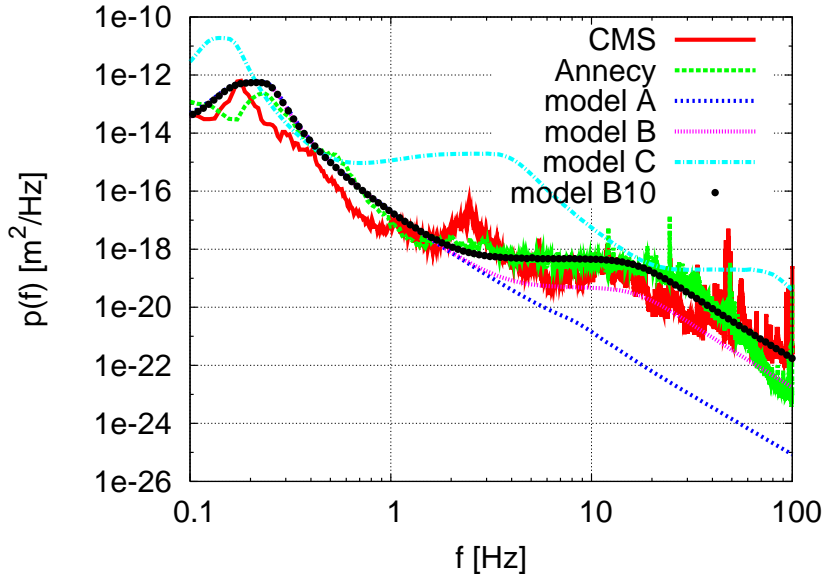


Fig. 3.65: Ground motion power spectral density for several sites.

deployed.

Mechanical stabilisation system for Main Linac and BDS

To reduce the motion of the ML quadrupoles for high frequencies (≥ 1 Hz), each quadrupole will be positioned on an active stabilisation system, see §5.18. For the integrated simulations a theoretical fit of the measured transfer functions of the current design has been used as shown in Fig. 3.66. An integrated r.m.s. movement of 1 nm above 1 Hz has been demonstrated. The peak at 0.2 Hz of the quadrupole stabilisation is close to the micro-seismic peak which is unfavourable. A targeted future design is shown in the figure.

For the BDS, the same design as for the ML has been assumed in simulation, though a more dedicated system could be envisaged.

Mechanical stabilisation system for the final doublet

To reduce the beam offset jitter for high frequencies the final doublet system, which includes the last quadrupoles QD0 and QF1, will be put on a large mass, the pre-isolator, that is fixed to the tunnel floor. In addition an active stabilization can be deployed, see §5.18.2 and §5.18.3, in the following the simulation is limited to the stand-alone usage of the pre-isolator. For such a system an achieved integrated r.m.s. movement of 0.13 nm above 4 Hz has been reported. The preisolator has two support points that each have their own transfer function, as shown in Fig. 3.67. The resonance at 50 Hz is caused by the vibration of the cantilever and is designed to be at the beam repetition rate. For the integrated simulations these transfer functions are implemented. A discrepancy between the two different transfer functions of the mechanical stabilisation of the ML and BDS, and the final doublet system, and therefore between the quadrupole positions will impact luminosity due to dispersion. Therefore, the transfer functions should be tuned to have a similar shape, especially at lower frequencies. Simulations have shown that a tuning of the quadrupole stabilisation by, for example, a low-pass filter will ease the task of the orbit feedback [191].

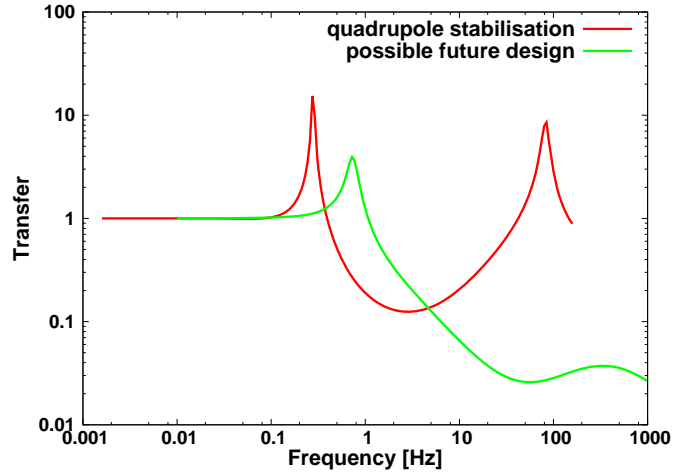


Fig. 3.66: Amplitude of the theoretical transfer functions of the quadrupole stabilisation.

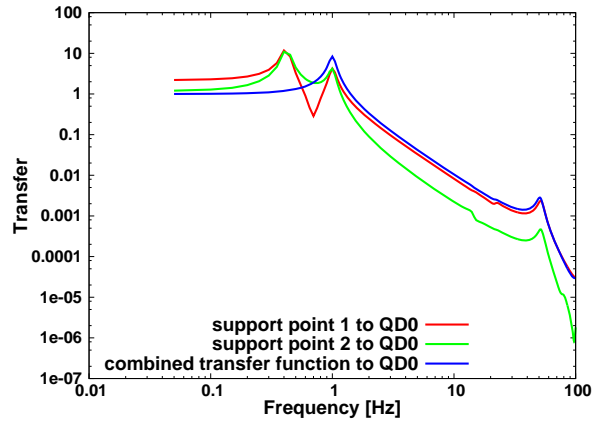


Fig. 3.67: Amplitude of the theoretical transfer functions of the preisolator of the final doublet system.

Dynamic magnetic fields

The beam position will be sensitive to stray magnetic fields in the nanotesla regime. A review has been performed in [192]. Examples of possible sources of stray fields are the earth's magnetic field, the RF system, nearby equipment (e.g., vacuum systems, power cables inside the tunnel), other external sources (e.g., railways, power lines) or the Drive Beam. The impact of stray fields with frequencies below about 1 Hz will be strongly reduced by the orbit feedback systems. Furthermore, at high frequencies (\geq kHz) structures and beam pipes provide shielding. It is important to note that the CLIC beamline will not be sensitive to stray fields with a frequency of 50 Hz (and its harmonics), e.g., fields related to the power grid, due to its explicitly chosen 50 Hz repetition rate. In the review, it was shown that the long transfer line is most sensitive, while also the BDS will be affected. Specifications for the cabling have been provided and it was also shown that stray fields coming from the Drive Beam will not affect the Main Beam.

If necessary, mitigation techniques can be applied; in [192] several options have been discussed.

As an example, a feed-forward system after the turnaround loop to correct the beam position is foreseen. Furthermore, shielding of the individual magnetic field sources should significantly reduce the stray fields.

The dynamic magnetic fields have not been taken into account in the integrated simulations as measurements and realistic power spectra of these magnetic fields are missing and more detailed studies of the shielding effect for dynamic fields in the nanotesla regime are required.

Quadrupole strength jitter

Besides the tight position stabilisation requirements of the ML quadrupoles, the quadrupole strength stability is of equal importance. Figure 3.68 shows luminosity loss as a function of quadrupole strength jitter for respectively the ML, BDS without final doublet (FD), and final doublet. For the ML a misaligned beamline is assumed and subsequently one-to-one correction is performed. For the BDS a perfect beamline is assumed. The result is in agreement with the current specifications for the relative quadrupole strength jitter, which, as an example, for the ML quadrupole is 0.5×10^{-4} .

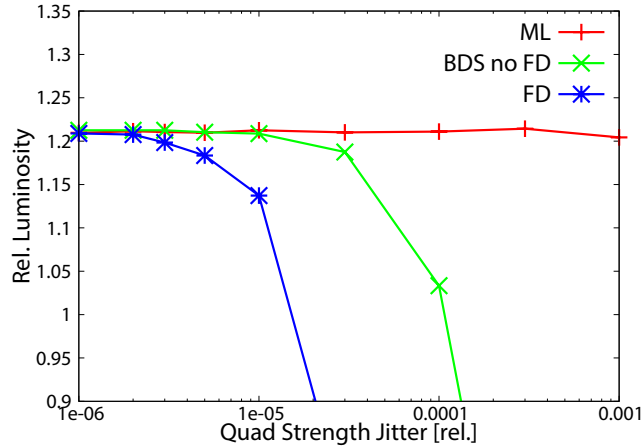


Fig. 3.68: Relative loss of peak luminosity as a function of the quadrupole strength jitter for the ML, BDS without final doublet (FD), and with final doublet. Note that the luminosity loss is only due to quadrupole strength jitter and that no other dynamic effects, e.g., ground motion, has been applied.

Resistive-wall wakefields in the collimators

The resistive-wall wakefields from the small gap collimators can turn out to affect even the single bunch. This effect has been studied in Ref. [193] and in Ref. [194]. These wakefields are included in the integrated simulations and cause an overall luminosity reduction of about 1% and an additional luminosity loss caused by beam position jitter induced by dynamic imperfections of about 0–1%. The assumed material for the colimator jaws is beryllium and copper-coated titanium.

3.8.4.2 Integrated beam-based orbit feedback design

To counter low-frequency ground motion beam-based feedback will be applied. Here two complementary feedbacks are deployed, the IP feedback and the fast orbit feedback.

IP feedback

The IP feedback corrects the beam position at the IP by measuring the deflection angles of the colliding beams and adjusting the beam position with a dipole kicker positioned near QD0, see §5.15. An additional intra-train feedback is foreseen, but is not taken into account here and considered as a reserve option.

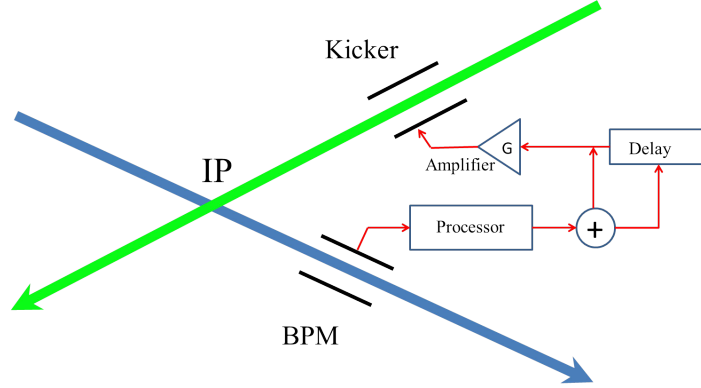


Fig. 3.69: Schematic of IP feedback system. Taken from Ref. [195].

Figure 3.69 shows the key components of the system: a BPM based on stripline pickups for registering the position (and hence kick angle) of the outgoing beam; a fast analog front-end signal processor; delay loop; an amplifier to provide the required output drive signals applying a certain gain factor, G ; and a kicker for applying an angular correction to the opposite incoming beam. The kicker is placed between QD0 and the IP. The BPM is placed in the post-collision extraction line and should have a resolution better than about $30\ \mu\text{m}$.

Intrapulse IP feedback

As mentioned, the IP feedback system could also be used as an intra-train feedback. However for CLIC, the extremely short nominal bunch spacing (0.5 ns) and very short nominal pulse duration (156 ns) make the intra-train feedback implementation technically very challenging.

Therefore, this system is not implemented in the feasibility studies, but currently considered as a reserve option. An extensive review including beam-beam simulations can be found in Ref. [195].

The system has been estimated to have a total latency of 37 ns, which makes one correction every 74 bunches, i.e., 4 iterations per train. It could reduce the luminosity loss due to beam-beam offset at the beginning of the pulse by approximately a factor of 4.

Fast orbit feedback

To correct the orbit there are two options, either the quadrupoles can be moved or dipole kickers can be deployed, see §5.18 and §5.2. From an optics point of view the solutions are very similar. The current baseline for the ML is quadrupole movers and dipole kickers as an alternative option.

The fast orbit feedback system in the ML and BDS has 2122 BPMs and 2105 correctors. By measuring the beam position in the BPMs and reducing the offset from the nominal value with the correctors, the beam will stay close to the nominal orbit and retain its low emittance. The simulated pulse-to-pulse orbit correction feedback is a global feedback based on a singular value decomposition (SVD) of the response matrix of the system with systematically adjusted weights for the different singular values to reduce the noise propagation and optimise the luminosity. For a detailed description of the fast orbit feedback system, see §5.15.

RF jitter

The basic feedback algorithm will encounter problems in the presence of beam energy jitter. This beam energy jitter is caused by small deviations of the acceleration gradients from their nominal values. In the dispersive collimation section of the BDS, such energy variations result in beam offsets up to the millimetre range. Since the usual beam offset due to ground motion is not larger than a few micrometers, the orbit feedback reacts strongly on the large offsets created by the energy variations. The result is a mis-steering of the beam and the resulting luminosity loss is not tolerable. To counteract this effect, we use the fact that the beam offsets due to energy variations follow a special pattern, given by the dispersion function. By removing this dispersion pattern from the BPM measurements the luminosity can be recovered almost fully. The use of this so-called dispersion filter is only necessary in the horizontal plane, since the coupling to the vertical plane can be neglected. The remaining luminosity loss due to the energy jitter coupling with the orbit feedback is as low as about 0.1%. Nominal design values of the RF jitter itself causes an additional luminosity loss of about 1%. This was not added in the subsequent simulations.

BPM resolution

Measurement errors, notably BPM noise, degrade the effectiveness of the pulse-to-pulse feedback, as a BPM measurement error will directly propagate into the orbit correction. To obtain the required BPM resolution in the BDS, simulations have been performed without other dynamic effects. In Fig. 3.70 the relative luminosity loss is shown as a function of the BPM resolution. It can be seen that a BPM resolution of 50 nm is required in the BDS to limit the luminosity loss to 2%, while the BPM resolution in the ML can be more relaxed. However, due to consideration of static imperfections in the FD, tighter BPM resolution might be required. The constraint on the BPM resolution can be mitigated by running with a lower gain of the feedback.

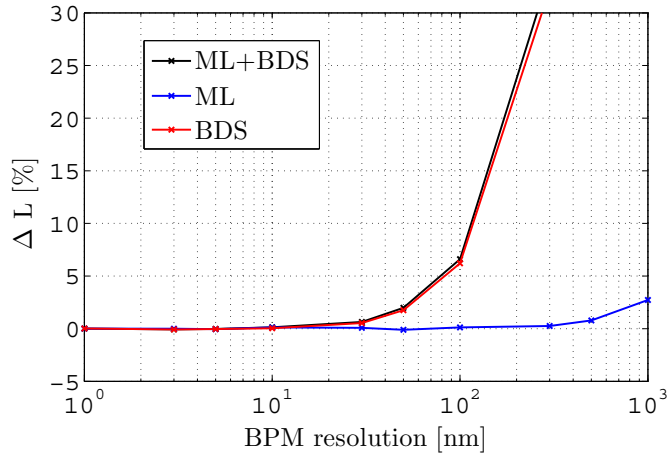


Fig. 3.70: Relative peak luminosity loss as a function of the BPM resolution for the ML and BDS, separated and combined. Note that this is only due to BPM noise and that no other dynamic effect, e.g., ground motion, has been applied.

3.8.4.3 Transverse feedback performance*Simulation setup*

All simulations have been performed tracking the ML and the BDS with PLACET [175] and GUINEA-PIG [176]. In accordance with §3.8.4.2 and other sections, a BPM resolution of 100 nm is assumed for

the ML BPMs and 50 nm for the BDS BPMs. For each study 50 machines have been simulated with different seeds.

Modeling of static imperfections

The foreseen emittance growth budget due to the static imperfections of the RTML, ML and BDS combined is a growth from 5 nm normalized geometric emittance at the exit of the damping rings to 20 nm at the start of the BDS, which corresponds to a peak luminosity of about $2.4 \times 10^{34} \text{cm}^{-2} \text{s}^{-1}$. Instead of integrating the static imperfections, which is something that will be implemented in the foreseeable future, a simplified approach is taken here. For the simulations, no static imperfections are implemented, but an emittance of 20 nm is simulated at the beginning of the ML. Thus it is assumed that the whole static budget is appropriated. The foreseen budget for luminosity loss due to dynamic imperfection in the ML and BDS is about 20% of luminosity. The nominal peak luminosity is $2 \times 10^{34} \text{cm}^{-2} \text{s}^{-1}$.

Short-term luminosity loss

For the current design, i.e., including the preisolator and quadrupole stabilisation, Fig. 3.71 shows that the luminosity is well preserved over a long time period of 60 s, which is about the maximum time for which the used ground motion models are valid. The remaining jitter on the luminosity is caused by the remaining high frequencies of the ground motion and the BPM resolution.

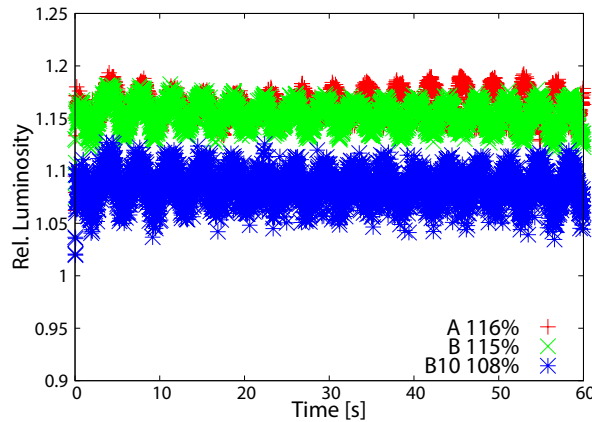


Fig. 3.71: Example of luminosity for the current design over a longer time scale (60 s) for several ground motion models averaged over 50 seeds.

The systematic motion is due to the discrepancy between the transfer functions of the stabilisation of the final doublet and the rest of the beamline.

In Table 3.38 the relative luminosity performance for several stabilisation systems is shown. It can be concluded that depending on the ground motion different stabilisation measures are required. Note that for ground motion model A mitigation methods can even lower the luminosity performance. This is due to offsets between the preisolator and the rest of the beamline, which is caused by a discrepancy between the two transfer functions. Note that an enhanced quadrupole stabilisation can improve the luminosity performance significantly.

Table 3.38: Overview of the relative luminosity performance (and luminosity loss in %) with respect to the nominal luminosity of $2 \times 10^{34} \text{cm}^{-2}\text{s}^{-1}$ for different ground motion models and stabilisation systems. Simulations including the collimator wakefields are also added.

Ground Motion Model	no GM/+ coll.	A	B	B10/+ coll.
No stabilisation	1.21 (0) / 1.20 (0)	1.19 (2)	0.96 (25)	0.53 (68)
Preisolator only	–	–	1.13 (8)	0.88 (33)
Preisolator + quad. stabilisation	–	1.16 (5)	1.15 (6)	1.08(13) / 1.06 (14)
Preisolator + targeted future design	–	–	–	1.18 (3) / 1.17 (3)

Luminosity evolution for large time scales

The pulse-to-pulse orbit correction relies on the fact that the response matrix of the system is reasonably stable. However for longer time scales of the ground motion the system and thus the response matrix will be significantly changed, after which the response matrix has to be recalculated and additional optimization has to be performed. To estimate the lifetime of the pulse-to-pulse orbit correction, ground motion over longer time scales has been studied. Assuming a perfectly aligned machine at $t = 0$ and a known response matrix, ground motion has been applied for a certain time based on the ATL-law, where the amplitude taken here is based on measurements from the LEP-tunnel, which might change up to a factor five. Note that the amplitude is also highly site-dependent [190]. After applying the pulse-to-pulse beam-based orbit feedback feedback the resulting luminosity is shown in Figure 3.72 as a function of the time. It can be seen that after about half an hour further optimization is required. Tuning of the BDS sextupole knobs can recover almost all luminosity loss.

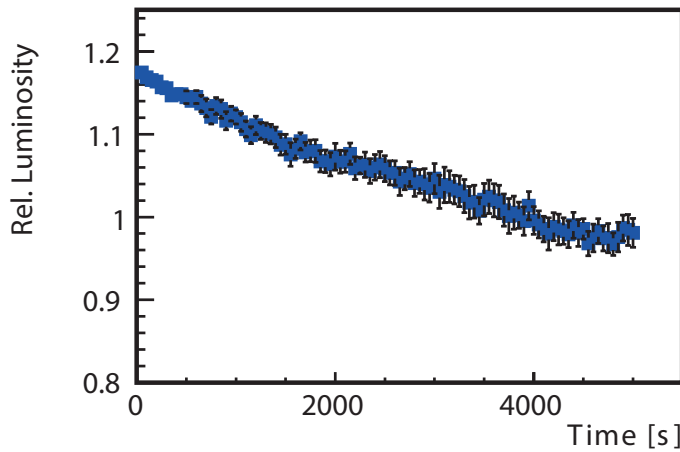


Fig. 3.72: Luminosity evolution for long time scales of ground motion. Here pulse-to-pulse beam-based orbit feedback is used. After about 30 minutes, the luminosity is decreased by 10%. To correct for this loss, further optimization procedures, e.g., tuning of the BDS sextupole knobs, are required.

Relative offsets between a BPM and its quadrupole will induce a mis-steering by the orbit feedback. Such an offset can be caused, for example, by residual misalignment, the quadrupole stabilisation system or external fields that might degrade the BPM measurement. Figure 3.73 shows the relative luminosity loss for randomly distributed BPM drifts in respectively the ML, BDS without final focus (FF) and without final doublet (FD). It can be seen that the constraints are similar to the BPM resolution

constraints. It is expected that these constraints can be met.

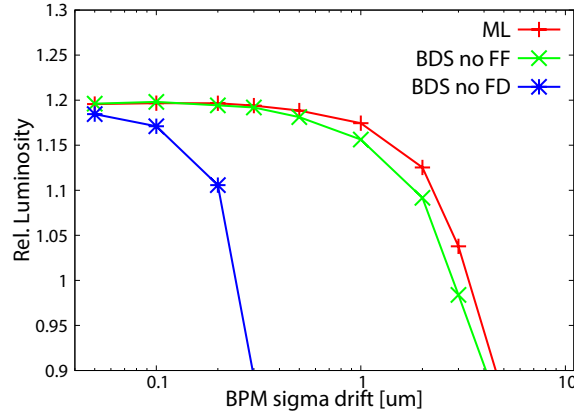


Fig. 3.73: Relative luminosity loss as a function of the BPM drifts for the ML, BDS without final focus (FF) and without final doublet (FD). Note that the luminosity loss is only due to BPM displacements and that no other dynamic effects, e.g., ground motion, has been applied.

3.8.4.4 Longitudinal imperfections

In CLIC, three critical longitudinal tolerances exist that directly impact the luminosity:

- The relative arrival time of the colliding bunches at the interaction point.
- The relative phasing of the two ‘crab’ cavities.
- The relative phasing between Drive Beam and Main Beam in the linac and the drive-beam current.

Relative main-beam arrival time

If the two beams do not arrive at the same time at the nominal collision point, they will collide before or after this point. Since the beta-function increases around the collision point, the beam sizes will in this case be larger than nominal, which leads to a luminosity reduction. The tolerance on the main-beam-to-main-beam timing jitter is $22\mu\text{m}$ for 1% luminosity loss.

Phasing of the ‘crab’ cavities

‘Crab’ cavities are used in CLIC to rotate the bunches before the collision such that they collide with no crossing angle, see Ref. [185]. A difference of the RF phases in the ‘crab’ cavities on the electron and the positron side leads to a horizontal offset of the two beams at collision. While the static difference can be corrected with the orbit feedback system, the dynamic difference needs to remain limited. A relative phase stability of 0.01° is required to limit the luminosity loss to 1%.

Drive-beam phase and amplitude jitter

Jitter of the drive-beam current, bunch length or phase in the decelerators will lead to jitter of the amplitude or phase of the RF that accelerates the beam in the ML. This will lead to energy errors of the Main Beam along the linac, which in turn can lead to luminosity loss via two main effects. First, the energy bandwidth of the BDS is limited, see Fig. 3.74. Hence, a too large energy jitter of the beam entering the

BDS will lead to luminosity loss. Secondly, the beam energy error along the linac can lead to emittance growth. Both effects are discussed below in more detail.

Luminosity loss due to energy errors

The Main Beam is accelerated with an average RF phase of about 12° . Consequently a phase jitter of $\Delta\phi = 0.1^\circ$ leads to an effective gradient error of 3.6×10^{-4} . The RF phase is not constant along the linac. Over the main part a phase typically smaller than 12° is used to provide a correlated energy spread in the beam for BNS damping. At the end of the linac a phase of 30° is used in order to compress the beam energy spread to the target r.m.s. value of 0.35%. Hence phase jitter in the end of the linac will impact the beam energy more than at the beginning.

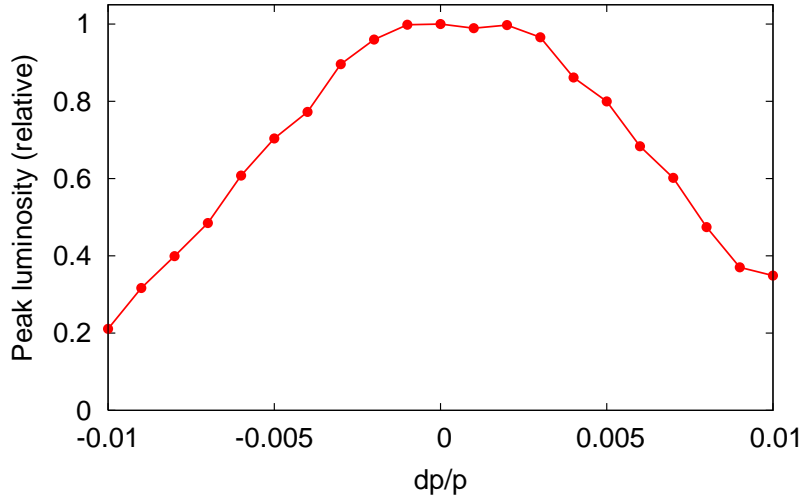


Fig. 3.74: Energy bandwidth of the BDS

Simulations have been performed that vary the RF phases and amplitudes independently and randomly in the electron and positron linac. Four types of errors are considered:

- An RF phase error $\sigma_{\phi,coh}$ of constant size along the whole ML.
- An independent RF phase error $\sigma_{\phi,inc}$ for each Drive Beam decelerator of the linac.
- An RF amplitude error $\sigma_{G,coh}$ of constant size along the whole ML. This can be caused by a variation of the beam current $\sigma_{I,coh}$ or a variation of the bunch length $\sigma_{\sigma_z,coh}$.
- An independent RF amplitude error $\sigma_{G,inc}$ for each Drive Beam decelerator of the linac, which can again be caused by a current or bunch length variation.

The results for coherent errors along the ML are shown in Fig. 3.75. The luminosity loss can be approximated as [196]

$$\begin{aligned} \frac{\Delta\mathcal{L}}{\mathcal{L}} \approx & 0.01 \left[\left(\frac{\sigma_{\phi,coh}}{0.2^\circ} \right)^2 + \left(\frac{\sigma_{\phi,inc}}{0.8^\circ} \right)^2 \right. \\ & + \left(\frac{\sigma_{I,coh}}{0.75 \times 10^{-3}I} \right)^2 + \left(\frac{\sigma_{I,inc}}{2.2 \times 10^{-3}I} \right)^2 \\ & \left. + \left(\frac{\sigma_{\sigma_z,coh}}{1.1 \times 10^{-2}\sigma_z} \right)^2 + \left(\frac{\sigma_{\sigma_z,inc}}{3.3 \times 10^{-2}\sigma_z} \right)^2 \right] \end{aligned}$$

Here, $\sigma_{\phi,coh}$ is the r.m.s. amplitude of the relative phase error between main and Drive Beam, integrated over the ML structure fill time, and assuming that the error is the same in each drive-beam decelerator. $\sigma_{\phi,inc}$ is assumed to be independent from one decelerator to the next. The errors for the drive-beam current and bunch length are similarly defined as $\sigma_{I,coh}$, $\sigma_{\sigma_z,coh}$, $\sigma_{I,inc}$ and $\sigma_{\sigma_z,inc}$.

In the drive-beam generation complex, these tolerances are valid for constant errors along the pulse. The tolerances are significantly larger for errors that vary along the pulse [197].

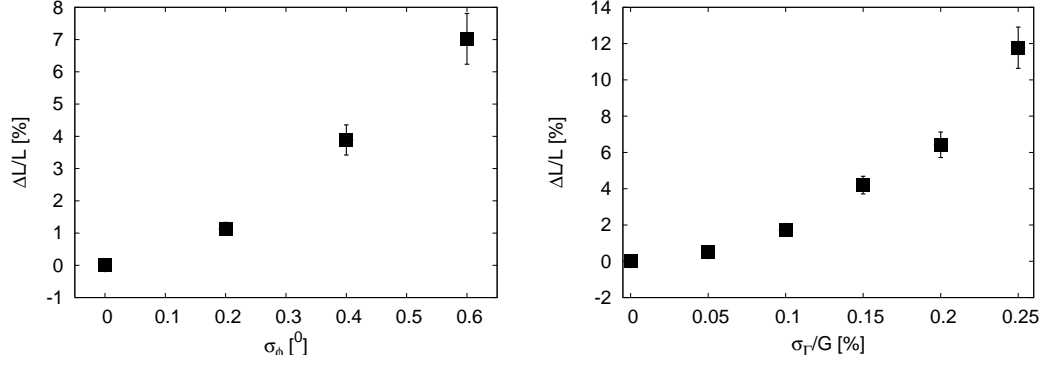


Fig. 3.75: The relative luminosity loss for a perfectly aligned machine as a function of the coherent RF phase (left) and amplitude jitter (right)

Emittance Growth

The increase of the beam emittance due to RF jitter is particularly important in case spurious dispersion has built up. To evaluate this, the ML has been simulated with an initial emittance of 10 nm. The initially perfect machine has been subjected to 10^6 s of ATL-like ground motion and a one-to-one steering has been performed. This yields an average total emittance of about 20 nm at the end of the ML, which corresponds to the nominal target emittance. The emittance growth due to RF jitter is shown in Fig. 3.76. An emittance growth of 0.4 nm is expected to lead to a luminosity loss of 1%. As can be seen, this corresponds to a coherent phase jitter of 0.3° , which is comparable to the corresponding tolerance for energy related luminosity loss. The situation is similar for coherent gradient jitter. Also for incoherent phase and gradient jitter the tolerances for the two mechanisms are very similar.

Further study will be needed to explore potential mitigation techniques that can reduce the RF-jitter induced emittance growth. One method may for example be to introduce one dispersion correction knob per decelerator.

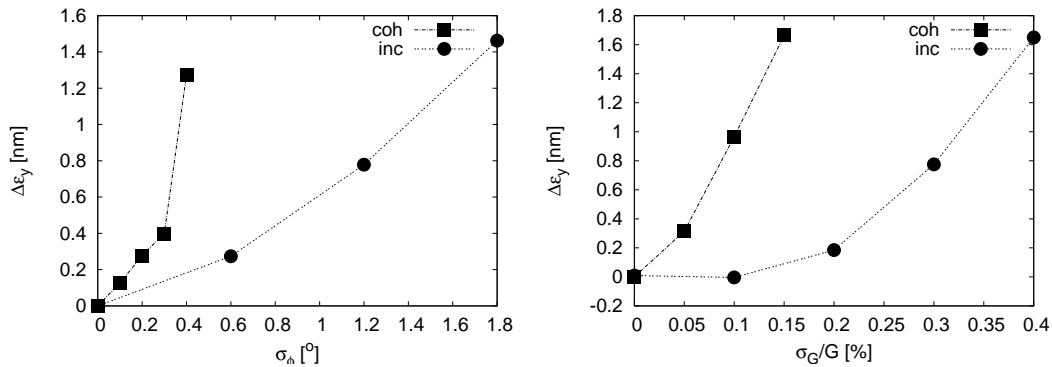


Fig. 3.76: The sensitivity of the ML to RF jitter after 10^6 s of ground motion and one-to-one correction.

Tolerances in the RTML

Along the RTML, individual bunches perform a longitudinal motion. This motion consists of the desired bunch-length compression in the bunch compressors, an unavoidable but static shift due to non-linearities in the lattice and of an unfavourable dynamic bunch-phase jitter. It is this dynamic phase jitter that has to be kept small, thus imposing tight tolerances on the average bunch energy, i.e., booster linac amplitude and bunch compressor RF phases, as well as on the bend angles of the bunch compressor chicanes. At the same time, the r.m.s. bunch energy has to jitter by less than 0.2% and the r.m.s. bunch length by less than 1%.

As seen in the previous section, the relative phasing of Main Beam and Drive Beam has to be better than 0.2° (12 GHz) for errors coherent along the Drive Beam sections and better than 0.8° (12 GHz) for errors incoherent along the Drive Beam sections. The relative phasing of electrons and positrons at the IP has to be better than 0.4° (12 GHz). These constraints facilitate the specification of the allowed beam phase errors at ML entrance for the two different phase references under consideration. In case of external phase references (EPR) the beam phase stability in front of the ML has to be better than $\sigma_{\phi\text{MB-DB}} < 0.2^\circ$ (12 GHz), since any phase error of the Main Beam will remain unchanged along the entire ML and will thus be coherent in all drive-beam sections. In case the outgoing beams are used as reference (OBR) two values need to be specified. Since the Main Beam including a possible phase error is used as phase reference for the RF of the second bunch compressor and the Drive Beam the relative phasing will always be correct. Hence, the allowed beam phase error is limited to $\sigma_{\phi\text{IP}} < 0.4^\circ$ (12 GHz) by the relative phasing of electrons and positrons at the IP. On the other hand, any phase error imposed on the Main Beam behind the phase measurement has to stay below $\sigma_{\phi\text{MB-DB}} < 0.2^\circ$ (12 GHz) to avoid spoiling the relative phasing of Main Beam and Drive Beam.

In Ref. [198] requirements to match above-mentioned phase stability as well as bunch length and energy have been studied in detail for the RTML. Since error sources were studied individually each of them was allowed to fully exploit above-mentioned specifications. That means, all values given below are upper limits. A possible benefit from a feed-forward system after the turn around loops (see §3.3) has not been taken into account. According to this study, the stability of the chicane dipoles must be better than a few 10^{-4} and 10^{-3} for the first and second bunch compressors respectively. This is well above their stability requirement of 10^{-5} . For the turn-around loops and the central electron arc tracking simulations have shown that the magnetic jitter should stay below 10^{-4} assuming that the magnets within each arc cell are powered by a single power supply per magnet type. Since the bunches pass the bunch compressor RF at zero crossing any RF phase jitter will produce a bunch energy jitter, which in turn will be converted into a bunch phase jitter in the chicanes. At the second bunch compressor the RF phase must be stable to 0.24° (12 GHz). The RF phase of the first bunch compressor must be stable to 0.08° (2 GHz) (OBR) or 0.14° (2 GHz) (EPR). RF amplitude errors need to stay below 2% for both bunch compressors. An amplitude jitter of the booster linac will introduce an energy jitter which will be converted in the BC2 chicane into a bunch phase jitter. It has to stay below 0.1%. On the other hand, the booster linac phase has to stay below 2° . A phase error of the incoming bunch will be fully converted into an energy error at the ML entrance. It has to stay below 0.4° (2 GHz) (OBR) or 0.7° (2 GHz).

3.8.5 Multi-Bunch Effects

In the CLIC main linac long-range wakefields may induce multi-bunch effects that can compromise the beam stability and must be kept under tolerance threshold. The effect of a bunch-generated wakefield on the trailing bunches is referred as multi-bunch effect. Persistent wakefields in the accelerator cavities, and resistive-wall wakes, are sources of long-range wakefields. Their impact on the beam has been studied and tolerances on their levels have been evaluated.

3.8.5.1 *Vacuum and Fast Ion-Beam Instability*

The residual gases (H_2 , H_2O , CO , N_2 , etc.) present in the vacuum chamber of an accelerator are ionized by the beam and can either cause ion accumulation around trains of electron bunches or seed electron clouds around trains of positron bunches. The rest gas is usually ionized by the beam via scattering ionization, but, when the beam becomes transversely very small and the beam electric field sufficiently high, field ionization may also set in and lead to significantly larger ionization rates. The latter phenomenon causes in fact full ionization of a certain volume around the beam. In an electron machine, the ions can be trapped between subsequent bunches and accumulate to a level capable of exciting a two-stream instability. In uniformly filled rings, the ion instability can be of conventional type, i.e., the number of trapped ions rapidly increases over the accelerator because there is no gap to clear them from the chamber and reset the accumulation process. However, even when there are more trains of bunches circulating in a ring, separated by long enough gaps as to clear the ion cloud in-between trains, a strong instability could still develop over a train length, which is called fast beam ion instability (FBII). When FBII occurs, individual ions last only for a single passage of the electron beam and are not trapped for multiple turns. This type of instability can also occur in a linear machine, because it does not depend on the periodicity of the structure but only on the propagation of a train of bunches able to trap ions down a sufficiently long machine. This is a head-tail effect which affects only the bunches in the last part of a train. The bunches in the head are totally unaffected. The basic conditions for the possible onset of the FBII could be met at several stages for the CLIC electron beams.

In the long transfer line, detailed macroparticle simulations have shown that partial pressures of 1 nTorr for both H_2O and CO are sufficient to drive the electron beam unstable in the vertical plane. The instability manifests itself with both coherently growing vertical offset motion and emittance growth in the second part of the bunch train. The coherent motion also exhibits clear frequencies, on which it is excited (depending on the ion oscillation frequencies), whereas the emittance growth amounts to about 50% for bunches in the second half of the train and has some peaks of 100% increase for a few bunches in the very tail of the train. The main result of this study is that in the long transfer line a vacuum better than 1 nTorr is required against FBII. This poses a serious constraint on the design of the vacuum system [199].

Studies of beam stability during FBII have also been performed for the Main Linac. Both acceleration and increasing beta functions have been taken into account in the macroparticle simulations. In presence of acceleration the situation is more complex than in the transfer line, because the decreasing beam size causes the trapping condition to change along the linac. At the beginning of the linac ions will be trapped inside the beam, while toward the end of the linac more and more ions are cleared between the bunches since the beam sizes shrink. This is positive for beam stability, as it limits the ion accumulation around the beam, and adds up to the effect of the higher energy, which is also stabilizing. On the other hand, because of small beam size, the field ionization sets in relatively early. This negates the beneficial effects of the increased beam rigidity and loss of trapping, and makes the beam unstable for partial pressures of relatively heavy gas species (mass number above 10) higher than few nTorr. Consequently, also in the Main Linac, partial pressures of 1 nTorr are specified as the upper limit for species like CO_2 or H_2O [200]. Macroparticle simulations have shown that the same pressure tolerances of about 1 nTorr per species as in the Main Linac can be safely extended to the BDS. Furthermore, it was also calculated that a vacuum degradation by up to 3 orders of magnitude can be tolerated over few metres before the IP in terms of beam stability [201].

Pressure thresholds have been calculated for the CLIC electron Main Linac with an energy scaled version to 1 TeV and an alternative lattice with 500 GeV centre-of-mass energy, and the values have been compared with the nominal 3 TeV case. The vacuum level is assumed to be tolerable if no FBII is predicted to develop. In particular, three different realistic vacuum compositions have been assumed in our study, as summarized in Table 3.39.

Numerical simulations with pressure scans were run for the different operating options, each one

Table 3.39: Vacuum compositions

	Unbaked	Baked	Baked and NEG pumped
H ₂ ($A = 2$)	40%	80%	90%
H ₂ O ($A = 18$)	40%	10%	4%
CO ($A = 28$)	10%	5%	3%
CO ₂ ($A = 44$)	10%	5%	3%

with the three possible vacuum compositions. In post-processing, the Fourier spectra of the bunch centroid offsets over the bunch train at the end of the Main Linac were evaluated. A vacuum pressure was considered to lead to FBII when the Fourier spectrum exhibited at least one resonant frequency line exponentially growing above the noise level. It was found that hydrogen does not contribute significantly to FBII and the threshold values are mainly determined by the other gas components (H₂O, CO and CO₂), which explains the higher thresholds in presence of NEG vacuum. Table 3.40 summarizes the pressure thresholds for the different vacuum compositions and Main Linac options, and shows a direct comparison with the nominal 3 TeV case (first column)

Table 3.40: Pressure thresholds for all three vacuum compositions and each Main Linac version

Vacuum Composition	Nominal 3 TeV	Scaled 1 TeV	Alternative 500 GeV
	$N_b = 312$ $N = 4 \times 10^9$	$N_b = 1248$ $N = 1.33 \times 10^9$	$N_b = 354$ $N = 6.8 \times 10^9$
Unbaked	7 nTorr	3 nTorr	10 nTorr
Baked	20 nTorr	8 nTorr	20 nTorr
Baked and NEG pumped	50 nTorr	20 nTorr	60 nTorr

The first row of the table also displays the different number of bunches and bunch charge considered for each case, since these two parameters have a significant impact on the condition for FBII development. Furthermore, another important difference between these three options is the lower fraction of the Linac affected by field ionization due to the larger beam sizes with lower energies. Different optics, lower energy, higher number of bunches, and higher charge per bunch combine in a way that hardly changes the instability thresholds in the case of 500 GeV from the nominal 3 TeV case. On the other hand, with the proposed set of parameters, the scaled Linac at 1 TeV exhibits thresholds for the instability onset lower by more than a factor 2 with respect to the nominal case, posing therefore the tightest requirements on the vacuum quality. Thanks to a near-to-equal partitioning of the ‘active’ gas components H₂O, CO and CO₂, which enhances the Landau damping from frequency spread, tolerable pressures in NEG vacuum are in all cases above a factor 2 higher than those needed in baked vacuum.

3.8.5.2 Resistive-Wall Wakefield Effects

It is a well-known effect in accelerator physics that the interaction of a particle beam with the vacuum chamber, which has a finite value of conductivity, can lead to energy loss as well as coherent instabilities in the transverse plane. In fact, while the energy loss due to resistive wall is generally negligible, the defocussing kicks felt by the beam particles in the tail of a bunch, or bunch train, and generated by the image currents trailing behind the sources (i.e., the bunch, or bunch train, head) can add up over the

path of the beam and result in jitter amplification or emittance growth. The effects of resistive wall can be studied in time domain via macroparticle simulations. The beam particles are tracked with periodic kicks coming from the integrated effect of the resistive wall wakefields, so that the orbit stability can be assessed, or the offset amplification can be quantified. Another possible approach consists of using existing analytic formulae to calculate the rise times of coupled bunch instabilities under the effect of the resistive-wall impedance. In general, coupled-bunch phenomena associated to resistive wall are much stronger than single-bunch effects, although the large short-range wakefield from coated pipe walls can actually play a significant role for the short CLIC bunches.

For the long transfer line, an analytic estimation of both jitter amplification and emittance growth has been given for the Main and the Drive Beam. With a copper vacuum chamber (conductivity $59 \mu\Omega^{-1}\text{m}^{-1}$) of radius $a = 0.1$ m for the Drive Beam and $a = 0.06$ m for the Main Beam, the emittance growth and the amplification of injection errors are found to be adequately small (well below 10%). However, a large copper chamber turns out to be mandatory, because, with stainless steel (conductivity $1.4 \mu\Omega^{-1}\text{m}^{-1}$), the minimum radius would be about twice the one required in copper [199].

The multi-bunch effects of resistive-wall have been estimated through macroparticle simulations for the BDS. A realistic aperture model has been considered, including the restrictions due to collimators and to the magnet constraints in the Final Focusing System. The minimum values of the beam pipe radius could be established, above which the resistive-wall effect becomes negligible on the multi-bunch scale and for different energy options. In particular, the study showed that the beam chambers need to be in copper, with a minimum aperture of 12 mm at 500 GeV, 10 mm at 1 TeV and 10 mm at 3 TeV [202].

Analytic simulations following the formalism described in Ref. [203] can also be applied to the resistive-wall wakes, in order to evaluate their impact on the beam jitter. In case of quadrupole misalignment for instance the amplification factor due to resistive-wall wakefields has been found to be $F_{\text{quad}} \approx 0.012$.

3.8.5.3 Long-range wakefields in the accelerating structures

Two causes can induce long-range wakefields in the accelerator cavities: beam offsets at injection and misalignments. Long-range wakefields generated by the leading bunches cause deflecting transverse kicks on the trailing bunches. The largest wakefield amplitude allowed in the main linac was calculated for the CLIC parameter optimisation phase, and has a value of $6.6 \text{ kV.pC}^{-1}\text{m}^2$ [203]. This wakefield affects only the first following bunch, so that each bunch has a direct effect only on its first follower. Given this value, it is possible to calculate the direct wakefield impact parameter, a_1 , from bunch to bunch. This parameter describes by how much an oscillation of the first bunch is amplified at the subsequent bunches, because of the long-range wakefield effects. This parameter, integrated over the main linac length \hat{s} for point-like bunches, is [203]:

$$a_1 = i \int_0^{\hat{s}} \frac{W(\Delta z) N e^2 \beta(s)}{2E(s)} ds \quad (3.13)$$

where:

Δz is the bunch-to-bunch distance

W is the wakefield

N is the number of particles per bunch

E is the energy along the linac

β is the Twiss parameter along the linac

In the main linac case, $a_1 \sim 1.5$, which is acceptable. The theoretical description of Eq. 3.13 can be extended to calculate the indirect effect of each bunch on the whole train of following bunches. This

calculation has been applied to study the beam stability in case of three possible imperfections that might cause beam blow up:

- Coherent jitter of all bunches of the incoming beam, which leads to scattering of the final bunches. Result of the calculation proved that the amplification factor is $F_{\text{coherent}} \approx 1$, which is acceptable;
- Random bunch-to-bunch jitter of the incoming beam. In this case the amplification factor is $F_{\text{rms}} \approx 4.9$. This seems to be the limit of acceptability;
- Specific combinations of offsets of the incoming bunches. The worst combination can be found via a singular value analysis of the indirect multi-bunch effect matrix A . In such case, the largest singular value defines the worst case: $F_{\text{worst}} \approx 20$.

The simulations show very good agreement with the theory, see Fig. 3.77. In case of non point-like bunches, numerical simulations show that the effect of the long-range wakefields is reduced, see Fig. 3.78.

Misalignment of the accelerating structures can also lead to emittance growth. A simulation has been performed where only the long-range wakefields are misaligned: for an r.m.s. misalignment of $7 \mu\text{m}$ an emittance growth of 0.13 nm is found after one-to-one correction. In case of point-like bunches the emittance growth is only 0.037 nm , see Fig. 3.79.

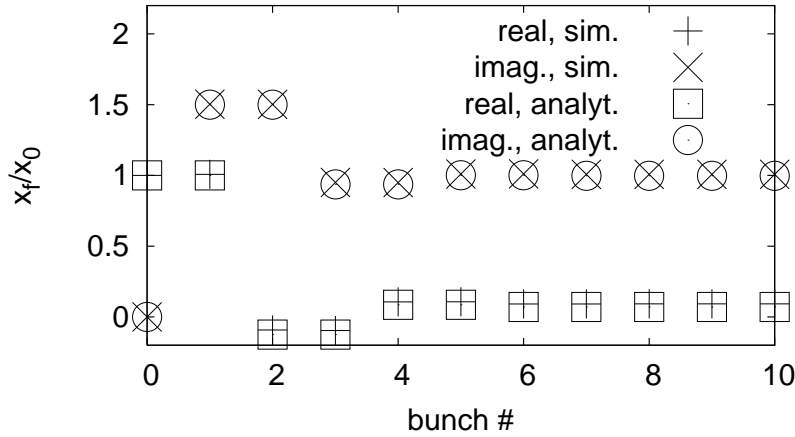


Fig. 3.77: Normalized amplitudes of the bunches at the end of the main linac for an offset incoming train. Point-like bunches are assumed in the calculation and in the simulation.

3.8.5.4 Kink instability

In CLIC the multi-bunch kink instability is a potential concern. If bunches collide with a small vertical offset in the interaction point they are strongly deflected. After the collision the bunches will have parasitic collision with the incoming bunches from the other train. Due to the kick angle received at the interaction point, the outgoing bunches will have a vertical offset with respect to the incoming ones which will kick them in the vertical direction. If the whole incoming train has the same offset Δy_0 this offset will be amplified by the kicks as

$$\Delta y = \frac{\Delta y_0}{1 - n_c \frac{4Nr_e}{\gamma\theta_c^2} \frac{\partial y'}{\partial \Delta y}} \quad (3.14)$$

where:

N is the number of particles per bunch

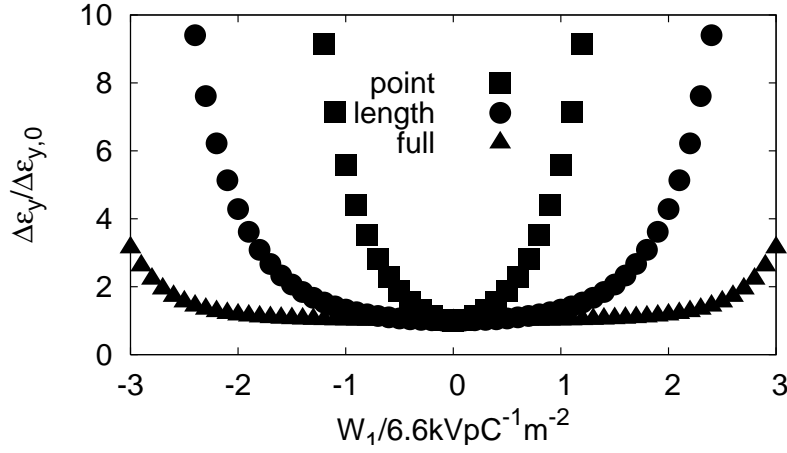


Fig. 3.78: Emittance growth as a function of the wakefield at the second bunch for point-line bunches, realistic bunches with no initial incoherent energy spread, and bunches with initial energy spread.

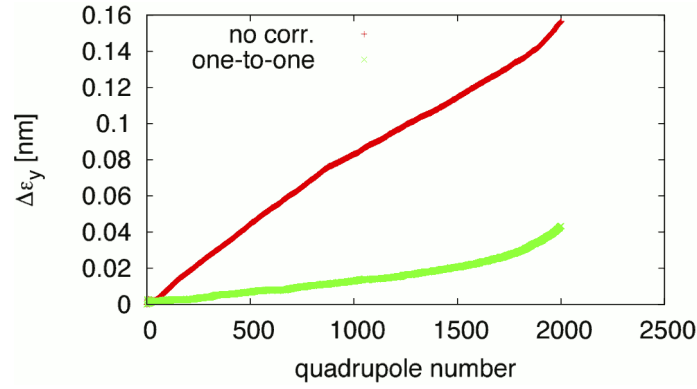


Fig. 3.79: Emittance growth for static misalignment of the accelerating structures before and after one-to-one steering.

- r_e the classical electron radius
- θ_c the full crossing angle between the beams
- n_c the number of parasitic crossings
- γ the relativistic factor of the beam

In CLIC, the derivative of the deflection angle y' on the beam-beam offset is $42 \times 10^3 \text{ nm}^{-1}$, taking into account the impact of the coherent pairs. For a free drift space of 3 m one finds $n_c = 40$ and hence $\Delta y/\Delta y \approx 1.06$: the offset amplification is very small.

3.8.6 Conclusions

A complete set of detailed lattices exists, covering the entire low-emittance transport region from the exit of the damping rings to the interaction point. These lattices have been optimized to provide robustness

against imperfections, already in the design phase. Some room for improvement still exists in some subsystems.

In the main linac full specification of the necessary beam-based alignment procedures has been outlined, leading to excellent performance. In the RTML, a set of BBA procedures to cure static imperfections still has to be specified and tested, but this should not present particular problems. In the BDS, beam-based alignment procedures have been outlined and show good performance, although they do not yet fully achieve the target performance. They need to be improved both in terms of performance and speed of convergence.

Studies of dynamic effects in the main linac and beam delivery systems have been performed. A simulation framework for the simulation of ground motion effects has been developed to facilitate the algorithm design and optimization, and to verify the luminosity preservation in spite of ground motion. These simulations delivered guidelines for the design of the stabilization transfer function of the system, and proved that the luminosity target can be achieved.

Multi-bunch effects have been also addressed, proving that their impact is considerably smaller than for single-bunch effects.

Detailed integrated studies including simultaneous dynamic and static effects need to be performed in order to estimate the interplay between the two regimes, and evaluate how the many different effects integrate with each other on the different time scales. For instance, RF-jitter and its correction through feedback loops must be included in the static alignment procedures. Another improvement toward more realistic simulations will consist in replacing the mirror simulation of positron bunches through electrons, with two independent simulation of both lines, also to evaluate the performance of the BDS beam-based alignment procedures in case of static imperfections. The RTML design and performance optimisation must be completed and finally detailed studies of machine commissioning using pilot-bunches, as well as failure modes and other operational aspects must also be carried out.

REFERENCES

References

1. Rinolfi, L. *et al.* *The CLIC electron and positron polarized sources* CERN-OPEN-2010-017. CLIC-Note-817 (CERN, Geneva, 2009). <<http://cdsweb.cern.ch/record/1269911/files/CERN-OPEN-2010-017.pdf>>.
2. Nakanishi, T. *et al.* Large enhancement of spin polarization observed by photoelectrons from a strained GaAs layer. *Phys. Lett. A* **158**, 345–349 (1991).
3. Nakamura, S., Drachenfels, W., Durek, D. & *et al.* Acceleration of polarized electrons in ELSA. *Nucl. Instr. and Meth. A* **441**, 93–106 (1998).
4. Luh, D. A. *et al.* *Recent Polarized photocathode R&D at SLAC* SLAC-PUB-9603 (SLAC, Stanford, CA, USA, 2002). <<http://www.slac.stanford.edu/cgi-wrap/getdoc/slac-pub-9603.pdf>>.
5. Humensky, T. B. *et al.* SLAC's polarized electron source laser system and minimization of electron beam helicity correlations for the E-158 parity violation experiment. *Nucl. Inst. and Meth. A* **521**, 261–298 (2004).
6. Zhou, Z., Brachmann, A., Maruyama, T. & Sheppard, J. C. *Polarized Photocathode R&D for Future Linear Colliders* SLAC-PUB-13514 (SLAC, Stanford, CA, USA, 2009). <<http://www.slac.stanford.edu/cgi-wrap/getdoc/slac-pub-13514.pdf>>.
7. Zhou, F., Brachmann, A. & Sheppard, J. *Preliminary design of a bunching system for the CLIC polarized electron source* SLAC-PUB-13780. CLIC-Note-813 (SLAC, Stanford, CA, USA, 2009). <<http://www.slac.stanford.edu/pubs/slacpubs/13750/slac-pub-13780.pdf>>.
8. Artru, X. *et al.* Polarized and unpolarized positron sources for electron-positron colliders. *Nucl. Instr. and Meth. B* **266**, 3868–3875 (2008).
9. Artru, X., Chehab, R., Chevallier, M. & Strakhovenko, V. Advantages of axially aligned crystals used in positron production at future linear colliders. *Phys. Rev. ST Accel. Beams* **6**. doi:10.1103/PhysRevSTAB.6.091003. <<http://prst-ab.aps.org/pdf/PRSTAB/v6/i9/e091003>> (2003).
10. Suwada, T. *et al.* First application of a tungsten single-crystal positron source at the KEK B factory. *Phys. Rev. ST Accel. Beams* **10**. doi:10.1103/PhysRevSTAB.10.073501. <<http://prst-ab.aps.org/pdf/PRSTAB/v10/i7/e073501>> (2007).
11. Dadoun, O. *et al.* *Study of a hybrid positron source using channeling for CLIC* CLIC-Note-808 (CERN, Geneva, 2009). <<http://cdsweb.cern.ch/record/1248436/files/CLIC-Note-808.pdf>>.
12. Poirier, F. *et al.* *Dynamics on the positron capture and accelerating sections of CLIC* CERN-OPEN-2011-034. CLIC-Note-877 (CERN, Geneva, 2011). <<http://cdsweb.cern.ch/record/1368465/files/CERN-OPEN-2011-034.pdf>>.
13. Ferrari, A., Latina, A. & Rinolfi, L. *Design Study of the CLIC Injector and Booster Linacs with the 2007 Beam Parameters* CERN-OPEN-2008-017. CLIC-Note-737 (CERN, 2008). <<http://cdsweb.cern.ch/record/1124323/files/CERN-OPEN-2008-017.pdf>>.
14. Vivoli, A. *et al.* *The CLIC Positron Capture and Acceleration in the Injector Linac* CERN-OPEN-2010-020. CLIC-Note-819 (CERN, Geneva, 2010). <<http://cdsweb.cern.ch/record/1277226/files/CERN-OPEN-2010-020.pdf>>.
15. Bulyak, E. & *et al.* in *POSIPOL 2007 Workshop, 23-25 May 2007, Orsay, France* (2007).

16. Rinolfi, L., Antoniou, F., Braun, H.-H., Papaphilippou, Y. & Schulte, D. in *Proc. 23rd IEEE Particle Accelerator Conf., 4-8 May 2009, Vancouver, British Columbia, Canada* (2009), 2945–2947. <<http://accelconf.web.cern.ch/accelconf/PAC2009/papers/we6rfp065.pdf>>.
17. Bulyak, E., Gladkikh, P., Skomorokhov, A. & Omori, T. in *Proc. 1st Int. Particle Accelerator Conf., 23-28 May 2010, Kyoto, Japan* CLIC-Note-855 (2010), 2123–2125. <<http://accelconf.web.cern.ch/accelconf/IPAC10/papers/tupd093.pdf>>.
18. Bulyak, E. in *Proc. 2011 Particle Accelerator Conf., 28 March - 1 April 2011, New York, USA* (2011), 229–231. <<http://accelconf.web.cern.ch/accelconf/PAC2011/papers/mop064.pdf>>.
19. Omori, T. in *CLIC09 Workshop, 12-16 October 2009, CERN* (2009).
20. Yakimenko, V. & et al. in *CLIC09 Workshop, 12-16 October 2009, CERN* (2009).
21. Liu, W., Gai, W. & Kim, K.-J. in *Proc. 22nd Particle Accelerator Conf., 25-29 June 2007, Albuquerque, New Mexico, USA* (2007), 2918–2920. <<http://accelconf.web.cern.ch/accelconf/p07/PAPERS/THPMN090.PDF>>.
22. Liu, W., Gai, W., Rinolfi, L. & Sheppard, J. in *Proc. 1st Int. Particle Accelerator Conf., 23-28 May 2010, Kyoto, Japan*, (2010), 4131–4133. <<http://accelconf.web.cern.ch/accelconf/IPAC10/papers/thpec035.pdf>>.
23. Zang, L. *Study and optimization of Undulators-based polarized positron sources for linear colliders* (University of Liverpool, 2010). <http://research-archive.liv.ac.uk/1445/2/ZangLei_Sept2010_1445.pdf>.
24. Adderley, P. A. *et al.* Load-locked dc high voltage GaAs photogun with an inverted-geometry ceramic insulator. *Phys. Rev. ST Accel. Beams* **13**. doi:10.1103/PhysRevSTAB.13.010101. <<http://prst-ab.aps.org/pdf/PRSTAB/v13/i1/e010101>> (2010).
25. Artru, X., Baier, V. N., Chehab, R. & Jejcic, A. Positron source using channeling in a tungsten crystal. *Nucl. Instr. and Meth. A* **334**, 443–454 (1994).
26. Artru, X. *et al.* in *Proc. 6th European Particle Accelerator Conf., 22-26 June 1998, Stockholm, Sweden* (1998), 1394–1396. <<http://accelconf.web.cern.ch/AccelConf/e98/PAPERS/MOP53C.PDF>>.
27. Artru, X. *et al.* in *Proc. 6th European Particle Accelerator Conf., 22-26 June 1998, Stockholm, Sweden* (1998), 1394–1396. <<http://accelconf.web.cern.ch/AccelConf/e98/PAPERS/MOP53C.PDF>>.
28. Baier, V., Katkov, V. & Strakhovenko, V. Radiation yield of high-energy electrons in thick crystals. *Phys. Stat. Solid. (b)* **133**, 583–592 (1986).
29. Artru, X. *et al.* Positron sources using channeling - a comparison with conventional target. *Particle Accelerators* **59**, 19–41 (1998).
30. Rinolfi, L. *et al.* in *Proc. 23rd IEEE Particle Accelerator Conf., 4-8 May 2009, Vancouver, British Columbia, Canada* (2009), 2945–2947. <<http://accelconf.web.cern.ch/accelconf/PAC2009/papers/we6rfp065.pdf>>.
31. Braun, H., Corsini, R., Delahaye, J.-P. & Tecker, F. *CLIC 2008 Parameters* CERN-OPEN-2008-021. CLIC-Note-764 (CERN, 2008). <<http://cdsweb.cern.ch/record/1132079/files/CERN-OPEN-2008-021.pdf>>.
32. Vivoli, A. *et al.* *The CLIC Positron Capture and Acceleration in the Injector Linac* CERN-OPEN-2010-020. CLIC-Note-819 (CERN, 2010). <<http://cdsweb.cern.ch/record/1277226/files/CERN-OPEN-2010-020.pdf>>.

REFERENCES

33. Antoniou, F. & Papaphilippou, Y. in *Proc. 11th European Particle Accelerator Conf., 23-27 June 2008, Genoa, Italy* (2008), 685–687. <<http://accelconf.web.cern.ch/accelconf/e08/papers/mopp062.pdf>>.
34. Halbach, K. Permanent magnet undulators. *J. Phys. Colloques* **44**, 211–216 (1983).
35. Elleaume, P., Chavanne, J. & Faatz, B. Design considerations for a 1 ÅSASE undulator. *Nucl. Inst. and Meth. A* **455**, 503–523 (2000).
36. Verdier, A. in *Proc. IEEE 18th Particle Accelerator Conf., 27 March - 2 April, 1999, New York, USA* (1999), 398–400. <<http://accelconf.web.cern.ch/accelconf/p99/PAPERS/WEDR3.PDF>>.
37. *MAD-X Homepage* <<http://mad.web.cern.ch/mad>>.
38. *Low Emittance Rings Workshop 2010* <<http://ler2010.web.cern.ch>> (2010).
39. *Low Emittance Rings Workshop 2011* <<http://lowering2011.web.cern.ch>> (2011).
40. Stulle, F., Schulte, D., Snuverink, J., Latina, A. & Molloy, S. in *Proc. XXV Linear Accelerator Conf., 12-17 September 2010, Tsukuba, Japan* (2010), 88–90. <<http://accelconf.web.cern.ch/accelconf/LINAC2010/papers/mop019.pdf>>.
41. Korostelev, M. *Optics Design and Performance of an Ultra-Low Emittance Damping Ring for the Compact Linear Collider* (EPFL, Lausanne, 2006). <<http://lphe.epfl.ch/publications/theses/these.mk.pdf>>.
42. Papaphilippou, Y., Braun, H.-H. & Korostelev, M. in *Proc. 11th European Particle Accelerator Conf., 23-27 June 2008, Genoa, Italy* (2008), 679–681. <<http://accelconf.web.cern.ch/accelconf/e08/papers/mopp060.pdf>>.
43. Aiba, M. *Nucl. Instr. and Meth.* paper submitted.
44. Levichev, E. *et al.* in *Proc. 23rd IEEE Particle Accelerator Conf., 4-8 May 2009, Vancouver, British Columbia, Canada* (2009), 2757–2759. <<http://accelconf.web.cern.ch/accelconf/PAC2009/papers/we6pfp105.pdf>>.
45. Braun, H., Levichev, E. B., Papaphilippou, Y. & Siniatkin, K. S. & Zolotarev. *Alternative design of the CLIC Damping Ring Lattice* CERN-OPEN-2011-016. CLIC-Note-849 (CERN, 2010). <<http://cdsweb.cern.ch/record/1347751/files/CERN-OPEN-2011-016.pdf>>.
46. Antoniou, F., Martini, M., Papaphilippou, Y. & Vivoli, A. in *Proc. 1st Int. Particle Accelerator Conf., 23-28 May 2010, Kyoto, Japan* (2010), 3542–3544. <<http://accelconf.web.cern.ch/AccelConf/IPAC10/papers/wepe085.pdf>>.
47. Schoerling, D. *et al.* Design and System Integration of the Superconducting Wigglers for the CLIC Damping Rings. *Phys. Rev. ST Accel. Beams* **15** (2012).
48. Vivoli, A. & Martini, M. in *Proc. 1st Int. Particle Accelerator Conf., 23-28 May 2010, Kyoto, Japan* (2010), 3557–3559. <<http://accelconf.web.cern.ch/accelconf/IPAC10/papers/wepe090.pdf>>.
49. Raubenheimer, T. Tolerances to Limit the Vertical Emittance in Future Storage Rings. *Particle Accelerators* **36**, 75–119 (1991).
50. Wootton, K. P. *et al.* in *Proc. 2nd Int. Particle Accelerator Conf., 4-9 September 2011, San Sebastian, Spain* (2011), 1102–1104. <<http://accelconf.web.cern.ch/accelconf/IPAC2011/papers/tupc046.pdf>>.
51. Korostelev, M. & Zimmermann, F. in *Proc. 10th European Particle Accelerator Conf., 26-30 June 2006, Edinburgh, Scotland, UK* (2006), 873–875. <<http://accelconf.web.cern.ch/accelconf/e06/PAPERS/MOPLS135.PDF>>.

52. Renier, Y., Antoniou, F., Bartosik, H., Papaphilippou, Y. & Wootton, K. P. in *Proc. 2nd Int. Particle Accelerator Conf., 4-9 September 2011, San Sebastian, Spain* (2011), 2205–2207. <<http://accelconf.web.cern.ch/accelconf/IPAC2011/papers/wepc080.pdf>>.
53. Laskar, J. Frequency analysis for multi-dimensional systems. Global dynamics and diffusion. *Physica D: Nonlinear Phenomena* **67**, 257–281 (1993).
54. Piwinski, A. *Handbook of Accelerator Physics* (ed Chao, A.) (World Scientific, 1999).
55. Martini, M. *Intra-Beam scattering in the ACOL-AA machines* CERN-PS-84-9-AA (CERN, 1984). <<http://cdsweb.cern.ch/record/151638/files/cm-p00047664.pdf>>.
56. Bjorken, J. & Mtingwa, S. *Particle Accelerators* **13**, 115 (1983).
57. Bane, K. *A Simplified Model of Intrabeam Scattering* SLAC-PUB-9226 (SLAC, 2002). <<http://www.slac.stanford.edu/cgi-wrap/getdoc/slac-pub-9226.pdf>>.
58. Rumolo, G., Bruns, W. & Papaphilippou, Y. in *Proc. 11th European Particle Accelerator Conf., 23-27 June 2008, Genoa, Italy* (2008), 661–663. <<http://accelconf.web.cern.ch/accelconf/e08/papers/mopp050.pdf>>.
59. Rumolo, G. & Zimmermann, F. *Practical User Guide for HEADTAIL* CERN-SL-Note-2002-036 AP (CERN, 2002). <<http://cdsweb.cern.ch/record/702717/files/sl-note-2002-036.pdf>>.
60. Yin Vallgren, C. *et al.* Amorphous carbon coatings for the mitigation of electron cloud in the CERN Super Proton Synchrotron. *Phys. Rev. ST Accel. Beams* **14**, 071001 (2011).
61. Palmer, M. A., Alexander, J. P., Billing, M. G., Calvey, J. R. & et al. in *Proc. 1st Int. Particle Accelerator Conf., 23-28 May 2010, Kyoto, Japan* (2010), 1251–1255. <<http://accelconf.web.cern.ch/accelconf/IPAC10/papers/tuymh02.pdf>>.
62. Mounet, N., Metral, E. & Rumolo, G. in *Proc. 2nd Int. Particle Accelerator Conf., 4-9 September 2011, San Sebastian, Spain* (2011), 778–780. <<http://accelconf.web.cern.ch/accelconf/IPAC2011/papers/mops075.pdf>>.
63. Zotter, B. *Transverse mode-coupling and Head-Tail Turbulence* ISR-TH/82-10 (CERN, 1982). <<http://cdsweb.cern.ch/record/137720/files/SCAN-0009026.pdf>>.
64. Adolphsen, C. & et al. *Zero Order Design Report for the Next Linear Collider* SLAC-R-474 (SLAC, 2002). <<http://www.slac.stanford.edu/cgi-wrap/getdoc/slac-r-474.pdf>>.
65. Naito, T. *et al.* in *Proc. 1st Int. Particle Accelerator Conf., 23-28 May 2010, Kyoto, Japan* (2010), 2386–2388. <<http://accelconf.web.cern.ch/accelconf/IPAC10/papers/weobmh02.pdf>>.
66. Belver-Aguilar, C., Faus-Golfe, A., Barnes, M. J., Rumolo, G. & Zannini, C. in *Proc. 2nd Int. Particle Accelerator Conf., 4-9 September 2011, San Sebastian, Spain* (2011), 1012–1014. <<http://accelconf.web.cern.ch/AccelConf/IPAC2011/papers/TUPC011.pdf>>.
67. Alesini, D. & Marcellini, F. RF deflector design of the CLIC test facility CTF3 delay loop and beam loading effect analysis. *Phys. Rev. ST Accel. Beams* **12**, 031301 (2009).
68. Emma, P. *A spin rotator system for the NLC* NLC-Note-7 (SLAC, Stanford, CA, USA, 1994).
69. Latina, A., Solyak, N. & Schulte, D. in *Proc. 1st Int. Particle Accelerator Conf., 23-28 May 2010, Kyoto, Japan* (2010), 4608–4610. <<http://accelconf.web.cern.ch/accelconf/IPAC10/papers/thpe040.pdf>>.

REFERENCES

70. Stulle, F., Adelmann, A. & Pedrozzi, M. *Conceptual design of bunch compressors and turn around loops for a multi-TeV linear collider* EUROTeV-Report-2008-025. CLIC-Note-xxx (CERN, 2008). <http://www.eurotev.org/sites/site_eurotev/content/e328/e329/e1082/e1500/EUROTeV-Report-2008-025.pdf>.
71. Stulle, F., Schulte, D., Snuverink, J., Latina, A. & Molloy, S. in *Proc. XXV Linear Accelerator Conf., 12-17 September 2010, Tsukuba, Japan* (2010), 88–90. <<http://accelconf.web.cern.ch/accelconf/LINAC2010/papers/mop019.pdf>>.
72. Stulle, F. *Beam phase and energy tolerances in the CLIC RTML* CERN-OPEN-2011-048. CLIC-Note-874 (CERN, 2011). <<http://cdsweb.cern.ch/record/1406047/files/CERN-OPEN-2011-048.pdf?subformat=pdfa>>.
73. Schulte, D. in *Proc. 23rd IEEE Particle Accelerator Conf., 4-8 May 2009, Vancouver, British Columbia, Canada* (2009), 4664–4666. <<http://accelconf.web.cern.ch/accelconf/PAC2009/papers/fr5rfp055.pdf>>.
74. Wang, D., Schulte, D., Gao, J. & Stulle, F. *Design Study of the CLIC Booster Linac with FODO Lattice* EUROTeV Report 2008-092 (CERN, 2009). <<http://ebookbrowse.com/eurotev-report-2008-092-pdf-d46450179>>.
75. Syratcev, I. *To be published*
76. Jeanneret, J. B. & Braun, H.-H. in *Proc. 11th European Particle Accelerator Conf., 23-27 June 2008, Genoa, Italy* (2008), 3014–3016. <<http://accelconf.web.cern.ch/accelconf/e08/papers/thpc017.pdf>>.
77. Jeanneret, J. B. *et al.* in *Proc. 11th European Particle Accelerator Conf., 23-27 June 2008, Genoa, Italy* (2008), 3017–3019. <<http://accelconf.web.cern.ch/accelconf/e08/papers/thpc018.pdf>>.
78. Stulle, F., Schulte, D., Snuverink, J., Latina, A. & Molloy, S. in *Proc. 1st Int. Particle Accelerator Conf., 23-28 May 2010, Kyoto, Japan* (2010), 3013–3015. <<http://accelconf.web.cern.ch/accelconf/IPAC10/papers/wepec054.pdf>>.
79. Snuverink, J. *et al.* in *Proc. 1st Int. Particle Accelerator Conf., 23-28 May 2010, Kyoto, Japan* (2010), 3398–3400. <<http://accelconf.web.cern.ch/accelconf/IPAC10/papers/wepe023.pdf>>.
80. d’Amico, E. & Guignard, G. Special lattice computation for the CERN Compact Linear Collider. *Phys. Rev. ST Accel. Beams* **4**, 021002 (2001).
81. Garcia, H. & *et al.* *Simulations of emittance measurements at CLIC (to be published)*
82. Sands, M. *Emittance growth from radiation fluctuations* SLAC-AP-047 (SLAC, Stanford, CA, USA, 1985). <<http://www.slac.stanford.edu/cgi-wrap/getdoc/slac-ap-047.pdf>>.
83. Saldin, E. L., Schneidmiller, E. A. & Yurkov, M. V. On the coherent radiation of an electron bunch moving in an arc of a circle. *Nucl. Instr. and Meth. A* **398**, 373–394 (1997).
84. Nodvick, J. S. & Saxon, D. S. Suppression of Coherent Radiation by Electrons in a Synchrotron. *Phys. Rev.* **96**, 180–184 (1954).
85. Latina, A., Eliasson, P. & Schulte, D. in *Proc. 10th European Particle Accelerator Conf., 26-30 June 2006, Edinburgh, Scotland, UK* (2006), 864–866. <<http://accelconf.web.cern.ch/accelconf/e06/PAPERS/MOPLS130.PDF>>.
86. Schulte, D. in *Proc. 23rd IEEE Particle Accelerator Conf., 4-8 May 2009, Vancouver, British Columbia, Canada* (2009), 3808–3810. <<http://accelconf.web.cern.ch/accelconf/PAC2009/papers/th6pfp045.pdf>>.

87. Balakin, V. E., Novokhatsky, A. V. & Smirnov, V. P. in *Proc. 12th Int. Conf. on High Energy Accelerators, 11-16 August 1983, Fermilab, Batavia, IL, USA* (1983), 119–120.
88. Latina, A., Eliasson, P. & Schulte, D. in *Proc. 22nd Particle Accelerator Conf., 25-29 June 2007, Albuquerque, New Mexico, USA* (2007), 2844–2846. <<http://accelconf.web.cern.ch/accelconf/p07/PAPERS/THPMN061.PDF>>.
89. Schulte, D. in *Proc. 23rd IEEE Particle Accelerator Conf., 4-8 May 2009, Vancouver, British Columbia, Canada* (2009), 3808–3810. <<http://accelconf.web.cern.ch/accelconf/PAC2009/papers/th6pfp045.pdf>>.
90. Schulte, D. in *Proc. 21st IEEE Particle Accelerator Conf., 16-20 May 2005, Knoxville, TN, USA* (2005), 1251–1253. <<http://accelconf.web.cern.ch/accelconf/p05/PAPERS/RPPP011.PDF>>.
91. Schulte, D. in *Proc. 20th IEEE Particle Accelerator Conf., 12-16 May 2003, Portland, OR, USA* (2003), 2727–2729. <<http://accelconf.web.cern.ch/accelconf/p03/PAPERS/RPAB004.PDF>>.
92. Schulte, D. & Raubenheimer, T. in *Proc. IEEE 18th Particle Accelerator Conf., 27 March - 2 April, 1999, New York, USA* (1999), 3441–3443. <<http://accelconf.web.cern.ch/accelconf/p99/PAPERS/FRA24.PDF>>.
93. Leros, N. & Schulte, D. in *Proc. 8th European Particle Accelerator Conf., 3-7 June 2002, Paris, France* (2002), 461–463. <<http://accelconf.web.cern.ch/accelconf/e02/PAPERS/MOPRI059.pdf>>.
94. Eliasson, P. & Schulte, D. in *Proc. 21st IEEE Particle Accelerator Conf., 16-20 May 2005, Knoxville, Tennessee, USA* (2005), 1141–1143. <<http://accelconf.web.cern.ch/accelconf/p05/PAPERS/RPPP009.PDF>>.
95. Leros, N. & Schulte, D. in *Proc. 19th IEEE Particle Accelerator Conf., 18-22 June 2001, Chicago, Illinois, USA* (2001), 1687–1689. <<http://accelconf.web.cern.ch/accelconf/p01/PAPERS/TPPH014.PDF>>.
96. Schulte, D. & Tomas, R. in *Proc. 23rd IEEE Particle Accelerator Conf., 4-8 May 2009, Vancouver, British Columbia, Canada* (2009), 3811–3813. <<http://accelconf.web.cern.ch/accelconf/PAC2009/papers/th6pfp046.pdf>>.
97. Schulte, D. *Effect of RF-Phase Jitter on the Main-Beam Emittance in CLIC* CERN-OPEN-2000-101. CLIC-Note-432 (CERN, 2000). <<http://cdsweb.cern.ch/record/435664/files/open-2000-101.pdf>>.
98. Schulte, D. & Tomas, R. in *Proc. 23rd IEEE Particle Accelerator Conf., 4-8 May 2009, Vancouver, British Columbia, Canada* (2009), 3811–3813. <<http://accelconf.web.cern.ch/accelconf/PAC2009/papers/th6pfp046.pdf>>.
99. Schulte, D., Wilson, E. J. N. & Zimmermann, F. in *Proc. XXII International Linear Accelerator Conf., 6-20 August, 2004, Lubeck, Germany* (2004), 138–140. <<http://accelconf.web.cern.ch/accelconf/l04/PAPERS/MOP43.PDF>>.
100. Zimmermann, F. & Schulte, D. *Phase and Amplitude Tolerance in the CLIC Main Linac* CERN-OPEN-2003-055. CLIC-Note-588 (CERN, Geneva, 2003). <<http://cdsweb.cern.ch/record/693451/files/open-2003-055.pdf>>.
101. Schulte, D. in *Proc. 23rd IEEE Particle Accelerator Conf., 4-8 May 2009, Vancouver, British Columbia, Canada* (2009), 4664–4666. <<http://accelconf.web.cern.ch/accelconf/PAC2009/papers/fr5rfp055.pdf>>.
102. Schulte, D. *To be published*

REFERENCES

103. Jeanneret, J. B., Rumolo, G. & Schulte, D. in *Proc. 1st Int. Particle Accelerator Conf., 23-28 May 2010, Kyoto, Japan* (2010), 3401–3403. <<http://accelconf.web.cern.ch/accelconf/IPAC10/papers/wepe024.pdf>>.
104. Rumolo, G. & Schulte, D. in *Proc. 23rd IEEE Particle Accelerator Conf., 4-8 May 2009, Vancouver, British Columbia, Canada* (2009), 4658–4660. <<http://accelconf.web.cern.ch/accelconf/PAC2009/papers/fr5rfp053.pdf>>.
105. Rumolo, G. & Schulte, D. in *Proc. 11th European Particle Accelerator Conf., 23-27 June 2008, Genoa, Italy* (2008), 655–657. <<http://accelconf.web.cern.ch/accelconf/e08/papers/mopp048.pdf>>.
106. Grudiev, A., Cappelletti, A. & Kononenko, O. in *Proc. XXV Linear Accelerator Conf., 12-17 September 2010, Tsukuba, Japan* (2010), 94–96. <<http://accelconf.web.cern.ch/accelconf/LINAC2010/papers/mop021.pdf>>.
107. Schulte, D. *Pulse Shaping and Beam Loading Compensation with the Delay Loop* CERN-OPEN-2000-146. CLIC-Note-434 (CERN, Geneva, 2000). <<http://cdsweb.cern.ch/record/448697/files/open-2000-146.pdf>>.
108. Schulte, D. & Syratchev, I. in *Proc. 20th International Linear Accelerator Conf., 21-25 Aug 2000, Monterey, CA, USA* (2000). <<http://accelconf.web.cern.ch/accelconf/l00/papers/MOA04.pdf>>.
109. *CLIC Lattice repository* <<http://clicr.web.cern.ch/CLICr/MainBeam/BDS/>>.
110. Schuler, P. in *CLIC08 Workshop, 4-17 October 2008, CERN* (2008). <<http://indico.cern.ch/getFile.py/access?contribId=291&sessionId=38&resId=0&materialId=slides&confId=30383>>.
111. Resta-Lopez, J. *et al. Status report of the baseline collimation system of CLIC. Part II* arXiv:1104.2431. CLIC-Note-883 (CERN, 2011). <<http://cdsweb.cern.ch/record/1344632/files/CLIC-Note-883.pdf>>.
112. Schulte, D., Guignard, G., Leros, N. & d’Amico, E. T. in *Proc. 19th IEEE Particle Accelerator Conf., 18-22 June 2001, Chicago, Illinois, USA* (2001), 3033–3035. <<http://accelconf.web.cern.ch/accelconf/p01/PAPERS/RPAH082.PDF>>.
113. Burkhardt, H. *et al. Halo and tail generation computer model and studies for linear colliders* EUROTeV-Report-2008-076 (EUROTeV, 2008). <http://www.eurotev.org/reports/_presentations/eurotev_reports/2008/e1533/EUROTeV-Report-2008-076.pdf>.
114. Agapov, I., Blair, G., Malton, S. & Deacon, L. BDSIM: A particle tracking code for accelerator beam-line simulations including particle-matter interactions. *Nucl. Instr. and Meth. A* **606**, 708–712 (2009).
115. Linsen, L. in *CLIC meeting, 17 June 2011* (2011).
116. Burkhardt, H., Blair, G. A. & Deacon, L. C. in *Proc. 1st Int. Particle Accelerator Conf., 23-28 May 2010, Kyoto, Japan* (2010), 4307–4309. <<http://accelconf.web.cern.ch/accelconf/IPAC10/papers/thpd014.pdf>>.
117. Raimondi, P. & Seryi, A. Novel Final Focus Design for Future Linear Colliders. *Phys. Rev. Lett.* **86**, 3779–3782 (2001).
118. Tomàs, R. Nonlinear optimization of beam lines. *Phys. Rev. ST Accel. Beams* **9**, 081001 (2006).
119. Zamudio, G. & Tomàs, R. *Optimization of the CLIC 500 GeV Final Focus system and design if a new 3 TeV Final Focus system with $L^*=6.0$ m* CERN-OPEN-2011-035. CLIC-Note-882 (CERN, 2010). <<http://cdsweb.cern.ch/record/1368480/files/CERN-OPEN-2011-035.pdf>>.

120. Dalena, B., Schulte, D., Tomas, R. & Angal-Kalinin, D. in *Proc. 23rd IEEE Particle Accelerator Conf., 4-8 May 2009, Vancouver, British Columbia, Canada* (2009), 3874–3876. <<http://accelconf.web.cern.ch/accelconf/PAC2009/papers/th6pfp074.pdf>>.
121. Oide, K. Synchrotron-Radiation Limit on the Focusing of Electron Beams. *Phys. Rev. Lett.* **61**, 1713–1715 (1988).
122. Tomàs, R. *et al.* *Summary of the BDS and MDI CLIC08 Working Group* CERN-OPEN-2009-018. CLIC-Note-776 (CERN, Geneva, 2008). <<http://cdsweb.cern.ch/record/1216866/files/CERN-OPEN-2009-018.pdf>>.
123. Dalena, B., Schulte, D. & Tomas, R. in *Proc. 1st Int. Particle Accelerator Conf., 23-28 May 2010, Kyoto, Japan* (2010), 3416–3418. <<http://accelconf.web.cern.ch/accelconf/IPAC10/papers/wepe029.pdf>>.
124. Shinton, I. R. R. & Jones, R. M. in *5th CLIC-ILC BDS+MDI meeting, 10 September 2010, CERN* (2010). <<http://indico.cern.ch/getFile.py/access?contribId=1&resId=1&materialId=slides&confId=106655>>.
125. Barranco, J., Martin, E. & Tomas, R. *Luminosity studies in a traveling focus scheme in the CLIC Final focus* to be published as CLIC Note.
126. Seryi, A. in *3rd CLIC-ILC BDS+MDI meeting, 19 July 2010, CERN* (2005). <<http://indico.cern.ch/conferenceDisplay.py?confId=106655>>.
127. Mutzner, R., Rumolo, G., Pieloni, T. & Rivkin, L. *Multi-Bunch effect of resistive wall in the beam delivery system of the Compact Linear Collider* CERN-THESIS-2010-073. CLIC-Note-818 (CERN, 2010). <<http://cdsweb.cern.ch/record/1266868/files/CERN-THESIS-2010-073.pdf>>.
128. Schulte, D. in *CLIC08 Workshop, 4-17 October 2008, CERN* (2008). <<http://indico.cern.ch/getFile.py/access?contribId=287&sessionId=40&resId=0&materialId=slides&confId=30383>>.
129. Eliasson, P., Korostelev, M., Schulte, D. & Tomas, R. in *Proc. 10th European Particle Accelerator Conf., 26-30 June 2006, Edinburgh, Scotland, UK* (2006), 774–776. <<http://accelconf.web.cern.ch/accelconf/e06/PAPERS/MOPLS094.PDF>>.
130. Dalena, B. *et al.* in *Proc. Int. Workshop on Future Linear Colliders LCWS11, 26-30 September 2011, Granada, Spain*, (2011). <<http://arxiv.org/pdf/1202.0562v1>>.
131. Swoboda, D., Dalena, B. & Tomas, R. *CLIC spectrometer magnet interference computation of transversal B-field on primary beam* CERN-OPEN-2010-016. CLIC-Note-815 (CERN, Geneva, 2010). <<http://cdsweb.cern.ch/record/1266884/files/CERN-OPEN-2010-016.pdf>>.
132. Ambattu, P. *et al.* *CLIC crab cavity specifications* EuCARD-REP-2010-003. EuCARD-IAR-S1-Combined-1038471-v3 (CERN, 2010). <<http://indico.cern.ch/getFile.py/access?resId=0&materialId=paper&confId=76184>>.
133. Rumolo, G. *Parameter Specification. Vacuum System for the CLIC Beam Delivery System* EDMS 992781 v.2 (CERN, 2010). <https://edms.cern.ch/file/992781/2/Vacuum_system_BDS.doc>.
134. Garion, C. & Kos, H. in *Proc. 23rd IEEE Particle Accelerator Conf., 4-8 May 2009, Vancouver, British Columbia, Canada* (2010), 363–365. <<http://accelconf.web.cern.ch/accelconf/PAC2009/papers/mo6rfp007.pdf>>.

REFERENCES

135. Mainaud Durand, H., Touzé, T., Griffet, S., Kemppinen, J. & Lackner, F. in *Proc. 11th International Workshop on Accelerator Alignment, 3-7 September 2010, DESY, Hamburg, Germany* (2010). <http://iwaa2010.desy.de/e107506/e107507/e113203/e119271/IWAA2010_HMD_CLIC.pdf>.
136. Aihara, H., Burrows, P. & Oreglia, M. *SiD Letter of Intent* SLAC-R-944 (SLAC, Stanford, CA, USA, 2009). <<http://arxiv.org/pdf/0911.0006v1.pdf>>.
137. ILD. *The International Large Detector Letter of Intent* DESY 2009-87. Fermilab-Pub-09-682-E. KEK Report 2009-6. 2009. <<http://arxiv.org/pdf/1006.3396v1.pdf>>.
138. Artoos, K. *et al.* in *Proc. 23rd IEEE Particle Accelerator Conf., 4-8 May 2009, Vancouver, British Columbia, Canada* (2009), 3636–3638. <<http://accelconf.web.cern.ch/accelconf/PAC2009/papers/th5rfp081.pdf>>.
139. Tomàs, R. *Technical specifications of the CLIC Final Doublet quadrupoles* EDMS 976036 (CERN, Geneva, 2009). <https://edms.cern.ch/file/976036/2/Technical_specification_of_the_CLIC_FD_Q.pdf>.
140. Nosochkov, Y. & Seryi, A. Compensation of detector solenoid effects on the beam size in a linear collider. *Phys. Rev. ST Accel. Beams* **8**, 021001 (2005).
141. Dalena, B., Schulte, D., Tomas, R. & Angal-Kalinin, D. in *Proc. 23rd IEEE Particle Accelerator Conf., 4-8 May 2009, Vancouver, British Columbia, Canada* (2009), 3874–3876. <<http://accelconf.web.cern.ch/accelconf/PAC2009/papers/th6pfp074.pdf>>.
142. Dalena, B., Schulte, D. & Tomas, R. in *Proc. 1st Int. Particle Accelerator Conf., 23-28 May 2010, Kyoto, Japan* (2010), 3416–3418. <<http://accelconf.web.cern.ch/accelconf/IPAC10/papers/wepe029.pdf>>.
143. Murray, J. J. *Effects Of Superposition Of Detector Solenoid And FFS Quadrupole Fields In SLC And Correction Methods* SLAC-CN-237 (SLAC, Stanford, CA, USA, 1983). doi:10.2172/6829177. <<http://www.osti.gov/bridge/servlets/purl/6829177-IO94me/6829177.pdf>>.
144. Swoboda, D., Dalena, B. & Tomas, R. *CLIC spectrometer magnet interference computation of transversal B-field on primary beam* CERN-OPEN-2010-016. CLIC-Note-815 (CERN, Geneva, 2010). <<http://cdsweb.cern.ch/record/1266884/files/CERN-OPEN-2010-016.pdf>>.
145. Sadeh, I., Abramowicz, H., Ingbir, R., Kananov, S. & Levy, A. *A Luminosity Calorimeter for CLIC* LCD-Note-2009-002 (CERN, 2009). <<http://lcd.web.cern.ch/LCD/Documents/Documents/LCD-2009-002.pdf>>.
146. Grah, C. & Saproonov, A. Beam parameter determination using beamstrahlung photons and incoherent pairs. *Journal of Instrumentation* **3**, P10004 (2008).
147. Burrows, P. N. *et al.* in *Proc. 21st IEEE Particle Accelerator Conf., 16-20 May 2005, Knoxville, Tennessee, USA* (2005), 1359–1361. <<http://accelconf.web.cern.ch/accelconf/p05/PAPERS/RPPP013.PDF>>.
148. Burrows, P. N. *et al.* in *Proc. 10th European Particle Accelerator Conf., 26-30 June 2006, Edinburgh, Scotland, UK* (2006), 852–854. <<http://accelconf.web.cern.ch/accelconf/e06/PAPERS/MOPLS123.PDF>>.
149. Resta-Lopez, J., Burrows, P. N. & Christian, G. Luminosity Performance Studies of the Compact Linear Collider with Intra-train Feedback System at the Interaction Point. *Journal of Instrumentation* **5**, 09007 (2010).

150. Rumolo, G. in *11th MDI meeting, 19 March 2010, CERN* (2010). <<http://indico.cern.ch/getFile.py/access?contribId=1&resId=0&materialId=slides&confId=86050>>.
151. Maruyama, T. in *Linear Collider Workshop of the Americas, 29 September - 3 October 2009, Albuquerque, New Mexico, USA* (2009). <<http://ilcagenda.linearcollider.org/getFile.py/access?contribId=201&sessionId=13&resId=1&materialId=slides&confId=3461>>.
152. Esberg, J. & et al. *To be published*
153. Schulte, D. *Study of Electromagnetic and Hadronic Background in the Interaction Region of the TESLA Collider* TESLA-97-08 (Hamburg University, Hamburg, 1997). <<http://cdsweb.cern.ch/record/331845/files/shulte.pdf>>.
154. Dalena, B. & Schulte, D. in *Proc. 1st Int. Particle Accelerator Conf., 23-28 May 2010, Kyoto, Japan* (2010), 3404–3406. <<http://accelconf.web.cern.ch/accelconf/IPAC10/papers/wepe025.pdf>>.
155. Burkhardt, H., Blair, G. A. & Deacon, L. C. in *Proc. 1st Int. Particle Accelerator Conf., 23-28 May 2010, Kyoto, Japan* (2010), 4307–4309. <<http://accelconf.web.cern.ch/accelconf/IPAC10/papers/thpd014.pdf>>.
156. Salt, M. D. *et al. Background at the Interaction Point from the CLIC Post-Collision Line* EuCARD-CON-2010-031. CLIC-Note-847. CERN-ATS-2010-160 (CERN, 2010). <<http://cdsweb.cern.ch/record/1299164/files/CERN-ATS-2010-160.pdf>>.
157. Ferrari, A. Conceptual design of a beam line for post-collision extraction and diagnostics at the multi-TeV Compact Linear Collider. *Phys. Rev. ST Accel. Beams* **12**, 021001 (2009).
158. Vorozhtsov, A. *Preliminary Design and Cost Estimate of CLIC Main Beam Normal Conducting Magnets Required for the Post-Collision Line* EDMS 1097652 v.1. CLIC-Note-863. ATS/Note/2011-024 TECH (CERN, 2010). <https://edms.cern.ch/file/1097652/1/ATSNote_CLIC_MB_PostCollisionLine_edms_1097652.pdf>.
159. Appleby, R., Salt, M. D., Deacon, L. C. & Gschwendtner, E. in *p* (2011), 1060–1062. <<http://accelconf.web.cern.ch/accelconf/IPAC2011/papers/tupc028.pdf>>.
160. Ishida, T. in *Proc. 22nd Particle Accelerator Conf., 25-29 June 2007, Albuquerque, New Mexico, USA* (2007), 686–688. <<http://accelconf.web.cern.ch/accelconf/p07/PAPERS/TUXKI03.PDF>>.
161. Walz, D., Jurow, J. & Garwin, E. L. Water Cooled Beam Dumps and Collimators for the Stanford Linear Accelerator. *IEEE Transactions on Nuclear Science* **12**, 867–871 (1965).
162. Walz, D. R., Amann, J. W., Arnold, R., Seryi, A. & et al. in *Proc. 1st Int. Particle Accelerator Conf., 23-28 May 2010, Kyoto, Japan* (2010), 3341–3343. <<http://accelconf.web.cern.ch/accelconf/IPAC10/papers/wepe003.pdf>>.
163. Mereghetti, A., Maglioni, C. & Vlachoudis, V. *FLUKA and Thermo-mechanical Studies for the CLIC Main Dump* CERN-OPEN-2011-030. CLIC-Note-876 (CERN, Geneva, 2011). <<http://cdsweb.cern.ch/record/1355402/files/CERN-OPEN-2011-030.pdf>>.
164. Agapov, I., Blair, G., Malton, S. & Deacon, L. BDSIM: A particle tracking code for accelerator beam-line simulations including particle-matter interactions. *Nucl. Instr. and Meth. A* **606**, 708–712 (2009).
165. Agostinelli, S., Allison, J., Amakoe, K. & et al. GEANT4 : A Simulation toolkit. *Nucl. Instr. and Meth. A* **506**, 250–303 (2003).

REFERENCES

166. Schulte, D. in *Proc. XXII International Linear Accelerator Conf., 6-20 August, 2004, Lubeck, Germany* (2004), 144–146. <<http://accelconf.web.cern.ch/accelconf/104/PAPERS/MOP45.PDF>>.
167. Field, R. C. Beamstrahlung monitors at SLC. *Nucl. Instr. and Meth. A* **265**, 167–169 (1988).
168. Bonvicini, G. & Welch, J. Large angle beamstrahlung as a beam-beam monitoring tool. *Nucl. Instrum. Meth. A* **418**, CLNS-1523, 223–232 (1998).
169. Apyan, A. in *Proc. 2nd Int. Particle Accelerator Conf., 4-9 September 2011, San Sebastian, Spain* (2011), 1057–1059. <<http://accelconf.web.cern.ch/accelconf/IPAC2011/papers/tupc027.pdf>>.
170. Schulte, D. *Study of Electromagnetic and Hadronic Background in the Interaction Region of the TESLA Collider* TESLA-97-08 (Hamburg University, Hamburg, 1997). <<http://cdsweb.cern.ch/record/331845/files/shulte.pdf>>.
171. *Handbook of Accelerator Physics and Engineering* (eds Chao, A. & Tigner, M.) (World Scientific, 1998).
172. Schulte, D. in *Proc. 6th European Particle Accelerator Conf., 22-26 June 1998, Stockholm, Sweden* (1998), 478–481. <<http://www.cern.ch/accelconf/e98/PAPERS/MOP52C.PDF>>.
173. Oide, K. Synchrotron-Radiation Limit on the Focusing of Electron Beams. *Phys. Rev. Lett.* **61**, 1713–1715 (1988).
174. Tomàs, R. Nonlinear optimization of beam lines. *Phys. Rev. ST Accel. Beams* **9**, 081001 (2006).
175. Latina, A. *et al.* in *Proc. 11th European Particle Accelerator Conf., 23-27 June 2008, Genoa, Italy* (2008), 1750–1752. <<http://accelconf.web.cern.ch/accelconf/e08/papers/tupp094.pdf>>.
176. Schulte, D. in *Proc. 5th Int. Computational Accelerator Physics Conf., 14-18 September 1998, Monterey, CA, USA* (1998). <<http://cdsweb.cern.ch/record/382453/files/ps-99-014.pdf>>.
177. Schulte, D. in *Proc. 23rd IEEE Particle Accelerator Conf., 4-8 May 2009, Vancouver, British Columbia, Canada* (2009), 4664–4666. <<http://accelconf.web.cern.ch/accelconf/PAC2009/papers/fr5rfp055.pdf>>.
178. Latina, A., Eliasson, P. & Schulte, D. in *Proc. 22nd Particle Accelerator Conf., 25-29 June 2007, Albuquerque, New Mexico, USA* (2007), 2844–2846. <<http://accelconf.web.cern.ch/accelconf/p07/PAPERS/THPMN061.PDF>>.
179. Schulte, D. in *Proc. 21st IEEE Particle Accelerator Conf., 16-20 May 2005, Knoxville, TN, USA* (2005), 1251–1253. <<http://accelconf.web.cern.ch/accelconf/p05/PAPERS/RPPP011.PDF>>.
180. Eliasson, P. & Schulte, D. Design Of Main Linac Emittance Tuning Bumps For The Compact Linear Collider And The International Linear Collider. *Phys. Rev. ST Accel. Beams* **11**, 011002 (2008).
181. Schulte, D. & Raubenheimer, T. in *Proc. IEEE 18th Particle Accelerator Conf., 27 March - 2 April, 1999, New York, USA* (1999), 3441–3443. <<http://accelconf.web.cern.ch/accelconf/p99/PAPERS/FRA24.PDF>>.
182. Tenenbaum, P. *Application of Kick Minimization to the RTML Front End* SLAC-TN-07-002 (SLAC, Stanford, CA, USA, 2007). <<http://www.slac.stanford.edu/cgi-wrap/getdoc/slac-tn-07-002.pdf>>.

183. Touzé, T., Mainaud Durand, H. & Missiaen, D. P. in *Proc. 23rd IEEE Particle Accelerator Conf., 4-8 May 2009, Vancouver, British Columbia, Canada* (2009), 3639–3641. <<http://accelconf.web.cern.ch/accelconf/PAC2009/papers/th5rfp082.pdf>>.
184. Press, W. H., Teukolsky, S. A., Vetterling, W. T. & Flannery, B. P. *Numerical Recipes in Fortran 90* (Cambridge Univ. Press, 2007).
185. Dalena, B. *et al.* in *Proc. Int. Workshop on Future Linear Colliders LCWS11, 26-30 September 2011, Granada, Spain*, (2011). <<http://arxiv.org/pdf/1202.0562v1>>.
186. White, G., Schulte, D. & Walker, N. J. in *Proc. 10th European Particle Accelerator Conf., 26-30 June 2006, Edinburgh, Scotland, UK* (2006), 3041–3043. <<http://accelconf.web.cern.ch/accelconf/e06/PAPERS/THPCH104.PDF>>.
187. Schulte, D. *Feedback Studies EUROTeV-Report-2007-065* (CERN, 2007). <http://www.eurotev.org/reports__presentations/eurotev_reports/2007/e1074/EUROTeV-Report-2007-065.pdf>.
188. Seryi, A., Hendrickson, L., Raimondi, P., Raubenheimer, T. O. & Tenenbaum, P. G. in *Proc. XX International Linac Conf., 21-25 August 2000, Monterey, CA, USA* (2000). <<http://www.slac.stanford.edu/cgi-wrap/getdoc/slac-pub-8596.pdf>>.
189. Shiltsev, V. Observations of Random Walk of the Ground in Space and Time. *Phys. Rev. Lett.* **104**, 238501 (2010).
190. Shiltsev, V. Review of observation of ground diffusion in space and in time and fractal model of ground motion. *Phys. Rev. ST Accel. Beams* **13**, 094801 (2010).
191. Snuverink, J. *et al.* in *Proc. 2nd Int. Particle Accelerator Conf., 4-9 September 2011, San Sebastian, Spain* (2011), 1048–1050. <<http://accelconf.web.cern.ch/accelconf/IPAC2011/papers/tupc023.pdf>>.
192. Snuverink, J. *et al.* in *Proc. 1st Int. Particle Accelerator Conf., 23-28 May 2010, Kyoto, Japan* (2010), 3398–3400. <<http://accelconf.web.cern.ch/accelconf/IPAC10/papers/wepe023.pdf>>.
193. Rumolo, G., Latina, A. & Schulte, D. in *Proc. 10th European Particle Accelerator Conf., 26-30 June 2006, Edinburgh, Scotland, UK* (2006), 780–782. <<http://accelconf.web.cern.ch/accelconf/e06/PAPERS/MOPLS096.PDF>>.
194. Resta-Lopez, J. & *et al.* *Current status of the baseline collimation system of the compact linear collider* submitted for publication as a CLIC note.
195. Resta-Lopez, J., Burrows, P. N. & Christian, G. Luminosity Performance Studies of the Compact Linear Collider with Intra-train Feedback System at the Interaction Point. *Journal of Instrumentation* **5**, 09007 (2010).
196. Schulte, D. & Tomas, R. in *Proc. 23rd IEEE Particle Accelerator Conf., 4-8 May 2009, Vancouver, British Columbia, Canada* (2009), 3811–3813. <<http://accelconf.web.cern.ch/AccelConf/PAC2009/papers/th6pfp046.pdf>>.
197. Schulte, D., Wilson, E. J. N. & Zimmermann, F. in *Proc. XXII International Linear Accelerator Conf., 6-20 August, 2004, Lubeck, Germany* (2004), 138–140. <<http://accelconf.web.cern.ch/accelconf/l04/PAPERS/MOP43.PDF>>.
198. Stulle, F. *Beam phase and energy tolerances in the CLIC RTML* CERN-OPEN-2011-048. CLIC-Note-874 (CERN, 2011). <<http://cdsweb.cern.ch/record/1406047/files/CERN-OPEN-2011-048.pdf?subformat=pdfa>>.
199. Jeanneret, J. B. *et al.* in *Proc. 11th European Particle Accelerator Conf., 23-27 June 2008, Genoa, Italy* (2008), 3017–3019. <<http://accelconf.web.cern.ch/AccelConf/e08/papers/thpc018.pdf>>.

REFERENCES

200. Jeanneret, J. B., Rumolo, G. & Schulte, D. in *Proc. 1st Int. Particle Accelerator Conf., 23-28 May 2010, Kyoto, Japan* (2010), 3401–3403. <<http://accelconf.web.cern.ch/accelconf/IPAC10/papers/wepe024.pdf>>.
201. Rumolo, G. in *11th MDI meeting, 19 March, 2010, CERN* (2010). <<http://indico.cern.ch/getFile.py/access?contribId=1&resId=0&materialId=slides&confId=86050>>.
202. Mutzner, R., Rumolo, G., Pieloni, T. & Rivkin, L. *Multi-Bunch effect of resistive wall in the beam delivery system of the Compact Linear Collider* CERN-THESIS-2010-073. CLIC-Note-818 (CERN, 2010). <<http://cdsweb.cern.ch/record/1266868/files/CERN-THESIS-2010-073.pdf>>.
203. Schulte, D. in *Proc. 23rd IEEE Particle Accelerator Conf., 4-8 May 2009, Vancouver, British Columbia, Canada* (2009), 4664–4666. <<http://accelconf.web.cern.ch/accelconf/PAC2009/papers/fr5rfp055.pdf>>.

Chapter 4

Accelerator Physics description of the Drive Beam complex



S. Kimball

4.1 Drive-Beam accelerators

4.1.1 Overview

The two Drive-Beam Accelerators (DBAs) generate the 4.2 A, 142 μ s long drive-beam pulses and accelerate them to a final energy of ~ 2.4 GeV, using normal conducting fully-loaded accelerating structures with an RF frequency of 999.5 MHz. The two DBAs are identical and have a total length of 2.6 km, including injectors and bunch compressors, and provide Drive-Beam pulses for the positron and the electron main linacs. Key design goals of the DBAs are to ensure the high-pulse current, short bunch length and stability of the beam current, energy and phase.

The DBA injectors (DBIs) produce electron beam pulses with a bunch charge of $q_b = 8.4$ nC, an r.m.s. bunch length of about 3 mm and an r.m.s. normalized emittance of 100 μ m and bring them to a beam energy of 50 MeV. The beam pulses are then accelerated to 300 MeV in the first stage of the DBA linacs (DBL1), individual bunches are compressed from 3 mm to 1 mm in a magnetic chicane, and then accelerated to their final energy of 2.4 GeV in the second stage of the DBA linacs (DBL2). The schematic layout of one Drive-Beam accelerator is shown in Fig. 4.1.

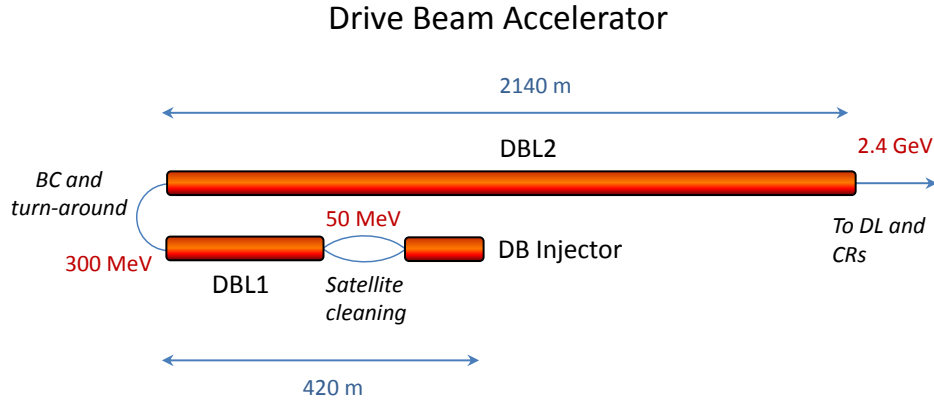


Fig. 4.1: Schematic layout of a Drive-Beam accelerator

Table 4.1 shows the main parameters for the DBA injector and the DBA linac.

4.1.2 System descriptions

4.1.2.1 e^- source and injector

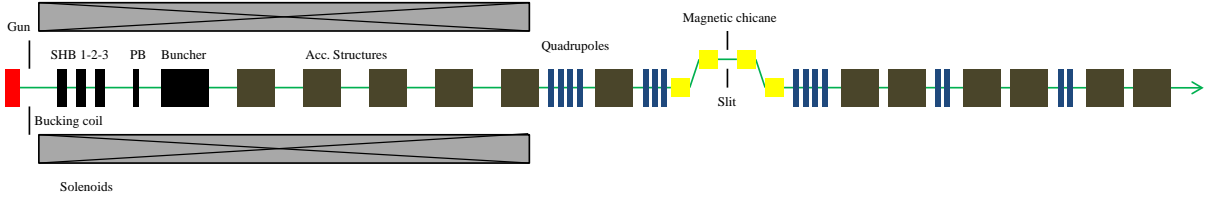
The Drive-Beam pulses are generated by a 140 keV thermionic gun. The gun is followed by a bunching system similar to the one used in CTF3 at CERN [1]. It is composed of three sub-harmonic bunchers (SHB) which operate at a frequency of 499.75 MHz, followed by a pre-buncher (PB) and a travelling-wave buncher, both operating at 999.5 MHz. A schematic layout of the DBI is shown in Fig. 4.2.

Up to the pre-buncher the average beam momentum is 140 keV/c. After the buncher the beam momentum is increased to about 4.2 MeV/c, where the velocity of electrons is sufficiently close to that of light. From then on, 12 units of travelling-wave structures are used to accelerate the beam up to about 50 MeV.

Focusing of the beam is provided by solenoid magnets in the first part of the line, and by quadrupole magnets after the fifth structure, where the beam energy is about 26 MeV. At that point, a magnetic chicane with four dipole magnets and a momentum collimation is used to clean the longitudinal phase space. After the magnetic chicane, six accelerating structures accelerate the beam up to about 50 MeV.

Table 4.1: Main parameters of DBA and DBA injector

Parameter	Symbol	Value	Unit
Injector parameters			
Beam energy	E	50	MeV
Bunch length	σ_b	3	mm
Energy spread r.m.s.	$\Delta E/E$	< 1	%
Normalized transverse emittance	$\gamma\epsilon$	< 100	μm
Drive Beam linac parameters			
RF frequency	f_{RF}	1	GHz
No. of structures in injector	$N_{\text{s.INJ}}$	12	–
No. of structures at DBL1	$N_{\text{s.DBL1}}$	92	–
No. of structures at DBL2	$N_{\text{s.DBL2}}$	715	–
Final beam energy	E_f	2.4	GeV
Bunch charge	q_b	8.4	nC
Initial bunch length	$\sigma_{b,i}$	3	mm
Final bunch length	$\sigma_{b,f}$	1	mm
Bunch separation	Δt_b	0.6	m
Pulse length	τ_{pulse}	142	μs
No. of bunches /pulse	N_b	70882	–
Energy spread	$\Delta E/E_f$	< 0.35	%
Normalized r.m.s. transverse emittance	$\gamma\epsilon$	< 110	μm

**Fig. 4.2:** Layout of the Drive Beam injector.

4.1.2.2 Drive-Beam Linac 1 (DBL1)

The first linac (DBL1) consists of 92 accelerating structure and brings the beam energy to 300 MeV. As will be discussed in §4.1.3.3, each FODO cell in DBL1 holds two accelerating structures for improved beam stability. A strong short-range wakefield, which is introduced by the high bunch charge, tends to create a positive energy chirp. The accelerating structures are operated at the RF phase angle of 27.5° , so as to ensure the energy slope suitable for bunch compression in this condition.

4.1.2.3 Bunch compressor

Four types of preliminary design have been studied for the bunch compressor so far, as discussed in §4.1.3.3. To compensate potentially large phase jitters, a chicane with $R_{56} = -0.1$ m has been chosen. However, this does not accomplish a full bunch compression, leaving some remaining energy chirp. The accelerating phase in the second linac section (DBL2) is such as to compensate the chirp and minimize the final energy spread.

4.1.2.4 Drive-Beam Linac 2 (DBL2)

The second linac (DBL2) consists of 715 accelerating structures and produces a final beam energy of 2.4 GeV. As in DBL1, the optics design of DBL2 adopts a FODO lattice. The RF phases of the cavities have been chosen in accordance with the final energy spread (0.35% or less) that is required for subsequent sections. For improved tunability of the system, each FODO cell contains two accelerating structures from 300 MeV to 1.5 GeV and four accelerating structures from 1.5 GeV to the end. This will reduce the cost and will make the DBL2 shorter.

4.1.3 Accelerator physics issues

4.1.3.1 DBI design and performance

The design of the thermionic gun is very similar to the one used in CTF3 [1]. It produces a continuous e^- beam at 140 keV with an r.m.s. energy spread of 0.16 keV, and transverse normalized emittance not larger than $3.5 \mu\text{m}$. Such beam parameters are identical to the ones at CTF3. The main differences are that CLIC requires a longer pulse ($140 \mu\text{s}$ versus $1.5 \mu\text{s}$) and a higher repetition rate (50 Hz).

The RF frequency of the Drive Beam linacs is 999.5 MHz. Only every second RF bucket is occupied by a bunch. The bunch phase is switched periodically from even to odd buckets to allow subsequent frequency multiplication [2]. In order to achieve this beam time structure, the subharmonic bunching system (SHB), operating at 499.75 MHz, is built such that its RF phase can be switched by 180° in about 5 ns.

All three SHBs are travelling-wave 2-cell structures which are 15.6 cm in length and with an aperture radius of 4.7 cm (subject to reduction, if necessary, keeping 2 cm as a lower limit). The phase velocities and voltages of the SHBs are as shown in Table 4.2.

Table 4.2: Parameters for the SHBs

Buncher	Phase velocity [c]	Voltage [kV]
SHB1	0.93	35.0
SHB2	0.61	36.5
SHB3	0.73	38.8

The pre-buncher consists of a 999.5 MHz, 6 cm long travelling-wave single-cell structure. Realistic parameters from a scaling of the existing CTF3 pre-buncher have been assumed in the simulation. The accelerating gradient is 1.2 MV/m and the beam aperture is 4.7 cm as for the SHB.

After the bunching system, the buncher is used to further reduce the bunch length and accelerate the bunches. The energy spread must also be kept as small as possible. These goals are achieved by using an 18-cell travelling-wave buncher with an increasing phase velocity in the first 12 cells and with phase velocity equal to the speed of light in the last six cells. The accelerating field is 4.2 MV/m in each cell, reducing, if necessary, the beam aperture in the cells which should be larger than 1 cm. The specification of the buncher is given in Table 4.3.

The beam energy at the exit of the buncher is about 4.2 MeV. Following the buncher, 12 units of travelling-wave structures are used to accelerate the beam up to about 50 MeV. The specifications of these structures are given in Table 4.4.

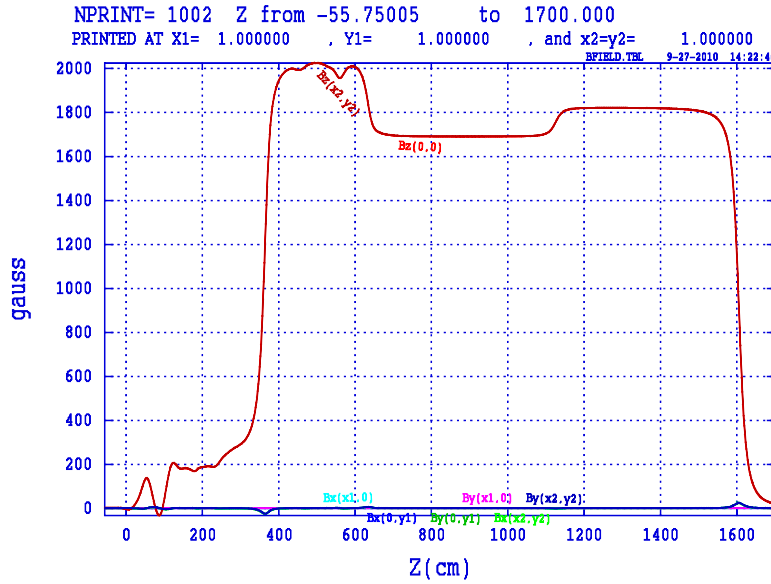
One of the main issues for the design of Drive-Beam accelerators is to limit the growth of the transverse beam emittance in the system, especially in the low-energy part below a few MeV, which can be induced by a strong space-charge force created by the large bunch charge (8.4 nC). For this reason, extensive PARMELA simulations have been carried out to assess the space-charge effect and to optimize

Table 4.3: Parameters for the buncher

Parameter [Units]	Value
Phase velocity [c]	
first 12 cells	0.68–0.99
last 6 cells	1
Phase advance per cell [π]	2/3
Total length [m]	1.681
Accelerating field [MV/m]	4.2
Beam aperture radius [cm]	4.7 (decreasing to keep the field constant)

Table 4.4: Parameters for the accelerating structures

Parameter [Units]	Value
Phase velocity [c]	1
Number of cells	10
Phase advance per cell [π]	2/3
Total length [m]	0.9998
Voltage [MV]	4.8
Beam aperture radius [cm]	4.7 (subject to reduction if necessary)

**Fig. 4.3:** Magnetic field profile inside the solenoids

the solenoidal magnetic field to use for beam focusing. The solenoid coils are placed starting from 50 cm downstream of the gun, producing a magnetic field which increases to about 2 kG at the buncher position, as shown in Fig. 4.2. A bucking coil is placed 10 cm after the gun with a reversed polarity, so that the

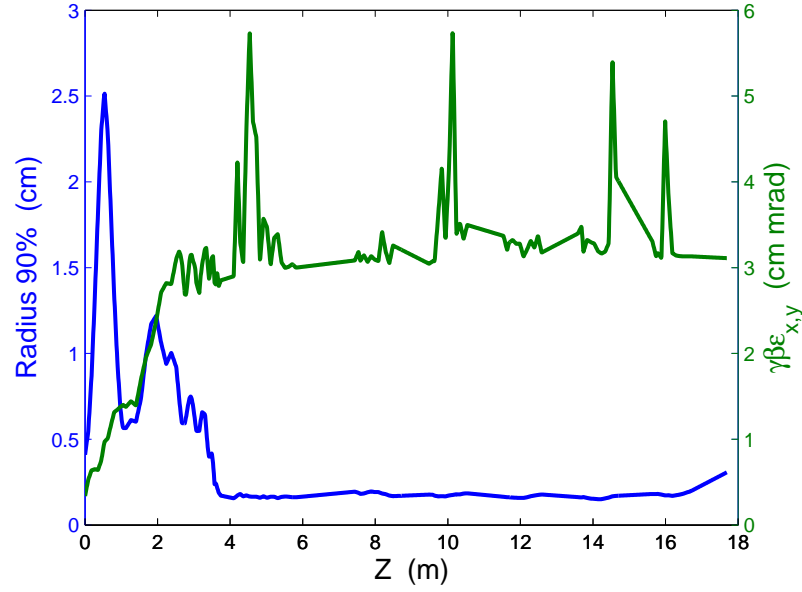


Fig. 4.4: Beam radius and transverse emittance inside the solenoids

gun cathode would not see any magnetic field. Solenoidal focusing is used up to the fifth accelerating structure, where the beam energy is about 26 MeV, thus the space-charge effect is considerably reduced. From then on, the beam focusing is provided by quadrupole magnets. The magnetic field profile inside the solenoids is shown by Fig. 4.3. The profiles of the beam radius and transverse emittance are shown in Fig. 4.4. The final value of the beam emittance in both planes is about $30 \mu\text{m}$, well below the target value of $100 \mu\text{m}$.

According to simulations, at a beam energy of 26 MeV the energy spread is around 2 MeV and the r.m.s. bunch length is about 11 mm. In order to trim the longitudinal phase space, a chicane is introduced for momentum collimation. The chicane is composed of four 15 cm-long rectangular dipole magnets, spaced by 50 cm, each providing a bending angle of 14.3° . This chicane creates an R_{56} parameter of 78 mm. The dispersion in the mid-point of the chicane is 16 cm and a horizontal slit with an aperture of 0.7 cm will be placed. This provides a momentum collimation of 1 MeV. The simulations have shown that up to 24% of the beam current is dumped at the chicane. This corresponds to a power of about 180 kW, which is considered technically feasible and acceptable. However, further optimization of the bunching system will be pursued for simplified design and reduced radioactivity in operation. In addition, accelerating structures upstream of the chicane will be operated off-crest so as to take advantage of the magnetic bunching and to further reduce the bunch length.

After the magnetic chicane, six more accelerating structures will accelerate the beam up to 50 MeV which is the final energy of the injector. Simulations have been performed assuming an intensity of 6 A produced by the gun during the pulse. The relevant beam parameters at 50 MeV are shown in Table 4.5.

4.1.3.2 *Satellite bunches and cleaning system*

Table 4.5 indicates that about 4.9% of the beam power is contained in so-called satellite bunches which adversely affect the system power efficiency and increase the hardware activation due to radiation. Figure 4.5 illustrates a proposed scheme for eliminating the satellite bunches in an early part of the Drive-Beam system. It is based on the use of two units of 1 GHz RF deflectors and fast kickers. With the beam

Table 4.5: Beam parameters at the end of the injector

Parameter [units]	Value
Energy [MeV]	50
Bunch charge [nC]	8.4
Bunch length (r.m.s.) [mm]	2.83
Energy spread (r.m.s.) [MeV]	0.45
Horizontal norm. emittance (r.m.s.) [μm]	32.9
Vertical norm. emittance (r.m.s.) [μm]	28.7
Satellites [%]	4.9

energy of approximately 50 MeV, the satellite power to be dumped would be about 70 kW.

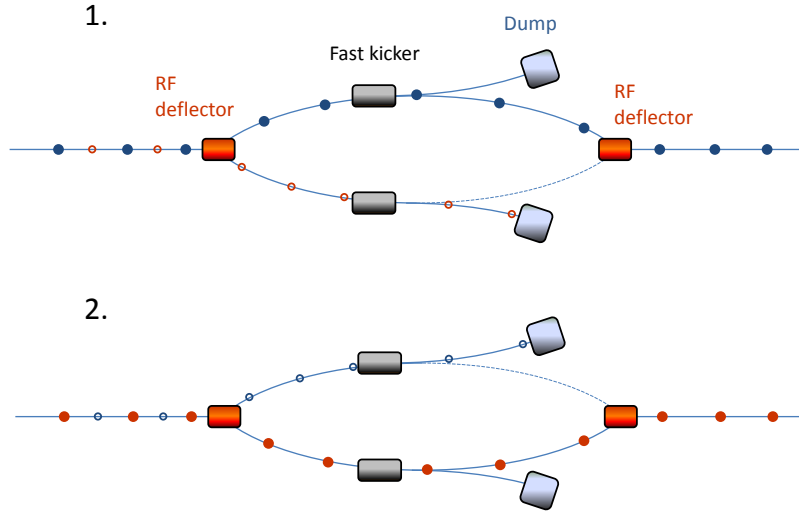


Fig. 4.5: Schematic layout of the satellite cleaning system. The main (solid dots) and satellite bunches (empty dots) are separated in two beamlines using an RF deflector. Every 244 ns, the bunch phase switches by 180° and satellite bunches are alternately sent to one line (1) or the other (2). Two fast kickers, alternately fired every 140 ns, are then used to send the unwanted satellite bunches into a dump. A second RF deflector, at a 180° betatron phase advance, is used to cancel the kick from the first one, recombining the orbits of the main bunch pulses.

4.1.3.3 Optics of the Drive-Beam Linacs

The Drive-Beam pulse consists of 24 short trains of about 2928 bunches each having a charge of $q_b = 8.4$ nC. The bunches alternate between odd and even buckets every 244 ns.

At the entrance of the PETS the specified bunch length is 1 mm r.m.s. with a tolerance of 1%. The tolerance for the bunch phase error here is $\sigma_{\Delta\phi} = 0.2^\circ$ at 1 GHz ($\sigma_{\Delta z} = 175 \mu\text{m}$) [3]. Within DBL1, which accelerates the beam to 300 MeV, the bunch length is compressed from 3 mm to 1 mm. Then the DBL2 brings the beam to its final energy of 2.4 GeV (see Fig. 4.1). In order to minimize the final bunch phase

4.1 DRIVE-BEAM ACCELERATORS

jitter caused by the energy jitter, a strong energy chirp created in DBL1 and a low R_{56} in the chicane are utilized. In DBL2, the large beam energy spread will be reduced to levels which are acceptable in the Drive-Beam decelerator. The beam is accelerated in DBL1 with an RF phase of 27.5° and in DBL2 with an RF phase of 18° , limiting the final energy spread to below 0.35%. The phases results in an average gradient reduction of about 5.5%.

The short-range wakefield structure used in simulations has been calculated using the method of Ref. [4], and compared with results from the ABCI code [5]. The long-range wakefield of the structure has been calculated from scaling of the 3 GHz CTF3 SICA structure [6].

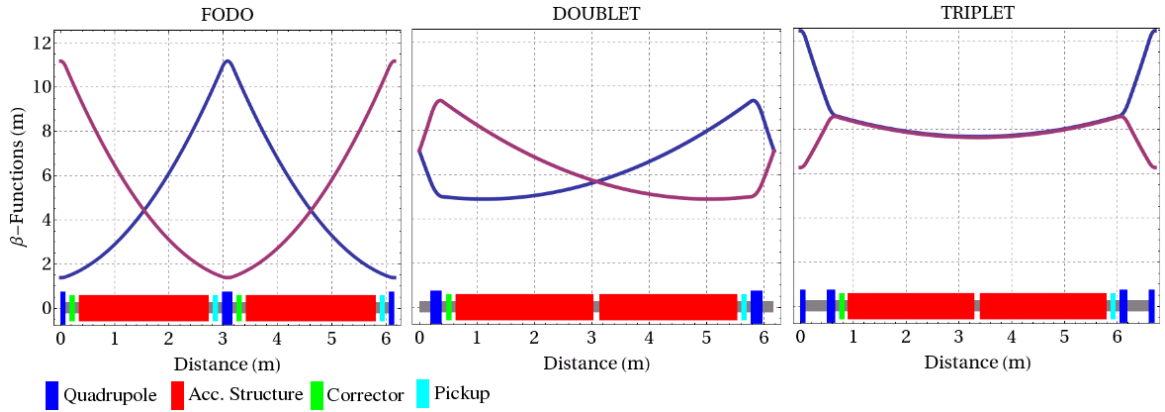


Fig. 4.6: Sketch of single-cell lattices used in calculations

Three types of lattice, based on FODO, doublet, and triplet, have been compared. All lattices contain two accelerating structures per cell and have roughly the same length. A strong focusing lattice will prevent a large amplification of any jitter of the incoming beam. However, it was found that obtaining small β -functions at high beam energy, particularly in the triplet lattice, requires a quadrupole field of 1 T which exceeds the reach of normal-conducting magnet technologies. A sketch of the lattices is shown in Fig. 4.6.

Since no estimate of the transverse jitter of the incoming beam has yet been worked out, only the jitter amplification is calculated. In the simulation, each bunch is cut into slices; the beam is set to an offset and tracked through the linac. The plots in Fig. 4.7 show the offsets of the beams in phase space at the end of the linac. To quantify the effect, an amplification factor, A , is defined as [7]:

$$A = \frac{\sigma_{x,0}}{\Delta x} \sqrt{\left(\frac{x_f}{\sigma_{x,f}}\right)^2 + \left(\frac{x'_f}{\sigma'_{x,f}}\right)^2} \quad (4.1)$$

where:

- $\sigma_{x,0}$ is the initial beam size,
- $\sigma_{x,f}$ is the final beam size,
- $\sigma'_{x,0}$ is the initial beam divergence,
- $\sigma'_{x,f}$ is the final beam divergence,
- Δx is the initial beam offset,

x_f is the final position of the slice,
 x'_f is the angle of the slice.

For a slice with nominal energy and without wakefield effects, $A = 1$.

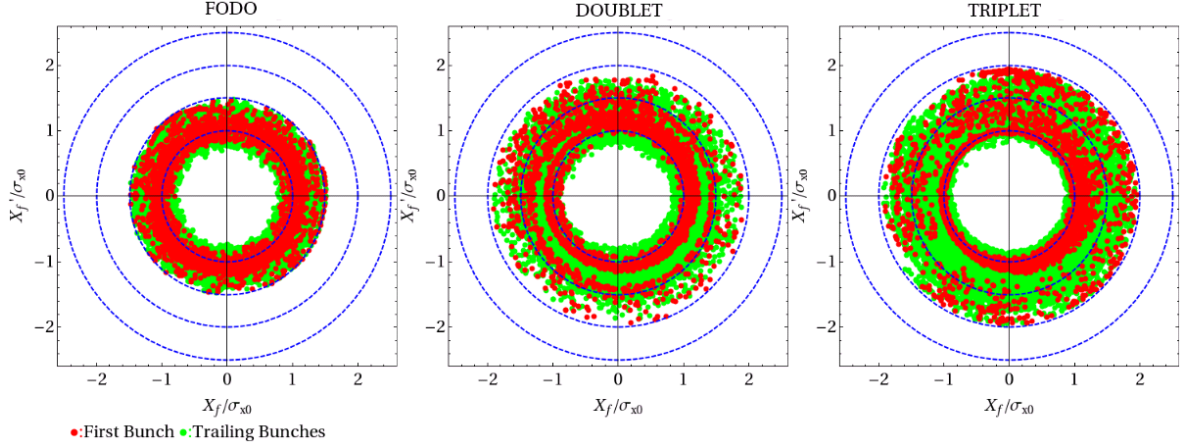


Fig. 4.7: The amplification factor of the beam at the end of the Drive-Beam accelerator for different type of lattices. The acceptable value of amplification would be less than 1.5.

For point-like bunches the offsets can be computed analytically [8]. However, since they lack energy spread, damping effects are ignored and the motion will be coherent, and as a result the amplification will be larger. Figure 4.8 shows the normalized amplitudes for the bunches at the end of the DBA, assuming an initial offset of the incoming train (with constant bunch charge).

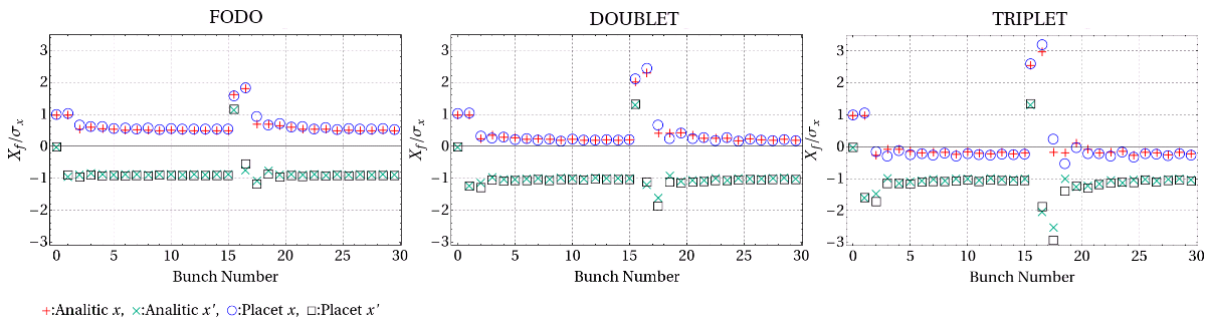


Fig. 4.8: Normalized amplitudes for the bunches at the end of the DBA in the case of an initial offset and point like bunches, for the different lattice types. Analytical computations were verified by numerical simulations done using the code PLACET.

In order to keep a constant beam current and constant beam loading, two bunches at overlapping points should have their charges halved. The normalized amplification, computed for a FODO lattice in

such cases, is given in Fig. 4.9. As can be seen in the figure the amplification on overlapping points is smaller for a ramped bunch charge.

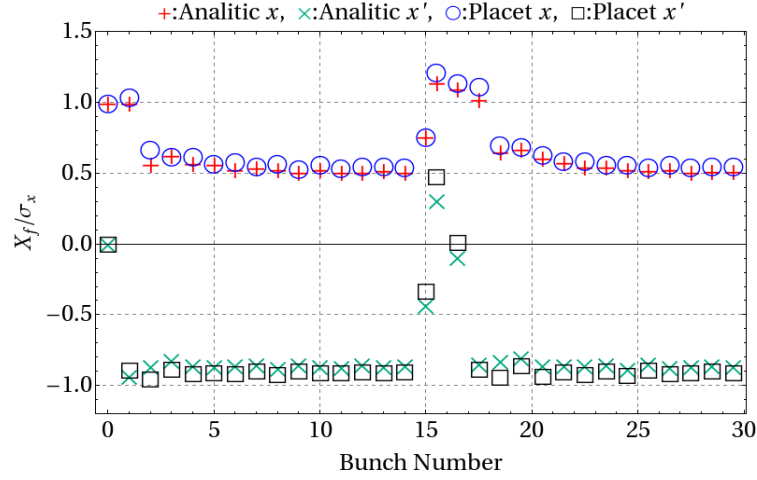


Fig. 4.9: Normalized amplitudes for the bunches at the end of the DBA in the case of an initial offset and point-like bunches, ramped charge, for a FODO cell. Analytical computations were verified by numerical simulations done using the PLACET code.

Alignment issues have been studied by conducting a simulation where all elements are assumed to have random misalignment with a normal distribution of $\sigma = 200 \mu\text{m}$ and $\sigma' = 200 \mu\text{rad}$. Each quadrupole magnet is assumed to be equipped with a beam position monitor (BPM) for all lattice types. Beams with nominal and offset energies were tracked to simulate dispersion correction and orbit correction. Figure 4.10 shows the emittance growth along the beamline throughout DBA1 and DBA2. For each of the three lattice types, 100 random number seeds were tried. For simplicity's sake the trajectory in the bunch compressor section of the beamline is assumed to be perfect. It was found that with the FODO and triplet lattice types the emittance growth is quite small, while with the doublet the growth rate exceeds 10%.

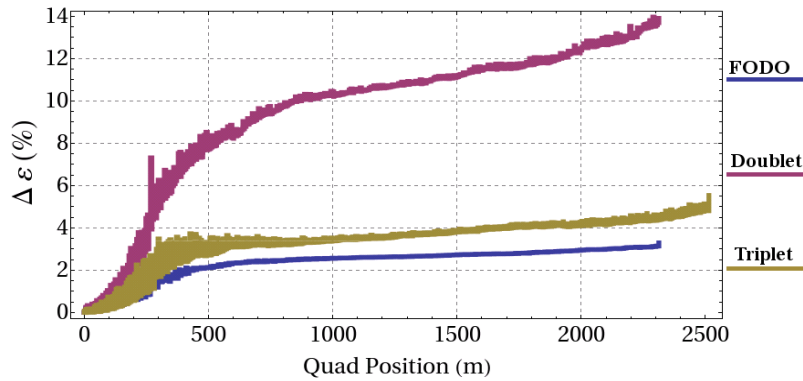


Fig. 4.10: Emittance growth along the beamline for FODO, doublet, and triplet lattices. The bunch compressor section is assumed to be perfectly aligned.

The simulation study above indicates that the FODO lattice offers the best solution in terms of the transverse amplification and emittance growth. The FODO lattice has the additional advantages of lower cost and simpler operation. Correction of static errors in the beamline will also be easier for the FODO lattice than for a triplet lattice. It should be possible to obtain better results for a triplet lattice with a shorter cell length, i.e., using a single accelerating structure per cell. However, this latter approach would dramatically increase the cost.

To the first order approximation, the phase error ($\delta\sigma\Phi$) or the bunch length error ($\delta\sigma$) expected after a magnetic chicane would be proportional to the energy jitter. Errors in quantities such as charge (δQ), phase ($\delta\sigma_{in}$) and energy (δE_{in}) of the incoming bunches, or in RF phase ($\delta\Phi_{RF}$) and gradient (δG) in the linac, can cause an energy jitter. The bunch compressor should compensate potentially large errors in these quantities as well as errors which are caused by beam loading. Currently we are looking into the single bunch case and have studied four types of compressor in order to define the longitudinal tolerances. Figures 4.11-4.12 show the phase shift and the variation of the bunch length after the chicane as a function of various types of initial errors.

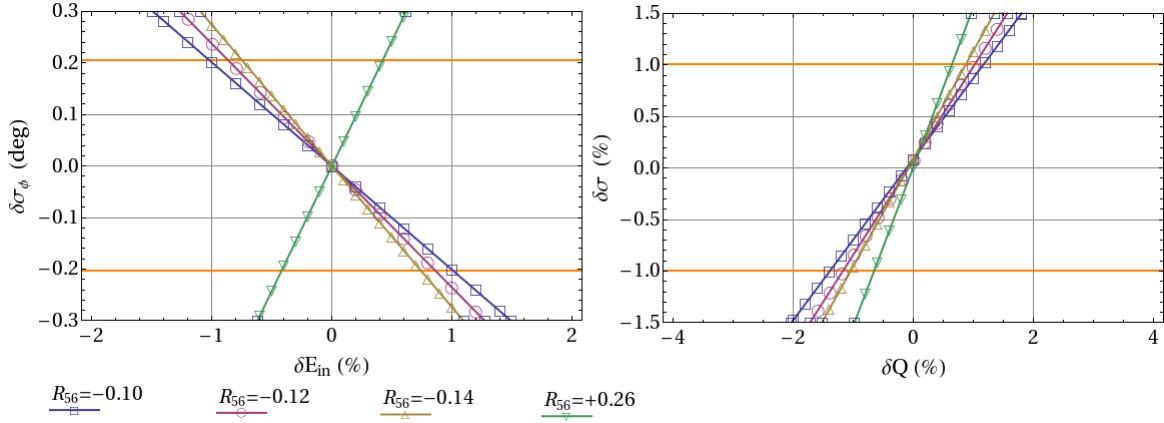


Fig. 4.11: Phase shift after the chicane vs. incoming bunch phase error (left) and bunch lengthening error vs. incoming bunch charge error (right). Orange lines show acceptable tolerances.

As can be seen from the figures above, large longitudinal errors can be compensated by the chicane with $R_{56} = -0.1$ m. However, the lower R_{56} of this compressor implies a larger effective gradient reduction compared to the compressor with $R_{56} = +0.26$ m which allows a more efficient use of the RF. The tolerances of DBA1 are summarized in Table 4.6.

Table 4.6: RF tolerances of DBL1

Parameter [Units]	Symbol	Value
RF power error [%]	δG	0.2
Beam current error [%]	δQ	0.1
RF phase error [$^\circ$]	$\delta\Phi_{RF}$	0.05

4.1 DRIVE-BEAM ACCELERATORS

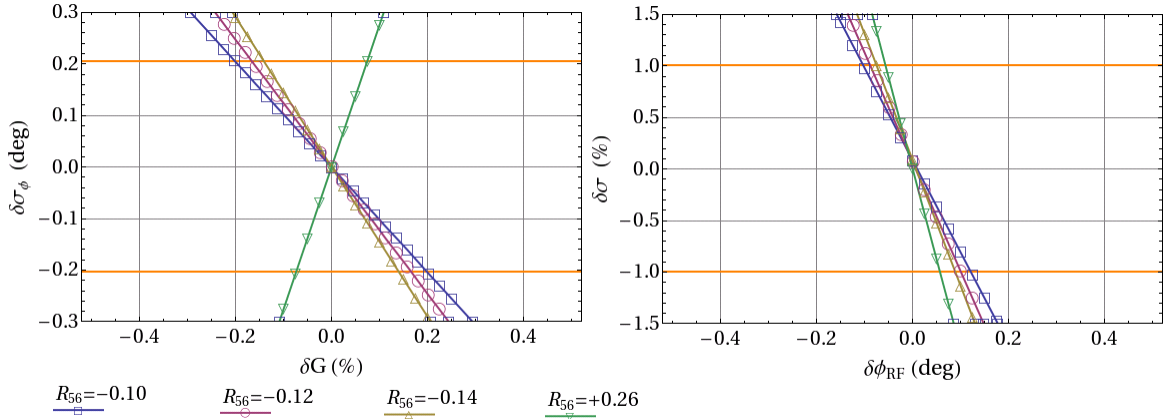


Fig. 4.12: Phase shift after the chicane vs. gradient error in linac (left) and bunch lengthening error vs. RF phase error in linac (right). Orange lines show acceptable tolerances.

4.1.4 Component specifications

4.1.4.1 Accelerating structures

The Drive Beam Accelerator (DBA) and injector for each Drive-Beam linac will consist of 819 identical travelling-wave accelerating structures to accelerate the beams to 2.4 GeV. Structures, operating at a frequency of 999.5 MHz, are composed of 21 cells, with a $2\pi/3$ phase advance per cell, giving a total structure length of 2.3 m. A klystron will feed 142 μ s long pulses of 15 MW into each structure, and 95% of this power is transferred into the 4.2 A beam due to fully beam-loaded operation.

4.1.4.2 Klystrons

The Drive-Beam linac complex has 1638 klystrons, operating at 999.5 MHz, each driven by individual pulse modulators. The klystrons should provide 140 μ s long pulses of 15 MW at a repetition rate of 50 Hz. Stringent requirements are placed on phase and power stability for klystrons in DBL1, of 0.05° and 0.2%, respectively (see Table 4.6).

4.1.4.3 Modulators

Each klystron requires a 150 kV pulse for 150 ms at a repetition rate of 50 Hz. This means an average power of 200 kW per modulator (considering the klystron efficiency and losses). The required reproducibility of the peak pulse amplitude is about 10^{-5} (in a frequency range between 6 kHz and 4 MHz). At lower frequencies, the RF feedback compensates the drift with systematic error feed-forward and RF feedback. Higher frequencies are naturally filtered by the machine

4.1.5 Magnets

The Drive-Beam linac has 1638 quadrupole magnets, i.e., one per klystron. Optics requirements impose a linear profile of the quadrupole strength along the linac, following the beam energy increase. Instead of individually powering each magnet, a powering strategy based on the use of several main converters has been adopted. Each one feeds a long string of magnets (between 30 and 60 units). The desired current slope is then obtained by active dissipative trimmers. This implies the use of a very small number of cables and a reduction in the number of bulky converters. For FODO (baseline) and doublet lattice types

the quadrupoles are assumed to have 20 cm effective length with 50 mm aperture. For the triplet, two types of quadrupole are needed with effective lengths of 22 cm and 16 cm. For all lattices the maximum field gradient is 23 T/m.

4.2 Drive-Beam Recombination Complex

4.2.1 Introduction

The Drive-Beam is accelerated to 2.37 GeV by the normal conducting 999.5 MHz linac (see §4.1) after which the Drive-Beam Recombination Complex (DBRC) compresses the bunch trains and raises its average current up to 100 A over the pulse. CLIC deploys three recombination stages: a Delay Line (DL) for the first factor of two, the first Combiner Ring (CR1) for a factor of three, and the second one (CR2) for the last factor of four. The beam injection into and extraction from the DL and CRs are accomplished by using RF deflectors. The beam from CR2 is then transported through a Long Turnaround (LTA) up to the sequential Turnarounds (TAs), which inject the beam into decelerating sections.

The DBRC at CLIC is designed to best preserve the transverse and longitudinal beam emittances. Additional design considerations include isochronicity, smooth linear optics, vacuum chambers with low impedance, beam diagnostics, and HOM-free active RF elements. The feasibility of bunch recombination has been successfully demonstrated at CTF3 (see Chapter 7 for details) with a low energy beam (120 MeV) and a compressed beam current up to 28 A (140 ns). The CLIC DBRC design represents a technically sound extrapolation which incorporates CTF3's operational experience and results. Table 4.7 summarizes the parameters of the CLIC Drive-Beam compared to those at CTF3.

Table 4.7: the main CLIC Drive-Beam parameters after recombination compared to those of CTF3

Parameter [units]	CTF3 (design)	CTF3 (obtained)	CLIC
Energy, $E_{\text{in,dec}}$ [GeV]	0.150	0.10–0.12	2.37
Average pulse current, I_{dec} [A]	35	28	100
Train duration, τ_{train} [ns]	140	140	244
No. bunches / train, N_b	1600	1600	2922
Bunch charge, Q_b [nC]	3	3	8.4
Bunch separation, Δ_b [ns]	0.083	0.083	0.083
r.m.s. bunch length, σ_s [mm]	1	1	1
Max. energy spread, $\Delta E/E$	0.01	0.015	0.01
r.m.s emittance, $\gamma\epsilon$ [μm]	100	80	150

4.2.2 DBRC design criteria

The DBRC transports the DBA beam up to the decelerator. The high efficiency for RF power extraction which is required at CLIC poses a major demand on the temporal and spatial structure of the Drive-Beam. Preservation of longitudinal and transverse emittances must be assured along the whole DBRC: the allowance in the growth of transverse emittance is defined by the ratio between the decelerator acceptance (150 μm [9]) and the DBA beam emittance. The tolerance in isochronicity is $R_{56} < \pm 1$ cm. To ensure the required operational performance, devices for controlling the beam trajectory and tuning, together with frequency structure, will be implemented throughout the beamline.

An isochronous cell structure, based on three dipoles and two symmetric quadrupole triplets, as inherited from CTF3, is employed in the design of the combiner rings at CLIC. The range of tunability of such a cell, with three independent quadrupole families, has been tested at CTF3. Figure 4.13 shows an example of the optical functions in one arc.

The beam energy spread, combined with chromaticity in the beamline, is a main source of single-bunch emittance growth. The relatively high natural energy spread of the Drive Beam ($\sim 2\%$ total) emanates from the fully beam-loaded linac, in which any beam current variation translates into energy variation.

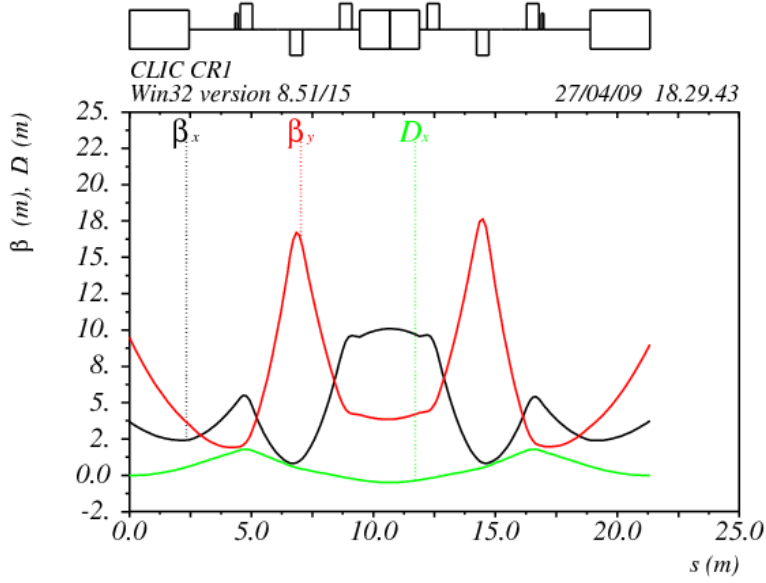


Fig. 4.13: Optical functions of a CTF3-type isochronous cell in CR1

The transverse and longitudinal chromaticity must be corrected simultaneously in order to ensure preservation of beam emittances in all dimensions in the phase space. A low dispersion function helps keep low values for the second order term T_{566} , which relates the bunch length to energy spread. This can be achieved with the isochronous arcs above mentioned. However, the sextupole magnets that are used to zero the T_{566} will increase other second order terms T_{16n} and T_{26n} , where $n = 1-6$. They relate the horizontal motions of the beam particles to the energy spread, thus presenting a challenge in preservation of the horizontal emittance. The increase in horizontal emittance then translates, through the terms T_{51n} and T_{52n} ($n = 1-6$), into an effective loss of the isochronicity.

Any phenomenon which increases the beam energy spread should, therefore, be avoided or be minimized. Incoherent synchrotron radiation will add an energy spread along the train due to different paths followed by successive bunches. The bending radii in all the rings are, therefore, optimized by taking into account the induced energy spread under perceived space constraints.

Recently a new isochronous cell, a Chasman–Green cell, has been proposed [10]: it is rendered isochronous by a short dipole magnet with a negative bending radius in its centre, where the dispersion is high. This solution has the advantage of not requiring a strong horizontal focusing, and therefore offers a much larger natural energy acceptance. Figure 4.14 shows an example of such a cell. This cell has been adopted in the latest design of the CLIC DL and the connecting transfer lines. It is expected to address the issue which was encountered at the DL of CTF3 with an earlier cell design, which had a shorter length and a larger bending angle, leading to a poor energy acceptance.

Another source of emittance growth is the non-achromaticity associated with the injection bump. In CTF3 the residual dispersion for bunches, which pass off-axis in the quadrupoles inside the injection bump, has been observed. The design of the injection section of CLIC CRs is based on a bump offset of 2–3 cm, as determined by the maximum kick (a few mrad) that is available from the RF kicker, together with the relatively low beta value there. After the bump the dispersion must be brought down to the level of the natural dispersion, i.e., $D_x \sim \pm 0.05$ m and $D'_x \sim \pm 0.01$. Solutions of achromatic injection bumps have been developed for CLIC, optimized in accordance with different recombination factors of the two CRs.

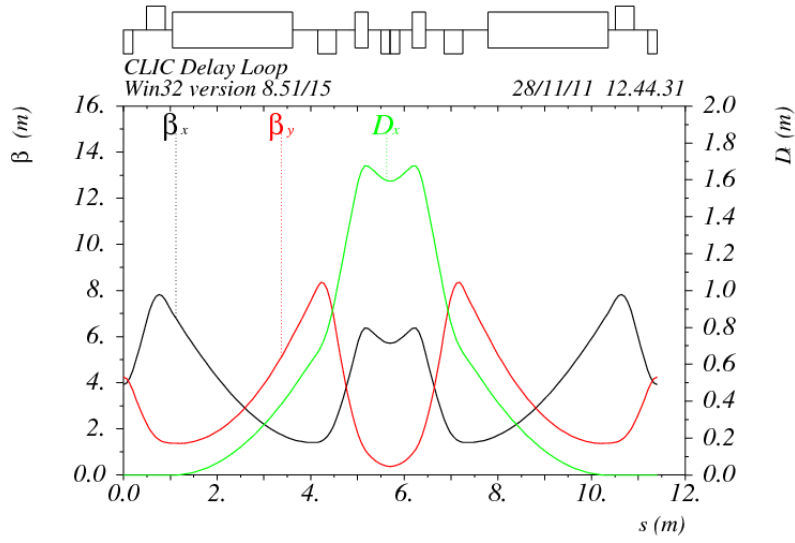


Fig. 4.14: Optical functions of a Chasman–Green type cell which has been adopted for the DL and transfer lines at CLIC.

When designing the CLIC recombination system special care has been put into maintaining low chromaticity optics. This is also based on CTF3 operation experience, where, for easing the commissioning and for reducing the sensitivity to mismatch and errors, the CR is currently operated with a tune value which is less by one unit than the original design optics.

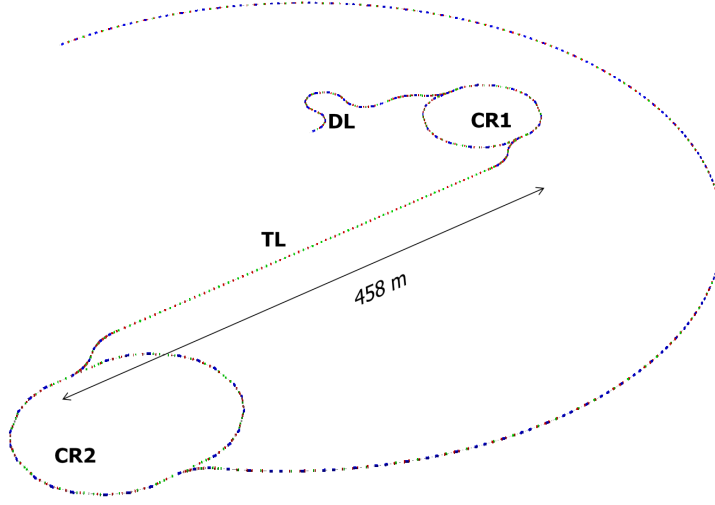
Coherent synchrotron radiation (CSR) is a source of an energy loss and increase in energy spread, which lead to an increase in the transverse beam emittance. Fortunately, however, the CLIC Drive Beam is less sensitive to effects of CSR than in the case with CTF3, thanks to the higher beam energy. In CTF3 the CSR effects are rendered negligible when the bunch length is stretched in the chicane before the DL up to 2 mm, as detailed in §4.2.6. The same method can be applied to CLIC. Simulations of the effects in the DL, where the dipole bending radius is shorter, have been carried out, and the results are summarized in §4.2.6.

4.2.3 Isochronous rings

The beamline lengths of the DBRC are determined by the temporal structure of the Drive Beam. The DL length (L_{DL}) is determined by the final bunch train duration ($L_{train} = 73.168 \text{ m} \approx 73 \text{ m}$), and by the length of the bypass (L_{bypass}). The design has with a small correction for the interleaving of the trains $L_{bypass} = L_{train}$, corresponding to $L_{DL} = 2L_{train}$. The lengths of CR1 and CR2 have to be multiples of the train length ($L_{CR1} = 4L_{train}$, $L_{CR2} = 6L_{train}$). Table 4.8 summarizes the main parameters of the beamline elements within the CLIC DBRC. The bunch length of the beam from DBA is 1 mm. It is stretched to 2 mm before entering the DBRC for mitigating collective effects driven by high peak currents. A chicane is used in the injection transfer line to serve as a bunch stretcher, as in the CTF3 system, so that the bunch length can be adjusted for minimizing the CSR effects. Out of the DBRC, the bunch length will be compressed, again, to 1 mm as it enters the Drive Beam decelerating section.

The geometrical layout of the complete DBRC, including the Long Turnaround (LTA), which shares the tunnel with the Main Beam Injector, is shown in Fig. 4.15. All the magnets are based on the normal conducting technology. The optics design is devised to allow a large range of tunability in transverse phase advances, essential for optimizing the system operation, as repeatedly witnessed at

CTF3.

**Fig. 4.15:** Schematic layout of the DBRC**Table 4.8:** CLIC DBRC main parameters

Parameter [units]	DL	CR1	CR2	LTA	TA
Emittance [μm]	150	150	150	150	150
Energy spread [%]	1	1	1	1	1
Bunch length [mm]	2	2	2	2	2
L [m]	146	293	439	1200	162
Combination factor	2	3	4	–	–
Final bunch distance [cm]	30	10	2.5	2.5	2.5
Final average current [A]	8.4	25	100	100	100
RF deflector freq. [GHz]	1.5	2	3	–	–
No. of dipoles	22/24	18	24	114	3 + 12
Dipole ρ [m]	6.9	8	9	57	5
Angle [$^\circ$]	21.32/2.37	20	15	2	20

The DL is a single-pass beamline which is traversed by odd-numbered trains. The even-numbered trains, on the other hand, will go through a bypass line which has a path length half that of the DL. As mentioned earlier, a new optical design based on the Chasman–Green isochronous cell is deployed in the CLIC DL, where a major improvement in the energy acceptance is expected, compared to the CTF3 case. This new cell design also allows a higher filling factor for the dipole magnets. Consequently, the bending radius has been increased from 4.7 m [11] to 7 m, helping to reduce the effects of the CSR.

The RF deflector of the DL operates at 1.5 GHz and will kick the beam by 5 mrad. In order to relax the design and operational parameters of septum magnets, a defocusing quadrupole is placed between the deflector and the septum. This quadrupole magnet acts on both the incoming and the outgoing beams thus increasing their relative separation at the location of septa. Figure 4.16 shows the optical functions of the DL, where the injection and extraction points are located in the first and last isochronous cells with slightly modified optical functions.

The CR1 consists of six isochronous arcs: two long opposite straight sections for injection and

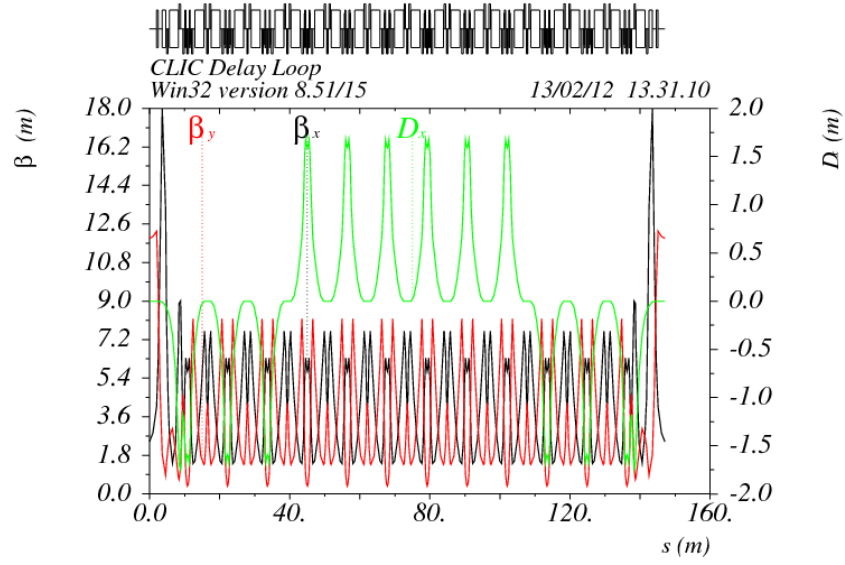


Fig. 4.16: Optical functions of the delay loop

extraction, and four short straight sections. Two of the short straight sections incorporate wigglers for tuning the path length. The CR2 has a similar structure. However, the CR2 is a ring where the bunches travel longer and it includes eight isochronous arcs. The CR2 adopts a longer bending radius which reduces the energy spread among bunches following different recombination arcs. Figures 4.17 and 4.18 show the optical functions of the CR1 and CR2, respectively.

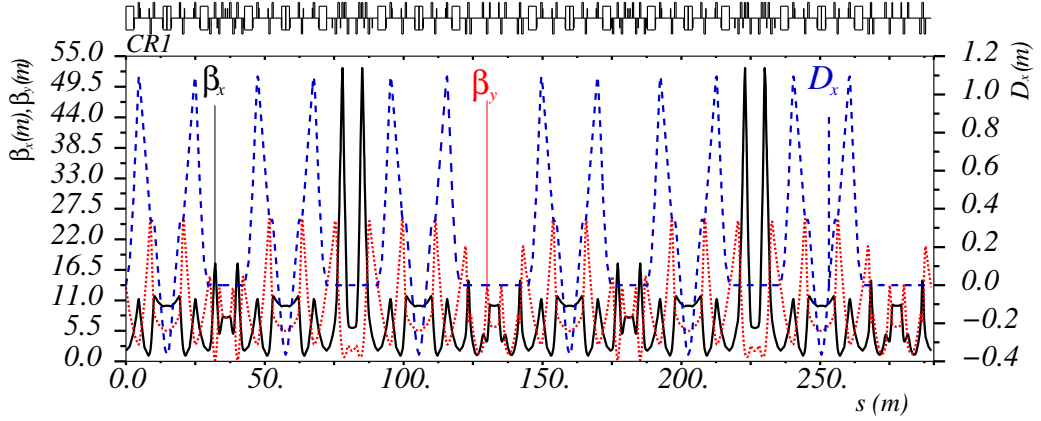


Fig. 4.17: Optical functions of the CR1

The injection bumps with the RF kicker are, by definition, not achromatic. The schemes of dispersion correction are different for the CR1 and CR2, as dictated by their different recombination factors. At the CR1, with a recombination factor of three, the correction can be achieved by using four additional static orbit correctors around each of the four 2 GHz RF deflectors, as shown in Fig. 4.19. This is because the bunches in the second and in the third turns receive kicks with the same value. The injected train is put on the ring's closed orbit with the help of both the RF deflectors and the correctors (Fig. 4.19(a)), while the trains already circulating in the ring follow the closed bump created by the correctors (Fig. 4.19(b)). At the CR2 with a combination factor of four, a static correction scheme cannot be applied, since the orbit bump in the third turn is different from that of the second and the fourth. Instead, two families of sextupole magnets are introduced to close the dispersion for all turns (Fig. 4.20).

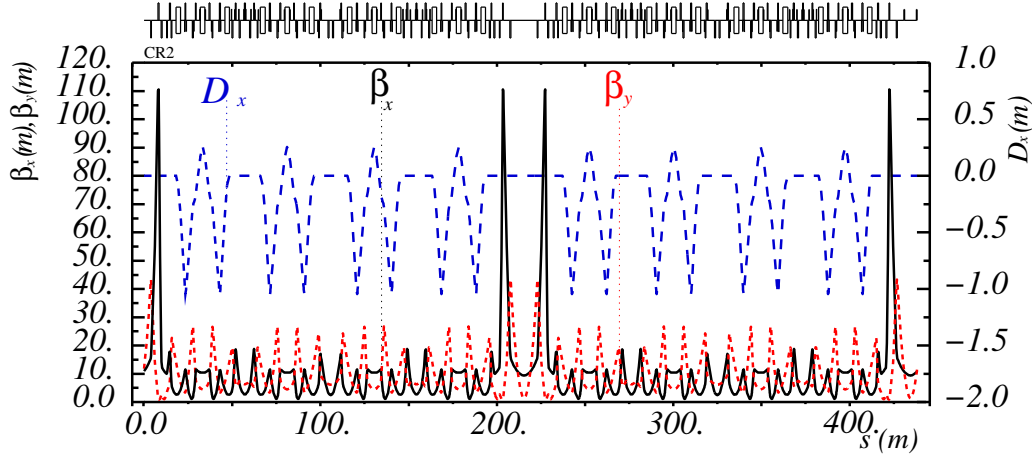


Fig. 4.18: Optical functions of the CR2

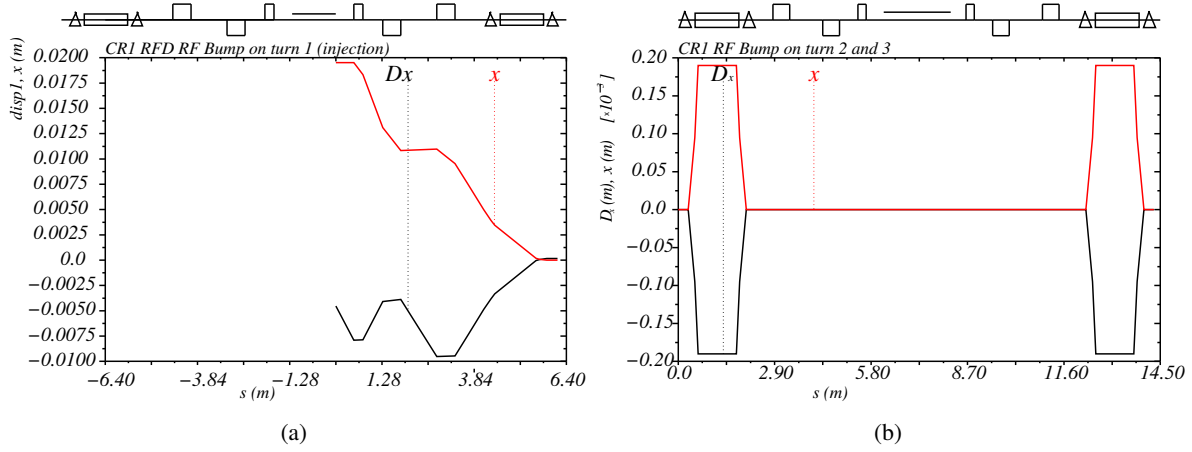


Fig. 4.19: CR1 achromatic injection bump trajectory and dispersion at injection (a) and at second and third turn (b). Rectangles centred around the line represent the RF deflectors, triangles – the magnetic correctors, the remaining rectangles – the quadrupoles, and the line above is the septum.

The beam injection into and extraction from the three rings is done through DC septa magnets placed in the straight sections. The lattices of these sections have been designed to reduce the required deflection angle. Magnets similar to the CTF3 septa can be used, in spite of the higher energy, creating a deflection angle of 25 mrad, with a septum thickness of 12 mm, a magnetic length of 650 mm, and a current of 2000 A. A longer magnet, with less stringent parameters, follows this septa and guides the beam into the nominal trajectory.

The Long Turnaround (LTA) arcs, which transport the recombined Drive-Beam up to the decelerator, have a total length of 1216 m. The CTF3-style isochronous cell with a long bending radius is adopted. The total bending angle of LTA is 228°. Figure 4.21 shows the optical functions of one LTA cell.

The Turnarounds (TAs) are located approximately every 800 m along the Main Linacs. Each TA features a feed-forward control of the beam phase, with its own phase monitor, as described in §5.15. While the beamline is isochronous, two chicanes are placed before and after the phase-controlling RF. The chicanes have a non-vanishing net R_{56} , and they are used for compressing the bunch length before the beams enter the decelerators. The layout of one TA and its optical functions are shown in Fig. 4.22.

The beam energy loss due to synchrotron radiation per 2π bending is $U_0(\text{MeV}) = 2.8/\rho(\text{m})$ for

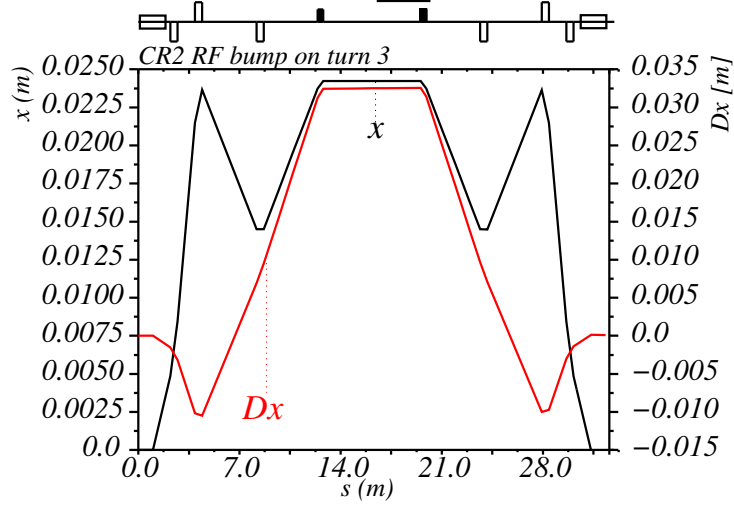


Fig. 4.20: CR2 achromatic injection bump trajectory and dispersion at the third turn. Rectangles centred around the horizontal line represent the RF deflectors, other empty rectangles represent the quadrupoles, filled rectangles represent the sextupoles and the line above is the septum.

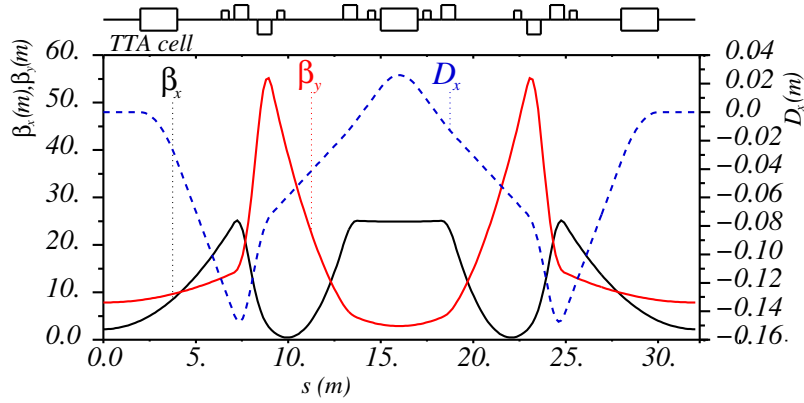


Fig. 4.21: Optical functions of the LTA cell. The LTA is composed of 28 such cells.

the nominal beam energy, where ρ is the dipole bending radius. Considering the different bending radius along the system and the different paths that each bunch will follow, the difference in energy loss between the bunches with the longest and the shortest path in the whole DBRC is $\Delta U = 2.2 \text{ MeV} (0.09\%)$, within the acceptance of the system.

4.2.4 Single particle dynamics

The most critical issue from the single particle dynamics point of view is the energy acceptance. Isochronicity implies relatively strong focusing. Consequently, non-linearities of the optical functions are very pronounced. Figure 4.23 shows an example from the CR1. The effects can lead to unacceptable emittance growth in all three planes. The lattice must be designed to mitigate them. First, keeping the low dispersion function helps reduce the strength of beam focusing. This is obtained with the isochronous arc, as described in the previous section. In addition, three or four families of sextupole magnets are used for further mitigation of non-linear effects. To preserve the dynamic aperture the phase advance in between cells must be carefully chosen so that the unwanted effects from sextupoles are cancelled out locally [12]. For example, the straight sections in between cells of the CR1 arc, which is made of three cells, are matched to deliver in both planes close to $4/3 \times 2\pi$ phase advance from cell to cell. For the same reason

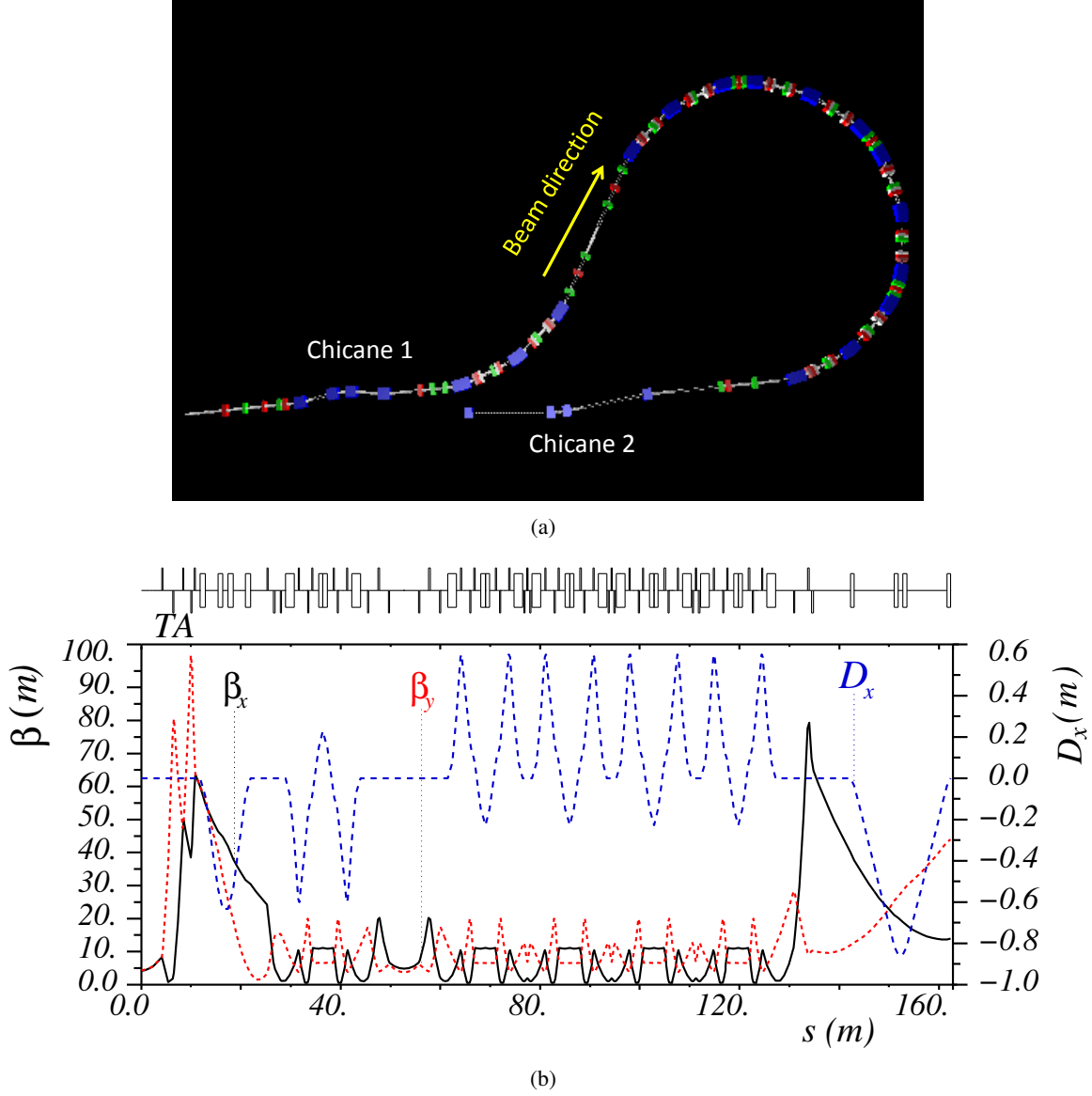


Fig. 4.22: Layout and optical functions of TAs

they contain harmonic sextupoles. The strengths of the sextupole magnets are adjusted to minimize T_{566} , non-linear terms up to third order in $\delta p/p$ of the horizontal dispersion and chromaticities. It is very difficult to find a design which results in all the above quantities being zero and a compromise solution needs to be found that adequately distributes the emittance growth among the planes. For that purpose the second order moments of the assumed input distribution are computed [13] and used as additional constraints in the optimization. Figure 4.23(b) demonstrates the result of such a correction, as obtained from calculations with the PTC [14] module of the MAD-X [15] program.

The lattice fulfils the requirements of preserving the bunch length and it delivers a recombined beam with emittances below 150 mm mrad, if the energy spread is kept smaller than $\pm 1\%$. For the momentum distribution obtained from the Drive-Beam accelerator simulations the r.m.s. bunch length increases by 1.3%, see Fig. 4.24(b). This corresponds to the fully recombined beam that is simulated by performing the tracking for all 24 pathways through DBRC and adding the obtained distributions. Figure 4.24(a) compares the distributions in the longitudinal phase space before and after DBRC. The effect of not entirely zeroed T_{566} in the rings is still visible as the extent of the deviation from the initial

4.2 DRIVE-BEAM RECOMBINATION COMPLEX

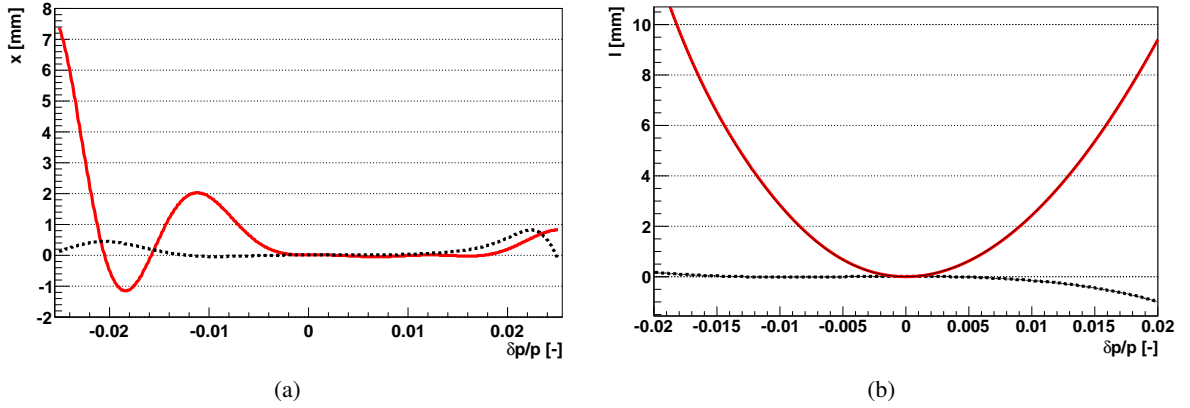


Fig. 4.23: Illustration of non-linear effects in CR1 and effect of the correction using sextupoles. Final position in the horizontal (a) and longitudinal (b) plane after tracking over 2.5 turns in CR1 starting with all coordinates zero but $\delta p/p$ varied. Continuous red line – no correction, dashed black line – with the sextupolar correction.

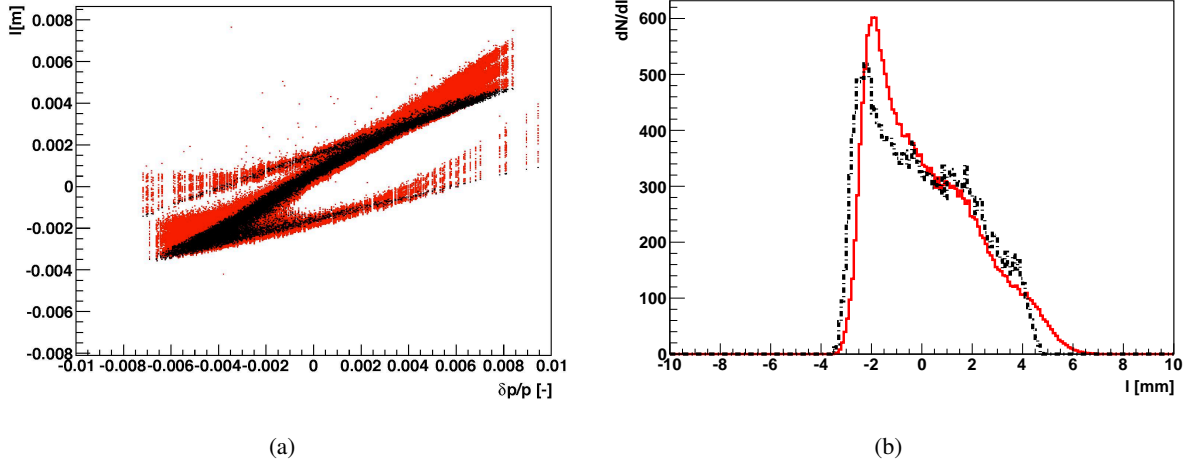


Fig. 4.24: Comparison of initial (black) and final (red) distributions in the longitudinal plane. (a) Scatter plot of longitudinal phase space for fully recombined beam. (b) Longitudinal position distribution.

distribution depends on the number of turns. The corresponding horizontal and vertical emittances are 124 mm mrad and 108 mm mrad, respectively. Figure 4.25 presents emittance evolution from DL up to the exit of LTA for the longest beam path, i.e., passing DL, three turns in the CR1 and four turns in the CR2. Table 4.9 gives numerical values for the emittance increase in various parts of the DBRC. In this case the final r.m.s. emittance is 143 μm in the horizontal plane and 112 μm in the vertical, while in the case of the shortest path it is respectively 108 μm and 104 μm .

Figure 4.26(a) shows the distribution of the action variable $2J_x = x_n^2 + p_{xn}^2$, where x_n and p_{xn} are the normalized coordinates. Clearly we observe a tail ranging above the value corresponding to the size of the beam envelope assumed for the decelerator studies. However, only 1.4% of electrons are above this threshold, see Fig. 4.26(a). In the vertical plane this value is equal to 0.3%, however, these are mostly the same electrons as the ones having large action in the horizontal plane since both are correlated with large momentum offset. Nevertheless, a collimation system should be installed before the decelerator to avoid uncontrolled losses.

In the current design the biggest increase of the emittance is observed in CR1 and in the injection line to CR2. The latter one is related to the design of the time variable injection bump of CR2, namely,

Table 4.9: Approximate emittance growth over DBRC from tracking the distribution obtained from DBA simulations (initial $\delta p/p$ r.m.s. = 0.35%).

	$\Delta\epsilon_x(\%)$	$\Delta\epsilon_y(\%)$
DL	1	1
TL1	1	1
CR1 – 3 turns	16	3
TL2	30	8
CR2 – 4 turns	31	10
LTA	43	12

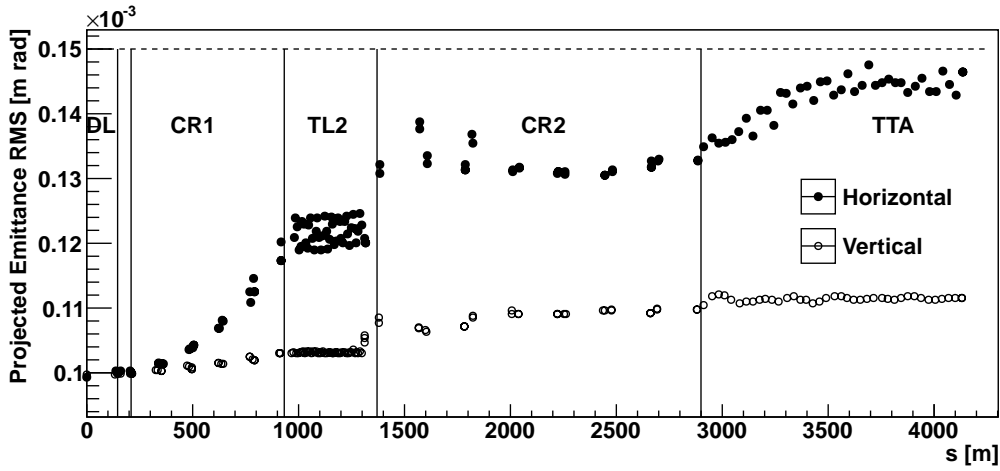


Fig. 4.25: Evolution of projected emittances (normalized) in transverse planes along DBRC for the bunches travelling the longest distance. The dashed line shows the allowed emittance budget. Vertical lines delimit different parts of the complex.

large divergence of the beam at the injection point. It forces large beta functions and strong optics in the injection line, which makes the non-linearities more pronounced. Studies to find a better solution will continue.

4.2.5 Beam loading in RF deflectors

The use of RF deflectors in the DBRC has been introduced in §4.1 and their technical details are discussed in §5.5.4. The deflectors are basically RF resonant cavities which are operated at their transverse mode frequencies so as to give horizontal kicks to the bunches at a selected timing and phase. The frequency of each deflector can be chosen as the minimum dictated by the bunch frequency and recombination factor, or as one of its multiples. Frequencies of 1.5, 2, and 3 GHz have been chosen, respectively, for deflectors in the DL, CR1, and CR2.

The HOMs and fields with tilted polarities of the RF deflectors will be addressed in ways similar to what was implemented at the upgraded CTF3 CR [16], so as to avoid excitation of beam instabilities.

The beam loading due to the high current through the RF structures is an important issue when defining the deflector parameters. The beam loading is generated by the interaction between the beam current and the off-axis components of the longitudinal electric field of deflecting modes. Unwanted deflecting fields can be excited by the beam if it passes through the deflectors with horizontal or vertical

4.2 DRIVE-BEAM RECOMBINATION COMPLEX

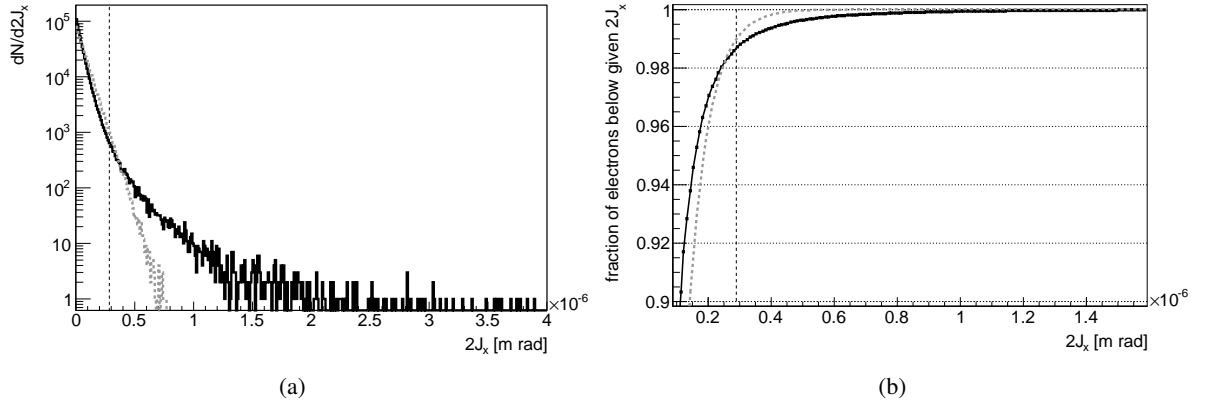


Fig. 4.26: (a) Distribution of the action variable at the end of LTA for the recombined beam. All 24 possible pathways were simulated and final distributions added. (b) Fraction of electrons with action below given value. Black continuous lines correspond to the obtained distribution and grey dotted ones to the distribution assumed in the decelerator studies, i.e., the gaussian with $\sigma = 150$ mm mrad emittance and vertical lines mark the 3σ value which is the size of the beam envelope used in the decelerator design.

offsets. In CTF3 these phenomena have been widely studied in both the CR and the DL [17].

The beam loading effects in CR1 and CR2 have been analysed assuming travelling-wave (TW) RF deflectors. Since the horizontal trajectory with constant deflecting field is parabolic, the beam will pass off-axis even in the case of perfect injection. Following the considerations reported in Ref. [17], it is possible to find a general scaling law for the beam loading effects in the following form:

$$\langle x_{\text{osc}} \rangle \propto \phi \frac{q}{E_0} f_{\text{RF}}^2 \frac{R}{Q} \frac{L_{\text{defl}}^3}{v_g} = q \phi^4 E_0^2 P_{\text{IN}}^{-3/2} f_{\text{RF}}^0 \xi(a/\lambda_{\text{RF}}) \quad (4.2)$$

where:

- $\langle x_{\text{osc}} \rangle$ is the average induced oscillation amplitude in the bunch train,
- ϕ is the injection angle,
- R is the transverse shunt impedance of the deflectors,
- Q is the quality factor per unit length,
- v_g is the group velocity (in general the TW RF deflectors are backward structures and v_g is negative),
- P_{IN} is the input power,
- L_{defl} is the deflector length,
- f_{RF} is the working frequency,
- E_0 is the beam energy,
- E_0 is the bunch charge,
- $\xi(a/\lambda_{\text{RF}})$ is a function of the ratio between the deflector iris radius a and the wavelength λ_{RF} .

This function takes into account the dependence of the R/Q and v_g from the iris radius. Typical behaviours of the ξ function show that it has a broadband maximum in a wide range of a/λ_{RF} . An

interesting result from Eq. (4.2) is that the beam loading effects do not depend on the RF frequency of the deflectors.

This is due to the fact that an increase of the frequency results in an increase of both the efficiency and the wake intensities. Moreover, a comparison of parameters of CTF3 and CLIC in Table 4.7 indicates that, with a fixed value of the maximum available input power, the effects of the beam loading at CLIC are three orders of magnitude bigger than that at CTF3. This means that at CLIC the beam loading is a very demanding issue even in the case of perfect injection.

The solution to this problem requires increasing the input power thus reducing the deflector length, and additionally, using a multiple number (N) of deflectors fed in parallel, instead of only one. Then, the effects of the wakefield can be reduced as $1/N^2$.

A dedicated tracking code has been written to calculate the effects of the beam loading at CLIC. The code allows studies in both cases of perfect injection ('systematic effect') and injection with errors.

In case of the CR1, the recombination factor of three reduces the beam loading effects relative to the CR2, because the beam loading is not perfectly 90° out-of-phase. Consequently, the number of multiple deflectors (N) to use at CR1 can be limited to two. The ratio between the Courant–Snyder (CS) invariants of each extracted bunch and its nominal projected emittance has been calculated for different phase advances between the two deflectors, and for different horizontal β -function values at the deflectors (β_{x_defl}). Figure 4.27 shows this ratio for the CR1 and CR2 as a function of the phase advance between the two RF deflectors, taken on the part of the ring not including the injection bump, and assuming $\beta_{x_defl} = 4$ m and 2 m, respectively. Here, the effects of injection errors are not taken into account. The results show that the beam loading is controllable and that the amplification factor can be even lower than 1 over a wide range of CR tunes, as explained in Ref. [17].

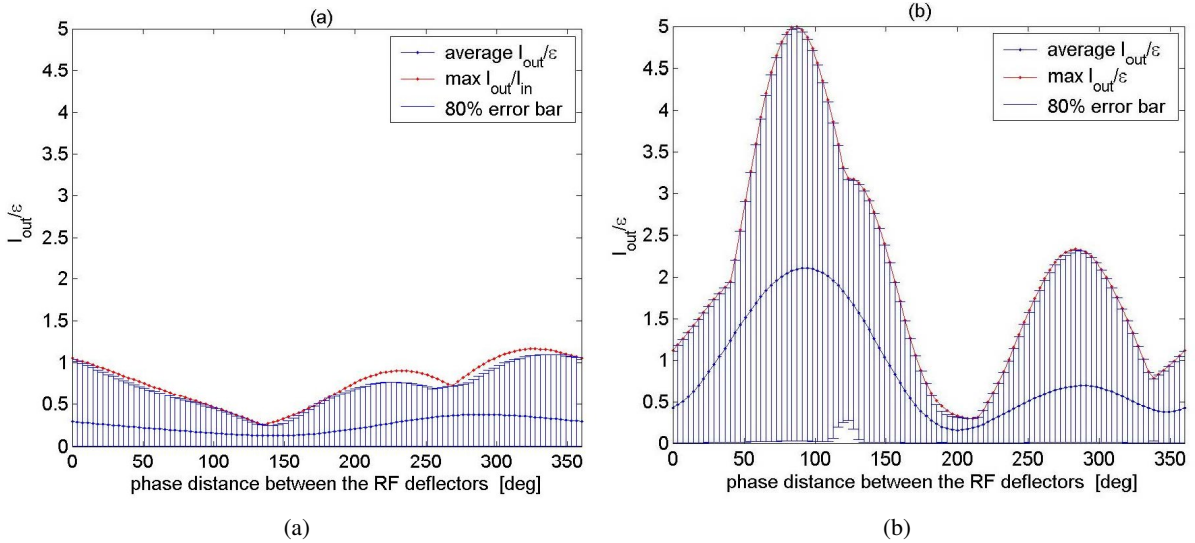


Fig. 4.27: Ratio between the output CS invariants of bunches and the nominal projected emittance for CR1 and CR2 (systematic effect).

The effect of injection errors has also been explored. In this case, an analysis is given for injection errors in angle and/or in phase which are located in an ellipse with a CS invariant equal to the projected emittance of the beam. For instance, Fig. 4.28 shows the amplification factor of an initial error in position as a function of the phase advances between the two deflectors. Similar results are obtained for other injection errors. There exists therefore a wide tune range for both CRs which minimizes the effect of transverse emittance growth due to RF beam loading.

An intuitive explanation of the fact that in CR2, for some horizontal tunes, there is a reduction of

the amplification factor can be found in Ref. [17] and can be easily extended to CR1.

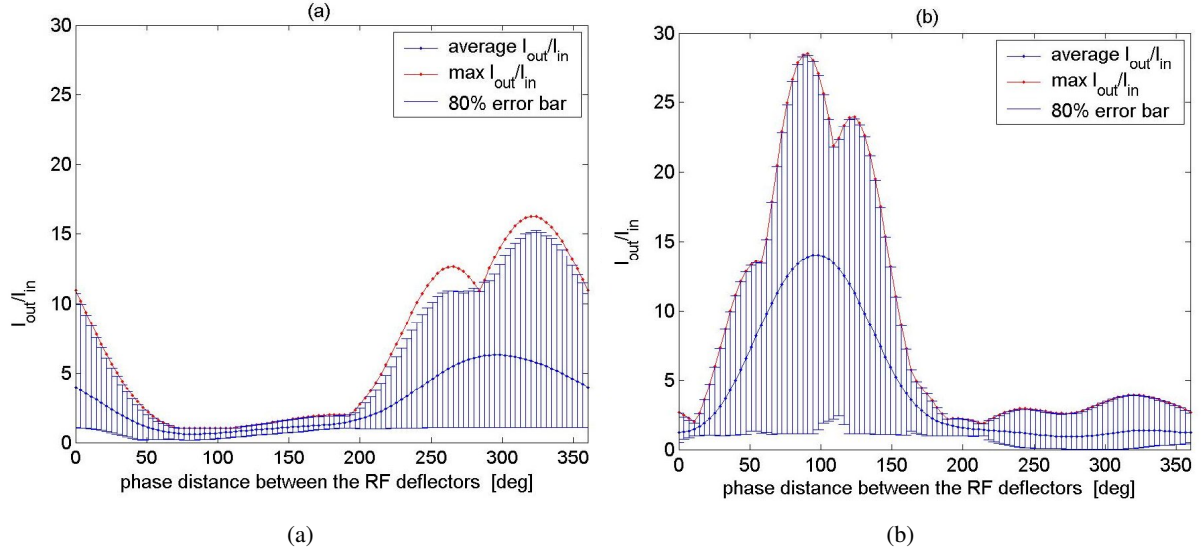


Fig. 4.28: Amplification factor for an initial error in position in CR1 and CR2.

4.2.6 Parametric studies of Coherent Synchrotron Radiation (CSR) effects

Coherent Synchrotron Radiation (CSR) emitted by high brightness bunches in transfer lines generates growth of the projected emittance in the bending plane, increase in energy spread and energy losses, and is one of the main emittance degradation sources to be cured in FEL Linacs. From the beam dynamics point of view the DBRC has to be regarded as a beam transport line. Even if the Drive-Beam bunch length is not comparable to that of FELs, the bunch intensity and the total number of dipoles that every bunch passes by are very high, and the effect of CSR cannot be neglected. The CSR effects will be more pronounced in the DL, due to the shorter dipole bending radius, as indicated in Table 4.8. A parametric study of the CSR effects has been carried out using the Elegant code [18] neglecting shielding effects. A DL configuration in which the single particle dynamics was not yet fully optimized was used. Full start to end simulations including CSR will be done at a later stage with the fully optimized configuration. We expect that the preliminary considerations deduced here will hold for the whole system.

Although the system as a whole is isochronous, the bunch length along the beamline is not constant, as determined by the values of the local R_{56} which oscillates around zero. As a consequence, the larger the initial bunch energy spread, the larger the oscillation in the bunch length, as shown by Fig. 4.29. This also affects the emission of CSR.

First simulations with a 1 mm-long bunch, with the nominal energy spread and intensity, showed a very strong degradation of the transverse emittance. Stretching the bunch, through a magnetic chicane placed before the DL, will reduce the CSR effects on the phase spaces. This bunch stretching introduces a correlation in the longitudinal phase space, which will be used together with the energy chirp, before the turnaround, to re-compress the bunch just before deceleration.

From here on a bunch length of 2 mm is assumed. Beam tracking with CSR off (10^4 macro-particles) and CSR on (2×10^5 macro-particles) has been carried out as a function of the initial transverse emittance ϵ_x and initial energy spread σ_p . Since the CSR effects depend not only on the r.m.s. values of the distribution, but also on the bunch shape, the particle distribution obtained by tracking the beam through the DBA has been used as input for the simulations (see §4.1.3.3), scaling each particle coordinate with the emittance and/or energy spread.

Figure 4.30 shows the horizontal emittance surface at the end of the DL as a function of ϵ_x

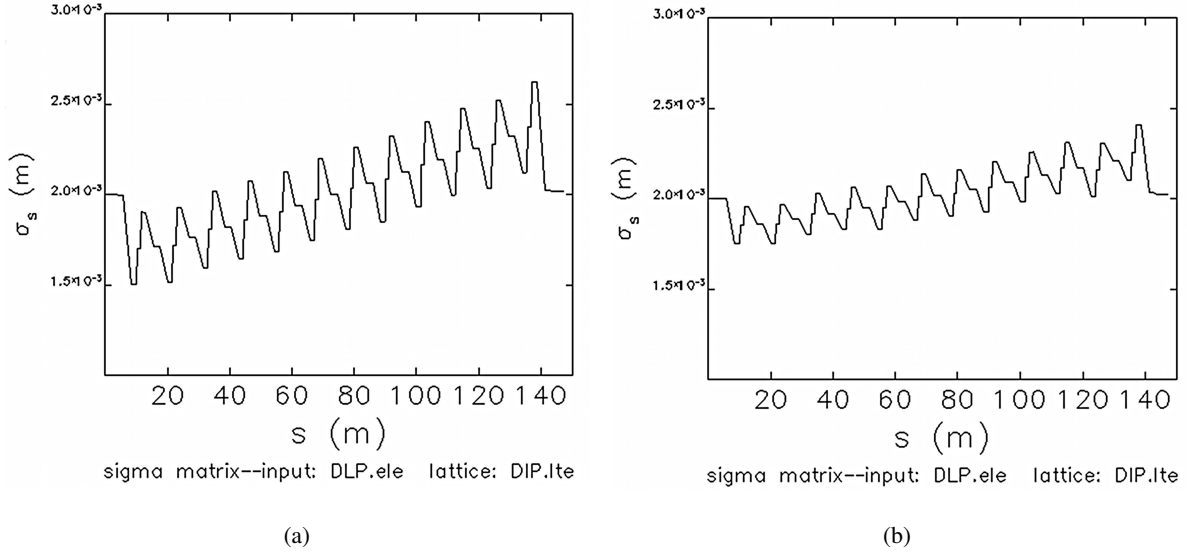


Fig. 4.29: Bunch length along the DL with two different values of the beam energy spread σ_p/p , 0.15% (a) and 0.3% (b)

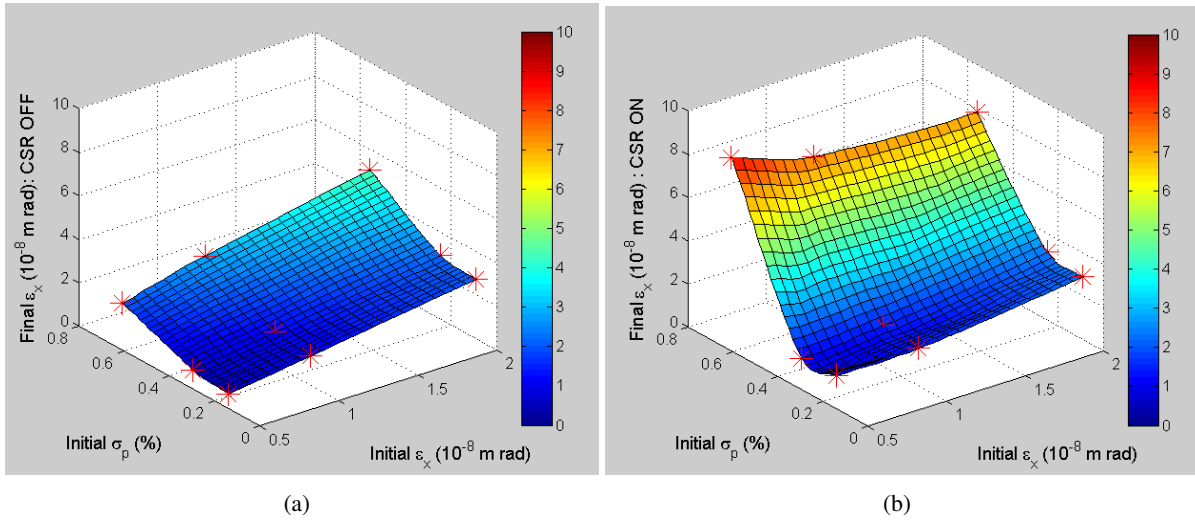


Fig. 4.30: Horizontal emittance at Delay Loop final point (a) with no CSR, (b) with CSR, as a function of initial beam transverse emittance and energy spread

and σ_p around the parameters of the particle coordinate distribution obtained by tracking through the linac ($\epsilon_{nx} = 50 \mu\text{m}$, three times smaller than the maximum emittance accepted by the decelerator, and $\sigma_p = 0.31\%$). In the absence of CSR the emittance growth is driven only by the energy spread, as already described in previous paragraphs, and is relatively high for smaller emittances (Fig. 4.30(a)). It should be considered that in these simulations the chromatic behaviour was not yet optimized: with the sextupole configuration described above the emittance degradation is much reduced.

Emittance growth strongly increases (Fig. 4.30(b)) when including CSR effects in the simulations. The smaller the initial emittance the stronger is this effect. Figure 4.31 shows the ratio between the emittance with CSR on and the emittance with CSR off. It shows that it is not worth using a small emittance beam from the injector, because the increased brightness will be lost due to CSR. The bunch length increase is lower than 3% in all considered cases (see Fig. 4.32(a)). It is interesting to notice

4.2 DRIVE-BEAM RECOMBINATION COMPLEX

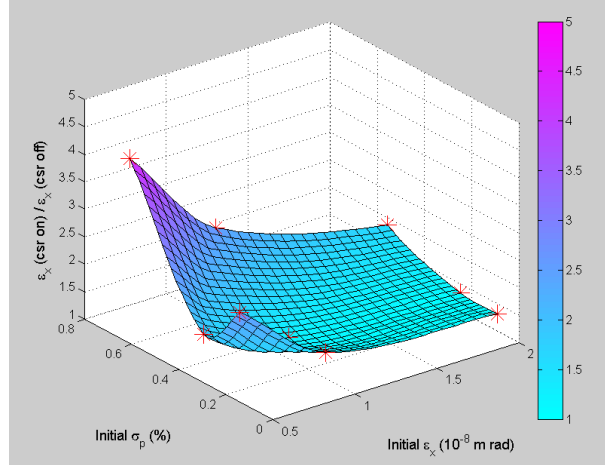


Fig. 4.31: Ratio between final emittance with CSR on and CSR off, as a function of initial beam transverse emittance and energy spread

that for values of the energy spread lower than nominal the bunch length increase is larger than in the nominal case. This is due to the above mentioned fact of the R_{56} oscillation. The final energy spread is also affected by CSR, and in this case the smaller the initial value, the higher the relative increase (see Fig. 4.32(b)).

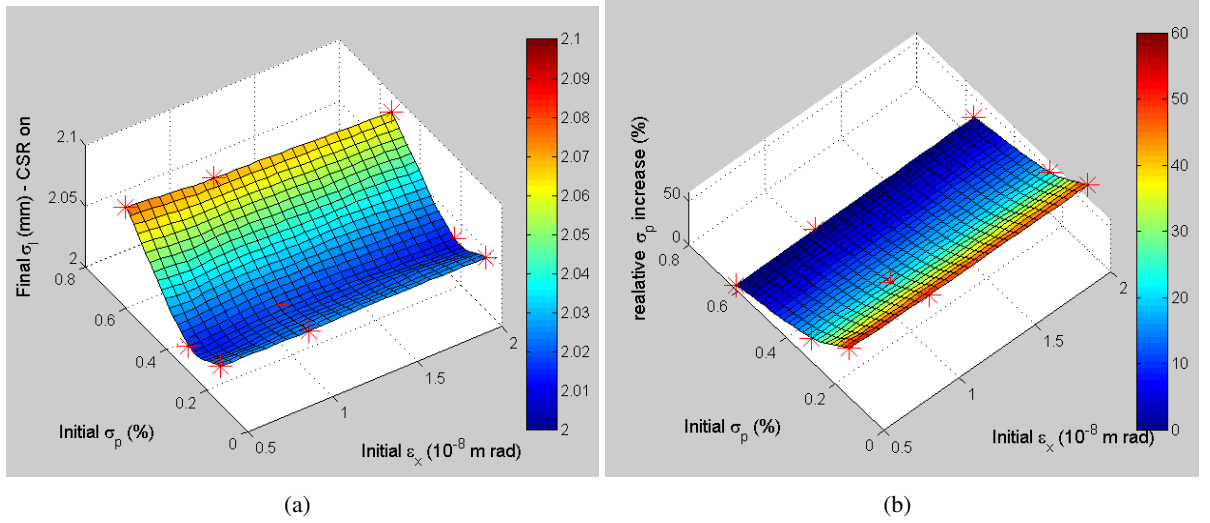


Fig. 4.32: Bunch length (a) and increase in energy spread as a function of initial beam transverse emittance and energy spread with CSR on

Vertical emittance is not directly affected by CSR, but only through the increase of the energy spread. In any case the effects are negligible and not reported in the figures.

Simulations along the whole DBRC with the optimized chromatic correction configuration and including shielding effects will be carried out for a more precise estimation of the effects. The simulations reported here support the choice of not increasing the bunch brightness, by reducing beam emittance or bunch length.

4.3 Beam transport

4.3.1 Overview

We discuss the beam transport lines which connect the Drive-Beam Recombination Complex (DBRC) (see §4.2) with the decelerator sections. As shown in Fig. 4.33, the Long Turnaround (LTA) will ‘turn around’ the direction of one half of the Drive-Beam toward the upstream end of the e^- main linac. The other half of the Drive-Beam will proceed toward the upstream end of the e^+ main linac. In the present site design of CLIC at CERN, the whole DBRC, up to the end of the LTA, is intended to be built at ground level, while the decelerator sections are placed underground. The task of the beam transport lines, therefore, is to provide the beams with descent paths to the Main Linac tunnels and deliver the beams up to the upstream ends of the Main Linacs. The total length of the beam transport line is 23.4 km for the e^- and 23.9 km for the e^+ . The beam line and its optics are presented in §4.3.2. Collective effects are discussed in §4.3.3 and the specification of the main components in §4.3.4. Table 4.10 gives the beam parameters among others that are relevant to the beam transport lines.

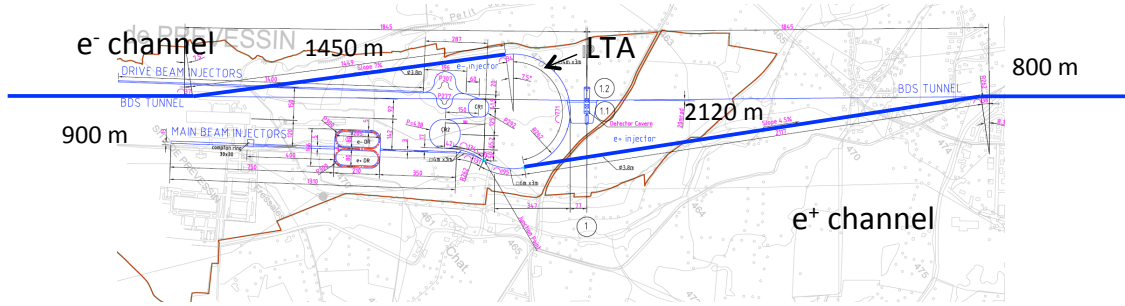


Fig. 4.33: The upstream part of the Drive-Beam transport showing the connection between the surface site and downstream ends of the two Main Linac tunnels

4.3.2 System description

4.3.2.1 Long transfer lines

Optical design

The Drive-Beam transport for CLIC is based on a FODO lattice with instrumentation and control devices suitable for beam tuning. The periodicity of the lattice is chosen to match the structure of the decelerator sectors, each 876 m long. This results in Twiss parameters that are identical at each extraction kicker that brings a bunch train into one of the turnaround loops.

An issue with a FODO beamline is spurious dispersion which can be induced by misalignment of quadrupole magnets. It becomes very acute in case of extremely long beamlines like those required at CLIC. To improve the situation the FODO structure of the Drive-Beam transport is built with long cells with weak quadrupole magnets, without introducing any dipole magnets. This reduces the chromaticity and makes the beamline less prone to generation of spurious dispersion.

The Drive-Beam transport in each sector has eight FODO cells with a phase advance per cell of $\mu_{\text{cell}} = 45^\circ$. Thus, each sector has a total phase advance $\mu_{\text{sector}} = 360^\circ$. Benefits of this design include reduced spurious dispersion, reduced impacts of beta-beating which could arise from optical errors at the entrance of the line, acceptably small maximum of the beta-function $\hat{\beta}$, which eases optical matching to the turnaround loops, and reduced power consumption and cost. Table 4.10 summarizes the relevant parameters. More details of the optimization of the optical design are discussed in Ref. [19].

4.3 BEAM TRANSPORT

Table 4.10: Parameters relevant to the design of the Drive-Beam transport lines. ‘Beam parameters’ and ‘Optics layout data’ give the design parameters. ‘Errors’ represent the assumed errors in simulation, as described in the text, whose results are summarized by ‘Impact of beam’. The Drive-Beam channels feeding the e^- and the e^+ Main Linacs have different lengths. Data depending on these lengths are quoted with (e^-/e^+).

Parameter [units]	Symbol	Value
Beam parameters		
Bunch population	n	5.25×10^{10}
Bunches per train	N_b	2928
Bunch spacing [ns]	δt	0.083
Train length [ns]	Δt	244
Beam current [A]	I	101
Beam energy [GeV]	E	2.4
Normalized emittance, end of DB linac [m]	$\epsilon_{n,x,y}$	10^{-4}
Normalized emittance, entrance of decelerators [m]	$\epsilon_{n,x,y}$	1.5×10^{-4}
Relativistic factor	$\gamma = E/m_e$	4697
Max r.m.s beam size [m]	$\sigma_{\beta,x,y} = (\epsilon_{n,x,y} \hat{\beta} / \gamma)^{1/2}$	2.14×10^{-3}
Momentum band	$\hat{\delta}_p$	± 0.02
Optics layout data		
Length (e^-/e^+) [m]	L	23 400 / 23 900
Number of sectors (e^-/e^+)	N_{sec}	24+3 / 24+4
DB sector length [m]	L_{sec}	876
Cell length [m]	L_{cell}	109.6
Number of cells (e^-/e^+)	N_{cell}	217/223
Phase adv. /cell [rad]	μ_{cell}	$\pi/4$
Total phase advance (e^-/e^+)[rad/2 π]	$\Delta\psi/2\pi$	27.1/27.9
Av. beta function [m]	β	144
Max. beta function [m]	$\hat{\beta}$	214.3
Min. beta function [m]	$\check{\beta}$	95.7
Chromaticity	C	-27
Errors		
Relative r.m.s. gradient error	$\sigma(k_1)/k_1$	10^{-3}
Transverse r.m.s. position of quadrupole [m]	$\sigma_Q(x,y)$	2×10^{-4}
Transverse r.m.s. position of BPM/quad [m]	$\sigma_{\text{BPM/Q}}(x,y)$	2×10^{-4}
Impact on beam		
Beta-beating	$\Delta\beta_{n,x,y}/\beta_{x,y}$	0.03
Relative emittance error, for:		
$\Delta x, y(s_0)/\sigma_{\beta,x,y}(s_0) = 0$	$\Delta\epsilon_{x,y}/\epsilon_{x,y}$	0.002
$\Delta x, y(s_0)/\sigma_{\beta,x,y}(s_0) = 0.3$	$\Delta\epsilon_{x,y}/\epsilon_{x,y}$	0.05
$\Delta x, y(s_0)/\sigma_{\beta,x,y}(s_0) = 1.0$	$\Delta\epsilon_{x,y}/\epsilon_{x,y}$	0.6

Optical errors

The effects of optical errors in the Drive-Beam transport have been examined with relatively conservative assumptions on the errors, as listed in Table 4.10. The assumed r.m.s. transverse position errors of 0.2 mm for quadrupole magnets and beam position monitors are achievable by the use of standard positioning devices and survey techniques. In addition to the alignment and strength errors of the quadrupole

magnets, injection errors have also been considered. The study was done with MAD-X tracking with effects of the orbit corrections taken into account. The Twiss functions and the emittances are re-built by a fit of the statistical tracking data with $\varepsilon^2 = \langle x^2 \rangle \langle x'^2 \rangle - \langle xx' \rangle^2$, $\alpha = -\langle xx' \rangle / \varepsilon$ and $\beta = \langle x^2 \rangle / \varepsilon$. They are then compared to the design values.

The simulation indicates that the beta-beating, as observed at the end of the line, is relatively small and peaks at 3% in the range $-0.02 \leq \delta_p \leq 0.02$ with a much smaller r.m.s value over the range. The robustness of the optical matching shown here is one of the benefits of the choice $\mu_{\text{sector}} = 360^\circ$. The r.m.s. value of the residual static orbit error is $\langle x^2 \rangle = \langle y^2 \rangle \simeq 0.5 \text{ mm}^2$. This can be corrected locally at each kicker.

In the absence of injection errors, the relative emittance growth $\Delta\varepsilon_{x,y}/\varepsilon_{x,y} = 0.002$ is negligible. However, an injection error would almost fully result into an emittance growth. Therefore, the trajectory at the injection point s_0 must be controlled within the level of $\Delta x(s_0)/\sigma_{\beta_x}(s_0) < 0.2$ and $\Delta y(s_0)/\sigma_{\beta_y}(s_0) < 0.2$ at the entrance of the long transfer line. A dump action will need to be initiated in case of an excessive injection orbit error.

4.3.2.2 Turnaround and bunch compressors

The Drive-Beam trains which initially travel in directions opposite to the Main-Beam line are brought to the decelerators through a 180° turn-around loop (TA), as described in §4.2. The optics design of each TA is similar to that of CR1, offering the isochronicity and achromaticity adequate for preserving the beam emittances in all co-ordinates.

Each TA is preceded by a chicane for longitudinal bunch de-compression, followed by another for bunch re-compression. The second chicane, installed between the downstream end of the TA and the entrance of the decelerator, is used also for fine-tuning the time synchronization of the Drive-Beam trains relative to the Main Beam. Each chicane consists of four dipole magnets, which are spaced longitudinally by several metres to provide room for RF kickers. Figure 4.34 shows a schematic view of a chicane. Each dipole, 1 m long, has a magnetic field strength of $B = 0.75 \text{ Tm}$. Thus it deflects the $2.5 \text{ GeV}/c$ beam by approximately 0.09 rad ($\simeq 0.5^\circ$). With a pole gap of $\simeq 0.03 \text{ m}$, the outer dimensions of the dipole magnets are $w = 0.31 \text{ m}$ and $h = 0.22 \text{ m}$ (i.e., dipole D2 type 1 in [20]).

Studies are at an early stage at CTF3 on synchronization between the Drive-Beam and the Main Beam, with a prototype system currently under construction. At present, the plane of bending in the chicane (i.e., horizontal or vertical) is an open issue. This design decision, together with numerous system integration studies, will be carried out during the project implementation phase. Topics of the study include implementation issues of the entire TA beam synchronization system, including the chicane, deflectors, RF amplifiers (see § 5.15.2.3), and other elements to be installed in the tunnel.

4.3.3 Accelerator physics issues

Strong collective effects can arise in a high-current beam of 101 A with a bunch train structure ($\Delta t \sim 240 \text{ ns}$). Two effects are of potential concern: multi-bunch resistive instabilities and positive-ion effects in the case of the electron beam.

4.3.3.1 Multi-bunch resistive wall instabilities

The long-range wakefield, which is produced by a bunch with an orbit displacement of $\Delta_{x,y}$ relative to the axis of the vacuum chamber, exerts transverse kicks to subsequent bunches. The growth in normalized amplitude, δA_n of subsequent bunches can be written as

$$\delta A_n \propto \Delta_{x,y} \sqrt{\frac{L}{\sigma}} \frac{1}{a^3} . \quad (4.3)$$

where:

4.3 BEAM TRANSPORT

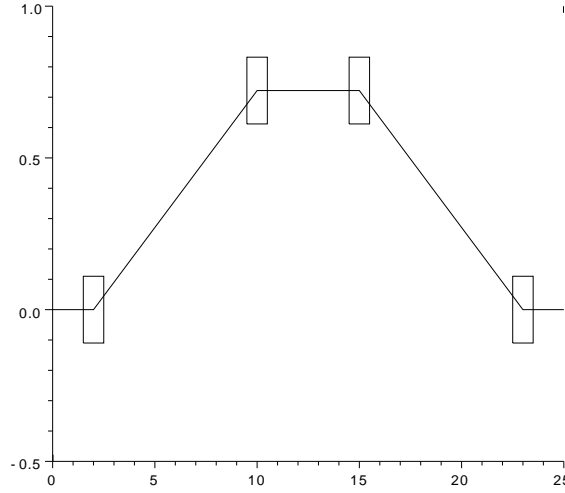


Fig. 4.34: Schematic diagram of a bunch compression chicane located between the downstream end of a turn-around and the entrance of every decelerator in the main tunnel. While the aspect ratio is not 1:1, the scales in metres are shown. The orientation (horizontal or vertical) is not fixed at the time of writing.

- L is the distance over which the bunches travel,
- σ is the electrical conductivity,
- a is the radius of the vacuum chamber,

A more complete discussion can be found in Ref. [21]. Cumulated along the DBRC, LTA and the descent tunnel, the $L_{\text{DBRC,LTA}}$ is ~ 2700 m. The length of the long transfer line is $L_{\text{LTL}} \sim 24000$ m. In the Drive-Beam transport a typical r.m.s. orbit displacement is 1 mm and the alignment errors of vacuum chambers are 2 mm r.m.s. The use of copper vacuum chambers with a large diameter is mandatory for keeping the relative emittance growth at $\Delta\epsilon_n/\epsilon_n < 0.1$ in order to ensure a total relative emittance growth to keep within the allowed budget of 50% between the end of the Drive-Beam linac and the entrance of the decelerator, see Table 4.10. This is compatible with the design consideration of the transport line from the optical viewpoint, which, as discussed in §4.3.2.1, favours a weak beam focusing. The contribution of the resistive wall instability must be considered all through the total path along the DBRC, the LTA, and the LTL. The emittance growth can be maintained at an acceptable level with the aperture (radius) $a_{\text{DBRC+LTA}} = 0.04$ m and $a_{\text{LTL}} = 0.1$ m, as summarized in Table 4.12.

4.3.3.2 Ion effects

Charged-particle beams ionize the residual gas in the vacuum chamber. In the case of an electron beam, the ionized electrons are repelled while the positive ions (typically, carbon monoxide, CO) are attracted toward the beam.

A study [21] shows that the ion density grows linearly within a train. With the short bunch spacing of $\delta t = 0.083$ ns (25 mm), the CO ions are fully trapped in each train but they are un-trapped between two neighbouring trains.

The ions induce tune-shifts $\Delta\nu_{x,y,\text{inc}}$, and cause beam instabilities associated with transverse displacements of the bunches. The instability is characterized by a rise-time τ_{rt} , or by $n_{rt} = L/(c\tau_{rt})$ for a given beam line of length L . Both the $\Delta\nu$ and n_{rt} grow linearly with L and with the vacuum pressure

p . With a total travelling path $L = 27$ km, between the end of the Drive-Beam linac and the entrance of the most distant decelerator, a pressure below $p = 10^{-10}$ mbar is required to preserve good beam quality. Table 4.12 gives relevant parameters. The reference [21] presents a more quantitative discussion.

4.3.4 Component specifications

4.3.4.1 Magnets

Table 4.11 summarizes the specifications for the magnets to be used in the Drive-Beam transport, as per the beam line design in accordance with Table 4.10. The field strengths quoted there include a margin of 10% for operation at the nominal beam momentum. The corrector magnets are for orbit correction in the presence of misalignment of the quadrupole magnets and the Earth's magnetic field $B_{\text{Earth}} = 4.7 \times 10^{-5}$ T.

The long transfer line will be suspended from the ceiling of the tunnel, and because of this installation requirement, the transverse profile of all the magnets there must fit within a square of $0.4 \text{ m} \times 0.4 \text{ m}$. Lightweight magnets, accommodating vacuum chambers with large apertures ($a = 0.1 \text{ m}$) will have to be built. The good field area of a quadrupole magnet in the present design is $r \leq 0.02 \text{ m}$ (20% of the radius of the vacuum chamber), in which the absolute field error satisfies $\Delta B l \leq 2.8 \times 10^{-5} \text{ Tm}$. A detailed technical study of all the magnets of the Drive-Beam complex is available in Ref. [22].

Table 4.11: Specifications for the magnets to be used in the Drive-Beam transport. Quoted errors are tolerances

Magnet	Variable	Value	Quantity (e^+/e^-)
Quadrupole	Integrated gradient Gl [Tm/m]	0.14	432/448
	Relative gradient error $\Delta Gl/Gl$	2.0×10^{-3}	
	Maximum field error $\Delta B l$	2.8×10^{-5}	
Dipole corrector	Integrated field Bl [Tm]	7.6×10^{-3}	432/448
	Maximum field error $\Delta B l$ [Tm]	2.8×10^{-5}	

4.3.4.2 Vacuum system

For adequate mechanical rigidity, the thickness t of the vacuum chamber must be greater than 3 mm. This thickness also reduces the electromagnetic radiation outside the vacuum system to an adequate level.

The requirement on the residual static pressure $p \leq 10^{-10}$ mbar requires the use of getters and a bake-out system in the long drift spaces. If the ratio of skin depth to the thickness of the getter exceeds one, for the r.m.s bunch frequency, evaporated getters must be avoided. The surface smoothness of the copper chamber must be in the μm range. With the large bunch train current, the bellows must be equipped with tight RF sliding elements to fit within the radius of the vacuum chamber. The large radius of the vacuum chamber allows the quadrupole assemblies to be free of getter and bake-out equipment. Table 4.12 summarizes the resultant parameters relevant to the vacuum system. Detailed specifications appear in Ref. [23].

4.3.4.3 Beam instrumentation

The long transfer line must be equipped with Beam Position Monitors (BPM) and Beam Loss Monitors (BLM).

4.3 BEAM TRANSPORT

Table 4.12: Parameters for the vacuum system and vacuum chamber in the Drive-Beam transport. The quoted total line length is for one beam complex

Parameter [units]	Symbol	Value
Total line length [m]	L	24 000
Radius [m]	a_{LTL}	0.1
Thickness [m]	t	0.003
Material	Copper	
Pressure [Torr]	p	10^{-10}
Beam		
Incoherent detuning	$\Delta v_{x,y}$	0.015
No. of rise-times	n_{rt}	0.18

Position measurement

Low-bandwidth (Low-BW) BPMs are used for regular measurement for the adjustment of bunch trains as single bodies, while high-bandwidth (High-BW) BPMs which operate at a bunch frequency of $\nu_0 = 12$ GHz are used for diagnosing the train structure. The latter is also used for fast beam interlocks.

A Low-BW BPM will be attached to each quadrupole magnet in the beam transport. The BPMs on horizontally-focusing quads will measure the horizontal orbit co-ordinate, while the BPMs on vertically-focusing quads will measure the vertical orbit co-ordinate. Table 4.13 gives the specifications. It indicates the aperture, quoted as ‘Normalized aperture’ in which good resolution, as specified, needs to be ensured. Beyond this aperture up to 0.05 m, the BPMs should still provide a response signal in the presence of the beam, although a degraded resolution is acceptable. With the total train charge $Q = 25 \mu\text{C}$, its duration $\Delta t = 244$ ns, and the low bandwidth frequency $f = 10^8$ Hz, the dynamic range is $\Delta Q = Q/\Delta t/f = 1 \mu\text{C}$. The full range of the high bandwidth BPM is the bunch charge with some margin. The quoted dynamic range and accuracy allow for the measurement of commissioning beam trains which will contain 10% of the nominal charge.

At least two High-BW BPMs are needed to detect any saw-tooth transverse structure within the train. A harmful saw-tooth structure can arise in a bunch train from the bunches which pass through the combiner rings for different numbers of turns. The High-BW BPMs should be placed at the entrance of the long transfer line. They also provide the beam dump system with trigger signals in case of excessive overall transverse oscillations.

Beam loss monitors

With the large diameter of the vacuum chamber ($a = 0.1$ m), no substantial beam losses are expected along the straight portions of the beamline. However, failures of extraction kickers must be considered, and a dedicated beam loss monitor should be prepared, together with a local beam dump, downstream of each kicker. A full train will deposit an energy of

$$H = nN_b E \simeq 6 \times 10^4 \text{ J.} \quad (4.4)$$

This energy is too large to allow repetitive impacts on a copper vacuum chamber. The detector must then be able to provide a signal able to prevent further beam injections. Beam trains twenty times less intense than nominal must be measurable. The sensitivity of the BLM must therefore be in the range $\delta H = H/1000 = 60 \text{ J}$ leaving an adequate relative sensitivity of 0.02 for the beams. The quoted number of joules is the quantity of energy deposited in the dump. The corresponding signal read by the detector will depend on its size and location w.r.t. the dump.

The bandwidth of the BLM must be high enough to prevent further injection of trains in the tunnel and to trigger a dump for those trains which are already on the way. Assuming that the trains can be dumped at the exit of turnaround loops, with a transit time of $\delta t_{TA} = 440$ ns, the bandwidth of the BLM must be $\nu_{BW} = 10/\delta t_{TA} \simeq 2 \cdot 10^7$ Hz. The specifications are summarized in Table 4.13.

Table 4.13: Specifications for the instrumentation of the Long Transfer Line of the Drive-Beam. Data is given for the nominal beam. Accuracy, resolution and stability as fractions of the normalized aperture (BPM) or dynamic range (BLM). The physical aperture of the BPM is the radius $a = 0.1$ m of the vacuum system. The quoted quantities apply to the whole of the Drive-Beam complex. ‘F’ = feedback needed and ‘I’ = interlock needed.

	Dynamic range	Normalized aperture	Relative accuracy	Relative resolution	Relative stability	BW	Quantity $e^+ + e^-$	F/I
Low BW BPM	$1 \mu\text{C}$	0.02 m	1.4×10^{-4}	10^{-4}	10^{-4}	10^8 Hz	880	no/no
High BW BPM	10 nC	0.02 m	1.4×10^{-3}	10^{-3}	10^{-3}	10^{10} Hz	4	no/no
BLM	6×10^4 J	–	10^{-3}	5×10^{-4}	5×10^{-4}	2×10^7	48	no/yes

4.4 Decelerators

4.4.1 Overview

The decelerators must serve as the stable and robust RF source for the Main Linacs. The two decelerator lines run in parallel with the two Main Beamlines for the full length of the Main Linacs. Each decelerator is divided into 24 sectors. In each sector a Drive-Beam train of 101 A, 2.4 GeV, and 244 ns length is decelerated and the kinetic energy of the beam particles is converted to RF power by power extraction and transfer structures (PETS) [24]. The beam current is determined by the power production requirement, while the initial energy is determined by requiring a maximum particle energy extraction of 90%. The length of the decelerator sectors is 878 m on average, but it actually varies from about 840 m to 1050 m to ensure the same power extraction efficiency in each sector (see §5.4). While the fill factor is constant along the linac to first order, it is slightly lower at the beginning due to a limited choice of quadrupole lengths. A detailed discussion of the beam physics of the CLIC decelerators is found in Ref. [25].

4.4.2 Beam and lattice parameters

Table 4.14 summarizes the main parameters for the decelerator lattice and beam for nominal operation. During a tune-up period, uncombined (0.5 GHz bunch spacing) low-current beams may be used with a shorter train length (as short as required for precise enough Beam Position Monitor (BPM) resolution).

Table 4.14: Decelerator parameters

Lattice parameters [units]	Symbol	Value
Decelerator sector average length [m]	L_{avg}	876
Decelerator sector length, longest sector [m]	L	1053
Number of PETS per sector	N_{PETS}	1492
Lattice FODO cell length [m]	L_{FODO}	2.01
Lattice FODO phase-advance (lattice start) [°]	ϕ_{FODO}	92
Lattice maximum beta function (lattice start)[m]	β_{F}	3.40
Lattice average beta function (lattice start) [m]	$\langle\beta\rangle$	1.25
Number of FODO cells, longest sector	N_{FODO}	524
Vacuum chamber inner radius	a_0 [mm]	11.5
Drive-Beam parameters (nominal beam) [units]	Symbol	Value
Average beam intensity [A]	I	101
Initial energy [GeV]	E_0	2.4
Maximum energy extraction efficiency [%]	η_{extr}	90
Minimal final particle energy [GeV]	E_{min}	0.24
Train length [ns]	t_{train}	244
Bunch frequency [GHz]	f_{bunch}	11.994
Bunch-to-bunch distance [mm]	z_{bb}	25.0
Bunch length [mm]	σ_z	1
Bunch form factor [%]	$F(\lambda(\sigma_z))$	96.9
Initial normalized emittance [μm]	$\epsilon_{\text{Nx,Ny}}$	150
PETS power production [MW]	P	135

4.4.3 System description

Each decelerator sector contains 1492 PETS. The inner radius of the PETS, and that of the vacuum chamber, is $a_0 = 11.5$ mm. The initial normalized emittance is assumed to be $\epsilon_{\text{Nx,Ny}} = 150 \mu\text{m}$. The large energy extraction, combined with significant transverse wakefields, leads to a need for strong beam

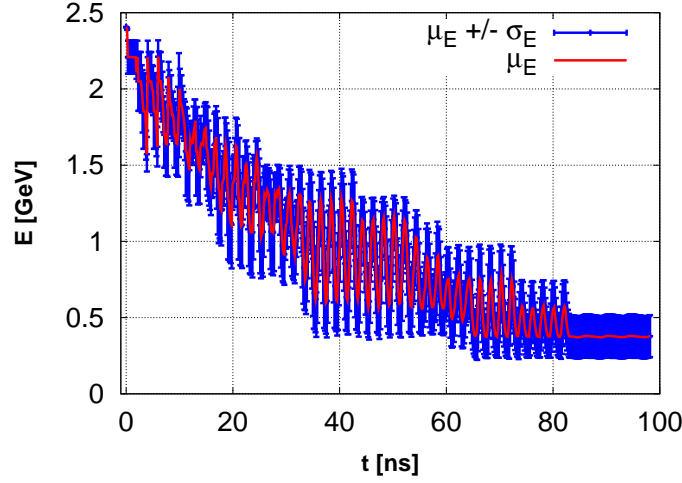


Fig. 4.35: Decelerator beam energy profile after deceleration. The head of the train (towards the left) is less decelerated to compensate for the accelerating structure beam loading. An up to 88 ns-long high-energy transient is followed by the steady-state part of the train which experiences full deceleration, whose first 15 ns only is shown in this figure. The final energy of the most decelerated steady-state particles, E_{\min} , is a factor $(1 - \eta_{\text{extr}}) = 0.10$ times the least decelerated particles in the head, which have lost a negligible amount of energy. The blue line (+) shows the mean $\pm 1\sigma$ energy spread for each bunch, while the red line (-) is the mean energy averaged over the 1 ns fill time of the PETS.

focusing in the decelerators. This is achieved by a FODO lattice design, with two quadrupole magnets implemented per CLIC module which is 2.01 m long (see §5.6). The phase-advance is 92 degrees per cell, the maximum beta is $\hat{\beta} = 3.40$ m, and an average beta function is $\langle \beta \rangle = 1.25$ m. The initial maximal r.m.s. beam size is $\sigma_{x,y} = 0.3$ mm. In the following, as a metric for decelerator beam envelope, the 3σ transverse beam envelope of the outermost slice of the beam is used. As for specifying the tolerances, a guideline is adopted so that no single instability source or error source should increase the beam envelope by more than 5%.

4.4.3.1 Energy spread

The bunches in the Drive-Beam will experience varying degrees of deceleration as they pass through the decelerator. While the first bunch sees little deceleration as the PETS is not yet loaded, the next bunches undergo a progressively larger amount of deceleration, and the subsequent main part of the Drive-Beam train with a steady 101 A beam intensity experiences full deceleration of up to 90%. The magnitude of deceleration experienced by the individual particles within a steady-state bunch also has a wide spread, because of the combination of the bunch length of 1 mm and the 12 GHz extraction mode. By the time the beam reaches the end of a decelerator sector, the final energy of the most decelerated steady-state particles, E_{\min} , is a factor $(1 - \eta_{\text{extr}}) = 0.10$ times the least decelerated particles in the head, which have lost a negligible amount of energy. Figure 4.35 shows the energy profile of the first 100 ns of the Drive-Beam train. The length of the high-energy transient building up at the head of the train may vary between 1 ns for tune-up beams and 88 ns for nominal beam loading operation mode (see §2.5.8). In both cases particles of all energies, from the high-energy head to the low energy steady-state portion of the train, must be transported without significant losses.

4.4 DECELERATORS

4.4.3.2 Focusing strategy

The strengths of quadrupole magnets are scaled so that the most decelerated particles maintain a constant phase-advance per cell, as proposed in Ref. [26]. The quadrupole gradient, therefore, has to decrease to 10% of the initial value along each decelerator. For a perfect machine and injection, however, the high-energy beam slices in the transient are contained within the envelope of the lower energy slices. If the strength of quadrupole magnets is chosen to match the most decelerated bunch within the beam, the FODO stability limit will be surpassed at the lattice end when the initial beam energy is lower than the lattice energy by a factor

$$E_{\text{unstable}}/E_0 < (1 - \eta_{\text{extr}}) \sin(\phi_{\text{FODO}}/2) / \sin(180^\circ/2) + \eta_{\text{extr}} \approx 0.97 \quad (4.5)$$

where:

η_{extr} is the energy extraction efficiency which is quoted in Table 4.14.

Since the deceleration scales with the beam current, there is a similar limit for the current, which can be written as:

$$I_{\text{unstable}}/I_0 > 1/\eta_{\text{extr}} - (1/\eta_{\text{extr}} - 1) \sin(\phi_{\text{FODO}}/2) / \sin(180^\circ/2) \approx 1.03. \quad (4.6)$$

4.4.3.3 Optics errors

The effect of injection errors on the beam envelope, r , is estimated as $\Delta r/r \sim \sqrt{|\Delta\beta|/\beta}$. Allowing for a maximum 5% increase of the minimal beam envelope, the tolerance on optics errors is specified as

$$\frac{|\Delta\beta|}{\beta} \leq 10\% \quad (4.7)$$

As long as the beam envelope is contained, the effect of optics errors on emittance growth and beam decoherence is of no concern. The beam decoherence is an important contribution for mitigating the effect of the transverse wakefields [25].

4.4.4 Accelerator physics issues

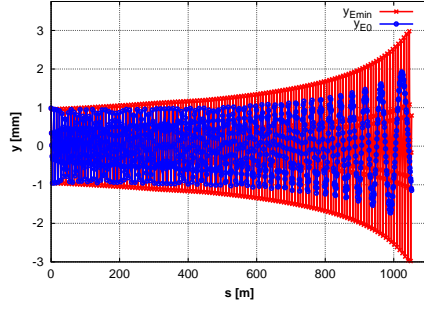
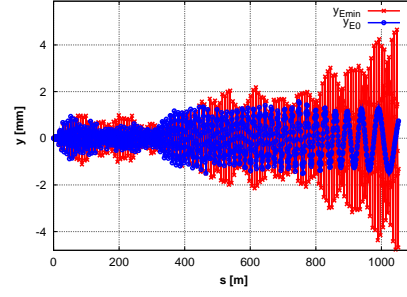
After deceleration the Drive-Beam ends up with a very large energy spread. Issues which significantly affect the beam envelope include: adiabatic undamping, transverse wakefields, and misalignment of quadrupole magnets.

4.4.4.1 Adiabatic undamping

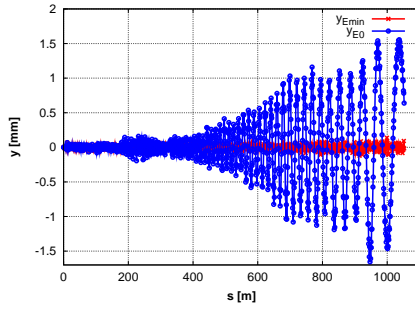
Even in an ideal situation where a perfectly aligned beamline receives a perfect beam injection, an increase of the beam envelope by a factor $\sqrt{1/(1 - \eta_{\text{extr}})}$ takes place due to adiabatic undamping. Figure 4.36(a) illustrates the development of the beam envelope in this ideal case, showing the growth of the 3σ envelope of maximum 3 mm. The maximum power extraction efficiency is driven by the adiabatic undamping and by the effects of transverse wakefields and quadrupole kicks described below.

4.4.4.2 Transverse wakefields

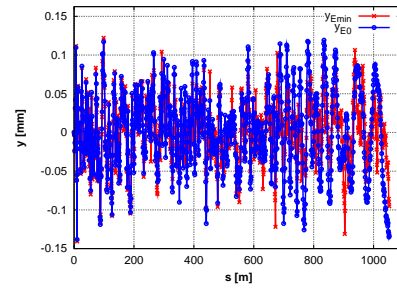
The higher order modes of the PETS will amplify beam jitters and offsets. The PETS have been designed to minimize the effect of transverse dipole wakes [24, 25]. With the baseline PETS parameters (see §5.5.2), the simulated amplification of the beam envelope due to the transverse dipole wake is less than

(a) Perfectly aligned machine (3σ particles)

(b) Uncorrected machine (0 ini. emit.)



(c) 1-to-1 corrected machine (0 ini. emit.)



(d) Dispersion-free corr. machine (0 ini. emit.)

Fig. 4.36: Example trajectory along the decelerator of a least decelerated particle (in blue, o) and a most decelerated particle (in red, x), for the cases of a perfectly aligned machine (a), an uncorrected machine (b), a 1-to-1 corrected machine (c) and a dispersion-free steered machine (d). Note the different vertical scales on the graph ordinate axes.

5% for all the following scenarios: 1σ injection offset, 1σ jitter on all transverse mode frequencies, and for a machine with baseline values for component misalignment.

4.4.4.3 Quadrupole kicks

Each decelerator sector contains up to 1050 quadrupoles. Each misaligned quadrupole adds a kick to the beam centroid and induces a transverse oscillation of the centroid of a given beam slice. A peculiar issue at the CLIC decelerators is that the beams at each point along the beamline have a large energy variation within the train and within the bunch. This requires an orbit correction scheme with a wide-energy bandwidth, and the solution at CLIC is to employ dispersion-free steering [27].

Figure 4.36(b) shows simulated orbit oscillations for quadrupole misalignment of $\sigma_{\text{quad}} = 20 \mu\text{m}$, resulting in slice centroid oscillations of several millimetres. Figure 4.36(c) shows the effect of applying a standard 1-to-1 beam steering technique. The beam centroid is brought to within an accuracy determined by the alignment and resolution of the BPMs. However, beam slices of different energies will follow dispersive orbits, and for slices with a large energy difference with respect to the centroid, the oscillations still drive the beam envelope to unacceptably large values. Figure 4.36(d) shows the performance of dispersion-free orbit correction. In this simulation both the component misalignments and wakefields are taken into account. It is seen that the beam envelope now remains within a fraction of a millimetre.

Figure 4.37 compares the simulated total 3σ beam envelope (worst of 100 machines) after no correction, 1-to-1 steering and dispersion-free steering, when including the effects of adiabatic undamping, PETS effects and quadrupole kicks. The minimum achievable envelope due to adiabatic undamping

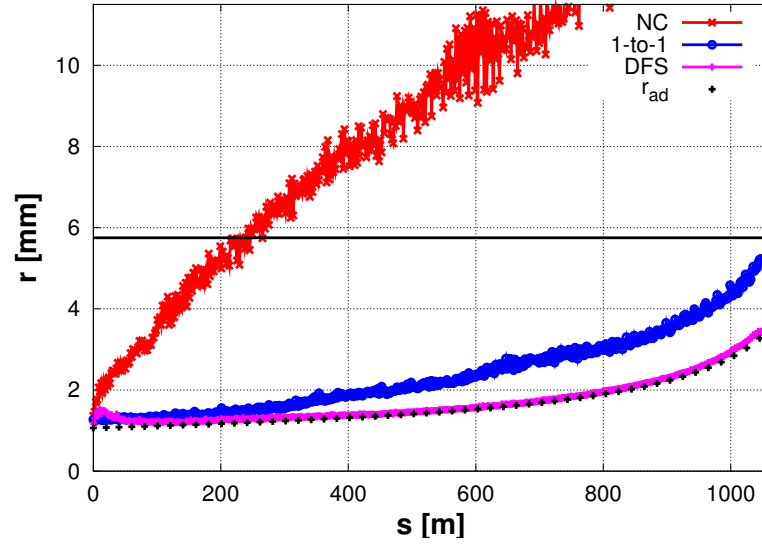


Fig. 4.37: The 3σ beam envelope (worst of 100 machines) along the decelerator lattice in the cases of no correction (red, x), 1-to-1 correction (blue, o) and dispersion-free steering (magenta, +). The minimum achievable envelope due to adiabatic undamping alone is plotted in black. We observe that the dispersion-free steering has taken out almost all residual particle movement, in all parts of the beam. From Ref. [25].

alone is plotted in black. We observe that the dispersion-free steering has taken out almost all residual transverse movement, in all parts of the beam.

4.4.4.4 Resistive-wall instability

The discussion on the resistive-wall instability of the Drive-Beam in the long beam transport has been presented in §4.3. We apply the same calculation techniques [28] to the decelerator. The decelerator sectors are much shorter (1 km, as opposed to 24 km). However, the aperture of the vacuum chambers in the decelerators is much smaller (11.5 mm, as opposed to 100 mm). Calculations have shown that use of copper for the vacuum chambers in decelerator sections would offer an adequate solution in terms of avoiding resistive-wall instabilities. With stainless steel ($\sigma_{ss} = 1.4 \times 10^6 \Omega^{-1}\text{m}^{-1}$), an injection offset of the Drive Beam train would be amplified by about 30% (not acceptable), while with copper ($\sigma_{Cu} = 5.9 \times 10^7 \Omega^{-1}\text{m}^{-1}$) the amplification is limited to about 1% (acceptable).

4.4.4.5 Ion effects

Effects of positive ions for the long beam transport have been discussed in §4.3. We apply the same calculation techniques [28] to the decelerator. For the decelerator, a conservative analytical estimate, which does not take into account the large energy spread, shows that a pressure of about 40×10^{-9} mbar yields one instability rise-time along the decelerator. This defines part of the specification for the vacuum system in the decelerator.

4.4.5 Component specifications

4.4.5.1 Quadrupoles

A total of about 42 000 quadrupoles are required for the 48 sectors of the decelerator. For nominal operation, the integrated gradient, $\int G dl$, decreases in proportion to the beam deceleration, from 12.2 T at the start of each decelerator to 1.22 T at the end. To accommodate the requirements of physics energy scans (see Chapter 8) and operational flexibility during system tuning, the strongest quadrupole magnets

need to operate at 8.5–14.6 T, and the weakest quadrupoles at 0.85–4.9 T [29].

Two magnet design schemes have been investigated, one based on electromagnets and the other on mechanically tunable permanent magnets, as discussed in §5.2. For electromagnets, a special powering strategy has been developed to reduce power dissipation in the cables and to reduce the power cost [29]. The requirement on the relative field accuracy of each individual magnet is 1×10^{-3} (r.m.s.), while the requirement on the pulse-to-pulse field stability is 5×10^{-4} (r.m.s.). The latter is tighter than the former, since the effect of the resulting orbit jitter cannot be taken out by static corrections.

4.4.5.2 Correctors

Beam steering in the decelerator can be performed by using dipole correctors, quadrupole movers or by moving the girders themselves. The following scenarios can be envisaged:

- Each quadrupole is provided with a horizontal and vertical dipole corrector. Assuming that the quadrupole misalignment is kept within $50 \mu\text{m}$ r.m.s., the maximum integrated field required is $\pm 2 \text{ mT m}$ (bipolar). The dipole correctors should ideally be integrated in the quadrupoles to ensure efficient correction for all Drive-Beam energies.
- Each quadrupole is installed on a vertical and horizontal mover. The corresponding maximum transverse offset required is $\pm 200 \mu\text{m}$. The use of quadrupole movers for correction is particularly interesting if permanent magnets are to be used for the decelerator quadrupoles, as it is planned to include moving parts. For either correctors or movers, robust performance is ensured if at least 2/3 of the quadrupoles are equipped with a steering device.

Since each girder will be positioned on horizontal and vertical movers for the active pre-alignment system, we can consider two additional scenarios:

- Each quadrupole is provided with only a horizontal or vertical dipole corrector (or, equivalently, with a horizontal or vertical mover). In this case, with only half the number of movers/correctors, we can almost completely recover the full steering performance of the line.
- Finally, we can use the girder movers only, with no correctors/movers. In this configuration, unlike the previous cases, the steering performance will be partially reduced. However, simulations show [30] that it stays within specification if the alignment tolerance of the quadrupole magnetic centre is $20 \mu\text{m}$ or smaller. This scenario is currently the one considered for the module design (see §5.6).

4.4.5.3 Beam Position Monitors

In order to perform orbit correction a sufficient number of Beam Position Monitors must be installed. The performance of the orbit correction depends on the accuracy and resolution of the BPMs, as well as the number of BPMs installed. These issues have been discussed in Ref. [31]. If the BPMs are installed on all quadrupoles, the orbit correction algorithms reduce the beam envelope close to the minimum achievable, assuming a BPM accuracy of $\sigma_{\text{acc}} = 20 \mu\text{m}$ and a BPM resolution of $\sigma_{\text{res}} = 2 \mu\text{m}$, with performance mostly independent of quadrupole misalignment. If the BPMs are installed on every other quadrupole magnet, assuming the same BPM accuracy and resolution, the orbit correction performance would be degraded if the quadrupole misalignment is substantially larger than the baseline value of $\sigma_{\text{quad}} = 20 \mu\text{m}$. As a compromise between cost, performance, and robustness, it is foreseen to install two BPMs per three quadrupoles. The BPM accuracy and precision must not deteriorate substantially for tune-up beams.

4.4.5.4 Component tolerances

Table 4.15 summarizes the tolerances of the beamline components in the decelerator. The quadrupole offset tolerance corresponds to what needs to be achieved by machine pre-alignment, which would allow successful beam-based tuning and robust performance. The requirement on the BPM accuracy is

4.4 DECELERATORS

to ensure sufficient performance of 1-to-1 steering in order to be able to proceed with dispersion-free steering. The requirement on the BPM resolution is for dispersion-free correction, in order to produce a beam envelope close to the minimum achievable for robust decelerator operation.

Table 4.15: Decelerator component tolerances

Component tolerances [units r.m.s.]	Symbol	Value
Quadrupole offsets [μm]	σ_{quad}	20
PETS offset [μm]	σ_{PETS}	100
Pitch/roll [mrad]	$\sigma_{\theta,\phi}$	1
BPM accuracy (mechanical + electrical) [μm]	σ_{acc}	20
BPM resolution [μm]	σ_{res}	2

4.4.5.5 Vacuum system considerations

The vacuum chambers of the decelerator have to be built with copper or the inner walls have to have a conductivity of the order of $\sigma_{\text{Cu}} = 5.9 \times 10^7 \Omega^{-1}\text{m}^{-1}$, to prevent an onset of resistive-wall instabilities. The vacuum pressure in the decelerator is required to be 40×10^{-9} mbar or less, to prevent an onset of fast-ion instabilities.

4.5 Dump lines

4.5.1 Overview

After leaving $\sim 90\%$ of its power in the PETS, the Drive-Beam (spent beam), at the end of each of the 48 decelerators, has to be bent away from the decelerator axis, and be disposed of at the beam dump. This has to be done in a way that leaves a sufficient amount of space for injecting the fresh Drive-Beam into the next sector. A single dipole magnet is used to sweep the spent beam for that purpose. At the same time, the radiation in the tunnel has to be maintained at a level sufficiently low for operation and maintenance. Thus the beam dumps are located 20 m downstream of the extraction point, 6 m away from the axis of the decelerators, and enclosed within concrete shielding.

A schematic view of the extraction and dump area is presented in Fig. 4.38. The free longitudinal space between two decelerators is $\Delta s = 8$ m. At the time of writing, the injection line of the fresh Drive-Beam train into the downstream decelerator has not been designed in detail, but much flexibility is allowed on its upstream side. The extraction dipole of the spent beam occupies the first half of the free space, leaving 4 m for a vertical dipole which brings the fresh beam onto the axis of the decelerator. The vertical clearance between the two lines is sufficient to install quadrupoles in the descending part of the fresh beam line at almost all of the longitudinal positions. The dump line will enter a separate tunnel 5 m downstream after leaving the extraction magnet. The dump cavern is isolated from the main tunnel by approximately 4 m of rock or concrete.

In this section, we present a proof of feasibility of the extraction system, then we build up the impact map of the spent beam on the dump. We show that an adequately thick metallic window will sustain the flow of electrons. We consider a water dump. A low-temperature excursion is met with a reasonable water flow in the beam impact area. No engineering study of the dump has yet been made. We rely on the experience at SLAC with a three times more powerful water dump [32]. We limit our discussion to a preliminary specification of the dump system.

In the following the design parameters and technical implementation of the dump lines are presented. In §4.5.2 there is a short overview of the spent beam parameters and in §4.5.3 the extraction dipole magnet is described. This dipole must spread the beam in order to afford a homogeneous impact map on the dump, with an acceptably low density on the entrance window of the dump. Therefore, this magnet features a special field configuration. In §4.5.4 there is a discussion of the beam dump.

4.5.2 Beam parameters

The parameters which are relevant to the dump line design are summarized in Table 4.16. The data of the beam entering a decelerator in this table differ somewhat from the nominal values at 3 TeV given in Appendix A. One reason for this is the need for a more powerful beam in the 500 GeV CLIC with a momentum larger by 8% and a bunch intensity larger by 8% (see §9.2). Some operational margin must be considered. The train population in Table 4.16 is 16% larger than the nominal value at 3 TeV and the beam momentum at the entrance of the decelerator is 4% larger. The corresponding total energy of a train is thus 21% larger than the nominal value. This covers the 500 GeV needs with an additional margin of 4% for the power which impacts the dumps.

The deceleration process was simulated [33] using these modified train parameters. The differential charge distribution with momentum of a bunch train after tracking along a decelerator model is shown in the upper left corner of Fig. 4.39. While most particles are decelerated from 2.5 GeV/c down to the 0.24 GeV/c, some electrons at the head of the trains and of the bunches are only partially decelerated. The distribution is therefore heavily skewed with a strong peak at low momentum and a tail vanishing at 2.5 GeV/c. The parameters of the decelerated train are given in Table 4.16. The key values for the design of the extraction and dump system are the total train population $N = 1.78 \times 10^{14}$ and the average power to absorb $P = 0.54$ MW. The time structure of the beam must also be considered for its dynamic thermal impact on the entrance window of the dump, see §4.5.4.

4.5 DUMP LINES

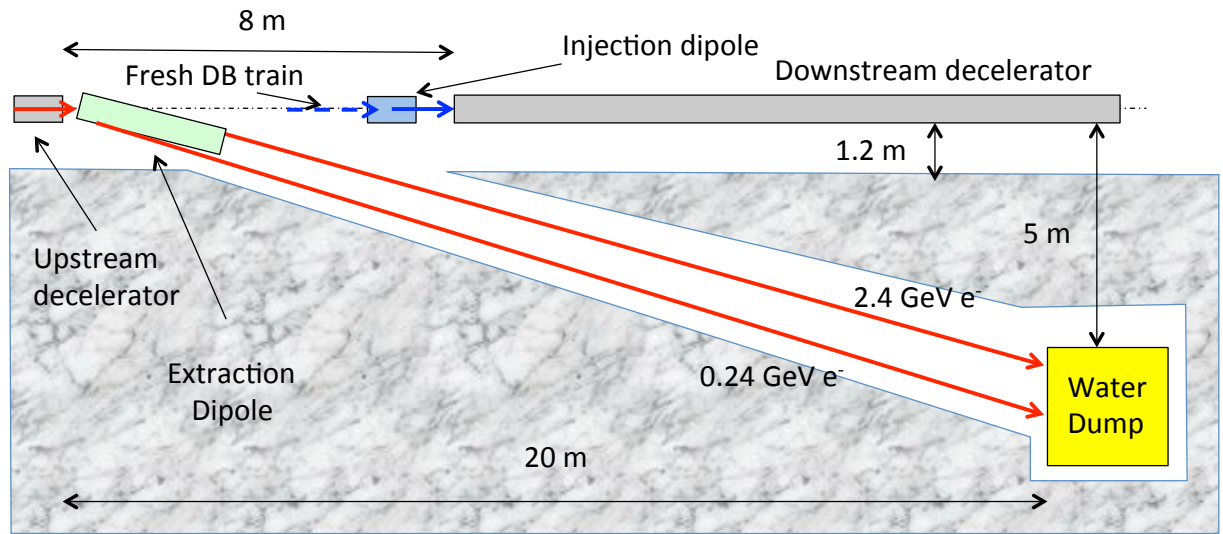


Fig. 4.38: A schematic view of the dump system. Top: a top view with the extraction dipole of the spent beam and the injection dipole of the fresh train which enters the decelerator of the next sector. The green rectangle is the extraction dipole and the blue one the injection dipole. Bottom: a side view of the 8 m longitudinal gap between two decelerators in the main tunnel. In red the spent beam, in blue the fresh Drive-Beam which is fed in the next decelerator. This beam is at height 2.45 m and enters horizontally from the left, out of the compression chicane (not seen here) which follows the turnaround. It is kicked down to reach the Main Linac beam level at 0.83 m.

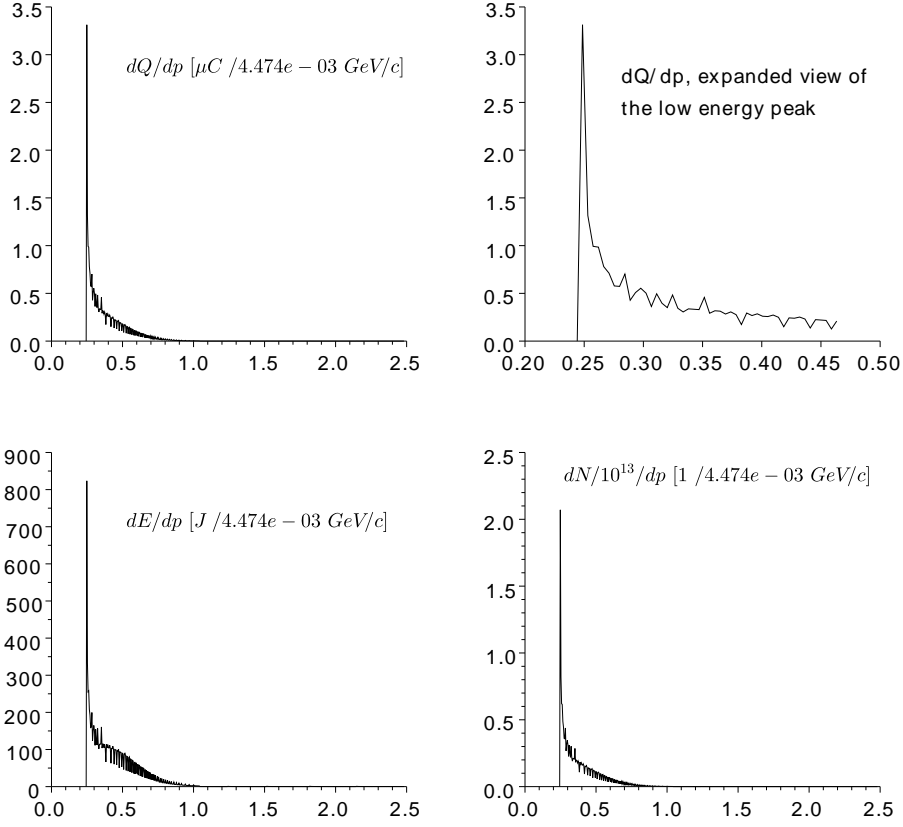
4.5.3 The extraction system

The spent beam must be swept out of the axis of the main linac and dumped safely at a transverse distance which is large enough to allow for sufficient shielding of the main linac. The horizontal transverse dilution must be large enough to avoid an excessive local beam density on the dump while keeping within a reasonable transverse size. These two criteria must be met in spite of the very large momentum spread of the beam, with a ratio maximum/minimum momentum of one order of magnitude. The extraction system must in addition be compact to limit the space occupancy in the main tunnel. The following criteria must therefore be met:

1. Use a simple and compact magnetic system to leave space for the beam line of the fresh Drive-

Table 4.16: CLIC Drive-Beam parameters out of a decelerator

Parameter [units]	Name	Value
Maximum momentum [GeV/c]	p_2	2.5
Final momentum range [GeV/c]	p_0, p_2	0.24, 2.5
Total electron population of a train	N	1.78×10^{14}
Train duration [ns]	δt_{train}	240
Total energy per train entering a decelerator [J]	$E_{\text{in,decel}}$	7.2×10^4
Total energy to dump per train [J]	$E_{\text{dump}} = E_{\text{out,decel}}$	1.08×10^4
Repetition frequency [Hz]	f_r	50
Average power to dump [W]	$P_{\text{dump}} = f_r E_{\text{dump}}$	0.54×10^6
Beam sizes [units]		
r.m.s size at p_0 [m]	σ_0	5×10^{-4}
r.m.s divergence at p_0 [rad]	σ'_0	7×10^{-4}
r.m.s divergence averaged [rad]	σ'	2.25×10^{-4}

**Fig. 4.39:** The momentum structure of the beam at the end of a decelerator. Upper left: the charge distribution. Upper right: an expanded view of the low momentum peak. Lower left: the energy density distribution. Lower right: the particle density distribution.

Beam train which is fed into the next sector.

2. Consider a dump located at $s_{\text{dump}} = 20$ m from the extraction point.
3. Build an impact map centred at $\Delta x \sim 6$ m away from the Drive-Beam axis to allow for enough

4.5 DUMP LINES

shielding between the dump cavern and the tunnel.

4. Strongly spread the low-momentum peak [$p_0 = 0.24, p_1 = 0.27$] GeV/ c of the spent beam.
5. Confine the spread of the high-momenta in order to limit the useful transverse size of the dump to $\Delta w \simeq 1$ m.

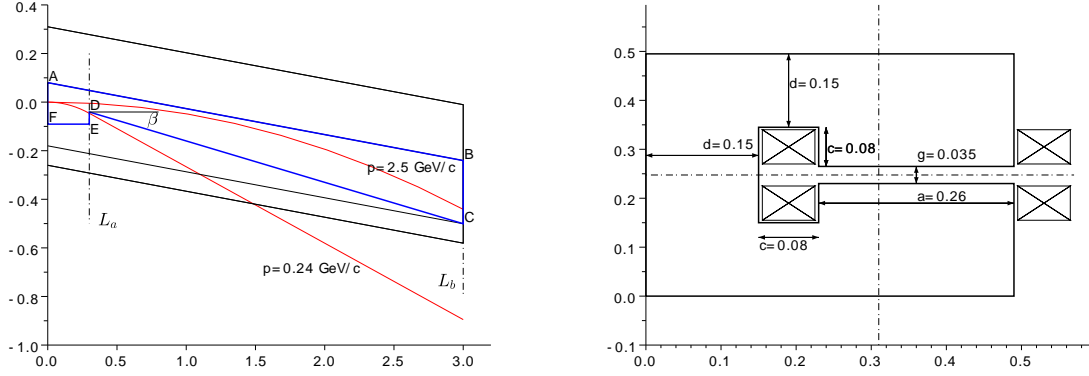


Fig. 4.40: The geometry of the extraction magnet. Left: a schematic top view of the magnet. Abscissa: the longitudinal s co-ordinate which is parallel to the decelerator axis. Ordinate: the horizontal coordinate x . The beam enters the magnet along s at $x = s = 0$. The area of nominal constant magnetic field B is delimited by the thick blue polygon. The thin black external line delimits the yoke (on the positive x -side) and the coil (negative x -side). The beam trajectories of the two extreme momenta are drawn in red. The coordinates of the points A to F and the angle β are given in Table 4.17. Right: an end-view of the magnet. The shape of the yoke in the gap is shown for the rear side of the magnet. It will be made narrower upstream according to the left part of the figure. More data are found in Table 4.17.

We propose to use a single dipole to extract the beam and drive it to the dump. It is shown in Fig. 4.40. Magnetic and geometric data are found in Table 4.17. The beam leaving the magnet must be approximately parallel for all momenta to keep within a reasonable transverse size at the dump. This is done by using a longitudinally skewed pole piece (the angle β in Fig. 4.40). A small rectangular segment at the entrance of the magnet provides the stronger spread which is needed to dilute the low-momentum peak up to $p_1 = 0.27$ GeV/ c . Its length L_a and the angle β are adjusted by simulation to superimpose the low and the high momenta in the dump, see Ref. [34]. The magnetic field $B = 0.8$ T is kept low in order to provide a sharp field edge on the extraction side (segment CD in Fig. 4.40). The field length is limited to $L_b = 3$ m. This makes the weakly populated momentum range above 2 GeV/ c to be folded on top of the lower momenta, further limiting the width of the dump, see upper left of Fig. 4.41. The gap size is fixed by the vertical beam divergence and the aperture is large enough to contain the whole beam in the vacuum system. The first-order calculations of the magnetic data and the shape of the vacuum chamber are discussed in Ref. [34]. The impact map on the dump is obtained by tracking [34] and using the data of Fig. 4.39. The results are shown in Fig. 4.41 and discussed in §4.5.4.

4.5.3.1 Space considerations in the main tunnel

We consider a longitudinal gap length of 8 m between two consecutive decelerators to house the extraction system of the spent beam. Figure 4.38 displays the extraction dipole discussed in §4.5.3 and located in this gap. Horizontally and on the side of the Main Beam, the transverse occupancy of the magnet is $\simeq 30$ cm compared with the separation of 67 cm between the Drive-Beam and the Main-Beam. The vacuum chamber on the downstream side of the magnet is already 20 cm away from the decelerator axis in the horizontal plane, see Fig. 4.40. Therefore the space following this magnet is free for the line of

Table 4.17: The parameters of the dipole for Drive-Beam dump extraction. Top part: magnetic and mechanical data. Bottom part: the geometry of the field area, see text and Fig. 4.40. The referential system is parallel to the decelerator axis. The origin is located at the entrance point of the beam in the magnet.

Parameter [unit]	Name	Value
Magnetic field [T]	B	0.8
Yoke length [m]	L	3
Gap [m]	g	0.035
Aperture [m]	a	0.26
Coil size [m]	c	0.08
Full yoke width [m]	w_1	0.49
Full width [m]	w	0.57
Full height [m]	h	0.395
Full current [A \times turn]	I	2.25×10^4
Apex of the yoke [unit]	s [m]	x [m]
A [m]	0.0	0.080
B [m]	$L_b = 3.0$	-0.241
C [m]	$L_b = 3.0$	$x_b = -0.501$
D [m]	$L_a = 0.3$	$x_a = -0.041$
E [m]	$L_a = 0.3$	-0.091
F [m]	0.0	-0.091
Skew angle [rad]	β	0.169

the fresh beam. In particular the bending magnet which is needed to bring the descending beam line into the horizontal axis of the downstream decelerator is short, i.e., $L = 1$ m and $B = 0.8$ T, and fits easily into the longitudinal gap, see Fig. 4.38. A quadrupole can even be installed on top of the extraction magnet near its upstream side if needed. While the fresh beam line remains to be studied, the extraction line does not impose strong limitations, especially considering the large freedom which is allowed on its incoming side where the distance between the compression chicane and the point of the kick-down is not constrained. It should also be noted that the gap length is not, properly speaking, a constraint. It was chosen to be short in order to limit the length of the main tunnel. Adding a few metres per gap, i.e., per sector, would have a minor impact on the overall project.

4.5.4 The dump

The energy deposition on the entrance window and in the water of the dump has been calculated with the beam distributions as shown in Fig. 4.41. The effective vertical beam size in the window is $\Delta y = 0.01$ m, see Ref. [34]. The maximum beam density on the window is then $d^2N_{\max}/dxdy = 3 \times 10^{16}$ electrons/m². With the short train length and the relatively long repetition frequency, the time structure of the temperature in the window exhibits a saw-tooth shape. The excursion ΔT associated with the saw-tooth is computed considering adiabatic heat deposition by a train (see diffusion length data in Table 4.18), and the maximum average temperature $\langle T \rangle$ at the window side facing the upstream vacuum is obtained by solving the heat equation, see Ref. [34]. Numeric data are given for a 2 mm thick window and different materials in Table 4.18. The temperature excursions are small compared to the allowed ΔT_{\max} associated to the ultimate tensile strength, see Table 4.18 and Ref. [35]. For the water absorber, considering an effective shower length $\Delta s \simeq 4L_R = 1.4$ m ($L_{R,\text{water}} = 0.35$ m), a temperature increase $\Delta T \leq 30$ K is obtained with a vertical water speed $v = 3 \times 10^{-3}$ m/s and a total useful flux $\phi \simeq 0.015$ m³/s, small enough to avoid unwanted turbulence, see Ref. [34].

4.5 DUMP LINES

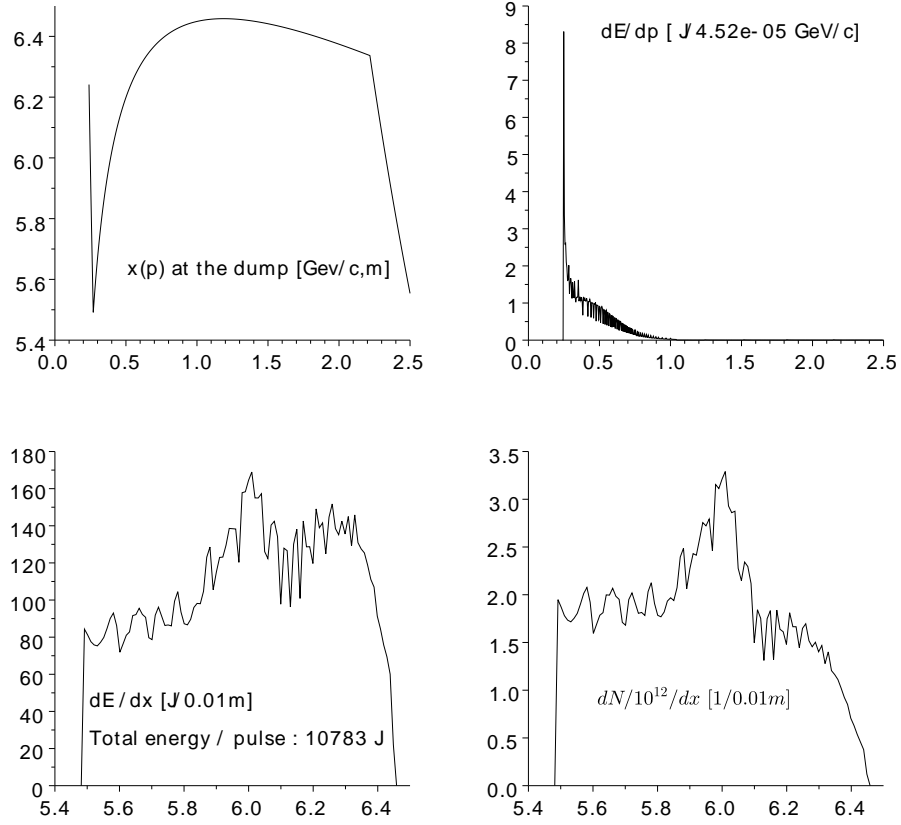


Fig. 4.41: The beam distribution on the dump. Upper left: the horizontal x position as a function of momentum. Upper right: the energy deposition as a function of the beam momentum. Lower left: the horizontal energy distribution in the dump water. Lower right: the horizontal distribution of electrons onto the dump window.

Table 4.18: Thermal data for the dump window for some metals. The diffusion length $d = (2D\delta t)^{1/2}$ is given for the two time scales δt_{train} and $\delta t = 1/f_r$ of Table 4.16.

Data [units]	Be	Al	Ti	Cu
dE/dz [J/m]	4.713e-11	6.977e-11	1.072e-10	2.011e-10
c_v [J/m ³ /K]	1.940e+06	2.240e+06	2.130e+06	3.290e+06
K [J/m/s/K]	1.590e+02	2.210e+02	2.000e+01	3.930e+02
D [m ² /s]	8.196e-05	9.866e-05	9.390e-06	1.195e-04
d_{train} [m]	6.272e-06	6.882e-06	2.123e-06	7.572e-06
$d_{50\text{Hz}}$ [m]	1.811e-03	1.987e-03	6.129e-04	2.186e-03
ΔT_{max} [K]	174	187	274	88
$\langle \hat{T} \rangle$ [K]	0.2	0.2	4.0	0.4
ΔT [K]	0.7	0.9	1.5	1.8

4.5.4.1 A preliminary specification for the Drive-Beam dump

The design of the dump remains to be made. It will be located longitudinally at $s_{\text{dump}} = 20$ m from the downstream side of the extraction magnet. The dimensions of the useful water volume are given in Table 4.19, together with the characteristics of the entrance window. These data are derived in Ref. [34]. Additional issues must be considered in the design. The overall volume of the dump will be much

larger than the useful volume. The cavern housing the equipment remains to be studied. Radiation issues require detailed FLUKA studies. Shielding, safe access to the area, and adequate ventilation with activated air require a dedicated study. Water activation (tritium production, carbon isotopes produced by oxygen decay) require filtering in the primary water circuit. Hydrogen and oxygen radicals produced by dissociation also require filtering in the primary water circuit. Finally, the vacuum of the extraction system and of the decelerator cannot be separated by a window. The dynamic pressure must be the same in both systems, namely $p = 40 \text{ nT}$.

Table 4.19: Preliminary parameters of the post decelerator beam dumps. The radiation length in water is $L_R = 0.36 \text{ m}$

Parameter [units]	Name	Value	Comment
Longitudinal position [m]	Δs	20	relative to extraction point
Transverse position of window centre [m]	Δx	6.0	relative to decelerator axis
Height of window centre [m]	Δy	0	relative to decelerator axis
Water useful volume			
Width [m]	Δx_v	1.7	$1 + 2L_R$
Height [m]	Δy_v	0.7	$2L_R$
Depth [m]	Δz_v	3	$8L_R$
Vertical water speed [m/s]	v	3×10^{-3}	
Total useful water flow [m ³ /s]	ϕ	1.15×10^{-2}	
Window size			
Width [m]	Δx_w	1.0	
Height [m]	Δy_w	0.1	
Thickness [m]	t	0.02	material Al, Ti or Cu

REFERENCES

References

1. Urschuetz, P. *et al.* in *Proc. 10th European Particle Accelerator Conf.*, 26-30 June 2006, Edinburgh, Scotland, UK (2006), 795–797. <<http://accelconf.web.cern.ch/AccelConf/e06/PAPERS/MOPLS101.PDF>>.
2. Braun, H. H. *et al.* *The CLIC RF Power Source: A Novel Scheme of Two-beam Acceleration for Electron-positron Linear Colliders* CLIC-Note-364. CERN-99-06 (CERN, Geneva, 1998). <<http://cdsweb.cern.ch/record/403637/files/CERN-99-06.pdf>>.
3. Schulte, D. & Tomas, R. in *Proc. 23rd IEEE Particle Accelerator Conf.*, 4-8 May 2009, Vancouver, British Columbia, Canada (2009), 3811–3813. <<http://accelconf.web.cern.ch/AccelConf/PAC2009/papers/th6pfp046.pdf>>.
4. Bane, K. *Short-range dipole wake-fields in accelerating structures for the NLC* SLAC-PUB-9663 (SLAC, Stanford, CA, USA, 2003). <<http://www.slac.stanford.edu/cgi-wrap/getdoc/slac-pub-9663.pdf>>.
5. Chin, Y. H. *User's Guide for ABCI Version 9.4 (Azimuthal Beam Cavity Interaction) and Introducing the ABCI Windows Application Package* KEK Report 2005-06 (KEK High Energy Accelerator Research Organization, 2005). <http://www-proc.kek.jp/Materials/Yoshii/ABCI_94_Manual.pdf>.
6. Geschonke, G. & Ghigo, A. *CTF3 Design Report* CERN-PS-2002-008-RF. CTF-3-NOTE-2002-047. LNF-2002-008-IR (CERN, Geneva, 2002). <<http://cdsweb.cern.ch/record/559331/files/ps-2002-008.pdf>>.
7. Schulte, D. *Beam Dynamics Simulation for the CTF3 Drive-Beam Accelerator* CERN-PS-2000-049-AE. CLIC-Note-452 (CERN, Geneva, 2000). <<http://cdsweb.cern.ch/record/453507/files/ps-2000-049.pdf>>.
8. Schulte, D. in *Proc. 23rd IEEE Particle Accelerator Conf.*, 4-8 May 2009, Vancouver, British Columbia, Canada (2009), 4664–4666. <<http://accelconf.web.cern.ch/accelconf/PAC2009/papers/fr5rfp055.pdf>>.
9. Adli, E. *A Study of the Beam Physics in the CLIC Drive Beam Decelerator* (University of Oslo, 2009). <<http://cdsweb.cern.ch/record/1239173/files/CERN-THESIS-2010-024.pdf>>.
10. Huang, N. Y. *et al.* in *Proc. 2nd Int. Particle Accelerator Conf.*, 4-9 September 2011, San Sebastian, Spain (2011), 2085–2087. <<http://accelconf.web.cern.ch/accelconf/IPAC2011/papers/wepc036.pdf>>.
11. Biscari, C., Alesini, D., Ghigo, A., Marcellini, F. & Jeanneret, J. B. in *Proc. 23rd IEEE Particle Accelerator Conf.*, 4-8 May 2009, Vancouver, British Columbia, Canada (2009), 2673–2675. <<http://accelconf.web.cern.ch/accelconf/PAC2009/papers/we6pfp076.pdf>>.
12. Streun, A. in *Proc. of CAS - CERN Accelerator School. Intermediate accelerator physics*, 15-26 September 2003, DESY, Zeuthen, Germany CERN-2006-002 (2003), 203–216. <<http://cdsweb.cern.ch/record/603056/files/CERN-2006-002.pdf?version=1>>.
13. Tomàs, R. Nonlinear optimization of beam lines. *Phys. Rev. ST Accel. Beams* **9**, 081001 (2006).
14. Schmidt, F., Forest, E. & McIntosh, E. *Introduction to the polymorphic tracking code: Fibre bundles, polymorphic Taylor types and "Exact tracking"* CERN-SL-2002-044-AP. KEK-REPORT-2002-3 (CERN, Geneva, 2002). <<http://cdsweb.cern.ch/record/573082/files/sl-2002-044.pdf>>.
15. *The MAD-X home page* <<http://frs.web.cern.ch/frs/Xdoc/mad-X.html>>.

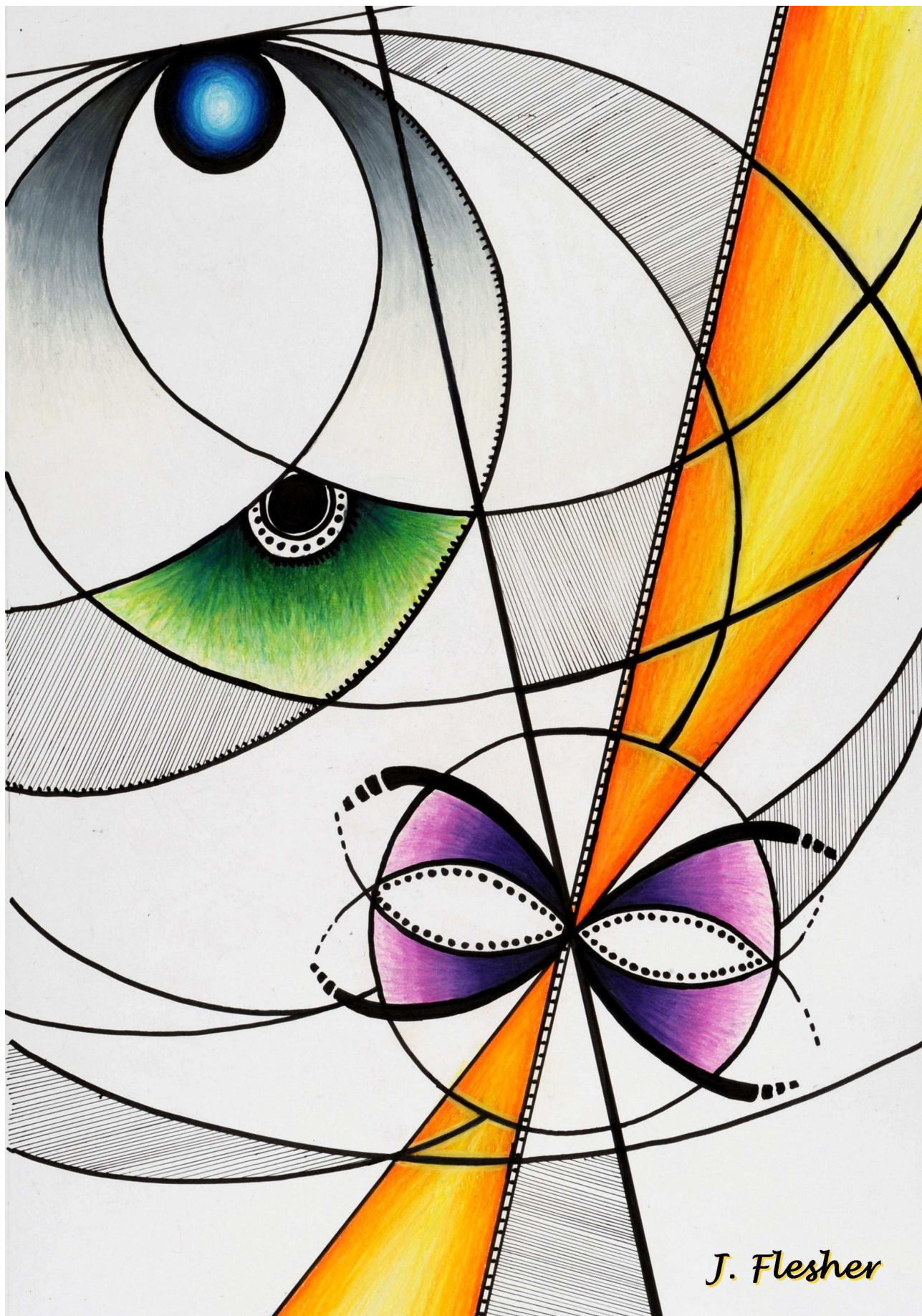
16. Marcellini, F. & Alesini, D. RF deflector design of the CLIC test facility CTF3 delay loop and beam loading effect analysis. *Phys. Rev. ST Accel. Beams* **12**, 031301 (2009).
17. Alesini, D. & Gallo, A. Effects of the beam loading in the RF deflectors of the CLIC test facility CTF3 combiner ring. *Phys. Rev. ST Accel. Beams* **7**, 034403 (2004).
18. Borland, M. Simple method for particle tracking with coherent synchrotron radiation. *Phys. Rev. ST Accel. Beams* **4**, 070701 (2001).
19. Jeanneret, J. B. & Braun, H. H. *Optimization of a Beam Transfer FODO Line* CERN-AB-2008-012. CLIC-Note-760 (CERN, Geneva, 2008). <<http://cdsweb.cern.ch/record/1122291/files/CERN-AB-2008-012.pdf>>.
20. Vorozhtsov, A. *Preliminary Design of CLIC Main Beam Magnets Required For The Beam Transport. Project Breakdown Structure (PBS): 1.3* CERN-ATS-Note-2011-044 TECH. EDMS 1139561 (CERN, Geneva, 2010). <<http://cdsweb.cern.ch/record/1354956/files/CERN-ATS-Note-2011-044%20TECH.pdf>>.
21. Jeanneret, J. B. *et al.* in *Proc. 11th European Particle Accelerator Conf., 23-27 June 2008, Genoa, Italy* (2008), 3017–3019. <<http://accelconf.web.cern.ch/accelconf/e08/papers/thpc018.pdf>>.
22. Vorozhtsov, A. *Preliminary Design of CLIC Drive Beam Magnets Required For The: Delay Line, Combiner Rings, Turn-Around, Transport to Tunnel, Long Transfer Line and Injector Linac* CERN-ATS-Note-2011-025-TECH. CLIC-Note-864. EDMS 1082761 (CERN, Geneva, 2010). <https://edms.cern.ch/file/1082761/1/ATSNote_CLIC_DB_edms_1082761.pdf>.
23. Jeanneret, J. B. *CLIC Parameter Specification. Vacuum of the Long Transfer Line* EDMS 930483 (CERN, Geneva, 2009).
24. Syratcev, I., Adli, E., Schulte, D. & Taborrelli, M. in *Proc. 22nd Particle Accelerator Conf., 25-29 June 2007, Albuquerque, New Mexico, USA* (2007), 2194–2196. <<http://accelconf.web.cern.ch/accelconf/p07/PAPERS/WEPMN071.PDF>>.
25. Adli, E. *A Study of the Beam Physics in the CLIC Drive Beam Decelerator* (University of Oslo, 2009). <<http://cdsweb.cern.ch/record/1239173/files/CERN-THESIS-2010-024.pdf>>.
26. Riche, A. J. *Maximum Energy Transfer Efficiency in CLIC Drive Beam and Proposal for a Method of Focusing, Derived from a very General Discussion on Focusing in Linacs* CLIC-Note-266 (CERN, Geneva, 1994). <<http://cdsweb.cern.ch/record/275691/files/SCAN-9501325.pdf>>.
27. Adli, E. & Schulte, D. in *Proc. 11th European Particle Accelerator Conf., 23-27 June 2008, Genoa, Italy* (2008), 547–549. <<http://accelconf.web.cern.ch/accelconf/e08/papers/mopp001.pdf>>.
28. Jeanneret, J. B. *et al.* in *Proc. 11th European Particle Accelerator Conf., 23-27 June 2008, Genoa, Italy* (2008), 3017–3019. <<http://accelconf.web.cern.ch/accelconf/e08/papers/thpc018.pdf>>.
29. Adli, E. & Siemaszko, D. *Drive beam magnets powering recommendations* (CERN, 2010).
30. Sterbini, G. & Schulte, D. in *Proc. 2nd Int. Particle Accelerator Conf., 4-9 September 2011, San Sebastian, Spain* (2011), 1036–1038. <<http://accelconf.web.cern.ch/accelconf/IPAC2011/papers/tupc019.pdf>>.
31. Adli, E. *Drive beam decelerator BPM functional specification* (CERN, 2009).
32. Walz, D., Jurow, J. & Garwin, E. L. Water Cooled Beam Dumps and Collimators for the Stanford Linear Accelerator. *IEEE Transactions on Nuclear Science* **12**, 867–871 (1965).

REFERENCES

33. Adli, E. *A Study of the Beam Physics in the CLIC Drive Beam Decelerator* (University of Oslo, 2009). <<http://cdsweb.cern.ch/record/1239173/files/CERN-THESIS-2010-024.pdf>>.
34. Jeanneret, J. B. *Dumping the Decelerated Beams of CLIC* CERN-OPEN-2011-039. CLIC-Note-887 (CERN, Geneva, 2011). <<http://cdsweb.cern.ch/record/1376685/files/CERN-OPEN-2011-039.pdf>>.
35. Fartoukh, S., Jeanneret, J. B. & Pancin, J. *Heat deposition by transient beam passage in spoilers* CERN-SL-2001-012-AP. CLIC-Note-477 (CERN, Geneva, 2001). <<http://cdsweb.cern.ch/record/498625/files/sl-2001-012.pdf>>.

Chapter 5

Technical description of the accelerator



J. Flesher

5.1 SOURCES

5.1 Sources

5.1.1 Overview

The CLIC Main Beam injectors are described in §3.1 which gives a general overview from an accelerator physics point of view. In the following, a more technical description of the most relevant components and concepts for the baseline configuration can be found. However, a detailed technical description of the injectors is not yet available since for the conceptual design the focus was on identifying the critical items.

The Main Beam injectors are in a central location close to the Interaction Point (IP). The polarized electron and unpolarized positron beams are accelerated up to 9 GeV and then transported along the Main Linac to each end of the linear collider. The Main Beam injectors consist of a polarized electron source with its pre-injector, a 5 GeV drive linac, two positron conversion targets followed by pre-injectors, and a common injector linac which accelerates both particle species up to 2.86 MeV. The injector linac is followed by pre-damping rings, damping rings, bunch compressors, and the booster linac. In this section the injectors are described up to the pre-damping rings. A schematic layout of the CLIC Main Beam injector complex is shown in Fig. 5.1.

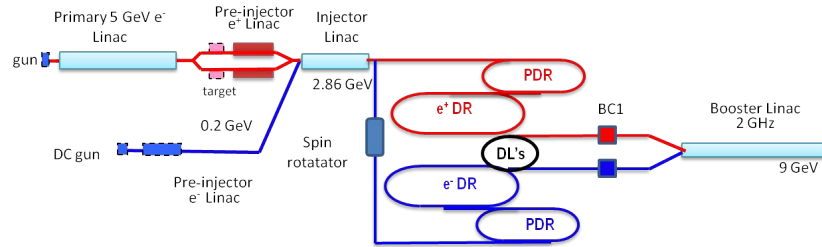


Fig. 5.1: Schematic layout of the Main Beam injector complex.

A polarized positron source has been studied for future upgrades beyond the baseline. More information can be found in §3.1.4.

The 2 GHz linac technology can be considered as conventional and is based on a system used for many years in major accelerator labs. The polarized electron source uses challenging technologies like a high-power laser, thin-film cathodes and an ultra high vacuum system. Its concept it is based on systems already used in existing facilities. The most challenging part is the positron production target, positron capturing, and subsequent transport of the large emittance to the damping rings. For this part the design is based on simulations which have been extensively benchmarked with data from existing facilities.

5.1.2 Technical description

5.1.2.1 e^- source and linac

The CLIC polarized electron source consists of a DC-photo gun, a 1 GHz bunching system, and a 2 GHz accelerator which accelerates the electrons up to 200 MeV before injection into the common injector linac. A spin rotator is needed in front of the pre-damping ring to orient the spin vertically for injection into the damping rings. A schematic diagram of the source is shown in Fig. 5.2. The most demanding components are the laser and the DC-photo gun with its GaAs cathode.

The CLIC polarized electron source is designed to take advantage, as much as possible, of proven technologies and installations. The SLC electron source and the ILC design are used as references for CLIC. In a recent experiment at SLAC using the gun test facility, the CLIC parameters have been demonstrated using this technology [1].

To produce polarized electrons, a circularly polarized laser is shone on a GaAs-type cathode.

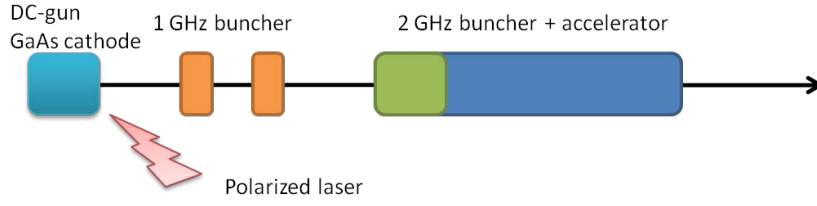


Fig. 5.2: Schematic of the polarized electron source and bunching system

A commercially available strained multi-layered GaAs cathode can be used. The cathode requires a very good vacuum environment to obtain long lifetimes. Several thousand hours of lifetime have been demonstrated provided that the pressure around the cathode can be kept in the 10^{-11} mbar range. The gun has to be equipped with a load-lock system for easy cathode exchange and activation.

An important deteriorating effect is ion back-bombardment [2, 3]. Since this damage is proportional to the current density, the total flux of electrons (measured in C/cm^2) that can be drawn under given vacuum conditions during a lifetime is limited. This limitation is not the dominant deteriorating factor for the CLIC source, since only less than $1000 C/cm^2$ per year are required whereas values of $\sim 10^5 C/cm^2$ have been demonstrated at JLAB and MAMI. In addition to ion back-bombardment, the interaction of the cathode surface with oxidizing gases also reduces photocathode lifetime. The harmful gas species may be present either in the residual gas or may be become enhanced due to electron/wall interaction in the vicinity of the cathode; for example due to beam loss or field emission. Experience at all source labs has shown that it is necessary to restrict beam loss current and field emission to levels of the order of nanoamperes. A recent experiment at JLAB has demonstrated that a correspondingly low value of field emission can be achieved at the CLIC design voltage of 140 keV [4, 5]. Concerning beam loss (1 nA is $< 10^{-4}$ of average beam current at CLIC), much lower relative losses have been demonstrated in c.w. operation [6], but in the case of CLIC a very careful design of electron optics must enforce this, because of the larger emittance and the presence of space charge effects. The losses induced after the bunching system (12%) are no threat for the photocathode since they happen far from it, which allows the induced gasses to be eliminated by differential pumping. The simultaneous achievement of state-of-the-art basic vacuum, low field emission and low losses should result in a cathode lifetime of at least three months under operational conditions at CLIC.

Table 5.1 summarizes the required laser parameters for the CLIC Main Beam polarized electron source with a margin factor of 3 allowing for longitudinal and transverse pulse shaping, beam transport, polarization control, and QE (Quantum Efficiency) drop. SLAC has demonstrated all the main parameters for the DC option, which is taken as the baseline for CLIC [7–10]. Figure 5.3 shows a schematic laser system as used at SLAC. This has undergone many improvements over the years, to increase output energy.

A flash-lamp pumped Ti:sapphire rod is inserted into a cavity which consists of a planar and a curved end mirror optimized to compensate thermal lensing in the rod. A quartz plate inside the cavity is used to tune the wavelength with an output bandwidth of ~ 0.7 nm. A Pockels-cell cuts out the required flat part (50–900 ns) from the $15 \mu s$ pulse produced in the cavity during the $22 \mu s$ pumping time. The drop of quantum efficiency and degradation of the flash-lamps is compensated through a feedback to the Pockels-cell. Multimodal beam is necessary for the required pulse length and a near flat-top profile after slicing. A second type of Pockels-cell system is capable of producing a pulse shape, which compensates for beam loading using remotely controllable arbitrary waveforms to the Pockels-cell driver. A linear polarizer and a pair of Pockels-cells provide the high degree of circular polarization. Two remotely controllable half-wave plates assure the helicity can be changed on the cathode. The beam transport is designed to preserve the polarization and to image the last Pockels-cell for helicity control.

5.1 SOURCES

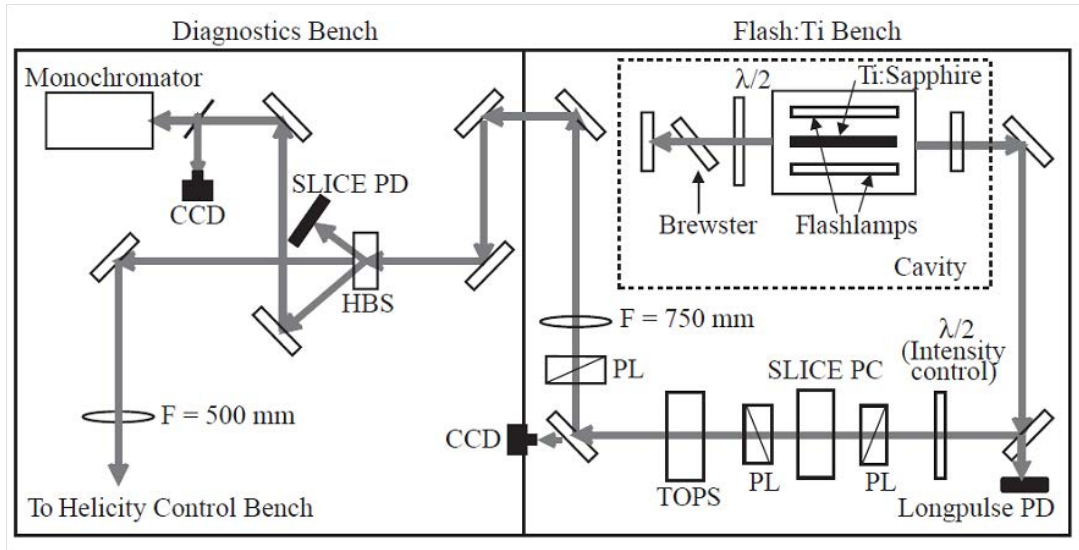


Fig. 5.3: Schematic laser system for CLIC

Table 5.1: Parameters of the laser system for the CLIC DC baseline as demonstrated at SLAC and the 1 GHz laser option

	CLIC 1 GHz	CLIC DC/ SLAC Demo
Electrons		
Number of electrons per bunch	3.72×10^9	1365×10^9
Charge/single bunch [nC]	0.96	–
Charge/macrobunch [nC]	300	300
Bunch spacing [ns]	1	DC
RF frequency [GHz]	1	DC
Bunch length at cathode [ps]	100	DC
Number of bunches	312	–
Repetition rate [Hz]	50	50
QE [%]	0.3	0.3
Polarization	>80%	>80%
Circular polarization	>99%	>99%
Laser		
Laser wavelength [nm]	780–880	865
Energy/micropulse on cathode [nJ]	509	–
Energy/macropulse on cathode [μJ]	159	190
Energy/micropulse laser room [nJ]	1526	–
Energy/macropulse laser room [μJ]	476	633
Mean power per pulse [kW]	1.5	2
Average power at cathode wavelength [mW]	8	9.5

The flash-lamps will require to be changed every month due to the 50 Hz repetition rate; this takes about 1 hour. Apart from general water circuit maintenance, the system demonstrated good long-term reliability. Humidity and temperature are controlled to avoid slow drifts and, with the feedback at the Pockels-cell, the system routinely delivers $< 0.5\%$ r.m.s. stability both in the laser and the electron beam.

Where the 1 GHz pulse structure is directly produced by the laser system an injection mode locked Ti:sapphire oscillator, using a gain-switched diode with external cavity tuning or several diodes to cover a broad range of wavelengths, could be used as the front end [11–13]. A Ti:sapphire amplifier pumped by a 1 GHz pulsed Nd-YLF diode-pumped laser system, similar to that of the PHIN laser [14, 15], at second harmonic wavelength could provide the energy per pulse necessary for CLIC. The system would also give tunable wavelength, variable pulse repetition rate, and pulse length for cathode R&D. The advantage of such a system is that the time structure of the beam is defined by the laser; the bunching efficiency is therefore optimal. Such a time structure, however, is demanding on the cathode due to space charge and surface charge limitations and its feasibility would have to be demonstrated.

For the baseline with a DC gun an efficient bunching system consisting of 1 GHz sub-harmonic pre-bunchers and a tapered buncher at 2 GHz followed by 2 GHz accelerating structures prepares the beam for injection into the injector linac. The bunching and acceleration have been simulated for a bunch spacing of 2 GHz, while the bunch spacing for the pre-injector linac has been revised recently to 1 GHz. This change would not change the conclusion of the study done at 2 GHz. A bunching system at 1 GHz with subsequent acceleration at 2 GHz should have a very similar performance as the one described below. The bunching system comprises two 1 GHz pre-buncher, one 5-cell tapered- β buncher, and a 2 GHz accelerator, as shown in Fig. 5.2. While two pre-bunchers are used to modulate the macro bunch, 5-cell tapered- β travelling-wave 2 GHz structures are used as a buncher to compress the micro bunches down to 14 ps FWHM at the end of the first 2 GHz accelerator [16]. According to the simulation 88% capture efficiency can be expected for such a system. Several solenoids are used to focus the beam from the gun to the first accelerating structure which also uses solenoid focusing all along its length.

The beam is subsequently accelerated to 200 MeV using the nominal 2 GHz RF structures. The 2 GHz RF system is described in §5.1.3. A loaded gradient of 18 MV/m has been chosen for the 1.5 m long accelerating structures. The total length of the linac, including the source, amounts to about 30 m.

The nominal beam consists of two bunch trains of 156 bunches spaced by 1 ns with a distance of 717 ns between the first bunches of the two sub trains, therefore the laser pulse length needs to reach at least 900 ns. The RF pulse length needed is around 1300 ns including the 389 ns filling time of the accelerating structure.

5.1.2.2 e^+ source and linac

The CLIC positron source aims for unpolarized beams for the baseline configuration. A conventional scheme has been studied in the past and was found feasible with a double target scheme [17]. Target heating and the resulting positron phase space have been found critical. Consequently the concept of hybrid targets (Fig. 5.4) has been studied and adopted as the baseline for CLIC.

The advantage of this scheme is the possibility to use thinner targets to reduce the energy deposition in the target. This also allows sweeping out unwanted particles in front of the final converter target. A 5 GeV electron beam impinges on a crystal tungsten target aligned along its $<111>$ axis. Photons produced via the channelling process go straight to an amorphous tungsten target while the charged particles are bent away, reducing the deposited energy. The channelling effect enhances the photon yield compared to a pure bremsstrahlung process. The tungsten target thickness and the distance between the two targets have been carefully optimized for maximum positron production [18]. The optimized target parameters and the distance between the two are listed in Table 5.2 for the crystal target and Table 5.3 for the amorphous target.

Downstream of the amorphous target, an Adiabatic Matching Device (AMD) collects the positrons

5.1 SOURCES

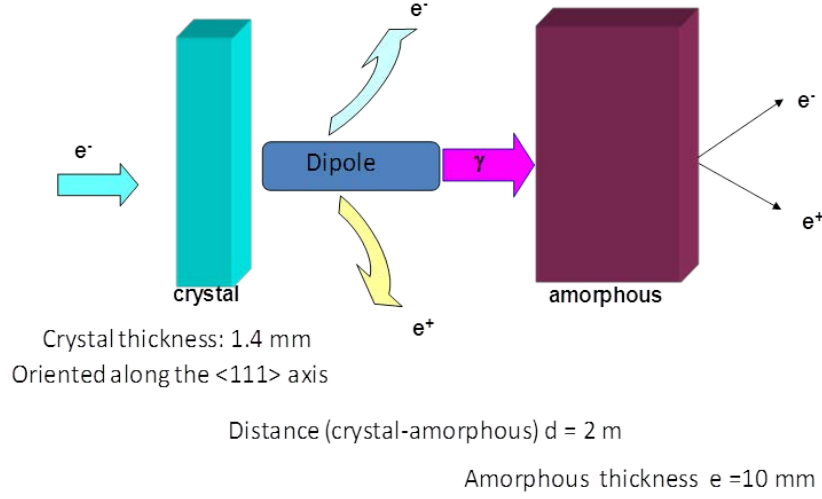


Fig. 5.4: The CLIC positron source based on hybrid targets.

Table 5.2: Crystal target parameters.

Material	Tungsten
Thickness (radiation length)	$0.4 \chi_0$
Thickness (length)	1.40 mm

Table 5.3: Amorphous target parameters.

Material	Tungsten
Thickness (radiation length)	$3 \chi_0$
Thickness (length)	10 mm
Distance to the crystal	2 m

by reducing their transverse momentum. It was simulated as a cylinder of 20 cm long and 20 mm radius with a magnetic field given by: $B = B_0/(1 + az)$, with $B_0 = 6$ T and $a = 55 \text{ m}^{-1}$.

The pre-injector linac captures and accelerates the positrons up to 200 MeV after which a bunch compressor reduces the bunch length before injection in the common injector linac. A typical four-magnet chicane has been used for the simulations of the bunch compressor. The 2 GHz accelerating structures are surrounded by solenoids. For the simulations 0.5 T was used for the solenoid fields and an aperture of 20 mm radius for the accelerating structures. The total simulated positron yield defined as positrons delivered to the pre-damping ring and matching its longitudinal and transversal acceptance was found to be $0.39 \text{ e}^+/\text{e}^-$. The whole positron source including the pre-injector linac will be about 40 m long. Two such sources will be installed in parallel from the beginning. The beam can be switched bunch by bunch between the two targets and later on recombined with RF deflectors operating at 1 GHz. For 3 TeV only one target station is needed but for the 500 GeV version two targets are probably necessary to guarantee the lifetime aimed for.

The positron source was designed to be able to survive at least one full year of CLIC operation

before a target has to be changed. Therefore, the Peak Energy Deposition Density (PEDD) was limited to below 35 J/g which has been found to be the damage limit corresponding to about 1000 days of operation (see §3.1.3.2). The CLIC positron source with its two parallel targets should therefore have a large operational margin since one target is already sufficient to deliver the full current at 3 TeV without exceeding these conditions. So far no detailed technical design of the target area including the AMD has been done for CLIC. A thick crystal target for positron production has been studied extensively at KEK including an operational run lasting several months, validating this concept and benchmarking simulations [19]. An experiment using the full hybrid target approach is under way at KEK [20]. Therefore, valuable data should be available to verify the concept for CLIC.

The positron-source drive linac consists of an electron source and a 5 GeV conventional 2 GHz linac. A total of 218 accelerating structures, as described in §5.1.3, will be used; the total length of the linac is about 500 m. The electron source can be a conventional DC-gun with a bunching system similar to the polarized source or an RF photo injector. The RF photo injector would allow easy tuning of the bunch population with a feedback on the laser amplitude in order to fulfil the positron beam current stability requirements at the entrance of the pre-damping ring. The CTF3 injector as well as the PHIN photo injector would fulfil the requirements of such a source.

5.1.2.3 Common e^+/e^- injector linac

The injector linac accelerates both e^- and e^+ from 200 MeV to 2.86 GeV. The main parameters of the linac are summarized in Table 5.4. The acceleration of the particles is provided by a total number of 120 travelling-wave accelerating structures whose parameters are summarized in Table 5.5. One 50 MW klystron will drive one accelerating structure in the common injector linac due to the special time structure of the beam. The RF pulse length has to be $3.6 \mu\text{s}$ to allow subsequent acceleration of electrons and positrons. The positrons follow the electrons with 2314 ns between the first electron and the first positron. Each particle species consists of two sub-trains each 156 ns long and spaced by 717 ns. This particular time structure is necessary to fulfil the damping ring and geometrical requirements of the main injector systems. Amplitude modulation of the RF system will be needed to compensate the beam loading for all trains sufficiently.

A triplet-based lattice has been studied so far by simulations where the drift spaces between the triplets are filled with accelerating structures [21]. The focusing strength has to be quite strong at the beginning of the linac to cope with the large positron phase space and can be relaxed towards the end of the linac. Detailed simulations have been done only for the positron beam starting from the simulated phase space at the end of the pre-injector linac and bunch compressor. The polarized electrons can use the same optics since their emittance is two orders of magnitude smaller.

Table 5.4: General parameters of the Injector Linac

Parameter	Value
Total length [m]	~ 300
Average accelerating field [MV/m]	15
Number of accelerating structures	120
Length of accelerating structures [m]	1.5
Energy gain [MeV]	22.5

5.1.3 Injector RF system and accelerating structure

The pre-injector linacs for electrons and positrons, the common injector linac, the booster linac, and the positron driver linac will use the same 2 GHz accelerating structure and RF system. The 2 GHz system is also used for the first bunch compressor (BC1). The only exception is the second bunch compressor (BC2), in front of the main linac, which will use a 12 GHz RF system.

The nominal 2 GHz RF system consists of two 50 MW klystrons and a cavity-type pulse compressor which is used to enhance the peak power. The compressed RF pulse is then distributed to four accelerating structures. The accelerating structure is a 1.5 m long quasi-constant-gradient structure running at a loaded gradient between 15 and 18 MV/m. In order to adapt the RF system to different beam currents and pulse length in the various linacs, the compression factor is optimized for each linac. The common injector linac will not use a pulse compression system due to the long RF pulse length needed. The configurations of the different linacs within the injector systems are summarized in Table 5.6. The main components of the RF system are described below.

5.1.3.1 Klystron and pulse compressor

We assume a conventional solenoid-focused 2 GHz klystron with an output power of 50 MW. The pulse length assumed for pulse compression is up to $8\ \mu\text{s}$. Such a klystron does not presently exist on the market but is assumed to be an extrapolation from the 3 GHz, 45 MW and $6\ \mu\text{s}$ klystrons currently used in CTF3. The klystron output power will be compressed using a SLED I type cavity with a Q of 2×10^5 . The nominal pulse compressor setup assumes a power gain sufficient to feed four accelerating structures with an input power up to 56 MW each depending on beam current and pulse length. The higher beam current, of the 500 GeV version of CLIC, will be required to feed only two structures per pulse compressor. An RF station would be completed with a solid-state modulator powering the klystron. The combination of two klystrons is required to allow for amplitude modulation with a constant phase over the trains for beam loading compensation.

5.1.3.2 Accelerating structure

A tapered quasi-constant-gradient accelerating structure has been designed to be used in the various injector linacs. The length of the structure has been driven by the need to accelerate a high beam current and to improve efficiency with a short filling time. The main parameters of the structure can be found in Table 5.5.

Table 5.5: 2 GHz accelerating structure parameters

Parameter	Value
Frequency [MHz]	1999
Structure length (30 cells) [m]	1.5
Filling time [ns]	389
Cell length and iris thickness [mm]	50, 8
Shunt impedance [$\text{M}\Omega/\text{m}$]	54.3–43.3
Aperture (a) [mm]	20–14
Cell size (b) [mm]	64.3–62.9
Group velocity (v_g/c) [%]	2.54–0.7
Phase advance per cell	$2\pi/3$

The structure will be operated in the booster linac at an average loaded gradient of 16 MV/m with an input power of 44 MW for a bunch charge of 4×10^9 electrons. For a single beam using 312 bunches

and a total pulse length of 545 ns the structure obtains an RF-to-beam efficiency of 16.5%.

The higher-order modes of this structure have been studied and the results have been used in the beam dynamics studies for the booster linac.

5.1.3.3 Different operational modes within the injector complex

Since each linac has a different time structure and current the operation mode for the RF systems differs from linac to linac. The 200 MeV pre-injector linacs are separate; one for positrons and one for electrons therefore the compressed RF pulse length is about 1300 ns for the nominal beam. A peak power gain of 2.5 can be assumed for such a configuration. In the injector linac the total RF pulse length amounts to 3600 ns and pulse compression is no longer useful; therefore one klystron feeds one accelerating structure which also allows more flexibility for the beam loading compensation given the fact that positrons will have a higher current than electrons in this linac. The delay between electrons and positrons amounts to $2.3 \mu\text{s}$ in the injector linac and $1.1 \mu\text{s}$ in the booster linac respectively. The different configurations for the 2 GHz RF system used in each linac are summarized in Table 5.6.

Table 5.6: Configuration of the 2 GHz RF systems for each linac of the injector complex.

Linac	Energy gain	Bunch population	RF pulse length	Power per structure	Loaded gradient	Power compress. gain	No. of structures	Length
	[MeV]	$[\times 10^9]$	[ns]	[MW]	[MV/m]			[m]
e^- pre-injector	200	4.3	1300–1700	54	18	2.3–2.5	18	30
e^+ pre-injector	200	11	1300–1700	56	15	2.3–2.5	9	40
Injector linac	2660	6	3600–4000	44	15	1	119	300
e^+ drive linac	5000	11	1300–1700	56	15	2.3–2.5	223	400
Booster linac	6140	4	1700–2000	44	16	2–2.3	256	473

The beam loading compensation which depends on the beam current will have to rely mainly on amplitude modulation. Studies for NLC/GLC showed that this is feasible for a similar RF system [22].

5.1.4 Cost considerations

Obviously the most expensive components of the injectors are related to the RF system, modulators, pulse compressors, klystrons, and accelerating structures. The cost and performance of the klystron is the dominating factor. We assume a 50 MW klystron; if a klystron with significantly higher power can be obtained for a similar price, savings for the RF system can be obtained as more structures can be powered by one RF station. Given the number of high-power RF components which are needed in the injector complex, detailed engineering studies should be done for their production. As a consequence, early prototyping of these items is important and should start in the project preparation phase.

5.1.5 Outlook for project preparation phase

The Main Beam injector complex design uses mostly well-established technologies and conservative parameters in order to ensure its reliability. Therefore, during the technical design the work would concentrate on cost optimization, prototyping of components (in particular the RF system) and the construction of a polarized electron source to get early operational experience.

More detailed and integrated simulations will have to be performed to get a more accurate picture of the beam performance and to obtain more detailed specifications for components. Trade-offs for cost optimizations have to be evaluated.

5.1 SOURCES

The prototyping of components will certainly include the 2 GHz RF systems. A complete RF station including modulator, klystron, pulse compressor, and accelerating structure should be built. For the positron production prototype, work for the adiabatic matching device and the target has to be done. In addition, some testing with a hybrid target would be desirable including detailed yield and lifetime studies.

Since the source is really the starting point of the CLIC Main Beam, a polarized electron source should be constructed including the DC-gun, a laser, the cathode handling system, and a short beamline to measure the beam properties including polarization.

Although several options have been studied for polarized positrons, no realistic solution is available today. A major R&D program would be necessary to advance towards a valid conceptual design.

5.2 Normal-conducting and permanent magnets

5.2.1 Overview

The acronym CLIC (Compact Linear Collider) points to a key aspect of the project: the compactness. Small magnet apertures and limited space for the magnet systems (e.g., on the two-beam modules in the CLIC main tunnel) are aspects impacting on the magnet design choices. For these and other reasons the CLIC baseline foresees the use of normal-conducting Electromagnets (EM) and, where they can be an advantage, of Permanent Magnet (PM) technologies in several cases pushed to their maximum operational limit in terms of compactness and magnetic saturation of the materials used. The use of Superconducting Technology (SC) may be necessary in some specific cases (e.g., for the Damping Ring wigglers) where the requirements are not achievable with EM and PM technologies.

The CLIC complex will contain a quantity of magnets well beyond the number of magnets previously produced for a particle accelerator. For example, the Drive Beam Quadrupole (DBQ) family will have more than 40 000 units and the Main Beam Quadrupole (MBQ) family more than 4000 units. The industrialization, cost optimization, quality control, assembly, and installation of such large numbers of magnets will be among the major challenges of the project.

5.2.2 Main Beam Quadrupoles

The Main Beam linac's magnetic lattice foresees the focusing of the e^+ and e^- beams with 4020 MBQs with a constant nominal gradient but of different magnetic lengths (see Table 5.7).

Table 5.7: List of Main Beam Quadrupole types (the numbers given are the totals for the two linacs).

Quadrupole type	Magnetic length [mm]	Quantity
Type-1	350	308
Type-2	850	1276
Type-3	1350	964
Type-4	1850	1472

The nominal gradient for the four types of MBQ is 200 T/m and the magnet aperture required is of ≥ 8 mm diameter bore.

The magnets were designed at CERN in 2009. During the same year, the procurement of the major components for Type-1 and Type-4 prototypes was launched. These prototypes will be needed to test and validate the active stabilization capability (see §5.18), to develop dedicated magnetic measurement systems for magnets with very small apertures, and to be assembled and tested in the Test Module-LAB and Test Module CLEX program (for more details see §2.10.4). The scope of this prototype program will be the validation of the magnet design, to investigate all the integration aspects inside the CLIC two-beam modules, and later to test the quadrupoles with beam (in CLEX).

Figure 5.5 shows the main views of the Type-4 prototype. The four types of MBQ differ only in the active (magnetic) length, so all cross-section dimensions and operational parameters are identical. The magnet bore (inter-pole aperture) is 10 mm.

Even if fully compatible with the two-beam module layout, the interconnection interfaces of the prototype (electrical and hydraulic) are not yet optimized for series production. The present configuration will provide a relatively robust coil interface in view of the expected frequent dismounting and re-assembly. Table 5.8 shows the main parameters for the Type-4 magnet. Parameters of the shorter Type-1, Type-2, and Type-3 such as weight, electrical and cooling parameters, are, of course, lower.

A key aspect to be investigated on the prototypes is the achievable mechanical tolerances for the iron quadrants. In order to investigate the best achievable performance in terms of magnetic quality (magnetic axis and magnetic field quality) we are trying to procure the iron quadrants machined at the

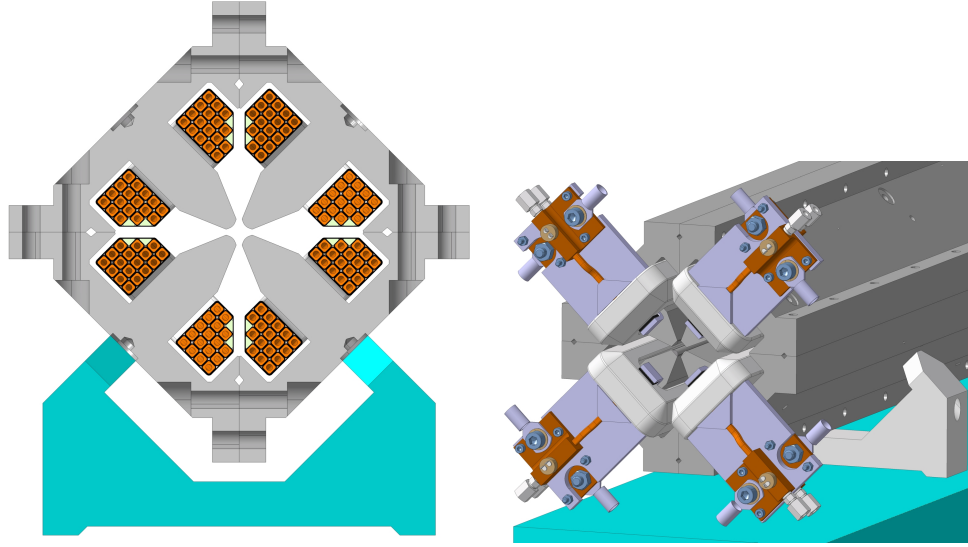


Fig. 5.5: Main Beam Quadrupole: cross-section and end view

Table 5.8: Main parameters for MBQ Type-4 prototype.

Parameter [unit]	Value
Yoke length [mm]	1844
Magnet length [mm]	1901.8
Yoke weight [kg]	$80 \times 4 = 320$
Conductor weight [kg]	$12.5 \times 4 = 50$
Total magnet weight [kg]	370
Cooling circuits per magnet	4
Height/width [mm]	5.6
Hole diameter [mm]	3.6
$x = y$ [mm]	1
r [mm]	1
Turns per pole	17
Conductor length per pole [m]	68
Current [A]	126
Current density [A/mm ²]	6.01
Resistance [mΩ]	241.3
Inductance [mH]	42.8
Power [W]	3831
Voltage [V]	30.4
Water velocity [m/s]	1.12
Water flow [l/min]	0.69
Pressure drop [bar]	4.26
Reynolds number	6147
Temperature rise [K]	20

best mechanical precision. An overall precision of 0.02 mm (on the 2 m long Type-4 quadrants) should be possible with ‘standard’ production techniques but has not yet been achieved. Analysis of the results and of the performances of the different prototypes are on-going and from the magnetic measurement and test with beam we expect to have indications of the necessary machining quality in order to fulfil the magnetic requirements as defined in the beam optics studies.

Another point to be investigated with the prototypes is the use of ‘standard’ steel (rather than special steel for magnetic applications, e.g., ‘Armco’ type). The finite-element analysis at the base

of the magnet design has shown that the magnetic characteristic of ‘standard’ steel (e.g., ‘AISI 1010’ type) would be sufficient to guarantee the required magnet performance, so it was decided to build the quadrants for the first two prototypes from tightly certified (and measured by CERN) ‘standard’ steel ingots. The analysis of the results is ongoing. Figure 5.6 shows coils and iron quadrants for the MBQ prototypes.

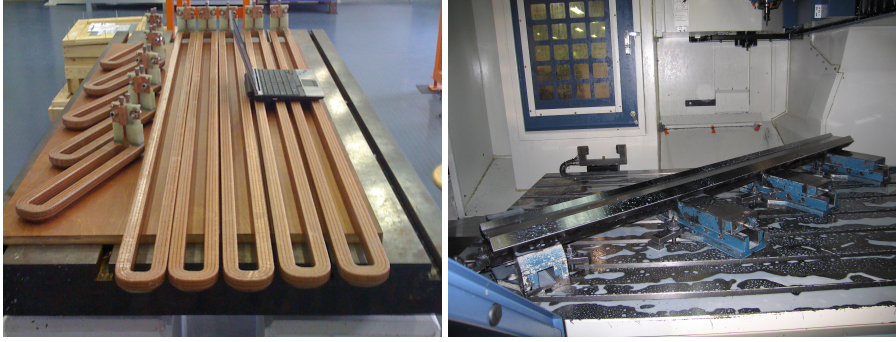


Fig. 5.6: Main Beam Quadrupole prototype procurement: coils and iron quadrant (during machining)

5.2.2.1 Main Beam Quadrupole beam-steering correctors

A beam-steering capability is required along the Main Beams. Depending on the type of MBQ, the dipole integrated strength for beam-steering correction varies from 10^{-3} Tm (for Type-1 MBQs) to 4×10^{-3} Tm (for Type-4). Steering capability is required in only one plane per magnet, alternatively vertical and horizontal.

Two main solutions are possible: a MBQ built-in correction scheme with extra coils in each magnet or an *ad hoc* small dipole corrector added to each MBQ. The second solution was retained as baseline since it is not clear how to place correction coils inside such a compact magnet working very close to the saturation limit (the nominal operation gradient set at 200 T/m). Furthermore, the use of correction coils would require a laminated structure for the magnet poles, different from the present baseline. The beam-steering correctors will be of four different types depending on the strength required. They will use laminated steel yokes and coils cooled by natural air convection due to small electrical power dissipation.

Figure 5.7 shows examples of the integration for two types of correctors (for Type-1 and Type-4 MBQ).

5.2.3 Drive Beam Quadrupoles

In order to keep the Drive Beam focused along the Main Linac decelerators, quadrupole magnets (Drive Beam Quadrupoles (DBQs)) are present all along the beam in a FODO configuration with one ‘F’ and one ‘D’ quadrupole on each module. The decelerators contain 20 740 quadrupoles in each linac.

The required quadrupole strength (in terms of integrated gradient) scales with the energy along the decelerator. In the nominal operation of CLIC, at the beginning of the decelerator (for a beam energy of 2.5 GeV at the decelerator entrance) [23], a maximum integrated gradient of 12.2 T per magnet is required; this is known as the ‘nominal maximum’ integrated gradient needed in the decelerator. The variation of gradient with position is shown in Fig. 5.8. Several different scenarios are shown, and the expected variation of gradient at each point of the decelerator is visible. At the entrance side, the strength must be tuneable from 8.5 T to 14.6 T per magnet (70% to 120% of the ‘nominal maximum strength’ of 12.2 T per magnet). The required range at the exit side is 0.85 T to 4.9 T (i.e., from 7% to 40% of the ‘nominal maximum strength’).

The main requirements for CLIC DBQs are given in Table 5.9. In the two-beam module layout,

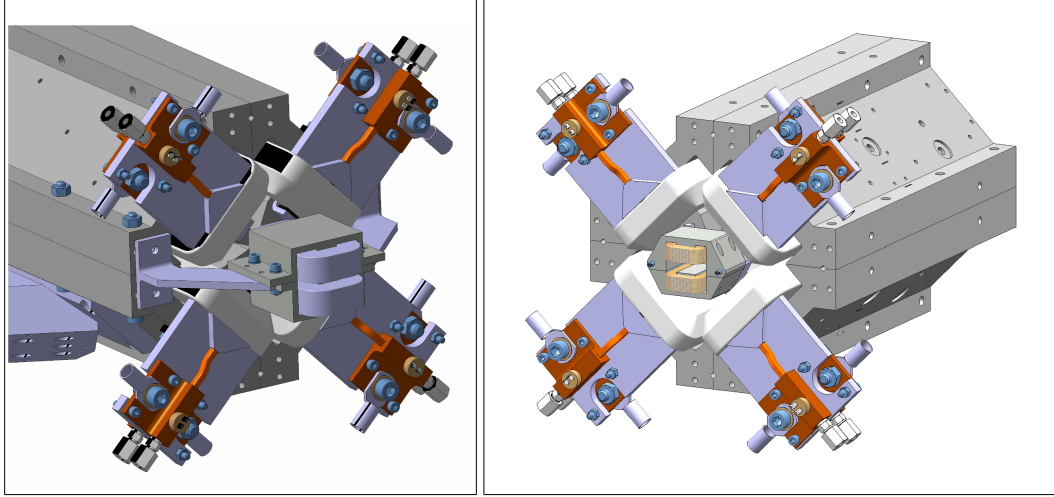


Fig. 5.7: View of the beam-steering corrector integration for the MBQ Type-4 (left) and Type-1 (right).

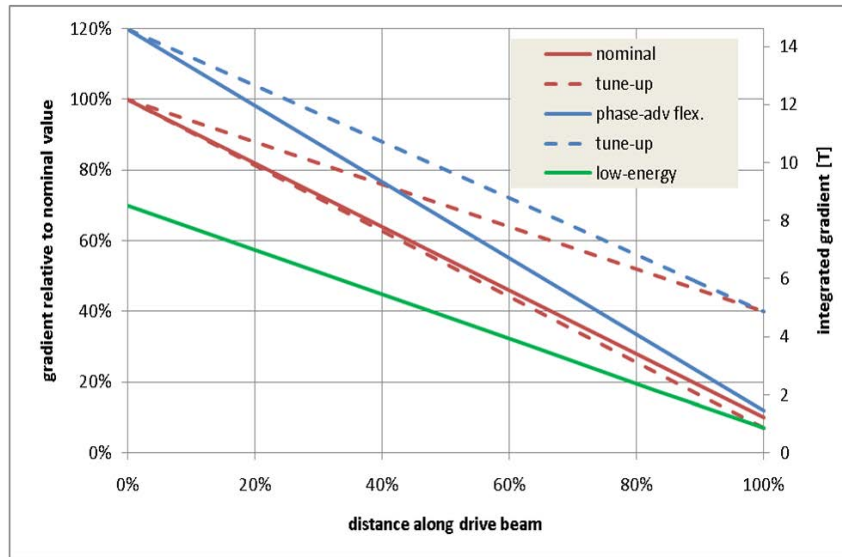


Fig. 5.8: Gradient requirements for Drive Beam Quadrupoles as a function of distance along the decelerator. Several scenarios are shown – nominal operation, phase advance flexibility, and low-energy operation. Envisaged limits for tuning up are shown with dashed lines. The percentages on the left vertical axis show the integrated gradients relative to the ‘nominal maximum strength’ of 12.2 T at the high-energy side.

the allocated space for each DBQ is constant. To fulfil the needed integrated gradient requirement, assuming a constant magnetic length of 0.15 m (compatible with the available length of 270 mm), the needed gradient should vary along the decelerator from 81.2 T/m to 8.12 T/m.

The design activity for 41 400 units of this family of magnets is proceeding on two fronts: a classical electromagnetic design and an option with tuneable permanent magnets.

5.2.3.1 Classical electromagnet design option

Several solutions are possible to meet the specified variations in integrated gradient:

- keep the magnetic length of each magnet constant and decrease the maximum gradient (by reducing the maximum current in the coils);

Table 5.9: Main requirements for Drive Beam Quadrupole

Parameter	High-energy side	Low-energy side
Number of magnets		41 400
Nominal maximum strength [T] (integrated gradient)	12.2	1.22
Stability		5×10^{-4}
Integrated gradient quality		0.1%
Good field region [mm]		11
Bore radius [mm]		13
Available width [mm]		391
Available height [mm]		391
Available length [mm]		270

- keep the current in the coils constant (and consequently the gradient) and decrease the magnetic length for each magnet;
- combine the solutions a) and b) to define a certain number of ‘magnet variants’ and set inside each variant an adequate couple magnetic length-gradient to obtain the required integrated gradient.

For the procurement of the DBQs needed for the Test Module-LAB and CLIC Test Module program (which require a maximum of 14 units) we are mainly investigating solution a) and we focus on achieving the maximum integrated gradient required (nominally 12.2 T for the beginning of the Decelerator). An important operational aspect to be investigated is the powering scheme for the full chain of 20 700 quadrupoles in each linac (see §5.8 for more details).

A classical EM magnet design is under study. Available longitudinal space on the modules is quite limited but a solution that will guarantee the needed maximum integrated gradient and field quality seems possible. The available space was optimized in order to get the maximum magnetic length (194 mm) in order to limit the gradient and consequently the electrical power.

Figure 5.9 shows a conceptual design of such a magnet. Figure 5.10 shows its excitation curve showing the different operation points:

- at the decelerator entrance (nominal integrated gradient of 12.18 T);
- at the decelerator end (integrated gradient of 1.22 T (i.e., 10% of the maximum);
- at the desired ‘ultimate’ value (120% of the nominal).

Figure 5.11 shows the expected field quality for the three different working points.

Prototypes are being designed; they will be mainly used for integration tests within the CLIC Test Module Program (see §2.10.4) and to investigate industrial manufacturing choices and technologies. Table 5.10 shows the main design and operational parameters for the magnet.

The integration of the DBQ is delicate due to the small space available on the modules and the presence of many critical components on the Drive Beam (DB) line. Figure 5.12 shows a cut-away view of the magnet integration with BPM, PET, vacuum pipe, bellows, and flanges.

5.2.3.2 Tunable Permanent Magnet option

Permanent Magnet design concept

The Permanent Magnet option has several advantages: limited or zero requirements for powering and cooling, limited power dissipation in the tunnel. The global requirement from the CLIC tunnel cooling and ventilation system is to keep the heat dissipation to air below 150 W/m all components and systems

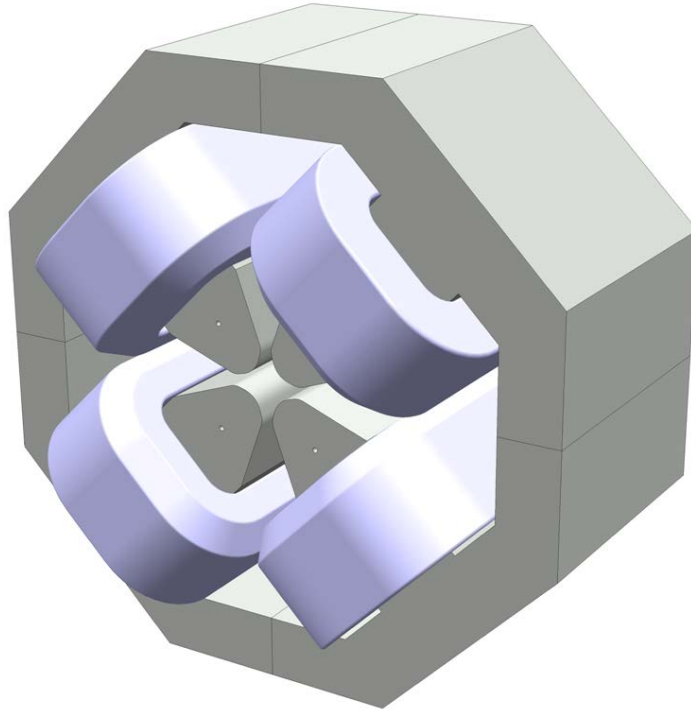


Fig. 5.9: Conceptual design of the Main Beam Quadrupole prototype (EM option design).

included. As this is a very challenging requirement, a magnet solution based on permanent magnets would be extremely advantageous.

Adjustable Permanent Magnet quadrupoles have been used extensively in other accelerators [24–26]. Several basic concepts were considered, including a hybrid electromagnet/permanent magnet design, with PMs in an outer yoke providing a quadrupole field which could be varied by coils mounted on the poles. However, in order to produce the required variation in field, the coil current density is nearly as high as in the conventional EM design. Consequently this design was abandoned.

The proposed design for the high-energy end uses a moving piece to adjust the quadrupole strength. Either a PM is moved, or part of the steel yoke, or a combination of both. The poles remain in place to ensure the field quality is constant as the strength is varied. Motion is symmetric about the mid-plane of the magnet. As the moving piece is moved away from the beam, the strength is reduced.

The PM design has been modelled in Opera-3D/TOSCA. A 3D representation of the magnet is shown in Figure 5.13. The quadrupole is of the ‘lozenge’ type with a gap in the mid-plane. There are four PMs which can be moved symmetrically in the vertical direction. The PMs are at an angle of 40° to the horizontal, and are connected by ‘bridges’ of magnetic steel at the top and bottom, which move with them. A ‘sandwich plate’ underneath the PMs is used to keep them in place against the large magnetic forces they experience when they are moved away from the maximum strength position. The parameters achieved are shown in Table 5.11.

The maximum strength (integrated gradient) falls slightly short of the ‘ultimate’ strength of 14.6 T (i.e., 120% of ‘nominal maximum strength’). This small change can almost certainly be compensated for by making small modifications to the design, and possibly by slightly increasing the length of the magnet.

At the maximum extent of its motion, the strength is reduced to 4.1 T. The same quadrupole design can therefore be used for about 55% of the decelerator line. Beyond this point, at least two other quadrupole families would be needed, to cover the whole range. This can easily be achieved using

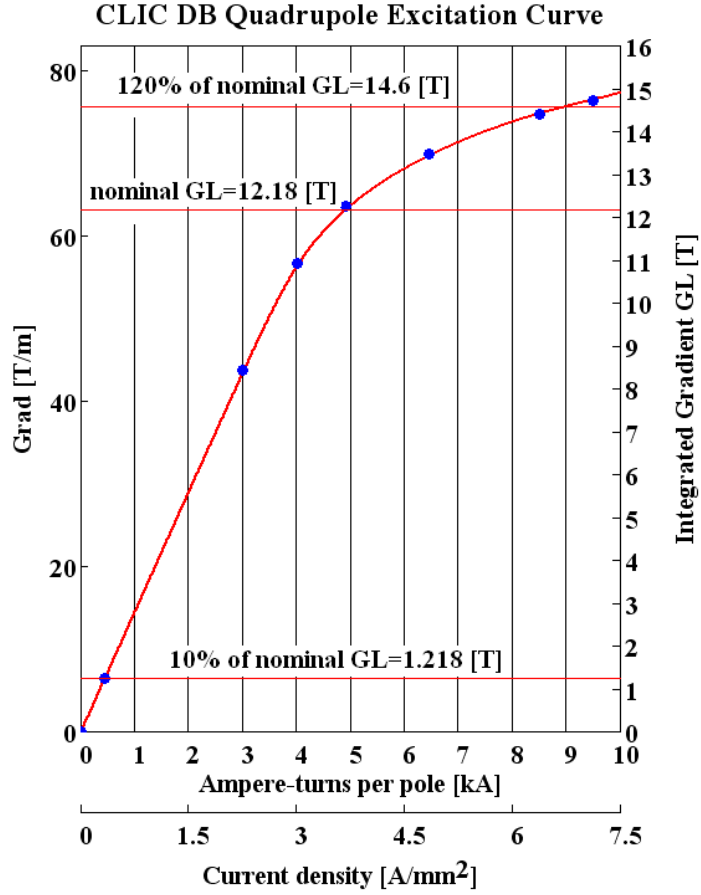


Fig. 5.10: Magnet excitation curve showing different operating points

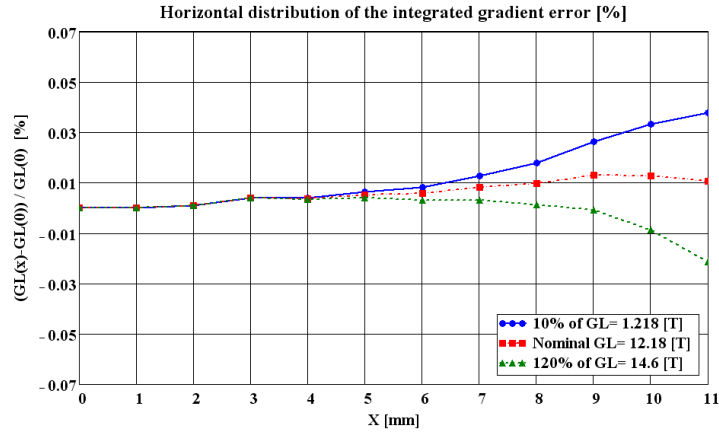


Fig. 5.11: Expected field quality for the three different working points

slight variations of the existing design.

The inscribed radius has been increased from the original value of 13 mm in order to accommodate lateral movement of the magnet to provide dipole correction. A horizontal or vertical movement of 1 mm is sufficient (at maximum gradient) to give the required integrated dipole field of $12 \times 10^{-3} \text{ Tm}$.

The maximum vertical force on each moving part has been estimated at 15 kN. An arrangement of motors and gearboxes has been designed that will withstand this level of force. The system will be able

5.2 NORMAL-CONDUCTING AND PERMANENT MAGNETS

Table 5.10: Main parameters for the Drive Beam Quadrupoles

Parameter	Units	Value		
Assembled magnet				
Magnet size H×S×L	mm×mm×mm	390×390×286		
Magnet mass	kg	149.2		
Full aperture	mm	26		
Good field region diameter	mm	11×2 = 22		
Yoke				
Yoke size H×S×L	mm×mm×mm	390×390×180		
Yoke mass	kg	29.4×4 = 117.6		
Coil				
Hollow conductor size	mm	6×6, ∅ = 3.5		
Number of turns per coil		52		
Total conductor mass	kg	31.6		
Operation mode				
		‘min’ (10%)	‘max’ (100%)	‘Ultimate’ (120%)
Magnetic length	mm	194.7	194	192.5
Gradient at Z=0	T/m	6.26	62.78	75.85
Integrated gradient ∫Gdl	T	1.218	12.18	14.6
Integrated gradient quality in GFR	%	0.04	0.01	0.02
Electrical parameters				
Ampere turns per pole	A t	432	4840	9100
Current	A	8.3	93	175
Current density	A/mm ²	0.3	3.6	6.8
Total resistance	mΩ	99	99	99
Total inductance	mH	40	40	40
Voltage	V	0.82	9.2	17.3
Cooling		Air (natural convection)	Water	Water
Cooling circuits per magnet		–	4	4
Water velocity	m/s	–	1.1	1.9
Water flow per circuit	l/min	–	0.6	1.1
Pressure drop	bar	–	2.2	5.7
Reynolds number		–	4122	8210
Temperature rise	K	–	5	10

to control the position of the moving parts to within 15 μm . This means that the field will be adjustable to the level of precision required (0.05% of the gradient). Higher-precision motion systems are available; this seemed a good compromise between cost and accuracy.

The complete magnet is shown in Fig. 5.14. The dimensions are greater than those specified in Table 5.11; however, the magnet has been shown to fit into a preliminary CAD model of the module. The motor overhangs longitudinally but it could easily be modified to point in the opposite direction or vertically upwards.

As for the MBQs, steering correction capability will be also needed for the DBQ magnets. Unlike the MBQ, the steering correction will be ‘static’; as baseline, a maximum correction value of $\pm 2 \times 10^{-3} \text{ Tm}$ is proposed. For the electromagnetic option, as well as the study for a solution with

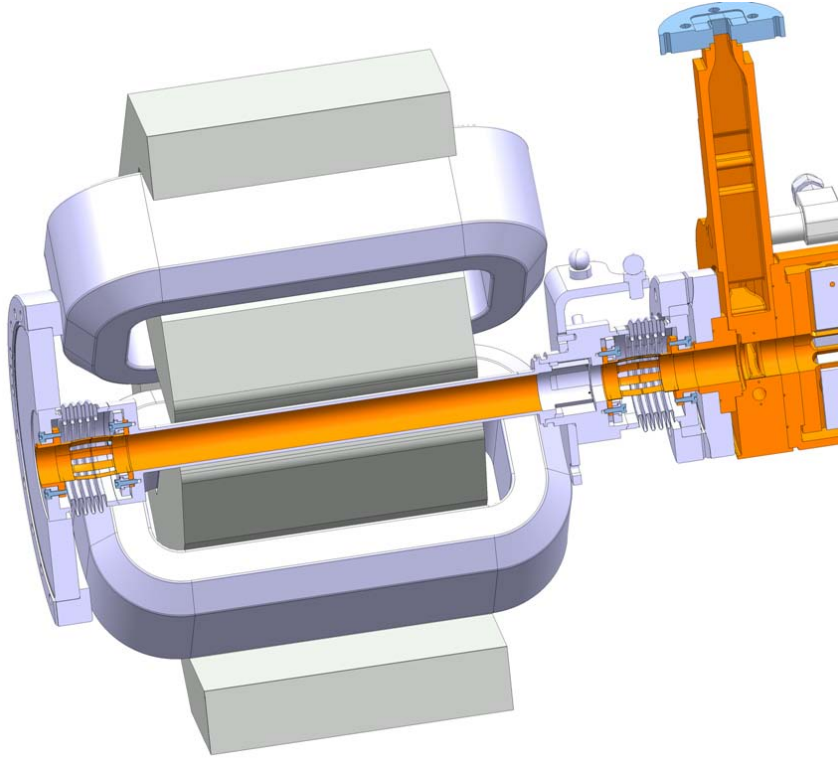


Fig. 5.12: View (section detail) of the MBQ prototype with other beamline components

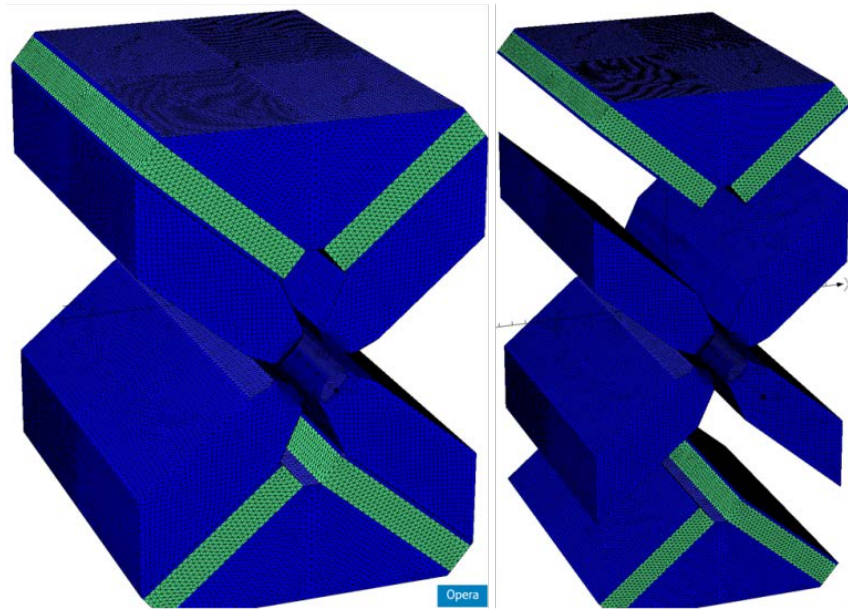
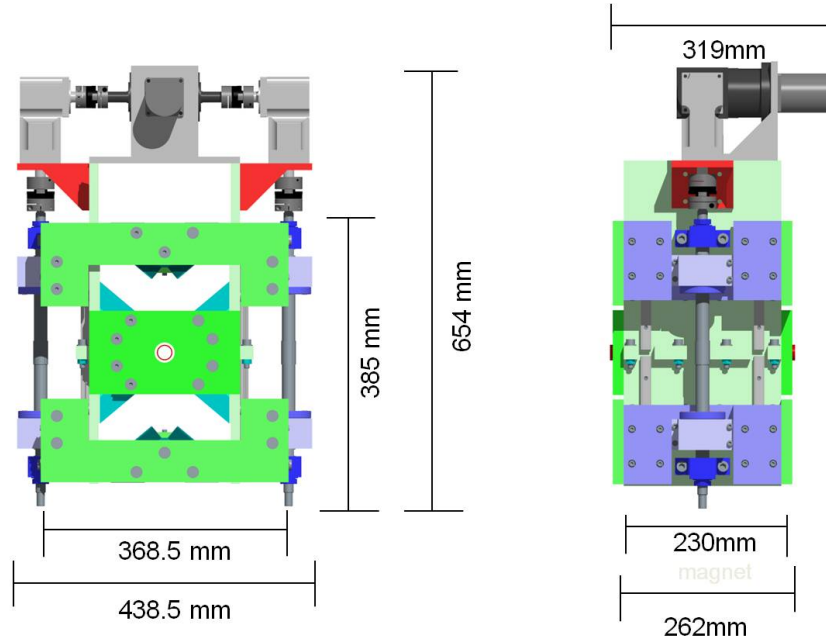


Fig. 5.13: A 3D representation of the high-strength quadrupole, modelled in FEA. The magnet is closed (left) and open (right) for maximum and minimum gradient respectively. The green blocks represent the PMs, which are magnetized parallel to their shortest dimension.

trim coils, there is the possibility to use the girder alignment actuators to apply the ‘static’ correction (by slightly shifting the quadrupole center vertically or horizontally). For the Tunable Permanent Magnet option, a solution adding a shift of the quadrupole geometric centre to the magnet tuning is under development.

Table 5.11: Parameters for the tuning PM design.

Parameter	Range of values	
Width [mm]	438.5	
Height [mm]	654	
Length [mm]	319	
Inscribed radius [mm]	14.8	
Gradient [T/m]	58.4	16.5
Strength [T]	14.2	4.1
Movement of top piece [mm]	0	58
Magnetic length [mm]	243	
Integrated gradient quality [%]	0.1	
Good gradient region [mm]	7.5	

**Fig. 5.14:** Proposed mechanism for controlling the magnet, showing overall dimensions. A single motor drives both moving parts up and down.

5.2.4 Final Doublet Quadrupoles

The Final Doublet Quadrupoles QF1 and QD0 will be the last magnetic elements of the Beam Delivery System (BDS). Both are challenging designs since the required gradients are at the limit of electromagnetic and permanent magnet technologies.

As explained in §3.6.3.1, it seems extremely difficult, particularly for QD0, to propose a design based on superconducting technology; the necessity for active stabilization of the magnet (see §5.12.2.2), the very limited available space, and the presence of the post-collision spent-beam vacuum chamber seem to exclude a superconducting solution.

For QF1, the situation is different due to its position further away from the Intersection Point (IP) and the resulting relaxed dimensional and logistic boundary conditions. In this case we intend to evaluate both solutions: one similar to that proposed for the QD0 and another based on standard superconducting technology.

A hybrid solution of electromagnets plus PM is proposed for the QD0 design and for QF1. In the case of QD0, the boundary conditions indicate a hybrid magnet design:

- extremely high gradient needed;
- limited space available;
- presence of the post-collision vacuum chamber ~ 35 mm away;
- the need for a wide tunability range;
- the need for active stabilization of the magnet.

Figure 5.15 shows the concept of the hybrid design for QD0. See §5.12.2.1 for details of this magnet design.

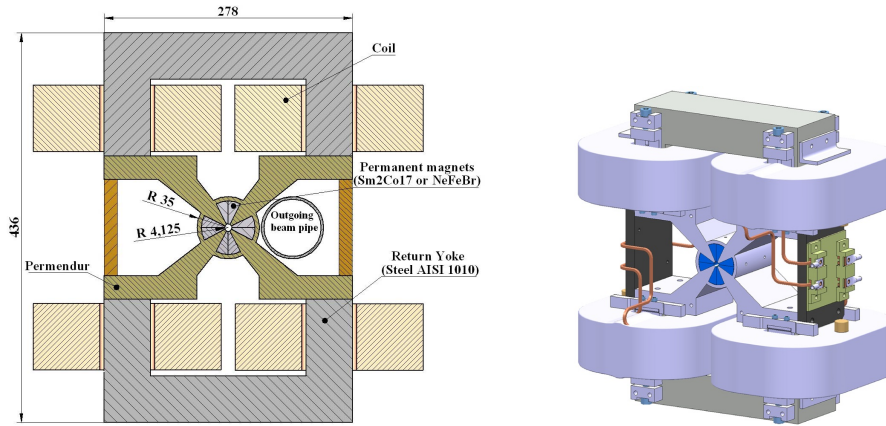


Fig. 5.15: Conceptual design (cross-section and global view) of the validation prototype for the QD0 quadrupole. Main components are visible: coils (copper air-cooled with optional thermalization water circuit), return yokes (in AISI1010 steel), central quadrupolar core (in Permendur), permanent magnet wedges (circular sector shaped).

5.2.5 Other magnets

5.2.5.1 Normal-conducting magnets

Reference [27] reports the global estimation in numbers and main parameters of the CLIC magnet sub-system.

We have started with the analysis of the most critical magnet families considering as critical:

- the ‘extreme’ operational parameters;
- the small dimensions or other tight logistic boundary conditions;
- the volume of the magnet procurement (number of units to be procured).

For example, the operational parameters could vary from the 575 T/m gradient of the QD0 down to the 0.008 T for the MBCO2 dipoles of the DB long transfer-lines. The dimensions could vary from the very compact cross-section of the QD0 to the very large post-collision dipoles. Since the proposed QD0 design is widely presented in other sections of the CDR (see §5.12.2.1), we report here, as an example of the magnet system variety, the first dimensioning for the ‘Mag4’ dipole, the largest of the post-collision magnet family. The main parameters of this magnet are presented in Table 5.12 and the cross-section is shown in Fig. 5.16.

Table 5.12: Main parameters of the post-collision dipole ‘Mag4’: the largest CLIC magnet.

Parameters	Value
Full aperture (horizontal) [mm]	444
Good field region (hor./ver.) [mm]	410/1394
Effective length [mm]	4000
Strength [T]	0.8
Yoke	
Yoke length [mm]	3750
Yoke cross-section area [m ²]	2.96
Yoke mass [kg]	87,227
Coil	
Conductor type [ID no. 8200]	30 mm×30 mm, $\varnothing=12$ mm
Conductor mass per m [kg/m]	6.99
Number of turns per coil	42
Number of pancakes per coil	6
Total conductor mass [kg]	6341
Electrical parameters	
Ampere turns per pole [A t]	148 770
Current [A]	3542
Current density [A/mm ²]	4.5
Total resistance [m Ω]	21.6
Total inductance [mH]	127.5
Voltage [V]	76.5
Power [kW]	271
Cooling	
Cooling circuits per magnet	12
Coolant velocity [m/s]	2.4
Cooling flow per circuit [l/min]	16.1
Pressure drop [bar]	3.9
Reynolds number	43 470
Temperature rise [K]	20

5.2.5.2 Permanent Magnets

Permanent Magnet technology could be extremely interesting in the following cases:

- limited available space for magnet design and integration;
- small magnet bore;
- limitation in electrical or powering consumption or powering dissipation (to air or to water).

One drawback of PM technology concerns the tuning capability. Owing to the absence of electrical current generating the magnetic field, the needed tuning capability must be done by the means of mechanical movements of the PM or iron blocks. This needs a delicate investigation of the magneto-mechanical behaviour of the structure, with exact determination of the mechanical movement/field variation transfer function.

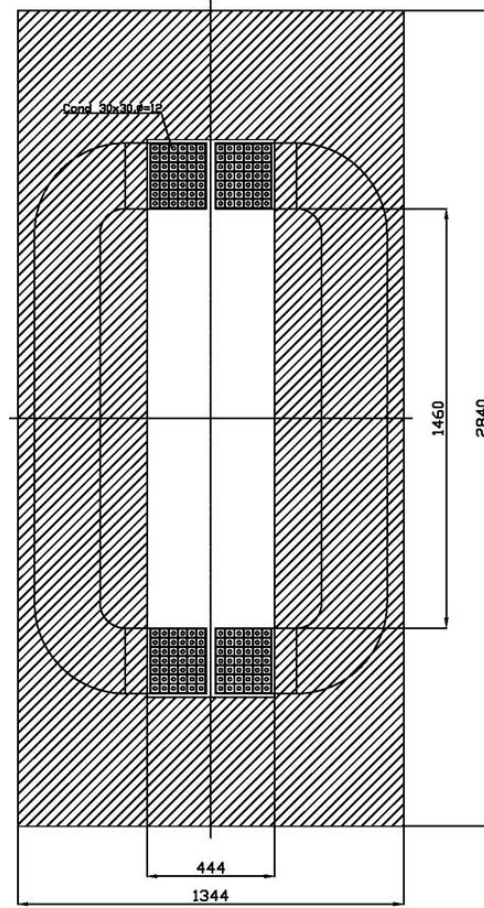


Fig. 5.16: Cross-section of the ‘Mag4’ post-collision dipole.

Another issue is the stability in time and under external magnetic field and radiation of the PM blocks (see §5.2.6.2 below)

5.2.6 Technical issues

5.2.6.1 Electromagnet technical issues

For the majority of magnets present in the CLIC accelerator complex, a classical electromagnet design seems possible and convenient from the point of view of the optimization of functionality, dimensions, technical service requirements, and cost.

The major technical issues affecting these magnets concern the procurement aspect: in some cases (e.g., DBQs and MBQs) the series of magnets to be procured is impressive. This aspect, together with the fact that in a lot of cases the magnets will be relatively small, imply production technologies and procurement schemes not typical for accelerator magnets but closer to standard electromechanical components (e.g., electrical motors or electromechanical actuators).

So, apart from the design optimization of the most important families of magnets, one of the main aspects to be investigated in the next years is the industrialization and procurement of such large series of magnets including new technical choices and alternative industrial solutions.

5.2.6.2 Permanent Magnet technical issues

For the DBQ optional design, the most challenging aspects, beside the design itself (relative small space available in the two-beam module for its integration), are similar to those of the electromagnets. We are

5.2 NORMAL-CONDUCTING AND PERMANENT MAGNETS

dealing with the largest magnet family of the accelerator complex (41 400 units). The small dimensions and relatively large production and production rate, will mean dealing with ‘standard’ electromechanical industry rather than with the more familiar ‘magnet industry’.

Another important aspect to investigate is the medium and long term stability of PM blocks:

- stability in time (the PM block should not magnetically degrade during the expected lifetime of the accelerator);
- stability with respect to external magnetic field (this point is extremely important for the QD0 that is placed inside the region of the experimental detector’s solenoid);
- stability with respect to radiation (this point is also critical for QD0 which will be placed just 3.5 m from the IP).

Industry can already supply materials that could fulfil these requirements (NdFeB and especially SmCo rare earth compounds) and further material performance improvements can be expected in the near future. A lot of investigation and testing must still be done to check the feasibility of these solutions for a real accelerator environment.

5.2.7 Component inventory

A systematic analysis and first dimensioning of all CLIC magnets is underway. The results will be the so-called ‘CLIC Magnet Catalogue’ where, for each magnet family or variant, will be listed:

- main dimensions;
- operating parameters;
- technical system requirements (electrical power consumption and cooling needs);
- procurement cost.

Input for such dimensioning is the data provided by the beam physics team who are defining the main parameters of the accelerator magnetic lattice (magnet strength, magnetic length, range of tunability, field quality, etc.)

5.3 Superconducting magnets

5.3.1 Overview

In the CLIC study 52 superconducting wigglers are foreseen in each of the two damping rings, in order to reduce the normalized horizontal beam-emittance to 500 nm, the normalized vertical emittance to 5 nm, and the normalized longitudinal emittance to 5960 eVm [28]. Figure 5.17 shows the emittance at the extraction point of the damping rings, as a function of the wiggler field B_0 and the wiggler's period length λ , including intra-beam scattering (IBS). The beam physics of the Damping Rings is described in §3.2.

The wigglers are increasingly more effective for higher magnetic field and shorter period length. Figure 5.18 shows the maximal field B_0 that can be achieved with different technologies. The requirements of CLIC can only be met by using superconducting wigglers with a field $B_0 \geq 2.5$ T and g/λ of about 0.4–0.5, where g is the gap between the magnetic poles and λ the period length of the magnetic flux density of the wiggler $B_y = B_y \sin 2\pi/\lambda$. The optimal working point for Nb-Ti technology can be found with a given gap of 20 mm at a period length of 50 mm and a maximal magnetic flux density of 2.5 T. For Nb₃Sn wire technology the optimal working point is at a period length of 40 mm and a maximal magnetic flux density of 2.8 T.

Table 5.13 gives an overview of recently installed superconducting wigglers in storage rings. The field requirements of the CLIC damping wigglers at the given gap and period length are not met by any of the currently installed superconducting wigglers; therefore, this section will present the results of short-model wigglers which meet the requirements of the CLIC damping rings.

Figure 5.19 shows the baseline design for the CLIC superconducting damping wigglers. We assume an infinitely long periodic wiggler. In this case, the flux distribution can be calculated by expanding the magnetic scalar potential $\Phi = \Phi_x \Phi_y \Phi_z$, with $\Phi_z = \cos(nkz)$ along the z -axis, where $k = 2\pi/\lambda$. In the air gap of the wiggler the two-dimensional Laplace equation can be written as

$$\Phi_x \frac{\partial^2 \Phi_y}{\partial y^2} - \Phi_x \Phi_y n^2 k^2 = 0. \quad (5.1)$$

As $B_y(y) = B_y(-y)$ the field is given by

$$B_y = \sum_n B_{0,n} \cosh(nky) \cos(nkz), \quad (5.2)$$

$$B_z = \sum_n -B_{0,n} \sinh(nky) \sin(nkz), \quad (5.3)$$

with $n \geq 1$ and odd.

5.3.2 Engineering considerations

The manufacturing process of a superconducting damping wiggler involves the following steps.

1. Manufacture and preassembly of iron-yoke and stainless-steel support structures.
2. Insulation of iron pieces with electrostatic epoxy coating for Nb-Ti or with Al₂O₃ plasma spray for the Nb₃Sn version.
3. Winding of approximately 13 km of superconducting strands per wiggler magnet. One wiggler magnet consists of about 30 modules each comprising 5 magnet poles.
4. In the case of Nb₃Sn: heat-treatment-mold assembly and heat treatment.
5. Impregnation-mold assembly and vacuum impregnation with Araldite MY740 (100 PP), hardener HY 906 (80 PP), and accelerator DY 073 (1 PP) or similar epoxy.
6. Cryogenic testing and ‘training’ of the wiggler module in a dedicated cryostat.

5.3 SUPERCONDUCTING MAGNETS

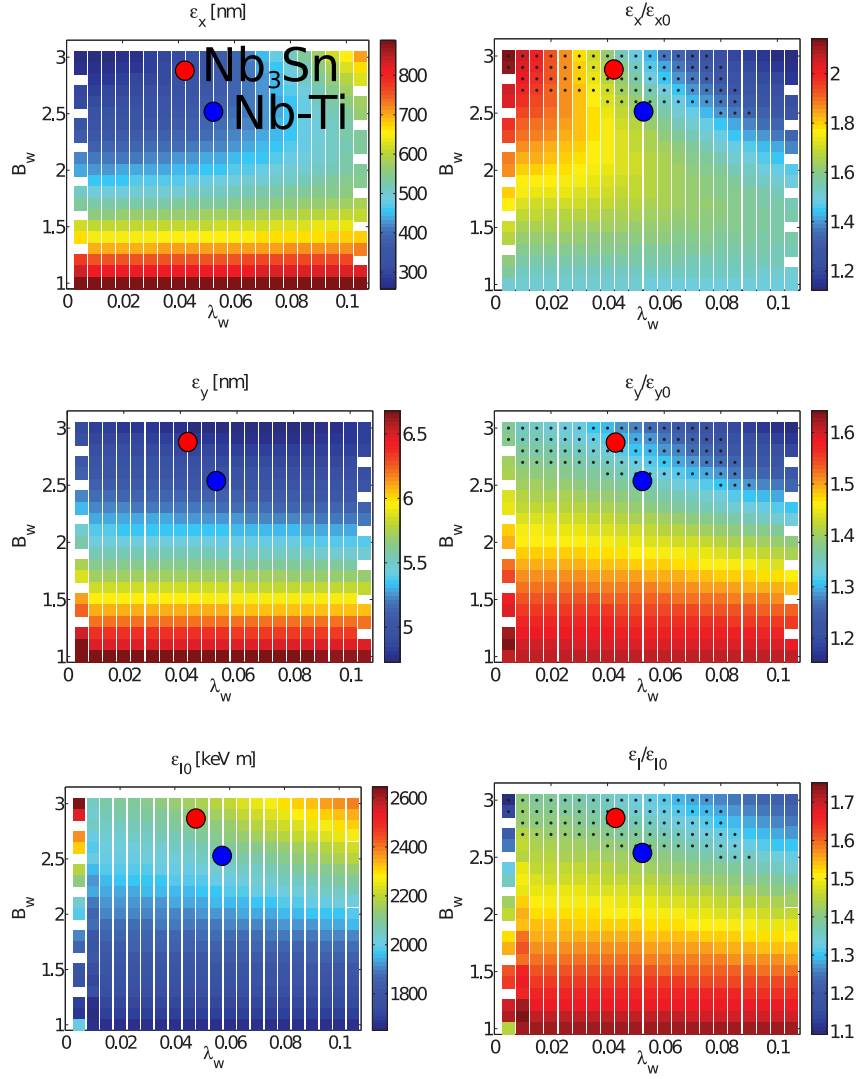


Fig. 5.17: Scaling of the extracted emittances with the wiggler field and period. In the left-hand plots the extracted emittances are shown, while in the right-hand ones the ratio between the extracted and the zero current emittances are shown. The black dots indicate solutions where all the emittance requirements are met. The longitudinal emittance is kept constant [29].

7. Integration of the magnet modules.
8. Magnetic field-quality measurements with Hall probes and stretched wire systems.

Either Nb-Ti or Nb₃Sn strands will be used for the magnet manufacture. Figure 5.20 presents the cross-sections of two suitable Nb-Ti strands for the CLIC damping wigglers. These strands were used for winding the two short-models (two-period configuration); see §5.3.3. Nb-Ti strands are ductile, can be insulated easily with standard organic insulation materials such as enamel, are widely available, have fine filaments in the range of 5 μm , and large unit lengths are available. However, the engineering current density, J_E , which scales linearly to the maximal achievable mid-plane flux for large currents, can be almost doubled by using Nb₃Sn as opposed to Nb-Ti wire technology. In addition, the temperature margin of Nb₃Sn technology is much larger, which increases the stability and consequently reduces the number of training quenches. The critical temperature of Nb-Ti is 9.6 K compared to 18.1 K of Nb₃Sn. Oxford Instruments' 'restack rod process' (RRP) for the production of Nb₃Sn strand is well suited for

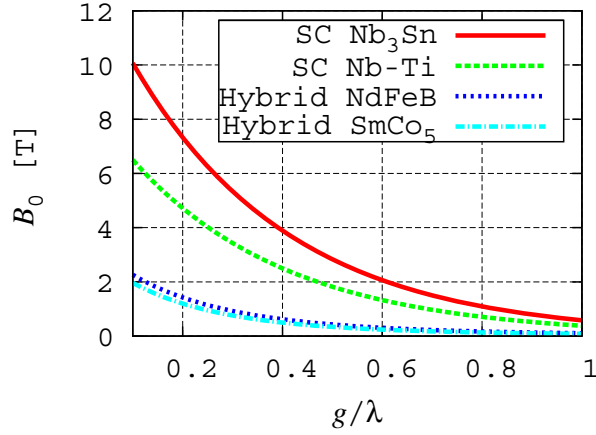


Fig. 5.18: Maximal mid-plane field B_0 versus g/λ in wiggler magnets employing superconducting technology and hybrid permanent magnet excitation. The superconducting wiggler curves are calculated with a finite-element program. The hybrid permanent magnet wigglers were fitted with Halbach's fit [30] and parameters from Ref. [31].

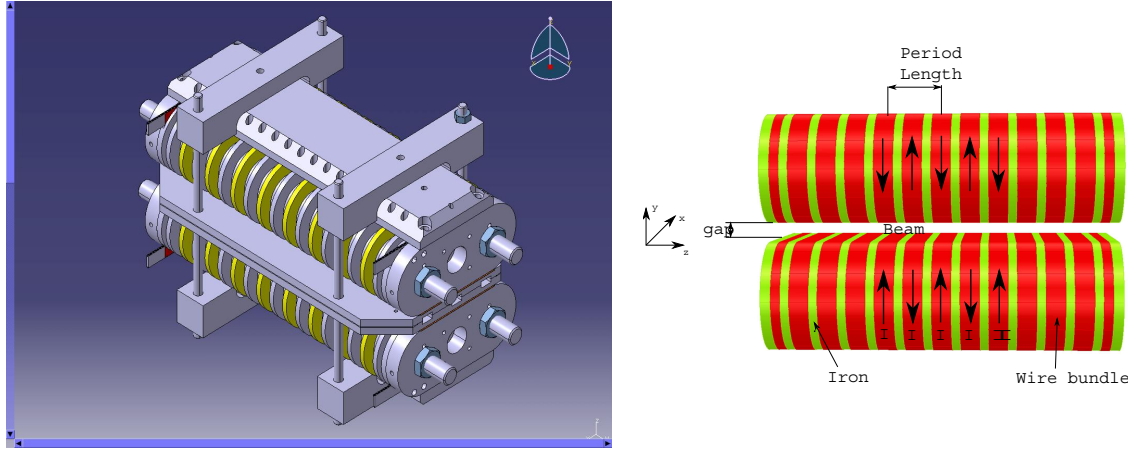


Fig. 5.19: Baseline design of CLIC damping wigglers.

the CLIC damping wigglers. Figure 5.21 presents a schematic of the RRP internal tin process (left) and a cross-section of the reacted strand (right). Table 5.14 summarizes the main parameters of the three different strands and the total amount of wire needed for 104 CLIC damping wigglers.

5.3.3 Parameters and technical choices for CLIC Damping Ring wigglers

Table 5.15 gives an overview of the main parameters of the baseline Nb_3Sn and Nb-Ti wiggler magnets. An Nb_3Sn wiggler magnet can be operated at a 50% higher mid-plane flux density and a higher operating temperature than a Nb-Ti wiggler magnet. Alternatively, Nb_3Sn allows the reduction of the period length to $\lambda = 40$ mm. With Nb-Ti superconducting material it is not possible to meet the requirements of the CLIC damping rings with a period length shorter than 50 mm.

5.3 SUPERCONDUCTING MAGNETS

Table 5.13: Superconducting wigglers with period < 70 mm produced by Budker INP, Russia compared to different options for the CLIC damping wigglers.

Technology	Installed at	Year	B_0	Pole-#	λ	g	g/λ	Vertical aperture
			[T]		[mm]	[mm]		[mm]
Nb-Ti	ELETTRA (Italy)	2002	3.7	45	64	16.5	0.26	11
Nb-Ti	CLS (Canada)	2005	2.2	61	34	13.5	0.40	9.5
Nb-Ti	DIAMOND (UK)	2006	3.75	45	60	16.5	0.28	11
Nb-Ti	CLS (Canada)	2007	4.34	25	48	14.5	0.30	10
Nb-Ti	DIAMOND (UK)	2009	4.25	45	48	13.5	0.28	10
Nb-Ti	LNLS (Brazil)	2009	4.19	31	60	18.4	0.31	14
Nb-Ti	ALBA (Spain)	2009	2.1	117	30.15	12.6	0.42	8.5
Nb-Ti	ANKA (Germany) similar to CLIC DRs	2012	2.5	80	50	≤ 20	0.40	13
Nb ₃ Sn	Storage ring similar to CLIC DRs	2014	2.8	100	40	≤ 20	0.50	13

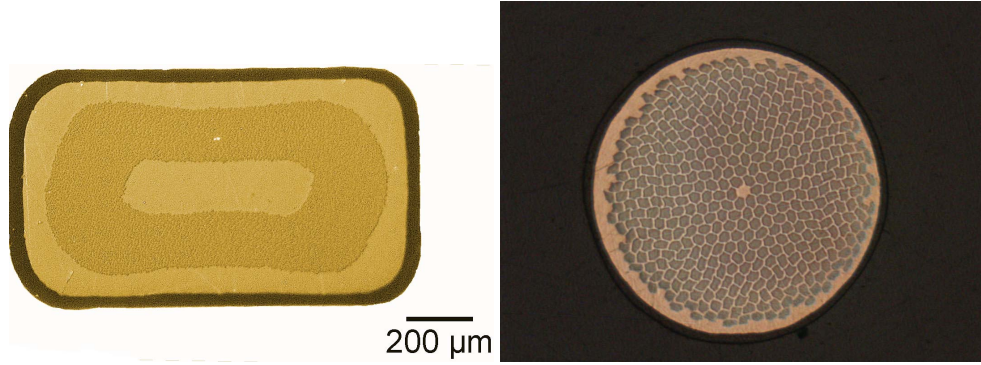


Fig. 5.20: Cross-section of two Nb-Ti strands suitable for the CLIC damping wigglers. Left: CERN LHC corrector wire # 3 [32], Right: strand produced by Bochvar Institute of Inorganic Materials, Moscow [33].

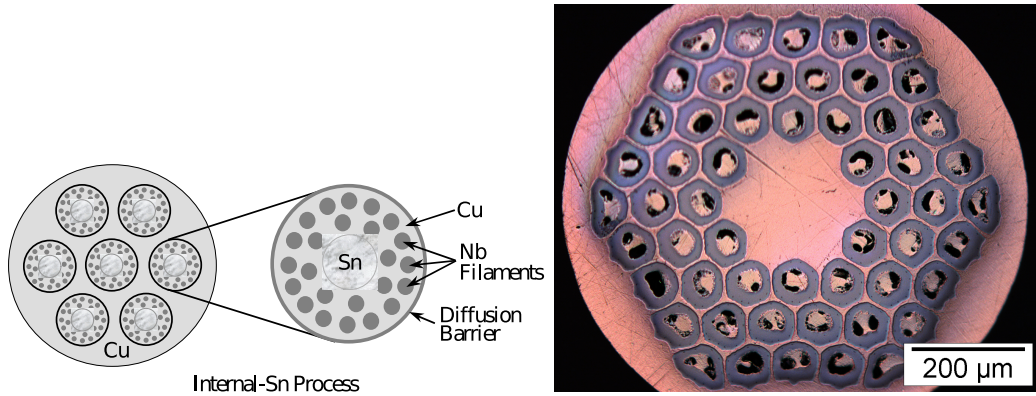


Fig. 5.21: Left: schematic of the RRP internal-tin process [34]. Right: cross-section of the reacted Nb₃Sn RRP strand from Oxford Instrument Technology (OST).

Figure 5.22 shows the modulus of the magnetic flux density, $B_{\text{mod}} = \sqrt{B_x^2 + B_y^2 + B_z^2}$. The maximal field B_{mod} in the 3D calculation is approximately 2–5% higher compared to the 2D calculation, and is caused by local field enhancement in the end coils. This field enhancement can be reduced by replacing

Table 5.14: CLIC damping wiggler strand options

	Nb-Ti BINP	Nb-Ti CERN	RRP Nb ₃ Sn
Strand diameter [mm]	0.85	0.61×1.13	0.81
Cross-section [mm ²]	0.57	0.69	0.52
Insulated diameter [mm]	0.92	0.73×1.25	0.94
Shape	round	rectangular	round
SC/Cu ratio	1.5/1	1/1.8	1.1/1
Maximal current [A]	700 (4.2 K, 50 mm) 830 (1.9 K, 50 mm)	730 (4.2 K, 40 mm) 950 (1.9 K, 40 mm)	1100 (4.2 K, 40 mm) 1000 (4.2 K, 50 mm)
Critical temperature [K]	9.6	9.6	18.1
RRR	100	>100	300
Filament diameter [μ m]	≤ 45	≤ 7	≤ 80
Insulation	Imidal varnish	PVA enamel	S-glass braid
Total [km]	1700	1700	1700

the central-post in the end coil by a non-magnetic material.

The field distribution (roll-off) along the pole in the transverse direction is shown in Fig. 5.23 (left). The good-field region (defined as the region with a field homogeneity better than 1 unit in 10 000) is ± 3.7 mm about the centre of the beam axis.

Figure 5.23 (right) shows the first, third, and fifth field harmonics for air gaps between 1 mm and 20 mm and a 40 mm period wiggler calculated with the finite element method. For a gap of 20 mm the third harmonic can already be disregarded.

The wiggler has to be designed such that the angle and displacement of the beam remains unchanged after the traverse of the magnet. Thus the following conditions have to be met: a zero first field integral $I_1 = \int B_y dz = 0$ (vanishing kick angle) and zero second field integral $I_2 = \iint B_y dz^2 = 0$ (zero displacement). Figure 5.24 presents two coil designs for the full-scale wiggler. It is possible to achieve the specifications with both designs. To reduce the fringe field and its effect on the second field integral, it is advisable to have an unsaturated iron end-pole.

Figure 5.24 (top) also shows that only the outermost wire bundle of *version-1* experiences forces towards the extremities of the wiggler. In the second design the three outer-most wire bundles experience forces towards the extremities of the wiggler. Therefore, *version-1* is preferable in terms of mechanical stability. A magnetic sensitivity analysis shows that the first field integral is compensated for all currents. However, the second field integral of *version-1* is more sensitive to changes in the current compared to *version-2*; see Fig. 5.25. In the CLIC damping rings the wigglers will be operated at a constant operating current. Therefore, the design can be optimized such that the first and second field integrals vanish. However, in the project preparation phase, one full-scale prototype wiggler will be tested in a synchrotron used for light-generation; there, the current has to be changed during operation. For this prototype the maximum second field integral of $7 \times 10^{-4} \text{ Tm}^2$ in one wiggler can be scaled to a maximal displacement of the beam of $x = e/\gamma m_e c \cdot I_2 \approx 0.1 \cdot I_2 \leq 70 \mu\text{m}$, which can be easily corrected in a synchrotron.

Figure 5.26 shows the field lines (left), the peak field on each Nb₃Sn strand (middle), and that the Lorentz force contracts the wire bundle (right). However, the centre of the forces is off-centre and closer to the central yoke which results in a net force towards the central post. Figure 5.27 (left) presents the net force on the whole wire bundle. Figure 5.27 (right) shows the net forces on a wiggler coil in the centre of the wiggler.

Since the critical current of Nb₃Sn is strain dependent, the strain on the conductor due to different thermal contraction factors of the materials, and the Lorentz forces were calculated. Figure 5.28 shows that the strain remains very small. The degradation due to strain in the Nb₃Sn conductor is well below 5%.

Before the integration of the wigglers in the damping rings the field maps of the wigglers must

5.3 SUPERCONDUCTING MAGNETS

Table 5.15: Main parameters of the Nb₃Sn and Nb-Ti baseline design

	Nb ₃ Sn	Nb ₃ Sn	Nb-Ti	Nb-Ti
Period length λ [mm]	40	50	50	50
Gap (beam stay clear) [mm]	13	13	13	13
Gap (magnetic) [mm]	18	18	18–20	18–20
Mid plane field [T]	2.5	3.7	2.5	3.0
Peak field [T]	7.9	10.5	6.2	7.5
Operating current [A]	1100	1000	660	790
Inductance at operating current [H]	0.5	1.5	1.5	1.5
Operating temperature [K]	~ 5	~ 5	4.3	1.9

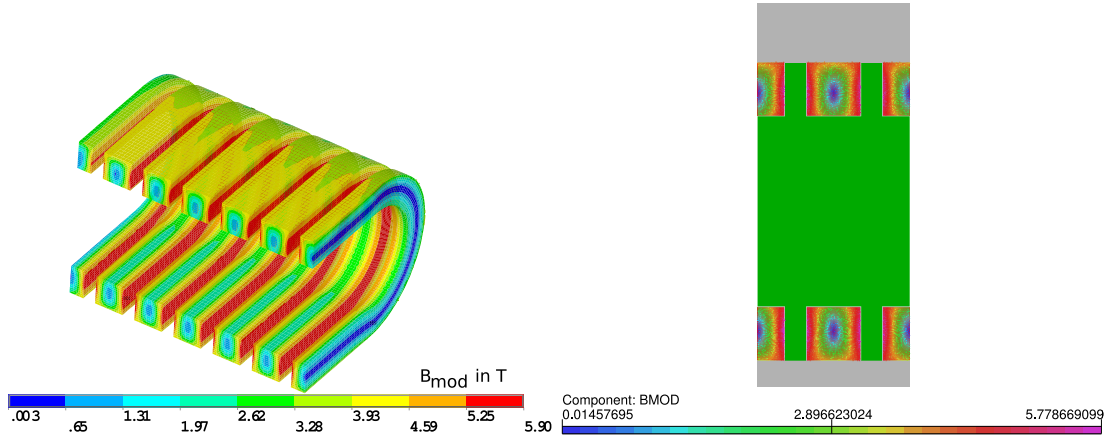


Fig. 5.22: Left: peak field (3D) on conductor calculated with the finite-element program ANSYS. Right: peak field (2D) on conductor calculated with the finite-element program Opera.

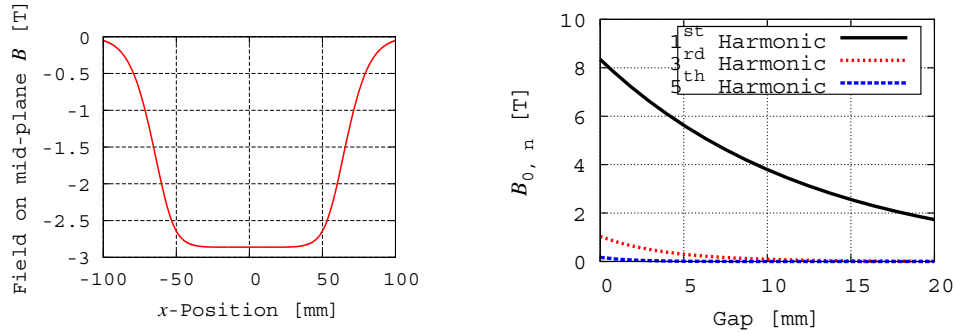


Fig. 5.23: Left: field distribution (roll-off) at the poles of the wiggler. Right: harmonics of the wiggler field at $y = 0$ with a period length of 50 mm.

be measured in a dedicated cryostat with three axis Hall-probes. These probes are moved through the wiggler gap on a sled driven by a linear actuator. The Hall-probes need to be calibrated *in situ* after each cool-down, using a calibration magnet and a zero-Gauss chamber. In addition, a precise measurement of the first and second field integrals with a pulsed stretched wire measurement system must be performed.

The influence of mechanical tolerances on the equilibrium emittance and the damping time (disregarding all higher-order effects) was estimated by calculating the zero-current emittance.

For this calculation we assume a Gaussian distributed period length with a mean $\mu(\lambda) = 56$ mm

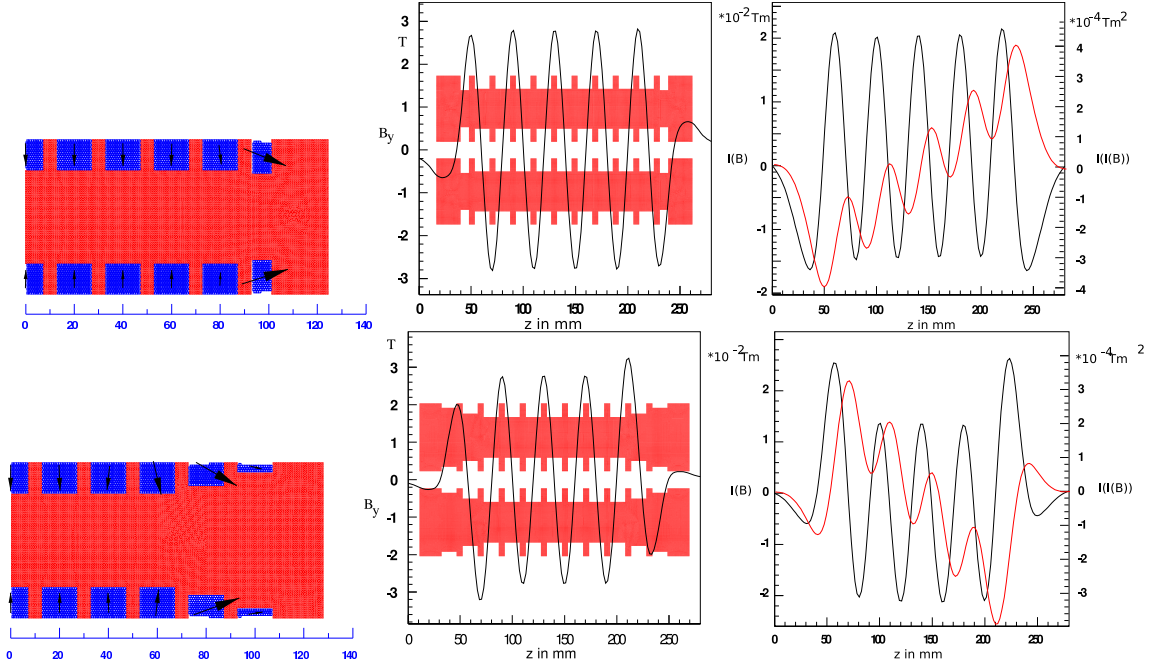


Fig. 5.24: Antisymmetric wiggler. Top: CERN design. Bottom: design similar to ANKA and BINP wigglers.

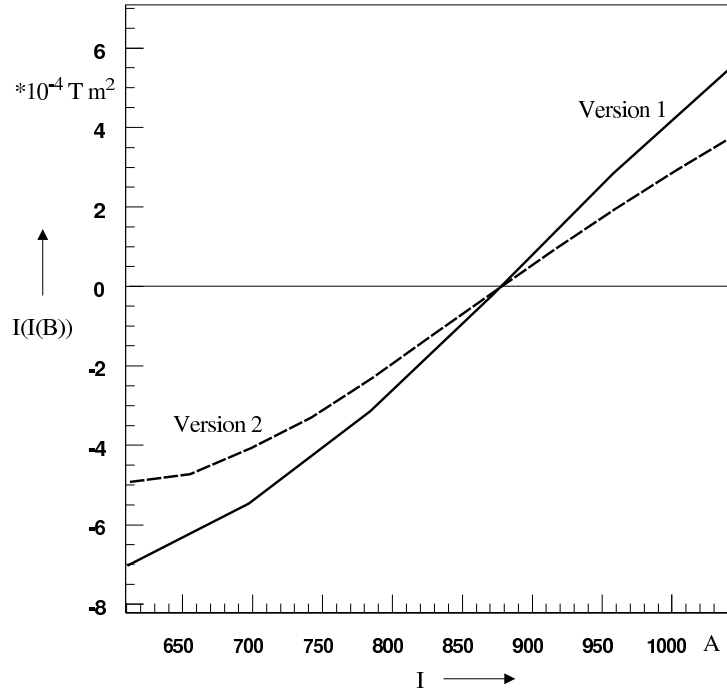


Fig. 5.25: Antisymmetric wiggler. Sensitivity analysis of the second field integral of the CERN (*version-1*) and the ANKA (*version-2*) design.

and a field amplitude with a mean $\mu(B_0) = 3$ T, a standard deviation¹ of $\sigma(B_0) = 0.2$ T and $\sigma(\lambda) = 1$ mm;

¹A standard deviation of $\sigma(B_0) = 0.2$ T corresponds to an error in the pole height of ± 1.5 mm if $B_p = \text{const}$ and $\lambda = \text{const}$.

5.3 SUPERCONDUCTING MAGNETS

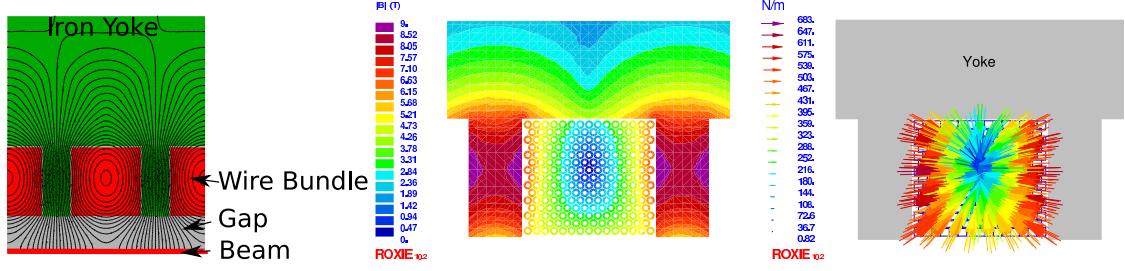


Fig. 5.26: Left: the field lines of a cross-section through the bottom part of a wiggler calculated by using the FEM code Opera 2D. The iron is depicted in green, air and insulation in gray, and the conductor in red. The beam is depicted at the bottom in red. Middle: peak field on conductor. Right: forces contracting the wire bundle as calculated with ROXIE 10.

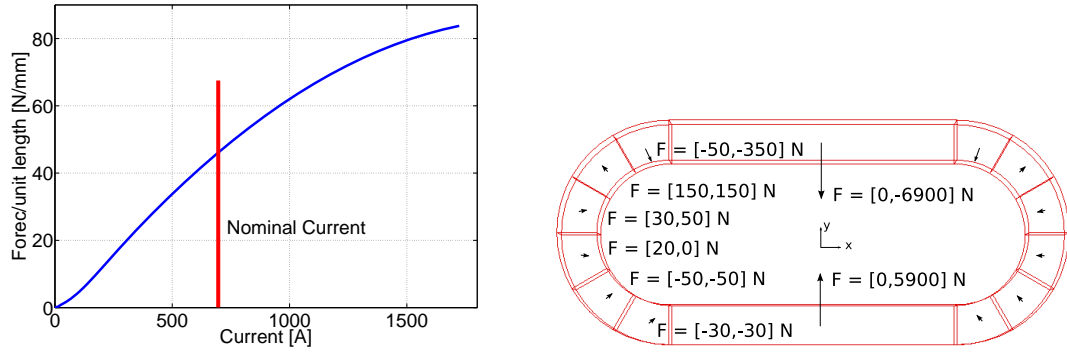


Fig. 5.27: Left: net force on wire bundle of a vertical racetrack wiggler versus current. Right: net force on wire bundle of a vertical racetrack wiggler.

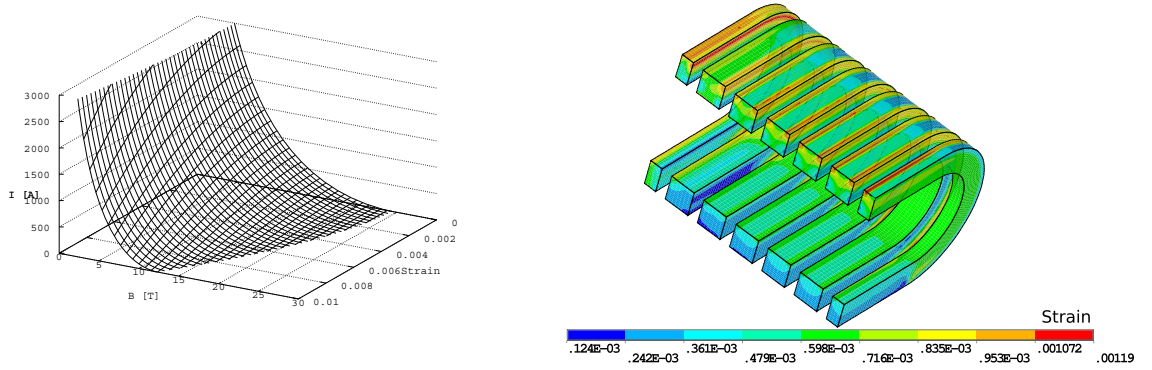


Fig. 5.28: Left: Summers' fit for OST RRP strand. Right: strain at 4.3 K and operating current.

then added over the contribution of each half-period

$$I_{2w}^G = \sum_{i=1}^{2N_w} \frac{\lambda B_0^2 e^2}{4p^2}, \quad (5.4)$$

$$I_{5w}^G = \sum_{i=1}^{2N_w} \frac{1}{30\pi^3} \frac{\beta_w B_0^5 \lambda^3 e^5}{p^5}. \quad (5.5)$$

For this study, the emittance generated in wiggler magnets is calculated for one million damping ring samples each equipped with 52 damping wigglers. Figure 5.29 shows a histogram for $\kappa = I_{5w}^G / I_{5w} \cdot I_{2w} / I_{2w}^G$ calculated with an average $\beta_w = 4.79$ m in the wiggler magnets.

The equilibrium horizontal zero-current emittance is, according to Ref. [35],

$$\gamma \epsilon_{x0} \approx \gamma \epsilon_{a0} \frac{J_{x0}}{J_{x0} + F_w} + \gamma \epsilon_{w0} \frac{F_w}{J_{x0} + F_w}, \quad (5.6)$$

where $F_w = I_{2w} / I_{2a}$ (I_{2a} is the damping generated in the arc section of the ring), ϵ_{a0} the normalized horizontal zero-current emittance generated in the arc section, and the contribution to the damping partition number from the arc cells $J_{x0} = J_x (1 + F_w) - F_w$. With the parameters above, and those in Appendix A and in Ref. [35], the overall expected emittance growth in the ring due to mechanical errors is less than 1%.

Notice that if the yaw, pitch, or roll angles obtained with magnet alignment do not meet the target values, higher-order field components are introduced which are not represented in the field model described above.

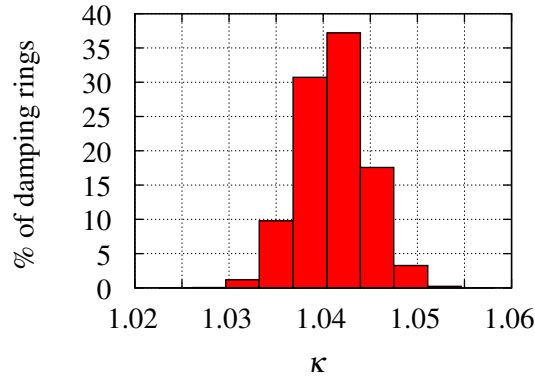


Fig. 5.29: Histogram of the influence of mechanical errors on emittance

Magnetic shims (known as magic fingers) can be used to compensate both for small errors of the first and second field integrals and for small multipole errors due to mechanical tolerances in the wiggler [36]. Additional steerers can be used for compensation of the field integrals.

5.3.4 Magnet prototypes and test results

Two Nb-Ti short-models were successfully manufactured in two independent collaborations. In the framework of the CERN collaboration with the Karlsruhe Institute of Technology (KIT), Germany, a 40 mm period, Nb-Ti short-model was manufactured. In the framework of the collaboration between CERN and the Budker Institute of Nuclear Physics (BINP), Russia, Nb-Ti short-models with a period length of 50 mm were manufactured. In addition, a Nb₃Sn trial racetrack coil was designed, manufactured, and tested at CERN.

5.3.4.1 CERN-KIT Nb-Ti short-model

In the framework of the KIT collaboration, a 40 mm period Nb-Ti wiggler short-model with two periods was designed, built, and tested at CERN. Figure 5.30 (left) shows some manufacturing steps of the short-model. Central posts and poles were manufactured separately by using soft iron plates with a thickness of 14 mm and 5.8 mm, which were bolted together during the process of winding. The winding direction has to be reversed after the completion of each winding block in order to achieve an alternating current

5.3 SUPERCONDUCTING MAGNETS

direction; see Fig. 5.19. The wire was turned through a loop in a groove located in the pole plate. Care was taken to pack the wire bundle as densely as possible to minimize voids that may result in cracking in the epoxy resin leading to premature quenches. A mold was used to impregnate the wiggler. For electrical insulation, 0.11 mm and 0.25 mm thick Nomex[®] sheets were used. The achieved insulation resistance is 127 M Ω at 150 V over a pulse of 60 s.

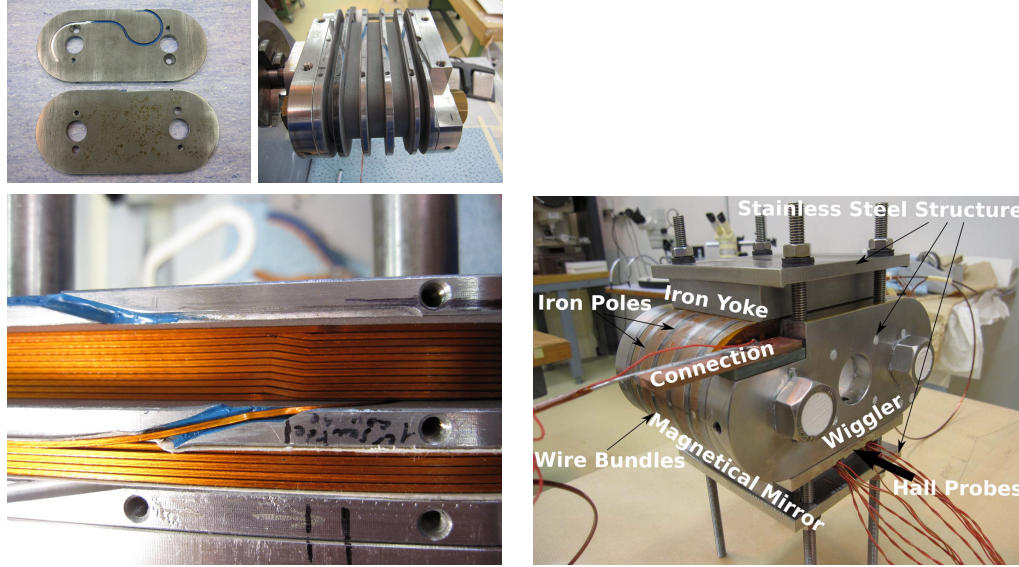


Fig. 5.30: Left: Manufacturing process of short-model wiggler. Right: Measurement configuration of wiggler in mirror configuration.

A magnetic mirror configuration was used to test half of the wiggler as shown in Fig. 5.30 (right). Nine Hall probes were glued on top of the magnetic mirror for field measurements. Figure 5.31 (right) shows a continuous Hall probe measurement during ramping at a pole at 4.2 K and 1.9 K. At 1.9 K a magnetic flux of 2.42 T was reached, meeting the CLIC damping ring specifications.

Figure 5.31 (left) shows the training characteristic of the wiggler. After twelve quenches the short-sample current I_{ss} of 730 A, which corresponds to an engineering current density of 730 A/mm² in the bundle, was achieved at 4.2 K. After cooling to 1.9 K, the current could be increased to 910 A, a value very close to the expected short-sample current of the superconducting material. This current increase shows the wiggler's mechanical stability. After a thermal cycle to 293 K and re-cooling to 4.2 K the same critical current was reached after only one quench [37]. The so-called training characteristic is thus conserved for thermal cycles, and an important point for the operation of the magnets in an accelerator. Although this magnet would fulfill the CLIC specifications only when cooled to 1.9 K, the successful testing of this short-model can be interpreted as a proof-of-principle for the Nb-Ti option.

5.3.4.2 CERN–BINP Nb-Ti short-model

The main parameters of the short-model wiggler manufactured at BNIP are presented in Table 5.16. The central post is machined from one piece of iron. The wire transition was achieved by mounting a G11 plate on top of the poles after the winding of the corresponding bundle was completed. The wiggler was then turned by 180 degrees and the next groove was wound in the opposite direction. Figure 5.32 shows a rendering and a photograph of the final wiggler.

The load line, for the strand parameters given in Table 5.14, is presented in Fig. 5.33 (left). Figure 5.33 (right) shows the results of the training of the wiggler. After a thermal cycle the first quench occurred at a current of 582 A. The second quench occurred at 673 A, above the operating current of 660 A. The training of the wiggler was very long, caused by the choice of a fast ramp-rate. The cho-

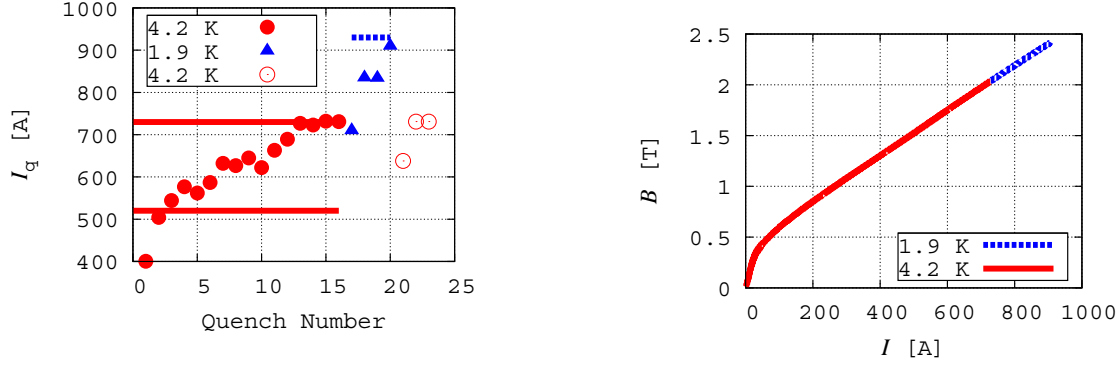


Fig. 5.31: Left: quench training. First measurement series at 4.2 K (•), second measurement at 1.9 K (▲), third measurement at 4.2 K after thermic cycle to 293 K (○). Right: on-axis amplitude magnetic flux density B_0 versus current I .

sen Nb-Ti strand has very large filaments, causing large inter-filament coupling losses. Experience has shown that these losses cause a quench if the ramp rate is larger than 0.5 A/s.

In the matching coils large forces occur which are directed towards the extremities of the wiggler. In the current design of the BINP short-model wiggler no pre-stress can be applied to compensate for these stresses and, in addition, the mechanical stability of the wire bundle of the matching coil in incompletely filled grooves is believed to be poor. Therefore, the quench performance may be improved by an appropriate clamping structure. As stated before, field enhancements in the end-coils can be reduced by using a non-magnetic material. However, experience has shown that introducing a mix of materials with different heat-expansion coefficients may cause premature quenches of the magnets due to unloaded and unsupported wire bundles. Further improvements can be obtained by reducing the depth of the iron grooves. In the present design, the mid-plane magnetic flux density is limited to $B_0 = 2.2$ T instead of the required $B_0 = 2.5$ T, because of too deep grooves. However, the mechanical structure and the field on the conductor will almost not be changed by upper grooves. A wiggler with adapted grooves but otherwise identical design will meet the specifications of CLIC damping rings, however, with the magnet operating at 95% on the load line [38].

Table 5.16: Main parameters of BINP short-model wiggler

Period [mm]	50
Magnetic field [T]	2.5
Gap [mm]	20
Design current [A]	660
Current margin [%]	5
Turns	28, 146, 289, 341, 289, 146, 28
Layers	2, 10, 19, 22, 19, 10, 2

5.3.4.3 CERN Nb_3Sn trial coil

As a first step towards damping wigglers that employ Nb_3Sn wire technology, a trial coil, shown in Fig. 5.34 (left), was tested. The Lorentz forces have a different magnitude and direction in case of a single coil compared to a periodic wiggler structure. Therefore, a mechanical retaining structure, shown in Fig. 5.34 (right), had to be used for testing the coil. Figure 5.35 presents the field distribution on the

5.3 SUPERCONDUCTING MAGNETS

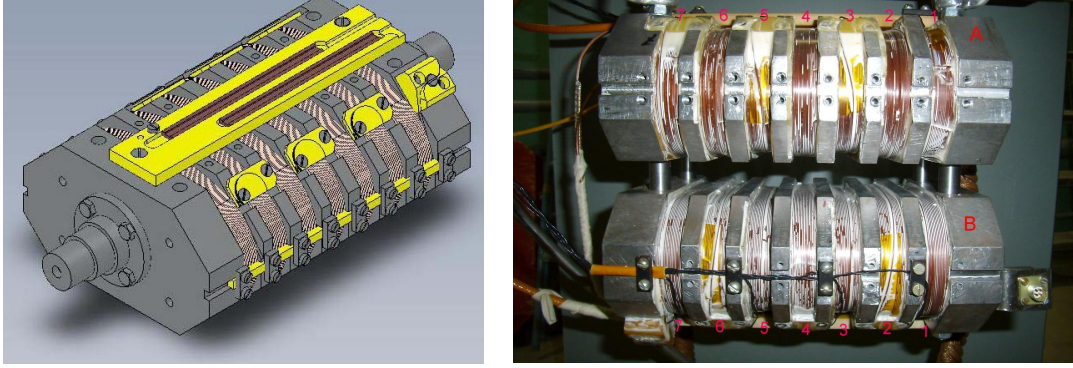


Fig. 5.32: Left: schematic design of short-model wiggler. Right: wound and potted short-model wiggler magnet.

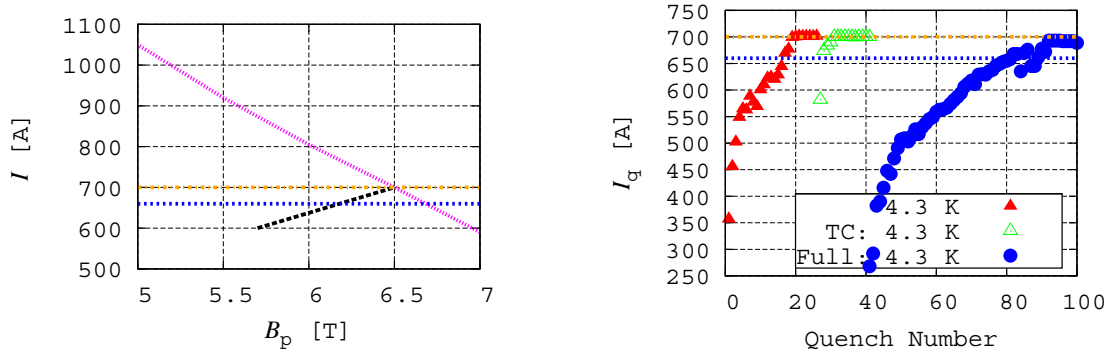


Fig. 5.33: Left: load line of the BINP short-model wiggler in black. The yellow, dashed line shows the short-sample current and the dashed blue line shows the operating current. The measured short-sample current is shown in pink. Right: training curve of the BINP short-model wiggler.

conductor for the maximum current reached during the test. The amplitude of the peak field is similar to the one in a wiggler magnet.

Figure 5.36 shows the quench currents I versus the peak field B_p on the conductors of the Nb_3Sn test coil. Note that the first quench was triggered at a current level close to the short-sample current limit. Unlike for the Nb-Ti prototypes, no ‘training’ is needed. A training quench is a special type of disturbance quench that occurs when the coil windings move slightly under the influence of electromagnetic forces and pressure changes during excitation. This may result in successively higher fields at subsequent quenches. High local stress due to imperfections in the winding and the epoxy resin can result in micro-cracks and/or a micro-movement of the wires which will raise the temperature locally. The better quench performance can be explained by the increased enthalpy margin of a Nb_3Sn coil. Nevertheless, care has to be taken during coil winding to densely pack the coil, because the Lorentz forces are directed towards the centre of the wire bundle (see Fig. 5.26), which results in a coil contraction during excitation.

Figure 5.36 shows in addition, that the Nb_3Sn test coil reached close to short-sample currents. Figure 5.37 presents the measured voltage across the coil at a constant ramp rate of 1 A/s. The coil is operated in the instability area of the superconducting material, where the flux-pinning force F_H is not sufficient to pin the flux-vortices. Strand measurements have shown that at 1.9 K the ‘self-field instabil-

ity' is the dominating mechanism that limits the performance of high- J_c wires, while the magnetization instability does not play a significant role. The minimum quench current due to the self-field instability is of the same order at 1.9 K and 4.2 K [39]. The noisy signal at 1.9 K and the fact that the maximal measured quench current at 1.9 K is only $\sim 2\%$ higher, shows that the quench current is close to the self-field stability current, and much smaller than the critical current. The critical current, indicates the maximum current which can be reached for a certain peak field, strain, and temperature; see Fig. 5.36, black line for 4.2 K and 1.9 K and zero strain.

To increase the flux-pinning force F_H and to ensure magnetic stability in type II superconductors, structural imperfections are needed in the superconductor. Such imperfections may be grain boundaries, lattice disturbances, grain morphology, impurities such as defined amounts of Zn, Mg, Fe, or Ni, or combinations thereof. In general, the increase of I_c depends on the temperature during heat treatment. Additional curing time and/or a higher temperature lead to a larger layer thickness, fewer grain boundaries, and therefore less pinning force. The applied RRP wire from OST was produced with a heat treatment optimized for high field applications. In the CLIC damping wigglers the conductors are operated in the intermediate and 'low' field range around 0 – 8 T. In this field range, the maximum pinning force is related to the average grain size and the grain size distribution in the Nb₃Sn layer. Therefore the quench current I is inversely proportional to the grain size, and thus proportional to the number of grain boundaries per unit volume. As a result, grain growth may be undesired [40] and a shorter (or lower temperature) heat treatment would increase the current margin for the CLIC damping wigglers.

The observed quench propagation was much slower at 974 A than at 1132 A (see Fig. 5.38). In the first phase of a quench, current sharing is present. Current sharing denotes the continuous commutation of the current from the superconducting to the normal conducting fraction of the strand [41]. To study current sharing, we varied the temperature and calculated iteratively the fraction of the current flowing in the superconductor I_s and in the copper matrix I_{Cu} , where the total current is $I = I_s + I_{Cu}$. The voltage drop over the superconductor is given by $U = U_0(I_s/I_c)^n$, and the resistance of the copper is a material property depending on the temperature, RRR, and applied magnetic field B . Figure 5.39 shows the result of the study. A copper-to-superconductor ratio of approximately 1, a residual resistivity ratio (RRR) of 250, and an n -value of $n = 70$ was assumed. The dissipated power density is well approximated by $P(I)/V = \rho(I)J^2$, where J denotes the applied current density, ρ the electrical conductivity, and V a reference volume. In the case of a higher operating current density, the power dissipation sets in at lower temperatures and reaches higher values. The associated quicker voltage build-up reduces the time until the quench is detected and can, therefore, reduce the quench load and, consequently, the hot-spot temperature. The quench load at 4.3 K and 1.9 K is in the range of 13–18.3 kA²s. The residual-resistivity-ratio (RRR) of the strand is around 250. This quench load relates to a hot-spot temperature of around 300 K.

No degradation of the coil's quench performance was observed over three thermal cycles and 21 quenches. After the training of the magnet at 1.9 K and one thermal cycle, the quench current at 4.2 K and 1.9 K reached almost the same level of > 1100 A. The results of this trial-coil testing shows that the use of Nb₃Sn superconducting material (with its higher enthalpy margin and higher critical current density) is within the technological reach for wiggler magnets. Wiggler magnets are particularly suited to this application because of the favourable force distribution, the short unit lengths of wire required, and the modular assembly and heat-treatment of the wiggler.

5.3.5 Magnet protection

The damping wiggler magnets need to be protected in the case of a quench. The estimation of the quench load for adiabatic conditions and at a uniform magnetic field gives a conservative estimation of the hot-spot temperature during a quench [38, 44]:

$$\int_{t_0}^{\infty} I^2(t) dt = \eta A^2 \int_{T_0}^{T_{\max}} \frac{c_v(T)}{\rho_E(B_s, T, \text{RRR})} dT, \quad (5.7)$$

5.3 SUPERCONDUCTING MAGNETS

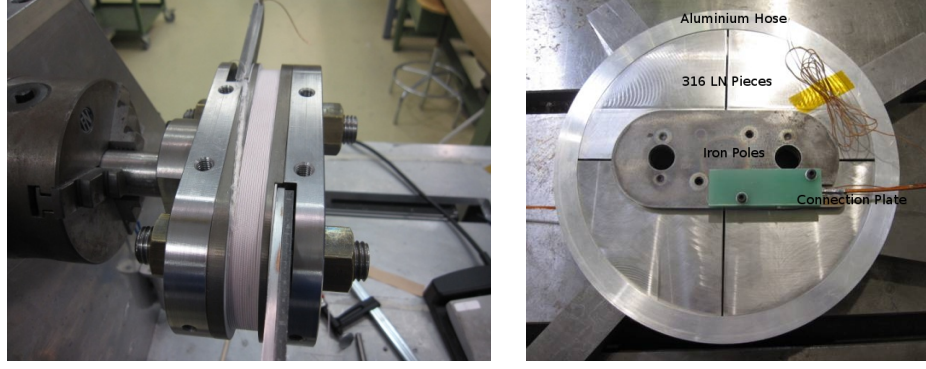


Fig. 5.34: Left: test coil during manufacturing. Right: test coil in retaining mechanical structure.

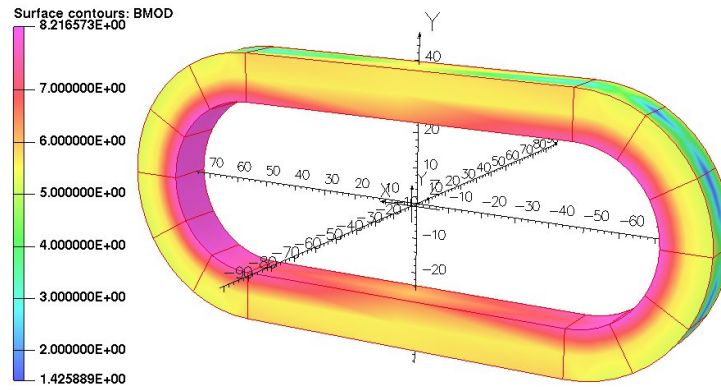


Fig. 5.35: Peak field at 1194 A (maximum current, $T = 1.9$ K).

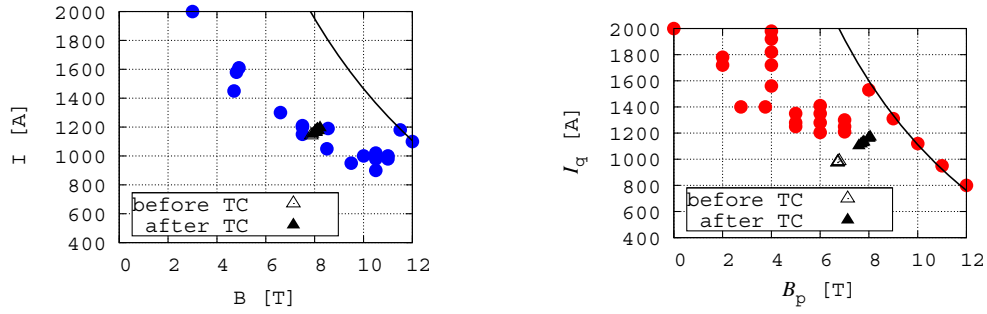


Fig. 5.36: Short-sample test results (red and blue points) as a function of the peak magnetic field and current of the test coil at 4.3 K (left) and at 1.9 K (right). The short-sample current was published in Ref. [42]. The black line shows the critical surface.

where $Z = \int_{t_0}^{\infty} I^2(t) dt$ is the quench load, t_0 is the time when a quench occurs, and $I(t)$ the current flowing in the magnet. η is the volumetric filling factor of the copper, A is the cross-section of the strand, T_0 is the operating temperature, and T_{\max} is the so-called hot-spot temperature. $c_v(T)$ is the volumetric heat capacity depending on the temperature T , and ρ_E is the electrical resistivity of the copper matrix, which depends on the applied magnetic flux density B_s , the temperature T and the residual resistivity RRR. Figure 5.40 shows the hot-spot temperature for a magnetic flux density of $B = 6$ T, an operating

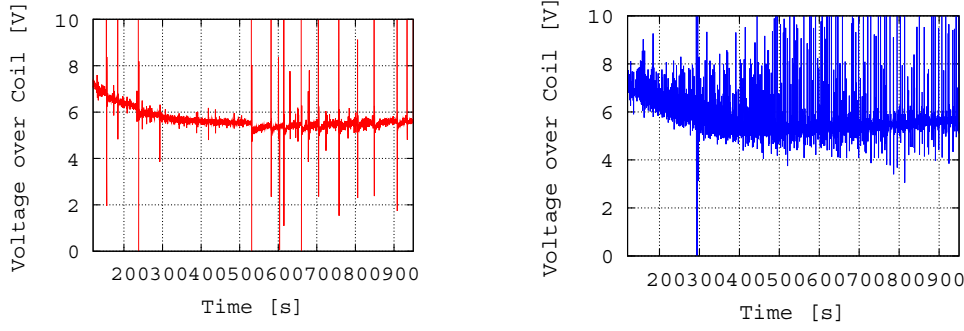


Fig. 5.37: Perturbations during the powering of the magnet with a ramp rate of 1 A/s. Left: $T = 4.3$ K. Right: $T = 1.9$ K.

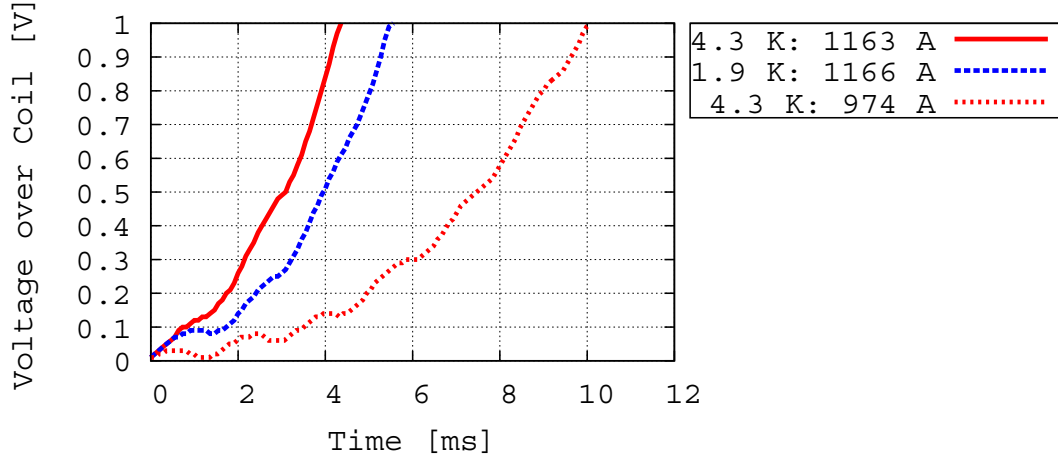


Fig. 5.38: Quench propagation after a quench at different currents at 4.2 K and 1.9 K.

temperature of $T_0 = 4$ K, and a RRR of 100.

It is more economical to power superconducting magnets in series because this reduces the number of power supplies and current leads into the cryostats. It is foreseen to power the 52 wigglers in four electrical circuits, that is, 13 wigglers powered in series. A disadvantage of this powering scheme is that in case of a quench the stored energy of all series-connected wiggler must be extracted from the powering circuit. The total stored energy in the baseline design is around 4.2 MJ per string. A PSpice simulation was performed to optimize the protection scheme and to estimate the energy dissipated in the quenched wiggler, as well as the energy dissipated into the supercritical helium.

Wigglers can be built and protected in modules; in the extreme each half period can be protected separately by means of a parallel resistor within the magnet coldmass, as it was done for the LHC beam diagnostics undulator [45]. The resistance increase after the occurrence of a quench was measured with the CERN short-model wiggler and used as an input to the PSpice simulation of the network.

Figure 5.40 shows a model for the resistance increase after a quench (top left) which was measured with the CERN short-model wiggler magnet, the dependency of the inductance on the current (top right) which is also extrapolated from CERN short-model wiggler magnet measurements. The voltages in the

5.3 SUPERCONDUCTING MAGNETS

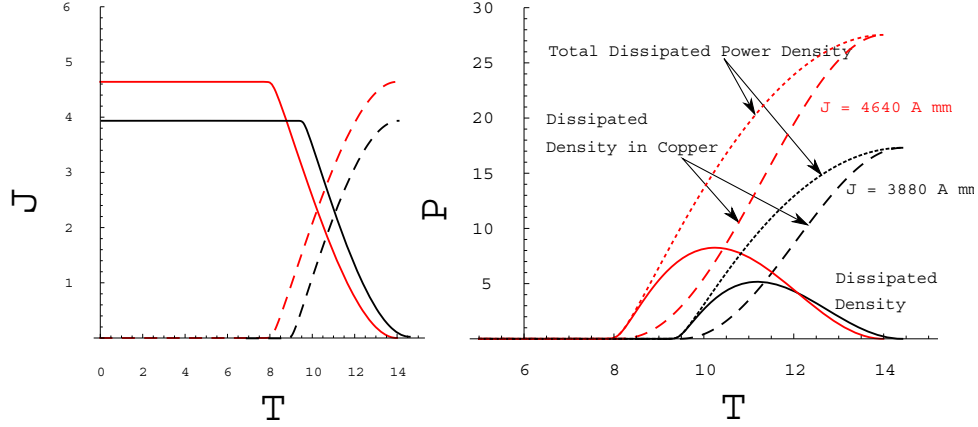


Fig. 5.39: Left: current sharing in the OST Nb₃Sn RRP strand with a current margin to critical current of 25% ($B_p = 6.7 \text{ T}$, $J = 4640 \text{ A mm}$) and 5% ($B_p = 7.5 \text{ T}$, $J = 3880 \text{ A mm}$). Right: dissipated power density in Nb₃Sn, copper and the entire strand. See Ref. [43].

circuit during the discharging of the circuit for the baseline design with $R_p = 20 \text{ m}\Omega$ and $R_{\text{ext}} = 1.2 \Omega$ (middle left), the energy deposited into the parallel resistors (middle right), and the dependency of the quench load on the parallel resistor R_p (bottom left) were simulated with PSpice. The dependency of the hot-spot temperature on the quench load (bottom right) was calculated with Eq. (5.7). These calculations show that to avoid any damage to the wiggler, the maximum stored energy in each wiggler module must be kept below 11 kJ, resulting in an inductance of 50 mH at the operating current of 660 A. Therefore, it is sufficient to sub-divide each wiggler into 30 modules that are protected with parallel dump resistors of 20 m Ω .

It is assumed that the energy extraction switch opens after a delay of less than 1 ms. Around 80% of the stored energy will be damped into the water-cooled, extraction resistor installed outside the string of magnets at ambient temperature. The remaining part of the energy is dumped into the cold helium bath. Note that the transient heat transfer to the helium bath, and thus the re-cooling time after a quench, can be influenced by the cold resistor design. The external extraction resistor was optimized such that the voltage across the string stays below 700 V and was chosen to be $R_{\text{ext}} = 1.2 \Omega$. This configuration will result in a maximal quench load of around $30 \text{ kA}^2\text{s}$ (0.03 MIITs) and result in a maximal hot-spot temperature below 200 K for the CERN LHC wire #3; see also Fig 5.40.

It will be essential to measure the resistance build-up in the Nb-Ti wire supplied by the Bochvar Institute and the RRP Nb₃Sn wire produced at OST. If the resistance increase is too slow to ensure magnet protection, quench heaters would need to be used to speed up the resistance build-up in the magnet. The following paragraphs give an overview of the required equipment for the magnet protection scheme.

5.3.5.1 Protection electronics

Within the protection scheme of the superconducting wiggler magnet circuits of the CLIC damping rings a dedicated electronic protection system will be used for the timely detection of quenches in the superconducting magnets and bus-bars. In case of a magnet or bus-bar quench, the system will activate the energy extraction systems and send a power abort signal to the respective power converter(s) and powering interlock controller. In addition the system will serve as a data acquisition system for the superconducting circuit and transmit all recorded data to the accelerator control system.

The protection electronics will be modular with one pick-up module attached to each individual magnet and a common evaluation and supervision unit. As an option the system can be additionally equipped with dedicated high-precision systems for the protection and supervision of bus-bar splices as

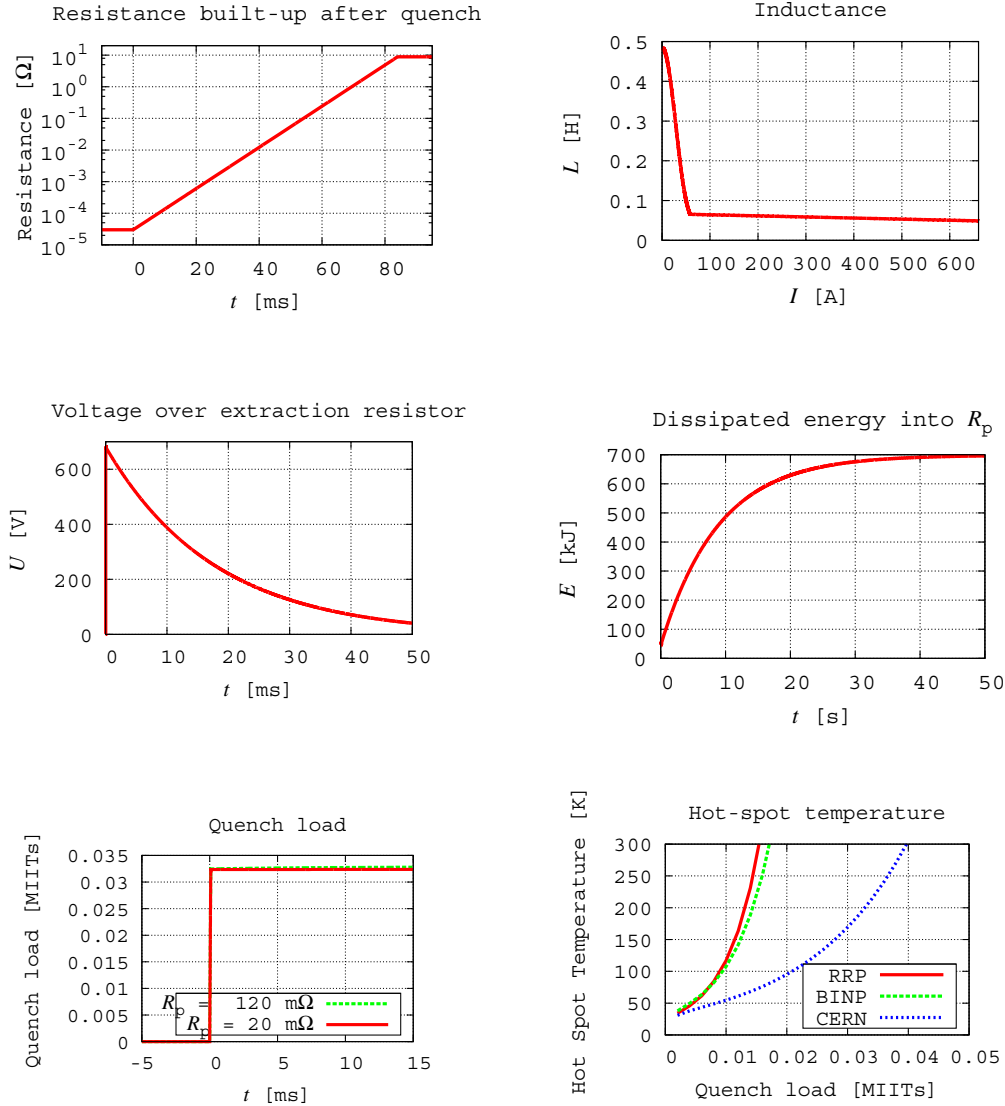


Fig. 5.40: Results of the circuit analysis

well as for the current leads. In addition the protection will be equipped with a dedicated current sensor monitoring the total current of the superconducting circuit.

The pick-up module will consist of an analog input stage and an analog-to-digital converter, electrically connected to the magnet with 3×2 redundant voltage probes and a galvanic separated digital interface, which provides the communication link to the evaluation and supervision unit. The evaluation and supervision unit, based on an embedded computer board, will collect the information from all attached pick-up modules and determine by a real-time software process the state of the superconducting circuit. The digital quench detection system concept, in combination with a dedicated current sensor, will allow the use of dynamic, current-dependent detection parameters. In the case of a quench it will activate the respective hardwired interlocks as described above.

The unit will be connected to the accelerator control system via a fieldbus or ethernet link. The evaluation and supervision unit will be integrated together with all pick-up modules in an electronic crate

housing the AC–DC power supplies. Owing to its modular design, the protection system can be adapted to different configurations of the superconducting circuits including test benches.

5.3.5.2 Magnet protection hardware

With internal resistors across each module of the wiggler magnet only a part of the total, stored magnetic energy will actually be extracted to the external extraction resistor, the quantity depending on the ratio of the external to internal resistance values. In the case of the Nb-Ti wiggler magnets the stored energy will be of the order of 4.2 MJ per circuit. Even with 17% dissipated in the internal resistors, the extracted energy is an order of magnitude higher than in the LHC corrector circuits. Consequently, a completely new design of the extraction resistors is required. Indirect water cooling appears to be the most appropriate way of evacuating the heat. For the Nb₃Sn wiggler magnets the extracted energy is similar.

The maximum extraction voltage of 700 V (dc) for the Nb-Ti baseline design magnets exceeds the capability of the electro-mechanical switch-gear in the extraction facilities of the LHC corrector circuits. Also, the requirement for a very short opening time cannot be met with such switches. Therefore, an IGCT-based solution is proposed as the basic choice for the extraction switch. With such a controllable semiconductor switch, the actual opening time will be a fraction of a millisecond. Development of the integration of an IGCT opening switch will begin shortly at CERN as a prelude to a possible upgrade of the LHC 600 A systems. A complete, bi-polar, prototype system should be ready within one year. It must be able to carry and commutate 1 kA, with a release voltage exceeding 1 kV (no radiation-hard thyristor drivers are required for the CLIC damping rings as they can be shielded).

The system will be housed in a standard Euro-rack. It can be either mono-polar or bi-polar (in current). For the bi-polar version back-to-back thyristors will be used. A design with series connection of two, redundant, devices will always be pursued for enhanced reliability of the opening function.

At currents up to 700 A no water-cooling will be required as long as dissipation into the surrounding air is permitted. With a voltage drop of typically 2×1.4 V the losses will not exceed 2 kW at 700 A.

5.3.6 Thermal and mechanical beam-pipe related design

The following paragraphs will describe quantitatively the various sources of heat load and will present a conceptual thermal design of the beam-pipe.

5.3.6.1 Synchrotron radiation

The most important source of heat load is synchrotron radiation. The angular distribution of frequency-integrated power $dP/d\Omega$ from periodic magnetic structures can be derived from the general expression for an arbitrary electron trajectory obtained by Schwinger (1949) [46]. For an electron following a sinusoidal trajectory we obtain the following form [47]:

$$\frac{dP}{d\Omega} = \frac{d^2P}{d\theta d\Psi} = 3 \frac{\gamma^2}{\pi^2} P_T f_K(\gamma\theta, \gamma\Psi) \quad (5.8)$$

where θ and Ψ are the observation angles in the horizontal and vertical directions, and P_T is the total power integrated over angles and frequencies

$$\{P_T\}_{\text{kW}} = 0.633 \{E\}_{\text{GeV}}^2 \{B\}_T^2 \{L\}_m \{I\}_A \approx \{9.8 \text{ kW}\}_{\text{Nb-Ti}}, \{12.1 \text{ kW}\}_{\text{Nb}_3\text{Sn}} \quad (5.9)$$

The angular dependence is given by

$$f_K(\gamma\theta, \gamma, \Psi) = \int_{-\pi}^{\pi} \sin^2 \alpha \left(\frac{1}{D^3} - \frac{4(\gamma\theta - K \cos \alpha)^2}{D^5} \right) d\alpha \quad (5.10)$$

where $D = 1 + (\gamma\Psi)^2 + (\gamma\theta - K \cos \alpha)^2$ and the deflection parameter K is given by

$$K = 0.934\{\lambda\}_{\text{cm}}\{B\}_{\text{T}} \approx 10.5 \text{ for Nb}_3\text{Sn} \text{ 11.7 for Nb-Ti.} \quad (5.11)$$

An example for the radiation spectrum generated by a CLIC Nb₃Sn damping wiggler, at 2 m from the source, is given in Fig. 5.41.

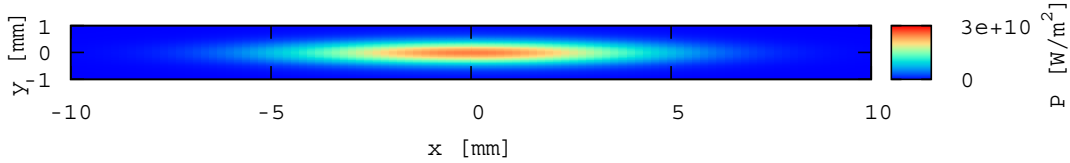


Fig. 5.41: Spectrum generated by a CLIC damping wiggler ($\lambda = 40$ mm, 2.8 T) at 2 m from the source

With the lattice design presented in Table 5.17 we can calculate the total heat load from synchrotron radiation on the beam-pipe downstream of a vertical absorber to < 1 W/m, as the beam-pipe is partially in the shadow of the upstream absorbers. The heat load ‘seen’ by the sixth and following magnets downstream of a horizontal absorber will be approximately 20 W/m for the Nb-Ti baseline design and 25 W/m for the Nb₃Sn design. Figure 5.42 shows the heat load distribution on the beam-pipe downstream of a vertical and a horizontal absorber. The horizontal aperture of the wiggler has to be chosen large enough to reduce the heat load from synchrotron radiation. Figure 5.43 shows the contribution of each wiggler to the total heat load on the last and preceding wiggler. More studies are required to optimize the space between the wigglers in order to accommodate the warm–cold vacuum transitions, absorbers, quadrupoles, and beam instrumentation.

The absorber design was optimized such that the load on the vertical and horizontal absorbers is balanced and reaches its maximal value, after some 10 absorbers. This maximum value corresponds to the emitted synchrotron power according to Eq. (5.9). Figure 5.44 shows the heat load on each absorber. The heat load on the vacuum chamber could be reduced by a factor of two if the horizontal gap of the horizontal collimator was closed to 7.5 mm. However, closing this absorber will result in an unbalanced absorber load: around 4 kW at the vertical absorbers and 18 kW at the horizontal absorbers.

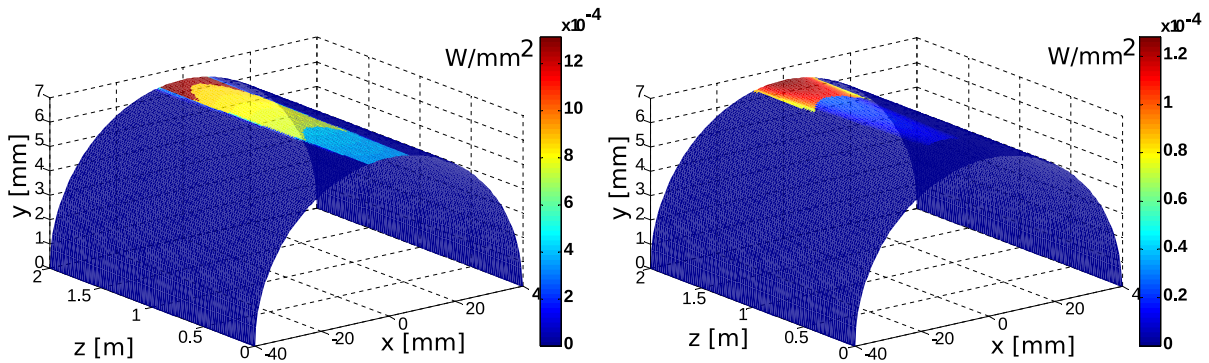


Fig. 5.42: Spatial distribution of synchrotron radiation on the beam-pipe for the 25th wiggler with a total heat load of 20 W/m (left) and the 26th wiggler with a total heat load of 1 W/m (right) for the Nb-Ti baseline design

5.3 SUPERCONDUCTING MAGNETS

Table 5.17: Lattice for heat load calculation of synchrotron radiation

Element	Length [m]	Vertical App. [mm]	Horizontal App. [mm]	Shape
Even numbered cells — Horizontal absorber				
Wiggler	2	13	80	Elliptical
Transition and quadrupole	0.25	13	80	Elliptical
Absorber	0.5	13.5	12.3	Rectangular
Transition	0.25	13	40	Elliptical
Odd numbered cells — Vertical absorber				
Wiggler	2	13	80	Elliptical
Transition and quadrupole	0.25	13.5	40	Elliptical
Absorber	0.5	9.5	12.5	Rectangular
Transition	0.25	13.5	40	Elliptical
Beam-pipe (heat load)	2	13	80	Elliptical

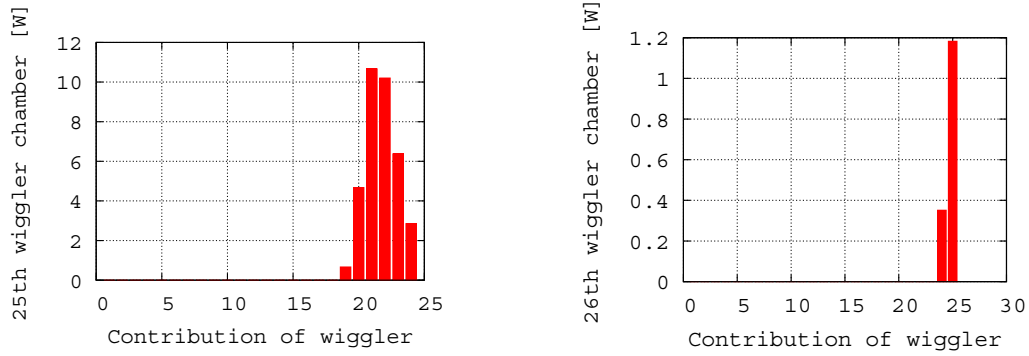


Fig. 5.43: Contribution to the heat load from downstream wigglers on the 25th (left) and the 26th (right) wiggler

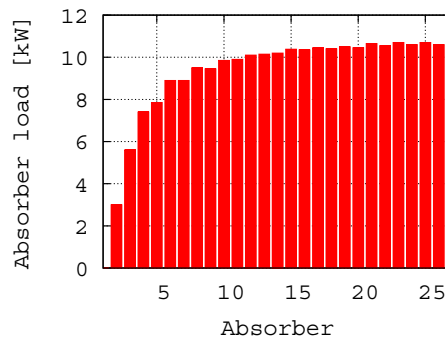


Fig. 5.44: Absorber load distribution

5.3.6.2 Attenuation

In the following paragraphs we will discuss where the synchrotron radiation is deposited. The critical photon energy ε_c of the CLIC damping wiggler can be calculated according to Ref. [48].

$$\varepsilon_c = 0.665 \{E\}_{\text{GeV}}^2 \{B_0\}_T \approx 13.5 \text{ keV for Nb-Ti, } 15.2 \text{ keV for Nb}_3\text{Sn}, \quad (5.12)$$

where E is the beam energy, and B_0 the amplitude of the wiggler's magnetic flux density.

The measured intensity I transmitted through a layer of material with thickness l is related to the initial intensity I_0 according to the Beer–Lambert law [49],

$$\frac{I}{I_0} = e^{-\mu l} \quad (5.13)$$

where l denotes the penetration depth. The attenuation coefficient is μ . If we limit the transmitted energy to 1% of the initial intensity, the penetration depth can be calculated to be

$$l = 4.6 \frac{1}{\mu}. \quad (5.14)$$

For a photon energy of $3\varepsilon_c \sim 5 \times 10^{-2} \text{ MeV}$, the attenuation coefficients for steel and the corresponding penetration depths are given in Table 5.18. The maximum penetration depth l_{max} , shown in Fig. 5.45, is also given in Table 5.18. The maximum penetration depth is at least one order of magnitude smaller than the material thickness of the beam-pipe. Therefore, all synchrotron radiation will be converted in the inner part of the beam-pipe into heat, and consequently, no heat will be deposited directly into the superconducting coils.

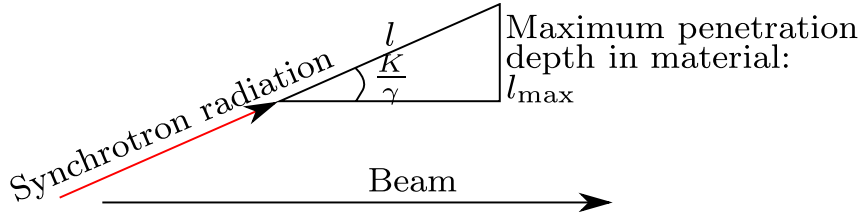


Fig. 5.45: Maximal penetration depth l_{max} of synchrotron radiation in the beam-pipe

Table 5.18: Attenuation coefficients and penetration depth [49] for a photon energy of $5 \times 10^{-2} \text{ MeV}$

Material	μ/ρ [cm ² /g]	ρ [g/cm ³]	μ [cm ⁻¹]	l [cm]	l_{max} [μm]
Al	0.3681	2.699	0.994	4.628	454
Cu	2.613	8.960	23.41	0.1965	19
Fe	1.958	7.874	15.42	0.298	29

5.3.6.3 Electron clouds

The heat load estimation due to electron clouds in the electron and positron damping rings was performed with the ECLOUD code [50]. Figure 5.46 (left) shows the heat load induced by electron clouds in the electron damping ring. The electron beam is not affected by multipacting for values of δ_{max} up to 2.4. Multipacting is a phenomenon of resonant electron multiplication in which a large number of electrons is built up, leading to large power losses and heating of the beam-pipe.

5.3 SUPERCONDUCTING MAGNETS

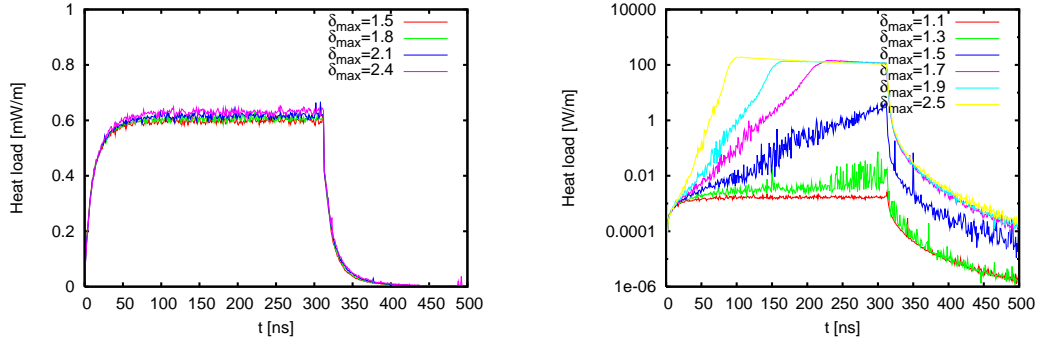


Fig. 5.46: Left: heat load induced by electron clouds in the electron damping ring. Right: heat load induced by positron clouds in the positron damping ring.

In the positron ring, multipacting appears for a secondary electron emission yield $\delta_{\max} > 1.3$ and causes significantly strong e-cloud effects over one train passage for values above 1.4–1.5; see Fig. 5.46 (right). As electron clouds cause not only heat load but also beam instabilities, low secondary electron emission yield coating such as amorphous carbon, TiZrV ternary alloy, called Non Evaporable Getter (NEG), or surface treated grooved copper [51] is needed for the positron damping ring.

5.3.6.4 Image currents

The average power deposition, per unit length, due to the wakefield of the beam in the extreme anomalous skin effect regime of a cold beam-pipe for aluminium or copper coating is, according to Ref. [52],

$$P/L = \frac{\Gamma(\frac{5}{6})cZ_0}{4b\pi^2} \frac{I_{av}^2}{\sigma_z^{\frac{5}{3}}\eta f_{RF}} B_{Mat} \approx 1 \frac{W}{m}. \quad (5.15)$$

While good conductors do enter the anomalous skin effect regime at cryogenic temperatures and high frequencies, poor conductors do not. For poor conductors such as uncoated stainless steel or NEG coating the heat load can be estimated by normal skin effect formulas [53]

$$P/L = \frac{\Gamma(\frac{3}{4})c\sqrt{Z_0}}{\sqrt{32}b\pi^2} \frac{I_{av}^2}{\sigma_z^{\frac{3}{2}}\eta f_{RF}} \frac{1}{\sqrt{\sigma_c}} \approx 32 \frac{W}{m}. \quad (5.16)$$

The presented values for the image current power deposition were calculated with the values given in Table 5.19. A material with poor conductivity is not acceptable because of its high heat load; therefore, all following calculations are assuming a well conducting beam-pipe, which is also required by beam dynamics.

5.3.6.5 Normal-conducting joints

First tests have shown that soldered joints have a resistance of $R < 20 \text{ n}\Omega$. As the wiggler will be built by using 30 modules (15 joints per metre) the losses due to joint resistances will amount to a total dissipated power of

$$P/L < RI^2/L = 15 \cdot 20^{-8} \Omega \cdot 660^2 \text{ A}^2 / 1 \text{ m} < 0.2 \text{ W/m}. \quad (5.17)$$

Table 5.19: Parameters of Eqs. (5.15) and (5.16) ([52] and [54])

Parameter	Value	Unit	Explanation
$\Gamma(\frac{5}{6})$	1.13		Gamma-function
B_{Al}	3.3×10^{-7}	$m^{\frac{2}{3}}$	Material specific constant, Al
B_{Cu}	3.9×10^{-7}	$m^{\frac{2}{3}}$	Material specific constant, Cu
σ_c	2×10^6	Sm^{-1}	Stainless steel conductivity at 4.3 K
Z_0	120π	Ω	Free space impedance
c	3×10^8	m/s	Speed of light
I_{av}	0.15	A	Average current
b	5.5×10^{-3}	m	Radius of beam-pipe (with safety margin)
σ_z	1.4×10^{-3}	m	Bunch length
ηf_{RF}	$0.22 \times 1 \times 10^9$	Hz	Fraction of the ring circumference occupied by a bunch train for 1 GHz frequency times frequency
	312		Number of bunches (2 trains \times 156 bunches)
	4.1×10^9		Bunch population
	427.5	m	Ring circumference
	1.4×10^{-6}	s	Orbital period
	1×10^{-9}	s	Bunch separation

5.3.6.6 Eddy currents

Eddy currents will occur during a quench of the wiggler due to the rapidly changing magnetic flux density; during the magnet ramp, eddy currents are negligible for ramp rates of less than 5 A/s. Figure 5.47 shows the magnetic forces on the beam-pipe during a quench. The eddy currents stay small; therefore, the magnetic forces on the wiggler are almost unaffected by the eddy currents ($F \sim B^2$). The dissipated power due to eddy currents in the beam-pipe for the two cases (thin and thick beam-pipe) is around 3 W/period or 75 W/m for a period of 100 ms. Therefore, a total energy of 7.5 J/m is dissipated. The dissipated energy due to eddy currents in the beam-pipe will not cause damage to the system and can, therefore, be neglected.

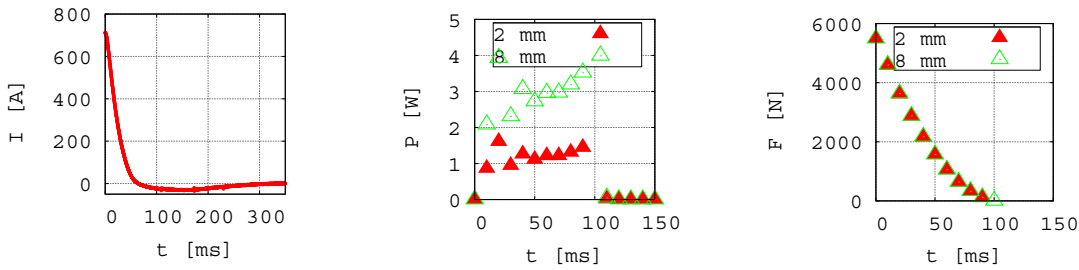


Fig. 5.47: Current decrease in the short-model wiggler after a quench (left), dissipated power in a stainless steel beam-pipe (middle), magnetic forces (right)

5.3.6.7 Cooling concept

We propose to develop a different cooling system than the standard superconducting wiggler cooling system (Fig. 5.48). For indirect cooling, the whole wiggler magnet is in an insulation vacuum. The helium is contained in the heat exchangers. In bath cooling, the magnet is immersed in liquid helium (LHe). To extract the heat, a copper liner cooled with gaseous helium contained in heat exchangers is

5.3 SUPERCONDUCTING MAGNETS

required (depicted in red). Further, a mechanically stable pipe that can withstand the pressure increase during a quench (in black) is needed. This pipe also insulates the beam vacuum from the surrounding liquid helium. Although indirect cooling requires the detailed thermal design of the superconducting coils, it has a number of advantages compared to bath cooling:

- Mechanically less demanding beam-pipe. Bath cooling would require a stainless steel beam-pipe to sustain the pressure increase during a quench. Without this requirement, a 2 mm smaller gap can be realized. The result is a more than 10% higher B_w .
- Less complex cryogenic structure because all helium is contained within the heat exchangers. The result is a smaller helium mass, smaller valves, tubes, etc.
- Cryostat design for exchangeable coils and vacuum pipes for maintenance and repairs is less complex.

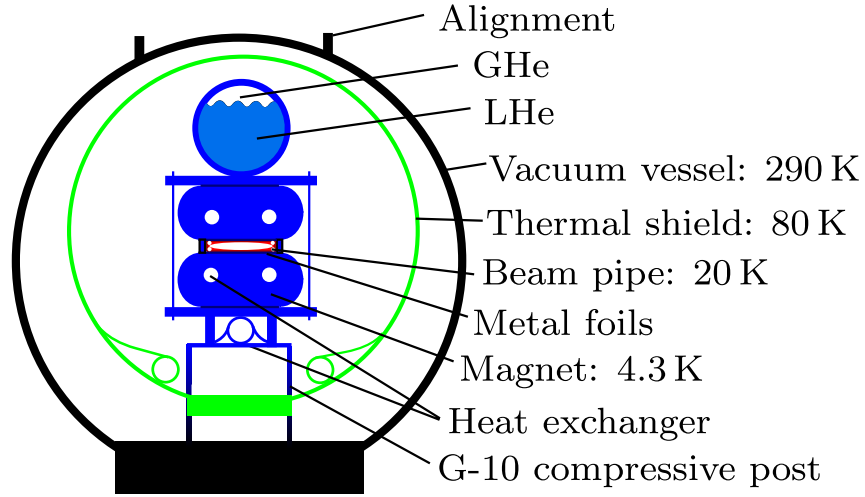


Fig. 5.48: Conceptual design of cryostat. The different colours represent the different temperature levels.

An insulating vacuum of 10^{-4} Pa is established to minimize the heat transfer to the superconducting coils by convection. The superconducting coils and the beam-pipe are mounted with minimal thermal contact and with materials such as glass-fibre reinforced plastics with a large strength-to-heat-conductivity ratio. All surfaces are wrapped with polished well-conducting metal foils or aluminized Mylar foils with small emissivities to reduce heat transfer by radiation.

The temperature of the beam-pipe is stabilized at around 20 K, where the heat conductivity k of copper is highest (Fig. 5.49). The result is an iso-thermal beam-pipe. Cryo-coolers for this temperature level are available, and radiation to the superconducting coils is kept to a minimum.

The heat loads are deposited in the centre of the cross-section of the 2 m long beam-pipe (Fig. 5.42) and have to be transported over $\lesssim 50$ mm to the outer side of the beam-pipe. The resulting temperature difference is smaller than $\Delta T < 1/2 \cdot \dot{Q}l/kA \approx 0.3$ K, with the heat load $\dot{Q} = 5$ W, the distance from the centre of the beam-pipe to the heat exchanger $l = 1$ mm, the average heat conductivity $k = 2000 \text{ W(mK)}^{-1}$ (RRR = 80), and cross-section $A \geq 2 \times 10^{-3} \text{ m}^2$.

The calculation of heat leak from other sources is straightforward and presented, for example, in Ref. [56]. Table 5.20 gives a summary of all heat load sources occurring in the CLIC damping wigglers at the different temperature levels.

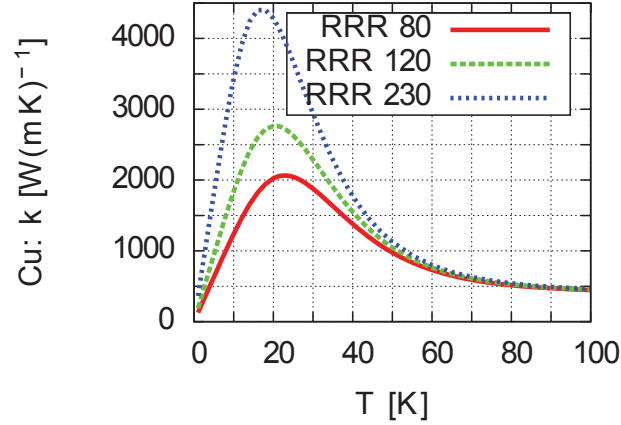


Fig. 5.49: Heat conductivity of OFHC copper over temperature. Data from [55].

Table 5.20: Summary of the average heat loads (all sources) at the different temperature levels in watts

	Shield 80 K	Beam-pipe 20 K	SC coils 4.2 K
Synchrotron radiation (HA)		20.0	
Synchrotron radiation (VA)		1.0	
Average SR		10.5	
Image currents		2.0	
E-clouds		0.02	
Radiation	16.3		0
Convection	1.0		0.10
Conduction	0.9		0.64
Joints	-		0
Current leads	72.0		0.16
Total (average)	90.2	12.5	0.9

5.3.7 Technical issues

An Nb-Ti prototype installed in a synchrotron with similar parameters as foreseen for the CLIC damping rings will allow to us verify the long-term stability of the field, radiation resistance under operating conditions, field quality, and the heat load calculations. Further, the technical auxiliary equipment such as cryostat, power supply, and magnetic shims (magic fingers) can be tested. However, the baseline design foresees operation with only 5% margin to the critical surface. Therefore, the Nb-Ti wigglers require a more sophisticated cryogenic system to ensure an operating temperature below 4.5 K at all times.

On the other hand, Nb₃Sn wigglers have a considerably higher temperature margin, allowing more options for the cryogenic system and allowing more reliable operation. For these reasons, Nb₃Sn models are under construction and the experience with them will lead to a feasibility study with a full-length Nb₃Sn prototype.

The thermal design of the beam-pipe has to be optimized and different coatings (e.g., amorphous carbon, TiZrV ternary alloy, or grooved copper) of the beam-pipe have to be studied.

It will be essential to measure the resistance build-up in the Nb-Ti wire supplied by the Bochvar Institute and the RRP Nb₃Sn wire produced at OST and then to update the circuit analysis accordingly.

Using the full-scale prototype, the quench detection system and the magnet protection system have to be tested including failure scenarios of the quench detection system, the power supply shutdown, and the extraction switch system.

The cooling of the string of magnets, the headers, the jumpers, current-leads, and the by-passes has to be validated and tested.

5.3.8 Outlook for project preparation phase

In the project preparation phase it is foreseen to merge the two independent collaborations CERN–KIT and CERN–BINP in order to manufacture a full scale Nb-Ti prototype wiggler (as described above) at BINP and then test it at ANKA, with CERN specifying the design parameters in consultation the collaboration partners. During the manufacture and testing of the Nb-Ti prototype, CERN will manufacture short-models, and a full-scale Nb₃Sn prototype with help from its collaboration partners. The remaining technical issues will be dealt with as described in §5.3.7. Table 5.21 gives an overview of the strategy of the superconducting magnet projects for CLIC.

Table 5.21: Outlook for project preparation phase

Nb ₃ Sn technology	Nb-Ti technology
CDR: First tests	
Conceptual design for short-model 5 test coils for insulation and heat treatment tests One vertical racetrack coil tested 2-period wiggler in mirror and full configuration	Conceptual Design for short-model Short-model at BINP successfully tested Short-model successful tested at CERN in mirror configuration
Project preparation phase: small prototype	
	Design and test modules Test splices and modularity Field quality assurance Validate and test magnet protection system Validate and test cooling of string of magnets, headers, jumpers, current-leads, and by-passes Validate and test vacuum and coatings
Project preparation phase: full-scale prototype	
Full scale Nb ₃ Sn prototype with cryogenic system to be tested e.g., at ANKA Design and manufacturing at CERN with input from ANKA and BINP	Full scale Nb-Ti prototype with cryogenic system manufactured at BINP with design input from CERN and tested at ANKA Manufacturing at BINP, design by a collaboration of CERN, BINP, and ANKA. Test at ANKA

5.4 Radio Frequency systems

5.4.1 Overview

The CLIC concept builds on advanced Radio Frequency (RF) systems, for both Drive Beam and Main Beam. Due to their special importance and novelty, the CLIC X-band RF systems (consisting of the Drive Beam Power Extraction and Transfer structures (PETS)), the CLIC Main Beam accelerating structures (AS), and the CLIC crab cavities, are be treated separately in §5.5. All other, more conventional RF systems are treated here. This section covers in particular the Drive Beam accelerating structures, the Drive Beam klystrons, the Damping Ring RF system, the RF deflectors.

Even though referred to as ‘conventional’ the RF systems described in this section have to meet very challenging specifications, in particular:

- ***Accelerating structures for Drive Beam generation***

The 1 GHz, traveling wave accelerating structures for the high-current (4.2 A) Drive Beam have to deal with potentially strong excitation of higher order modes; they furthermore have to operate in ‘full beam loading’ mode such as to maximize the RF to beam power transfer efficiency; this means that the amplitude of the forward traveling wave is zero at the structure output.

- ***Klystrons for Drive Beam generation***

The Drive Beam klystrons have to be optimized for maximum efficiency, since a total power of 184 MW at the accelerating structure inputs will be needed. The envisaged target value of above 70% requires very low perveance ($0.25 \mu\text{Perv}$) to reduce space charge effects (Perveance characterizes the dependence of the current on the anode voltage in the regime of space-charge limited [Child-Langmuir] emission, the unit μPerv is equal to $\text{M}\Omega^{-1}\text{V}^{-1/2}$). In order to obtain significant output power in the range of 15 to 20 MW, this requires multiple beam klystrons. In addition to the need for maximum efficiency, also the required amplitude and phase stability are very challenging, both for the klystron itself and the modulator providing the anode voltage pulse. Note also that maximum efficiency implies operation in saturation, which would not allow for amplitude regulation feed-back via the RF drive.

- ***RF deflectors for Drive Beam generation***

The bunch train compression scheme for the generation of the 100 A electron Drive Beam relies on the use of fast RF deflectors for injection into the delay lines and in the combiner rings. The design of these devices for failsave operation is very important for the overall running efficiency of the CLIC accelerator.

- ***The Damping Ring RF systems***

The Damping Ring RF systems have to deal with extremely large transient beam loading and must be stable enough not to blow up the extremely small emittances which will be created in the Damping Rings.

The above four systems have been studied in detail in the past years and the results are documented in the following four subsections.

All other RF systems, in particular also the challenging low level RF systems, are considered ‘conventional’ enough to be defined and worked on later in the technical design phase of the project.

5.4.2 Drive Beam accelerating structures

5.4.2.1 Introduction

The use of two identical Drive Beam Accelerators (DBA) is foreseen for the nominal CLIC scheme, i.e., for a centre-of-mass energy of 3 TeV. Each will accelerate a Drive Beam to 2.37 GeV. For a centre-of-mass energy of ~ 1.5 TeV or below, only one DBA would be needed (see §8.1). Because of the large beam current of 4.2 A (bunch charge 8.4 nC), Higher Order Modes (HOMs) can be excited by the beam

and would render it unstable – they required detailed study and mitigation. Several structure types, using different methods for HOM damping, have been investigated at different operating frequencies [57].

A Tapered Damped Structure (TDS) has been studied first. It is a downscaled version of a structure originally designed for the CLIC main accelerator. Higher order modes are damped in the TDS by coupling wide band silicon carbide (SiC) loads through waveguides to the accelerating cells. The accelerating mode is not damped if the cut-off frequency of these waveguides is chosen appropriately (above the fundamental mode frequency and below the first dipole mode frequency). A TDS designed for 1 GHz would be enormous in size and weight (outer diameter 1.3 m).

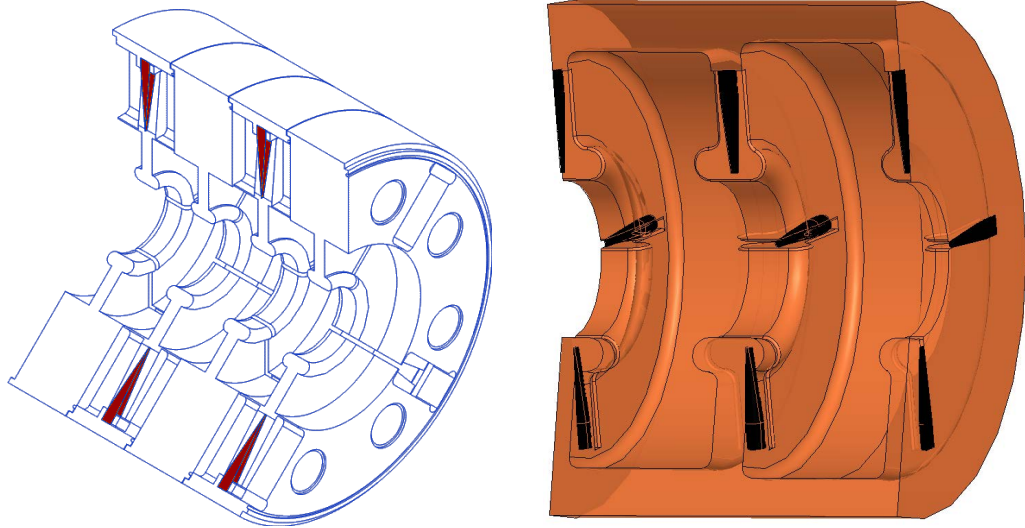


Fig. 5.50: Conceptual view of two SICA structures; left: The 3 GHz CTF3 structure; right: The baseline structure for the CLIC Drive Beam Accelerator at 1 GHz.

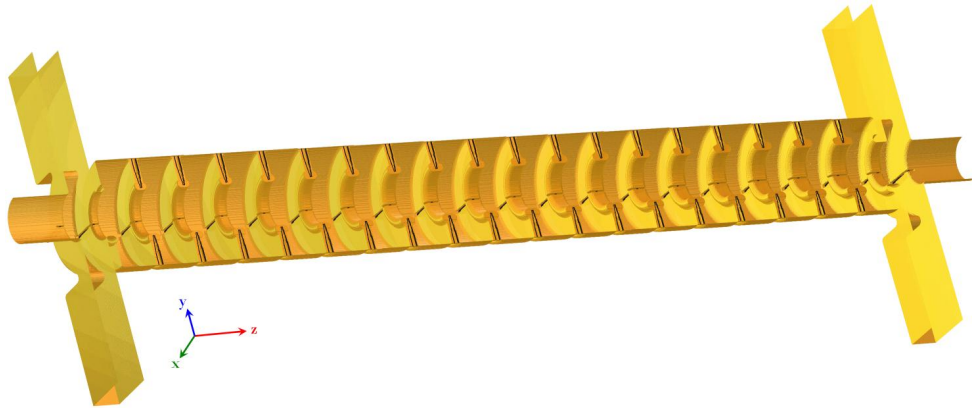


Fig. 5.51: Baseline SICA structure for the CLIC Drive Beam accelerator consisting of 21 cells (19 accelerating cells and a coupling cell at each end). The total length is 2.4 m.

Therefore, a second structure type has been developed, the Slotted Iris–Constant Aperture structure (SICA)[58]. In addition to strong damping, both TDS and SICA use detuning of the dipole modes along the structure, which improves the suppression of HOMs significantly and which goes hand in hand with a desired group velocity variation along the structure. But in contrast to the TDS structure, where this detuning is obtained by varying the iris aperture, the SICA structure uses different size nose cones in

every cell. The beam aperture is constant along the structure, which is advantageous, e.g., for reducing the short range wakefields and to ease measurements. Irises are radially slotted four times (dividing a disk in quadrants); the slots guide dipole and quadrupole modes into SiC loads situated outside the cells (see Fig. 5.50 left). Every other iris has those four slots rotated by 45° , which helps field homogeneity and mechanical stability. The dipole modes are strongly damped (Q typically below 20), while monopole modes are not influenced by the slots due to the structural symmetry.

Slot modes have been investigated in detail, they are even stronger damped (Q typically below 6) and do not degrade the performance. A total of 20 SICA structures operating at 3 GHz have been built by industry [59]. They have been installed in CTF3 in 2003, and the CTF3 Drive Beam linac has been operated routinely since then under full beam-loading conditions [60] at nominal parameters as well as higher gradients, powers, and currents, thus sufficiently validating the concepts of both SICA and full beam loading.

5.4.2.2 Structure optimisation

A simple scaling of the CTF3 SICA structure to 999.5 MHz would still lead to a considerable outer diameter of 520 mm, but since most of the outer part of the 3 GHz version has no basic electromagnetic functionality, a smart design modification could be developed where the higher order mode absorbers (SiC loads) are located directly in the iris slots, thus reducing the outside diameter to 300 mm (see Fig. 5.50, right). At the same time, the input power was lowered to 15 MW (peak) to match the klystron cost optimum (compare §5.4.3) when operating with one klystron per structure. Furthermore, the structure's fill time could be adjusted to 245 ns. In this way, frequency components of 4 MHz and multiples, contained in the noise which is added by the RF amplifier chain, are band-stop filtered. These noise components are particularly critical because once transmitted to the Drive Beam, they would add up coherently by the beam manipulation in the delay loop and the combiner rings. Calculations have shown that the phase noise requirements of the amplifier chain can be relaxed by more than a factor of four if the fill time deviates from the optimum of 245 ns by less than 5 ns.

Figure 5.52 shows the result of optimizing the group velocity of all structure cells (nose cone length) for different RF input powers, structure lengths (number of accelerating cells) and beam pipe apertures.

For all plotted points, an RF-to-beam efficiency of more than 95% and a structure fill time of 245 ± 5 ns could be obtained. Beam dynamics simulations have been performed to find a compromise between aperture and structure length for the 15 MW input power to minimize short and long range wake effects. The resulting structure is composed of 19 accelerating cells, two coupling cells, is 2.4 m long in total and has a beam pipe aperture (diameter) of 98 mm (see Fig. 5.51). The group velocity of this structure decreases linearly along the 19 accelerating cells. The accelerating gradient and the losses in each cell are also given in Fig. 5.53 for the loaded (solid line) and the unloaded case (dashed line). The total accelerating voltage (on crest) of one accelerating structure is 3.4 MV. Figure 5.54 shows the complex electric field of the accelerating mode along the 19 accelerating cells as it would be seen in a bead-pull measurement, simulated with GdfidL. The remaining tuning error of individual cells is smaller than 30 kHz but creates the small standing wave pattern that can be seen in Fig. 5.54 (right). This can be cured in a real structure by dimple tuning – as applied to the 3 GHz SICA structure (compare [59]). The input and output coupler have been adjusted to provide an input reflection of less than -30 dB over a bandwidth of 1 MHz around the operating frequency of 999.5 MHz (see Fig. 5.55).

5.4.2.3 Higher Order Mode Damping

Higher order modes and their reduction by damping and detuning have been studied in detail and are published in Ref. [61]. The results can be summarized as follows:

- Modes with magnetic symmetry planes in the x and y direction are practically not damped by the

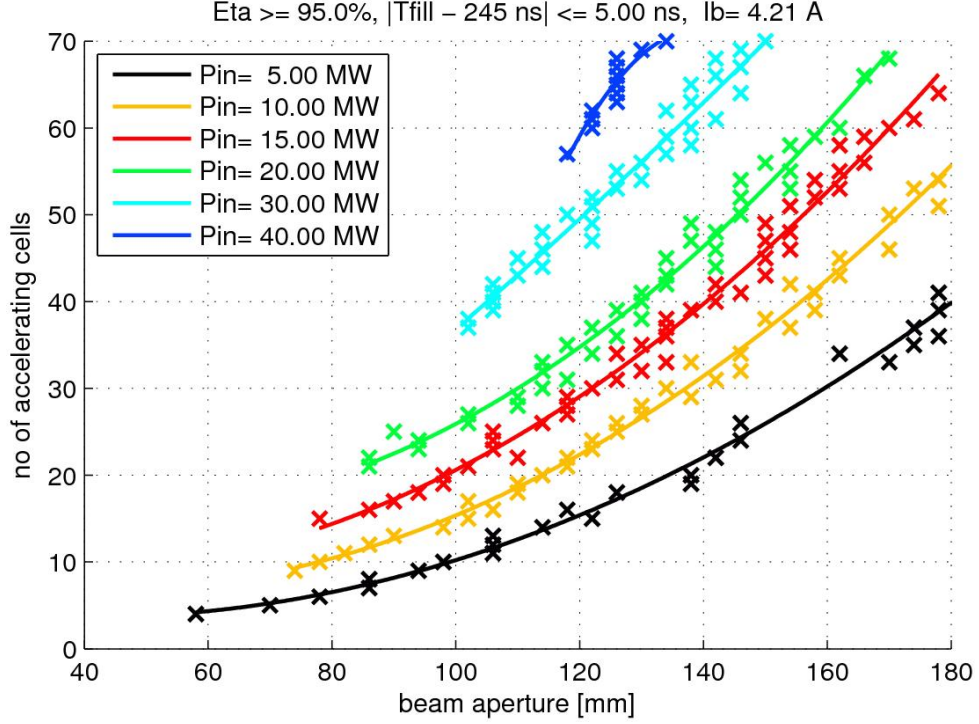


Fig. 5.52: Structure optimisation: For several input powers (colour coded) and beam pipe apertures (diameter), the number of accelerating cells and the group velocity in each cell can be chosen such that the RF-to-beam efficiency is above 95% while the fill time is 245 ± 5 ns. The CLIC DBA baseline structure has a beam pipe aperture of 98 mm and is made of 19 accelerating cells.

SiC loads. They are well detuned.

- The slots and the SiC loads have been optimized to efficiently damp dipole modes. It has been seen that the quadrupole modes in both polarizations couple only weakly to the beam. Therefore, the 45° rotation of the loads from one cell wall to its two neighbours to damp quadrupole modes is not employed any longer.
- Most of the dipole mode bands are additionally widely detuned.
- The accelerating mode is sufficiently decoupled from the SiC loads when machining accuracy is controlled to better than 0.1 mm.
- A number of slot modes exist – but they are very well damped.

Wakefields have been calculated with GdfidL for a bunch charge of 8.4 nC and a bunch length of 1 mm (normal distribution, standard deviation 1 mm). Figure 5.56 shows the longitudinal wake potential calculated along the beam axis for monopole modes.

The accelerating mode of the full structure has an overall (R/Q) of 2.3 k Ω (linac definition) and is excited by the considered bunch to a corresponding accelerating voltage of 60 kV. The excited wave runs out of the output couplers and thereby decays. The first HOM band is an order of magnitude less excited and resonates in the frequency band from 2.08 to 2.10 GHz (detuned by 20 MHz).

Transverse wakefields have been simulated with the same bunch characteristics (charge 8.4 nC, length 1 mm) but displaced by 10 mm in x and y direction, respectively (compare Fig. 5.51 for the orientation of x and y). The results are shown in Fig. 5.57. Monopole modes have been suppressed in the simulation by inserting an electric wall at $x=0$ (for W_x) and at $y=0$ (for W_y), respectively (the potentials are re-scaled by a factor of 1/2 to correct for the excitation by the mirror bunch). The dipole modes are

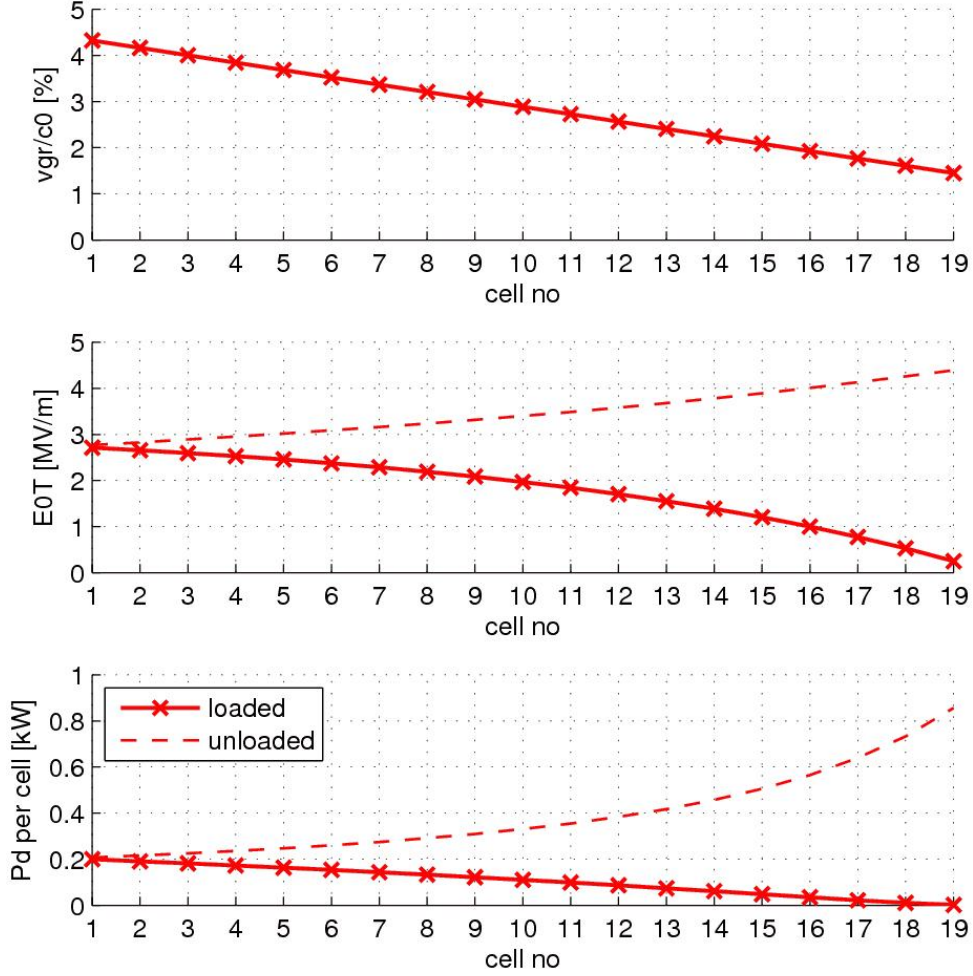


Fig. 5.53: Electromagnetic properties of the CLIC DBA structure for the 19 accelerating cells. Top: group velocity profile in reference to the speed of light; middle: the accelerating gradient for the loaded (solid line, beam current 4.2 A) and the unloaded (dash line) case; bottom: average dissipated power in each cell for the loaded and unloaded case for an RF duty cycle of 7.5%.

strongly damped by the SiC loads with a loaded Q -value of 21 in x direction and 17 in the y direction—here some power is additionally extracted by the output coupler. The kick factor of the full structure is about 70 V/pC/m^2 both in x and y direction.

5.4.2.4 Summary

Summarizing, the Drive Beam Accelerator (DBA) for each Drive Beam Linac will consist of 819 identical traveling wave structures to accelerate the beams to 2.37 GV. Structures are composed of 21 cells, giving a total structure length of 2.4 m. Klystrons will feed $140 \mu\text{s}$ long pulses of 15 MW into the accelerating $2\pi/3$ mode at 999.5 MHz and 95% of this power is transferred into the 4.2 A beam due to fully beam loading operation.

The most important parameters of the SICA structures for the Drive Beam accelerator at 3 and 1 GHz are summarized in Table 5.22.

5.4 RADIO FREQUENCY SYSTEMS

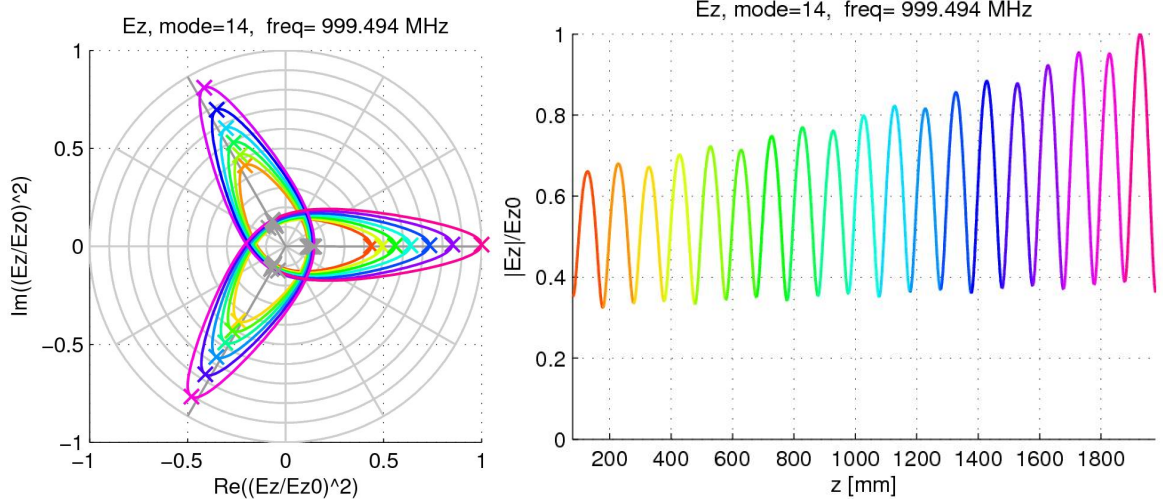


Fig. 5.54: The normalized electric field component E_z on the beam axis for the 19 accelerating cells, on the left squared in the complex plane and on the right the magnitude along the longitudinal position.

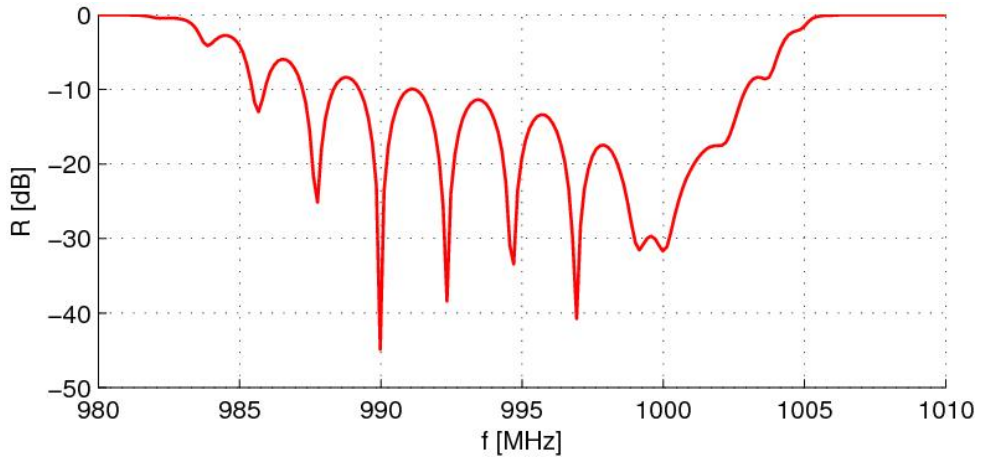


Fig. 5.55: Input reflection of the CLIC DBA structure. The input reflection is below -30 dB in a 1 MHz bandwidth around the operating frequency.

5.4.3 Drive Beam klystrons

5.4.3.1 Introduction

To feed each of 1638 accelerating structures with 1 GHz RF pulses of 15 MW, a total pulsed RF power of 24.57 GW is required. With the required pulse length of $150 \mu\text{s}$ and a repetition rate of 50 Hz, the corresponding average RF power at the accelerating structure input is 184 MW. This large average RF power requires highly efficient RF power generation to keep the overall power consumption at bay. As detailed above, these RF pulses must be controlled in amplitude in phase to an uncorrected intra-bunch jitter of below $\pm 0.05^\circ$ in phase and $\pm 0.2\%$ in amplitude. These requirements dictate the challenging specifications for the Drive Beam klystrons and their modulators.

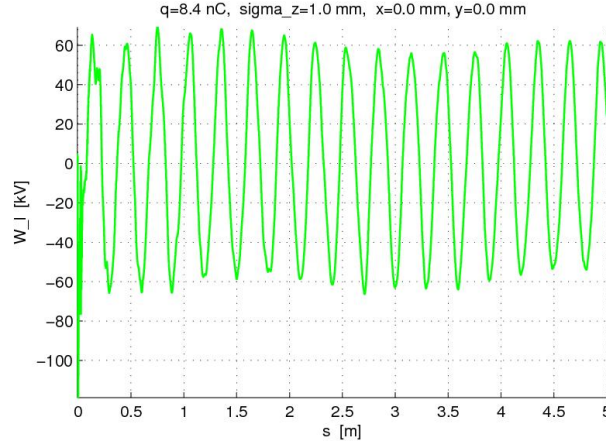


Fig. 5.56: Longitudinal wake potential at $x=y=0$ mm, generated by a charge of 8.4 nC with a length of 1 mm.

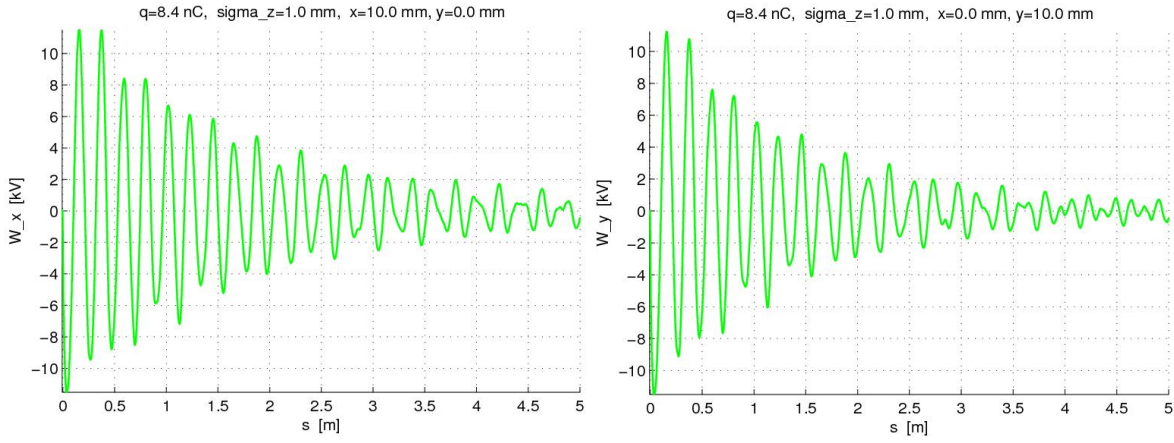


Fig. 5.57: Transverse wake potentials of the dipole modes for a displacement in x (top) and y (bottom) direction of 10 mm.

5.4.3.2 Which type of power source?

RF power sources other than klystrons have been considered, in particular in view of the need of highly efficient operation and the very challenging demand for phase stability.

Magnetrons can produce RF power with very good efficiency, they are however oscillators by nature, thus they must be phase-locked to an external drive with relatively large power (> -20 dBc). But even in this case the remaining phase noise is too large to be compatible with the stringent requirements cited above.

While klystrons use velocity modulation of a DC electron beam with subsequent drift spaces to reach density modulation, Inductive Output Tubes (IOTs) employ direct density modulation using an RF grid voltage, whereas the output circuit is an RF structure, loaded by the output waveguide, like in a klystron. IOTs are used in commercial TV transmitters and operate typically at 700 MHz and power levels of below 100 kW. Their advantages are the non-vanishing differential gain in the optimum efficiency working point and the modest DC voltage (< 50 kV); their disadvantage is their limited gain (~ 22 dB). It is possible to conceive HOM IOTs and multi-beam IOTs for larger single unit power reach, but this would involve a major R&D program. CPI has developed and tested a six-beam HOM-IOT, operated at 31 kV, which produced 920 kW with an efficiency of 62%.

Table 5.22: Parameters of the SICA Drive Beam accelerating structures

	3 GHz SICA (CTF3)			1 GHz SICA (CLIC)		
Operating frequency [MHz]	2998.55			999.5		
Beam current [A]	3.5			4.2		
Iris thickness [mm]	6.0			18		
Aperture diameter [mm]	34.0			98		
Phase advance / cell [°]	120			120		
Cell length [mm]	33.32			99.98		
Number of cells / structure	32			21		
Structure length (incl. couplers) [m]	1.22			2.40		
Fill time [ns]	98			245		
Input power [MW]	30			15		
Accelerating voltage unloaded [MV]	13.3			6.6		
Accelerating voltage loaded [MV]	7.9			3.4		
Peak surface field [MV/m]	33			30		
Beam loading [%]	97.4			99.9		
Efficiency [%]	92.5			95		
	1st cell	mid cell	last cell	1st cell	mid cell	last cell
Cavity diameter [mm]	82.95	79.00	74.39	240.77	231.40	215.56
Nose cone size [mm]	0.00	2.53	4.66	4.352	9.418	16.191
Group velocity accelerating mode [% c]	5.19	3.49	2.36	4.32	2.89	1.45
Q_0 accelerating mode	13 860	12 771	10 950	23 810	21 923	16 108
R'/Q (linac definition) [Ω/m]	3143	3292	3165	1107	1142	1004
Frequency 2 nd monopole [MHz]				2292	2369	2451
Phase advance 2 nd monopole [°]				84.8	75.6	65.8
Q_0 2 nd monopole mode				45 540	49 710	51 850
R'/Q 2 nd monopole [Ω/m]				853	914	932
Frequency 1 st dipole [MHz]	4147	4197	4097	1344	1375	1409
Phase advance 1 st dipole [°]				161	165	169
Q_{SiC} 1 st dipole mode	17.5	6.2	5.8	13	19	29
Kick factor 1 st dipole [V/pC/m ²]	555	668	843	66.9	81.9	92.3
Frequency 2 nd dipole [MHz]	4243	4279	4379	1517	1602	1783
Phase advance 2 nd dipole [°]				178	168	146
Q_{SiC} 2 nd dipole mode	3.4	17.3	24.4	6	5	6
Kick factor 2 nd dipole [V/pC/m ²]	206	254	197	19.3	14.5	4.0
Total number of structures		18			819	
Total energy gain [MeV]		127			2370	

5.4.3.3 Size and number of klystrons

An obvious question is to how best subdivide the total peak power on individual power sources — is it better to for large number of small devices or for a small number of large devices? The criteria to include in this consideration are of course the cost and availability of a single device, but also the complexity and operability of the complete system, the energy efficiency and the life time. A good starting point certainly is the largest commercial high power RF source in the UHF range with high efficiency: the 1.3 GHz multi-beam klystron developed for the X-FEL and the ILC—it produces 10 MW RF pulses of 1.5 ms pulse-length with a repetition rate of 20 Hz. Different versions of this tube have been developed and manufactured by Toshiba, Thales and CPI, and all three makes have consistently and reproducibly produced peak powers in excess of 10 MW with a gain of 48 dB to 49 dB and an electronic efficiency of around 65%.

A considerably larger MBK has been proposed [63]. It uses 27 small current density beamlets, thus

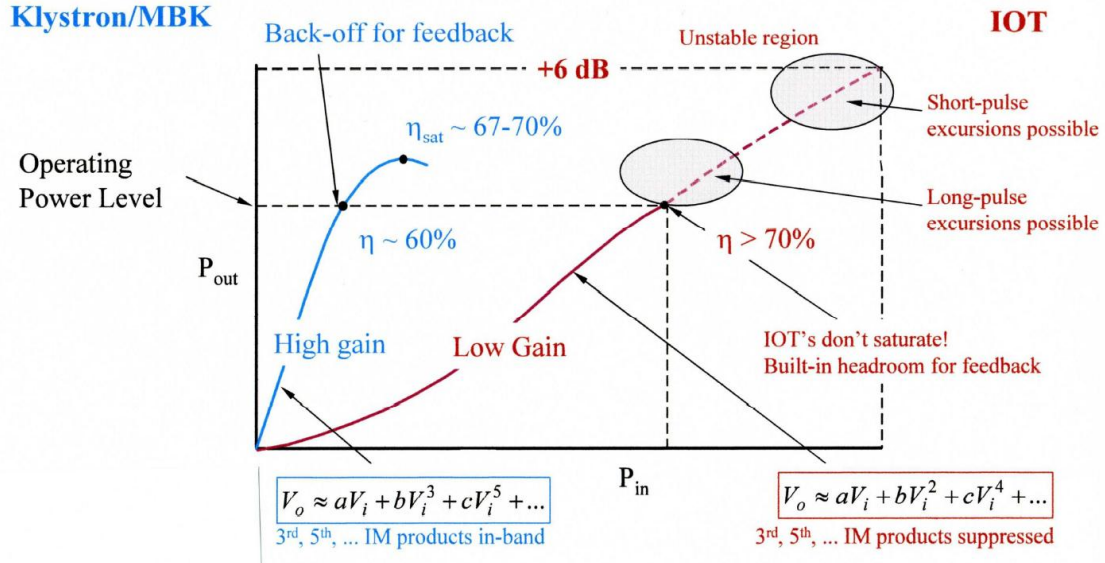


Fig. 5.58: Different characteristics of a klystron (blue) and an IOT [62]

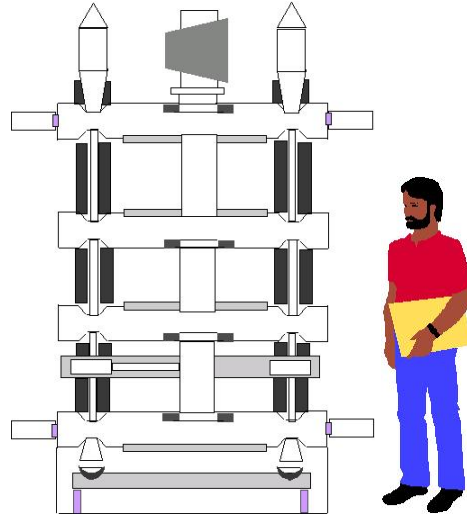


Fig. 5.59: Schematic layout of a CLIC 1 GHz, 50 MW 27-beam MBK

allowing large power with small current per beamlet (the focusing system is designed for a voltage of 154 kV DC and a current per beamlet of 15 A, resulting in a single beamlet perveance of $0.25 \mu\text{Perv}$). The MBK targets a peak power of 50 MW peak with an electronic efficiency in excess of 70%. A conceptual view of this is given in Fig. 5.59. The main idea behind this concept is to use a whispering gallery mode in the fundamental interaction cavities, which would allow for a common cavity for all beamlets with the possibility of efficient wrong-order-mode damping. The technical implementation of such a highly complex tube is however extremely challenging, resulting in many possible single point failures that are difficult to fix.

The other extreme would be to go to a large number of simple single-beam klystrons, which can be manufactured reliably and in large quantities; they should however still reach large efficiencies if the beam current can be kept low enough to keep the negative influence of space charge effects at

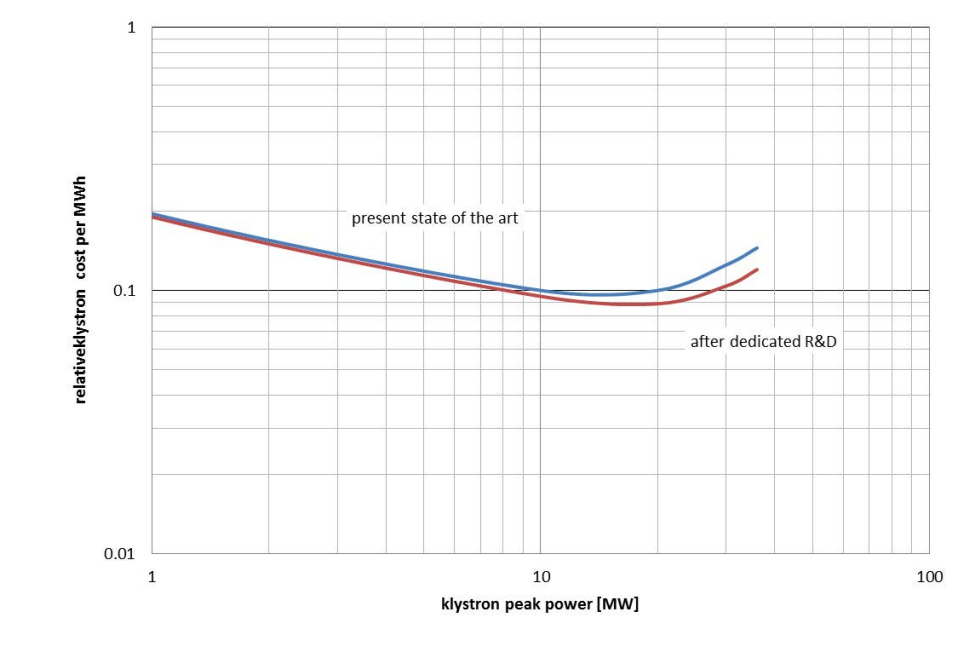


Fig. 5.60: Relative cost of the 1 GHz RF power generation including the cost of the klystron and considering tube lifetime [64], as a function of peak power

bay. The maximum possible efficiency will in this case rather be limited by technical feasibility and reproducibility, but it was concluded and confirmed by industrial partners that 70% efficiency is in reach.

As a compromise between these two extremes, we looked at the principal behaviour of the cost per MW for different size power sources and found that there is an optimum which will depend on the actual design (including large series production criteria), the technical difficulties and complexities, the operability and difficulty to intervene on a failing unit and the compatibility with modulators. It was also considered that typically very large power devices tend to have a shorter lifetime or MTBF. Figure 5.60 tries to summarize these findings by indicating in principle the cost optimum per MW peak power and per operating hour, including the finite lifetime of the device. Concluding from these findings and after many consultations with the relevant industrial partners, the klystron parameters used in this CDR are based on a modest extrapolation of the parameters of commercially available multi-beam klystrons, resulting in 15 to 20 MW peak power with acceptable efficiency for pulse lengths of $150 \mu\text{s}$ and a repetition rate of 50 Hz. This is in reach with relatively conventional modulators providing cathode voltage pulses of about 150 kV.

5.4.4 Drive Beam RF deflectors

5.4.4.1 Introduction

The bunch train compression scheme for CLIC relies on the use of fast RF deflectors (RFDs) for injection in the Delay Line (DL) and in the Combiner Rings (CRs). The three types of deflectors have different operating frequencies depending on the recombination factor of the rings (see §4.2). The frequencies of operation are 1.5 GHz, 2 GHz, and 3 GHz for the DL, CR1 and CR2, respectively.

The most demanding issues in the RFD design are those related to the beam dynamics, including both the beam loading effects on the fundamental deflecting mode (horizontal polarity) and the effects of the 90° tilted polarity (vertical polarity). These effects have been carefully investigated in the CTF3 case [65–67] and have been extended to the CLIC case [68]. The main results are given in §4.2.

To reduce the beam loading effects on the fundamental deflecting mode the proposed solution is to use multiple travelling wave (TW) RFDs as sketched in Fig. 5.61. Each TW RFD is a deflecting structure working on the deflecting TM_{11} -like mode [69].

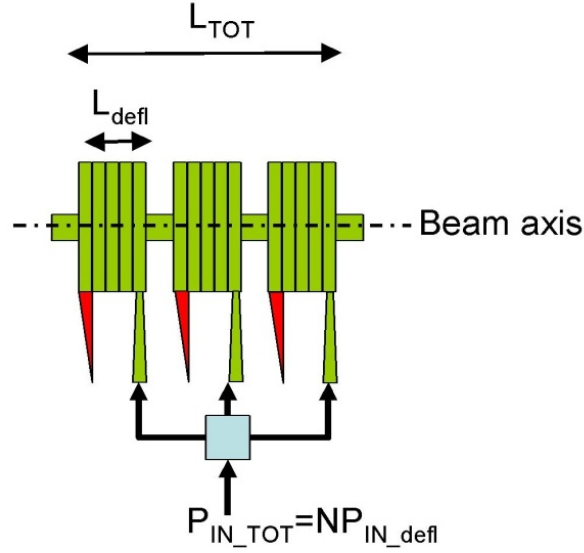


Fig. 5.61: Multiple travelling wave deflectors to reduce the beam loading effects.

5.4.4.2 RFD cell design

The sketch of a single RFD cells is given in Fig. 5.62 with typical electric and magnetic field lines (x is the deflection plane).

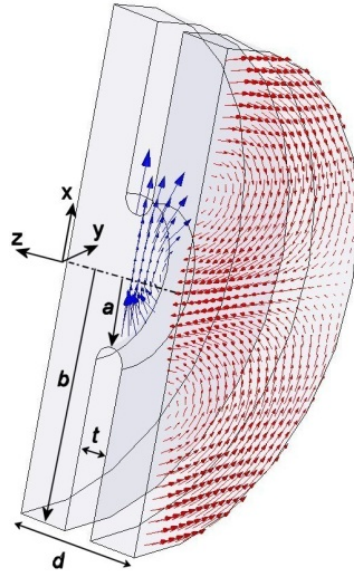


Fig. 5.62: Single cell of a TW RFD with the E and B field lines.

The design of the single cell can be done (similarly to accelerating structures) analyzing the deflectors parameters as a function of the iris aperture. Fig. 5.63 reports, as example, the main RFD parameters

in terms of transverse series impedance (Z_T), field attenuation constant (α) and group velocity for the three different RFDs. In the plot we have defined the transverse series impedance per unit length Z_T as:

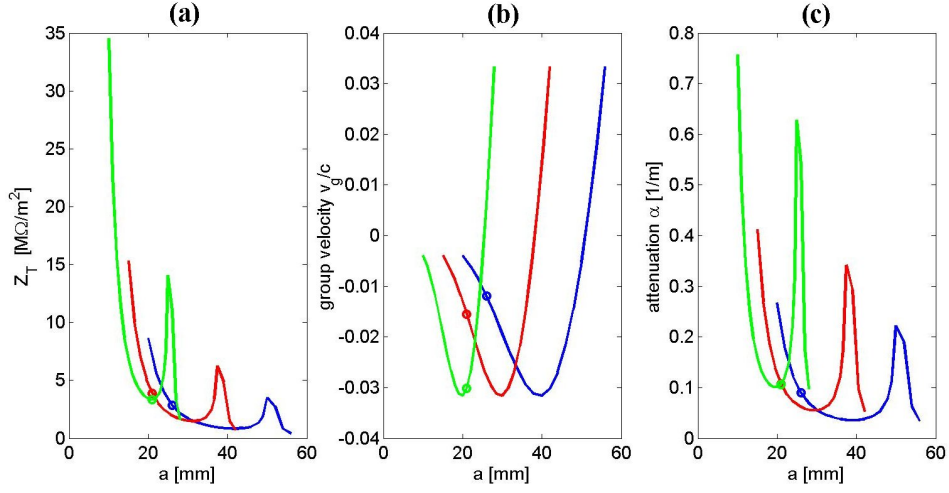


Fig. 5.63: Main RFD parameters in term of transverse series impedance (a), group velocity (b) and field attenuation constant (c) for the three different RFDs: blue curves (1.5 GHz RFD for the DL), red line (2 GHz RFD for the CR1) and green line (3 GHz RFD for CR2). The dots in the plots correspond to the parameters related to the final chosen iris apertures.

$$Z_T = \frac{E_T^2}{P} = \frac{\left| \int_0^d (\tilde{E}_x - c \tilde{B}_y) e^{j\omega_{RF}z/c} dz \right|^2}{d^2 P} \quad \left[\frac{\Omega}{\text{m}^2} \right] \quad (5.18)$$

where:

- P is the power flux along the structure
- E_T is the total equivalent deflecting field
- d is the cell period
- ω_{RF} is the angular RF frequency
- z is the longitudinal coordinate
- \tilde{E}_x, \tilde{B}_y are the transverse complex components of the electric and magnetic field on axis

The plot was done using the approximations and the calculations given in [69] and considering the $2\pi/3$ deflecting modes. The parameters depend, of course, also on the iris thickness (t) that has been considered for simplicity and according to the results obtained in [69] equal to 20 mm, 15 mm and 10 mm for the three different deflectors.

From Fig. 5.63(b) it can be seen that, in the range of iris apertures which give high series impedances, the RFDs are backward structures.

In the figures, the dots indicate the possible solution for the RFD of the DL and CRs, according to the considerations which follow.

5.4.4.3 Beam loading in the deflector

According to the beam loading calculations [68], the induced oscillations amplitudes due to the beam loading effects scales as:

$$\langle x_{acc} \rangle \propto \varphi \frac{q}{E_0} f_{RF} Z_T L_{defl}^3 = q \varphi^4 E_0^2 P^{-\frac{3}{2}} f_{RF}^0 \xi(a/\lambda_{RF}) \quad (5.19)$$

where:

- $\langle x_{osc} \rangle$ is the average induced oscillation amplitude in the bunch train
- φ is the deflection angle
- P is the input power
- L_{defl} is the deflector length
- f_{RF} is the working frequency
- E_0 is the the beam energy
- q is bunch charge
- $\xi(a/\lambda_{RF})$ is a form factor (function of the ratio between the deflector iris radius a and the wavelength) that shows a broadband maximum in a wide range of a/λ_{RF} .

From Eq. 5.19 it can be seen that, to reduce the beam loading effects, one has to increase the input power in order to reduce the deflector length. As reasonable values of the available input power for each deflector we have assumed 50 MW. Figure 5.64 shows the behaviour of the total deflector lengths, filling times and average dissipated powers per unit length as function of the iris aperture assuming this input power. The final iris apertures (shown in the plots as dots) have been chosen with the following criteria:

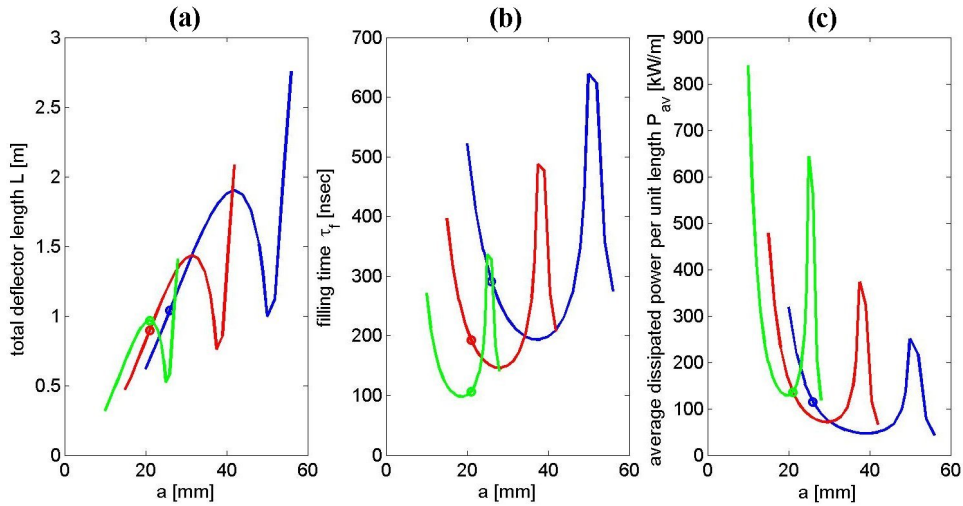


Fig. 5.64: Deflector lengths (a), filling times (b) and average dissipated powers per unit length (c) as a function of the iris apertures for the three different RFDs: blue curves (1.5 GHz RFD for the DL), red line (2 GHz RFD for the CR1) and green line (3 GHz RFD for CR2). The dots in the plots correspond to the parameters related to the final chosen iris apertures.

- minimization of the average dissipated power per unit length to simplify the cooling system and deflector realization,

5.4 RADIO FREQUENCY SYSTEMS

- minimization of the structure length to reduce the impact on beam dynamics in terms of short range wakefield,
- minimum radius of the cells equal to 20 mm to have enough stay clear and to reduce the impact on beam dynamics in terms of short range wakefield.

The RFD parameters calculated by HFSS are given in Table 5.23. They are slightly different with respect to the parameters plotted in Fig. 5.63 and Fig. 5.64 because in these plots the calculations have been performed using the mode matching technique with sharp edge irises [69].

Table 5.23: RFD parameters calculated by HFSS.

PARAMETER	DL	CR1	CR2
Working frequency f_{RF} [GHz]	1.5	2	3
TW mode of operation	TM ₁₁₀ -like $2\pi/3$		
Radius of the iris aperture a [mm]	25	20	20
Cell period d [mm]	66.62	49.97	33.31
Group velocity v_g/c	-0.016	-0.02	-0.028
Field Attenuation constant [1/m]	0.05	0.66	0.093
Transverse series impedance Z_T [$M\Omega/m^2$]	2.2	3.2	3.7
Number of multiple deflector N	2	2	6
Length of each single deflector L_{defl} [m]	0.6	0.45	0.15
Input power in each single deflector P [MW]		50	
Filling time of each deflector τ_F [ns]	110	80	16
Total deflecting structure length L_{TOT} [m]	1.2	0.9	0.8
Total input power P_{TOT} [MW]	100	100	300
Average deflecting field per unit length E_T [MV/m]	11	13	14
Average dissipated power per unit length [kW/m]	75	98	140
Deflection angle [mrad]		5	
Pulse length [μs]		140	
Repetition rate [Hz]		100	

Because of the high bunch current operation in the DL and CRs, the RFDs have to be designed with a proper mechanism to strongly detune and damp the 90° deflecting polarity. This is absolutely necessary to avoid the fast vertical beam instability observed for the first time in CTF3 [66] and caused by the vertical trapped modes. A possible solution to shift and damp these modes can be similar to that adopted for the new RF deflectors of CTF3 [66]. In these devices the frequency separation between the vertical and horizontal polarities has been strongly increased by appropriate design of the splitting-mode rods. In particular, with respect to the ‘classical’ RFD used as separators [69], these rods have been moved towards the axis of the structure.

The damping of the vertical modes has been realized by modifying the rods themselves that become special damping antennas connected to external loads. The mechanical drawing of the CTF3 new RFD is given in Fig. 5.65.

5.4.5 Damping Ring RF system

5.4.5.1 Introduction

In order to achieve high luminosity in CLIC, ultra-low emittance bunches have to be generated in both electron and positron DRs. To achieve this goal, large energy loss per turn in the wigglers has to be replenished by the RF system. This results in very strong beam loading transients affecting the longitudinal bunch position and the bunch length. In Table 5.24 the parameters of the DR and PDR are presented as

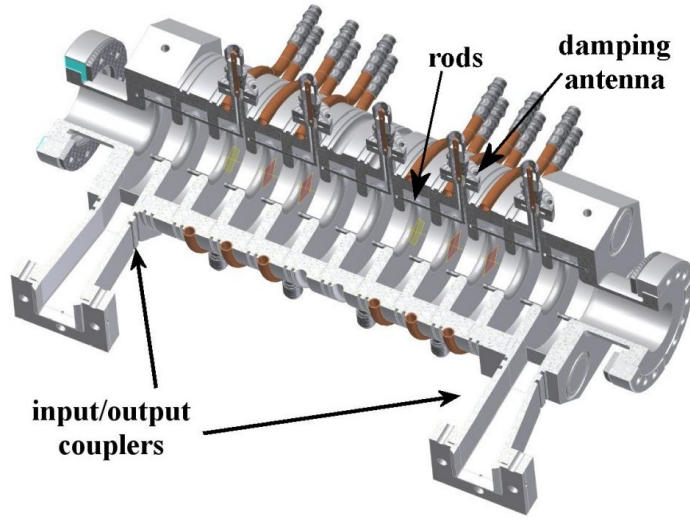


Fig. 5.65: Mechanical drawing of the CTF3 new RFD

they are specified in §3.2. The bunch spacing in the CLIC main linac is 0.5 ns (2 GHz bunch repetition frequency). The baseline design presented in Table 5.24 corresponds to a 1 GHz RF system where the bunch spacing is 1 ns. In this case, two trains of 156 bunches circulating in the DR symmetrically must be interleaved after extraction in order to provide the nominal bunch train structure. A possible alternative is based on a 2 GHz RF system with only one train of 312 bunches with nominal spacing and without bunch interleaving. The main disadvantage of this alternative is that the peak current is twice higher than in the baseline case. This has strong implications for several subsystems, one of which is the DR RF system. In the following, the baseline at 1 GHz with two bunch trains circulating in the DR is described. Several alternative solutions both at 1 GHz and at 2 GHz are described elsewhere [70].

Table 5.24: Parameters of the DR and PDR (§3.2).

Parameters [units]	DR	PDR
RF frequency: f [GHz]	1	1
Circumference: C [m]	427.5	389.15
Energy: E [GeV]	2.86	2.86
Momentum compaction: α_p	1.28×10^{-4}	3.72×10^{-3}
Bunch population: N_e	4.1×10^9	4.5×10^9
Number of bunches: N_B	312	312
Number of trains: N_T	2	2
Energy loss per turn: eV_A [MeV]	3.98	2.76
Energy spread in the bunch: σ_E/E [%]	0.12	0.1
Bunch length: σ_Z [mm]	1.8	4.6
RF voltage: V_C [MV]	5.1	10
Harmonic number: h	1426	1298
Synchronous phase: φ [°]	38.7	74.0
Synchrotron frequency: f_s [kHz]	3.45	39.1
Energy acceptance: $\Delta E/E$ [%]	2.34	1.7
Bucket length: $2\Delta Z$ [mm]	70	185

In addition, tight specifications from the Ring-To-Main-Linac (RTML) line and the main linac are set in order to provide nominal bunch and bunch train structure in the main linac. Two specifications are of the paramount importance for the DR RF system: 0.1° at 1 GHz (280 fs) r.m.s. spread in the bunch spacing from the nominal value of 0.5 ns and 2% r.m.s. bunch length spread along the bunch train (see §4.3).

The specifications for the PDR RF system are somewhat different since they are dominated by the DR injection acceptance. They are much more relaxed and do not cause any challenges in the PDR RF system design.

Below, fast transient effects due to strong beam loading affecting beam parameters within one revolution period are analysed. The long term stability of the RF systems and beam parameters are not considered; it is assumed that slow feedback system takes care of it.

5.4.5.2 Beam loading effect

Voltage modulation

Both high peak current and very high energy loss per turn contribute to a very strong loading of the cavity when the beam passing through. Strong voltage modulations are possible due to strong variation of the stored energy. The stored energy variation is expressed in terms of the beam parameters [70]:

$$\delta U = -(P_B - \langle P_B \rangle) \frac{N_B T_R}{N_T h} = -\frac{N_B N_e e V_A}{N_T} \left(1 - \frac{N_B}{h} \right) \quad (5.20)$$

Then a condition to keep the RF voltage variations small in an RF system with constant input RF power is derived:

$$|\delta U| \ll U = \frac{V_C^2}{2\omega R/Q} \quad (5.21)$$

In the following, R/Q of the RF system is optimized since all the other parameters in [57] and [58] are specified in Table 5.24 and cannot be changed.

Bunch phase modulation

Variation of the RF voltage results in the variation of the bunch phase along the train. There are two contributions: First, the phase of RF voltage is directly affected by the voltage excited in the cavity by the beam. Second, since the energy loss per turn must be constant for all bunches along the train, the synchronous phase slips to compensate the RF voltage reduction due to beam loading. The sum of the two contributions gives the total modulation of the bunch phase [70]:

$$\delta \varphi_B = \delta \varphi_1 + \delta \varphi_2 = \frac{\delta V_c}{V_c} \left(\tan \varphi + \frac{1}{\tan \varphi} \right) = \frac{\delta V_c}{V_c} \frac{1}{\cos \varphi \sin \varphi} \quad (5.22)$$

Bunch length modulation

Modulations of the RF voltage also results in the RF bucket distortions which are schematically shown in Fig. 5.66. Since the energy spread in the bunch is constant related to radiation damping the bunch get longer if the RF voltage is reduced.

The effect of the bunch lengthening can be estimated analytically in the case of the small amplitude harmonic oscillations [70]:

$$\frac{\delta \sigma_z}{\sigma_z} = -\frac{1}{2} \frac{\delta V_c}{V_c} \frac{1}{\sin^2 \varphi} \quad (5.23)$$

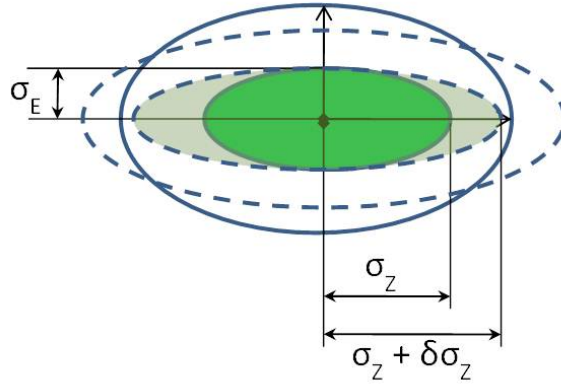


Fig. 5.66: Distortion of the RF bucket and the bunch longitudinal phase space due to RF voltage modulation is schematically shown.

5.4.5.3 Damping Ring RF system

Baseline solution proposed for the CLIC CDR is based on the two bunch trains circulating the DR in the same direction with a delay equal to the half of the DR circumference. Since the bunch spacing in the trains is twice the nominal one, the peak current and so the peak beam loading power is reduced by factor of two. In addition, RF system can be designed at lower frequency of 1 GHz which brings the advantage of providing more stored energy to cope with the strong beam loading effects. Thus, in the baseline, the DR RF system is designed in a way that the stored energy is so high that the RF voltage variation is kept small to minimize the transient effect on the beam phase to be below the specifications. The RF system is in its principle close to the standard RF system for high beam current storage rings e.g., KEK-B low energy ring (LER) [71]. It is also proposed to use the same type of cavities: ARES-type, which provides low R/Q necessary to mitigate the strong beam loading effects. Below the choice of basic parameters is shown in a few steps:

1. The specification for the bunch phase variation is given as 0.1° r.m.s. spread at 1 GHz. Since in the proposed RF system RF voltage modulations are small and very close to a linear variation from the first bunch in the train to the last one, the phase variation is linear as well. Knowing the distribution we can formulate the specification in a form corresponding to peak-to-peak variation of 0.3° which corresponds to 0.1° r.m.s.
2. Using equation (5.22) relative peak-to-peak RF voltage variation is estimated to be 0.26%.
3. Using variation of equation (5.21) relative peak-to-peak variation of the total stored energy is estimated to be 0.52%.
4. Equation (5.20) is used to calculate the absolute peak-to-peak variation of the total stored energy to be 0.318 J.
5. Knowing the relative and the absolute variation, the total stored energy itself can be calculated: 61.2 J.
6. Finally, given the total stored energy and RF voltage, the total R/Q of the RF system is calculated using equation (5.21).

In order to come from the parameters of the total RF system to the individual cavity parameters, an estimate of the admissible RF voltage per cavity V_0 is needed. To get it, the ARES-type cavity originally designed for KEK-B RF system at 0.509 GHz [71] is scaled to 1 GHz and modified to reduce R/Q . In Fig. 5.67 the original cavity geometry and some parameters are shown. The ARES cavity

5.4 RADIO FREQUENCY SYSTEMS

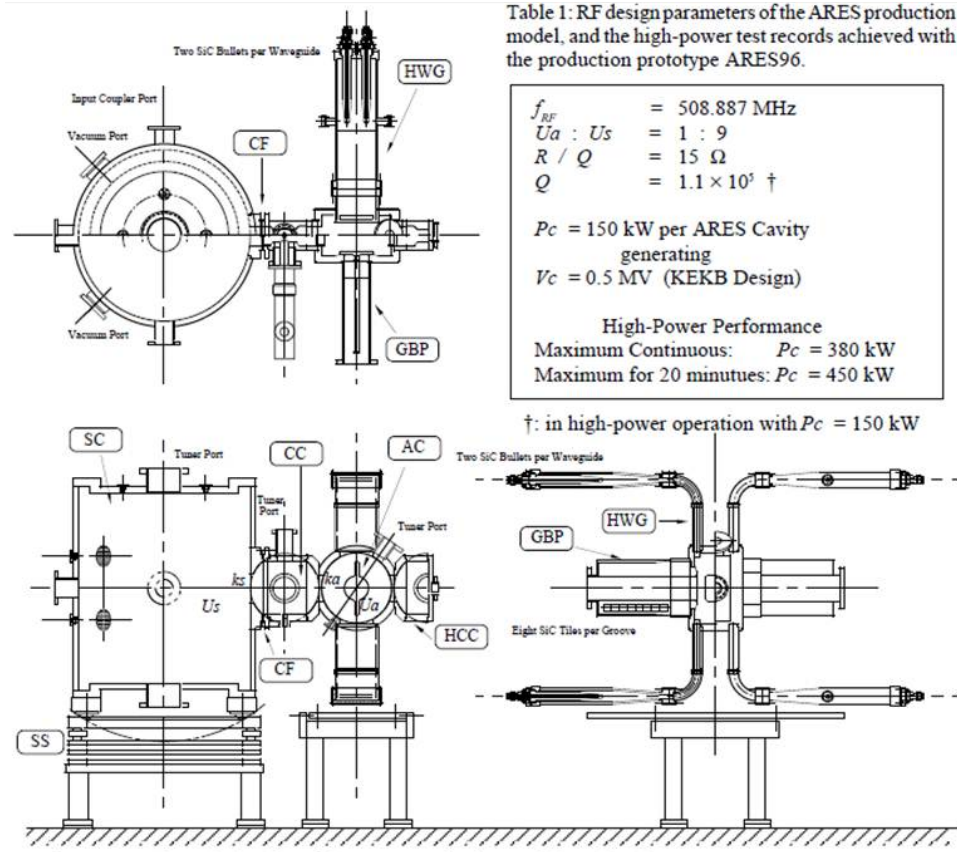


Fig. 5.67: Schematic drawings of the ARES cavity and some parameters are shown from [72].

consists of three cavities: storage cavity which operates at TE015 mode, accelerating cavity operating at fundamental TM010 mode and the coupling cavity connecting the storage and accelerating cavities. It is equipped with HOM damping and tuning features.

Furthermore, in Fig. 5.68, the process of cavity scaling and modification is schematically shown. It is done in two steps. First, all dimensions of the cavity are reduced as the ratio of frequencies. Making

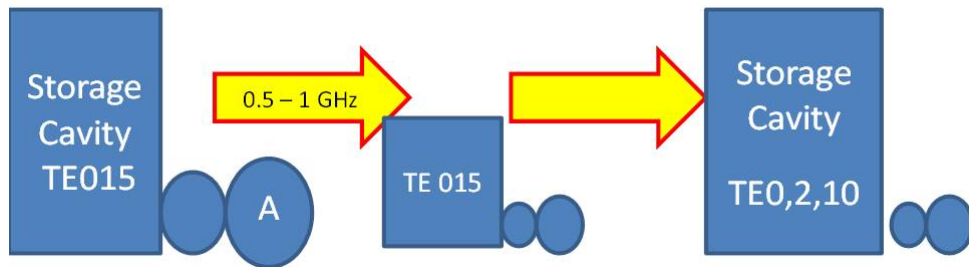


Fig. 5.68: Two step processes of cavity scaling and modification for R/Q reduction is schematically shown.

this scaling we assume that the admissible electro-magnetic field strength remains constant, so the RF voltage per cavity must be reduce linear with the frequency: $V_0 \sim 1/f$. The corresponding scaling of cavity parameters is presented in Table 5.25, where the original parameters at 0.509 GHz are presented in column (1) from [72] and the ones scaled to 1 GHz are in the column (2). The next step of cavity

modification in order to reduce R/Q of the cavity is the increase of the storage cavity volume. For example, if the storage cavity dimensions are increased up to approximately the same values as there were before the scaling from 0.509 to 1 GHz, the R/Q value of the cavity is decreased by a factor of approximately $2^3=8$ since most of the energy (90%) is located in the storage cavity. RF voltage per cavity remains the same. This reduction in R/Q of the cavity is more than enough for our purpose. In fact, in our case, an intermediate modification of the storage cavity is chosen to have comfortable voltage per cavity $V_0=319$ kV. This gives the number of cavities to be 16 and the corresponding $R_0/Q=2.1 \Omega$ per cavity.

Table 5.25: Parameters of the ARES cavity: Original parameters at 0.509 GHz, Parameters of the cavity scaled to 1 GHz and Parameters of the cavity modified at 1 GHz.

	Original	Scaled	Scaling law	Modified
Frequency: f [GHz]	0.509	1		1
Normalized shunt impedance (circuit): R_g/Q [Ω] ($\propto f^0$)	7.4	7.4	$(\propto f^{-3}) \equiv 1/8$	0.925
Unloaded Q -factor: Q ($\propto f^{-1/2}$)	110 000	78 000	$(\propto f^1) \equiv 2$	156 000
Aperture radius: r [mm]	80	40		40
Gap voltage range: V_g [kV]	500–866	250–433	–	250–433
Nominal – Maximum tested				

Finally, set of parameters of the RF system is calculated and summarized in Table 5.26. In addition, parameters of the KEK-B LER RF system [KEKBLLRF] which is based on the ARES cavities are presented for comparison.

Table 5.26: Parameters of the baseline CLIC RF system at 1 GHz and the KEK-B LER RF system from [71].

	CLIC	KEK-B LER
RF frequency [GHz]	1	0.509
Total stored energy [J]	61.2	106
Total R/Q [Ω]	33.8	148
RF voltage per cavity V_0 [kV]	319	500
Number of cavities	16	20
R_0/Q per cavity [Ω]	2.1	7.4
Q -factor	120 000	110 000
Total wall loss power [MW]	3.2	3.1
Average beam power [MW]	0.6	4.5
Total RF power [MW]	3.8	7.6
Number of klystrons	8	10
Required klystron power [MW]	> 0.5	> 0.8
Total length of the RF system [m]	$16 \times 2 = 32$	$20 \times 2.5 = 50$
Bunch phase modulation p–p [$^\circ$]	0.3 (train 22%)	3.5 (gap 5%)

In summary, the baseline solution for the CLIC DR RF system is close to what is already in operation for many years (KEK-B, etc.). There are no feasibility issues or showstoppers. The final cavity design both RF and mechanical are still to be done to finalize the parameters of the RF system. There are several alternative solutions both at 1 GHz and at 2 GHz which have been considered elsewhere [70] and which could lead to an improved design compared to the baseline, but requires some R&D effort before being adopted as a baseline.

5.4.5.4 PDR RF system

In PDR, the energy loss per turn is smaller and so the beam loading effect. At the same time total required RF voltage is higher which makes it easier for RF system to cope with the beam loading since the stored energy is higher for the same shunt impedance. Finally, the requirements on the bunch phase variation along the train are much more relaxed than in the DR because the only constraint comes from the longitudinal acceptance at the injection into the DR. In fact, an RF system based on the scaled Single Cell Cavity (SCC) developed and used in KEK-B high energy ring (HER) [73] satisfies fully these requirements. In Fig. 5.69, schematic view of the SCC unit is shown. Including the cryostat, tuning and HOM damping features it is about 3 m long.

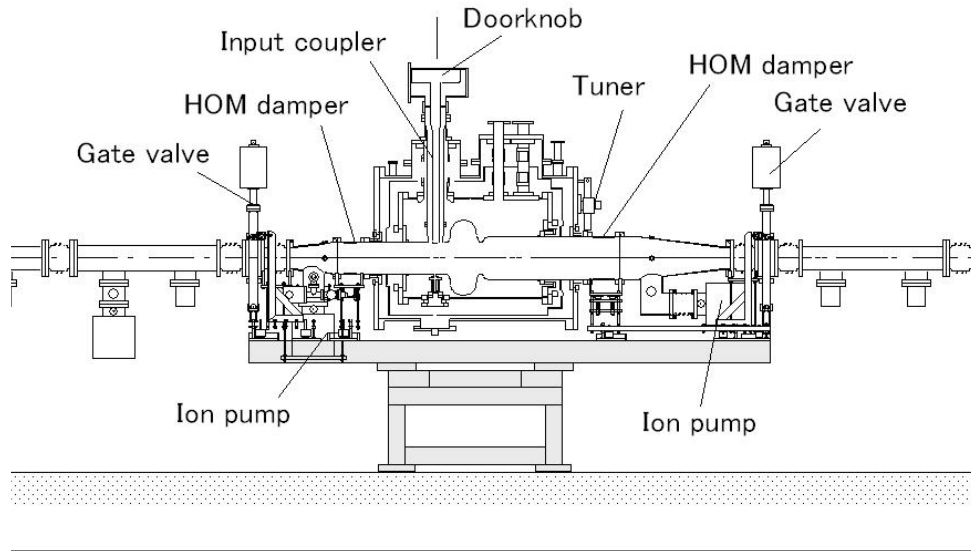


Fig. 5.69: Schematic view of SCC cavity is shown from [73].

The main parameters of the cavity and the achieved RF voltage per cavity are listed in Table 5.27, middle column. In the right column, parameters scaled to 1 GHz are presented. In the RF voltage per cavity scaling it is assumed that the gradient remains constant.

Table 5.27: Main parameters of the SCC cavity [73].

Frequency: f [GHz]	0.509	1
Normalized shunt impedance (circuit): R_0/Q [Ω]	46.5	46.5
Unloaded Q -factor: Q	$\sim 10^9$	$\sim 10^9$
Aperture radius: r [mm]	110	55
Beam loading power range: [MW] Nominal–Maximum tested	0.25–0.4	
Gap voltage range: V_0 [MV] Nominal–Maximum tested	1.5–2	0.75–1

Assuming that 1 GHz cavity can provide 1 MV voltage the total number of cavities is calculated as well as the other parameters of PDR RF system. They are presented in Table 5.28.

In the last row the bunch phase variation along the bunch train is shown: 1.5° at 1 GHz which corresponds to 1.25 mm. This is much smaller than the DR bucket length of 70 mm, so that the injection can be done very close to the centre of the bucket for all bunches in the train.

Table 5.28: Parameters of the PDR RF systems.

RF frequency f [GHz]	1
Total stored energy [J]	17
Total R/Q [Ω]	465
RF voltage per cavity V_0 [kV]	1000
Number of cavities	10
Q -factor	10^9
Total wall loss power [W]	100
Total cryogenic power [MW]	0.1
Average beam power [MW]	0.47
Total RF power [MW]	~ 0.5
Number of IOTs	10
Required IOT power [MW]	> 0.05
Total length of the RF system [m]	$10 \times 1.5 = 15$
Bunch phase modulation p-p [$^\circ$]	1.5 (train 22%)

5.4.5.5 RF power sources and wall plug power

Total RF power per DR approaches 4 MW level leaving no other choice for RF power source but a klystron. Assuming typical klystron efficiency of 50% and typical high voltage power supply efficiency of 80% total wall plug power is estimated to be at the level of 10 MW per DR.

In the case of the PDR, IOTs can be used as an RF power source which has typical efficiency which is higher than that of a klystron. Assuming typical IOT efficiency of 70% and typical high voltage power supply efficiency of 80%, the total wall plug power is estimated to be at the level of 1 MW per PDR including required cryogenic power.

5.4.5.6 Summary

To cope with the substantial beam loading, the proposed baseline solution for the CLIC Damping Rings uses the ARES cavity concept, which has been in operation at KEK-B for many years. It uses klystrons to produce the necessary RF power of 4 MW. For the CLIC Pre-Damping Ring, the KEK-B HER RF system is copied and adapted and could be operated with IOTs. Alternative concepts do exist but they are only mentioned here. For more detailed descriptions refer to Ref. [70].

5.5 X-band RF system

This section deals with the following systems:

- Main Linac accelerating structures (§5.5.1)
- RF design of the Power Extraction and Transfer Structure (§5.5.2)
- Two-beam RF system integration (§5.5.3)
- Crab cavity system (§5.5.4)

The RF system for the bunch compression in the Main Linac tunnel will be based on structures similar to the accelerating structures and no further details are given here.

5.5.1 Main Linac accelerating structures

5.5.1.1 RF design

The parameters of the CLIC Main Linac (ML) accelerating structure have been obtained as described in §2.1.5 (for more details see Refs. [74, 75]) based on an optimization that includes an improved understanding of high-gradient limits, wakefield-related beam dynamics constraints, and considers the performance and cost of CLIC at 3 TeV. Furthermore, compact couplers have recently been developed and HOM damping loads have been designed. The RF design has also been made consistent with details of the present manufacturing procedure, which is based on bonded asymmetrical disks, and with requirements coming from integration of the accelerating structure in the two-beam module described in §5.6. This refinement of the structure design has been made to produce the self-consistent parameter set described in this section.

Basic cell geometry and HOM damping

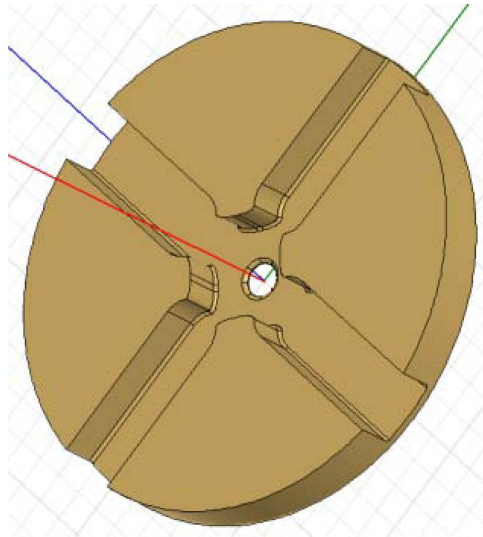


Fig. 5.70: Basic cell geometry of the accelerating structure with shown strong waveguide HOM damping

The basic cell geometry is shown in Fig. 5.70. The cell has an elliptical cross-section iris and convex elliptical cross-section outer walls in order to minimize surface fields. There are four damping waveguides incorporated in each cell to provide efficient damping. The Q -factor of the lowest dipole-band is below ten. The cell geometry is adapted to the manufacturing process based on the bonding of disks in which one side of the disks is flat and the other side carries all the cell features. This is the side facing out in Fig. 5.70. The geometry of the outer wall and damping waveguides has been optimized to

minimize both the pulsed, surface heating, temperature rise on the outer wall and the penetration distance of the fundamental mode into the damping waveguides while maintaining the same damping efficiency. This has been achieved through reducing both the aperture to the damping waveguide and the damping waveguide width. The smaller penetration distance allows a smaller overall transverse size since the HOM damping loads made of SiC can be placed closer to the axis without affecting the Q -factor of the fundamental mode. The distance from the axis of the structure to the tip of the SiC damping load is 50 mm. The geometry of the load placed in the damping waveguide is shown in Fig. 5.71. It is 30 mm long and is tapered from 1 mm \times 1 mm cross-section to 5 mm \times 5 mm over 30 mm and a 10 mm long part of the latter cross-section.

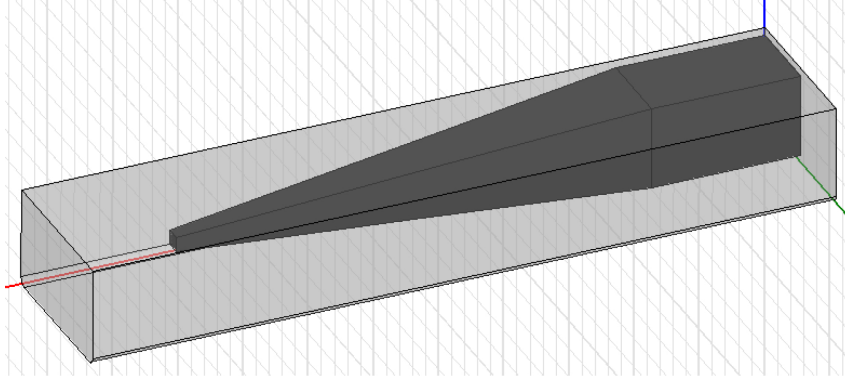


Fig. 5.71: Internal volume of a damping waveguide equipped with a HOM load made of SiC

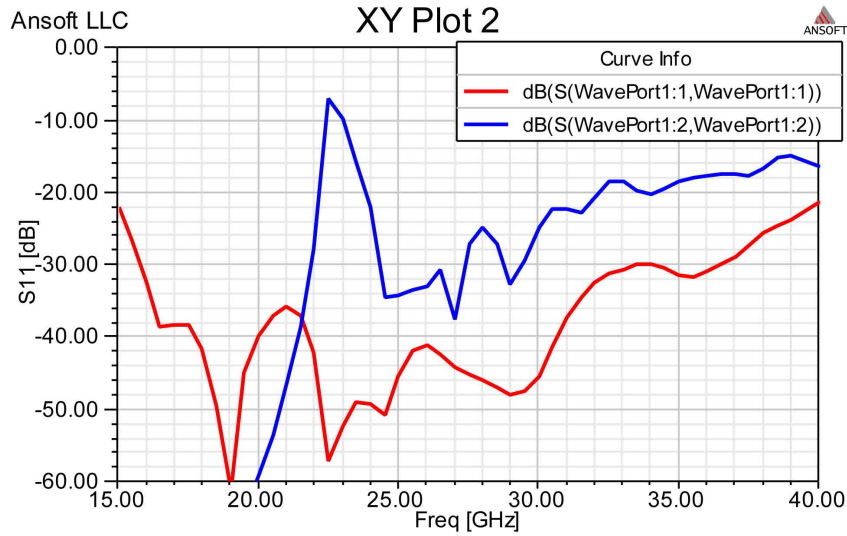
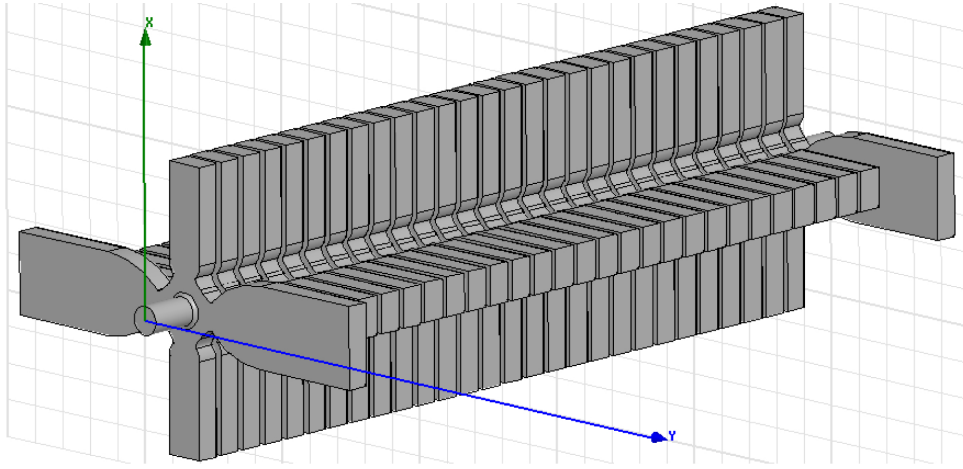
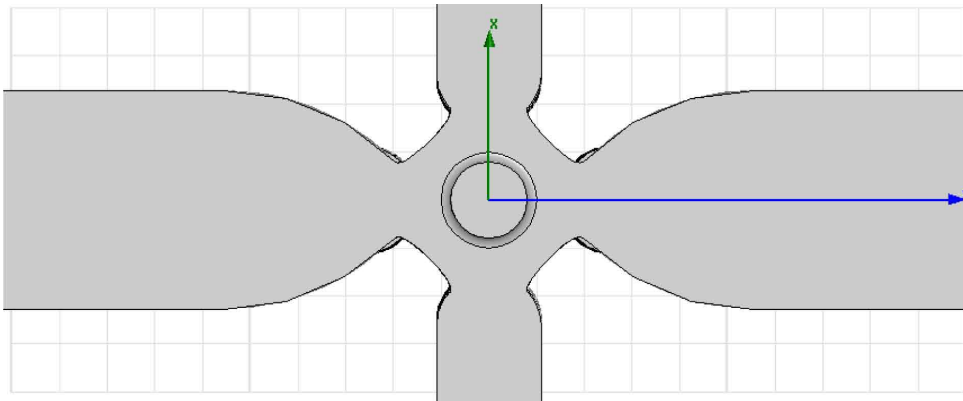


Fig. 5.72: Reflections from SiC load in the damping waveguide are shown both for TE10 (red) and for TE01 (blue) modes

This load configuration provides very broad band absorption of the wakefields and is used to terminate each damping waveguides of the structure. The reflections of the TE10 and TE01 waveguide modes from the load are calculated using HFSS frequency domain code [76] with measured SiC parameters [77] ($\epsilon' = 13$, $\tan\delta = 0.16$). The geometry of the load has been optimized to keep the reflections below -30 dB for TE10 mode and below -20 dB for TE01 mode. The final results are presented in Fig. 5.72. These reflections do not compromise the HOM damping performance which is primarily determined by the cell-to-damping-waveguide coupling.

Structure tapering and couplers**Fig. 5.73:** Internal volume of the full structure

The RF geometry of the full structure is shown in Fig. 5.73. It has 26 regular cells which are tapered along the length of the structure plus input and output coupler cells. The geometry of a coupler cell is shown in Fig. 5.74. The coupling is magnetic but the coupler cell geometry is quite different from that traditionally used and very much resembles the regular cell geometry. The only difference is that in the coupler cell, two opposite waveguides are of the standard WR-90 width forming a double-feed coupler cell. The other two damping waveguides are kept in place to maintain damping as efficient as in the regular cells. Furthermore, this naturally minimizes the quadrupolar kick, since the geometry is close to the regular cell geometry where the quadrupolar kick is cancelled by the symmetry. The coupler provides about the same acceleration as a regular cell and both surface magnetic and electric fields do not exceed maximum values in the rest of the structure. As a double-feed coupler it must be fed in phase from both sides. It is done using a magic-T, where the wakefields coming in the opposite direction from the coupler cell into the power waveguides are out of phase for the TE₁₀ mode and in phase for the TE₀₁ mode. Under these conditions both modes are guided to the forth arm of the magic-T which is terminated by a load. This provides efficient HOM damping in both planes in the coupler cells which is a non-negligible part of the full structure.

**Fig. 5.74:** Internal volume of the coupler cell

The main parameters of the structure are presented in Table 5.29. Following the beam dynamics requirements, the optimum average aperture radius to wavelength ratio is 0.11 resulting in the group velocity reaching, in the last cell, $0.83\% v_g/c$. At this rather low group velocity, the bandwidth of the

structure sets a lower limit to the rise time of the field level in a cell in the same way as in a high Q cavity. This rise-time limit is also shown in Table 5.29 together with the conventional filling time of a travelling-wave structure. The consequence of the limited bandwidth is that two ramps are necessary at the beginning of the pulse to simultaneously compensate for the structure bandwidth and for the beam-loading-induced bunch-to-bunch energy spread. The input pulse shape is shown in Fig. 5.75.

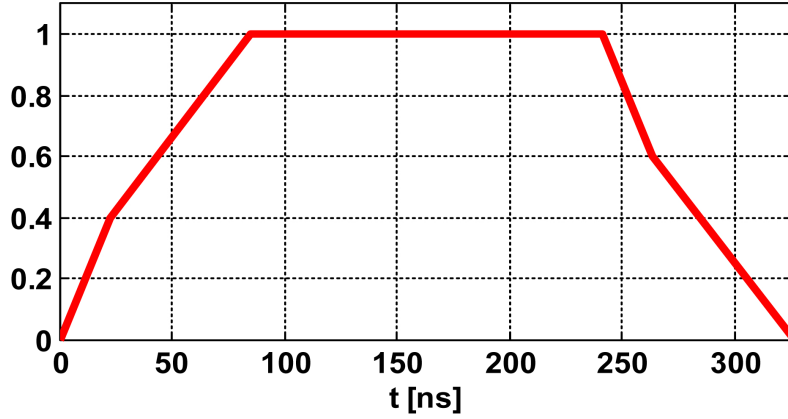


Fig. 5.75: Schematic shape of the input pulse

Table 5.29: Structure parameters

Average loaded accelerating gradient	100 MV/m
Frequency	12 GHz
RF phase advance per cell	$2\pi/3$ rad
Average iris radius to wavelength ratio	0.11
Input, output iris radii	3.15, 2.35 mm
Input, output iris thickness	1.67, 1.00 mm
Input, output group velocity	1.65, 0.83% of c
First and last cell Q -factor (Cu)	5536, 5738
First and last cell shunt impedance	81, 103 $M\Omega/m$
Number of regular cells	26
Structure length including couplers	230 mm (active)
Bunch spacing	0.5 ns
Bunch population	3.72×10^9
Number of bunches in the train	312
Filling time, rise time	67 ns, 21 ns
Total pulse length	244 ns
Peak input power	61.3 MW
RF-to-beam efficiency	28,5 %
Maximum surface electric field	230 MV/m
Maximum pulsed surface heating temperature rise	45 K

Both the iris radius and thickness are tapered linearly in order to provide an optimum distribution of various high-power parameters and to avoid the hot spots along the structure. The variations of these parameters are shown in Fig. 5.76. The unloaded structure gradient, the surface electric field rise and the temperature rise are made to be constant. In Fig. 5.76, the pink line shows the distribution of a new field quantity S_c [78] which serves as a limit for high gradient performance and to a certain extent combines both the power and the surface electric field constraints.

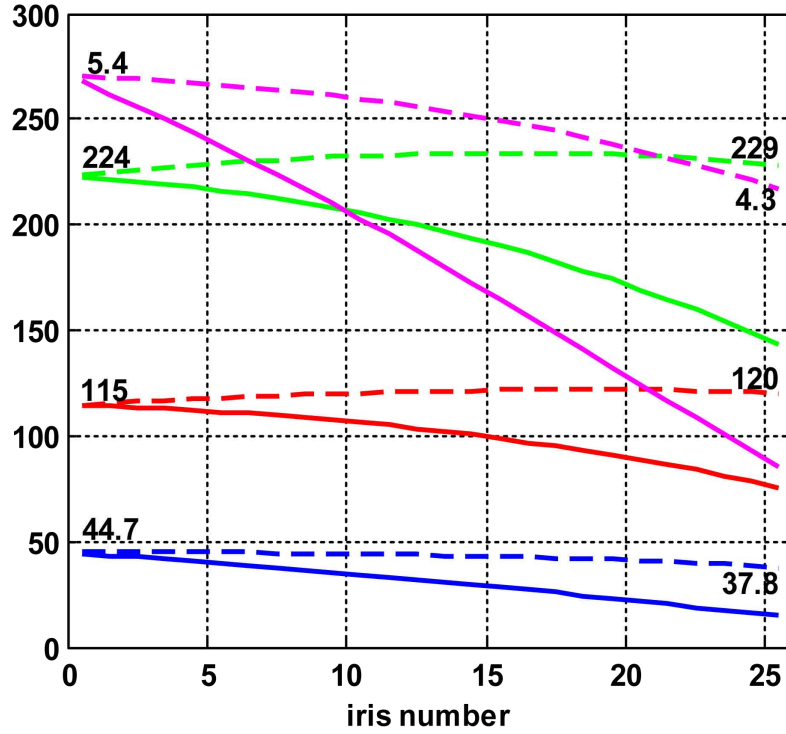


Fig. 5.76: The fundamental mode properties are shown in the regular cells. The solid lines, from top to bottom are: S_c [$\text{W}/\mu\text{m}^2$] (pink), surface electric field [MV/m] (green), accelerating gradient [MV/m] (red), pulse surface temperature rise [K] (blue). Dashed lines are unloaded and solid lines are beam-loaded conditions.

Structure wakefields

Table 5.30: Parameters of the lowest dipole-band modes.

Cell	First	Middle	Last
Q -factor	11.1	8.7	7.1
Amplitude [$\text{V} \cdot \text{pC}^{-1} \cdot \text{mm}^{-1} \cdot \text{m}^{-1}$]	125	156	182
Frequency [GHz]	16.91	17.35	17.80

The tapering also provides detuning of the higher order modes which is an important effect even for heavily damped structures. The relative contributions of the heavy damping and detuning to the transverse wakefield spectrum are illustrated in Fig. 5.77. Parameters of the lowest dipole-band modes calculated from the fitting to the impedance curves are listed in Table 5.30. The transverse wake of the full structure including coupler cells was computed in time domain using the parallel code GdfidL [79]. The results for both planes are shown in Fig. 5.78. The difference between the two planes comes only from the coupler cells and is very small. One can see that both wakes at the position of the second bunch, which is 0.15 m behind the first bunch, are below the 6.6 V/pC/mm/m, as required for beam dynamics.

Wakefield monitor

To achieve high luminosity in CLIC, the accelerating structures must be aligned to an accuracy of $5 \mu\text{m}$ with respect to the beam trajectory as specified in §3.4.5.3. Position detectors called wakefield monitors (WFM) are integrated into the first cell of every second structure for a beam-based alignment. The principle is based on measuring the wake signal excited by the beam and propagating from the cell to

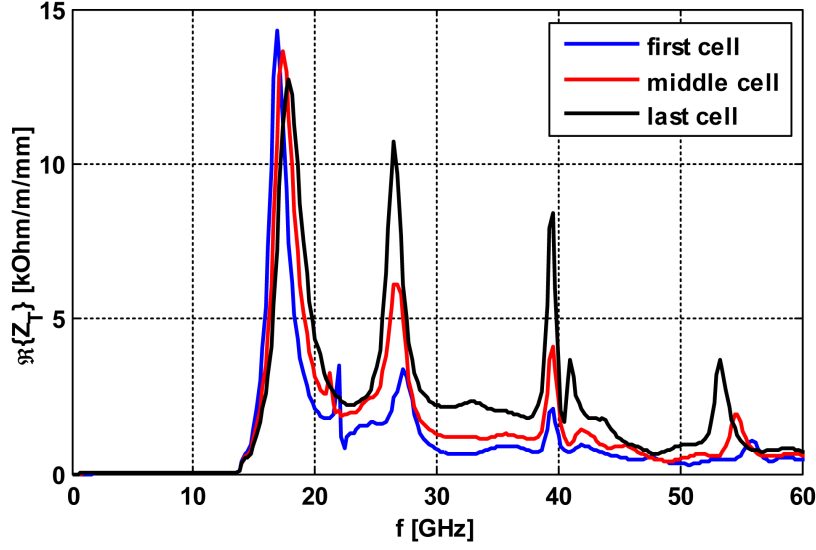


Fig. 5.77: Transverse impedances of the first (blue), middle (red) and last (black) cells

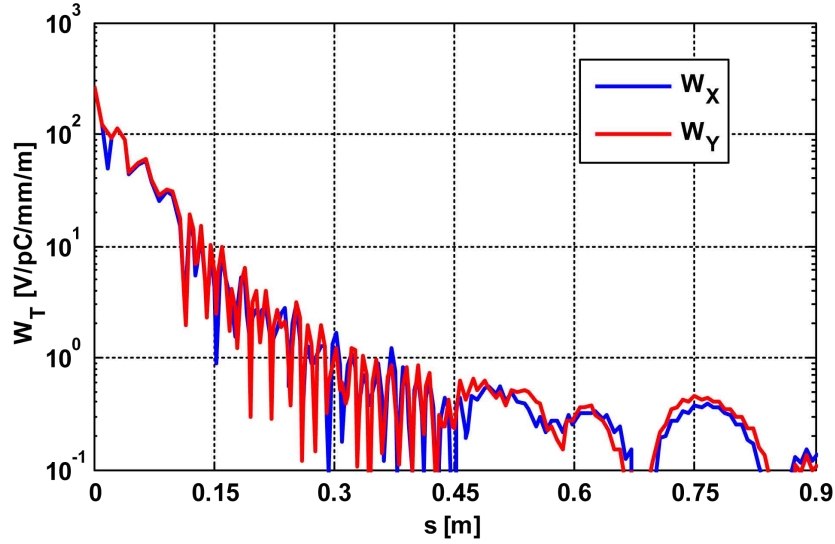


Fig. 5.78: The envelope of the transverse wakefields for both planes. The CLIC bunch spacing is 0.15 m.

the HOM loads through the damping waveguides. In a special cell, the WFM cell, four pickups are introduced between the cell and the HOM loads to measure this signal in all four damping waveguides. In Fig. 5.79 the geometry of such a pickup is shown as implemented in the CTF3 TBTS accelerating structure [80]. The signals from four pickups are combined to provide the measure of the horizontal and vertical displacements of the structure with respect to the beam in the same way as done in a cavity BPM.

Fabrication tolerances

Owing to the very large amount of structures, the implementation of tuning in the final design is not suitable, for this reason the tolerances are defined on the assumption that tuning is not possible. A detailed study of the required machining and assembly tolerances has been performed [81] and is summarized below.

- *Systematic errors*: inefficiency in acceleration due to RF de-phasing is mainly caused by system-

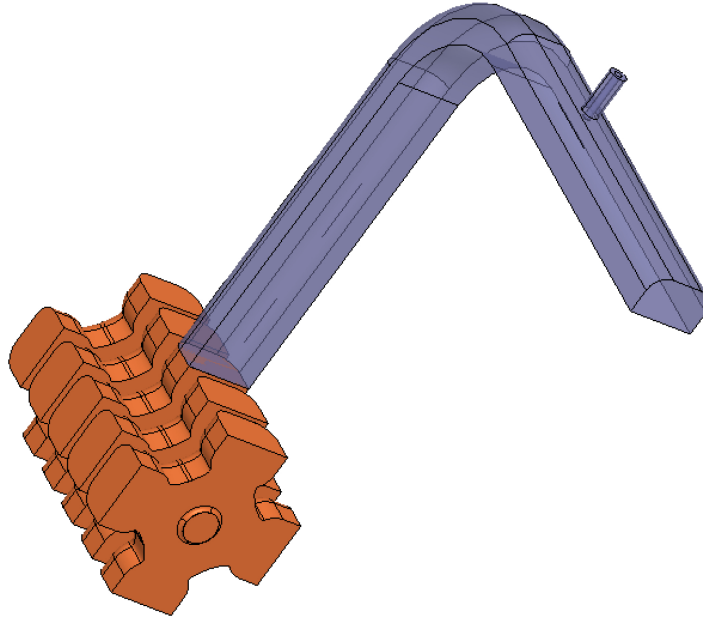


Fig. 5.79: Geometry of one of the four arms of the wakefield monitor

atic errors in the cell dimensions as it is a coherent effect. The most sensitive dimension is the transverse size of the cell, $2b$, where $1\text{ }\mu\text{m}$ systematic error causes $\sim 2\%$ reduction in the structure acceleration.

- *Random errors*: cell-to-cell frequency error due to random errors in cell dimensions causes mismatch, reflections, and appearance of field enhancement due to standing waves. Limiting the mismatch to $< -40\text{ dB}$ results in the same tolerance on the most critical dimension $2b$ of $\sim 1\text{ }\mu\text{m}$.
- *‘Bookshelving’*: systematic tilt of the disks introduces a transverse kick which is proportional to the accelerating gradient. Keeping the ratio of the transverse kick to the acceleration $dV_t/dV_z < 10^{-4}$ (see §5.2.3.2) requires the tilt to be below $140\text{ }\mu\text{rad}$.
- *WFM*: The required WFM accuracy must be below $3.5\text{ }\mu\text{m}$. This sets the limit on the cell shape accuracy such that the transverse alignment of the axis of the iris aperture (source of the short range wakes) with respect to the axis of the cell and damping waveguides (measuring the wakes) must be at least better than $3.5\text{ }\mu\text{m}$.

In summary, micrometre tolerance level is required in cell disk fabrication and several micrometres in the structure assembly in order to satisfy stringent beam dynamics requirements without additional tuning.

Accelerating structure engineering design

In its final configuration, the accelerating structure (see Fig. 5.80) [82] is composed of 26 regular cells as well as input and output compact couplers recently developed. Each disk has an external diameter of 80 mm and comprises damping waveguides housing the silicon carbide damping material. Four manifolds extend the damping waveguides and allow for sufficient pumping conductance [83]. One of them is connected to the main vacuum reservoir. Cooling circuits are also integrated into the structure to extract the RF power dissipation during all operations modes. Alignment spheres are placed on the external reference surfaces to allow for the alignment of the beam axis. Wakefield monitors [84], integrated into the first cell of every second structure for beam-based alignment, are used to align the accelerating structure to the beam axis with an accuracy of 5 mm.

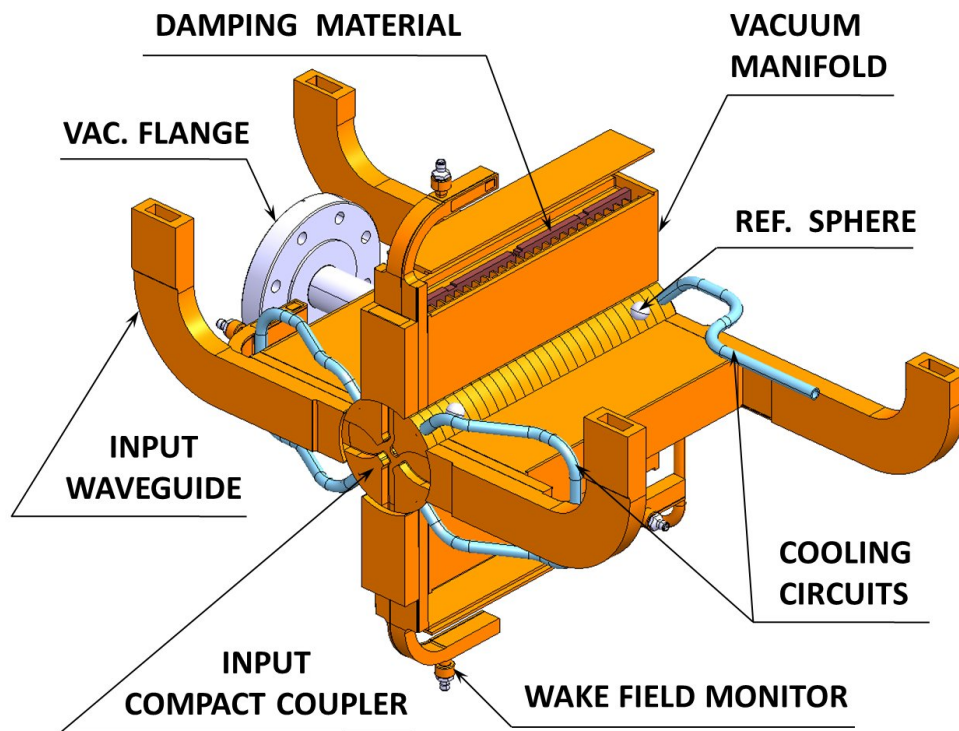


Fig. 5.80: 3D view of the CLIC accelerating structure

For each disk (see Fig. 5.81), the required geometry, dimensions, and tolerances are based on the RF requirements. A high-precision region has been identified for the definition of the requirements. In the internal region 'A', the shape tolerance of the RF cells is ± 2.5 mm and the surface roughness, R_a , is 0.025 mm.

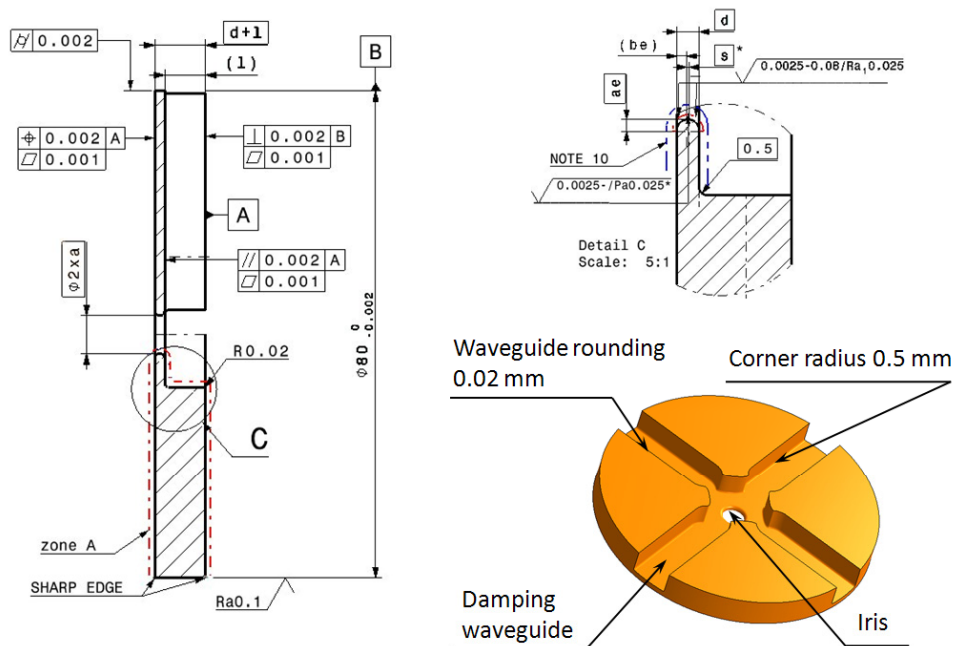


Fig. 5.81: Main tolerances for accelerating structure disk

Both the iris radius and thickness are tapered linearly in order to provide an optimum distribution of various high-power parameters and to avoid hot spots along the structure. Tuning holes are provided only for the prototype phases. For series production, fabrication tolerances should satisfy the stringent beam dynamics requirements without additional tuning (see *Fabrication tolerances* above).

A 0.02 mm rounding of the waveguides has been implemented to avoid sharp edges. The waveguide corner radius of 0.5 mm permits a reduction of the pulse surface heating, (see Fig. 5.81). Integrated compact couplers have been developed to reduce the length of the structure. The geometry of the compact coupler cell is very similar to that of the regular cell (see Fig. 5.82). In the coupler cell, two opposite waveguides of the standard WR-90 width form a double-feed coupler cell. The other two damping waveguides are kept in place to maintain damping as efficiently as in the regular cells.

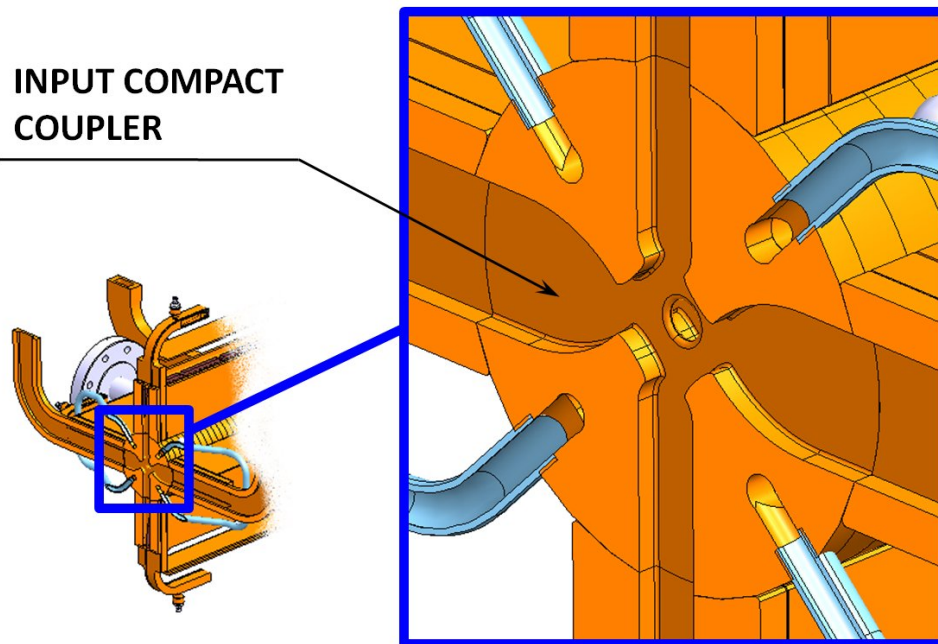


Fig. 5.82: Transversal cut of the accelerating structure compact coupler disk

5.5.1.2 Accelerating structure fabrication, assembly, and integration issues

For the engineering design and fabrication of the accelerating structure [85], the concept of a superstructure has been introduced. A superstructure is composed of two accelerating structures, assembled together as one unit (see Fig. 5.83).

The fabrication of the accelerating structure is based on the following main steps:

- diamond machining;
- surface treatment including chemical etching;
- joining of the disks by diffusion bonding at about 1000°C in a hydrogen atmosphere;
- vacuum baking at 650°C.

The different components of the superstructure are fabricated using conventional technologies, namely milling and turning. To fulfil the beam physics requirements, ultraprecise machining is required. The ultraprecision parts are the disks and the vacuum manifolds. To machine the disks the procedure foresees two main steps: pre-fabrication and ultra-precision machining. The pre-fabrication includes pre-turning and pre-milling, as well as all needed stress reliefs, to achieve an accuracy of few tens of

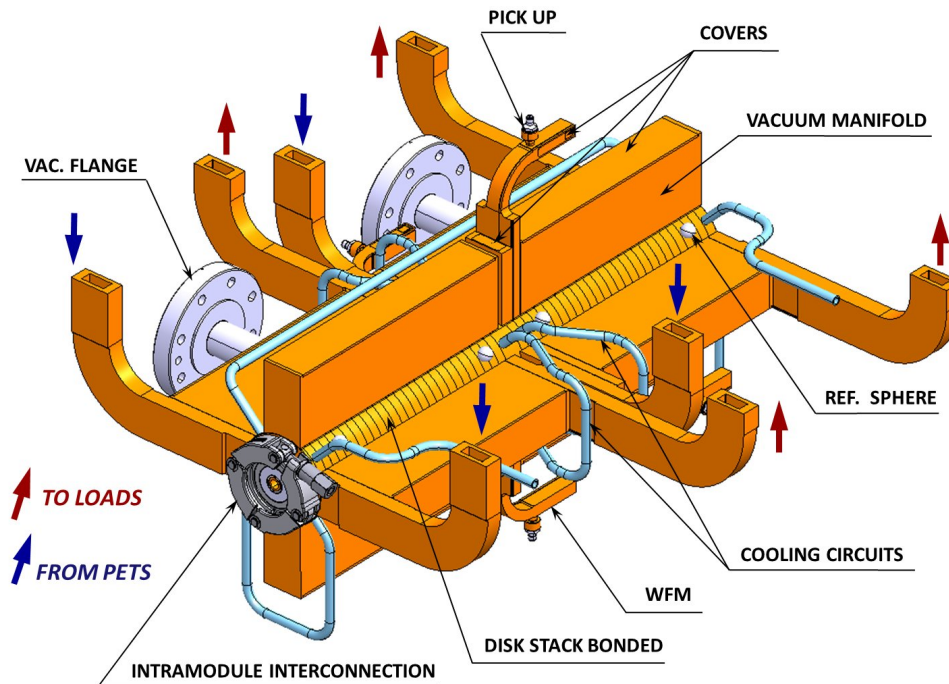


Fig. 5.83: 3D view of a superstructure

microns. Several tests are being conducted to study the influence of annealing cycle parameters (mainly temperature and time) on flatness and surface quality. For the moment the adopted annealing temperature varies from 180°C to 240°C, and the holding time from 4 to 2 hours respectively. The quality of this milling is important in order not to make any sharp ridges or burrs. The shape accuracy down to 5 mm is then achieved by ultraprecision machining. Special care is taken for the transition from the turning surface of the elliptical iris to the milled flat surface. For surface quality considerations, turning of the iris up to the ‘nose’ needs to be the last operation (see Fig. 5.84).

Turning to milling transition area



Fig. 5.84: Detail of iris region machining

Many accelerating structure disks were fabricated by different vendors, although at present few

European companies are able to fulfil the technical specification. Both iris shape and damping waveguide profiles are within specification. Based on these results, we can conclude that the existing 3D-milling technology is well established, cost effective and delivers the accuracy of the fabrication within our specifications.

The accelerating structure disks and vacuum manifolds undergo a very detailed cleaning procedure, implying chemical etching for about 30 s, followed by ultrasonic cleaning in de-ionized water as well as in clean alcohol.

The assembly of the superstructure components is comprised of several other steps (see Fig. 5.85), namely:

- diffusion bonding of the disks under hydrogen at a temperature of about 1000°C. Before bonding, alignment of the cells to better than 5 μm in total is accomplished by using a dedicated V-shaped support;
- pre-assembly and brazing of vacuum manifolds and waveguides;
- brazing of the vacuum manifold and waveguide assembly to the bonded disk stack at a temperature of about 950°C;
- brazing of cooling tubes and interconnection bellows at a temperature of about 900°C;
- brazing of the two equipped stacks to form a superstructure;
- installation of the silicon carbide damping loads. Silicon carbide damping loads are fired at about 1000°C before bolting them to the vacuum manifold;
- welding of the interconnection vacuum flanges and vacuum manifold covers;
- the superstructure is then installed in a clean stainless container with separate high vacuum and baked in a vacuum furnace at 650°C for at least 10 days. The required vacuum level is 10^{-9} mbar.

Typical braze alloys are 25Au/75Cu, 35Au/65Cu, and 50Au/50Cu. The assembly is leak-checked after each brazing cycle.

Quality control, based on a dedicated quality assurance system, is made to check the conformity during the whole fabrication process. The main quality controls are geometrical verifications and RF measurements based on bead pulling. Figure 5.86 shows the RF measurement set-up of a typical CLIC accelerating structure recently built for high-power tests. Throughout all assembly steps, it is mandatory to preserve the alignment tolerance. Straightness measurements, before and after the different heat cycles, show that the variation is within tolerance. Dedicated tooling has been designed to hold the structure during handling and transport operations. The impact of the different fabrication errors on the superstructure power production has been studied (see the section on *Fabrication tolerances* above). Coupons are also added at each fabrication step and analysed for contamination. The baseline assembly procedure is now well established and fully validated following high-power tests.

5.5.1.3 Results from testing accelerating structures

The baseline design for the main linac accelerating structure is described earlier in this section. The TD26 is the name given to the corresponding test structure. Two families of prototype accelerating structures for CLIC have been produced and tested to date; these are close to the final baseline design which has not yet been tested.

The first family is called T18 and TD18 which is a strongly tapered low group velocity accelerating structure described in detail in Ref. [86]. This was the first structures developed using new design criteria resulting in a low group velocity and input power but a very strong tapering. The accelerating gradient reaches 126 MV/m in the last cell for 100 MV/m average acceleration along the structure. The objective of this structure was to launch an early high-gradient test structure after the frequency change of CLIC from 30 GHz to 12 GHz to demonstrate the feasibility of 100 MV/m. A total of four undamped (T18)

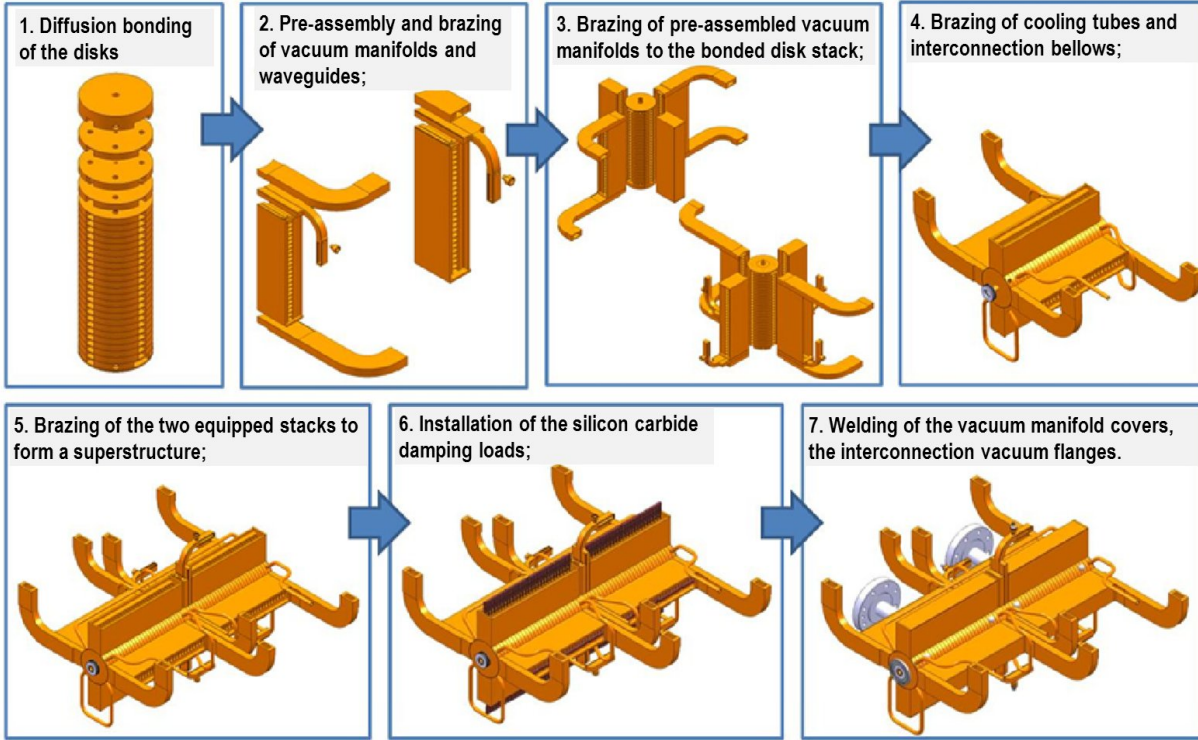


Fig. 5.85: Main assembly steps of superstructure

and two damped (TD18) structures of this family have been tested up to now at 11.4 GHz using the test facilities at SLAC and KEK.

The second family is called T24 and TD24 [87] which is a quasi-constant gradient structure, therefore less tapered and with lower surface fields than T18. This structure family has been optimized both for RF-to-beam efficiency and high-gradient constraints. This structure and its RF parameters are very similar to the TD26 baseline which has mainly an optimized filling factor due to compact couplers and integrates the RF loads. The TD24 is a test structure which has damping waveguides but not load material. Two T24 structures have been tested at 11.4 GHz and one TD24 in the TBTS at 12 GHz.

The main results described here are the successful demonstration of undamped and damped CLIC-type structures running at 100 MV/m unloaded gradient with the design RF pulse length of 240 ns and a breakdown rate below 3×10^{-7} as required. The latest test of a damped TD24 at KEK, which is still ongoing, fulfilled the CLIC specifications using the nominal CLIC RF pulse shape with a 160 ns flat top. The next steps are to fully integrate the short coupler design and the HOM loads into a fully-featured TD26 and demonstrate the same performance.

Structure test facilities

The CLIC collaboration is taking advantage of klystron-based test facilities originally constructed for the NLC/GLC project at SLAC and KEK. The X-band frequency for these facilities is 11.424 GHz. At SLAC two facilities, ASTA and NLCTA [87], can be used to test accelerating structures, PETS, and high power RF components. Two 50 MW klystrons are combined into a pulse compressor providing up to 300 MW of RF power for a typical pulse length of 240 ns. At KEK the NEXTEF [88] facility is being used. Here two 50 MW tubes are combined providing about 90 MW of RF power for testing. NEXTEF and NLCTA are equipped with a sophisticated control and data acquisition system allowing 24 hour operation. Most of the results described below have been obtained in these two test facilities.

At CERN a klystron-based test stand [89] with one klystron and pulse compressor at 11.994 GHz is

5.5 X-BAND RF SYSTEM

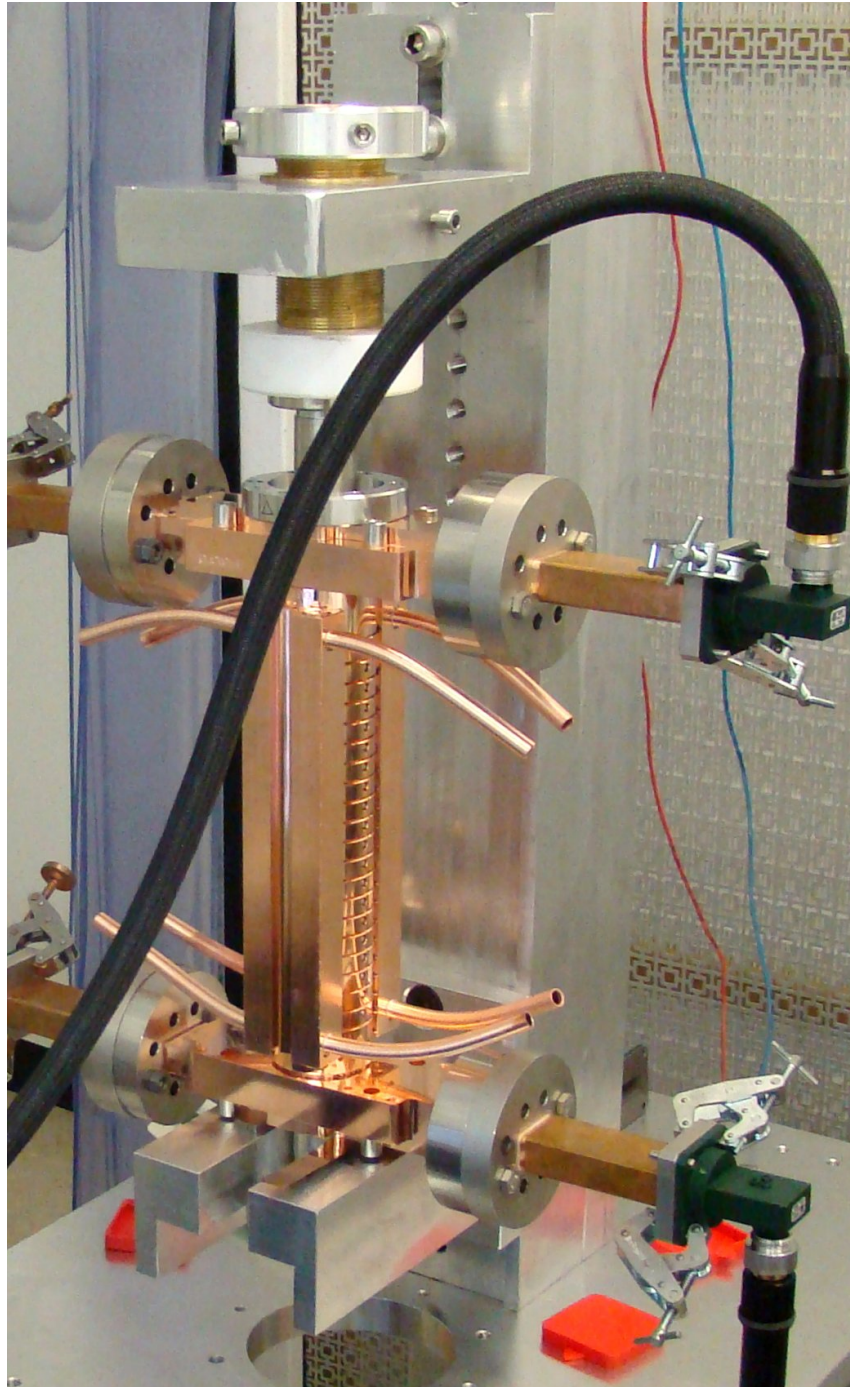


Fig. 5.86: RF measurement set-up of a test accelerating structure

under construction and began commissioning with a full RF system and test structure in May 2012. The two-beam test stand TBTS [90] in CTF3 is equipped with a power production structure (PETS) which allows extraction of up to 200 MW of RF power at 11.994 GHz from the CTF3 Drive Beam. This power can be used for structure testing. At the same time a separate probe beam enables direct acceleration measurements of the structures under test.

Results obtained

The main goal of the high power testing is to demonstrate that it is possible to operate this CLIC prototype accelerating structures at 100 MV/m average loaded gradient and 240 ns nominal pulse length with a breakdown probability below 3×10^{-7} /pulse/m.

A total of nine prototype accelerating structures belonging to the two families described above have been successfully high power tested so far. With the exception of two CERN-built structures they have been built in collaboration between KEK and SLAC. KEK purchased and oversaw the fabrication and quality control of the disks while SLAC did the surface preparation and assembly following the procedures developed for NLC/GLC [91]. The two structures mentioned here made by CERN followed the same fabrication procedures.

All of these structures have been processed above 100 MV/m up to a pulse length between 230 ns and 252 ns depending on the test facility used. The typical conditioning procedure applied was to start at a pulse length as short as 50 ns, process above 100 MV/m and then lengthen the pulse length in several steps to reach the nominal pulse length of 240 ns with a square pulse. After the initial processing-breakdown probabilities as a function of gradient and pulse length have been measured systematically. The amount of dark current, the Fowler-Nordheim-enhancement factor, β , as well as the dark current energy spectrum were measured using the instrumentation available at the NEXTEF facility at KEK [92]. The conditioning was typically continued at a fixed gradient and pulse length for some time. An important observation during the conditioning experiments was that the breakdown rate at a fixed gradient continues to decrease as a function of time even after more than 1000 hours of operation. For example, the recent conditioning of a T24 structure at KEK showed an exponential reduction of the breakdown rate at 100 MV/m and 252 ns pulse length with an e-folding time of 186 hours as shown in Fig. 5.87. Breakdown probabilities in the CLIC target range have been obtained so far after 1000–2000 hours of conditioning.

The scaling of the breakdown probability as a function of gradient is illustrated for some structures in Fig. 5.88. Typically the probability increases by a factor of 10 for about 7 MV/m increase in gradient. It was found that the curves could be described approximately with an E^{30} law [93] which was used for scaling results in this report. The breakdown probability depends strongly on the RF pulse length. For a fixed breakdown probability the accelerating gradient scales as $t^{-1/6}$ with pulse length. An example of a measurement of the breakdown rate dependence on RF pulse length is shown in Fig. 5.89 for the TD18 measured at KEK. The high power testing has been done so far using a square pulse; the nominal RF pulse shape for CLIC however is a 88 ns ramp followed by 156 ns flat top (see §5.4.3 for details). Experimental studies in the past indicated that the pulse length relevant for the breakdown probability is the pulse duration above 85% of the maximum power. Therefore in the following it is assumed that the equivalent square pulse length of 180 ns will have the same breakdown rate as the CLIC nominal 240 ns ramped pulse shape. The latest testing of a TD24 structure at KEK used the CLIC design pulse shape and confirmed this assumption.

Since each test facility has individual features and constraints, the testing of these structures has not been done under identical conditions. This is true for the conditioning procedure applied as well as for the breakdown detection hardware and strategy. Despite these differences very consistent results could be achieved which confirm the robustness and reproducibility for this type of structure. The most relevant breakdown probabilities obtained after conditioning are summarized in Table 5.31 together with the conditions of the experiments. The last column indicates which operational gradient could be expected from the measurement results applying the scaling laws mentioned above to extrapolate to CLIC parameters.

For the time being it has not been possible to test these accelerating structures with high power and nominal beam loading, therefore all the testing has been done unloaded. In the loaded case the input power to the structure is slightly higher and the field distribution along the structure is changed according to the loading; on the whole the accelerating field is higher at the beginning of the structure and lower

at the end of structure. The assumption used in this document is that the net breakdown rate will change very little in the loaded case while the distribution of the breakdowns in the structure might change. Experiments are planned to verify this assumption.

T24#3 BDS vs time normalized at 252ns 100MVm

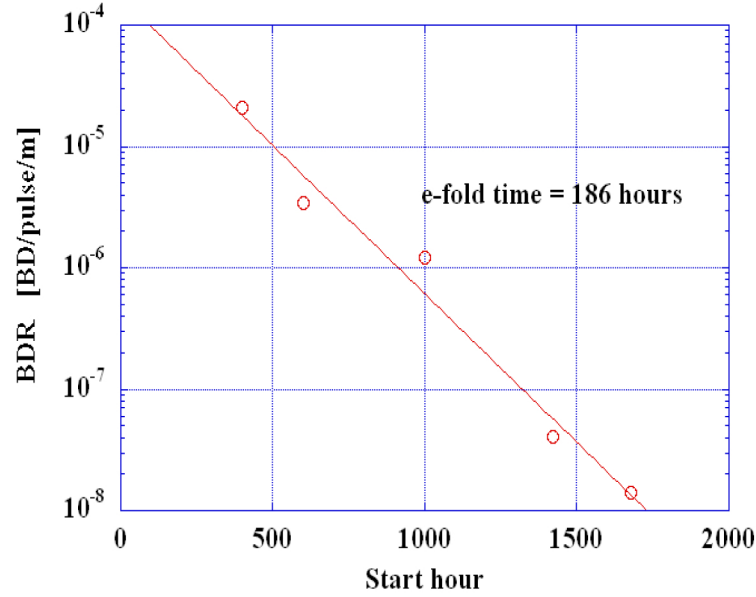


Fig. 5.87: Breakdown rate as a function of conditioning time for a particular working point

Relevance of the results for CLIC

Most of the results to date have been obtained at 11.424 GHz instead of the nominal 12 GHz. RF breakdown is, in general, a frequency-independent phenomenon [93]. In addition the 5% frequency difference is insignificant thus the results at 11.424 GHz are relevant for CLIC.

The T18 series of prototype structures were the first structures which could be reliably operated at a gradient of 100 MV/m with the necessary pulse length. Therefore these experiments demonstrated that such a gradient is obtainable in X-band structures. Moreover, the aperture range, an important parameter for breakdown and short range wakefields, matches the CLIC requirements and is similar to the CLIC TD26 structure. From the implementation of heavy waveguide based damping in the TD18 structures an important conclusion could be drawn for the TD26 base line structure.

It is expected that the compact coupler and the actual loads in the damping waveguides can be implemented in a way which does not reduce the high gradient performance. Therefore the difference between TD24 and TD26 from the point of view of high power testing is considered to be insignificant. Therefore the RF design of the CLIC structure can be validated with high power tests of TD24 structures.

Table 5.31 summarizes the high power test results of the T18 and T24 series of structures. In the last column the average accelerating field is given which is expected from these measurements for the CLIC specific parameters of 100 MV/m average loaded gradient, 180 ns equivalent flat top and 3×10^{-7} /pulse/m breakdown rate. The scaling was done using $BDR \sim G^{30} t_p^5$.

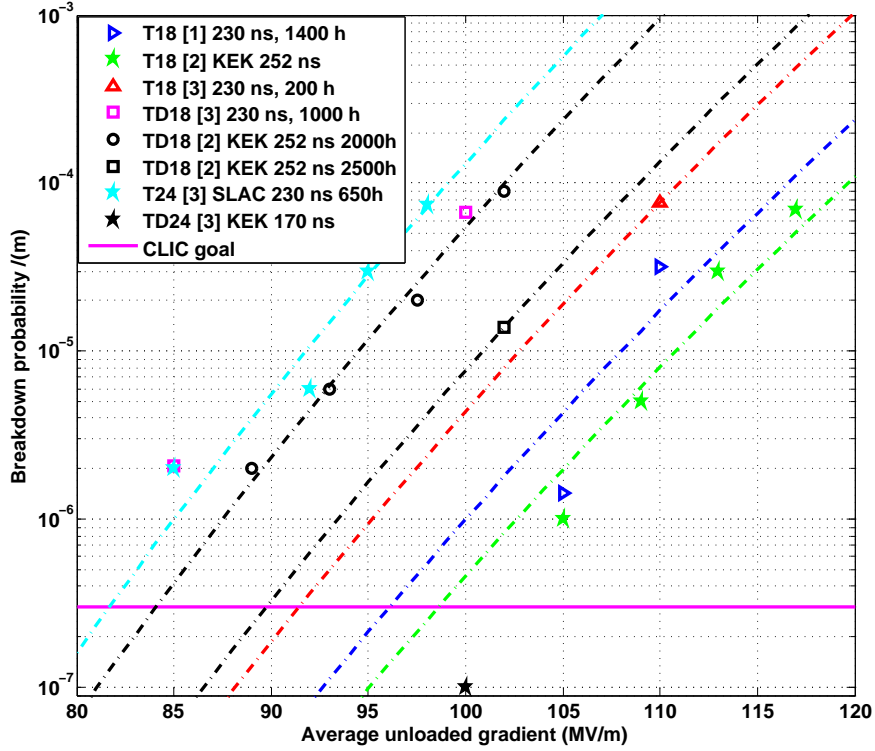


Fig. 5.88: Breakdown rate as a function of unloaded gradient for different structures. The lines show an E^{30} dependence fitted to the data points. The testing of the TD24 at KEK was still ongoing when this plot was made and therefore the data point shown should be considered as preliminary.

Additional results with importance for CLIC

During the study for NLC/GLC, significant results concerning normal conducting X-band structures have been obtained and are relevant for CLIC [94]. About 40 structures have been produced and tested for a total of 25 000 hours with high power during the R&D effort. Scaling laws for pulse length dependence and gradient dependence of the breakdown rate have been extensively studied and are used within the CLIC study.

In particular, for a final test at SLAC, eight structures have been fabricated and conditioned during more than 1500 hours. The structures continued to improve their breakdown rate at a constant gradient exponentially with a time constant between 500 and 700 hours. A degradation as a function of time was not observed. These structures have been tuned and beam was accelerated successfully and according to the predictions. The yield for structures successfully built and conditioned was $>70\%$ once the geometry was fixed.

A number of venting tests have been done in order to probe the robustness of this kind of structure. Structures have been vented with nitrogen, filtered air, unfiltered air. The performance of the structure could be recovered quickly in each case.

A pair of structures of the DDS type equipped with damping slots and damping loads at the end of the manifolds has been tested in the ASSET facility at SLAC [95]. The wakefields have been measured with beam validating the simulations for the design as well as the capability to build such structures with the necessary accuracy. In addition higher order mode signals have been used to measure the beam position in the structure with a resolution below 1 micron, thus demonstrating the possibility of beam-

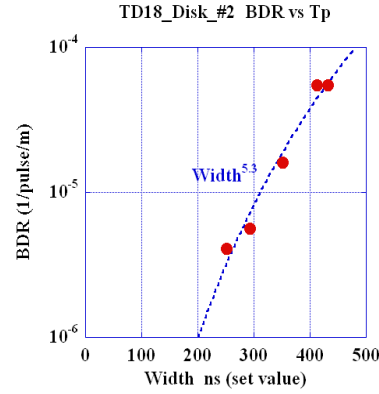


Fig. 5.89: Breakdown rate as a function of pulse length as measured at KEK for the TD18. The fitted curve shows the typical $BDR \approx \tau^5$ dependence.

Table 5.31: Summary of breakdown rate measurements for fixed gradient in the final stage of conditioning and predicted usable unloaded gradient at CLIC parameters

Structure name	Unloaded gradient	Flat top pulse length	Breakdown rate	Conditioning hours	Expected gradient for a trip rate of 3×10^{-7} and 180 ns flat top
	[MV/m]	[ns]	[1/pulse/metre]		[MV/m]
T18 #1 SLAC	105	230	1.0×10^{-6}	1400	105
T18 #1 SLAC	106	230	3.1×10^{-7}	1200	110
T18 #2 KEK	105	252	1.0×10^{-6}	3900	107
T18 #3 SLAC	110	230	7.7×10^{-5}	288	95
T18 #5 CERN/SLAC	90	230	1.3×10^{-6}	560	89
TD18 #1 SLAC	100	230	7.6×10^{-5}	1300	87
TD18 #2 KEK	102	252	1.4×10^{-5}	2500	95
T24 #4 SLAC	98	230	7.4×10^{-5}	650	85
T24 #3 KEK	120	252	1.6×10^{-6}	1700	120
TD24 #3 KEK 12 GHz TBTS	100	160	$< 10^{-7}$	ongoing	103

based alignment based on these signals [96]. A waveguide damped structure based on a former 30 GHz

design had been tested in the past at ASSET and the measurement confirmed the damping properties calculated [97].

The transverse kick to the beam caused by a breakdown occurring in a structure has been measured in NLCTA and a typical magnitude of 10 keV/c r.m.s. was found [98]. Studies have also been performed on what happens if one does not switch off the RF drive after a breakdown and allow several subsequent pulses before intervening. It appears that if a structure is operated at a low breakdown rate, a single event can be tolerated without provoking immediate breakdowns on subsequent pulses. These results can be used in defining a future operational scenario for CLIC.

5.5.2 Power Extraction and Transfer Structure (PETS): RF design

The CLIC Power Extraction and Transfer Structure (PETS) is a passive microwave device in which bunches of the Drive Beam interact with the constant impedance of the periodically loaded waveguide and excite preferentially the synchronous mode. The RF power produced is collected downstream of the structure by means of the RF power extractor; it is delivered to the main linac structure using the waveguide network connecting PETS to the accelerating structures. The RF power generated by the bunched beam in a constant impedance periodic structure in general can be expressed as:

$$P = I^2 L^2 F_b^2 \omega_0 \frac{R/Q}{V_g^4} \times \left(\frac{1 - \exp(-L\tau)}{L\tau} \right)^2, \quad (5.24)$$

$$\tau = \frac{\omega_0}{2QV_g}$$

where:

I	is the beam current
L	is the active length of the structure
F_b	is the single bunch form factor
ω_0	is the bunch frequency
R	is the impedance per unit length
Q	is the quality factor
V_g	is the group velocity

For the CLIC accelerating structure parameters such as peak RF power – P_S , RF pulse length – T_S and structure length – L_S , the Drive Beam current after all the combinations in combiner rings is well established:

$$I_{DB} = \frac{P_S T_S}{L_S} \times \frac{N_C c}{E_{DB} \eta_{DB} \eta_{RF}} \quad (5.25)$$

where:

N_C	is the Drive Beam combination factor
E_{DB}	is Drive Beam initial energy
η_{DB}	is the Drive Beam energy extraction efficiency
η_{RF}	is RF network transfer efficiency
c	is the speed of light

5.5 X-BAND RF SYSTEM

In general, the decelerating module (see Fig. 5.90), consisting of PETS, quadrupoles, BPMs, and high power RF networks, must not be longer than the accelerating structure it drives, to ensure maximum effective accelerating gradient. For a given CLIC unit layout, where the number of PETS (m) and number of the accelerating structures (n) are fixed, the active length and thus the impedance of the PETS are determined.

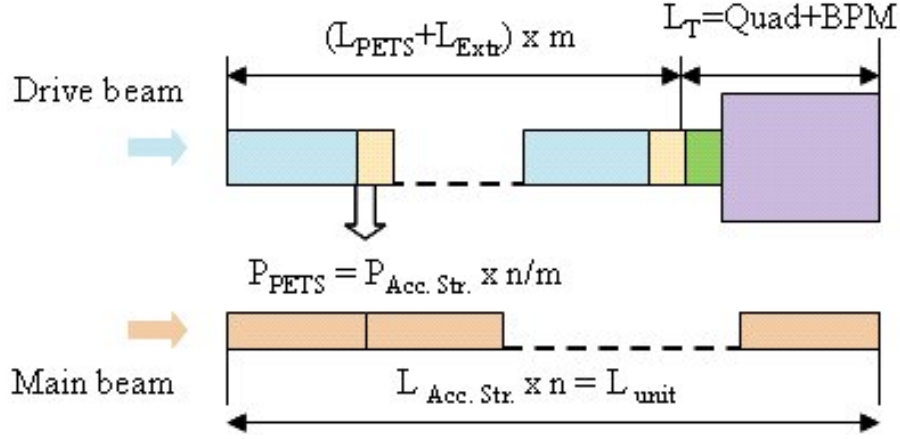


Fig. 5.90: Generic layout of the CLIC unit

At a given frequency λ_0 , the normalized impedance of the periodical structures with high group velocity ($V_g/c > 0.2$) and fixed RF phase advance (ϕ), and iris thickness (t) scales with the structure aperture radius approximately as:

$$\frac{R/Q}{\beta_g} = \left(\frac{a}{\lambda_0} \right)^{-3.7} G(\lambda_0, \phi, t) \quad (5.26)$$

where:

$$\beta_g = V_g/c$$

a is the PETS aperture radius

G is the geometric parameter connecting the RF phase advance and iris thickness (see an example in Fig. 5.91)

Using Eqs. 5.24, 5.25 and 5.26 we can then write the expression for the PETS aperture radius using the given parameters of the rest of the system which are summarized in Table 5.32:

$$\frac{a}{\lambda_0} = \left[I_{DB}^2 (L_S \times n - L_T - L_E \times m)^2 F_b^2 \frac{\pi G}{P_S \lambda_0 2 n m} \right]^{0.27} \quad (5.27)$$

In the presence of deceleration, the final energy spread in the Drive Beam will be $\sim 90\%$ in order to achieve high efficiency of the RF power extraction; therefore, a FODO lattice is required to prevent beam losses along the decelerator. To ensure the beam stability, one metre quadrupole spacing is needed [100]. This naturally defines the number of accelerating structures per CLIC unit: $n = 4$ and limits possible choices for the PETS configuration in a module to: $m = 1, 2$ and 4 .

The RF power extractor length (L_E) is determined by Eq. 5.27 and the constraints on the beam aperture. In most cases, when the beam aperture is expected to be kept constant, the choice of aperture defines the power extraction strategy. Throughout the PETS optimization for the different aperture radii, a number of different RF power extractors have been developed. Briefly, the history of this development

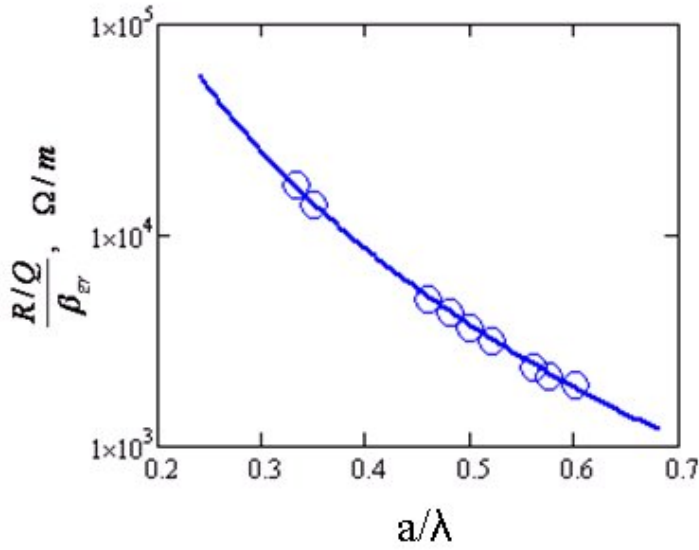


Fig. 5.91: Impedance of the 12 GHz periodical structure ($\phi = 90^\circ, t/\lambda = 0.08$ and $G = 290$) vs. structure aperture calculated using Eq. 5.26 – solid line, and simulated with EM computer code HFSS [99] – circles.

Table 5.32: Input parameters for the PETS design

Accelerating structure length	0.25 m
RF peak power/structure	64 MW
RF pulse length	241 ns
Drive beam energy	2.4 GeV
Drive beam energy extraction efficiency	0.9
Single bunch form factor (F_b^2)	0.93
Combination factor (N_C)	12
RF network transfer efficiency	0.96
Drive Beam current	101 A
Quadrupole + BPM length (L_T)	0.4 m

is summarized in Fig. 5.92. If the aperture radius $a/\lambda < 0.27$, then classical couplers can be used similar to those in the accelerating structure. When the aperture radius range is within: $0.42 < a/\lambda < 0.78$, as is the common approach, extractors are equipped with a choke reflector [101], to prevent the propagation of the generated RF power in the overmoded waveguide circuit. For the larger apertures, $a/\lambda > 0.8$, a special mode-mixing quasi-optical technique has been developed [102]. However, the general trend is as follows: the bigger the aperture, the more length/space is needed to extract RF power efficiently. This is also true for the special matching elements that are necessary to connect the extractor and the structure's regular part.

The actual choice of the PETS layout is a result of a compromise between multiple constraints and the structure cost/performance:

- Using Eq. 5.27, we have first estimated the range of PETS aperture and active length variations for the different m under the condition: $L_E = 0$. With the results obtained, when the smallest aperture radius is $a/\lambda > 0.4$ ($m = 4$), more accurate calculations have been done assuming that $L_E = 3\lambda$.
- RF power production efficiency is limited by ohmic losses which are determined by the structure Q -factor and filling time.

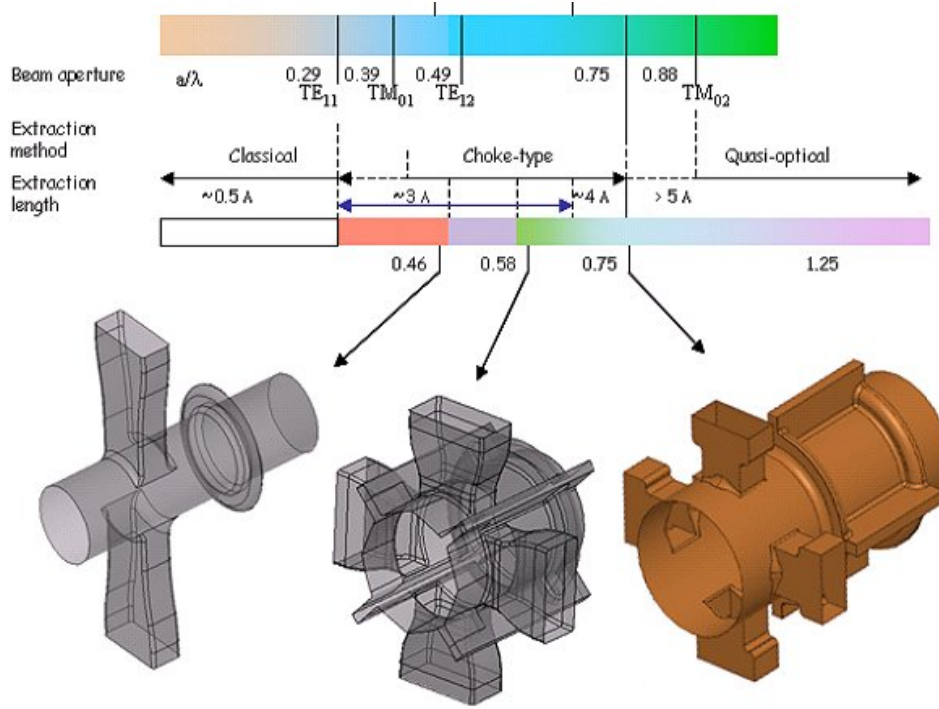


Fig. 5.92: The RF power extractor design specifics depending on the extraction aperture radius a/λ .

- The high RF power performance in periodic structures is governed by the RF constraints. For accelerating structures, that RF power density on the structure surface determines the performance through the quantities S_c and $P/\lambda c$ (see §2.3.2). In our case this condition can be explained in a simple way: the PETS aperture radius should be at least larger than the sum of the accelerating structure input aperture radii it drives: $(a \times m)/(a_s \times 4) > 1$. In this way the power density is not higher than in the accelerating structures.
- Another important issue is the beam stability along the decelerator, which can be spoiled by transverse HOM kicks. As a first approximation, the transverse kick integrated along the module is proportional to $a^{-3} \times L_{\text{PETS}} \times m$.

All these arguments are summarized in Table 5.33 for the different PETS layouts.

Table 5.33: Three different PETS layouts

m	Power [MW]	a/λ_0	L_{active} [m]	Efficiency	$\frac{a \times m}{a_s} \times 4$	$a^{-3} \times L_{\text{active}} \times m$ [cm ⁻²]
4	66.7	0.318	0.075	0.994	2.52	0.0597
2	133.3	0.477	0.225	0.991	1.89	0.0265
1	266.7	0.625	0.525	0.989	1.24	0.0138

Comparing the three solutions, we conclude that the layout with $m=2$ is the best compromise in terms of RF high power production reliability and beam stability. It is also the most cost effective, when considering the complexity of the RF waveguide network, total active length of the PETS, and number of RF power extractors. The actual PETS aperture was slightly reduced from $a/\lambda = 0.477$ down to $a/\lambda = 0.46$, to avoid the coupling to the quadrupole mode in the power extractor region.

For the fixed aperture, changes of iris thickness and phase advance in a high group velocity structure, such as the PETS, do not significantly modify the longitudinal impedance. However, the transverse HOM impedance and HOM damping performance are sensitive to these variations, see Fig. 5.93. In general, the lower phase advances favour impedance reduction of the trapped HOM of the higher bands, whilst the thinner irises are beneficial for the stronger damping of the lowest dipole band. To facilitate the fabrication technology the iris thickness $t/\lambda = 0.08$ (2 mm) and 90° phase advance per cell were chosen.

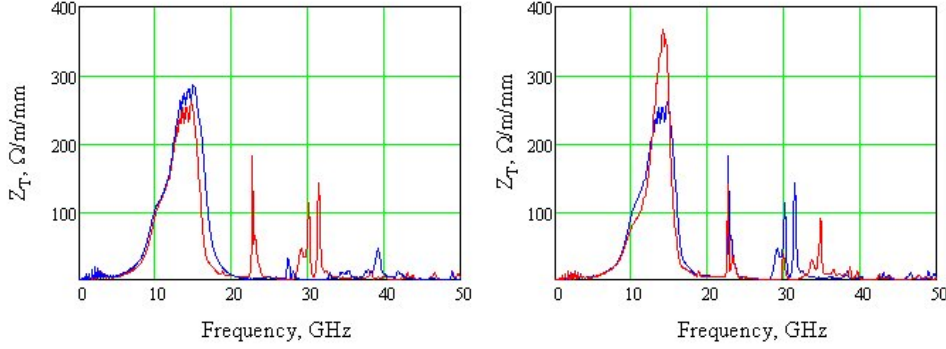


Fig. 5.93: Transverse impedances calculated with EM computer code GdfidL [103] for the fixed iris thickness ($t/\lambda = 0.08$) and different phase advances: 90° in blue and 120° in red (left). Transverse impedances for the fixed phase advance ($\phi = 120^\circ$) and different iris thicknesses: $t/\lambda = 0.08$ in blue and $t/\lambda = 0.14$ in red (right).

In its final configuration, the PETS comprises eight octants (bars) separated by the 2.2 mm wide damping slots. Each of the bars is equipped with HOM damping loads, as shown in Fig. 5.94. This arrangement follows the need to provide strong damping of the transverse HOM modes. The two extremities of the PETS bar are equipped with a special cell, which acts like a $\lambda/4$ transformer and matches the PETS impedance to the impedance of the 23 mm aperture circular waveguide. To guarantee a fairly even concentration of the electric field on the iris surface, the tip of the iris has a slightly convex (33 mm radius) shape, whilst the bottom of the cell is kept flat, see Fig. 5.95. The sharp edges of the corrugated profile on the bar were smoothed out by a 0.9 mm rounding. The ceramic loads are clamped to the bar's sides with a special stainless steel plate.

The electric field distribution across the PETS aperture does not maintain full circular symmetry. The electrons travelling at radial distances larger than 60% of the PETS aperture radius, would receive a transverse kick from the octopolar component of the decelerating mode. The situation improves significantly if every second structure is turned by 22.5° to get a cancellation of focusing and defocusing deflections [104], see Fig. 5.96. The 12 GHz CLIC PETS parameters are summarized in Table 5.34.

5.5.2.1 PETS power extractor

The PETS compact RF power extractor base line design is shown in Fig. 5.97. The power extractor converts the TM_{01} mode in 23 mm diameter circular waveguide into a TE_{10} mode in a rectangular WR90 waveguide with a calculated efficiency of 99.4%. Together with losses in the PETS, the overall power production and extraction efficiency is calculated to be 98.5%. The isolation of the forward power after the double choke, as well as matching at operating frequency are below -50 dB, see Fig. 5.98. In this design the peak surface electric field at a nominal power is 44 MV/m, which is 28% lower than in the PETS regular part. The double choke configuration ensures good isolation for the relaxed fabrication tolerances and is essential for the PETS ON/OFF RF circuit. The 3 dB combining RF waveguide network is integrated into the design. The total length of the extractor is 24.2 mm.

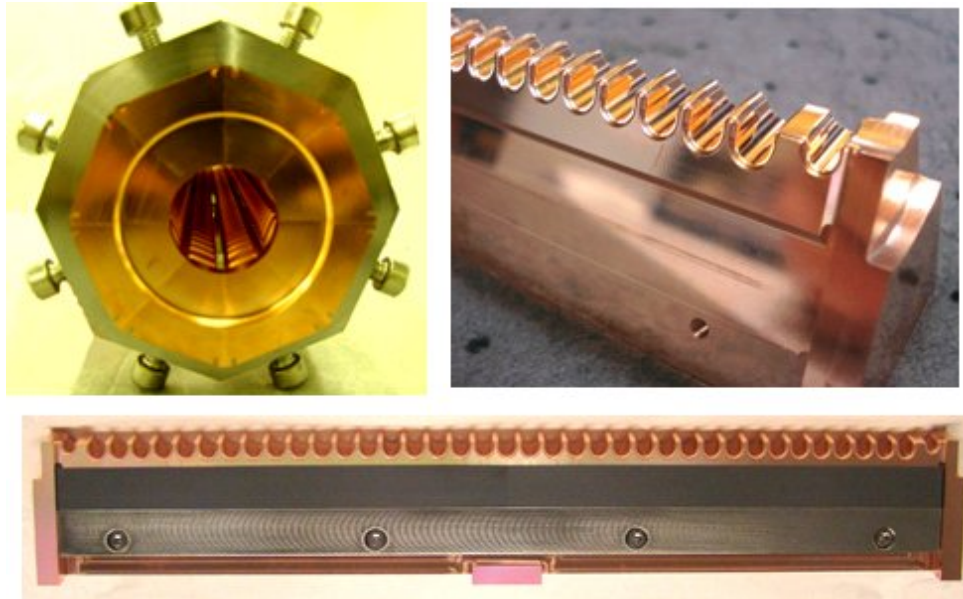


Fig. 5.94: The front view of the pre-assembled PETS body (top left), zoom of the PETS single bar (top right) and view of the single bar equipped with damping loads (bottom)

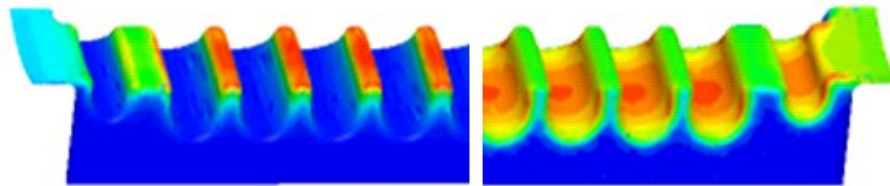


Fig. 5.95: Electric (left) and magnetic (right) field plots on the surface of the single PETS bar

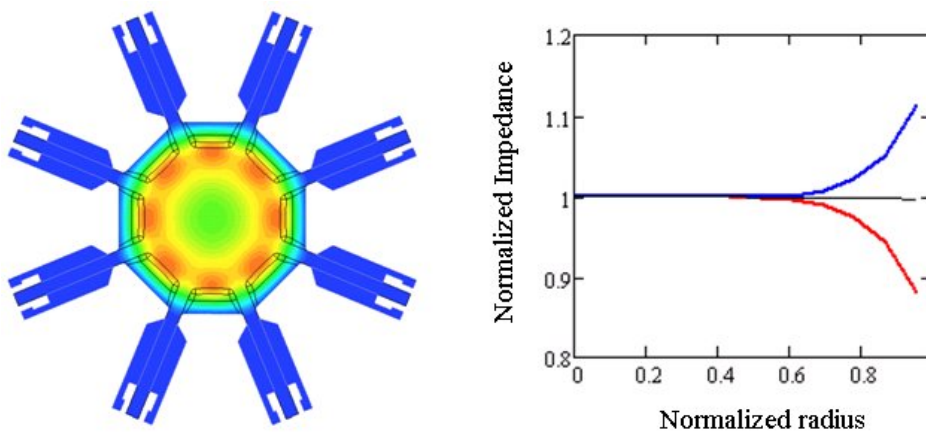
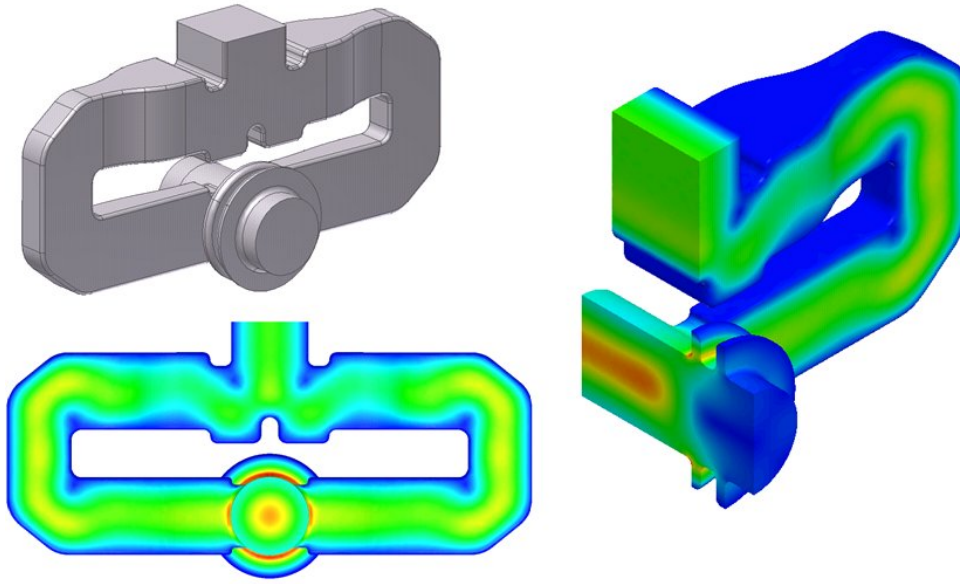


Fig. 5.96: The electric field distribution across the PETS aperture in the middle of the regular cell is shown to the left. The normalized radial impedance distributions are shown to the right. Here in red is the impedance calculated towards the slot centre, in blue towards the iris centre and in black the impedance averaged over the two structures rotated by 22.5° with respect to each other.

Table 5.34: The 12 GHz CLIC PETS parameters.

Aperture	23 mm
Iris thickness	2.0 mm
Cell length	6.253 mm
Phase advance/cell	90°
Corrugation depth	4.283 mm
R/Q	2290 Ω/m
$\beta=V_g/c$	0.453
Q -factor	7200
Active length	0.213 m (34 cells)
RF pulse length	241 ns
Drive Beam current	101 A
Output RF power	133.7 MW
Peak surface electric field	56 MV/m
Peak surface magnetic field	0.08 MA/m
Pulsed temperature rise	1.8°C
Breakdown trip rate	1×10^{-7} 1/pulse/metre

**Fig. 5.97:** RF design of the PETS double-choke RF power extractor with integrated 3 dB combiner. In colour the electric field plots are shown.

5.5.2.2 Transverse HOM damping in PETS and Drive Beam stability

The PETS must deal with high current electron beams and provide extremely stable beam transport for about one kilometre. Strong damping of any deflecting HOM in the PETS is required to prevent significant beam losses. In the PETS, the synchronous frequency of the lowest transverse mode is only 8.3% higher than the operating one. Therefore, methods that are commonly used for accelerating structure damping such as cut-off waveguides, or choke cavities are impractical. The only way to damp transverse wake is to use its symmetry properties — damping with slots. In the presence of longitudinal slots, the transverse mode field pattern is dramatically distorted so that a considerable amount of energy is now stored in the slots. The new TEM-like nature of the mode significantly increases the group velocity, in

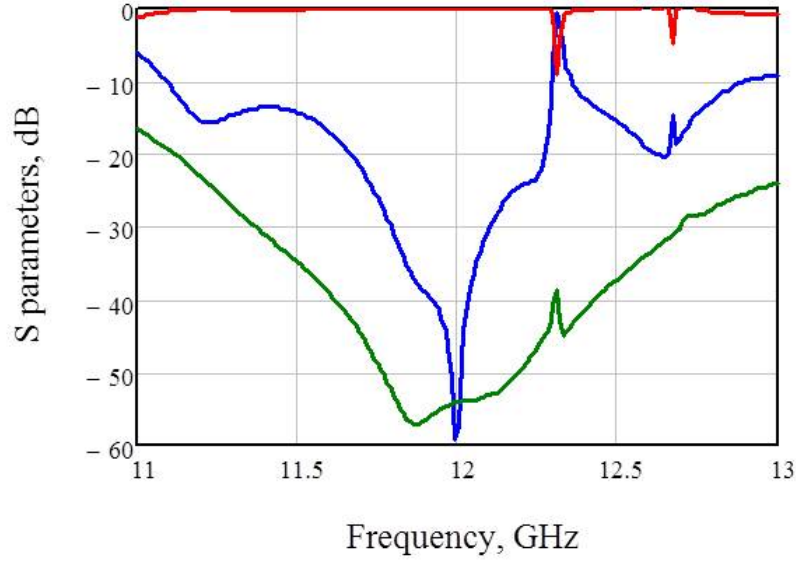


Fig. 5.98: The S-parameters of the compact RF power extractor calculated with HFSS. Here the extraction is shown in red, the reflection is in blue, and radiation through the double-choke reflector is shown in green.

our case from $0.52c$ to almost $0.73c$. Still, there is practically no damping (radiation) in this configuration. To provide the damping, one must incorporate the radial impedance gradient in the slot, in order to create the radial component of the Poynting vector. This is done by introduction of lossy dielectric material close to the slot opening. In addition, the proper choice of the load configuration with respect to the material properties makes it possible to couple the slot mode to a number of heavily loaded modes in the dielectric, see Fig. 5.99. As for the load damping material, we have used SiC parameters as a baseline, for which the different vendors provide well-defined and reproducible dielectric properties. It is beneficial, in terms of damping, to place the loads as close to the slot opening as possible. However, the actual load radial position was optimized in order to minimize the evanescent coupling of the decelerating mode. As a criteria, we constrain the decelerating mode external Q -factor (Q_ϵ), to be at least 100 times higher than the PETS ohmic Q -factor (Q_Ω). To relax the tolerances on the load position, a load radial offset of 18.5 mm was chosen, giving the ratio $Q_\epsilon/Q_\Omega = 500$.

Computer simulation is for the moment the only method to study the very low PETS impedances. The two most advanced parallel finite element time-domain codes T3P [105] and GdfidL were used to simulate the PETS transverse wakes. For a similar simulated geometry, good agreement between GdfidL and T3P has been observed, see Fig. 5.100.

To analyse the beam dynamics along the decelerator in the presence of strong deceleration and wakefields, the computer code PLACET [106] is used. The code requires discrete mode parameters as inputs, which are used to reconstruct the transverse wake generated by the charged bunch:

$$\begin{aligned} W_\perp(z) &= 2q \times \sum_i \frac{K_{\perp i}}{1-\beta_i} \sin\left(\frac{\omega_i z}{c}\right) e^{-\frac{\omega_i z}{2Q_i(1-\beta_i)c}} \times \left\{1 - \frac{\beta_i z}{L(1-\beta_i)}\right\} \\ W_{\perp i}(z) &= 0, \quad z > L \frac{1-\beta_i}{\beta_i} \end{aligned} \quad (5.28)$$

where:

K_\perp is the transverse mode loss factor,

$\beta = V_g/c$ is the group velocity,

Q is the loaded quality factor,

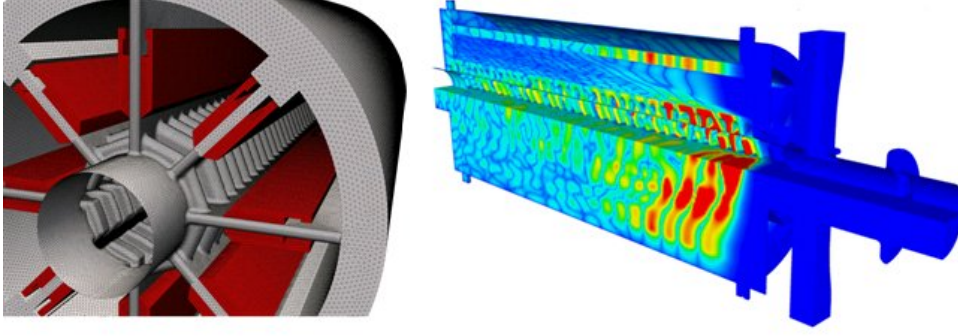


Fig. 5.99: The PETS geometry as used in T3P simulations (left). A snapshot of excited wakefields calculated by T3P as the bunch is about to leave the PETS (right). Strong damping in the lossy dielectric loads can be directly observed.

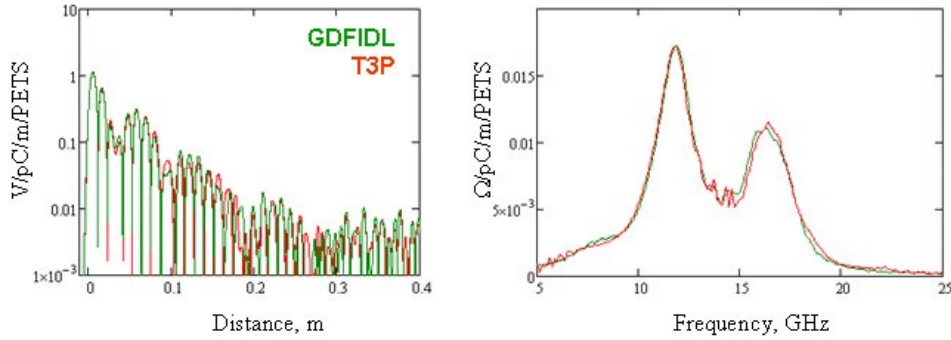


Fig. 5.100: The comparison between transverse wakes and impedances calculated by GdfidL and T3P

- ω is the angular frequency
- L is the PETS active structure length.

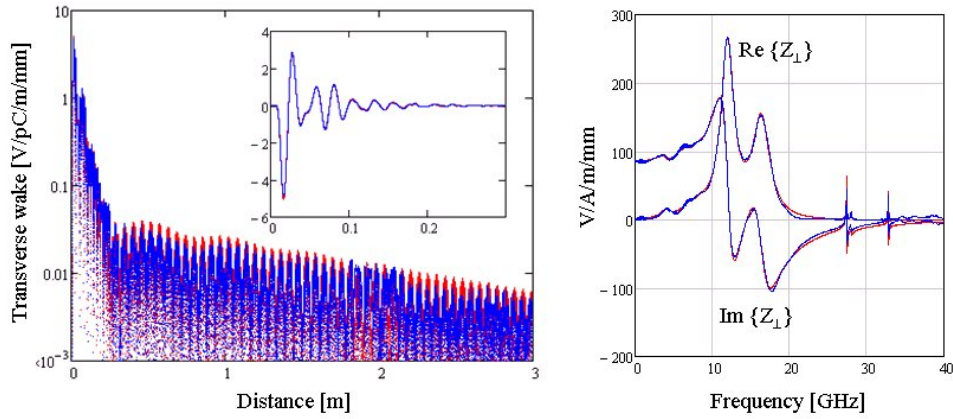
A special computer algorithm was developed which analyses the wake simulated by time-domain computer code and then approximates the results with a limited number of discrete modes using Eq. 5.28. The model obtained is then benchmarked with GdfidL/T3P results simulated for the different PETS length, to check the consistency of the model. The comparison between the transverse wake simulated for the PETS nominal length by GdfidL and the one reconstructed from an eight mode model together with the corresponding impedances is shown in Fig. 5.101. The mode parameters are summarized in Table 5.35. From this analysis we can also determine the HOM damping performance. In our case, the two most dangerous modes are around 12 GHz and 16.4 GHz and have effective loaded Q factor of about 6.5.

The efficiency of transverse HOM damping in the PETS will be studied experimentally in the Test Beam Line (TBL), where 16 PETS will be installed and tested with a 30 A Drive Beam. In the longer term, during mass production of many thousands of damping loads, a certain deviation of the load material properties can be expected. This will affect the frequency and Q -factor of the damped modes. The effects of the modes Q -factors and frequency modification were studied with PLACET, see Fig. 5.102 and Fig. 5.103.

It was found that, even with Q -factor values twice as high, the beam quality along the decelerator practically did not change. Initial amplitude jitter amplification also remained well below a factor of 2 in the frequency range of the lowest dipole band. We have calculated that the loaded Q -factors of the dipole modes in the lowest band are about inversely proportional to changes in the dielectric loss tangent of the

Table 5.35: The transverse modes parameters used in the model

Mode #	F GHz	$K_{\perp}/(1-\beta)$ V/pC/m/mm	$Q \times (1-\beta)$	$\beta = V_g/C$
1	3.95	0.073	3.4	0.43
2	6.92	0.108	5.5	0.67
3	8.5	0.139	5	0.7
4	12.01	3.99	6.82	0.67
5	16.4	3.37	6.3	0.56
6	27.41	0.063	527	0.18
7	28	0.023	156	0.03
8	32.82	0.034	943	0.02

**Fig. 5.101:** The PETS transverse wake (left) and impedance (right). Here the blue colour corresponds to the GdfidL results and red one is the model reconstruction. One can see good agreement between the two.

damping material. From our experience, the different vendors normally provide the lossy ceramic with less than 10% deviation of the material properties. Thus we can conclude that transverse HOM damping technology developed for the PETS is robust and delivers enough margin to provide stable Drive Beam transportation along the decelerator.

The effect of the PETS power extractor transverse impedance on the beam stability was studied separately. The power extractor does not hold the circular symmetry and thus the transverse impedances for the two symmetry planes are different. For both polarizations, the impedances are dominated by two modes trapped in the double choke. These two modes are naturally damped by radiating them into the circular waveguide. However, for the horizontal polarization, many low-impedance un-damped modes are present (see Fig. 5.104). These modes are associated with the volume of the extractor's RF power combiner. The beam jitter amplification along the decelerator was simulated assuming, as the worst case scenario, that extractor impedances for both polarizations are similar to the one in the horizontal plane. Also the Q-factors of all the modes were artificially doubled, to provide a certain margin to the results obtained by GdfidL simulations. The calculated jitter amplification at the end of the decelerator gives us an extra 5% to the PETS budget (compare Fig. 5.102 and Fig. 5.104). This could be considered as a reasonably small perturbation.

5.5.2.3 PETS 'ON/OFF' operation strategy

During normal machine operation, the main accelerating structure and/or the PETS will periodically experience a breakdown. To maintain overall luminosity, the present strategy requires locally (in a single

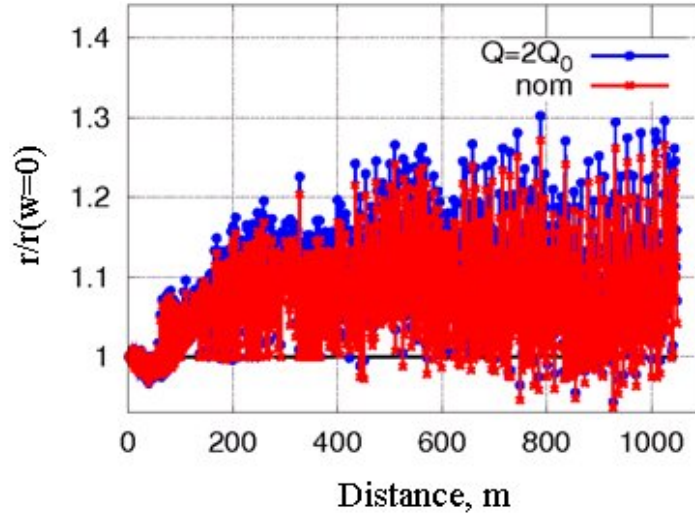


Fig. 5.102: The beam jitter amplification along the decelerator normalized to the case without transverse wake effects. The simulations have been done in approximation of the ‘real’ machine, when quadrupoles are randomly misaligned by $\pm 5 \mu\text{m}$, which approximates a machine aligned with 1-to-1 steering and the Drive Beam population was adopted for the beam loading compensation in the main linac. The beam is injected with offset and jitter as follows: $y(z) = \sigma_y + (\sigma_y/N) \sum \sin(k_n z)$, where σ_y is the initial transverse r.m.s. beam size, and k_n is the wave number for dipole mode n .

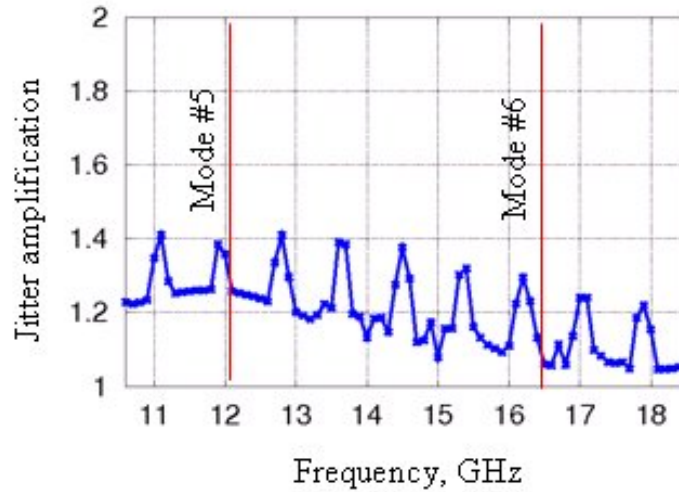


Fig. 5.103: The beam jitter amplification at the end of decelerator vs. frequency of the single deflecting mode. Here the wake amplitude was taken as the sum of all the mode kick factors and the Q -factor was doubled compared to the ones for modes 5 and 6 in Table 5.35.

PETS) a termination of RF power production in response to any breakdown. Another important requirement is the capability of the system to provide a gradual ramp up of the generated power in order to re-process either structure. A system has been developed based on an external high power variable RF reflector [107], as illustrated in Fig. 5.105. Providing the whole range of reflections from 0 to 1, it can fully or partially terminate the RF power transfer from the PETS to the accelerating structure. In general, the reflected RF power will be returned to the PETS. In order to mitigate this effect, a fixed internal RF reflector is placed at the upstream end of the PETS, thus recirculation of RF power inside the

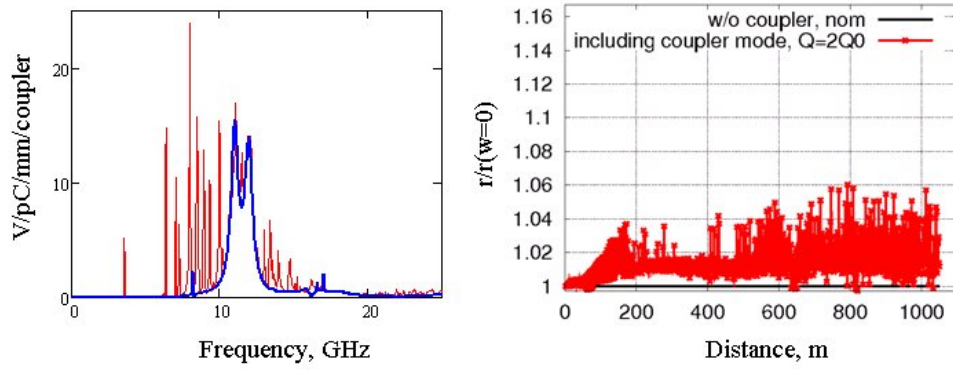


Fig. 5.104: The PETs extractor transverse impedances are shown left. Here the horizontal polarization is shown in red and vertical polarization is shown in blue. The beam jitter amplification along the decelerator normalized to the case without transverse wakes effects is shown right.

PETS is established. If at the operating frequency the electric length of such an RF circuit is tuned to be $L = \lambda_0(n+1/4)$, then the cancellation of the RF power generation from the Drive Beam can be achieved.

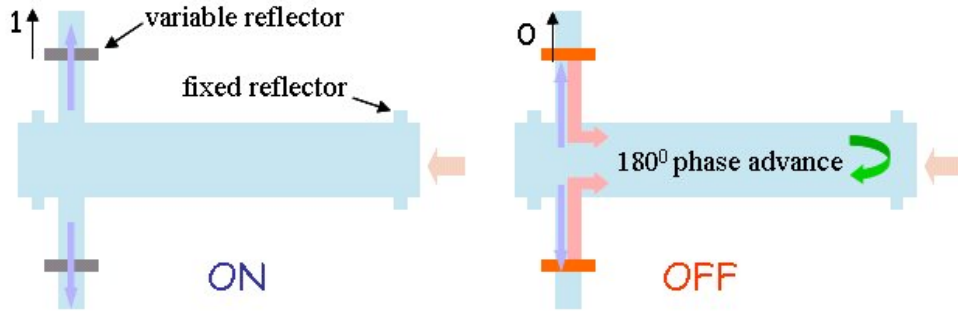


Fig. 5.105: Schematic diagram of the PETS ON/OFF operation strategy

A three-port waveguide RF circuit was chosen as the baseline configuration for the variable RF reflector design. In such a device, the reflection can be varied from 0 to 1, if one of the ports is equipped with an RF short circuit where the RF phase of reflection can be changed progressively through 180° . A new type of compact variable reflector has been developed, which is arranged as a sequence of the different RF circuits, see Fig. 5.106. This configuration provides the possibility for mechanical movement of the piston without electrical contact and to change gradually the phase of the reflection. To prevent RF wave propagation in the coaxial part, it is equipped with an RF filter composed of three choke reflectors with isolation better than -60 dB over a broad frequency range. At any intermediate position of the piston and nominal CLIC RF power level, the surface electric field does not exceed 43 MV/m. The linear stroke $S = 7.7$ mm ($S/\lambda_0 = 0.31$) is required to switch the device from full transmission to full reflection. Because of its compact design, the reflector provides a very broad, about 2 GHz at -3 dB level, RF transmission frequency bandwidth in the ON position. This is important in order to prevent the parasitic RF phase and amplitude modulation of the generated RF signal [108].

The pulse time structure was studied for the intermediate piston positions, based on the HFSS simulations of the transfer matrices for all the components, including PETS, power coupler, fixed and variable reflectors. The single bunch response of the PETS calculated with GdfidL was used as input. The results are shown in Fig. 5.107. Here the ramped nature of the generated RF pulses is optimized for the beam loading compensation in the main accelerating structure [109].

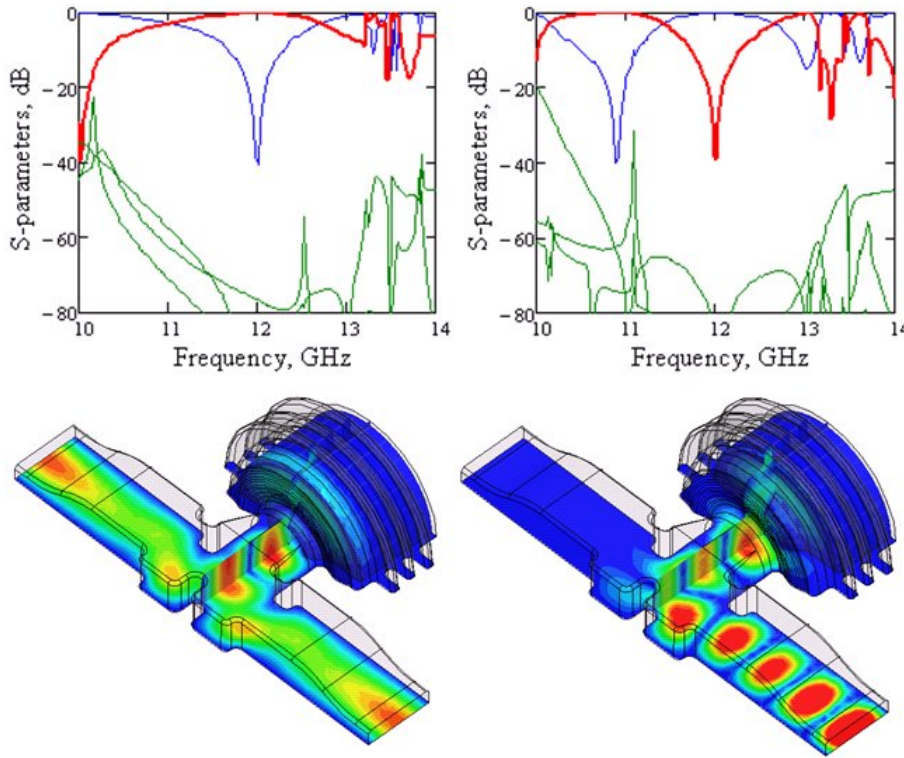


Fig. 5.106: Illustrations of the variable reflector operating in ON (left) and OFF (right) positions (electric fields are shown in a half geometry). In the S-parameters plots, the transmission is shown in red, the reflection in blue and radiations through the triple choke filter of the three possible modes are shown in green.

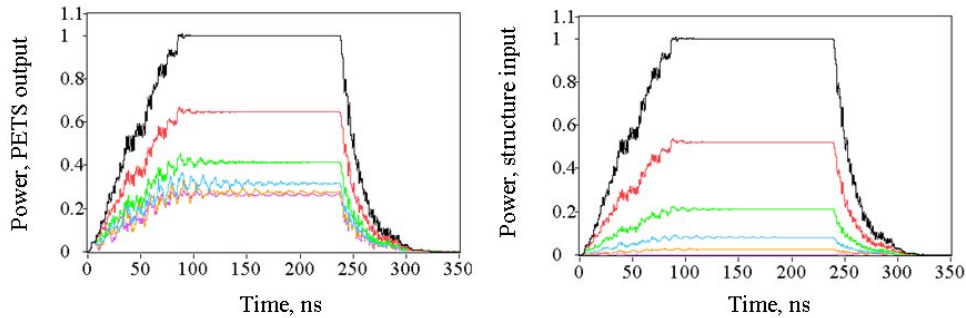


Fig. 5.107: RF pulse envelopes at the PETS output (left) and the structure input (right). Here the reducing amplitudes correspond to the different piston positions.

The RF power levels at the PETS output and at the structure input, as functions of the piston displacement, are summarized in Fig. 5.108. In the OFF position, the RF power extracted from the Drive Beam in the PETS is suppressed down to 25% of its original value, which is expected to be enough to prevent, or to reduce dramatically the probability of RF breakdown in the PETS itself.

The high RF power prototype of the variable reflector has been built and has replaced the previous external recirculation loop in the TBTS PETS. In this new configuration the internal recirculation can be established and the ON/OFF proof-of-principle experiments will be conducted.

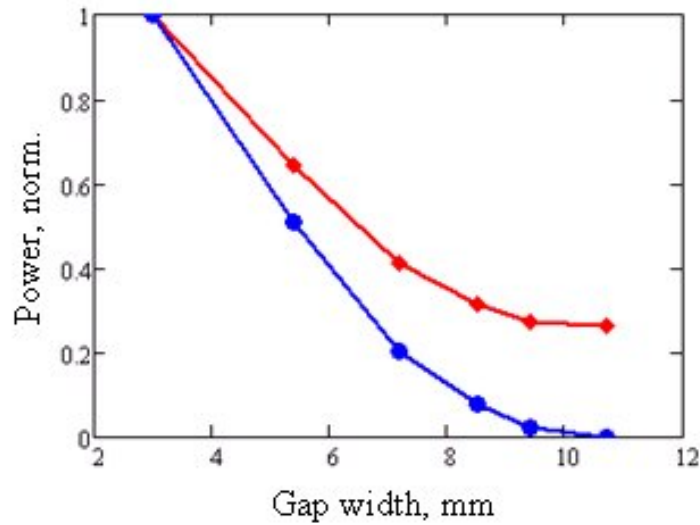


Fig. 5.108: Normalized steady-state RF power levels at the structure input (blue) and the PETS output (red) for the different piston positions

5.5.2.4 PETS fabrication, assembly and integration issues

Following the two-beam module layout, the concept of the ‘PETS unit’ has been introduced. A PETS unit consists of an assembly of two PETS, together with the corresponding mini-tank, and output coupler (see Fig. 5.109). The components of the PETS units are fabricated using conventional machining technologies and are assembled at a final stage using electron-beam welding (EBW). To gain in compactness, the PETS coupler also integrates the ON/OFF mechanism, as shown in Fig. 5.110.

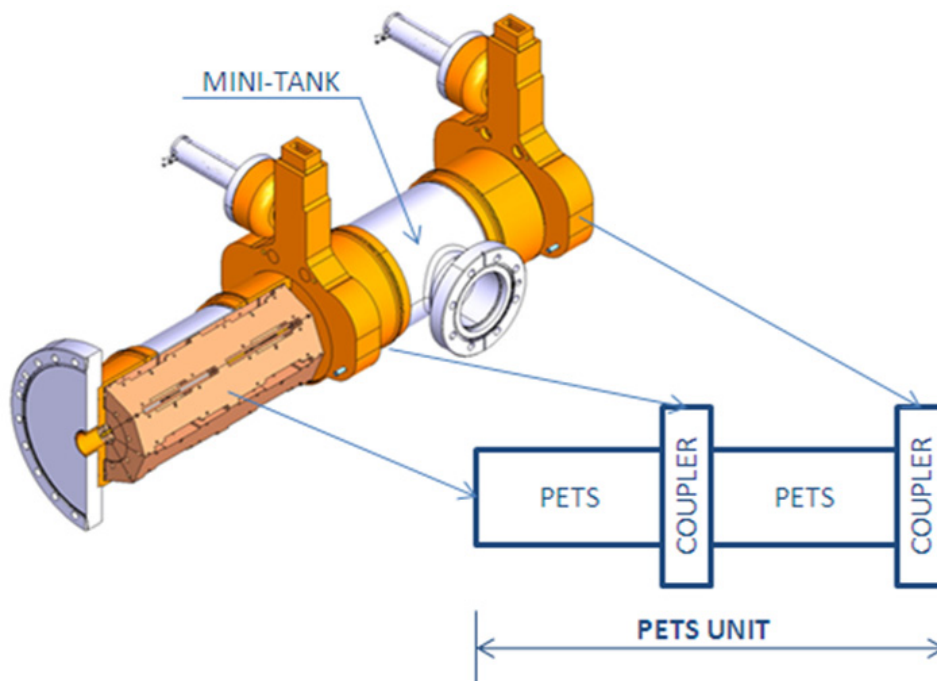


Fig. 5.109: General view of the PETS unit

The PETS bars and couplers undergo a very detailed cleaning procedure, including chemical etching. Silicon carbide damping loads are fired at about 1000°C before bolting them to each side of the

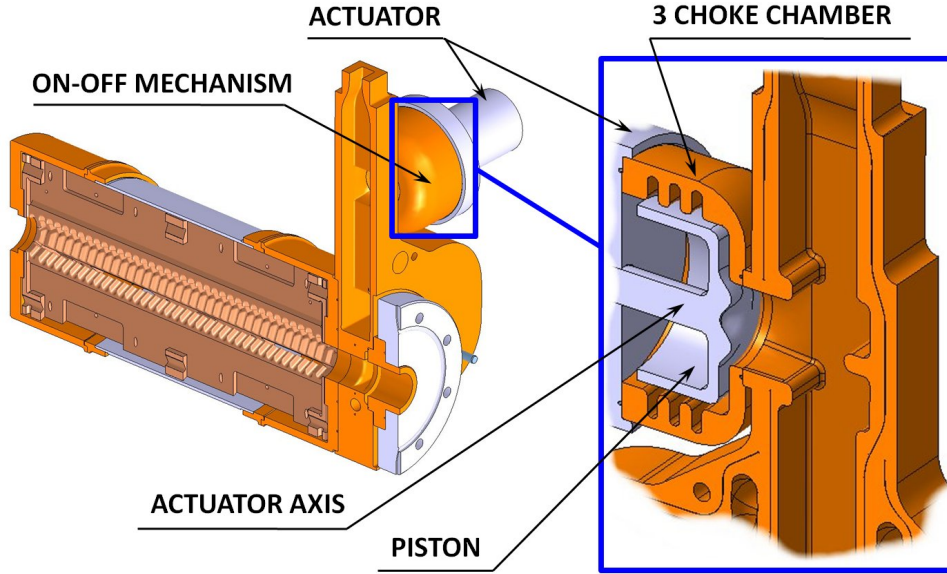


Fig. 5.110: Closer view of the single PETS with details of the integrated ON/OFF mechanism

bar. Afterwards, the 8 PETS bars are assembled by EBW under very clean conditions, and briefly baked under vacuum at about 200°C.

The fabrication of the PETS units also includes other steps:

- brazing of the two coupler halves with the RF flange
- brazing of the coupler assembly to the mini-tank interface pieces
- brazing of the extremity rings to the mini-tank

The last operation foresees the EBW of the coupler to the mini-tank assembly, see details in Fig. 5.111. A simplified version of this assembly procedure was successfully applied to the scaled 11.4 GHz PETS version, as shown in Fig. 5.111. At present, all brazing cycles are done under a partial pressure hydrogen atmosphere (few tens of mbar) and at a temperature varying from 900°C to 1000°C.

The fabrication and/or assembly errors can potentially detune the PETS synchronous frequency and thus affect the RF power production:

$$P(\omega) = P(\omega_0) \times \left| \int_0^L \exp \left(i \frac{\omega - \omega_0}{2c} \frac{1 - \beta}{\beta} z \right) dz \right|^2 \quad (5.29)$$

The impact of the different fabrication errors on the PETS power production has been studied, see Fig. 5.112. The most dangerous error is the PETS period corrugation depth; however, for an accepted level of the power reduction <0.1% (<35 MHz detuning) a $\pm 20 \mu\text{m}$ fabrication accuracy can be tolerated. The PETS assembly errors most likely will modify the PETS aperture (R) due to the bar's radial displacement. We have calculated that a $\pm 120 \mu\text{m}$ modification of the PETS aperture will also give a 0.1% power reduction. Another assembly error can come from the radial misalignments of the individual bars. In this case the PETS transverse symmetry will be distorted. This can cause the decelerating mode to couple out through the damping slot. We have calculated the dependence of the PETS external Q -factor (Q_ε), determined by RF losses in the damping loads, for the different radial displacement of a single bar and of the two neighbouring bars, see Fig. 5.113. It appears that the ratio Q_ε / Q_Ω remains above 100 for <140 μm radial displacement in both cases (Q_Ω is the PETS ohmic Q -factor).

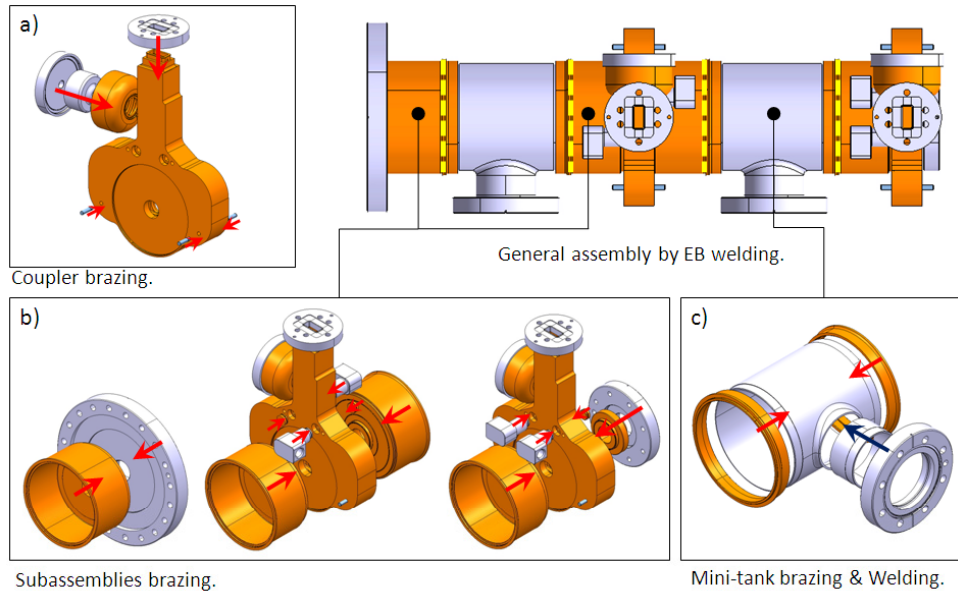


Fig. 5.111: Main assembly steps of PETS unit

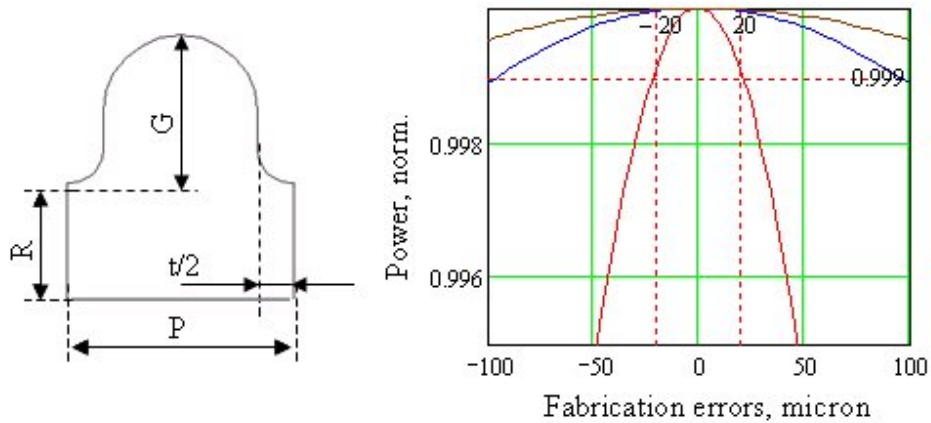


Fig. 5.112: Generic geometry of the PETS regular cell (left). The power production efficiency calculated for the different types of fabrication errors (right). Here the cell length (P) is shown in blue, corrugation depth (G) is in red and iris thickness is in brown.

Quality controls, based on a dedicated quality assurance system, are made to check the conformity during the whole fabrication process. The main quality controls are geometric controls and RF measurements. The required tolerances for the PETS bar fabrication are shown in Fig. 5.114. Two regions have been specified for the definition of the tolerance requirements. In the internal region 'A', the shape tolerance of the RF cells is $\pm 7.5 \mu\text{m}$ and the surface roughness is $0.1 \mu\text{m}$.

At present a few European companies are able to produce the PETS bars within the technical specification. The machining procedure includes conventional milling steps interleaved by annealing steps which are required to release the stresses. Several tests are being conducted to study the influence of annealing cycle parameters (temperature and time) on flatness and surface quality. For the moment the adopted annealing temperature varies from 180°C to 240°C and the holding time from 4 to 2 hours.

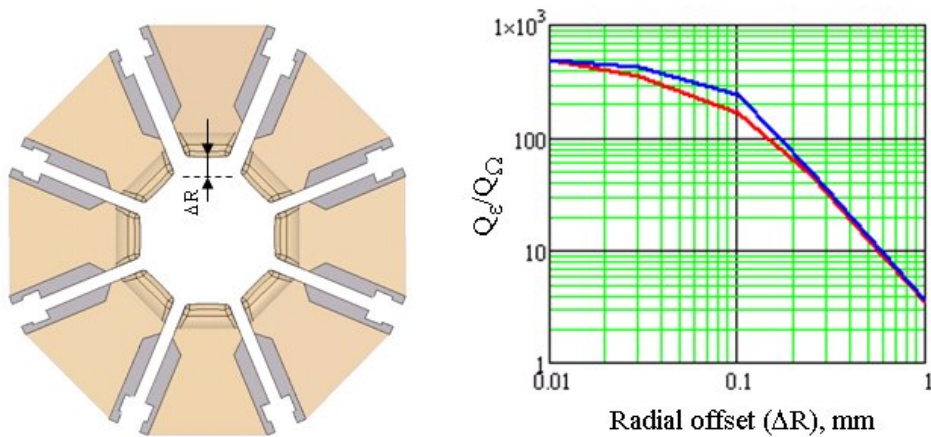


Fig. 5.113: The illustration of the possible single bar radial miss alignment (left). The ratio Q_{ϵ}/Q_{Ω} as a function of the single bar (blue) and of the two neighbourhood bars (red) radial displacements (right).

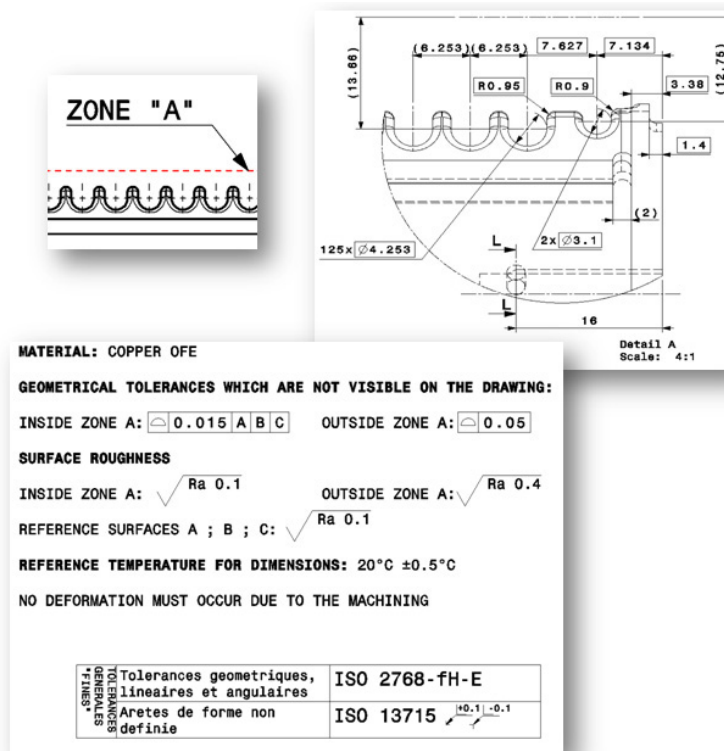


Fig. 5.114: The PETScell bar fabrication tolerances requirements

A typical result from geometrical control of the cells is shown in Fig. 5.115. In this case the achieved shape accuracy of $\pm 3\ \mu\text{m}$ is well within the specification.

To illustrate the achieved 12 GHz PETScell RF characteristics, a one metre long TBTS PETScell is given as an example. This PETScell was also the most challenging in terms of fabrication. The S-parameters measured at low RF power levels are shown in Fig. 5.116. The ohmic efficiency of 91.2% and the group delay of 10.1 ns were measured and are very close to the expected values: 91.14% and 9.98 ns respectively.

A special method was developed to measure the PETScell synchronous frequency. In the PETScell case,

5.5 X-BAND RF SYSTEM

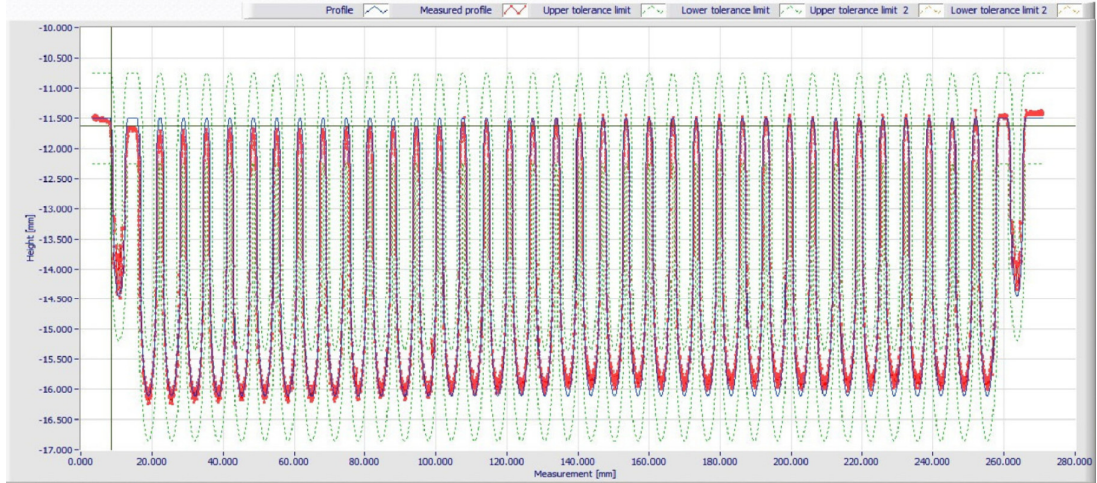


Fig. 5.115: Measured shape accuracy of a typical PETS bar

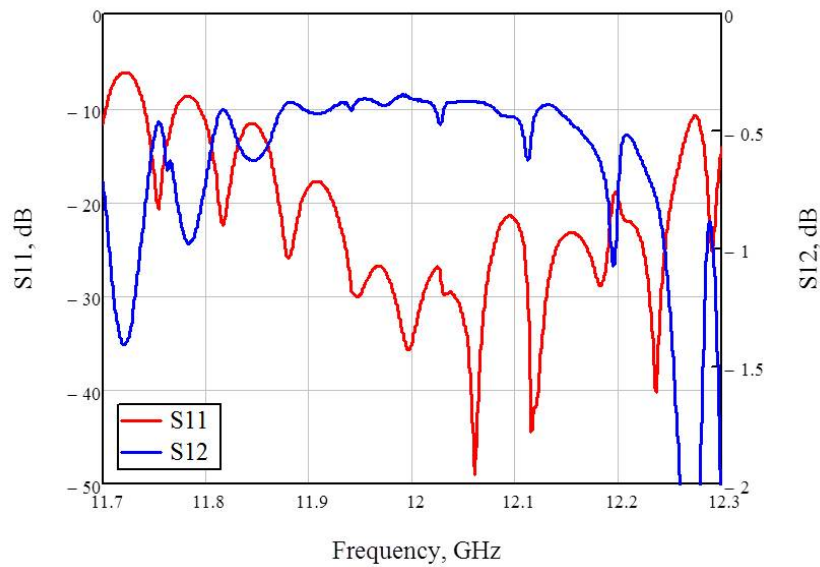


Fig. 5.116: The TBTS PETS low RF power measurement results

the standard bead-pull technique was not practical due to the over-moded PETS nature. Instead, a sliding antenna moving on an electronic ruler along one of the damping slots was used. This way, with a small (< -50 dB) coupling to the antenna, the fields were measured without any perturbation of the PETS decelerating mode. An example of antenna measurements at a fixed frequency and the reconstructed PETS dispersion curve are shown in Fig. 5.117. The measured PETS synchronous frequency was 9 MHz lower than the design value. This corresponds to about $6 \mu\text{m}$ of the cell shape fabrication accuracy.

Many PETS bars were fabricated by different vendors and, based on our experience, we can conclude that existing 3D-milling technology is well established, cost effective, and delivers the accuracy of the PETS fabrication within our specifications.

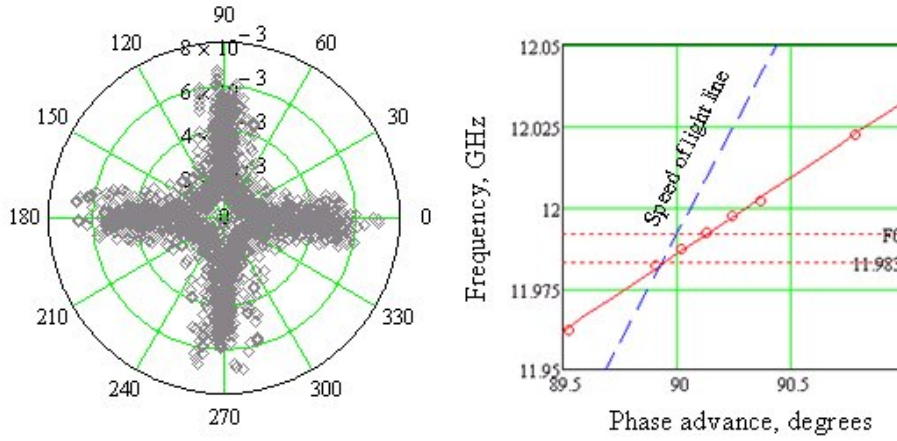


Fig. 5.117: The complex transmission at the PETS synchronous frequency 11.985 GHz measured with sliding antenna (left). The reconstructed PETS dispersion curve (right).

5.5.2.5 PETS high-power RF tests results

The main objective of the PETS testing program is to demonstrate the reliable production of the nominal CLIC RF power throughout the deceleration of the Drive Beam. These experiments are ongoing in CTF3 and results are discussed in detail in Chapter 7. However, in order to understand the ultimate performance of the PETS and to accumulate enough statistics for the breakdown trip rate characterization, the PETS was also tested using an external high-power RF source, similar to that which is normally used for testing the accelerating structures.

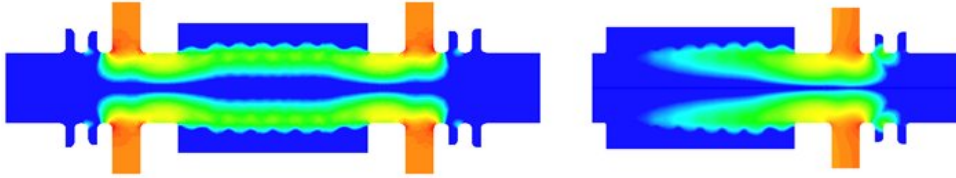


Fig. 5.118: RF power density distribution along the PETS for the RF source (left) and the beam (right) driven configurations

Comparing the two approaches in terms of the actual power flow in the PETS, see Fig. 5.118, the tests with the external RF power source were conducted in more demanding conditions than those needed for CLIC. There is an extra input coupler and uniform RF power distribution along the structure. The experiments with an external RF power source were done at the Accelerating Structure Test Area (ASTA), which was constructed and commissioned at SLAC in 2008 [110].

To do these tests, two 11.424 GHz scaled versions of the 12 GHz PETS were designed and fabricated. The PETS#1 was not yet equipped with damping material. The structure was tested at SLAC during 2009 and showed good performance; providing nominal CLIC parameters in terms of peak power and pulse length, but with higher-than-nominal breakdown trip rate: $\sim 2 \times 10^{-6}$ /pulse/m. The PETS#2 was equipped with damping material and represented the full PETS features. Following the experience gained after the PETS#1 testing, the fabrication, cleaning, and assembly procedures were significantly improved when preparing the PETS#2. For illustration, a few stages of the PETS#2 assembly process are shown in Fig. 5.119. The results of the PETS#2 low RF power measurements are summarized in Fig. 5.120. The structure was installed in ASTA (see Fig. 5.121) and tested during autumn 2010.

The history of the PETS#2 high power processing is summarized in Fig. 5.122. In total, 275 hours

5.5 X-BAND RF SYSTEM

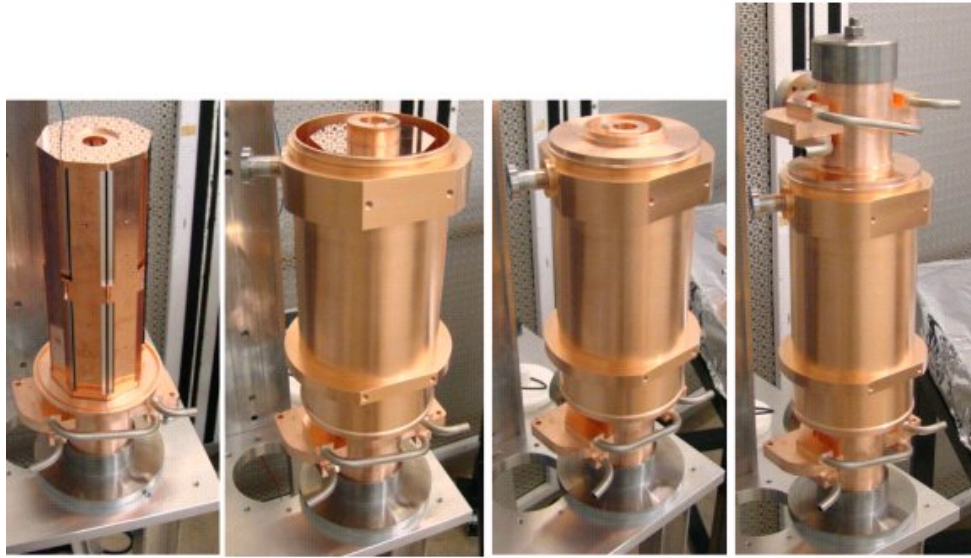


Fig. 5.119: Stages of the PETS#2 assembly process

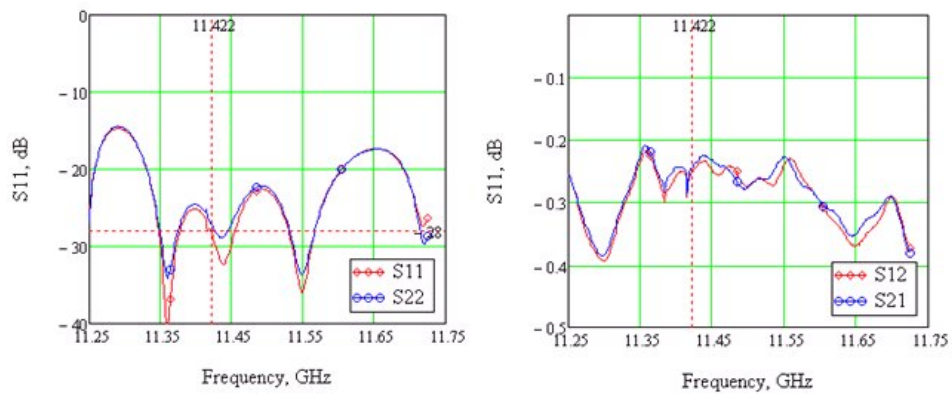


Fig. 5.120: The PETS#2 measured reflection (left) and transmission (right)

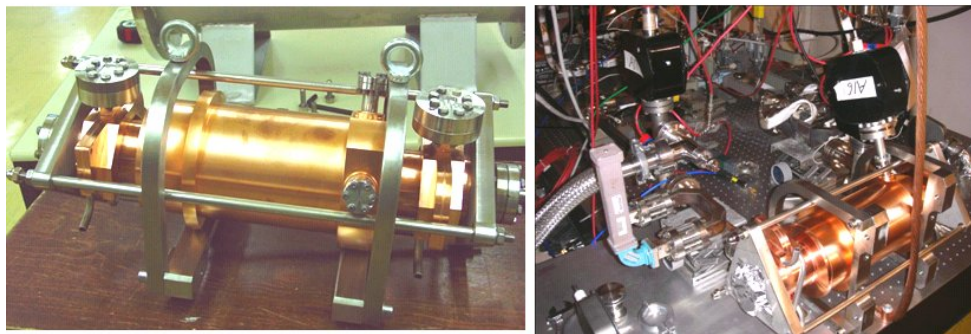


Fig. 5.121: The PETS#2 before shipping to SLAC (left). The PETS#2 installed in the ASTA experimental area (right).

of testing time were accumulated. It should be emphasized that the whole RF network in ASTA was conditioned at the same time, which somewhat limited the power production stability at a high power

level due to the frequent vacuum interlock trips in the different waveguide components.

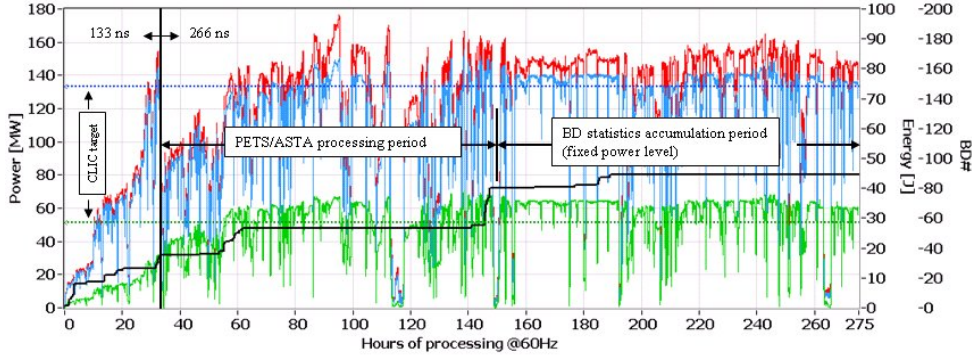


Fig. 5.122: The history of the PETS#2 high power processing at ASTA. Here in green is pulsed energy; in blue is RF power averaged over 266 ns, in red is a peak power, and in black is the accumulated number of breakdowns.

The breakdown activity in the PETS was registered in different ways: measuring the reflected and transmitted signals, with vacuum gauges and Faraday caps mounted at both PETS extremities. In the case of an event identified as a PETS breakdown, the RF power was shut down on the next pulse and restarted a few tens of seconds later, when vacuum interlocks permitted. In total, 91 breakdowns were registered during the whole testing period. Analysing each event we observed:

The breakdowns were detected primarily due to the activity in the Faraday cup channels.

The breakdowns fell into two categories: the first, when measurable changes of reflected signal were detected (type-1) and the second, when only Faraday cups channels showed the activity (type-2), see Fig. 5.123. The frequency of appearance was pretty evenly distributed between the two types.

None of the breakdowns showed measurable changes in the transmitted pulse shape and so, no missing energy was observed. In the real CLIC environment all these events would be practically undetectable and potentially would not affect the Drive Beam quality.

During the last 125 hours of testing, the PETS was running at pulsed parameters above the nominal CLIC ones. The statistical distributions of average RF power and registered breakdowns are shown in Fig. 5.124 and the typical RF pulse shape during that period is shown in Fig. 5.125.

To make an appropriate breakdown trip rate analysis, we have counted only the pulses with an average power above CLIC nominal. There were 1.55×10^7 such pulses in 125 hours. With 8 registered breakdowns, the PETS breakdown trip rate was 5.3×10^{-7} /pulse/PETS. Most of the breakdowns were located in the upper tail of the distribution and happened during the earlier stage of the run, which make the integrated BDR estimate rather conservative. During the last 80 hours, no breakdowns were registered giving a BDR $< 1.2 \times 10^{-7}$ /pulse/PETS.

The feasibility of the PETS operation at a peak RF power level $\sim 7\%$ higher and with RF pulses $\sim 10\%$ longer compared to the CLIC requirements was successfully demonstrated in klystron-driven experiments at SLAC. The tests at a fixed power level were considered complete when the measured breakdown trip rate was close enough to the CLIC specification of 1×10^{-7} /pulse/m. In this test this occurred after 80 hours of operation without any breakdown (BDR $< 2.4 \times 10^{-7}$ /pulse/m). The demonstration has been done in a more demanding environment than needed for CLIC with an extra input coupler and a uniform RF power distribution along the structure.

5.5.2.6 RF waveguide distribution network

In the CLIC module, the single PETS provides RF power for the two accelerating structures by means of RF distribution network based on the WR90 rectangular RF waveguide, see Fig. 5.126.

5.5 X-BAND RF SYSTEM

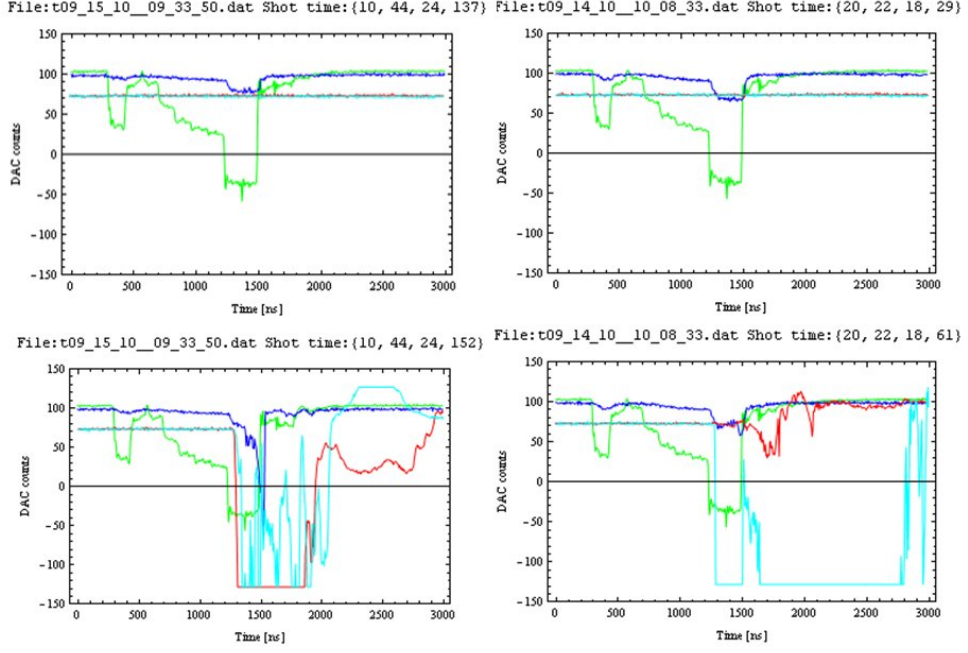


Fig. 5.123: The raw data logged into the breakdown counter. On the top are pre-breakdown pulses and on the bottom are breakdown events. Here incident power is in green, reflected is in blue, the Faraday cup signal at the PETS output is in red and in turquoise is the Faraday cup signal at the PETS input. Two types of events are shown. On the left is a ‘type-1’ event and on the right is a ‘type-2’ event.

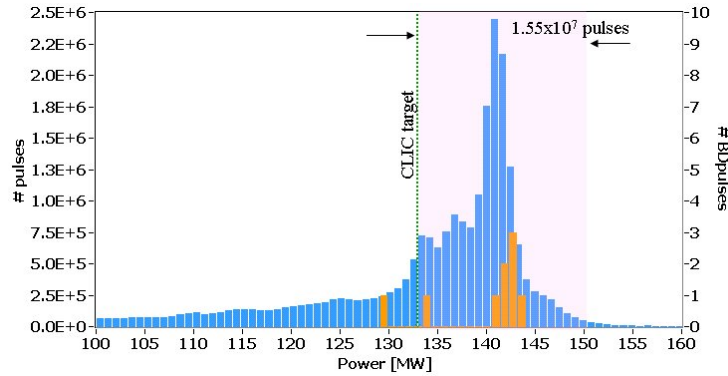


Fig. 5.124: The statistical average RF power distribution (blue) and distribution of registered breakdowns (orange)

In this configuration the broadband PETS and the narrow-band structures have a strong cross-communication. Thus, the isolation between them is necessary to avoid circulation of the reflected signals in the system. To do that, we have developed a compact E-plane 3 dB hybrid, see Fig. 5.127. It provides good matching in a broad frequency range. In this design, the maximum surface field at the nominal RF power level is 38 MV/m.

Another important requirement is the need for independent transverse alignment (of $\sim \pm 0.1$ mm) of the two linacs during machine operation. To avoid the mechanical stresses in a waveguide network we suggest using the choke-mode flange. This device allows for an electrically contact-free connection between the waveguides and the possibility to misalign transversely the two waveguides without introducing any RF phase errors. A fixed 11.424 GHz prototype of the choke-mode flange with circular groove and 2.5 mm wide slot was built (see Fig. 5.128) and tested in ASTA at SLAC at a high RF power level. It had reached $90 \text{ MW} \times 200 \text{ ns}$ (the maximum pulsed power available in ASTA at that time) with-

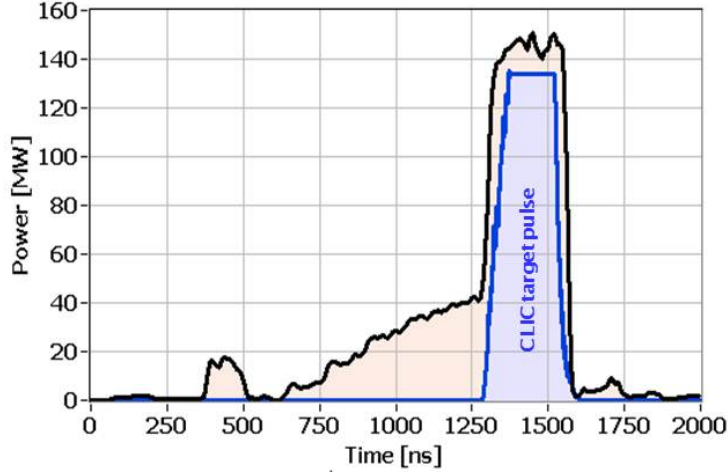


Fig. 5.125: Typical RF pulse shape in ASTA. Here, for convenience, we also plotted the shape of the CLIC target pulse.

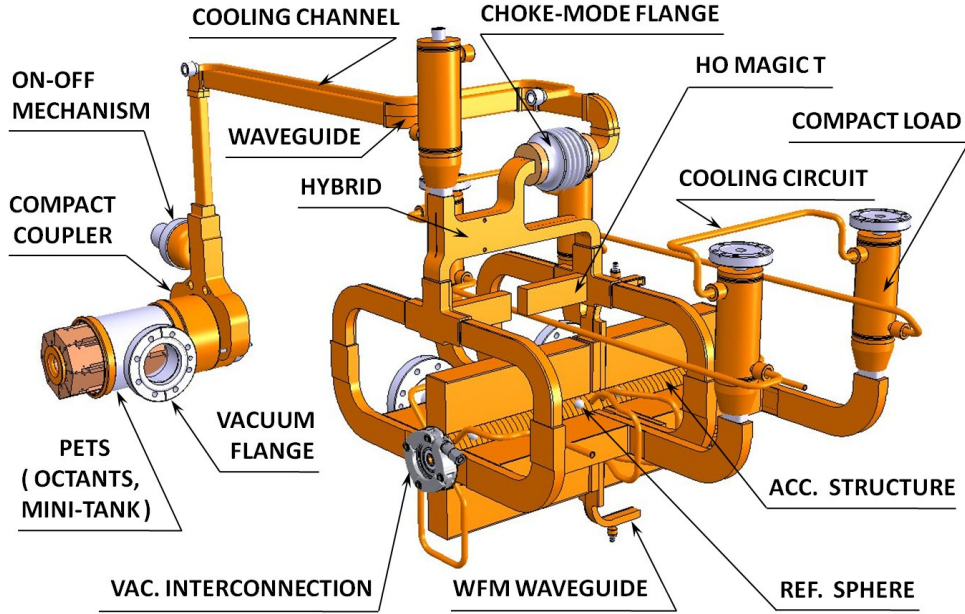


Fig. 5.126: Schematic view of the CLIC module RF system

out showing any breakdown activity. Unfortunately, with the circular choke configuration, the transverse shift along the narrow wall of the waveguide causes the coupling to the TM_{02} mode resonance which has a frequency very close to the operating one. This effect could be clearly seen in the measured spectrum of reflection in Fig. 5.128. We have replaced the circularly symmetric choke with the double-sector choke, as shown in Fig. 5.129, in order to avoid the resonance condition for the trapped symmetrical mode. In addition, the two cylindrical RF absorbers were installed in the vacuum chamber behind the choke to cancel any resonances in this volume over a broad frequency range. In this configuration, even for the relative shear shift of the waveguides by ± 0.5 mm in both directions, good (below -40 dB) matching can be obtained. We have calculated that a 1° twist and a 3° tilt also can be tolerated.

In order to avoid the situation where an unwanted HOM could be trapped at the structure's output coupler region and thus reduce the peak power level per load, it was decided to use two RF loads per accelerating structure. In total, including the load which is needed to terminate the differential port of

5.5 X-BAND RF SYSTEM

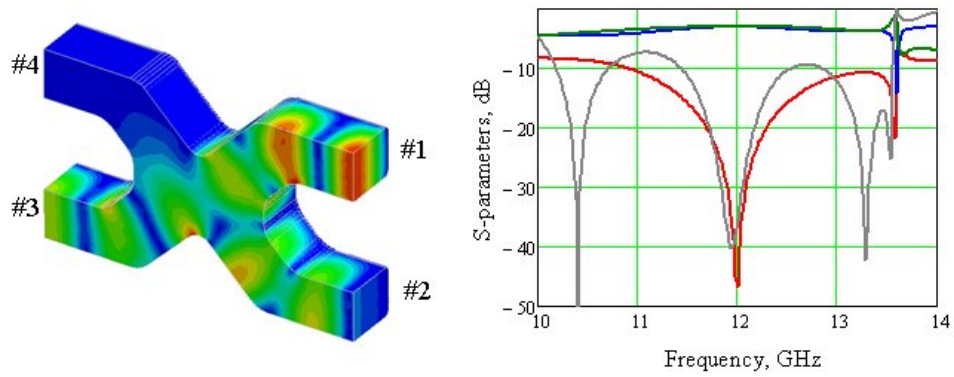


Fig. 5.127: Electric field plot and S-parameters of the compact E-plane 3 dB hybrid calculated with HFSS (electric field is shown in half geometry). In the S-parameters plot, the S11 is shown in red, the S12 is shown in blue and the S13 is shown in green. For illustration, the S11 for the case when ports 2 and 3 are short-circuited is shown in grey.

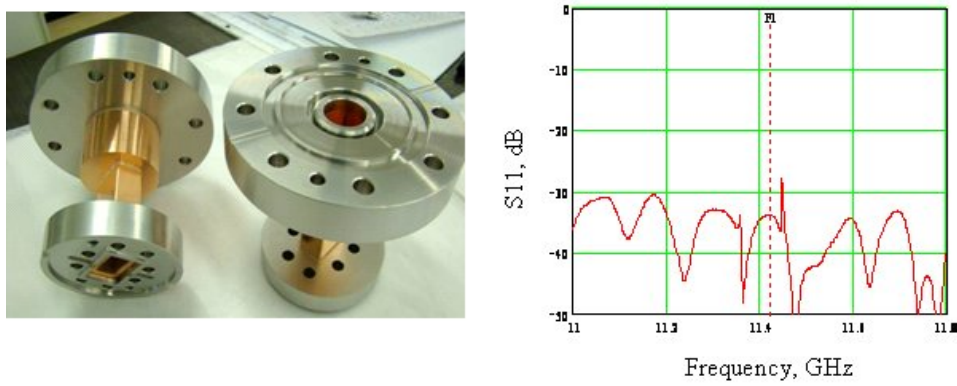


Fig. 5.128: The 11.424 GHz choke-mode flange prototype is shown (left) and the measured reflection of the whole assembly is shown (right)

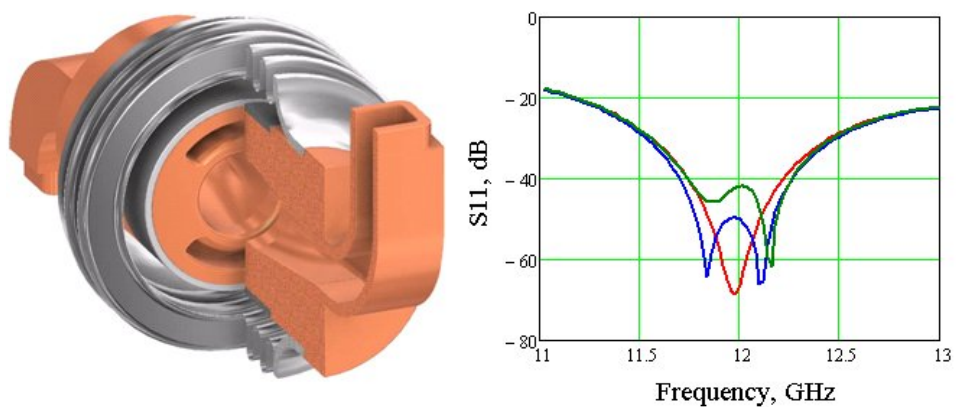


Fig. 5.129: Schematic view of the double-sector choke flange. In the S-parameters plot the reflection for the fully aligned flange is shown in red, for the 0.5 mm shift along the wide wall in blue, and for the 0.5 mm shift along the narrow wall is shown in green.

the 3 dB hybrid, five loads per single PETS are needed. This makes the RF load the most common RF component. For the nominal beam current in the main linac, the $7\text{ MW} \times 240\text{ ns}$ RF pulses at 50 Hz (90 W average power) should be dissipated in a single load. During the structure's initial RF processing period the RF power will be about factor of two higher than the nominal. These moderate peak and average RF power requirements made it possible to design a compact, 10 cm long, 'dry' RF load where the RF power is absorbed in a lossy ceramic (SiC) cylinder, see Fig. 5.130 and Fig. 5.131. The generated heat is evacuated through the direct interface between the ceramic and the external copper jacket equipped with a water cooling circuit. The load provides a good matching and its parameters are rather insensitive to the variations of the lossy ceramic RF properties. For the 15 MW peak RF power, the electric field on the ceramic surface does not exceed 7 MV/m for the normal component and 3 MV/m for the tangential component of the electric field.

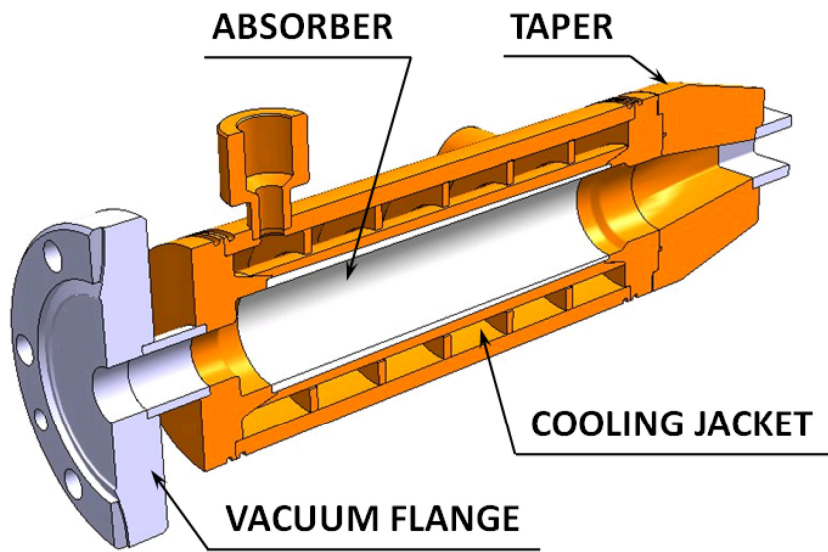


Fig. 5.130: Schematic view of the CLIC 'dry' RF load

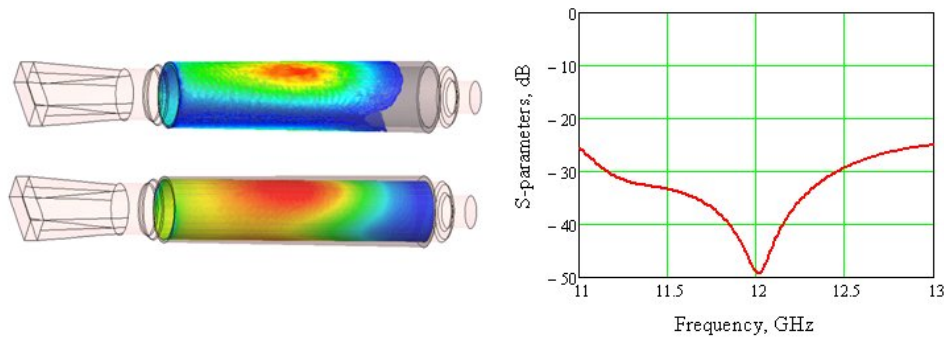


Fig. 5.131: The RF power density (top left) and electric field (bottom left) distributions inside the volume of the absorbing cylinder. The load reflection simulated with HFSS is shown right.

5.5.3 Two-beam RF system integration

5.5.3.1 Two-beam RF system layout

The smallest modular part of the RF system is called an ‘RF unit’. An ‘RF unit’ is composed of a PETS feeding a super-structure (two accelerating structures assembled as one mechanical unit) via the corresponding RF network. The RF network consists of several RF components, such as an E-hybrid, a choke mode flange and high-power loads.

The schematic view of an ‘RF unit’ with all related components is shown in Fig. 5.132.

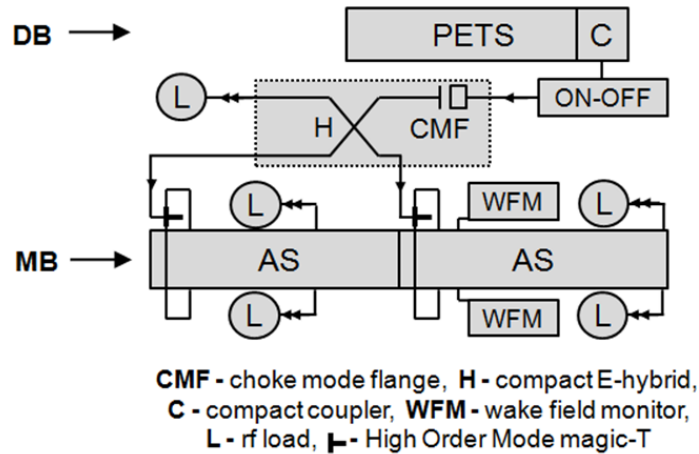


Fig. 5.132: Schematic view of an ‘RF unit’

The total number of RF units is 71 406. The inventory of components per RF unit is given in Table 5.36.

Table 5.36: Component inventory

Item	Number per RF unit		Total number
PETS	1	(8 octants)	71 406
PETS compact coupler	1		71 406
PETS on-off mechanism	1		71 406
RF components			
E-hybrid	1		71 406
Choke-mode flange	1		71 406
High-power load	5		357 030
Splitter	2		142 812
Accelerating structures	2	(26 cells each)	142 812
WFM	1		71 406

5.5.3.2 Operational scenarios

The 12 GHz RF system in the CLIC two-beam scheme consists of a PETS structure, an RF network, and two accelerating structures. RF diagnostics are needed to determine the accelerating gradient and the

phase of the Main Beam with respect to the RF. In addition, diagnostics are used to detect RF breakdown in either the PETS or accelerating structures.

From the point of view of RF instrumentation there are two types of RF units. The first two units and the last unit of each Drive Beam decelerator will be equipped as reference units. A schematic layout of the reference units is shown in Fig. 5.133. The other RF units will have only the RF signals picked up at the output loads of the accelerating structures to detect malfunctions. A reference unit has a beam phase monitor and a directional coupler to determine the PETS output amplitude and phase as well as the output power signals from the accelerating structures. Both phase measurements are needed to correctly time the Drive Beam with respect to the Main Beam.

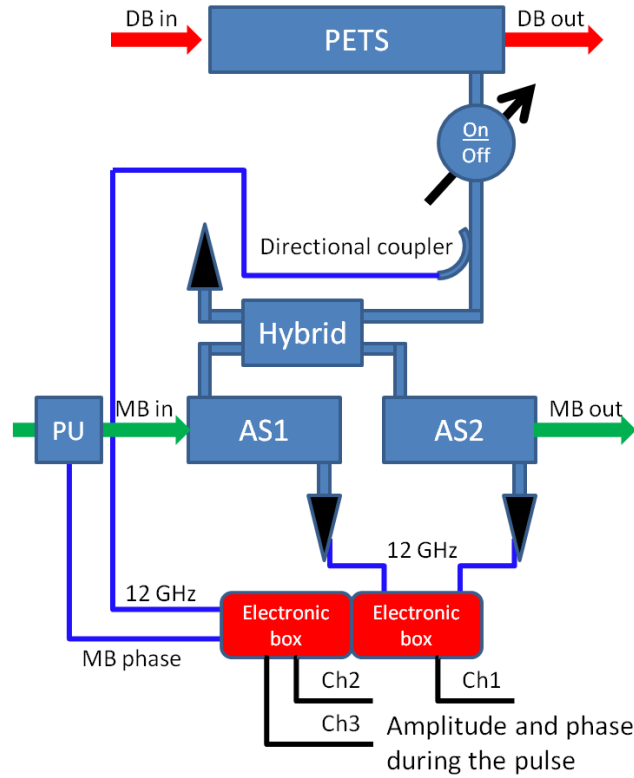


Fig. 5.133: A schematic view of the RF diagnostics of a reference two-beam unit

In both types of units the PETS output power is compared to the power measured at the output of the structures. This measurement allows breakdowns to be detected and checks that the whole RF unit works as foreseen. Standard RF units are equipped only with accelerating structure output-power detection. This allows breakdowns in the accelerating structures to be detected along with problems with the ON/OFF mechanism. A breakdown in the PETS can be detected by comparing the structure outputs with the PETS output power measurement in the reference units.

When persistent breakdowns are detected in a PETS structure or in the RF network, the power production for the corresponding PETS can be reduced by a factor of four using the ON/OFF mechanism. Since there is no indication that a single breakdown in a PETS structure would have a significant influence on the Drive Beam, the PETS structures would only be switched off in case of several consecutive breakdowns, in order to protect the PETS. If a breakdown in an accelerating structure is detected, the baseline scenario requires that the power to the structure be switched off for the next pulse using the ON/OFF mechanism. The RF unit would remain off for a defined time t_1 and then will be ramped up

to nominal power during a time period t_2 . Based on the procedures currently used in prototype tests, t_1 and t_2 are both equal to 20 s. It therefore takes a total of 40 s after a breakdown to recover the RF unit for acceleration. It is likely that this time can be reduced and tests will be performed to determine the optimum times.

Breakdowns in accelerating structures can kick the beam transversally. Measurements have been made in NLCTA and are currently underway in CTF3 [111]. Kicks have been measured up to approximately 5–35 kV which is large enough to lose that pulse for luminosity production but small enough not to harm the collimation system or the accelerator. By specifying a maximum 1% luminosity loss due to structure trips, this results in a maximum permissible trip rate of 3×10^{-7} /m/pulse for the 3 TeV case. In the 500 GeV case, a trip rate of 1.6×10^{-6} /m/pulse would be permitted. In order to compensate for the energy loss of structures in recovery mode, sufficient overhead has to be installed into the machine. The 5% energy overhead specified for CLIC allows for all trips within a 6σ distribution for the specified breakdown rate and 40 s recovery time. The energy overhead is permanently installed and the structures are powered but dephased. To activate the overhead, the phase of the Drive Beam with respect to the Main Beam is changed. This can be done pulse-by-pulse and sector-by-sector in the turnaround loops of each Drive Beam.

The scenario described above corresponds to the worst case because a detailed knowledge of the breakdown-kick distribution is still lacking and it is assumed to react on each breakdown. First studies indicate that in the low breakdown rate regime, most breakdowns are single events and do not cause the operation of the accelerating structures to become unstable. It is thus likely that it is not necessary to stop the RF for each breakdown. Breakdown kicks, statistics, and recovery will be studied in detail in the next few years in CTF3 and the klystron-based test areas to define the operational scenarios more precisely.

5.5.4 Crab cavity system

As the main linacs have a 20 mrad crossing angle and the bunches have a slender profile, crab cavities are required to rotate bunches so they collide head on (in a frame that moves perpendicularly to the relative velocity of the colliding bunches). Without crab cavities 90% of the achievable luminosity would be lost. They apply a z-dependent horizontal deflection to the bunch that is nominally zero at the centre of the bunch. It is important that the relative centre of rotation be identical for the two bunches otherwise they miss each other at the IP. In order to achieve identical centres of rotation the RF phases of the two cavities must be in perfect synchronism.

The crab cavity is located prior to the final dipole as shown in Fig. 5.134 but sufficiently close to be at 90° phase advance from the IP. Key challenges associated with maximizing luminosity are the accurate phase synchronization of cavities on opposing beam lines at the level of 4.4 fs (19 milli-degrees at 12 GHz) and adequate damping of wakefields. The requirement for beam to cavity synchronization is modest and depends on the depth of focus at the IP, it is of the order of degrees rather than milli-degrees. Cavity amplitude stability is modest being at the level of 2%.

As every sixth RF bucket is filled the crab cavities could be operated at any frequency which is a multiple of 1.99903 GHz, however the availability of power sources and major infra-structure guides the baseline frequency choice as 11.9942 GHz. Consideration of worst case beam-loading dictates an RF power requirement above 100 kW. High power RF at 11.9942 GHz could be provided either by klystrons or by a Drive Beam and PET structures. The Drive Beam for the main linac is not easily made available near the IP and it is also thought that phase jitter generated in the PET structures is likely to be too large for the phase synchronization target to be met. The SLAC XL5 klystron delivers up to 50 MW at 12 GHz and hence without using a SLED this power level is an initial constraint. Klystrons will have phase jitter on their output coming primarily from modulator droop and ripple. Whilst in principle this can be corrected, the difficulty of making an accurate phase measurement and correcting phase on a timescale much less than the 156 ns bunch train length looks insurmountable. It is proposed to use one klystron to

drive crab cavities on both linacs as illustrated in Fig. 5.134. Waveguide lengths from the klystron to the cavities are estimated to be at least 40 m with at least one bend to go round the detector.

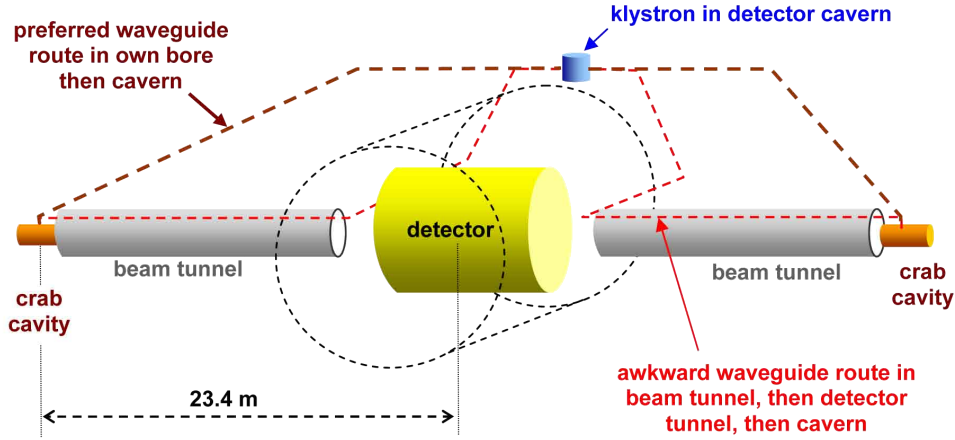


Fig. 5.134: Configuration of crab cavity RF system

A key challenge for the system is to maintain identical RF path lengths to better than $1\ \mu\text{m}$ between the power splitter and each cavity. With an advanced optical interferometer it may be possible to provide reference phases at the cavities that are synchronized to 1 fs.

5.5.4.1 Crab cavities

The kick requirement for the 1.5 TeV CLIC beam is 2.55 MV at 11.9942 GHz when $R_{12} = 23.4\ \text{m}$. This kick increases in inverse proportion to the frequency. The acceptable phase synchronization tolerance increases with frequency. The two big concerns for the CLIC crab cavity are vertical wakefield kicks and synchronization. Choosing a lower frequency certainly requires a larger RF source, it might reduce wakefield kicks but will probably make the phase synchronization target more difficult to achieve. Available infrastructure dictates baseline development at 11.9942 GHz.

Beam loading only occurs in crab cavities when the bunch is off axis and changes its sign depending on the side that the beam passes. At the location of the crab cavity, bunch offsets can be large. Beam loading in the CLIC crab cavities is likely to be unpredictable and cannot be controlled by feedback. The proposed solution for maintaining the correct cavity amplitude is to have a power flow through the cavity that is significantly higher than the maximum beam loading power requirement. This is most easily realized with a high group velocity travelling-wave (TW) cavity. A disc loaded waveguide TW structure is well proven as a deflecting cavity and has been selected as the baseline structure. The number of cells is kept small to achieve the power flow and reduce wakefields. The minimum number of cells required depends on the maximum achievable surface field without breakdown and the R/Q .

The constraints taken for the baseline development are a maximum surface field of $115\ \text{MVm}^{-1}$, a maximum cavity power of 20 MW, and a kick of 2.55 MV. Initial studies favoured the $2\pi/3$ mode hence the cell length becomes fixed at 8.3375 mm. The cell equator is adjusted to give the correct frequency. Initial studies considered an iris thickness of 2 mm and two ranges of iris radii. The first iris radius range yielding negative group velocities and meeting the constraints was 4.7 mm to 5.7 mm with a corresponding minimum cell number between 10 and 13. The second iris radius range yielding positive group velocities was 6.2 mm to 6.65 mm with a corresponding cell number range of 15 to 16. Essential work required before the project preparation phase is to demonstrate that a surface field limit of $115\ \text{MVm}^{-1}$ gives dipole structures that do not break down and there are no pulse heating issues for the 2 mm iris proposed.

Wakefields from the CLIC crab cavities should not reduce the luminosity by more than 2%. At

5.5 X-BAND RF SYSTEM

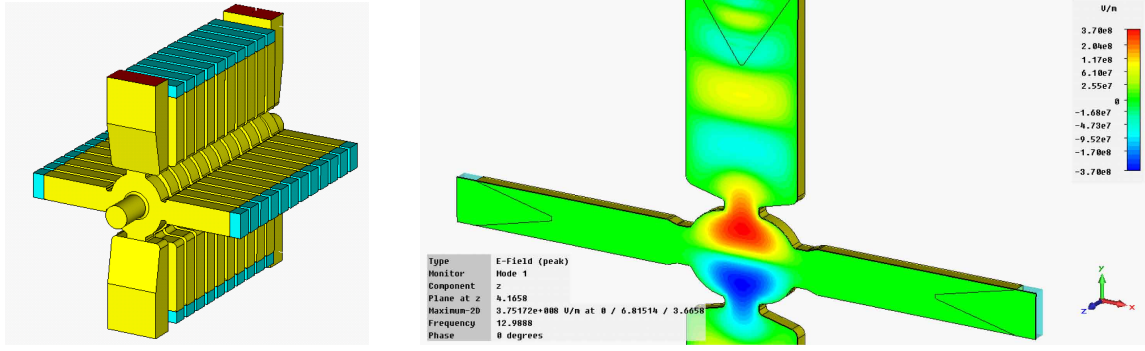


Fig. 5.135: Ten-cell crab cavity with waveguide damping (length ~ 90 mm)

1.5 TeV and with a beam offset of $35 \mu\text{m}$, the tolerable transverse wake potential W_t can be determined from the beam delivery parameters as 0.3 V/pC in the vertical plane and 1.38 V/pC in the horizontal plane. These wakefield tolerances need to be met for all offsets between the beam and the cavity centre axis, likely to be dominated by cavity alignment. The most dangerous modes are the dipole modes in the fundamental dipole passband in the vertical plane, particularly the mode with the same phase advance as the crabbing mode known as the ‘same order mode’ or SOM. By using an elliptical cell cross-section, the SOM frequency can be adjusted while the crabbing mode is kept at constant frequency. When the SOM is at a frequency which is a half integer multiple of 1.99903 GHz , the vertical wake is minimized and is relatively insensitive to manufacturing tolerances. For the CLIC crab cavity the SOM is tuned to be resonant at 13 GHz . With elliptical cells and small bunch offsets a moderate $Q \sim 600$ is required. Studies have indicated that the required damping Q factors can be achieved by using standard waveguide dampers with elliptical cells. This cavity design is to be regarded as the baseline. Illustrations of circular cells with waveguide dampers are given in Fig. 5.135. Longitudinal modes in the crab cavity do not pose any threat to the beam in the TeV regime.

5.6 Two-beam module

5.6.1 Overview

The CLIC two-beam configuration along most of the length of the Main and Drive linacs consists of ‘repeated modules’ [112] and [113]. Each Main Linac contains more than 10 000 such modules. The Drive Beam generates in each of the Power Extraction and Transfer Structures (PETS)(see §5.5.2) the RF power for two accelerating structures (see §5.5.1). Each module contains up to four PETS (see Fig. 5.136). Space for quadrupoles in the main linac is made by leaving out two, four, six, or eight accelerating structures and suppressing the corresponding PETS (see Fig. 5.137).

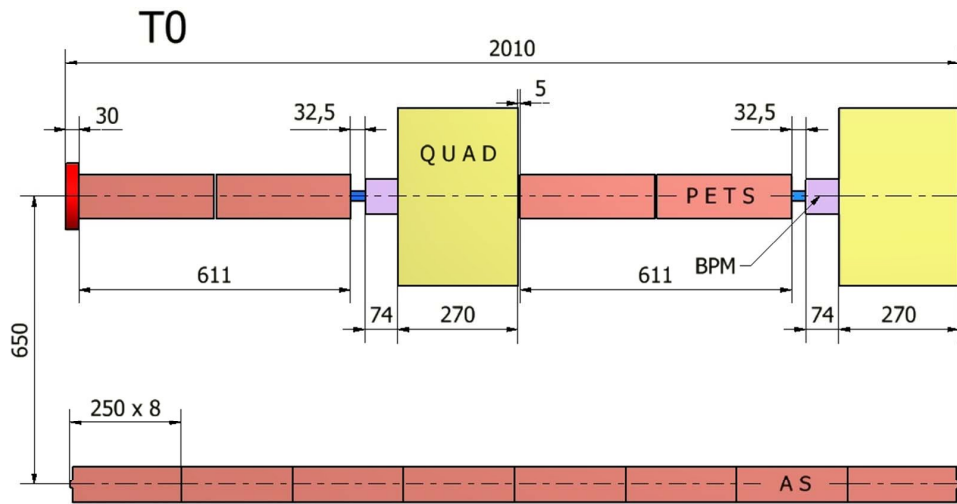


Fig. 5.136: Schematic layout of CLIC Type-0 module

In order to accommodate all needed configurations five types of modules are needed. Type-0 modules contain only accelerating structures in the Main Beam line (see Fig. 5.136) whereas Type-1 to Type-4 modules have Main Beam Quadrupoles (MBQs) of variable length, replacing 2, 4, 6 or 8 accelerating structures correspondingly (see Fig. 5.137).

The module components are mounted on alignment girders. The module length is determined mainly by considerations about the mechanical and thermal stability of the overall system. Presently a value of 2010 is chosen. Drive Beam linac simulations show that the Drive Beam Quadrupole spacing must be about 1 m with a quadrupole length of about 270 mm to produce sufficient strength. The remaining space is available for two PETS and the BPM. A length of 30 mm has been reserved for inter-girder connections. A few modules with only Main Beam and Drive Beam quadrupoles are needed where each Drive Beam is fed into and out of a Drive Beam linac sector.

5.6.2 Introduction

The two-beam module design has to take into consideration the requirements for the different technical systems. The main components are designed and integrated to optimize the filling factor and gain in compactness. Figure 5.138, shows a 3D view of a typical two-beam module, with the main components, such as accelerating structures, PETS and quadrupoles. In the following subsections all main technical systems are described. Some repetition of the material shown also in the specific chapters of these systems is unavoidable and wanted.

5.6 TWO-BEAM MODULE

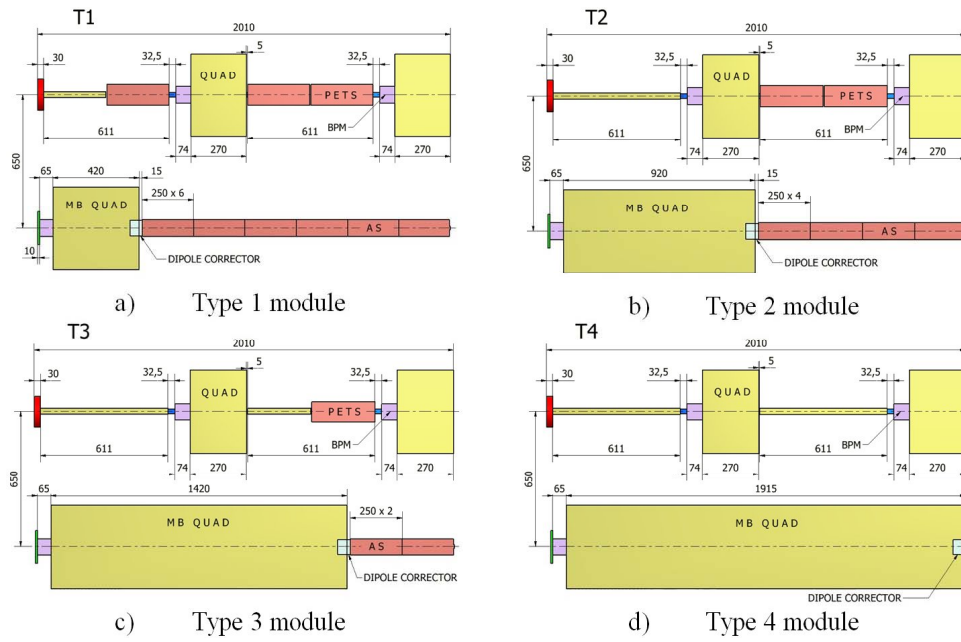


Fig. 5.137: Schematic layout of CLIC modules with different Main Beam quadrupoles

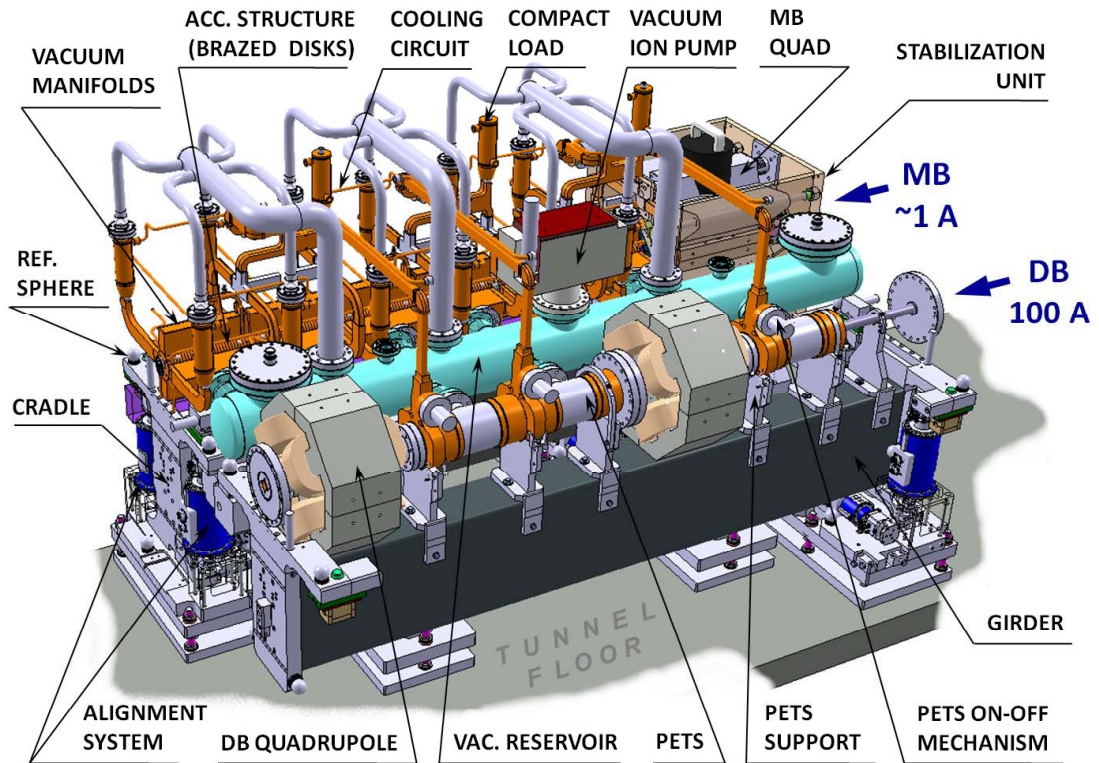


Fig. 5.138: 3D view of a Type-1 CLIC two-beam module

5.6.3 RF system

The main components of the RF systems are the accelerating structures, the PETS, and the RF network comprising the inter-beam waveguides and the RF components. The main parameters of the RF structures

are listed in Table 5.37.

Table 5.37: Main parameters of the RF structures

	Length [mm]	Aperture [Ø, mm]	Gradient [MV/m]	Power [MW]
PETS	308	23	6.5	136
AC	230	5	100	64

The design of the accelerating structures is based on OFE copper disks bonded together to form a stack. The design is based on the idea of using four waveguides to suppress the long-range transverse wakefields [114]. The cell geometry is adapted to the manufacturing process based on the bonding of disks with one side being flat and the other side carrying all the cell features. The geometries of the outer wall and damping waveguides have been optimized to minimize both the pulsed surface heating temperature rise on the outer wall and the penetration distance of the fundamental mode into the damping waveguides while maintaining the same damping efficiency. A so-called compact coupler will be used. In the coupler cell, two opposite waveguides are of the standard WR-90 width forming a double-feed coupler cell. The other two damping waveguides are kept in place to keep the damping as efficient as in the regular cells. HOM damping loads are mounted inside the damping waveguides. For this four manifolds will be brazed onto the disks. One of these will be connected to the central vacuum reservoir providing sufficient conductance to reach the required vacuum level. Two accelerating structures will be brazed together to form a superstructure. Details of assembly of the accelerating structures are given in §5.5.1.2. Position detectors called Wakefield Monitors (WFM) are integrated into the structure for beam-based alignment. One WFM is installed for each superstructure, at the beginning of the second accelerating structure. It consists of a waveguide which extends the damping waveguide with the same section. There are four waveguides per superstructure which are folded through 90°. Two coaxial RF pick-ups are implemented on the WFM waveguide: one on the large side to extract the TM-like modes and the other one on the small side to detect the TE-like modes. Details of this design are shown in Fig. 5.139.

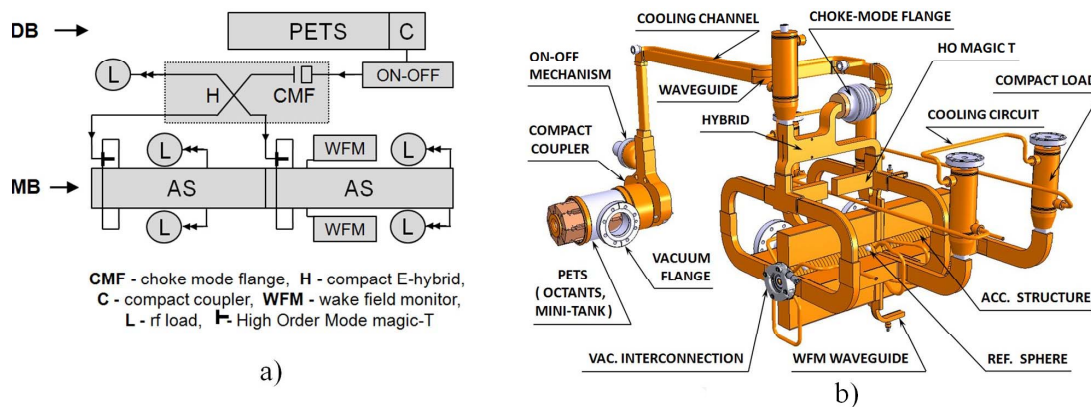


Fig. 5.139: Layout of CLIC Module RF Network; schematic (a) and 3D model of an assembly (b)

The CLIC Power Extraction and Transfer Structure (PETS) is a passive microwave device in which Drive Beam bunches interact with the impedance of the periodically loaded waveguide and excite pref-

entially the synchronous mode. The RF power produced is collected at the downstream end of the structure by means of the Power Extractor and delivered to the accelerating structure. In this layout, a single PETS should produce RF power for two accelerating structures. The PETS is comprised of eight octants separated by damping slots. Each of the slots is equipped with HOM damping loads. This arrangement follows the need to provide strong damping of the transverse modes. In periodic structures with high group velocities, the frequency of a dangerous transverse mode is rather close to the operating one. The only way to damp it is to use its symmetry properties. To do this, only longitudinal slots can be used. These slots also naturally provide high vacuum conductivity for the structure pumping. The upstream end of the PETS is equipped with a special matching cell and output coupler. The PETS octants are installed in a vacuum tank, which is directly brazed to the outside coupler.

During machine operation, it will be necessary to locally turn the RF power production off when either a PETS or an accelerating structure fails due to breakdown. The compact coupler, collecting and guiding the RF power from the PETS and transferring it to the accelerating structure, also integrates the so-called ‘ON-OFF’ mechanism.

The PETS (see Fig. 5.140) in the present configuration are composed of eight copper bars (see Fig. 5.141 (left)) milled with $15\ \mu\text{m}$ shape accuracy. Special slots between them are filled with absorbers for damping of the transverse high-order modes. Compact couplers (see Fig. 5.141 (right)) were designed to combine a few functions.

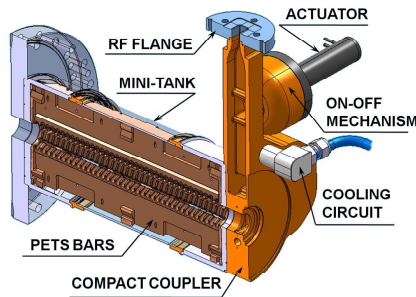


Fig. 5.140: 3D model of an assembly of one PETS

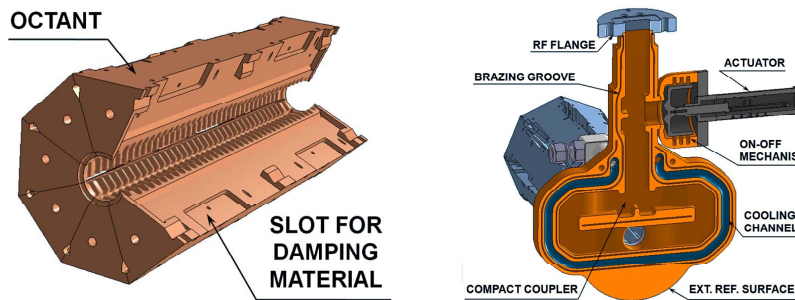


Fig. 5.141: Octants composing the PETS (left) and a compact coupler combined with ‘ON-OFF’ mechanism (right)

Being part of the RF network (see Fig. 5.139) they also provide an external reference of the DB for the alignment system and play the role of support. The ‘ON-OFF’ mechanism is implemented directly to the coupler body. The water cooling channel is machined inside each coupler and conduction cooling is used for the bars. The vacuum ‘mini-tank’, surrounding the PETS, is centred and fixed by electron beam welding on couplers thanks to specially machined grooves. The vacuum port on each ‘mini-tank’ is connected to the main vacuum reservoir, where the ion pump is fixed.

The CLIC two-beam RF network, starting from the PETS compact coupler, includes all the RF

components needed for the power extraction and distribution from PETS to ACS, such as standard X-band rectangular WR-90 waveguides, hybrids, and loads. A choke-mode flange, guaranteeing the power transmission without electrical contacts, is then required to cope with independent MB and DB alignment during operation. The next important component in the RF chain is the choke mode flange (CMF), which allows moving and aligning two beams independently. Its location is between the ‘ON-OFF’ mechanism and the hybrid, distributing the RF power between two adjacent accelerating structures. Figure 5.142 illustrates the layout of the RF network near the accelerating structure inputs.

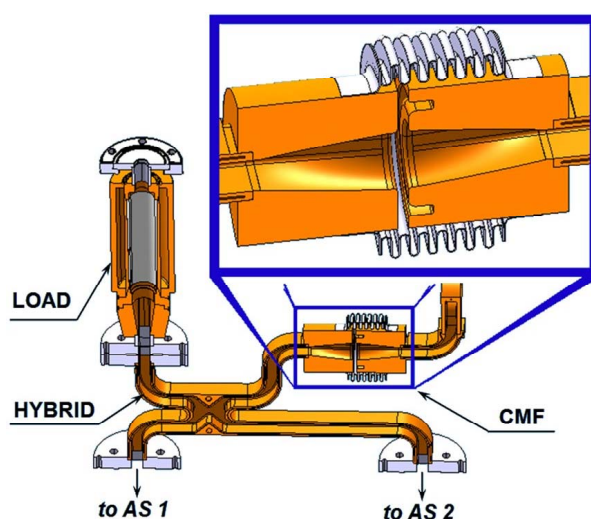


Fig. 5.142: 3D model of the choke mode flange, hybrid and load

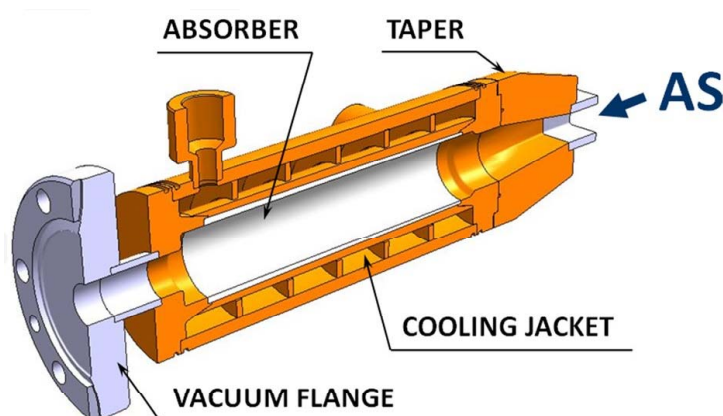


Fig. 5.143: Mechanical design of compact load

An RF load (see Fig. 5.143) is attached to one of the hybrid ports to avoid the reflection to the corresponding PETS. The RF splitters are used to equally feed the accelerating structures. The micro-precise assembly connections play a significant role for both vacuum and RF systems. Where possible, joints are implemented by brazing and welding. However in some places, where the assembly cannot be done without RF flanges, the ones recently designed at CERN were adopted.

5.6.4 Cooling system

Most of the RF input power is dissipated as heat in the module structures. All module types require a different cooling layout, because of the Main Beam Quadrupole which comes in four different configurations. Apart from the thermal dissipation, requirements for the cooling system are governed by the requirements of vacuum, alignment, and mechanical stability. Furthermore, vibration should also be taken into account. Vibrations of the lattice elements, if not properly corrected, can result in a loss in performance by creating unacceptable emittance growth in the linear accelerator and relative beam–beam offsets at the interaction point. The circulating water used to cool the lattice quadrupoles will increase magnet vibration levels which must remain compatible with the stringent stability requirements of the Main Beam Quadrupole. For a Type-1 module, the power dissipation induced in the main components is summarized in Table 5.38. The power dissipation values are given for unloaded beam conditions, which represent the worst case, for the sizing of the cooling circuit. The power dissipation between unloaded and loaded beam conditions varies by less than 15%. Considering the tight alignment and stabilization tolerances, the main components in the module are foreseen to be cooled in parallel as shown in Fig. 5.144. The accelerator is supposed to run at several power levels. Therefore, not only should the nominal centre-of-mass energy of 3 TeV be taken care of by the cooling system but also other intermediate settings such as 0.5 TeV. The total power dissipation for the modules of a 21 km long linac is about 70 MW, and about 95% is cooled by water.

Table 5.38: Power dissipation in a Type-1 two-beam module

	Quantity	Unit power dissipation [W]	Total power dissipation [W]
AS	6	411	2466
PETS	3	88	264
MB Quadrupole	1	890	890
DB Quadrupole	2	171	342
Loads	12	179	2148
RF network	3	11	33
Total			6143

The two-beam module cooling directly influences the size of the pipes to be housed in the underground tunnel. Considering a temperature difference across the two-beam module of 20 K, the corresponding volumetric water flow-rate is 3500 m³/h, leading to 600 mm diameter cooling pipes. About 65% of the flow passes through the super-accelerating structures. The temperature difference for each accelerating structure is then 5 K. To cope with longitudinal movements, resulting in a beam-to-fundamental-mode phase change, dimensions will be pre-compensated for the nominal operating temperature. Transverse movements affect the transverse wakefields and tilts give fundamental mode-driven kicks. The overall impact on the beam is being evaluated. Between unloaded and loaded conditions, the mass-flow rate can be adjusted to minimize the temperature profile of the accelerating structure.

5.6.5 Vacuum system

The present baseline for the two-beam module vacuum system excludes the possibility of heating the vacuum enclosure for geometrical stability reasons, leading thus to an unbaked system. Field ionization studies [115], [116] on the fast-ion beam instability result in a vacuum specification that is lower than the usual unbaked vacuum pressure (of the order of 10^{-7} – 10^{-8} mbar) by two orders of magnitude. As mitigation of this problem high speed pumping and a large vacuum conductance are needed. More details

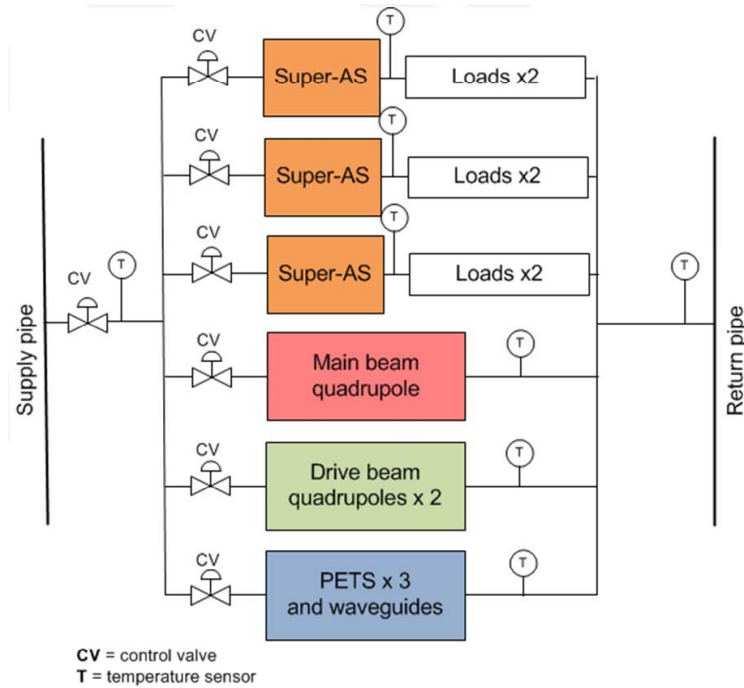


Fig. 5.144: Schematic layout for the two-beam module cooling

are given in §5.7.2.1. Figure 5.145 illustrates the layout.

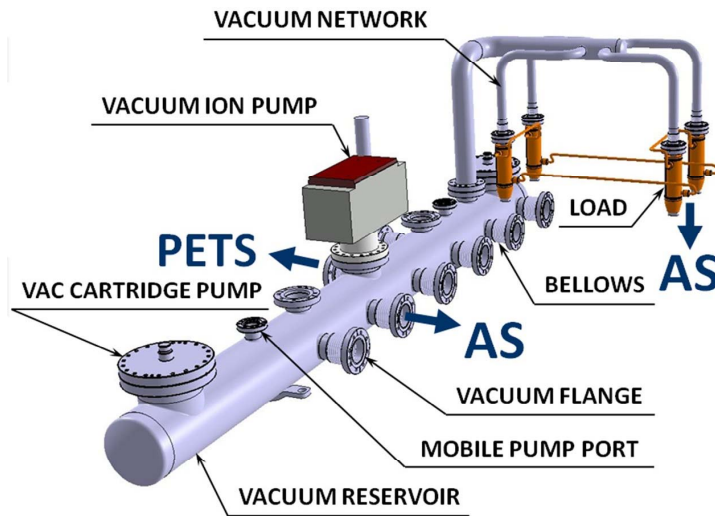


Fig. 5.145: 3D model of the CLIC module vacuum system

One vacuum ion pump and two cartridge pumps are connected directly via flanges. An additional pumping port, equipped with a roughing valve is foreseen for connection of a mobile turbo-molecular pump station, which will be used for initial pump down. The interconnections between main components should sustain the vacuum forces, provide an adequate electrical continuity with low impedance and remain flexible so as not to restrict the alignment. The damping material must be used in the interconnection space to avoid wakefields. The AS–AS interconnection design is shown in Fig. 5.146.

The vacuum envelope is mainly the ensemble of RF components. In addition the vacuum chambers for the quadrupoles are needed. For the Drive Beam Quadrupoles, it will consist of a stainless steel tube, copper coated, with an aperture of 23 mm and an outer diameter of 26 mm. For two-beam modules other

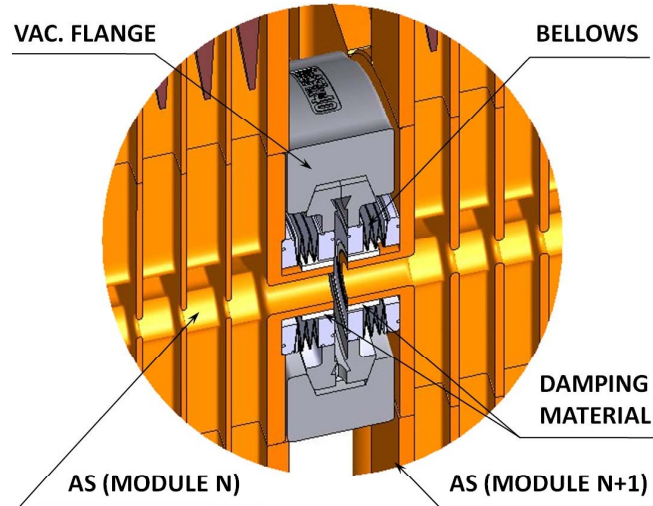


Fig. 5.146: 3D model of the module vacuum interconnection

than Type-0, drift tubes are required for the Drive Beam, based on the same design as the Drive Beam Quadrupole beam pipe, as well as a vacuum chamber for the Main Beam Quadrupole. The conductance of this chamber is limited leading to distributed pumping. A specific vacuum chamber shape has been developed to allow for the installation of two NEG strips in two antechambers. The vacuum chamber has to be installed during the assembly of the magnet.

The pumping system must not induce vibrations, especially to the Main Beam Quadrupole stabilization system. A combination of NEG pumps with high pumping speed and a sputter ion pump is used. A pumping port equipped with a roughing valve has to be foreseen for the connection of a mobile turbo-molecular pumping station or a leak detector.

The high filling factor required to minimize the costs means a very limited space allocated for the beam line interconnections. For the Main Beam, the interconnections consist of the continuity of the vacuum enclosure. Low impedance interconnections are not required; nevertheless, damping materials have to be installed in the interconnection gap to avoid wakefields. The vacuum envelope in these interconnections is based on bellows to assure flexibility and module alignment capability as well as an all metal connection. A dismountable solution with flanges and a metallic seal is preferred to avoid contamination by metallic dust. The same concept is used for the Drive Beam but in addition a low impedance continuity has to be assured to carry the image current of the high intensity beam (100 A). More details can be found in §5.7.

5.6.6 Magnet system

The magnet system is composed mainly of the Drive Beam Quadrupoles and of the Main Beam Quadrupoles.

5.6.6.1 Main Beam quadrupoles

Among the major components of the two-beam modules will be the Main Beam Quadrupoles (MBQs) needed for the focusing of the Main Beams along the linacs. The MBQs have different lengths as shown in Table 5.39. The total number of MBQs is 2010 units per linac. The four types of MBQs have the same cross-section with a magnetic aperture of 10 mm and a nominal gradient of 200 T/m.

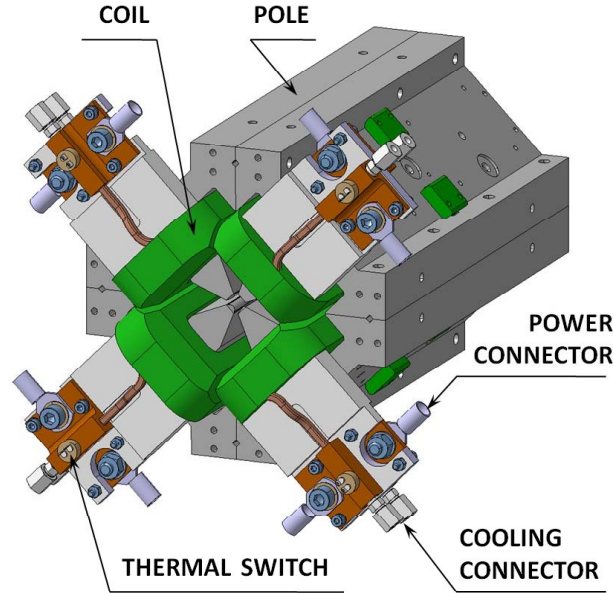
A very compact electromagnetic design for the MBQ was developed at CERN in 2009. Figure 5.147 shows a view (detail) of the Type-4 MBQ. The cross-section of the magnet is optimized for the beam requirements, while the interconnections (electrical and hydraulic) are, for the moment, optimized for the MBQ ‘prototype phase’ with frequent dismounting of the assembly planned for tests and pro-

Table 5.39: Main Beam Quadrupoles types (quantities for the two linacs)

Quadrupole type	Magnetic length [mm]	Quantity
Type-1	350	308
Type-2	850	1276
Type-3	1350	964
Type-4	1850	1472

cedures checks. This interconnection layout is fully compatible with the two-beam module integration, but for the final configuration the interconnection will probably be better integrated in the module layout considering series installation, access, optimized routing of technical service lines, etc.

Several prototypes of the MBQ (two Type-1 and two Type-4) are under procurement and will be tested with, and without, beam in the coming years.

**Fig. 5.147:** 3D view of the Main Beam quadrupole prototype

A beam-steering corrector capability on the Main Beam is also required. The corrector design which has been retained is for an ‘*ad hoc*’ small dipole to be added to each MBQ magnet. A basic calculation together with an integration study was done in order to check the feasibility of this solution.

Fig. 5.148 shows an example of the integration of such correctors. More details on the magnet design can be found in §5.2.2.

5.6.6.2 Drive Beam Quadrupoles

Each two-beam module contains two Drive Beam Quadrupoles (DBQ). The decelerators therefore contain 41 400 quadrupoles in total. This will be the largest family of magnets in the CLIC complex.

In the two-beam module baseline proposal, the allocated space for the DBQ is constant all along the decelerators, while the working gradient varies by one order of magnitude along the decelerator (from 81.2–8.12 T/m). This condition will satisfy the beam optics requirements along each decelerator sector, i.e., to provide an integrated gradient varying from 12.2 T down to 1.2 T as the average Drive Beam

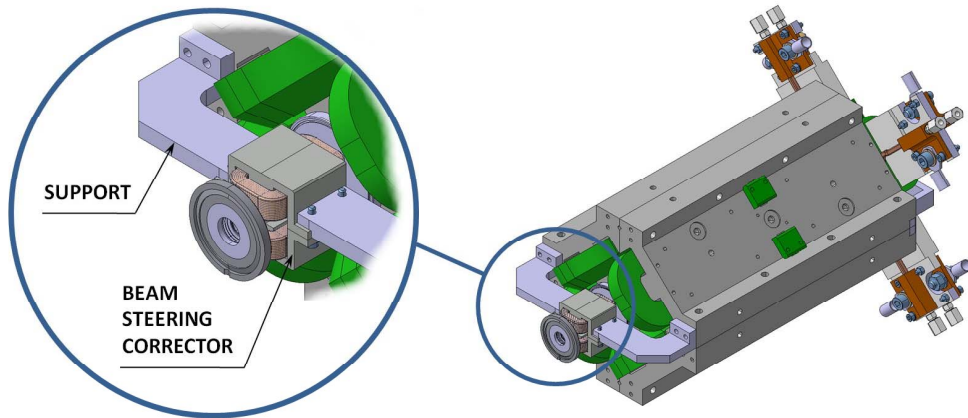


Fig. 5.148: 3D view of the beam steering corrector integration

energy decreases from 2.5 GeV down to 0.25 GeV.

The R&D activity for this family of magnets is proceeding along two lines: a classical electromagnetic (EM) design and a tuneable permanent magnet (PM) solution.

Figure 5.149 illustrates an integration study for the EM magnet solution and outlines the vacuum chamber, interconnection flanges, BPM and part of the PETS. See §5.2 for more technical details of the magnet solutions under investigation.

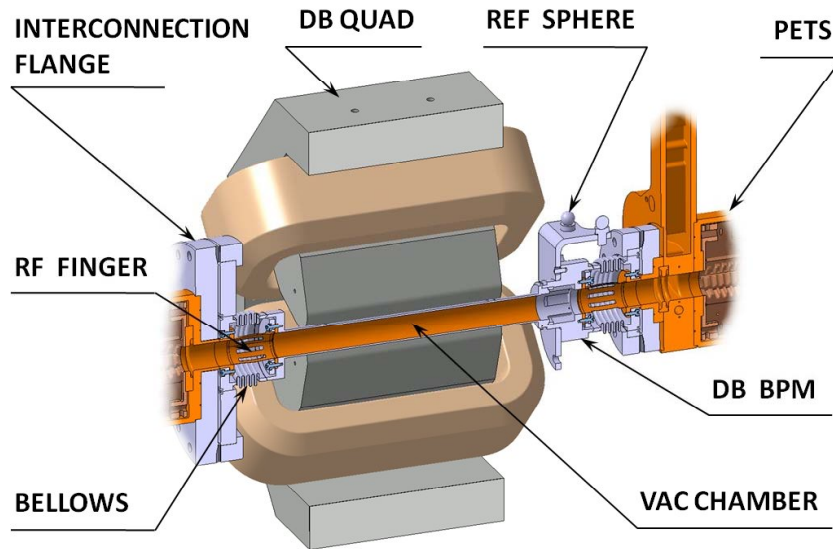


Fig. 5.149: 3D view of the MBQ prototype with BPM, PETS, vacuum chamber, and other ancillary components

5.6.7 Magnet powering system

The radiation levels in the Main Linac tunnel may reach 120 mSv/year, implying a substantial impact on the powering of the 50 000 magnets. If the power converters were to be placed in the tunnel, several aspects would be affected, namely the mean time between failures, efficiency, precision, control, and volume. Therefore, the powering of all magnets is done from dedicated radiation-free caverns, one per

accelerating sector. Whereas the specification for the power converters is eased by the radiation-free environment, much more cabling will be required since the mean distance between a two-beam module magnet and its power converter is about 260 m.

The powering strategy of the Main Linac quadrupoles, as described in §5.8, has been established in order to minimize both length and cross-section of the cables by adopting a cable sharing strategy for the Main Beam Quadrupoles and a trimming strategy for the Drive Beam Quadrupoles. The principle is based on the feeding of series-connected magnets, between 10 and 60 units, by modular power converters and the trimming of small currents in between each magnet in order to reach the current profile requirements.

The trimmers are only dissipative since the current profile requirement shows a monotonic slope. Besides, the precision on the trimmed current is very low (about 1%) when compared to the main magnet current. For these reasons, the trimmers can be implemented in the high-radiation areas, close to the modules, allowing savings on cabling costs. Each trimmer, as shown in Fig. 5.150, contains a dissipative active component like a MOSFET or a bipolar transistor, together with a fast-loop PI controller for reaching the needed trimmed current, between 0.1 A and 10 A. The control signals are exchanged with the control room through the CLIC front-end Acquisition and Control Module (ACM) (see §5.13) at a rate of up to 100 Hz.

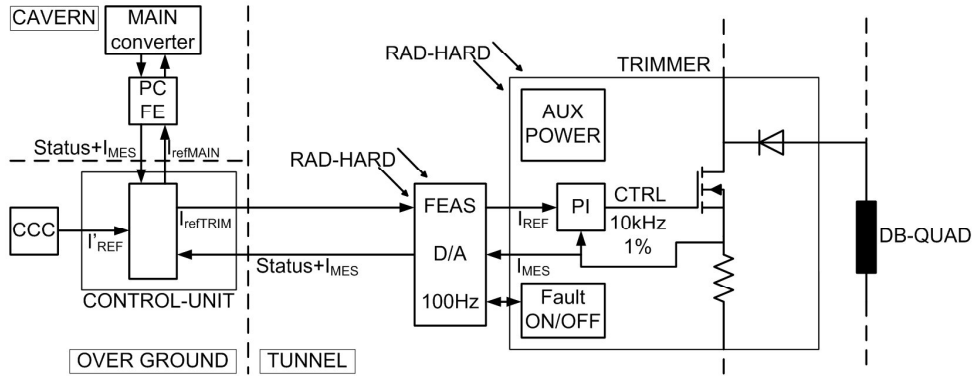


Fig. 5.150: Working principle of the trimmers

The Drive Beam decelerator requires several operational profiles including flexibility around the nominal point. The dimensioning of the main modules and the trimmers allow for the worst case operation. Because of the sizing of the magnets and their saturated curves at higher fields, the needs in current do not fit a linear curve, as illustrated by Fig. 5.151. Above 110% flexibility, the power consumption of the whole linac is strongly affected (viz. a 24 MW increase).

The main converters, powering the Drive Beam Quadrupoles, are rated to optimize the power dissipation to air. With a higher rated voltage, the dissipation is dominated by the trimmers, whereas at lower voltages, the dissipation is dominated by the cables. As illustrated in Fig. 5.152, an optimum is found for a rated voltage of 220 V, at any given current. In total $N + 1$ identical modules will be operated in parallel in order to provide some redundancy, with N corresponding to the minimal number of modules needed to provide the nominal current. For $N = 1$, twice the nominal power has to be installed. The overall overrating decreases when N increases. Considering the weak dependency between the power dissipation and the module current rating, a divider of the maximum current requirement (124 A) has been chosen, namely 42 A. Finally, the trimmers are rated for 4 A/12 V and dissipate a maximum power of 33 W.

5.6 TWO-BEAM MODULE

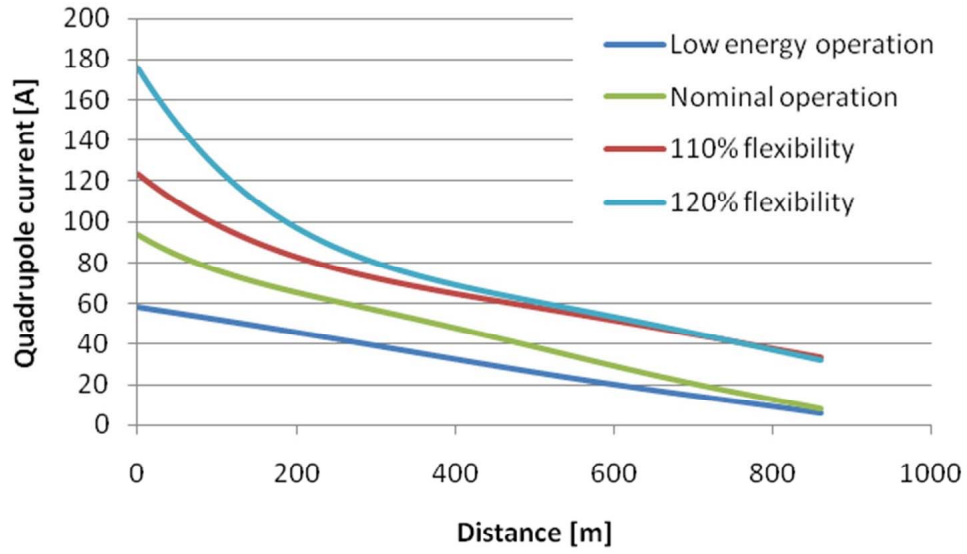


Fig. 5.151: Current profile and at different operation points and their corresponding power consumption

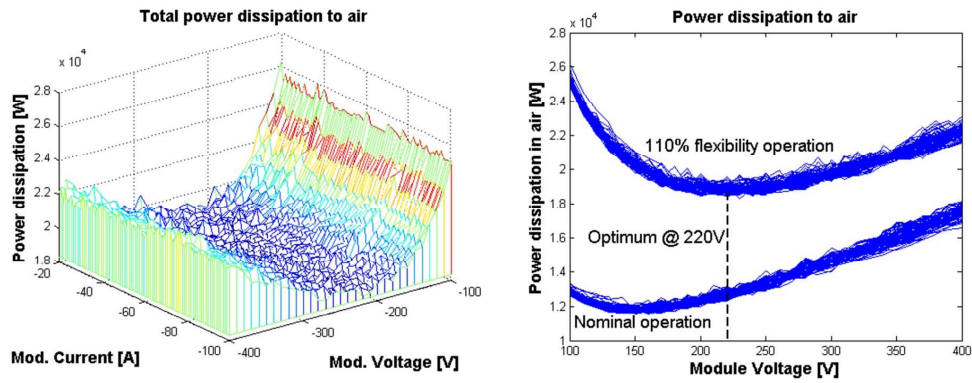


Fig. 5.152: Power dissipation to air as a function of the converters ratings

Because of the distribution of the Main Beam Quadrupoles, the powering of the Main Linac is not constant along the tunnel, as illustrated in Fig. 5.153. Between the first and the last sector, there is a factor 3 in the installed power, which impacts the number of cable trays, power dissipation in the tunnel, and length of the dedicated radiation-free cavern.

The above-mentioned powering strategies allow for a reduction in the amount of cable trays in the tunnel. Nine trays are considered as a worst case, including the Main Beam Quadrupoles and dipole correctors, the Drive Beam Quadrupoles, the transport magnets, and the AC power brought to the caverns.

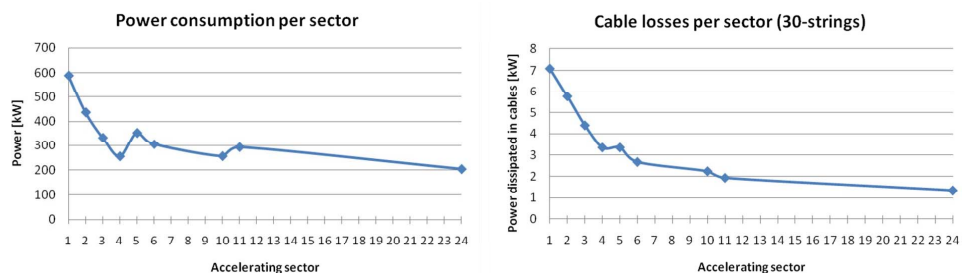


Fig. 5.153: Magnet and dissipated power for Main Beam quadrupoles along each accelerating sector

5.6.8 Supporting system

The micro-precision CLIC structures will be aligned on girders. The girder construction constraints are mainly dictated by beam physics and RF requirements. All girders are mechanically interconnected in a so-called ‘snake system’ (Fig. 5.154). This system allows for the precise alignment on the overall length of the two linacs.

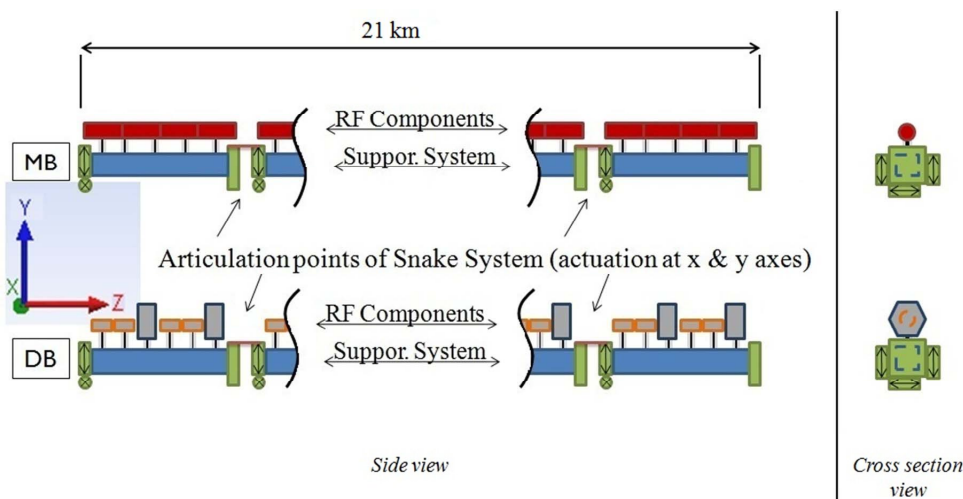


Fig. 5.154: Supporting ‘snake-system’ concept

A fundamental issue for proper operation of the snake system is the stiffness of the girders and the V-shaped supports. It is expected that the girders and the V-shaped supports will have higher stiffness values compared to other components of the CLIC two-beam modules. Therefore, the possible static deflection of the girders and V-shaped supports is taken into account at an early stage, while calibrating the actuators. For component alignment, it is necessary to transfer the reference, representing the beam axis, to the outside surface of the RF structures. This means that the supporting system must also include a feature for this reference transfer.

Damping and isolation of the dynamic behaviour of the two-beam modules are additional requirements for the girders in order to maintain the micrometric alignment of the particle beam. The main requirements for the girders are summarized in Table 5.40.

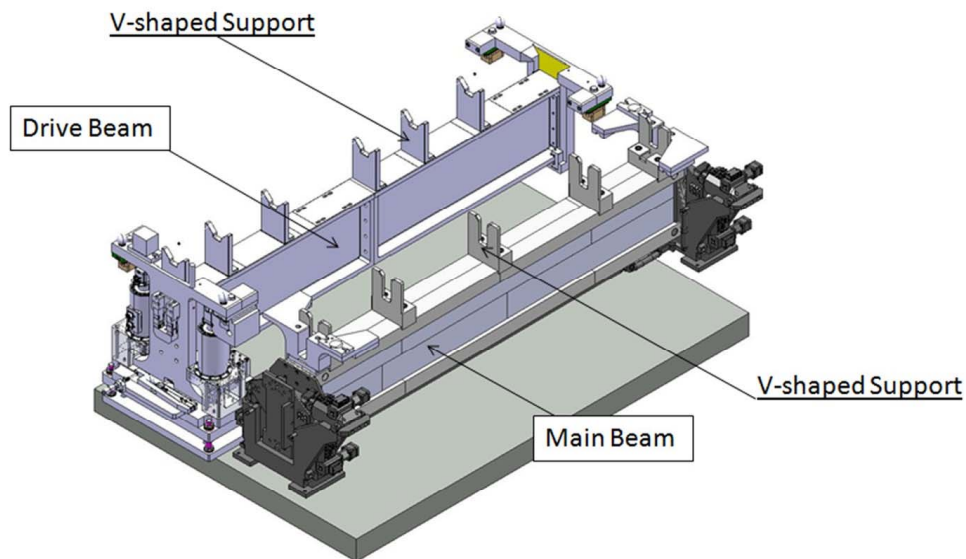
The basic guidelines of the study for the girder were the technical requirements and the preliminary weight estimation for the two-beam module. Girder material choice was important, along with feasibility control at this step of the study. Industrial materials (e.g., aluminium, stainless steel and others) were

Table 5.40: Girder technical requirements

Parameter	Requirement
Modulus of elasticity	≥ 400 GPa
Mass per girder (universal)	≤ 240 kg
Maximum vertical deformation in loaded condition	$10\ \mu\text{m}$
Maximum lateral deformation in loaded condition	$10\ \mu\text{m}$
Maximum weight on top of the girder (distributed)	400 kg/m

excluded due to the stringent girder technical specification. Alternative materials (e.g., carbon fibre or metal foams) could not meet the length specification for the girders. Therefore, the baseline material for the two-beam module girders was chosen to be silicon carbide (SiC) and as an alternative material the, newly developed, Epument mineral cast. Both the selected baseline and alternative materials meet the technical requirements and, in addition, allow optimized solutions with adequate damping behavior for possible accelerator dynamic loads (girder eigen-frequencies = 50 Hz).

The components between the RF components and the girder are the so-called V-shaped supports (Fig. 5.155). The design of such a component has raised issues of stiffness and space availability.

**Fig. 5.155:** CLIC two-beam module Type-0 supporting system

The V-shaped supports have to be firmly fixed on the SiC girder, which has very high rigidity but is brittle. Mechanical fixing methods are not compatible with such a condition. Therefore it has been decided to either glue or braze the V-shaped supports to have them fully integrated onto the girder (Fig. 5.156). A clamp with an intermediate part made of ‘soft’ material will be used to fix the RF components.

Based on the two-beam module integration constraints, only the external envelope of the girder was given in the technical specification. Therefore, according to the fabrication methods and the available precise machining applications (for the reference surfaces), different cross-sections were investigated.

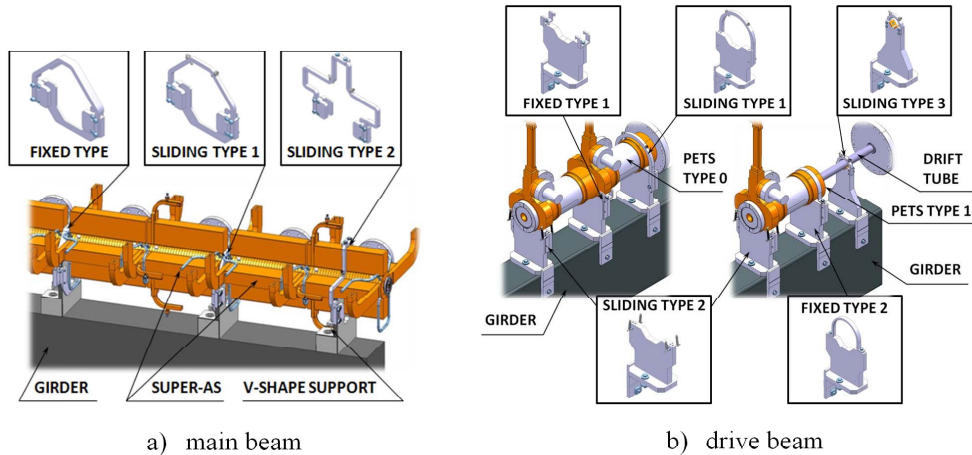


Fig. 5.156: Typical configurations of V-shaped supports

Internal girder reinforcements were analysed and simulations for different I-shaped and H-shaped girder cross-sections performed. Two baseline configurations of the prototype two-beam module girders were selected: one solid and one hollow, reinforced, I-shaped girder. These two configurations were chosen for different reasons:

- The solid I-shaped girder provides stability and stiffness for the two-beam module. The reference surfaces are simply obtained by high-precision machining.
- The hollow I-shaped girder is formed by glued standardized SiC beams. The machining of the reference surfaces is, in this case, achieved by pre-stressing the overall girder on its longitudinal axis.

Prototype girders of the two-beam module were procured and delivered to CERN in December 2010 [117, 118]. Extensive alignment tests are being conducted in parallel with precision assembly investigations.

5.6.9 Alignment system

Pre-alignment of the two-beam modules will take place when beam is off. It will consist of two steps: a mechanical pre-alignment (see §5.17) which will pre-align all the components within ± 0.1 mm with respect to the Metrological Reference Network (MRN), and an active pre-alignment fulfilling the requirements described here. For a sliding window of 200 m, the standard deviations of the transverse position of each component with respect to the straight fitting line must be inferior to a few microns. The total error budget in the determination of the position of components has been calculated. It corresponds to 14 mm for the RF accelerating structures and 17 mm for the Main Beam Quadrupoles [119].

The pre-alignment can be divided in two parts: the determination of the position of the components and re-adjustment of the supports.

5.6.9.1 Determination of the position of the components

See also §5.17 which deals with the general strategy of alignment [120, 121].

The determination of the position of the components is performed via a combination of two measurement networks:

5.6 TWO-BEAM MODULE

- a Metrological Reference Network (MRN) consisting of overlapping stretched wires provides an accuracy and precision of a few microns over at least 200 m, and
- a Support Pre-alignment Network (SPN) associates proximity sensors (capacitive based Wire Positioning Sensors (cWPS)) to each support which measure with respect to a stretched wire. This system provides a precision and accuracy of a few microns over 10–15 m.

Both networks will perform measurements with respect to the same stretched wire alignment reference. Overlapping stretched wires will be located between the two beams, as illustrated in Fig. 5.157.

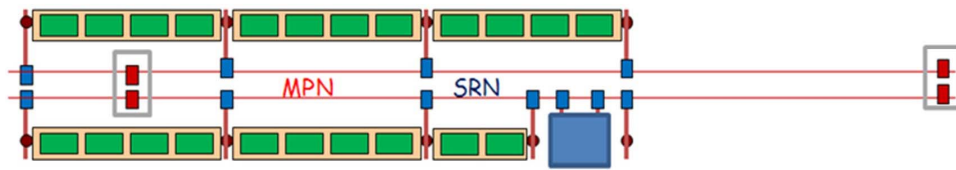


Fig. 5.157: Module and measurements networks

Each cradle of DB or MB girder will be equipped with one cWPS and a two-axis inclinometer. Each MBQ interface plate will be equipped with two cWPS and a two-axis inclinometer. A temperature probe will be installed on each support, close to the sensors in order to correct dilatation effects.

The MRN network (see Fig. 5.158) will consist of complete metrological plates and intermediate metrological plates.

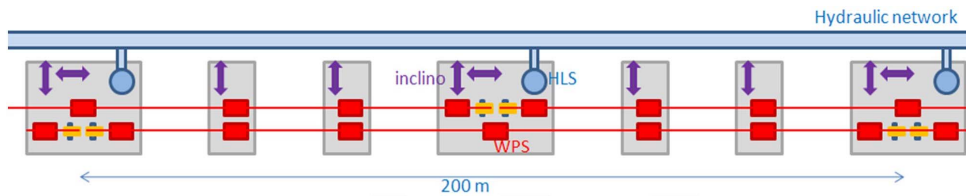


Fig. 5.158: Configuration of MRN network

Every 100 m, a complete metrological plate will be located at the extremities of one wire, and at the level of the sag of the overlapping wire. This plate will host three cWPS, one per wire, and one HLS sensor allowing computation of the catenary of the stretched wire. Intermediate plates, hosting two cWPS and one two-axis inclinometer, will provide redundancy in the determination of the straight reference computed from the overlapping wires.

With the combination of these networks, the position of each sensor will be known and determined in a general coordinate system. Prior to this installation, during the ‘fiducialisation’ process, the zero of each component will be determined in the support reference and, at the same time, the position of each sensor will be measured with respect to the support reference. This will be carried out on a 3D Coordinate

Measuring Machine (CMM), with an uncertainty of measurement of 0.3 mm. This allows the position of the zero of each component to be calculated in the general coordinate system. All the components will be equipped with non magnetic mechanical interfaces for 0.5 inch diameter spheres, while supports will be equipped with non-magnetic mechanical interfaces for 1.5 inch diameter spheres. These mechanical interfaces will be measured on the CMM during ‘fiducialisation’ process, and will allow the checking of the position of the components on their supports after transport, just before installation [122].

5.6.9.2 Re-adjustment of the supports

DB components (PETS and DB quad) and MB accelerating structures will be pre-aligned on girders linked by a so-called articulation point allowing displacements along 3 DOF, while MBQ supports will be re-adjusted independently from the other supports within 5 DOF [123]. Linear actuators will support girders and cam movers will support MB quadrupole interface plate. These two solutions for re-adjustment will provide sub-micrometric resolution over a range of ± 3 mm. A pre-alignment zone has been defined in the underground tunnel (see CLIC tunnel typical cross-section) and corresponds to the interface with ground. This includes shimming which will compensate for floor imperfections and long-term local variations. It also includes mechanisms for initial pre-alignment (resolution of manual displacements better than a few hundred microns along vertical, radial, and longitudinal axes, within a range of ± 5 mm). Once the initial pre-alignment is carried out, these mechanisms will be clamped to the floor so as to be as rigid as possible.

Several issues must however be taken into account:

- 1 Firstly, the integration of the alignment systems must be considered. Hydraulic networks linking HLS sensors follow the equipotential surface of the Earth’s gravitational field; this will not be the case with the tunnel which will be laser straight. So every few hundred metres along the tunnel, sensors will compensate for the slope (see Fig. 5.159). Overlapping stretched wires, located between two beams, will be protected, but access for maintenance will be difficult. A mechanical solution has been found by adding a removable wire at the level of the stretching devices which is accessible every 100 m.

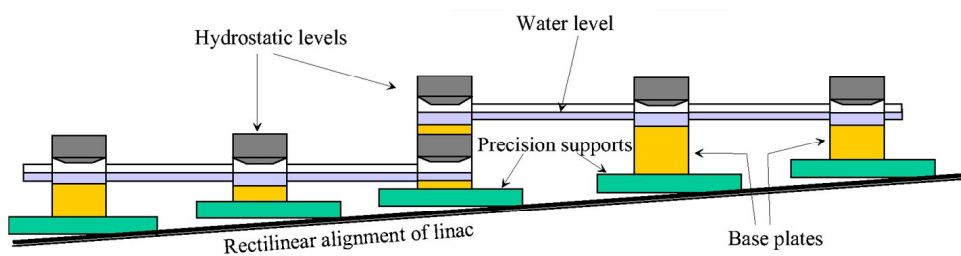


Fig. 5.159: Configuration of HLS network in a laser straight tunnel

- 2 A second issue is the constraints on the re-adjustment system from the other systems, which will apply additional transverse loads on the actuators and on the associated mechanics. Simulations concerning their impact is ongoing; these constraints will be studied on the two-beam module prototypes.
- 3 A third issue is the difference of temperature of the components between installation and operation. Fiducialisation and pre-alignment of the components on their supports will be performed at

a standard temperature of 20°C, which will be modified during operation, generating dilatation of the components on the girders (mainly in the longitudinal direction) and misalignments. Simulations concerning misalignments are under way and will be validated on the two-beam module prototypes. Temperature variation in the tunnel will also imply dilatation of the supports on which the position of the sensors have been determined. Temperature probes will be added on each support to correct dilatation effects. This means that the distance between sensors on their support and the stretched wire should be minimized. The sag of the wire could be limited (shorter length of wires, develop wires with small linear mass and high resistance to traction). In this case, materials with low expansion coefficients should be used for the sensor supports.

- 4 A fourth issue is the location of the alignment references which are between the two beams, inside the module: the alignment systems will already be installed and used for the pre-alignment of the module, which implies installation of the module from above and not from one side.

5.6.10 Stabilization system

To preserve the ultra-low transverse emittances during beam transport requires mechanical stabilization of all 3992 MBQs (see §5.18). The integrated r.m.s. [124] of the absolute vertical displacements of the magnetic field centres of each quadrupole must stay below 1.5 nm for frequencies above 1 Hz. Similarly, it should stay below 5 nm in the horizontal direction.

To reach such a level of mechanical stability for the CLIC MBQ, ground vibration measurements in operating particle accelerators [125] have shown that a mechanical stabilization system is needed under each quadrupole. At each MBQ, the interconnected girders and supports with accelerating structures will be interrupted by the independent MBQ support. The MBQ will be supported by the stabilization system that is supported inside a magnet girder placed on the eccentric cams of the alignment system. The MBQ stabilization strategy is based on a stiff actuating support with stiff piezoelectric actuators, the measurement of the relative displacement between the quadrupole and an inertial reference mass (seismometer), and an active reduction of the transmission of vibrations to the magnet support at low frequencies [124]. The main reason for the choice of this strategy is the robustness against external disturbances. The actuators are mounted in pairs in a parallel structure with flexural hinges, inclined and in the same plane. Each actuator pair is mounted inside an x-y guide that will allow vertical and horizontal motion but will block motion along and around (roll) the longitudinal axis of the magnet. A conceptual drawing of the quadrupole stabilization system for a Type-4 module is shown in Fig. 5.160. The stabilisation system for Types 1 to 3 will be very similar but with a shorter magnet girder. The number of actuator pairs depends on the magnet type.

The displacement range and the stiffness of the actuators also allows one to reposition the quadrupole in vertical and lateral direction between beam pulses with steps up to 50 nm in a range of $\pm 5 \mu\text{m}$.

In order to be able to reduce the vibrations of the quadrupole magnet to the required level with the stabilization equipment, the vibration background in the CLIC main tunnel should be kept low. Several commercial systems can isolate by more than a factor 10 at several Hz, however this ratio drops quickly for a frequency of 1 Hz. Some former experiments on quadrupole stabilization for particle accelerators were compared in Refs. [124] and [126]. A general observation from those experiments is the sharp decrease at 1 Hz for the ratio of integrated r.m.s. displacement with and without stabilization. The main reasons behind this are the resolution limits of the instrumentation and actuators, control stability issues, and difficulties in the design of mechanical systems with low resonant frequencies.

The vibration background is composed of seismic background combined with technical noise. While the seismic background is site dependent, the technical noise is created by human activity and technical infrastructure and can be reduced by appropriate design choices. Vibrations can be transmitted to the quadrupole magnet via the floor through the magnet support or directly to the quadrupole magnet. The seismic background combined with the technical noise can be considered as a broadband excitation

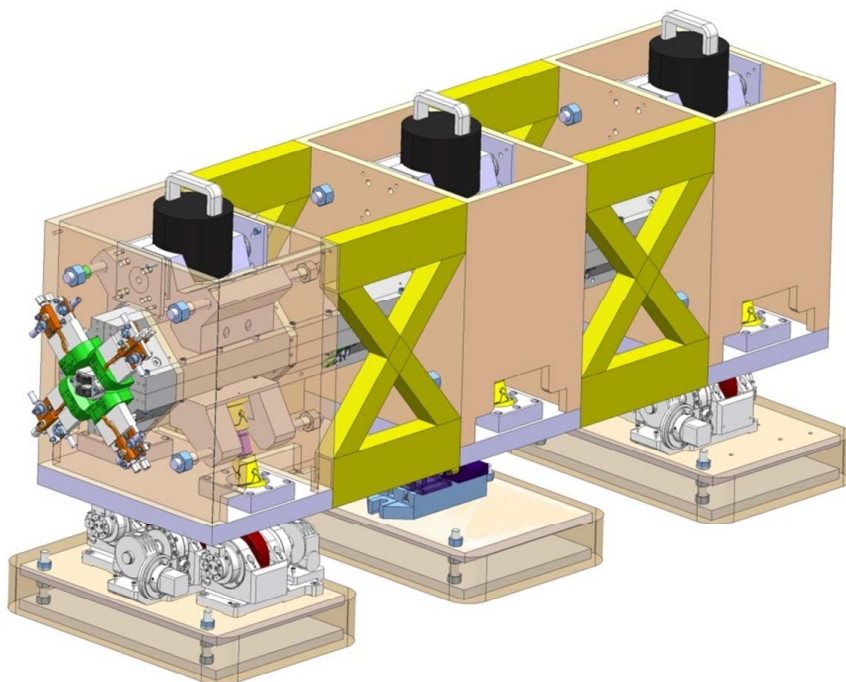


Fig. 5.160: Conceptual drawing of the quadrupole stabilization system for the Type-4 MBQ

with decreasing amplitude with increasing frequency.

Requirements emerge between the stabilization system, the pre-alignment system, the two-beam module design, the tunnel and general services design, and finally the accelerator environment. Such interactions are described in detail in §5.18 and are summarized in Table 5.41 and Table 5.42. It is possible that these tables are not complete and in some cases not precise. They indicate, however, the level of integration needed between different technical systems.

5.6.11 Beam instrumentation

The two-beam module beam instrumentation mainly consists of Beam Position Monitors (BPM) and Beam Loss Monitors (BLM). The present design of the BLM system is not advanced enough to be integrated in the mechanical layout of the module at this stage; all activities linked to the BLM developments are covered in §5.9.7. Beam instrumentation in much smaller quantities, for intensity, transverse and longitudinal profiles, will be located at special girders at the end of each Drive Beam decelerator for the Main Beam, and on modules of Types 1–4 for the Drive Beam. This section presents the integration of the Main Beam and Drive Beam BPMs in the two-beam modules.

CLIC modules will be produced in large quantities and so the BPM system is extensive. The Main Beam contains about 4000 BPMs while the Drive Beams require about 42 000 BPMs, i.e., two Drive Beam BPMs per module. In the Main Beam, there will be a BPM for each quadrupole for module Types 1–4. The requirements for the module BPMs are shown in Table 5.43.

The Main Beam BPM consists of two cavities: a position cavity measuring both x and y directions, and a reference cavity measuring beam charge and phase. Both cavities are resonant at 14 GHz. The reference cavity has two monopole mode-coupling ports which allows for redundancy of the readout electronics to ensure optimal reliability, as required for the orbit feedback controller. The main BPM will be connected rigidly to the quadrupole with no possibility to adjust its position. Alignment targets are mounted on the top, in order to measure the relative BPM position with respect to the quadrupole. The BPM is not connected to the Wire Position System, (WPS). A 3D image of the Main Beam BPM is

Table 5.41: Requirements of the module influencing the stabilization design

Requirement	Solution
Robustness against external direct forces for alignment and stability reasons	Stiff stabilization support
Integration in module design, beam height at 620 mm	Compact design of the stabilization, the alignment, and the intermediate stage. Stiffness of the intermediate stage increased by building the girder around the magnet.
Compatibility of stabilization and nano positioning with pre-alignment and fiducialisation	Stiff stabilization support without elastomers Ultra-precise flexural actuator guidance Ultra-precise x-y position measurement between alignment of intermediate stage and quadrupole.
Robustness against stray magnetic fields	Mechanical components in low permeability material No magnetic coils in the inertial reference mass
Radiation hardness	No electronics near the beam Screened rack space Radiation-hard electronics in local controller No elastomers in stabilization support
Transportable	x-y guidance lockable in longitudinal direction
Fast uncontrolled change of the actuators not allowed (Machine protection)	Detect power cut Actuators with small leakage currents Measurement of x-y position magnet in nano-positioning stage

depicted in Fig. 5.161.

For the Drive Beam BPM, the current plan is to use short stripline BPMs, only 25 mm long, with position signals processed at baseband in a bandwidth of 4–40 MHz. The strip lines are built into the quadrupole vacuum chamber, as shown in Fig. 5.162.

The Drive Beam BPMs are rigidly connected to the quadrupole, via a special support and one end is welded to the vacuum chamber that goes through the quadrupole. The other end is connected to the PETS via an RF-shielded bellows. Not shown in the picture are target balls mounted on the top side of the BPM, which will enable measurement of the mechanical centre with respect to the quadrupole centre. The very short distance to the PETS, and its 100 MW 12 GHz RF, is of particular concern and RF leakage into the BPM will be studied in the near future.

For the Main Beam BPM, down-mixing to an IF band followed by fast sampling is proposed as the baseline solution, while for the Drive Beam direct sampling is proposed. The main parameters of the systems are shown in the Table 5.44.

Each processing channel is capable of injecting a test tone into its cavity or adjacent stripline to verify operation of its complementary processing channel. The real calibration, to establish the phase and scale of the position signal may be done with beam. For more detailed information on the BPM system see §5.9.2.

Owing to the long distances (~ 1 km) between the underground alcoves where electronics could be

Table 5.42: Requirements of stabilization for module design

Requirement	Solution
Low vibration background in the tunnel:	
–Seismic background	Site selection
–Technical noise from surface and human activity	Depth of the tunnel
–Amplification at resonant frequencies of components in the neighbourhood of the Main Beam quadrupoles and their supports.	Design the components and their supports with high resonant frequencies and structural damping.
–Machines: pumps, motors, etc.	Minimize the beam height
	Distance from tunnel and modules
	Vibration absorbers under equipment
–Vacuum	Vacuum pumps should be off during beam, vacuum with NEG and ion pumps.
–Water cooling	Damping of flow pulsations
	Avoid low frequency resonances of pipes
	Damped water pipe supports
	Reynolds number as low as possible
–Ventilation	Transverse tunnel ventilation
–Electronics cooling fans	Avoid excess induced vibrations transmitted to module
–Acoustic noise	Sound level in tunnel should be minimized
–Transmission of vibrations to the floor	Selection of concrete for tunnel floor, discontinuities between caverns and tunnel
Limited external forces creating shear in piezo electric actuators	Vacuum and beam interconnects with low lateral and longitudinal stiffness
	Flexible link for water cooled cables
High resolution, low noise requirements	Short cables
	Local amplifiers, conditioners, ADC, DAC
	Stable power supply
	Screening from AC and pulsed signal cables
Small controller latency	Local controller hardware
Compatibility of the pre-alignment stage with the stabilization and nano-positioning	Mechanically very stiff pre-alignment stage
	Minimization of the load carried by the pre-alignment stage
	Minimization of the beam height
Air temperature stability	Optimized temperature regulation with transverse ventilation in ventilation sectors

installed, the amount of cables needed to transport acquisition and control signals, would be enormous, and take up too much space in the tunnel. Also the cost of such a system would be prohibitive. This thus demands a local radiation-hard acquisition and control system per module (every 2 m), which digitizes and transmits the data via an optical link, to servers, located in one of the alcoves or in a surface building. For each module ~ 270 signals have to be transmitted, all having different sampling frequencies and repetition rates (see §5.13.3.2)

5.6 TWO-BEAM MODULE

Table 5.43: Requirements for the BPM systems for the CLIC two-beam modules

Region	Accuracy	Spatial resolution	Temporal resolution	Beam aperture	Bunch frequency	Beam current	Pulse duration	Quantity
Main Beam	5 μm	50 m	10 ns	8 mm	2 GHz	1 A	156 ns	4196
Drive Beam	20 μm	2 mm	10 ns	26 mm	12 GHz	100 A	240 ns	41 484

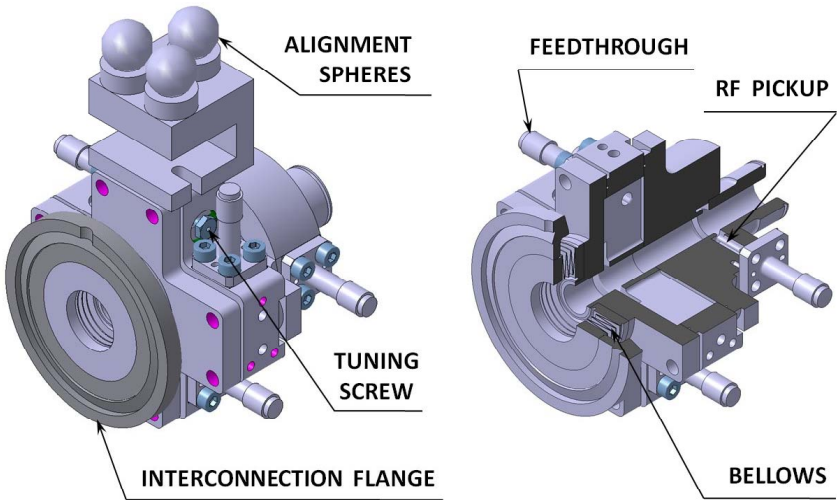


Fig. 5.161: Main Beam cavity BPM

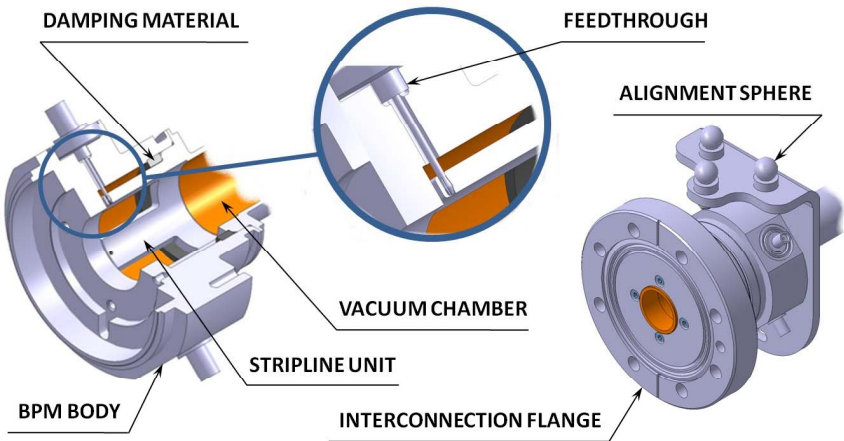


Fig. 5.162: Drive Beam BPM

Table 5.44: Requirements for the BPM system for the CLIC two-beam modules

BPM Type	Freq.	BW (max)	Ultimate Res.	Temp Res.	IF freq.	Sampling freq. Processor Type	Quantity
Cavity BPM	14 GHz	40 MHz	50 nm	10 ns	200 MHz	~160 MS/s	4800
Strip line BPM	20 MHz	40 MHz	1 μ m	10 ns	–	~160 MS/s	43 000

5.6.12 Handling and transport

The space required for module transport and installation in the tunnel has a major influence on the tunnel cross-section. Studies were therefore carried out to identify how the modules could be transported and installed in the tunnel. These studies had the secondary goal of feeding some design requirements related to transport and installation into the module design.

The large number of modules and module supports to be transported and installed in the tunnel means that it is important to optimize the whole sequence of module transport to allow rapid transport and installation. Table 5.45 shows the number of modules.

Table 5.45: Module and supports — transport study input data

Item	Quantity (3 TeV)		Quantity (500 GeV)		Dimensions [mm]	Mass [kg]
	Per sector	Total	Per sector	Total		
Module	436	20 924	436	4248	2010×1550×1200	1500
Module support	436	20 924	436	4248	–	200

Before a module arrives at its installation point its supports will be installed and aligned; the geodesic survey equipment is installed before the module arrives at its point of installation. Installation in this order means that the module has to be transferred horizontally over the stretched survey wire equipment before being lowered into place on its supports. This results in the constraint that the module will have to be supported from above during the transfer from the tunnel transport vehicle onto its supports.

A conceptual design of the vehicle with its own on-board lifting equipment was produced in order to reserve the necessary space in the tunnel integration design work (for more details see §6.5.4.1).

Although module installation logistics should aim for sequential installation, the installation process must allow installation of modules between two previously installed modules in the event of supply delays. In addition the system must be able to remove a previously installed module if major repairs are needed.

A key requirement for module design identified during the study is the need for a clear interconnection plane between modules so that they can be lowered into their final position without interference with the adjacent modules(s). As the clearance between adjacent modules will be minimized (10 mm or less) modules will need to be carefully guided during the installation process.

In addition to the clear interconnection plane, adapting the module design for transport requires the use of lifting points and support points to allow the whole sequence of transport and handling operations. These operations will be needed during the phases of module assembly, testing, storage, road transport to access points, lowering, tunnel transport, and installation. The module design effort includes the design of any transport restraints and special lifting beams to be used when handling fully assembled modules

5.6 TWO-BEAM MODULE

during the installation process.

5.6.13 System integration

The module integration started with a combination of 3D envelopes, reserving the space for the main components. This permitted, at a very early stage, a better understanding of the module component sizing and optimization in accordance with the physics requirements and space allocation. The schematic views were also very helpful. Both the basic 3D model and a schematic of the Type-1 Module are shown in Fig. 5.163. The Type-1 Module, where two accelerating structures are replaced by a focusing magnet, is the most interesting from the point of view of integration. This is because of its density of parts and, consequently, its complexity; all possible components are involved. This provides an opportunity to explore the feasibility and assembly issues during integration.

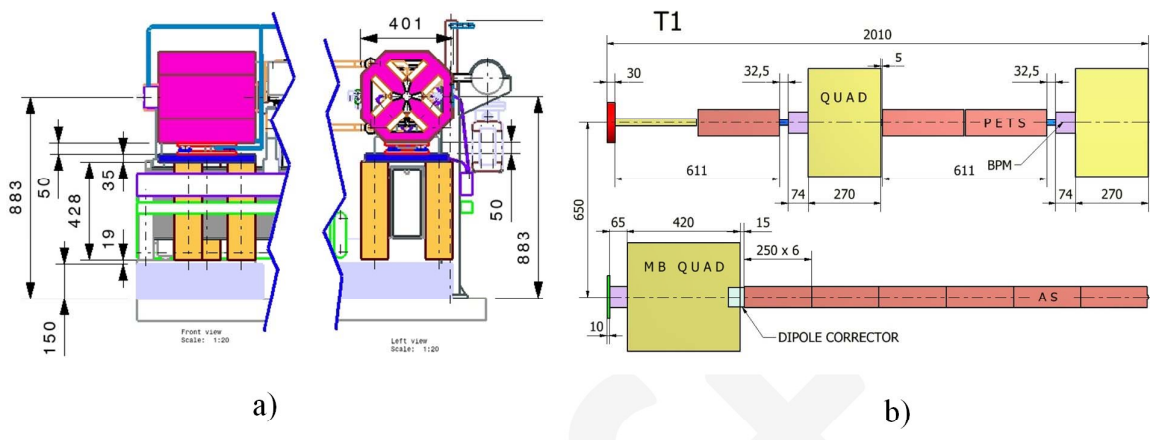


Fig. 5.163: Space distribution between module components in vertical (a) and longitudinal (b) directions

As a first step, the vertical space budget was determined. 150 mm were reserved for the floor level compensation and pre-alignment system devices. The optimal girder cross-section was then studied, including the cradles, equipped with actuators for re-positioning of the supported components. The cross-section of the DB quadrupole is slightly more space-demanding compared to the MB magnet. Once fixed on the girder, it defines the horizontal plane of the beams, 883 mm from the tunnel floor. Later, other solutions were studied and tested for the different technical systems. The baseline configuration was frozen at the end of May 2010.

5.6.14 Component inventory

The number of two-beam modules as a function of type and energy is given in Table 5.46 and the number of components is given in Table 5.47.

Table 5.46: Number of two-beam modules

Energy	Type-0	Type-1	Type-2	Type-3	Type-4	End sectors	Total	No. of sectors
3 TeV	16 748	308	1268	954	1462	184	20 924	48
500 GeV	2358	368	1490	—	—	32	4248	10

Table 5.47: Number of components (excluding the 8 m long end sections for each decelerator)

Components	Quantity per module					Total	
	T0	T1	T2	T3	T4	3 TeV	500 GeV
AS	8	6	4	2	0	142 812	27 032
PETS	4	3	2	1	0	71 406	13 516
MBQ	0	1	1	1	1	3992	1858
DBQ	2	2	2	2	2	41 480	8432
DB BPM	1.3	1.3	1.3	1.3	1.3	27 653	5621
BLM	0.5	1.5	1.5	1.5	1.5	14 362	3966
WFM	4	3	2	1	0	71 406	13 516
MB girders	1	1	1	1	0	19 278	4216
DB girders	1	1	1	1	1	20 740	4216
MB linear movers	3	6	6	6	6	74 196	18 222
DB linear movers	3	3	3	3	3	62 220	12 648
Cam movers	0	5	5	5	5	19 960	9290

5.6.15 Cost considerations

The two-beam modules represent nearly one third of the total cost of the CLIC project. Very large series productions will be needed for the fabrication of the two-beam modules. The two-beam module cost was estimated by applying learning curves to the current prototype costs. Based on LHC experience with magnet production and typical learning percentage values [127], the learning factor has been chosen to be 0.85–0.93 depending on the type of operation. For repetitive machine operation it is usually equal to 0.9–0.95. For equally-shared hand assembly and machining operations, the learning factor is 0.85. For a learning factor of 0.9, and three production lines, the average unit cost of a series of 10 000 units is about one quarter of the prototype cost. The two-beam module cost drivers are the RF system (65%) and support systems including alignment (15%). Cost studies have been conducted for the RF structures and girders, and they are in agreement with the CERN cost estimates. For the RF structures, tolerance and surface quality significantly affect the cost. In the next phase, the impact of relaxed tolerances has to be studied in detail. Potential savings can be made by reducing the high number of components in the current two-beam module. The feasibility of having longer components (such as girders and RF structures) or merging functionality (common Main Beam and Drive Beam girders) has to be studied. Alternative machining and materials will also have to be analysed. For example, low-cost WPS are currently under development. The reduction of the number of girders would lead to a decrease in the number of actuators and sensors, as the number of supports to be aligned would be lower. Several parameters influence the cost, and for each of these cost-performance optimization has to be done.

5.6.16 Outlook for the project implementation phase

A key component of the project implementation phase will be the increasing direct involvement of industry. Industrialization is a critical issue for cost-effective production of the key technologies. Alternative technologies have to be studied in collaboration with industry, to improve performance and lower the cost. The main studies which have to be conducted in this phase are:

- The baseline engineering design for the RF structures requires several fabrication steps, increasing the possibility of misalignment and overall cost. In addition, diffusion bonding under a hydrogen atmosphere necessitates a long period of vacuum baking which is very costly. The assembly procedure has to be optimized and new heat cycles explored;
- Support system: Longer and/or MB-DB common girder configurations need to be investigated;

5.6 TWO-BEAM MODULE

- Vacuum system: Mini pumps mounted directly onto each RF structure minimize the vacuum forces and simplify the vacuum network;
- Number of components: Longer RF structures, aiming at a reduction in the overall number of components.

5.7 Vacuum system

5.7.1 Introduction

In particle accelerators, beams travel under vacuum primarily to reduce the beam-gas interactions, i.e., the scattering of beam particles by the molecules of the residual gas. These interactions are responsible for machine performance limitations such as reduction of beam lifetime (nuclear scattering) and of luminosity (multiple Coulomb scattering), intensity limitation by pressure instabilities (ionization) and, for positive beams only, electron-induced instabilities (e.g., beam blow-up).

Beam-gas scattering often leads to non-captured particles and nuclear cascade when these particles are lost on the beampipes. These effects increase the radiation dose rates in the accelerator tunnels and, upstream from the detectors, increase the background seen by the detectors in the experimental areas, leading to material activation, dose rates to intervention crews, premature degradation of tunnel infrastructures like cables and electronics, and finally a higher probability of single events induced by neutrons which can destroy the electronics in the tunnel and in the service galleries.

As with other particle accelerators, the design of the beam vacuum system in the CLIC accelerator complex must obey severe constraints which have to be considered at the design stage since retrofitting mitigation solutions is often impossible or very expensive. Among them, the vacuum system has to be designed to minimize beam impedance and radiofrequency higher-order-modes (HOM) generation and optimise the beam aperture in particular in the magnets. It has also to provide enough ports for the pumps and for the vacuum diagnostics and to allow for bake-outs to achieve ultra-high vacuum (UHV) pressures ($<10^{-8}$ Pa). The impact of other constraints like integration, material and personnel safety, RF and HV conditioning issues and costs often lead to a compromise in performance of all systems of an accelerator. This explains why these issues need to be addressed at the design stage.

The CLIC complex involves all major beam-induced constraints on the vacuum system: synchrotron radiation, electron cloud, sparking and degassing induced by high electric fields. In addition, the CLIC damping rings contain superconducting magnets and therefore vacuum issues for accelerators operating at cryogenic temperatures like heat loads, synchrotron radiation and induced magnet quenches also need to be addressed.

Synchrotron radiation will dominate the dynamic vacuum in the predamping rings, damping rings, combiner rings and in other sections with small bending radius like delay loops and bunch compressors. The electron cloud, if not mitigated, is expected to build up in the predamping and damping rings. The risk of sparking and of outgassing induced by high electric fields will be dominating in the Main Linac. Therefore, most of the CLIC complex requires high and ultra-high vacuum.

The difficulty in the design of the beam vacuum system of this accelerator complex results from the combination of several of these beam-induced effects. The predamping and damping rings illustrate these difficulties as they combine the effects of synchrotron radiation and electron cloud. In addition to their specific requirements, the feedback effect of the photo-electrons generated by the synchrotron radiation on the electron cloud has to be prevented.

Some parts of the CLIC complex are more conventional from the vacuum point of view; e.g., for the Drive Beam Accelerator (DBA) the vacuum system will be similar to that of Linac4 and for the transfer lines to the Main Linac the vacuum system will rely on a standard UHV mechanical design and pumping scheme. The only concern is the cost issue since long and expensive cabling is needed as is remote control and monitoring.

The performance of high intensity and high-energy particle accelerators can be limited by beam-induced vacuum dynamic effects. With the CLIC complex all vacuum configurations, each with their own problems, are present exposing the beam vacuum system to many constraints like thermal desorption as well as synchrotron radiation, ion instabilities, electron cloud and induced desorption.

Different vacuum categories and the corresponding technologies can be distinguished according to the vacuum chamber temperature (cold or room temperature), baked or unbaked system, coated or

5.7 VACUUM SYSTEM

uncoated chambers. The choice of the technology drives the vacuum performance as well as the cost of the system.

5.7.2 Room temperature vacuum systems

5.7.2.1 Unbaked systems

For an unbaked vacuum system, the static vacuum performance is determined by water. The thermal outgassing of water is time dependent. It decreases with t^{-1} where t is the pumping time in hours. The usual value for standard materials such as copper or stainless steel is:

$$Q [\text{mbar} \cdot \text{l} \cdot \text{s}^{-1} \cdot \text{cm}^{-2}] = 2 \times 10^{-9} \cdot t^{-1} [\text{h}]$$

As the system is unbaked, no distributed pumping like getter coating can generally be used. Thus only lumped pumps are used and the pumping performance can be limited by the conductance. Usually the vacuum for a standard unbaked system is of the order of 10^{-7} to 10^{-9} mbar.

Main Linac

The CLIC Main Linac is composed of two-beam modules integrating the two beams with their subsystems. The vacuum specificity of these modules is that heating is not allowed in order to maintain the good geometrical accuracy and alignment. The field ionization studies resulted, for fast ion beam instability, in a vacuum specification of 10^{-9} mbar [128]. Given the large surface areas to be pumped, high pumping speed and large vacuum conductance are needed. Both beam vacuum enclosures are linked by waveguides.

The vacuum envelope is mainly composed of RF systems such as accelerating structures, power extraction structures, and waveguides. Some additional vacuum chambers have been designed; the first is for the Drive Beam Quadrupoles (DBQs). Two vacuum chambers for the DBQs have to be installed in each module composed of a stainless steel tube, copper coated, with an aperture of 23 mm and an outer diameter of 26 mm. For non-standard modules, drift tubes are required for the Drive Beam, probably based on the same design as the DBQ beampipe. A vacuum chamber for the Main Beam Quadrupoles (MBQ) is also needed. The conductance of this chamber is very low since the pole radius is 5 mm and the length of the quadrupole is up to 2 m. It therefore requires distributed pumping. A specific vacuum chamber has been designed to allow the installation of two NEG strips in two antechambers (Fig. 5.164). The NEG strips are supported by ceramic supports to minimize the heat transfer and air-flow cooling is needed to avoid a large temperature increase in the chamber during NEG activation. The wall thickness of the chamber must be optimized to not reduce the vacuum conductance. The vacuum chamber is squeezed between the two halves of the magnets during its assembly. The vacuum performance is measured on a prototype based on a more pessimistic design than the present one [129]. The NEG has been activated with only a marginal temperature increase of the vacuum chamber wall.

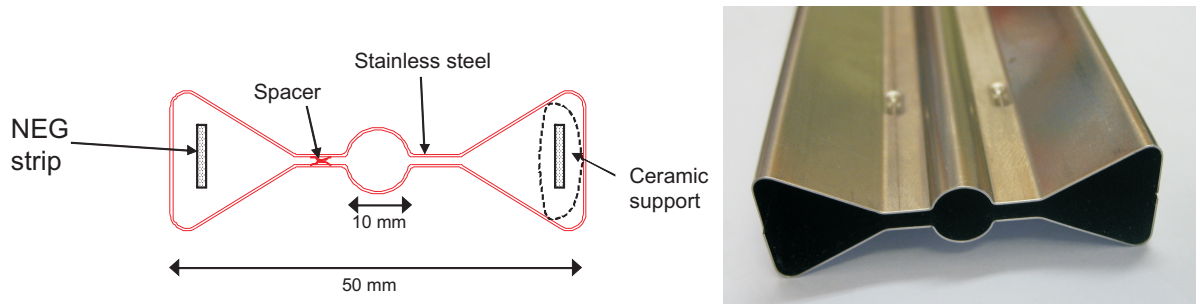


Fig. 5.164: Conceptual design and prototype of the Main Beam quadrupole vacuum chamber

The longitudinal conductance in the accelerating structures proper is very limited due to the small

aperture (typically 5 mm). This requires radial pumping. To achieve this, a longitudinal vacuum manifold is integrated in the design of the accelerating structures and brazed with them. The pumping system has to be vibration free not to induce vibration sources especially to the quadrupole stabilization system. A combination of NEG cartridge pumps with high pumping speed and a sputter ion pump is used. The latter is used to pump noble gas species as well as methane. In the present design, the pumping system is composed of a common reservoir, equipped with the pumps, that is linked to the accelerating structures and the power extraction structures. Each reservoir has a pumping port equipped with a roughing valve for the connection of a mobile turbo-molecular pumping station or a leak detector. The performance of the pumping system for the static vacuum is presented in Fig. 5.165. An average pressure along both beams in the range of 2×10^{-9} mbar is reached after 100 hours of pumping. It is worth pointing out that the vacuum performance of such a system is limited by the conductance between the accelerating structures and the vacuum reservoir. An alternative pumping solution based on a very compact pump, combining ion pump and NEG cartridge, is under study.

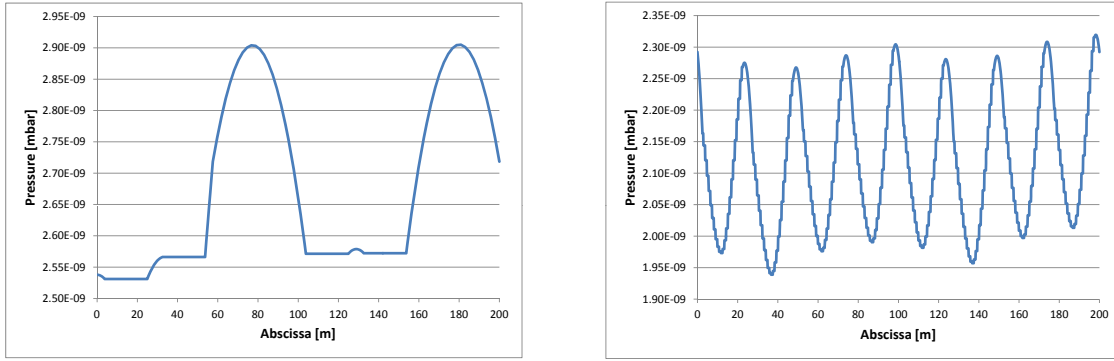


Fig. 5.165: Calculated static pressure profiles after 100 hours of pumping for the Main and Drive Beam respectively

The very high filling factor of the main linacs leaves a very limited space for the beam line interconnections, especially for the Main Beam. For the Main Beam, the interconnections consist in the continuity of the vacuum enclosure. Low-impedance interconnections are not required; however, damping material has to be used to avoid wakefields. The vacuum envelope in these interconnections is based on a bellows to assure flexibility and module alignment capability, as well as an all-metal connection. A dismountable solution with flanges and a metallic seal is preferred to avoid the contamination by metallic dust. The same base concept is used for the Drive Beam but in addition a low-impedance continuity has to be assured to carry the image current of the high intensity beam (~ 100 A). Flexible elements in copper-based alloy (CuBe) are used to shield the bellows (Fig. 5.166).

Sectorisation of the vacuum system is required to ease installation and commissioning, local intervention and leak detection and to limit a vacuum degradation. A manageable sector length of around 200 m is proposed. Sector valves must be installed on both beams at the same longitudinal locations.

Machine detector interface and post-collision line

The QD0 sector consists of an incoming beam chamber inside the magnet and a post-collision chamber passing through the magnet structure. For the CLIC design we have chosen room-temperature QD0 magnets as opposed to the superconducting QD0 planned for the ILC. This means that the CLIC QD0 will not be able to profit from the high capacity cryo-pumping available within a magnet cold bore. However, simulations for CLIC and ILC [130] show that incoherent instabilities and beam-gas background are acceptable in this region up to pressures of 10^5 nTorr and 10^3 nTorr, respectively. These relatively relaxed

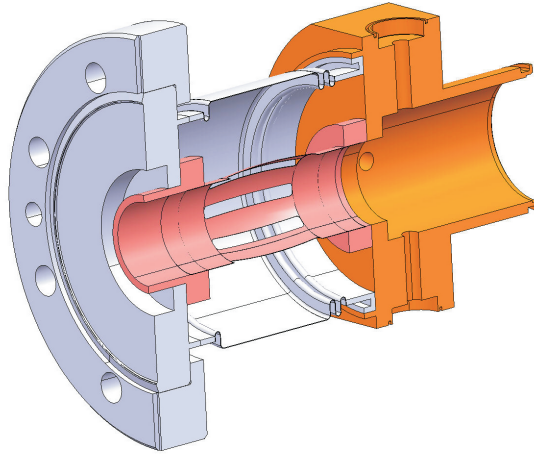


Fig. 5.166: Concept of the Drive Beam interconnection

pressure requirements suggest that lumped pumping from the extremities of the magnet may be feasible.

The baseline is therefore to make a unbaked system using ultra-high vacuum (UHV) materials and procedures to obtain a vacuum pressure of 40 nTorr or less in the decelerator. The layout of the QD0 magnets limits the chamber diameter to 7.6 mm and pump separation to about 4 m. Assuming a clean, unbaked vacuum system, a static pressure profile after 100 hours of pumping has been calculated (see Fig. 5.167). This corresponds to an average pressure of $3.6 \cdot 10^2$ nTorr. This conforms with the requirement of beam-gas background, but gives little margin for additional beam-induced outgassing. The beam pipe in the QD0s should therefore be kept under vacuum to minimize contamination with water vapor.

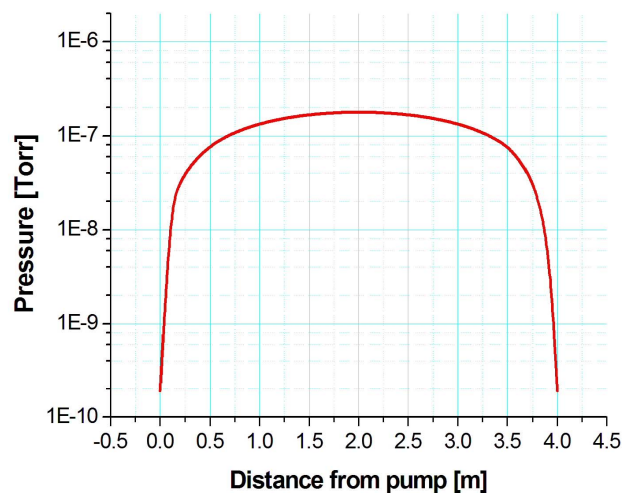


Fig. 5.167: Pressure profile in the QD0 after 100 hours

An additional constraint is imposed by the detector push-pull concept, which implies that the beam vacuum must be broken to switch detectors. The system must therefore be designed so that the required operating pressure can be obtained within about 24 hours of re-connecting the push-pull sector inside the detector.

The MDI region is planned to be physically sectorised with ultra-high vacuum valves as shown in Fig. 5.168. Two valves are required in the space between QD0 and the experiment to allow the detectors to be exchanged (push-pull) whilst maintaining the QD0 and experimental beam pipe either under vacuum, or filled with a clean, inert gas.

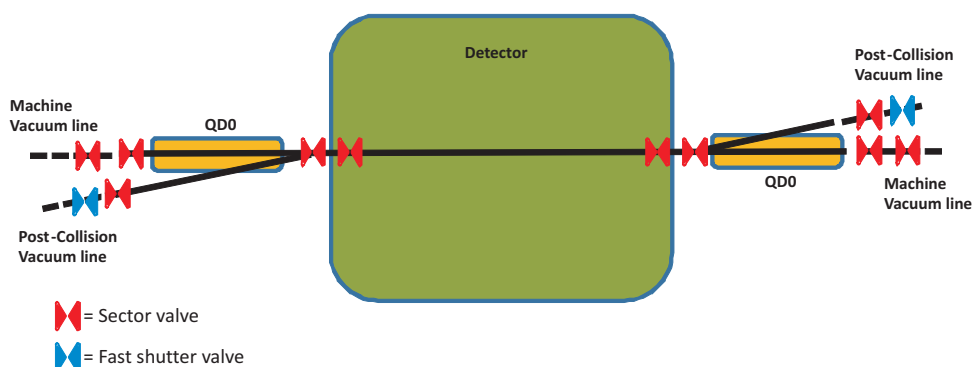


Fig. 5.168: Sectorisation scheme of the experimental area

Both QD0 and post-collision sectors will require a self-contained system of pumps and vacuum instruments for measurement of pressure and to allow interlock of the sector valves. The small sector between the two push-pull valves will be pumped and interlocked with a mobile (removable) vacuum system.

The QD0 sector will be pumped by sputter-ion pumps, with additional lumped NEG or sublimation pumps as necessary.

Beam impedance aspects of this sector have not yet been considered. A low-resistivity coating may be required, particularly on the QD0 sector.

The post-collision line will consist of a series of stainless steel vacuum chambers in stepped or conical forms inside the magnetic and absorber elements. As the absorbers are outside the vacuum chambers, the chambers will be designed with windows upstream of the intermediate dump absorbers and an exit window separating the collider vacuum system from the main dump body.

The pressure has a less demanding requirement in the medium vacuum range, allowing for a conventional un-baked system design. However it will require a high pumping speed due to the large surface area and beam-induced outgassing. A combination of sputter-ion, turbo-molecular and mechanical pumps will be used.

The post-collision line is separated from the collider beam line to allow independent interventions to these sectors. A fast shutter may be installed on each post-collision line to prevent contamination of the experimental sector due to incidents in the post collision line.

5.7.2.2 Baked systems

For an unbaked system, the vacuum is driven by adsorbed gas molecules with intermediate binding energies in the range of 17 to 25 kcal/mol, namely water. By heating up the surface, the binding energy is lowered and adsorbed gas molecules can be evacuated from the vacuum system. After a bake-out cycle, the typical outgassing rate for stainless steel or copper is around 10^{-12} mbar·l·s⁻¹cm⁻². The outgassing is then dominated by H₂ diffusing out of the metallic walls.

5.7 VACUUM SYSTEM

Coated chambers

Combiner rings and delay loops

The four combiner rings (CR) constitute the CLIC Drive Beam frequency multiplication system after the delay loops. They are characterized by very high beam currents during the bunch train pulse, reaching at most about 100 A at the CR2 extraction.

The vacuum requirement is mainly imposed by ion effects. Dynamic pressures in the range of 10^{-9} mbar should be sufficient to keep both incoherent tune-shift and transverse displacement of bunches to an acceptable value.

The CR vacuum chamber diameter and material are defined by the beam pipe wall impedance and the multi-bunch resistive wall instability. The needed high electrical conductivity imposes high purity copper as the material of choice. The limitation in the emittance growth due to the mentioned instability is fulfilled for a beam pipe inner diameter of about 80 mm.

The limited acceptable emittance growth requires very smooth inner wall surfaces, possibly in the mm range. The very high pulse current (from 20 to 100 A) demands the shortest path for image currents and very firm contacts in the RF shields. Any sudden aperture modification of the inner wall should be avoided.

Despite the peculiarities related to the beam structure, the conceptual design of the CLIC CRs has similarities with that of modern synchrotron radiation facilities. For example, length and electron energy are close to that of SOLEIL and MAX-IV light sources. As for those accelerators, the main gas load in the CRs is induced by synchrotron radiation bombardment onto the inner walls in the arcs and the nearby straight sections. Despite the fact that the injected electrons circulate in the rings for only a few turns, the high bunch-train current generates a significant amount of synchrotron radiation power. The total synchrotron radiation power can be evaluated by calculating the energy U_0 emitted by one electron per turn

$$U_0[keV] = \frac{88.5 \cdot E^4[GeV]}{\rho[m]} \quad (5.30)$$

where:

- E is the electron energy (2.7 GeV)
- ρ is the bending magnet radius (9 m for CR2)

Therefore, $U_0=310.2$ keV. The average single-train current is:

$$I = \frac{n_e \cdot e[C]}{\Delta t[s]} \quad (5.31)$$

where:

- n_e is the number of electron per train
- e is the electron charge
- Δt is the single-train duration

For $I=25$ A as at the entrance of CR2: $n_e=3.8 \times 10^{13}$ electrons/train; the emitted power P in the CR2 is, therefore, about 18 kW. The average synchrotron radiation power per arc is about 2 kW.

The photon flux can be evaluated by:

$$N[s^{-1}] = 8.08 \times 10^{20} \times E[GeV] \times I[A] \quad (5.32)$$

For an equivalent steady-state current of 58.9 mA, the total photon flux along the CR2 is therefore $1.13 \times 10^{20} \text{ s}^{-1}$.

In modern accelerators, in particular light sources, Ti-Zr-V film coatings are extensively used. This non-evaporable getter (NEG) material has in this context a twofold benefit after in situ activation by heating. First of all, it provides the vacuum system with a very high distributed pumping speed for the most abundant gasses released by vacuum chambers. Then, as its surface is very clean after the dissolution of the oxide layer, the desorption yields induced by photon and electron bombardment undergo a dramatic decrease [131] when compared with those of traditional materials.

NEG coating is also proposed for all vacuum chambers of the CLIC CRs to efficiently reduce the effects of synchrotron radiation induced desorption. This choice has a heavy impact in the design of the four rings. In fact, the vacuum system must be bakeable up to 250°C and, as a consequence, severe restrictions are imposed to vacuum bellows and valves, any monitor installed in the beam pipe, and the machine commissioning and operation. The installation of permanent bakeout equipment is proposed. In case of space constraints for the beam pipes of the magnets, the thin multilayer solution can be implemented as was done for hundreds of LHC vacuum chambers [132]. This solution needs only an additional thickness of 0.5 mm.

The installation of ion pumps is also proposed to remove gas molecules that are not adsorbed by the NEG material.

The production of synchrotron radiation is the main objective of light sources: most of the photons are extracted along dedicated vacuum chambers toward the experimental areas. In general, water-cooled vacuum chambers and massive copper absorbers intercept the photons that are not extracted and collide with the inner walls of the vacuum system. In the CRs, synchrotron light is a by-product of the electron trajectory and the removal of the associated thermal power is complicated by the very high bunch-train current and the related resistive-wall effects. For example, the use of massive photon absorbers would be hindered by the associated discontinuities. A viable solution would be removal of the heating power essentially by water cooling the vacuum chambers; small tapers welded directly on the beam pipe would be in any case necessary to shadow the BPM and vacuum bellows from synchrotron light. Long-term behavior of the vacuum chambers under pulsed synchrotron power has to be assessed.

The vacuum sectorization of the CRs follows the arc structure: one vacuum sector per arc, six vacuum sectors for CR1, eight for CR2. As a consequence, a single vacuum sector is about 50 m long in both CRs. The volume of one vacuum sector is about 0.250 m^3 while the inner surface area is about 13 m^2 .

The pressure reading in each vacuum sector is provided by combined gauges. The ion pump current is also used to trigger vacuum interlocks.

Long transfer lines

Both the main and the Drive Beams have to be transported from the injector complex towards the main linac heads. These transfer lines have a length of around 21 km. The field ionization studies resulted for fast ion beam instability in a vacuum specification of 10^{-10} mbar and the transverse resistive wall instability analysis led to an aperture of 120 mm and 200 mm for the main and Drive Beams, respectively [133, 134].

Vacuum chambers are in copper, 2 and 2.5 mm thick for the main and Drive Beams, respectively. To reach the vacuum specification, distributed pumping is used by means of NEG coating. A NEG thickness of around $0.7 \mu\text{m}$ could be used to avoid skin effects (need to be lower than $1.3 \mu\text{m}$). The NEG bake-out is carried out at 120°C during 24 hours. It is then activated at around 230°C during 24 hours. A permanent bake-out system is foreseen. Additional sputter ion pump are used for noble gases and methane.

These long transfer lines have a FODO cell structure with a cell length of 438 m for the Main

5.7 VACUUM SYSTEM

Beam and 109.6 m for the Drive Beam. The vacuum system layouts are shown in Fig. 5.169 and 5.170.

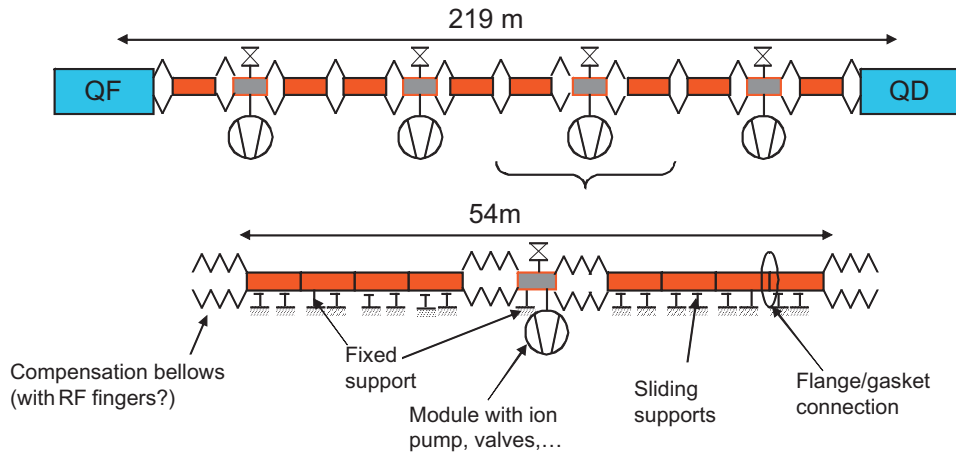


Fig. 5.169: Conceptual layout of the vacuum system for the Main-Beam long transfer line (one half cell represented)

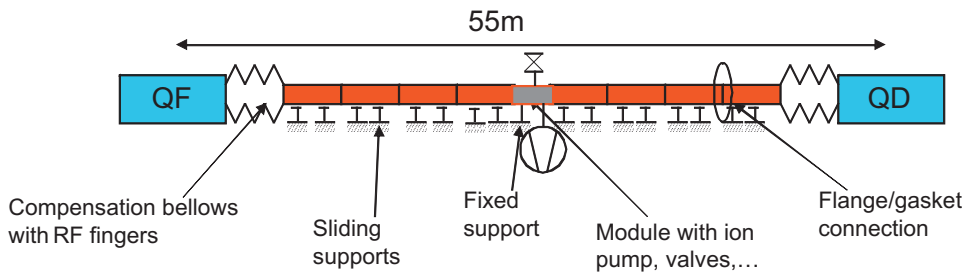


Fig. 5.170: Conceptual layout of the vacuum system for the Drive-Beam long transfer line (one half cell represented)

Fixed modules, are used, equipped with an ion pump, a roughing valve for the connection of a mobile turbo-molecular pumping station or a leak detector, gauges. Compensation based on shielded bellows has to be used mainly for the thermal expansion of the vacuum chambers during the bake-out and NEG activation. The high intensity Drive Beam requires low impedance and smooth transitions.

The vacuum system in the long transfer lines is sectorized. A sector length of 438 m is proposed.

Vacuum in experimental areas

The vacuum sector in experimental areas must combine BDS vacuum requirements with the needs of the surrounding detectors. CLIC detectors have requested a geometry consisting of a cylindrical section inside the vertex detector with symmetric cones on either side. The vacuum system design (chambers, supports, instrumentation) within each detector must be optimized to present the minimum radiation length within the detector acceptance. Low-Z materials such as beryllium and aluminium also have high secondary emission yields. Optimizing the vacuum chamber for physics may therefore imply the use of coatings and/or in-situ heating of the chamber to maintain vacuum stability.

An additional constraint is imposed by the detector push-pull concept, which implies by definition that the beam vacuum must be separated to switch detectors. The system must therefore be designed so that the required operating pressure can be obtained within 24 hours of re-connecting the push-pull sector.

The experimental area sector will require a self-contained system of pumps and vacuum instruments for measurement of pressure and interlock of the sector valves. This UHV sector will be pumped by sputter-ion pumps, with additional NEG or sublimation pumps as necessary. Gas loads from the adjacent unbaked QD0 and post-collision sectors may require additional pumps to be installed.

Uncoated chamber – Drive-Beam linac

The two Drive Beam linacs are 2.6 km long and are each composed of about 819 RF accelerating structures, in addition to injectors and bunch compressors (see §4.1). In addition to the RF cavity and coupler the basic cell, with a length of about 3.1 m, includes a quadrupole magnet, beam monitors and vacuum components. The aperture varies from 10 cm in the RF cavities to 4 cm in the quadrupoles.

The required dynamic pressure, defined by ion trapping (see §4.3), is about 5×10^{-11} mbar. This degree of vacuum is achieved with *in-situ* baking. The proposed pumping system is based on integrated NEG and ion pumps installed between the RF cavity and the quadrupole.

The open technical issue is the in-situ bakeout of the cells, including the RF structures. The lowest heating temperature for an efficient baking is 150°C; it is not excluded that dedicated air ovens will be designed for the heating of the RF cavities. Higher temperatures provoke intolerable thermal expansion and the consequent need for special vacuum bellows and RF fingers. In addition it has to be proved that after heating the dimensional tolerances remain within the acceptable range. If in-situ bakeout is unfeasible, pressures of a few ntorr could be obtained after about 4 days of pumping by NEG and lumped ion pumps.

At the present stage of the project, NEG thin film coating on the inner surfaces is excluded. The very high surface current excludes the application of the film in the cavities and in the vicinity of the couplers. The vacuum chambers in the quadrupoles are too small to provide a relevant pumping to the rest of the cells.

In case of bakeout, the maximum length of the vacuum sector is limited by the available electrical power for the heating. Based on experience with the LHC, a typical vacuum sector would encompass about 30 basic RF cells. As a consequence, at least 25 vacuum sectors are necessary for each Drive-Beam linac.

5.7.3 Cryogenic vacuum systems (Damping Rings)

5.7.3.1 Generalities on cryogenic vacuum systems

Cryogenic vacuum presents specific challenges, with both advantages and disadvantages for an accelerator system. When we introduce temperature as a variable parameter, it is convenient to reason in terms of density (number of free molecules per unit volume) and not of pressure. At constant density, reducing temperature reduces the molecule's mobility, hence the conductance, which scales as \sqrt{T} . From 300 K to 20 K, conductance is reduced by a factor 3.9, while to 4 K it is reduced by a factor 8.6.

At the surfaces bounding vacuum, molecules impinging on a cold surface stick to it at a rate (sticking probability equals ratio between the number of molecules adsorbed to the total number of impinging molecules, per unit time) which depends *inter alia* on temperature and the gas species. More generally, a cold wall acts as a cryopump, reducing the pressure of adsorbed gases and hence the density of free molecules.

It is worth noting that the vapor pressure of hydrogen remains high at fairly low temperature unless the cold bore is operated at 1.9 K, as in the case of the LHC. A further problem due to the presence of a cold bore is that of the heat load to the vacuum chamber's walls, which is then evacuated to the refrigeration system. In case of a 1.9 K vacuum chamber, a beam screen is necessary to intercept the heat load as with the LHC.

Photodesorption has early been identified as a source of vacuum degradation in storage rings

and has extensively been studied. Yields have been measured as a function of critical energy, angle of incidence, substrate material and coatings as well as temperature. In particular, it has been shown that primary photodesorption yield, i.e., for desorption of tightly bound molecules (in opposition to recycling desorption of previously cryosorbed molecules) decreases with decreasing temperature [135]. The set of equations determining free molecular density in presence of primary and recycling photodesorption, cryopumping and vapour pressure has been formalized [136].

Synchrotron radiation and beam-induced multipacting are sources of heat load to the walls. At the same time, electron clouds produce beam instability, so that mitigation of electron cloud through reduction of SEY may be desirable anyway at warm as much as at cold. The electronic energy distribution of a metal being only very slightly perturbed by temperature due to Fermi-Dirac statistics, SEY does not depend directly on temperature, but only indirectly through surface coverage by cryosorbed gas species. A consistent experimental program to determine SEY at cold from different substrates and in presence of different compositions of residual gas is ongoing.

5.7.3.2 *Damping Rings: constraints for vacuum and surfaces*

The upper limit for the gas density in the electron DR is determined by the rise time of fast-ion instability [137]. In this effect, positive ions get trapped and oscillate in a bunch train, accumulating around the electron beam in an ion-cloud. A tune shift is induced at the end of the train. The rise time of the fast ion instability is inversely proportional to pressure, typically 1.1 ms at 10^{-9} mbar; this time is about one revolution time, which is too fast to be controlled. A vacuum better than 10^{-10} mbar is therefore desirable in the electron ring.

In the positron ring, the gas density is set by the lifetime of the beam, as determined by the beam-gas interaction [138]. A vacuum level of 10^{-9} mbar is a sufficiently low operating pressure.

Synchrotron radiation is produced in a wiggler as a vertically flat cone, strongly peaked in the forward direction (see §5.3). Most of this radiation is absorbed in the warm absorbers, and only 0.1% hits the wiggler's vacuum chamber walls, with a total of 20 W/m impinging on the 25th wiggler and 1 W/m on the 26th wiggler in the case of the Nb-Ti superconducting wigglers. Photons generate photoelectrons with a yield Y ; these primary electrons are accelerated by the beam towards the vacuum chamber walls and generate in their turn secondary electrons, with a yield (Secondary Electron Yield SEY) δ . There are several consequences of the build-up of this electron cloud around a positron bunch. In the positron ring, the electron cloud may cause tune shift and beam instability by electrons trapped in a bunch train. This effect has been studied in [139], concluding that only a SEY below 1.3 could ensure stable operation. A most obvious effect is beam-induced multipacting [140], where secondary electrons created at the wall receive a momentum kick from the beam and traverse the chamber to collide with the opposite wall in exactly one bunch spacing, thus producing new electrons in resonance with the bunch spacing. In both Damping Rings, electron cloud and beam-induced multipacting may produce pressure increase by electron induced desorption and heat load to the walls by electrons. However, it has been shown that in the electron ring, multipacting does not affect the beam and that for $SEY < 2.4$, the heat load remains below 1 mW/m. The situation is very different for the positron ring, where multipacting appears above a SEY of 1.3, causing a significantly stronger electron cloud over 1 train passage for values above 1.4 to 1.5. For SEY above 1.4, the heat load grows beyond 1 W/m and therefore becomes unacceptable.

5.7.3.3 *Damping Ring layout and vacuum layout*

The present layout of the CLIC DRs is described in 2.6. As a reminder, the damping rings are of racetrack shape, with 26 wigglers in each of the two long straight sections, interspersed with quadrupoles in a standard FODO structure. The synchrotron radiation cones generated in the wigglers are absorbed by horizontal and vertical absorbers in the warm sections downstream of each wiggler, while a terminal absorber at the end of the straight section absorbs the remaining photon power. Space for injection/extraction and

for the RF cavities is reserved at the dispersion-free region at the end of the long straight sections. Vacuum sectorization has to separate the more delicate elements, like the injection/extraction devices and the RF cavities, from the cold straight sections. Due to reduced space in the cells of the long straight sections, these may accommodate only a limited number of sector valves, with the scope of allowing for separate heating up of a limited portion of the ring. Finally, the terminal absorbers have to be separated from the rings. A conceptual view of the vacuum sectorization is shown in Fig. 5.171.

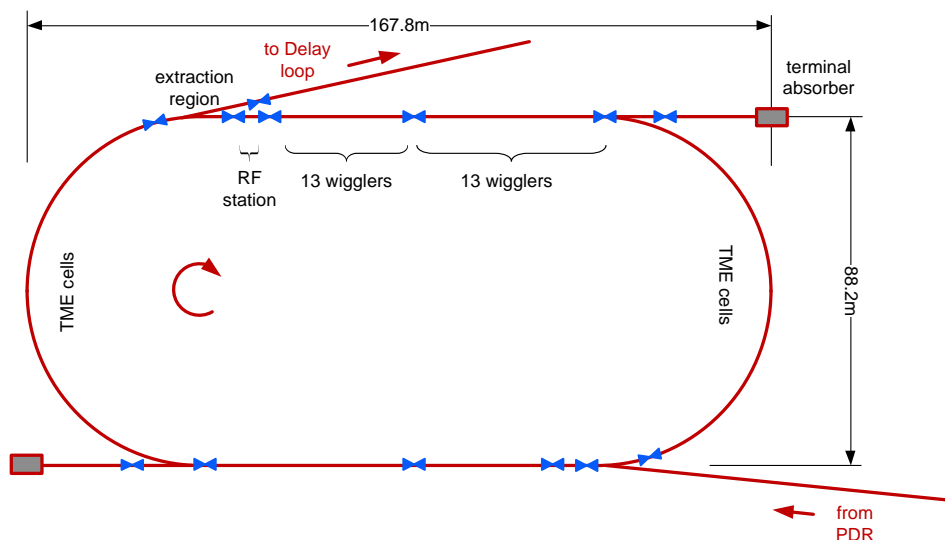


Fig. 5.171: Sectorization scheme for the vacuum of a DR. The sectorization is identical for both DRs

To limit the required refrigeration power for the superconducting wigglers, the heat load by synchrotron radiation is taken by warm absorbers interspersed between the cold wigglers. The DR straight section layout appears therefore as a succession of cold wigglers and warm absorbers, alternating cold and warm vacuum-chamber segments.

The length of one wiggler and hence of its cold vacuum chamber is 2 m, while the warm part comprising the absorber and quadrupole spans approximately 1 m. Localized pumping may be installed between two wigglers. As ultra-high vacuum pumps, sputter-ion pumps and lumped NEG pumps should be used both in the straight sections and in the arcs, while pumpdown should be assured by mobile turbomolecular pumping groups, installed at some convenient locations along the arc and the straight sections. In the straight sections, gas evacuation from the central part of the wiggler would be limited by the reduced conductance of the vacuum chamber portion inside the wiggler. Distributed pumping is naturally present if the vacuum chambers' walls are at the same temperature as the wiggler, between 1.9 K and 5 K depending on the superconductor, or may be obtained by opportune NEG coating or NEG stripes, located in the larger horizontal portion of the vacuum chamber left free by the beam.

5.7.3.4 Vacuum chamber – the options

A trade-off between beam aperture (13 mm minimal) and the magnetic field strength (20 mm magnetic gap) determine the vertical dimension of the vacuum chamber. The horizontal dimension is limited only by integration in the cryostat and by mechanical stability. As explained in §5.3, the wiggler may work at 1.9 K or at 5 K depending on the strand's material and stability. As the vacuum chamber may be in thermal contact with the wiggler or isolated from it, any temperature value between 2 K and 300 K should be considered as possible. As discussed earlier, a beam screen is only useful if the vacuum chamber is operated below 2 K.

Values of molecular conductance for different gas species and different temperatures for an elliptical wiggler vacuum chamber, as shown in Fig. 5.172, are presented in Table 5.48.

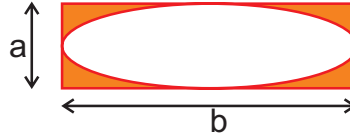


Fig. 5.172: Elliptical vacuum chamber, $a = 13$ mm, $b = 80$ mm, $l = 2$ m

Table 5.48: Molecular conductance, disregarding non-zero sticking effects, for a 2 m long, 80 mm \times 13 mm wide wiggler vacuum chamber. A more accurate estimation should be obtained by Test-Particle Monte-Carlo simulation, including non-zero sticking

Half vacuum chamber conductance [l/s]	300 K	20 K	4 K
H ₂ (M=2)	13	3.3	1.5
CH ₄ (M=14)	4.9	–	–
Ne (M=20)	4.1	1.1	–
CO, N ₂ (M=28)	3.5	0.9	–

In the electron ring, to reach the required dynamic pressure, the wiggler's vacuum chamber should be baked out or, even better, NEG coated. This affects the design of the wiggler, which should either be assembled around a closed and pumped vacuum chamber, or should be able to withstand heating of the chamber up to 150-250°C. If heating is not possible, it may be necessary to widen the vacuum chamber to increase its conductance, by an appropriately designed antechamber, which could also accommodate NEG strips, as proposed in the past for LEP.

The challenge is similar for the positron ring. SEY is increased by the presence of cryosorbed gas species on the chamber's wall, so a bakeout is necessary to deplete the surfaces before cooldown. If the wiggler's design does not allow for *in-situ* heating, the only solution which has shown to lower the SEY in an unbaked system is an amorphous carbon coating [141, 142].

5.7.4 Vacuum control

The vacuum control of the CLIC complex is based on the standard architecture for which the active components, i.e., pumps, gauges and valves are installed in the tunnel whereas the controllers are grouped and located in dedicated radiation-free areas. Thus, long cables between the controllers and the vacuum elements have to be used. For the main linac, the distance between two consecutive underground technical rooms (UTR) is around 880 m inducing cable lengths up to around 450 m.

Combined gauges, Pirani and cold or hot cathode ionization gauges, depending on the pressure requirements, are usually used for UHV applications to cover a pressure range from atmosphere to a pressure down to 10^{-11} mbar. In addition, ion pumps are also used to provide a reliable pressure measurement. Vacuum ports for the gauges have to be as close as possible to the beam pipe to give a representative pressure in the beam pipe. Vacuum ports are usually close to lumped pumps.

Vacuum sector valves are installed to ease the installation sequence and the commissioning of the vacuum system, allow local intervention on the vacuum system and also limit the effect of a leak (vacuum degradation) or accidental opening of the vacuum enclosure. Sector valves are electro-pneumatically actuated gate valves with different flange sizes. All-metal sector valves are used because of the low outgassing rate and the high radiation hardness.

Pressure interlocks must be generated and supplied to their control systems to protect machine beam components and vacuum system. The signals must be reliable to avoid unnecessary beam dump.

Redundancy may be required to limit the beam downtime in case of failure of one vacuum gauge and also to increase the reliability of the triggering signals. The vacuum system must allow full remote control.

5.7.5 Technical issues

5.7.5.1 *Synchrotron radiation*

In the Damping Rings, the required emittance reduction is achieved by generation of synchrotron radiation in the superconducting wigglers. Primary photons, emitted in a strongly peaked narrow cone, may be hitting only one side of the vacuum chamber but are scattered and reflected at the vacuum chamber walls. Both primary and reflected photons induce photodesorption, i.e., desorption of neutral molecules, thus contributing to the dynamic residual gas pressure in the vacuum chamber. They also produce photoelectrons, believed to be involved in the photodesorption mechanism via electron stimulated desorption [143]. Photoelectrons eject secondary electrons from the vacuum chamber walls with a yield δ or SEY, thus contributing to the build-up of an electron cloud. Finally, synchrotron radiation deposits power on the vacuum chamber, which is particularly undesirable for a cold bore, as this power has to be evacuated at cold temperature, thus increasing the refrigeration plant load.

The two fundamental parameters describing photodesorption and photoelectron production are the photodesorption yield, η (molecules/photon) and the photoelectron yield, Y (electrons/photon).

Partially triggered by the LHC, extensive studies have been dedicated to determining the photodesorption and photoelectron yield from bare and NEG-coated technical surfaces for accelerator vacuum chambers. A complete overview of literature on photodesorption theory and results may be found in [143]. Desorbed gases are typically H_2 , CO , CO_2 , H_2O and CH_4 . The photoelectron yield is measured experimentally in the framework of e-cloud studies, from bare and NEG-coated surfaces. A summary of experimental results may be found in [144], a work which underlines the importance of suppressing primary photoelectrons via an antechamber to make full use of surfaces of low SEY.

Amorphous carbon coating has shown promising results in limiting SEY. It also features low photodesorption yield [141]. Reflection and photoelectron yield are needed to completely characterize a coating which may mitigate dynamic vacuum and electron effects, without needing an in-situ bakeout. Photoelectron emission from amorphous carbon coated vacuum chamber wall should be studied in dedicated experiments in a synchrotron radiation beam. For photoelectron yield measurements, the set-up should permit separate assessment of the reflectivity R of the wall and photoelectron yield, as explained in [145], which requires changing the orientation of the vacuum chamber wall with respect to the light pencil. Before starting measuring amorphous carbon coatings, previous results from bulk copper or NEG-coated copper may be used for calibration.

5.7.5.2 *Dynamic vacuum in the main linac accelerating structures and its relation with dark current and breakdown*

The dynamic vacuum is influenced by two phenomena: gases released by electron-stimulated desorption (ESD) due to the bombardment of surfaces with electrons released by field emission inside RF structures ('dark current'), and gases released during RF breakdown.

Dark current is regularly emitted by RF structures, due to the mechanism of electron field emission from high electric field regions. These electrons may either be captured by the accelerating fields and exit the cavity, or impinge on the surfaces and release gas molecules by ESD (and also be multiplied by secondary emission leading to multipacting phenomena). Released gas molecules have energy of a few eV and may entirely fill the cavity during a 230 ns RF pulse. After collision with a cavity wall they are then slowed down to thermal velocities and travel only a few fractions of a mm during a pulse. Simple estimates, taking into account the amount of dark current collected outside test structures and known values for ESD coefficients [146], lead to doubt that the local pressure inside the RF structure during an RF pulse may be higher than the dynamic vacuum threshold. Table 5.49 summarizes these first estimates,

showing that the local pressure can be higher than the acceptable threshold. It should be underlined that this phenomenon may happen simultaneously in all the structures along the machine.

Table 5.49: Amount of gas released inside an RF structure, based on a simple geometrical scaling (ratio approximately 40) between the dark current collected outside it and the amount of electrons assumed to be trapped inside and impinging on walls. The ESD coefficients for unbaked copper are taken from [147], the geometry of the cell is assumed to be TD18-like.

ESD coefficient for H ₂	2.00×10^{-1}
Total H ₂ molecules per RF pulse	9.11×10^8
Equivalent H ₂ pressure [Torr]	1.12×10^{-8}
ESD coefficient for CO	3.00×10^{-2}
Total CO molecules per RF pulse	1.37×10^8
Equivalent CO pressure [Torr]	1.68×10^{-9}

The total amount of gas is however minimal, and its pressure will quickly decrease below the threshold in a few ms while it is ‘diluted’ in the whole volume on its way to the pumps, making it very difficult to measure in view of its low amount and fast timescale. Fig. 5.173 illustrates its projected time dependence.

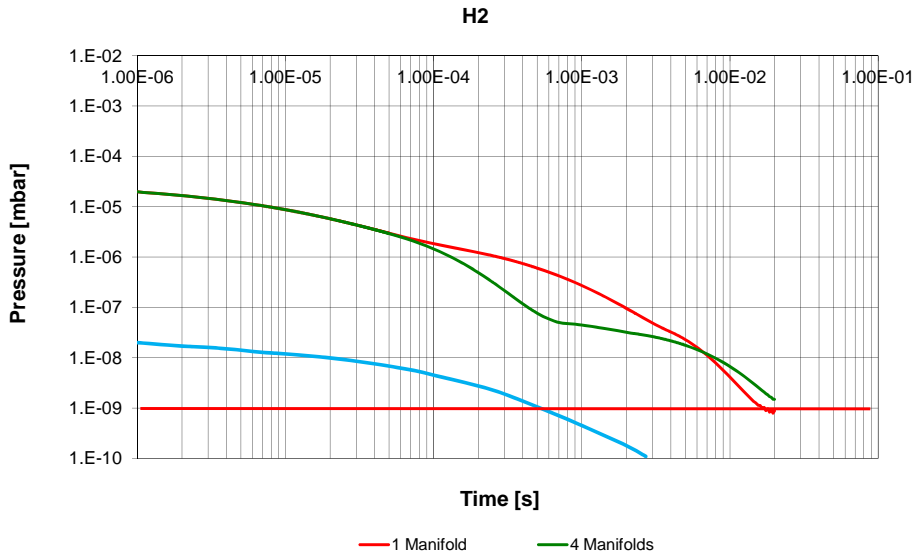


Fig. 5.173: Green and red curves: time evolution of the pressure in the mid-cell of a structure for hydrogen, calculated with thermal equivalence model [148], in the case of a breakdown. Blue curve: estimated time evolution in the case of molecules released by ESD in an RF pulse.

The release of gas bursts during breakdowns has been studied with a dedicated test stand. Breakdowns are produced on samples facing a tip exposed to very high fields, releasing in the breakdown an energy of approximately 1 J stored in a capacitor bank, which compares well with the energies released inside RF structures [149]. The amount of gas released at each breakdown has been carefully measured [150] and is of the order of 2×10^{12} molecules for both H₂ and CO. The time for pressure recovery after the gas burst release has been calculated by MC and FEM codes [151, 152] for RF accelerating structures and ancillary components of the current design, and is given in Table 5.50. This means that if a break-

down happens during one RF pulse in a given structure, full pressure recovery for H_2 is obtained before the next RF bunch train, and 4 pulses are needed for full recovery in the case of CO. It should be noted that the criterion for dynamic vacuum is an average over the entire machine, and larger pressures can be tolerated locally. Moreover for pressures up to 10^{-5} mbar of CO no measurable decrease of breakdown field has been measured in the DC breakdown tests [153], meaning that any overpressure below this limit should have no effect on the triggering of subsequent breakdowns.

Table 5.50: Pressure after 20 ms (equivalent to a 50 Hz repetition rate) and recovery time to 10^{-9} mbar

Gas	Molecules released	Pressure after 20 ms	Time to reach 10^{-9} mbar
H_2	2×10^{12}	1×10^{-9} mbar	20 ms
CO	2×10^{12}	5×10^{-7} mbar	80 ms

In conclusion, the effects of RF breakdowns on dynamic vacuum seem to be acceptable with the present design of the RF structures. The effects of dark currents appear to be close or above the limit of acceptability. To have better estimates which may lead also to a possible solution, an experimental program for accurate ESD measurement is under way. It is also foreseen to launch extensive simulations of dark current trajectories which, coupled with accurate ESD values and further MC and FEM vacuum simulations will allow better predictions. Together with this, the RF test benches will be extensively instrumented.

5.7.5.3 *Dynamic cold vacuum*

In cold vacuum situations, pressure profile calculation is paramount for the determination of the correct vacuum layout to guarantee a maximal pressure below 10^{-10} mbar, as required to limit the rise time of fast ion instability. As seen above, warm and cold sections alternate in the Damping Rings. A model of dynamic cold vacuum should be established on the basis of a thermal model of the unique ring vacuum chamber, to account for intermediate temperature zones. It should include a correct modeling of the cold wall sticking, vapor pressures, synchrotron-radiation induced desorption and recycling of cryosorbed gas, based on the vast literature of experimental results on this subject. The dynamic pressure profile calculation could first be done with an electrical network simulation, based on the electrical analogy, then it should be refined by a Test-Particle Monte-Carlo. Only such a calculation can give an answer to questions like lumped versus distributed pumping, presence or not of an antechamber, opportune coating to absorb photons and reduce photodesorption.

5.7.5.4 *Technological challenges*

In-situ bakeout

Ultra-high vacuum usually requires bake out of the vacuum system. It is used to reduce gas output as well as to activate NEG coating. The technological challenge is for the damping rings, namely the wiggler, or Drive-Beam linac, combiner rings or experimental chamber for which the space around the vacuum chamber is very limited and/or the chamber should be thermally insulated to avoid heating surrounding elements. The vacuum chamber may be wrapped with an isolated ultra-thin heater [154, 155] and thermal insulation should be designed to protect the surrounding elements. Heater wrapping developed for SOLEIL is as thin as 0.7 mm, while for the LHC it is as thin as 0.3 mm.

5.7 VACUUM SYSTEM

Coatings in small vertical aperture

Magnetron plasma sputtering for thin films is well developed at CERN. The limited (vertical) dimension of the vacuum chamber imposes some development work. The smallest vacuum chamber with a NEG coating was a 8 mm diameter one, but the quality of the coating was not guaranteed and the rate of production of a valid coating was poor. With amorphous carbon, the fragility of the graphite rod used as electrode will require some special design to permit achievement of a good-quality coating over its 2 m length.

5.7.5.5 Integration of vacuum system, interfaces

The integration of the vacuum system in the accelerators has to be considered from the beginning. Otherwise, this could lead to integration and/or performance issues as well as cost increases. Vacuum system integration shall proceed in parallel with the following activities: expertise provided to beam-related components (magnets, beam instrumentation, radio-frequency systems, etc.), engineering of vacuum related components (beampipes, bellows, pumping ports, etc.) and machine integration including cabling and services. The vacuum system has to be considered as a whole from the beam pipes to their supports and sector valves.

Interfaces with the vacuum system have to be carefully defined and designed, as examples for the vacuum chambers supports or UHV connections of radio-frequency or beam instrumentation systems.

5.8 Powering CLIC

5.8.1 Overview

CLIC will require more than 70 000 power converters to supply power to its magnets and klystrons. Several technical issues including machine availability, power quality, and feasibility are addressed and powering strategies are proposed. The Drive Beam (DB) linac consumes about two thirds of the total power consumption with requirements on the modulators that have so far not been reached. The DB decelerator contains about two thirds of the total number of magnets. A powering scheme using groups of series connected magnets and small current trimmers is presented. Efforts have been made to improve the overall machine availability by implementing redundancy for the converters and a failure-tolerant operation strategy. Finally, the specifications of the power converters for all the CLIC magnets show the grouping strategy to adopt. Imposing uniformity across the CLIC magnets regarding their current needs will allow a reduction in the number of power converter families and the improved management of spares.

5.8.2 Powering the Main Linac

The Main Linac is that part of the machine which contains the highest density of magnets and power converters. The main component of the linac is the serial connection of 860 modules in each of the 48 accelerating sectors. Between each accelerating sector, a dedicated, radiation-free, cavern houses most of the power converters which feed current to the magnets through long cables (up to 450 m). The power to be dissipated in air is limited by ventilation issues and does not allow individual powering of all the magnets. Therefore a series powering strategy consistent with beam physics requirements and reliability requirements is needed.

Each accelerating structure contains two quadrupoles for steering the DB and some contain one larger quadrupole for the Main Beam (MB) with a small dipole corrector as illustrated in Fig. 5.174. The density of MB quadrupoles is not constant along the linac (Fig. 5.175). There is a high number in the few first sectors reducing towards the end of the tunnel or the interaction point. This has an impact on the size of the caverns and the number of cable trays needed to bring the current to the magnets.

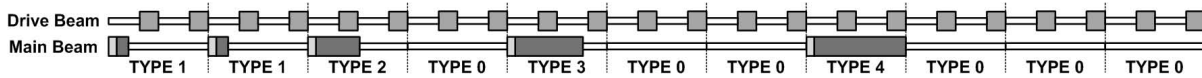


Fig. 5.174: Possible module sequence in the tunnel

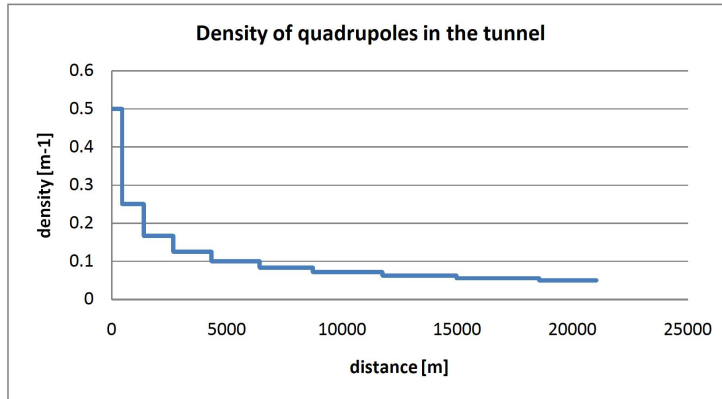


Fig. 5.175: Density of MB quadrupoles in the tunnel

5.8.2.1 Main Beam magnet powering (cable sharing solution)

All the Main Beam magnets have the same current requirements with a flexibility of $\pm 1\%$ and a precision of 100 ppm. Some magnets can be by passed for ballistic steering. In order to reduce the power dissipation in the tunnel, the power cables are shared between the magnets and converters so only the difference current between two consecutive magnets flows through the cables. The flexibility requirements for the currents of the MB quadrupoles are guaranteed as illustrated in Fig. 5.176. In addition, if in some cases the currents of two consecutive magnets are identical, a failure tolerant operation is possible by shorting the failed converter and disconnecting the cable as in Fig. 5.177. The converters are two-quadrant DC converters to allow an isolated magnet to be by passed. The converters, which will be located in radiation-free caverns, are also put in strings; the number of converters per string depends on the allowed common mode voltage of the magnets to ground.

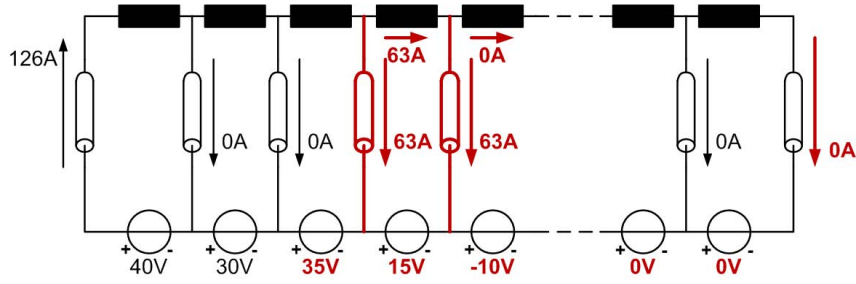


Fig. 5.176: Current distribution for ballistic steering

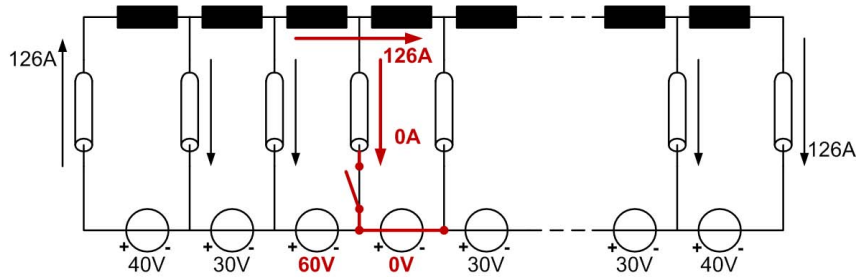


Fig. 5.177: Example of failure-tolerant operation

5.8.2.2 Drive Beam magnet powering

The field requirements, and hence the current requirements, for powering the DB quadrupoles are distributed along each accelerating sector as a monotonic slope from higher to lower energy in the Power Extraction and Transfer Structures (PETS) as shown in Fig. 5.178. Instead of individually powering each magnet, one main converter feeds a string of magnets (see Fig. 5.179), consisting of typically between 30 and 60 units limited by the common-mode voltage from the magnet to ground. The slope in current is made by active dissipative trimmers. This powering strategy implies the use of a very small number of cables and a reduction in the number of bulky converters. A modular and redundant approach is chosen, so all the main converter sub-modules are identical, no matter the needs in current.

The required precision on the trimmers is only $\pm 1\%$, while the precision of the higher current is 500 ppm. The simple design of the trimmer allows a radiation-tolerant solution to be implemented in the tunnel, saving thousands of kilometres of cables. Also, this powering strategy implements a failure-tolerant operation allowing up to 20 failed trimmers in one accelerating sector, as long as 99% of the operating current is maintained in the magnet corresponding to the failed trimmer. When a failed trimmer

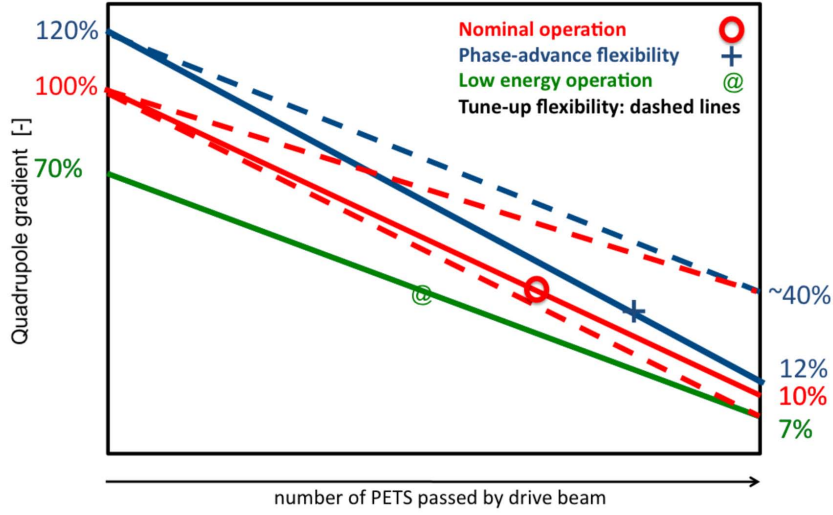


Fig. 5.178: Flexibility requirement in current profile

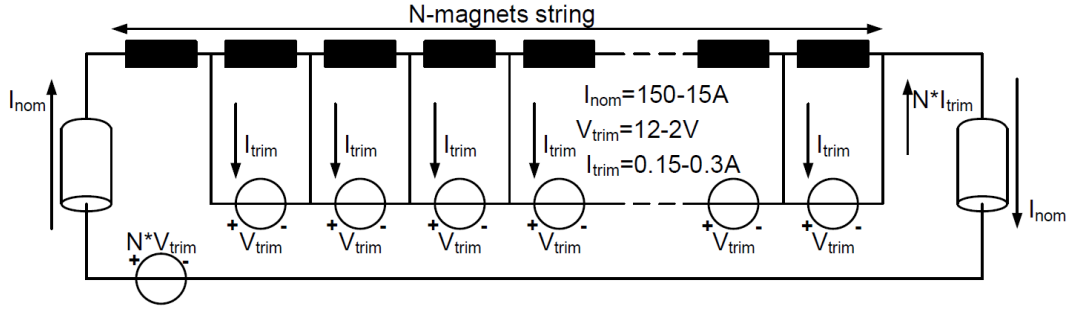


Fig. 5.179: Converter and trimmer solution

is shorted as in Fig. 5.180, two consecutive magnets can share the same current without significant impact on the beam envelope. The shorted failure mode is guaranteed by an embedded crowbar.

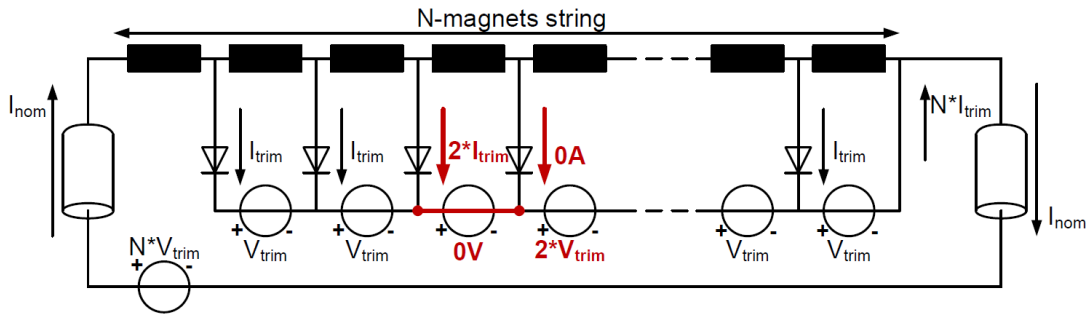


Fig. 5.180: Failure scenario in one of the trimmers

5.8.2.3 Main Beam injection complex

The MB injection consists of linacs, transport lines, and damping rings. The magnets in the linacs and the transport lines are mostly fed with DC current with a precision of about 50–100 ppm which is possible with existing power converters. The damping rings consist of a number of warm magnets and

5.8 POWERING CLIC

superconducting wigglers. One converter will feed all the wigglers of a single line. The set-up time requirement for the current is about 1 A/s.

5.8.2.4 Drive Beam injection complex

The DB injection is mostly made up of combiner rings and transport lines to the Main Linac. Around 10 000 magnets are to be fed with a DC current with a precision of about 50–100 ppm. These converters will be mostly located above ground. The DB linac has 1639 quadrupoles, one per klystron, with a similar field profile to that in the DB decelerator in the Main Linac. The same powering strategy with main converters and trimmers will be applied, allowing for a failure-tolerant operation and redundancy in the main converters.

5.8.3 Drive Beam linac modulators

The klystron modulators will be operated at 150 kV/160 A (~ 24 MW per modulator) in pulsed mode for a pulse length of $140 \mu\text{s}$. To meet the specified RF power quality, which is derived directly from the accelerator performance requirements, the modulator voltage absolute precision and pulse-to-pulse reproducibility of about 10^{-5} will require an extended development. Ripple and pulse-to-pulse precision on the high voltage should be controlled, either from low-level RF control or ideally from the modulator control, meaning that a high voltage precision measurement will be needed. The efficiency target (including modulator efficiency and pulse efficiency) is 90%.

The system contains the modulator that feeds the klystron which feeds the cavities with RF power as shown in Fig. 5.181. The precision requirement on the pulse can be achieved with either a direct voltage measurement feedback, RF feedback, or beam phase measurement. The klystron contains a feed-forward system from the modulator and a feedback from the cavity. Ideally these systems should be de-coupled so the precision requirement should come from the modulator. Note that repeatability is more important than precision itself, since low-frequency drift can be corrected by RF feedback to the klystron. The required bandwidth of the pulse precision is 10^{-5} between 6 kHz and 4 MHz in the first 10% of the lattice. The remainder requires only a precision of 10^{-4} , which is still beyond the actual state of the art. At lower frequencies, the RF feedback compensates the drift with systematic error feed-forward and RF feedback. Higher frequencies are naturally filtered by the machine.

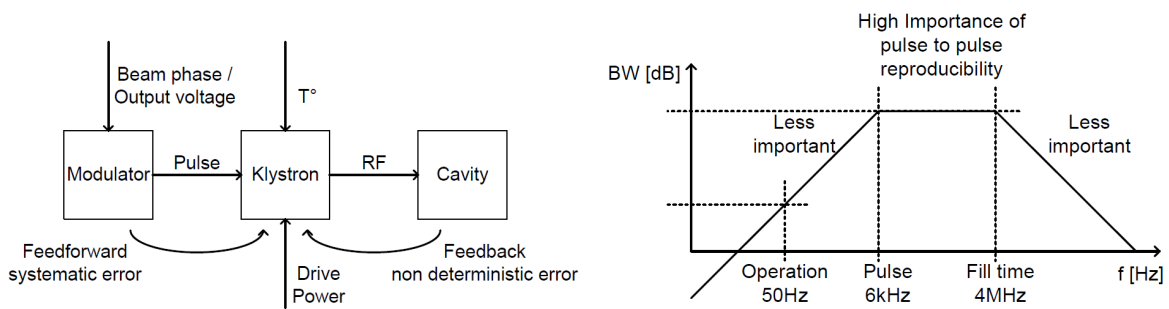


Fig. 5.181: Modulator/Klystron on the system level and pulse requirements

The specification on the measurement performance is much tighter than the actual state of the art, in both precision and bandwidth (see Fig. 5.182). If the modulator is to work without any feedback coming from RF, then this requirement becomes compulsory. However, the use of indirect high-bandwidth measurement on the RF phase to implement a fast in-pulse feedback on the modulator voltage and/or on the klystron RF-input modulation must be studied in parallel.

Considering the pulse length, the number of klystrons to feed (more than a thousand), and the need to minimize the total power consumption from the accelerator, voltage rise- and fall-times become

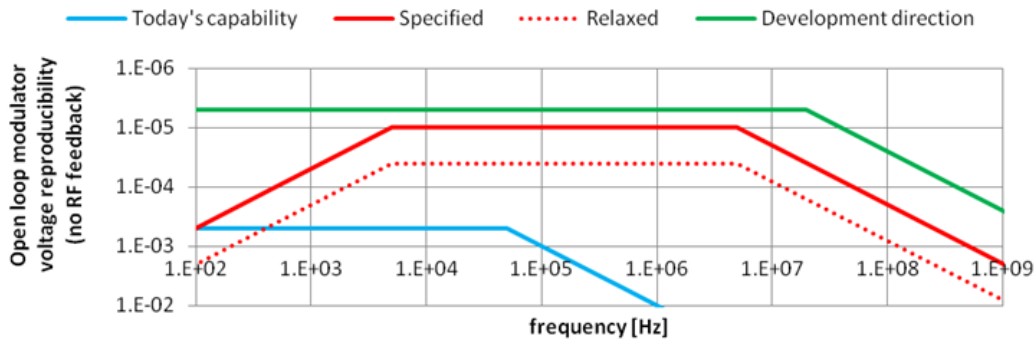


Fig. 5.182: Bandwidth requirement on the voltage measurement and state of the art

sensitive parameters for the selection of the optimum modulator topology (it is specified to reach not more than $10\ \mu\text{s}$ for total rise/fall/set-up time). Transformer-less topologies may be more efficient than solutions using pulse or resonant transformers (considering their bandwidth limitation affecting the pulse rise- and fall-times), however, they present more challenges in terms of reliability. To optimize the overall machine availability, a modular and parallel solution must be developed in order to counteract the poor mean time between failures due to the high number of modulators. Several topologies must be studied and compared, including, but not limited to, resonant, fully solid-state, monolithic and multiple pulse transformer solutions.

5.8.4 Reliability and redundancy

5.8.4.1 Reliability requirements (Machine Protection)

The required machine availability will be given by the Machine Protection Working Group. Technical shutdowns will be scheduled for global machine maintenance during which failed converters can be replaced if a redundant system has taken the lead. During operation, the down-time caused by failure in converters must not exceed a few per cent. With the amount of converters in the machine, the Mean Time Between Failure (MTBF) is expected to be only a few hours. Therefore, redundant and failure-tolerant systems are compulsory.

5.8.4.2 Sensitive areas and recommendations

For reliability, the most sensitive area is the DB decelerator with its 41 400 magnets to be powered. As described previously, the magnets will be arranged in powering groups containing one converter and several trimmers. The converters will be composed of identical modules to reach all current profiles with an N+1 redundancy. The trimmers can have up to 20 failures per accelerating sector without affecting the beam dynamics. These recommendations will allow a failure-tolerant operation and high machine availability if the failed modules or trimmers are replaced during the scheduled maintenance days.

The other sensitive areas include the klystron modulators (which will be modular with N+1 redundancy to increase their reliability), the DB injection complex (11 000 magnets), the MB injection complex (7000 magnets) and finally the MB accelerator (4000 magnets underground). Special care must be taken with the converters that sit underground since their repair time must include the time for tunnel cool-down and travel to and from the tunnel. The modules must be designed in such a way as to facilitate their replacement.

5.8 POWERING CLIC

5.8.4.3 Machine inertia

In case of failure or fast abort of the machine, the current in the magnets must be maintained to within 90% of its nominal value for at least 2 ms. This leads to a requirement that the L/R time constant of the system has to be higher than 20 ms. In case of the failure of the power converter itself, the requirement on the crowbar response is proportional to $(LC)^{1/2}$ and the tolerated loss δ before activating the crowbar is typically 2.5%.

5.8.4.4 Machine availability

A first approach for predicting the availability of the machine is carried out with the decelerator. Its reliability has been estimated with composite models including failure rates and Markov chains. The reliability of the Main Linac is a function of the reliability of the main redundant converters and the trimmer chains with failure tolerance. The time-scale for reliability is defined as the mean time between scheduled maintenance days and the availability of the machine as a function of the scheduled maintenance is given in Fig. 5.183. The availability of the Main Linac is strongly affected by the trimmers after the failure tolerance has been reached. An obvious availability optimum is reached for this case, and the reliability study must be carried out for the whole powering system.

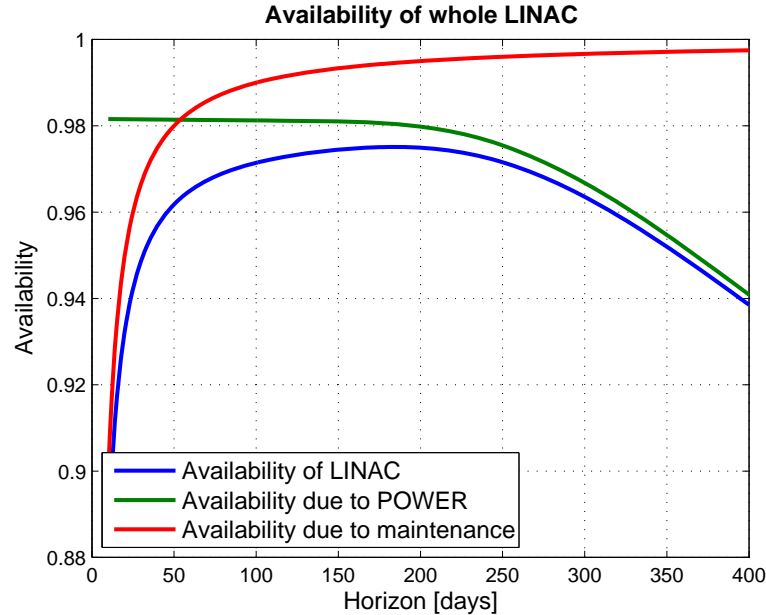


Fig. 5.183: Expectations on the machine availability due to the reliability of the Drive Beam decelerator

The presented model gives a fair approximation of the expected downtime. The aim of such a study is the optimization of the given system in terms of reliability with variables independent of the technology and variables which are directly linked with the hardware. Parameters such as redundancy and time between scheduled maintenance days can be changed within the model itself. Technically speaking, the optimization of parameters such as failure rates or mean time to repair depends on the power converters themselves. Accurate crowbar control, easy replacement of a module, or immunity against surges and explosions of a neighbouring module must be carefully designed to ensure failure tolerance.

5.8.5 Powering and grid considerations

The power consumption of CLIC needs careful consideration. With such an amount of power, the percentage of grid power fluctuation has to be minimized in order to respect the utility grid frequency

fluctuation constraints, to limit voltage flickers produced by step-down transformer voltage drops, and to reduce electrodynamic efforts in transformer windings. For these reasons, the charging of the capacitor banks of the pulsed converters might induce power transients on the 400 kV network that can affect its stability and quality. Therefore, a constant power load to the grid must be assured. Another direction for study would include optimal charger efficiency and modulator power management in case of sudden shutdown.

5.8.6 Components inventory

5.8.6.1 Magnets

The CLIC machine contains about 70 000 warm magnets of various types with different current needs as listed in Table 5.51. About two thirds are located underground in the Main Linac tunnel.

Table 5.51: Magnet distribution across sectors

Sector	Magnet type	Quantity
Main linac	DB quadrupole	41 400
	MB quadrupole	3992
	Dipole corrector	3992
Drive Beam injection	Dipole	1604
	Quadrupole	3813
	Sextupole	1804
	Corrector	3813
Drive Beam linac	Quadrupole	1638
Damping rings	Wiggler	208
	Dipole	280
	Quadrupole	1802
	Sextupole	952
	Corrector	1024
Main Beam injection	Dipole	568
	Quadrupole	1637
	Sextupole	276
Beam delivery system	Dipole	432
	Quadrupole	192
Total		69 427

5.8.6.2 Converter families

It is important for the optimization of the manufacturing and subsequent maintenance to group the magnets into the smallest number of powering families. The magnets of the DB accelerator should have similar requirements to those in the decelerator in order to be able to use the same converters. The current needs of the other magnets should be made as uniform as possible, within a particular sub-type. At this point in the project, several converter families have been established according to the power needs as shown in Table 5.52. The corresponding magnets might have to be corrected, e.g., in the number of turns to fit into one of the families.

5.8.7 Outlook for project preparation phase

Drive Beam linac:

Table 5.52: Converter families

Current	Voltage	Power	Quantity	Magnets to be powered
±1 A	±5 V	5 W	3992	Main Beam correctors
4 A	12 V	33 W	41 400	Drive Beam trimmers
42 A	220 V	10 kW	4512	Drive Beam decelerator (+accelerator)
100 A	10 V	10 kW	2144	Damping Ring and Drive Beam sextupoles
±100 A	±10 V	10 kW	3092	Damping Ring skew quads and dipole correctors
±130 A	±10 V	1.3 kW	788	Damping Ring skew quads and steerers
130 A	10 V	1.3 kW	1004	Damping Ring quadrupoles
130 A	20 V	2.6 kW	3448	Main Beam quadrupoles types 1&2 and damping ring quadrupoles
130 A	40 V	5.2 kW	3092	Main Beam quadrupoles types 3&4 and Drive Beam dipoles and sextupoles
±250 A	±10 V	2.5 kW	312	Damping Ring steerers
500 A	15 V	7.5 kW	1265	Drive Beam quadrupoles and damping rings combined-function magnets
500 A	30 V	15 kW	816	Damping Ring quadrupoles
900 A	15 V	13.5 kW	8	Wigglers
900 A	35 V	31.5 kW	1184	Drive Beam dipoles
900 A	60 V	54 kW	260	Drive Beam and Damping Ring dipoles
n/a	n/a	n/a	n/a	Main Beam injection magnets, post collision line magnets, beam delivery system magnets

- Maximize charger efficiency and power quality.
Objective: better than 90% efficiency with constant power consumption.
- Minimize rise, fall and settling time of the pulse.
Objective: for 140 μ s pulse, less than 10 μ s total for rise, fall and set-up time.
- Guarantee exceptional pulse-to-pulse voltage reproducibility.
Objective: 10^{-5} from pulse_{n-1} to pulse_n (RF feedforward gives long-term precision).
- Optimize volume.
Objective: mechanical implementation compatible with one system every 3 m.

Decelerator:

- Hardware validation of the main converters using the trimming principle.
Objective: study and validation of the dynamics, failure process, and radiation hardness.

Reliability:

- Modular approach optimization for reliability.
Objective: improvement of machine availability.

5.9 Beam instrumentation

5.9.1 Overview of the CLIC beam instrumentation needs

In this section we refer to the design of the CLIC 3 TeV machine. Beam dynamics considerations dictate most of the requirements for beam instrumentation. Wherever needed, we make the distinction between instrumentation needs (primary requirements on the raw measurements) and the diagnostics potential, i.e., the potential to obtain derived physics parameters or performance indicators from the direct measurements.

CLIC is expected to perform with extremely tight tolerances on most beam parameters; a few examples: extremely small emittance beams are generated in the damping rings and this small emittance must be conserved over more than 40 km of beam transport lines. This transport requires a very precise control of the beam trajectory, hence very precise and numerous beam position monitors. At the interaction point, the beam is then focused to only a few nanometers in size requiring specific instrumentation. Before entering the main linac, the bunch length must be shortened and controlled with 10 fs-level resolution. In summary the dominating requirement for the instrumentation of the Main Beam is very high resolution, often beyond the presently achieved.

The situation for the Drive Beam is somewhat different: The Drive Beam has a moderate energy but an extremely high intensity and high bunching frequency. It is used to generate the radio frequency power required to accelerate the Main Beam. One could call the Drive Beam complex ‘nothing more’ than a power source, the equivalent of a gigantic 12 GHz klystron distributed over a distance of 48 km, which is supposed to run with the best efficiency and reliability. Here the most important requirement for instrumentation is stability and high reliability for machine protection.

The total number of instruments foreseen for the Drive and Main beams complex are given in Table 5.53 and Table 5.54 respectively. The distribution between instruments located in underground areas (grey) or in surface buildings (white) is indicated. On the first sight the number of instruments is very large and exceeds at least by an order of magnitude the number of instruments built for the LHC. But taking for example the beam position monitors, one has to realize that the demand is quite ‘standard’ in the sense that the beam position is sampled in both planes at a quarter betatron wavelength. The scale of the project then generates the large number of instruments; there is little room for specifying less instruments without severely compromising the performance of the project.

Table 5.53: Number of beam instruments for the Drive Beam complex

Instrument type	DB injector	DB tunnel	DB total
Intensity	38	240	278
Position	1834	44 220	46 054
Beam size	32	768	800
Energy	18	192	210
Energy spread	18	192	210
Bunch length	24	288	312
Beam loss/halo	1730	44 220	45 950
Beam phase	16	192	208
Total	3710	90 312	94 022

The following subsections describe in detail the present concepts and designs of all CLIC instrument types. Each subsection starts with a summary table expressing the needs for a given kind of measurement, both in terms of expected performance but also mentioning the number of devices to be installed along the accelerator. The tightest requirements are extracted from each table and discussed in detail. The technology chosen as a baseline solution for CLIC is presented with a status of its cur-

Table 5.54: Number of beam instruments for the Main Beam complex

Instrument type	MB injector	Underground	Total
Intensity	86	98	184
Position	1539	5648	7187
Beam size	34	114	148
Energy	19	54	73
Energy spread	19	4	23
Bunch length	17	58	75
Beam loss/halo	1936	5854	7790
Beam polarization	11	6	17
Tune	6	0	6
Beam phase	–	96	96
Luminosity	–	2	2
Total	3667	11 934	15 601

rent development. In some cases, the instruments have been already designed, integrated in the machine layout, or laboratory tests or even beam tests have been performed. For some others, the design of the instruments is only discussed at the conceptual level, relying on future achievements to be obtained in the framework of other accelerator projects.

The following text is a very comprehensive summary of all the studies performed so far for the CLIC beam instrumentation. It is structured the following way:

- Beam Position Monitoring Pickups (see §5.9.2)
- Beam Position Monitoring Electronics (see §5.9.3)
- Transverse Profile Measurements (see §5.9.4)
- Longitudinal Profile Measurements (see §5.9.5)
- Beam Intensity Measurements (see §5.9.6)
- Beam Loss monitoring (see §5.9.7)
- Beam Energy Measurements (see §5.9.8)
- Polarization Measurements (see §5.9.9)
- Luminosity Monitoring (see §5.9.10)

In order to avoid any misunderstanding, we show here definitions of ‘Accuracy’ and ‘Resolution’, two important terms used throughout this section:

- *Accuracy*: Value quantifying the absolute calibrated response of a measurement device within a well-defined standard frame (for example: beam position in mm relative to magnetic axis of adjacent quadrupole);
- *Resolution*: The resolution is the smallest increment that can be induced or discerned by the measurement device within the given conditions.

5.9.2 Beam Position Monitoring Pickups

An overview of the requirements for beam position monitoring is shown in Table 5.55. The requirements are expressed in terms of the expected position accuracy and resolution and the expected time resolution. The variation of the beam intensity and also the variation of the beam pipe aperture are quoted to highlight the various situations found along the entire accelerator complex.

Table 5.55: Beam Position Monitors by Region and Function

Sub-systems	Intensity [A]	Train duration / bunch frequency [ns]/[GHz]	Accuracy / resolution [μm]	Time resolution [ns]	Quantity	Beam aperture [mm]
Main Beam						
Injectors	0.5	156/1	100/50	10	83	40
PDRs	0.5	156/1	40/20	10	600	20/9
DRs	0.5	156/1	40/2	Turn by turn 10	600	20/9
RTML	1	156/2	40/10	Turn by turn 10	1424	Various
Main Linac	1	156/2	5/0.05	10	4196	8
BDS	1	156/2	5/0.003	10	200	Various
MDI & PCL	1	156/2	1000/100	10	12	Various
Drive Beam						
Source and linac	4	140 μs /0.5	20/20	10	660	40
Frequency	4 \rightarrow 100	140 μs \rightarrow 24 \times 240 ns	40/10	10	210	80
Multiplication		0.5 \rightarrow 12				
Complex						
Transfer to tunnel	100	24 \times 240 ns	40/10	10	872	200
Turnaround	100	240/12	40/10	10	1920	40
Decelerator	100	240/12	20/2	10	41 484	26
Dump lines	100	240/12	20/2	10	96	40

5.9.2.1 Main Beam Linac BPM

The Main Beam linac requires one BPM per quadrupole, a total of 4196 BPMs. Resolution requirements of 50 nm (even tighter in the Beam Delivery System) as well as accuracy and stability requirements make resonant cavity position monitors the only obvious choice. Single-bunch spatial resolution better than these requirements has already been demonstrated in several systems [156] using very narrow band resonating cavities. But the required temporal resolution implies to use a broader bandwidth. The largest presently deployed system with comparable bandwidth and spatial resolution consist of 36 BPMs [157, 158], so the CLIC system will provide the additional challenge due to its large scale.

Table 5.56: Main Beam Linac Beam Position Monitor Specifications

Parameter	Value
Quantity	4196
Nominal current	1.2 A
Bunch frequency	2 GHz
Single bunch charge	$3.72 \times 10^9 \text{ e}^-$ (600 pC)
Beam duct aperture	8 mm
Position resolution	50 nm r.m.s.
Temporal resolution	10 ns
Accuracy	5 μm
Stability	100 nm

Baseline Choices

The Main Beam linac BPM consists of two cavities [159] as depicted in Fig. 5.184, a position cavity measuring both X & Y, and a reference cavity measuring beam charge and phase. The position cavity supports degenerate X and Y dipole modes at 14 GHz. The signals are brought out on four dipole-mode selective couplers, two for each of the X and Y position signals. The reference cavity, with monopole mode frequency also at 14 GHz, provides the beam charge and phase signal used to normalize the position signals. The reference cavity has two monopole mode coupling ports. Redundancy of readout is required to insure that one can identify spurious measurements, which might otherwise risk machine damage from mis-steering the beams by the real-time orbit feedback.

Monopole mode in dipole cavity

As the BPM position cavity output waveguides are designed to couple only to cavity dipole modes, the monopole mode of the dipole cavity has essentially no external damping. We have studied the effect of this undamped monopole mode on longitudinal beam dynamics. We require that the energy variation due to the BPM longitudinal mode along the bunch train is small ($<10^{-4}$) when summed over all BPMs. We find this condition is met if the monopole mode frequency of the dipole cavity is sufficiently far from a harmonic of the 2 GHz bunch spacing. For example, if the monopole mode frequency is at least 200 MHz away from $N \cdot 2$ GHz, we find that the monopole mode, summed over the Main Beam bunch train, leads to an energy variation along the train of ~ 1 kV per cavity, or ~ 2 MeV if summed coherently over the 2000 cavities in one linac. This amounts to less than 10^{-5} of total energy at 250 GeV operation or $\sim 10^{-6}$ at 1.5 TeV, compared to the requirement of $<10^{-4}$. The energy difference is reduced even more by detuning of the cavity monopole mode.

Future Activities and Options

Three MB BPMs will be fabricated and tested, both on the bench and in CTF3. Bench tests will include verification of design including the ease manufacturing, mode frequencies and couplings, and accuracy of mode centres. Beam tests will include verification of coupling, resolution, accuracy, and stability. In addition we will proceed with the design and prototyping of cavity BPM processing electronics. We will investigate an alternate design for the pickup based on a choke-mode cavity.

5.9.2.2 Beam Delivery System BPMs

The Beam delivery system requires a BPM resolution at least ‘as good or better’ than the Main Beam linac with the added complication of beam pipe apertures varying between 8 and 25 mm. The larger aperture BPMs must operate at a lower frequency than that chosen for the main linac BPMs, even as low as 3 GHz. The required performance can be achieved by scaling the demonstrated performance of existing BPMs. Fortunately the BPMs requiring 3 nm resolution have small pipe diameter and can be handled with essentially the same pickup and electronics as envisioned for the Main Beam linac BPM. The signal-to-noise in these BPMs is adequate to meet the resolution requirements. Though this resolution has not yet been observed in a particle beam, recent results are approaching the requirements [159].

5.9.2.3 Damping Ring BPMs

The CLIC damping ring complex, including pre-damping rings, requires BPMs capable of turn-by-turn resolution. Given the short length of the bunch train (156 ns) compared to the revolution time of the ring (1.6 μ s), RF transient loading is an important issue. Therefore a few BPMs must provide temporal resolution within the 156 ns bunch train. We expect it will be convenient to provide 10 ns temporal resolution for all of DR and PDR BPMs.

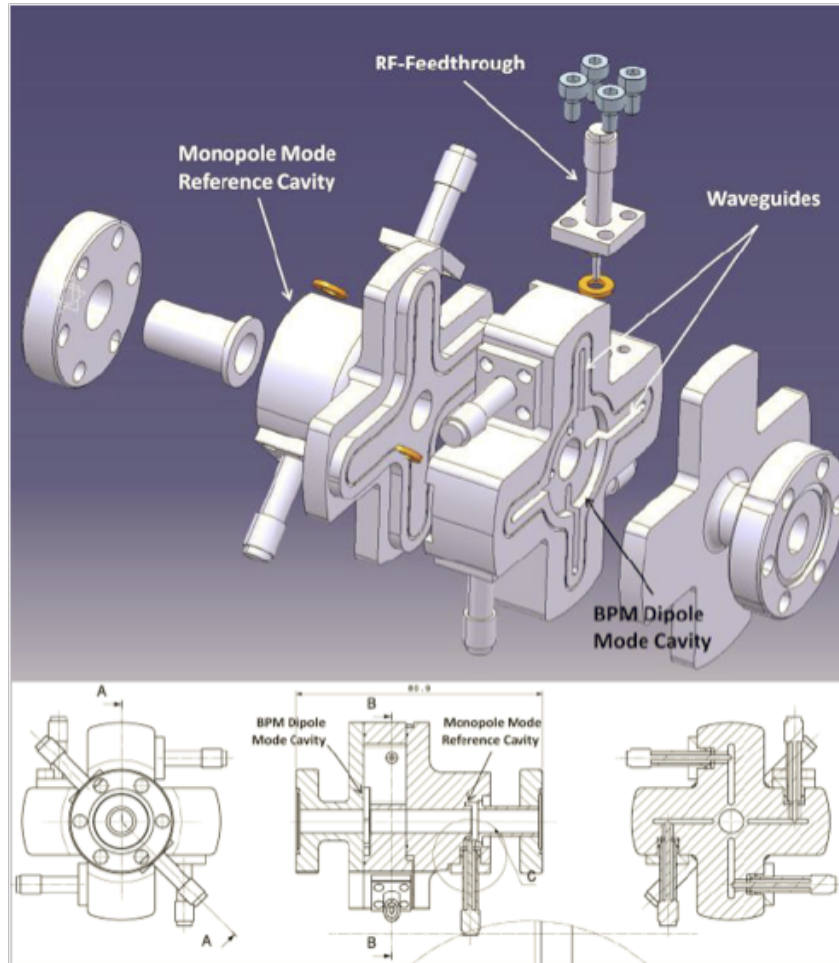


Fig. 5.184: Main Beam Linac Cavity BPM

Table 5.57: Damping Ring Beam Position Monitors

Parameter	Value	Comments
Quantity	1200	e^+ & e^- PDR's & DR's
Nominal current	600 mA	During train passage
Revolution frequency	608 kHz	
Bunch frequency	1 GHz	
Single bunch charge	600 pC	
Beam duct aperture	20 / 9 mm	
Position resolution	10 μ m	
Temporal resolution	100 ns	
Accuracy	20 μ m	Centre with external fiducials

Baseline Choices

A conventional high-current ring BPM system is appropriate. Small button pickups will be used to maintain low beam impedance. Low coupling to the beam is adequate given the large beam current here. In general, the requirements are similar compared to those of many light sources.

5.9.2.4 Drive Beam decelerator BPMs

The BPMs for the Drive Beam decelerator represent a unique combination of issues:

1. Quantity: 41 580 pieces; these account for 75% of all CLIC BPMs
2. Bunch structure; the function of the DB decelerator is to produce > 100 MW RF power at 12 GHz, some small fraction of which can propagate to the BPM, making the bunch frequency a poor choice for processing BPM signals.
3. Temporal resolution of 10 ns requires developing an adequate position signal throughout the bunch train.
4. Required resolution of $2\ \mu\text{m}$ in a beam aperture of 23 mm requires amplitude measurement at high resolution, about one part in 6000 in amplitude and requiring accurate calibration.
5. Dynamic range: the system must electrically ‘survive’ the signals generated for extreme cases of non centred beams at any fill pattern up to 240 ns pulse length up to 8.3 nC/bunch.

Table 5.58: Drive Beam decelerator BPMs

Parameter	Value	Comments
Quantity	41 580	Total for all decelerators
Nominal current	100 A	
Bunch frequency	12 GHz	
Single bunch charge	8.3 nC	
Beam duct aperture	23 mm	
Position resolution	2 μm r.m.s. & full charge, single bunch to 240 ns train	
Temporal resolution	10 ns	Centre with external fiducials
Accuracy	20 μm	
Wakefields	Under study	

Baseline Choices

The present concept foresees to use short stripline BPMs, only 25 mm long, with position signals processed at baseband in a bandwidth of 4 – 20 MHz. The striplines are to a large extent integrated into the aperture of the quadrupoles in order to meet the space constraints of the two-beam module (see Fig. 5.185).

Time-Domain Analysis

The BPM was modeled in GdfidL (see Fig. 5.186) for beam response and wakes (see Fig. 5.187). Initial analysis indicated trapped modes; in particular we find a resonant mode close to the 12 GHz bunch spacing apparent in the transverse wake. Addition of a ring of SiC rf damping material at the base of the striplines damps this resonance without significantly affecting the beam position signal as depicted in Fig. 5.188 and Fig. 5.189.

In the following steps the damped BPM design was analysed for beam response and wakes. We compared the time-domain analysis with an analytic model and found excellent agreement (see Table 5.59). Transverse wakes were calculated for the analytical model from the beam voltages induced on the striplines, integrated over the number of bunches in the round-trip time of the stripline signal [160].

The bunch train longitudinal wake was obtained by convoluting the single bunch wake from GdfidL with the 12 GHz bunch fill pattern. The results are depicted on Fig. 5.190. No coherent buildup of the wake over the train is observed.

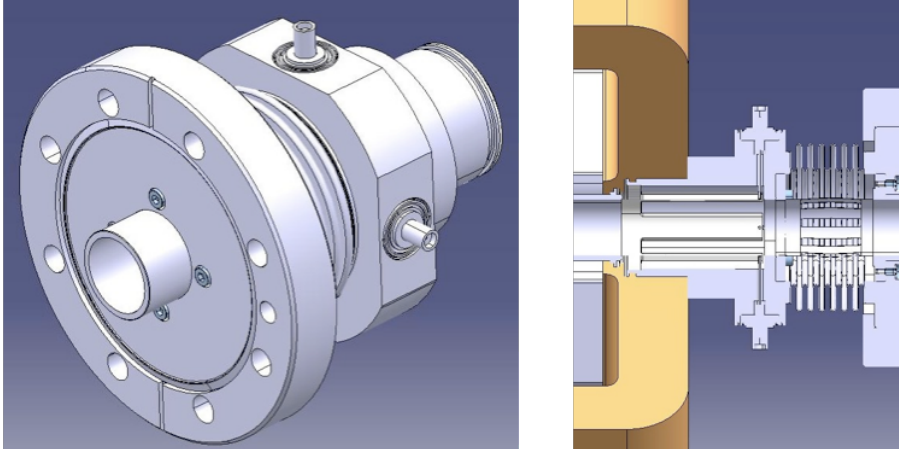


Fig. 5.185: left: 3D model of a Drive Beam Decelerator BPM – right: BPM integrated in the CLIC module.

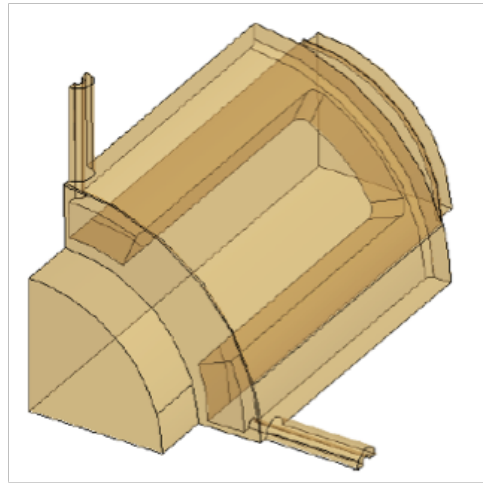


Fig. 5.186: GdfidL model of Drive Beam BPM.

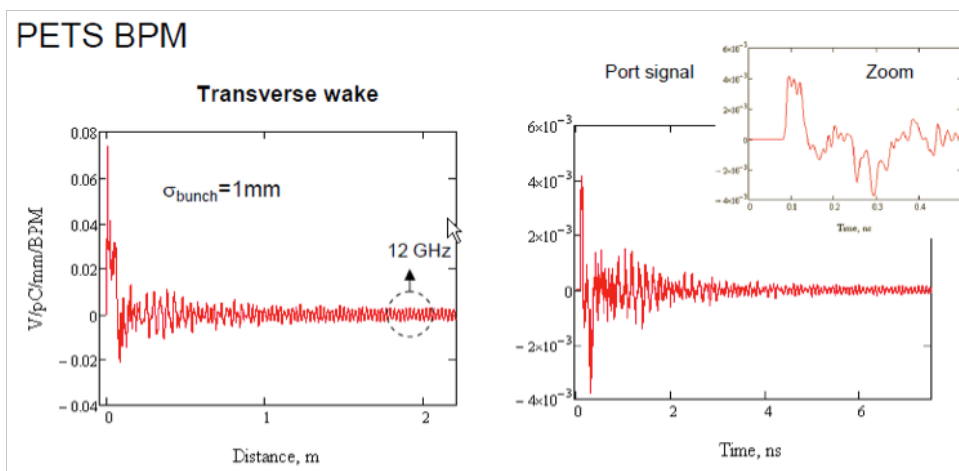


Fig. 5.187: Undamped stripline BPM transverse wake and port signal.

A prototype Drive Beam BPM will be tested in the lab in 2012, followed by beam tests of four units in CTF3.

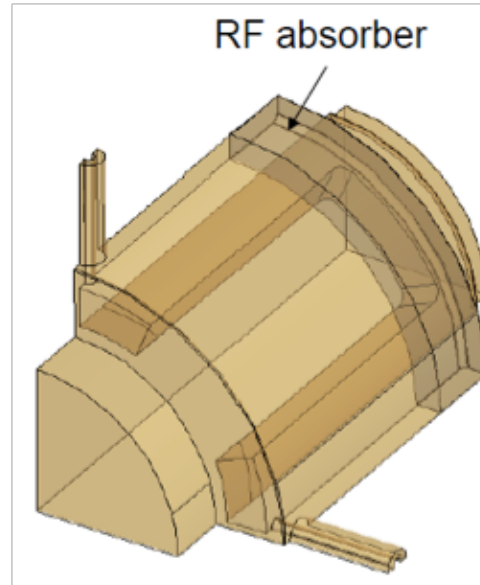


Fig. 5.188: Drive Beam BPM with RF absorber added.

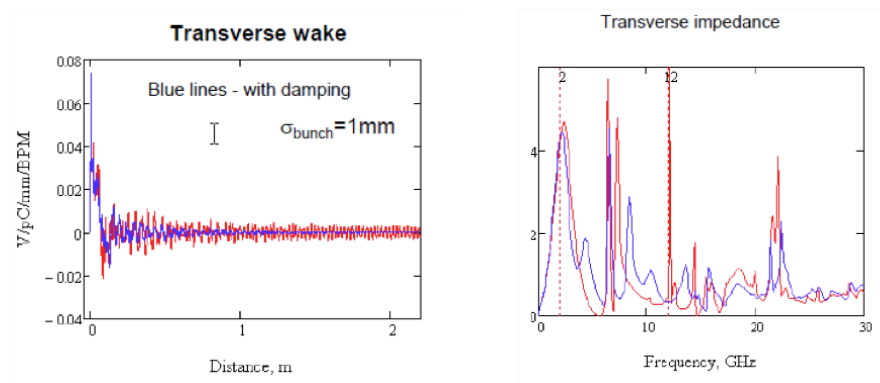


Fig. 5.189: Transverse wake and transverse impedance of Drive Beam BPM. Undamped (red) and damped (blue). The damping material removes the narrow lines above the BPM processing frequency.

Table 5.59: Comparison of GdfidL and analytic model of Drive Beam BPM response

Parameter	GdfidL	Analytic	Comments
Signal amplitude	0.16 fJ	0.15 fJ	Signal energy for 1 pC single bunch, evaluated at 2 GHz in 100 MHz bandwidth
Transverse scale	0.146/mm	0.148/mm	Dipole/monopole sensitivity
Transverse wake	31 mV/pC/mm	27 mV/pC/mm	

5.9.2.5 Other BPMs: Drive Beam transfer line example

The Drive Beam linac, its transfer lines and turnarounds and other beam systems require another 5000 BPMs with requirements less demanding than those of the Main Beam linac or Drive Beam decelerator. We plan to instrument these areas with slightly modified versions of the previously detailed BPM designs. As an example we look at the one of the more challenging of these systems, the Drive Beam long transfer line BPMs, the challenge coming from the large beam duct diameter. Here we chose for the baseline

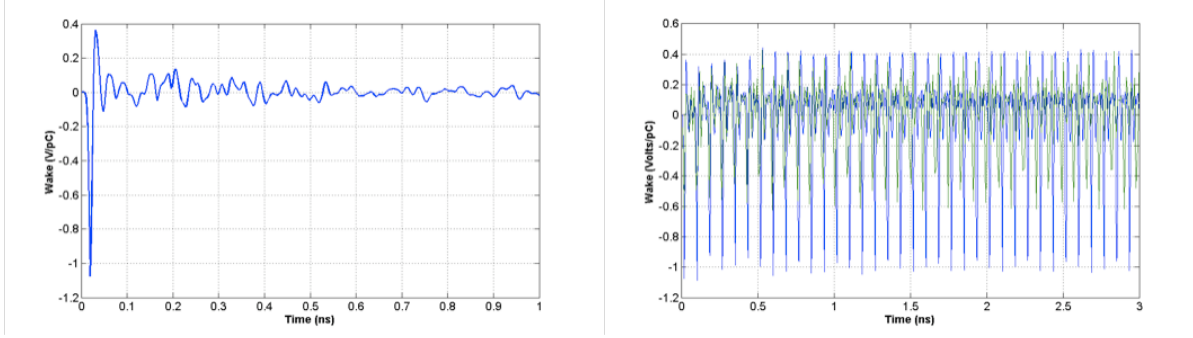


Fig. 5.190: Single bunch and bunch train longitudinal wake calculated by GdfifL.

design a button BPM with small 6 mm diameter buttons. The presence of high frequencies in the beam bunch spectrum precludes large buttons due to the existence of narrow-band beam impedances at the TE11 mode resonance around the button edge. Choosing to process the signal in a 20 MHz bandwidth around a centre frequency of 200 MHz, we find that we can meet the $10\ \mu\text{m}$ resolution requirement for an intensity as low as a single bunch at nominal bunch charge.

Table 5.60: Long Transfer lines BPM requirements

Parameter	Value	Comments
Quantity	872	e^+ & e^- long transfer lines
Nominal current	100 A	
Bunch frequency	12 GHz	
Single bunch charge	8.3 nC	
Beam duct aperture	200 mm	
Position resolution	$10\ \mu\text{m}$	
Temporal resolution	10 ns	
Accuracy	$40\ \mu\text{m}$	Centre wrt external fiducials

5.9.3 Beam Position Monitoring Electronics (Processors)

Three different types of BPM processor are presently under consideration to serve the various types of BPM systems. These have much in common; they are all based on maximizing the processing done digitally to take advantage of modern, high resolution, fast sampling ADCs. We minimize the amount of critical analog components, especially ones requiring critical matching. Online calibration is an important aspect of these designs.

At this point we base the designs on 16-bit, 160 Msample/sec ADCs, but the designs scale easily to faster sampling devices. The higher the sampling rate, the easier it is to meet requirements for analog components, especially the large and potentially expensive analog filters in the signal paths.

Table 5.61 gives the overview of which processor will be used for each part of the accelerators. The processor types are explained in more detail in the following subsections.

5.9.3.1 Cavity BPM Processor

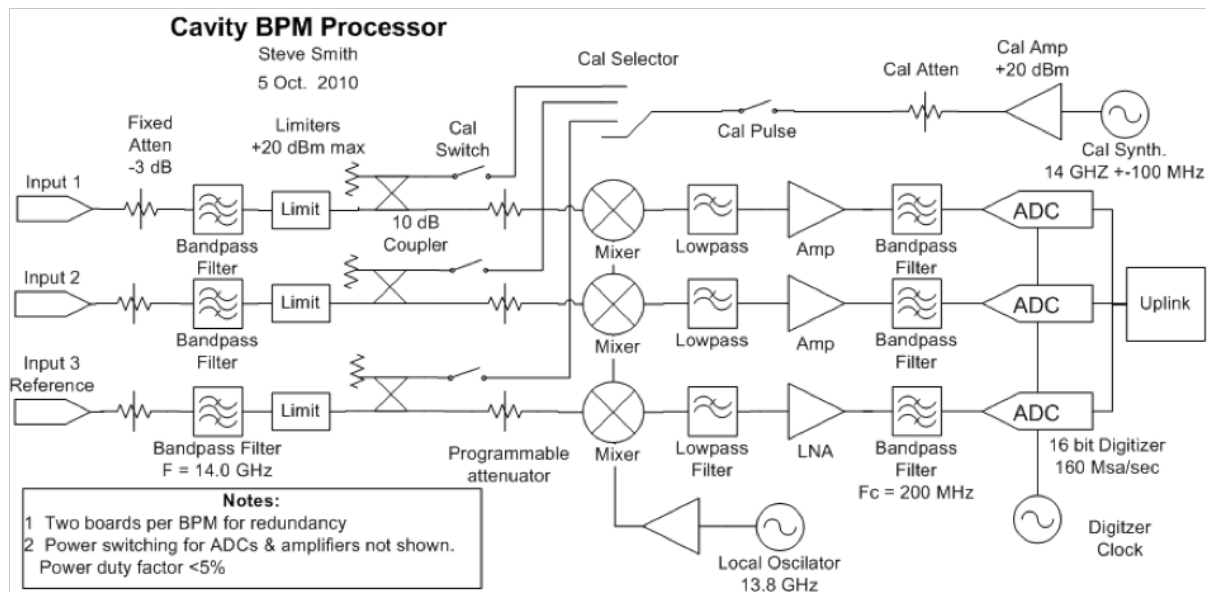
A cavity BPM processor is designed to measure 6 signals at 14 GHz, two signals for each transverse position and two reference channels for the intensity and phase. Three signals would be enough, but seen the importance of the system for the luminosity performance of the accelerator all physically available

Table 5.61: Beam Position Monitor Processor Types

Processor Type	Freq.	BW	Ultimate	Time res.	Pickup Type	Qty
Cavity BPM	14 GHz	40 MHz	50 nm	10 ns	Cavity	4800
Damping Ring	2 GHz	40 MHz	1 μm	10 ns	Button	1200
Direct sampling	2–500 MHz	40 MHz	1 μm	10 ns	Button/strip	48 000

signals on the output ports of the cavity pickups are measured for redundancy. For convenience, and further redundancy, the six signals are spread across two mezzanine acquisition boards, either of which is able to provide full measurement capabilities to the required accuracy and resolution. The processing scheme (see Fig. 5.191) consists of bandpass filters, programmable attenuation, down-conversion, lowpass filtering, low-noise amplification, anti-alias filtering and the standard high-resolution ADC per channel. Further processing is performed digitally, including down-conversion from IF, digital filtering, normalizing to amplitude and phase of the Reference channel, phase rotation, I/Q demodulation, scaling and offset compensation. A digital filter with bandwidth less than the analog bandwidth of the system is chosen since the band-limiting digital filters are exactly matched.

Each processing channel is capable of injecting a test tone into its cavity to verify operation of its complementary processing channel.

**Fig. 5.191:** Cavity BPM Processor Mezzanine Card, two required per cavity BPM for redundancy.

The ADC is assumed to be at least as fast and accurate as the present Linear Technologies 16-bit, 160 Msamples/s LTC2209, with a low-power sleep mode suitable for $\leq 5\%$ duty factor at 50 Hz operation. At 160 Msamples/s, position can be reported in 6 ns intervals, though successive measurements at this rate are correlated due to bandwidth limitations in the processing chain, probably about 20 MHz.

5.9.3.2 Button/Stripline Baseband BPM Processor

Used principally for the Drive Beam decelerator BPMs, this type of processor acquires 4 signals in a bandwidth of 2 – 200 MHz directly from a button or stripline BPM. The processing scheme (see Fig. 5.192) consists of lowpass filters, programmable attenuation, low-noise amplification, anti-alias

filtering and the standard high-resolution ADC per channel. Further processing is performed digitally, including digital filtering, amplitude estimation, and estimating position from $Y = R/2 \cdot \Delta/\Sigma$. Two of the input channels are capable of emitting a test tone to calibrate the gain ratio of the two adjoining channels via the inter-pickup coupling. The ADC is assumed to have the same performances as the ones chosen for the cavity BPM described previously.

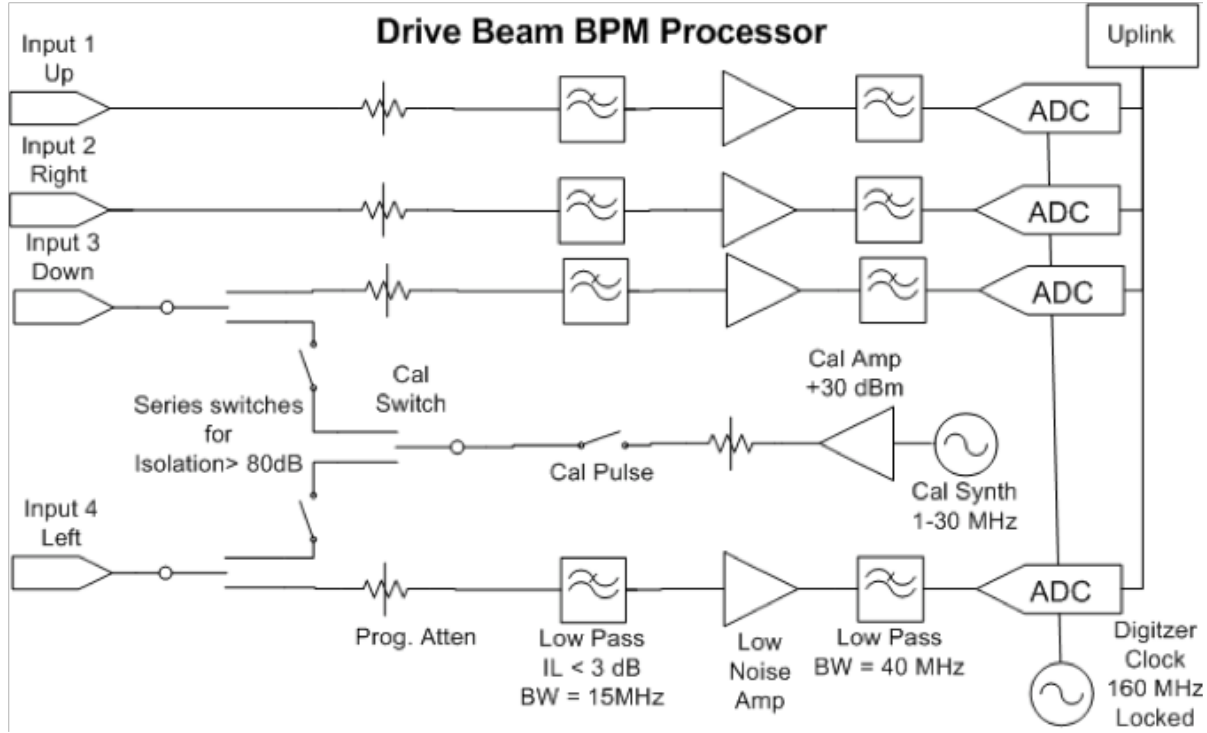


Fig. 5.192: Baseband Button/Stripline BPM Processor mezzanine card.

5.9.3.3 Damping Ring BPM Processor

The damping ring processor looks very much like the Baseband Button/Stripline BPM processor with the addition of analog downconversion from 1 or 2 GHz to a finite IF before the digitizer. Nevertheless since it likely has many more operational modes and a turn by turn storage capability, we anticipate a different implementation. There are commercially available electronics for ring BPMs used in almost every third generation light source, which meet these needs. This will be further investigated in the technical design phase of the project.

5.9.4 Transverse Profile Measurements

5.9.4.1 Overview

An overview of the requirements for transverse profile monitoring is shown in Table 5.61. It presents the evolution of the normalized beam emittance through the CLIC complex with the corresponding expected spatial resolution and the number of devices requested. The beam energy is also indicated as it may influence the choice of detector technology. The typical charge densities are mentioned, as they will set an upper limit above which intercepting devices like screens or wire scanners would get damaged. For best thermal-resistant materials like C, Be or SIC, the limit corresponds to charge density of 10^6 nC/cm² [161]. This number refers to the survival of material to single shot pulse, and does not take into account the heat dissipation effects that would need to be considered in the final design (repetition rate of the machine, cooling of the material).

In most cases, the measurement of the beam size serves directly to compute the transverse beam emittance. For ultra-relativistic beam energy, it is classically done using either the 4 profiles method [162] or a quadrupolar scanning method [163]. The first method relies on the use of several beam size monitors installed at different locations on the beamline and the emittance can be deduced using the nominal optic of the machine. The other method only requires one profile monitor, where the beam size is measured as a function of the strength of a focusing element. This latter method is obviously cheaper because only requires a single monitor but the beam optic needs to change accordingly, which may lead to unexpected beam losses. An alternative solution has been proposed and tested on the CTF2 [164] scanning five quadrupoles or more in such a way that the beam size stays constant at the profile monitor while the phase advance through the beam line changes.

The use of intercepting devices, like screens, degrade the beam emittance due to multiple scattering effects as the beam passes through the screen and for this reason it becomes safer to dump the beam afterwards. The best solution would then be to measure the beam emittance using 4-profiles method and non-intercepting devices, which in some cases is unfortunately not feasible.

Table 5.62: Transverse beam size requirements

Sub-systems	Emittance [nm.rad]	Energy [GeV]	Resolution [μm]	Quantity	Charge density [nC/cm ²]
Main Beam					
e ⁻ source & pre-injector complex	10 ⁵	0.2	50	2	< 5 × 10 ⁵
e ⁺ source & pre-injector complex	93 × 10 ⁵	0.2	50	4	< 5 × 10 ⁵
Injector linac (e ⁻ /e ⁺)	1/93 × 10 ⁵	2.86	50	2	< 5 × 10 ⁵
Pre-Damping Rings (H/V)	63 000/1500	2.86	50/10	4	< 5 × 10 ⁶
Damping rings (H/V)	< 500/5	2.86	10/1	4	< 5 × 10 ⁸
RTML	510/5	2.86–9	10/1	70	< 5 × 10 ⁸
Main Linac	600/10	9–1500	10/1	48	< 5 × 10 ⁸
Beam Delivery System	660/20	1500	10/1	8	< 5 × 10 ⁸
MDI & Post-collision line	> 660/20	< 1500	1000	6	< 5 × 10 ³
Drive Beam					
Source and linac	100	2.37	50	10	< 40 × 10 ⁶
Frequency multiplication complex	100	2.37	50	20	< 40 × 10 ⁶
Transfer to tunnel	100	2.37	50	2	< 40 × 10 ⁶
Turn around	100	2.37	50	96	< 1.5 × 10 ⁶
Decelerator	150	< 2.37	50	576	> 1.5 × 10 ⁶
Dump lines	> 150	< 2.37	100	96	> 1.5 × 10 ⁶

With the total number of required devices at 948, the measurements of transverse beam size is a becoming a very large system, corresponding to the 3 times the total number of such devices actually in use at CERN in the whole accelerator complex. Typical imaging systems used in CTF3 are presented in §7.2.8.

The beam emittance is significantly reduced in the damping rings and the performances of transverse profile become extremely challenging from the damping rings till the end of the Beam delivery system, with a 1 micron resolution. Several detection systems, which have already proven their capability to measure very small beam size are presented in the following subsections.

5.9.4.2 Optical Transition radiation imaging systems

The spatial resolution of $50\text{ }\mu\text{m}$, as requested from the Main Beam source to the end of the injector linac, can be easily achieved using Optical Transition Radiation (OTR) screens [165] or wire scanners [166]. The expected charge densities are still compatible with the use of standard and robust interceptive techniques. OTR screens provide images of the beam in a single shot, whereas wire scanners only give beam profiles over several shots. However, wire scanners have the advantage of being less interceptive than screens, where the beam is normally required to be dumped afterwards. These technologies have been used for 20–30 years and state-of-the-art devices have even pushed the resolution limit down to few microns [167–170].

A typical imaging system, as used on CTF3, is depicted in Fig. 5.193. It is composed of a vacuum tank equipped with a motorized arm, capable of inserting two OTR screens with different reflectivity coefficients and a calibration target. Visible photons are emitted by the screen, reflected vertically downwards and focused onto a CCD camera using a radiation-hard lens. The light intensity is adjustable using a remotely controlled Optical density filter wheel. Lead shielding blocks are installed all around the camera to minimize radiation damage as much as possible.

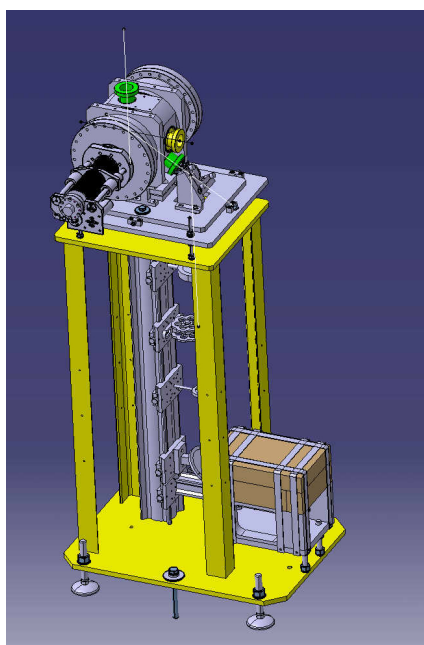


Fig. 5.193: CTF3 OTR screen assembly.

The major limitations for the use of OTR screen resides in the beam induced thermal load. As an example, the instantaneous temperature rise in thin graphite screen has been calculated as a function of beam energy and beam size for the case of the Main Beam and the Drive Beam. The results are shown on Fig. 5.194 and clearly indicate that below $500\text{ }\mu\text{m}$ for the MB and 3 mm for the DB screen cannot survive the full beam charge. This is a strong constraint, which can only be overcome by limiting the number of bunches or reducing the pulse train length.

5.9.4.3 High resolution transverse profile measurement using OTR

Spatial resolution better than one micron have been recently measured by observing the beam size contribution to the Point Spread Function (PSF) of a standard OTR imaging system [171, 172]. Originally the PSF is an image generated by a point-like source and projected by an optical system on a detector (e.g., CCD camera). The source is provided by optical transition radiation from a conductive target. The PSF must bear information about the source structure, the optical system, and the distribution of electrons

5.9 BEAM INSTRUMENTATION

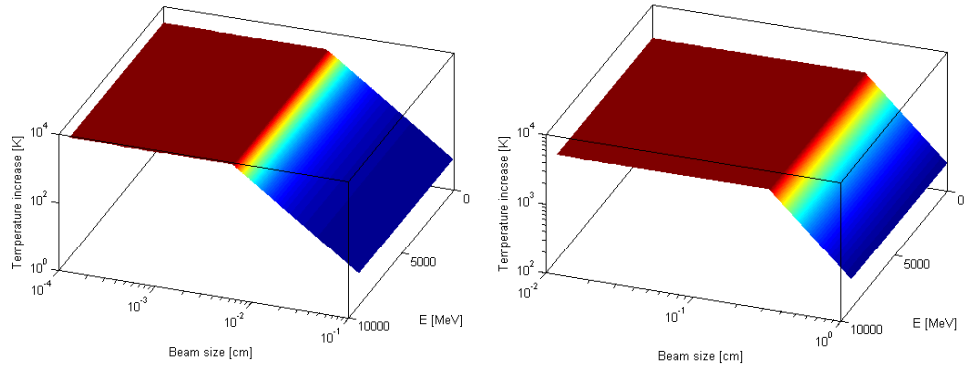


Fig. 5.194: Temperature increase of screen as a function of beam size and beam energy for the Main Beam (left) and Drive Beam (right)

(the beam size). It was predicted that the source is non-uniform, but has a minimum in the centre. The width of the PSF (as well as the sensitivity to the transverse beam size) is defined by the optical system, but the visibility is determined by the beam size. A typical vertical polarization component of OTR PSF measured at ATF2 is shown in Fig. 5.195(left) while Fig. 5.195(right) shows projected OTR PSF measured for three different beam sizes. A clear sensitivity to a micrometer beam is observed. Nevertheless, additional investigations and systematic measurements are required to optimize the optical system and light density on a CCD and to convert the current system into a ‘turn-key’ device.

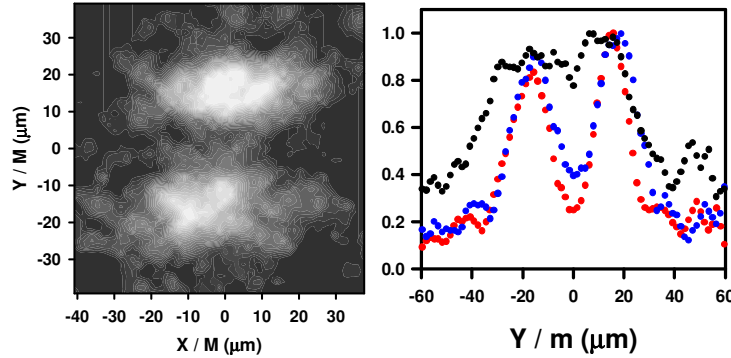


Fig. 5.195: High-resolution beam size measurement using OTR PSF technique (m is the magnification factor and X and Y are the CCD coordinates). Left - typical OTF PSF vertical polarisation component; Right - projected OTR PSF measured for three vertical beam sizes: SAD predictions are $\sigma = 7.2 \mu\text{m}$ (black), $\sigma = 3.4 \mu\text{m}$ (blue), and $\sigma = 1.7 \mu\text{m}$ (red).

Of course, thermal limitations linked to the use of an intercepting device remain true in this case and would most likely limit this technique to single bunch observation or low intensity beams.

5.9.4.4 Synchrotron light imaging

CLIC will collide beams with nanometers beam size, which strongly relies on the generation of ultra-low emittances in the damping rings, putting very tight requirements on the spatial resolution of beam size monitors. This problem has been studied in detail during the last 10 years either in the context of performance optimization of 3rd generation synchrotron light sources or in the framework of the ILC / CLIC studies with an R&D program performed to prove the feasibility of low emittance generation in damping rings. This work has led to the developments of several techniques, which can provide beam size measurements with resolution of the order of one micron. Two of them are based on the use of

Synchrotron Radiation (SR) [173]. For highly relativistic particles, the spatial resolution of SR imaging system is intrinsically limited by diffraction, which can be minimized by using shorter wavelength. To provide micron size resolution, imaging systems were further developed in the X-ray regime [174–176]. Another innovative techniques has been proposed and successfully tested in PSI [177, 178] based on the measurements of the Point Spread Function (PSF) on an imaging system. The beam size is not seen anymore as an image of the beam, but as a modulation of the PSF of a simple imaging system and sub-micron resolution have already been achieved. At ATF2 in KEK, very small beam profiles have been measured as well using a Laser Wire Scanner [179]. The latter device is discussed in more details in the next paragraph.

5.9.4.5 *Micron-size resolution using laser-wire scanners*

The most critical issue for transverse profile monitoring has been identified since several years and refers to one-micron resolution beam size measurements in a linear part of the machine. In the CLIC complex, this type of device will be required from the exit of the Damping Ring to the Beam Delivery system. This covers more than 80 km of beam line and a total of more than 100 devices will be required. Contrary to the rings or turnarounds, where synchrotron radiation could be envisaged as a natural source of light for instrumentation, there is no natural source of photons in a linear accelerator. The use of intercepting devices must be restricted to single bunch mode to prevent any beam-induced damages.

Basic principle of a laser-wire scanner

Laser-wire systems employ a finely focused laser beam to scan across an electron beam to measure its transverse profile and thereby determine its emittance [180]. Laser light is compton scattered off the electron beam and either the scattered photons (or, at high electron beam energy, the scattered electrons) are detected downstream. Laser-wires are well suited for use at CLIC because they are relatively non-invasive devices that can be used continuously during machine operation and they can also be used for very high intensity beams, whereas solid wires would be destroyed. They can also be used for beam sizes approaching the wavelength of the laser-light. Typically light of wavelength 532 nm has been used to date, however shorter wavelength light has been used at SLC [181]. The interplay between laser-wire location and the corresponding technical requirements on the laser-wire systems, including compton signal extraction, needs to be integrated into the beamline design throughout the machine.

Existing systems at electron machines

The state of the art at electron ring machines was achieved at the ATF [182] using a CW laser plus focusing cavity centred on the electron beam and at PETRA [183], where a Q-switched injection-seeded laser is used. A schematic of the optical set-up is shown in Fig. 5.196.

Both the ATF and PETRA systems measure the horizontal and vertical dimensions of the electron beam. The ATF system measured successfully electron beams of size $5.5\ \mu\text{m}$. The PETRA system measured electron beams of size of $48\ \mu\text{m}$, aiming at automation and turnkey operation; a single scan at PETRA takes less than one minute, limited by the laser repetition rate (20 Hz).

Micron-scale laser-wires

At the micron scale needed for some locations in CLIC (e.g., the BDS) systematic effects are very important, including uncertainties due to laser optical aberrations and the unknown horizontal size of the electron beam, which enters via a convolution with the laser intensity distribution at the focus.

Micron-scale electron beams were measured at the ATF extraction line [184] where beams of the order $3\ \mu\text{m}$ vertical size have been measured.

At the ATF2 laser wire, the laser is focused at the interaction point by a custom doublet lens of

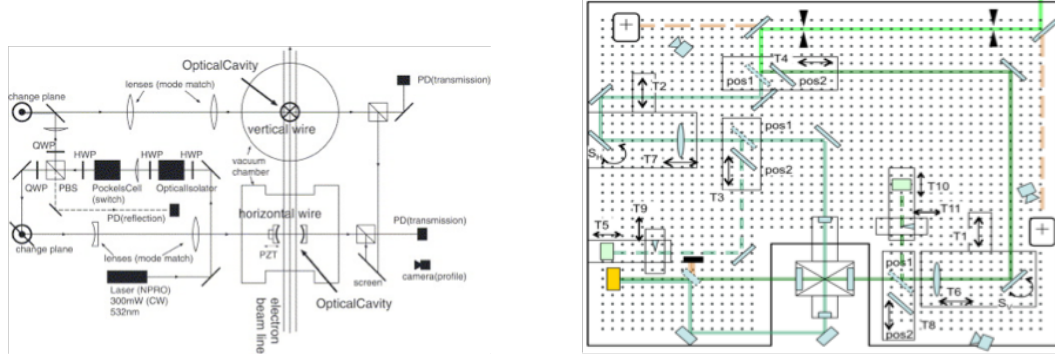


Fig. 5.196: (left) Layout of the optical components of the ATF Damping ring laser-wire [181]; The symbols stand for photodiodes (PD), half-wave plate (HWP), quarter-wave plate (QWP), polarizing beam splitter (PBS), and piezo actuator (PZT). (right) Layout of the PETRA III laser-wire system; in this system the vacuum chambers are fixed and the laser light is scanned from a vertically mounted optical table.

focal length 56.6 mm. The lens consists of three elements, the first two elements with curved surfaces and then a vacuum window, which is an integral part of the lens design. The first curved surface is aspheric to correct for spherical aberrations. All of the optical elements are made of fused silica to withstand both high laser power and a high radiation environment; the use of a single material has implications for the chromatic aberrations of the system, which in turn has implications for the spectral energy spread of the laser system. The lens also has a high damage threshold anti-reflective coating to prevent the formation of ghosts within the lens, which could destroy it. A full discussion is provided in [183].

Ongoing R&D at ATF2 is concentrated on understanding these systematic effects and on pushing the measurement scale down to one micron or less. Other challenges include increasing the speed of scanning and the ease of turnkey operation; ongoing R&D at PETRA III is addressing these aspects. Two measurement examples are given in Fig. 5.197.

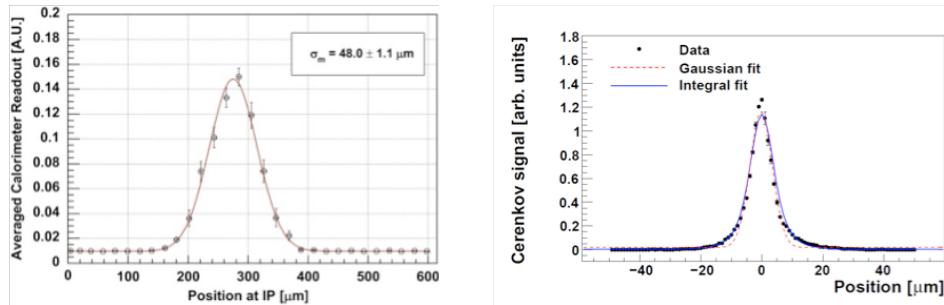


Fig. 5.197: Vertical laser-wire scans. (a): PETRA III [182]. Right: ATF-Extraction line [183] including a fit to a Gaussian and also an integral fit incorporating Rayleigh range effects. These affect the convoluted laser-wire scan shape as the Rayleigh range of the laser is comparable to the horizontal size of the electron beam and therefore the assumption that the laser size is the same across the whole electron beam is no longer valid. However, it is difficult to disentangle this effect from aberrations of the laser or lens and requires careful modeling.

Laser System

Additional challenges are presented by the laser-systems themselves; ongoing R&D [185] is centered on developing fiber lasers because of their many attractive properties which are important for laser-wire operation. To achieve the smallest beam size possible (limited by the optics and the laser wavelength), it is important that the spatial beam quality of the laser is as close as possible to a perfect Gaussian. This is

measured by a quantity called the M^2 of the laser, where an M^2 of 1 is a perfect Gaussian and beams with poorer quality spatial output have higher M^2 s. So that the focused spot of the laser is not limited by its spatial quality it is desirable to have an $M^2 < 1.1$. This can be difficult to achieve with high power solid state lasers (e.g., Nd:YAG), as thermal effects in the laser rod tend to distort the output mode. Optical fibers are waveguides, and if a single mode waveguide is used as a fiber laser the output will be very nearly perfectly Gaussian, at any level of amplification. For visible and near infrared light, a single mode fiber will be < 10 mm in diameter, which limits the amount of energy it would be possible to extract from the fiber. However, recently photonic crystal fibers have been developed [186] which have a core surrounded by air holes that mean it is possible to have large diameter cores (up to 100 mm is possible) while still remaining single spatial mode, allowing the use of these fibers for high power applications.

For the laser-wire experiments at the ATF [183] a pulse energy of 200 mJ and duration 400 ps (FWHM, so ~ 168 ps) was used, giving a peak power of 500 MW. However, the electron pulse duration was ~ 30 ps, so it would be possible to use a less energetic shorter pulse. Calculations have shown that a power of 10 MW (e.g., 50 mJ in 5 ps) should be acceptable for these experimental conditions, an energy achievable in fiber systems (although not at high repetition rates). Research is ongoing to produce energies greater than 100 mJ in the near infrared at repetition rates high enough for intra train scanning.

Pointing Stability

Fibers can also be made polarization maintaining, that is, the polarization state of the light out of the fiber is the same as that coupled in. This is important as the smallest achievable spot size depends on the laser wavelength and therefore it is preferable to work in the visible or UV regions. However, Er and Yb doped fibers lase in the near infrared (1.55 μ m and 1 μ m respectively) and so it is necessary to convert this output via harmonic generation to shorter wavelengths, which requires linearly polarized light.

Another advantage of fiber lasers is their efficiency. Continuous wave fiber lasers can have efficiencies (absorbed pump power to laser output) of 85%, which means that very little pump power is transferred to the fibre as heat and this, combined with the high surface area to volume ratio of fibres, means that they do not need active cooling which considerably reduces the complexity of the system and removes the need for circulating water. The pump diodes require water-cooling but as pump light can be delivered via fibre the pump diodes can be situated at a distance from the main fibre laser somewhere more accessible and easier to service.

In terms of pulse width, Yb doped fibers can support pulses down to 50 fs [187], which enables the use of very high peak powers for the laser-wire, which is important because the cross-section for Compton scattering is small. This may also be useful as electron bunch durations become shorter.

Light Distribution

Depending on the type of laser employed for the laser-wire scanner, different approaches for light distribution to the interaction location have to be considered. Where the power of the laser exceeds 10 GW per pulse, or pulse duration falls below 100 fs, a vacuum piped transport system must be used; this is not expected to be necessary for CLIC laser-wire systems where, instead, simple pipes to protect people from accidentally crossing the beam path should be sufficient. Laser transport can be achieved by expanding the beam to a large spot size and using mirrors to steer it from the laser room to the interaction region (final focus and scan location). Depending on the total distance and the laser power, optical components of different sizes might be used. For example, at the PETRA laser-wire, transport of the laser beam of approximately 10 MW power is achieved by expanding the laser beam to approximately 20 mm diameter by a Galilean telescope with output lens aperture of 2". Mirrors of 2" diameter are sufficiently large to accommodate the beam without diffraction effects.

The Rayleigh range for a perfect Gaussian laser mode ($M^2 = 1$) with 20 mm diameter is about 600 m. According to the propagation equation of a Gaussian beam [188] within 100 m propagation the

size of the laser changes by only $\pm 1.5\%$. In real conditions, when $M^2 > 1$, the same collimation of the laser beam can be achieved on a reduced distance. For the case of the laser employed at PETRA, $M^2 = 2.6$ and the maximum distance with a variation of the size within 1.5% reduces to approximately 40 m. For longer transport distances, collimated beams must be expanded to larger sizes therefore optics with a diameter of 3–4 inches must be used. The cost of optics scale almost as D^2 (where D the diameter of the optical element).

The last case to consider is that of a laser with a power < 100 kW. This includes a configuration where a master mode-locked oscillator, synchronized to the accelerator, is transported to different locations to be successively amplified by a local amplifier. In this case it would be possible to transport the laser using 100s of metres of optical fibres thus making the transport line practically alignment-free. Moreover, costs are drastically reduced due to the diminished number of optical elements.

Scanning Systems

The scanning system at the ATF DR employs motors to move the vacuum chamber, to which the laser final focus system is fixed. A similar moving system is employed at the ATF2, where the laser final focus lens is fixed to the vacuum vessel in order to know precisely the relative position of the laser waist with respect to the beam position. The scanning system at PETRA III has two modes; one where the laser final focus lens systems are moved using stepper motors using a feedback readout system and the other employing a tilted mirror driven by a piezo stack; both stepping modes have intrinsic step resolution better than $1\ \mu\text{m}$. The scanning range of the stepping motor mode is 25 mm, with a 500 ms overhead for stepping the stages; combining this with the 20 Hz repetition rate of the laser and using 20 steps for a scan, with 5 shots per step gives $(5 \times 50\text{ ms} + 500\text{ ms}) \times 20 = 15\text{ s}$ for a complete scan. The piezo-driven mode has a scanning range of the order of 1 mm and, after moving the stages into place, can perform a scan with 20 steps and five shots per step in $5 \times 50\text{ ms} \times 20 = 5\text{ s}$.

By employing a mode-locked laser system that is locked to the inter-bunch spacing, significantly faster scan rates could be achieved and this would be necessary in order to determine the beam size train by train in some locations in CLIC. Potential solutions involving electro-optic scanning systems have been explored [189]; it may be possible to test this system, which should be capable of scanning at a laser repetition frequency of 130 kHz, at PETRA III.

Electron Bunch Jitter

Transverse position jitter between bunches (and, depending on the scanning scheme, trains of bunches) will add in quadrature to the laser-wire scan and must be subtracted either from an overall average, or bunch-by-bunch using information from BPMs. Preliminary simulations [190] of wakefield effects in the ILC linac have indicated that wakefields do not seem to affect significantly the Gaussian nature of ILC bunches, but do affect their centroid positions early in the train. Similar studies need to be performed for CLIC.

Laser Wire Scanner at very high energy

All the LWS developments and tests are performed on electrons with an energy of a few GeV. Some extrapolations of the laser wire scanner properties are discussed below. The evolution of the Compton cross-section to higher energies and the corresponding characteristics of the scattered photons and degraded electrons, are particularly important to define the best detection scheme. Fig. 5.198 shows how the Compton scattering cross-section changes with beam energy. Above 1 GeV, the cross-section starts decreasing and for 50 GeV electrons it has been already reduced by a factor of two. At CLIC top energy, the initial value is dropped by one order of magnitude. Even if it is not major issue, this must be taken into account in the design of the final system, adapting the laser power accordingly to still provide a decent signal to be detected. Moreover, at very high energies, the cross-section for electron-positron pair

creation is increasing and must be taken into account as well.

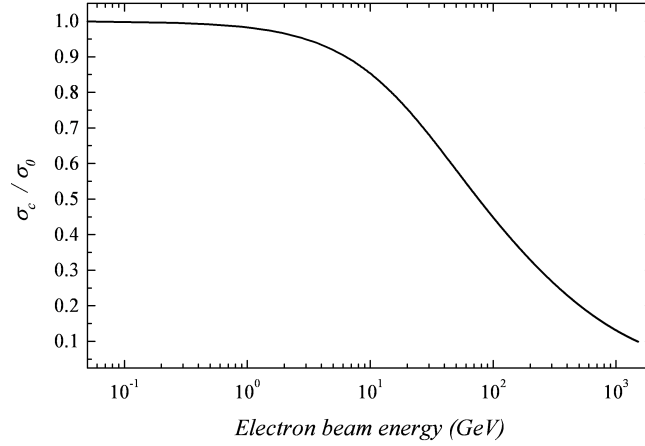


Fig. 5.198: Evolution of the Compton scattering cross-section as a function of the electron beam energy. The value is normalized to the Thomson cross-section. The calculation assumes a 266 nm wavelength laser and a 90° collision angle between the laser and the particles.

Signal Detection

The properties of the scattered photons and degraded electrons depend on the electron beam energy as depicted respectively in Fig. 5.199 and Fig. 5.200.

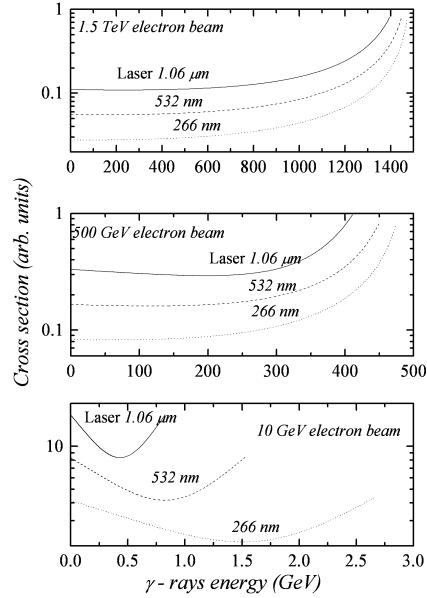


Fig. 5.199: Energy spectrum of the scattered photons assuming 1.5 TeV (a) 500 GeV (b) and 10 GeV (c) incident electron energy and three different laser wavelength (1060, 532 and 266 nm)

At very high energies, the initial electron energy is mostly converted into the emission of a high-

energy g -ray and the scattered particles are left with only a small fraction of its initial energy. The scattered photon spectrum peaks on the highest energy photons. Moreover, the photon's spectrum, which remains fairly broad for electron beams of moderate energy, gets sharply peaked around the highest energy as the electron beam energy increases. In linear collider, detecting these high-energy photons is a real concern, particularly difficult because most of the photons flux is emitted in a small angle inversely proportional to the electron energy. At energies close to 1 TeV, this cone angle becomes smaller than one mrad. Along a linac, their measurement becomes impractical and would require deviating the initial electron beam in order to insert the detector. On the contrary, the measurement of the degraded electrons could be simpler. Their energy spectrum is relatively independent of the initial electron beam energy (see Fig. 5.200) and, at very high energy the energy difference between the Main Beam and the scattered particle is large enough to design an efficient detection scheme.

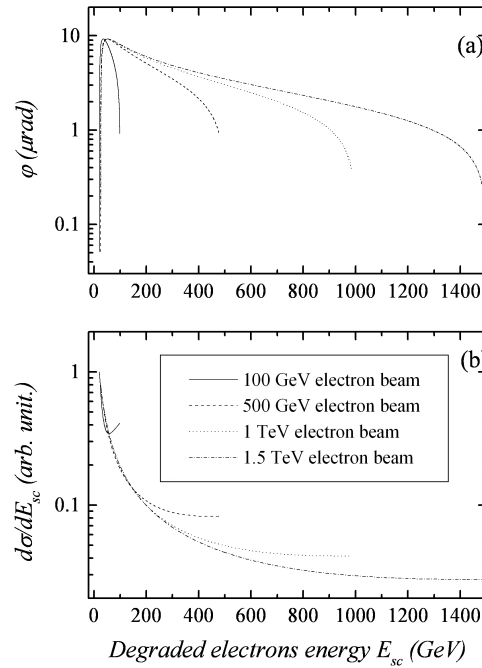


Fig. 5.200: Properties of the Scattered electrons for different beam energy: (a) angular emission and (b) energy spectrum of the scattered electrons.

For light of wavelength 532 nm, the energy loss of the electron beam is insignificant ($< 5\%$) for electron beam energies less than about 2 GeV and for the CLIC Drive Beam (2.4 GeV) the maximum energy loss is 6%. Below this approximate energy, the Compton signal must be detected via the scattered photons, and in order to do this, a magnetic field is necessary to separate them from the main electron beam. At energies above this level, the scattered electrons can be measured because they will be over-focused by downstream quadrupoles, however the energy spread of these scattered electrons is large and so they will leave the Main Beam at widely different locations, making efficient detection difficult. Full simulation of a laser-wire system for the ILC was performed in [191] where it was shown that it would preferable to locate laser-wire after a large bend downstream of the linac in order to reduce linac-related backgrounds.

At the ATF and PETRA, the scattered Compton photons are detected by a crystal calorimeter (scintillation crystals attached to a photomultiplier), respectively CsI crystals at ATF (extraction line and DR systems) and lead tungstate crystals at PETRA. A Cherenkov detector was also employed at the ATF extraction line to verify that there were no systematic differences from the crystal detectors. A system based on Cherenkov detector is useful in order to differentiate the signal from synchrotron related backgrounds; such a system can also be located in difficult to access positions in the beam-line, with the

Cherenkov light directed to photomultipliers situated well away from the beam-line. Such a system is currently under test at the ATF2.

Laser Wire Scanner in the BDS

The implementation of the four laser wire scanners foreseen in the CLIC BDS is shown in Fig. 5.201. They are distributed along the diagnostic section over a few hundred metres.

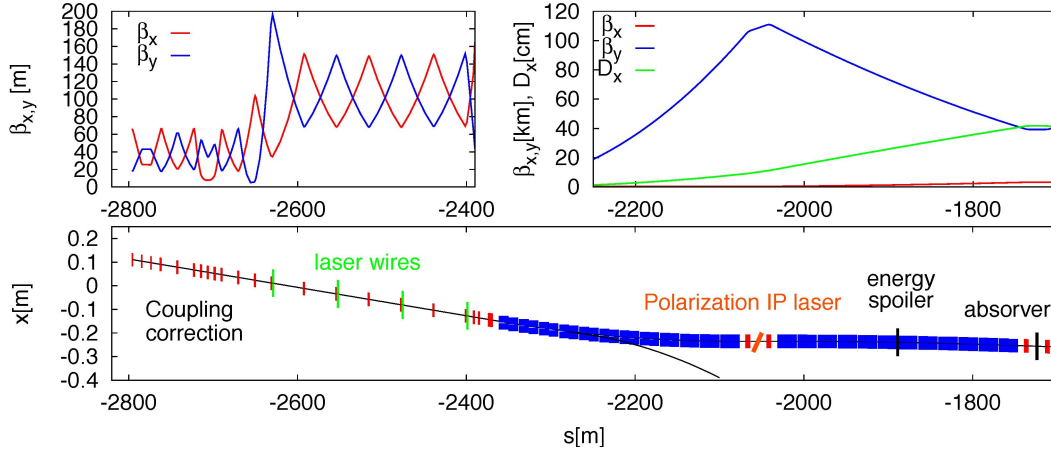


Fig. 5.201: Beam optics in the BDS with the implementation of four Laser Wire Scanners

The detection of scattered electrons (photons) is foreseen to be integrated in the first dipoles of the energy collimation area as indicated on Fig. 5.202.

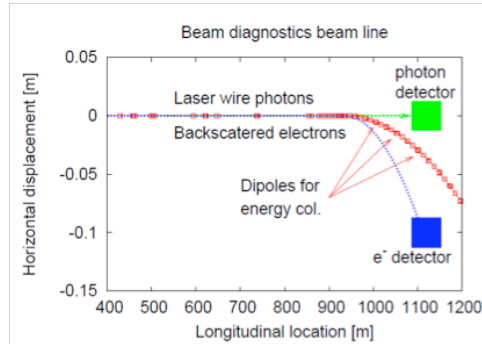


Fig. 5.202: Detection scheme in the BDS at the end of the diagnostic section

5.9.4.6 Diffraction radiation as a non-invasive beam size measurements

Diffraction Radiation (DR) appears when a relativistic charged particle (typically an electron) moves in the vicinity of a medium (a target) with impact parameter (the shortest distance between the target and the particle trajectory) as depicted on Fig. 5.203. The electric field of the particle interacts with the target atoms polarizing them. The polarized atoms oscillate emitting radiation known as DR with a very broad spectrum. The spatial-spectral properties of the radiation are very sensitive to a very broad range of electron beam parameters. However, the energy loss due to the process is so small that the electron parameters remain nearly the same as the initial ones. It makes it possible to develop non-invasive diagnostics tools.

DR in optical wavelength range (ODR) was applied for transverse beam parameter monitoring at ATF@KEK [192], FLASH@DESY [193] and APS@ANL [194]. Since the year 2000 the properties of

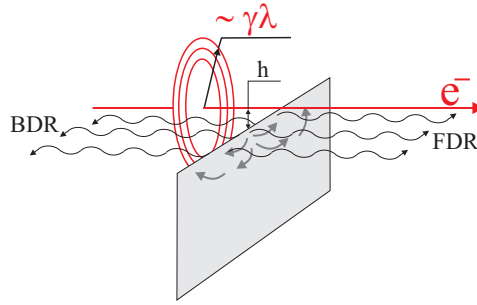


Fig. 5.203: Principle of diffraction radiation generation

ODR from a slit target [195, 196] were investigated as a possible tool for high-resolution non-invasive transverse beam size measurement (see Fig. 5.204 left). Fig. 5.204 right represents a typical ODR vertical polarization component measured with a CCD camera at KEK-ATF.

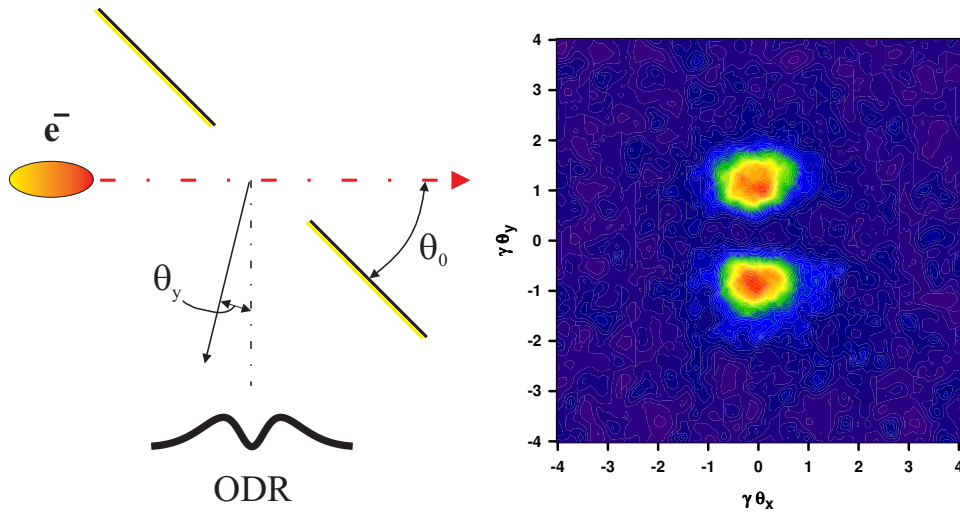


Fig. 5.204: Scheme of ODR generation from a slit target (left), Typical ODR vertical polarization component measured with a CCD camera

The visibility of the ODR pattern was measured on ATF2, compared with the simulated data and the beam size was determined. The comparison between the wire scanner and the ODR measurement is represented in Fig. 5.205. The achieved sensitivity to the beam size was as small as 13 μm .

The resolution of the current system was defined by the diffraction limit, system configuration (like the precision of the slit geometry and alignment), non-optimal measurement system, as well as by the residual contribution from synchrotron radiation (SR). To be able to achieve the resolution smaller than 10 μm , an upgrade of such a system should be followed up measuring DR in EUV or X-ray spectral-range. An experimental validation of such a scheme has been proposed during the next years on the CESR-TA ring at Cornell/USA.

5.9.4.7 Transverse profile monitoring in the Post-collision line

After the collisions, the beam is finally dumped. A set of beam imaging systems is foreseen along the line to make sure the beam is steered and diluted correctly over the dumps. These systems do not require a high resolution since the beam in the dump line is growing in size to few millimeters at minimum.

Typical beam footprints on the entrance window of the water dump are shown in Fig. 5.206 for

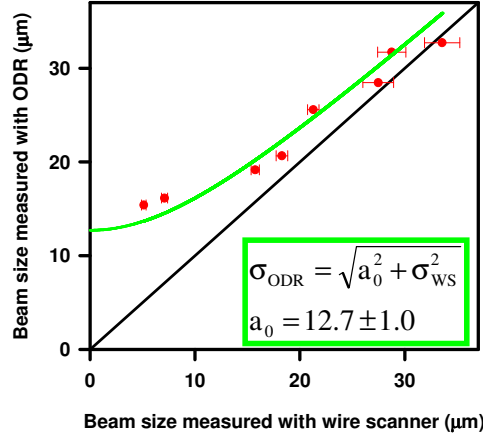


Fig. 5.205: Sensitivity of Diffraction radiation for beam size measurement

non-colliding and colliding beams. The typical beam size is as big as few millimeters for non-colliding beams and increases up to several centimeters in the vertical axis for largely disrupted beams.

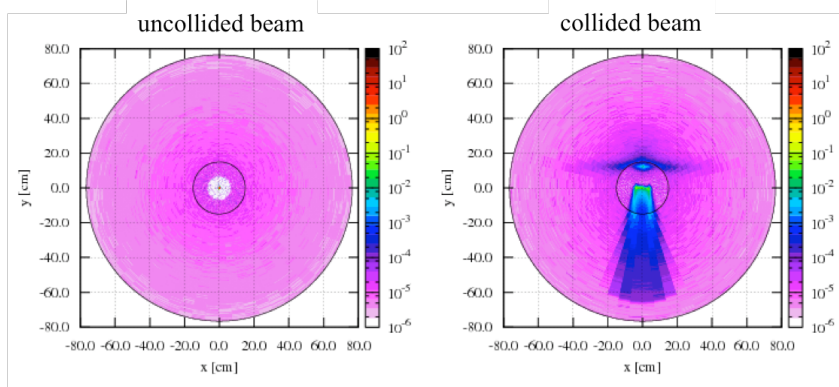


Fig. 5.206: Beam footprint on the water-dump entrance window and in the 1 mm thick 30 cm diameter Titanium window. Non-collided beam deposits 4.3 J/cm³ compared to only 0.13 J/cm³ once the beam is colliding (~ 6.3 W). The two different vertical spots visible on the entrance window during collisions correspond to the beamstrahlung photons (up) and the disrupted beam (below).

The total diameter of the screen should be as large as 30 cm. Similar screens with 60 cm diameter have been already developed for the LHC beam dumping system [197] and do not represent any critical issues.

5.9.4.8 Imaging systems for the high-energy spread beam in the Drive Beam Decelerator

The beam intensity reaches up to 100A in the CLIC Drive Beam complex and especially in the decelerator. With such large intensities, the impedance of the beam line must be kept as low as possible to avoid instabilities and resonances, potentially degrading the beam quality. Thus a replacement chamber has been incorporated in the mechanical design of such OTR tank in such a way that the beam propagates in constant beam pipe when the screens are not used. Such an assembly is depicted in Fig. 5.207 with the replacement chamber is red.

Optical Transition Radiators provide a very reliable source with a total number of photons per proton in the wavelength range λ_a, λ_b given by:

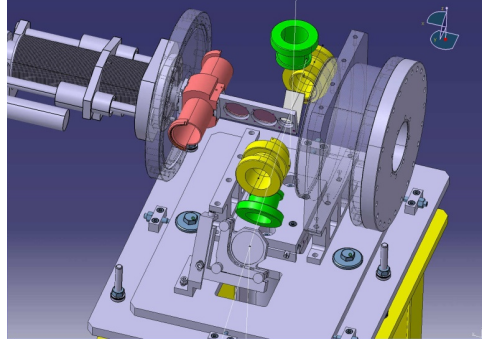


Fig. 5.207: CTF3 OTR vacuum vessel and its replacement chamber.

$$N_{\text{OTR}} = \frac{2\alpha R}{\pi} \left[\left(\beta + \frac{1}{\beta} \right) \cdot \ln \left(\frac{1+\beta}{1-\beta} \right) - 2 \right] \ln \left(\frac{\lambda_b}{\lambda_a} \right) \quad (5.33)$$

where:

- α is the fine structure constant
- β is the proton velocity
- λ is the relativistic factor
- R is the optical reflectivity of the screen

At the end of the decelerator, the beam is characterized by a large transverse size and a very high energy spread. Following the equation mentioned just before, the OTR photon yield and the cone angle of emitted light present a not negligible dependency on the beam energy as depicted in Fig. 5.208. In the case of the CLIC decelerator, it leads to a factor 2 difference in light intensity emitted by electrons of low and high energy. Full simulations including the efficiency of the optical system should be done to estimate the errors in imaging such beams with OTR.

Several decades of research on ceramic phosphors at CERN [198] and at other laboratories has led to the extensive use of doped alumina ceramic screens, i.e., $\text{Al}_2\text{O}_3:\text{Cr}^{3+}$, for accelerator beam observation. Alumina (type AF995 [199]) is doped with 0.5% chrome sesquioxide and at room temperature two principal lines of luminescence at 692.9 and 694.3 nm are generated with a decay time of 3.4 ms [200]. These screens are also compatible with ultrahigh vacuum systems, they exhibit good response linearity, and their radiation resistance is high. For example, in tests made at CERN, screens have withstood integrated relativistic proton fluxes of up to 10^{20} protons/cm².

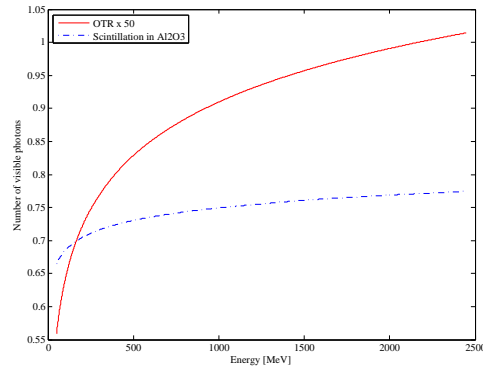
The energy dependence of both a carbon OTR screen and chromium-doped alumina is presented in Table 5.63. The number of photons generated by the Al_2O_3 screen is proportional to the deposited energy inside the screen. The photon yield mentioned for alumina is expressed in photon per MeV of deposited energy and does not change strongly in the typical energy range of the CLIC decelerator. Moreover, the number of photons generated by luminescence is much higher than the OTR photons. For high-energy particles, alumina has shown sensitivities starting for 10^7 – 10^8 protons when observed with a normal CCD camera. Even if the melting point for alumina is 2000°C, one should not use it with temperature higher than 1650°C.

5.9.4.9 Summary of CLIC Transverse profile monitor

A summary of the transverse profile monitoring systems is presented in Table 5.64 and indicates what would be the technology choice for the different part of the accelerator complex. It gives baseline sce-

Table 5.63: OTR and luminescent screen parameters

Screen	OTR Carbon	$\text{Al}_2\text{O}_3:\text{Cr}^{3+}$
Density (g/cm^3)	1.7	3.96
Specific heat (J/gK)	0.7–2.4	1.09
Melting point ($^\circ\text{C}$)	3527	2000
Light directivity	0.07 mrad	isotropic
Photons yield	$10^{-2}(\text{ph}/\text{p}^+)$	$10^4(\text{ph}/\text{MeV})$

**Fig. 5.208:** Comparison of visible photons yield for an OTR in aluminum and a photo-luminescent screen in Chromium doped Alumina

nario, where existing developments are mature enough to fulfill the requirements. In many cases, there are two technologies mentioned, as required to cover the full dynamic range of beam intensities.

Table 5.64: Transverse beam size monitors

Sub-systems	Quantity	Technology choice		Testing site
		Baseline	Alternatives	
Main Beam				
e [−] & e ⁺ injector complex	10	OTR	OTR	CERN
PDR and DRs	8	XSR	LWS/OSR-PSF	SLS, PETRA, Soleil, Diamond,..
RTML	70	OTR	OTR/OSR PSF	ATF2
Main Linac and BDS	56	LWS	XDR	CESR-TA
		OTR	OTR-PSF	ATF2
		LWS	XDR	CESR-TA
PCL	6	OTR	Scintillating screens	CERN
Drive Beam				
Source and linac	10	OTR/LWS	ODR	FELs
FM complex	20	OSR/XSR	XSR	SLS, PETRA, Soleil, Diamond,..
Transfer to tunnel	2	OTR/LWS	ODR	FELs
Turnarounds	96	OSR	XSR	SLS, PETRA, Soleil, Diamond,..
Decelerator and dump lines	672	OTR	Scintillating screens	CERN

Alternative solutions are indicated as well, if they exist. They would correspond to better technologies in term of performance or cost but would need further R&D to prove their feasibility in the case of CLIC beams. For information, the places where such technologies could be tested are mentioned in

the last column.

5.9.5 Longitudinal Profile Measurements

5.9.5.1 Overview and general discussion on technologies

An overview of the specifications for longitudinal profile monitors is given in Table 5.65. It presents the evolution of the bunch length and spacing all along the CLIC complex with the expected time resolution and the number of devices requested. Similarly to transverse profile monitoring, the typical charge density is quoted in the table and highlights the preference for non-intercepting devices as soon as this value gets higher than 10^6 nC/cm². The time resolution mentioned in the table is specified for both bunch and train length, the latter value expressing the needs to measure the evolution of the bunch length along the pulse duration. Several diagnostic techniques can be envisaged at the moment to measure the longitudinal behavior of the beam with high resolution. Four of them are actually considered to cover the CLIC requirements as non-interceptive devices: Streak camera using optical radiation. Measurements of the frequency spectrum of Coherent radiation, power spectrum of the direct electro-magnetic field of the particles and electro-optical techniques using short laser pulses. These techniques should then be classified depending on their expected performances either in terms of resolution but also on their capacity to fully resolved the longitudinal beam profile (P) or simply provide an r.m.s. bunch length (L). It is generally agreed that in locations like bunch compressors where the bunch length is modified on purpose, the tuning of the system would require the full knowledge of the longitudinal profile, which can only be measured using expensive and complex system. The evolution the bunch length in straight sections could be done only using an r.m.s. value, hopefully performed using simpler and cheaper devices.

The bunch length is manipulated several times along the complex. The way positrons are generated induces that they would have a longer bunch length than the electron roughly by a factor 2. Nevertheless on the Main Beam from the source to the end of the damping ring the bunch length is never shorter than 1 ps and can be measured with a resolution better than 500 ps using optical photons emitted either from SR in the rings or TR in straight sections and state of the art Streak Cameras [201]. This would also satisfy most of the requirements on the Drive Beam side. An example of a bunch length measurement using the streak camera in CTF3 is shown in Fig. 5.209.

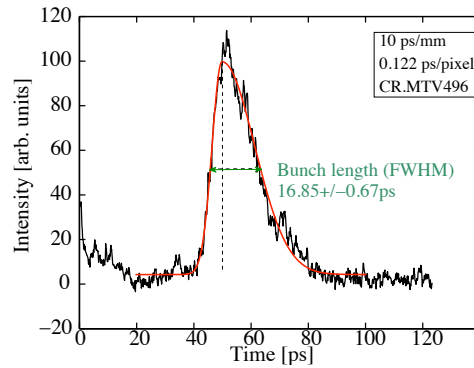
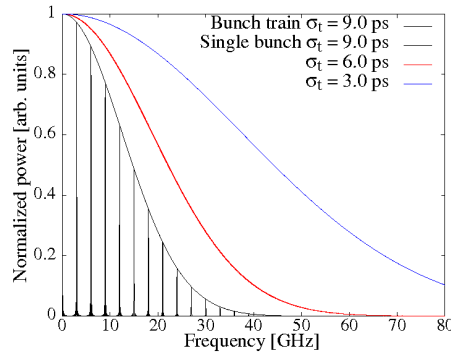


Fig. 5.209: An example of the CTF3 single bunch spectrum measured with the streak camera using synchrotron light from the Combiner Ring.

Although streak cameras can provide an accurate single shot measurement of a single bunch profile, they cannot measure in a single shot the evolution of the bunch length over the full pulse train length. RF devices measuring the beam power spectrum at high frequency, see Fig. 5.210, would then cover this requirement. Such systems have been developed at CTF2 [202], CTF3 [203, 204], and elsewhere, based on either diode a power measurement using diodes, or down-mixing techniques where more sensitivity is required. The choice of operational frequency, f_{op} , of the detector depends on the required bunch length

Table 5.65: Longitudinal beam profile requirements

Sub-systems	Bunch length [mm]	Energy [GeV]	Resolution Bunch[ps]/Train[ns]	Quantity	Charge density [nC/cm ²]
Main Beam					
e ⁻ injector complex	5	0.2	2 / 10	3 ^P	< 5×10 ⁵
e ⁺ injector complex	11	0.2	5 / 10	5 ^P	< 5×10 ⁵
Injector linac (e ⁻ /e ⁺)	1 / 5	2.86	0.5 / 10	2 ^P	< 5×10 ⁵
Pre-Damping Rings (H/V)	5	2.86	2 / 10	2 ^P	< 5×10 ⁶
Damping rings (H/V)	1.5	2.86	0.5 / 10	2 ^P	< 5×10 ⁸
RTML					< 5×10 ⁸
- Bunch compressors 1	0.300	2.86	0.1 / 10	4 ^P	
- Booster linac	0.300	2.86→9	0.1 / 10	0	
- Transfer lines - turnarounds	0.300	9	0.1 / 10	4	
- Bunch compressor 2	0.044	9	0.02 / 10	4 ^P	
Main Linac	0.044	9→1500	0.02 / 10	48 ^L	< 5×10 ⁸
Beam Delivery System	0.044	1500	0.02 / 10	2 ^P	< 5×10 ⁸
Sub-systems	Bunch length/spacing [mm]/[GHz]	Energy [GeV]	Resolution Bunch[ps]/Train[ns]	Quantity	Charge density [nC/cm ²]
Drive Beam					
Source and linac	4 / 0.5	→2.37	1 / 10	8	< 40×10 ⁶
Frequency multiplication		2.37	1 / 10		< 40×10 ⁶
- Delay loops	2 / 0.5			6	
- TL1	2 / 1			2	
- Combiner ring 1	2 / 3			2	
- TL2	2 / 3			2	
- Combiner ring 2	2 / 12			2	
- TL3	2 / 12			2	
Transfer to tunnel	2 / 12	2.37	1 / 10	4	< 40×10 ⁶
Turn arounds		2.37	0.5 / 10		< 1.5×10 ⁶
- Bunch compressor 1	2 / 12			96	
- Turnarounds	1.4 / 12			0	
- Bunch compressor 2	1 / 12			96	
Decelerator	1 / 12	< 2.37	0.5 / 10	48 ^L	> 1.5×10 ⁶
Dump lines	1 / 12	< 2.37	0.5 / 10	48 ^L	> 1.5×10 ⁶

**Fig. 5.210:** Power spectrum for a train of Gaussian bunches, with r.m.s. bunch length $\sigma_t = 9$ ps and separated by $\tau = 333.3$ ps (black) and the single bunch envelope for $\sigma_t = 9$ ps (black) $\sigma_t = 6$ ps (red) and $\sigma_t = 3$ ps (blue).

dynamic range needing to be covered and should be chosen to be $f_{op} = 1/(2\pi\sigma_b)$ to obtain the highest sensitivity, where, f_{op} is in GHz, and σ_b is in femtoseconds. Although there is in principle no limit to the bunch length that these devices can measure, D-band waveguide based RF detectors are the highest frequencies currently used for this type of measurement and hence put a recommendation on the sensitivity reach to about 0.09 mm (300 fs). RF based detectors should be installed close to a streak camera for an initial calibration, and once calibrated can be used as online monitoring tool of the bunch length, if the bunch shape is known, or of the form factor, see Fig. 5.211 and 5.212.

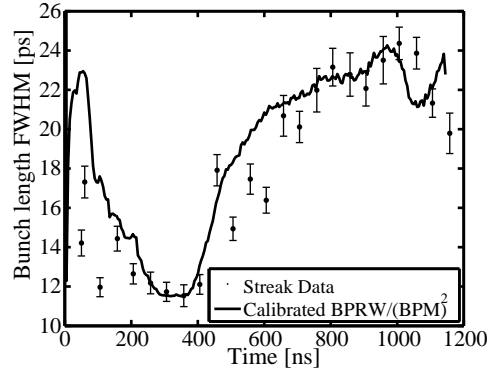


Fig. 5.211: Bunch Length measurement comparing a calibrated BPRW and the Streak Camera measurement in CTF3.

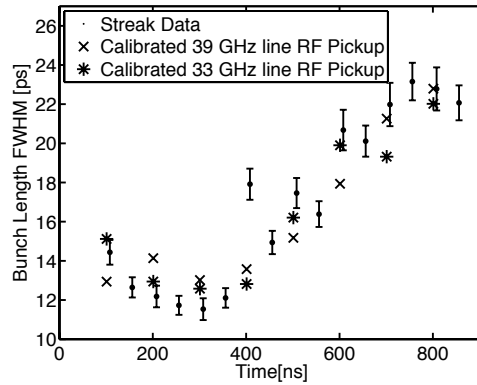


Fig. 5.212: Examples of calibrated 33 and 39 GHz RF pickup signals in CTF3 compared to Streak Data.

For areas of the machine where the bunch length is shorter than 0.15 mm, alternate techniques to the RF pickup should be investigated, as described in more details in the following paragraphs.

5.9.5.2 Longitudinal profile monitor with 20 fs time resolution

Table 5.65 shows that for the Main Beam the most stringent requirements for bunch profile measurement occur at bunch compressor BC2 and downstream from BC2. The requirement is to measure the detailed longitudinal profile of the 44 μm (150 fs) r.m.s. bunch with a resolution of 6 μm (20 fs) r.m.s., at high charge density. A full knowledge of the bunch profile is desired rather than just a moment of the bunch distribution, and the measurement must be totally non-intercepting. The optimum solution to this problem is electro-optic measurement of the bunch Coulomb field, which can yield very reliable results at CLIC parameters of energy, charge and emittance.

Principle of Operation

Electro-optic and related techniques have proved to be extremely promising for the measurement of electron beam longitudinal profiles where the ultra-short electron bunches have structure in the range from picoseconds down to tens of femtoseconds (and indeed below). The principle of electro-optic longitudinal diagnostics (see Fig. 5.213) is to accurately measure the temporal profile of the Coulomb field of the extreme relativistic electron beam, without intercepting the beam itself, through optical non-linearities induced in an electro-optic crystal within the electron beam line. The crystal is placed adjacent to the electron beam, but the beam does not traverse the crystal, making this a completely non-intercepting technique. The Coulomb field sweeping through the appropriately chosen crystal renders the material birefringent during the field transit; this birefringence is probed by a chirped (or sometimes ultra short) optical probe laser pulse that is passed through the crystal parallel to the electron beam axis, and in synchronism with the electron bunch.

Once the probe laser beam has interacted with the electron (or positron) bunch, the bunch is then extracted from the beamline. The resulting time-varying rotation of the polarization of the optical pulse can then be sensitively detected using all-optical techniques to yield a temporal (or longitudinal) evolution of the Coulomb field, which itself is a measure of the charge density longitudinal profile within the bunch.

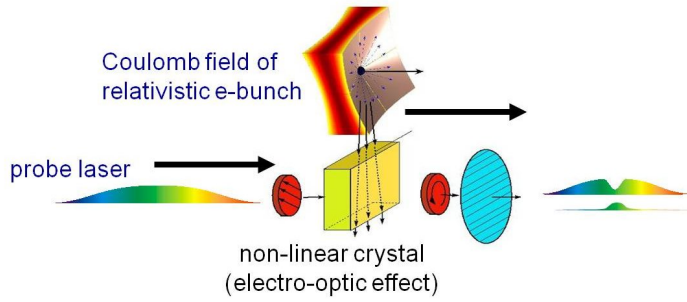


Fig. 5.213: Principle of operation of electro-optic detection.

There are a number of different ways of implementing this general principle that have been applied to single shot electron beam diagnostics, each with its own particular merits. We discuss each of the demonstrated techniques briefly, before a more detailed discussion of the preferred (baseline) choice for CLIC high resolution profile monitoring. It is useful in discussing the capabilities to separate the effects of the non-linear laser-electron beam interaction (the encoding process), and the readout of the optical information (the decoding of the temporal information).

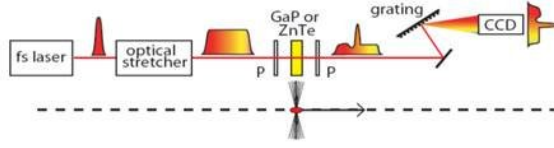
Demonstrated time-explicit single-shot EO techniques

Three techniques of EO longitudinal diagnostics have been demonstrated in accelerator experiments, spectral decoding (SD) [205], Spatial Encoding [206], and Temporal Decoding [207] (see Fig. 5.214). Of these, SD and TD have been most extensively developed and demonstrated.

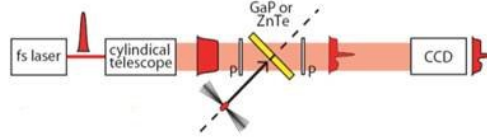
In all techniques, the encoding of the bunch profile is via the Coulomb field at a radially offset distance. This introduces a time resolution limit through the relativistic angular spread of the Coulomb field, which dictates the faithfulness of the Coulomb field temporal profile as a measure of the bunch charge density profile. This limit, with $\Delta t_{\text{res}} \sim 2R/c\gamma$, can be ignored for multi-GeV and TeV electron beams. Note that the same limit applies to any technique reliant on the temporal structure of Coulomb field at a radially offset position, such as in coherent diffraction radiation techniques.

Spectral decoding: While SD is the simplest, and most widely implemented, technique it is fundamentally limited in its time resolution through the readout process. While the precise value of the time

Spectral Decoding



Spatial Encoding



Temporal Decoding

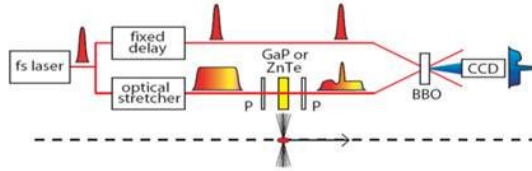


Fig. 5.214: Schematic of different EO techniques. In both Spectral Decoding and Temporal an ultrashort laser pulse is chirped before injection into the accelerator and interaction with the electron beam. In TD, the encoded information is retrieved by optical cross-correlation with a synchronized ultrashort pulse. In Spatial Encoding, an ultrashort pulse is used for the beam-interaction, with the cross-correlation integral to the geometry of the interaction region.

resolution limit will depend on the laser parameters in a given implementation, in practice the resolution will always be $\Delta t_{res} > 1$ ps. We therefore do not discuss this technique further here, other than to note that with further developments, by e.g., FEL facilities, this technique may become a feasible alternative for certain streak camera diagnostics.

Spatial encoding: In SE an ultrashort laser pulse with a large (~ 5 mm) transverse beam size interacts with the Coulomb field pulse in a non-collinear geometry. This arrangement leads to a time-space mapping of the EO interaction, as different transverse parts of the probe arrive at the EO crystal with different time delays. Through imaging of the probe beam, and use of polarization optics to convert the EO interaction into an optical intensity variation, it becomes possible to read out the effect of the EO interaction as a function of time. Spatial encoding has been demonstrated at the FFTB (SLAC) [207], and at FLASH (DESY) [208], with observed temporal signals of ~ 300 fs and ~ 100 fs respectively. In both of these implementations a contribution to the limited time resolution can be attributed to the complex fiber-optic ultrashort optical pulse transport required for their specific implementations, but which is not inherent to the technique itself. In the FLASH example, the limitations expected from the encoding process (as will be described below) were being approached. SE has a significant advantage over TD, in that the low pulse energies available from commercial ultrafast laser oscillator systems are sufficient. This follows from the fact that the decoding process is linear in laser intensity. The limitations arise from i) the encoding process, which will be broadly similar to all the other techniques, and (ii) the pulse duration of the probe pulse. In practical implementations this second constraint restricts the ultimate

time resolution to an estimated $\Delta t_{\text{res}} > 50$ fs.

Temporal decoding: In TD, the ultrafast optical beam is split into two separate beams, a probe and a gate. The probe is stretched to a pulse length of ~ 20 ps, typically by passing through a grating pair. This stretched pulse samples the bunch-induced birefringence in the electro-optic crystal, and the stretched duration sets the time window for the measurement. The decoding process is through an optical cross correlation measurement, where the gate beam serves as a short-pulse reference. The cross-correlator produces a time-space mapping in a similar way to that described for SE.

The stretched probe pulse is focused on to the electro-optic crystal inside the accelerator beam pipe at the measurement location – the measurement of the Coulomb field is done at a specific point, rather than an extended region as in SE. The phase retardation induced in the crystal by the bunch field is translated into an intensity modulation on the stretched pulse by passing it through an arrangement of polarisers. This encoded intensity is then cross-correlated with the short pulse in a β -Barium Borate (BBO) crystal. The non-collinear nature of the cross correlation geometry provides a mapping of time to spatial position in the BBO crystal and the CCD [209], as shown schematically in Fig. 5.215. The use of a time-space mapping for the decoding avoids the limitation seen in SD. However, it comes at the expense of requiring significantly higher laser pulse energies for the non-linear decoding process. The probe laser typically used for TD has been a 1 kHz repetition rate amplified Ti:S laser with pulse length ~ 30 fs, wavelength 800 nm and pulse energy > 1 mJ.

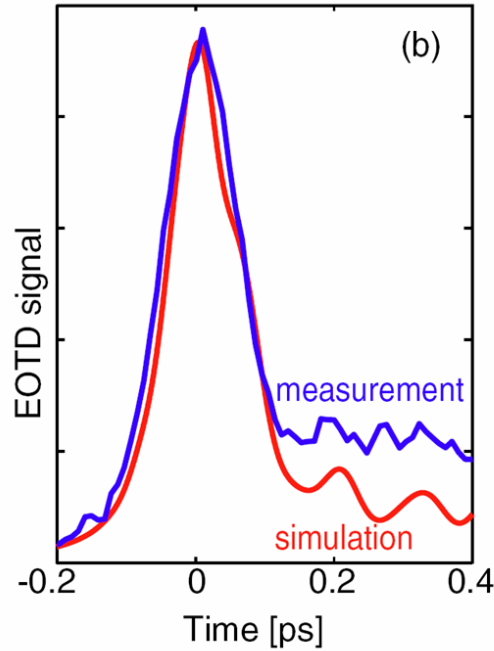


Fig. 5.215: Shortest measured electron bunch profile (at DESY FLASH). The optimum fitted Gaussian curve sigma is 79.3 ± 7.5 fs.

In experiments undertaken at FLASH, single-shot TD has been demonstrated with time resolution of 120 fs FWHM (~ 60 fs r.m.s.). The same campaign of measurements was also able to successfully benchmark the EO-determined profile against transverse deflecting cavity measurements. A scheme for in-situ absolute time calibration of the diagnostic, through effectively recording two snapshots of the same electron bunch with known 1–20 ps time delay between snapshots, was also demonstrated. The high time resolution measurements were near the limit of the gate pulse duration, but were principally restricted by the temporal limits of the encoding process. To minimize the encoding limit, a very thin

65 μm thick GaP crystal was used. To achieve the improved ~ 20 fs time resolution for CLIC, it will be necessary to improve on both the encoding and the decoding capability.

Both SE and TD (in the form described above) may reasonably be expected to have similar time resolution capabilities. Both require a short gate pulse or probe pulse for the time-space mapping, and both have similar encoding limitations. However, the use of an optical cross-correlator, albeit with the additional requirement for high pulse energies, opens up the potential to exploit established ultrafast optical characterization processes such as Frequency Resolved Optical Gating (FROG) or its many variants. In the following ‘FROG’ is taken to refer to this general class of ultrafast measurement techniques, rather than a specific implementation. In a FROG measurement the temporal profile of a cross-correlation is obtained, together with the spectra (of the cross-correlation) as a function of time. This two-dimension time-frequency information can then be deconvolved to provide temporal information on a time resolution shorter than that of any individual pulse in the cross-correlation. It is this capability that is routinely applied in autocorrelation-FROG characterization of sub-10 fs optical pulses, with information obtained at a resolution shorter than the optical pulse. In the context of CLIC diagnostics, it is proposed that TD, enhanced with FROG capability, will allow the optical characterization to deliver the desired 20 fs resolution.

Electro-optic materials and temporal resolution

There are temporal resolution limitations that arise from the EO crystal response. These limitations are often best summarized as a detection frequency cut-off, rather than directly as a temporal resolution. For example, for a 0.2 mm thick ZnTe crystal electric field Fourier components with a frequency lower than 2.8 THz are detected with minimal distortion, while higher frequency Fourier components are detected with reduced efficiencies. For a 0.2 mm thick GaP crystal, Fourier components up to about 8 THz are detected with minimal distortion.

The EO material response curves are strongly dependent on the material, and on the material thickness. The two materials ZnTe and GaP, shown in Fig. 5.216 are the most common used in EO diagnostics, and in electro-optic THz spectroscopy. The cutoff shown at ~ 5 THz and 9 THz, respectively, can be described as arising from a propagation phase mismatch between the probe laser and the Coulomb field propagating within the material; for thinner crystals the relative mismatch is reduced, giving rise to the higher cutoff. However, this advantage unfortunately has the drawback of a reduced signal magnitude. For even vanishingly thin crystals a cutoff in the response will remain, arising from the rapid change in refractive index of the material for frequencies approaching the optical phonon resonances. An ideal detection material would be free from such resonances and response cutoffs, and have a near uniform response from 0–20 THz or higher. Alternative EO materials exist that have both large EO coefficients and a response curve that can include frequencies up to 20 THz or higher (e.g., DAST, GaSe). However, the response for a fixed crystal orientation and Coulomb field - laser geometry does not span the full bandwidth; the crystal orientation can be chosen to provide a broad response centred at a given frequency. To achieve the full bandwidth required for 20 fs r.m.s. resolution diagnostics, it is proposed that a detector comprising multiple crystals, of different orientation or material, is used to provide a small set (2–3) of simultaneous measurements. These measurements will then be ‘spliced’ into a single faithful temporal profile of the beam; we note that the algorithms necessary for this splicing of explicit temporal information remain to be developed and tested. The ‘splicing’ of time-implicit spectral information from spectral upconversion measurements should be straightforward. A single laser system, and single beam-interaction assembly, is envisaged for the multiple-crystal detection, and should not add significantly to the system complexity over that of a single-crystal arrangement. Fig. 5.217 shows simulation results. The bunch profiles have been chosen to demonstrate the effect expected for ultrashort time scale charge density variations.

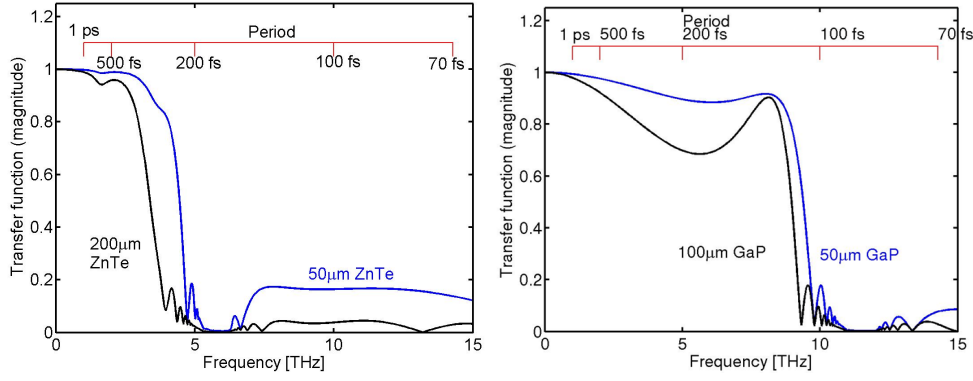


Fig. 5.216: Normalized amplitude spectral response functions for the two commonly used EO crystals, and for different crystal thicknesses. The form of these response functions means that the temporal response of the EO encoding cannot be treated as a simple r.m.s.-like quantity.

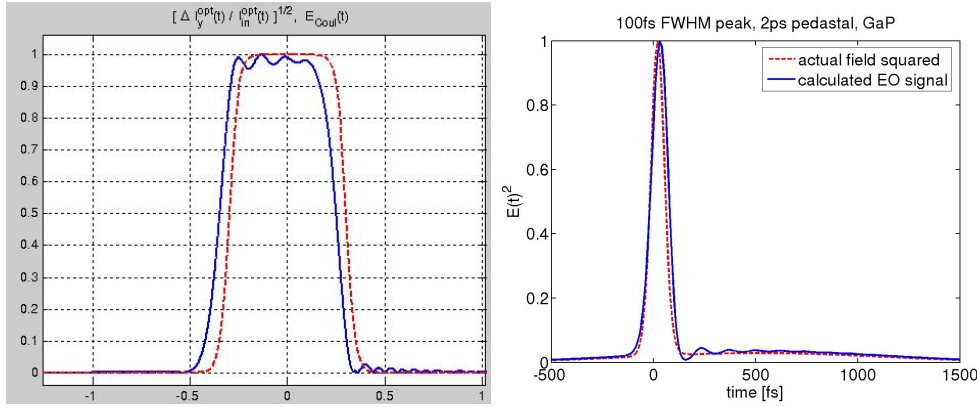


Fig. 5.217: Example simulations of EO profiles (blue) obtained for given charge bunch profiles (red).

High resolution (& time implicit) techniques – spectral up-conversion

Based on a more detailed description of the EO encoding process described in [210], which explains the encoding in terms of optical sideband generation via sum and difference frequency mixing of the optical and terahertz fields in the crystal, a new technique called Spectral Upconversion [211] has been developed (see Fig. 5.218). The technique directly measures the Fourier spectrum of the electron bunch, through first upconverting the far-IR–mid-IR spectrum to the optical region, followed by optical spectral imaging. The technique uses a long-pulse (>10 ps) laser probe, for which laser transport in optical fibre becomes relatively trivial. The laser system can be significantly simpler than the ultrafast amplified systems of TD. In measuring the Fourier spectrum of the bunch, there is a loss of phase and explicit time information when compared with TD, but this comes at the gain of diagnostics system simplicity and expected reliability. When coupled to the multiple-crystal detection arrangement, the response bandwidth is sufficient to characterize bunches with 20 fs resolution, and potentially even shorter.

Note that through up converting the Coulomb spectrum to the optical, region, the relative bandwidth of the spectrum is reduced by more than an order of magnitude; it becomes possible to measure the full spectrum with a single CCD detector with well-calibrated response. Single-bunch, or intratrain measurements become possible through selected timing of the probe laser pulse. In addition this method can measure non-propagating long wavelength components not accessible to radiative techniques such as CSR, CTR, CDR and Smith-Purcell.

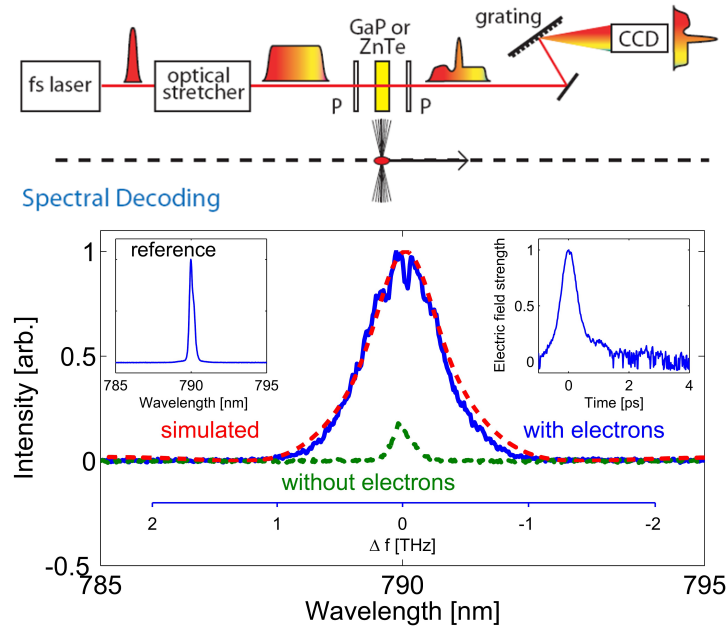


Fig. 5.218: (Top) general concept of the Spectral Upconversion technique. A quasi-monochromatic $\sim 10\text{--}50$ ps duration pulse interacts with the electron beam, to produce an output optical pulse that has the spectrum of the bunch Coulomb field imposed on it as optical sidebands. (Bottom) Results from a demonstration experiment, as described in Ref. [211].

Envisaged CLIC systems

Of the systems described above, temporal decoding has best demonstrated time resolution, and the potential for even higher time resolution with the FROG-TD system. TD currently requires complicated, and expensive, amplified ultrafast lasers to obtain the higher time resolution. Single-shot SD requires much simpler ultrafast laser oscillators, but suffers from an intrinsic temporal limitation that can, in certain circumstances, causes severe measurement artifacts in the measured bunch profile [205] which make it unsuitable for the 20 fs resolution monitors (although for low time resolution measurements it may still be a suitable approach).

Spectral upconversion offers a relatively simple method for obtaining spectral information of the bunch temporal profile, including the long-wavelength non-propagating spectral components; it is able to do this with high repetition rate laser systems, so when coupled to optical array detectors and suitably fast read-out will be able to perform single bunch measurements, or a sequence of measurements throughout a bunch train. It therefore provides an option for intratrain feedback systems.

It is proposed that for 20 fs time resolution requirements, both time explicit FROG-EO systems and time-implicit spectral up-conversion system be developed for CLIC. The specific locations of time-explicit, low rep rate diagnostics and systems appropriate for feedback still remains to be identified.

Development work required for CLIC Technical Design Phase

For CLIC implementation, development will need to address operational reliability of the diagnostic, as well as the more challenging task of achieving the higher time resolution to the 20 fs r.m.s.

The higher time resolution is to be achieved by the use of current and alternative EO materials, and the yet-to-be demonstrated multiple-crystal detectors to achieve sufficient detection bandwidth. The

testing of a range of alternative materials in EO diagnostic systems will need to be undertaken; this will address issues of signal calibration and splicing of multiple-crystal data; of signal-noise and bandwidth relationships, and crystal robustness in accelerator environments; Much of the initial development can be undertaken with laser-lab experiments only, without the need for more complicated accelerator tests.

The material investigations and multiple-crystal developments will feed into both of the two approaches for the EO diagnostic systems, the time-explicit ‘FROG’ Temporal Decoding EO system, and the time-implicit spectral up-conversion system. The amplified laser systems currently required for Temporal Decoding, and which will certainly be required for the FROG-TD systems, suffer significant problems of day-day reliability and alignment stability. Development should be aimed at first demonstrating FROG-TD, and then minimising the pulse energy requirements for FROG-TD detection. Minimising the laser pulse energy requirements will allow the complexity of the laser system to be reduced, with concurrent improvement in reliability. Optical-fibre ultrafast oscillators, which are now commercially available, have shown themselves to be reliable systems for low pulse energy ultrashort pulses. While fibre systems delivering the ultrashort pulses with the expected requirement of 10–50 μJ pulse energy are not available currently, independent developments in laser technology (driven partly by accelerator applications such as FEL seeding) offer the likelihood that such system will be available in the 2–5 year time frame. The spectral up-conversion approach has a distinct advantage in simplicity, cost, and reliability of the required laser systems, albeit at the loss of explicit time profile information. Low pulse energies are suitable, as no optical-nonlinear process is required in retrieving the coulomb field spectral information. The quasi-monochromatic laser would deliver relatively long pulse durations (~ 10 ps), which greatly simplifies the laser transport requirements. Appropriate laser systems will need to be identified or developed; Yb fibre laser systems are a potentially low-cost and robust option, and are being developed in the context of EO diagnostics by FEL laboratories. The spectral up-conversion laser power requirements will be largely driven by signal-noise; to adequately specify the laser requirements, further testing and development of spectral up conversion is needed.

5.9.5.3 *Cost-effective high-resolution bunch length monitor (coherent diffraction radiation)*

Bunch length and profile can be derived from the spectral analysis of a coherent radiation generated by an electron/positron beam at a wavelength range comparable to or longer than the bunch length [212, 213]. The advantage of the method is that it does not have any theoretical limitation on the resolution for the bunch length measurements, i.e., for shorter bunches a shorter wavelength range has to be measured. In practice, the accuracy depends on the technology of the detection system. The technology is significantly different when comparing optical, near-infrared or far-infrared wavelength ranges. Therefore, each bunch length range must be considered separately.

The coherent radiation spectrum, $S(\omega)$, is defined by the following equation

$$S(\omega) = S_e(\omega) \cdot [N + N \cdot (N - 1) \cdot F(\omega)] \quad (5.34)$$

where:

$S_e(\omega)$ is the single electron spectrum

N is the bunch population

$F(\omega)$ is the longitudinal bunch form factor and the measurement purpose

Coherent Diffraction Radiation (CDR) generated by a charged particle passing by a conducting screen is one of the best candidates [214]. Recent developments in theory of the phenomenon allow us to predict the single electron spectrum with relevant accuracy [215].

There are two major tasks the CDR technique can fulfill. The first one is the online monitoring of the bunch length both throughout a train and shot-by-shot, when the bunch length is shorter than 500 fs,

where RF pickup reaches its sensitivity limit. The second task is to measure longitudinal bunch form factor and bunch profile through the analysis of CDR spectrum.

Vacuum system

The CDR monitor only requires a moderate space in the accelerator beam line, i.e., be compact, robust and light. A schematic drawing is demonstrated in Fig. 5.219. It will be based on a typical accelerator vacuum chamber with a CDR generating cavity. The current design is based on accumulative experience of many groups developing CDR diagnostics. Nevertheless the cavity length, depth and angle of the incoming surface will be finalized during the project preparation phase. For that purpose we shall use advanced electromagnetic simulation tools (Gdfidl and ACE3P (SLAC)) to optimize the cavity and to predict the single electron spectrum essential for determining the longitudinal bunch form factor and profile.

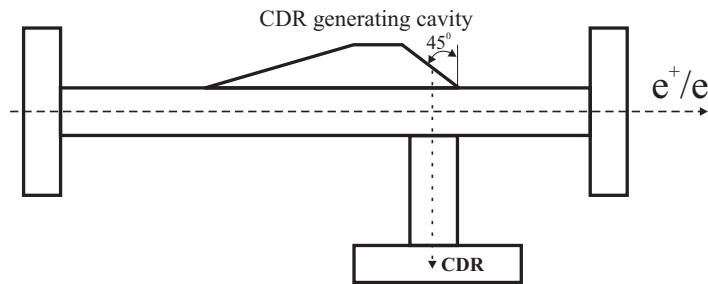


Fig. 5.219: Schematic drawing of a CDR generator.

During the project preparation phase a prototype of the CDR generator will be built and tested with beam in the CTF3 facility.

Measurement system

To fulfill the challenging requirements of 10 ns train resolution, an extremely fast detector should be envisaged. Schottky Barrier Diode (SBD) based detector would be an appropriate choice with a typical time response of FWHM = 250 ps (see, for instance, Fig. 5.220 [216]). One may see that the detector has a long tail of about 2 ns, nevertheless, it still satisfies the CLIC requirements of 10 ns resolution throughout the train.

Typical beam signals measured at CTF3 by a CDR target are shown in Fig. 5.221. They are capable of following the fast bunch length variations observed along the pulse. Higher amplitudes indicate shorter bunches.

There are a few SBD detectors commercially available (see Tables 5.66 and 5.67). They cover the optimal bunch length (σ_z) region from 9 ps to 90 fs. With a lower accuracy, bunch lengths of a few femtoseconds can be monitored.

Table 5.66: SBD detectors from Millitech, Inc.

Type	DXP-42	DXP-28	DXP-22	DXP-19	DXP-15	DXP-12	DXP-10	DXP-08	DXP-06	DXP-05
Band	K	Ka	Q	U	V	E	W	F	D	G
Freq.[GHz]	18–26	26–40	33–50	40–60	50–75	60–90	75–110	90–140	110–170	140–220
σ_z [ps]	6.1–8.8	4.0–6.1	3.2–4.8	4.0–2.7	2.1–3.2	1.8–2.7	1.4–2.1	1.1–1.8	0.9–1.4	0.7–1.1

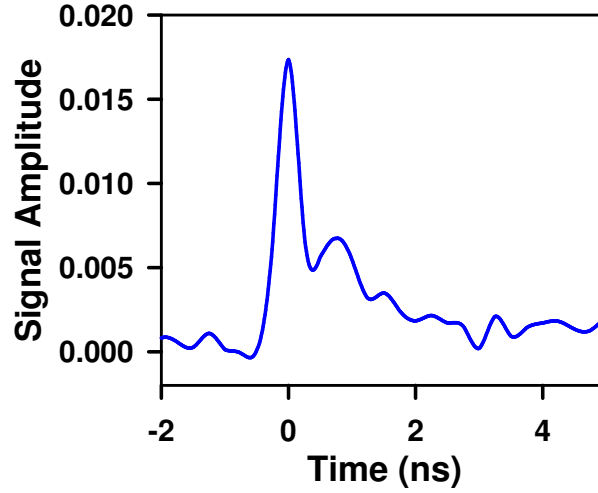


Fig. 5.220: Schottky Barrier Diode detector response.

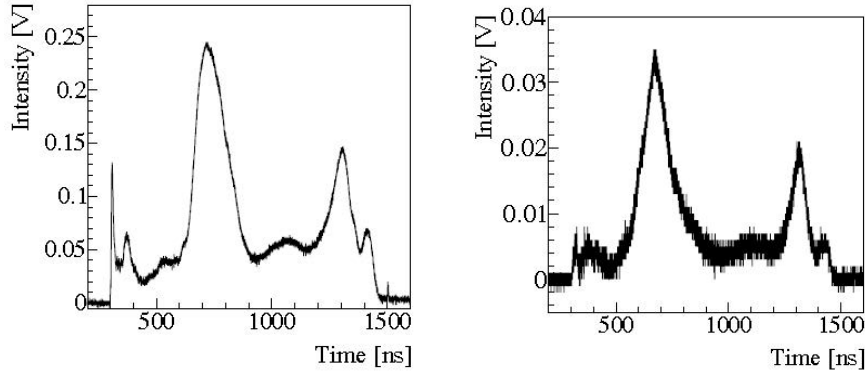


Fig. 5.221: CDR power signals measured with two SBD detectors: DXP-08 40 - 60 GHz (left) and DXP-12 60 - 90 GHz (right) [217, 218].

Table 5.67: SBD detectors from VDI Virginia Diodes, Inc. The unit of frequency is Ghz and of σ_z is ps

Type	WR4.3ZBD	WR3.4ZBD	WR2.8ZBD	WR2.2ZBD	WR1.9ZBD	WR1.5ZBD	WR1.2ZBD	WR1.0ZBD	WR0.8ZBD	WR0.65ZBD
Freq.	170–260	220–330	260–400	330–500	400–600	500–750	600–900	750–1100	900–1400	1100–1700
σ_z	0.61–0.94	0.48–0.72	0.40–0.61	0.31–0.48	0.27–0.40	0.21–0.31	0.18–0.27	0.14–0.21	0.11–0.18	0.09–0.14

The CLIC bunch length monitor using coherent diffraction radiation should measure the bunch spectrum in single shot using a grating and an array of diodes. The final design of the detector will be finalized during the project preparation phase.

5.9.5.4 Diagnostics of the bunch combination in the Drive Beam complex

The evolution of the bunch combination frequency needs to be monitored in order to optimize the Drive Beam generation process. Phase errors should be measured after the delay loop and within the Combiner Rings in order to diagnose potential optics or ring length errors contributing to phase errors in the final 12 GHz Drive Beam, which should be less than a few picoseconds of phase error for optimal power production. Studies have shown [219], that a path length error in the delay loop, resulting in 15 ps of

bunch spacing error, can introduce a power production efficiency drop by as much as 30%.

Non-interceptive phase monitor diagnostics based on streak cameras imaging synchrotron radiation or button pickups coupled to electronics based on either high frequency diodes or down mixing techniques, have been developed at CTF3 [220, 221]. These solutions can be adapted for use in CLIC. These techniques are complementary and are based on a single shot measurement. The streak camera provides a phase measurement within a few hundreds of picoseconds time window and a few picoseconds or sub-picoseconds of resolution. The button pickup, see Fig. 5.222, with the corresponding electronics, see Fig. 5.223, can monitor phase errors along the full pulse train with nanosecond time resolution, determined largely by the ADC sampling choice, and a phase precision of about 5° of 12 GHz (1–2 ps). Improved sensitivity could be obtained with more sensitive electronics components.

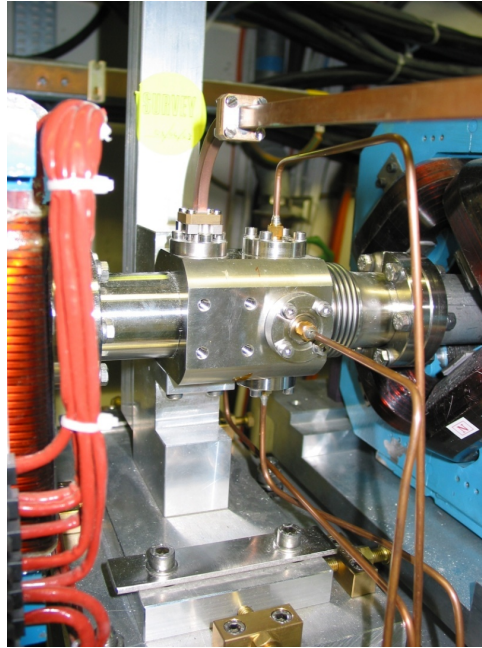


Fig. 5.222: Button pickup ‘BPR’ installed in the CTF3 Combiner Ring

Button pickup ring-length measurement based on down-mixing electronics – ‘BPRS’

The BPRS electronics has a 3 GHz local oscillator with an adjustable phase shifter control. As a consequence, the output of the down mixed signal will be maximized if the signal is in phase with the local oscillator and zero if $\pi/2$ out of phase. A perfect factor of four combination, without phase errors, the ring length of the Combiner Ring should be $(C \pm 1/4 \cdot \lambda)$, where C is a constant and λ is the wavelength corresponding to the 3 GHz RF deflector in the Combiner Ring (see Fig. 5.224). Hence, the periodicity of the output BPRS signal, for a well adjusted ring length, should be exactly the time taken for the beam to complete four turns as shown in Fig. 5.225. This signal is hence used to adjust the ring length in a multi-turn measurement and can also monitor any phase variations along the pulse train, which will be reflected in an amplitude drop in the resulting down mixed signal, for a uniform current.

The concept of the BPRS measurement can be extended to monitoring path length errors in the delay loop, or in other Combiner Rings in CLIC, by modifying the electronics in order to be sensitive to phase errors of different frequencies of interested. For example, it is foreseen in CTF3 to modify the electronics of a button pickup after the delay loop, in order to be sensitive to residual 1.5 GHz phase errors, originating from a path length error in the delay loop. Simulations have shown, that by using a 1.5 GHz reference local oscillator, with an adjustable phase control, and with small modifications to the down mixing components in the electronics, that such a detector can be sensitive to phase errors of the

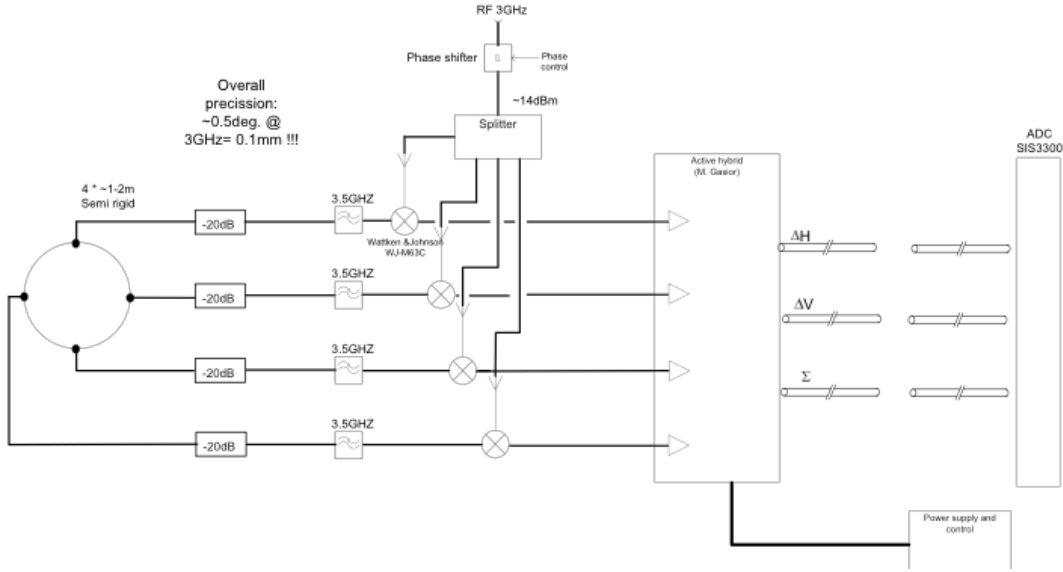


Fig. 5.223: Button pickup ‘BPR’ electronics installed in CTF3 for ring length measurements

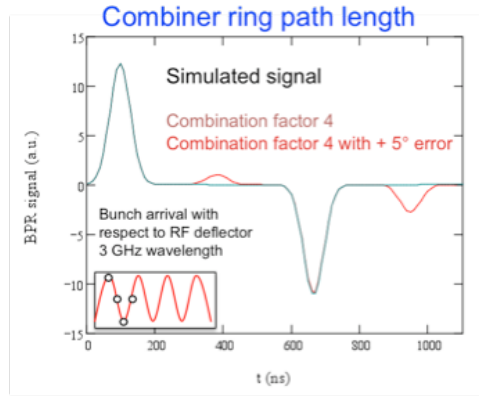


Fig. 5.224: A schematic of the sensitivity of the BPR sum signal to phase errors during a factor of $N=4$ combination, with a perfect 3 GHz incoming beam

order 1 - 2 ps.

Button pickup phase measurement based on high-frequency diodes – ‘phase monitor’

Another method to identify errors in the combination is by measuring directly the beam power contained in various beam harmonics as depicted in Fig. 5.226. Two ‘phase monitor’ devices have been installed in CTF3, one just after the delay loop, and the other one inside the Combiner Ring. The principle of these two detectors, explained in the following, can be adapted to measuring the particular beam frequency spectrum, during the various beam combinations of the CLIC Drive Beam generation.

In CTF3, the beam power spectrum is collected by the four antennae of the BPR button pickup shown in Fig. 5.222. The four signals are combined, to be position insensitive, and re-divided into four channels where attenuation is applied where needed. The signals are then band-pass filtered around a particular beam harmonic of interest, with a bandwidth of ~ 100 MHz and measured with a diode, see Fig. 5.226. The signals are digitized with a 12-bit ADC sampling at 96 MS/s. The phase monitor in the delay loop monitors the beam power at central frequencies of 7.5 GHz, 9.0 GHz, 10.5 GHz, and 12.0 GHz

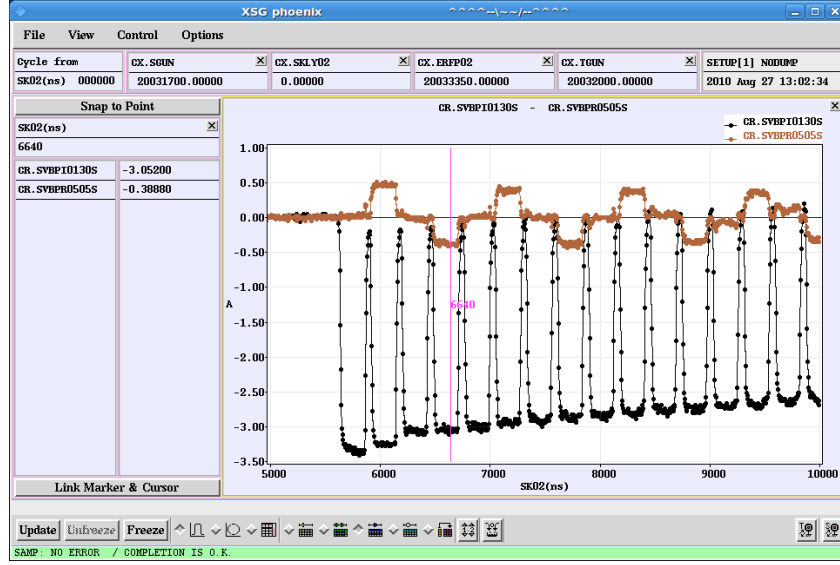


Fig. 5.225: Measurement of the Combiner Ring length, tuned for a factor of four combination, using the BPRS signal, with the beam stored over many turns

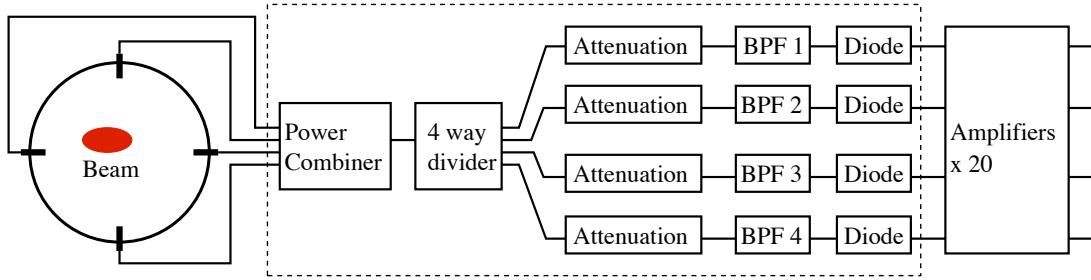


Fig. 5.226: A schematic of the 'phase monitor' electronics based on bandpass filters and diodes

to be sensitive to residual 1.5 GHz spacing errors in the combined 3 GHz beam. The one in the Combiner Ring monitors the frequency bands around 6.0 GHz, 9.0 GHz, 12.0 GHz, and 15.0 GHz where after a perfect 12.0 GHz combination, the 12.0 GHz component should increase to a maximum in the fourth turn, whilst the other signals are suppressed.

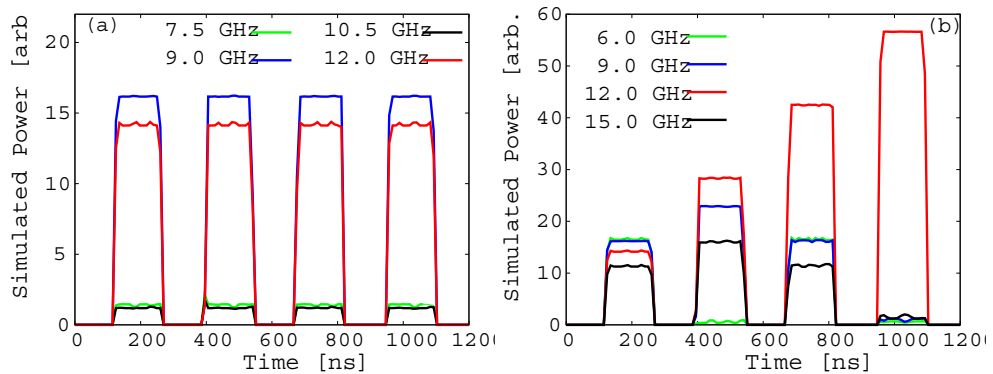


Fig. 5.227: Simulation of the expected phase monitor signals after the delay loop (a) and in the Combiner Ring (b) for a perfectly combined beam with uniform bunch length along the train.

Fig. 5.227 shows a simulation of the expected phase monitor signals measured in the CTF3 de-

lay loop and the Combiner Ring for a combination without phase errors and a uniform bunch length, $s_b = 15$ ps, along the bunch train. Deviations from the relative power measurements, in each frequency for each turn, would indicate a path length error, and hence these signals can provide tuning knobs for the operators. Relative changes to these signals can also be sensitive to bunch length variations, in particular if the bunches are $s_b > 10$ ps and hence measurements with the phase monitor should be normalized, on-line, to calibrated bunch length measurements using the BPRW, see Fig. 5.211.

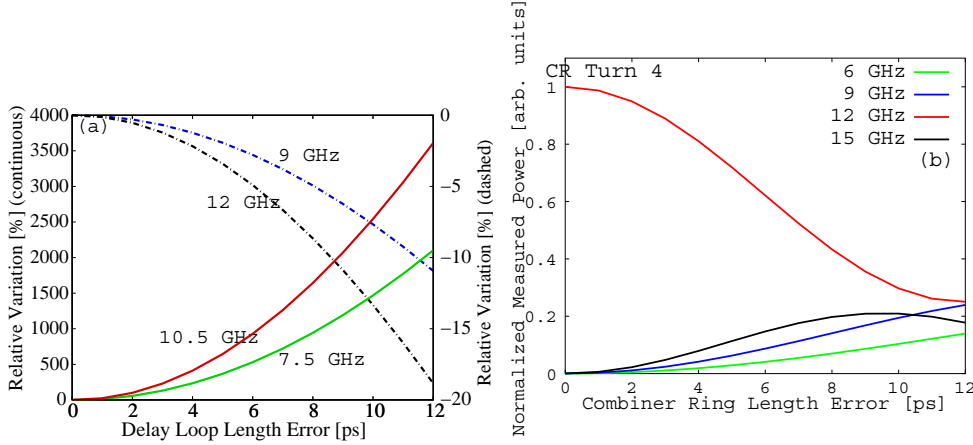


Fig. 5.228: Sensitivity of the phase monitors to path length errors in the delay loop (left) and in the combiner 4th turn (right), for different detection frequencies.

The amplitude changes of the phase monitor signals are shown as a function of the error in the ring lengths in picoseconds in Fig. 5.228(left) for the delay loop and Fig. 5.228(b) for the Combiner Ring, during the fourth turn.

Although the phase measurements presented in the following paragraph were done in conditions where losses developed in the fourth turn and an imperfect combination is measured, see Fig. 5.229, this data is still useful to demonstrate the ability of developed diagnostics to be sensitive to phase errors during the beam combination measurement.

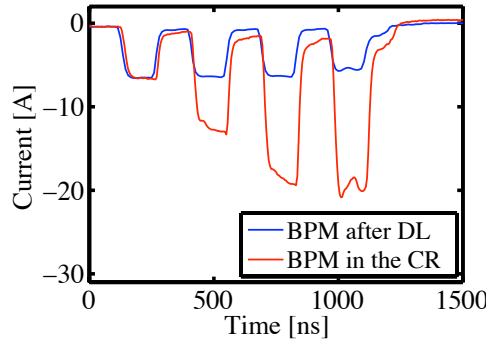


Fig. 5.229: Intensity measurements after the delay loop (blue) and inside the Combiner Ring (red), as measured during a beam diagnostics commissioning run in November 2009 at CTF3.

The combination factor four as measured by the streak camera in the Combiner Ring is shown in Fig. 5.230.

An example of the power measured for the phase monitor on this same measurement day, normalized to current and bunch length, is shown in Fig. 5.231. As expected, the 12 GHz power measurements dominate for the combination. But, due to the poor combination, there is a residual signal from the other frequency components, predominately 6 GHz. These unwanted harmonics should be much suppressed

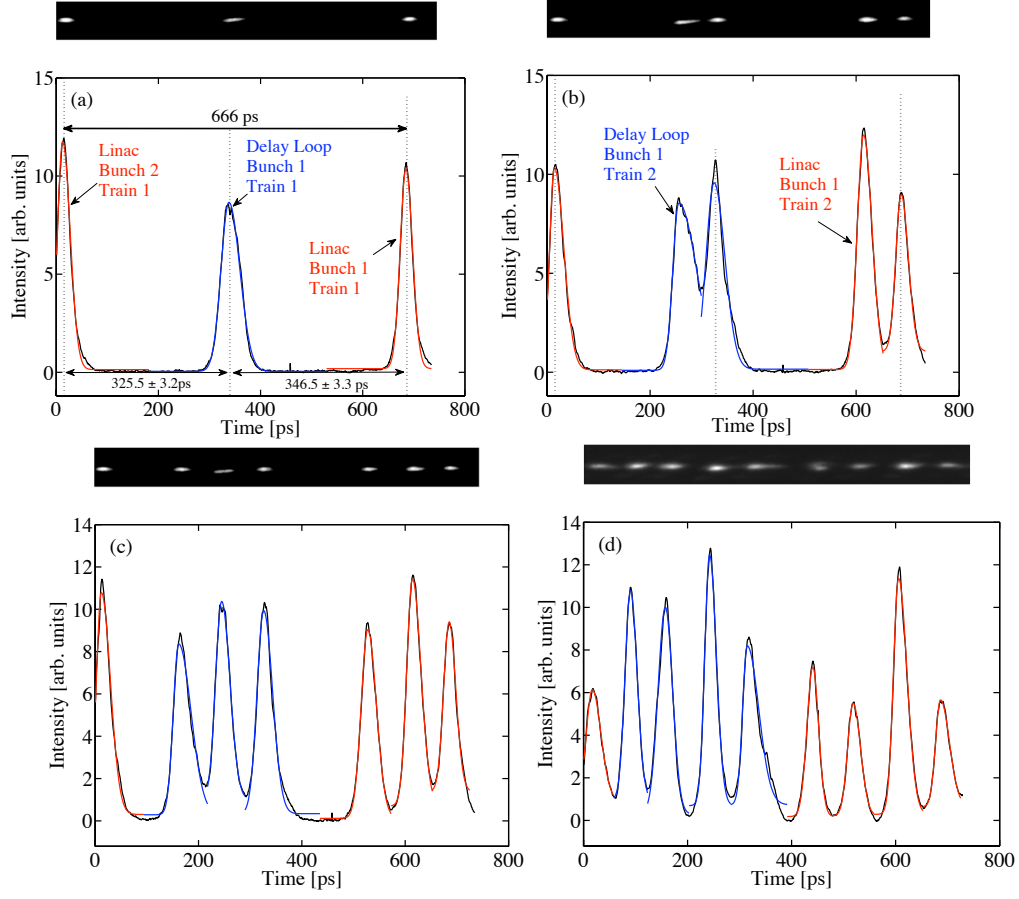


Fig. 5.230: Streak camera bunch spacing measurement for subsequent turns in the Combiner Ring, showing a sensitivity to measuring phase errors during the bunch frequency multiplication process. 50 ps/mm sweep speed – (a) First turn (b) Second turn (c) Third turn (d) Fourth turn.

in the phase monitor measurements in case of a better combination.

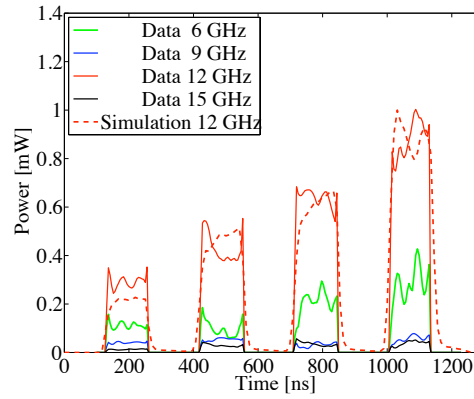


Fig. 5.231: Phase monitor power measurement, normalized to the intensity measured with a BPM and the bunch length measured with the BPRW device. Residual 6 GHz signals indicate a phase error during the combination.

The observed bunch spacing error is related to non-zero dispersion at the measurement point [222], and corrections to the dispersion are currently being addressed at CTF3. The dispersion, the ring length and the isochronicity of the rings are all items in the beam optics that are currently being understood

at CTF3. The relevant optics tuning knobs are being identified and updated phase measurements are currently being performed.

5.9.5.5 Summary of CLIC longitudinal profile monitors

A summary of the longitudinal profile monitoring systems is presented in Table 5.68 and indicates what would be the technology choice for the different part of the accelerator complex. It gives baseline scenario, where the technology is mature enough to fulfill the requirements. In many cases, there are two technology mentioned, which basically indicates that two different types of devices are needed to cover the full dynamic range of beam intensities.

Table 5.68: Longitudinal profile monitors: (P) stands for full longitudinal profile measurements and (R) for r.m.s. bunch length or form factor measurements

Sub-systems	Quantity	Technology choice	Testing site
Main Beam			
e ⁻ & e ⁺ injector complex	10	Streak (P) / RF pick-up (R)	CTF3
PDRs and DRs	4	Streak (P) / RF pick-up (R)	CTF3
RTML	12	EOS (P) / CDR / CSR (R)	XFELs
Main linac and BDS	50	EOS (P) / CDR (R)	XFELs
Drive Beam			
DB source and linac	8	Streak (P) / RF pick-up (R)	CTF3
FM complex	16	Streak (P) / RF pick-up (R)	CTF3
Transfer to tunnel	4	Streak (P) / RF pick-up (R)	CTF3
Turnarounds	192	Streak (P) / RF pick-up (R)	CTF3
Decelerator and dump lines	96	Streak (P) / RF pick-up (R)	CTF3

Longitudinal profile monitors for bunches of the order of one picosecond are developed in CTF3 and relies on the use streak camera and RF devices to respectively. For shorter bunches as required in the CLIC Main linac, EO techniques and coherent radiation techniques would be the preferred solution but RF deflecting cavity [223] could well be envisaged if necessary to provide reliable cross calibration for these two others technologies. Most likely, the development of very short bunch instrumentation is not possible at CERN at the moment and should be carried out in collaborations with XFEL's project like the ones in PSI, DESY or SLAC.

5.9.6 Beam Intensity Measurements

5.9.6.1 Overview

An overview of the requirements for beam intensity measurements is presented in Table 5.69. The change of beam pipe diameter is mentioned in the table, as it would give an indication on possible standardization of devices.

5.9.6.2 Accuracy limit of state of the art devices

Drive beam intensity measurement accuracy, resolution, and stability requirements are driven by several applications. Maintaining stable accelerating gradient requires reproducibility and stability of Drive Beam current to 10^{-3} . Survival of electronics in the tunnel requires Drive Beam loss less than 10^{-5} while potential access restrictions for personnel due to activation of tunnel components limits losses at less than 10^{-4} in each decelerator sector.

Table 5.69: Requirements for Beam intensity measurements

Sub-systems	Intensity [A] (312 x part/bunch) for DB	Train duration [ns]/ bunch frequency [GHz]	Accuracy / resolution [%]	Time resolution [ns]	Quantity	Beam aperture [mm]
Main Beam						
e ⁻ injector Complex	6×10^9	156/1	2/0.5	10	6	40
e ⁺ injector Complex	8×10^9	156/1	2/0.5	10	34	40
Injector Linac (e ⁻ /e ⁺)	$4.4/6.4 \times 10^9$	156/1	2/0.5	10	50	40
PDRs	$4.4/6.4 \times 10^9$	156/1	2/0.5	10	10	20/9
DRs	4.1×10^9	156/1	2/0.5	10	10	20/9
RTML	4.1×10^9	156/2	2/0.5	10	54	various
Main Linac	3.7×10^9	156/2	1/0.1	10	48	8
Beam Delivery System	3.7×10^9	156/2	1/0.1	10	4	various
Spent Beam Line	3.7×10^9	156/2	1/0.1	10	3	various
Drive Beam						
Source and Linac	4.2	1 / 140.3	0.1 / 0.01	10	10	40
Frequency Multi.			0.1 / 0.01	10		80
- Delay Loops	4.2	288 / 243.7			12	
- TL1	8.4	288 / 243.7			2	
- Combiner ring 1	0.4–25.2	96 / 243.7			4	
- TL2	25.2	96 / 243.7			2	
- Combiner ring 2	25.2–101	24 / 243.7			4	
- TL3	101	24 / 243.7			2	
Transfer to Tunnel	101	24 / 243.7	0.1 / 0.01	10	4	200
Turn arounds	101	1 / 243.7	0.1 / 0.01	10	96	40
Decelerator	101	1 / 243.7	0.1 / 0.01	10	96	26
Dump lines	101	1 / 243.7	0.1 / 0.01	10	48	40

Establishing absolute accuracy better than 1% is very challenging. But combining 1% absolute calibration accuracy with inter-calibration between devices measuring a common beam under low-loss conditions established with loss monitors will suffice. The high Drive Beam current (100 A) makes detection of small fractional beam losses straightforward. The inter-calibration procedure relaxes the need for say 10^{-4} absolute calibration to one of 10^{-4} diurnal stability. Localization of losses within a Drive Beam decelerator section is facilitated by a combination of loss monitors and beam position monitor sum signals similarly inter-calibrated to the beam charge monitors to a few $\times 10^{-4}$ in low-loss conditions.

5.9.7 Beam Loss Measurements

5.9.7.1 Overview

The main tasks of a beam loss monitor (BLM) systems are to prevent damage to accelerator components and to provide diagnostics for daily operation. As an integral part of the CLIC machine protection system, the CLIC BLM system should detect potentially dangerous beam instabilities and prevent subsequent injection into the Main Beam linac and the Drive Beam decelerators. Additionally the BLM system will provide information for beam diagnostics by localizing and characterizing the beam loss distribution. This includes the ability to measure the time structure of the loss, which can indicate the origin of the beam perturbations. These two roles can also be decoupled in two separate systems. In the CDR we focus on the protection requirements of the BLMs. Only for the damping and pre-damping rings additional requirements have been specified. Where further measurements for diagnostics purposes could

be desirable, future studies are outlined in the following sections.

Table 5.70 lists the beam parameters and significant loss fraction for each machine sub-system. The estimated number of electrons required to damage a beamline component is based on the structural yield limit for energy deposited in copper, [224]. Limits are more strongly dependent on the charge density, rather than the energy of the beam.

Table 5.70: Beam parameters and loss limits in the CLIC Complex

Sub-systems	Beam Energy [GeV]	Electrons per bunch train	Train duration	Estimated number of electrons to damage beam line component	Number of electrons for loss of 1 Watt/m [m ⁻¹ s ⁻¹]
Main Beam					
e ⁻ and e ⁺ injector complex	0–2.86	1.16×10 ¹²	156 ns		2.18×10 ⁹ (at 2.86 GeV)
PDRs and DRs	2.86	1.16×10 ¹²	156 ns	3.48×10 ⁸ (at extraction)	2.18×10 ⁹
RTML	9	1.16×10 ¹²	156 ns	6.94×10 ⁸	
Main linac	9–1500	1.16×10 ¹²	156 ns	3.48×10 ⁸	6.94×10 ¹⁰ –4.16×10 ⁶
BDS	1500	1.16×10 ¹²	156 ns	1.16×10 ⁸	4.16×10 ⁶
Spent Beam Line	1500		156 ns		4.16×10 ⁶
Drive Beam					
Injector complex	0–2.4		140 μs	1.54×10 ¹³	2.60×10 ⁹ (at 2.4 GeV)
Decelerator	2.4–0.24	1.53×10 ¹⁴	240 ns	1.54×10 ¹²	2.60×10 ⁹ –2.60×10 ⁸
Dump lines	0.25(peak)	1.53×10 ¹⁴	240 ns		2.60×10 ⁸

5.9.7.2 Summary of CLIC Beam Loss Monitor requirements & baseline choice

The main requirements for a baseline BLM technology choice are described and summarized in Table 5.71.

Response time and time resolution

The machine protection strategy for CLIC will be based on the a ‘next cycle permit’ concept [225] where after each cycle; the next cycle permit is revoked and only re-established once beam and equipment checks are passed. The highest envisaged repetition rate of 100 Hz leads to the required BLM response and processing time of less than 8 ms for all CLIC sub-systems except the pre-damping rings and damping rings, where a response time of 1 ms is required to assist with orbit control.

The time resolution for protection purpose is equal to the cycle repetition interval for all sub-systems (except the pre-damping and damping rings).

System sensitivity and dynamic range

The system must be sensitive enough to measure the onset of any loss, which exceeds the acceptable threshold. With the exception of the two-beam modules and the BDS, the beam losses should not exceed 1 W/m. To avoid luminosity losses due to beam loading variations in the two-beam modules the total beam losses should not exceed 10⁻³ over each Main Beam and 10⁻³ over each Drive Beam decelerator. To detect the onset of these losses, the sensitivity requirements are specified to be the signal produced by a loss rate of a factor of 100 less. For the BDS, the sensitivity requirements are determined by the expected losses on each collimator, as described in §3.5.3.1. The sensitivity requirements are used to

define the lower end of the dynamic range.

The upper end of the dynamic range is derived from the signal of a dangerous beam loss (loss causing component damage). In general, during beam operation, losses are required to stay safely (at least a factor of 10) below the estimated damage level. Therefore, to limit the required dynamic range of the BLMs, the upper end is defined as a factor of 10 below the estimated damage level.

Table 5.71 summarizes the presently specified needs for CLIC beam loss monitoring.

Table 5.71: Requirements for BLMs in the CLIC complex

Sub-systems	Dynamic range	Sensitivity [Gy/pulse]	Response time[ms]	Quantity	Recommended
Main Beam					
e ⁻ and e ⁺	10 ⁴	10 ⁻⁷	<8	95	
Injector complex					
PDRs and DRs	10 ⁴	10 ⁻⁹ (Gy/ms)	1	1396	Insensitive to synch. rad.
RTML	10 ⁴	10 ⁻⁷	<8	1443	
Main Linac	10 ⁶	10 ⁻⁹	<8	4196	Distinguish losses from DB
BDS (energy spoiler + collimator)	10 ⁶	10 ⁻³	<8	4	
BDS (betatron spoilers + absorbers)	10 ⁵	10 ⁻³	<8	32	
BDS (except collimators)	>10 ⁵	< 10 ⁻⁵	<8	588	
Post-collision Line	10 ⁶	10 ⁻⁷	<8	56	
Drive Beam					
Injector complex	5×10 ⁴	5×10 ⁻⁶	8	4370	
Decelerator	5×10 ⁶	5×10 ⁻⁸	8	41 484	Distinguish losses from MB
Dump lines	5×10 ⁶	5×10 ⁻⁸	8	96	

5.9.7.3 Baseline Technology Choices

Ionization chambers similar to the ones used at the LHC for example, are specified as the baseline choice of BLM system in all machine subsystems except for the damping and pre-damping rings. The LHC ionization chamber itself has a very high dynamic range of at least 10⁸. The LHC readout electronics, based on current to frequency conversion, have a dynamic range of 10⁵. Together with the LHC ionization chambers the sensitivity is 7×10⁹ Gy (in the shortest time integration interval) [226]. The measurement range can be easily shifted up by 1–3 orders of magnitude by reducing the monitor sensitivity (i.e., reducing sensitive volume and/or gas pressure) and/or by the choice of the electronics components to cover the requirements in Table 5.71 with the exception of the beam delivery system. Currently under development is readout electronics for CERN injector BLM systems, which are expected to cover a dynamic range of 10⁶. The Main Linac and Decelerator could also safely be operated with a somewhat reduced dynamic range, should 1–5×10⁶ turn out to be technically too challenging.

For the high signals expected in the beam Delivery System, the same type of readout electronics can be used with Secondary Emission Monitors (SEM) [227].

The baseline choice of BLM system in the damping rings is a Cerenkov radiator coupled to a photomultiplier, a system used at the Advanced Photon Source (APS) for the Linear Coherent Light Source (LCLS) free electron laser [228].

The total number of BLMs required is currently estimated to be greater than 50 000. However, the total number of BLMs could be substantially reduced either by halving the number of ionization chambers for the Drive Beam decelerators or with the use of alternative technologies such as fibres or long ionization chambers in the main tunnel. The alternative technologies are briefly discussed as future

activities and options in §5.9.7.11.

5.9.7.4 *Beam Loss Monitoring of the Drive Beam excluding the two-beam modules*

The Drive Beam injector complex consists of the linacs, the delay loops and Combiner Rings, the long transfer lines and the transfer lines to each Drive Beam in the main tunnel. Due to the high intensity Drive Beam, it is currently foreseen to install one BLM per quadrupole, at total of approximately 4300 BLMs. The average distance between BLMs is between 2 and 50 m. In the transfer lines, where the BLM spacing is high, the vacuum chamber is large (100 mm in diameter) and the operational losses are expected to be low. For some subsystems, it is possible that the number of BLMs required would be reduced if destructive losses were detected by the vacuum gauges rather than with BLMs.

5.9.7.5 *Beam Loss Monitoring of the Main Beam (excluding the damping rings, two-beam modules and beam delivery system)*

The Main Beam injector complex (apart from the damping rings) consists of the pre-injector and injector linacs, the booster linac, bunch compressors, diagnostic sections, the turnarounds and the long transfer lines to the main linac. It is foreseen to install approximately one BLM per quadrupole in every subsystem. In the long transfer lines there are only 96 quadrupoles over 21 000 m, i.e., approximately one every 210 m, whereas in parts of the transfer lines to the tunnel there is one quadrupole every 0.5 m.

5.9.7.6 *Beam Loss Monitoring in the damping rings*

In each of the damping rings, there are 502 quadrupoles, 102 dipoles, 288 sextupoles, 356 steerers, 48 skew quads and 52 wigglers. In each of the pre-damping rings there are a total of 196 quadrupoles, 38 dipoles, 102 sextupoles, 156 steerers, 38 skew quads and 40 wigglers. It is foreseen to install one BLM for each quadrupole, a total of 1396 BLMs.

To assist with orbit control, the BLM system in the CLIC damping ring complex should respond within 1000 turns, i.e., within about one millisecond. To ensure that the superconducting wigglers do not quench, the losses should not exceed 1 W/m corresponding to a loss of 2×10^6 electrons per metre per millisecond. Based on FLUKA simulations of continuous losses for the 2.4 GeV Drive Beam, this would result in a dose near the beamline of approximately 10^{-7} Gy in one millisecond. To detect the onset of these losses, the BLMs should be sensitive a factor of 100 less, i.e., approximately 10^{-9} Gy.

At the extraction point of the damping rings, the beam becomes destructive when 0.03% of a bunch train is lost. Using this as an approximation for the damage potential within the damping rings, damage to a beamline component occurs when 3.5×10^8 electrons hit a single aperture restriction. Based on FLUKA simulations for the 2.4 GeV Drive Beam, a loss of 3.5×10^8 electrons results in a dose close to the beam line of approximately 10^{-4} Gy. The upper limit of the dynamic range requirement should allow for the detection of 10% of destructive losses. The required dynamic range for the BLM system in the damping rings is 10^4 .

To avoid synchrotron radiation, the BLMs in the straight sections should be placed immediately after each quadrupole and absorber. In the arc sections, the BLMs should be placed immediately after each dipole and absorber or between the doublets. Whilst the absorbers are expected to pick up most of the synchrotron radiation, it is possible that some radiation would reach BLMs at these locations. The use of Cerenkov detectors, which are typically insensitive to synchrotron radiation, might lead to more freedom in positioning the detectors to optimize detecting the loss signal. However, exposure to synchrotron radiation should still be limited to avoid radiation damage to BLM components.

5.9.7.7 Beam loss monitoring in the two-beam modules (main linac and Drive Beam decelerators)

Beam loss monitoring for the two-beam modules requires careful consideration. The system would ideally be able to distinguish between losses from each of the two beams, 65 cm apart. The BLMs should be sensitive to signals from lost electrons with an energy range of 9 to 1500 GeV in the Main Beam and 2.37 to 0.237 GeV in the Drive Beam. Table 5.72 lists the different BLM requirements at various positions in the CLIC tunnel. For the Drive Beam, they are specified for losses at the maximum and minimum energies. For the Main Beam they are specified for each of the module types, which depend on the energy of the beam.

Table 5.72: Summary of the BLM requirements in the two-beam modules

	Dynamic range	Sensitivity [Gy/pulse]	Response time [ms]	Longitudinal position resolution [m]
DB side, 2.4 GeV	5×10^5	10^{-7}	< 8	1
DB side, 0.24 GeV	2×10^5	$5 \cdot 10^{-8}$	< 8	1
MB side Type 1, 9–100 GeV	10^6	10^{-9}	< 8	2
MB side Type 2, 100–250 GeV	10^6	10^{-9} – 10^{-8}	< 8	~ 5
MB side Type 3, 250–750 GeV	10^6	10^{-9} – 10^{-8}	< 8	~ 10
MB side Type 4, 750–1500 GeV	10^5	10^{-8}	< 8	~ 10

To distinguish between losses in the horizontal and vertical planes, one BLM for each quadrupole is required, a total of 41 484 for the Drive Beam decelerators and 4196 for the Main Beam linacs. The longitudinal resolution of the BLM system should be less than the spacing between quadrupoles, which is approximately 1 m in the Drive Beam decelerators and always higher in the Main Beam. The response time should be less than 8 ms to allow the system to react from train to train.

Simulations have been performed using the Monte Carlo code FLUKA [225, 229, 230] to determine the sensitivity and dynamic range requirements for BLMs in the two-beam modules. Losses at the maximum and minimum energies for each beam were simulated to determine the resulting spatial distribution of absorbed dose. For each beam energy, two loss scenarios were simulated. In one, the loss was simulated at single point representing the location of an aperture restriction, i.e., at the end of a PETS just before the quadrupole in the Drive Beam and the end of an accelerating structure just before the quadrupole in the Main Beam. In the other, the losses were simulated continuously along the beam pipe, an approximation of losses at multiple aperture restrictions, to represent standard operational losses due to beam gas interactions. The simulations are described in greater detail in [231]. Examples of the resulting dose distributions are shown in Fig. 5.232 and Fig. 5.233.

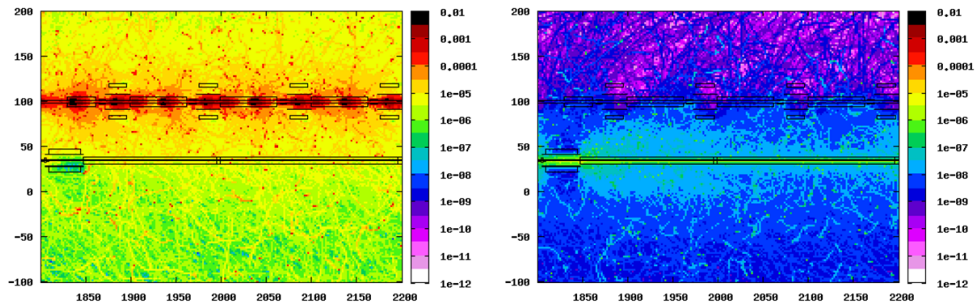


Fig. 5.232: Dose in Gray per pulse (bunch train) due to maximal operational losses of the DB at 2.4 GeV (left) and MB at 9 GeV (right).

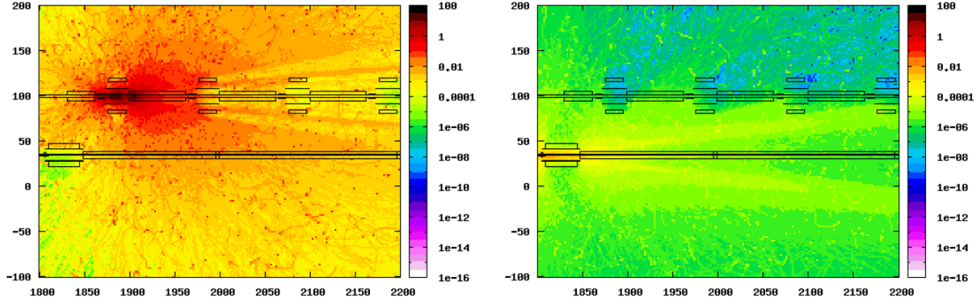


Fig. 5.233: Doses in Gray due to damaging loss of the DB at 2.4 GeV (left) and the MB at 9 GeV (right).

Whilst ideally the BLM system should be sensitive to the losses due to beam gas interaction, it is required that the system is at least sensitive to the losses at which the machine can no longer operate. It is assumed that the limiting factor in normal operation will be imposed by beam dynamic considerations, where losses of no more than 10^{-3} of the total beam intensity along the 20 km main linac, and no more than 10^{-3} of the total beam intensity along each decelerator section (average length 876 m), can be tolerated due to luminosity losses from beam loading variations. From Fig. 5.233, a loss of 10^{-3} of a bunch train along the linac would result in an absorbed dose close to the quadrupole, a possible location of the BLM, of approximately 10^{-5} Gy for the Drive Beam, and approximately 10^{-7} Gy for the Main Beam. To see the onset of such losses the sensitivity requirements were determined to be 10^{-7} Gy per pulse and 10^{-9} Gy per pulse respectively. Similar plots for losses at other energies were used to make estimates for the sensitivity requirements in Table 5.71.

The dynamic range of the BLM system should allow for the detection of beam losses at a factor of 10 below the point at which they become destructive. The losses become destructive respectively on the Drive Beam or the Main beam when 1% or 0.03% of a single bunch train hits a single aperture restriction. This corresponds to approximately 1.5×10^{12} and 3.5×10^{10} electrons from the drive and Main Beams respectively. In the Drive Beam, the aperture restrictions are located at the end of the PETS just before a quadrupole and in the Main Beam at the end of the accelerating structure just before the quadrupole. From Fig. 5.232, destructive losses at 9 GeV in the Main Beam and 2.4 GeV in the Drive Beam result in doses of 0.01 - 0.1 Gy near the beamline. Based on these results, the dynamic range is determined to be between 4×10^5 and 10^6 . Similar plots for losses at other energies were used to make estimates for the dynamic range requirements listed in Table 5.72.

The system should be able to detect the onset of failures in the cold-start up scenario described in [225, 229], where the number of electrons per bunch train would be reduced by a factor of 100 in the Drive Beam and 150 in Main Beam. Thus an additional requirement is that the BLM system should always be sensitive to a signal over a factor of 150 less than that produced by a destructive beam loss at nominal intensity. It is clear that this is always the case from Table 5.72, where the upper limit of the dynamic range is defined by the signal at 10% of destructive loss, and the dynamic range is always greater than 150.

As shown in Fig. 5.232, the absorbed doses are similar from destructive loss at 2.4 GeV at the quadrupole near the loss point and the subsequent upstream quadrupole. This is also the case for losses at 0.24 GeV. Therefore, due to the close spacing between the quadrupoles in the Drive Beam, it would be feasible for machine protection purposes to place one BLM every two quadrupoles. However the ability to distinguish between losses in the horizontal and vertical planes would be lost.

5.9.7.8 Beam Loss Monitoring in the beam delivery system (BDS)

Between the main linac and the interaction point there are 18 collimators (9 spoilers and 9 absorbers), 206 dipoles, 70 quadrupoles and 18 sextupoles for each BDS. As the BDS is highly critical in terms

of damage potential, it is foreseen to install one BLM per dipole, quadrupole, skew quadrupole and collimator, a total of 624 BLMs. The BLM response time should be less than 8 ms to allow the system to comfortably react from train to train.

The BLMs should be sensitive to losses on the BDS collimators during standard operation. In the main linac, the largest part of operational losses is expected to originate from beam-gas interactions. It is estimated that, due to the beam-gas interactions in the main linac and BDS, approximately 0.02% of the beam will hit the collimators in the BDS [189]. Assuming the losses are evenly distributed over each of the collimators this would correspond to approximately 2×10^7 electrons per bunch train hitting each spoiler. Based on FLUKA simulations of losses at 1.5 TeV in the main linac, a loss of 2×10^7 electrons at a single location would lead to doses of approximately 0.002 Gy in a region near the spoiler.

It is likely that most of the halo losses will occur on the first betatron spoilers whereas the remaining spoilers will see a much smaller fraction of the beam. Therefore sensitivity requirements of the BLMs are specified to be a factor of ten lower, i.e., 2×10^{-4} Gy, such that significant losses on any spoilers are detected.

The dynamic range of the BLMs for the collimators should allow for the detection of 10% of destructive losses. The first spoiler and the first absorber (momentum cleaning) should withstand the impact of a full bunch train, 1.16×10^{12} electrons. This is to happen regularly during commissioning and not so often during normal operation. The other collimators (betatron cleaning) can only withstand a fraction of the beam (sacrificial devices). To ensure the survivability of the betatron cleaning collimators, the beam loss on each collimator should be no more than approximately 1%, 1.16×10^{10} electrons per bunch train. Based on FLUKA simulations of losses at 1.5 TeV in the main tunnel, this would lead to an absorbed dose in a position near the collimators of approximately 100 Gy for the first (momentum cleaning) spoiler and absorber and 1.0 Gy for the betatron collimators. Using the sensitivity requirement as a lower limit, the dynamic range is required to be approximately 10^6 for the momentum collimators and less than 10^5 for the remaining collimators.

It should be noted that the sensitivity and dynamic range requirements are currently based on estimates of dose distribution from simulations of loss at single aperture restrictions in the main linac. The dose distribution resulting from losses on a spoiler and absorber is likely to be substantially different. However, for the baseline technology choice, a change in two orders of magnitude of the specified requirements would be reasonably achievable.

The beam becomes destructive to standard BDS beamline components when approximately 0.01% of a bunch train, 1.16×10^8 electrons, is lost at a single aperture restriction. Based on FLUKA simulations of losses at 1.5 TeV in the main tunnel, this results in a dose of 0.01 Gy near the beam line.

5.9.7.9 Beam Loss Monitors in the Post-collision line

The key components of the spent beam line are shown in Fig. 5.234. The most significant beam losses are expected to occur in the protection absorbers of the window-frame magnets and in the intermediate and main dumps [232].

The four window-frame magnets separate the electrons, positrons and beamstrahlung photons. The power loss in the magnet absorbers is expected to be between 1 and 11 kW. All ‘opposite-sign’ particles are then stopped by the upper part of the intermediate dump, which should absorb 140 kW of power, whilst ‘same-sign’ particles with energies less than 250 GeV are stopped by the lower part of the dump, which should absorb 170 kW of power. Between the intermediate dump and the main dump there are four C-type magnets to disperse the remaining beam before it impacts on the main dump, which should absorb 14 MW of beam power.

It is currently foreseen to install 28 BLMs for each spent beam line: four per window frame magnet, four at the intermediate dump (due to the asymmetric losses on the dump), one for each C-shaped magnet and four at the main dump. However the BLMs might be repositioned when better

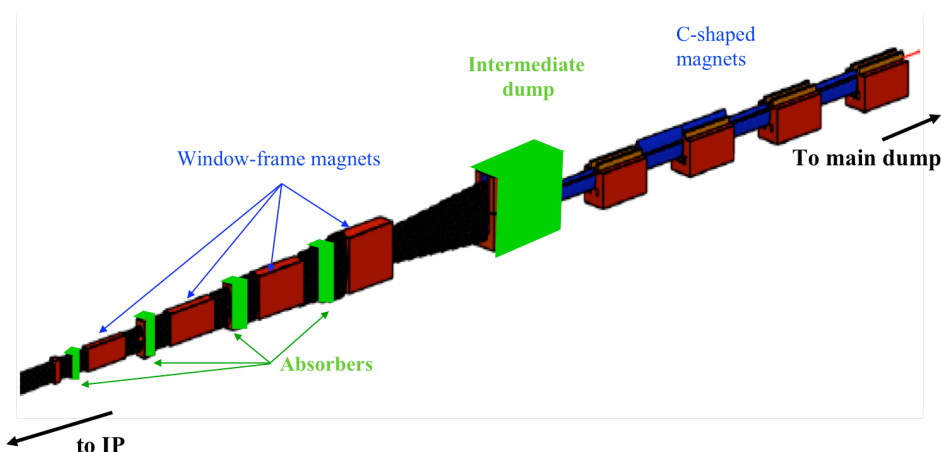


Fig. 5.234: Schematic of the Post-collision line with a succession of absorbers and an intermediate dump

information about the expected loss distribution at each component is known.

The specifications for sensitivity and dynamic range currently represent collective requirements of all BLMs in the spent beam line. The sensitivity requirement is based on detecting the onset of losses of 1 W/m. According to FLUKA simulations of continuous losses at 1.5 TeV along a beam line, the resulting absorbed dose near the beam line is approximately 10^{-5} Gy per pulse, for losses of 1 W/m. The sensitivity requirement is therefore specified to be a factor of 100 less to detect the onset of these losses. Whilst an upper limit for the dynamic range not known, the specified dynamic range is set to match that for the collimators in the BDS. In the case where the upper limit of dynamic might not be consistent with BLMS sensitive enough to detect of 1 W/m, the BLMs would be rearranged with different thresholds for their different measurement purposes. This would be determined for the technical design report and is not considered to be a conceptual problem.

5.9.7.10 Future Activities and Options

In the time period before the project preparation phase, the focus of future activities will be to reduce the total cost of the system, to refine the BLM requirements listed in the previous sections and to refine described BLM systems for the purpose of beam diagnostics.

The issue of cost will be addressed primarily by testing alternative technologies for the two-beam modules, which account for approximately 85% of the required number of BLMs with ionization chambers as baseline technology choice.

To better determine the BLM requirements, simulations will be performed that are more specific to each CLIC subsystem, particularly for subsystems such as the damping rings and BDS where detecting beam loss is crucial, and where the estimated loss signals are currently based on simulations of beam loss in the main linac. Simulations will also be adapted to the type of technology considered or tested. Estimates of requirements are currently based on values for absorbed dose in air, a reasonable approximation for the expected loss signal in ionization chambers. However, future simulations for calculating the detector signals for CLIC requirements and for CTF-3 testing must take into account the expected loss signal in the respective detector. For example, the signal in Cerenkov detectors is dependent on the angle and type of incoming radiation so current estimates of absorbed dose near the beam line would not be sufficient for estimating the detector requirements.

A BLM system used for diagnostic purposes should distinguish between losses from each beam in the two-beam modules. Current simulations indicate that the worst ‘cross-talk’ between signals appears to be from losses of the Main Beam at low energy (9 GeV) and of the Drive Beam at high energy (2.4 GeV): From Fig. 5.233, in a region close to the Main Beam, a destructive loss from the Drive Beam

provokes a signal of similar magnitude to that of a destructive loss from the Main Beam. A single monitor in this region would not be able to distinguish between the losses. For machine protection purposes this is not a problem since the loss would not go unnoticed. For beam diagnostic purposes, Monte Carlo studies will be used to investigate optimizing the position of BLMs for distinguishing the location of loss signals. Furthermore, due to the difference in time structure between the Main Beam and the Drive Beams, a BLM system with a very high temporal resolution that could distinguish between the destructive losses from each of the beams could be considered as an alternative technology.

5.9.7.11 Alternative BLM technologies summary

Some of the detectors to be investigated before the Technical Design Report are summarized in this section. The use of long ionization chambers (long hollow coaxial cable filled with argon and CO₂) [233, 234] are currently considered for use in the two-beam modules and their characteristics are summarized in Table 5.73.

Table 5.73: Summary of the alternative BLM systems considered for two-beam modules

	Dynamic range	Sensitivity [nC/Gy]	Response time	Longitudinal position resolution
Long ionization chambers (Ar + CO ₂) (FERMILAB & SLAC)	10 ⁴ (SLAC)	2 × 10 ² cm ⁻¹ (FERMILAB)	~μs	m – km
Cherenkov fibres (with SiPM) under investigation at CTF3	10 ⁴ (typical)	10 ⁵ cm ⁻²	~50 ns	10 cm
Plastic scintillating fibres (with PMT)	< 10 ⁷	< 10 ⁸ cm ⁻²	~ns	m

The advantage of long ionization chambers is that they are cheap, easy to install and have uniform sensitivity. Whilst the potential radiation damage to the cable isolation could be of concern, the system at SLAC survived 20 years running without problems. However, due to the fact that long ionization chambers have to be placed further from the beam line than the standard short ionization chambers, their sensitivity and dynamic range may not meet the requirements for the two-beam modules. Optical fibers for the two-beam modules would offer a better response time if it is required. Cerenkov fibers have a high tolerance to radiation and are insensitive to synchrotron radiation whereas scintillating materials typically offer much better sensitivity and dynamic range but suffer damage at much lower radiation levels.

A Cerenkov fibre system where two parallel fibers attached to SiPM readout is currently under study [235, 236] and it is foreseen that several tests will be performed at the CTF3 facility CLEX in 2012.

5.9.8 Beam Energy Measurements

5.9.8.1 Overview

An overview of the requirements for beam energy measurements is shown in Table 5.74 for the Main and the Drive Beam respectively. The table presents the evolution of the beam energy and its energy spread through the CLIC complex with the corresponding expected resolution and the number of devices requested. The typical charge densities are mentioned since they will set an upper limit above which intercepting devices like screens or wire scanners would get damaged.

Table 5.74: Requirements for Beam Energy measurements

Sub-systems	Energy [GeV]	Energy spread [%]	Accuracy [%]	Resolution [%]	Time resolution [ns]	Quantity	Charge density [nC/cm ²]
Main Beam							
e ⁻ injector complex	→0.2	3.5→0.1	1	0.5	10	2	< 5×10 ⁵
e ⁺ injector complex	→0.2	6→3.5	1	5	10	4	< 5×10 ⁵
Injector linac (e ⁻ /e ⁺)	→2.86	0.1 / 2.7	1	0.5	10	2	< 5×10 ⁵
Pre-Damping Rings	2.86	0.5	0.1	0.05	10	2	< 5×10 ⁶
Damping Rings	2.86	0.134	0.1	0.05		2	< 5×10 ⁸
<u>RTML</u>			0.1	0.05	10		< 5×10 ⁸
- Bunch compressors 1	2.86	1.17				4	
- Booster linac	2.86→9					2	
- Transfer lines	9					2	
- Turnarounds	9						
- Bunch compressor 2	9	1.26				4	
Main Linac	9→1500	1.3→0.3		0.02	10	48	< 5×10 ⁸
BDS	1500	0.3→1		0.02	10	2	< 5×10 ⁸
Drive Beam							
Source and linac	→2.37	1	0.1	0.01	10	10	< 40×10 ⁶
Frequency multiplication	2.37	1	0.1	0.01	10	6	< 40×10 ⁶
Transfer to tunnel	2.37	1	0.1	0.01	10	0	< 40×10 ⁶
<u>Turnarounds</u>	2.37		0.1	0.01	10		< 1.5×10 ⁶
- Bunch compressor 1		0.3				48	
- Turnarounds							
- Bunch compressor 2						48	
Decelerator	< 2.37	→90	0.1	0.01	10	0	> 1.5×10 ⁶
Dump lines	0.237 < x < 2.37	< 90	0.1	0.01	10	48	> 1.5×10 ⁶

The beam energy and its energy spread need to be carefully monitored all along the complex. Once emitted from their conversion target, the positron beam has an energy spread of 6% a factor of two bigger compared to the electrons. Their energy spread is further reduced in the injector linac and in the damping rings. In the RTML, the two consecutive bunch compression stages introduce a time correlated energy spread necessary to shorten the bunch length. The energy spread increases then up to 1.3% but is reduced by roughly a factor of three as the beam is accelerated along the Main Linac. In the BDS, the beam energy needs to be precisely monitored since very tight beam energy stability is mandatory to ensure optimum final focusing conditions.

5.9.8.2 Beam energy and energy spread measurement in Spectrometer line

A spectrometer uses the Lorentz force, $F=q \cdot [E+p \times B]$, to transfer information about particle momentum into particle position. If a particle of charge q and momentum p passes through a magnetic field B it will ‘experience’ a force F , which will result in a change in path direction as depicted in Fig. 5.235. Assuming a deflection in the horizontal plane, the measurement of the horizontal beam position and size in the spectrometer line will directly provide a measurement of the beam energy and its energy spread. Experimentally it requires minimizing the natural transverse beam size at the position of the monitors ((d) and (e)) by using a set of quadrupoles (a). The alignment of the beam entering the bending magnet is also crucial and needs to be precisely measured and corrected if necessary.

The monitor accuracy and resolution will depend on the accuracy of the beam position measure-

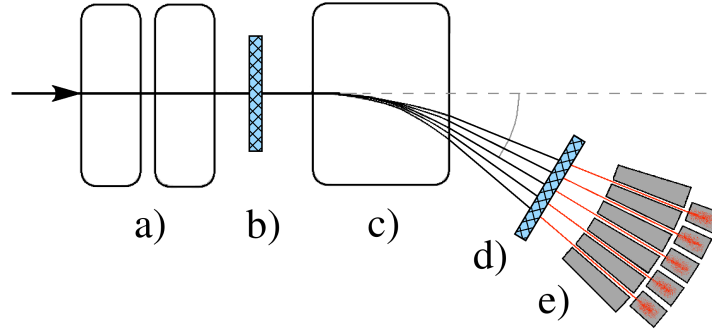


Fig. 5.235: Schematic of spectrometer line: (a) set of quadrupoles (b) beam position monitoring before the bending magnet (c) bending magnet (d) beam position and profile monitor in the spectrometer line (e) horizontally segmented beam dump

ment and on knowing the value of the bending magnet field from its precise calibration. Magnets can be calibrated accurately down to few ppm and state-of-the-art BPMs can provide accuracy and resolution of few microns and 50 nm respectively, which would provide beam energy measurements with an accuracy and resolution better than 10^{-3} and 10^{-5} respectively.

Energy spread is typically measured using beam profile monitors installed at the end of the spectrometer line. Contrary to the beam position monitor, they are mostly interceptive devices, as discussed previously in §5.9.4. In this context, thermal limitations have to be taken into account in the choice of the detector technology and implemented as well in the final design of devices.

Energy spread measurement using OTR screens

The optics of the beam line is made in such a way that the beam size at the location of the monitor is large enough in order to minimize the thermal stress in the OTR screen. Typical beam sizes will be of the order of 1 cm. A limitation of OTR in imaging large beam size is actually illustrated in Fig. 5.236. It shows a decrease of the light intensity captured by the camera, as the beam is moving out of the centre of the screen. This effect depends on the electron energy, as the OTR photons are emitted in a cone of $1/\gamma$ aperture, and on the numerical aperture of the optical system.

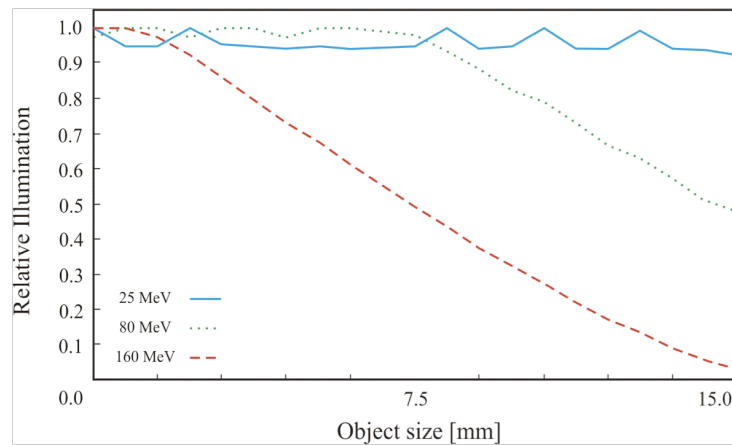


Fig. 5.236: Illumination plot simulating the relative number of OTR photons arriving on the camera with Zemax

The effect has been studied in details on the CTF3 machine, as depicted in Fig. 5.237. As the beam is moved toward the edge of the screen, the light intensity drops out quickly and the beam profile is truncated. Several alternatives have been proposed by developing OTR screens with different surface

shape (parabolic) or different surface state (diffusive screen) and have already shown promising results [237].

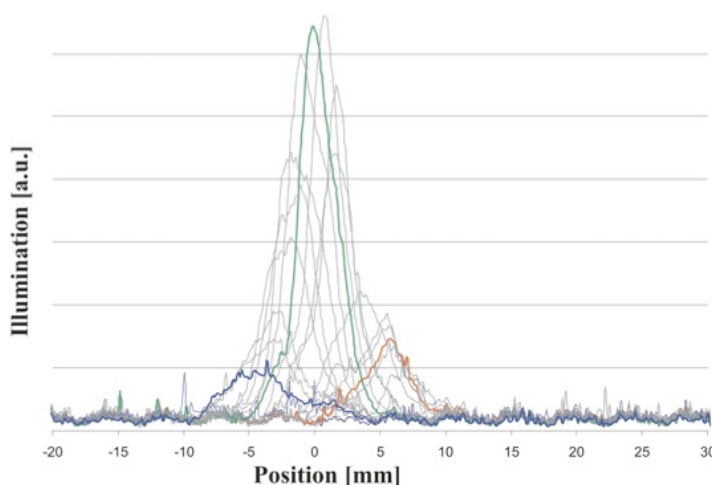


Fig. 5.237: Illumination plot as measured on CTF3 using a flat highly reflective OTR screen in aluminum. The beam energy was 100 MeV.

Another parasitic effect also observed on CTF3 was due to the synchrotron radiation emitted by the bending magnet at the entrance of the spectrometer line (see Fig. 5.238). Some of the photons were emitted in the direction of the beam, reflected by the OTR screen and detected by the camera, producing then a large background signal potentially degrading the quality of the measurement.

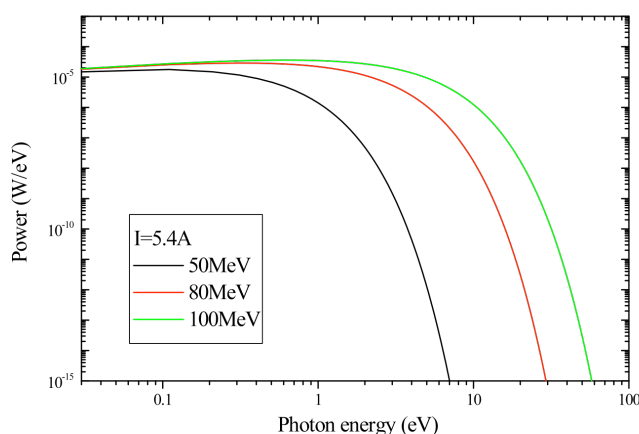


Fig. 5.238: Typical synchrotron radiation spectrum for several beam energies assuming a bending magnet with a radius of 100 cm

In order to overcome this limitation, the mechanical design of the OTR screen was modified to incorporate a thin carbon foil, mounted just upstream of the OTR screen, which will absorb and reflect the synchrotron radiation from the main bending magnet. Such screens [238] (as depicted in Fig. 5.239) are already in use in the present CTF3 spectrometer line imaging system.

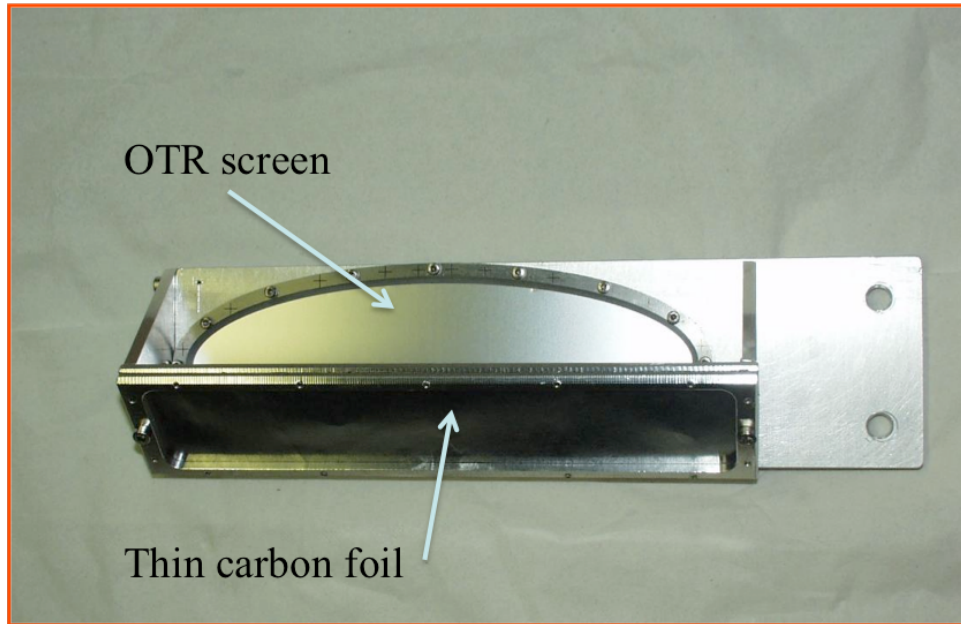


Fig. 5.239: Pictures of a typical aluminum OTR screen in the CTF3 spectrometer lines with a carbon foil to stop SR photons produced in the upstream bending magnet

Time resolved energy spread measurement using segmented dumps

Time resolved measurements have been developed during the last years on CTF3, and despite several technologies were tried [239], the detection system found to be the most simple and robust is based on a device, called segmented dump. It is composed of parallel metallic plates designed to stop the incident particles. By measuring the deposited charge in each segment, the beam profile can be reconstructed. The material and the dimension of the segments must be optimized depending on the beam parameters. In particular, they need to be long enough to stop the particles. On the other hand, the segment thickness must be chosen to provide an optimized spatial resolution, which will tend to degrade due to multiple Coulomb scattering [240] inside the segments. Moreover, because of the high power carried by the beam, thermal changes must be considered as a crucial issue as well as radiation effects that will influence the long-term behavior the detector. An example of a typical geometry developed for the CTF3 linac [241] and designed for beam energies below 100 MeV is depicted in Fig. 5.240. The present system uses of a multi-slit collimator installed just upstream of the segmented dump. Its role is to capture as much beam power as possible, keeping the deposited power in the segments low enough to avoid water-cooling. However the slit width needs to be large enough to detect enough particles and provide comfortable signal amplitudes.

Monte-carlo simulations using FLUKA [232] have been performed in order to choose the optimal material for the collimator and the dump segments and to optimize the detector geometry for best sensitivity and thermal behavior. A typical energy deposition inside the detector is presented in Fig. 5.241 for the CTF3 beam parameter.

Several segmented dumps have been built and installed at several location along the CTF3 linac and are now regularly for the optimization of the machine [242]. As an example, a typical energy spectrum is displayed on Fig. 5.242, and shows a fast high energy transient at the beginning of the pulse followed by a long steady state with typically 2–3% energy spread.

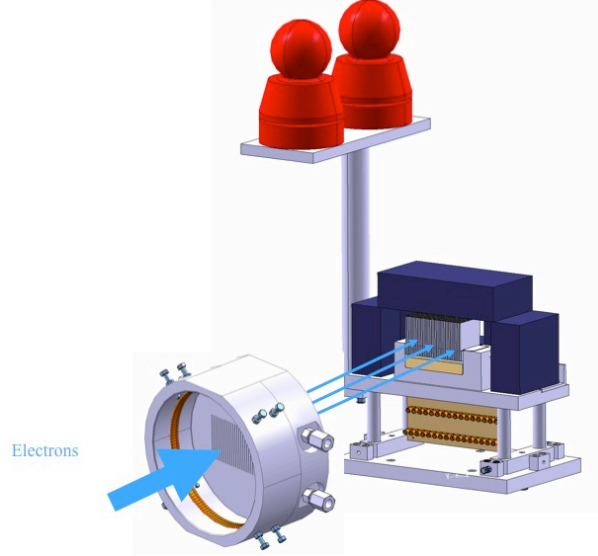


Fig. 5.240: Segmented beam dump assembly with a 20 cm long multi-slit collimator (32 vertical slits, each 400 μm wide) made out of iron and 32 tungsten segments, 2 mm wide and 5 cm long, spaced by 1 mm. Radiation hard ceramics are used as insulating material between plates.

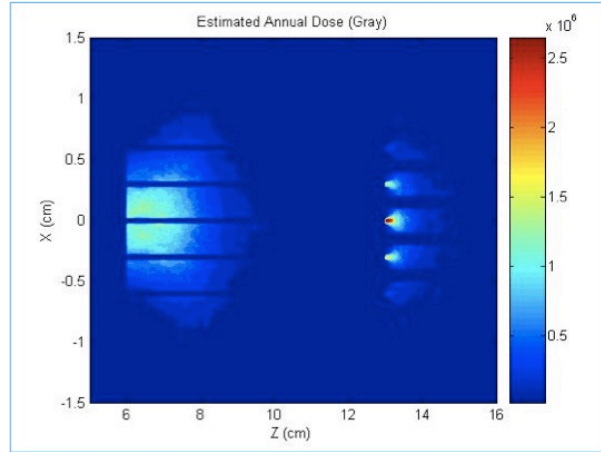


Fig. 5.241: Energy deposition (GeV/cm^3) in a segmented dump simulated using FLUKA. The beam energy is 120 MeV.

5.9.8.3 High Precision BPM for Energy measurement in the Beam Delivery System

Beam energy measurements in the Beam Delivery System are crucial because the final focusing system performance is closely related to the good knowledge of the beam energy within a resolution of 2×10^{-4} . It is then foreseen to measure beam energy using bending magnets (> 200 in total) and the high precision BPMs. As sketched in Fig. 5.243, the BPM, as required for beam position monitoring would provide measurements with a resolution better than 100 nm. By combining several BPMs along the BDS, the estimation of the beam energy will be accurate enough to fulfill the requirements.

5.9.8.4 Time-resolved spectrometry on the CLIC Drive Beam decelerator

In normal beam conditions, the Drive Beam progressively loses its energy as it propagates along the decelerator. A typical time resolved spectrum at the end of the decelerator is shown in Fig. 5.244. It is characterized by a fast transient lasting 100 ns. The overall beam energy spread is of the order of 90%.

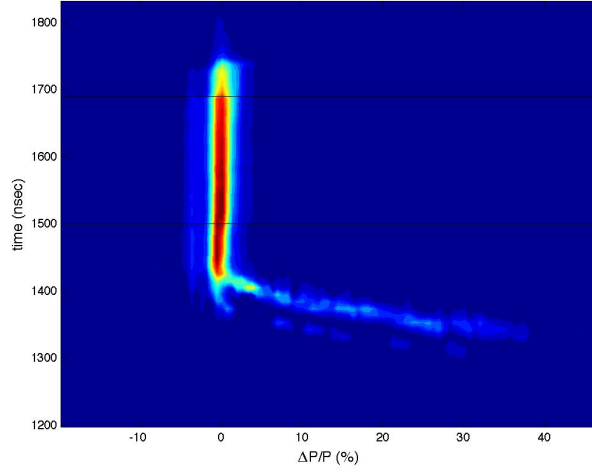


Fig. 5.242: Typical Time resolved energy measurement as measured on the CTF3 linac. Beam energy of 100 MeV.

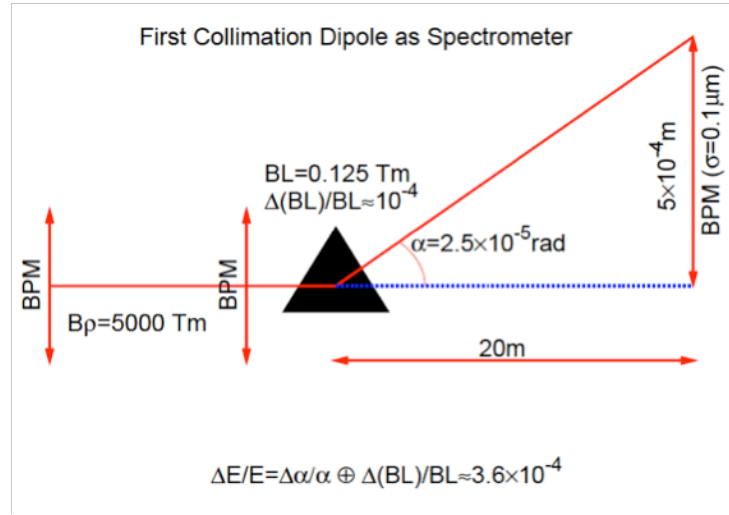


Fig. 5.243: Energy measurement scheme as foreseen in the Beam Delivery System

The other extreme case, even if it should not happen frequently, would correspond to the case where all the PETS of a decelerating sector are switched off. The beam will not interact with the structures and will not be decelerated, as depicted on the second plot of Fig. 5.244.

The measurement of the DB energy and energy spread before and after the decelerator is required as a proof of the efficiency of the CLIC RF power production.

Similarly to what is foreseen in the CLIC injector complex, the beam will be dumped in a spectrometer line at the end of each decelerator. The classical techniques to measure energy spread discussed in paragraph 5.7.7.2 X-REF cannot be used anymore due to the high beam power carried by the beam. Moreover, due to the high energy spread, the device should be based on a technology, which is not sensitive to energy variation.

A possible solution could use the emission of Cherenkov photons in air (or glass). To highlight the performance on Cherenkov radiation in this particular context, a comparison between OTR and Cherenkov photons yield is presented as a function of beam energy in Fig. 5.245. The calculation assumes a Cherenkov cell of 1 cm length. The number of photons produced by OTR is lower than the one produced by Cherenkov in air. The energy threshold to emit Cherenkov photons in air is around 20 MeV and, contrary to OTR, the light yield is then perfectly constant with beam energy.

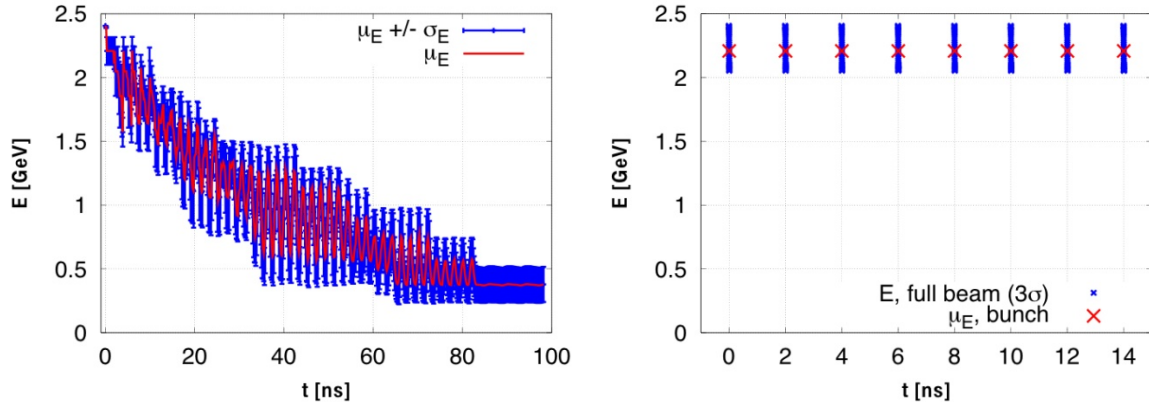


Fig. 5.244: Minimum and maximum energy spread at the end of the Drive Beam decelerator

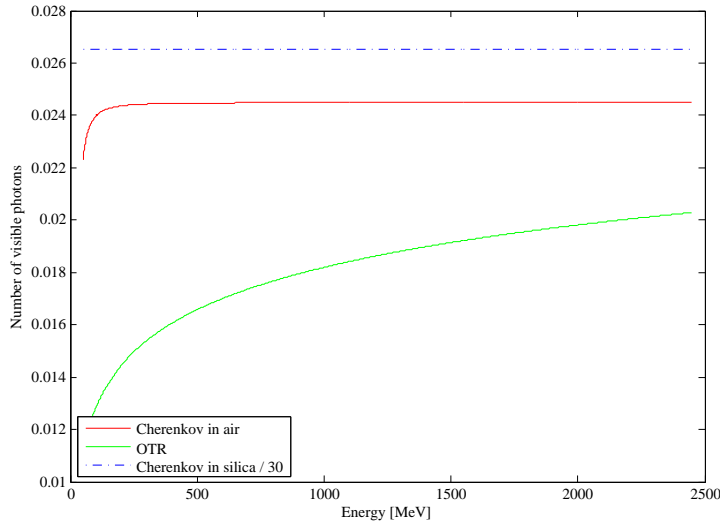


Fig. 5.245: Evolution of the number of photons produced by OTR and Cherenkov in air or quartz as function of beam energy

To measure the beam energy spread, segmented devices would need parallel glass / gas cells, generating Cherenkov photons, which are then transported via optical fiber to a linear CCD or multi-anode photomultiplier. Gas cells can be as small as few cm long and would not suffer from the high beam power. Such a system is currently in preparation to be tested on the CTF3 during the project preparation phase.

5.9.8.5 Summary of CLIC beam energy monitors

A summary of the beam energy monitoring systems is presented in Table 5.75 and indicates what would be the technology choice for the different part of the accelerator complex. It gives baseline scenario, where the technology is mature enough to fulfill the requirements. In many cases, there are two technology mentioned, which basically indicates that two different types of devices are needed to cover the full dynamic range of beam intensities.

5.9.9 Beam Polarization Measurements

The main electron beam is polarized and its polarization must be measured and maintained through the whole complex. The specifications for polarization measurements have not been studied in details so far,

Table 5.75: Overview of energy measurements

Sub-systems	Quantity	Technology choice	Testing site
Main Beam			
e^- & e^+ injector complex	8	BPM / OTR / seg. dump	CERN
PDRs and DRs	2	BPM / XSR	Sync. light sources
RTML	12	BPM / XSR	FELs
Main Linac and BDS	52	BPM	ATF2
Drive Beam			
DB source and linac	10	BPM / OTR / Cherenkov	CERN
FM complex	6	BPM / OTR	CERN
Turnarounds	96	BPM / OTR	CERN
Decelerator and dump lines	48	BPM / Cherenkov	CERN

but it is however clear the several monitors would be required all along the Complex as indicated in the following Table 5.76.

Table 5.76: Quantity of polarization monitors required in CLIC

Sub-systems	Quantity
Injector complex	3
Pre-Damping Rings	2
Damping Rings	2
RTML	8
Beam Delivery System	2

No developments were initiated so far concerning the CLIC needs but electron polarization is classically measured using Mott polarimetry [243] at low beam energy and Compton back-scattering above few GeVs [244]. A detailed design of the CLIC polarimeters will be initiated during the TDR phase of the project.

5.9.10 Luminosity Monitoring

The concept and the design of the luminosity monitors are presented in §3.7.3.2 as a part of the description of the Post Collision Line.

5.10 Beam transfer systems

5.10.1 Introduction

Challenging kicker systems are required for both the Main Beam and Drive Beam of CLIC. Figure 5.246 shows an overview of the kickers in the CLIC facility: the required kicker systems are described herein, together with the principal technological challenges for specific systems. For the Main Beam, the injection and extraction stripline kickers from the Pre-Damping Rings (PDR) and Damping Rings (DR) are described in detail, as these have extremely high demands on stability and ripple. Beam coupling impedance considerations, stability, technical design ideas, the possibility of a double kicker system, droop compensation and an inductive adder are all discussed. For the Main Beam, the interaction point kicker system is also described. For the Drive Beam, the combiner ring and turn-around kickers are described, and consideration is given to the loop phase compensation kickers.

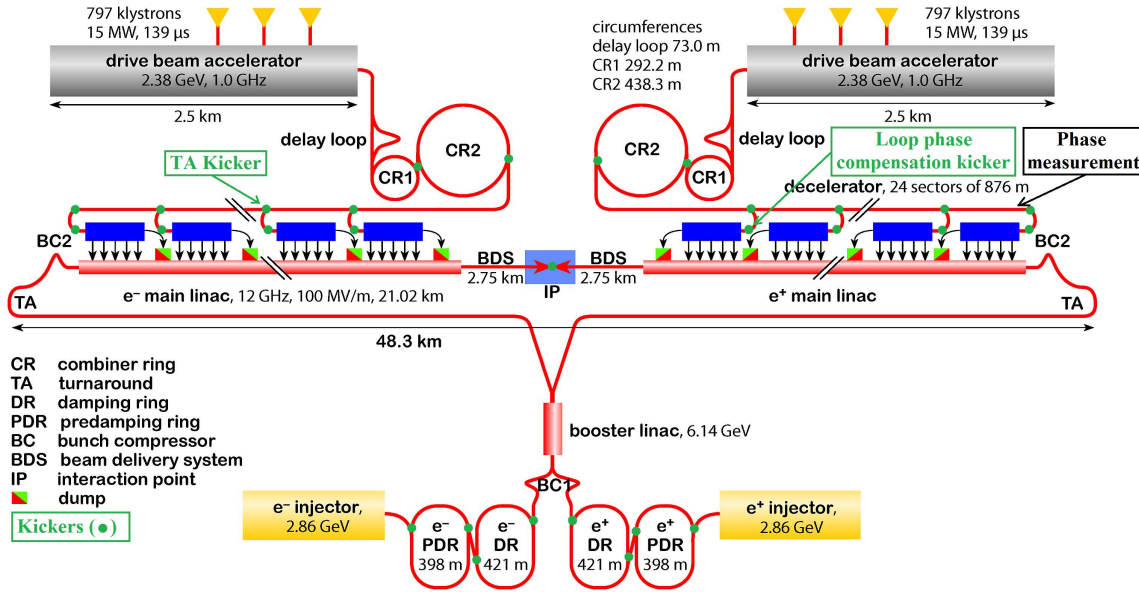


Fig. 5.246: Overview of the kickers in the CLIC facility

5.10.2 Main Beam

The design of the injectors for CLIC is based on a central complex, housing all the subsystems, to prepare the Main Beams. The Main Beams are subsequently transported, via two long transfer lines, to the starting point of each main linac at the extremities of the collider facility.

5.10.2.1 Injection and extraction from PDR and DR

The CLIC design relies on the presence of PDR and DR to achieve the very low emittance, through synchrotron radiation damping, needed for the luminosity requirements of CLIC. To achieve high luminosity at the Interaction Point (IP), it is crucial that the beams have very low transverse emittance: the PDR and DR provide emittance damping in all three dimensions. The PDR is required to decouple the wide aperture requirements of the incoming beams from the final emittance requirements of the main linac. The design parameters of the PDR and DR are dictated by target performance of the collider (e.g., luminosity), the injected beam characteristics or compatibility with the downstream system parameters: the emittances of the beams in the damping rings must be reduced by several orders of magnitude [245]. The injection and extraction layouts have been investigated with the preliminary PDR lattice, with the goal of using common equipment designs for both systems. The difference in the injected emittances between e⁺ and e⁻ means that the injection layouts are slightly different for the two PDR rings, as shown

in Fig. 5.247. For the e^+ ring, two kicker units are needed to provide a total deflection of approximately 4 mrad, while for the e^- ring a single kicker unit with 2 mrad is sufficient. Two different magnetic septa thicknesses are needed, and also two gap heights, with a 20 mm version needed for the e^+ PDR injection system only (Table 5.77). The required currents are reasonable, although the 13.7 kA for the e^+ PDR septum may pose some issues for cooling, and a longer (3.0 m) magnet could be envisaged to reduce the field and hence current by 33%.

Another issue is the required field stability of the septum. This is calculated on the assumption that a variation of approximately 4×10^{-2} mrad is required for PDR injection, 4×10^{-3} mrad for PDR extraction and DR injection, and 4×10^{-4} mrad for DR extraction [246], which translates as a stability of $\pm 2 \times 10^{-6}$. This stability will present interesting challenges for the power supply, unless the septum inductance can be made sufficiently large to provide filtering of the current.

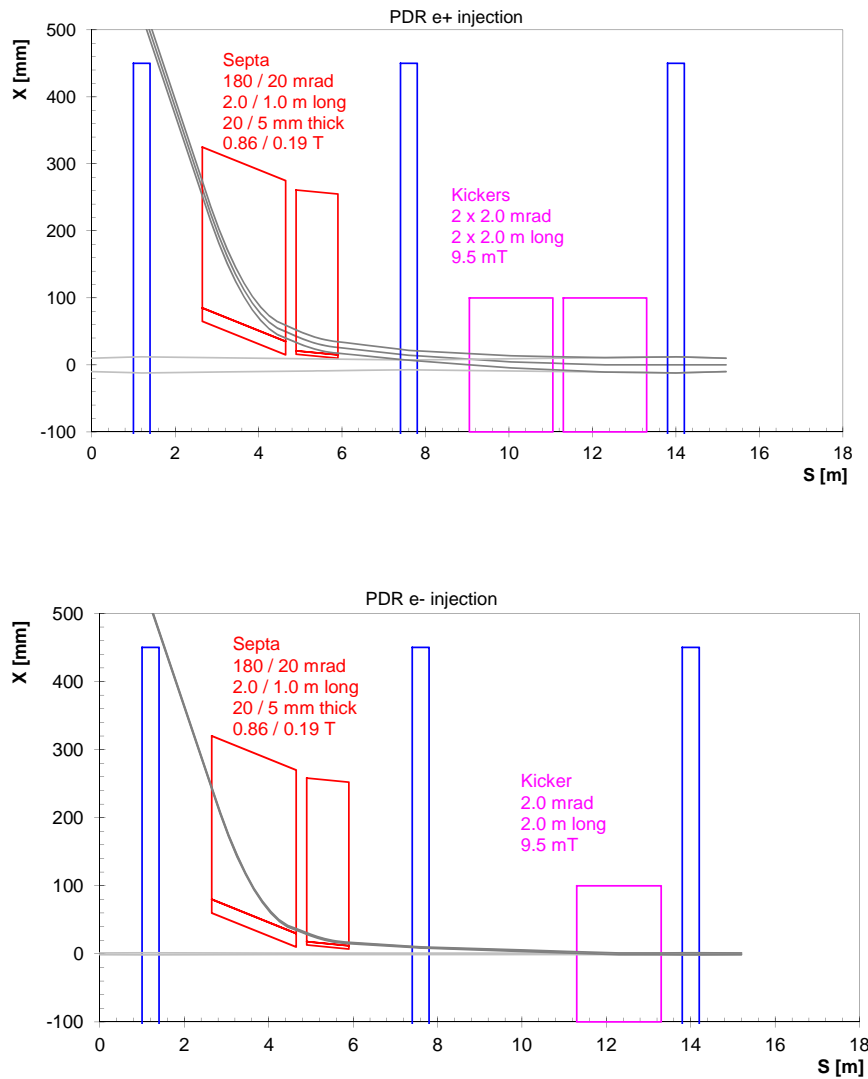


Fig. 5.247: Layout of PDR injection regions for e^+ ring (top) and e^- ring (bottom), with 2.0 m-long thick (20 mm) septa and 1.0 m-long thin (5 mm) septa, and 2.0 m-long kicker modules. This arrangement would require two free drifts each 6.0 m long for the injection system.

For the PDR extraction, the same kicker and septum modules are initially foreseen as for the PDR

injection. Protection of the extraction septa against unsynchronized or partial kicks will probably be necessary, which could require the addition of space in the layout for a passive diluter or absorber.

The layouts for extraction from the DR are shown in Fig. 5.248. The same quadrupole spacing and free drift is assumed, as the extraction systems can be installed symmetrically with respect to the injection regions.

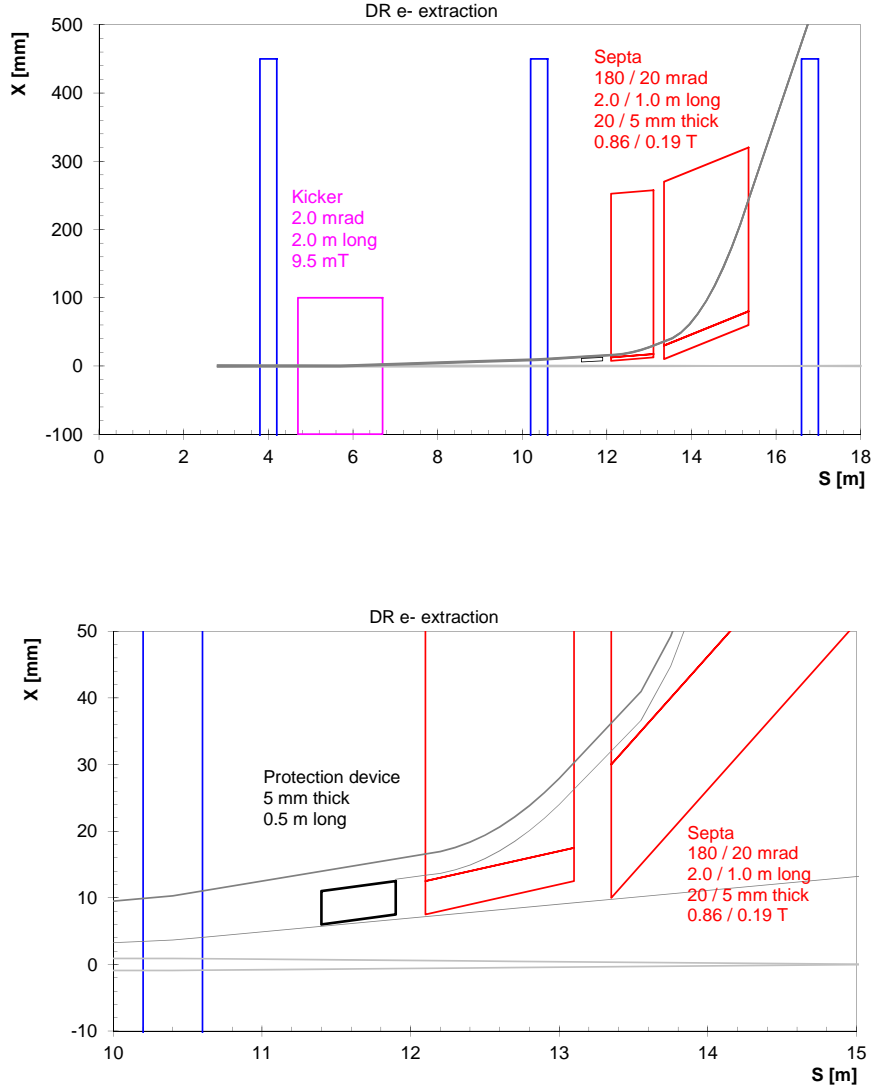


Fig. 5.248: Layout of DR extraction regions for e^+ and e^- rings (top), and zoom showing protection of extraction septum from kicker sweep (bottom), with 5.0 mm thick and 0.5 m long diluter. Kicker strengths and septum strengths/thicknesses can be further optimized at the cost of increasing the number of equipment variants.

5.10.2.2 Damping Ring and Pre-Damping Ring kickers

In order to limit the beam emittance blow-up due to oscillations at extraction the combined flat top ripple and droop of the field pulse for the DR extraction kickers must be less than $\pm 0.02\%$. In addition, the total allowable beam coupling impedance in each ring is also very low. This section discusses initial ideas for achieving the demanding requirements for the PDR and DR kickers.

Table 5.77: PDR/DR injection and extraction septum specifications

Parameter [units]	PDR e ⁺ inj. thin	PDR e ⁺ inj. thick	PDR/DR thin	PDR/DR thick
Beam Energy [GeV]	2.86	2.86	2.86	2.86
Deflection Angle [mrad]	20	180	20	180
Gap height [mm]	20	20	5	5
Septum thickness [mm]	5	20	5	20
Length [m]	1.0	2.0	1.0	2.0
Injection Stability	$\pm 2 \times 10^{-3}$	$\pm 2 \times 10^{-4}$	$\pm 2 \times 10^{-3} / \pm 2 \times 10^{-4}$	$\pm 2 \times 10^{-4} / \pm 2 \times 10^{-5}$
Extraction Stability	–	–	$\pm 2 \times 10^{-4} / \pm 2 \times 10^{-5}$	$\pm 2 \times 10^{-5} / \pm 2 \times 10^{-6}$
Pulsed mode	DC	DC	DC	DC
Available length [m]	~2.5	~1.5	~2.5	~1.5
Vacuum [mbar]	10^{-10}	10^{-10}	10^{-10}	10^{-10}
Gap field [T]	0.19	0.86	0.19	0.86
Coil current [kA]	3.0	13.7	0.8	3.4

Table 5.78: PDR & DR kicker specifications (2 GHz baseline)

Parameter [units]	PDR	DR
Beam Energy [GeV]	2.86	2.86
Deflection Angle [mrad]	2	1.5
Aperture [mm]	40	20
Field rise and fall time [ns]	700	1000
Pulse flat top duration [ns]	~160	~160
Flat top reproducibility	$\pm 1 \times 10^{-4}$	$\pm 1 \times 10^{-4}$
Injection stability [per system]	$\pm 2 \times 10^{-2}$	$\pm 2 \times 10^{-3}$
Extraction stability [per system]	$\pm 2 \times 10^{-3}$	$\pm 2 \times 10^{-4}$
Injection field homogeneity [%]	$\pm 0.1^a$	$\pm 0.1^a$
Extraction field homogeneity [%]	$\pm 0.1^a$	$\pm 0.01^b$
Repetition rate [Hz]	50	50
Available length [m]	~3.4	~1.7
Vacuum [mbar]	10^{-10}	10^{-10}
Pulse voltage per stripline [kV]	± 17.0	± 12.5
Stripline pulse current (50Ω load) [A]	± 340	± 250

^a Over 3.5 mm radius.^b Over 1 mm radius.

Jitter in the magnitude of the DR extraction kicker waveform translates into beam jitter at the IP [1]. Thus the PDR and DR kickers, in particular the DR extraction kicker, must have a very small magnitude of jitter. Table 5.78 shows the specifications for the PDR and DR kickers [246]: the specified stabilities include all sources of contributions such as ripple and droop. The values in Tables 5.77 and 5.78 will be refined as the optics design progresses.

Striplines will be used for the kicker elements (see following sections). The angle of deflection

(θ_E), in radians, due to an electric field between untapered stripline plates, is given by:

$$\theta_E = \arctan \left(\frac{V \cdot L \cdot c}{d \cdot p \cdot \beta \cdot c} \right) \quad (5.35)$$

where:

- V is the potential difference between the deflector plates
- L is the overall length of the deflector plates
- d is the plate separation,
- $\beta \cdot c$ is particle velocity,
- c is the velocity of light in free space (3×10^8 m/s)
- p is the beam momentum in units of GeV/c.

The angle of deflection (θ_B), in radians, due to a magnetic field is given by:

$$\theta_B = \left(\frac{0.3 \cdot B \cdot L}{p} \right) \quad (5.36)$$

where B is magnetic flux-density [T].

It can be shown that the deflection due to the magnetic field is independent of the impedance of the striplines and the electric and magnetic deflections are equal for $\beta=1$. In order that the electric and magnetic fields seen by the beam do not annul each other the striplines must be ‘charged’ from the beam exit end of the striplines. The electrical parameters shown in the last two rows of Table 5.78 can be derived from Eqs. 5.35 and 5.36.

Beam coupling impedance

The allowable broad band impedances, in the CLIC PDR and DR, are $1 \Omega \times n$ for longitudinal beam coupling impedance and $10 \text{ M}\Omega/\text{m}$ in the transverse plane: these values would result in beam stability against single bunch effects [247]. Since the allowable impedances are for the complete PDR and DR, which are composed of many systems including both injection and extraction kicker systems, the permissible beam coupling impedances, per kicker system, are assumed to be 5% of the longitudinal impedance allowance, i.e., $\frac{Z_0}{n} = 0.05 \Omega$, and 2% of the transverse impedance allowance, i.e., $200 \text{ k}\Omega/\text{m}$.

Figure 5.249 shows the real part of the longitudinal beam coupling impedance for an SPS extraction (MKE) magnet [248] and an LHC injection (MKI) magnet [249] in Ω/m length of ferrite: if an equivalent ferrite loaded kicker magnet with a length of 3 m is used for a CLIC kicker system, the real part of the longitudinal beam coupling impedance will be three times that shown in Fig. 5.249. The total longitudinal beam coupling impedance of DAΦNE striplines [250] (Fig. 5.250), predicted by numerical simulations, is also shown in Fig. 5.249: these striplines have an overall length of approximately 0.94 m. The predicted and measured longitudinal beam coupling impedance, for the DAΦNE striplines, are in reasonable agreement [251].

Figure 5.249 shows that, with or without serigraphy, the real longitudinal beam coupling impedance of the MKE magnets exceeds $0.05 \Omega \times n$ at all frequencies up to 1 GHz. The MKI magnets employ a more effective beam impedance reduction technique [249], and the real part of the longitudinal beam coupling impedance is within specification over the complete frequency range considered above. The DAΦNE striplines have a longitudinal impedance of less than 1Ω for frequencies above 420 MHz: there is, however, a peak in the impedance spectrum of $\sim 14 \Omega$ at $\sim 100 \text{ MHz}$. The low-frequency impedance

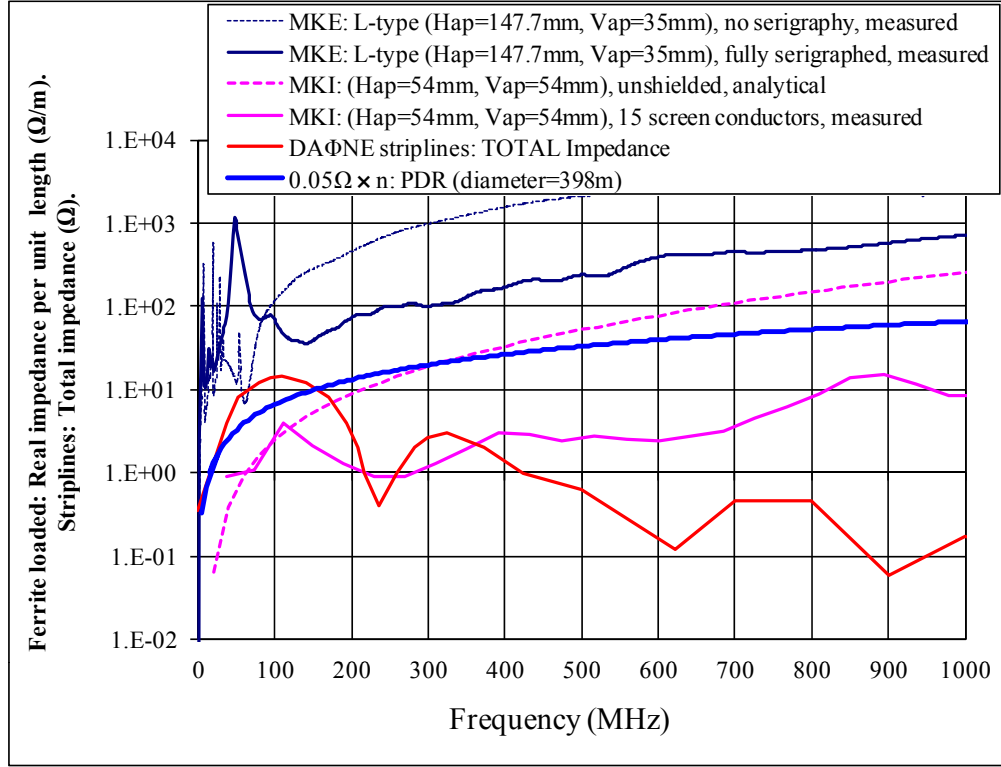


Fig. 5.249: Longitudinal beam coupling impedance, both with and without beam impedance reduction techniques, for an MKE magnet (real impedance), an MKI magnet (real impedance) and DAΦNE striplines (total impedance, 0.94 m overall length). A fraction (5%) of the allowable longitudinal beam coupling impedance Z_0^{\parallel}/n , for the PDR, is also shown.

peak of the striplines is a fundamental characteristic of the striplines. The equation for the longitudinal impedance (Z_0^{\parallel}) of untapered strip-line BPMs is:

$$Z_0^{\parallel} = 2Z_c \left[\frac{\phi_0}{2\pi} \right]^2 \left[2\sin^2 \left(\frac{\omega L}{c} \right) - i \sin \left(\frac{2\omega L}{c} \right) \right] \quad (5.37)$$

where:

- Z_c is the (even mode) characteristic impedance of one stripline with the beam pipe – each stripline is assumed to be terminated with impedance Z_c at the upstream end
- ϕ_0 is the angle each stripline subtends to the pipe axis (coverage angle)
- L is the length of each stripline

Much research has been carried out, for ILC & DAΦNE, into tapered, elliptical cross-section, striplines and wide-band feedthroughs. An elliptical cross-section of stripline minimizes the variation of the vertical dimension of the beam pipe between the injection region and the adjacent dipole region and increases the deflection efficiency [250].

By tapering the transition between the stripline structure and the adjacent beam pipe (Fig. 5.250) it is possible to [250]:

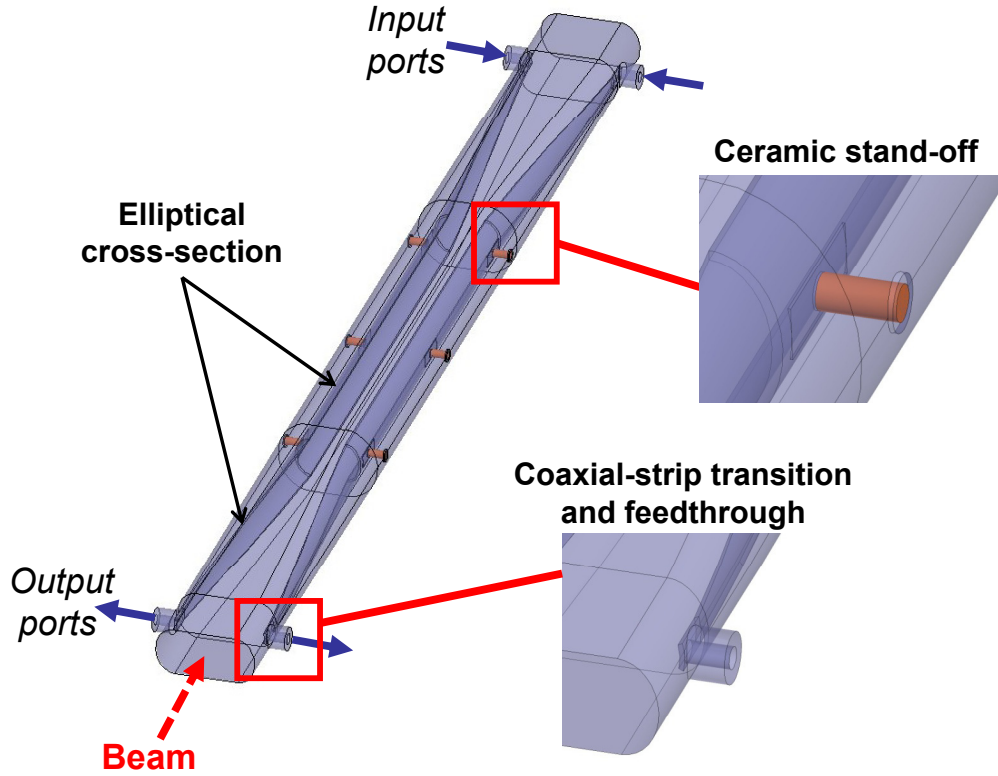


Fig. 5.250: DAΦNE striplines [250], 0.94 m overall length and each taper $\sim 30\%$ of overall length

reduce the non-uniformity of transverse deflection as a function of the transverse position;
 reduce the beam coupling impedance of the striplines;
 reduce the reflection coefficient at high frequency.

Eq. 5.37 is valid for untapered striplines, each of which is terminated with impedance Z_c at their upstream end [252]. Eq. 5.37 can be re-written as follows to allow for the effect of tapers:

$$Z_0^{\parallel} = 2Z_c \left[\frac{\phi_0}{2\pi} \right]^2 \left[2\sin^2 \left(\frac{\omega L_e}{c} \right) - i\sin \left(\frac{2\omega L_e}{c} \right) \right] \left(\left[\sin^2 \left(\frac{\omega l}{c} \right) \right] / \left[\frac{\omega l}{c} \right]^2 \right) \quad (5.38)$$

where (Fig. 5.249):

- l is the length of a single taper (Fig. 5.251)
- L_e is the effective length of each stripline ($L_e = L - l$) (Fig. 5.249)
- L is the overall length of a stripline

The percentage of taper is defined to be the length of a single taper relative to the overall length of the striplines, namely;

$$Taper(\%) = \frac{l}{L} \times 100$$

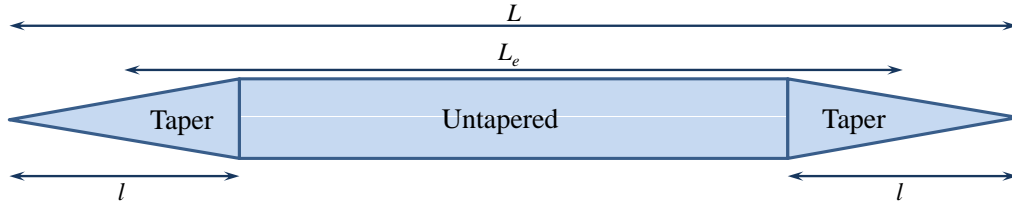


Fig. 5.251: Definition of lengths for a tapered stripline (courtesy S. Smith)

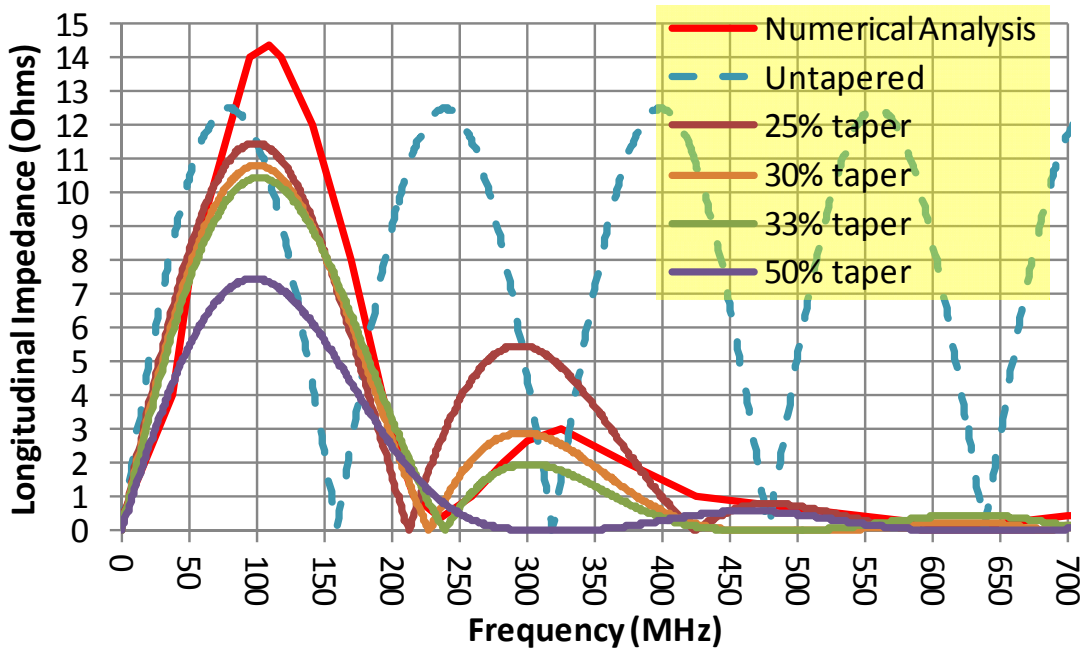


Fig. 5.252: Longitudinal beam coupling impedance, for DAΦNE striplines ($\sim 30\%$ taper), as determined by a numerical analysis [253], and Eqs. 5.37 and 5.38

Figure 5.252 shows the longitudinal beam coupling impedance for the DAΦNE striplines (taper, at each end, of $\sim 30\%$ [253] of the 0.94 m overall stripline length [‘Numerical Analysis’]) together with the results of Eqs. (3 and 4). After the first low-frequency impedance peak the analytical solution for a 30% taper is very similar to the numerical analysis of the DAΦNE striplines, providing confidence in Eq. 5.38 modified to include tapers. In addition, numerical analysis of a stripline with a 10% taper also shows good agreement between the numerical analysis and Eq. 5.38 [254].

As pointed out in Ref. [255] the uniformity of the deflecting field, as a function of the transverse coordinates, for a given transverse section of the kicker, depends on the coverage angle of the striplines. The optimum case, for circular electrodes, is for a coverage angle of 80° ; even so the inhomogeneity of the field can be a few tens of per cent inside the good field region [255]. However, for CLIC, although the field uniformity specifications are extremely demanding (Table 5.78) the required good field uniformity region is relatively small. Simulations have commenced to study the field uniformity issues and the initial results are promising [254].

Eq. 5.37 shows that for a coverage angle of $\pi/2$ radians per stripline, a peak of longitudinal beam coupling impedance of $Z_c/4$ Ohms occurs at a frequency close to $c/(4L)$: hence the frequency of the peak is dependent upon the length of the stripline. Thus, from Eq. 5.37, for a $50\ \Omega$ even-mode characteristic impedance and an overall stripline length of 0.94 m, a longitudinal impedance peak of $12.5\ \Omega$ is expected at 80 MHz. The frequency of this impedance peak is moved upwards by tapers and is approximately 100 MHz with 25% tapers, which is reasonably consistent with the DAΦNE stripline simulation results shown in Fig. 5.251.

From Fig. 5.249, striplines have a significantly lower longitudinal beam coupling impedance, than a screened MKI magnet, at frequencies above 400 MHz: in addition, the imaginary component of the longitudinal beam impedance (not shown in Fig. 5.249) is known to be significant, for the MKI magnet, above 600 MHz [256]. The use of striplines rather than a screened ferrite loaded magnet is supported by experience at KEK/ATF, where metallized ceramic tubes were used to reduce the beam coupling impedance of ferrite loaded kickers: the thickness of the metallization was difficult to accurately control and, as a result, two kickers had very different pulsed magnetic characteristics [257].

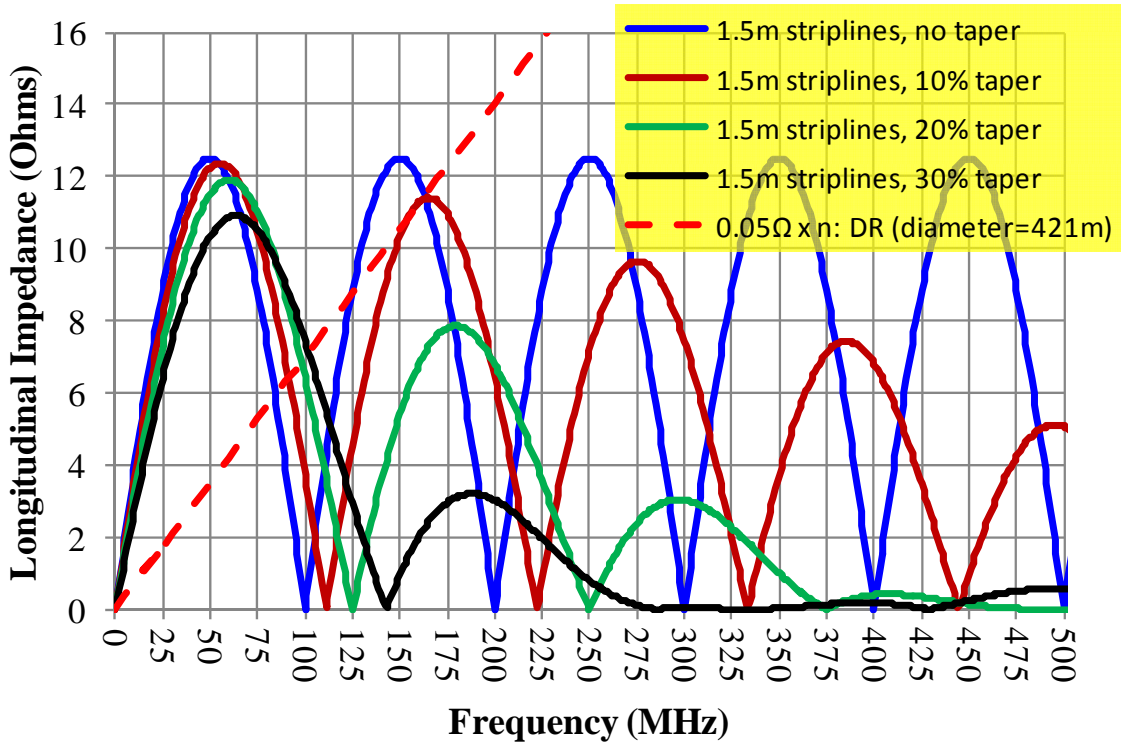


Fig. 5.253: Longitudinal beam coupling impedance, for striplines of ($L=$)1.5 m overall length (suitable for DR) and a coverage angle of 90° per stripline, with a taper at each end, calculated from Eqs. 5.37 and 5.38

Figure 5.253 shows longitudinal beam coupling impedance, for striplines of 1.5 m overall length (length suitable for DR) and a coverage angle of 90° per stripline, with a taper at each end whose length is expressed as a percentage of overall length; the longitudinal beam coupling impedance is calculated from Eqs. 5.37 and 5.38. The permissible longitudinal beam coupling impedance, of $\frac{Z_0}{n} = 0.05\ \Omega$ per kicker system, is also shown on Fig. 5.253: short tapers are required, for 1.5 m long striplines, to ensure that the longitudinal beam coupling impedances in the range from 150 MHz to 170 MHz, are less than $0.05\ \Omega \times n$. Depending upon the degree of tapering, the calculated longitudinal impedance at 55 MHz is a factor of up to 3.3 greater than $0.05\ \Omega \times n$.

Figure 5.254 shows the longitudinal beam coupling impedance for striplines with an overall length of 1.5 m and 3 m, with a coverage angle of 90° per stripline and a 20% taper at each end: the first

impedance peak occurs at a frequency of 60 MHz and 30 MHz for the 1.5 m and 3 m long striplines, respectively: thus the 1.5 m striplines have a lower ratio of the maximum value of calculated longitudinal impedance to $0.05 \Omega \times n$ at frequencies below ~ 40 MHz. However the 3 m long striplines have the advantage that, for a given percentage taper, the impedance peaks are more rapidly damped.

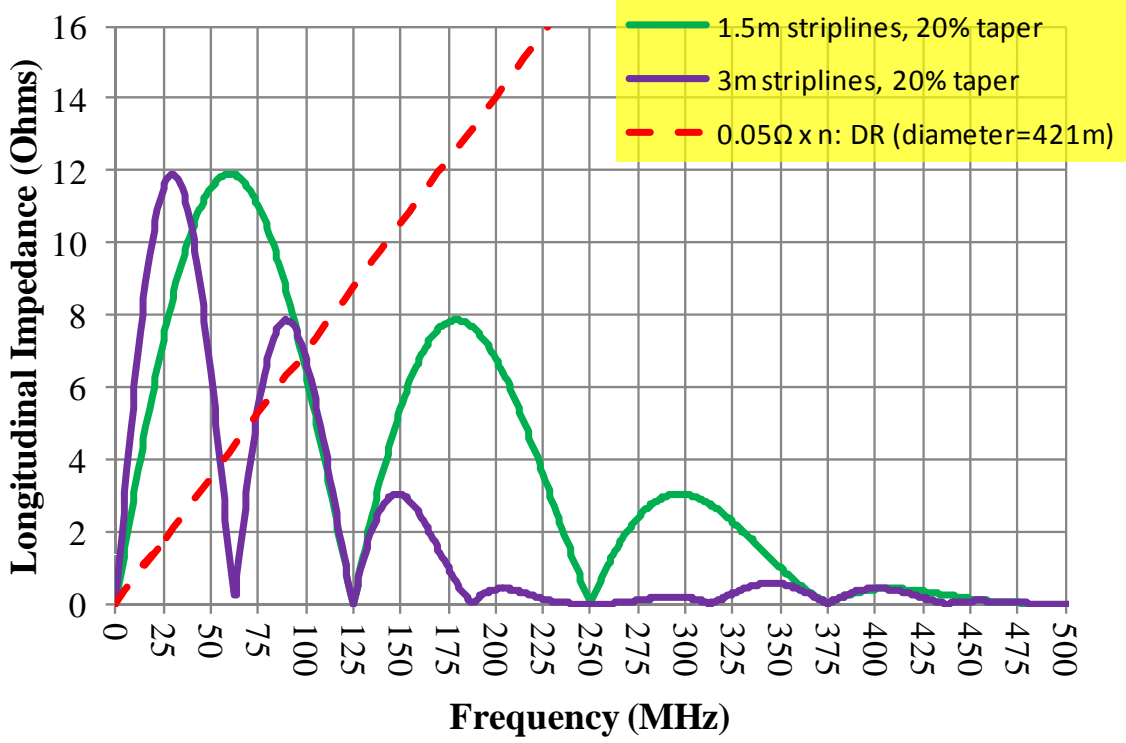


Fig. 5.254: Longitudinal beam coupling impedance, for striplines of ($L =$) 1.5 m and 3 m overall length with a coverage angle of 90° per stripline, with a 20% taper at each end, calculated from Eqs. 5.37 and 5.38

Beam stability simulations are required to assess the effect of the longitudinal beam coupling impedance exceeding $0.05 \Omega \times n$ at low frequencies and to determine whether, for the longitudinal beam coupling impedance, two sets of 1.5 m striplines are better than a single set of 3 m striplines, or vice-versa.

Reference [252] shows the following equation for the transverse impedance (Z_0^\perp) of strip-line BPMs:

$$Z_0^\perp = \left[\frac{Z_0^\parallel}{\omega} \right]_{\text{pair}} \left[\frac{c}{b^2} \right] \left[\frac{4}{\phi_0} \right]^2 \sin^2 \left(\frac{\phi_0}{2} \right) \quad (5.39)$$

where:

- b is the inside radius of the (round) beam pipe
- Z_0^\parallel is calculated from either Eq. 5.37 [252] or from Eq. 5.38
- L_e is the effective length of each stripline ($L_e = L - l$) (Fig. 5.249)
- L is the overall length of a stripline

Figure 5.255 shows transverse beam coupling impedance, for striplines with an overall length of 1.5 m (length suitable for DR), with a taper at each end whose length is expressed as a percentage of overall

stripline length: the transverse impedances are calculated from Eq. 5.39, assuming a beam-pipe inside radius of 0.024 m. A transverse broadband impedance of less than 10 M Ω /m, for the complete DR, would result in beam stability against single bunch effects [247]. The allowable transverse impedance per kicker system is assumed to be 2% of the beam stability criteria, i.e., 200 k Ω /m: the 1.5 m striplines are below this limit.

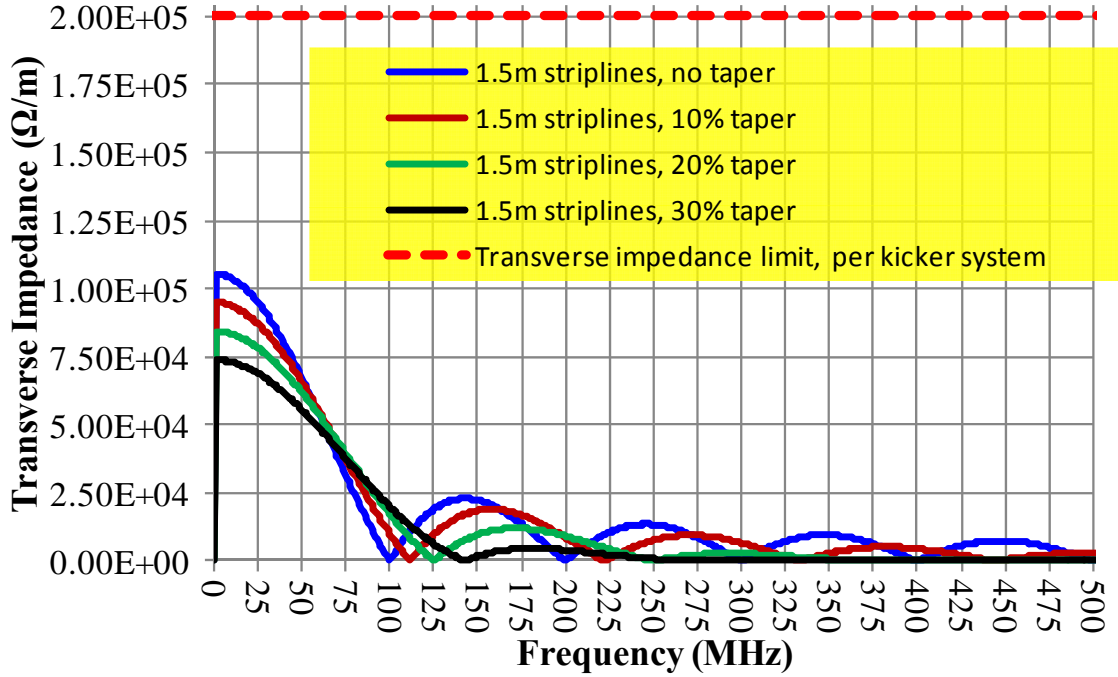


Fig. 5.255: Transverse beam coupling impedance for striplines of ($L =$)1.5 m overall length (length suitable for DR), with a taper at each end (expressed as a percentage of overall length), calculated from Eq. 5.39. For calculation purposes, the inside radius of beam-pipe for the striplines is assumed to be 0.024 m.

Caveat re. beam coupling impedance

Recent research into the striplines [254] has highlighted a significant difference between stripline BPMs and a stripline kicker. For a stripline kicker, in order to inject or extract beam, the two striplines will be pulsed to equal magnitude but opposite polarity voltages, i.e., in odd mode. When driven in odd mode there is a virtual ground mid-way between the striplines. Hence the odd mode characteristic impedance of each stripline is dependent upon the proximity of each stripline to both the beam pipe and the virtual ground.

In the case of the stripline BPMs, the striplines are not driven by an external pulse generator and therefore the characteristic impedance of the stripline is dependent upon the proximity of the beam pipe (there is not a virtual ground mid-way between the BPM striplines). The beam coupling impedance is dependent upon this, even mode, characteristic impedance (see Eqs. 5.37 and 5.38). During the time when beam is circulating in the PDR and DR, to reduce the emittance, and the kicker striplines are not driven by the pulse generator, the beam coupling impedance can be evaluated in a similar way to that of BPM striplines – however the even mode characteristic impedance of the kicker striplines must then be considered. The even mode characteristic impedance, of the kicker striplines, will be greater than the odd mode characteristic impedance: thus if each stripline is terminated in its even mode characteristic impedance (to minimize beam coupling impedance), the termination is not matched for the odd mode characteristic impedance. The effect of an impedance mismatch upon field rise-time and ripple requires

further research – but the effect of an impedance mismatch can be minimized by:

- Minimizing the electrical delay of coaxial cable between the pulse generator and the striplines;
- Minimize the ratio of the even mode to odd mode characteristic impedance of the striplines, i.e., for a $50\ \Omega$ even mode characteristic impedance per stripline, ensure that the odd mode characteristic impedance per stripline is as close as possible to $50\ \Omega$ while still achieving the required field homogeneity.

The difference between the even mode and odd mode characteristic impedances can be minimized if the beam pipe is close to the striplines. However a beam pipe close to the striplines may not be consistent with achieving the required field homogeneity and voltage hold-off: this requires detailed studies.

Note: an odd mode characteristic impedance of a stripline of less than $50\ \Omega$ does not relax the requirement of a broadband impedance of $50\ \Omega$ for the coaxial feedthroughs: the feedthrough of the $50\ \Omega$ termination should ideally be $50\ \Omega$ so that the beam image current ‘sees’ an impedance matched to the even mode characteristic impedance for each stripline.

Conclusions for beam coupling impedance

Striplines will be used for the kicker systems in the CLIC PDR and DR: for striplines with an even mode characteristic impedance of $50\ \Omega$, initial analytical calculations show that their transverse beam coupling impedance is within the allowable $200\ \text{k}\Omega/\text{m}$ per kicker system. In order to limit the magnitude of the longitudinal beam coupling impedance at frequencies after the first, low frequency, peak, tapers of approximately 10% and 25% are required for the DR and PDR striplines, respectively. Power deposition in the resistive terminator of the stripline, attributable to the circulating beam, will be calculated from the real part of the longitudinal beam coupling impedance of the striplines and a spectrum of the beam: this will allow the effect of tapers, upon calculated power deposition, to be evaluated.

Beam stability simulations are required, for both the PDR and DR, to assess the effect of the longitudinal beam coupling impedance exceeding $0.05\ \Omega \times n$ at low frequencies and to determine whether, for the longitudinal beam coupling impedance, two sets of 1.5 m striplines are better than a single set of 3 m striplines, or vice-versa.

Simulations have commenced to study the homogeneity of the integrated field [254]. To maximize the efficiency of the stripline kickers, the length of the taper should be minimized, however sufficient taper is required to reduce the high-frequency longitudinal beam coupling impedance to an acceptable level [258]. In addition, tapers affect the non-uniformity of transverse deflection as a function of the transverse position [250], [259], so the length of taper needs to be optimized for the field homogeneity too. It is envisaged that, to minimize the contribution of the stripline assembly to the overall machine beam coupling impedance, the same beam pipe cross-section will be used for the striplines as is used for the surrounding elements: if it proves impossible to find a design which meets all of the requirements, then the stripline beam pipe cross-section could be changed. From the point of view of beam coupling impedance it may be even better to taper the beam-pipe rather than the striplines, but this requires further investigation.

Once the electromagnetic simulations are completed, striplines will be prototyped under the Spanish Science Industry Program.

System stability

Figure 5.256 shows a simplified schematic of a stripline kicker system. The two striplines are driven to an equal magnitude of voltage but of opposite polarity. A High Voltage DC (HVDC) power supply charges a Pulse Forming Network (PFN) or a Pulse Forming Line (PFL). The fast switch is then closed

to launch a pulse towards the striplines (note: for simplicity, Fig. 5.256 only shows one of the two HVDC supplies, PFL/PFN and fast switches). The pulse propagates through the striplines and is then deposited in a terminating resistor. The characteristic impedances of the PFL/PFN, transmission lines, striplines and terminating resistors are matched as far as possible to minimize reflections, which could cause ripple on the flat top of the deflection waveform: however it may not be feasible to match the odd mode characteristic impedance of the striplines to the characteristic impedance of the other elements of the kicker system (see caveat above). The PFL and fast switch, shown in Fig. 5.256, could be replaced with an Inductive Adder. This is discussed later.

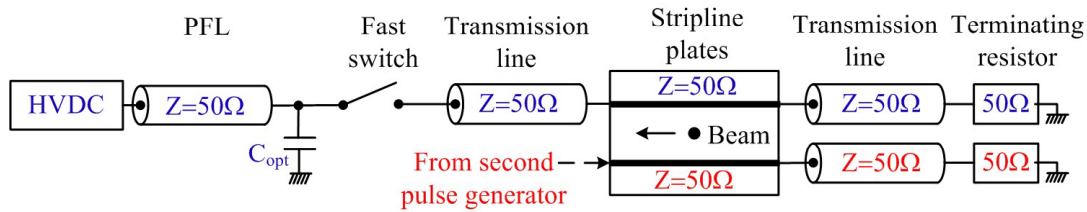


Fig. 5.256: Simplified schematic of stripline kicker system

To limit the beam emittance blow-up due to oscillations, the pulse power modulators for the DR kickers must provide extremely flat, high-voltage, pulses: specifications call for a 160 ns duration flattop of 12.5 kV, 250 A, with a combined ripple and droop of not more than $\pm 0.02\%$ (Table 5.78). Figure 5.257 shows the definition of the pulse required for the CLIC DR & PDR.

- Rise time: is the time needed to reach the required voltage (including settling time);
- Settling time: is the time needed to damp oscillations to within specification;
- Droop & ripple: window during which the combined droop and ripple must be within specification;
- Reproducibility: maximum difference allowed between two consecutive pulses.
- Fall time: time for voltage to return to zero.

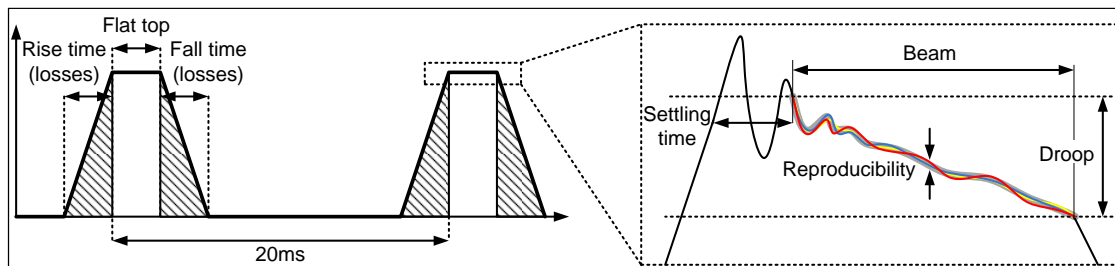


Fig. 5.257: Definition of pulse required for CLIC DR & PDR

Possible sources of ripple, droop and irreproducibility of the deflection waveform include:

- PFN: a PFL or inductive adder will likely give lower ripple – thus a PFN will not be considered further;

- HVDC supplies (reproducibility is expected to be acceptable for slow charging of PFL);
- Attenuation in the PFL and transmission lines;
- Switch (dynamic characteristic, and both short term and long term temperature effects);
- Feedthroughs;
- Striplines;
- Terminating resistor (frequency dependence of value, long-term stability and temperature will affect ripple and reproducibility of the waveform);
- Non-ideal impedance matching of the system.

Several of these items will be discussed in the following sub-sections.

The demanding specifications for droop and ripple can be relaxed for an individual kicker if a double kicker system is employed [257]: in this case the overall response of the double kicker system must meet the specifications.

Double kicker system

Experience at KET/ATF

Extraction from the DR with a single kicker system requires a very uniform and stable field pulse with ultra-low ripple (Table 5.78). A double kicker system (Fig. 5.258), consisting of two identical ferrite loaded kicker magnets and a single power supply, has been developed at KEK [257], [260], [261]. The first kicker extracts the beam from a damping ring and the second kicker, displaced from the first kicker by a suitable Betatron phase, results in anti-phase ripple to that of the first kicker (Fig. 5.259).

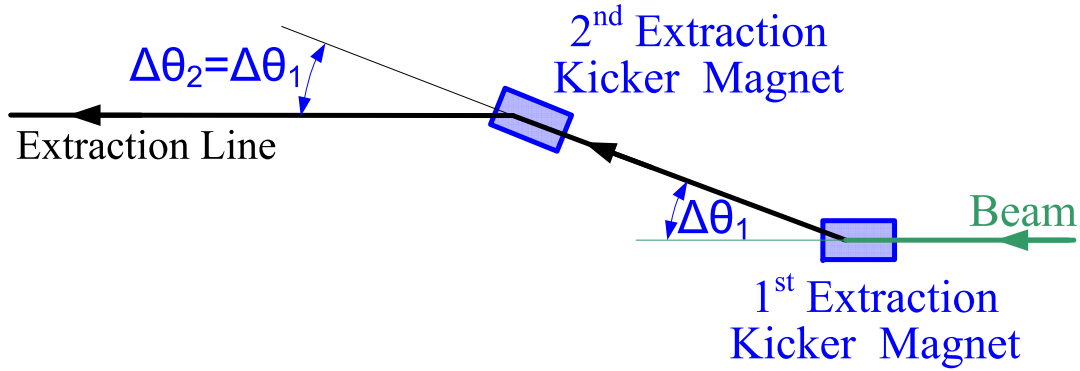


Fig. 5.258: first and second kickers separated by a betatron phase of $2n\pi$: for a betatron phase of $(2n-1)\pi$ the second kick would be in the other direction

Theoretically, using a double kicker system, the effect of ripple in the two kickers and small variations in the output of the HVDC supplies can be completely cancelled. In addition, theoretically, the double kicker can compensate for field inhomogeneity in each stripline kicker; this therefore permits the field uniformity requirement of an individual stripline kicker to be relaxed, while still achieving excellent overall effective deflection uniformity. However this places demanding requirements on the beam optics.

Measurements have been carried out at the KEK/ATF with a double kicker: the two kickers were nominally identical, ferrite loaded, transmission line magnets. However, to reduce beam coupling impedance, the inside of the ceramic tube in the magnet apertures was coated with 1 μm thick Titanium

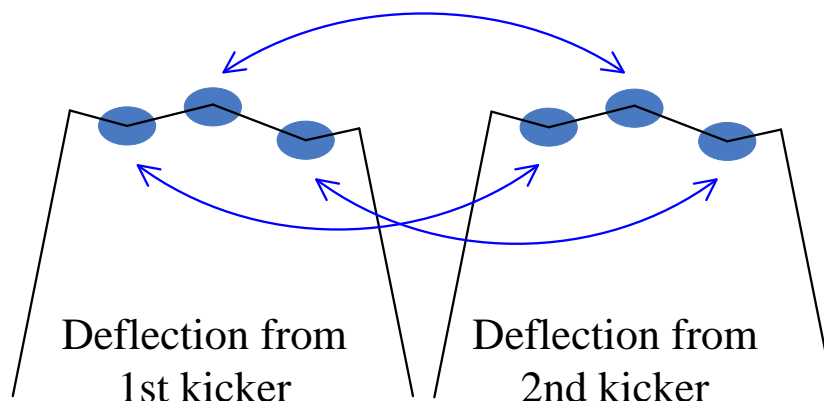


Fig. 5.259: Exactly the same flat top ripple from both kickers ideally results in ripple cancellation

Nitride (TiN): the thickness of the TiN coating is probably not uniform. This is evidenced by the fact that the second kicker had an apparent deflection of only 83% of the first kicker (for approximately the same current flow [257]): this deflection was determined from measurements of the beam orbit, shot by shot, in the extraction line [257]. The two KEK kickers each had 25 cells and were manufactured to high mechanical accuracy. In addition the ferrite used (TDK-PE14) was from a single manufactured batch: thus magnetically the two kickers should perform in a very similar manner.

The phase advance of the two kickers, although nominally π , was experimentally determined to minimize the jitter angle in two kicker mode. Subsequently, to measure the equivalent jitter in single kicker mode, the 2nd kicker was replaced with a dipole [261]: the strength of the dipole was adjusted to give the same average beam trajectory as for the double kicker. The dipole had a small aperture and a high stability power supply thus its field uniformity and field stability are believed to be very good. All measurements were made with single bunches, i.e., at a particular time on the kick field waveform.

BPMs were used to determine the ripple of the double kicker system. The ATF Damping Ring had button BPMs with a positional resolution of $20\text{ }\mu\text{m}$ to $30\text{ }\mu\text{m}$. The extraction line used both Cavity BPMs ($2\text{ }\mu\text{m}$ resolution) and Stripline BPMs ($20\text{ }\mu\text{m}$ to $30\text{ }\mu\text{m}$ resolution). The KEK double kicker achieved a factor of ~ 3.3 reduction in kick jitter angle, with respect to a single kicker [261]. The resolution of the BPMs limited the optimization of the phase advance and thus the jitter angle reduction. The resolution of the Cavity BPMs was limited, at the time, by the readout electronics. Improvement in the electronics now allows a resolution of approximately 100 nm [262].

Research into double kicker systems is planned at CERN to try to achieve a greater improvement in jitter reduction: two identical stripline kickers and high precision BPMs will be used.

Double kicker for CLIC

For CLIC, assuming a 10 m separation between the 1st and 2nd kickers, the time of flight is $\sim 33.3\text{ ns}$ for the beam and $\sim 50\text{ ns}$ for the kicker current pulse. In order that the beam bunches and kicker field are synchronized in time at the second kicker system either:

- the two kicker systems must be in parallel (Fig. 5.260) or,
- for a series connection a $\sim 16.7\text{ ns}$ delay loop is required for the beam.

Feeding two parallel kickers from a common HVDC supply and single switch (Fig. 5.260) is the best option as it avoids the need for an additional delay loop for the Main Beam. In order to synchronize in time the beam bunches and kicker field at the 2nd kicker system, there is an additional transmission cable between the switch and second stripline kicker whose temporal delay is the same as the time of flight of the beam. However this transmission cable has the undesirable effect of introducing extra attenuation and dispersion of the electrical pulse arriving at the second stripline kicker in comparison with the pulse arriving at the first stripline kicker.

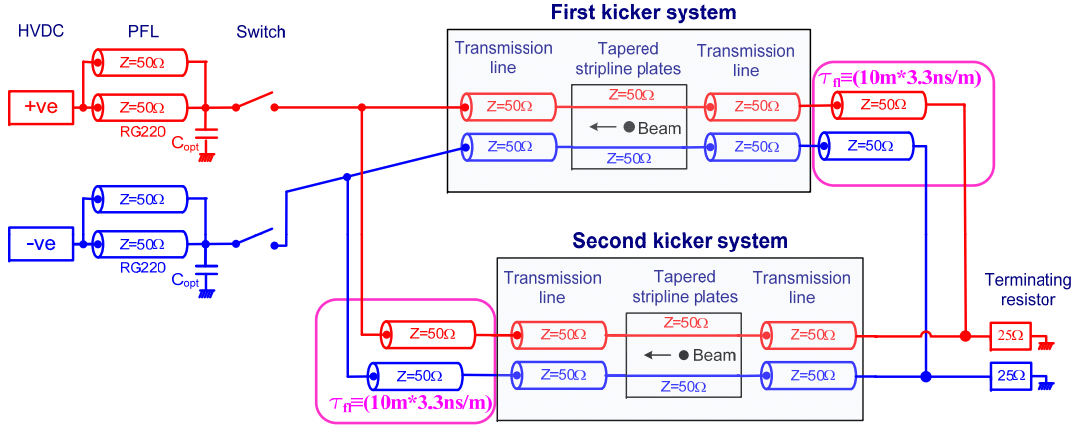


Fig. 5.260: Schematic of double kicker system, supplied in parallel, for the CLIC DR

Impedance matching considerations

Initial considerations of impedance matching of striplines, for electrical pulses, indicate that to achieve a pulse ripple of not more than 0.02%, impedances should be matched to better than 2.8%. However given the relatively long allowance for field rise and fall times (Table 5.78), and provided that transmission line lengths are minimized, there may be time for ripple, introduced due to impedance mismatches, to be damped to a suitably low level before the end of the specified rise or fall time. However making use of the relatively long allowance for rise and fall times would have the disadvantage of increasing power dissipation, and hence heating, in the switches and terminating resistors.

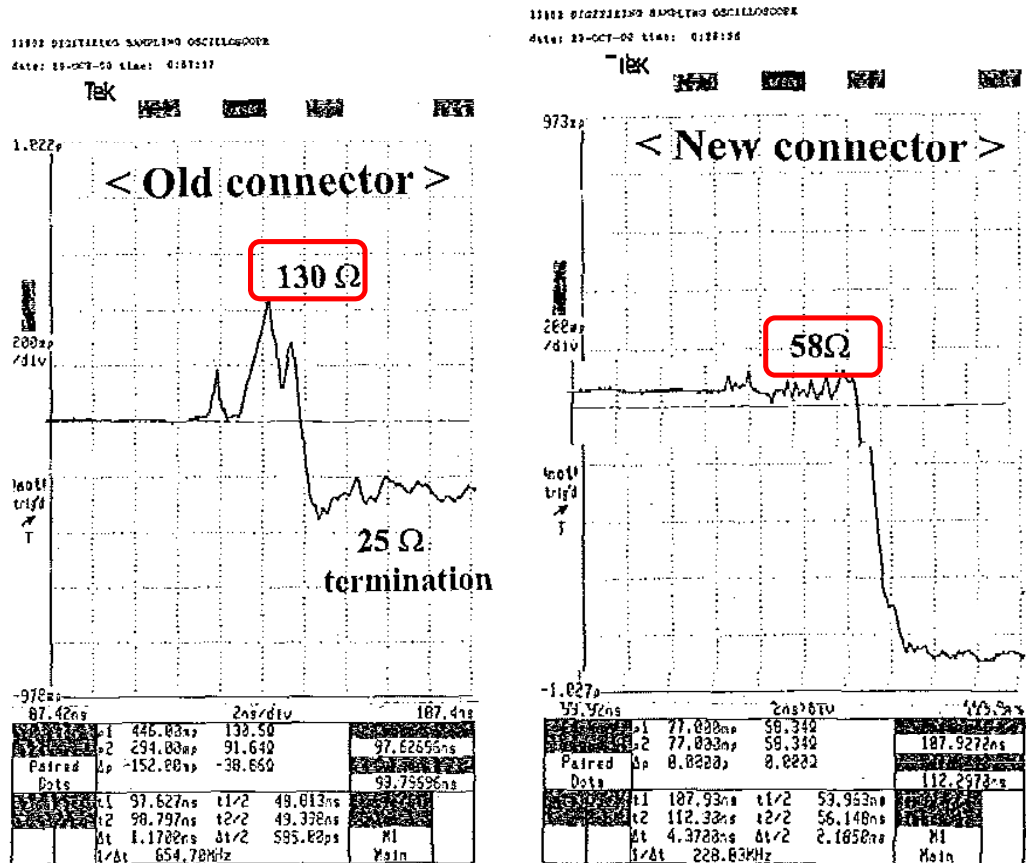
Feedthrough connectors can be a significant source of impedance mismatch. KEK/ATF and INFN/DAΦNE both carried out research and development concerning feedthrough connectors to achieve good impedance matching over a wide range of frequencies. The KEK/ATF feedthrough connector, developed using HFSS, had a predicted S11 reflection coefficient below 0.02 up to 300 MHz [261]; this corresponds to impedance matching to 4%. A measurement with a step waveform showed an impedance of up to 58 Ω [261]; this is not as good as predicted but considerably better than the 'old' feedthrough connector performance (Fig. 5.261). The new feedthrough connector performance is shown in Fig. 5.262.

In order to minimize thermal effects the rise and fall times of the electrical pulse must be as short as feasible. Thus research and development of HV feedthrough connectors is required for the CLIC DR kicker systems in order to be able to achieve the required voltage hold-off together with adequate impedance matching over a wide frequency range. Identification and procurement of suitable HV feedthroughs is presently part of the Spanish Science Industry Program.

In addition to the feedthrough connectors, the transmission lines, striplines and terminating resistors are all possible sources of impedance mismatches: the usual datasheet value for the real impedance

of suitable, commercial, HV transmission line, at 1 MHz, is $50\ \Omega$ with a tolerance of $\pm 1\%$. In addition, the impedance matching of the PFL and semiconductor switches is important. For the terminating resistor, due to the presence of parasitic components, the impedance value will be frequency dependent. Temperature and long-term stability will affect ripple and reproducibility of the waveform. All of these effects require further research and development.

Fig. 5.261: Measured step-response of old (left) and new (right) KEK/ATF feedthrough connector [261]

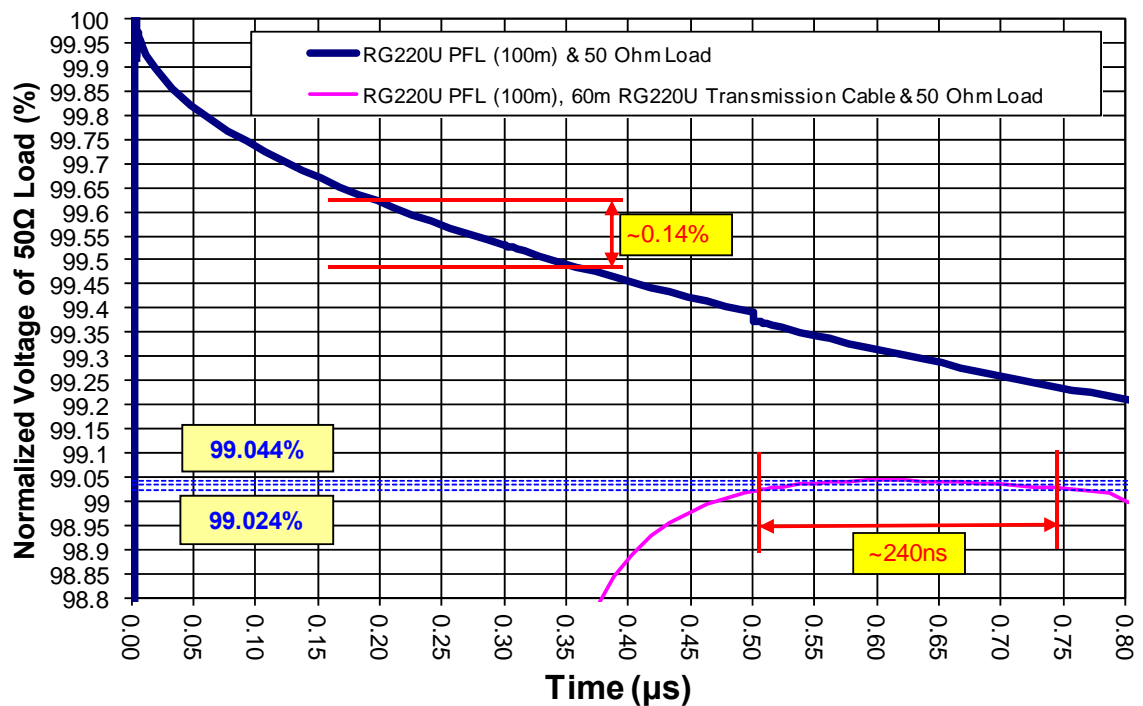


In addition to the above the semiconductor switches used will have an on-state resistance which will be temperature dependent; thus the on-state resistance will depend upon pulse duration and ambient temperature. Hence it is desirable to minimize the duration of the electrical pulse, i.e., by minimizing the rise and fall times and designing the system to minimize impedance mismatches so that ripple is damped rapidly.

Compensation of droop

If a PFL is used, one of several problems for deflection stability is PFL droop. Impedance matched PFLs deliver low ripple pulses, but low attenuation and dispersion are essential (especially with longer pulses) to control droop and 'cable tail'. However it is possible to make use of the frequency dependent attenuation and dispersion, of the transmission line, to compensate for PFL droop, but increased cable tail is a potential problem (Fig. 5.263).

Figure 5.263 shows PSpice predictions for load current, for a 100 m long PFL of RG220U coax, with a transmission line that is firstly modelled as lossless then subsequently is modelled as 60 m of RG220U coax. In both cases an ideal $50\ \Omega$ terminating resistor is modelled. Over a 160 ns period the

Fig. 5.262: New feedthrough connector developed at KEK/ATF**Fig. 5.263:** PSpice predictions for load current, for a 100 m long PFL of RG220U coax with a transmission line that is (a) lossless, (b) 60 m of RG220U

lossless transmission line gives a predicted droop of 0.14%; when the 60 m of RG220U is modelled, the load current is flat to within $\pm 0.01\%$ over a 240 ns period: however $\pm 0.01\%$ is significant in comparison with the required $\pm 0.02\%$ stability for the DR extraction kicker system.

Inductive adder

An inductive adder [263–269], instead of a PFL or PFN, is a promising means of compensating for ripple as well as attenuation and dispersion in transmission lines. The inductive adder shown in Fig. 5.264 consists of: a multi-cell primary circuit, a single secondary winding, and a fast pulse transformer with adequate voltage isolation. Each primary circuit has a fast switch. The switches can be turned on and off independently, via trigger circuits, to provide some pulse shaping: for the CLIC DR and PDR kickers the control of the primary switches could be digital [263] (on-off), analogue [269] (gain control of semiconductor switch) or a combination of these two schemes. The combined digital and analogue control scheme could involve many primary cells, each primary capacitor charged to a high voltage, controlled in a digital sense and several cells, possibly at lower voltage, controlled in an analogue manner [270–272]. In order to cancel ripple, by suitable control of primary cells, it is expected that high bandwidth switches will be required.

The inductive adder concept is also good for machine protection and reliability as it inherently contains redundant primary switches. Thus if one or just a few of many primary switches fail, a substantial portion of the required deflection is delivered to the beam.

The inductive adder concept is being studied further [270–272] and it is planned to build a prototype 12.5 kV version for evaluation and testing. In order to minimize ripple generated by the inductive adder considerable effort will be required to ensure that, as far as reasonably possible, the characteristic impedance of the adder is matched to that of the system.

Figure 5.265 shows an 18 kV inductive adder designed and built at LLNL.

Figure 5.266 shows a schematic of an inductive adder with constant voltage layers, a digital modulation layer and an analogue modulation layer. The analogue modulation layer can work either passively or actively. For passive analogue modulation, when the full load current flows through R_a the voltage drop across R_a is maximum: during the pulse a proportion of the current transfers to the magnetizing inductance L_m , thus reducing the voltage drop across R_a and compensating for droop.

For active modulation the semiconductor switches in the analogue modulation layer are operated in their linear region and provide a shunt path for the current which flows through resistor R_a . By controlling the current sharing between the resistor and the switch, it is possible to modulate the voltage over the resistor R_a and hence the load voltage. If the semiconductor switches are operating at their minimum on-state resistance, a significant portion of the current flows through the switch and hence the voltage drop across R_a is minimized.

Figure 5.267 shows predictions for an inductive adder with various values of capacitance per layer, with and without an analogue modulating layer. Without a modulation layer, 320 μF of capacitance per layer is required, for the DR adder, to keep the load voltage droop below 0.02%. To demonstrate active analogue modulation the capacitance per layer was reduced to 20 μF and the current of the shunt switch was modulated. Without an analogue modulation layer, 20 μF per layer results in a load voltage droop of $\sim 0.4\%$; with analogue modulation the droop was reduced to less than 0.01%. The simulation results, presented in Fig. 5.267, show that analogue modulation can be applied to theoretically achieve the required droop with a substantially reduced value of capacitance per layer

5.10.2.3 Interaction Point (IP) kickers

The design luminosity of CLIC requires transverse beam sizes at the nanometer level at the Interaction Point (IP), as well as stabilisation of the beam collision overlap at the sub-nanometre level. Ground motion effects can generate relative vertical offsets of the two colliding beams at the IP which will significantly degrade the luminosity. A beam-based intra-train feedback system in the interaction region can correct the relative beam-beam offset and steer the beams back into collision. In addition, this feedback system may help to considerably relax the required tight stability tolerances of the final doublet magnets. Since this IPFB system has to operate in an environment with high background radiation, the

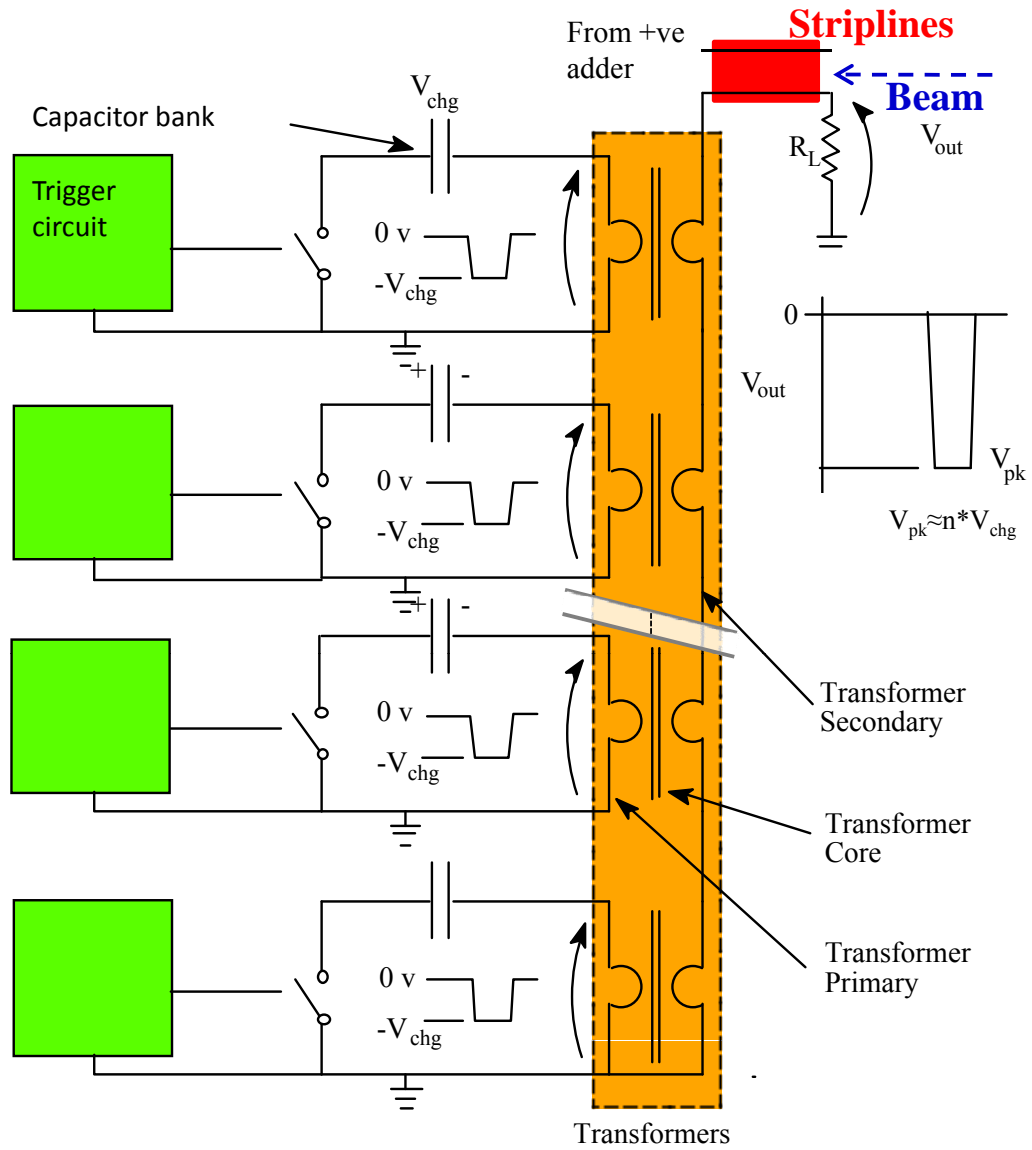


Fig. 5.264: Multi-cell inductive adder

choice of the position of the IPFB components is a compromise between the reduction of the latency time and the minimisation of the background/backsplash effects on the FB electronic components.

A fast FB system (Fig. 5.268) has been developed at Oxford University [273]-[274]. The principle of the 'Feedback On Nanosecond Timescale' (FONT) scheme is:

- Measure the deflected outgoing bunches of one beam with a BPM and kick the other beam to eliminate the relative vertical offset at the IP;
- The feedback loop assesses intra-train performance and an RF amplifier dynamically modulates the correction signal to the kicker. The system assumes that any fast time structure in the vertical

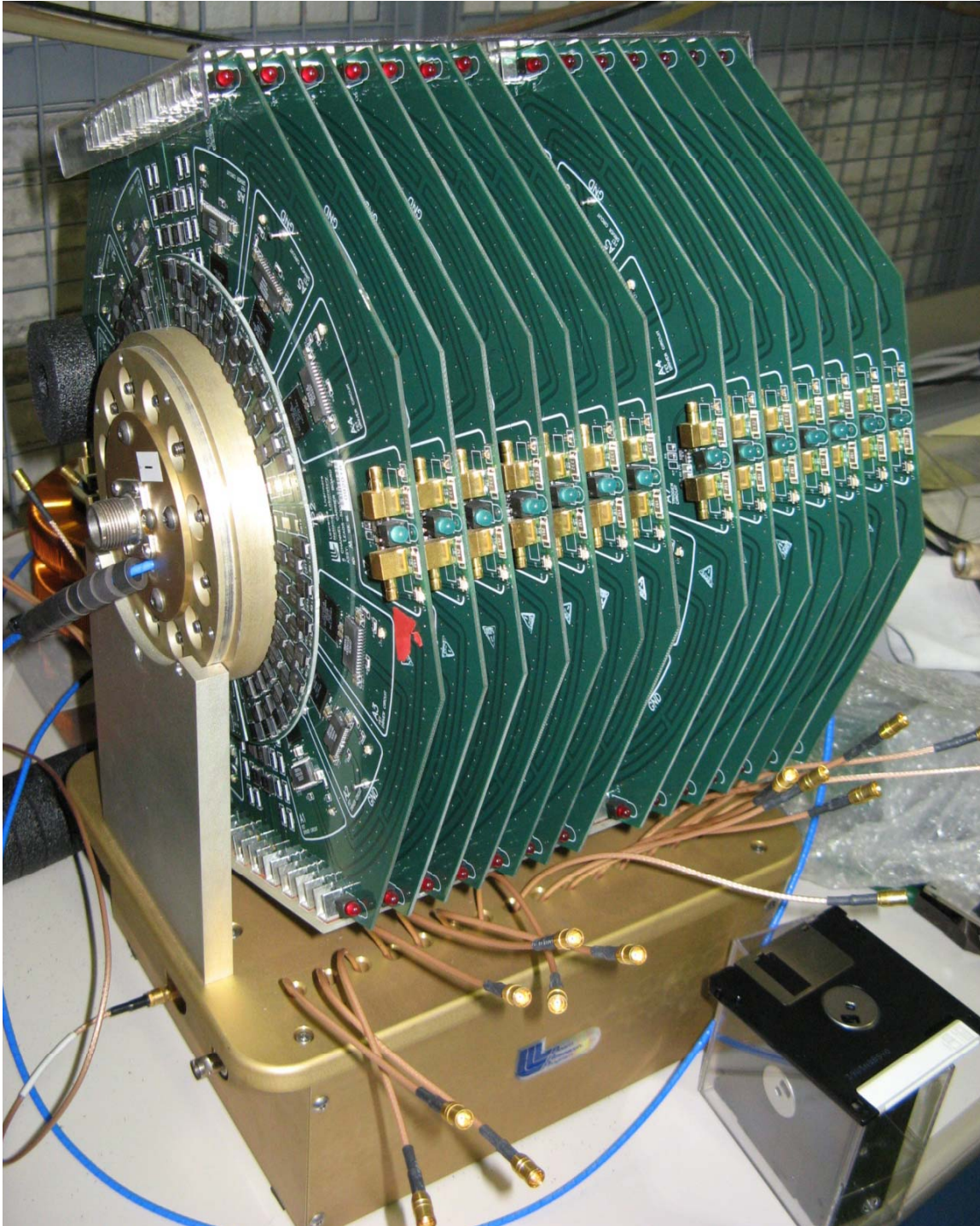


Fig. 5.265: Multi-cell, 18 kV, inductive adder supplied by LLNL to KEK/ATF

- position within each bunch train is within the bandwidth capability of the amplifier to correct;
- There is a need to minimize the IPFB latency so as to allow multiple passes through the FB loop within the 156 ns bunch train duration;
 - The distance of components from the IP has to be minimized to reduce latency: hence the BPM and kicker should be located within the detector; the current design has these components located about 4 m from the IP. Thus radiation-hard components are required for the kicker and amplifier.

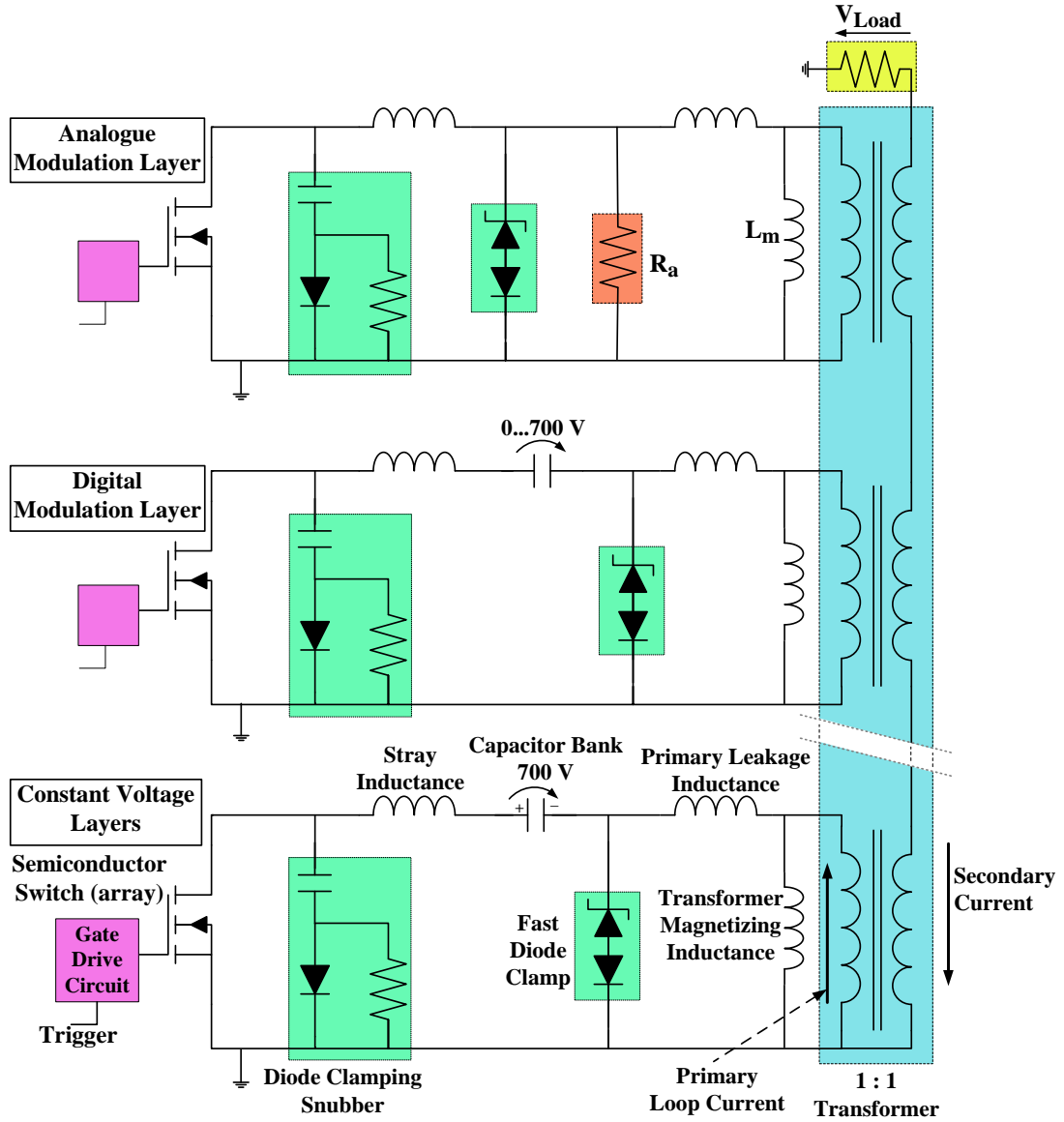


Fig. 5.266: Schematic of an inductive adder with constant voltage layers, a digital modulation layer and an analogue modulation layer

- Correction of a 1.5 TeV e^+/e^- beam requires that the stripline voltages of 1.5 kV per nrad of beam deflection.

A prototype system with bandwidth, latency and kick requirements suitable for CLIC is described in Ref. [273]. Further details of the system components and simulation of its performance are given in §5.15.3 and §3.8.4.2 respectively.

5.10.3 Drive Beam

The Drive Beam kicker systems comprise (Fig. 5.246):

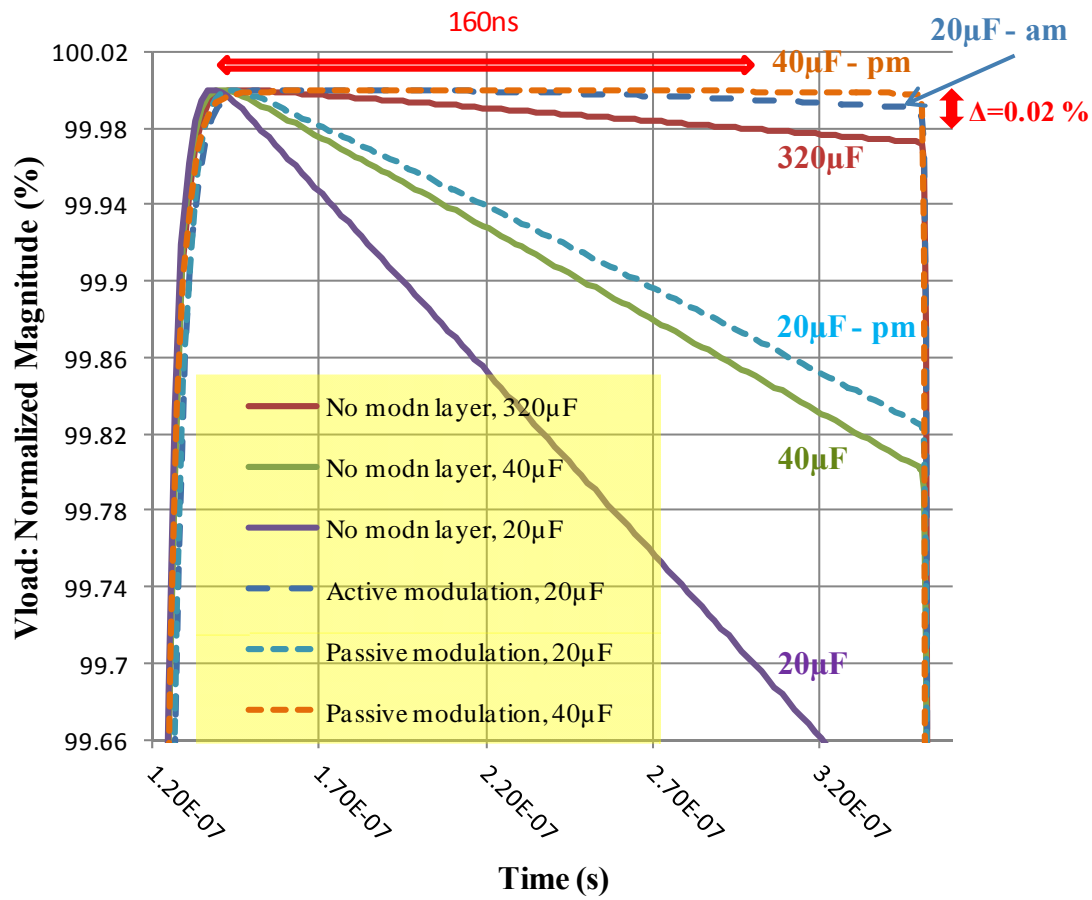


Fig. 5.267: Predictions for an inductive adder with various values of capacitance per layer, with and without an analogue modulating layer

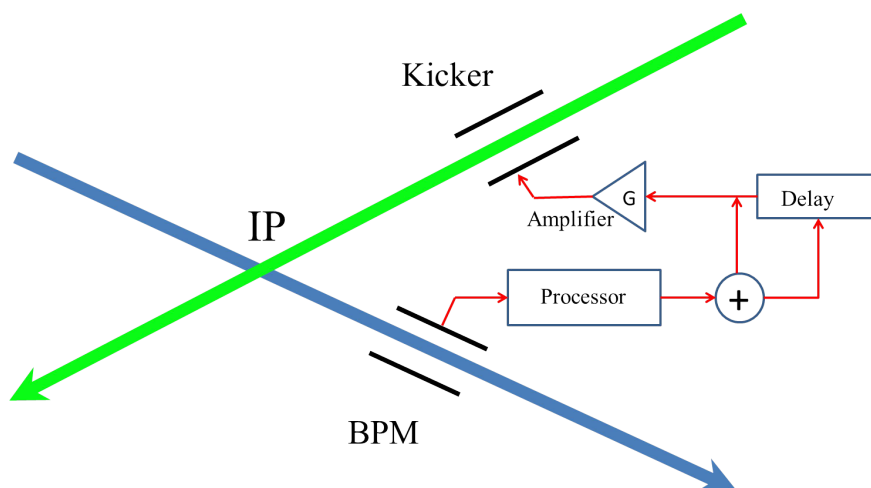


Fig. 5.268: Concept of the IP feedback system [273–275]

5.10 BEAM TRANSFER SYSTEMS

- Four kicker systems for extraction of the beams from both CR1 and CR2;
- 48 turn-around kickers for providing beam to the decelerators;
- 192 loop phase compensation kickers.

5.10.3.1 Combiner Ring and turnaround kickers

Table 5.79 shows the specifications for the existing CTF3 extraction kicker as well as for the CLIC CR extraction kickers and the turn-around kickers. The most challenging requirement for the CR extraction kickers is the burst-rate of up to 688 kHz for 140 μ s, each 20 ms: continuous operation of up to 3 MHz has been demonstrated with kickers, although this has been for either a capacitive load (i.e., not a 50 Ω load) [276–278] or for short duration pulses [279]. The turn-around kickers have similar specifications to the CR kickers except that the turn-around kickers do not have a burst-rate requirement and their rise/fall time requirements are relaxed.

Table 5.79: Drive Beam: CR extraction and turnaround kicker specifications

Quantity [units]	CTF3 CR extraction	CLIC CR1 extraction	CLIC CR2 extraction	Turnaround
Beam energy [MeV]	300	2380	2380	2380
Total kick deflection angle [mrad]	7	2.5	2.5	2.5
Stripline plate separation [mm]	40	20	20	20
Maximum stripline length [m]	1.7	3	3	3
Rise/fall time [μ s] (0.25% to 99.75%)	$\leq 0.07/\leq 0.07$	$\leq 0.15/\leq 0.15$	$\leq 0.15/\leq 0.15$	$\sim 5/20,000$
Pulse duration [ns]	200	up to 450	Up to 450	up to 450
Flat-top reproducibility [%]	± 0.1	± 0.1	± 0.1	± 0.1
Flat-top stability [%] (including droop)	± 0.25	± 0.25	± 0.25	± 0.25
Repetition rate				
Initial [Hz]	5	–	–	–
Nominal [Hz]	50	50	50	50
Burst mode [kHz]	none	688 for 140 μ s	172 for 140 μ s	none
Average [Hz]	–	4800	1200	–
Pulse voltage [kV] (across 50 Ω load)	12.6	10	10	10
Pulse current [A] (into 50 Ω load)	252	200	200	200

5.10.3.2 Loop phase compensation kicker system

Loop phase compensation kickers will be used to synchronize the phase between the Drive Beams and the Main Beam. A phase Feed-Forward (FF) system [280] will consist of a phase measurement, just in front of the Drive Beam Turn Around loop, to determine phase errors with respect to a reference phase and kickers for phase correction. The kicker system must be capable of changing the path length by up to $\pm 700 \mu$ m ($\pm 375 \mu$ rad) spread over four kickers. This yields 16 kickers and amplifiers per loop phase compensation system (Fig. 5.269).

Stripline kickers with an active length of 1 m and an aperture of 50 mm will likely be used to match the space restrictions; the aperture requirement is based on a 0.5% r.m.s. energy spread, and a 1 m dispersion, yielding a 5 mm r.m.s. spread to the beam width in the middle section of the chicane. (This 5 mm aperture only allows for $\sim \pm 4\sigma$ transmission and either the lattice design or the kicker aperture

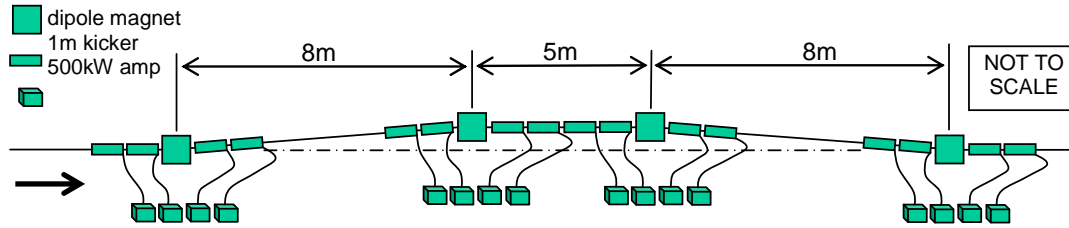


Fig. 5.269: Conceptual layout of kicker/amplifier system in the Drive Beam turnaround chicane

may need to be adjusted appropriately.) This system comprises 16 amplifiers per Drive Beam, i.e., 768 amplifiers in total, with a peak amplifier power of approx. 410 kW - allowing some margin (e.g., for a slightly higher energy spread than assumed) brings this to around 500 kW. (This requirement could be reduced if full kick at full bandwidth is found not to be essential). We assume the following parameters for the amplifier specification:

Speed: 10 ns: with bandwidth limitation shared equally between kicker and amplifier. The amplifier bandwidth is split equally between the amplifier modules and the combining system - each needs a 70 MHz bandwidth. Each kicker is connected to its amplifier with pair of coaxial cables.

Amplifier architecture: modular, MOSFET: this is a standard solution for fast, high-power amplifiers, but the output from many low power modules will have to be combined. It allows extremely high power densities and (relatively) low cost. Assuming each module provides $\sim 1\text{--}2$ kW, around 512 (or 256) modules would be required to provide ~ 500 kW per amplifier/kicker. An example of a module with the required power and speed is shown in Fig. 5.270

5.10.4 Conclusions

There are several very challenging kicker systems required for both the Drive Beam and Main Beam of CLIC. The PDR and DR kickers are particularly challenging due to their requirements of excellent field homogeneity, low beam coupling impedance and ultra-low ripple/droop. Striplines with suitable tapers can achieve the required beam transverse and longitudinal coupling impedances except for the low frequency longitudinal impedance. Studies of field homogeneity have commenced: a set of prototype striplines will be prototyped under the Spanish Science Industry Program. Striplines will likely be used for all the CLIC kicker systems.

An inductive adder is being investigated for the pulse generators for the PDRs and DRs. The inductive adder will be designed to permit pulse shaping and is expected to be inherently highly reliable and provide good machine protection.

The other challenging Main Beam kicker system is the IP feedback kicker, which must have very low latency and work in an environment with high background radiation. The technology developed has demonstrated a feedback latency of only 37 ns for a system deployed about 4 m upstream of the CLIC IP.

The combiner ring extraction kickers are also demanding because of the requirement for a high burst-rate. The turn-around kickers are similar to those required for the combiner ring extraction kickers except that the turn-around kickers do not have a burst-rate requirement. A large and challenging kicker and associated amplifier system is required to provide phase correction at the drive-beam turnarounds.

5.10 BEAM TRANSFER SYSTEMS

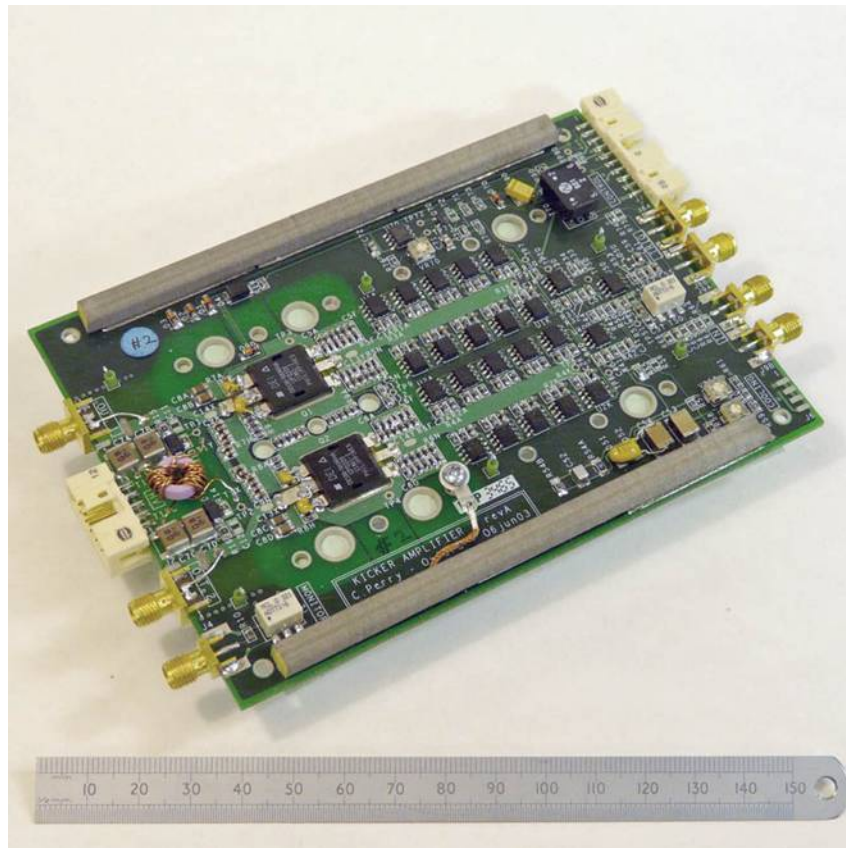


Fig. 5.270: Example of a possible MOSFET-based amplifier module

5.11 Beam intercepting devices

5.11.1 Introduction

In the preparation phase of this CDR a survey of beam intercepting devices has been conducted in order to identify those devices or systems, which need, at this early stage a demonstration of their feasibility. It should be clear that the objective of these feasibility studies was a full technical design. This section presents the result of the feasibility studies for the following three systems:

- Main Beam Dump
- Collimation System
- Photon Absorbers in the damping rings

All other systems in the CLIC accelerators are considered less critical and their feasibility is not considered for this report.

5.11.2 Main Beam dump

In order to better cope with the challenge of absorbing the 14 MW CLIC Main Beam, a water beam dump at the end of the CLIC post-collision line has been proposed. The present baseline design is inspired by the studies of D. Walz et al. (1967) for the SLAC 2.2 MW water dump [281], which has been operated for over 40 years. The same concept has been adopted as baseline for the ILC main dump conceptual design where a power of 18 MW must be absorbed [282].

The main design choices for the CLIC Main Beam dump, as far as materials, water flow rate and major dimensions are concerned, are driven by the peak energy density in water from the uncollided beam at 1.5 TeV. Also the total deposited power at the 14 MW level, as well as some hydraulic and thermo-mechanical considerations play a big role in the conceptual design.

The CLIC main water dump consists of a cylinder, filled with water, potentially pressurized at 10 bar, 10 m long, and with a diameter of 1.8 m, surrounded by a 15 mm thick titanium vessel of the same shape. A 1 mm thick circular titanium window was hollowed in the upstream dump face, centred on the dump axis, and with a diameter of 30 cm.

5.11.2.1 Energy deposition in the Main Beam dump

The energy/power deposition by the primary beam on the water dump and its enclosing vessel was calculated using the FLUKA Monte Carlo simulation code [283] [284]. Two different beam scenarios were considered: the 1.5 TeV uncollided electron beam with a transverse Gaussian beam profile centred on the dump axis, with $\sigma_{\text{hor}} = 1.79$ mm and $\sigma_{\text{ver}} = 3.15$ mm; no beam divergence was considered. For the collided beam the secondary particles produced in the electron–positron interactions at 3 TeV centre-of-mass energy were simulated with the GUINEA-PIG package [285] and were transported along the post-collision line up to the dump with the DIMAD tracking code [286]. Energy spectra of the collided electrons, the coherently scattered electrons and the bremsstrahlung photons arriving at the dump are shown in Fig. 5.271. The average number of particles reaching the dump is shown in Table 5.80.

Figure 5.272 shows (upper frame) the longitudinal distribution of the peak energy in the water dump: the fine (Cartesian) mesh used for the uncollided beam shows a maximum of $\sim 230 \text{ J.cm}^{-3}$ per bunch train, whereas the coarser cylindrical mesh used for the collided beam shows a maximum value smaller by a factor of about 25, clearly due to the lower particle density of the collided beam at the dump.

Table 5.81 shows the peak energy and total power on the water dump and on the titanium vessel/window for the uncollided and the collided beam scenarios. As expected, the case of uncollided beam is more severe than the one of collided beam, as far as peak energy deposition and total load are concerned.

5.11 BEAM INTERCEPTING DEVICES

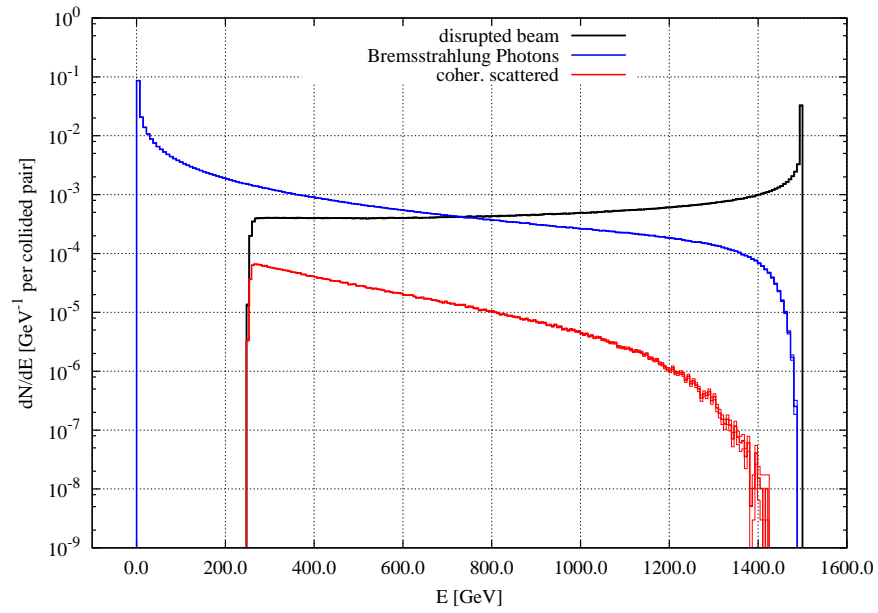


Fig. 5.271: Energy distribution of the particle types reaching the dump, per electron–positron collided pair. The statistical confidence range is plotted for the given binning (200 bins for each particle spectrum)

Table 5.80: Average number of particles reaching the dump, per electron–positron collided pair, for each particle type

Particle yield per collided pair	
Disrupted e^-	0.9199
Coherent e^-	0.0185
Bremsstrahlung γ	2.1894

Table 5.81: Peak energy and total power on the water dump and on the titanium vessel/window for the un-collided and the collided beam scenarios. Statistical uncertainties on the total values are below 0.1%.

	Max [J cm ⁻³ per bunch train]		Total power [W]	
	uncollided	collided	uncollided	collided
H ₂ O	230 ± 1	9.10 ± 0.01	13.8 M	13.4 M
Ti window	4.35 ± 0.36	83.8 ± 1.0 m	6.24	4.91
Ti vessel (side)	569 ± 18 μ	903 ± 29 μ	8.45 k	9.07 k
Ti vessel (upstr. face)	32.0 ± 13.2 μ	2.15 ± 0.13 m	9.07	45.7
Ti vessel (dwnstr. face)	245 ± 6 m	39.1 ± 6.2 m	1.12 k	944

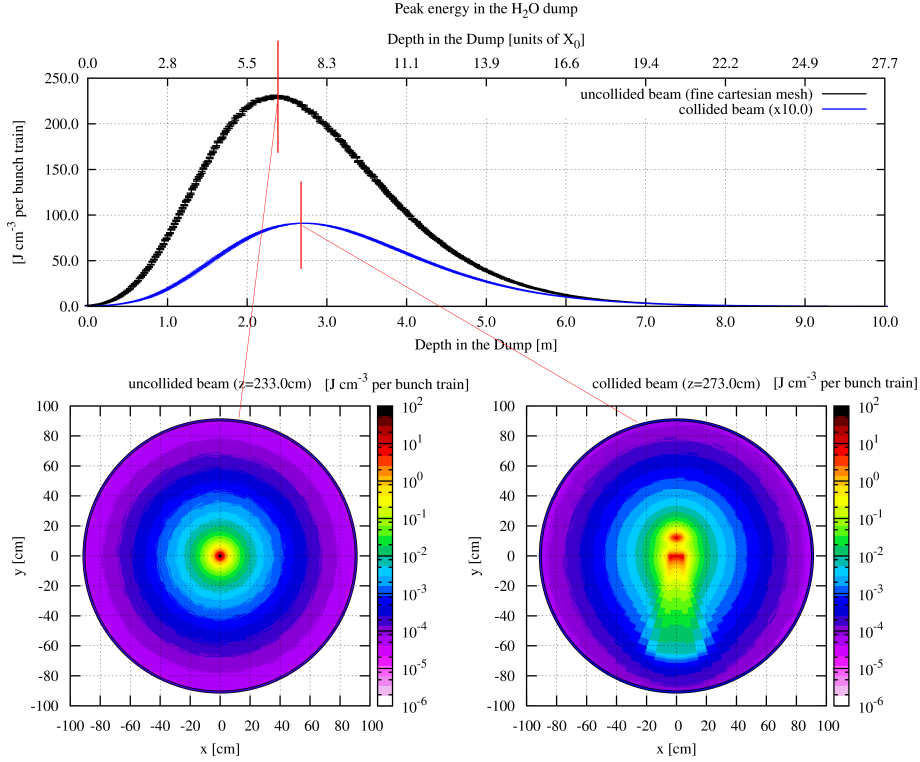


Fig. 5.272: Upper frame: longitudinal distribution of the peak energy in the water dump for the uncollided and the collided beam (the curve is zoomed by a factor of 10 for the sake of clarity); the statistical uncertainties are plotted as well. Lower frame: maps of energy deposition on the transverse plane at the location of the two maximum values; statistical uncertainties on plotted values are at most $\sim 16\%$.

The induced nuclide production in the dump was estimated; in case of uncollided beam, the short lived radio-nuclides are (with half-lives in brackets) ^{15}O (2 minutes), ^{13}N (10 minutes) and ^{11}C (20 minutes) are produced with rates of $1.19 \times 10^{15} \text{ s}^{-1}$, $5.51 \times 10^{13} \text{ s}^{-1}$ and $3.39 \times 10^{14} \text{ s}^{-1}$, respectively. The long-lived nuclides ^7Be (53.6 days) and ^3H (12.3 years) have a production rate of $1.14 \times 10^{14} \text{ s}^{-1}$ and $3.12 \times 10^{14} \text{ s}^{-1}$, respectively: these last values are roughly a factor of two higher than those expected at the TESLA Main Beam dump [287], designed for a lower energy of 250 GeV, but with an average current higher by a factor of five. Lower values by $\sim 3\%$ are expected for the collided beam.

5.11.2.2 Water bath of the Main Beam dump

Water is supposed to circulate in the dump in a closed loop, externally cooled: the primary water circulates across the beam axis in the tank by means of a vortex-flow system (or similar), and it unloads the removed heat on a separated, secondary fluid in a heat exchanger, external to the tank. A continuous water flow of at least 25–30 litre/s, at an average speed of 1.5 m/s, is required to remove the power deposited in the innermost part of the dump and maintain the peak temperature of water slightly below its boiling point. A safety factor of at least two should be applied to these values.

In case of no (or inefficient) heat removal, the sudden increase in the temperature of water in the region of the beam spot is of the order of $\Delta T \sim 55 \text{ K}$ per pulse [288]. Consequently, water reaches the boiling point after few bunch trains: on such a short timescale, the beam must be interlocked and a safety system must be activated to evacuate the vapour pressure generated in the tank. The initial pressurization at 10 bar moves the boiling point of water to 180°C : a larger margin of manoeuvre is thus allowed, but some drawbacks are introduced; the sudden energy deposition also generates a dynamic pressure

wave in the water bath. In the region of the beam spot, the instantaneous increase in the pressure can be estimated to $\Delta p \sim 560$ bar [288]. While propagating from the region of the beam spot to the tank walls, the amplitude of this pressure wave decays exponentially to a value of about 6–7 bar, if no free water surface is found along the path. Explicit numerical simulations in AUTODYN®[289] confirm this scenario, clearly showing the azimuthal propagation of the pressure wave in water. The initial amplitude is almost linearly proportional to the initial pressure of the bath. The pressure wave causes an overstress on the dump walls and window at each bunch train, to be added to the stresses due to the 10 bar hydrostatic pressure. Nonetheless, when the wave is reflected back from the tank walls, the pressure at the walls may increase by a factor of 3.4 [288].

The analysis shows the need for stiffeners, and possibly some type of shock absorbers in critical locations, in order to guarantee the dump structural integrity. The use of gas–water mixtures for a more effective damping of the pressure wave is not a priori excluded. However, details of the choice and the scheme of such a hydraulic circuit are beyond the aim of this preliminary conceptual study.

5.11.2.3 Main Beam dump window

For the present study a circular window has been considered, 30 cm in diameter, 1 mm thick, made of a titanium alloy (Ti-6Al-4V, i.e., ASTM G5, or UNS R56400), and directly cooled by the circulating water inside the dump. With such a simplified preliminary design, the window itself cannot withstand all alone the hydrostatic pressure of 10 bar. Therefore stiffeners, a double/triple parallel windows system and/or a window concept such as a hemispherical window must be considered. Details of this design are beyond the scope of this conceptual design report.

The thermal transient behaviour due to the direct impact of the beam was analysed. An estimated average power of 6.24 W is deposited on the window by the beam, which generates stresses inversely proportional to the beam spot size. ANSYS® [289] numerical simulations show that the deposited power instantaneously increases the temperature by about 0.44°C, in transitory, while in case of steady state during continuous beam dumping the increase in the temperature of the window stabilizes around 26.4°C after few seconds. An almost-perfect convective cooling of the window by means of the internal primary water (Fig. 5.273) has been considered. The temperature limit on the window is not driven by the melting point of the chosen material, but by the boiling point of the cooling water, and by the yield limit of the material at this temperature.

5.11.3 Collimation system

5.11.3.1 Overview

The CLIC collimation system is explained in detail in §3.5.3.3, it consists of pairs of spoilers and absorbers in order to remove the unwanted halo of the beam. The CLIC collimation system is driven by their cleaning capabilities and has to be able to survive a possible accident scenario; Fig. 3.42 in §3.5.3) shows the longitudinal position of the spoilers in the BDS. The collimation system was simulated by means of FLUKA [284] for a possible beam accident scenario, as well for normal cleaning operation.

- For the accident scenario it was assumed that the full train of 312 pulses with intensity of 3.72×10^9 electrons at 1.5 TeV (representing a total energy of 280 kJ), hits the front face of the energy spoiler(ESP) and, with lower probability, the horizontal or vertical spoilers (XSP/YSP). For the simulation, a shallow depth of the beam was used with an impact parameter of 2 mm assuming a beam spread of $780 \times 22 \mu\text{m}^2$ in horizontal \times vertical for the energy spoiler ESP and $8 \times 1 \mu\text{m}^2$ for the transverse spoiler XSP.
- During normal operation all spoilers should see only a fraction of beam (of the order of 10^{-6}). For the sake of simulation, since no beam distribution hitting the collimator was available, we assumed a beam spread similar to that the accident case.

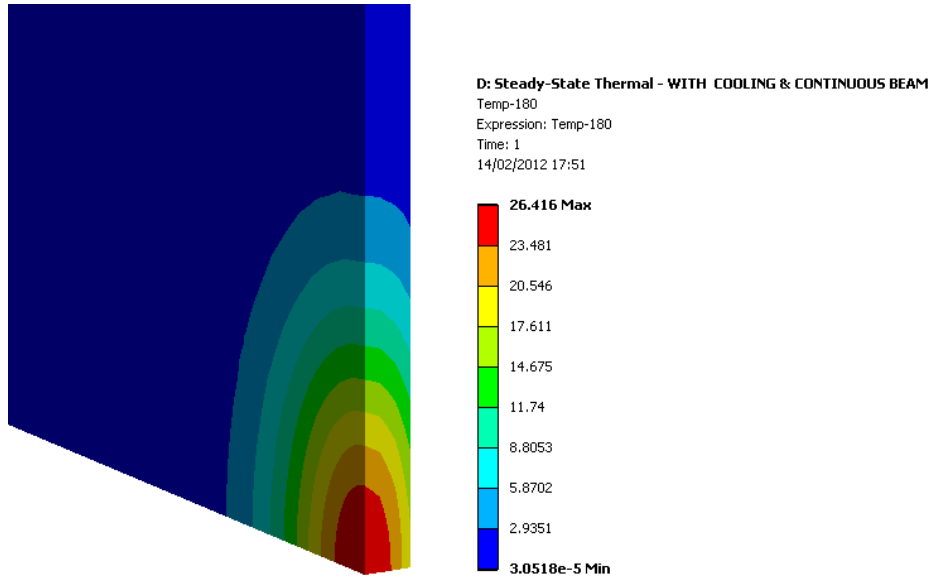


Fig. 5.273: Steady-state temperature distribution in the window due to continuous beam hitting and water-cooling on the internal side (back)

With the FLUKA calculations we attempted to address the following items both for instantaneous effects and for long term operation [290]:

- energy deposition calculation, with focus on the peak energy density to verify the survival of the object;
- long-term effects: DPA (Displacement Per Atom) and activation, assuming an operation of 200 days per year with a pulse train of $312 \times 3.72 \times 10^9$ electrons every 20 ms;
- secondary effects, charge particle production and especially muon production as seen by the experiments;
- dose on the downstream magnets, important for the survival of the coil insulation.

5.11.3.2 Simulation results

Energy deposition

Figure 5.274 shows the energy deposition map on a beryllium ESP spoiler for the accident scenario with 2 mm impact parameter. Although the total beam energy is equivalent to 280 kJ, the spoiler stops only a tiny fraction of the beam close to 6 J, about 36.5 MeV out of 1.5 eV for every primary electron hitting the spoiler. This energy deposition produces a peak energy density of the order of 600 J/cm^3 , which will generate, assuming adiabatic conditions, an instantaneous temperature rise of 450 K. The ESP spoiler will survive the accident scenario, since it is practically transparent to the beam, and only a tiny fraction of 2.4×10^{-5} will be stopped on the jaws. The remaining energy will continue downstream, therefore a dedicated study will be required to ensure the protection of the downstream elements that will be exposed on the accidental beam.

In the case of the XSP (Figs. 5.275 and 5.276) the considerably smaller beam spread as well as the heavier materials used (titanium for the jaws and copper for coating), results in a very high-energy deposition with a peak-energy density of 30 kJ/cm^3 as shown in Fig. 5.277. Obviously, the jaw material

5.11 BEAM INTERCEPTING DEVICES

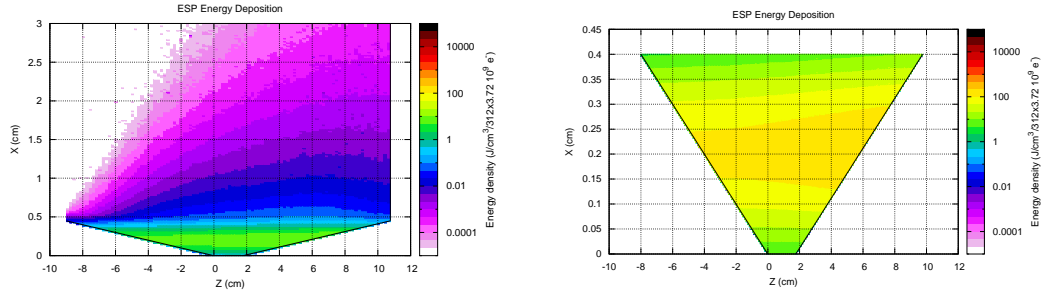


Fig. 5.274: Energy density map for ESP in the case of the accident scenario with 2 mm impact parameter. Left plot shows all collimator, right plot only the first 4mm where the maximum is located.

and the coating will not survive this huge energy density therefore a replacement of the spoiler after such a failure scenario would be required.

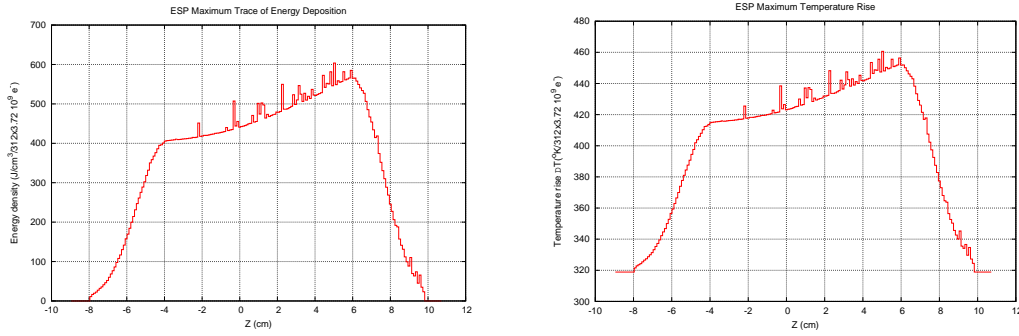


Fig. 5.275: Trace of the maximum energy density for the ESP accident scenario (left). Conversion to instantaneous temperature rise assuming adiabatic conditions on the beryllium jaw (right).

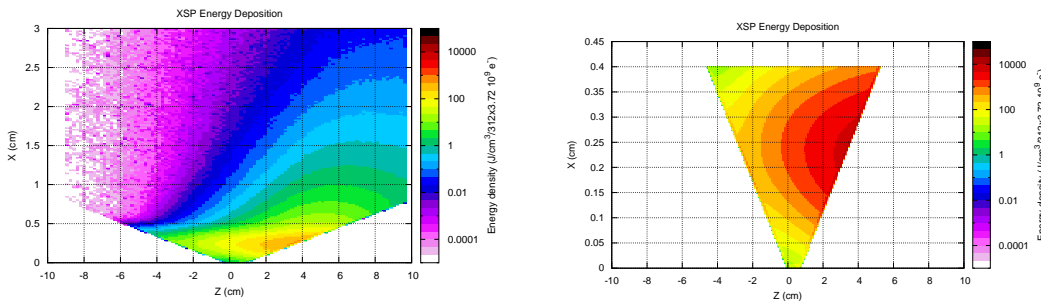


Fig. 5.276: Energy density map for XSP in the case of the accident scenario with 2 mm impact parameter. Left plot shows all of the collimator, right plot only the first 4 mm where the maximum is located.

Secondary particle production

The main mechanism of secondary particle production on the collimator is the indirect interaction of the electron beam with the spoiler through photo-nuclear interactions from the bremsstrahlung photons. Figure 5.278 shows the particle production fluencies out the ESP spoiler as well the associated muon

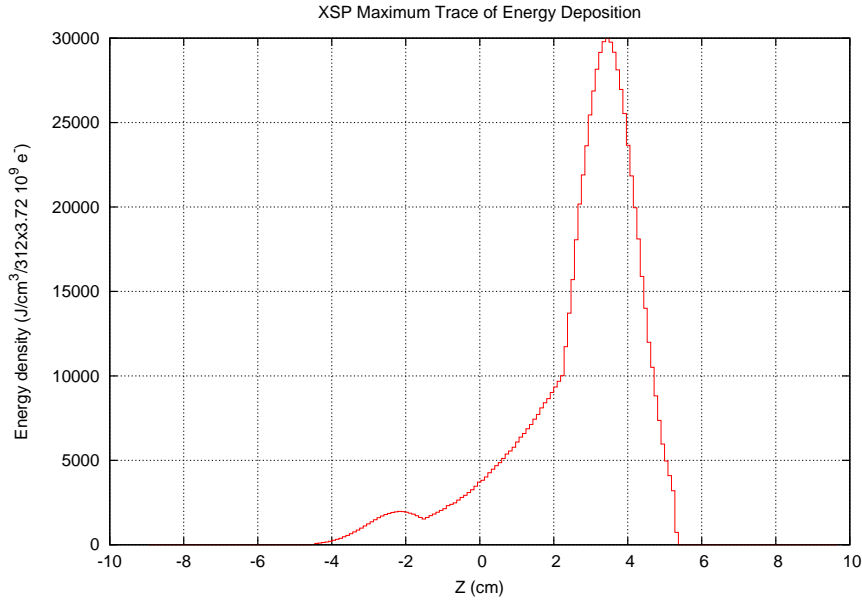


Fig. 5.277: Trace of the maximum energy density for the XSP accident scenario

production is shown in Fig. 5.279. Muons being minimum-ionizing particles are those which have a higher probability of reaching the experiments at the interaction point. Muons are produced by two mechanisms: by decays in-flight of charged mesons or directly in the spoiler through muon-pair production. The dominant mechanism is the in-flight decays of charged mesons with a relative ratio of 400:1. However, the correct evaluation of the muon spectrum reaching the experiments will strongly depend on the material present in the flight path of the muons. A possible remedy would be additional shielding after the spoiler in order to allow the charged mesons to interact before they decay.

Damage calculations (DPA)

According to the design parameters, the ESP should be exposed to fractions of 10^{-6} of the full beam, with a very small impact parameter. Assuming an operation of 200 days per year with a pulse train of $312 \times 3.72 \times 10^9$ electrons every 20 ms, and a damage threshold for beryllium of 31 eV, the maximum DPA obtained on the ESP spoiler is very low, of the order of 2.5×10^{-6} /year (Fig. 5.280).

Activation calculation

Figure 5.281 shows the activation simulation after one year of operation with the same assumptions as in the DPA calculation, for various cooling times. The core of the ESP spoiler during the operation will reach a maximum activity of 200 mSv/h during operation, which very quickly will drop to values below 0.1 mSv/h after one hour of cooling due to the very light and short-lived residual nuclei produced.

5.11.4 Photon Absorbers in the Damping Rings

A system of superconducting wigglers providing strong damping and extremely low emittance is an essential part of the CLIC damping ring. The CLIC damping ring operates with electron (or positron) beams with the energy of 2.86 GeV and average beam current up to 170 mA [291] [292]. Twenty-six wigglers will be installed in each of two straight sections of the CLIC damping ring. These wigglers produce radiation with a high total power up to 300 kW. The wigglers have a peak field of 2.5 T and will

5.11 BEAM INTERCEPTING DEVICES

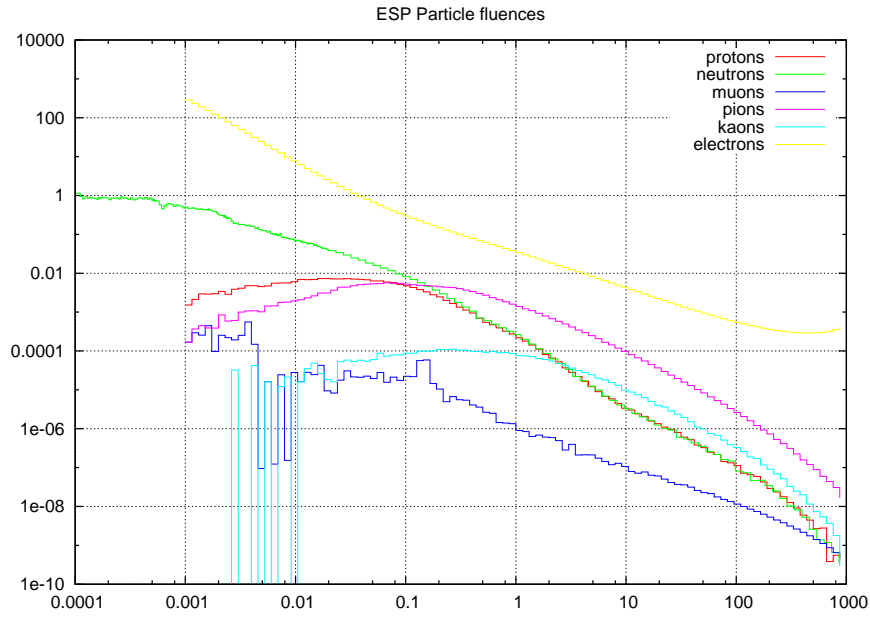


Fig. 5.278: Secondary particle fluences escaping the ESP spoiler

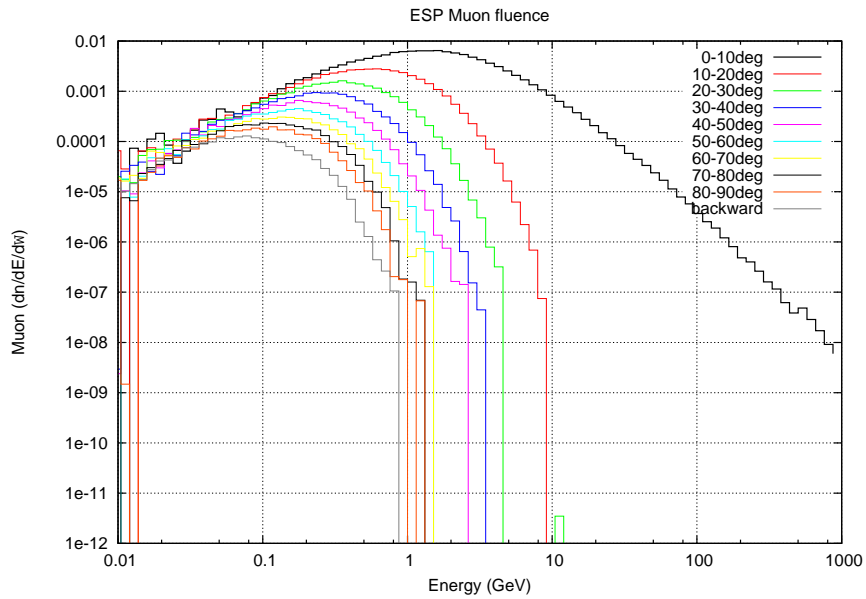


Fig. 5.279: Double differential muon fluence as a function of the energy and polar angle arriving to the interaction points

generate synchrotron radiation with a critical energy of 9.62 keV with a spectrum given in Fig. 5.282 and emitted in a concentrated light cone with a small opening angle of ~ 3.2 mrad. As shown on the plot the maximum energy of these photons is of the order of 50 keV, resulting in an attenuation length of about 19 mm on copper. The total power to be absorbed per wiggler is of the order of 8 kW.

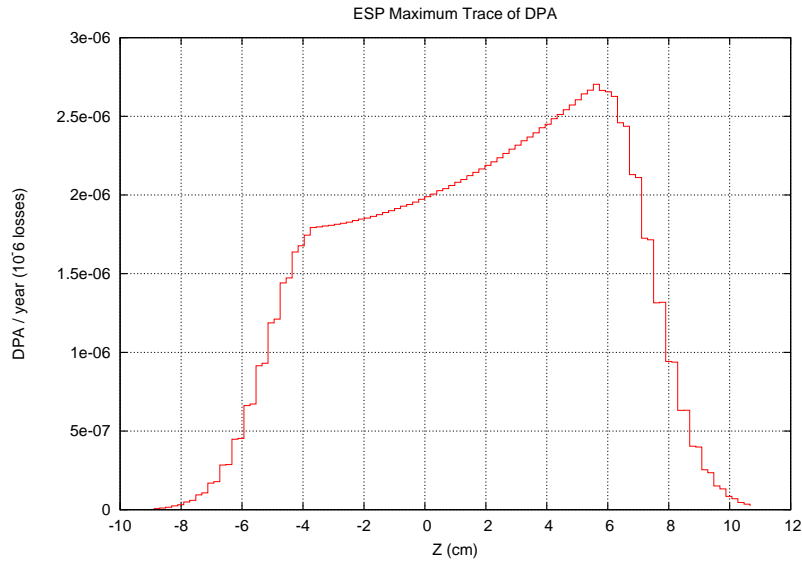


Fig. 5.280: Maximum trace of Displacement Per Atoms (DPA) for one year irradiation

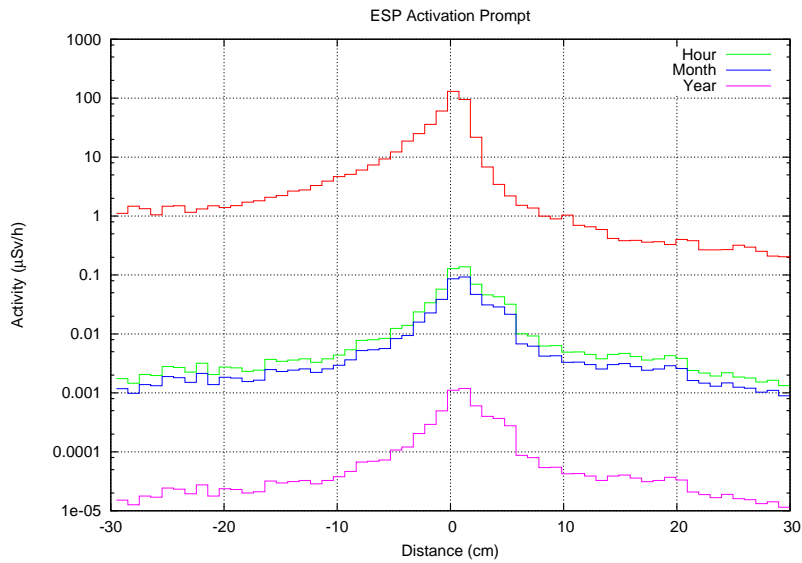


Fig. 5.281: Activity of the ESP spoiler after one year of operation. The red curve shows the prompt activity in (mSv/h) which quickly drops to low values after 1 hour of cooling. Cooling times of one month and one year are also shown.

The vertical absorber is a copper block with dimensions of $6 \times 90 \times 300 \text{ mm}^3$ (see Fig. 5.283), while the horizontal absorber is shown in Fig. 5.284. Ray tracing simulations [291] were performed to estimate the energy density seen by the wiggler absorbers depicted a total power load of 8 kW with 95 W/mm^2 maximum power density. Owing to the high surface density of deposited power a water cooling system is foreseen on the upper and lower plates of the absorber.

The line of absorbers in the focusing and defocusing quadrupoles of the wiggler section allows

5.11 BEAM INTERCEPTING DEVICES

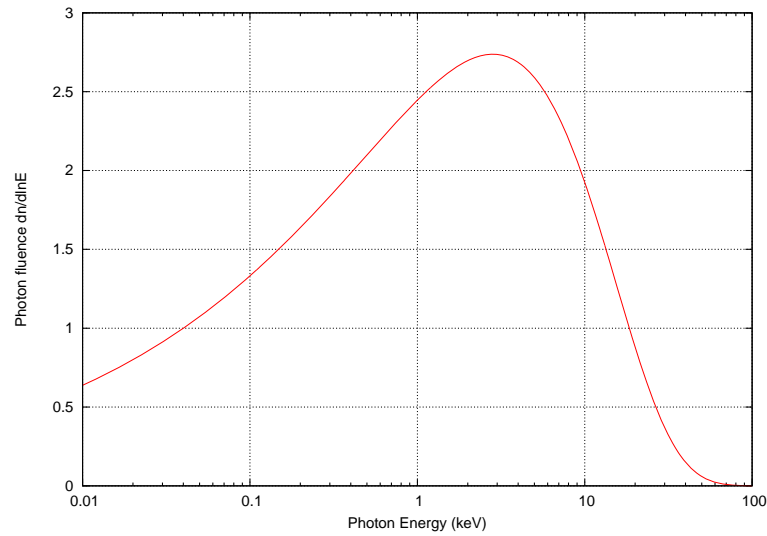


Fig. 5.282: Synchrotron radiation photon spectrum of 2.424 GeV electrons with a 2.5 T bending magnet

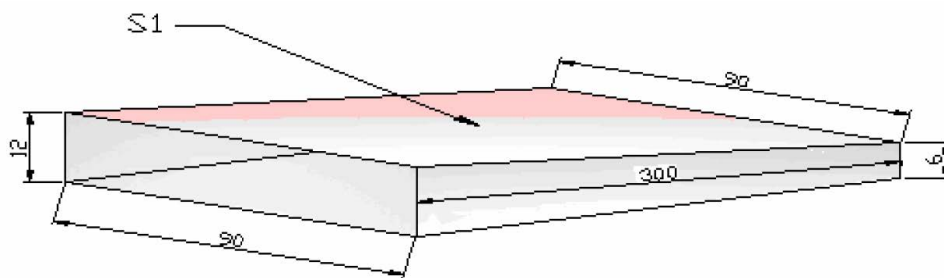


Fig. 5.283: 3D sketch of the vertical absorber

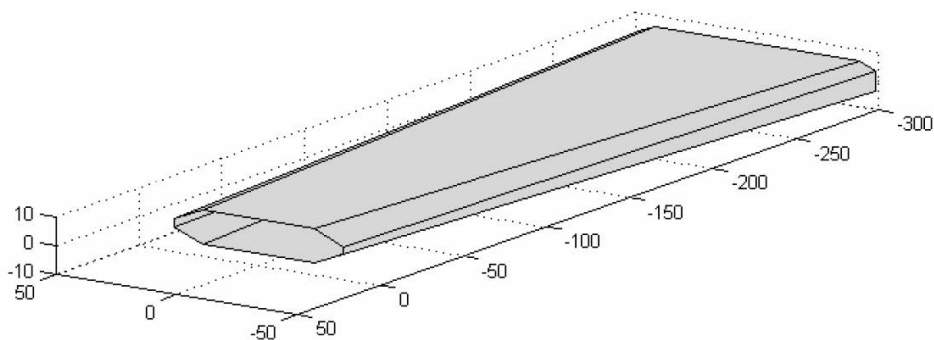


Fig. 5.284: 3D sketch of the horizontal absorber

intercepting around 210 kW of radiation power. The remaining 90 kW (for the ideal on-axis trajectory) should be stopped by a lump copper water-cooled absorber downstream the first bending magnet after the wiggler section. The optimization shows that the most advantageous shape of the final absorber is trapezoidal: in this case we can reduce the power density and improve heat transfer from the illuminated

strip on the absorber body to the cooling tubes. The total length of the final absorber is about 5 m.

5.11.5 Conclusion

Although many detailed design questions are left open at the present stage, it seems that for steady-state operation of the machine and for some setup scenarios a technical solution for beam intercepting devices can be found. Some other (unlikely) failure scenarios lead to a complete destruction of the beam spoilers. During the technical design phase more detailed studies for the machine protection will lead to a more quantitative assessment of the likelihood of such failure scenarios and to possible mitigation strategies.

5.12 Machine Detector Interface

5.12.1 Overview

The BDS at CLIC has a single interaction point where two detectors share the beam-time in a so-called ‘push–pull’ mode. The two experiments alternate between their data-taking and garage positions, moving by ~ 30 m on independent platforms equipped with air pads or rollers and alignment features.

In and around the detector region are several accelerator components necessary for proper machine operation and for luminosity optimization. One of the critical elements is the final focusing quadrupole QD0, which focuses the beam to the small vertical size of 1 nm r.m.s. The distance L^* of the downstream end of this quadrupole to the interaction point must be minimized to allow as strong focusing as possible. In the present layout L^* is 3.5 m, implying that the quadrupole is mounted inside the detector. The required strong gradient is achieved with a hybrid magnet composed of permendur, reinforced with permanent magnets, and with additional and tunable field strength provided by coils, as described in §3.6.3.1 and §5.12.2.1.

Any movement of the quadrupoles with respect to the beam would affect the transverse position of the beam at the interaction point by a comparable amount. To ensure that the luminosity loss due to this effect is kept below the two per cent level, the position must be stabilized to 0.15 nm r.m.s. in the vertical plane for frequencies above 4 Hz. The stabilization of the QD0 is hence one of the main challenges in CLIC.

Multiple approaches ensure this stabilization level at the IP, namely:

- incorporating a robust active pre-alignment system crossing the detector,
- adopting a permanent magnet arrangement for the QD0 quadrupoles to prevent vibrations due to cooling,
- supporting the QD0s from stable mechanical supports mounted off pre-isolator masses so as to be completely decoupled from technical noise produced by the detector, and
- providing an active stabilization system for the QD0s.

Laboratory tests have demonstrated that the 0.15 nm stability level (at 4 Hz and above) can be reached if the stability of the mechanical QD0 support is better than ~ 5 nm. In addition, recent measurements in the CMS experimental area have shown that this value can be reached in a well-designed underground experimental area. Although the results obtained to date are very encouraging, work must continue to integrate all of the needed elements within the limited space available. It is also important to demonstrate their performance in the stray field of the main experimental solenoid, and in the CLIC radiation environment.

The QD0 quadrupole is mounted inside a rigid support tube, supported by a massive pre-isolator, described in §5.12.2.3, which also holds the horizontally focusing quadrupole QF1 and some higher order chromatic correction magnets. Inside the support tube the magnet position is mechanically stabilized by a continuously active system based on capacitive sensors and piezo-actuators, described in §5.12.2.2. Mechanical structures are, wherever possible, optimized to have their first resonances around (multiples of) the 50 Hz machine frequency.

An active pre-alignment system ensures that the average position is corrected to within 10 mm r.m.s. with respect to the BDS elements and with respect to the other QD0 magnet. Special channels for laser light have been reserved through the detector to allow monitoring of the relative QD0 positions, as described in §5.12.3.

Complementing the mechanical stabilization system, the intra-pulse feedback system (§5.12.4.1) measures the position of the outgoing beam and applies a calculated kick to the other incoming beam to optimize the luminosity. Although bunch-to-bunch correction is not possible, the latency time of this feedback loop is small enough to allow several iterations within one 156 ns bunch train. As described in

§3.6.6 this may lead to a significant improvement of the mean luminosity. Further feedback and feed-forward systems are implemented in the main linacs and beam delivery systems to ensure beam stability for frequencies below 4 Hz.

The vacuum pressure requirements are not excessively challenging in the machine interface region, but the vacuum system layout is challenging due to requirements for the operation of the two detectors in push-pull mode. Access must be provided to the vacuum valves that separate the sections and the time for pumping after changes of detector must be minimized. The vacuum strategy and layout is described in §5.12.4.2 and the accessibility issues are an important part of the overall integration as described in §5.12.4.3.

Finally the detectors must be located in suitable caverns with infrastructure and services. In §5.12.4.4 we describe the requirements for the civil engineering and services and the suggested approach to cover these needs. Figure 5.285 shows a general view of the CLIC interaction region.

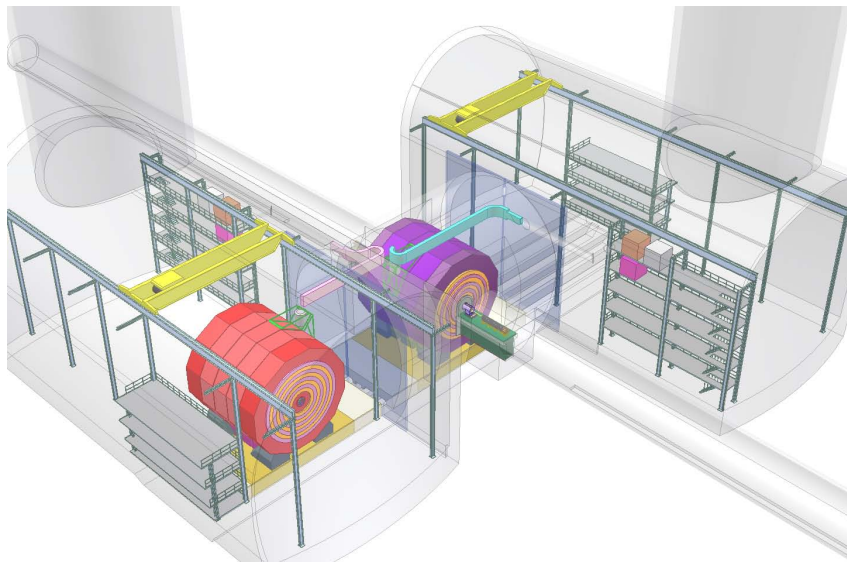


Fig. 5.285: General view of the interaction region at CLIC.

5.12.2 Technical description

5.12.2.1 QD0 magnet assembly

Magnet design

Owing to the specific layout of the CLIC Machine Detector Interface (MDI) (see §3.6.3.1) the space for the QD0 magnet is quite limited in the horizontal plane but not in the vertical one. For this configuration it seems advantageous to adopt a classical ‘8’ (or ‘two leaves’) quadrupole design. Figure 5.286 shows the conceptual design of the proposed cross-section for the QD0 magnet. The ‘8’ design is easily recognizable; the electro-magnetic (EM) coils are placed on the top and bottom return steel yokes.

The maximum strength achievable in an iron-dominated quadrupole magnet is limited by the saturation of the poles and by the pole shape-factor that causes, above a certain gradient and saturation, a ‘short circuiting’ of the magnetic flux lines across the poles outside the magnet aperture.

To limit this effect and to increase the maximum achievable gradient, four blocks of permanent magnet (PM) with adequate magnetization directions are added to the structure between each pair of poles. Each one of the four PM blocks is composed of two parts with different magnetization directions. It should be noted that the PM blocks do not actively contribute to the quadrupolar magnetic field in the magnet bore, but they act mainly to optimize the magnetization inside the iron poles. They compensate

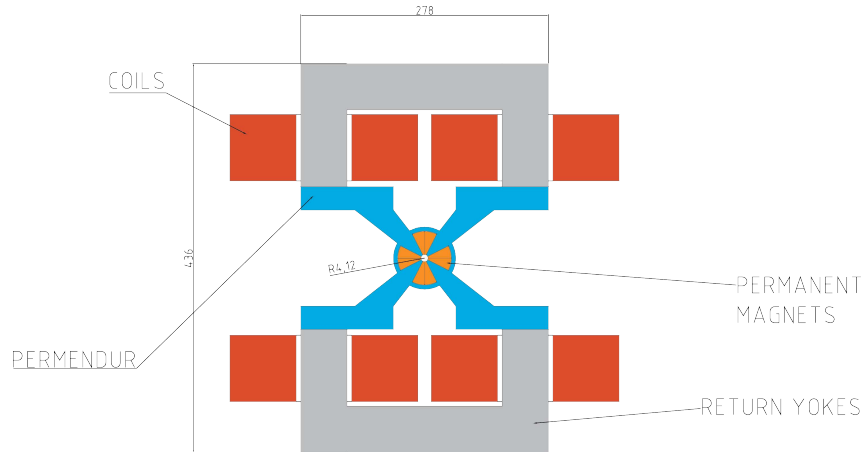


Fig. 5.286: Conceptual design of the QD0 cross-section.

spurious magnetic components that are not useful for building up the magnetic gradient in the aperture but that would add only to the saturation of the poles and the ‘short circuits’ between them [293].

The ring-like structure that links the four poles provides support and rigidity; high magnetic forces are generated in the structure when it is powered, while magnetic field quality is strongly dependent on the precise geometry of the poles. The presence of the ring, built-in during the pole machining (by a wire-erosion process), guarantees the mechanical stability and hence the correct geometry. A drawback of the ring is the short-circuiting of some magnetic flux that causes a reduction of gradient inside the magnet aperture by approximately 20 T/m.

In order to achieve higher gradient values, the central part of the structure is made of ‘permendur’, a Fe-Co alloy characterized by a high magnetic saturation level compared with classical low-carbon magnetic steel. Depending on the type of permanent magnet material chosen (among the SmCo or NdFeB families) the maximum gradients expected (with coils powered at 5000 A turns) are approximately:

- 530 T/m (with Sm₂Co₁₇),
- 590 T/m (with Nd₂Fe₁₄B).

We recall that the nominal gradient is 575 T/m as given in Table 3.27 (see §3.6.3.1).

The EM coils work at very low current density ($\sim 1.0 \text{ A/mm}^2$). This avoids the use of an active cooling system for the coil pancakes, which reduces vibrations of the structure, relevant for the QD0 stabilization (see §5.12.2.2).

Varying the current from zero to 5000 A turns corresponds to varying the gradient between $\sim 50 \text{ T/m}$ to $\sim 590 \text{ T/m}$ and permits a wide tunability of the magnet. The use of four independent power supplies should allow for compensation of potentially small differences between the pole performances (due to PM block tolerances, reproducibility, and to mechanical errors or deformations).

Figures 5.287 and 5.288 show the magnetic induction of the structure with coils powered at zero and 5000 A turns respectively. The major difference is in the magnetization (in strength and direction) of the magnet poles.

Short prototype

A prototype model with full-scale cross-section, working at nominal conditions, but with much shorter length (full QD0 length: 2730 mm), is under construction [294]. A view of the prototype is given in Fig. 5.289.

The aims of this prototype are:

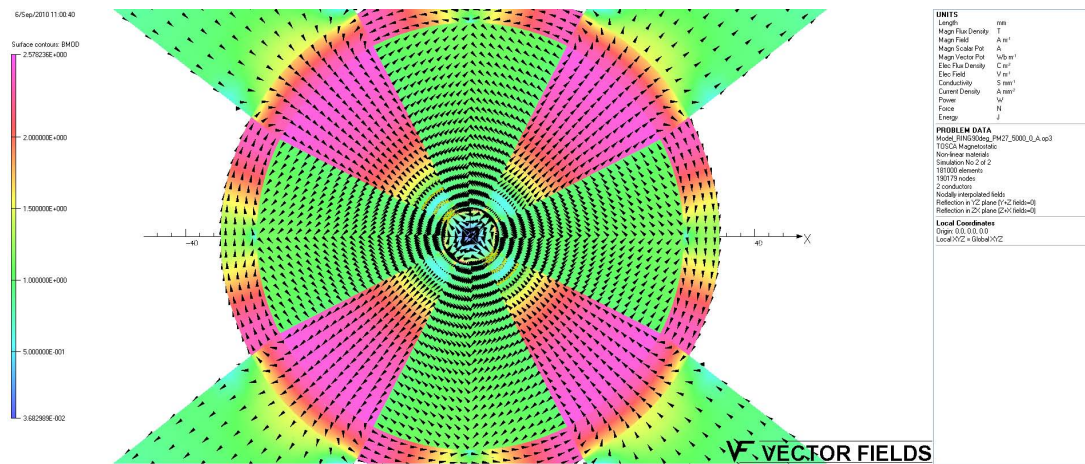


Fig. 5.287: Magnetic behaviour of the magnet with 0 A turns in the coils (the gradient in the magnet bore is in this case ~ 50 T/m)

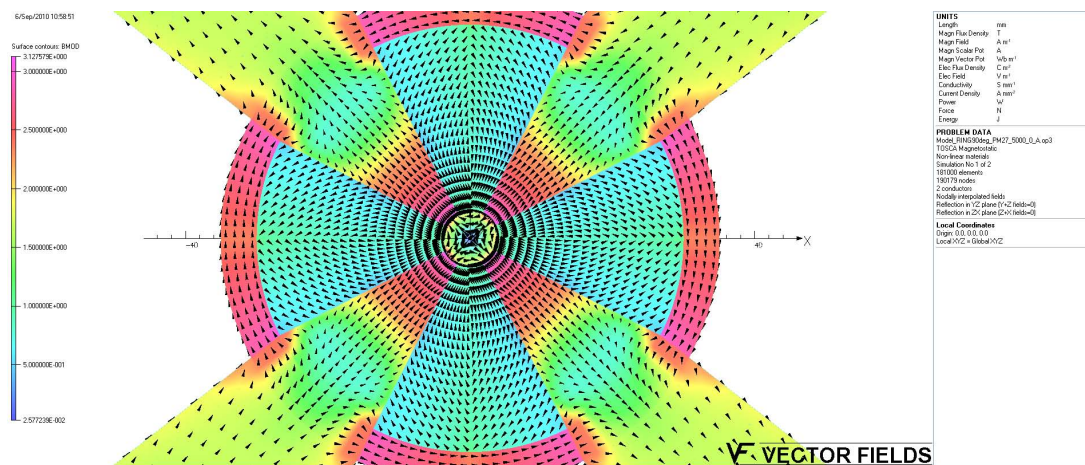


Fig. 5.288: Magnetic behaviour of the magnet with 5000 A turns in the coils (Gradient in the magnet bore is ~ 530 T/m)

1. to validate the concept of the 'hybrid magnet',
2. to check the behaviour of PM blocks of different materials working under an external high magnetic field generated by the EM coils (note that the PM blocks are easily dismountable),
3. to check the mechanical soundness of the assembly, a critical aspect for the required field quality,
4. to provide a real case study for the new magnetic measurement systems (by rotating coils compatible with 7–8 mm diameter magnet aperture) under development at CERN.

Towards a final magnet design

The two major differences between the design of the short prototype and the one for the longer version for the real MDI are (see Figs. 5.290 and 5.291):

1. For a longer structure installed in a very confined environment, like the MDI, temperature control must be provided even if the coil works at a very low current density (~ 1.0 A/mm²). For this reason, and also in order to give more stiffness to the coil assemblies, longitudinal bars (of non-magnetic metal) are included in the coil pancakes to stabilize the temperature of the coils.

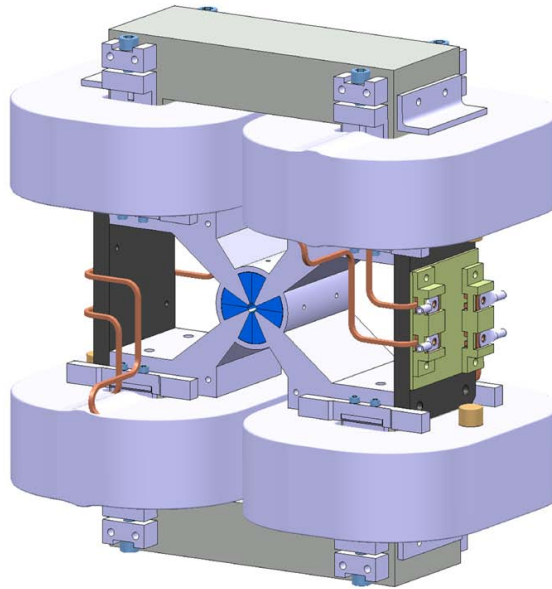


Fig. 5.289: Hybrid QD0 short prototype

2. In the longer structure, the coils are supported independently of the magnet core. This simplifies the active stabilization since the coils are the heaviest part of the magnet assembly and the cooling water flow does not directly affect the magnet core, which requires active stabilization.

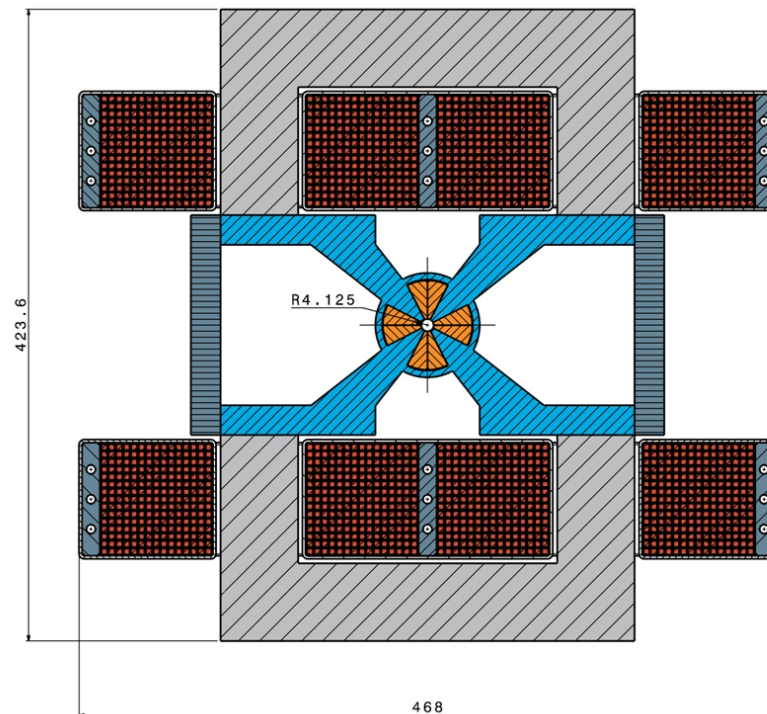


Fig. 5.290: QD0 with thermalization coils

The fundamental mechanical characteristics of the structure (fundamental resonance frequencies, intrinsic structure stiffness, etc.) must be characterized for the design of proper stabilization. As an

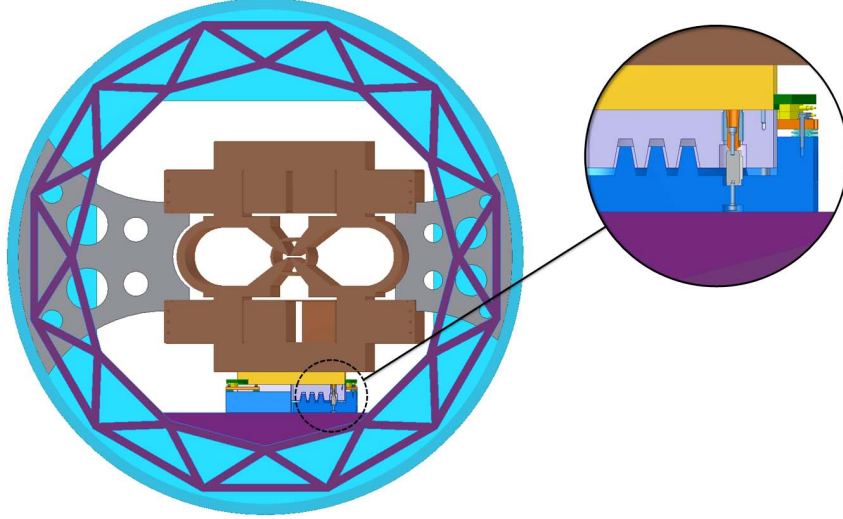


Fig. 5.291: Magnet/coils independent support. The integration of the stabilization foot in the support is shown in more detail on the right-hand side.

example, Fig. 5.292 shows the first resonance frequency and oscillation mode for a structure in which the return yokes are composed of single ‘Steel 1010’ pieces but the core part (made in permendur) is composed of 27 elements of 100 mm individual length (this is a possible solution if these components are manufactured by wire-erosion).

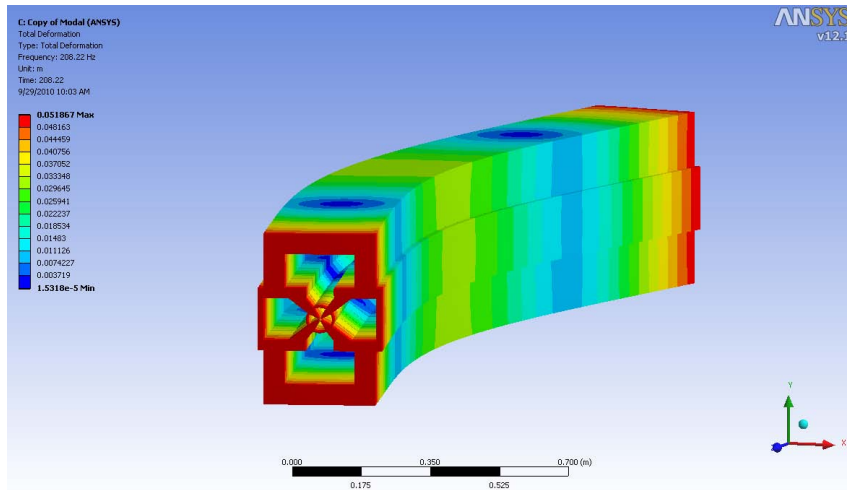


Fig. 5.292: First resonance frequency and oscillation mode for a full-length QD0 core assembly

5.12.2.2 QD0 stabilization

The very strong gradient of the QD0 quadrupoles, necessary to produce the extremely small vertical beam spot size of 1 nm r.m.s., has the side effect that any offset between the axis of the quadrupole and the beam trajectory leads to a displacement of the beam at the interaction point by a comparable amount. To avoid luminosity loss, the vertical position of the quadrupole must therefore be stabilized to 0.15 nm r.m.s. for frequencies of 4 Hz and above. This is achieved by an active stabilization system, complemented by a passive pre-isolator (see §5.12.2.3) and beam-based feedbacks (see §5.12.4.1). The stabilization of the QD0 quadrupoles is indeed one of the main challenges in CLIC.

The active stabilization system must measure vibrations and counteract them by a compensating motion on QD0. To work in the harsh and crowded environment of the Interaction Region (IR), the sensors and actuators must be compact, light compared to the QD0 weight, resistant to magnetic fields (QD0 being inside the detector solenoid), and resistant to radiation. They must operate at the sub-nanometre scale in the frequency range from 0.1 Hz to 100 Hz. A large number of sensors have been studied [295] and several geophones, piezoelectric and chemical sensors have been identified as possible candidates. Piezoelectric actuators are suitable for this application. Stabilization to the sub-nanometre level has been proven to be feasible using commercial equipment on a simplified QD0 prototype. A stabilization of 0.13 nm r.m.s. at 4 Hz has been achieved in the laboratory at the end of a cantilevered prototype where the initial displacement is maximal, see Fig. 5.293 [296] [297].

The QD0 is isolated from ground motion with a large commercial table combining passive and active isolation, with the addition of an extra feedback on QD0 to compensate for the structural resonances. A study is now underway to replace the commercial stabilization system by a more compact device. The current test set-up has the following dimensions: $24 \times 24 \times 5 \text{ cm}^3$. The lower part is dedicated to a rigid stabilization table equipped with four actuators that allow movements in three degrees-of-freedom with integrated relative capacitive gauges and elastomer for movement guidance [298]. Figure 5.294 shows a preliminary design of such a device. The passive part of the stabilization scheme is still under investigation, but the stabilized support is mounted on a passive pre-isolation system, described in §5.12.3.

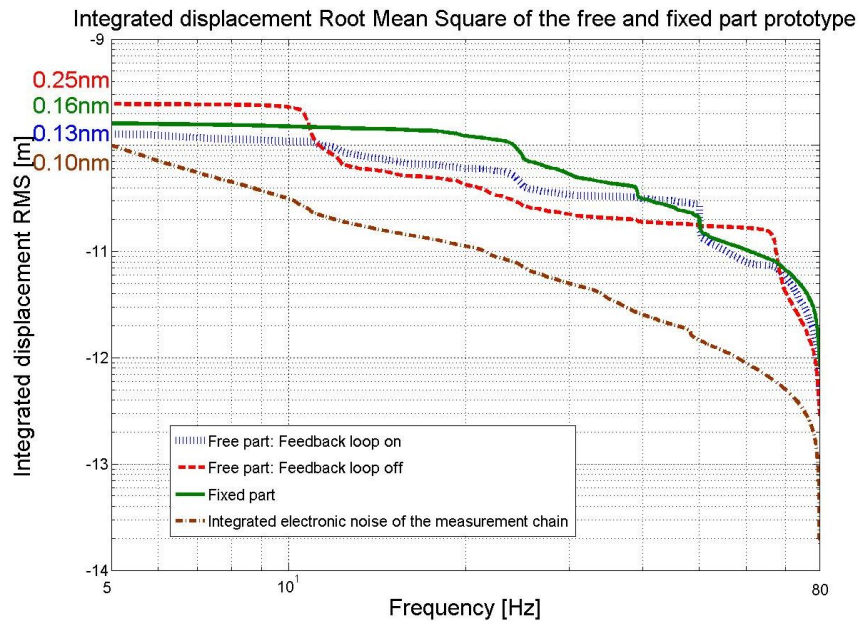


Fig. 5.293: Stabilization of a QD0 prototype to 0.13 nm for frequencies above 4 Hz

Since this compact device only stabilizes in a relative manner, an absolute sensor like the ones used for the QD0 prototype study has to be added to the magnet support.

The best longitudinal locations for the isolation device under QD0 have not yet been determined. They need to take into account the positions where maximal compensation is needed, the restricted space available, and cost. For lack of space, the support may need to be cantilevered. A possible integration below the QD0 magnet, with stabilization systems at the Gauss points, is shown in Fig. 5.291.

In order to limit the number of stabilization components, the QD0 design must minimize vibration induced by technical noise; thus the luminosity calorimeters and QD0 coils are supported independently. The whole support is mounted on a pre-isolator that is described in the next section.

The QD0 stabilization is complemented by a combination of active and passive systems to minimize beam jitter. The beam position is also corrected by an intra-pulse feedback system to maximize

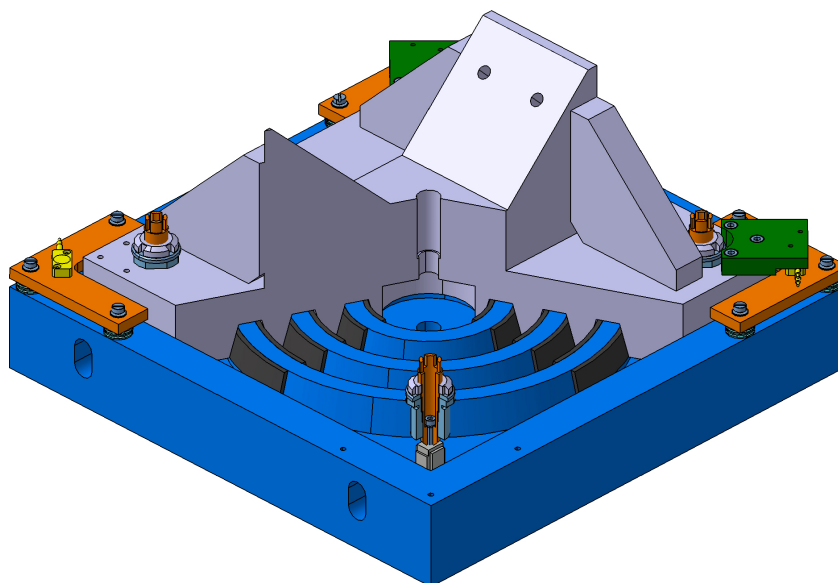


Fig. 5.294: Preliminary design of a stabilization device

performance as described in §5.12.4.1. In previous studies, the overall performance was clearly limited by the linear controller characteristics. An adaptive controller has been designed and combined with stabilization devices that have passed feasibility tests. Recent simulations show that a performance of 0.02 nm r.m.s. at 0.1 Hz should be sufficient. However, to achieve this performance, the integrated sensor noise must be below 0.13 pm r.m.s. at the IP at 0.1 Hz, i.e., 0.13 mm at the BPM. The final combination of systems must comply with the model shown in Fig. 5.295. This curve specifies what is needed to obtain the desired stabilization performance [298]. The calculated transfer function for the final quadrupoles has been included in the integrated beam dynamics simulations, see §3.8. The simulations show good performance even for relatively noisy sites.

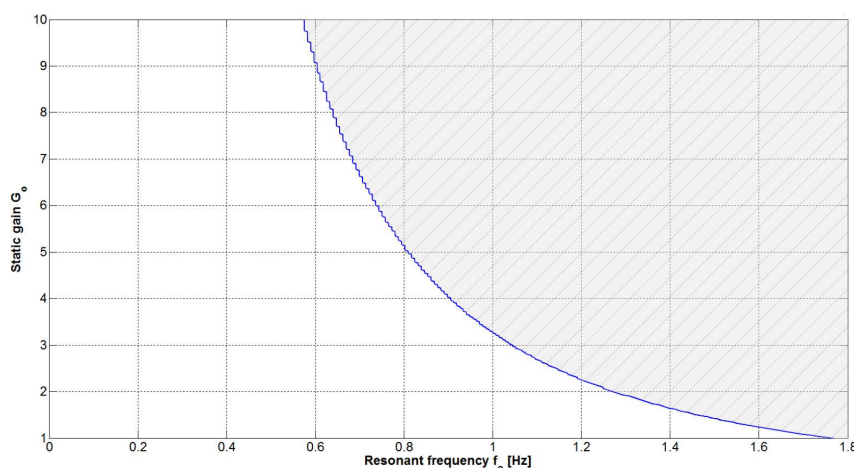


Fig. 5.295: Pattern for an active/passive isolation system for CLIC if the stabilization criterion is to be met. The isolation system studied is a second order low-pass filter characterized by three parameters: the static gain, the resonant frequency, and the damping factor. The pattern shown is taken in a domain where it is independent of the damping factor.

5.12.2.3 QD0 and QF1 pre-isolation

The ground micro-seismic motion at frequencies above 4 Hz, either natural or generated by machinery, can be effectively reduced by a passive mechanical low-pass filter [299]. A simple one-dimensional spring-mass system, with its first resonant frequency at $f_0 = (1/2\pi) \times \sqrt{K/M}$ Hz, where K is the spring constant and M the mass, shows a transfer function similar to Fig. 5.296.

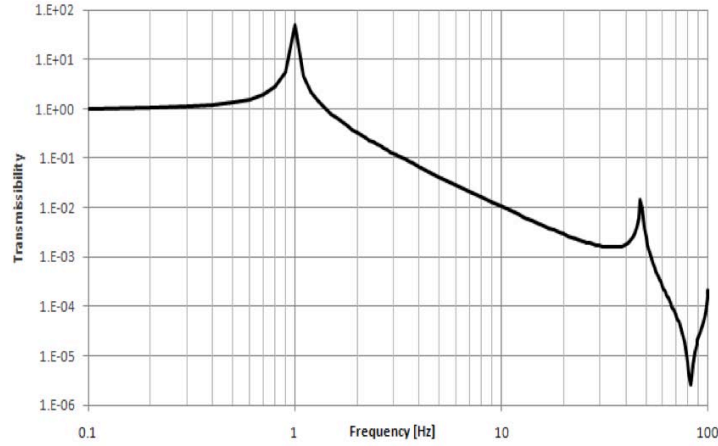


Fig. 5.296: Transfer function of a spring-mass system tuned at 1 Hz

At frequencies below f_0 the ground motion is transmitted to the mass without any attenuation, whilst at frequencies above f_0 the motion of the suspended mass is attenuated by a factor $(f/f_0)^2$. At frequencies close to the resonance, the motion can be amplified and a damping system is usually required. In reality, at higher frequencies, other resonances internal to the spring and the mass appear. They do not affect the attenuation performance, but rather limit the effective frequency bandwidth.

The layout of the CLIC final-focus complex with the QD0 and QF1 doublet is shown in Fig. 5.297. The common support ensures that QD0 and QF1 move coherently.

The two magnets are supported by rigid girders that are fixed on top of a massive concrete block, weighing about 80 tons and resting on several springs (in blue in Fig. 5.297) whose rigidity is tuned in order to have a vertical resonance of the whole assembly at 1 Hz. Vertical ground motion at frequencies below 1 Hz just bypasses the pre-isolator, without being attenuated or amplified; ground motions at frequencies above 1 Hz are reduced by a factor f^2 up to the first internal resonant mode, which can be tuned to be in the bandwidth 30–50 Hz.

The system provides a reduction of the r.m.s. vertical displacement from about 3 to 0.1 nm at 4 Hz and it works in combination with the pre-alignment and the active stabilization, of which it actually constitutes the first element.

5.12.3 QD0 pre-alignment

The final doublet quadrupoles must be pre-aligned very precisely for the luminosity optimization procedure to converge. The pre-alignment for the QD0 must fulfill the following requirements:

- determination of the transverse position of QD0 with respect to the other components of the last 500 m of the Beam Delivery System (BDS), within 10 mm r.m.s.; longitudinally this requirement

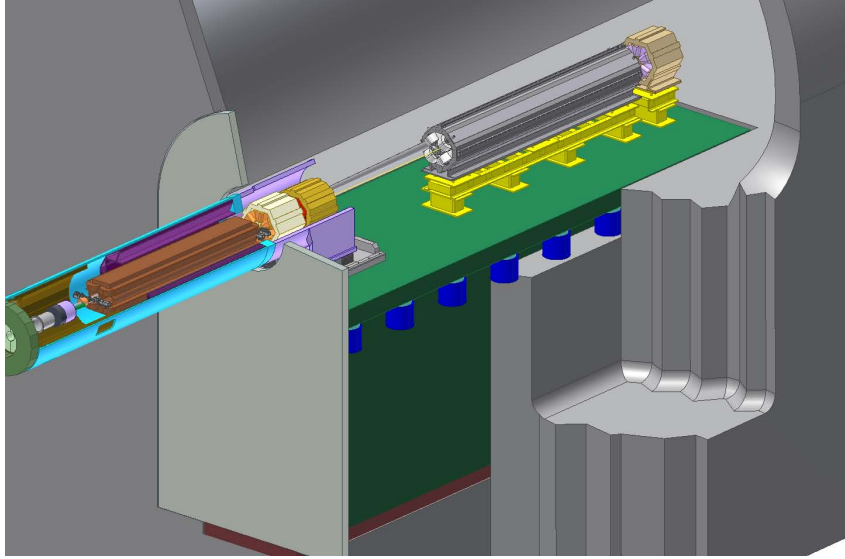


Fig. 5.297: Layout of the pre-isolator, with the concrete mass supporting the two final-focus quadrupoles QD0 and QF1.

is 20 microns r.m.s. between QD0 and QF1;

- monitoring of the position of one QD0 with respect to the other QD0 within $10\ \mu\text{m}$ r.m.s.;
- determination of the position of the left-side components with respect to the right-side components of the tunnel within $\pm 0.1\ \text{mm}$ r.m.s.;
- adjustment of the position remotely and with high-resolution (sub-micrometre).

The procedure can be summarized as follows:

- (1) The position measurement technique is the same as for the Main Beam quadrupoles [300, 301], except for the Metrologic Reference network. The mechanical zero position of QD0 is measured with respect to the sensor mechanical interfaces on a Coordinate Measurement System (accuracy $< 1\ \mu\text{m}$). Once in the tunnel, QD0 is equipped with two Wire Positioning Systems (WPS) and one biaxial inclinometer, installed on the measured mechanical interfaces. The WPS determines the position (radial, vertical, yaw, and pitch) of QD0 with respect to a stretched wire. The two-axis inclinometer provides the roll information as well as redundancy in the pitch axis. In the BDS Metrologic Reference Network (MRN) used to define the straight line for pre-alignment, the length of the last wire is 500 m, with no overlap in the last 250 m, due to space constraints. For the same reason, the Hydrostatic Levelling System (HLS) that monitors sag does not extend to QD0 (see Fig. 5.298). The catenary of the wire has to be extrapolated for the last few metres of the tunnel.

Capacitive sensors determine the relative longitudinal position of QD0 wrt QF1 with sub-micron precision. The sensors are coupled to each component, and measure without contact the distance to targets located at each end of a calibrated carbon bar.

- (2) The position of the QD0 magnets is monitored in two steps.
 - First, the (X,Y) position of the four magnet ends is monitored with respect to the centres of four ‘reference rings’ by four proximity RASNIK systems per ring as shown in Fig. 5.299 [302].
 - Secondly, the position of the centre (X,Y) of each ring is transferred radially, by means of Zerodur spokes, to RASNIK alignment systems placed in six optical paths equally distributed

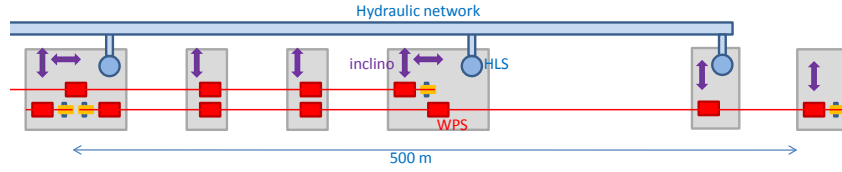


Fig. 5.298: Schematic layout of the pre-alignment equipment in the last 500 m of the tunnel

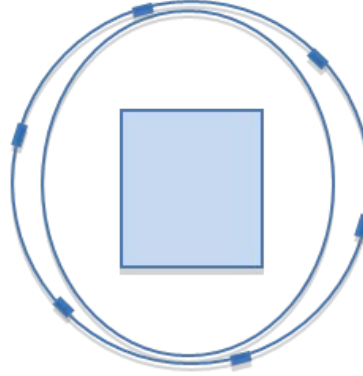


Fig. 5.299: A reference ring placed near a facing of a QD0 magnet

over ϕ , with their optical axes in the z direction as illustrated in Fig. 5.300 [303].

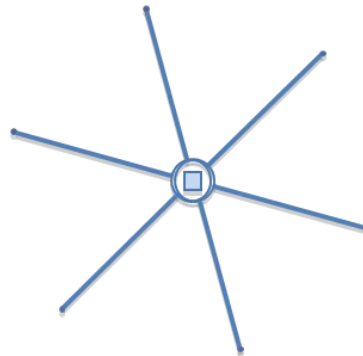


Fig. 5.300: The QD0, reference ring and radial (X,Y) transfer spokes seen in the z direction

- (3) The Final-Focus (FF) beamlines are like two antennas around the IP and the ‘ideal straight lines’ meet at the IP. Permanent monitoring systems provide the relative position of the two antennas, within ± 0.1 mm. A similar system is used at the LHC: the spatial distances between the two reference lines of the FF (stretched wires) and a common reference line (a wire stretched in a parallel dedicated gallery) are determined at three locations on each side. Survey galleries and boreholes between the galleries and the tunnels house the alignment equipment [304].
- (4) The adjustment system is the same as for the Main Linac quadrupoles. The eccentric cam-based adjustment system is a three-point system, with four contact points, providing five degrees of freedom (DOF). This system is used in several other accelerators or synchrotrons (e.g., at PSI and SLAC), but not with the sub-micron resolution required for CLIC. The FF system includes an additional remote adjustment of the longitudinal axis, using a stepper motor.

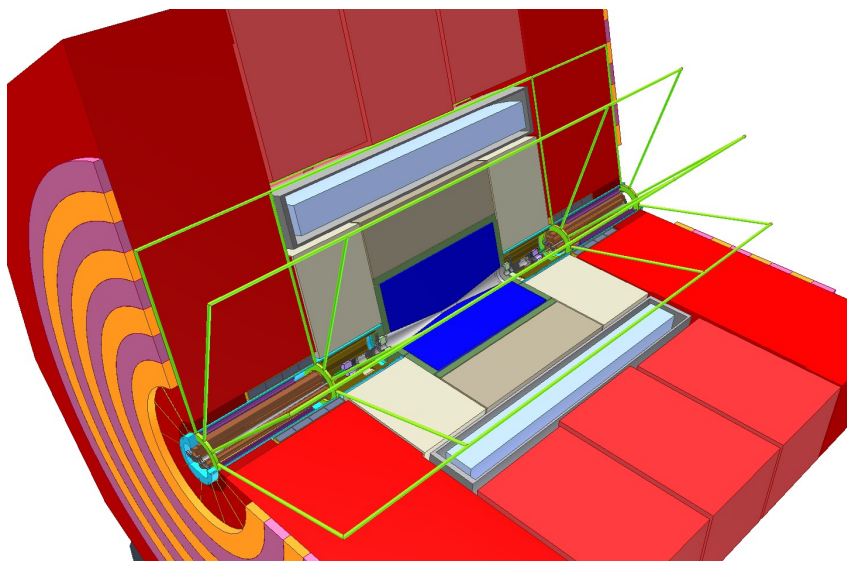


Fig. 5.301: Integration of the rings in the detector.

5.12.4 Push–pull system

The two detectors, CLIC_ILD and CLIC_SiD, have a similar layout based on a superconducting solenoid and an iron return yoke consisting of massive end-caps and a barrel region split longitudinally in three rings. This concept allows a surface assembly with pre-commissioning of the solenoid, followed by independent lowering of the rings in the underground cavern in the same way as was done for the CMS detector. The central ring of the barrel supports the cryostat of the superconducting coil as shown in Fig. 5.301. The calorimeters and the tracker are situated within the free bore volume of the vacuum tank. The differences in the two layouts come from the peak magnetic field, the free bore (diameter of the coil), the choice of the inner detector technology, and a different L^* . Figure 5.302 shows the main dimensions of CLIC_SiD and CLIC_ILD.

The thickness of the yokes must provide magnetic self-shielding to reduce the fringe field, radiation self-shielding to limit the dose to personnel in the cavern during data-taking, and shielding against an accidental beam loss. Compact detectors in a short experimental region anyway provide very efficient radiation shielding.

The thickness of iron in the movable parts (doors) of the endcaps is constrained by space available along the beam line, by the required L^* , and by keeping the QD0 support tubes as short as possible to provide vibration immunity. For simplicity, the longer experiment (CLIC_ILD) might add end-coils [305] to reduce its length to match the 12.80 m overall length of the CLIC_SiD detector, while still suppressing the fringe field.

Figure 5.303 shows the QD0 magnet with the different sections of vacuum tank and separating valves required for opening the detectors and for push–pull operation.

Both detectors have an approximate weight on the order of 13 000 tons dominated by the weight of the iron yoke with an overall height of 14 m and a total length along the beam of 13 m. Table 5.82 summarizes the main parameters of CLIC_SiD and CLIC_ILD.

In push–pull operation, while one detector is taking data on the beamline, the other is in its garage position. The distance between the two detector axes along the push–pull direction is 28 m, while 15 m is the distance from the beam axis to the beginning of the garage area in the experimental cavern.

Measurements of the stray field in the CMS experimental cavern have shown [306] that stray fields should not exceed 50 G otherwise work in the area will become rather difficult. The self-shielding of the return yoke must ensure that 50 G is not exceeded at a horizontal distance of 15 m from the beam axis.

5.12 MACHINE DETECTOR INTERFACE

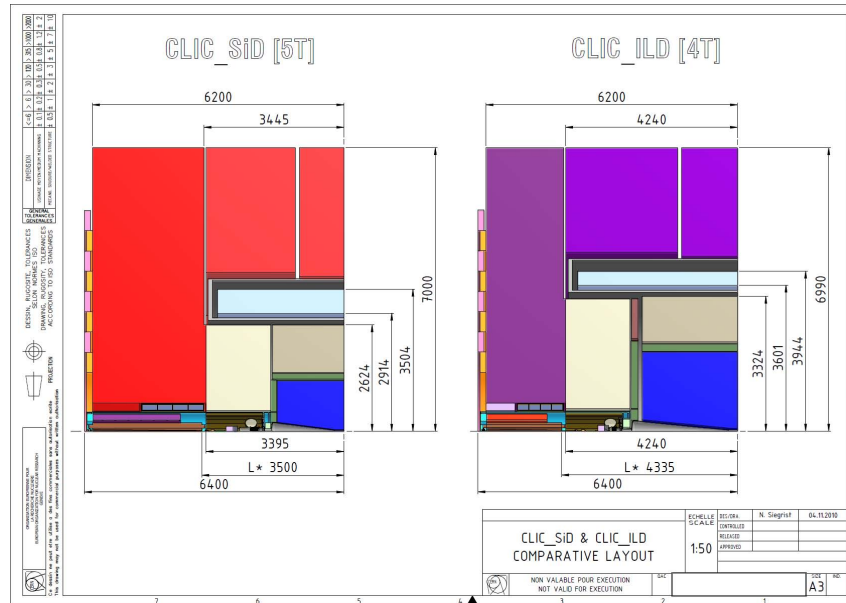


Fig. 5.302: Quarter views of the two basic detector layouts of CLIC_SiD and CLIC_ILD

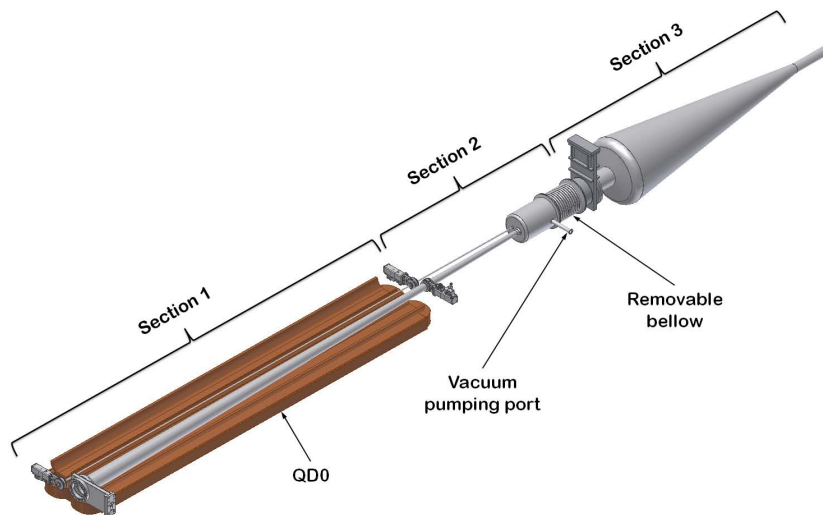


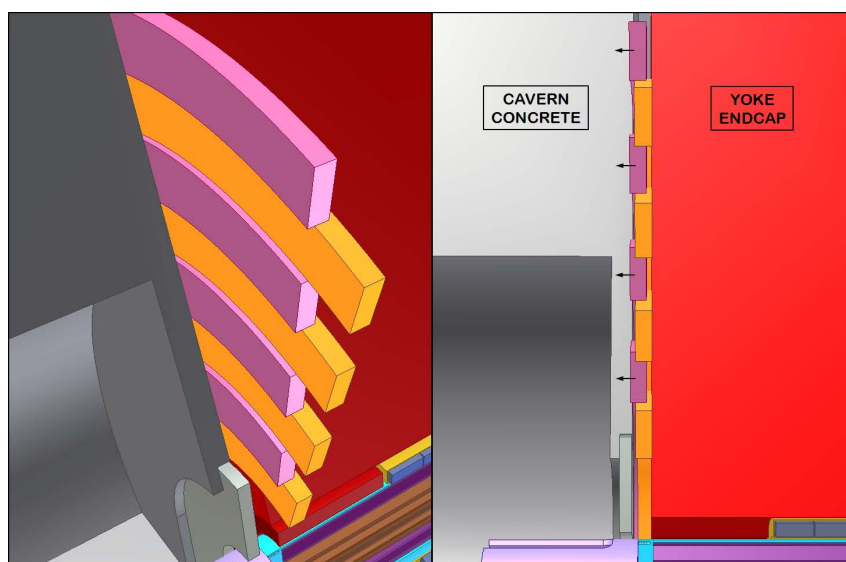
Fig. 5.303: View of QD0 magnet and vacuum sections and valves

Similarly the off-beam detector if energized in its cavern must not distort the field map of the on-beam detector by more than 0.01% inside its tracking volume (ILC criteria).

For personnel working in the cavern during beam operations, the maximum exposure to ionizing radiation is from potential beam losses. The iron yoke itself provides enough shielding for beam losses inside the detector, but there can also be losses in the region of the final-focus magnets, at the interface between the endcap and the cavern wall. For this region, shielding is provided by concentric shielding rings on the back side of the endcap iron, interleaved with shielding rings that are fixed on the cavern wall. The latter can be moved in and out by pneumatic or hydraulic jacks, thus creating a chicane system that closes perfectly the gap between the endcap and the tunnel wall. Figure 5.304 shows the detail of the chicane system for radiation shielding. Simulations of this system show the radiation dose remains at very acceptable levels even if a full bunch train is lost on the QD0 magnet.

Table 5.82: Main detector dimensions and weights

Parameter	CLIC_SiD	CLIC_ILD with end-coils
Detector length [m]	12.40	12.40
Overall length with shielding rings [m]	12.80	12.80
Detector diameter on flat [m]	14.00	13.98
Free bore [mm]	5448	6852
Coil inner diameter [mm]	5828	7202
Coil outer diameter [mm]	7008	7888
Coil length [mm]	6230	7890
L^* [mm]	3500	4340
Bore in endcap for support tube and anti-solenoid [mm]	1380	1380
Radial height vacuum tank [mm]	1020	828
Vacuum tank length [mm]	6690	8350
Coil weight [t]	201	173
Vacuum tank weight [t]	128	173
Endcap weight [t]	2900	2100
Barrel weight [t]	5000	4700
Complete return yoke [t]	10 800	9900
Detector total weight [t]	12 500	11 800

**Fig. 5.304:** Radiation chicane made of concentric ring modules.

5.12.4.1 Intra-pulse feedback system

The beam-based IP intra-train feedback (FB) system was outlined in §3.6.6. The schematic layout of the components is shown in Fig. 5.305.

Prototypes of the BPM, signal processor, feedback circuit, kicker and drive amplifier have been developed and tested with beam by the FONT Collaboration [307–310]. Key parameters are the latency

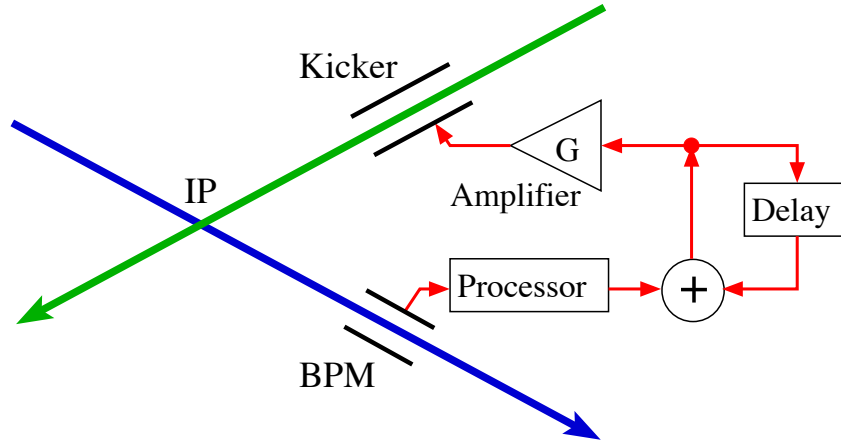


Fig. 5.305: Schematic layout of the IP feedback components.

of the components, which impacts upon the luminosity recovery potential, and the drive power of the amplifier, which determines the angular deflection that can be given to the beam. A short (~ 10 cm long) stripline BPM provides a fast-input beam position signal, and a short (~ 25 cm long) kicker provides the correcting beam angular deflection. These are compact, intrinsically fast, high-bandwidth components of ‘standard’ design. Actual devices with geometries optimized for the tight space constraints of the CLIC IR will need to be engineered as the IR design evolves. For the layout shown in Fig. 5.305, with the BPM and kicker located approximately 3 m from the IP, the beam round-trip time-of-flight delay is about 20 ns.

A prototype BPM signal processor has been designed (Fig. 5.12.4.1 (top)) with micron-level resolution, and a latency of 5 ns has been demonstrated [309]. A high-power kicker drive amplifier that meets CLIC requirements has been built (see Fig. 5.12.4.1 (bottom)) and tested with beam at ATF [310]. In order to optimize the latency, the feedback circuit was integrated into the amplifier board; a combined (feedback circuit + amplifier + kicker rise-time) latency of 8 ns was measured [310]. Assuming these demonstrated prototype latencies yields a total system latency of $33 \mu\text{s}$. For the FB performance simulations described in §3.6.6 a latency of 37 ns was assumed, which allows an extra 4 ns of delay, for additional cabling and/or adjustment of the electronics location near the IP. With further optimization of the component locations and cabling, and development of faster electronics, a total latency as low as 30 ns may be achievable.

5.12.4.2 Vacuum system

The MDI baseline is a non-baked system using ultra-high vacuum (UHV) materials and procedures to obtain the pressures specified in §3.6.7. The layout of the QD0 magnets limits the chamber diameter to 7.6 mm and pump separation to ~ 4 m. Assuming a clean, unbaked vacuum system, a static pressure profile after 100 hours of pumping has been calculated (see Fig. 5.307). This corresponds to an average pressure of 3.6×10^2 nTorr. This conforms with the requirement of beam-gas background, but gives little margin for additional beam-induced outgassing. The QD0s should therefore be kept under vacuum to minimize contamination with water vapour.

The MDI region is separated into physical sectors with ultra-high vacuum valves as shown in Fig. 5.308. Two valves are required in the space between QD0 and the experiment to allow the detectors to be exchanged (push-pull) whilst maintaining the QD0 and experimental beam pipe either under vacuum, or filled with a clean, inert gas. The post-collision line is separated from the collider beamline to allow independent interventions in these sectors. A fast shutter may be installed on each post-collision line to prevent contamination of the experimental sector due to incidents in the post-collision line.

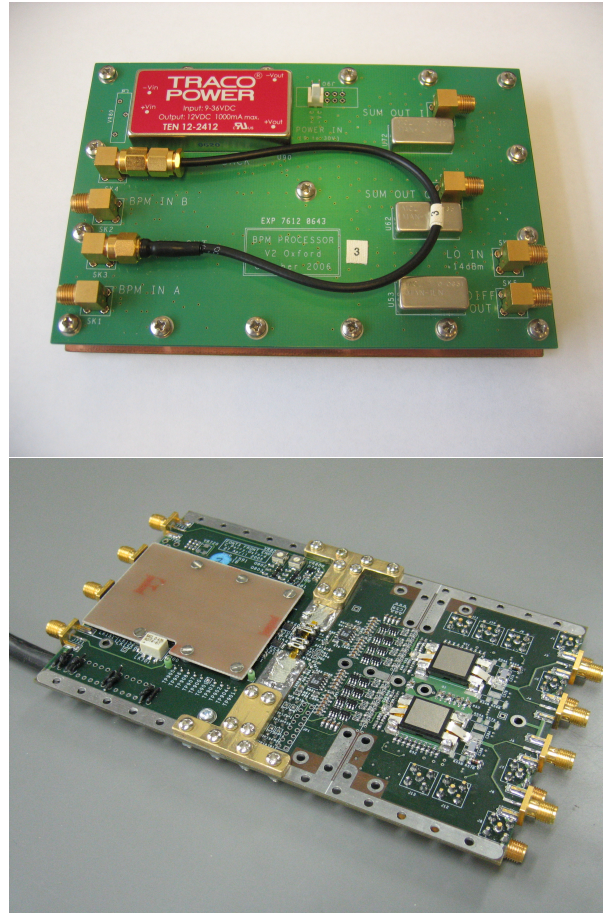


Fig. 5.306: Prototype modules for the IP Feedback system: (top) BPM signal processor and (bottom) integrated feedback circuit and drive amplifier.

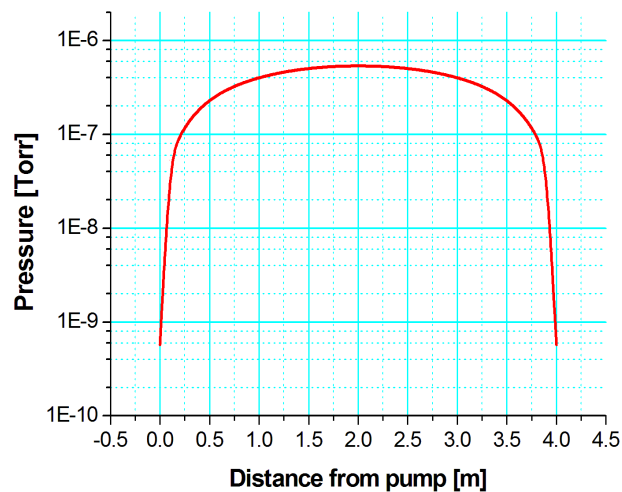


Fig. 5.307: Static pressure profile in QD0 region after 100 hours of pumping

Each of the sectors (QD0, experimental, post-collision) requires a self-contained system of pumps and vacuum instruments for measurement of pressure and interlock of the sector valves. The small sector

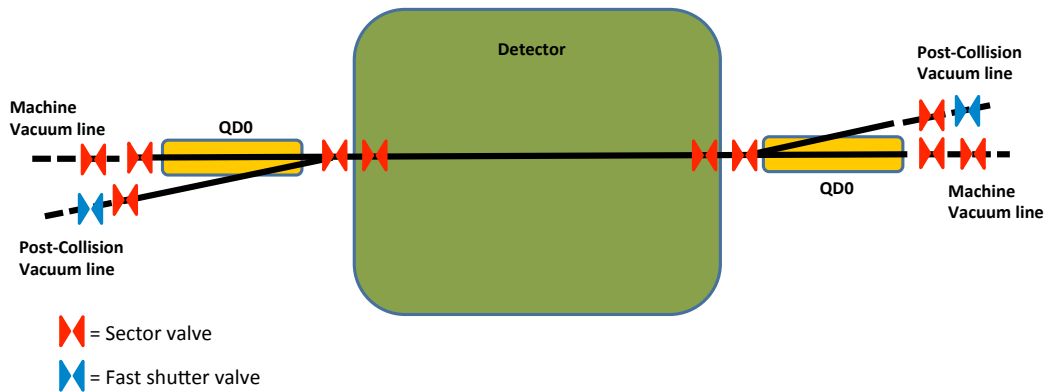


Fig. 5.308: Sectorization of vacuum in MDI region

between the two push–pull valves is pumped and interlocked with a mobile (removable) vacuum system.

The UHV detector and QD0 sectors are pumped by sputter-ion pumps, with additional NEG or sublimation pumps as necessary. The post-collision line requires a high pumping speed due to the large surface area and beam-induced outgassing. A combination of sputter-ion, turbo-molecular, and mechanical pumps is used.

The post-collision line consists of stainless-steel vacuum chambers in stepped or conical forms inside the magnetic and absorber elements. As the absorbers are outside the vacuum chambers, the chambers have windows upstream of the intermediate dump absorbers and an exit window separating the collider vacuum system from the main dump body.

5.12.4.3 Overall integration

The forward region includes several important components with quite different functions: the final-focusing magnets QD0, the Lumical and Beamcal calorimeters, the beam position monitors and kickers for the beam diagnostics and correction, the beampipe, the sensors and piezo-actuators for the active stabilization of QD0. Two independent support tubes with distinct functions and stiffness provide the mechanical support. Both are flanged together at their ends and cantilevered from the tunnel wall by a strong retaining bracket. This bracket has a stiff flange that allows a bolted connection to the support tube flange, a sliding pad underneath, as well as the pre-alignment mechanics. The whole system sits on a pre-isolator. Figure 5.309 shows the detail of the connecting part between tunnel and detector whereas Fig. 5.310 depicts in more detail the front part of the support tube. Additional integration problems arise due to the 20 mrad crossing angle of the incoming and outgoing beams. The QD0s are aligned with respect to the incoming beam. The push–pull procedures require breaking the vacuum system each time; therefore there are valves on the beampipe, between the QD0s and the Beamcals, for quick, safe and reliable vacuum operations.

Both detectors move on independent platforms made of reinforced concrete with a size of approximately $3 \times 16 \times 2 \text{ m}^3$. The design is similar to the plug of the PX56 shaft at CMS, which has been successfully operated and surveyed up to 2500 t. The gross weight of the detector plus platform is around 15 000 (13 000 + 2000) t.

The platforms are in contact with the floor through a set of (possibly anti-seismic) supports, which redistribute the total load. First finite-element calculations confirm that with a thickness of 2 m the local

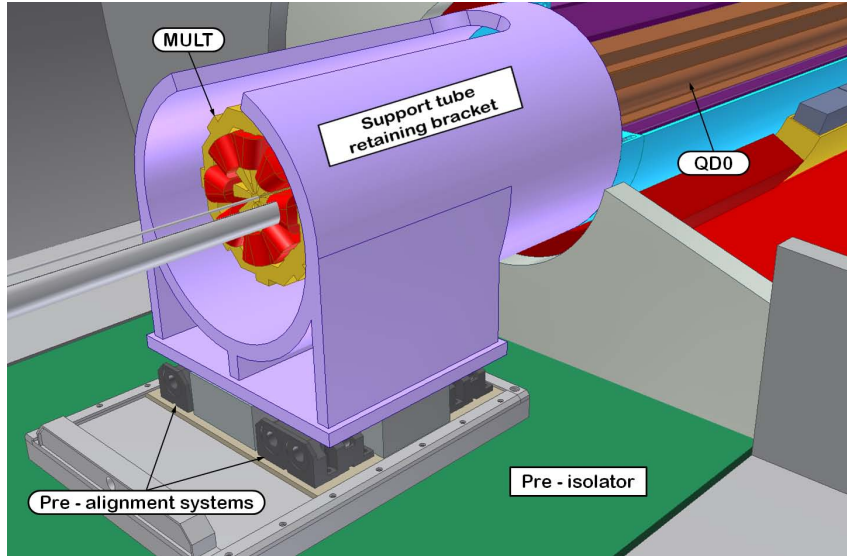


Fig. 5.309: Rear part of support tube with QD0, retaining bracket and pre-alignment underneath

stress and deformation remain well below the permissible values.

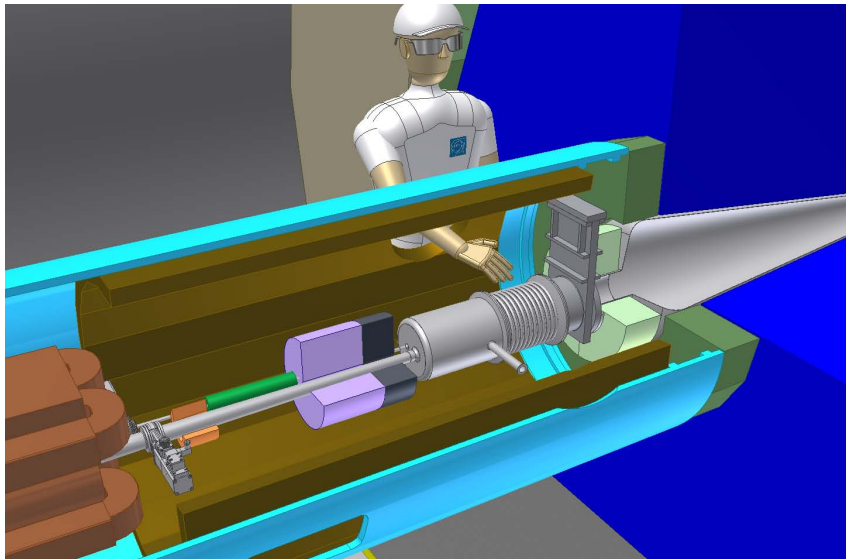


Fig. 5.310: Front part of support tube structure with QD0, BPM and kicker, vacuum valve, BeamCal and the transition region to the barrel parts

The moving system can move a total mass of 15 000 t and may use either air pads or heavy-duty rollers. The friction factor is 1.5% and 5% respectively. In both cases, as an example, a set of pulling hydraulic strands jacks, with a sufficient capacity, commercially available, can be integrated into the design without major difficulties. A guiding rail system with indexing capability at the interaction point can achieve the required alignment precision on the beam of ± 1 mm and 0.1 mrad between consecutive push-pull operations.

The floor underneath the platforms contains deep trenches to host the cable chains and provide access for the maintenance of the air pads or the heavy-duty rollers.

5.12.4.4 Experimental Area

Apart from supporting the two experiments, the layout of the underground interaction region has to satisfy many requirements [311]. These include minimizing the volume to be excavated and the cost, integration of services, personnel access, ventilation, survey galleries, and general safety features. At the present stage, the detector is to be assembled in its surface hall and lowered in large units into its underground cavern. Therefore there is only a crane of limited capacity (of the order of 40 t) in each underground area. Each experimental cavern has its own access shaft. This access shaft is situated at the end of the cavern outside the region covered by the opened experiment. The experiment has a diameter of ~ 14 m, with an additional 1.5 m on each side for the frame structure supporting external racks. To provide some lateral margin for the lowering, a shaft diameter of 18 m is reasonable. Since the elements to be lowered are much longer in one dimension than the other, the lift, the ventilation ducts and the emergency staircase can be located inside the same shaft. Figures 5.311 and 5.312 give the main dimensions. More details on the civil engineering aspects can be found in Chapter 6.

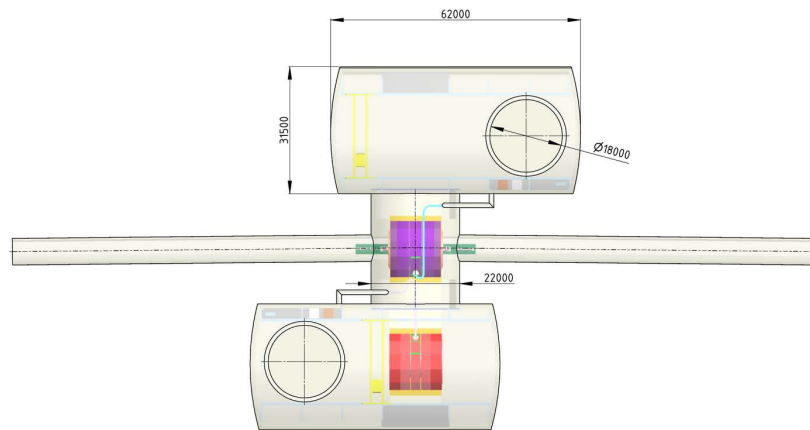


Fig. 5.311: Top view of the experimental area with dimensions

5.12.5 Component inventory

The main components of the Beam Delivery System are listed in Table 5.83.

5.12.6 Cost considerations

The Machine Detector Interface region contains a limited number of elements and most of them do not represent a large investment. One major cost item is of course the civil engineering of the experimental areas. The cost of the detectors is considered separately from the MDI.

5.12.7 Outlook for the project preparation phase

The proof of principle of a stabilization strategy has been validated in the laboratory with a representative prototype and with robust simulations. However, there is still important work to be carried out for the technological validation of the solution in the MDI region and its environment. The current stabilization device could be modified as new results are obtained.

IP feedback issues that require further study include the background (electromagnetic and neutron) radiation environment in the FB region, and the corresponding impact upon the radiation hardness requirements for the electronics components. Depending on the outcome, some local shielding may be

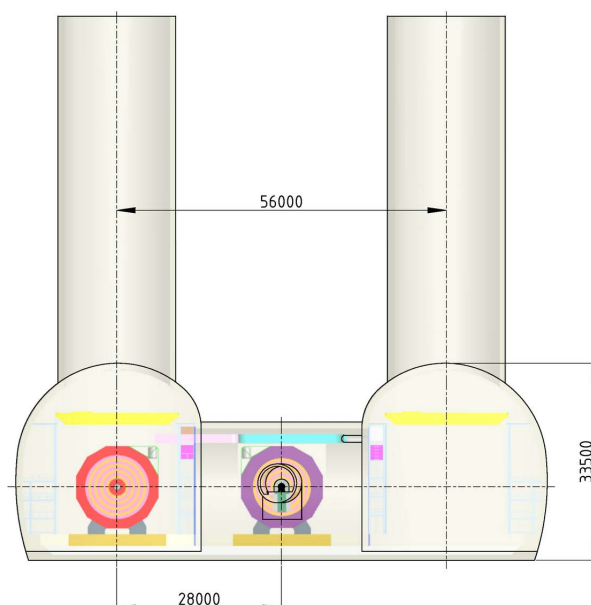


Fig. 5.312: Side view of the experimental area with dimensions

Table 5.83: Components in the MDI region

Items	Number	Comments
QD0 magnet	4	To be replaced in case of important energy changes
QD0 rectifiers	2×4	One rectifier per pole
QD0 stabilization systems	2	Sensors plus piezo-actuators plus pre-isolators plus support tubes
QD0 pre-alignment systems	2	
Vacuum system	1	One beryllium chamber in the detector region, two QD0 chambers plus vacuum into the post-collision beam region
IP feedback system	4	Four Beam Position Monitors, four kickers and associated electronics
Anti-solenoids	4	Adapted to each detector

required. Attention also needs to be paid to insulation against RF pickup, as well as prevention of RF broadcast into the neighbouring environment.

The development of the real, full-size QD0 magnet design (working in an accelerator environment and with a length of 2.73 m) is not a priority for the Conceptual Design. Nevertheless some studies to check the feasibility of a longer quadrupole, based on the proposed design, have been launched. For the QD0 pre-alignment, additional work is needed to develop a method to displace the wire stretcher to the tunnel when QD0 is dismantled.

More work is required to incorporate two detectors with different L^* values, if this cannot be avoided.

The combined effect of all feedback systems (including IP feedback) and the active and passive stabilization in the presence of ground motion and other perturbations will be simulated in more detail.

5.13 Controls

5.13.1 Introduction

The scale of the CLIC project (see §5.2 where the number of magnets in CLIC is detailed and §5.9 where the impressive amount of beam instrumentation is listed) determines the control system architecture as a largely distributed ‘three-tier’ control system including very sophisticated applications programs for the operation of the accelerators. In general, the CLIC control system can be considered as a larger-scale version of the present control system of the LHC and its injectors (see Ref. [312])

Some special consideration has to be given to the front-end tier. For all CLIC accelerators excluding the Main Linac tunnel it is proposed to use a ‘classical’ approach where controls electronics are housed in racks close to the accelerators and connected to front-end computers. This is also the basis of the control system for CTF3 and although the scale of the CLIC project means that the distances and the number of components to be controlled are larger than in CTF3, there should be no fundamental difficulty on controlling the CLIC injector complex.

The Main Linac tunnel for various reasons can not be controlled in the same way: firstly this part of the accelerator generates a very high number of control signals (about 100 signals per metre), i.e, close to 5 million analog control signals over both 24 km Main Linacs. Building the acquisition system for this number of channels in the classical modular approach would simply not be possible in terms of available space and also in terms of cost. In addition, very strict limitations on heat dissipation (see §6.4) and the high-radiation environment in the CLIC Main Linac tunnel, impose a new front-end architecture. We propose the development of a compact acquisition module, to serve as a dedicated acquisition and control module (ACM) for all signals of the two-beam modules (see §5.6) while the processing of the signals and calculations based on the signals is done outside the tunnel where heat dissipation and radiation are less critical.

The development of such an ACM with very low power dissipation, potentially pulsed-power operation and radiation hardness represents a technological challenge. But ensuring that all the teams that have responsibility for equipment in the modules (instrumentation, RF, vacuum, quadrupole stability, alignment, etc.) accept a common control interface also represents a sociological challenge.

The following sections describe briefly the main components of the classical ‘three-tier’ controls system architecture as proposed for CLIC where special emphasis is given to the ACM module design. Beam-synchronous timing is generally also considered a functionality of the control system, but due to its fundamental importance for CLIC, and since the current stability requirements have not yet been achieved, a separate section (§5.15) is dedicated to it.

5.13.2 Controls architecture

The control system for CLIC is based on a so-called ‘three-tier’ architecture: a resource tier that gathers information from equipment located close to the accelerators; a middle tier of servers to manage the communication between tiers; and a top tier that provides the Graphical User Interface (GUI) for the operators in the control centre.

The software applications suite covers all important aspects of accelerator controls: optics (Twiss, machine layout), parameter space, settings generation and management (generation of functions based on optics, functions and scalar values for all parameters), trim (coherent modifications of settings, translation from physics to hardware parameters), equipment control, and beam-based measurements.

The software architecture, shown in Fig. 5.313 is based on three main principles. It is modular (each module having high cohesion, providing a clear applications programming interface), layered (with three isolated logical layers — database and hardware access layer, business layer, user applications), and distributed. It should also provide homogeneous application software to operate all parts of the CLIC complex.

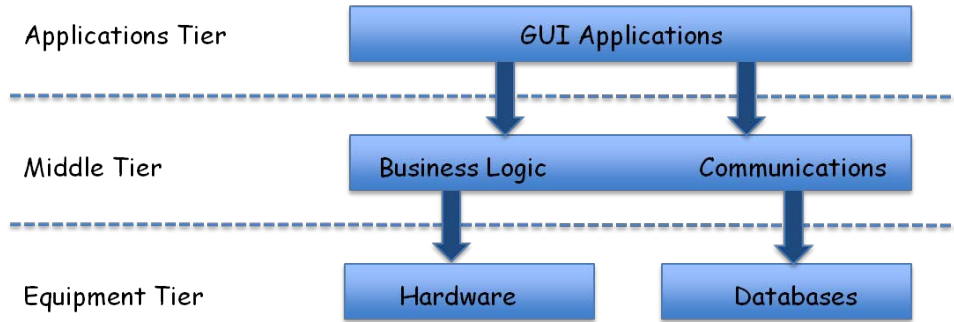


Fig. 5.313: The control software architecture

5.13.2.1 *Application tier*

At the top level — the application or presentation layer — consoles (PCs) in the CLIC control centre run GUIs that allow machine operators to control and optimize the CLIC accelerator complex and supervise the state of key systems. Dedicated displays provide real-time summaries of key machine parameters.

The operator consoles are the fastest, commercially available PCs running interactive applications, fixed displays and video displays. The CLIC control system is isolated from public networks.

Given the scale of the CLIC complex, we assume that the control centre is split into ‘hubs’ dedicated to major elements of the machine: Drive Beam, Main Beam, injectors, 2-beam acceleration, and site infrastructure; with each ‘hub’ containing at least 20 PCs each with multiple screens.

5.13.2.2 *Middle tier*

The middle tier of the control system consists of multiple servers:

- Application servers host the software required to generate, steer, and monitor the CLIC beams and run the supervisory control and data acquisition systems.
- File servers contain the operational applications. The middle tier also includes the central timing that provides and distributes the information on the operational parameters of the accelerator.
- Database servers contain the CLIC layout and the controls configuration, as well as all of the machine settings needed to operate the machine or to diagnose machine behaviour (see §5.13.7 for details)

The middle tier needs to consist of a farm of ~ 1000 multi-core processors each with performance equivalent to the 2012 state-of-the-art level.

5.13.2.3 *Equipment tier*

The equipment tier is where the interaction with the machine components takes place. This is described more fully below.

5.13.3 Front-end Acquisition and Control Module (ACM) for the Main Linac

5.13.3.1 *Scope*

Here we describe the requirements and constraints that apply to the design of the CLIC front-end Acquisition and Control Module (ACM), which is a special solution uniquely for the CLIC Main Linac. We give the signal requirements for the different users and the many constraints in terms of architecture, radiation hardness, power consumption, and remote diagnostic and configuration. Some 20 924 instances of this module are needed for the 3 TeV CLIC machine.

5.13.3.2 Signal acquisition and control channels

There are five different types of CLIC module (see §5.6). For each type of module more than 200 acquisition channels and about 170 control channels are needed per module in order to measure and control the properties of the beam, the RF parameters, the module alignment and stabilization, vacuum, and the cooling systems. Tables 5.84 and 5.85 give a summary, by sub-system, of the acquisition and control signals required per CLIC module. It can be clearly seen that the data rate for acquisition is dominated by the signals coming from beam instrumentation and from RF and is around 6 Mbits/s per ACM. Given the capacity of state-of-the-art optical fibres, there should be no data transmission bottleneck to and from the ACMs to the alcoves.

Table 5.84: Front-end acquisition channels in one 2 m long TBA module

	Number of signals	Signal frequency	Sampling frequency [Samples/s]	Resolution [bits]	Readout frequency [Hz]	Total data rate [kbits/sec]
Beam instr.	39	100 MHz	200×10^6	16	50	1060
RF instr.	23	50 MHz–1 GHz	200×10^6 – 2×10^9	10–12	50	1980
Cooling	72	DC	1	12	1	0.03
Alignment	34	DC	100	16–24	1	78
Stabilization	21	1 kHz	2×10^3	20	100	840
Vacuum	12	10–100 Hz	1×10^3	16	1	0.02
Power	2	DC	DC	12	150	6

Table 5.85: Front-end control channels in one 2 m long TBA module

	Number of signals	Signal frequency	Resolution [bits]	Transmission frequency [Hz]	Total data rate [kbits/sec]
Beam instrumentation	26	–	16	50	2.0
RF instrumentation	4	DC	1	50	0.2
Cooling	88	<1 kHz	–	1	–
Alignment	28	DC	16	50	1210
Stabilisation	6	DC	18	100	12
Vacuum	20	10–100 Hz	–	1	–
Power	2	DC	12	100	20

5.13.3.3 Basic concepts

Owing to the long distance (~ 878 m) between the underground alcoves (see Chapter 6), it is not foreseeable to locate the acquisition and control electronics for the 436 modules of one ‘sector’ in these alcoves. The required space for the electronics for such a large number of modules and the cost for the cabling to and from such a number of modules to the alcoves would be prohibitive.

The proposed solution, therefore, consists of a local ACM per CLIC TBA module (every 2.01 m), located as close as possible to each module. The actual position of the ACM has yet to be decided and depends on the form factors of the chosen hardware platforms. The module should, however, be positioned as far as possible from the beam pipes to limit the amount of radiation they are subjected to. Figure 5.314 shows the schematic layout of a typical CLIC module.

The ACM is responsible for the acquisition and transmission of control signals under rather severe constraints on the radiation hardness (see §5.13.3.4 below) and power consumption (see §5.13.3.5

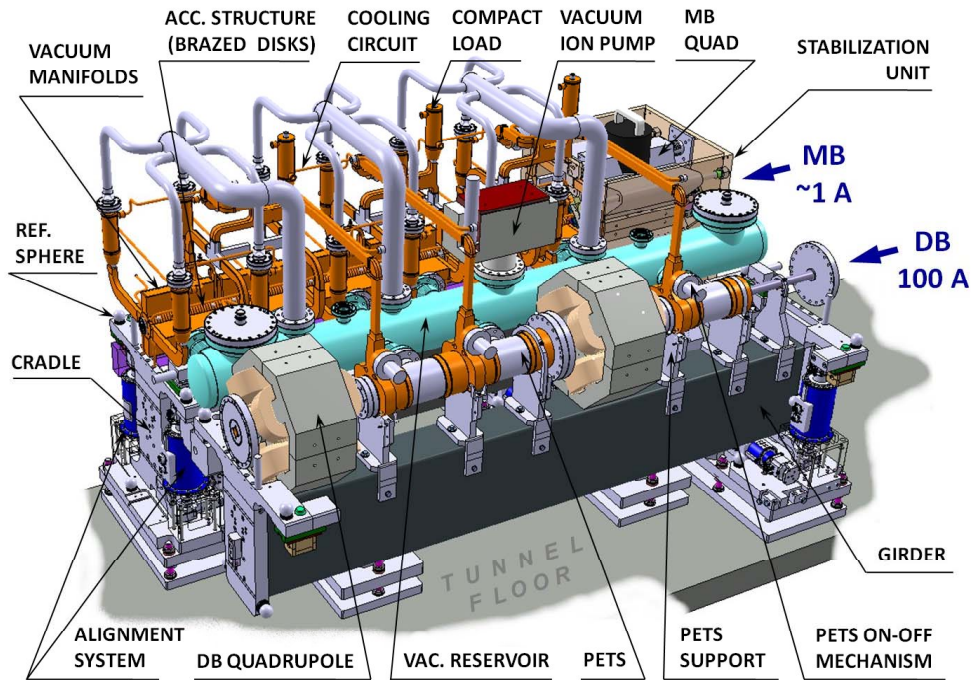


Fig. 5.314: 3D view of a typical CLIC module

below).

In the light of these constraints, a generic approach must be found in order to provide an ‘open’ CLIC module acquisition and control solution that would accommodate the controls requirements for the different CLIC sub-systems.

In order to provide this openness, the module acquisition and control solution shall offer the following services:

- A modular architecture based on a single form-factor card cage allowing the insertion of similar hardware modules dedicated to each CLIC sub-system.
- For each hardware module, a common hardware part (carrier concept) dealing with powering, data communication and diagnostics, and a specific part (one or multiple mezzanines) implementing the sub-system-specific acquisition and controls actions (DACs, ADCs, etc.).
- A fast deterministic communication bus for the transport and synchronization of data from all hardware modules.
- A common redundant power unit providing a standard set of voltage sources.
- A communication unit for the bi-directional and synchronous data transfer between the acquisition and control module and the CLIC control system.

5.13.3.4 Radiation hardness

A simulation [313] shows that the annual absorbed dose close to the modules can exceed 1000 Gy/year (see Fig. 5.315). The electronics normally have a lifetime of 10–15 years, and should hence either be designed to withstand a dose of 15 kGy or be shielded to reduce the radiation effect. As stated above, the final location of the ACM has not yet been decided. From the figures, it can be seen that the space below the tunnel floor would be best location although there may be access and space issues as there are a number of services (e.g., cooling) to be installed here.

5.13 CONTROLS

As shown in Fig. 5.316 and Fig. 5.317, the neutron flux is also very high and could produce single-event upsets and, even worse, single-event latch-ups, which could destroy the electronic modules.

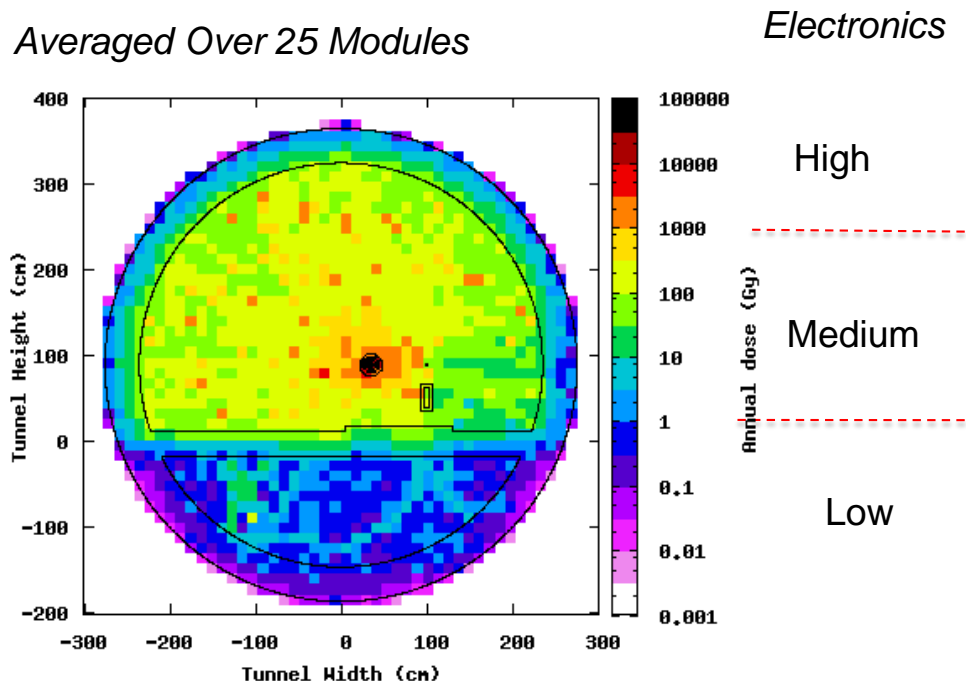


Fig. 5.315: Annual absorbed dose in main tunnel. Estimate of damage to electronics for a MB energy of 1.5 TeV

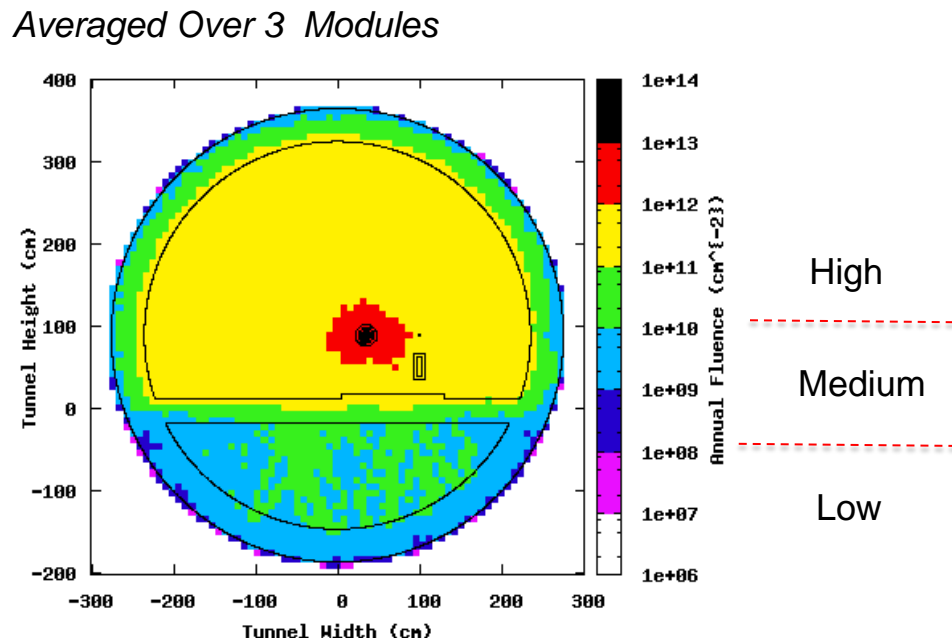


Fig. 5.316: 1 MeV neutron equivalent flux. Estimate of damage to electronics for a MB energy of 1.5 TeV

5.13.3.5 Power dissipation to air

The total power dissipation to air in the tunnel is limited to 150 W/m. Taking into account the dissipation of other systems this leaves much less than one W for each acquisition and control signal. Switching off

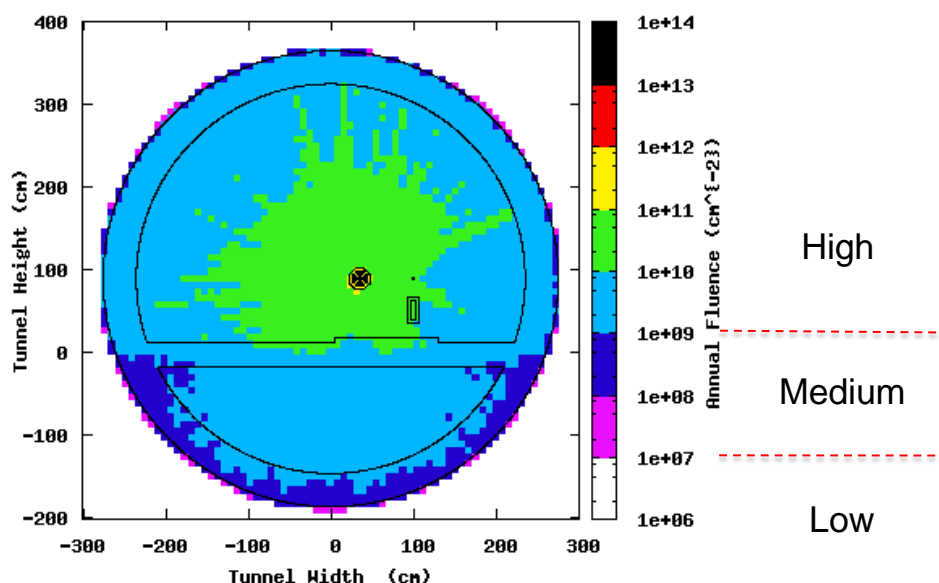
Averaged Over 3 Modules

Fig. 5.317: $>20\text{MeV}$ neutron flux. Estimate of damage to electronics for a MB energy of 1.5 TeV

the ADCs (and perhaps also other components of the system) between consecutive beam pulses should be investigated. If components can be switched off for 10 ms in a 50 Hz pulsing machine, then the power consumption for these components is reduced by 50%.

5.13.3.6 Digitization and data transmission

Taking into the account the constraints on power consumption and radiation, it is clear that the digitizing of signal acquisitions should take place at the lowest possible hardware level and that no local processor, nor operating system should be used inside the ACM. The acquisition and control unit should perform the following tasks:

- The prompt digitizing of the incoming signals from the CLIC sub-systems
- The execution of commands and configuration actions, as received from the higher level(s) of the CLIC control system
- The execution, for some systems, of pulse-to-pulse feedback loops
- The synchronization of acquisitions and commands with the CLIC timing system
- The time stamping of the acquisitions
- The pulsing of hardware components of the system, in synchronization with the CLIC timing system
- The bi-directional transmission of data via optical link(s) to the next-higher layer of control system.

Currently, two candidate hardware platforms are being investigated: one based on the open standard known as ‘MicroTCA for Physics’ which is supported by the PICMG consortium [314] and the other based on the PXI standard from National Instruments [315].

5.13.3.7 Communication topology

The ~ 400 signals going to and from each ACM must be collected and analysed in the underground alcoves, which are located at 878 m intervals along the tunnel. The link between the ACMs and the alcoves

must be immune to EMC interference and provide a protocol for high-speed synchronized transactions with the CLIC timing system. All transactions related to remote configuration and diagnostics (see next section) must also pass through this communication link.

White Rabbit (WR) [316] is a time-deterministic, low-latency ethernet-based network which enables transparent timing distribution with sub-nanosecond accuracy. It is being developed to replace the General Machine Timing (GMT) system currently used at CERN and will be the foundation for the control system of the Facility for Antiproton and Ion Research (FAIR) at GSI. White Rabbit takes advantage of the latest developments for improving timing over ethernet, such as IEEE 1588 (Precision Time Protocol) and Synchronous Ethernet. White Rabbit is an excellent candidate for the communication between the ACMs and the FECs located in the alcoves and is the proposed solution.

The ACMs are connected to series of WR switches located in the alcoves. For reasons of redundancy, each ACM has two separate optical-fibre connections. To further reduce the length of fibres needed, it has been decided to ‘daisy-chain’ ACMs together as shown in Fig. 5.318 below. Each alcove has connections to 438 ACMs which are arranged into 36 ‘daisy-chained’ groups; two times 17 groups of 12 ACMs and two groups of 14 ACMs as shown schematically in Fig. 5.319.

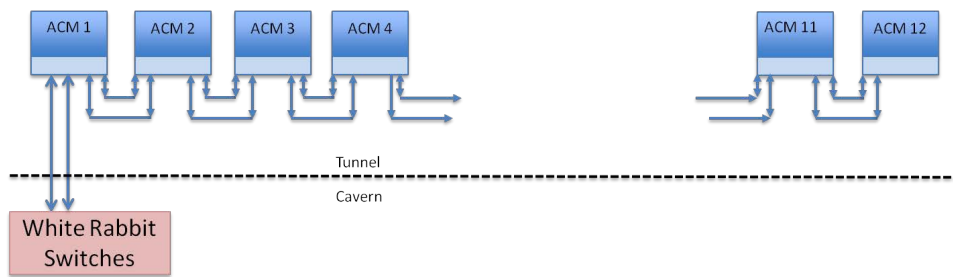


Fig. 5.318: A schematic of the ‘daisy-chaining’ of ACMs and the connection to a WR switch

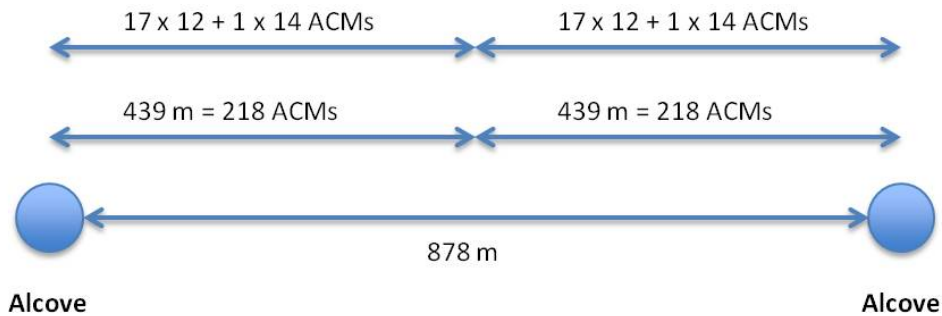


Fig. 5.319: A schematic of two alcoves and the numbers of ACMs which need to be connected

The 72 fibres arriving in each alcove are connected to 18-port WR switches which are the current state-of-the-art [317]. Five such WR switches are needed to handle all the acquisition and controls signals from the ACMs; giving a total of 90 inputs/outputs. There are a small number of free ports providing for limited redundancy. The proposed configuration in each alcove is shown in Fig. 5.320.

5.13.3.8 Remote configuration and diagnostic facilities

The quantities and the underground location of the ACMs represent a unique challenge in terms of operations. Specific aspects should be addressed in terms of operational availability and long-term maintenance and evolution of these systems. The following mandatory services shall be implemented at the level of the acquisition and control units:

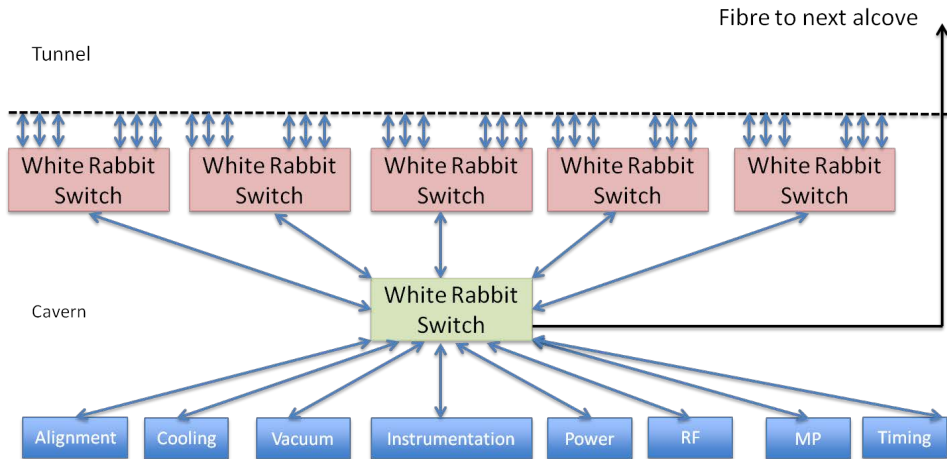


Fig. 5.320: A schematic of connections inside an alcove

- Monitor in real-time, through the communication link, the correct functioning of any internal hardware component of the system.
- In case of malfunction, disable parts of the system in order to allow the operation of CLIC in degraded mode.
- Remotely upgrade firmware and configuration parameters.

5.13.3.9 Front-end computers

In each alcove there is a dedicated front-end computer (FEC) for each module sub-system: beam instrumentation, RF, cooling, alignment, stabilization, vacuum, and power converters. In addition there is a FEC dedicated for timing and another FEC dedicated to machine protection. The FECs will be the fastest real-time computer available at the time of their installation. For the slower signals (e.g., vacuum and cooling, where real-time processing speed is not so important), Programmable Logic Controllers (PLCs), or their equivalent, may be used. The FECs are inter-connected via a further 18-port WR switch as shown in Fig. 5.320.

In order that the FECs can send information, via the middleware services, to the CLIC Control Centre the alcoves must have a connection to the surface. As there is only surface access every fourth alcove, it is necessary to link four alcoves via separate fibres. In the alcove which has access to the surface, a dedicated switch takes care of the connection to the surface.

5.13.4 Security

5.13.4.1 Network infrastructure security

The CLIC control system should be protected, not only from malicious external access, but also from inadvertent errors by operators and failures in the system. To achieve this there is a formal separation of the technical network, where the control components are connected, and the general-purpose network.

5.13.4.2 Role-based access

A role-based solution to grant access to the controls equipment and certain critical settings is part of the standard controls communication infrastructure. This system works by assigning permissions to roles rather than individual accounts. An access token — containing information about the user, the application, their location, their role, etc. — is obtained during the authentication phase and is used

5.13 CONTROLS

to grant or deny actions. This allows for filtering, control, and traceability of any modifications to the controls equipment. Access to the LHC control system is currently controlled by such a solution [318, 319].

5.13.4.3 *Software Interlock System (SIS)*

A Software Interlock System (SIS) is provided to further protect the CLIC machine. The SIS provides continuous surveillance of a large number of monitored devices grouped in different permit structures providing alarms and beam inhibits when necessary.

To allow for an automatic and failsafe operation of CLIC, a generic sequencer is required. The sequencer offers all the different functionalities required for hardware commissioning, beam commissioning, and CLIC beam operations.

5.13.5 Alarms and diagnostics

An alarm service performs the collection, analysis, distribution, definition, and archiving of information about abnormal situations, fault states, either to dedicated alarm consoles, running in the control room, or to specific applications.

The alarm system does not actually detect the fault states. This is done by user surveillance programs (agents), which run either on the front-end computers in the alcoves or on central servers on the surface and has been demonstrated on the LHC and its injectors [320].

The controls infrastructure of CLIC has to span large distances and is based on heterogeneous equipment, all of which needs to be constantly monitored. The purpose of the diagnostics and monitoring is to provide the operators and equipment groups with tools to monitor the accelerator and beam controls infrastructure with easy-to-use first-line diagnostics, as well as to solve problems or help decide on responsibilities for the first line of intervention.

5.13.6 Machine timing

The sequencing of 50 Hz cycles and important actions within them is controlled by a central timing facility. This system receives ‘legal’ time from a traceable source such as a GPS Disciplined Oscillator (GPSDO) and broadcasts it, along with other events of interest, to a set of event receivers distributed along the accelerator. The event receivers are available in different form factors to suit the needs of each subsystem, and are able to produce pulses to synchronize hardware and interrupts to the host for real-time task synchronization.

In addition, these event receivers also have the capability of time-tagging pulses for diagnostics purposes. The operators receive a more abstract view of the overall sequencing thanks to application software which translates between the different operational processes and the actual events on the timing link.

5.13.7 Data management services

Data management is fundamental to the operation of the accelerator complex throughout its full life cycle from design to dismantling [321]. Various types of data have to be covered by services that include data flow, data persistence, data processing, program and human interfaces to the data, verification and quality of the data.

Two categories of data management services can be distinguished, namely to handle configuration data and logging data [312]. All data that needs to be gathered and stored for the operation of CLIC can be categorized as configuration or logging data. As the requirements and characteristics are very different, they drive the choice for the supporting technical infrastructure and implementation. Table. 5.86 illustrates the main differences between the two data categories.

Table 5.86: Differences between configuration and logging data.

	Configuration data	Logging data
Purpose	Use an information model that reflects reality as close as possible so as to correctly exploit the installation	Keep track of live data over time for online monitoring and offline analysis and correlation
Data model	Complex/very complex model with 100 interdependent entities with many relations, constraints, and data-centric business logic	Simple time-series or event-based model (time, ID, value), the data type of the logged value may be complex
Data evolution	Quite static, slow data modifications (updates); the actual values have the highest importance; a history of the value updates ensures a heuristic approach; Total volume < 10 GB	Very dynamic with a continuous growth of data adding by data (inserts, no updates); Total yearly volume > 100 TB (i.e., 2011 scale for LHC operation)
Data criticality	Ranging from low for offline equipment installation data to very high for online accelerator parameter settings data; the integrity of the data is essential	High criticality, especially for the online usage of correlated measurement data during beam commissioning and beam operation; the correctness of the data is not guaranteed by the service

Within each of these two data categories, several logical data domains are to be covered. The ones that are listed below are directly linked to the operation of the accelerator installations.

5.13.7.1 Configuration data

Since the information needs to represent correctly the reality of the described data domain, a relational database management system is used for the data foundation. The following list contains the data domains of configuration data that have to be covered, as is already the case for the existing accelerator installations throughout the world.

Installation layout

This data domain concerns logically identified components of the accelerator that are installed and positioned. The domain scope includes the equipment on and around the beam path, as well as the related systems such as remote controls electronics and electrical powering circuits.

Controls configuration

Both the hardware and software configuration of the controls system are covered by this data domain. The full topology of the hardware infrastructure allowing remote command of all controllable devices, sensors and actuators, through the different layers and communication mechanisms is described and used by the software. All software instances from high-level applications to front-end processes are parameterized, deployed and scheduled for their specific purpose. The ensemble of this data domain

enables efficient and secure remote control of the accelerator equipment and particle beams.

Settings of operational parameters

This domain concerns the run-time settings of operational parameters that are applied to the accelerator at a moments time. The parameters can be at the level of an individual controllable device or a higher-level collection or aggregate. A history of these settings is essential to revert a parameter or a set of parameters to a previous working point of operation.

5.13.7.2 Logging data

The individual channels for which data is logged need to be described. Their configuration may include the details of the software components of the data acquisition chain. Computational and correction algorithms may complement the metadata in order to render the logged data in a specific required format.

The estimated number of data acquisition channels for a 50-kilometre-long CLIC installation is in the order of 6 million. Several systems such as RF and beam instrumentation read out at 50 Hz, corresponding to the basic cycle of CLIC. Some of this distributed information must be combined, processed, and fed back into actuators for adjustment of the consecutive cycle. In order to verify the correct functioning of the accelerator systems and the expected behaviour of the beams, most of this information needs to be stored for a certain period of time and scrutinized.

Given the fact that certain acquisition channels are able to distinguish individual particle bunches, the raw data rate, which can be read out and is eligible to be stored, exceeds 100 GB per second. It is also anticipated that global or local data snapshots of systems or subsystems be taken and stored, following interlocking events. The overall yearly data is in the exabyte range (i.e., millions of terabytes). Despite the evolution of information technology and supporting hardware, all raw data cannot be kept indefinitely. Consequently, different periods of data retention need to be defined, each with a higher level of averaging of the raw data. Overall data reduction should roughly be three orders of magnitude to reach annual volumes in the petabyte range. These amounts of data can still be managed and used for correlation, statistics and analysis work on a continuous basis.

The input–output mechanisms and storage media have to be tailored and tuned to high-performance data transfer. Therefore, a data model without the overhead of explicit object relationships and integrity constraints is more appropriate for logging data.

5.13.8 Conclusions

The CLIC project comprises several different accelerators, each of which needs a solution for controls. This complex of accelerators resembles the present scheme at CERN for the LHC and its injector chain. Hence a control system as a scaled version of the present LHC system can be envisaged. The basic functionality of a three-tier system has to be provided and the solutions for the front-end computers following the industrial standards available at the time of construction.

An exception to this general solution is the acquisition and control of the two-beam acceleration modules in the Main Linac. For this several challenges will have to be addressed as technology develops over the next few years:

- The scale of the 3 TeV CLIC machine requires an unprecedented amount of controls equipment to be installed within a limited space and under radiation constraints. For each of the 20 924 CLIC two-beam modules (see Table. 5.46) an acquisition and control module (ACM) chassis will be installed, which contains 10–20 electronics modules. This gives a total of between 100 000 and 200 000 individual electronics modules. An enormous industrialization and procurement effort is required to produce and deliver such a quantity of electronic cards.

- The tunnel of the CLIC Main Beam is a very hostile environment for electronics. We propose to separate the data acquisition from the data processing by installing Acquisition Control Modules (ACM) very close to every CLIC two-beam module. This a new and, and yet un-tested, concept for an accelerator control system front-end.
- From simulations, the radiation levels in the CLIC Main Beam tunnel are one or two orders of magnitude higher than in the LHC. Even by removing most of the electronics from the tunnel, it is not clear at the present moment that the ADC cards installed in the ACMs can survive the estimated annual absorbed dose rate of 1000 Gy/year.
- Another major challenge is to limit the amount of heat given off by the ACM into the tunnel. Over the next few years, various low-power solutions will be studied as will the possibility of switching off the ACM between beam-pulses.

5.14 Fine time generation and distribution

5.14.1 Background

The goal of a timing system is to provide a common time reference in a distributed environment. This reference is usually the result of counting ticks of a clock signal from an arbitrary instant. The clock signal, $a(t)$, is ideally of perfect periodicity and stability. Real-world clocks, however, present imperfections [322] in both amplitude and phase as expressed in Eq. 5.40.

$$a(t) = A(1 + \alpha(t)) \sin(\omega t + \varphi(t)) \quad (5.40)$$

where ω is the angular frequency of the clock signal.

Amplitude noise can often be controlled through hard amplitude limiters or automatic gain stages. These signals do not suffer from amplitude modulation, $\alpha(t)$, so we will ignore the $\alpha(t)$ term from now on. The random variations in the zero-crossing of the pseudo-periodic signals arise from the $\varphi(t)$ term, usually called phase noise. Ignoring amplitude modulation, Eq. 5.40 can be re-written as

$$a(t) = A \sin\left(\omega \left(t + \frac{\varphi(t)}{\omega}\right)\right) \quad (5.41)$$

showing that the $\varphi(t)/\omega$ term, which has dimensions of time, represents the time deviations in zero-crossing between the perfect and the imperfect periodic waveforms. Here $\varphi(t)$ is a random signal whose rms value is in principle a good indicator of clock quality. Dividing that r.m.s. value by ω gives the clock jitter. Phase noise is important because this imperfect clock is typically distributed to many receivers, where local counting is done and the common time reference is generated. In order to compensate for delays in cables and fibres, a constant correction is applied to the local time base, but this assumes the clock is a perfect copy of itself at intervals of T , where T is any multiple of the clock period. If this is not the case, as in all real-life clocks, the delay compensation mechanism does not fully achieve its goal.

5.14.1.1 Phase noise and jitter

Unfortunately, all clocks ultimately diverge in phase and even frequency, in such a way that the r.m.s. calculation of jitter increases as the averaging time grows. In order to tackle this problem, it is useful to work in the frequency domain. The Fourier transform of $\varphi(t)$, noted $\Phi(f)$ has the same energy as the time-domain signal. This result, expressed mathematically in Eq. 5.42, is known as Parseval's theorem [323].

$$\int_{-\infty}^{+\infty} |\varphi(t)|^2 dt = \int_{-\infty}^{+\infty} |\Phi(f)|^2 df \quad (5.42)$$

The units of the left-hand side (LHS) of Eq. 5.42 are rad^2s . A real-life signal would be bounded in time. If we call $\varphi_T(t)$ a signal which is non-zero only between times $-T/2$ and $+T/2$, its Fourier transform is

$$\Phi_T(f) = \int_{-T/2}^{+T/2} \varphi_T(t) e^{-j2\pi ft} dt \quad (5.43)$$

Re-writing Eq. 5.42 with the truncated signal and dividing both sides by T we have

$$\frac{1}{T} \int_{-T/2}^{+T/2} |\varphi_T(t)|^2 dt = \int_{-\infty}^{+\infty} \frac{|\Phi_T(f)|^2}{T} df \quad (5.44)$$

Since the LHS of Eq. 5.44 is clearly a measure of the power of the signal, the term $\frac{|\Phi_T(f)|^2}{T}$ on the RHS can be interpreted as a Power Spectral Density (PSD). In fact, the Wiener–Khinchine theorem

[324] tells us that

$$S_{\varphi}^{II}(f) = \lim_{T \rightarrow \infty} \frac{1}{T} |\Phi_T(f)|^2 \quad (5.45)$$

where $S_{\varphi}^{II}(f)$ is the two-sided PSD of the random process $\varphi(t)$. Multiplying by two, we get the one-sided PSD which is the most usual measure of oscillator phase noise. It is also customary to average m finite-time measurements to get an approximation of the one-sided PSD

$$S_{\varphi}(f) \approx \frac{2}{T} \left\langle |\Phi_T(f)|^2 \right\rangle_m \quad (5.46)$$

Taking the square root of Eq. 5.44 we would have the phase noise r.m.s. value, and dividing the result by the nominal frequency gives the jitter. The problem is that increasing the integration limits results in an increasingly larger measured jitter.

In real life, however, an application is only sensitive to jitter generated between two finite limits in the PSD curve. Figure 5.321 shows a typical plot of a one-sided PSD ($S_{\varphi}(f)$) of the phase noise for an oscillator. Integration limits are set between f_L and f_H . Phase noise below f_L corresponds to variations which are so slow as to be common mode for all timing receivers under all circumstances. For example, for a machine with a repetition rate of 50 Hz such as CLIC, phase noise below say 1 mHz will give an almost constant contribution during the 20 ms cycle and therefore will not affect the performance of the timing system. In addition, it is estimated that all perturbations below 5 Hz in Fourier frequency can be dealt with by appropriate inter-pulse feedback strategies. Reasons for establishing an upper limit in integration stem mainly from the inability of some systems to react to such fast variations, i.e., to limitations in bandwidth. These limitations can be in electronics, such as the bandwidth of the input stage of a digital gate, or in electromechanical systems such as an RF accelerating cavity. It is important to justify lower and upper integration limits for a given application based on both requirements and an intimate knowledge of the system.

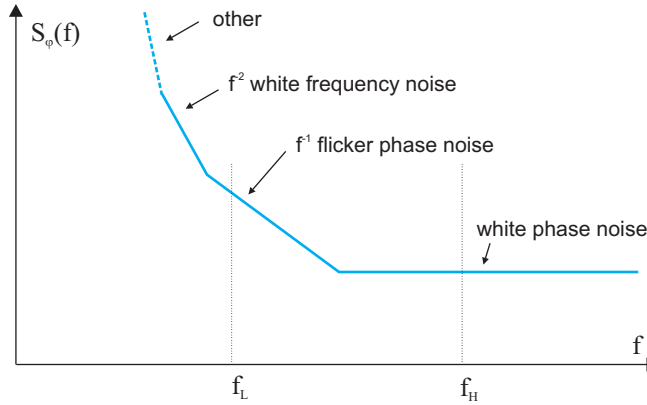


Fig. 5.321: One-sided PSD of phase noise for a typical oscillator.

Figure 5.321 also illustrates different types of noise, which can be identified by the different slopes of their PSDs in a log–log graph [322]. White phase noise dominates the high frequency area and has a flat distribution. Moving towards lower frequencies, we find flicker (pink) phase noise, which is characterized by a PSD scaling as f^{-1} . Since frequency is the derivative of phase, white frequency noise — arising from white noise in the frequency-setting elements of an oscillator — features an f^{-2} slope in the phase noise PSD diagram. Higher order f^{-n} terms can also be present. This low-frequency area of the graph will feature quick divergence under integration, and corresponds to the problematic long time-spans mentioned earlier for the time-domain representation.

5.14.1.2 Phase-locked loops

Phase-locked loops [325] are an invaluable tool in cleaning up the jitter of clocks, among many other possible applications. Figure 5.322 depicts their internal structure.

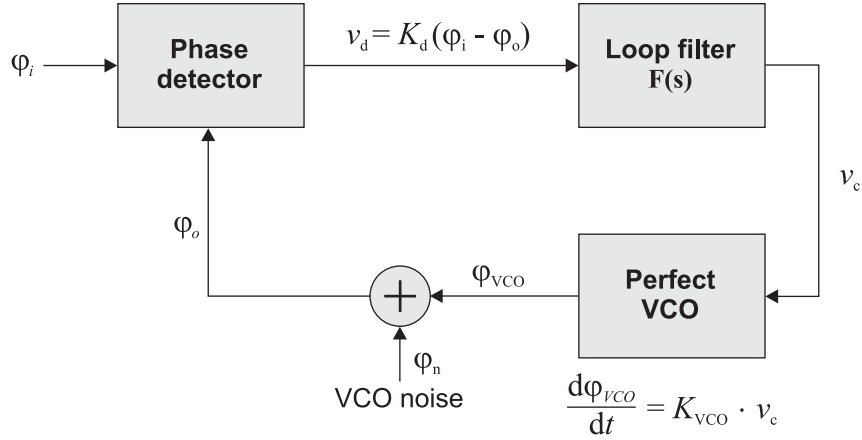


Fig. 5.322: Block diagram of a phase-locked loop.

The phase detector block generates an output voltage v_d proportional to the phase difference between the input and output of the PLL. In Laplace space, its output is therefore

$$V_d(s) = K_d (\Phi_i(s) - \Phi_o(s)) \quad (5.47)$$

The next block after the phase detector is the loop filter, which outputs the control signal for the Voltage-Controlled Oscillator (VCO)

$$V_c(s) = F(s) \cdot V_d(s) \quad (5.48)$$

The VCO outputs a signal with a frequency proportional to its input voltage. Since frequency is the derivative of phase, this means that the phase of the signal at the output of the VCO is proportional to the integral of the VCO control voltage

$$\Phi_{VCO}(s) = \frac{K_{VCO} \cdot V_c(s)}{s} \quad (5.49)$$

Since there are no perfect VCOs, we have included a VCO noise source in the diagram, contributing phase ϕ_n . Calculating the output phase ϕ_o from the two sources in the diagram (reference input phase ϕ_i and VCO phase noise ϕ_n) again in Laplace space gives

$$\Phi_o(s) = H(s) \cdot \Phi_i(s) + E(s) \cdot \Phi_n(s) \quad (5.50)$$

where $H(s)$ is called the system transfer function, defined as

$$H(s) = \frac{K_{VCO} K_d F(s)}{s + K_{VCO} K_d F(s)} \quad (5.51)$$

and $E(s)$ is the so called error transfer function, defined as:

$$E(s) = 1 - H(s) = \frac{s}{s + K_{VCO} K_d F(s)} \quad (5.52)$$

In typical clock-cleaning applications, $H(s)$ is a low-pass filter, while $E(s)$ is high-pass. Cut-off frequencies are dictated by PLL parameters, and most importantly the loop filter $F(s)$. The PSD of the

phase noise of φ_i will be filtered by $|H(s)|^2$ while the phase noise PSD of the VCO will be filtered by $|E(s)|^2$. This means that the low frequency noise in the PSD of φ_o will come from the reference φ_i and the high-frequency noise will come from φ_n . The transition from one noise source to the other will be at a frequency determined by the loop parameters. After careful study of the PSDs of φ_i and φ_n it is the task of the designer to choose a cut-off frequency that will minimize the overall area under the φ_o PSD curve, and consequently the time-domain jitter. In typical systems — like the transmission of a very stable clock over a channel which adds high-frequency noise — the VCO is worse than the reference at low frequencies and better at high frequencies. The point in frequency where the two PSD plots (reference and VCO) cross is in that case an optimum setting for PLL bandwidth, as shown in Fig. 5.323.

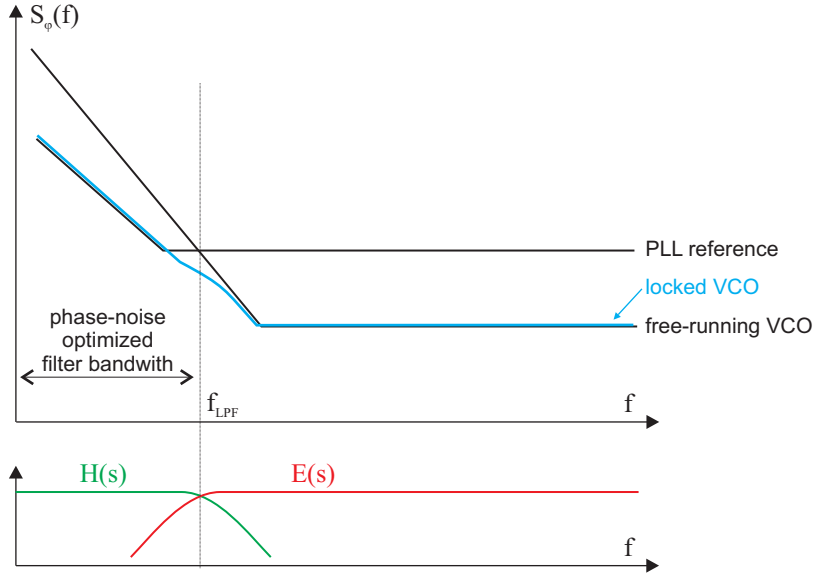


Fig. 5.323: Optimal choice of PLL bandwidth for jitter-cleaning applications.

In Fig. 5.322 the phase detector is shown as perfect, with no noise added to it as for the VCO. In practice, phase detector noise is also a concern, but mathematically it is equivalent to reference noise, so that the above formalism can be applied, replacing reference noise by reference plus phase detector noise.

5.14.2 CLIC timing requirements

The main requirements in terms of clock signal distribution come from three subsystems: the Low Level RF control for the Drive Beam, instrumentation for the Main Beam, and the two-beam acceleration scheme. The following paragraphs examine each one separately. The conclusion is that CLIC will need the distribution of precise clock signals at the level of some tens of femtoseconds of jitter over different bandwidths.

5.14.2.1 Drive Beam RF system requirements

In Ref. [326] the jitter of the 1 GHz field in the accelerating cavities of the Drive Beam is specified as 50 fs integrating between 5 kHz and 20 MHz. It is also said that with appropriate feed-forward control in the Main Beam, this figure could be relaxed by a factor of 10. However, the reference phase noise fed to the LLRF system is only responsible for a small percentage of the final jitter in the electromagnetic field. Taking this contribution to be 10% results in a specification of 50 fs for the jitter of the reference clock signal distribution to each one of the 326 accelerating structures in each linac.

5.14.2.2 Beam instrumentation requirements

Longitudinal profile monitors could be based on distributed lasers and changes in optical properties of bi-refractive materials induced by the Main Beam. These monitors have the task of measuring 150 fs bunches with a resolution of 20 fs [327]. The precision required from the clock signal, which allows the synchronization of the lasers with the beam, would therefore be in the few tens of femtoseconds, integrated between 5 Hz and a few hundreds of kHz (the bandwidth of the PLL locking the laser to the reference).

5.14.2.3 Two-beam acceleration system requirements

The two-beam acceleration scheme in CLIC requires a very precise synchronization between the Drive Beam and the Main Beam. Figure 5.324 depicts a possible synchronization solution. A controller measures the phases of the Drive and the Main Beam with respect to a reference line, and uses that information to control the amplitude of a kicker pulse which modifies the trajectory of the Drive Beam in order to keep it well synchronized with the Main Beam. The required precision of this alignment is around 40 fs [328], so the timing reference precision clearly needs to be better than that. The bandwidth of the kickers, in the several MHz region, would set a natural upper limit for integration of phase noise.

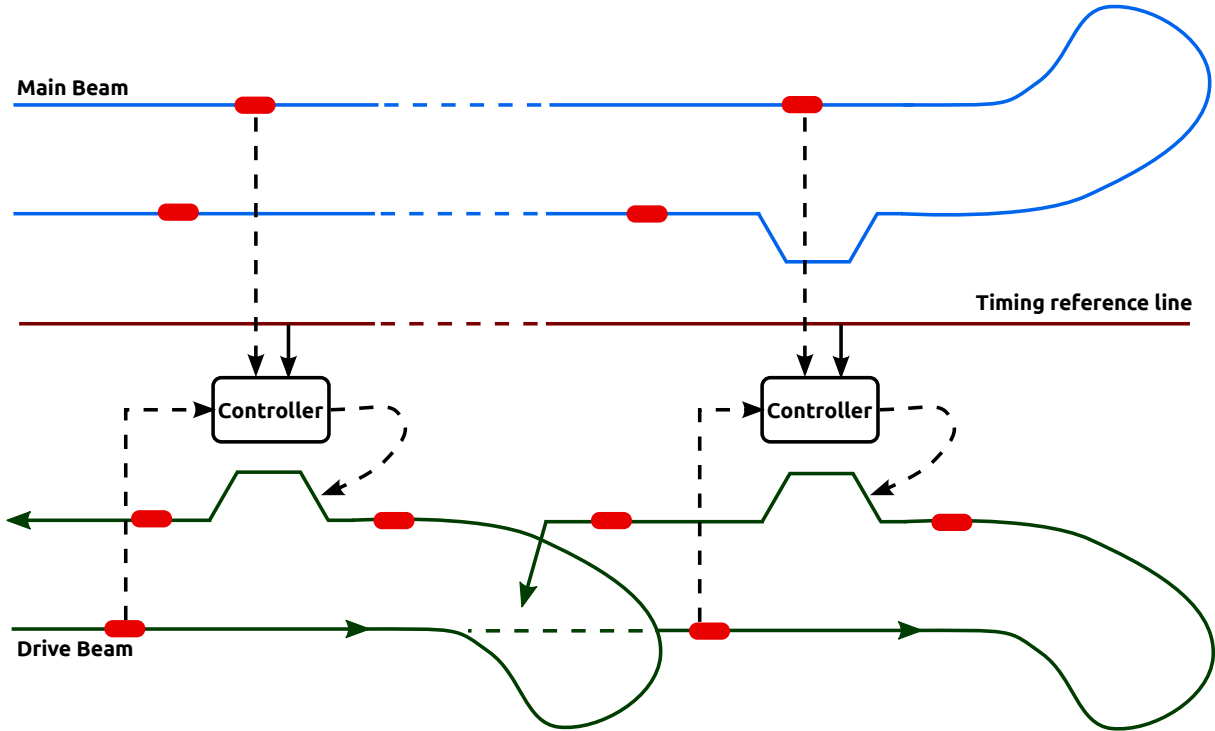


Fig. 5.324: Timing reference line usage for inter-beam synchronization (adapted from Ref. [328]).

5.14.3 Technical description

This subsection describes the two main types of solutions currently developed and tested for the distribution of precise timing signals in the femtosecond realm [329]. Both types have achieved synchronizations better than 20 fs over distances of several hundreds of metres.

5.14.3.1 Continuous wave systems

Figure 5.325 shows a simplified view of a system based on a Continuous-Wave (CW) laser modulated in amplitude by the RF or microwave signal to be transmitted. A fraction of the light reaching the destina-

tion bounces back from a Faraday Rotator Mirror (FRM) and is, in the process, shifted in frequency by 100 MHz using a Frequency Shifter (FS). Another FRM reflects a sample of the light signal as it leaves the source. These two signals, upon mixing together, produce a beat at 100 MHz whose phase can be easily measured. The key feature of this system is that the heterodyning process preserves phases, so a phase shift induced in the optical frequency by a change of length in the fibre will show up as exactly the same phase shift at the RF (100 MHz) frequency, which is much easier to measure. Once the phase of the beat signal is detected, it can be used to digitally shift the phase of the recovered RF signal at the receiving end of the link. It is important to note that what is really measured in this method is the phase delay, not the group delay of the modulation which is ultimately what we are interested in. In order to compensate for group delay, a first-order correction — based on actual measurements of a given fibre type for a range of temperatures — is applied to the raw phase delay measurements.

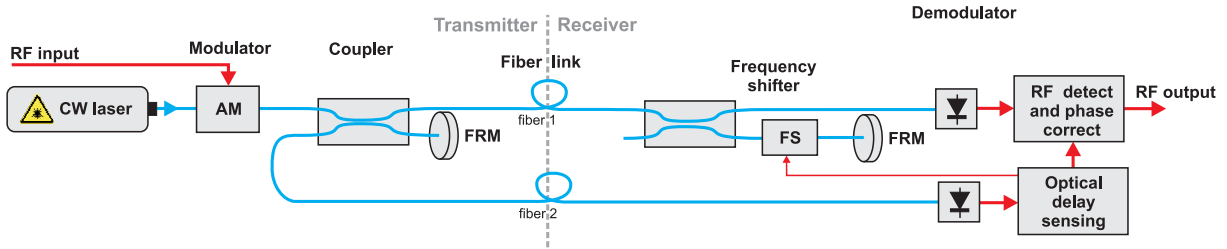


Fig. 5.325: Continuous-wave system for femtosecond timing distribution (simplified).

5.14.3.2 Pulsed systems

In the pulsed system depicted in Fig. 5.326, a mode-locked laser is synchronized with the external RF signal, which determines its repetition rate. Narrow light pulses come out of the laser and travel through a dispersion-compensated fibre to the receiver, where a fraction of the light is reflected back towards the emitter. An optical cross-correlator measures the degree of coincidence of the two pulse trains and the result is used to control a piezo actuator that changes the fibre length so as to keep a constant group delay. This mechanical actuator is unavoidable because the cross-correlator needs the pulses to overlap, at least partially, in order to give a meaningful reading. On the other hand, the pulsed system controls group delay directly, so no *ad hoc* conversion between phase delay and group delay is needed.

5.14.4 Technical issues

Both types of systems have been successfully deployed over distances of several hundred metres, so the 25 km needed by CLIC is unknown territory. In the case of the CW system, one potential source of concern is the need for a model of phase-group delay corrections vs. temperature. If the temperature is not uniform over the complete length of the fibre, as can easily be the case in CLIC, a solution will need to be found.

Another potential issue is Brillouin scattering, a non-linear effect which is especially strong in optical fibres, due to the large optical intensities in the fibre core. Brillouin scattering in fibres leads to a limit of the optical power which can be transmitted, since above a certain power threshold, most of the light is scattered or reflected. This is especially a problem for narrow-band optical signals, and for long fibre lengths. In the pulsed system, Brillouin scattering is not much of an issue, since the power spectral density, which is the important quantity, is much smaller than for narrowband CW systems.

Synchronization of lasers with the optical reference is another field which needs further work. Currently, only synchronizing with an RF signal has been tested, but an all-optical system would be much more precise and avoid the extra optical-electrical conversion. On the optical source side, it is important to find lasers with a coherence length which will allow efficient stabilization on a 25-km fibre link.

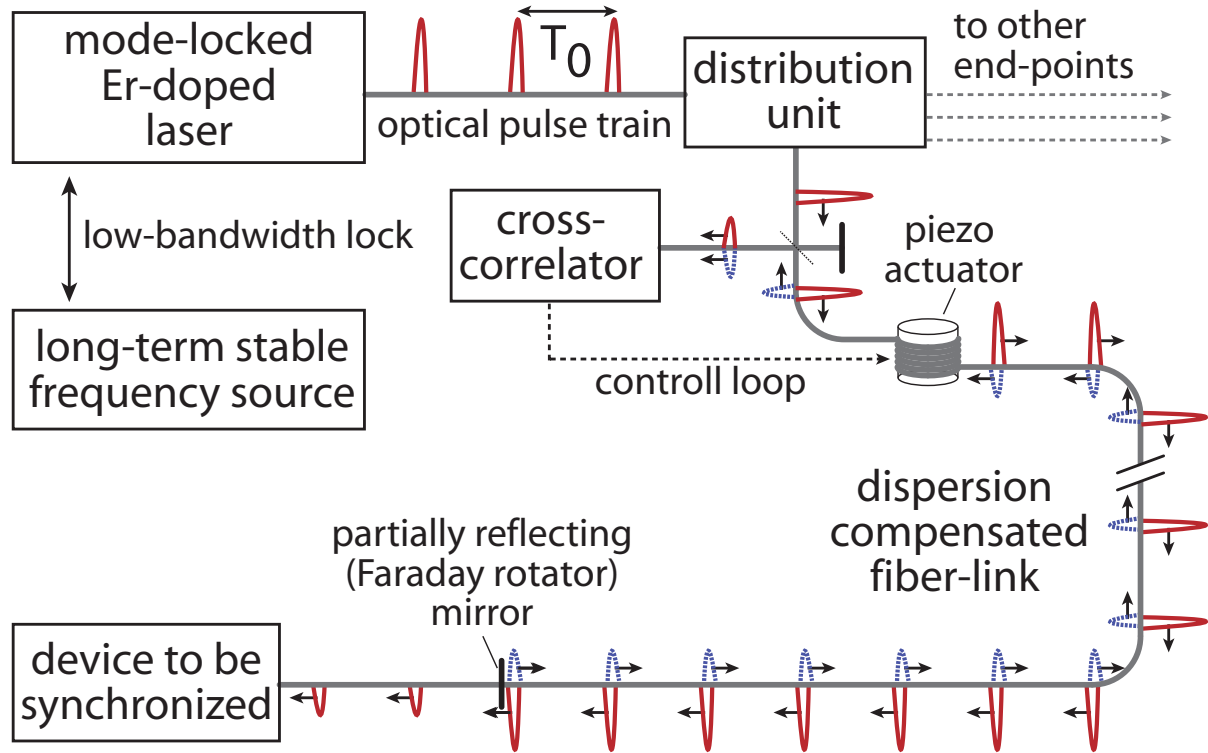


Fig. 5.326: Pulsed system for femtosecond timing distribution (courtesy of F. Loehl).

For the pulsed system, a major difficulty will be the dispersion control of the optical fibres, as the fibre length increases. Additional problems due to nonlinearities are not expected to be any more significant than with shorter fibre links.

Another major difficulty in both schemes will be Polarization Mode Dispersion (PMD), which can deteriorate the long-term timing stability especially for long link-lengths. The polarization state of light transmitted through a single mode fibre changes constantly, due to birefringence in the fibre. The larger this bi-refringence, the larger the propagation delay difference between the two polarization modes. Since the pulses or the CW light travel in different polarization states on both ways through the fibre, the travel times for both ways are unequal. The fibre bi-refringence and therefore the polarization state of the light further changes with temperature, which has the consequence that even if the light propagation delay for one round-trip is stabilized, the timing at the end of the link still shifts, since the propagation delays for both directions change in different ways.

Finally, one very important difference between the solutions currently deployed and the CLIC scenario is the scale of the project. Current implementations do not scale very well beyond some tens of destinations. This is mainly due to the number of ports typically available in optical components, such as splitters/combiners. For CLIC, one of the challenges will be to explore in detail the real needs of each destination and come up with a strategy for partitioning the system in such a way that a reasonable compromise between performance and cost can be found.

5.14.5 Cost considerations

The typical cost of an individual link is not very high. But taking into account the hundreds of destinations needed in CLIC, it is very important to carefully study ways in which costs can be reduced. CW systems have fewer opto-mechanical components and therefore have, in principle, the potential to be more cost-effective, but this remains to be studied in detail. Irrespective of the technology used, one important aspect which can have a major impact on cost is whether the CLIC synchronization system

can be partitioned into several loosely-coupled subsystems.

5.14.6 Outlook for project preparation phase

As can be seen from the previous discussion, there are many open questions which remain to be answered:

- The most important challenge is to make the existing solutions work with fibre lengths of around 25 km. This will involve work on the coherence length of laser sources and also an investigation of the problems induced by Brillouin scattering at high optical powers. A demonstrator of each technology needs to be built before an optimal decision can be taken for the best compromise between price and performance;
- Synchronizing remote lasers with the general timing system also needs to be investigated further, especially if an all-optical system is to be considered. In relation to this investigation, arrival-time monitors need to be studied since they are the most important diagnostics tool required to achieve good timing stability;
- A detailed study on the partitioning of the timing system among its different clients would potentially allow several semi-independent systems and have an important impact on costs. This study should be combined with an investigation of ways to extend the number of links supported by current solutions.

5.15 Real-time feedback equipment

5.15.1 Overview and background information

At CLIC, real-time feedback techniques will have to be used to achieve the very tight requirements related to controlling parameters of the different particle beams for all those cases where the requirements can not be met by the design of the appropriate equipment. Three accelerator systems for which the tolerances cannot be met uniquely by today's engineering techniques have been identified and are described in detail in the following sections:

- The stabilization of the Main Beam trajectory in the CLIC Main Linac
- The intra-train alignment of the vertical positions of the two Main Beams at the Interaction Point
- The time synchronization between the Main Beam and the different Drive Beam trains.

The time synchronization between the two Main Beams could also be the object of a real-time feedback system, in addition to a 'slow' feedback correction from one pulse to the next, which will be implemented anyway. Such a feedback would require a unique 'femto-second' precision global timing system covering the entire CLIC infrastructure; however it remains to be seen if such a system is needed, if it is feasible, and if its cost can be justified by its benefits. Technical details are described in §5.14

Any feedback system comprises three main elements: measure what happens, compare with what should happen, compute and apply corrections. The goal of this section is to describe the feedbacks listed above.

5.15.2 Stabilization of the beam trajectory in the CLIC Main Linac

5.15.2.1 Ground motion

Without any counter-measures, ground motion (GM) would be a severe problem for the operation of CLIC as it displaces the components of the beam-line relative to one other. The most affected components are displaced quadrupoles (QPs), which add dipole fields to the usual QP-fields and deflect the beam. As a result, the beam trajectory can oscillate along the beam-line. Such oscillations result in two problems at the interaction point (IP): beam size growth and beam-beam offset, both of which lead to luminosity decrease. In general, lower GM frequencies ($< 1\text{--}4$ Hz) tend to induce beam size growth, while higher frequencies are responsible for jitter-like beam-beam offsets.

Much work has been done in the last decades to measure and model ground motion properties. For CLIC two types of model are used. For short time-scales (up to one minute) the models of Ref. [330] and slightly modified versions are used. Ground motion on longer time-scales is modelled with the ATL law [331]. Ground motion is dealt with in greater detail in §3.8.

Ground motion mitigation

In order to suppress the ground motion induced effects, one passive and four active mitigation systems are planned (see Fig. 5.327).

- **Beam trajectory feedback** aims to steer the beams into the reference trajectory of the beam position monitors (BPMs). To accomplish this task the QPs are used as corrector magnets by moving them mechanically. This is achieved by the positioning capabilities of the stabilization system (see §5.17). Because of the beam repetition rate of 50 Hz, the sampling rate is fixed for the trajectory feedback. This limitation causes this feedback to be effective largely for frequencies below 1–4 Hz. The trajectory feedback is therefore only efficient at reducing beam size growth and slowly changing beam-beam offsets.

One severe technical problem of the correction of the beam trajectory by moving the quadrupoles is the offset of the Beam Position Monitors (BPMs). The BPMs are mechanically fixed to the

yoke of the quadrupoles and hence they move with the magnet. This means that through the control system the knowledge of the displacement of the quadrupole before the last beam pulse has to be used to correct the new readings of the BPMs. This can be made to work technically, but since the requested resolution of the BPMs is of the order of 50 nm, a large residual of the quadrupole movement might remain in the readings. For this reason a solution with small dipole correction coils is studied, but this leads to integration problems. Either one has to give up some longitudinal space for these correctors or accept a magnetic interference of these corrector dipoles with the quadrupoles. Currently we retain as baseline the steering of the trajectory by moving the quadrupoles.

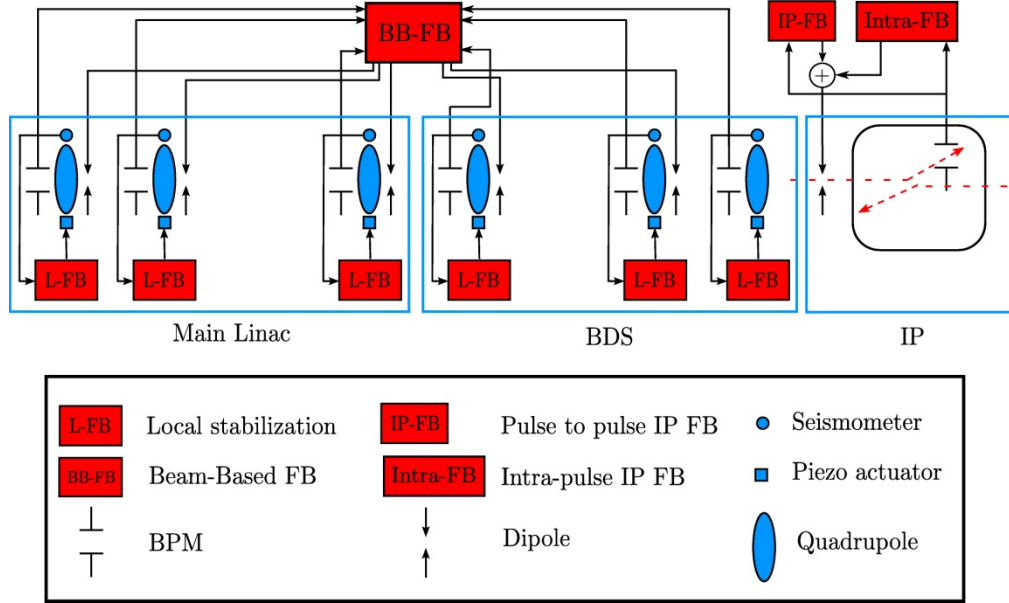


Fig. 5.327: Overview of the different systems to counteract ground motion effects, along the main linac and BDS of CLIC

- **Local stabilization system.** In order to suppress frequencies in the 5–100 Hz range, each quadrupole is equipped with a local stabilization system. This active feedback system uses the signals measured by a seismometer on top of the QP to compute, via a control algorithm, appropriate output signals that are applied to an actuator consisting of two to six legs per QP, depending on the QP weight. By changing the length of these legs via piezo-actuators the associated QP can be positioned in x and y . More details are given in §5.17.
- **IP feedback.** If two beams collide at the IP with a transverse offset, the outgoing beams receive a kick, due to the beam–beam interaction. This additional kick changes the trajectory of the beam in the post-collision line, which can be measured by dedicated BPMs. For small enough beam–beam offsets the kick angle is a roughly linear function of the beam–beam offset and provides the input to the so-called ‘IP feedback’, which calculates and applies a correction to a kicker located about 3.5 m upstream of the IP. Since the IP feedback has the same sampling rate as the beam trajectory feedback, the beam–beam offset will only be reduced for frequencies $< 1\text{--}4$ Hz. More details about the IP feedback are presented in §3.8.
- **Mechanical pre-isolator** of the final doublet quadrupole. The beam–beam offset at the IP is by far most sensitive to the vertical position of the final doublet QPs of the BDS. Even though the IP feedback reduces the beam–beam offset for low frequencies the high-frequency beam–beam offset induced by the offset of the FD is not acceptable. To counteract this problem a passive mechanical pre-isolator is used. It consists of a heavy concrete block supported by metal beams.

This huge mass-spring system significantly reduces the high-frequency components of the beam–beam offset. The mechanical pre-isolator is the only ground motion counter-measure not depicted in Fig. 5.327. More details are given in §5.12.

- ***Intra-train feedback*** is able to act within the bunch train length of 156 ns. It uses the same BPM as the IP feedback and is explained in more detail later.

Integrated simulations

To evaluate the ability of the five counter-measures to preserve the luminosity of CLIC in spite of ground motion, a full-scale simulation framework was set up. This framework includes a ground motion generator based on the models of ref. [330], beam tracking performed by the tracking code PLACET, and luminosity calculation with the simulation software GUINEA-PIG. Apart from the intra-train feedback all counter-measures described above are included in the simulations. The trajectory feedback and the IP feedback are implemented with the help of the octave interface for PLACET. The stabilization system and the mechanical pre-isolator are taken into account by modifications of the ground motion generator. The simulations aim to show the luminosity preservation up to one minute. Results of these integrated simulations are given in §3.8.

5.15.2.2 The proposed trajectory feedback system

The trajectory feedback takes the beam positions measured in the 2122 BPMs and calculates displacements for 2104 QPs, in order to steer the beam back onto the reference trajectory of the BPMs. Apart from the two QPs of the FD (QF1 and QD0), all QPs are used as actuators. The use of nearly all QPs as correctors ensures that the residual beam excursions are kept to a minimal level. Since the beam travels through the beam-line in trains with a separation of 20 ms, the sampling time of the system is fixed. The maximum frequency that can be resolved is 25 Hz. Since Nyquist’s theorem for discrete systems limits the magnitude of the controller transfer function for frequencies close to this 25 Hz, fundamental limitations are imposed on the performance. The effects of ground motion can only be suppressed for frequencies below 1–4 Hz, while frequencies above will be amplified. The suppressed, low frequencies contribute more significantly to a beam size growth, while the amplified higher frequencies result in jitter-like beam–beam offset. Therefore the main goal of the trajectory feedback is to counteract the beam size growth due to ground motion whilst amplifying beam jitter as little as possible. The design of the trajectory feedback is optimized in order to reduce the effect of BPM measurement noise, whilst correcting most ground-motion-induced beam oscillations efficiently.

An overview of the system structure is given in Fig. 5.328. The variable k is used as the time index and $1/z$ represents the unit time shift operator of the z -transform. The z -transform is the equivalent of the Laplace transform for discrete-time systems. The function between the magnetic centres of the QPs m_k and the BPM measurements y_k in the accelerator can be modelled via the orbit response matrix R . Since the beam produces a BPM measurement every 20 ms, the accelerator model also contains a shift operator. In principle, the steering of the beams is a straightforward task. The reference trajectory r_0 has to be subtracted from the BPM measurements to obtain an error vector. This error vector has to be multiplied with the pseudo-inverse of R ($R^{-1} = V\Sigma^{-1}U^T$) in order to reconstruct the beam oscillation that requires QP movement. This anticipated QP movement has to be subtracted from the actuator setting u_{k-1} (integrating behaviour of $g(z)$). However, BPM noise n_k does not permit such a simple feedback solution. Instead time-dependent and directional filters have to be used to reduce the influence of BPM noise.

Every matrix can be split up by the singular value decomposition (SVD) algorithm into three matrices containing input (ground motion) and output (BPM signals) directions (columns of the matrices V and U), and the corresponding singular values (diagonal elements of the matrix Σ). BPM noise can be reduced by mode weighting in the diagonal matrix F . Another advantage of the SVD decomposition is

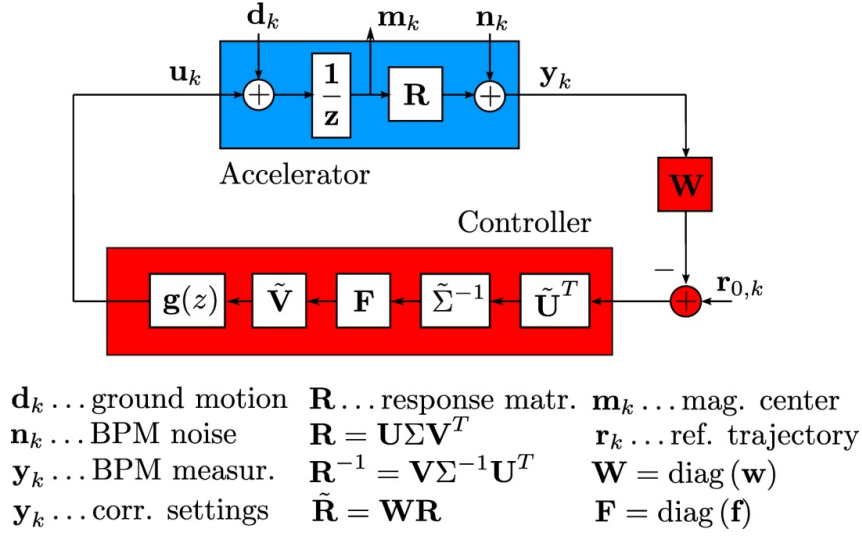


Fig. 5.328: Block diagram of the accelerator model and the controller structure of the trajectory feedback

the decoupling of the controller design. Each singular value and the associated ground motion and BPM direction corresponds to one feedback loop, which is independent of the other loops. The feedback design can therefore be reduced from one big system with 2104 inputs and 2122 outputs to 2104 independent feedback loops with one input and one output [332].

In order to further reduce noise a second weighting, the so-called BPM weighting, is introduced. The basic controller would act on all BPM readings in the same way. However, simulations have shown that BPM readings in the BDS have a higher significance for the associated luminosity loss. Hence the beam steering should be tighter in the BDS than in the rest of the machine. To accomplish this, the BPM readings are multiplied with a weighting function (diagonal matrix \mathbf{W}), that amplifies BPM readings from the BDS. Consequently, the necessary matrices for the trajectory controller have to be generated from the SVD of the augmented orbit response matrix $\tilde{\mathbf{R}} = \mathbf{W}\mathbf{R}$. Therefore, the matrices $\tilde{\mathbf{U}}$, $\tilde{\mathbf{\Sigma}}$ and $\tilde{\mathbf{V}}$ are used in the control algorithm instead of the original matrices \mathbf{U} , $\mathbf{\Sigma}$ and \mathbf{V} .

The feedback algorithm also includes frequency-dependent filters $g(z)$. Each element of the signal vector generated by the directional noise filter is connected with one individual filter $g(z)$ of the same type. The basic element of $g(z)$ is a simple discrete integrator, which adds up the necessary QP movements calculated by the directional filter. Additional filters are added to improve the BPM noise suppression, increase the stability margins of the feedback algorithm, and to advance the ground motion rejection for certain frequency ranges [333].

5.15.2.3 Further improvements

While for relatively short time-scales (a few minutes) a constant and known system model is a valid assumption, variations of accelerator systems can cause degradation of the feedback performance for longer periods of operation. In particular the trajectory response matrix \mathbf{R} of the main linac can change significantly due to drifts of the acceleration gradients. To counteract this gradually increasing mismatch between the system model and the real system behaviour an on-line system modelling tool was developed. It uses methods from system identification theory to estimate the time-varying response matrix, without stopping physics operation. This estimate is an important input for the feedback algorithm as well as for diagnostic tools. Modifications to the standard algorithm have been made to address the special nature of the main linac of CLIC.

5.15.3 The intra-train alignment of the vertical positions of the two Main Beams at the Interaction Point

A fast beam-based intra-train feedback (FB) system is foreseen to correct for the relative vertical displacement of the colliding beams at the IP by steering them back into collision. This FB system can be considered as the last line of defence against relative beam–beam offsets, and it may also help to relax the tight vibration tolerance of the QD0 quadrupoles. Intra-train FB is especially challenging at CLIC due to the extremely small bunch separation of 0.5 ns and bunch train length of only 156 ns. With current technology one cannot apply bunch-to-bunch corrections, but can only make a few correction iterations per train by using an all-analog FB system. No intra-train angle FB system is currently planned due to latency time constraints.

The key components are a beam position monitor (BPM) based on stripline pickups for registering the position (and hence deflection angle) of the outgoing beam; a front-end signal processor and feedback circuit; an amplifier to provide the required output drive signals; and a kicker for applying an angular correction to the opposite incoming beam. The BPM and kicker locations are shown in Fig. 5.329. The same hardware can be used to provide both the pulse-to-pulse IP feedback and the intra-train feedback.

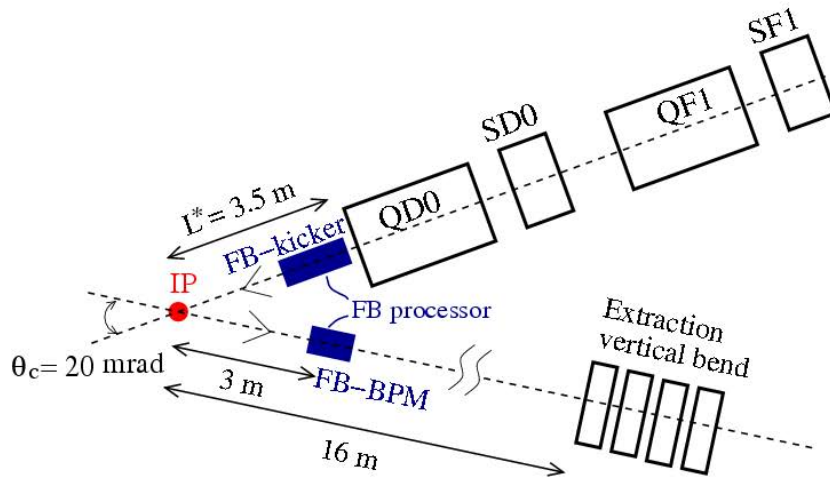


Fig. 5.329: Equipment location for IP and intra-pulse collision feedbacks

The functional layout of the components is shown in Fig. 5.330. Such a system would be deployed (to provide backup) on both sides of the IP. Details of prototype components and system tests with real beams are given in Ref. [334]. For this layout the total latency, due to beam time of flight and hardware delays, can be kept to 37 ns or less [335]. This allows for approximately three luminosity correction cycles during the bunch train duration, as shown in Fig. 5.331. This example corresponds to a simulation based on a single random seed of (very noisy) ground motion for the element misalignments in the BDS, and considers a perfect linac. A detailed description of the potential luminosity recovery performance is given in Ref. [335].

Prototypes of the BPM, signal processor, feedback circuit, kicker, and drive amplifier have been developed and tested with beam by the FONT collaboration [334, 336–338]. Key parameters are the latency of the components, which impacts upon the luminosity recovery potential, and the drive power of the amplifier, which determines the angular deflection that can be given to the beam. It is assumed that a short (~ 10 cm long) stripline BPM will be used to provide a fast-input beam position signal, and a short (~ 25 cm long stripline) kicker will be used to provide the correcting beam angular deflection. These are compact, intrinsically fast, high-bandwidth components of ‘standard’ design. Actual devices

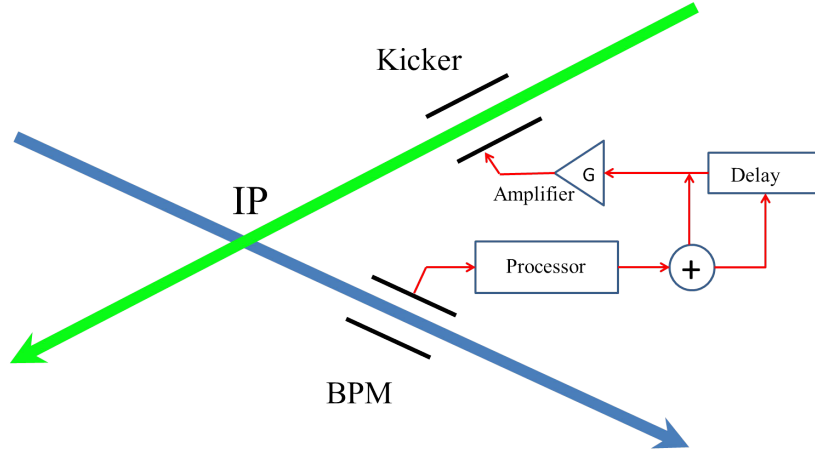


Fig. 5.330: Schematic layout of the IP feedback components

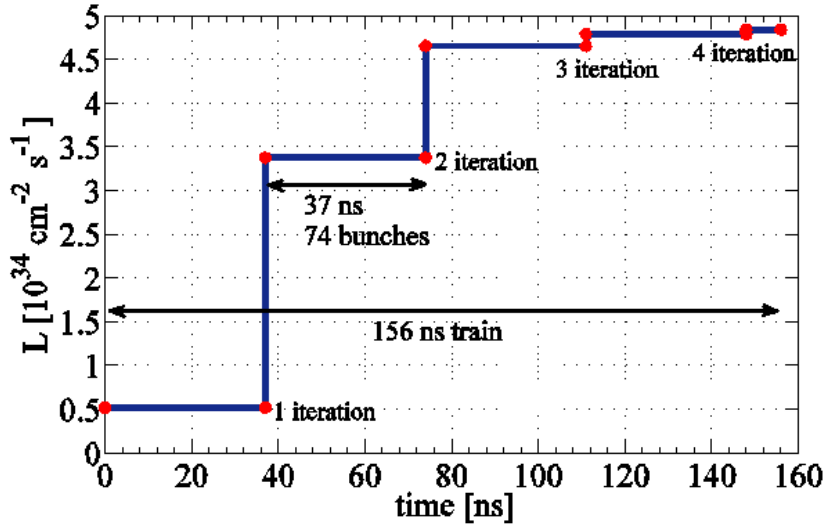


Fig. 5.331: Simulated luminosity versus bunch number for nominal CLIC 3 TeV parameters with intra-train bunch feedback 'ON'

with geometries optimized for the tight space constraints of the CLIC IR will need to be engineered as the IR design evolves. For the layout shown in Fig. 5.329, with the BPM and kicker located approximately 3 m from the IP, the beam round-trip time of flight delay is about 20 ns.

A prototype BPM signal processor has been designed (Fig. 5.332), with micron-level resolution, and a latency of 5 ns has been demonstrated [334]. A high-power kicker drive amplifier that meets CLIC requirements has been built (see Fig. 5.332) and tested with beam at ATF [338]. In order to optimize the latency the feedback circuit was integrated into the amplifier board; a combined (feedback circuit + amplifier + kicker rise-time) latency of 8 ns was measured [338]. Assuming these demonstrated prototype latencies yield a total system latency of 33 ns. For the FB performance simulations described in §3.8.4.1 a latency of 37 ns was assumed, which allows an extra 4 ns of delay, for additional cabling and/or adjustment of the electronics location near the IP. With further optimization of the component locations and cabling, and development of faster electronics, the latency might be reduced to 30 ns.

5.15 REAL-TIME FEEDBACK EQUIPMENT

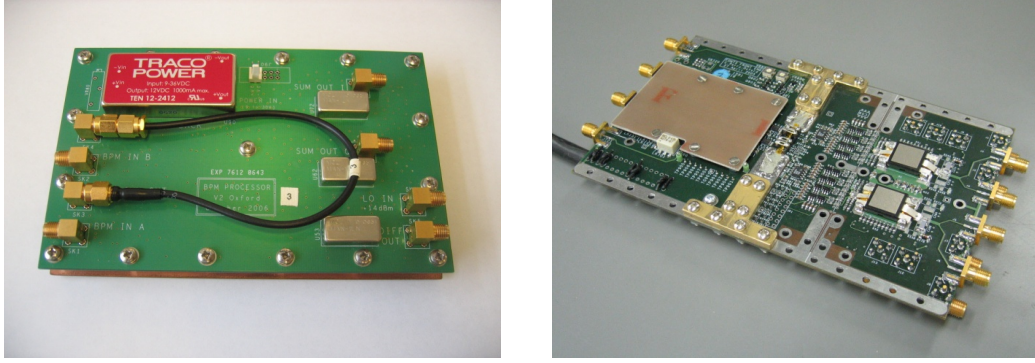


Fig. 5.332: Prototype modules for the IP Feedback system: a BPM signal processor (left) and an integrated feedback circuit and drive amplifier (right)

5.15.4 Time synchronization between the Main Beam and the different Drive Beam trains

5.15.4.1 Introduction

In order to be accelerated efficiently by the field in the RF cavities, the Main Beam should reach the cavities at the right phase of the accelerating field. If the phase is wrong, the Main Beam will not be accelerated properly, and as a consequence its emittance will blow up, and the luminosity will be reduced. A phase error of more than 0.2° (equivalent to 46 fs, or to $14\ \mu\text{m}$ for a beam travelling at the speed of light) would reduce the luminosity by more than 1%. Much effort will be expended in the design and implementation of the Drive Beam linac (modulator stability, klystron stability, low level RF, magnets) to obtain an intensity and phase stable Drive Beam. For the overall phase stability of the Drive Beam, missing the requested stability by less than a factor 10 seems feasible (see Chapter 4). The target for the feedforward system described below is therefore to control and correct in real-time the synchronization of each Drive Beam train with respect to the Main Beam to better than 46 fs, i.e., covering the missing order of magnitude in stability with a feedforward.

This feedforward will be implemented at each Drive Beam turnaround. The working principle is as follows; the Main Beam will be used as overall timing reference. For this the arrival time (or, better, the phase) of the outgoing Main Beam will be measured (by a special ‘Phase Monitor’ BPM) at each turnaround of the Drive Beam. The time will be measured by a high-precision oscillator, capable of keeping the information until the corresponding Drive Beam pulse arrives at the same location. In the worst case this time interval corresponds to almost twice the travel time of the Main Beam through the whole linac. The phase of the Drive Beam will be then measured by a second phase monitor located before the Drive Beam turnaround. The difference between the phase of the Main Beam and the phase of the Drive Beam train will be used to determine the power to be provided to a system of Beam Trajectory correctors, capable of modifying the path length of the Drive Beam train along the turnaround, hence adjusting the phase of the Drive Beam to the Main Beam to the required value. The system should be completed by at least two other phase monitors, located just before the entrance of the RF structure, in the Main Linac and in the decelerator respectively. The phase monitor installed on the Main Beam line will be used to verify if the distance covered by the Main Beam from the first BPM to the end of the Main Linac and back is the same as was used to compute the reference value (or if the reference itself has to be modified). The phase monitor installed on the Drive Beam line will also be used to cross-check the validity of the feedforward correction. Figure 5.333 illustrates the proposed feedforward and its components. One of the requirements of this feedforward is to be able to compensate phase variations inside the Drive Beam pulse, to make the phase of the pulse entering the decelerating structure as homogeneous as possible. So the Phase Monitor should be able to continuously measure the phase of a sliding fraction (typically 10–20 ns long) of the Drive Beam, and generate and send a continuously changing correction which will be applied to that part of the Drive Beam. The assumption has been made that the phase of the Main

Beam does not change significantly inside the Main Beam pulse (i.e., that the different bunches which constitute the Main Beam pulse are equidistant). If this was not the case, the feedforward correction would not be effective.

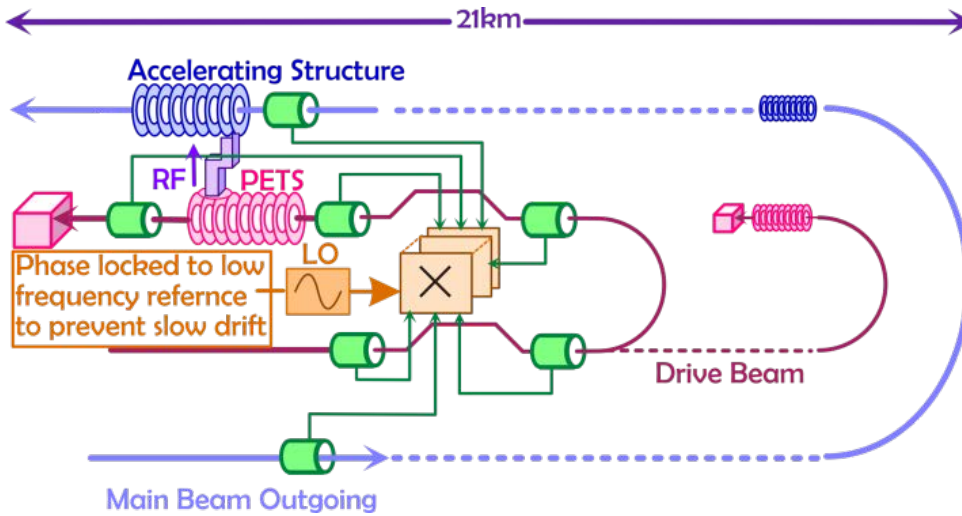


Fig. 5.333: Overall CLIC layout and the placement of the detectors (green cylinders) in the turnarounds.

5.15.4.2 Phase monitor

Requirements:

- high resolution (about 1/10 of a degree at 12 GHz or 20 fs);
- rejection, by means of properly designed filters, of RF noise and weak fields that may be generated elsewhere by the beam;
- very low coupling impedance, to avoid problems coming from interaction with the high beam current;
- adequate bandwidth to enable correction up to the bandwidth of the accelerating structures.

The Drive Beam can be expected to excite a variety of modes during its transport. These modes will travel down the beam pipe, and could pollute the signal from the phase monitor. A set of notch filters at both sides of the monitor will reflect these unwanted fields. These notch filters are implemented as bumps in the beam pipe. Their geometry is tuned to reject all possible propagating modes in the frequency range of interest. The RF design of an assembly with several independent notches is underway. By placing the notch filters an integer number of half-wavelengths apart, a resonant volume for the operating TM01 mode is also established (See Fig. 5.334).

This beam-induced signal is coupled out of the beam pipe through four slots placed symmetrically around the beam pipe circumference. The slot cut-off frequency is above 12 GHz in order to ensure only a weak coupling of the generated fields. The field intensity in each slot can be tuned by adjusting the slot thickness (d) (See Fig. 5.335). A waveguide is connected to each slot, followed by a transition to a standard 50 Ω coaxial line, and a commercial vacuum feed-through.

The amplitude of the signal coupled out will depend on the particular distance between the notches. It can vary from zero, if an even number of half-wavelengths is established in-between, to its maximum, if the half-wavelength number is odd. The magnetic field plots in the case of the TM01 mode is illustrated in Fig. 5.336.

This effect has been used, on the one hand, to minimize the amplitudes of the unwanted (TE11 and TE21) modes as much as possible, and on the other hand to maximize the amplitude of the useful TM01

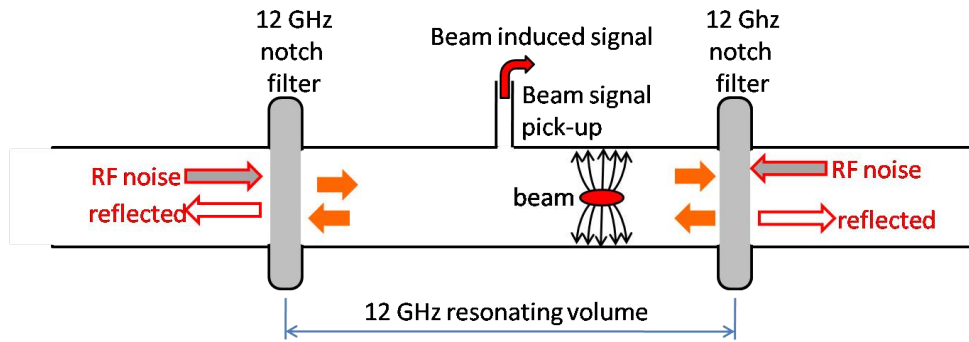


Fig. 5.334: Schematic of a pick-up with filters for noise rejection

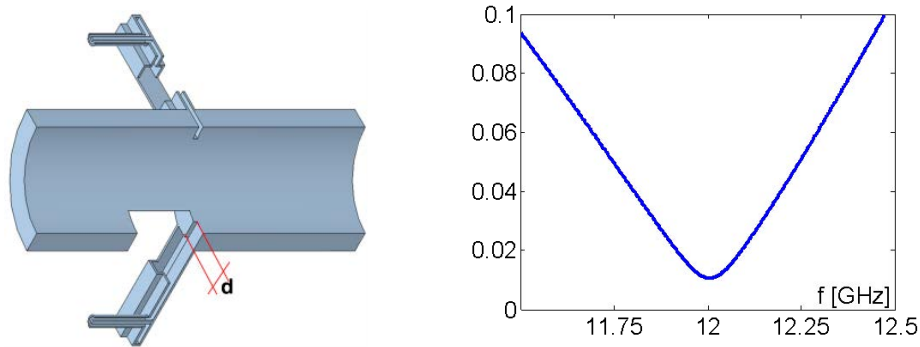


Fig. 5.335: Geometry of the pick-up (left) and the reflection frequency response of the waveguide to coaxial transition (right)

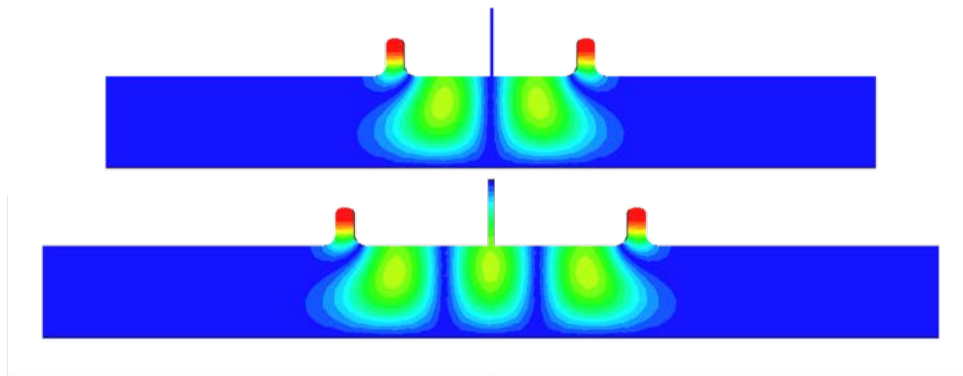


Fig. 5.336: Resonating modes in the volume between the notches: $n=2$ (top) and $n=3$ (bottom)

mode. Simulations of such a geometry yield typical values of $Q = 7000$ and $R = 60 \text{ k}\Omega$ for a structure built of aluminium. The requirements for time-sampling resolution (detector bandwidth) and restrictions on RF power extractions require the reduction of both these values.

To do that, a few methods can be used:

1. If the structure is built of stainless steel, both the Q -factor and the impedance can be reduced by about a factor of six;
2. Coupling the resonating fields to the special external loads, or increasing the coupling to the pick-up waveguide network.
3. Appropriate changing of the distance between the notches.

In the last case, the resonant frequency of the TM01 mode is shifted to where the notch filters have lower rejection, and the fields are thus less sharply contained in the notch delimited volume. Further, the frequency of maximum impedance is also shifted and the amount of extracted beam power is reduced. The pick-up impedance spectra for the cases with no coupling (solid lines), with coupling ($\beta = 5.6$ at 12 GHz) to the waveguide (dashed lines) together with the filter rejection response (solid red line) are shown in Fig. 5.337.

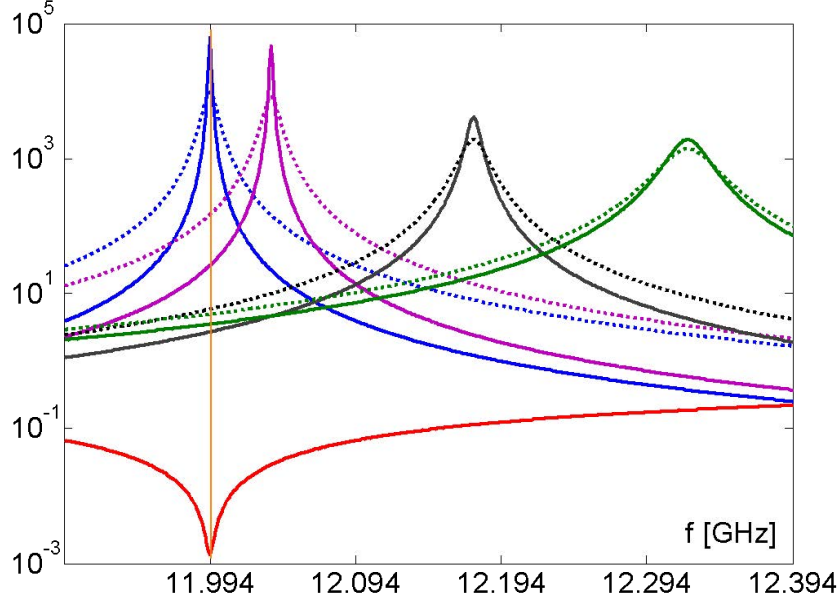


Fig. 5.337: Different cases of monitor shunt impedance (vertical scale in Ω) and notch frequency response

5.15.4.3 Detection electronics

In order to achieve the required very high resolution of this monitor, the design of the detection electronics is vital. Additionally, a very stable phase reference is required. Precision oscillators have been found which have less than 5 fs integrated timing jitter. Much progress has been made on femto-second stabilized reference lines in the last few years, in the context of XFEL construction. These links have been demonstrated over about one kilometre, but the possibility of extension over 24 km from the central distribution point cannot yet be inferred. However, for CLIC, the physical layout of the accelerator allows for an alternate phase reference, using low phase noise local oscillators, synchronized to the outgoing Main Beam rather than a central timing reference (see Fig. 5.333). The time between the passage of the outgoing Main Beam and the arrival of the Drive Beam (and the Main Beam again) is at most $160 \mu\text{s}$. In Fig. 5.338 the effects of beam path filtering on the LO jitter are presented. Fig. 5.339 shows more technical details characterizing the electronic circuits for phase detection.

For the signal detection itself, the performance is limited chiefly by device non-linearity and noise. While device non-linearity typically decreases with lower input power, the noise will increase relative to the signal. To mediate between these two conflicting goals, a strategy of parallelization will be used. The input signals from both the local oscillator and phase monitor will be split N ways, and detected on N mixers. The baseband signals will then be added together to increase the signal-to-noise ratio. As we are mixing directly to baseband, the dominant non-linear term will be the second-order term which mixes to DC, and which will thus be indistinguishable from the phase term. As this second-order term is proportional (in mV) to the square of the input amplitude, we must pick an operating point where its contribution is small enough, and then parallelize over enough devices to bring down the noise.

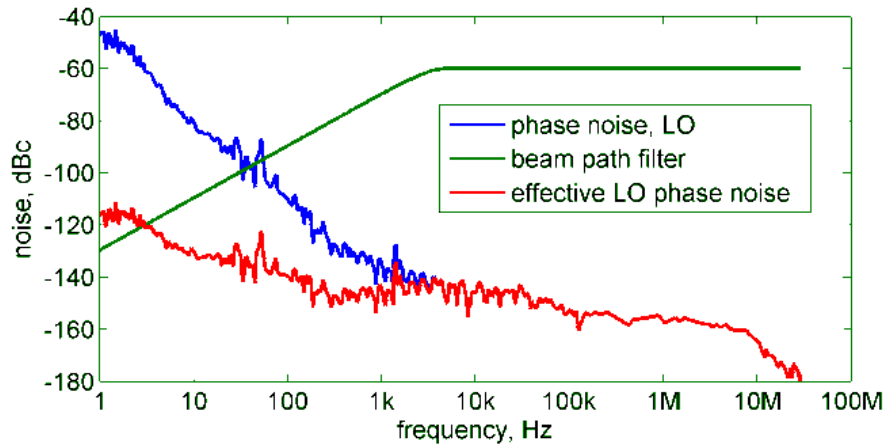


Fig. 5.338: Oscillator timing jitter and beam path filtering

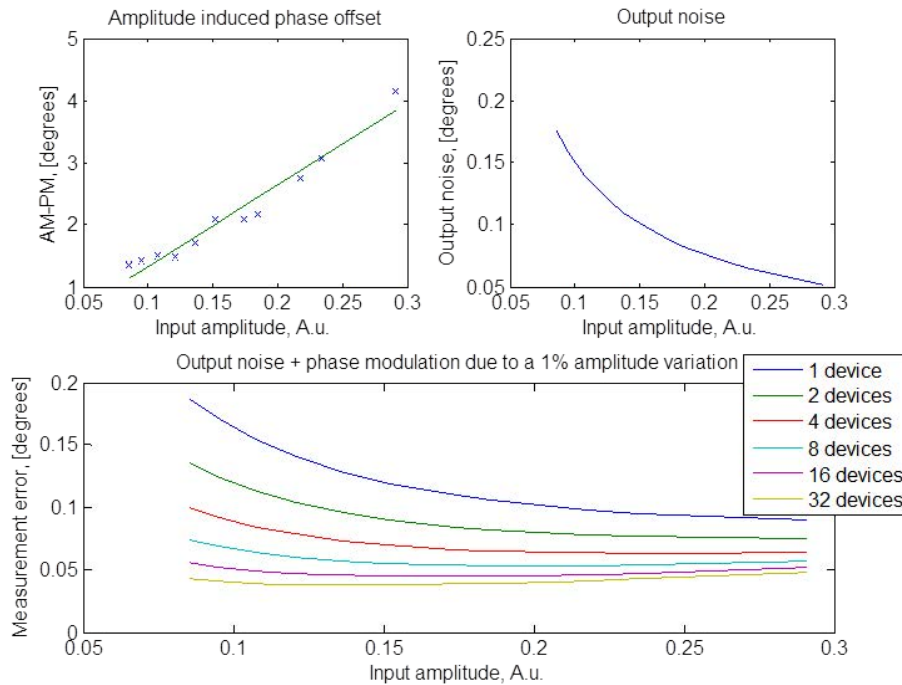


Fig. 5.339: Mixer linearity measurements, noise, and use of multiple devices

Detection electronics based on a similar approach were already produced some years ago with 30 GHz RF and a wider detection bandwidth.

5.15.4.4 Correction: conceptual system design

Here we describe the system which will be used to adjust the length of the Drive Beam trajectory in the turnaround. A schematic view of the system is shown in Fig. 5.340. The assumed specifications are:

- Required kick angle at each bend: $\pm 375 \mu\text{rad}$, spread over four kickers, with one amplifier per kicker. This yields 16 amplifiers per Drive Beam, i.e., 768 amplifiers in total.
- Stripline kickers with an active length of 1 m and a clear aperture of 50 mm. The aperture requirement is based on a 0.5% r.m.s. energy spread, and a 1 m dispersion, yielding a 5 mm r.m.s.

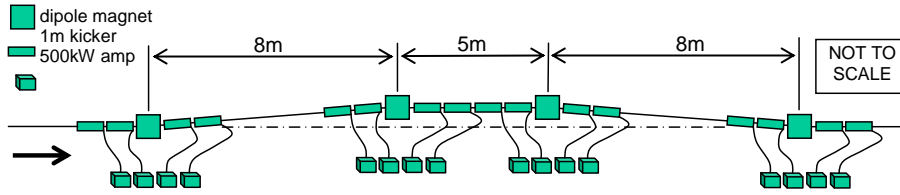


Fig. 5.340: Conceptual layout of kicker/amplifier system in the drive beam turnaround chicane

spread to the beam width in the middle section of the chicane. (This 5 mm aperture only allows for $\sim \pm 4\sigma$ transmission and either the lattice design or the kicker aperture may need to be adjusted accordingly.)

- These parameters yield a peak amplifier power of ~ 410 kW which, allowing some margin (e.g., for a slightly higher energy spread than assumed), brings this to around 500 kW. (This requirement could be reduced if full kick at full bandwidth is found not to be essential.)

5.15.4.5 Amplifier design

We assume the following parameters for the amplifier specification:

- **Speed: 10 ns:** with bandwidth limitation shared equally between kicker and amplifier. The amplifier bandwidth is split equally between the amplifier modules and the combining system — each needs a 70 MHz bandwidth. Each kicker is connected to its amplifier by a pair of coaxial cables.
- **Amplifier architecture: modular, MOSFET:** this is a standard solution for fast, high-power amplifiers, but the output from many low-power modules will have to be combined. It allows extremely high power densities and (relatively) low cost. Assuming each module provides ~ 1 (or 2) kW, around 512 (or 256) modules would be required to provide ~ 500 kW per amplifier/kicker. An example of a module with the required power and speed is shown in Fig. 5.341 [339]. (Note that vacuum tubes are also capable of the high peak powers and high voltages needed to drive the kickers directly, and should not be discounted.)

5.15.4.6 The case for having an additional absolute timing reference available

If a femto-second global timing system is deployed at CLIC (see §5.14), distributing a precise time reference over the entire 50 kilometres of the CLIC installation, the strategy for synchronizing the Drive Beams trains with the Main Beam will be modified to benefit from this facility. In this case, the arrival times of the two Main Beams, before entering the final turnaround, will be measured and compared with an absolute reference. The difference between the measured arrival time and the expected reference will be used to drive the system which adjusts the Main Beam path length in the turnaround. This adjustment would have to be achieved through a set of amplifiers/kickers similar to the ones described above. The phase of each Drive Beam train entering its turnaround will also be compared with an absolute reference (and not with the arrival time of the Main Beam), and the difference between measured and expected values will be used, as described above, to adjust the Drive Beam path length in the turnaround.

Obviously a combination of both approaches can be used, or one solution can be used to diagnose the performance of the other.

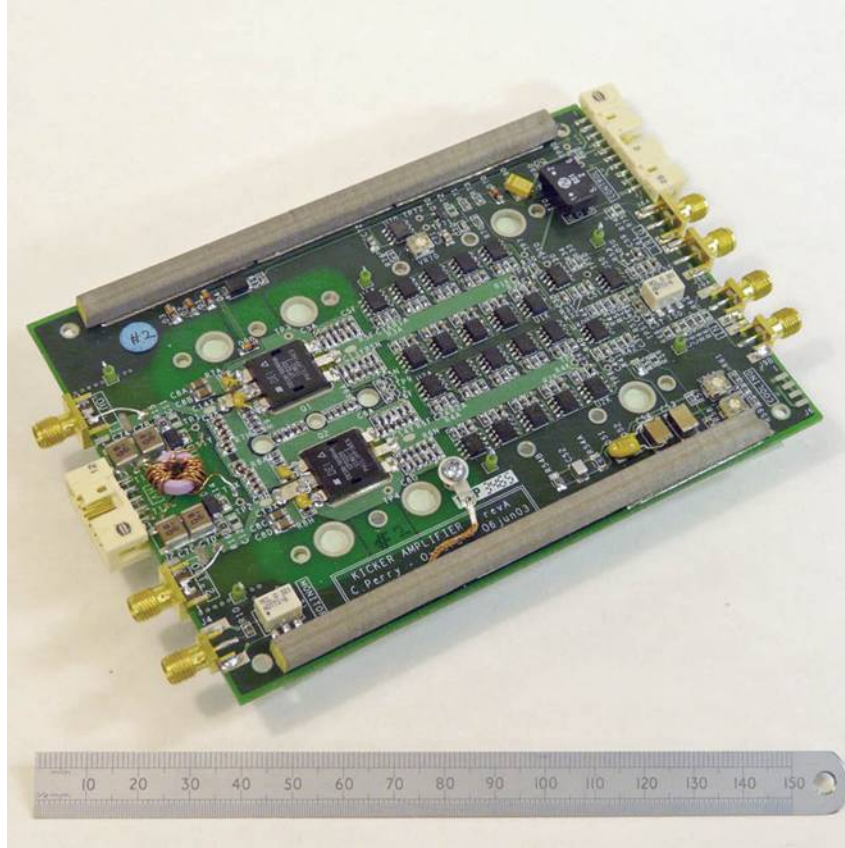


Fig. 5.341: Example of a possible MOSFET-based amplifier module.

5.15.5 Component inventory of all real-time feedbacks

A list of components required for the real-time feedbacks described above are given in Table 5.87.

5.15.6 Outlook for project preparation phase

Among the three topics presented here the last (i.e., the phase synchronization between the Main Beam and the Drive Beam) is the one where the existing CLIC Test Facility at CERN (CTF3) can be used to gain experience in the techniques involved. CTF3 produces a CLIC-like Drive Beam, which is first accelerated by a linac, and then recombined up to a factor 8 and sent into some PETS in the Two-Beam Test Stand (TBTS), where its energy is transferred to an Accelerating Structure and used to accelerate a probe beam. With this setup many quantities can be accurately measured and synchronized, starting with the generation of the two beams, the RF accelerating pulses in the linac, and the Drive Beam behaviour in the combiner ring. This will require the installation of a femto-second timing system and the distribution of its signal over the entire CTF3 site, and the installation of some of the phase monitors as described above. In addition a feedback system, which measures the phase of the Drive Beam in the combiner ring and corrects it in the transfer line towards the TBTS can be envisaged.

Table 5.87: Real-time feedback components

Systems	Number
Beam-based trajectory feedback	
Main Linac BPMs	4018
Beam Delivery System BPMs	226
Correctors (QP stabilization systems)	4208
Central processing unit	2
Communication network	2
IP and intra-train collision feedback	2 systems, one on each IP side
Fast kickers	2
Amplifiers	2
Stripline BPMs	2
Front-end signal processor	2
Feedback electronics circuit	2
Main Beam–Drive Beam feedforward	48 (24×2) systems
Stripline kickers	768 (16×24×2)
Amplifiers	768
Phase monitors	336 (7×24×2)
Precision oscillators	48 (24×2)
Detection electronics units (DEU)	48
Mixers (if 8 per DEU)	384

5.16 Machine protection

5.16.1 Overview

The machine protection for CLIC has to cope with a wide variety of failures, from real-time failures (RF breakdowns, kicker misfiring), to slow equipment failures, to beam instabilities (caused, for example, by temperature drifts and slow ground motions).

Owing to the many different types of accelerator components and the beams of various characteristics throughout the entire complex, the CLIC machine protection is an extensive subject. The machine protection has the mission to protect the various machine components from damage caused by ill-controlled beams. The severity of the damage is given by the financial impact of the damage and the reduction in the operational availability of the facility. The risk equivalent is given by the product of the fault rate and the impact of the fault (i.e., in statistical terms risk is the expectation value of the fault impact). This concept is illustrated by some examples for downtime in Table 5.88.

Table 5.88: Examples of risks

Downtime	Frequency	Risk equivalent (for 6 month running per year)
3 months	1 per 5 years	10%
1 day	10 per year	0.05%
2 years	1 per 10 000 years	0.04%

Special attention should be given to those cases where the impact is high even if the frequency is low, as frequencies of rare events are usually difficult to estimate *a priori*. Furthermore, for very high impact events, also the collateral damage to the Organization itself must be taken into account.

The machine protection system should reduce the risk to a level where the risk becomes acceptable. An acceptable risk can be expressed by the notion that the total expected operational downtime from all risk terms should be smaller than a few per cent and likewise, that the total expected financial impact is also less than a few per cent of the operational cost.

5.16.2 Specific dangers of CLIC beams

5.16.2.1 Beam power and destructive capacity

The beam power — given by the product of the beam charge, the particle energy, and the cycle repetition rate (50–100 Hz) — is impressive both for the Drive Beam (70 MW) and the Main Beam (14 MW) and this makes a sustained disposal of this power such a demanding task. However, for the purpose of the definition of safe beam, the destructive potential is primarily determined by the charge density of the beams. Table 5.89 summarizes various beams: a single (one of 24) Drive Beam Train (DBT), the Main Beam at the extraction septum of the Damping Ring (MB-DR), and the Main Beam at the exit of the main linac, and the Main Beam at the betatron collimation section (MB- β coll). Columns 2–4 show the characteristics of the beam. The next two columns give the energy deposition density (expressed in Jg^{-1}) in copper due to direct ionization loss by firstly the incident beam particles (based on tabular values for minimum ionization multiplied with 1.4 to take into account the relativistic rise), and secondly the shower core particles [340]. The table shows that the effect of the charge density of the incident beam is far more significant than the effect of the shower core. These figures can be put further into perspective by dividing them with the safe beam limit of 77 Jg^{-1} , which corresponds to a temperature rise of 200°C in copper, a value at which copper will structurally fail [341–343]. The last column shows this damage potential for the incident beam and demonstrates that the Drive Beam is over two orders of magnitude

above safe beam, while the Main Beam is around four orders of magnitude above safe beam.

Table 5.89: Beam characteristics and energy density

Beam (see text)	Particle energy [GeV]	Pulse charge [μC]	Beam size [mm^2]	Energy density in copper [Jg^{-1}]		Damage potential
				Incident beam	Shower core	Incident beam
DBT	2.4	25	1	4.8×10^3	40	0.8×10^2
MB-DR	2.8	0.20	125×10^{-6}	3.2×10^5	0.34	0.5×10^4
MB- β coll	1.5×10^3	0.18	40×10^{-6}	9.1×10^5	120	1.5×10^4

5.16.3 Failure types

We distinguish the following types of failure in CLIC.

5.16.3.1 Fast failures

These failures occur at time-scales corresponding to the beam passage through the accelerator complex. Because of the continuous beamline nature, it will be difficult, if not impossible to detect a failure and dump the beam. The major sources of these ‘in flight’ failures are:

- an RF breakdown could potentially produce enough transversal kick to send the Drive Beam or the Main Beam off trajectory into some accelerator component;
- a misfiring of a kicker can send the beam off trajectory into the extraction channel (Here the most critical element is the septum magnet);
- a klystron trip in the Drive Beam linac may potentially disrupt the beam enough to provide large losses. Taking into account the maximum signal distance to the source (~ 1.7 km at $2/3$ the speed of light) and the length of the linac (2.5 km), the Drive Beam linac has potentially the equivalent of three Drive Beam trains in the pipeline; i.e., a beam of more than two orders of magnitude above damage level.

5.16.3.2 Inter-cycle failures

These are mainly equipment failures that happen in the interval between two successive machine cycles (10–20 ms). The major sources of equipment failures are:

- power supply failures,
- positioning system failures,
- vacuum system failures.

5.16.3.3 Slow failures

This last category contains the failures that develop at time-scales larger than the repetition rate of CLIC. These are the failures that cause a slow onset of losses due to drifts in temperature, alignment, or beam feedback saturations. Under normal conditions, the beam feedback system should keep these drifts under control. Any deviation of the expected behaviour should be considered as potentially dangerous.

5.16.4 Protection strategies

The baseline machine protection of CLIC consists of various strategies to deal with each type of failure.

5.16.4.1 Passive protection

For in-flight failures, where detection and beam abort are impossible, the protection will be based on passive protection in the form of masks and spoilers.

The passive protection must be made robust enough to provide full protection for the whole pulse. Many of the systems are already designed along this principle. As an example, the energy collimation is capable of withstanding a full beam impact of the Main Beam in case of an energy error [344].

5.16.4.2 Real-time protection

Where the geometry of the CLIC complex provides the possibility to take a ‘short-cut’ in the signal path, protection in real-time is an option that can be considered. Without detailing them all, the most obvious options are in the rings, the turnarounds, and in the Drive Beam linac (i.e., real-time source inhibit).

For the next design phase a more detailed study will be performed of the failures in the Drive Beam linac in order to determine the need for special, fast devices to dispose of the 140 μ s-long Drive Beam in a safe way.

5.16.4.3 Beam Interlock System (BIS)

In case of an equipment failure during the inter-cycle period, a Beam Interlock System (BIS) will assure that the next cycle is inhibited. Owing to the finite time for detection and treatment, the BIS will handle only failures up to 2 ms before the next cycle is set off. The timeline of the equipment interlock decision is given in Fig. 5.342.

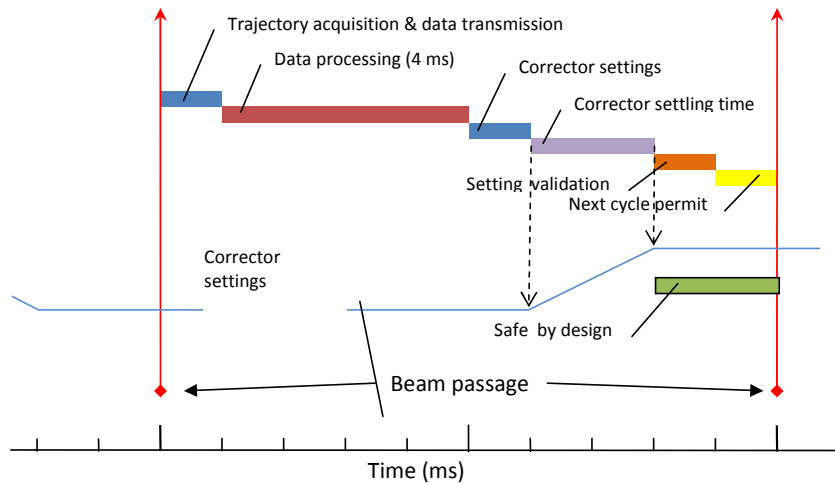


Fig. 5.342: Timeline showing beam passages, trajectory feedback, setting validation and Next Cycle Permit (NCP)

5.16.4.4 Safe by design

To cover the 2 ms blind period prior to the each cycle, all magnet circuits in critical beam transport structures must have enough inertia to remain within tolerance for 2 ms after a power converter fault. Here the required tolerance is determined by a safe passage of the beam. Preliminary studies have shown

that tolerances at the level of $\sim 10\%$ are acceptable, corresponding to magnet circuits with a L/R time larger than 20 ms.

The same principle of fault tolerance must be applied to all active equipment: vacuum, positioning systems, RF-HV, kicker-HV, and any mission critical beam instrumentation.

5.16.4.5 Post-cycle analysis and Next-Cycle Permit

The repetition rate of CLIC allows almost 10 ms to analyse the performance of a cycle and to decide whether it is safe to commit the machine for the next cycle. After every cycle the Next-Cycle Permit (NCP) is systematically revoked and is only re-established if a predefined list of beam and equipment quality checks has been passed. It should be noted that the NCP is not a ‘Yes/No’ decision as it will specify what the allowed intensities are for the various beams in the next cycle (see §5.16.7 below). The timeline of the quality checks and NCP is given in Fig. 5.343.

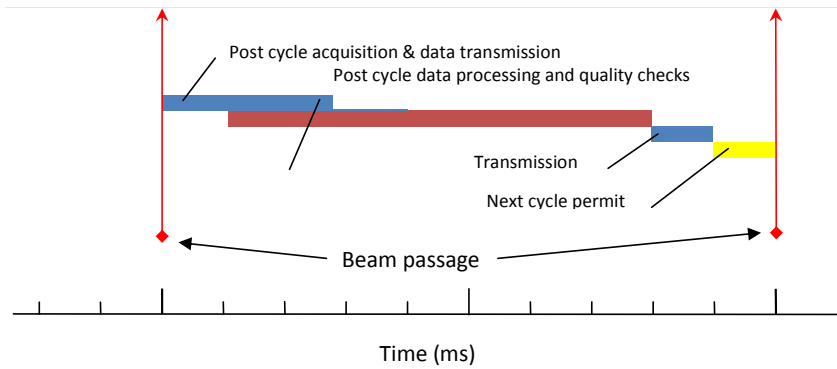


Fig. 5.343: Timeline showing beam passage, post cycle analysis and Next Cycle Permit (NCP)

The reliability of these quality checks, which can be implemented in a combination of hardware and embedded software, should be such that the number of false ‘PASS’ decisions is lower than the requirements from the tolerable risks. The number of false ‘VETO’ decisions should be low enough to limit the impact of the machine protection system on the total availability of the CLIC beam. Strict test procedures must be defined to certify the reliability of the post-cycle analysis. These test procedures must revalidate the system every time a quality check implementation has been modified.

Although the results of all beam observation systems will be scrutinized for abnormalities, the workhorse of the system and the line of last defence for detecting any failure is the beam-loss monitoring discussed in §5.9.7.

5.16.5 Beam Interlock System layout

The schematic layout of the BIS is shown in Fig. 5.344. Conceptually it is based on the BIS used in the LHC [345]. However, in this case there are four interlock chains (i.e., two for the Drive Beams and two for the Main Beams). The interlock chains follow the beam paths in both directions and are connected to a central interlock controller.

5.16.6 Fault analysis

For the technical design of the CLIC machine protection system, a detailed analysis of all failure scenarios will be made in order to estimate the risks and to derive the required reliability of the system components. A full failure catalogue can be established by convoluting the component classes with the full set of failure classes. Combined failure scenarios (e.g., multiple breakdowns, collective power

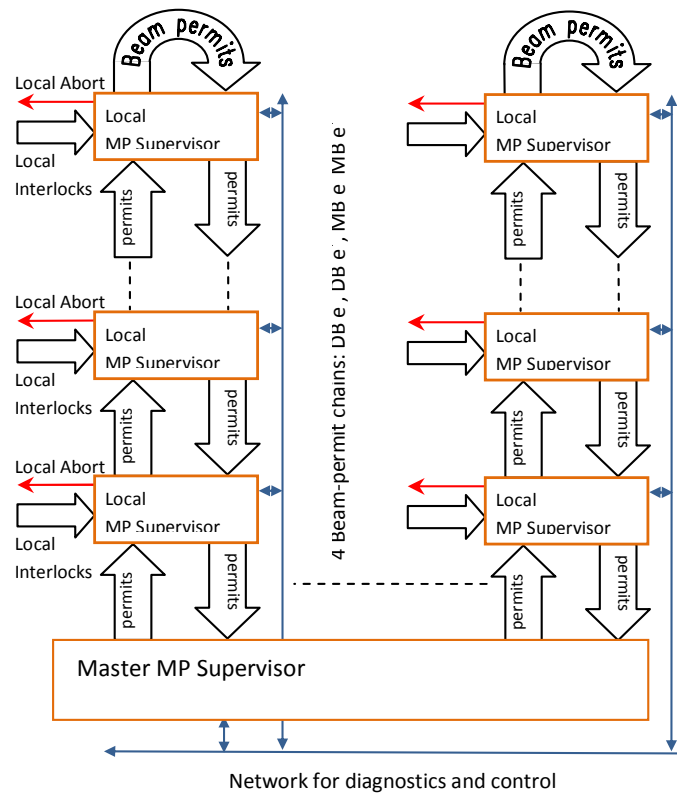


Fig. 5.344: Schematic layout of the Beam Interlock System

converter trips) must be considered as well. For every entry in the failure catalogue, the component multiplicity, expected failure frequency, direct damage, collateral damage and mean time to repair have to be obtained to complete the study. For those cases where the resulting risk is too high, or where the required reliability cannot be obtained, redundant solutions should be implemented.

In addition to aiding the risk analysis, this fault catalogue also forms the basis for the evaluation of the operational availability of the system.

5.16.6.1 Critical case studies

For the current conceptual design stage of the project, only the most critical failure scenarios are examined. Primarily, this involves simulating the most likely failures and evaluating the potential damage. Various studies have been undertaken [346, 347]. This approach will be complemented by identifying the most critical accelerator components (usually aperture restrictions), determining which beam disturbance is required for reaching these components, and then identifying those failures that may cause these disturbances.

5.16.7 Operational scenarios

Safe operation of CLIC requires that potentially harmful beams must not be allowed into the machine. In this context, the term ‘potentially harmful’ depends on the knowledge on the current state of the machine. At a ‘cold’ start-up, i.e., when the machine is completely unknown, only beam that cannot cause structural damage to any of the accelerators components is safe. Once the machine is probed by such a safe pilot beam, the charge density of the beam can be increased in steps by the beam control system, as long as permitted by the post-cycle analysis of every previous step.

5.16.7.1 Drive Beam

The CLIC Drive Beam, a 140 μs -long pulse with a bunch frequency of 0.5 GHz and energy of 2.4 GeV, is produced in a 2.5 km long linac. Each cycle consists of a header (121 bunches) – to ‘preload’ the cavities of the fully-loaded Drive Beam linac – followed by 24×24 sub-pulses (121 bunches each). The header is discarded at the end of the linac, whilst the following 24×24 sub-pulses are recombined in the delay loop and combiner rings, to form 24 ‘trains’ of 24×121 bunches with a 12 GHz bunch structure. The trains will be transferred to the 24 decelerating sectors where their energy is extracted and transferred to the Main Beam.

Starting with an unknown machine, all 24 distinct paths of the recombination complex will initially be tested with a safe pilot beam of 30 bunches. The scheme to safely reach the nominal intensity will consist of gradually adding bunches to the end of the pulse: in sequence H+30b (header + pilot), H+60b, H+1SP+30b (header + one sub-pulse + pilot for next sub-pulse), H+1SP+60b, H+2SP+30b, etc. Once we have reached H+24SP+30b, we have produced the first train, plus a pilot for the second train. At this point the recombination complex and the first decelerator are fully tested. The test of each subsequent turnaround and decelerator sector will also start with a safe pilot beam; however, the intensity may now be increased more rapidly, i.e., 30b, 60b, 1SP, 2SP, 3SP...24SP.

The precise increase in the number of sub-pulses during the intensity ramp of the decelerator trains has to be studied. It should be noted that a single sub-pulse will lead to a Drive Beam train of full length but spaced with 24 times the nominal bunch spacing, i.e., every bunch is followed by 23 missing bunches. Adding subsequent sub-pulses to the Drive Beam linac train, will change this spacing, i.e., for

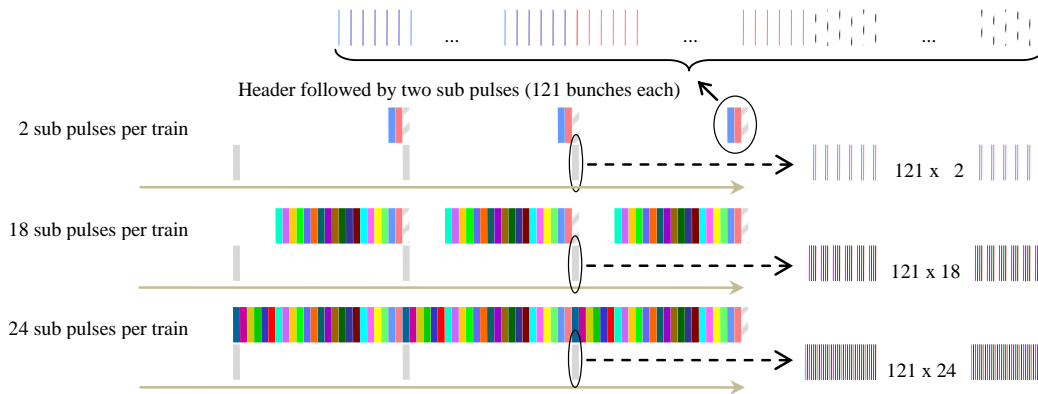


Fig. 5.345: Three cases for different number of sub pulses per decelerator train to illustrate the resulting non continuous bunch structure of the decelerator trains

n sub-pulses the Drive Beam train will consist of n bunches followed by $24 - n$ missing bunches. This particular bunch structure will have influence on the energy of the Drive Beam in the decelerator as the leading bunches will lose only very little energy. Hence the trajectory of the decelerator beam should be

carefully tracked during the intensity ramp. And the effect of closing the bunch gap on the beam energy and the beam trajectory, towards the end of the intensity ramp should be known and anticipated.

To speed up the intensity ramp, the testing of the 23 following decelerators could, in principle, proceed in parallel. This implies that each first sub-pulse of a decelerator train is to be preceded by a header that will be discarded at the end of the linac, unless it is preceded by the last sub-pulse for the previous decelerator train. This further implies that any special voltage program of the RF, which is there to optimize the non loaded cavity state seen by these header pulses, will have to be repeated for every decelerator header.

Figure 5.345 illustrates effect of combining a limited number of sub pulses for the decelerator trains. It also shows the production of various decelerator Drive Beams in parallel, requiring the addition of extra header pulses.

5.16.7.2 Main Beam

To obtain a safe Main Beam for cold start-up, the brilliance needs to be reduced by over four orders of magnitude with respect to nominal. The nominal Main Beam consists of 312 bunches spaced by 0.5 ns. A reduction in the number of bunches from 312 to a single bunch reduces the brilliance by a factor 300. Decreasing the current per bunch will give another factor of three. A further brilliance reduction can be obtained by increasing the emittance of the beam in the damping ring through controlled orbit distortions in the damping ring, allowing — in accordance with the available aperture — a factor 3 in the horizontal plane and a factor 20 in the vertical plane. The overall brilliance reduction that can be achieved is 5×10^4 , in the bulk part of the required level of reduction to provide safe beam for the main linac.

The intensity strategy will then consist of first gradually reducing the emittance and increasing the bunch current to nominal values and then to increase the number of bunches.

Beam position measurements (BPM) requirements

It should be noted that the BPM requirements for optimum luminosity operation are much tighter than the requirements for safe operation with nominal beams. While luminosity optimization demands a resolution that is a fraction of the beam size, machine protection demands to be able to steer the beam sufficiently clear from the aperture restriction of the betatron collimation section. The required clearance in the collimators for a beam of 1.2×10^4 above damage level is 4.4σ . Doubling this figure for a safety margin leaves us as available space 6σ in the horizontal plane and 46σ in the vertical plane (the half-aperture in the collimator being $a_x = 15 \sigma_x$ and $a_y = 55 \sigma_y$). The resolution for the beam positioning measurements should be of the same order. Based on a minimum beam size at the end of the linac of $\sigma_x = 2.0 \mu\text{m}$, $\sigma_y = 0.35 \mu\text{m}$, the requirements for the BPM resolution are $\sigma_x = 12 \mu\text{m}$, $\sigma_y = 16 \mu\text{m}$. Compared with the 50 nm resolution required for nominal beam, these requirements are about 250 times less stringent. To put this number in perspective, a single bunch with a factor of three less in intensity has an expected resolution degradation by a factor of 60, given by $1/3$ (intensity) times $1/20$ (cavity filling time).

5.16.8 Technical issues

The following technical issues related to machine protection have to be considered in more detail.

Protective masks

The masks, which protect all injection and extraction channels in case of kicker misfiring, have to be studied and designed. This may require further study of materials able to withstand the impact of a high-intensity or high-brilliance beams. If no suitable material is available to withstand the impacting beam, one has to rely on masks with renewable surfaces combined with highly reliable kicker systems. The

system should be designed such that the expected impact of mask replacements (in operational cost and time) is reduced to an acceptable level.

Drive Beam linac real-time protection

The scenarios for real time failures in the Drive Beam linac are to be studied. In case the impact of a failure is too large, internal beam dumps triggered by a real-time beam interlock system of the linac will be required.

Emittance control of the damping rings

Methods to spoil the horizontal and vertical emittance of the beam in the damping rings in a controlled way have to be implemented. This is not only required for enlarging the emittance during the intensity/brilliance ramp of the Main Beam, it may also be required to blow up the beam on very short time scales (possibly to complement an internal beam dump system) to protect against equipment errors in the damping rings.

Fault catalogue and fault simulation

A catalogue of all fault classes is to be established. The impact of the fault classes has to be studied in detail by simulation or other means.

Intensity ramp

The intensity ramp-ups of the Main Beam and Drive Beam have to be simulated, in particular to ensure that with the degraded beam observation performance (i.e., reduced resolution due to reduced intensity) the beam can still be sufficiently well observed and optimized to validate the safety of the next intensity increase.

5.16.9 Component inventory

The number of identifiable components for the machine protection system consists of:

- passive protective masks (note: these masks are to be considered as an integral part of the extraction and injection channel designs);
- real-time protection systems;
- Beam Interlock System (BIS);
- post-cycle analysis and Next Cycle Permit system;
- Quench Protection System (QPS). Although not mentioned here, the superconducting wigglers of the damping rings require a quench detection and energy extraction system. From the experience with Quench Protection Systems in other accelerators, this is not a critical issue.

In total, the hardware requirements for these systems are relatively modest; of the order of a hundred crates and processors. Owing to the relatively small module count, there are no specific cost considerations. The technical implementation for the post-cycle analysis system may further be guided by the system choice made for the acquisition and control system.

5.16.10 Outlook for the project preparation phase

All simulation studies mentioned above in §5.16.8 can be performed for the project preparation phase.

A number of issues outlined can also be tested in CTF3 or an equivalent facility. Most notably the following tests are foreseen:

5.16 MACHINE PROTECTION

- development and test of a prototype beam interlock system;
- test of the Next Cycle Permit concept;
- tests of Drive Beam intensity ramps, optionally including the parallel generation of multiple trains (i.e., non-continuous filling of the Drive Beam linac).

5.17 Active pre-alignment systems

5.17.1 Overview

The pre-alignment of the accelerator components will take place when beam is off. It will consist of two steps: a mechanical pre-alignment within ± 0.1 mm r.m.s. with respect to the Metrological Reference Network (MRN), and an active pre-alignment. The second step concerns only the components of the Main Linac (ML) and the Beam Delivery System (BDS), which have tighter tolerances on pre-alignment than the other parts of CLIC. The objectives of active pre-alignment are that, after computation, for a sliding window of 200 m, the standard deviations of the transverse position of each component with respect to a straight line fit must be less than a few μm .

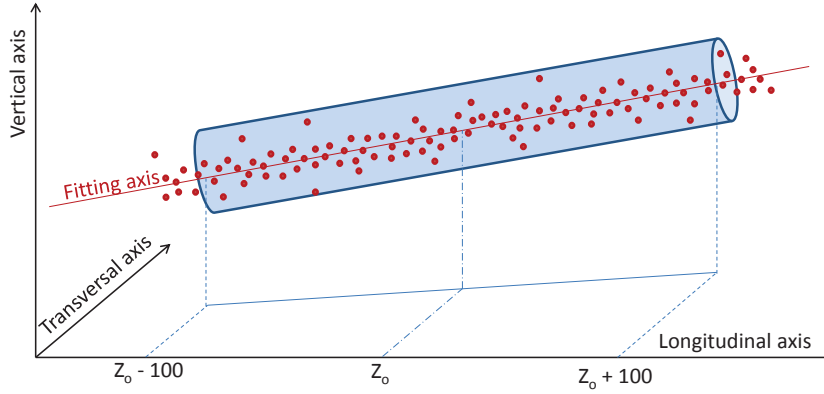


Fig. 5.346: Objectives of active pre-alignment

The radius of the cylinder in Fig. 5.346 corresponds to the total error budget in the determination of the position of components. Along the Main Beam (MB), it equals $14 \mu\text{m}$ r.m.s. for the RF structures and $17 \mu\text{m}$ r.m.s. for the Main Beam quadrupoles [348]. In the BDS, the total error budget is $10 \mu\text{m}$ r.m.s. for all components [349].

Active pre-alignment can be divided into two parts: the determination of the position of each component, by alignment systems, and the re-adjustment of components to the best position, by using actuators.

The determination of the position of each component is carried out as follows. Firstly, as it is not possible to implement a straight alignment reference line over 20 km, overlapping references of at least 200 m will reconstruct the straight reference [350]. This is the aim of the primary network: the Metrologic Reference Network (MRN), which propagates the precision and accuracy of the alignment needed: a few μm over more than 200 m. A secondary network: the Support Pre-alignment Network (SPN), framed by the MRN network, associates sensors to each support to be aligned, with a precision of a few μm precision over 10 m. A third step is required to link the support to the components to be aligned: this is the Alignment and Fiducialisation of each Component on the supports (AFC). The components must be pre-aligned accurately and precisely on their support and the mean axis (or their zero) must be perfectly determined with respect to the mechanical interface of the sensors belonging to the SPN network.

The technical solution described below consists of stretched wires with Wire Positioning Sensors (WPS). WPS sensors are biaxial ecartometers, based on capacitive technology, providing transverse off-sets, in the sensors frame of reference, with respect to a stretched wire. The resolution is sub-micrometric over a range of 10 mm [351].

Once the position of the components is known, the re-adjustment phase can take place. In order to

simplify the re-adjustment, several components are pre-aligned on supports. Two types of supports are involved: girders for the RF components of the Main Beam and the Drive Beam and interface plates for MB quadrupoles. DB and MB girders will be interlinked with their extremities, based on the cradles. This allows movement in the transverse girder interlink plane within 3 degrees of freedom (DOF), while the longitudinal direction is adjusted with micrometric mechanical guiding. The MB quadrupole is mounted on an interface plate allowing an adjustment along 5 DOF (the longitudinal axis will be blocked longitudinally after initial mechanical alignment) [352].

5.17.2 Re-adjustment solutions

Cam movers are proposed for the 5 DOF re-adjustment of the MB quadrupole interface plate and high-resolution linear actuators are proposed for the 3 DOF re-adjustment of the DB and MB girders as shown in Fig. 5.347.

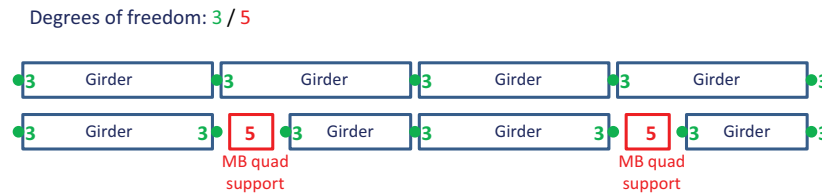


Fig. 5.347: Degrees of freedom of components supports

The eccentric, cam-based adjustment system is a 3-point system, with four interfaces to the ground, providing 5 DOF. This system, which supports the girders of the Swiss Light Source (SLS) at PSI and the undulators of the XFEL at SLAC, is used in several other accelerators or synchrotrons, though not with the sub-micrometric displacement resolution required for CLIC.

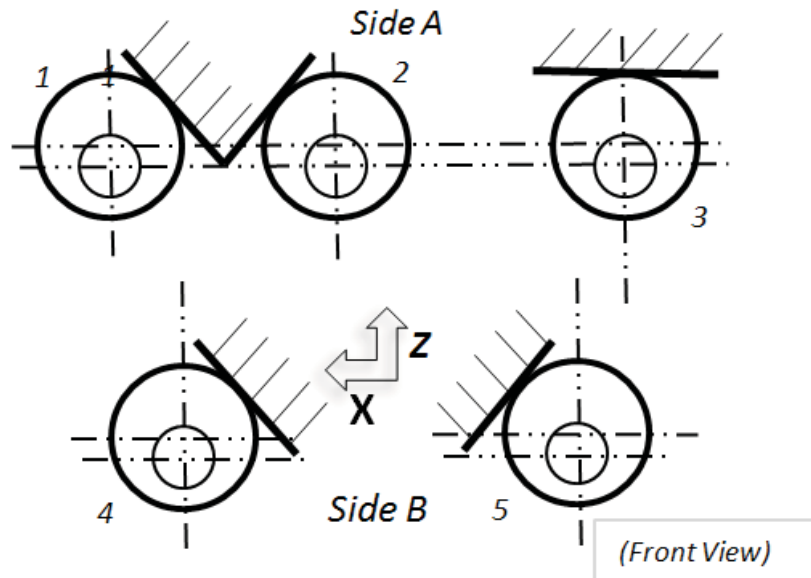


Fig. 5.348: Cam movers configuration (SLS)

The cam-based system from SLS (see Fig. 5.348), with slight improvements is being studied on a 1 DOF mock-up, in particular the sine wave response and the repeatability in short- and long-range alignment [353]. Latest results show a repeatability on full stroke (10 mm) better than $0.3 \mu\text{m}$ using a

standard spherical bearing and cylindrical cam surface. The re-adjustment resolution of vertical and radial translations on a 5 DOF mock-up has been validated below $2\text{ }\mu\text{m}$ over a range of $\pm 3\text{ mm}$ [354].

The re-adjustment concept, using linear actuators and cradles linking two adjacent girders as an articulation point, was validated in CTF2 [355]. Owing to changes in the size of components and to a considerable increase of load, some question marks were raised concerning the clearances and the kinematics of such a solution; consequently a new design has been proposed. This new solution has been validated on the two-beam test module [356, 357].

For the BDS, as no continuity between component supports is required, pre-alignment will be performed with 5 DOF using the cam-mover solution mentioned above.

5.17.3 Metrologic Reference Network (MRN)

This network consists of parallel wires linked, in at least three points (more points are needed for redundancy), by means of Wire Positioning Sensors (WPS) coupled on a common metrological plate (see Fig. 5.349). The mechanical interfaces of these sensors will have been precisely and accurately determined from a Coordinate Measuring Machine (CMM) with sub-micrometric precision [358].

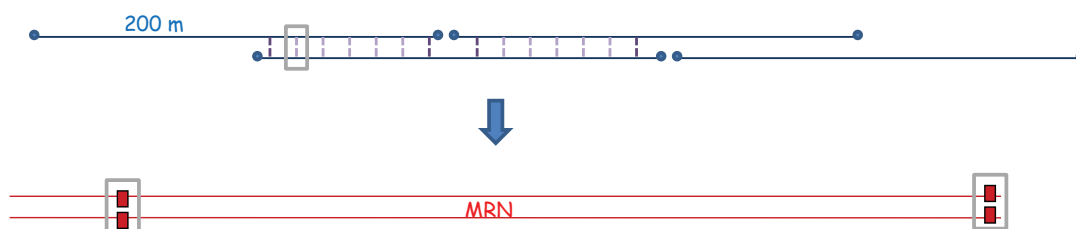


Fig. 5.349: MRN configuration

The main issues concerning the use of stretched wires as reference for alignment are firstly their long-term stability with respect to perturbing effects like variations of temperature, humidity, creep, and air currents, and secondly the modelling of its catenary. A Hydrostatic Levelling System (HLS) coupled with a WPS system is a good solution to continuously model the vertical shape of the stretched wire. The catenary of a stretched wire can be computed knowing at least three differences of height between WPS sensors located along the wire, following the minimal configuration shown below [359].

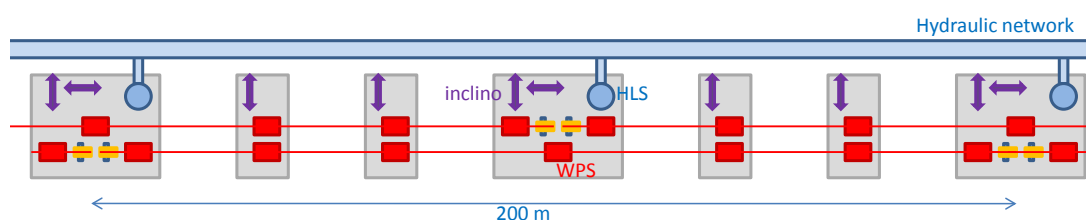


Fig. 5.350: Metrological plates of MRN network

The HLS system is based on the communicating vessel principle (see Fig. 5.350); the free surface of water provides the reference frame. This water network is composed of vessels connected to each other by pipes, partially filled with water, allowing water and air to circulate freely. A sensor is fitted to each vessel in order to determine the distance to the free surface of liquid. Several measurement technologies are possible: optical, capacitive, ultrasonic, but sub-micrometric resolution will only be reached by using capacitive technology [360].

5.17.4 Support Pre-alignment Network (SPN)

Owing to the SPN network, each support will be pre-aligned with respect to the MRN (see Fig. 5.351). To do this, each sensor must provide precise and accurate measurements, e.g., the position of the zero of each sensor is known with respect to its mechanical interface connected to the support and so each sensor can be installed on its support with micrometric precision. Each capacitive-based WPS (cWPS) is equipped with a flat, chamfered, conical type interface capable of being installed with micrometric precision.

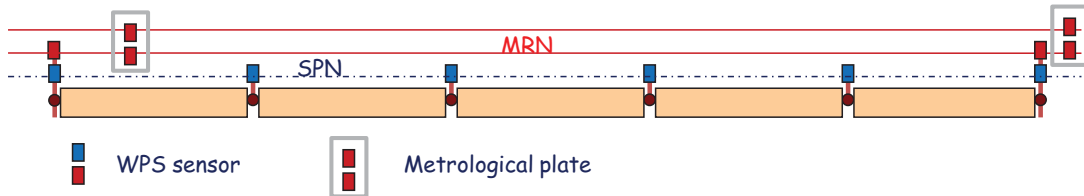


Fig. 5.351: Combination of MRN and SPN networks

Using the same system alignment for MNR and SPN networks simplifies configuration: the stretched wire reference will be used for both networks. As there are two parallel beams, a single reference installed between the two beams can be used, as shown in Fig.5.352 below:

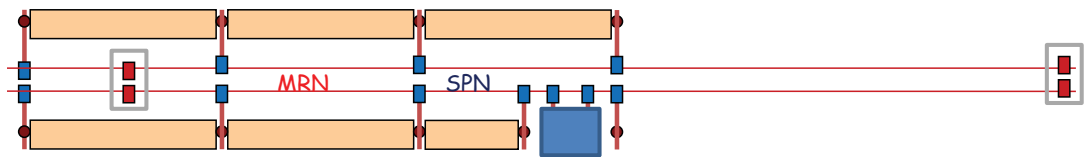


Fig. 5.352: Special configuration of MRN and SPN networks for modules

The longitudinal position between DB and MB supports will be measured and adjusted during installation with Laser Tracker measurements.

In the BDS area, the configuration shown in Fig. 5.353 will be adopted:

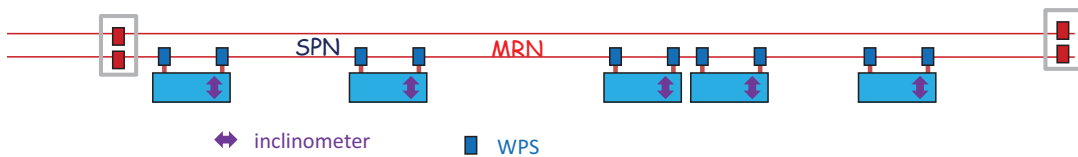


Fig. 5.353: BDS configuration

5.17.5 Alignment and fiducialisation of components (AFC)

Owing to the combination of MRN and SPN networks, the position of each sensor will be known and determined in a general coordinate system (see Fig. 5.354). Prior to the installation, during the fiducialisation process, the zero of each component will be determined in the support coordinate system, and at the same time the position of each sensor will be measured with respect to the support frame of reference. This will be carried out on a 3D Coordinate Measuring Machine (CMM), with an accuracy of $0.3 \mu\text{m} \pm 1 \text{ ppm}$ of the measured value. This allows the position of the zero for each component to be calculated in the general coordinate system. All the components will be equipped with non-magnetic



Fig. 5.354: Pre-alignment of components on the same support

mechanical interfaces for 0.5 inch diameter spheres, while supports will be equipped with non-magnetic mechanical interfaces for 1.5 inch diameter spheres. These mechanical interfaces will be first measured on a CMM during dimensional control, then during the fiducialisation process, thus allowing the control of the position of the components on their supports after transport, prior to installation [361, 362].

Table 5.90: Component inventory

Component [units]	No. of components per module type					MRN (200 m)	BDS&MDI (per comp.)	Total
	Type-0	Type-1	Type-2	Type-3	Type-4			
WPS	2	5	5	5	5	33	2	62 892
Inclinometer	2	4	4	4	4	16	1	54 064
HLS						1.2		284
Wire [m]						400		94 400
Hydraulic pipes [m]						200		47 200
Cam movers		5	5	5	5		5	24 080
Linear actuators	3	6	6	6	6			74 196
Metrological plates						16		3776
Stretching devices [sets]						1		236
Mechanical settlement i/f	2	7	7	7	5		4	61 812
Metrological targets	8	14	14	14	8	48	4	195 724
Total Number	16 748	308	1268	954	1462	236	824	

5.17.6 Cost considerations

With the proposed configuration, a very large number of components are required (as can be seen in Table 5.90) and so ways of reducing these numbers need to be considered. One of the first ideas is to decrease the number of actuators and sensors, by reducing the number of supports to be aligned. The length of a module is currently 2.01 m, and one of the first studies to be launched for the project preparation phase will be to look at the possibility of extending this length, or grouping DB and MB components of the same module on a single support. Although the idea of lengthening the girders is initially appealing, this increases the volume in which components will have to be pre-aligned and dimensionally controlled to a few μm . Similarly, long-term stability (in particular against thermal expansion) will be more difficult to achieve. The coupling of DB and MB components on the same girder must also be considered. In this case, the loads applied on a support will be doubled and a new way of re-adjustment will have to be found. Also, the adjustment of the position of the components of one beam with respect to the other beam is no longer possible as all components are pre-aligned on the same support.

In order to decrease the cost, low-cost WPS are under development. One prototype of an optical

WPS (oWPS) is being validated: its cost will be an order of magnitude lower than the cWPS. At the same time, a low-cost cWPS is under study.

We also plan to use a WPS sensor measuring with respect to two parallel wires at the same time. This solution will be feasible with oWPS sensors. A first mechanical procedure allowing efficient stretching of two wires at the same time through WPS sensors and protection was validated on 6 m.

5.17.7 Outlook for the project preparation phase

The stretched wire systems are the only available solution in order to answer CLIC requirements. No inter-comparison or cross-checks with other alignment systems could be performed. The development of an alternative optical solution would allow a real comparison and validation of alignment systems, in terms of performance, integration and cost.

A collaboration with NIKHEF has started [363], to develop short-range and long-range laser alignment systems based on their so-called ‘RASNIK’ and ‘RASCLIC’ systems.

An alternative solution, LAMBDA (Laser Alignment Multipoint Based Design Approach), is also under study at CERN [364]. This approach is based on the use of a laser beam under vacuum, considered as the alignment reference, and sensors distributed along the beam, coupled to the support to be aligned. Each sensor consists of three parts: a measurement surface, a convergent lens, and a CCD camera; thus the observation of the speckles on the measurement surface is performed indirectly by the CCD, which reduces the angular sensitivity of the system. According to a first simulation study, an angular orientation better than 0.2 mrad is sufficient for micrometric movements. Mechanical or optical shutters used as measurement surface will not alter the beam and will keep the straightness of the beam. Each shutter should be positioned to better than 12 μm to ensure sub-micrometric measurement accuracy.

5.18 Main Beam quadrupole stabilization equipment

5.18.1 Overview

One of the required actions to preserve the ultra-low transverse emittances during the beam transport is the mechanical stabilization of all 3992 Main Beam Quadrupoles (MBQs). More precisely, if $\Phi_x(f)$ is the power spectral density of the vertical absolute displacement of the quadrupole and more exactly that of the magnetic field centre, it is required that the integrated r.m.s. $\sigma_x(f)$, defined as

$$\sigma_x(f) = \sqrt{\int_f^\infty \Phi_x(v) dv} \quad (5.53)$$

shall stay below 1.5 nm above 1 Hz (see §3.8). Similarly, it shall stay below 5 nm in the lateral direction. The stabilization of structures at the nanometer scale is a concern in various fields of precision engineering [365] like interferometers [366], microscopes [367], or in manufacturing [368]. The concept proposed to reach such a stability for the CLIC MBQ is a mechanical stabilization system under each quadrupole, in the presence of a low vibration background in the CLIC main tunnel. This low vibration background is better obtained in a deep tunnel and by avoiding or minimizing vibration sources in the underground buildings. At first, the stability of the magnetic centre at the level mentioned above is assumed to correspond to the mechanical stability of the external magnet yoke due to its high mechanical stiffness. This will be verified with independent measurements (laser interferometry).

The presence of actuators with ultra-high displacement resolution in the stabilization system described in the next chapters led to the additional study to fine position or ‘nano position’ the MBQ in order to steer the beam [369]. For this alternative to dipole correctors or as an additional feature, it is required to move the MBQ by steps up to 50 nm between two pulses each 20 ms (50 Hz) in a range of ± 5 microns vertically and laterally. The requested position should be reached after about 5 ms with a precision of ± 1 nm.

At each MBQ, the interconnected girders and supports with accelerating structures will be interrupted by the independent MBQ support. The MBQ will be supported by the stabilization system that is supported inside a magnet girder placed on the eccentric cams of the alignment system (see §5.17).

The following additional requirements were identified:

- The stabilization system should be fully integrated in the module design. The combined height of alignment and stabilization should allow a beam height at 620 mm.
- The stabilization system should be compatible with the stringent alignment requirements.
- The stabilization system should be compatible with the accelerator environment.
- Transport, handling and installation of the stabilization system should be compatible with the installation planning.

The objective of this chapter is to demonstrate the ability to fulfill all these requirements using the same supports for the MBQ. To this purpose, the following items are addressed successively: description of the different sources of perturbations, presentation of the concept adopted to support the MBQ, two experimental validations of that concept, and a list of identified technical issues.

5.18.2 Ground vibration at various sites

Several comparisons of measurements of the ground vibrations are available in the literature [370, 371]. A database was built up at DESY and is available at [372]. The vibrations measured on the ground are composed of a seismic background superimposed with the technical or ‘cultural’ noise linked to human activities. The measurement of the seismic background was made in deep and remote locations, in geologically stable rock configurations such as e.g. the Salt Mine Asse (depth 900 m) and the Seismic Station

Moxa [372]. In such locations, integrated r.m.s. displacements of 0.5 nm at 1 Hz were measured. Models have been developed to represent this seismic background, like the ATL law [373] or the USGS Low-Noise Model [374]. Figure 5.355 shows measurements made by CERN in 2009 in various representative locations during the night.

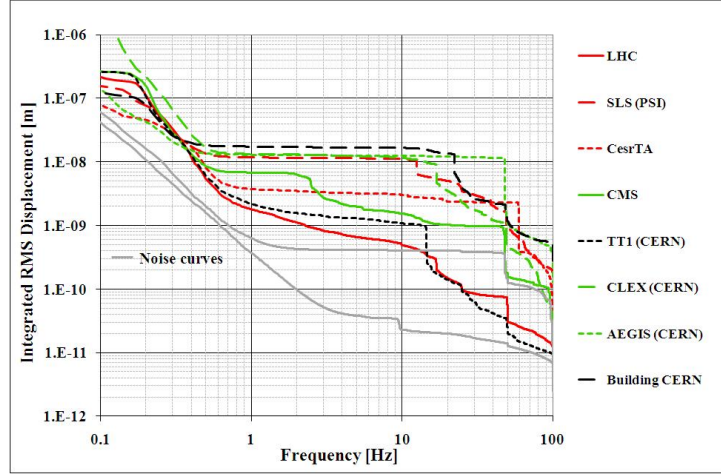


Fig. 5.355: Integrated vertical r.m.s. displacement at various locations in particle accelerators.

On Fig. 5.356, the night time P.S.D. of three operational particle accelerators (LHC (CERN) [375, 376], CesrTA (Cornell), and SLS (PSI)) are compared. The seismic background below 1 Hz is very similar and corresponds essentially to coherent micro-seismic waves. For such waves, the ground moves the same way over several kilometres. Above 1 Hz, the technical noise from the surface is attenuated by the depth of the tunnel (LHC 80 m, CesrTA 15 m, SLS surface building). For frequencies above 1 Hz, vibrations are coherent to a maximum of 40 m on continuous concrete slabs and to only a few metres in a tunnel structure with expansion joints. Day and night time variation was studied in [370] and can vary up to a factor five for sites on the surface and a factor two for deep tunnels. Measurements in a shallow tunnel without technical infrastructure at CERN (TT1, about 10 m deep) showed an variation of $\sim 2\text{--}5$ nm between night and day. Measurements on the surface during the day can reach values of 25 nm r.m.s. vertical displacement at 1 Hz and higher, as measured at several locations.

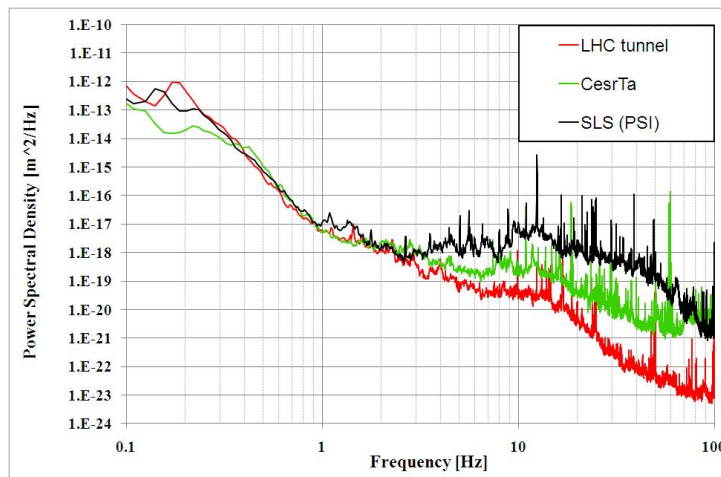


Fig. 5.356: Power Spectral Density of the vertical ground motion in three particle accelerators in operation

From the representative measurements in accelerator environments, and by taking into consideration the depth of the tunnel and measured day and night variations, the vertical integrated r.m.s. displace-

ment at 1 Hz can be estimated to vary between 2–5 nm in a deep CLIC tunnel with a geological structure and a running technical infrastructure comparable to the LHC. Furthermore, one can see that, to reach the required stability, the stabilization support should reduce the amplitude of the ground motion by roughly a factor four in the frequency range between 1 and 20 Hz. The ground motion above 20 Hz does not provide a significant contribution to the integrated r.m.s. at 1 Hz in the measured particle accelerators locations.

5.18.3 Technical noise

The technical noise is a generic term gathering all the sources of vibrations arising from the human activity. A model of the technical noise is presented in Ref. [376]. The propagation of technical noise through the ground and the structures has to be avoided as much as possible. Measurements have shown that such vibrations are rather quickly attenuated in a concrete floor; the influence of the technical cavern of an experiment, like ATLAS in the LHC, is greatly reduced after about 100 m. By adapting the civil engineering of caverns, like for the Laser Megajoule [377], and by using preventive measures such as e.g., vibration absorbers it is possible to further limit the impact of technical infrastructure on the main tunnel. The seismic background combined with the technical noise can be considered as a broadband excitation with decreasing amplitude with increasing frequency. Although not a vibration source, it is useful to mention here the vibration amplification at resonant frequencies of components and their support structures as a source of increase of vibration amplitudes. To limit this, the design of components and supports should increase the natural frequencies as much as possible. As a result of this, the support height, i.e., the beam height from the floor should be kept low. The major technical vibration sources in the main tunnel itself are presented below.

5.18.3.1 Water cooling

After the ground motion, the vibrations induced by water cooling can be expected to be the most important vibration source. In CLIC, a large fraction of the power will be dissipated in the PETS, ACS, the Drive Beam and Main Beam quadrupoles and this heat is evacuated by cooling water (see §6.2.8). Several vibration measurements were performed on water cooled components with very different results due to very different conditions. Turbulent water flow creates a broadband excitation and amplification at resonances of magnet supports or even of surrounding ACS [378] can increase the integrated r.m.s. by more than 100 nm. Transmission of pump vibrations, pipe resonances and vibrations created by flow adjusting valves and gauges can also lead to a large r.m.s. increase as measured in [379]. Forces acting directly on the quadrupole will create lower displacements with a stiffer magnet support as confirmed by measurements in [380] and specifically for soft versus rigid stabilization systems in [381]. The choice of a very rigid stabilization system [382] seems hence the right choice. A prototype CLIC MBQ with adjustable features will allow to test and reduce the influence of cooling water.

5.18.3.2 Vacuum and vacuum pipes

The vacuum in a central vacuum reservoir connected to both beams will be obtained with ion pumps and NEG during beam operation. Although no vibrations can be expected from this vacuum system after shutting down the primary vacuum pumps, the vacuum reservoir will easily transmit vibrations longitudinally and between drive and Main Beam and should hence be carefully designed.

5.18.3.3 Ventilation

A compartmented, transversal and hence smaller air flow rather than a longitudinal air flow is currently foreseen for the CLIC ventilation (see §6.4.2). This should be more compatible with the vibration stability than a longitudinal air flow.

5.18.3.4 Acoustic noise

The acoustic noise has several sources common with the technical noise transmitted through the floor but is transmitted through acoustic pressure waves that created forces acting directly on the MBQ and other components. This effect was studied and measured in [371] and it was concluded that the effect is not negligible. As demonstrated in the next chapter, an appropriate counter measure is to have a stiff stabilization support and a rigid magnet as they will be more robust against forces, acting directly on the quadrupole. On the other hand, the technical noise and the acoustic level in the CLIC tunnel should be kept as low as possible.

5.18.4 Stabilization

In a passive suspension, consisting of a simple spring k in parallel with a dashpot c , an overshoot appears on the transmissibility between the ground excitation and the payload response at a frequency corresponding to the resonance of the payload on the suspension stiffness (see e.g., the black dashed curve in Fig. 5.357(a), tuned to have a resonance at 20 Hz). Then, for higher frequencies, the curve is decreasing, and the isolation (transmissibility below one) starts at $\sqrt{2}f_n$ (where $2\pi f_n = \sqrt{k/m}$).

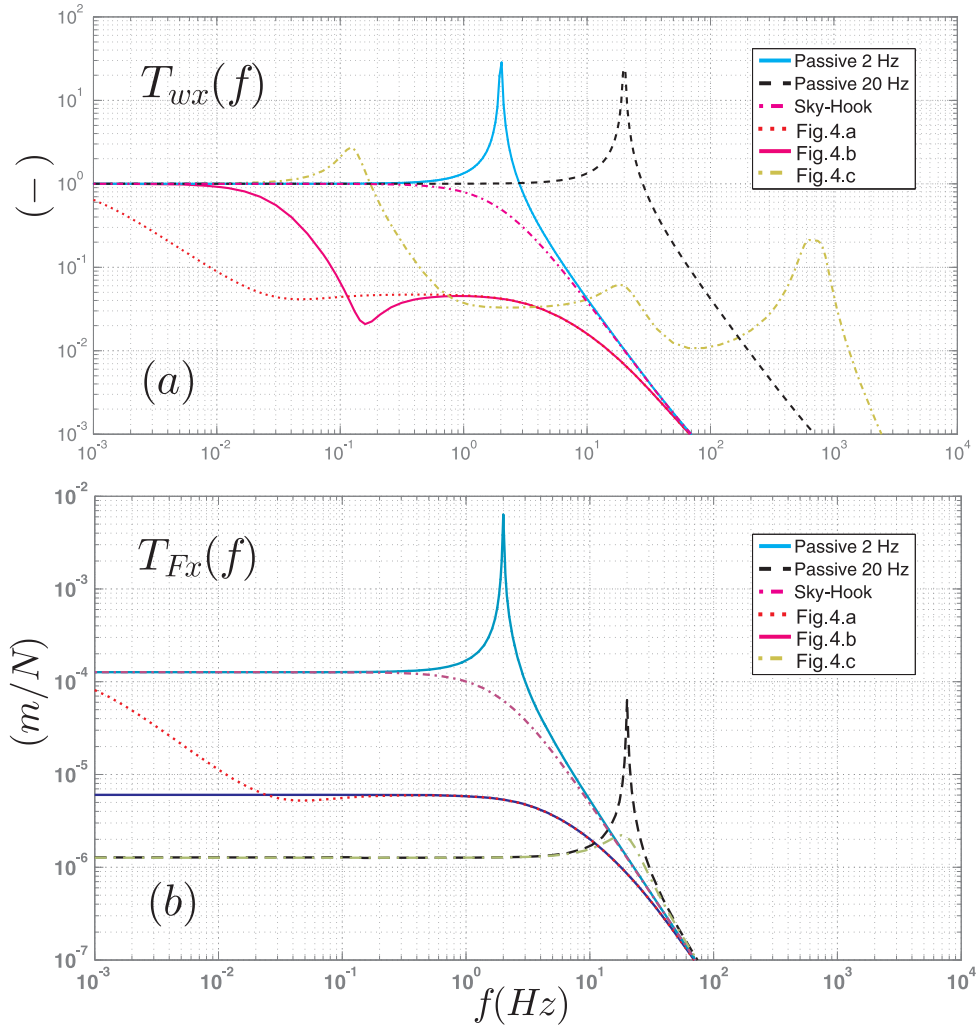


Fig. 5.357: Various passive and active control strategies. (a) Transmissibilities $T_{wx}(f)$ between the ground and the quadrupole; (b) Compliance $T_{Fx}(f)$ between a force applied on the quadrupole and the resulting displacement.

In order to increase the passive isolation, the first idea is to reduce the value of f_n as much as

possible. However, as the resonance frequency of the system decreases (e.g., resonance tuned at 2 Hz in Fig. 5.357(a)), it also becomes rapidly unacceptably sensitive to any external force directly applied on the quadrupole at very low frequency, and especially at the resonance frequency. This is illustrated in Fig. 5.357(b), showing the transmissibility (compliance) between a force applied on the quadrupole and its vertical displacement x . This is a reason why we are restricted to active isolation. A velocity feedback (so called *sky-hook damper* [383–385]) can remove the overshoot at the resonance (Fig. 5.357(a)), but does not reduce the compliance at very low frequency (Fig. 5.357(b)). Figure 5.358 shows three other configurations of active isolation strategies. The first two ones are based on the use of a reference mass, mounted either on the payload (Fig. 5.358(a) [386, 387]) or directly on the ground (Fig. 5.358(b) [388–391]). The feedback law is based on the measurement of the relative displacement between the reference mass and the payload. The transmissibilities are also shown in Fig. 5.357(a). At very low frequency, and for comparable plant, the strategy (b) has the advantage over (a) to be more robust to external forces (see Fig. 5.357(b)).

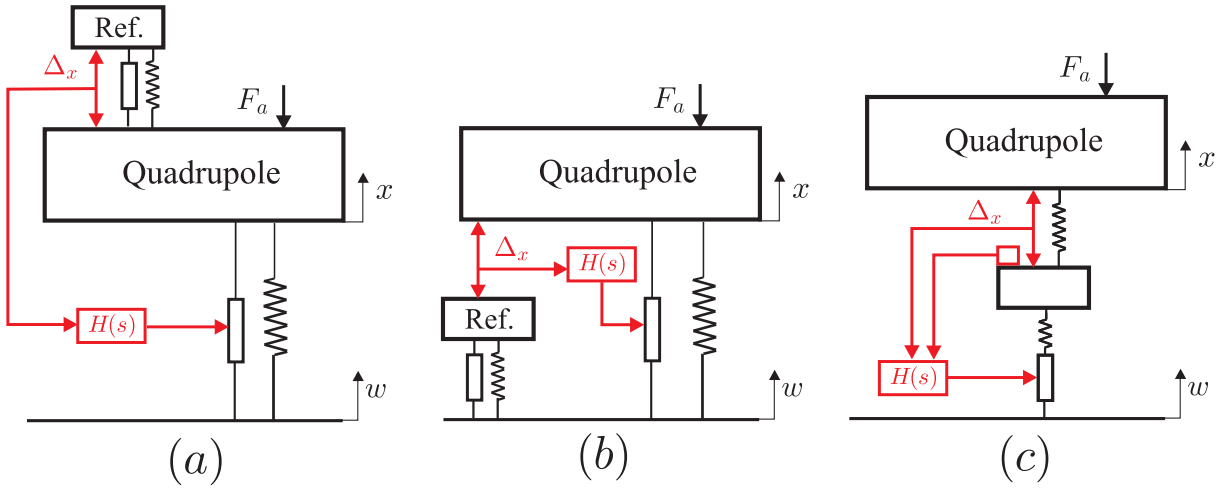


Fig. 5.358: Three strategies used for active vibration isolation.

The third strategy (Fig. 5.358(c) [392–394]) is an example of two-stages active mount. It is constituted of an intermediate mass mounted on a stiff piezoelectric stack and in series with an elastomeric layer. In this case, the feedback is based on a combination of the measurement of the relative displacement between the two masses and the absolute velocity of the intermediate mass. The typical transmissibility and compliance are also shown in Fig. 5.357. This strategy has already been used in previous studies on quadrupole stabilization [371, 395].

For the stabilization of MBQ, it has been decided to use the strategy (a), with a seismometer for the reference mass, stiff piezoelectric actuators like in [396, 397], and an active reduction of the transmissibility $T_{wx}(f)$ at low frequencies (mainly the range between 1 Hz and 20 Hz) [375]. Details of the strategy can be found in [382]. This stiff version of the strategy (a) has advantages to be more robust to technical noise than solutions using elastomers, and fulfil all the requirements mentioned in §5.17.

5.18.4.1 Modelling of quadrupole motion

Four different types of MBQ are defined with lengths between 420 mm (Type-1; about 100 Kg) and 1915 mm (Type-4; about 400 Kg). In this section, only the Type-4 is considered, as it is the longest and most challenging to stabilize. The supporting strategy adopted is described in [382, 398, 399]. Actually, it is inspired from the concept of a Stewart platform [400–402]. This is a well known concept that has been applied for both vibration isolation and precise positioning of ground and space structures. To

5.18 MAIN BEAM QUADRUPOLE STABILIZATION EQUIPMENT

tackle with the slender shape of the quadrupole, the six legs are mounted as depicted in Fig. 5.359. The orientations of the legs result from a tradeoff between the following requirements: provide a good stability in the longitudinal direction, manoeuvrability in both vertical and lateral directions, allow a sufficient resolution in the vertical direction, and ensure a static equilibrium when no control is applied. Assuming that the quadrupole is rigid, the dynamic equations of the system are

$$M\ddot{\mathbf{x}} = \mathbf{F} \quad (5.54)$$

where $M = \text{diag}(m, m, m, I_\theta, I_\phi, I_\psi)$ is the mass matrix, $\mathbf{x} = (x, y, z, \theta, \phi, \psi)$ is the vector describing small displacements of the quadrupole, and \mathbf{F} is the vector of resulting forces and torques applied by the legs on the quadrupole. \mathbf{F} is related to the axial forces in each leg by

$$\mathbf{F} = B\mathbf{f} \quad (5.55)$$

where $\mathbf{f} = (f_1, f_2, \dots, f_6)^T$ is the vector of active control forces in the six legs and B the force jacobian matrix. Assuming that there is no damping in the legs, f_i is given by

$$f_i = k_a(-q_i + \Delta_i + w_i^l) \quad (5.56)$$

where k_a is the axial stiffness of each leg, q_i and w_i^l are respectively the displacement of the quadrupole and the ground in the direction of the leg. Δ_i is the elongation of the leg due to a voltage V_i applied to the piezoelectric stack

$$\Delta_i = nd_{33}V_i \quad (5.57)$$

where nd_{33} is a characteristic of the actuator.

Replacing (5.55) and (5.56) in (5.54) gives

$$M\ddot{\mathbf{x}} + K\mathbf{x} = B\mathbf{u} + k_a B\mathbf{w}^l \quad (5.58)$$

or again

$$M\ddot{\mathbf{x}} + K\mathbf{x} = B\mathbf{u} + k_a B E \mathbf{w} \quad (5.59)$$

where $K = k_a B B^T$ is the stiffness matrix, \mathbf{w} and \mathbf{w}^l are the ground excitation vector and the ground excitation vector in the legs, and E is the excitation matrix projecting \mathbf{w} in the directions of the legs. $\mathbf{u} = (u_1, u_2, \dots, u_6)^T$ is the vector of control forces, where $u_i = k_a \Delta_i$. In the configuration described in Fig. 5.359, the quadrupole is supported by three pairs of legs (A, B and C). Assuming that the motion of the ground is the same for the two legs of each pair, the excitation vector is $\mathbf{w} = (u_A, v_A, w_A, u_B, v_B, w_B, u_C, v_C, w_C)^T$.

Let J be the Jacobian matrix relating the elongations velocities of the legs $\dot{\mathbf{q}}$ and the velocity vector $\dot{\mathbf{x}}$ as $\dot{\mathbf{q}} = J\dot{\mathbf{x}}$. According to the virtual work principle, we have

$$\mathbf{F}^T \delta \mathbf{x} = \mathbf{f}^T \delta \mathbf{q} = \mathbf{f}^T J \delta \mathbf{x} \quad (5.60)$$

After identification, we have $\mathbf{F} = J^T \mathbf{f}$. Comparing with (5.55) leads to $B = J^T$.

The analytical expression of J is found as follows. First, let us split the velocity vector $\dot{\mathbf{x}}$ into translational and rotational components such as $\dot{\mathbf{x}}^T = (\mathbf{v}^T, \boldsymbol{\omega}^T)$ where $\mathbf{v}^T = (\dot{x}, \dot{y}, \dot{z})$ and $\boldsymbol{\omega}^T = (\dot{\theta}, \dot{\phi}, \dot{\psi})$. Then, the velocity of the fixation point of leg i is

$$\mathbf{v}_i = \mathbf{v} + \boldsymbol{\omega} \times \mathbf{p}_i \quad (5.61)$$

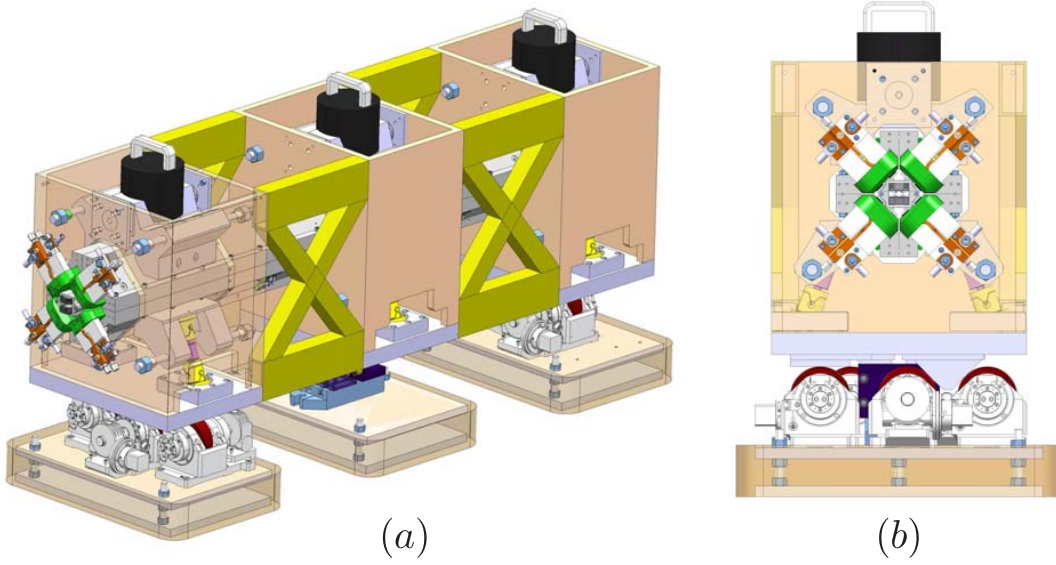


Fig. 5.359: Conceptual drawing of the quadrupole mounted on six active legs, integrated on the alignment stage: (a) Perspective view; (b) Front view.

where \mathbf{p}_i is the coordinate of the extremity of leg i in the reference frame fixed on the quadrupole. If $\mathbf{1}_i$ is a unit vector in the direction of leg i , the velocity of the extension of the leg is obtained by projecting \mathbf{v}_i along $\mathbf{1}_i$

$$\dot{q}_i = \mathbf{1}_i^T \mathbf{v}_i = \mathbf{1}_i^T (\mathbf{v} + \boldsymbol{\omega} \times \mathbf{p}_i) \quad (5.62)$$

or

$$\dot{q}_i = \mathbf{1}_i^T \mathbf{v}_i = \mathbf{1}_i^T (\mathbf{v} - \mathbf{p}_i \times \boldsymbol{\omega}) \quad (5.63)$$

Proceeding the same way for each leg, we have finally

$$J = \begin{pmatrix} \dots & \dots \\ \mathbf{1}_i^T & -\mathbf{1}_i^T \tilde{\mathbf{p}}_i \\ \dots & \dots \end{pmatrix} \quad (5.64)$$

where $\tilde{\mathbf{p}}_i$ is the antisymmetric matrix calculated from \mathbf{p}_i to express the cross product.

5.18.4.2 Quadrupole stabilization

The general idea applied to stabilize the quadrupole is based on the measurement of the relative displacement between the quadrupole and an inertial reference. In the configuration described in Fig. 5.359, three seismometers are mounted on the quadrupole, one above each pair of legs. After integration, let $\mathbf{x}^m = (x_A, y_A, z_A, x_B, y_B, z_B, x_C, y_C, z_C)^T$ be the vector of the measured displacements. \mathbf{x}^m is related to \mathbf{x} through

$$\mathbf{x}^m = S\mathbf{x} \quad (5.65)$$

where S is the matrix linking the two sets of coordinates. Then, for each pair of legs, the lateral and vertical motion of the quadrupole are used in a local feedback loop. For example, for the first pair of legs, the forces exerted by the actuators on the quadrupoles $\mathbf{u} = (u_1, u_2)^T$ are

$$\mathbf{u} = k_a \begin{pmatrix} \Delta_1 \\ \Delta_2 \end{pmatrix} = -k_a H(s) \begin{pmatrix} \sin \beta & \cos \beta \\ -\sin \beta & \cos \beta \end{pmatrix} \begin{pmatrix} x_A \\ z_A \end{pmatrix} \quad (5.66)$$

where $H(s)$ is the compensator, and β is the inclination of the leg with respect to the vertical direction. It can be a scalar or a vector, depending on the control authority required in the vertical and the lateral direction. Figures 5.360(a) and (b) show an example closed loop transfer functions respectively in the lateral and vertical direction. Each figure shows, for the three pairs of legs, the transmissibility between the ground and the quadrupole.

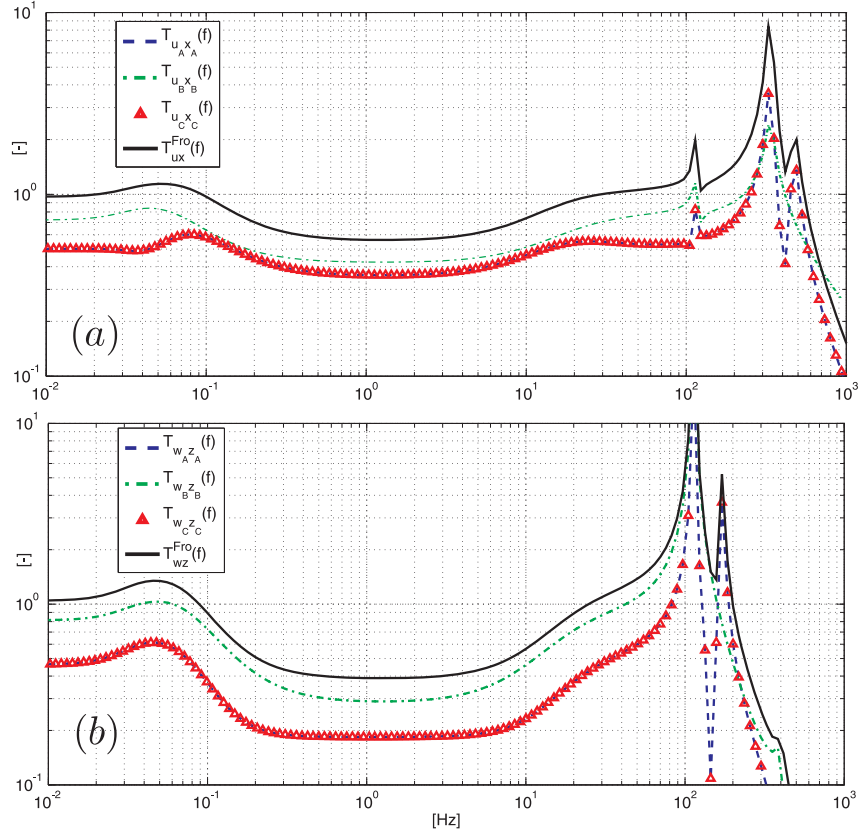


Fig. 5.360: Closed-loop transmissibility between the ground and the quadrupole for the three pairs of legs in the lateral (a) and vertical (b) direction.

To include these results in beam simulations, it can be more convenient to dispose of a unique scalar quantity, representative of the stabilization in each direction. To this aim, the Frobenius norm (r.m.s. norm) can be calculated from these curves. It is also shown in Fig. 5.360 for each direction.

5.18.5 Technical description of the real-time feedback

5.18.5.1 Sensors

As presented in §5.18.4, the strategy adopted to stabilize the MBQ is based on the measurement of the relative displacement between the quadrupole and an inertial reference mass. To achieve the stability requirements, the sensor must have a resolution of at least 0.1 nm in a frequency range between 1 Hz and 50 Hz. Actually, such a reference mass is contained in a broadband seismometer. For the purpose of the feasibility demonstration, tri-axial broadband seismometers [403] are used to measure the velocity under and above the stabilization support. The velocity is also integrated to get the displacement, used in the feedback loop. The seismometers have been characterized and have the required resolution and

frequency range for the stabilization. Initially, a seismometer is placed on the magnet for each actuator pair.

For the nano-positioning, displacement transducers based on strain gauges or capacitive gauges are integrated in the actuators during the validation. The gauges in the actuators can be eventually replaced by x–y position gauges that measure directly the position of the magnet with respect to the base of the stabilization support. Several solutions for this as for instance optical encoders with the required resolution and precision are commercially available.

5.18.5.2 Actuators

A stiff actuating support that can reach the defined stabilization and *nano-positioning* specifications in lateral and vertical direction should fulfil a certain number of requirements. First, the stability and positioning requirements apply for the integrated magnetic length of the magnet, i.e., that at least six degrees of freedom (d.o.f.) should be addressed. In order to stabilize the MBQ to 1 nm integrated r.m.s. vertical displacement at 1 Hz as expressed in Eq. 5.53, a vertical resolution of about 0.1 nm is needed. For the positioning, the combination of actuators, guidance and sensors should result in movements with a precision and repeatability of 1 nm. Parallel mechanisms with inclined actuators mounted with rotary joints as e.g., Stewart platforms, are stiff structures with high accuracy and load capacity and hence well adapted. Such parallel configurations are more precise than stacked serial configurations where guidance imperfections are difficult to correct. For the mentioned resolution and precision, the rotary joints need however to be replaced by flexural hinges to avoid friction, hysteresis and backlash. A second advantage of using flexural joints is that they give a way to deal with so-called workspace singularities of parallel manipulators [404]. In certain configurations, a structure with rotary joints will win a d.o.f. and the structure can move with all actuators locked. With flexural joints, the structure will maintain certain stiffness at a singularity configuration. The flexural stiffness of the joints introduces however bending forces and shear forces acting on the piezo actuators during operation but even more during assembly due to parts tolerances. Very sturdy, preloaded high load HVPZT piezo actuators with the required resolution were selected for the first testing [405]. A parametric design of the flexural joints was made to find an optimum between angular stiffness, assembly induced stresses and high longitudinal stiffness for overall structure stiffness [406]. The design (Fig. 5.361(left)) allows also different angular stiffness of the hinge for perpendicular directions. The design of the architecture of the parallel structure, i.e., number, position and orientation of the actuator legs, is a trade-off between the number of addressed d.o.f., the combined stiffness of the actuating structure and quadrupole, the required resolution, the available space and the cost of the actuating support. As the tolerances for stabilization and nano-positioning are defined for the plane transverse to the beam, the longitudinal d.o.f. can be blocked and the architecture results in a design with inclined actuator pairs in the same plane. The *roll* or rotation around the longitudinal axis is not suitable and should hence also be blocked by the guidance.

Figure 5.361(right) shows the pair of actuators mounted with flexural hinges inside an x–y guide that blocks the longitudinal direction. The x–y guide is a hyperguided support that is fixed around the magnet and that is held by eight flexural guides inside a rigid frame. The hyperguided support allows motion in vertical and lateral direction but is much stiffer in the longitudinal direction. In order to block the roll of the magnet, two bellows connect between the external rigid frame and the support attached to the magnet. A bellow is very rigid in torsion but allows vertical and lateral motion. The proposed guidance has two main advantages: the structure is lockable in the longitudinal direction and becomes hence transportable by protecting the piezo actuators. Secondly, an x–y position sensor can be placed in the x–y guide as mentioned in §5.18.5.1 to measure directly the position of the magnet with respect to the base of the stabilization system. The described structure can be repeated a number of times over the length of the quadrupole and the external rigid frames can be connected between them to form a rigid girder around the magnet as shown in Fig. 5.359.

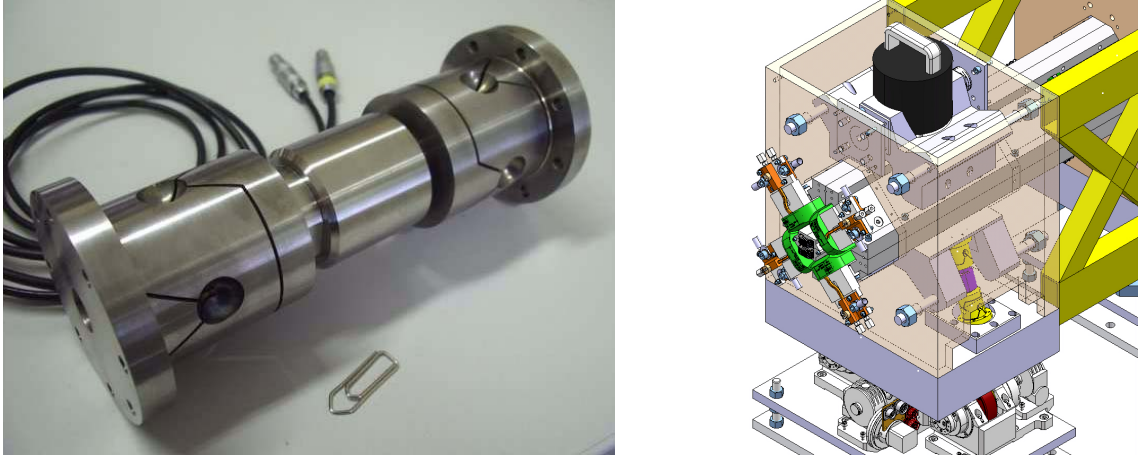


Fig. 5.361: (Left) Actuator with two prototype hinges; (Right) Detail of the x-y guidance.

5.18.5.3 Real-time controller

The main requirements for the CLIC stabilization electronics is a robust, low noise, low latency, high accuracy and resolution, low band and radiation resistant feedback control loop. A flexible configuration was chosen for the experimental validations on the test benches. It is based on a National Instruments PXI-8106RT real time controller with 2.16 GHz dual core processor with M series acquisition card. The hardware has been sufficient to start the study as shown by the experimental validation and gives information for the design of the custom built electronics that needs to be developed. The controller design is well advanced and the same controller can be used at the moment on each actuator pair as described in [382].

Noise, signal and resolution

Due to the high required resolution, the noise in the sensor, cabling, ADC and DAC electronics should be reduced to the minimum. This implies for the cabling a short path, for the moment 5 m, between sensor, actuators and the amplifiers and digital conversion that hence need to be next to the module. After optimization and experimental validation, the noise in the different components was characterized as described in [407]. Such curves can be used as a minimum specification for the noise levels. The minimum required ADC and DAC resolution is 18 bits (resolution including noise level), this without DC offsets.

Controller latency

The required maximum delay time between input signal and output signal from the controller was determined empirically with the controller hardware used in the experimental validation [407] and was also verified in the mathematical model of the controller. In order to have the full performance, the latency should be in the order of 50 μ s.

5.18.6 Experimental validations

To validate the strategy and to demonstrate the technical feasibility with the selected hardware components, two intermediate test benches were constructed. The first one is a single DOF scaled vertical test bench with a low payload combining a single high resolution actuator with a single axis of a broadband seismometer and with the PXI based controller. This bench was dedicated to study and validate the feasibility of low frequency vibration isolation to the required level with a minimum amount of components. It helped to determine the required specifications of the hardware components, the real time

DAQ software and the controller software. The nano-positioning capability using the same support was verified.

The objective of the second test bench was twofold. Firstly, to increase the payload mass and the actuator load capacity to the level of the equivalent actuator load of the MBQ. The dummy magnet has the mass and dimensions of MBQ Type-1 and weights can be added for the equivalent actuator load of other magnet types. Secondly, to increase the number of degrees of freedom and hence number of sensor and actuator channels, to control the vertical and lateral motions.

5.18.6.1 Test bench 1

The experimental setup consists of a guided piezoelectric stack, mounted in a double membrane flexural guide to allow only a vertical motion. Two seismometers are used to measure the vibrations at both ends of the actuator. The aim of the experiment is to stabilize a small mass placed on the top of the membrane, in this case the seismometer itself (Fig. 5.362(a)).

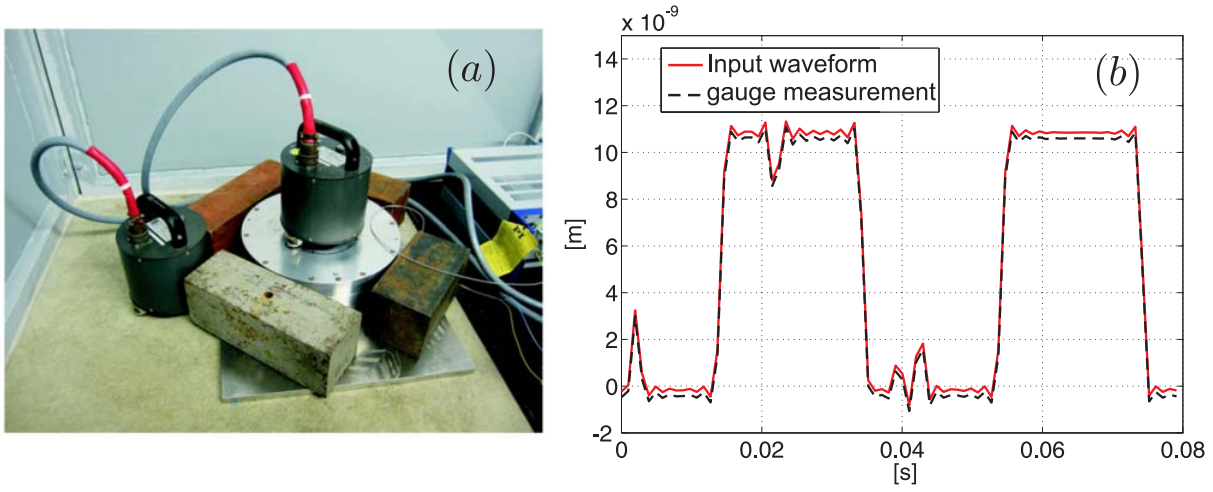


Fig. 5.362: (a) Picture of the scaled test bench; (b) Nano-positioning experiment.

The test bench is placed in a tunnel (ISR-I8) where the amplitude of the ground motion is similar to the values measured in the LHC tunnel. Day and night variations allow to study the test bench with a background varying between 2 and 7 nm vertical integrated r.m.s. at 1 Hz.

For the stabilization of the top seismometer, the controller is based on the measurement of the absolute velocity and is designed as follows: a proportional gain, a Butterworth high pass filter at 0.5 Hz, introduced in the controller to remove the drift in the signals, and a lag at 30 Hz to improve the stability. Figure 5.363 shows the integrated r.m.s. displacement of the top seismometer for two experiments, one performed during the day and one performed during the night. During the day, at 1 Hz, one sees that the feedback control has reduced $\sigma_x(f)$ from 6.1 nm to 1.5 nm, i.e., a reduction by a factor four. During the night, when the ground motion is even lower, σ_x is reduced from 2 nm to 0.6 nm at 1 Hz, and 0.45 nm at 4 Hz.

The nano-positioning capability of the leg has been tested with a square wave input, with an amplitude of 10 nm and a frequency of 50 Hz (Fig. 5.362(b)). The displacement measured with a capacitive gauge follows the input signal with the required precision. This result was obtained in open loop.

The stabilization results shown in Fig. 5.363, that correspond to the requirements, were obtained with a controller that uses only the seismometer placed on the membrane, i.e., only based on feedback. Improvements are still expected from an optimized combination of feedback and feed-forward of the seismometer placed on the floor and optimization of the hardware. Although the results were obtained for a small mass, the ratio of mass to the stiffness of the used actuator is the same as for the final load

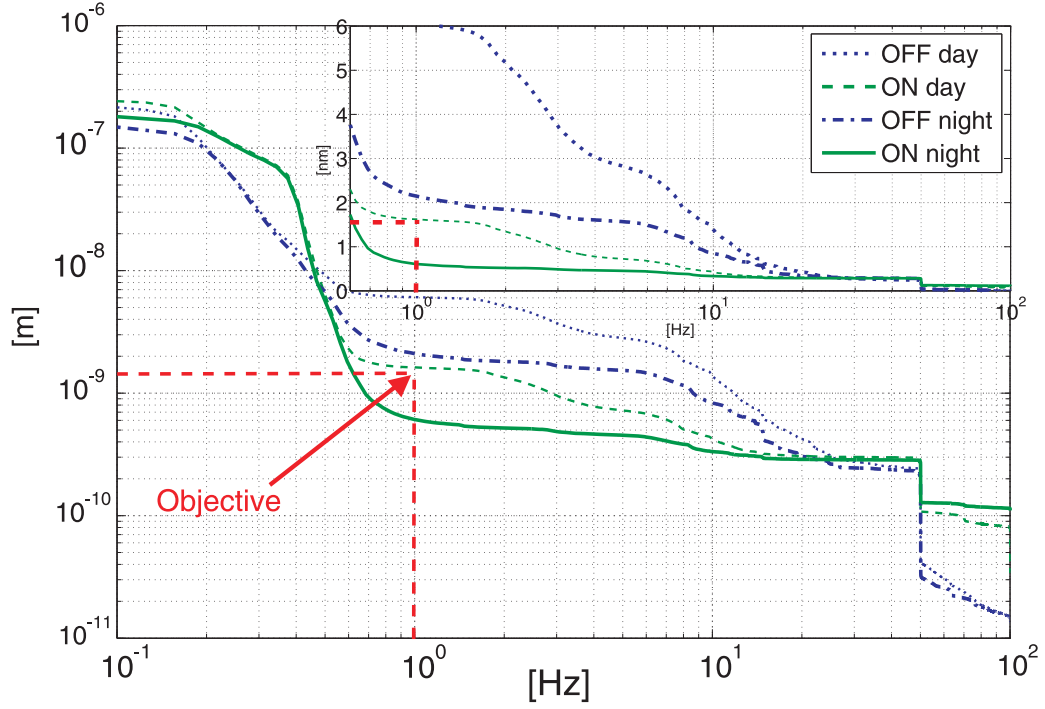


Fig. 5.363: Comparison of r.m.s. integrated of the top displacement $\sigma_x(f)$, for the test bench 1, when the controller is ON and OFF, during the day and during the night.

and the stiffness of the high load actuator. This was confirmed with the results of test bench 2.

5.18.6.2 Test bench 2

This second test bench is inspired from [396, 397], but designed to be modular, in order to allow to address a certain number of difficulties including: the validation of the selected high load actuator, the stabilization in both vertical and lateral direction, the nano-positioning in both vertical and lateral direction, mounting, jointure and guide design.

A compact mass with the dimensions and mass (100 Kg) of Type-1 MBQ is supported on one side by two passive mounts and on the other side by two active mounts. Figure 5.364 shows a drawing of the mechanical model (left) and a picture of the test bench (right). The two passive supports are used as guide to allow only two DOF on the active side. Each active mount is composed of a piezoelectric stack actuator, mounted with two flexible joints to avoid backlash and friction.

The governing equations are detailed in the §5.18.4.1. However, in this case, the number of variables is reduced: $\mathbf{x} = (x_A, y_A)$, $M = \text{diag}(m, m)$, $\mathbf{f} = (f_1, f_2)^T$ and $\mathbf{w} = (u_A, w_A)^T$ and

$$J = \begin{pmatrix} \sin \beta & \cos \beta \\ -\sin \beta & \cos \beta \end{pmatrix}; \quad K = 2k_a \begin{pmatrix} \sin^2 \beta & 0 \\ 0 & \cos^2 \beta \end{pmatrix}; \quad E = J \quad (5.67)$$

where β is the inclination of the legs with respect to the vertical. The controller consists of a Butterworth high pass filter at 0.5 Hz, and a double lead at 30 Hz. The same compensator is applied in the vertical and the lateral direction, and used to command the actuators after multiplication by the jacobian matrix. Figures 5.365(a) and (b) show the measured transmissibility between the ground and the mass respectively in the lateral and vertical direction.

These preliminary results show that a reduction by a factor two is achieved in the lateral direction, and a factor 5 in the vertical direction, similar to the results obtained with the first test bench.

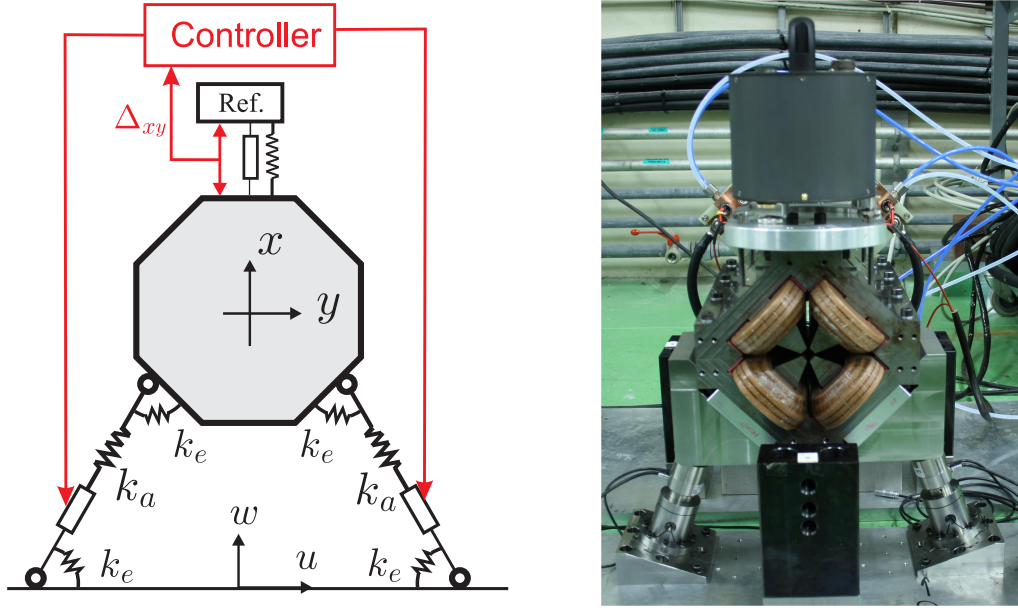


Fig. 5.364: (Left) Model and (Right) picture of the two DOF test bench

Similarly to Fig. 5.363, Fig. 5.366 shows the integrated r.m.s. displacement of the top seismometer for two experiments, one performed during the day and one performed during the night. During the day, at 1 Hz, one sees that the feedback control has reduced $\sigma_x(f)$ from 5.7 nm to 2.1 nm, i.e., a reduction by a factor 2.5. During the night, when the ground motion is even lower, σ_x is reduced from 2 nm to 0.9 nm at 1 Hz, and 0.7 nm at 4 Hz.

In order to test the nano-positioning capability of the test bench, two time histories have been used as input for the two actuators. The corresponding displacement of the mass has been measured in the lateral and vertical direction by capacitive gauges, and is shown in Fig. 5.367(a). Figure 5.367(b) shows the corresponding measured extensions of the legs after multiplication by J . Figure 5.367(c) shows the resulting trajectory of the mass in the vertical plane, measured with capacitive gauges.

Again the positioning was performed without feedback based on the displacement measurement, i.e., in open loop. Although the test was performed in an environment with a high level of background vibrations (integrated r.m.s. above 20 nm at 1 Hz) as visible on the displacement measurements, the trajectory corresponds practically with the ± 1 nm precision requirement.

5.18.7 Technical issues

5.18.7.1 Compatibility with accelerator environment

The stabilization sensors, actuators and eventual elastomers for damping should be radiation hard and insensitive to stray magnetic fields. Furthermore, the required resolution, i.e., μV , very high precision and small latency demands short lead wires imposing local controller hardware screened from radiation [408]. In the following points the criticality for the main components will be discussed together with possible solutions.

Sensors

For the feasibility demonstration on the first two test benches, commercially available broadband seismometers [403] were used that are not adapted to the presence of radiation and stray magnetic fields. Electrochemical seismometers SP500 [409] were developed and tested at the Stanford Linear Accelerator Centre and found not sensitive to magnetic fields. Furthermore, they are stated to be radiation hard

5.18 MAIN BEAM QUADRUPOLE STABILIZATION EQUIPMENT

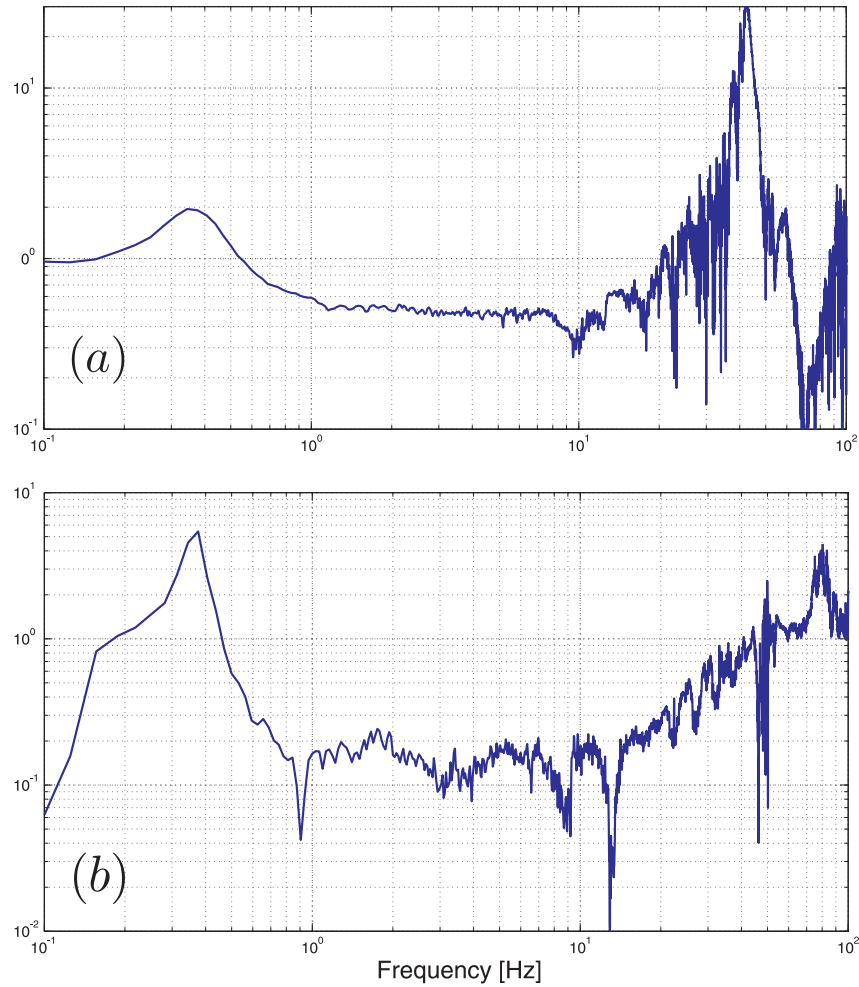


Fig. 5.365: Transmissibility between the ground and the mass of the test bench in the (a) lateral direction and (b) vertical direction.

but no complete results are available to validate this. The SP500 can be considered as a prototype that needs further development to solve inconveniences and further testing to show compatibility.

Another approach consists of adapting a traditional broadband seismometer. The main reason why traditional broadband seismometers are not radiation hard is the presence of electronics inside the device. Secondly, traditional broadband seismometers are sensitive to magnetic fields because of the coil surrounding the high permeability seismic mass that is used for force feedback. A solution was studied and tested on an optical seismometer without force feedback in [410]. They removed all electronics from a broadband seismometer for reasons not linked to radiation. In doing so, they have found a way of making seismometers radiation hard by placing all radiation sensitive components far from the beam. Secondly, they have removed the force feedback from the broadband seismometer. If additionally, all the components such as the spring and the seismic mass are made of low permeability materials, the seismometer is not sensitive to stray magnetic fields. Here again, more work is needed but the results given in the article, especially the obtained sensitivity and noise level are a strong indication of the technical feasibility to build a sensor that is compatible with an accelerator environment.

Actuators

Piezo electrical actuators are devices that are commonly used in nuclear reactors, radioactive waste management [411] and particle accelerators [412]. As they are solid state devices based on ceramics, they can

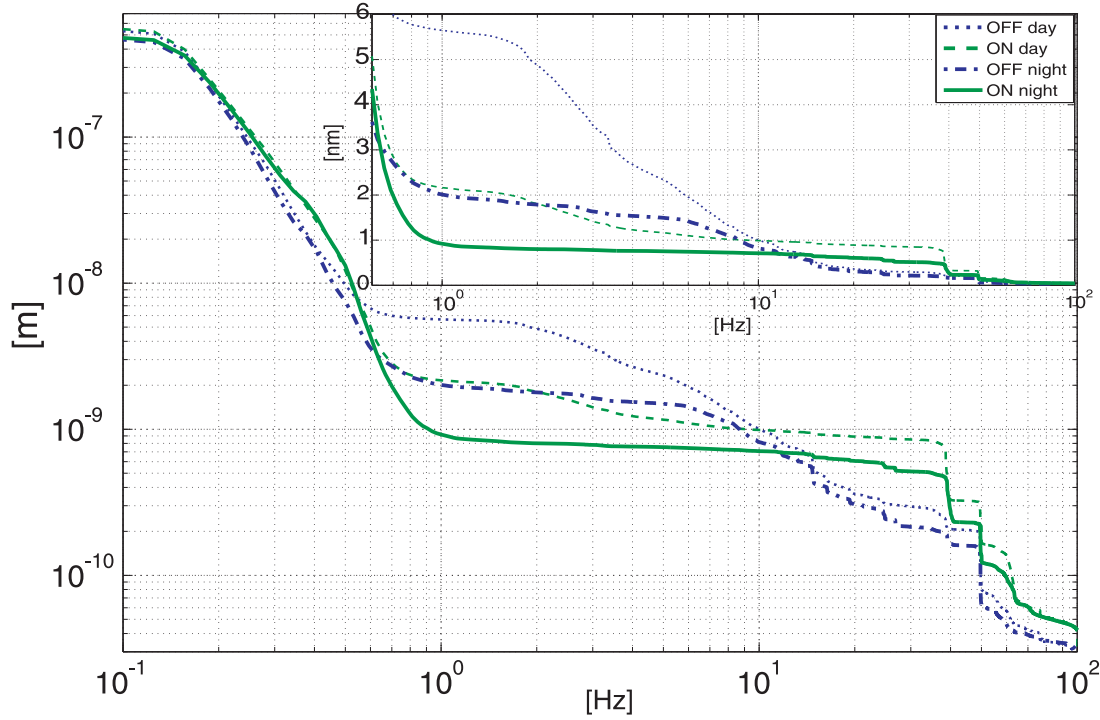


Fig. 5.366: Comparison of r.m.s. integrated of the top displacement $\sigma_x(f)$, for the test bench 2, when the controller is ON and OFF, during the day and during the night.

be considered radiation hard, especially if the amount of polymers used during production is minimized or even completely removed [413]. It is important to use only non-magnetic materials in the housing in order not to introduce dynamic forces due to varying stray magnetic fields of the quadrupole magnet.

Controller hardware

As some of the controller hardware needs to be placed near to the CLIC module, care should be taken in the design in order to allow radiation hard components. The design of the module should foresee rack space close to the module that is screened from radiation.

5.18.7.2 Compatibility with the alignment stage

The ground motion is a broad band excitation with decreasing amplitude with increasing frequency. This excitation is amplified on the accelerator components at the support resonant frequencies. This is a constant worry in light sources and several lessons were learned from this for the CLIC MBQ support. In the first place, an eccentric cam alignment system based strategy was selected for the first Type-4 MBQ alignment system for its expected rigidity. Secondly, an effort was made in the CLIC module design to lower the beam height to 620 mm. A significant advantage is the relatively low mass of the MBQ. The mass of the stabilization system and intermediate parts should nevertheless be minimized. Even if the Hertzian contact of an eccentric cam system can be designed theoretically extremely stiff, measurements in light sources have shown that the whole support can show resonances at rather low frequencies, this however for payloads of several tons.

The eventual impact of a spurious mode of the alignment stage at e.g., 30 Hz in series with the studied stabilization system with the resonance at 350 Hz (rigid option) is considered (Fig. 5.368(a)). The performance of the stabilization is strongly affected at that frequency. However, with the input of a typical low level ground vibration spectrum, the spurious mode at 30 Hz does not make a significant contribution at 1 Hz (Fig. 5.368(b)).

5.18 MAIN BEAM QUADRUPOLE STABILIZATION EQUIPMENT

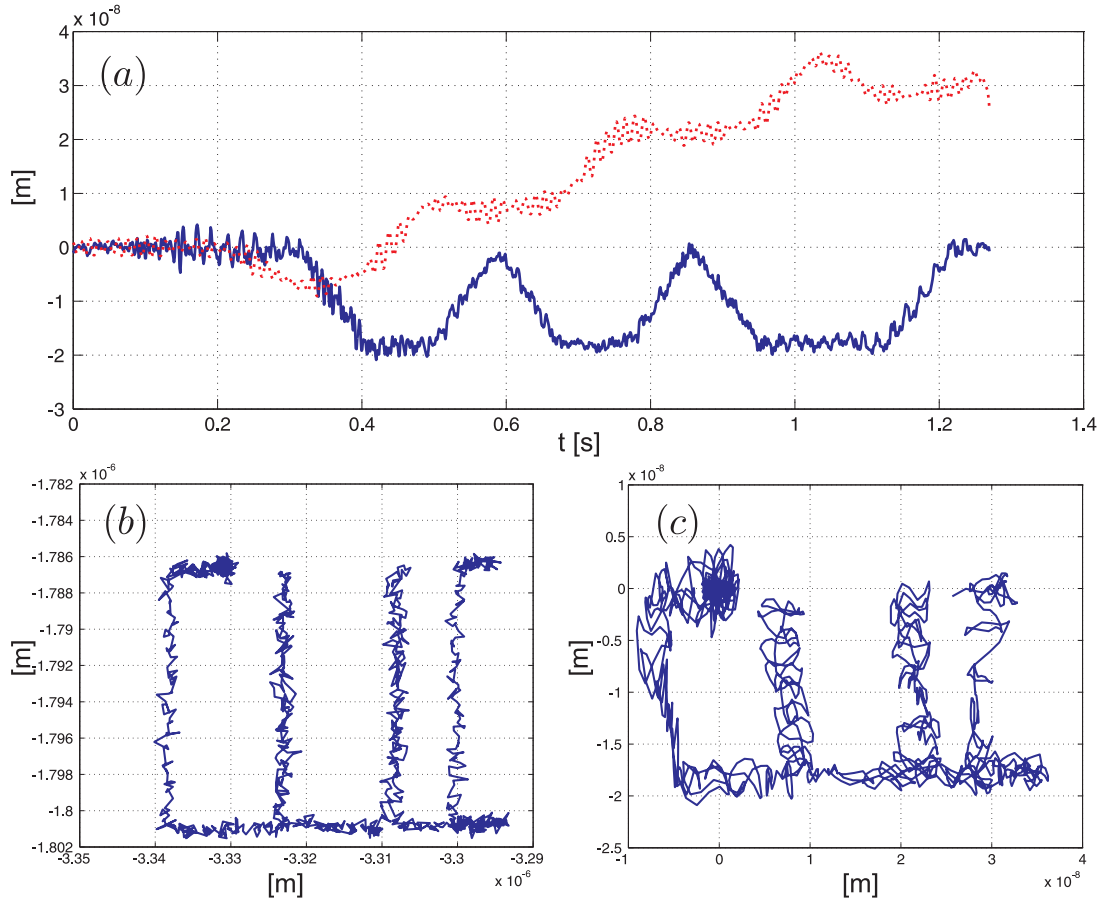


Fig. 5.367: Positioning experiment: (a) Time histories of the vertical (solid line) and lateral (dashed line) displacement of the mass measured by the capacitive gauge; (b) Extension of the legs after multiplication by J ; (c) Resulting trajectory of the mass in the vertical plane.

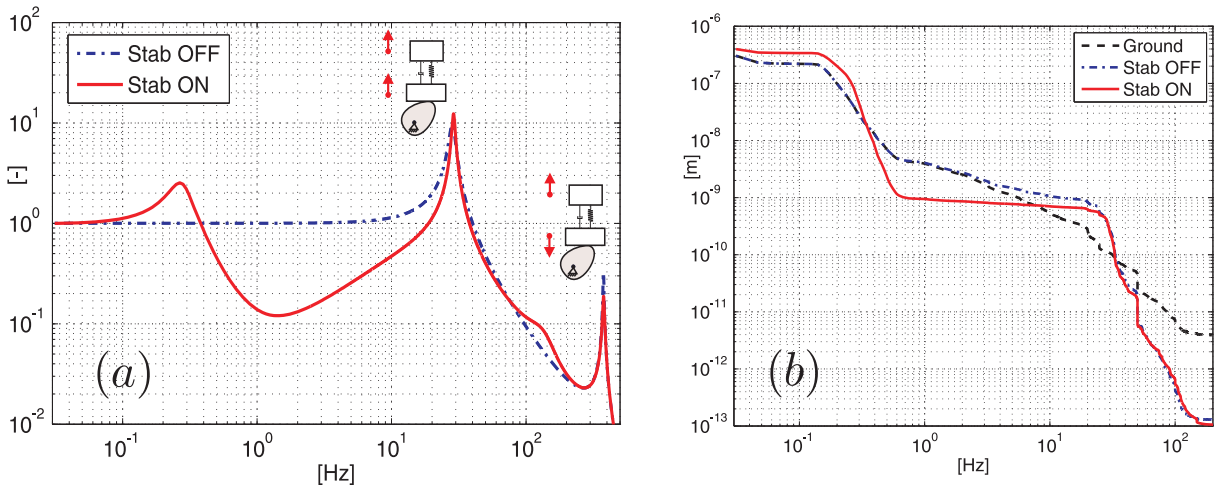


Fig. 5.368: Positioning experiment: (a) Transmissibility between the ground and the quadrupole for a two-DOF system with stabilization on/off; (b) Integrated r.m.s. displacement with a spurious mode at 30 Hz of the alignment support.

Next, for compatibility with the alignment requirements, the stabilization support should be several

times stiffer than the alignment support in order to be able to align against external forces acting directly on the quadrupole as for instance the vacuum bellow forces and cooling tube forces. This would be e.g. problematic for soft stabilization systems. For the fast nano-positioning, the alignment stage should be as stiff as possible in lateral and vertical direction. An additional requirement arises with respect to the measurement of the magnetic field centre with respect to the external references on the quadrupole magnet. Such references on the magnet would be positioned far from the stretched alignment wire in the tunnel and are hence not precise. The x–y guide equipped with x–y position sensors makes it possible to position precisely the magnet with respect to the interface between the magnet girder and the alignment system. This interface is much closer to the alignment wire. Furthermore, as described below, the MBQ should be transportable together with the locked x–y guide, it would be possible to do the fiducialization of the magnet installed on the stabilization system in a very precise position.

5.18.7.3 *Other technical issues*

Air temperature stability in the tunnel

Because of the required precision of the stabilization, the components of the stabilization should remain as much as possible at the same temperature and changes should be as slow as possible. This is especially the case for the seismometers and the control electronics. Temperature changes can create low frequency drifts of input and output signals and can create sensitivity changes of components.

Transportability

Because of the large number of MBQs (3992), they should be installed in the tunnel together with the stabilization system. This is challenging because of the used ceramic piezo actuators that are very sensitive to traction, shear and bending forces. Strict specifications can be made for transport and handling with respect to maximum acceleration and allowed inclination. To relax such specifications to a reasonable level, it is foreseen to lock the magnet inside the x–y guide and magnet girder. The locking forces can be made in the longitudinal direction where they will not act on the actuator.

Machine protection

As the range for the nano-positioning is $\pm 5 \mu\text{m}$, a fast uncontrolled change of the position of the actuators could be a problem for machine protection. First, without precautions, at a power-cut, the piezo actuators will move very fast to their zero position. The lead wires to the actuator can however be opened at the detection of the power-cut. The actuator will move back to the zero position very slowly as there are almost no leak currents inside piezo actuators. Secondly, an uncontrolled change of position can be detected with the x–y position sensor.

5.18.8 **Component inventory**

In general, the stabilization system can be split up in five main component groups: the sensors, the actuators, the mechanical flexural guides in the magnet girder, the DAQ, control and external communication hardware, and the cabling between module and control rack (not detailed in the table). As described above, the stabilization system will be built of a certain number of sensor and actuator pairs. The number of actuator pairs will depend on the MBQ magnet type, i.e., magnet mass and length and is determined by taking into account the mass per actuator, the resulting resonant frequency of the actuators and the stiffness of the quadrupole. Each actuator pair is equipped with lateral and vertical sensors for velocity and position measurements. The following table is based on a first conservative estimation (maximum required pairs) for the required number of actuator pairs for each MBQ type. For the conceptual design as well as for the experimental validation it should be noted that the actuators, sensors, DAQ, controls and communication units (i.e., all components other than the mechanical supports) are all commercially available products.

Table 5.91: Inventory of the equipment for Main Beam quadrupole stabilization

Component	Number			
	Type-1	Type-2	Type-3	Type-4
Piezoelectric actuator	4	6	6	6
Piezoelectric amplifier	4	6	6	6
Flexural joint	8	12	12	12
x-y guide	1	3	3	3
Magnet girder	1	1	1	1
x-y inertial sensor	2	3	3	3
Power supply inertial sensor	1	1	1	1
x-y position sensor	1	3	3	3
x-y position sensor conditioner	1	3	3	3
DAQ, control and communication unit	1	1	1	1

5.18.9 Cost considerations

The main cost driver for the stabilization system is the number of actuator pairs needed for each magnet type. This number also determines the number of x-y inertial and position sensors, flexural joints and mechanical parts, number of amplifiers, conditioners and control channels and finally the number of cables. The reduction of the earlier described number of DOF from six to four was already mainly driven by the resulting cost reduction. The further reduction of number of actuator pairs for any MBQ type would mean a significant cost reduction. This seems feasible for some of the magnet types but shall be confirmed after a complete detailed technical design and experimental validation on each MBQ magnet type. This reduction will be one of the main items in the technical design phase. At the time of writing, only few providers of actuators and sensors with the required resolution and signal to noise ratio are available (market leaders). Several providers exist however that sell equipment that is not far from the requirements. It is reasonable to expect that the economically and technically fast growing market of components for nano-technology will also increase the number of providers in the following years. A cost consideration can be made about the solution of nano-positioning of the MBQ in between beam pulses with the actuators of the stabilization system. The ability of fast and ultra precise adjustment of the quadrupole position within a range of several microns ($\pm 5\mu\text{m}$ proposed at the moment) in between beam pulses can increase the time in between required adjustments of the MBQ with the alignment system based on cam movers. The cam movers cannot make adjustments in between beam pulses and some beam time will be required for each repositioning. Nano-positioning with piezo actuators can hence increase the amount of available beam time.

5.18.10 Outlook for project preparation phase

- For the purpose of the demonstration, a broadband seismometer has been used as inertial reference to validate experimentally the strategy. Even if this procedure managed to fulfil the stability requirements, the performances are limited for two reasons. The first is that, as the signal is integrated to get the displacement, the noise is also integrated. The second is that the sensitivity of the seismometer falls rapidly above 80 Hz. A better adapted sensor could significantly improve the results. The development of an inertial reference coupled to an optical measurement technology is a promising direction, fully compatible with the accelerator environment.
- The conceptual design of the stabilization system must evolve to a complete design to be implemented on a Type-4 and Type-1 prototype MBQ. Such stabilized magnets shall be extensively tested together with the alignment system, eventually in an accelerator environment. The number

of actuator pairs and the x-y guide shall be optimized for all four magnet types for performance and cost. The performance of the x-y position sensor shall be tested.

Once the controller is well known, the flexible PXI solution shall be replaced by less flexible electronics, radiation resistant and optimized for noise, resolution, latency and cost.

- Optimization of the integration with alignment and beam-based feedback.
- Another stabilization system is under study for the final focus quadrupoles (see §3.8) that might give additional information.

REFERENCES

References

1. Zhou, F., Brachmann, A., Maruyama, T. & Sheppard, J. C. *Polarized Photocathode R&D for Future Linear Colliders* SLAC-PUB-13514 (SLAC, Stanford, CA, USA, 2009). <<http://www.slac.stanford.edu/cgi-wrap/getdoc/slac-pub-13514.pdf>>.
2. Aulenbacher, K. *et al.* The MAMI source of polarized electrons. *Nucl. Instr. and Meth. A* **391**, 498–506 (1997).
3. Grames, J. *et al.* in *AIP Conf. Proc. 915. Proc. 17th International Spin Physics Symposium, 2-7 October 2006, Kyoto, Japan* **915** (2006), 1037–1044. doi:10.1063/1.2750949. <<http://dx.doi.org/10.1063/1.2750949>>.
4. Poelker, M. in *EIC Meeting at The CUA, 29-31 July 2010, Edward J. Pryzbyla University Center at CUA* (2010). <http://www.jlab.org/~hornt/EIC_at_CUA>.
5. Adderley, P. A. *et al.* Load-locked dc high voltage GaAs photogun with an inverted-geometry ceramic insulator. *Phys. Rev. ST Accel. Beams* **13**, 010101 (2010).
6. Barday, R. & Aulenbacher, K. in *AIP Conf. Proc. 915. Proc. 17th International Spin Physics Symposium, 2-7 October 2006, Kyoto, Japan* **915** (2006), 1019–1024. doi:10.1063/1.2750946. <<http://dx.doi.org/10.1063/1.2750946>>.
7. Brachmann, A. *et al.* *Ultra-stable flashlamp-pumped laser* SLAC-PUB-10290 (SLAC, Stanford, CA, USA, 2002). <<http://www.slac.stanford.edu/pubs/slapubs/10250/slac-pub-10290.pdf>>.
8. Humensky, T. B., Alley, R., Brachmann, A. & *et al.* SLAC's polarized electron source laser system and minimization of electron beam helicity correlations for the E-158 parity violation experiment. *Nucl. Instr. and Meth. A* **521**, 261–298 (2004).
9. Brachmann, A. *et al.* *Laser development for future photocathode research at SLAC* SLAC-PUB-11373 (SLAC, Stanford, CA, USA, 2005). <<http://www.slac.stanford.edu/pubs/slapubs/11250/slac-pub-11373.pdf>>.
10. Nogueira, G. T., Xu, B., Coello, Y., Dantus, M. & Cruz, F. C. Broadband 2.12 GHz Ti:sapphire laser compressed to 5.9 femtoseconds using MIIPS. *Optics Express* **16**, 10033–10038 (2008).
11. Poelker, M. High power gain-switched diode laser master oscillator and amplifier. *Appl. Phys. Lett.* **67**, 2762–2764 (1995).
12. Hovater, C. & Poelker, M. An injection modelocked Ti:sapphire laser for synchronous photoinjection. *Proc. 1997 Particle Accelerator Conf., 12-16 May 1997, Vancouver, Canada* **3**, 2861–2863 (1998).
13. Ciarrocca, M., Avramopoulos, H. & Papanicolas, C. N. in *Proc. 5th European Particle Accelerator Conf., 10-14 Jun 1996, Barcelona* (1996), 1499–1501. <<http://accelconf.web.cern.ch/accelconf/e96/PAPERS/THPL/THP045L.PDF>>.
14. Kurdi, G. *et al.* *Development of the CTF3 photo-injector laser system* (Central Laser Facility, STFC, UK, 2007). <http://www.clf.rl.ac.uk/resources/PDF/ar06-07_s7rdi_ctf3photoinjector.pdf>.
15. Petrarca, M., Martyanov, M., Csatari Divall, M. & Luchinin, G. Study of the Nd:YLF powerful laser amplifiers for the CTF3 Photo Injectors. *IEEE Journal of Quantum Electronics* **47**, 306–313 (2011).
16. Zhou, F., Brachman, A. & Sheppard, J. *Preliminary design of a bunching system for the CLIC polarized electron source* CERN-OPEN-2010-025. CLIC-Note-813 (CERN, Geneva, 2009). <<http://cdsweb.cern.ch/record/1308186/files/CERN-OPEN-2010-025.pdf>>.

17. Kamitani, T. & Rinolfi, L. *Positron production for CLIC* CERN-OPEN-2001-025. CLIC-Note-465 (CERN, Geneva, 2000). <<http://cdsweb.cern.ch/record/492189?ln=en>>.
18. Dadoun, O. *et al. Study of a hybrid positron source using channeling for CLIC* CLIC-Note-808 (CERN, Geneva, 2009). <<http://cdsweb.cern.ch/record/1248436?ln=en>>.
19. Suwada, T. & et al. in *Proc. 23rd IEEE Particle Accelerator Conf., 4-8 May 2009, Vancouver, British Columbia, Canada* (2009), 518–520. <<http://accelconf.web.cern.ch/accelconf/PAC2009/papers/mo6rfp066.pdf>>.
20. Takahashi, T. in *International Workshop on Linear Colliders 2010 (ECFA-CLIC-ILC Joint Meeting), 18-22 October 2010, Geneva, Switzerland* (2010). <<http://ilcagenda.linearcollider.org/getFile.py/access?contribId=471&sessionId=77&resId=0&materialId=slides&confId=4507>>.
21. Vivoli, A. *et al. The CLIC Positron Capture and Acceleration in the Injector Linac* CERN-OPEN-2010-020. CLIC-Note-819 (CERN, 2010). <<http://cdsweb.cern.ch/record/1277226?ln=en>>.
22. Li, Z., Raubenheimer, T. O. & Miller, R. in *Proc. IEEE 18th Particle Accelerator Conf., 27 March - 2 April, 1999, New York, USA* (1999). <<http://accelconf.web.cern.ch/accelconf/p99/PAPERS/FRA43.PDF>>.
23. Adli, E. *Draft Drive Beam Decelerator Magnet Specification* EDMS 992790 (CERN, 2009). <https://edms.cern.ch/file/992790/3/decelerator_magnet_specification.pdf>.
24. Bondarchuk, E. *et al. Hybrid Quadrupole With Variable Gradient And Precise Regulation Of The Magnetic Center. IEEE Transactions on applied superconductivity* **16**, 1566–1569 (2006).
25. DiMarco, J., Drozhdin, A., Finley, D. & et al. in *Proc. 17th International Conf. on Magnet Technology (MT-17), 24-28 September 2001, Geneva, Switzerland* (2001). <<http://lss.fnal.gov/archive/2002/conf/Conf-01-269-E.pdf>>.
26. Gottschalk, S. C., De Hart, T. E., Kangas, K., Spencer, C. M. & Volk, J. T. in *Proc. 21st IEEE Particle Accelerator Conf., 16-20 May 2005, Knoxville, Tennessee, USA* (2005), 2071–2073. <<http://accelconf.web.cern.ch/accelconf/p05/PAPERS/MPPT029.PDF>>.
27. Schulte, D. *et al. List of Magnet Requirements for CLIC* CERN. <<https://edms.cern.ch/document/1000727/5>> (2010).
28. Schoerling, D. *et al. Design and system integration of the superconducting wiggler magnets for the Compact Linear Collider damping rings. Phys. Rev. ST Accel. Beams* **15**, 042401 (4 2012).
29. Antoniou, F., Martini, M., Papaphilippou, Y. & Vivoli, A. in *Proc. 1st Int. Particle Accelerator Conf., 23-28 May 2010, Kyoto, Japan* (2010), 3542–3544. <<http://accelconf.web.cern.ch/AccelConf/IPAC10/papers/wepe085.pdf>>.
30. Brown, G., Halback, K., Harris, J. & Winick, H. Wiggler and undulator magnets - A review. *Nucl. Instr. and Meth.* **208**, 65–77 (1983).
31. Korostelev, M. *Optics design and performance of an ultra-low emittance damping ring for the compact linear collider* (EPFL, 2006). <<http://lphe.epfl.ch/publications/theses/these.mk.pdf>>.
32. Brunning, O. *et al. LHC Design Report. Volume v.1: the LHC Main Ring* CERN-2004-003-V-1 (CERN, Geneva, 2004). <<http://cdsweb.cern.ch/record/782076?ln=en>>.
33. *Bochvar Institute of Inorganic Materials, Moscow* <<http://www.bochvar.ru>> (2010).

REFERENCES

34. Naus, M. T. *Optimization of Internal-SnNb3Sn Composites* (University of Wisconsin-Madison, 2002). <http://magnet.fsu.edu/~lee/asc/pdf_papers/theses/mtn02phd.pdf>.
35. Emma, P. & Raubenheimer, T. Systematic approach to damping ring design. *Phys. Rev. ST Accel. Beams* **4**, 021001 (2001).
36. Safranek, D. *et al.* Nonlinear dynamics in a SPEAR wiggler. *Phys. Rev. ST Accel. Beams* **5**, 010701 (2002).
37. Schoerling, D. *et al.* in *Proc. 1st Int. Particle Accelerator Conf., 23-28 May 2010, Kyoto, Japan* (2010), 3174–3176. <<http://accelconf.web.cern.ch/accelconf/IPAC10/papers/wepd039.pdf>>.
38. *Field Computation for Accelerator Magnets. Analytical and Numerical Methods for Electromagnetic Design and Optimization* (ed Russenschuck, S.) (Wiley-VCH, 2010).
39. Bordini, B. & Rossi, L. Self Field Instability in High-JcNb3Sn Strands With High Copper Residual Resistivity Ratio. *IEEE Transactions on Applied Superconductivity* **19**, 2470–2476 (2009).
40. *Engineering superconductivity* (ed Lee, P. J.) (Wiley-Interscience, New York, 2001).
41. Stekly, Z. J. & Zar, J. L. Stable superconducting coils. *IEEE Transactions on Nuclear Science* **12**, 367–372 (1965).
42. Bordini, D., Maccaferri, R., Rossi, L. & Tommasini, D. in *Proc. 11th European Particle Accelerator Conf., 23-27 June 2008, Genoa, Italy* (2008), 2404–2406. <<http://accelconf.web.cern.ch/AccelConf/e08/papers/wepd003.pdf>>.
43. Walters, C. R. *Design of multistrand conductors for superconducting magnet windings* BNL-18928. AADD-74-2 (Brookhaven National Laboratory, Upton, NY, 1974). <<http://ccdb4fs.kek.jp/cgi-bin/img/allpdf?198010209>>.
44. Wilson, M. N. *Superconducting Magnets* (Oxford University Press, USA, 1983).
45. Maccaferri, R., Facchini, M., Jung, R. & *et al.* in *Proc. 9th European Particle Accelerator Conf., 5-9 July 2004, Lucerne, Switzerland* (2004), 1630–1632. <<http://accelconf.web.cern.ch/accelconf/e04/PAPERS/WEPKF017.PDF>>.
46. Schwinger, J. On the classical radiation of accelerated electrons. *Phys. Rev.* **75**, 1912–1925 (1949).
47. Kim, K.-J. Angular distribution of undulator power for an arbitrary deflection parameter K. *Nucl. Instr. and Meth. A* **246**, 67–70 (1986).
48. Wiedemann, H. *Particle accelerator physics* (Springer, Berlin, 2007).
49. Hubbell, J. H. & Seltzer, S. M. *Tables of X-ray mass attenuation coefficients and mass energy-absorption coefficients from 1 keV to 20 MeV for elements Z = 1 to 92 and 48 additional substances of dosimetric interest* <<http://www.nist.gov/physlab/data/xraycoef/index.cfm>> (2010).
50. Rumolo, G., Ruggiero, F. & Zimmermann, F. Simulation of the electron-cloud build up and its consequences on heat load, beam stability, and diagnostics. *Phys. Rev. ST Accel. Beams* **4**, 012801 (2001).
51. Suetsugu, Y., Fukuma, H., Shibata, K., Pivi, M. T. F. & Wang, L. in *Proc. 1st Int. Particle Accelerator Conf., 23-28 May 2010, Kyoto, Japan* (2010), 2021–2023. <<http://accelconf.web.cern.ch/accelconf/IPAC10/papers/tupd043.pdf>>.
52. Podobedov, B. Resistive wall wakefields in the extreme anomalous skin effect regime. *Phys. Rev. ST Accel. Beams* **12**, 044401 (2009).

53. Podobedov, B. Resistive wall wakefields in the extreme anomalous skin effect regime. *Phys. Rev. ST Accel. Beams* **12**, 044401 (2009).
54. *CLIC parameter list 3 TeV* <<http://clic-meeting.web.cern.ch/clic-meeting/clicktable2010.html>> (2010).
55. NIST. *Cryogenic material properties* <<http://cryogenics.nist.gov/MPropsMAY/materialproperties.htm>> (2010).
56. Lebrun, P. in *CAS - CERN Accelerator School on Superconductivity and Cryogenics for Accelerators and Detectors* (eds Russenschuck, S. & Vandoni, G.) (2002), 348–362. <<http://cdsweb.cern.ch/record/503603>>.
57. Carron, G. *et al.* in *Proc. 20th International Linear Accelerator Conf., 21-25 Aug 2000, Monterey, CA, USA* (2000), 416–418. <<http://accelconf.web.cern.ch/accelconf/l00/papers/TUA16.pdf>>.
58. Jensen, E., Syratchev, I. & Wuensch, W. in *Proc. 19th IEEE Particle Accelerator Conf., 18-22 June 2001, Chicago, Illinois, USA* (2001), 855–857. <<http://accelconf.web.cern.ch/accelconf/p01/PAPERS/MPPH040.PDF>>.
59. Jensen, E. in *Proc. XXI Int. Linear Accelerator Conf., 19-23 August 2002, Gyeongju, Korea* (2002), 34–36. <<http://accelconf.web.cern.ch/accelconf/l02/AUTINDEX/..%5CPAPERS%5CM0401.PDF>>.
60. Corsini, R. *et al.* in *Proc. 9th European Particle Accelerator Conf., 5-9 July 2004, Lucerne, Switzerland* (2004), 39–41. <<http://accelconf.web.cern.ch/accelconf/e04/PAPERS/MOCH02.PDF>>.
61. Wegner, R. & Jensen, E. *CLIC Drive Beam Accelerating Structures* CLIC-Note-945(2012) (CERN, 2012).
62. Wright, E., Bohlen, H., Lenci, S. & Balkcum, A. in *2nd ILC Accelerator Workshop, 14-27 August 2005, Snowmass, Colorado, USA* (2005). <http://www.slac.stanford.edu/econf/C0508141/proc/pres/ILCAW0214_TALK.PDF>.
63. Jensen, E. & Syratchev, I. in *AIP Conf. Proc. 807. 7th Int. High Energy Density and High Power RF Workshop, 13-17 June 2005, Kalamata, Greece* (2006), 90–99. doi:10.1063/1.2158763. <http://proceedings.aip.org/resource/2/apcpcs/807/1/90_1?ver=pdfcov>.
64. Jensen, E. in *Proc. XXV Linear Accelerator Conf., 12-17 September 2010, Tsukuba, Japan* (2010), 717–719. <<http://accelconf.web.cern.ch/accelconf/LINAC2010/papers/th103.pdf>>.
65. Alesini, D. & Gallo, A. Effects of the beam loading in the RF deflectors of the CLIC test facility CTF3 combiner ring. *Phys. Rev. ST Accel. Beams* **7**, 034403 (2004).
66. Alesini, D. & Marcellini, F. RF deflector design of the CLIC test facility CTF3 delay loop and beam loading effect analysis. *Phys. Rev. ST Accel. Beams* **12**, 031301 (2009).
67. Alesini, D., Biscari, C., Chigo, A. & Marcellini, F. Beam instability induced by rf deflectors in the combiner ring of the CLIC test facility and mitigation by damped deflecting structures. *Phys. Rev. ST Accel. Beams* **14**, 022001 (2011).
68. Alesini, D., Biscari, C. & Ghigo, A. in *Proc. 1st Int. Particle Accelerator Conf., 23-28 May 2010, Kyoto, Japan* (2010), 4360–4362. <<http://accelconf.web.cern.ch/accelconf/IPAC10/papers/thpd037.pdf>>.
69. Bernard, P., Lengeler, H. & Vaghin, V. *On the design of disc-loaded waveguides for RF separators* CERN-68-30 (CERN, 1968). <<http://cdsweb.cern.ch/record/275758/files/CERN-68-30.pdf>>.

REFERENCES

70. Grudiev, A. *Conceptual design of the CLIC damping ring RF system at 1 and 2 GHz (Baseline and Alternatives)* CERN-OPEN-2011-031. CLIC-Note-879 (CERN, 2011). <<http://cdsweb.cern.ch/record/1357338/files/CERN-OPEN-2011-031.pdf>>.
71. Akai, K. *et al.* in *Proc. 6th European Particle Accelerator Conf., 22-26 June 1998, Stockholm, Sweden* (1998), 17491751. <<http://www.cern.ch/accelconf/e98/PAPERS/TUP10G.PDF>>.
72. Kageyama, T. *et al.* in *Proc. 1st Asian Particle Accelerator Conf., 23-27 March 1998, Tsukuba, Japan* (1998), 773–775. <<http://accelconf.web.cern.ch/accelconf/a98/APAC98/6D039.PDF>>.
73. Morita, Y. *et al.* in *Proc. 1st Int. Particle Accelerator Conf., 23-28 May 2010, Kyoto, Japan* (2010), 1536–1538. <<http://accelconf.web.cern.ch/accelconf/IPAC10/papers/tupeb011.pdf>>.
74. Grudiev, A., Braun, H.-H., Schulte, D. & Wuensch, W. in *Proc. XXIV Linear Accelerator Conf., 29 September - 3 October 2008, Victoria, British Columbia, Canada* (2008), 527–529. <<http://accelconf.web.cern.ch/accelconf/LINAC08/papers/tup055.pdf>>.
75. Grudiev, A. & Wuensch, W. in *Proc. XXIV Linear Accelerator Conf., 29 September - 3 October 2008, Victoria, British Columbia, Canada* (2008), 933–935. <<http://accelconf.web.cern.ch/accelconf/LINAC08/papers/thp062.pdf>>.
76. Ansoft Corporation - HFSS <www.ansoft.com>.
77. Luong, M., Wilson, I. & Wuensch, W. in *Proc. IEEE 18th Particle Accelerator Conf., 27 March - 2 April, 1999, New York, USA* (1999), 821–823. <<http://accelconf.web.cern.ch/accelconf/p99/PAPERS/MOP68.PDF>>.
78. Grudiev, A., Calatroni, S. & Wuensch, W. New local field quantity describing the high gradient limit of accelerating structures. *Phys. Rev. ST Accel. Beams* **12**, 102001 (2009).
79. Bruns, W. *The GdfidL Electromagnetic Field simulator* <www.gdfidl.de>.
80. Peauger, F., Farabolini, W., Girardot, P. & *et al.* in *Proc. XXV Linear Accelerator Conf., 12-17 September 2010, Tsukuba, Japan* (2010), 641–643. <<http://accelconf.web.cern.ch/accelconf/LINAC2010/papers/tup098.pdf>>.
81. Zennaro, R. *Study of the machining and assembly tolerances for the CLIC accelerating structure* EUROTeV-Report-2008-081 (CERN, 2008). <http://www.eurotev.org/sites/site_eurotev/content/e328/e329/e1082/e1532/EUROTeV-Report-2008-081.pdf>.
82. ATIA - a multi-platform CAD/CAM/CAE commercial software suite developed by Dassault Systemes company <<http://www.3ds.com/products/catia>>.
83. Samoshkin, A., Gudkov, D. & Riddone, G. in *Proc. XXV Linear Accelerator Conf., 12-17 September 2010, Tsukuba, Japan* (2010), 91–93. <<http://accelconf.web.cern.ch/accelconf/LINAC2010/papers/mop020.pdf>>.
84. Peauger, F., Farabolini, W., Girardot, P. & *et al.* in *Proc. XXV Linear Accelerator Conf., 12-17 September 2010, Tsukuba, Japan* (2010), 641–643. <<http://accelconf.web.cern.ch/accelconf/LINAC2010/papers/tup098.pdf>>.
85. Riddone, G. *et al.* in *Proc. 1st Int. Particle Accelerator Conf., 23-28 May 2010, Kyoto, Japan* (2010), 3819–3821. <<http://accelconf.web.cern.ch/accelconf/IPAC10/papers/thpea064.pdf>>.
86. Zennaro, R. *et al.* in *Proc. XXIV Linear Accelerator Conf., 29 September - 3 October 2008, Victoria, Canada* (2008), 533–535. <<http://accelconf.web.cern.ch/accelconf/LINAC08/papers/tup057.pdf>>.

87. Adolphsen, C. in *Proc. 20th IEEE Particle Accelerator Conf., 12-16 May 2003, Portland, Oregon, USA* (2003), 668–670. <<http://accelconf.web.cern.ch/accelconf/p03/PAPERS/ROPC006.PDF>>.
88. Matsumoto, S. *et al.* in *Proc. XXIV Linear Accelerator Conf., 29 September - 3 October 2008, Victoria, Canada* (2008), 906–908. <<http://accelconf.web.cern.ch/accelconf/LINAC08/papers/thp053.pdf>>.
89. Schirm, K. M. *et al.* in *Proc. 1st Int. Particle Accelerator Conf., 23-28 May 2010, Kyoto, Japan* (2010), 3990–3992. <<http://accelconf.web.cern.ch/accelconf/IPAC10/papers/thpeb053.pdf>>.
90. Ruber, R. J. M. Y., Ziemann, G. V., Ekeloef, T., Johnson, M. & *et al.* in *Proc. 11th European Particle Accelerator Conf., 23-27 June 2008, Genoa, Italy* (2008), 2821–2823. <<http://accelconf.web.cern.ch/accelconf/e08/papers/wepp139.pdf>>.
91. Wang, J. W., Lewandowski, J. R., Van Pelt, J. W., Yoneda, C. & *et al.* in *Proc. 1st Int. Particle Accelerator Conf., 23-28 May 2010, Kyoto, Japan* (2010), 3819–3821. <<http://accelconf.web.cern.ch/accelconf/IPAC10/papers/thpea064.pdf>>.
92. Higo, T., Matsumoto, S., Yokoyama, K., Fukuda, S. & *et al.* in *Proc. 1st Int. Particle Accelerator Conf., 23-28 May 2010, Kyoto, Japan* (2010), 3699–3701. <<http://accelconf.web.cern.ch/accelconf/IPAC10/papers/thpea012.pdf>>.
93. Grudiev, A., Calatroni, S. & Wuensch, W. New local field quantity describing the high gradient limit of accelerating structures. *Phys. Rev. ST Accel. Beams* **12**, 102001 (2009).
94. Doebert, S., Adolphsen, C., Bowden, G. B., Burke, D. L. & *et al.* in *Proc. 21st IEEE Particle Accelerator Conf., 16-20 May 2005, Knoxville, Tennessee, USA* (2005), 372–374. <<http://accelconf.web.cern.ch/accelconf/p05/PAPERS/ROAC004.PDF>>.
95. Jones, R. M., Adolphsen, C. E., Wang, J. W. & Li, Z. Wakefield damping in a pair of X-band accelerators for linear colliders. *Phys. Rev. ST Accel. Beams* **9**, 102001 (2006).
96. Doebert, S., Adolphsen, C., Jones, R. M., Lewandowski, J. R. & *et al.* in *Proc. 21st IEEE Particle Accelerator Conf., 16-20 May 2005, Knoxville, Tennessee, USA* (2005), 2804–2806. <<http://accelconf.web.cern.ch/accelconf/p05/PAPERS/TPPT044.PDF>>.
97. Achard, C. *et al.* *An Asset Test of the CLIC Accelerating Structure* CERN-PS-2000-044-RF. CLIC-Note-443 (CERN, Geneva, 2000). <<http://accelconf.web.cern.ch/accelconf/e00/PAPERS/THP2A18.pdf>>.
98. Adolphsen, C. in *Proc. 21st IEEE Particle Accelerator Conf., 16-20 May 2005, Knoxville, Tennessee, USA* (2005), 204–206. <<http://accelconf.web.cern.ch/accelconf/p05/PAPERS/TOPE002.PDF>>.
99. Ansoft Corporation - HFSS <www.ansoft.com>.
100. Schulte, D. *Stability of the drive beam in the decelerator of CLIC* CERN-PS-2002-052-AE. CLIC-Note-528 (CERN, Geneva, 2002). <<http://accelconf.web.cern.ch/accelconf/e02/PAPERS/MOPRI044.pdf>>.
101. Syratcev, I. V. *Mode Launcher as an Alternative Approach to the Cavity-Based RF Coupler of Periodic Structures* CERN-OPEN-2002-005. CERN-PS-RF-NOTE-2002-013. CLIC-Note-503 (CERN, Geneva, 2002). <<http://cdsweb.cern.ch/record/533650?ln=en>>.
102. Syratcev, I. V. *Efficient RF Power Extraction from the CLIC Power Extraction and Transfer Structure (PETS)* CERN-OPEN-2003-017. CLIC-Note-571 (CERN, Geneva, 2003). <<http://cdsweb.cern.ch/record/621402?ln=en>>.
103. Bruns, W. *The GdfidL Electromagnetic Field simulator* <www.gdfidl.de>.

REFERENCES

104. Riche, A. & Schulte, D. in *Proc. 1998 Linear Accelerator Conf., 23-28 August 1998, Chicago, IL, USA* (1998), 118–120. <<http://accelconf.web.cern.ch/accelconf/198/PAPERS/MO4031.PDF>>.
105. Candel, A. E., Kabel, A. C., Ko, K. & et al. in *Proc. ICAP 2006, 2-6 October 2006, Chamonix, France* (2006), 176–178. <<http://accelconf.web.cern.ch/accelconf/icap06/PAPERS/WEMPMP03.PDF>>.
106. Schulte, D., Guignard, G., Leros, N. & d’Amico, E. T. in *Proc. 19th IEEE Particle Accelerator Conf., 18-22 June 2001, Chicago, Illinois, USA* (2001), 3033–3035. <<http://accelconf.web.cern.ch/accelconf/p01/PAPERS/RPAH082.PDF>>.
107. Syrathev, I. & Cappelletti, A. in *CLIC08 Workshop, 14-17 October 2008, CERN* (Geneva, 2008). <<http://indico.cern.ch/getFile.py/access?contribId=140&sessionId=50&resId=1&materialId=slides&confId=30383>>.
108. Syrathev, I. & Cappelletti, A. in *Proc. 1st Int. Particle Accelerator Conf., 23-28 May 2010, Kyoto, Japan* (2010), 3407–3409. <<http://accelconf.web.cern.ch/accelconf/IPAC10/papers/wepe026.pdf>>.
109. Grudiev, A., Cappelletti, A. & Kononenko, O. in *Proc. XXV Linear Accelerator Conf., 12-17 September 2010, Tsukuba, Japan* (2010), 94–96. <<http://accelconf.web.cern.ch/accelconf/LINAC2010/papers/mop021.pdf>>.
110. Tantawi, S. *Test Facilities and Component Developments 2nd Collaboration Meeting on X-Band Accelerator Structure design and TEST program*, KEK, Japan. 2008.
111. Adolphsen, C. in *Proc. 21st IEEE Particle Accelerator Conf., 16-20 May 2005, Knoxville, Tennessee, USA* (2005), 204–206. <<http://accelconf.web.cern.ch/accelconf/p05/PAPERS/TOPE002.PDF>>.
112. Delahaye, J.-P. in *Proc. 1st Int. Particle Accelerator Conf., 23-28 May 2010, Kyoto, Japan* (2010), 4769–4771. <<http://accelconf.web.cern.ch/accelconf/IPAC10/papers/frxcmh01.pdf>>.
113. Riddone, G., Schulte, D., Syrathev, I. & et al. in *Proc. 11th European Particle Accelerator Conf., 23-27 June 2008, Genoa, Italy* (2008), 607–609. <<http://accelconf.web.cern.ch/accelconf/e08/papers/mopp028.pdf>>.
114. Peauger, F., Farabolini, W., Girardot, P. & et al. in *Proc. XXV Linear Accelerator Conf., 12-17 September 2010, Tsukuba, Japan* (2010), 641–643. <<http://accelconf.web.cern.ch/accelconf/LINAC2010/papers/tup098.pdf>>.
115. Jeanneret, J. B., Rumolo, G. & Schulte, D. in *Proc. 1st Int. Particle Accelerator Conf., 23-28 May 2010, Kyoto, Japan* (2010), 3401–3403. <<http://accelconf.web.cern.ch/accelconf/IPAC10/papers/wepe024.pdf>>.
116. Rumolo, G. & Schulte, D. in *Proc. 23rd IEEE Particle Accelerator Conf., 4-8 May 2009, Vancouver, British Columbia, Canada* (2009), 4658–4660. <<http://accelconf.web.cern.ch/accelconf/PAC2009/papers/fr5rfp053.pdf>>.
117. Gazis, N., Riddone, G., A., S. & et al. *Study of the supporting system for the CLIC Two-Beam Module* CERN-OPEN-2010-023. CLIC-Note-857 (CERN, Geneva, 2010). <<http://cdsweb.cern.ch/record/1308174/files/CERN-OPEN-2010-023.pdf>>.
118. Gazis, N., Riddone, G., Samoshkin, A. & et al. Study and application of micrometric alignment on the prototype girders of the CLIC Two-Beam Module. *Key Engineering Materials* **495**, 96–99 (2011).

119. Schulte, D. in *Proc. 23rd IEEE Particle Accelerator Conf., 4-8 May 2009, Vancouver, British Columbia, Canada* (2009), 4664–4666. <<http://accelconf.web.cern.ch/accelconf/PAC2009/papers/fr5rfp055.pdf>>.
120. Mainaud Durand, H., Touzé, T., Griffet, S., Kemppinen, J. & Lackner, F. in *Proc. 11th International Workshop on Accelerator Alignment, 3-7 September 2010, DESY, Hamburg, Germany* (2010). <http://iwaa2010.desy.de/e107506/e107507/e113203/e119271/IWAA2010_HMD_CLIC.pdf>.
121. Touzé, T. in *Proc. 11th International Workshop on Accelerator Alignment, 3-7 September 2010, DESY, Hamburg, Germany* (2010). <http://iwaa2010.desy.de/e107506/e107507/e113375/e119274/IWAA2010_TT_CLIC.pdf>.
122. Griffet, S. *Fiducialisation and pre-alignment* EDMS 1096130 (CERN, 2010). <https://edms.cern.ch/file/1096130/2/Fidu_Pre-Align_Note-Technique_V2_EN.pdf>.
123. Lackner, F. *et al.* Development of an eccentric cam-based active pre-alignment system for the CLIC Main Beam quadrupole magnet. *Diamond Light Source Proceedings MEDSI-6, Oxford, UK* **1**, 4 (2010).
124. Collette, C. *et al.* Active quadrupole stabilization for future linear particle colliders. *Nucl. Instr. and Meth. A* **621**, 71–78 (2010).
125. Collette, C., Artoos, K., Guinchard, M. & Hauviller, C. Seismic response of linear accelerators. *Phys. Rev. ST Accel. Beams* **13**, 072801 (2010).
126. Artoos, K. *et al.* in *Proc. 1st Int. Particle Accelerator Conf., 23-28 May 2010, Kyoto, Japan* (2010), 2824–2826. <<http://accelconf.web.cern.ch/accelconf/IPAC10/papers/wepeb058.pdf>>.
127. Wright, T. P. Learning curve. *Journal of the Aeronautical Science* (1936).
128. Rumolo, G. *Vacuum System for the CLIC Two-Beam Modules. Parameter Specification* EDMS 992778 v.2 (CERN, 2010). <https://edms.cern.ch/file/992778/2/Vacuum_system_Main_Linac.doc>.
129. Garion, C. & Kos, H. in *Proc. 23rd IEEE Particle Accelerator Conf., 4-8 May 2009, Vancouver, British Columbia, Canada* (2010), 363–365. <<http://accelconf.web.cern.ch/accelconf/PAC2009/papers/mo6rfp007.pdf>>.
130. Maruyama, T. in *Linear Collider Workshop of the Americas, 29 September - 3 October 2009, Albuquerque, New Mexico, USA* (2009). <<http://ilcagenda.linearcollider.org/getFile.py/access?contribId=201&sessionId=13&resId=1&materialId=slides&confId=3461>>.
131. Chiggiato, P. & Kersevan, R. Synchrotron radiation-induced desorption from a NEG-coated vacuum chamber. *Vacuum* **60**, 67–72 (2001).
132. Rathjen, C. *et al.* in *Proc. 21st IEEE Particle Accelerator Conf., 16-20 May 2005, Knoxville, Tennessee, USA* (2005), 2744–2746. <<http://accelconf.web.cern.ch/accelconf/p05/PAPERS/RPPE043.PDF>>.
133. Rumolo, G. *Vacuum System for the CLIC long transfer line. Parameter Specification* EDMS 992775 v.2 (CERN, 2010). <https://edms.cern.ch/file/992775/2/Vacuum_system_Long_Transfer_Line.doc>.
134. Jeanneret, J. B. *et al.* in *Proc. 11th European Particle Accelerator Conf., 23-27 June 2008, Genoa, Italy* (2008), 3017–3019. <<http://accelconf.web.cern.ch/accelconf/e08/papers/thpc018.pdf>>.

REFERENCES

135. Baglin, V. *Etude de la photo-désorption de surfaces techniques aux températures cryogéniques* (Université Denis Diderot, 7 UFR de Physique, Paris, 1997).
136. Turner, W. C. in *Proc. IEEE 15th Particle Accelerator Conf., 17-20 May 1993, Washington, USA* (1993), 3833–3835. <http://accelconf.web.cern.ch/accelconf/p93/PDF/PAC1993_3833.PDF>.
137. Rumolo, G., Jeanneret, J. B., Papaphilippou, Y. & Quatraro, D. in *Proc. 11th European Particle Accelerator Conf., 23-27 June 2008, Genoa, Italy* (2008), 658–660. <<http://accelconf.web.cern.ch/accelconf/e08/papers/mopp049.pdf>>.
138. Grafström, P. in *Proc. of CAS - CERN Accelerator School. Course on Vacuum in Accelerators, 16-24 May 2006, Platja d'Aro, Spain* (2006), 231–226. <<http://cdsweb.cern.ch/record/1047067/files/p213.pdf>>.
139. Rumolo, G., Papaphilippou, Y. & Bruns, W. in *Proc. 11th European Particle Accelerator Conf., 23-27 June 2008, Genoa, Italy* (2008), 661–663. <<http://accelconf.web.cern.ch/accelconf/e08/papers/mopp050.pdf>>.
140. Gröbner, O. in *Proc. 1997 Particle Accelerator Conf., 12-16 May 1997, Vancouver, B.C., Canada* (1997), 3589–3591. <<http://accelconf.web.cern.ch/accelconf/pac97/papers/pdf/4P004.PDF>>.
141. Yin Vallgren, C. *et al.* Amorphous carbon coatings for the mitigation of electron cloud in the CERN Super Proton Synchrotron. *Phys. Rev. ST Accel. Beams* **14**, 071001 (2011).
142. Yin Vallgren, C. in *Proc. 1st Int. Particle Accelerator Conf., 23-28 May 2010, Kyoto, Japan* (2010), 2375–2377. <<http://accelconf.web.cern.ch/accelconf/IPAC10/papers/weoamh03.pdf>>.
143. Hilleret, N. in *Proc. of CAS - CERN Accelerator School. Course on Vacuum in Accelerators, 16-24 May 2006, Platja d'Aro, Spain* (2006), 87–116. <<http://cdsweb.cern.ch/record/1046854/files/p87.pdf>>.
144. Suetsugu, Y. *et al.* First experimental and simulation study of the secondary electron and photo-electron yield of NEG materials (Ti-Zr-V) coating under intense photon irradiation. *Nucl. Instr. Meth. A* **554**, 92–113 (2005).
145. Baglin, V. in *Proc. 6th European Particle Accelerator Conf., 22-26 June 1998, Stockholm, Sweden* (1998), 2169–2171. <<http://www.cern.ch/accelconf/e98/PAPERS/TUP18H.PDF>>.
146. Calatroni, S. in *International Workshop on Linear Colliders 2010 (ECFA-CLIC-ILC Joint Meeting), 18-22 October 2010, Geneva, Switzerland* (2010). <<http://ilcagenda.linearcollider.org/getFile.py/access?contribId=300&sessionId=83&resId=1&materialId=slides&confId=4507>>.
147. Vorlaufer, C. *Modification of Ultra-High Vacuum Surfaces Using Free Radicals* (Vienna Tech. Univ., Vienna, 2002). <<http://cdsweb.cern.ch/record/547706/files/thesis-2002-014.pdf>>.
148. Garion, C. in *Proc. 2nd Int. Particle Accelerator Conf., 4-9 September 2011, San Sebastian, Spain* (2011), 1569–1571. <<http://accelconf.web.cern.ch/accelconf/IPAC2011/papers/tups021.pdf>>.
149. Kildemo, M. New spark-test device for material characterization. *Nucl. Instr. and Meth. A* **530**, 596–606 (2004).
150. Descoeudres, A., Levinsen, Y., Calatroni, S., Taborelli, M. & Wuensch, W. Investigation of the dc vacuum breakdown mechanism. *Phys. Rev. ST Accel. Beams* **12**, 092001 (2009).

151. Garion, C. Monte Carlo method implemented in a finite element code with application to dynamic vacuum in particle accelerators. *Vacuum* **84**, 274–276 (2010).
152. Garion, C. *Breakdown induced dynamic pressure in a CLIC accelerating structure* EDMS 1095288 (CERN). <<https://edms.cern.ch/document/1095288/1>>.
153. Ramsvik, T., Calatroni, S., Reginelli, A. & Taborelli, M. Influence of ambient gases on the dc saturated breakdown field of molybdenum, tungsten, and copper during intense breakdown conditioning. *Phys. Rev. ST Accel. Beams* **10**, 042001 (2007).
154. Jimenez, J. M. in *Proc. 11th European Particle Accelerator Conf., 23-27 June 2008, Genoa, Italy* (2008), 1959–1961. <<http://accelconf.web.cern.ch/accelconf/e08/papers/weobm04.pdf>>.
155. Al-Dmour, E. in *Proc. 11th European Particle Accelerator Conf., 23-27 June 2008, Genoa, Italy* (2008), 31–35. <<http://accelconf.web.cern.ch/accelconf/e08/papers/mozbg01.pdf>>.
156. Walstong, S. *et al.* Performance of a High Resolution Cavity Beam Position Monitor System. *Nucl. Instr. and Meth. A* **578**, 1–22 (2007).
157. Smith, S. R. *et al.* in *Proc. 23rd IEEE Particle Accelerator Conf., 4-8 May 2009, Vancouver, British Columbia, Canada* (2009), 754–756. <<http://accelconf.web.cern.ch/accelconf/PAC2009/papers/tu3grc05.pdf>>.
158. Heo, A., Kim, E.-S., Kim, H.-S. & *et al.* in *Proc. 23rd IEEE Particle Accelerator Conf., 4-8 May 2009, Vancouver, British Columbia, Canada* (2009), 3603–3605. <<http://accelconf.web.cern.ch/accelconf/PAC2009/papers/th5rfp070.pdf>>.
159. Lunin, A. *et al.* in *Proc. 1st Int. Particle Accelerator Conf., 23-28 May 2010, Kyoto, Japan* (2010), 1185–1187. <<http://accelconf.web.cern.ch/accelconf/IPAC10/papers/mope087.pdf>>.
160. *Handbook of Accelerator Physics and Engineering* (eds Chao, A. & Tigner, M.) (World Scientific, 1998).
161. Bravin, E. & Lefevre, T. in *Proc. 2003 Particle Accelerator Conf., 12-16 May 2003, Portland, Oregon, USA* (2003), 2464–2466. <<http://accelconf.web.cern.ch/accelconf/p03/PAPERS/WPPB024.PDF>>.
162. Rimbault, C. *et al.* in *Proc. 11th European Particle Accelerator Conf., 23-27 June 2008, Genoa, Italy* (2008), 1257–1259. <<http://accelconf.web.cern.ch/accelconf/e08/papers/tupc087.pdf>>.
163. Limborg, C., Gierman, S. & Power, J. in *Proc. 20th IEEE Particle Accelerator Conf., 12-16 May 2003, Portland, Oregon, USA* (2003), 2667–2669. <<http://accelconf.web.cern.ch/accelconf/p03/PAPERS/WPPG033.PDF>>.
164. Tenenbaum, P., Braun, H. H. & Chautard, F. in *Proc. 1997 Particle Accelerator Conf., 12-16 May 1997, Vancouver, Canada* (1997), 479–481. <<http://accelconf.web.cern.ch/accelconf/pac97/papers/pdf/8W017.PDF>>.
165. Honkavaara, K. *et al.* in *Proc. 2003 Particle Accelerator Conf., 12-16 May 2003, Portland, Oregon, USA* (2003), 2476–2478. <<http://accelconf.web.cern.ch/accelconf/p03/PAPERS/WPPB028.PDF>>.
166. Back, C. H., King, F., Collet, G., Kirby, R. & Field, C. *A Novel Wire Scanner for High Intensity Pulsed Beams* SLAC-PUB-8061 (SLAC, 1999). <<http://www.slac.stanford.edu/cgi-wrap/getdoc/slac-pub-8061.pdf>>.

REFERENCES

167. Castellano, M. & Verzilov, V. A. Spatial resolution in optical transition radiation beam diagnostics. *Phys. Rev. ST Accel. Beams* **1**, 062801 (1998).
168. Ross, M. *et al.* A Very High Resolution Optical Transition Radiation Beam Profile monitor SLAC-PUB-9280 (SLAC, 2002). <<http://www-spires.slac.stanford.edu/cgi-wrap/getdoc/slac-pub-9280.pdf>>.
169. Okugi, T. *et al.* Evaluation of Extremely Small Horizontal Emittance. *Phys. Rev. ST Accel. Beams* **2**, 022801 (1999).
170. Hayano, H. in *Proc. XX Int.l Linac Conf., 21-25 August 2000, Monterey, CA, USA* (2000), 146–148. <<http://accelconf.web.cern.ch/accelconf/l00/papers/MOC01.pdf>>.
171. Aryshev, A. *et al.* A novel Method for sub-micrometer transverse electron beam size measurements using optical transition radiation. *J. Phys.: Conf. Ser.* **236**, 012008 (2010).
172. Xiang, D. & Huang, W. Theoretical considerations on imaging of micron size electron beam, with optical transitions radiation. *Nucl. Instr. and Meth. A* **570**, 357–364 (2007).
173. Hofmann, A. *The Physics of Synchrotron Radiation* 346. <<http://dx.doi.org/10.1017/CBO9780511534973>> (Cambridge University Press, 2004).
174. Iida, K. *et al.* Measurement of an electron-beam size with a beam profile monitor using Fresnel zone plates. *Nucl. Instr. and Meth. A* **506**, 41–49 (2003).
175. Takano, S., Masaki, M. & Ohkuma, H. X-ray imaging of a small electron beam in a low-emittance synchrotron light source. *Nucl. Instr. and Meth. A* **556**, 357–370 (2006).
176. Kocsis, M. & Snigirev, A. Imaging using synchrotron radiation. *Nucl. Instr. and Meth. A* **525**, 79–84 (2004).
177. Andersson, A., Rohrer, M., Schlott, V., Streun, A. & Chubar, O. V. in *Proc. 10th European Particle Accelerator Conf., 26-30 June 2006, Edinburgh, Scotland, UK* (2006), 1223–1225. <<http://accelconf.web.cern.ch/accelconf/e06/PAPERS/TUPCH090.PDF>>.
178. Sjoström, M., Tarawneh, H. & Wallen, E. J. in *Proc. 10th European Particle Accelerator Conf., 26-30 June 2006, Edinburgh, Scotland, UK* (2006), 1193–1195. <<http://accelconf.web.cern.ch/accelconf/e06/PAPERS/TUPCH079.PDF>>.
179. Lefevre, T. *Laser Wire Scanners: Basic process and perspectives for the CTFs and CLIC Machines* CERN-OPEN-2002-010. CERN-PS-BD-NOTE-2001-015. CLIC-Note-504 (CERN, 2002). <<http://cdsweb.cern.ch/record/535808/files/open-2002-010.pdf>>.
180. Agapov, I., Blair, G. A. & Woodley, M. Beam emittance measurement with laser wire scanners in the International Linear Collider beam delivery system. *Phys. Rev. ST Accel. Beams* **10**, 112801 (2007).
181. Ross, M. C. *et al.* A laser-based beam profile monitor for the SLC/SLD interaction region. *Nucl. Instr. and Meth. A* **379**, 363–365 (1996).
182. Honda, Y., Sasao, N., Araki, S., Higashi, Y. & *et al.* Upgraded laser wire beam profile monitor. *Nucl. Instr. and Meth. A* **538**, 100–115 (2005).
183. Bosco, A. *et al.* A two-dimensional laser-wire scanner for electron accelerators. *Nucl. Instr. and Meth. A* **592**, 162–170 (2008).
184. Boogert, S. T. *et al.* Micron-scale laser-wire scanner for the KEK Accelerator Test Facility extraction line. *Phys. Rev. ST Accel. Beams* **13**, 122801 (2010).
185. Corner, L., Nevay, L. J. & Walczak, R. in *Proc. 1st Int. Particle Accelerator Conf., 23-28 May 2010, Kyoto, Japan* (2010), 3227–3229. <<http://accelconf.web.cern.ch/accelconf/IPAC10/papers/wepd058.pdf>>.

186. Photonics, N. *PHOTONIC CRYSTAL FIBERS* <<http://www.nktp Photonics.com/side5215.html>>.
187. Ilday, F., Buckley, J., Kuznetsova, L. & Wise, F. W. Generation of 36-femtosecond pulses from a ytterbium fiber laser. *Optics Express* **11**, 3550–3554 (2003).
188. Siegman, A. E. *Lasers* (Mill Valley, Calif.: University Science Books, 1986).
189. Bosco, A., Boogert, S. T., Boorman, G. E. & Blair, G. A. A large aperture electro-optical deflector. *Applied Phys. Lett.* **94**, 211104 (2009).
190. Agapov, I. *et al.* Tracking studies of the Compact Linear Collider collimation system. *Phys. Rev. ST Accel. Beams* **12**, 081001 (2009).
191. Blair, G. A., Malton, S., Agapov, I. V., Latina, A. & Schulte, D. in *Proc. 11th European Particle Accelerator Conf., 23-27 June 2008, Genoa, Italy* (2008), 2859–2861. <<http://accelconf.web.cern.ch/accelconf/e08/papers/wepp158.pdf>>.
192. Karataev, P. *et al.* Experimental observation and investigation of the prewave zone effect in optical diffraction radiation. *Phys. Rev. ST Accel. Beams* **11**, 032804 (2008).
193. Chiadroni, E. *et al.* in *Proc. 22nd Particle Accelerator Conf., 25-29 June 2007, Albuquerque, New Mexico, USA* (2007), 3982–3984. <<http://accelconf.web.cern.ch/accelconf/p07/PAPERS/FRPMN027.PDF>>.
194. Lumpkin, A. H., Berg, W. J., Sereno, N. S., Rule, D. W. & Yao, C.-Y. Near-field imaging of optical diffraction radiation generated by a 7-GeV electron beam. *Phys. Rev. ST Accel. Beams* **10**, 022802 (2007).
195. Karataev, P. *et al.* Beam-size measurement with Optical Diffraction Radiation at KEK Accelerator Test Facility. *Phys. Rev. Lett.* **93**, 244802 (2004).
196. Karataev, P. V. Pre-wave zone effect in transition and diffraction radiation: Problems and Solutions. *Phys. Lett. A* **345**, 428–438 (2005).
197. Lefevre, T. *et al.* in *Proc. 8th European Workshop on Beam Diagnostics and Instrumentation for Particle Accelerators, 20-23 May 2007, Venice, Italy* (2007), 132–134. <<http://accelconf.web.cern.ch/accelconf/d07/papers/tupb28.pdf>>.
198. Johnson, C. D. *Development and Use of Alumina Ceramic Fluorescent Screens* CERN-PS-90-42-AR (CERN, 1990). <<http://cdsweb.cern.ch/record/212834/files/CM-P00059425.pdf>>.
199. *AF995R from Saint Gobain Ceramiques Avancees Desmarquest* <<http://www.saint-gobain.com>>.
200. McCarthy, K. J. *et al.* Characterization of the Response of Chromium-doped Alumina Screens in the Vacuum Ultraviolet Using Synchrotron Radiation. *J. Appl. Phys.* **92**, 6541 (2002).
201. HAMAMATSU. *Hamamatsu Femtosecond Streak camera Ũ model FESCA 200* <http://jp.hamamatsu.com/products/opto-meas/pd357/pd360/fesca/index_en.html>.
202. Martinez, C. *Determination of Longitudinal Electron Bunch Lengths on Picosecond Time Scales* CERN-THESIS-2009-011 ; CERN-OPEN-2000-020 (Univ. Polytec. Catalunya, Barcelona, 1999). <<http://cdsweb.cern.ch/record/1164160/files/CERN-THESIS-2009-011.pdf>>.
203. Dabrowski, A. E. *et al.* in *Proc. 22nd Particle Accelerator Conf., 25-29 June 2007, Albuquerque, New Mexico, USA* (2007), 4069–4071. <<http://accelconf.web.cern.ch/accelconf/p07/PAPERS/FRPMS045.PDF>>.

REFERENCES

204. Dabrowski, A. E., Adli, E., Bettoni, S., Corsini, R. & et al. in *Proc. XXV Linear Accelerator Conf., 12-17 September 2010, Tsukuba, Japan* (2010), 647–649. <<http://accelconf.web.cern.ch/accelconf/LINAC2010/papers/tup100.pdf>>.
205. Berden, G. *et al.* Electro-Optic Technique with Improved Time Resolution for Real-Time, Non-destructive, Single-Shot Measurements of Femtosecond Electron Bunch Profiles. *Phys. Rev. Lett.* **93**, 114802 (2004).
206. Cavalieri, A. *et al.* Clocking femtosecond X-rays. *Phys. Rev. Lett.* **94**, 114801 (2005).
207. Berden, G. *et al.* Electro-Optic Technique with Improved Time Resolution for Real-Time, Non-destructive, Single-Shot Measurements of Femtosecond Electron Bunch Profiles. *Phys. Rev. Lett.* **93**, 114802 (2004).
208. Berden, G. *et al.* Benchmarking of Electro-Optic Monitors for Femtosecond Electron Bunches. *Phys. Rev. Lett.* **99**, 164801 (2007).
209. Steffen, B. *et al.* Electro-optic time profile monitors for femtosecond electron bunches at the soft x-ray free-electron laser FLASH. *Phys. Rev. ST Accel. Beams* **12**, 032802 (2009).
210. Jamison, S. P., MacLeod, A. M., Berden, G., Jaroszynski, D. A. & Gillespie, W. A. Temporally resolved electro-optic effect. *Optic Letters* **31**, 1753–1755 (2006).
211. Jamison, S. P., Berden, G., Phillips, P. J., Gillespie, W. A. & MacLeod, A. M. Upconversion of a relativistic Coulomb field THz pulse to the near-IR. *Appl. Phys. Lett.* **96**, 231114 (2010).
212. Lai, R. & Sievers, A. J. Determination of Charged Particle Bunch Shape from Coherent far-infrared Spectrum. *Phys. Rev. E* **50**, 3342–3344 (1994).
213. Fiorito, R. B. & Rule, D. W. Diffraction radiation diagnostics for moderate to high energy charged particle beams. *Nucl. Instr. and Meth. B* **173**, 67–82 (2001).
214. Castellano, M. *et al.* Measurement of Coherent Diffraction Radiation and its Applications for Bunch Length Diagnostics in Particle Accelerators. *Phys. Rev. E* **63**, 056501 (2001).
215. Castellano, M., Cianchi, A., Orlandi, G. & Verzilov, V. A. Effects of diffraction and target finite size on coherent transition radiation spectra in bunch length measurements. *Nucl. Instr. and Meth. A* **435**, 297–307 (1999).
216. Bartolini, R., Karataev, V. & Rehm, G. in *Proc. 23rd IEEE Particle Accelerator Conf., 4-8 May 2009, Vancouver, British Columbia, Canada* (2009), 4707–4709. <<http://accelconf.web.cern.ch/accelconf/PAC2009/papers/fr5rfp074.pdf>>.
217. Micheler, M. *et al.* in *Proc. 1st Int. Particle Accelerator Conf., 23-28 May 2010, Kyoto, Japan* (2010), 1143–1145. <<http://accelconf.web.cern.ch/accelconf/IPAC10/papers/mope071.pdf>>.
218. Micheler, M. *et al.* Longitudinal beam profile monitor at CTF3 based on coherent diffraction radiation. *J. Phys.: Conf. Ser.* **236**, 012021 (2010).
219. Adli, E. in *CLIC Beam Physics Meeting, 03 November 2010* (2010). <<http://indico.cern.ch/getFile.py/access?contribId=0&resId=1&materialId=slides&confId=112624>>.
220. Ferrari, A. *et al.* in *Proc. 6th European Workshop on Beam Diagnostics and Instrumentation for Particle Accelerators, 5-7 May 2003, Mainz, Germany* (2003), 211–213. <<http://accelconf.web.cern.ch/accelconf/d03/papers/PT18.pdf>>.
221. Dabrowski, A. E. *et al.* in *Proc. 1st Int. Particle Accelerator Conf., 23-28 May 2010, Kyoto, Japan* (2010), 1107–1109. <<http://accelconf.web.cern.ch/accelconf/IPAC10/papers/mope058.pdf>>.

222. Corsini, R., Ferrari, A., Rinolfi, L., Royer, P. & Tecker, F. Experimental results on electron beam combination and bunch frequency multiplication. *Phys. Rev. ST Accel. Beams* **7**, 040101 (2004).
223. Krejcik, P., Akre, R., Bentson, L. & Emma, P. in *Proc. 19th IEEE Particle Accelerator Conf., 18-22 June 2001, Chicago, Illinois, USA* (2001), 2353–2355. <<http://accelconf.web.cern.ch/accelconf/p01/PAPERS/WPAH116.PDF>>.
224. Jonker, M. *et al.* in *Proc. 1st Int. Particle Accelerator Conf., 23-28 May 2010, Kyoto, Japan* (2010), 2860–2862. <<http://accelconf.web.cern.ch/accelconf/IPAC10/papers/wepeb071.pdf>>.
225. Ferrari, A., Sala, P. R., Fassò, A. & Ranft, J. *FLUKA: A multi-particle transport code* SLAC-R-773. CERN-2005-010. INFN-TC-2005-11 (SLAC, Stanford, CA, USA, 2005). <<http://www.slac.stanford.edu/cgi-wrap/getdoc/slac-r-773.pdf>>.
226. Holzer, E. B. *et al.* *Beam Loss Monitoring System for the LHC* CERN-AB-2006-009 (CERN, 2005). <<http://cdsweb.cern.ch/record/930275/files/ab-2006-009.pdf>>.
227. Dehning, B., Ferioli, G., Holzer, E. B. & Kramer, D. *Very High Radiation Detector for the LHC BLM System Based on Secondary Electron Emission* CERN-BE-2010-028 (CERN, 2007). <<http://cdsweb.cern.ch/record/1301520/files/CERN-BE-2010-028.pdf>>.
228. Berg, W., Dooling, J. C., Pietryla, A. F., Yang, B. X. & Nuhn, H.-D. in *Proc. XXIV Linear Accelerator Conf., 29 September - 3 October 2008, Victoria, British Columbia, Canada* (2008), 492–494. <<http://accelconf.web.cern.ch/accelconf/LINAC08/papers/tup043.pdf>>.
229. Agosteo, S., Magistris, M., Mereghetti, A., Silari, M. & Zajacova, Z. Shielding data for 100–250 MeV proton accelerators: Double differential neutron distributions and attenuation in concrete. *Nucl. Instr. and Meth. B* **265**, 581–598 (2007).
230. Battistoni, G. *et al.* in *AIP Conf. Proc. 896. Proc. Hadronic Shower Simulation Workshop 2006, 6-8 September 2006, Fermilab* (eds Albrow, M. & Raja, R.) **896** (2007), 31–49. doi:10.1063/1.2720455. <<http://scitation.aip.org/getpdf/servlet/GetPDFServlet?filetype=pdf&id=APCPCS000896000001000031000001&idtype=cvips&prog=normal>>.
231. Sapinski, M. *et al.* in *Proc. 1st Int. Particle Accelerator Conf., 23-28 May 2010, Kyoto, Japan* (2010), 2869–2871. <<http://accelconf.web.cern.ch/accelconf/IPAC10/papers/wepeb074.pdf>>.
232. Salt, M. D. *et al.* in *Proc. 1st Int. Particle Accelerator Conf., 23-28 May 2010, Kyoto, Japan* (2010), 3389–3391. <<http://accelconf.web.cern.ch/accelconf/IPAC10/papers/wepe020.pdf>>.
233. Panofsky, W. K. H. *The use of a long co-axial ion chamber along the accelerator* SLAC-TN-63-57 (SLAC, 1963). <www.slac.stanford.edu/cgi-wrap/getdoc/slac-tn-63-057.pdf>.
234. Krueger, F. P. *Tevatron Beam Loss Monitor Specifications* Fermilab Engineering Note 1680.00 ES 158450 (FNAL, Batavia, IL, USA, 1982).
235. Wulf, W. F. & Korfer, M. in *Proc. 9th European Workshop on Beam Diagnostics and Instrumentation for Particle Accelerators, 25-27 May, 2009, Basel, Switzerland* (2009), 411–413. <<http://accelconf.web.cern.ch/accelconf/d09/papers/weoa01.pdf>>.

REFERENCES

236. Intermite, A., Putignano, M. & Welsch, C. P. in *Proc. 9th European Workshop on Beam Diagnostics and Instrumentation for Particle Accelerators*, 25-27 May, 2009, Basel, Switzerland (2009), 228–230. <<http://accelconf.web.cern.ch/accelconf/d09/papers/tupb27.pdf>>.
237. Welsch, C. P., Bravin, E. & Lefevre, T. in *Proc. 10th European Particle Accelerator Conf.*, 26-30 June 2006, Edinburgh, Scotland, UK (2006), 1220–1222. <<http://accelconf.web.cern.ch/accelconf/e06/PAPERS/TUPCH089.PDF>>.
238. Lefevre, T. *et al.* in *Proc. 10th European Particle Accelerator Conf.*, 26-30 June 2006, Edinburgh, Scotland, UK (2006), 1205–1207. <<http://accelconf.web.cern.ch/accelconf/e06/PAPERS/TUPCH083.PDF>>.
239. Lefevre, T. *et al.* in *Proc. 7th European Workshop on Beam Diagnostics and Instrumentation for Particle Accelerators*, 6-8 June 2005, Lyon, France (2005), 60–62. <<http://accelconf.web.cern.ch/accelconf/d05/PAPERS/POM014.PDF>>.
240. Motz, J. W., Olsen, H. & Koch, H. W. Electron Scattering without Atomic or Nuclear Excitation. *Review of Modern Phys.* **36**, 881–928 (1964).
241. Lefevre, T., Braun, H., Bravin, E., Dutriat, C. & Welsch, C. P. in *Proc. 8th European Workshop on Beam Diagnostics and Instrumentation for Particle Accelerators*, 20-23 May 2007, Venice, Italy (2007), 340–342. <<http://accelconf.web.cern.ch/accelconf/d07/papers/wepcl4.pdf>>.
242. Dabrowski, A. E. *et al.* in *Proc. XXIV Linear Accelerator Conf.*, 29 September - 3 October 2008, Victoria, British Columbia, Canada (2008), 585–587. <<http://accelconf.web.cern.ch/accelconf/LINAC08/papers/tup081.pdf>>.
243. Grames, J. M. *et al.* Unique electron polarimeter analyzing power comparison and precision spin-based energy measurement. *Phys. Rev. ST Accel. Beams* **7**, 042802 (2004).
244. Woods, M. *Compton Polarimetry at a 1TeV collider* SLAC-PUB-7744 (SLAC, 1998). <<http://www.slac.stanford.edu/cgi-wrap/getdoc/slac-pub-7744.pdf>>.
245. Papaphilippou, Y. *CLIC Damping ring beam transfer systems* CERN. <<http://indico.cern.ch/getFile.py/access?contribId=2&resId=1&materialId=slides&confId=87738>> (2010).
246. Papaphilippou, Y. *CLIC Parameter Specification. Kickers for the CLIC Damping and Pre-damping Rings* EDMS 989080 (CERN, 2009). <[https://edms.cern.ch/file/989080/2/Param_spec_kick_DR_v1_1_\(2\).docx](https://edms.cern.ch/file/989080/2/Param_spec_kick_DR_v1_1_(2).docx)>.
247. Koukovini-Platia, E. *et al.* *Impedance of the CLIC-DRs: What we know so far and what else we need to study?*. CERN. <<http://indico.cern.ch/getFile.py/access?contribId=0&resId=0&materialId=slides&confId=110595>> (2010).
248. Gaxiola, E. *et al.* *The SPS Fast Extraction Kicker System in LSS6* LHC-PROJECT-Report-913. CERN-LHC-Project-Report-913 (CERN, Geneva, 2006). <<http://accelconf.web.cern.ch/AccelConf/e06/PAPERS/THPCH143.PDF>>.
249. Barnes, M. J., Caspers, F., Ducimetiere, I., Garrel, N. & Kroyer, T. in *Proc. 22nd Particle Accelerator Conf.*, 25-29 June 2007, Albuquerque, New Mexico, USA (2007), 1574–1576. <<http://accelconf.web.cern.ch/accelconf/p07/PAPERS/TUPAN086.PDF>>.
250. Alesini, D. *Fast RF Kicker Design* LNF-INFN. <http://www.sinap.ac.cn/ICFA2008/ppt/apr.24/RF_fast_Kicker_Alesini.pdf> (2008).
251. Marcellini, F., Alesini, D., Guiducci, S. & Raimondi, P. in *Proc. 23rd IEEE Particle Accelerator Conf.*, 4-8 May 2009, Vancouver, British Columbia, Canada (2009), 1739–1741. <<http://accelconf.web.cern.ch/accelconf/PAC2009/papers/tu6rfp082.pdf>>.

252. *Handbook of Accelerator Physics and Engineering* (eds Chao, A. & Tigner, M.) (World Scientific, 1998).
253. Alesini, D., Guiducci, S., Marcellini, F. & Raimondi, P. in *Proc. 10th European Particle Accelerator Conf., 26-30 June 2006, Edinburgh, Scotland, UK* (2006), 1502–1504. <<http://accelconf.web.cern.ch/accelconf/e06/PAPERS/TUPLS009.PDF>>.
254. Belver-Aguilar, C., Faus-Golfe, A., Barnes, M. J., Rumolo, G. & Zannini, C. in *Proc. 2nd Int. Particle Accelerator Conf., 4-9 September 2011, San Sebastian, Spain* (2011), 1012–1014. <<http://accelconf.web.cern.ch/accelconf/IPAC2011/papers/tupc011.pdf>>.
255. Alesini, D., Guiducci, S., Marcellini, F. & Raimondi, P. *Fast Injection Kickers for DAFNE and ILC Damping Ring* Note: I-17 (INFN - LNF, Accelerator Division, Frascati, 2006). <<http://www.lnf.infn.it/acceleratori/dafne/NOTEDAFNE/I/I-17.pdf>>.
256. Day, H. A., Jones, R. M., Barnes, M. J., Caspers, F. & et al. in *Proc. 2nd Int. Particle Accelerator Conf., 4-9 September 2011, San Sebastian, Spain* (2011), 784–786. <<http://accelconf.web.cern.ch/accelconf/IPAC2011/papers/mops078.pdf>>.
257. Imai, T., Nakai, K., Hayano, H., Urakawa, J. & Terunuma, N. in *Proc. XX Int.l Linac Conf., 21-25 August 2000, Monterey, CA, USA* (2000), 77–79. <<http://arxiv.org/pdf/physics/0008133v1.pdf>>.
258. Rodríguez, I., Toral, F., Barnes, M. J., Fowler, T. & Ravida, G. in *Proc. 1st Int. Particle Accelerator Conf., 23-28 May 2010, Kyoto, Japan* (2010), 3299–3301. <<http://accelconf.web.cern.ch/accelconf/IPAC10/papers/wepd087.pdf>>.
259. Rodríguez, I. *Calculation methodology and fabrication procedures for particle accelerator stripline kickers* (Universidad Politécnica de Madrid, 2009).
260. Imai, T., Hayano, H., Terunuma, N. & Urakawa, J. *Highly Stable Beam Extraction by Double Kicker System* KEK Preprint 2002-16. KEK Accession No. 200227016 (KEK, Tsukuba, 2002). <<http://ccdb5fs.kek.jp/cgi-bin/img/allpdf?200227016>>.
261. Imai, T. *Development of Double Kicker System for Stable Beam Extraction* (Dept. of Physics, Tokyo University of Science, 2002).
262. Terunuma, N. in *Proc. 1st Int. Particle Accelerator Conf., 23-28 May 2010, Kyoto, Japan* (2010), 2397–2399. <<http://accelconf.web.cern.ch/accelconf/IPAC10/papers/wezmh02.pdf>>.
263. Watson, J. A. *et al.* in *Proc. 19th IEEE Particle Accelerator Conf., 18-22 June 2001, Chicago, Illinois, USA* (2001), 3738–3740. <<http://accelconf.web.cern.ch/accelconf/p01/PAPERS/FPAH031.PDF>>.
264. Cook, E. G. *et al.* in *Proc. Int. Power Modulator Conf., 30 June - 3 July 2002, Hollywood, California* (2002). doi:10.1109/MODSYM.2002.1189427. <<http://ieeexplore.ieee.org/stamp/stamp.jsp?tp=&arnumber=1189427>>.
265. Cook, E. G., Allen, F. V., Anaya, E. M., J., G. E. & et al. *Solid-State Modulator R&D at LLNL UCRL-JC-149976. SLAC-WP-040*. Submitted to International Workshop on Recent Progress of Induction Accelerators, 29-31 October 2002, Tsukuba, Japan (UCRL, Berkeley, USA, 2002). <<https://e-reports-ext.llnl.gov/pdf/241699.pdf>>.
266. Cassel, R. L., Nguyen, M., Pappas, G. C., deLamare, G. E. & et al. in *Proc. XXII International Linear Accelerator Conf., August 6-20, 2004, Lubeck, Germany* (2004), 697–699. <<http://accelconf.web.cern.ch/accelconf/104/PAPERS/THP42.PDF>>.
267. Cook, E. G. *et al.* in *Proc. 21st IEEE Particle Accelerator Conf., 16-20 May 2005, Knoxville, Tennessee, USA* (2005), 637–639. <<http://accelconf.web.cern.ch/accelconf/p05/PAPERS/ROAB008.PDF>>.

REFERENCES

268. Burkhart, C., Cook, E. D., Brooksby, C., Cassel, R. & Beukers, T. *Inductive Adder Modulators for ILC DR Kickers* Cornell University. <https://wiki.lepp.cornell.edu/ilc/pub/Public/DampingRings/CornellWorkshopTalks/Burkhart_Inductive_Adder_Modulator.ppt> (2006).
269. Gower, E. J. & Sullivan, J. S. in *Conference Record. Power Modulator Symposium, 2002 and 2002 High-Voltage Workshop, 30 June - 3 July 2002, Hollywood, USA* (2002), 321–324. doi:10.1109/MODSYM.2002.1189479. <<http://ieeexplore.ieee.org/stamp/stamp.jsp?tp=&arnumber=1189479>>.
270. Holma, J. & Barnes, M. J. *The Pulse Power Modulator Development for the CLIC Damping Ring Kickers* (CERN, to be issued).
271. Holma, J., Barnes, M. J. & Ovaska, S. J. in *Proc. 18th International Pulsed Power Conf., 19-23 June, 2011, Chicago, USA (TO BE PUBLISHED)* (2011).
272. Holma, J. & Barnes, M. J. in *Proc. 2nd Int. Particle Accelerator Conf., 4-9 September 2011, San Sebastian, Spain* (2011), 3409–3501. <<http://accelconf.web.cern.ch/accelconf/IPAC2011/papers/thpo032.pdf>>.
273. Burrows, P. N. in *Proc. 2003 Particle Accelerator Conf., 12-16 May 2003, Portland, Oregon, USA* (2003), 687–689. <<http://accelconf.web.cern.ch/accelconf/p03/PAPERS/ROPC011.PDF>>.
274. Resta-Lopez, J. & Burrows, P. in *Proc. 1st Int. Particle Accelerator Conf., 23-28 May 2010, Kyoto, Japan* (2010), 2791–2793. <<http://accelconf.web.cern.ch/accelconf/IPAC10/papers/wepeb045.pdf>>.
275. Burrows, P. N. *et al.* in *Proc. 10th European Particle Accelerator Conf., 26-30 June 2006, Edinburgh, Scotland, UK* (2006), 852–854. <<http://accelconf.web.cern.ch/accelconf/e06/PAPERS/MOPLS123.PDF>>.
276. Barnes, M. J. *et al.* in *Proc. IEEE International Pulsed Power Conf., 13-17 June 2005, Monterey, USA* (2005), 178–181. doi:10.1109/PPC.2005.300554. <<http://ieeexplore.ieee.org/stamp/stamp.jsp?tp=&arnumber=4084181>>.
277. Barnes, M. J. & Wait, G. D. in *Proc. 10th Int. IEEE Pulsed Power Conf., 10-13 July 1995, Albuquerque, USA 2* (1995), 1335–1340. doi:10.1109/PPC.1995.599802. <<http://ieeexplore.ieee.org/stamp/stamp.jsp?tp=&arnumber=599802>>.
278. Wait, G. D. & Barnes, M. J. in *Proc. 10th Int. IEEE Pulsed Power Conf., 10-13 July 1995, Albuquerque, New Mexico, USA 2* (1995), 1341–1346. doi:10.1109/PPC.1995.599803. <<http://ieeexplore.ieee.org/stamp/stamp.jsp?tp=&arnumber=599803>>.
279. Naito, T. *et al.* in *Proc. 1st Int. Particle Accelerator Conf., 23-28 May 2010, Kyoto, Japan* (2010), 2386–2388. <<http://accelconf.web.cern.ch/accelconf/IPAC10/papers/weobmh02.pdf>>.
280. Schulte, D. *et al.* in *Proc. XXV Linear Accelerator Conf., 12-17 September 2010, Tsukuba, Japan* (2010), 103–105. <<http://accelconf.web.cern.ch/accelconf/LINAC2010/papers/mop024.pdf>>.
281. Walz, D. R., Jurow, J. & Garwin, E. L. *Water Cooled Beam Dumps and Collimators for the Stanford Linear Accelerator* SLAC-PUB-95 (SLAC, Stanford, CA, USA, 1965). <<http://www.slac.stanford.edu/cgi-wrap/getdoc/slac-pub-0095.pdf>>.
282. Walz, D. R., Amann, J. W., Arnold, R., Seryi, A. & *et al.* in *Proc. 1st Int. Particle Accelerator Conf., 23-28 May 2010, Kyoto, Japan* (2010), 3341–3343. <<http://accelconf.web.cern.ch/accelconf/IPAC10/papers/wepe003.pdf>>.

283. Battistoni, G. *et al.* in *AIP Conf. Proc.* 896. *Proc. Hadronic Shower Simulation Workshop 2006, 6-8 September 2006, Fermilab* (eds Albrow, M. & Raja, R.) **896** (2007), 31–49. doi:10.1063/1.2720455. <<http://scitation.aip.org/getpdf/servlet/GetPDFServlet?filetype=pdf&id=APCPCS000896000001000031000001&idtype=cvips&prog=normal>>.
284. Ferrari, A., Sala, P. R., Fassò, A. & Ranft, J. *FLUKA: A multi-particle transport code* SLAC-R-773. CERN-2005-010. INFN-TC-2005-11 (SLAC, Stanford, CA, USA, 2005). <<http://www.slac.stanford.edu/cgi-wrap/getdoc/slac-r-773.pdf>>.
285. Schulte, D. *Study of Electromagnetic and Hadronic Background in the Interaction Region of the TESLA Collider* TESLA-97-08 (Hamburg University, Hamburg, 1997). <<http://cdsweb.cern.ch/record/331845/files/shulte.pdf>>.
286. Servranckx, R. V., Brown, K. L., Schachinger, L. & Douglas, D. *Users Guide to the Program DIMAD* SLAC-R-285 (SLAC, Stanford, CA, USA, 1990). <<http://www.slac.stanford.edu/cgi-wrap/getdoc/slac-r-285.pdf>>.
287. Bialowons, W., Maslov, M., Schmitz, M. & Sytchev, V. *Concept of the High Power e+/e- Beam Dumps for TESLA* TESLA Report 2001-04 (DESY, Hamburg, 2001). <http://tesla.desy.de/new_pages/TESLA_Reports/2001/pdf_files/tesla2001-04.pdf>.
288. Mereghetti, A., Maglioni, C. & Vlachoudis, V. *FLUKA and Thermo-mechanical Studies for the CLIC Main Dump* CERN-OPEN-2011-030. CLIC-Note-876 (CERN, Geneva, 2011). <<http://cdsweb.cern.ch/record/1355402/files/CERN-OPEN-2011-030.pdf>>.
289. *ANSYS - Simulation Driven Product Development - v. 12.1* <<http://www.ansys.com>>.
290. Vlachoudis, V. & et al. *Energy deposition calculations on the BDS spoiler system* CLIC-Note-932 (CERN).
291. Kuzminykh, V., Levichev, E. B. & K.V., Z. *SR Power Evacuation System From Damping Wigglers of the CLIC DR* CLIC-Note-658 (CERN, Geneva, 2006).
292. Schoerling, D. *et al.* Design and System Integration of the Superconducting Wigglers for the CLIC Damping Rings. *Phys. Rev. ST Accel. Beams* **15** (2012).
293. Halbach, K. in *Proc. 1986 Linear Accelerator Conf., 2-6 June 1986, Stanford, CA, USA* (1986), 407–410. <<http://www.osti.gov/bridge/servlets/purl/5330846-RBrRdi/5330846.pdf>>.
294. Modena, M. *Technical Specification of the CLIC Final Focus Short QD0 Hybrid Prototype* EDMS 1065698. 13th CLIC MDI Meeting on 7/5/2010 (CERN, 2010). <<http://indico.cern.ch/getFile.py/access?contribId=1&resId=0&materialId=slides&confId=89765>>.
295. Bolzon, B. *Etude de la stabilisation des quadrupoles de la ligne de faisceau d'un futur collisionneur linéaire* (Université de Savoie, France, 2007). <http://tel.archives-ouvertes.fr/docs/00/23/85/53/PDF/these_bolzon.pdf>.
296. Brunetti, L. *et al.* in *Proc. 11th European Particle Accelerator Conf., 23-27 June 2008, Genoa, Italy* (2008), 1335–1337. <<http://accelconf.web.cern.ch/accelconf/e08/papers/tupc115.pdf>>.
297. Redaelli, S. *Stabilization of Nanometre-Size Particle Beams in the Final Focus System of the Compact Linear Collider (CLIC)* CERN-AB-2004-026 (ABP). CLIC-Note-595 (Université de Lausanne, Lausanne, Switzerland, 2003). <<http://cdsweb.cern.ch/record/740518/files/ab-2004-026.pdf>>.

REFERENCES

298. Balik, G. & et al. in *MECATRONICS 2010, 8th France-Japan and 6th Europe-Asia Congress on Mechatronics, Yokohama, Japan* (2010). <http://hal.in2p3.fr/docs/00/62/88/17/PDF/Mecatronics_2010.pdf>.
299. Ramos, F. *Dynamic analysis of the FF magnets pre-isolator and support system (to be published)*
300. Lackner, F. *et al.* Development of an eccentric cam-based active pre-alignment system of the CLIC Main Beam quadrupole magnet. *Diamond Light Source Proceedings MEDSI-6, Oxford, UK* **1**, 4 (2010).
301. Mainaud Durand, H., Touzé, T., Griffet, S., Kemppinen, J. & Lackner, F. in *Proc. 11th International Workshop on Accelerator Alignment, 3-7 September 2010, DESY, Hamburg, Germany* (2010). <http://iwaa2010.desy.de/e107506/e107507/e113203/e119271/IWAA2010_HMD_CLIC.pdf>.
302. Aefsky, S., Amelung, C., Bensinger, J. & et al. The optical alignment of the ATLAS muon spectrometer endcaps. *J. Instrum.* **3**, 11005 (2008).
303. Van der Graaf, H. *Monitoring of the position of QDO magnets in the CLIC MDI area. Technical proposal* EDMS 1143037 v.1 (CERN, 2011). <<https://edms.cern.ch/file/1143037/1/ConceptQD0.pdf>>.
304. Coosemans, W., Mainaud Durand, H., Marin, A. & Quesnel, J.-P. in *Proc. 7th Int. Workshop on Accelerator Alignment (IWAA 2002), 11-14 November 2002, SPring-8, Japan* (2002). <<http://www.slac.stanford.edu/econf/C0211115/papers/023.PDF>>.
305. Gerwig, H. in *CLIC09 Workshop, 12-16 October 2009, CERN* (Geneva, 2009). <<http://lcd.web.cern.ch/LCD/Documents/Documents/LCD-OPEN-2009-001.pdf>>.
306. Gaddi, A. *Mechanical works in magnetic stray fields* CMS-S-ER-0001. EDMS 973739 (CERN, 2008). <<https://edms.cern.ch/file/973739/1/Mechanics-in-stray-field.pdf>>.
307. Burrows, P., Hartin, T., Hussain, A. M. & et al. in *Proc. 9th European Particle Accelerator Conf., 5-9 July 2004, Lucerne, Switzerland* (2004), 785–787. <<http://accelconf.web.cern.ch/accelconf/e04/PAPERS/MOPLT107.PDF>>.
308. Burrows, P. N. in *Proc. 2003 Particle Accelerator Conf., 12-16 May 2003, Portland, Oregon, USA* (2003), 687–689. <<http://accelconf.web.cern.ch/accelconf/p03/PAPERS/ROPC011.PDF>>.
309. Burrows, P. N. *et al.* in *Proc. 21st IEEE Particle Accelerator Conf., 16-20 May 2005, Knoxville, Tennessee, USA* (2005), 1359–1361. <<http://accelconf.web.cern.ch/accelconf/p05/PAPERS/RPPP013.PDF>>.
310. Burrows, P. N. *et al.* in *Proc. 10th European Particle Accelerator Conf., 26-30 June 2006, Edinburgh, Scotland, UK* (2006), 852–854. <<http://accelconf.web.cern.ch/accelconf/e06/PAPERS/MOPLS123.PDF>>.
311. Gerwig, H. *MDI engineering issues for a CLIC Detector* CERN. <<http://ilcagenda.linearcollider.org/getFile.py/access?contribId=50&sessionId=6&resId=0&materialId=slides&confId=4175>> (2010).
312. Roderick, C., Billen, R. & Teixeira, D. D. in *Proc. 13th Int. Conf. on Accelerator and Large Experimental Physics Control Systems, 10-14 October 2011, Grenoble, France* (2011), 1232–1134. <<http://accelconf.web.cern.ch/AccelConf/icalepcs2011/papers/thchaust06.pdf>>.
313. Mallows, S. & Otto, T. *Ionizing Radiation Estimates for the CLIC Main and Drive beams* (CERN, Geneva, 2010).

314. *PICMG* <<http://www.picmg.org>>.
315. *National Instruments. PXI Platform* <<http://www.ni.com/pxi/>>.
316. Serrano, J. *et al.* in *Proc. 12th Int. Conf. on Accelerator and Large Experimental Physics Control Systems, 12-16 October 2009, Kobe, Japan* (2009), 93–95. <<http://epaper.kek.jp/icaleps2009/papers/tuc004.pdf>>.
317. *White Rabbit Switch Technical Specification* <<http://www.ohwr.org>>.
318. Charrue, P. *et al.* in *Proc. 10th Int. Conf. on Accelerator and Large Experimental Physics Control Systems, 15-19 October 2007, Knoxville, USA* (2007), 90–92. <<http://accelconf.web.cern.ch/accelconf/ica07/PAPERS/TPPA04.PDF>>.
319. Sliwinski, W., Charrue, P. & Yastrebov, I. in *Proc. 13th Int. Conf. on Accelerator and Large Experimental Physics Control Systems, 10-14 October 2011, Grenoble, France* ISBN: 0-470-01168-8 (2011), 702–704. <<http://accelconf.web.cern.ch/AccelConf/icaleps2011/papers/wemmu009.pdf>>.
320. Buttner, M., Lauener, J., Sigerud, K., Stapley, N. & Charrue, P. in *Proc. 10th Int. Conf. on Accelerator and Large Experimental Physics Control Systems, 15-19 October 2007, Knoxville, USA* (2007), 588–590. <<http://accelconf.web.cern.ch/accelconf/ica07/PAPERS/RPPA35.PDF>>.
321. Billen, R., Le Roux, P., Peryt, M., Roderick, C. & Zaharieva, Z. in *Proc. 12th Int. Conf. on Accelerator and Large Experimental Physics Control Systems, 12-16 October 2009, Kobe, Japan* (2009), 61–63. <<http://epaper.kek.jp/icaleps2009/papers/tub001.pdf>>.
322. Rubiola, E. *Phase Noise and Frequency Stability in Oscillators* ISBN: **9780511812798** (Cambridge University Press, 2009).
323. Oppenheim, A. V., Willsky, A. S. & Hamid Nawab, S. *Signals and Systems* 2nd ed. ISBN: **0138147574** (Prentice Hall, 1996).
324. Papoulis, A. & Unnikrishna Pillai, S. *Probability, Random Variables and Stochastic Processes* 4th ed. (McGraw Hill, 2002).
325. Gardner, F. M. *Phaselock Techniques* 3rd ed. (Wiley, 2005).
326. Jensen, E. in *CLIC09 Workshop, 12-16 October 2009, CERN* (2009). <<http://indico.cern.ch/getFile.py/access?contribId=44&sessionId=8&resId=1&materialId=slides&confId=45580>>.
327. Lefevre, T. in *International Workshop on Linear Colliders 2010 (ECFA-CLIC-ILC Joint Meeting), 18-22 October 2010, Geneva, Switzerland* (2010).
328. Schulte, D. in *International Workshop on Linear Colliders 2010 (ECFA-CLIC-ILC Joint Meeting), 18-22 October 2010, Geneva, Switzerland* (2010). <<http://ilcagenda.linearcollider.org/getFile.py/access?contribId=194&sessionId=77&resId=2&materialId=slides&confId=4507>>.
329. Loehl, F. in *Proc. 2nd Int. Particle Accelerator Conf., 4-9 September 2011, San Sebastian, Spain* (2011), 1381–1383. <<http://accelconf.web.cern.ch/accelconf/PAC2011/papers/weoan2.pdf>>.
330. Seryi, A. & Napoly, O. Influence of ground motion on the time evolution of beams in linear colliders. *Phys. Rev. E* **53**, 5323–5337 (1996).
331. Shiltsev, V. Observations of Random Walk of the Ground in Space and Time. *Phys. Rev. Lett.* **104**, 238501 (2010).
332. Skogestad, A. & Postlewaite, I. *Multivariable Feedback Control: Analysis and Design* (Wiley-Interscience, New York, 2005).

REFERENCES

333. Pfingstner, J., Schulte, D., Snuverink, J. & Hofbaur, M. in *Proc. 2nd Int. Particle Accelerator Conf., 4-9 September 2011, San Sebastian, Spain* (2011), 511–513. <<http://accelconf.web.cern.ch/accelconf/IPAC2011/papers/mopo014.pdf>>.
334. Burrows, P. N. *et al.* in *Proc. 21st IEEE Particle Accelerator Conf., 16-20 May 2005, Knoxville, Tennessee, USA* (2005), 1359–1361. <<http://accelconf.web.cern.ch/accelconf/p05/PAPERS/RPPP013.PDF>>.
335. Resta-Lopez, J., Burrows, P. N. & Christian, G. Luminosity Performance Studies of the Compact Linear Collider with Intra-train Feedback System at the Interaction Point. *Journal of Instrumentation* **5**, 09007 (2010).
336. Burrows, P. N. in *Proc. 2003 Particle Accelerator Conf., 12-16 May 2003, Portland, Oregon, USA* (2003), 687–689. <<http://accelconf.web.cern.ch/accelconf/p03/PAPERS/ROPC011.PDF>>.
337. Burrows, P., Hartin, T., Hussain, A. M. & *et al.* in *Proc. 9th European Particle Accelerator Conf., 5-9 July 2004, Lucerne, Switzerland* (2004), 785–787. <<http://accelconf.web.cern.ch/accelconf/e04/PAPERS/MOPLT107.PDF>>.
338. Burrows, P. N. *et al.* in *Proc. 10th European Particle Accelerator Conf., 26-30 June 2006, Edinburgh, Scotland, UK* (2006), 852–854. <<http://accelconf.web.cern.ch/accelconf/e06/PAPERS/MOPLS123.PDF>>.
339. Burrows, C. P. for Perry. in *International Workshop on Linear Colliders 2010 (ECFA-CLIC-ILC Joint Meeting), 18-22 October 2010, Geneva, Switzerland* (2010).
340. Amsler, C. *et al.* Review of Particle Physics. *Phys. Lett. B* **667**. Section 27.5 electromagnetic cascades, 1–1340 (2008).
341. Resta-Lopez, J. & Fernandez-Hernando, L. *Review of the CLIC Energy Collimation System and Spoiler Heating* EUROTeV-Report-2008-050 (EUROTeV, 2008). <http://www.eurotev.org/sites/site_eurotev/content/e328/e329/e1082/e1566/EUROTeV-Report-2008-050.pdf>.
342. Nelson, W. R., Rokni, S. H. & Vylet, V. *Radiation calculations and shielding considerations for the design of the next linear collider* SLAC-PUB-7336 (SLAC, Stanford, CA, USA, 1996). <<http://www.slac.stanford.edu/pubs/slacpubs/7250/slac-pub-7336.pdf>>.
343. Fartoukh, S. D., Jeanneret, J. B. & Pancin, J. *Heat deposition by transient beam passage in spoilers* CERN-SL-2001-012-AP. CLIC-Note-477 (CERN, Geneva, 2001). <<http://cdsweb.cern.ch/record/498625/files/sl-2001-012.pdf>>.
344. Resta-Lopez, J. in *Proc. 23rd IEEE Particle Accelerator Conf., 4-8 May 2009, Vancouver, British Columbia, Canada* (2009), 2844–2846. <<http://accelconf.web.cern.ch/accelconf/PAC2009/papers/we6rfp026.pdf>>.
345. Todd, B., Dinius, A., Nouchi, P., Puccio, B. & Schmidt, R. in *Proc. 10th ICALEPCS Int. Conf. on Accelerator & Large Exp. Physics Control Systems, 10-14 October 2005, Geneva, Switzerland* (2005). <http://accelconf.web.cern.ch/accelconf/ica05/proceedings/pdf/P3_031.pdf>.
346. Adli, E., Eliasson, P., Elsen, E., Syratchev, I. & *et al.* *Studies of Selected Failure Modes in the ILC and CLIC Linear Colliders* EUROTeV-Report-2008-075 (CERN, 2008). <http://www.eurotev.org/reports__presentations/eurotev_reports/2008/e1571/EUROTeV-Report-2008-075.pdf>.

347. Adli, E., Schulte, D. & Syratchev, I. *A Study of Failure Modes in the CLIC Decelerator* CERN-AB-2008-014. CLIC-Note-757. EUROTeV-Report-2008-041 (CERN, Geneva, 2008). <<http://cdsweb.cern.ch/record/1122737/files/CERN-AB-2008-014.pdf>>.
348. Schulte, D. in *Proc. 23rd IEEE Particle Accelerator Conf., 4-8 May 2009, Vancouver, British Columbia, Canada* (2009), 4664–4666. <<http://accelconf.web.cern.ch/accelconf/PAC2009/papers/fr5rfp055.pdf>>.
349. Tomàs, R. *et al.* in *Proc. 1st Int. Particle Accelerator Conf., 23-28 May 2010, Kyoto, Japan* (2010), 3419–3421. <<http://accelconf.web.cern.ch/accelconf/IPAC10/papers/wepe030.pdf>>.
350. Mainaud Durand, H., Touzé, T., Griffet, S., Kemppinen, J. & Lackner, F. in *Proc. 11th International Workshop on Accelerator Alignment, 3-7 September 2010, DESY, Hamburg, Germany* (2010). <http://iwaa2010.desy.de/e107506/e107507/e113203/e119271/IWAA2010_HMD_CLIC.pdf>.
351. Mainaud, H. *Une nouvelle approche metrologique: l'écartométrie biaxiale. Application à l'alignement des accélérateurs linéaires* (Université Louis Pasteur, Strasbourg, France, 1996).
352. Mainaud-Durand, H. *The CLIC alignment studies : past, present and future* CERN-TS-Note-2005-028. TS-Note-2005-028 (CERN, Geneva, 2006). <[https://edms.cern.ch/file/590561/1/TS-Note-2005-028\(Mainaud\).pdf](https://edms.cern.ch/file/590561/1/TS-Note-2005-028(Mainaud).pdf)>.
353. Kemppinen, J. *Cam-based system for CLIC active pre-alignment: one degree of freedom tests* EDMS 1096186 (CERN, 2010).
354. Mainaud Durand, H. *et al.* in *Proc. 2nd Int. Particle Accelerator Conf., 4-9 September 2011, San Sebastian, Spain* (2011), 544–546. <<http://accelconf.web.cern.ch/accelconf/IPAC2011/papers/mopo029.pdf>>.
355. Bouché, J. M., Coosemans, W. & Pittin, R. *Active alignment system for CLIC 30GHz Modules in CTF2* CERN-OPEN-98-002. CLIC-Note-350 (CERN, Geneva, 1998). <<http://cdsweb.cern.ch/record/344917/files/open-98-002.pdf>>.
356. Mainaud Durand, H. *et al.* in *Proc. 2nd Int. Particle Accelerator Conf., 4-9 September 2011, San Sebastian, Spain* (2011), 547–549. <<http://accelconf.web.cern.ch/accelconf/IPAC2011/papers/mopo030.pdf>>.
357. Sosin, M. *et al.* in *Proc. Int. Particle Accelerator Conf., 20-25 May 2012, New Orleans, USA* (2012). <<http://cdsweb.cern.ch/record/1451297/files/CERN-ATS-2012-079.pdf>>.
358. Touzé, T. in *Proc. 11th International Workshop on Accelerator Alignment, 3-7 September 2010, DESY, Hamburg, Germany* (2010). <http://iwaa2010.desy.de/e107506/e107507/e113375/e119274/IWAA2010_TT_CLIC.pdf>.
359. Becker, F., Coosemans, W., Pittin, R. & Wilson, I. H. *An Active Pre-Alignment System and Metrology Network for CLIC* CERN-OPEN-2003-011. CLIC-Note-553 (CERN, 2003). <<http://cdsweb.cern.ch/record/604004/files/open-2003-011.pdf>>.
360. Mainaud-Durand, H. *Micrometric alignment metrology: means, developments and applications* TS-Note-2004-038 (CERN, Geneva, 2004). <<https://edms.cern.ch/file/473751/1/01-Mainaud.pdf>>.
361. Griffet, S. *Fiducialisation: state of the art* EDMS 1096102 (CERN, 2010). <https://edms.cern.ch/file/1096102/1/STATE_OF_THE_ART.pdf>.
362. Griffet, S. *Fiducialisation and pre-alignment* EDMS 1096130 (CERN, Geneva, 2010). <https://edms.cern.ch/file/1096130/2/Fidu_Pre-Align_Note-Technique_V2_EN.pdf>.

REFERENCES

363. Mainaud-Durand, H. *Proposal of a CERN/NIKHEF collaboration on CLIC pre-alignment studies* EDMS 1080845 (CERN, 2010).
364. Lackner, F., Touzé, T., Riegler, W. & Schmickler, H. *Technical proposal: Laser Alignment Multipoint Based - Design Approach* EDMS 1066954 (CERN, 2010). <https://edms.cern.ch/file/1066954/1/200410_TechProp_LaserCLIC_Lackner.pdf>.
365. Collette, C., Janssens, S., Artoos, K. & Hauviller, C. Active vibration isolation of high precision machine. *Diamond Light Source Proceedings MEDSI-6, Oxford, UK* **1**, 5 (2010).
366. Stochino, A. *et al.* The Seismic Attenuation System (SAS) for the Advanced LIGO gravitational wave interferometric detectors. *Nucl. Instr. and Meth. A* **598**, 737–753 (2009).
367. Carter, A. *et al.* Stabilization of an optical microscope to 0.1 nm in the three dimensions. *Applied Optics* **46**, 421–427 (2007).
368. Furutani, K., Suzuki, M. & Kudoh, R. Nanometer cutting machine using a Stewart-platform parallel mechanism. *Measurement Science and Technology* **15**, 467–474 (2004).
369. Schulte, D. in *Proc. 23rd IEEE Particle Accelerator Conf., 4-8 May 2009, Vancouver, British Columbia, Canada* (2009). <<http://accelconf.web.cern.ch/accelconf/PAC2009/papers/th6pfp045.pdf>>.
370. Amirikas, R., Bertolini, A., Bialowons, W. & Ehrlichmann, H. in *Proc. 36th ICFA Advanced Beam Dynamics Workshop, 17-21 October 2005, Kyoto, Japan* (2005). <http://vibration.desy.de/sites/site_ground-vibrations/content/e1454/e3974/e1475/infoboxContent1489/Nanobeam2005.pdf>.
371. Bolzon, B. *Etude des vibrations et de la stabilisation à l'échelle sous-nanométrique des doublets finaux d'un collisionneur linéaire* (University of Savoie, Annecy-le-Vieux, 2007). <<http://cdsweb.cern.ch/record/1100434/files/cer-002754217.pdf>>.
372. *Compilation of ground motion measurements* <<http://vibration.desy.de>>.
373. Baklakov, B. A. *et al.* in *Proc. IEEE Particle Accelerator Conf., 6-9 May 1991, San Francisco, California, USA* (1991), 3273–3275. <http://accelconf.web.cern.ch/accelconf/p91/PDF/PAC1991_3273.PDF>.
374. Peterson, J. *Observations and modeling of background seismic noise* 93-322 (U. S. Geological Survey, 1993). <<http://earthquake.usgs.gov/regional/asl/pubs/files/ofr93-322.pdf>>.
375. Artoos, K. *et al.* in *Proc. 23rd IEEE Particle Accelerator Conf., 4-8 May 2009, Vancouver, British Columbia, Canada* (2009), 3636–3638. <<http://accelconf.web.cern.ch/accelconf/PAC2009/papers/th5rfp081.pdf>>.
376. Collette, C., Artoos, K., Guinchard, M. & Hauviller, C. Seismic response of linear accelerators. *Phys. Rev. ST Accel. Beams* **13**, 072801–072811 (2010).
377. Beidneur, J. Génie civil : Laser megajoule, un chantier béton à haute précision. *Le Moniteur des travaux publics et du bâtiment* **5351**, 74–77 (2006).
378. Turner, J. L. *et al.* *Vibration Studies of the Stanford Linear Accelerator* SLAC-PUB-95-6867 (SLAC, Stanford, CA, USA, 1995). <<http://www.slac.stanford.edu/cgi-wrap/getdoc/slac-pub-6867.pdf>>.
379. Wang, D.-J., Ho, H. C., Wang, J. & Tsai, Z.-D. in *Proc. 21st IEEE Particle Accelerator Conf., 16-20 May 2005, Knoxville, Tennessee, USA* (2005), 1102–1104. <<http://accelconf.web.cern.ch/accelconf/p05/PAPERS/RPPE008.PDF>>.

380. Bolzon, B., Baud, J. P., Gaillard, G., Geffroy, N. & Jeremie, A. *Impact of flowing cooling water on the ATF2 final doublets vibrations* ATF-09-01 (KEK High Energy Accelerator Research Organization, 2009). <<http://atf.kek.jp/collab/ap/library/internal-reports/ATF-09-01.pdf>>.
381. Redaelli, S. *Stabilization of Nanometre-Size Particle Beams in the Final Focus System of the Compact Linear Collider (CLIC)* CERN-AB-2004-026-ABP. CLIC-Note-595 (Inst. Phys. Hautes Energies, Lausanne, 2003). <<http://cdsweb.cern.ch/record/740518/files/ab-2004-026.pdf>>.
382. Collette, C. *et al.* Active quadrupole stabilization for future linear particle colliders. *Nucl. Instr. and Meth. A* **621**, 71–78 (2010).
383. Karnopp, D., Crosby, M. J. & Harwood, R. A. Vibration control using semi-active force generators. *Journal of Engineering for Industry* **96**, 619–626 (1974).
384. Allison, S., Eriksson, L., Hendrickson, L., Himel, T. & Seryi, A. in *Proc. 19th IEEE Particle Accelerator Conf., 18-22 June 2001, Chicago, Illinois, USA* (2001), 1261–1263. <<http://accelconf.web.cern.ch/accelconf/p01/PAPERS/TPAH013.PDF>>.
385. Frisch, J. *et al.* in *Proc. XXII International Linear Accelerator Conf., 6-20 August, 2004, Lubeck, Germany* (2004), 684–686. <<http://accelconf.web.cern.ch/accelconf/104/PAPERS/THP36.PDF>>.
386. Saulson, P. R. Vibration isolation for broadband gravitational wave antennas. *Review of Scientific Instruments* **55**, 1315–1320 (1984).
387. Nelson, P. G. An active vibration isolation system for inertial reference and precision measurement. *Review of Scientific Instruments* **62**, 2069–2075 (1991).
388. Vervoordeldonk, M. J., Ruijl, T. A. & Rijs, R. M. G. in *Proc. ASPE Spring Topical Meeting* (2004). <http://www.aspe.net/publications/Spring_2004/04SP%20Extended%20Abstracts/1400B-Vervoordeldonk%20New.PDF>.
389. Vervoordeldonk, M. J. & Stoutjesdijk, H. in *Proc. 6th Int. Conf. of the European Society for Precision Engineering and Nanotechnology, 28 May - 1 June 2006, Baden near Vienna, Austria* (2006), 107–110. <<http://www.euspen.eu/content/Resources/Proceedings/Pages%20for%20proceedings%20sales%20-%20Baden.pdf>>.
390. Vervoordeldonk, M. J., Ruijl, T. A. M., Rijs, R. M. G. & Muller, J. C. A. US 2007/0035074. <<http://appft1.uspto.gov/netacgi/nph-Parser?Sect1=PTO1&Sect2=HITOFF&d=PG01&p=1&u=/netahtml/PTO/srchnum.html&r=1&f=G&l=50&s1=20070035074>>(2007).
391. Kar-Leung Miu, K. *A Low cost, DC-Coupled Active Vibration System* (Massachusetts Institute of Technology, 2008). <<http://dspace.mit.edu/bitstream/handle/1721.1/46061/374599635.pdf?sequence=1>>.
392. Fuller, C. R. & von Flotow, A. H. Active control of sound and vibration. *IEEE Control Systems* **15**, 9–19 (1995).
393. Schubert, D. W., Beard, A. M. & von Flotow, A. H. A practical product implementation of an active/passive vibration isolation. *Proc. of SPIE Vibration Monitoring and Control* **2264**, 38–49 (1994).
394. Schubert, D. W., Beard, A. M., Shedd, S. F., Earles, M. R. & von Flotow, A. H. 5,823,307. <

REFERENCES

395. Redaelli, S. *Stabilization of Nanometre-Size Particle Beams in the Final Focus System of the Compact Linear Collider (CLIC)* CERN-AB-2004-026-ABP. CLIC-Note-595 (Inst. Phys. Hautes Energies, Lausanne, 2004). <<http://cdsweb.cern.ch/record/740518/files/ab-2004-026.pdf>>.
396. Montag, C. Active stabilization of mechanical quadrupole vibrations for linear collider. *Nucl. Instr. and Meth. A* **378**, 396–375 (1996).
397. Montag, C. *Active Stabilization of Mechanical Quadrupole Vibrations in a Linear Collider Test Facility* (Hamburg University, 1997).
398. Artoos, K. *et al.* in *Proc. 23rd IEEE Particle Accelerator Conf., 4-8 May 2009, Vancouver, British Columbia, Canada* (2009), 3633–3635. <<http://accelconf.web.cern.ch/accelconf/PAC2009/papers/th5rfp080.pdf>>.
399. Collette, C. *et al.* in *Proc. The 12th IASTED International Conf. on Intelligent Systems and Control, 2-4 November 2009, Cambridge, Massachusetts, USA* (2009). <<http://cdsweb.cern.ch/record/1268422/files/EuCARD-CON-2009-031.pdf>>.
400. Spanos, J., Rahman, Z. & Blackwood, G. in *Proc. American Control Conf., 21-23 June 1995, Seattle, Washington, USA* (1995), 412–416. doi:10.1109/ACC.1995.529280. <<http://ieeexplore.ieee.org/stamp/stamp.jsp?tp=&arnumber=529280>>.
401. Hanieh, A. *Active Isolation and damping of Vibrations via Stewart Platform* (University of Brussels, 2004). <<http://www.ulb.ac.be/scmero/documents/these/Hanieh03.pdf>>.
402. Preumont, A. *Vibration Control of Active Structures An Introduction* 2nd ed. ISBN: 1402004966 (Kluwer Academic Publishers, Dordrecht, 2002).
403. *Guralp catalogue* <<http://www.guralp.com/product-range/seismometers/>>.
404. Kapur, P., Ranganath, R. & Nataraju, B. S. in *Proc. 12th IFToMM World Congress on the Theory of Machines and Mechanisms, 18-21 Juin 2007, Besancon, France* (2007), 521–526. <http://homepages.mcs.vuw.ac.nz/~donelan/cgi-bin/rs/publication_details?p=944&q=i>.
405. P-225, P-235 PICA- Power Piezo Stack Actuators. Preloaded High-Load Piezo Actuators (HVPZT) w/ Sensor Option Physik Instrumente GmbH & Co. <<http://www.physikinstrumente.com/en/products/prorder.php?sortnr=101750>>.
406. Artoos, K. *et al.* in *Proc. 1st Int. Particle Accelerator Conf., 23-28 May 2010, Kyoto, Japan* (2010), 1274–1276. <<http://accelconf.web.cern.ch/accelconf/IPAC10/papers/tuocmh02.pdf>>.
407. Artoos, K. *et al.* Study of the electronics architecture for the mechanical stabilization of the quadrupoles of the CLIC linear accelerator. *Journal of Instrumentation. Proc. Topical Workshop on Electronics for Particle Physics 2010 (TWEPP-10), 20-24 September 2010, Aachen, Germany* **5**, 9 (2010).
408. Artoos, K. *et al.* in *Proc. 1st Int. Particle Accelerator Conf., 23-28 May 2010, Kyoto, Japan* (2010), 2824–2826. <<http://accelconf.web.cern.ch/accelconf/IPAC10/papers/wepeb058.pdf>>.
409. *PMD Scientific, Inc.* <<http://www.pmdsci.com>>.
410. Zumberge, M., Berger, J., Otero, J. & Wielandt, E. An optical seismometer without force feedback. *Bulletin of the Seismological Society of America* **100**, 598–605 (2010).
411. Breeson, K. M. & Pepper, C. E. in *Proc. Waste management Symposia '94, 27 February - 3 March 1994, Tucson, AZ, USA* (1994). <<http://www.osti.gov/bridge/servlets/purl/10177989-fIvRYg/native/10177989.pdf>>.

- 412. Lilje, L., Simrock, S., Kostin, D. & Fouaidy, M. in *Proc. 8th European Particle Accelerator Conf., 3-7 June 2002, Paris, France* (2002), 2256–2258. <<http://accelconf.web.cern.ch/accelconf/e02/PAPERS/THPD0002.pdf>>.
- 413. *PICMA actuators* <<http://www.physikinstrumente.com>>.

Chapter 6

Civil engineering and technical services



S. Steed

6.1 OVERVIEW

6.1 Overview

Infrastructure costs for the CLIC project represent approximately one third of the overall budget. For this reason, particular emphasis has been placed on Civil Engineering and Services (CES) studies, to ensure a cost efficient conceptual design. This chapter provides an overview of the designs adopted for the key infrastructure cost drivers, such as; civil engineering, ventilation, water cooling, electrical supply, transport, and installation. Both the 500 GeV and 3 TeV machine concepts are considered.

6.2 Civil engineering

6.2.1 Overview

For the purposes of this CDR the civil engineering studies were based on the assumption that the CLIC facility will be sited on and around the existing CERN laboratory near Geneva, Switzerland. The proposed alignment for the near 50 km long 3 TeV machine straddles the France/Switzerland border, with the Interaction Region) fully located within existing CERN land on the Prévessin campus. Figure 6.1 is a schematic layout of the civil engineering complex for the CLIC project [1].

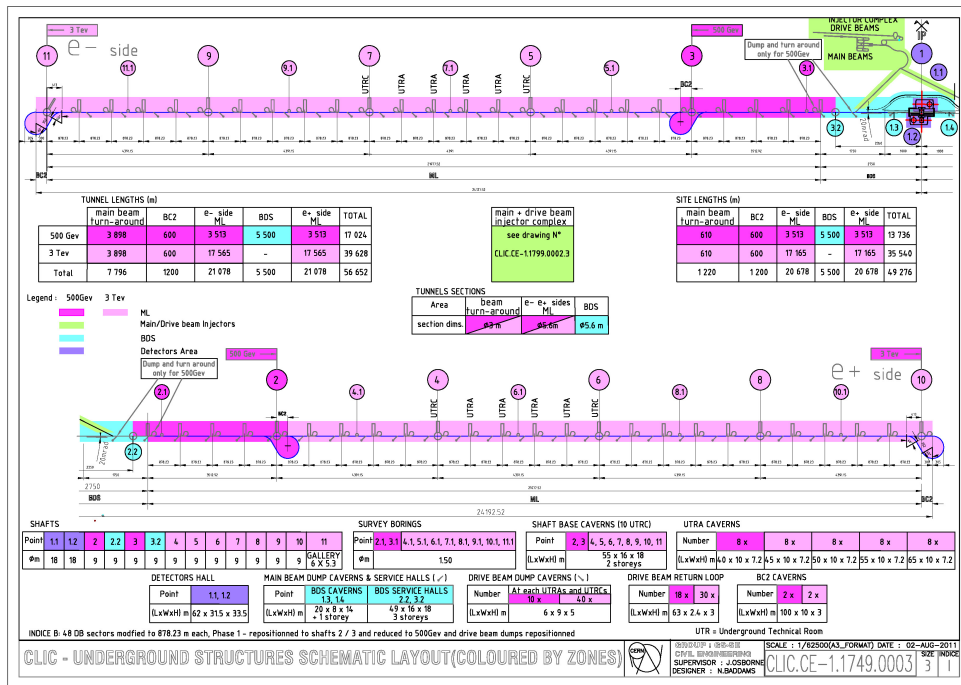


Fig. 6.1: Schematic layout of the civil engineering complex

The key features of this layout are:

- 20 mrad horizontal crossing angle and vertical plane symmetry about the collision point;
- Tunnels are laser straight, following the earth's curvature not like the ILC;
- Injection complex housed on the Prévessin campus with 'cut-and-cover' tunnels and surface buildings;
- Shafts and surface installations approximately every 5 km;
- Main Linac is housed within a single tunnel with an internal diameter of 5.6 m;
- 500 GeV machine from shafts 2 to 3, site length 17.74 km;
- 3 TeV machine from shafts 10 to 11, site length 49.28 km;
- Two independent caverns for detector assembly and maintenance with a common 'passageway' leading to a smaller Interaction Region (IR) cavern.

The CES studies presented in this chapter have been performed by the various technical experts within the CLIC team and in collaboration with certain ILC specialists. External consultancy firms ¹ have also contributed in some areas of these designs.

6.2.2 Location

The proposed siting for the 3 TeV CLIC project is in the north-western part of the Geneva region near the existing CERN laboratory. The near 50 km machine straddles the France/Switzerland border, with the IR fully located within existing CERN land on the Prévessin campus. The on-surface alignment of the accelerator tunnel is dotted with small villages, farmland and wooded areas.

The CERN area is extremely well-suited to housing the CLIC project, with the very stable and well understood ground conditions housing several particle accelerators in the region for over 50 years. The civil engineering works for the most recent machine, the LHC, were completed in 2005, so excellent geological records exist and have been utilized for this study to minimize the costs and risk to the project. The majority of the tunnel will be constructed in the stable molasse rock at depth of 100–150 m in an area with little seismic activity.

CERN and the Geneva region have all the necessary infrastructure at their disposal to accommodate such a project. Since Geneva is the home of many international organizations excellent transport and communication networks already exist. Geneva airport is only 5 km from the CERN site, with direct links; a newly constructed tramway gives direct access from the Meyrin site to the city centre (see Fig. 6.2).



Fig. 6.2: Tram stop outside the CERN Meyrin site

The governments of France and Switzerland have long standing agreements concerning the support of particle accelerators in the Geneva region, which make it very likely that the land could be made available free of charge, as it was for previous CERN projects.

¹ Amberg Engineering AG and Gadz Géotechnique Appliquée Deriaz SA

6.2.3 Land features

The proposed location for the accelerator is situated within the Swiss midlands embedded between the high mountain chains of the Alps and the lower mountain chain of the Jura. CERN is situated at the foot of the Jura mountain chain in a plain slightly inclined towards Lake Geneva. The surface terrain was shaped by the Rhone glacier which once extended from the Alps to the valley of the Rhone. The water of the area flows to the Mediterranean Sea. The absolute altitude of the surface ranges from 430 m to 500 m with respect to sea level. Figure 6.3 shows the potential siting for the CLIC tunnel in the region.

The physical positioning for the project has been developed based on the assumption that the maximum underground volume possible should be housed within the molasse rock and should avoid as much as possible any known geological faults or environmentally sensitive areas. In addition, it was assumed that the central injection complex and interaction region would be built on existing CERN land on the French Prévessin site. The shafts leading to the on-surface facilities have been positioned in the least populated areas. However, as no real discussions have taken place with the local authorities, the presented layouts can only be regarded as indicative, for costing purposes only. In certain areas, where the shafts would be either extremely deep or if a particularly environmentally sensitive area could not be avoided, inclined access tunnels have been foreseen. Although the typical depth of the tunnel below ground level is in the range of 100–150 m, at the French end the Main Linac is accessed via an inclined tunnel, since it is situated several hundred metres below ground level.

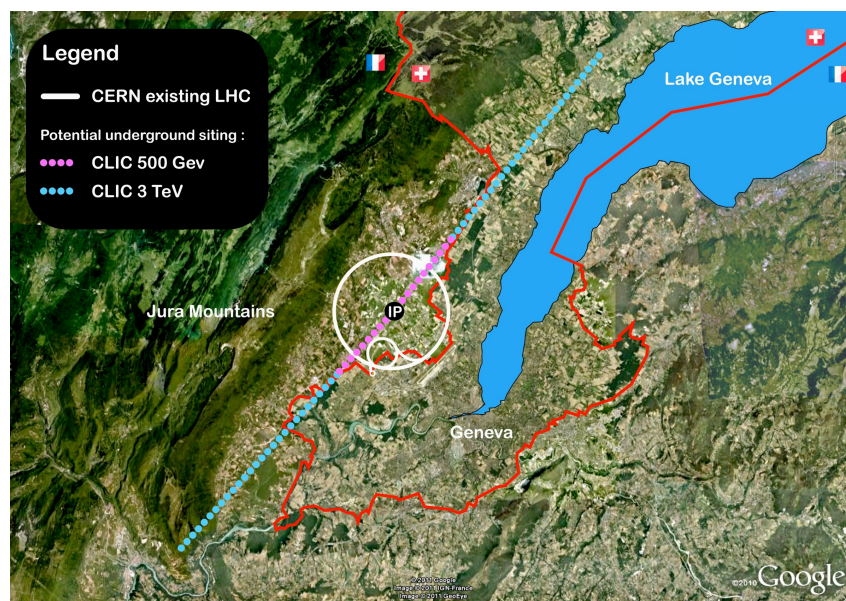


Fig. 6.3: Map showing a potential location for the CLIC accelerator complex

6.2.4 Geology

Most of the proposed path of CLIC is situated within the Geneva Basin, a sub-basin of the large North Alpine Foreland (or Molasse) Basin. This is a large basin which extends along the entire Alpine Front from South-Eastern France to Bavaria, and is infilled by molasse deposits of the Oligocene and Miocene age. The basin is underlain by crystalline basement rocks and formations of Triassic, Jurassic and Cretaceous age. The molasse, comprising an alternating sequence of marls and sandstones (and formations of intermediate compositions) is overlain by Quaternary glacial moraines related to the Würmian and Rissian glaciations. A simplified geological profile is shown in Fig. 6.4. The path crosses just below a well known fault at the valley of the Allondon river which is situated south-west of Geneva and filled with sands and gravels. Similarly, for the 3 TeV extension of the project, the tunnel will cross a second

sand- and gravel-infilled valley at Gland, situated north-east of Geneva. The tunnel at the south-west end will enter into some Jurassic limestone.

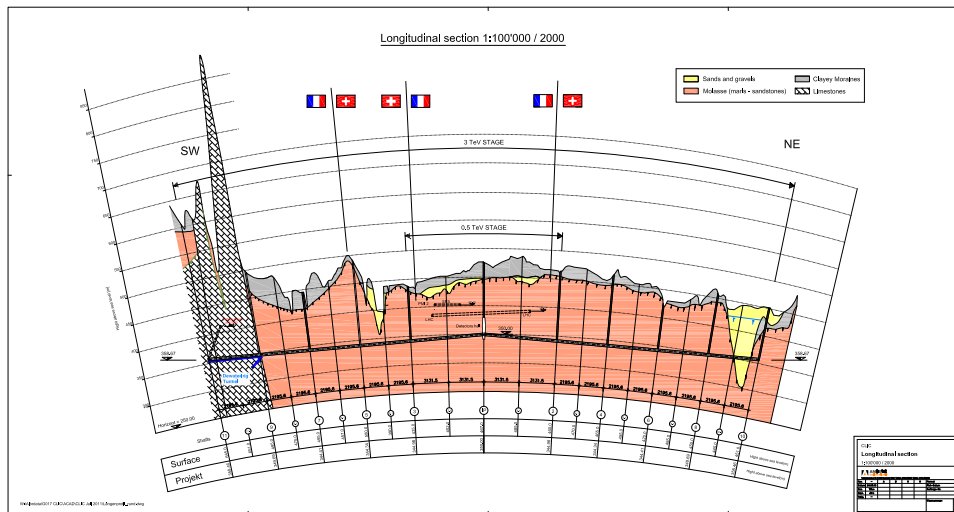


Fig. 6.4: Simplified geological profile. CLIC is mostly housed in the Molasse Rock

6.2.5 Site development

As most of the central campus is located on the CERN site at Prévessin, it is assumed for the CDR that the existing facilities such as; restaurants, main access, and road network are sufficient and have not been costed. However, for the parts located outside the existing fence line, but within CERN property, the following items will have to be included:

- Roads and car parks,
- Drainage networks,
- Landscaping and planting,
- Spoil dumps.

All temporary facilities needed for the construction works have also been included.

6.2.6 Construction methods

It is envisaged that Tunnel Boring Machines (TBMs) will be used for the main tunnel excavation followed by a second phase of excavation for the turnarounds, approximately every 800 m. In the molasse rock, a shielded TBM will be utilized, with single-pass pre-cast segmental lining, followed by injection grouting behind the lining. For planning and costing exercises, an average TBM advancement of 25 m per day, or 150 m per week is predicted. The second phase excavation will be executed using a 'roadheader' type machine. Figure 6.5 shows such machines.

Where the tunnel passes through any areas with potential water ingress, e.g., the 'Gland' depression, special excavation techniques such as freezing of the ground have been costed. Any new shafts that have to pass through substantial layers of water-bearing moraines (for example at CMS) will have to utilize this ground-freezing technique. This involves freezing the ground with a primary cooling circuit using ammonia and a secondary circuit using brine at -23°C , circulating in vertical tubes in pre-drilled holes at 1.5 metre intervals.

This frozen wall allows excavation of the shafts in dry ground conditions and also acts as a retaining wall. Figure 6.6 shows an example of this method.



Fig. 6.5: TBM (Gripper) type machine (left). Roadheader type machine (right)

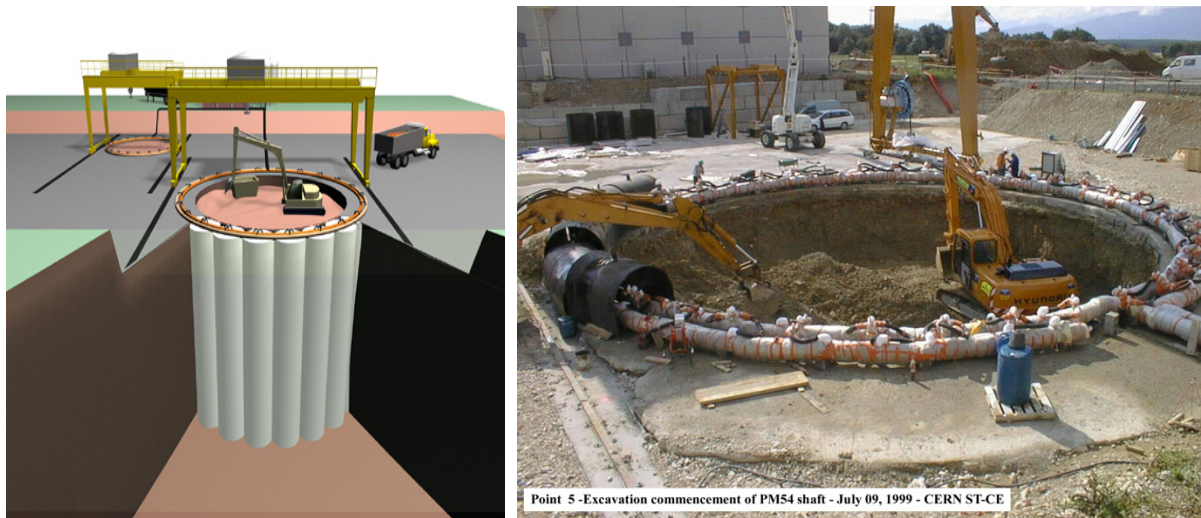


Fig. 6.6: Linking up cylinders of ice to construct a temporary wall

All the injection tunnels on the Préveessin site will be excavated using the ‘cut and cover’ technique. This method was used recently for the new 100 m long Linac4 injector for LHC. Figure 6.7 shows the Linac4 tunnel during construction.

6.2.7 Central injection complex

The complex (see Fig. 6.8) is located on CERN land in Préveessin and includes surface buildings and shallow underground galleries. It is divided into several parts: the Main Beam injectors, the Drive Beam injectors, and the experimental areas.

The Main Beam injector facility consists of six separate units with their own functionality and geometry: the primary e^- linac, the polarized e^- source, the positron target, the injector linac, the transfer line to the Damping Ring facility, and the booster linac. Figure 6.9 illustrates the geometry and structure of the underground part of the facility. The shallow galleries are cut-and-cover surface tunnels.

Surface buildings, which have been foreseen for the whole complex, will connect the underground facilities to the surface. Figure 6.10 shows the locations and geometries of the surface buildings for the Main Beam Injector, Drive Beam Injector and the experimental areas.

Cross-section B-B in Fig. 6.11 illustrates the way the klystron gallery for the Main Beam Injector is connected to the underground facility. There is a 5 metre vertical waveguide duct connecting the surface hall to the cut-and-cover tunnel. This 5 metre separation was recommended to address radiation protection issues.



Fig. 6.7: Excavation of LINAC4 using the cut and cover technique.

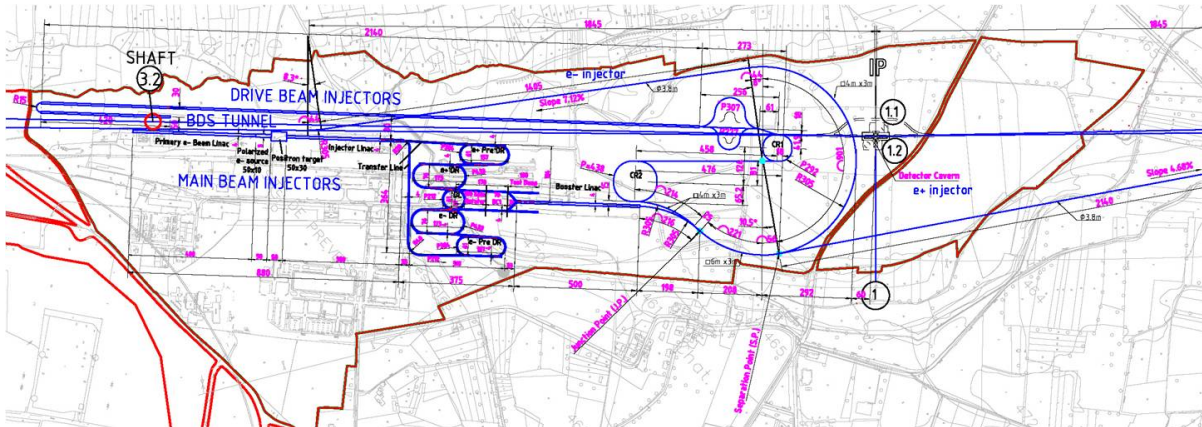


Fig. 6.8: Central injection complex – Plan view

The Drive Beam injector facility consists of four separate units with their own functionality and geometry: the Drive Beam Accelerator, the Delay Loop, Combiner Ring 1, and Combiner Ring 2. Figure 6.12 illustrates the geometry and structure of the facility.

Cross-section A–A in Fig. 6.13 illustrates how the largest building (2608 m long – 30 m wide – 9 m high), the klystron and modulator building for the Drive Beam injectors, is connected to the underground facility.

The inclined transfer tunnels transport the e^+ and e^- beams from the on-surface Injection Complex

6.2 CIVIL ENGINEERING

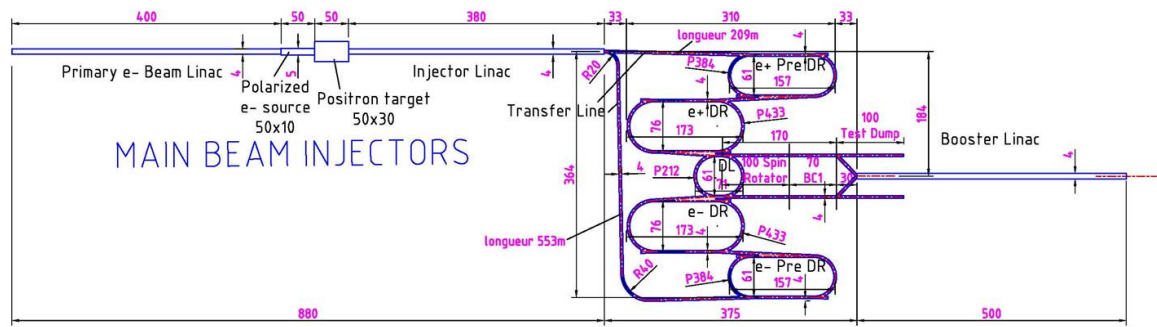


Fig. 6.9: Main Beam injectors – Overview

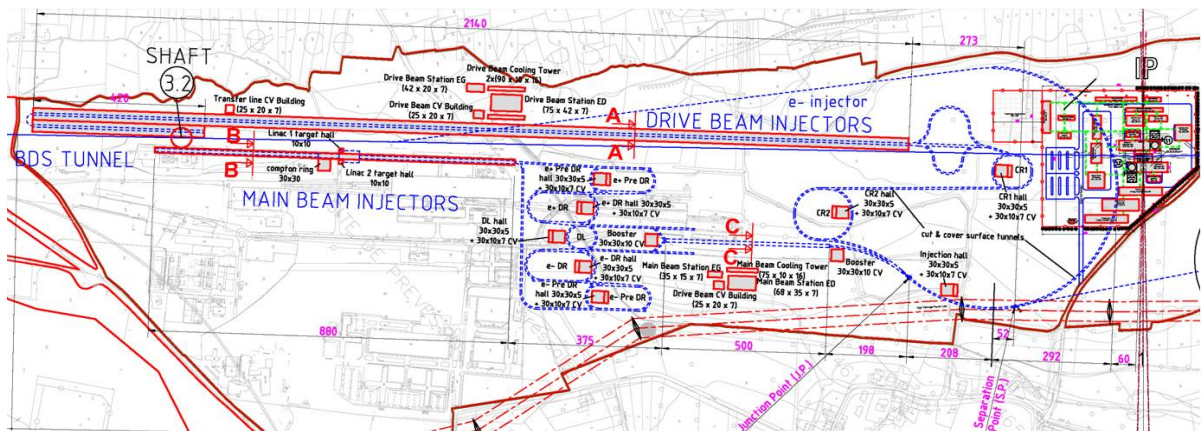


Fig. 6.10: Surface buildings (highlighted in red)

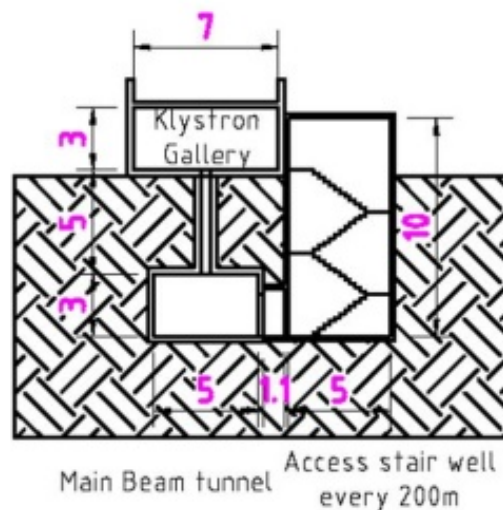


Fig. 6.11: Section B-B

to the deep-underground Main Linac. The e^- injector tunnel goes down with a slope of 7.12% while the e^+ injector tunnel has a smaller slope of 4.68%. These slopes are perfectly acceptable to allow ‘normal’ transport vehicles to operate safely.

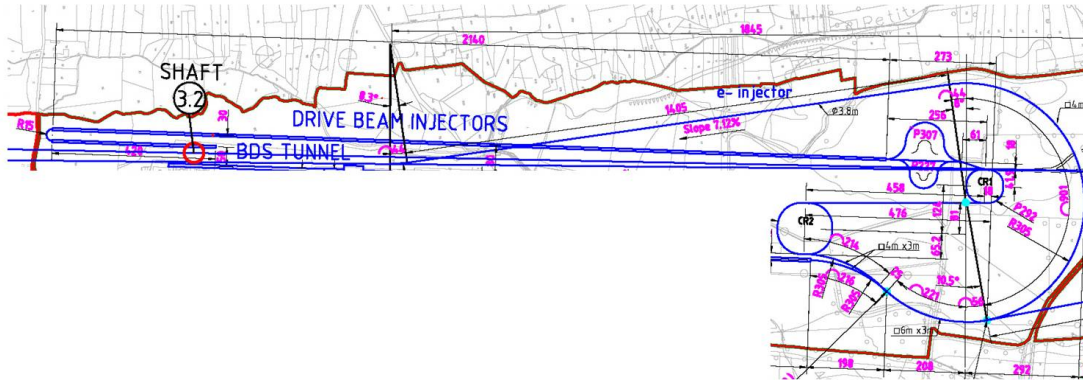


Fig. 6.12: Drive Beam Injectors – Plan view

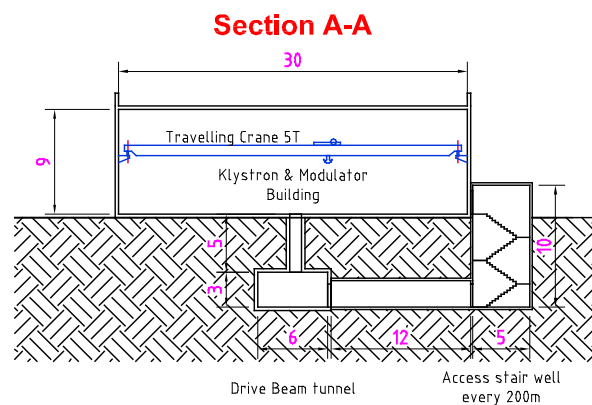


Fig. 6.13: Section A-A

The turnaround section of the e^- injector remains in the horizontal plane to ensure that the vertical and horizontal components of the beam transfer to the Main Linac are decoupled, i.e., there is no ‘spiral’ effect in the tunnel descent.

6.2.8 Main Linac

The internal diameter of the Main Linac tunnel has been fixed for the CDR at 5.6 m with a 10 cm margin to allow for construction tolerances. This diameter was defined by inserting all known machine components and services into a 3D model while maintaining a space for transport vehicles and safe passage of personnel. This diameter is within the common range of TBMs used for metro transportation tunnels, which means machinery and spare parts are more easily found on the market. A driving factor for the tunnel cross-section is the overhead ventilation ducting. Unlike the LHC tunnel, which uses the longitudinal ventilation concept, a semi-transversal ventilation scheme has been adopted.

In order to minimize vibration from the cooling pipes embedded in the tunnel floor, the *in situ* concrete will be formed of two sections separated by a vertical joint of compressible filler between the section housing the pipes and the section supporting the accelerator.

A typical cross-section of the Main Linac tunnel is shown in Fig. 6.14.

6.2.9 Drive Beam turnarounds

The Drive Beam turnarounds are located approximately every 800 m along the Main Linac. After completion of the TBM drive, these auxiliary structures will be excavated using a ‘roadheader-type’ machine.

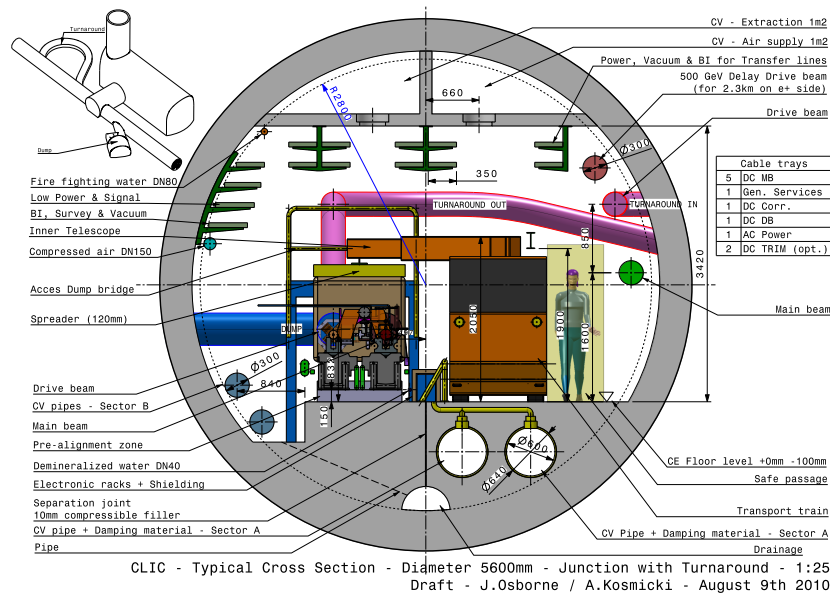


Fig. 6.14: Typical tunnel cross-section: 5.6 m

The Drive Beam must pass over the transport corridor both to enter and then to leave the turnaround. The radius of the turnarounds is 10 m. On the other side of the Main Linac, a 25 m long beam dump cavern is required at every turnaround. Figure 6.15 shows the Drive Beam turnaround and Drive Beam dump.

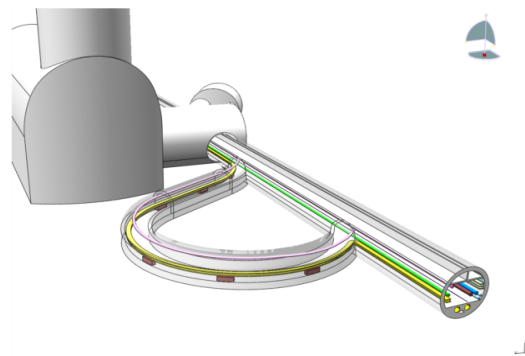


Fig. 6.15: Drive Beam turnaround and dump

6.2.10 Interaction Region and Beam Delivery System

In the middle of the CLIC complex are the IR and the Beam Delivery System (BDS). The BDS accommodates the incoming (and outgoing) beamlines to (and from) the IR, which hosts the detector caverns. Figure 6.16 shows the geometry and structure of the IR and BDS facilities.

The BDS consists of several facilities duplicated on both sides of the IR: Main Beam dump, BDS tunnel, Drive Beam dump, tune-up dump, shaft and service cavern, Drive Beam loop and dump complex.

The Main Beam dumps extend 315 m downstream from the IR (Fig. 6.17).

In order to prevent the radiation produced in the dump from propagating into the beam tunnel, a two metre thick concrete wall has to be built. Figure 6.18 shows the structure of the Main Beam dump cavern and tunnel with respect to the beam tunnel.

The Interaction Region consists of four main elements: two detector caverns, the transfer tunnel,

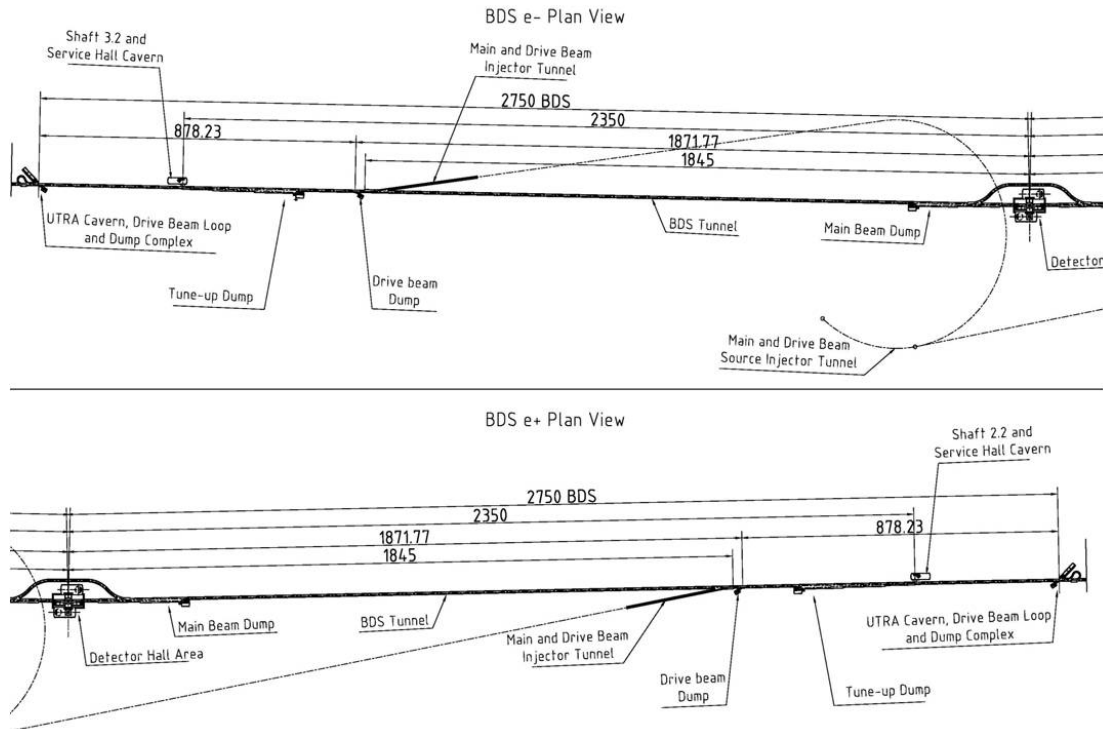


Fig. 6.16: BDS and IR – Plan view

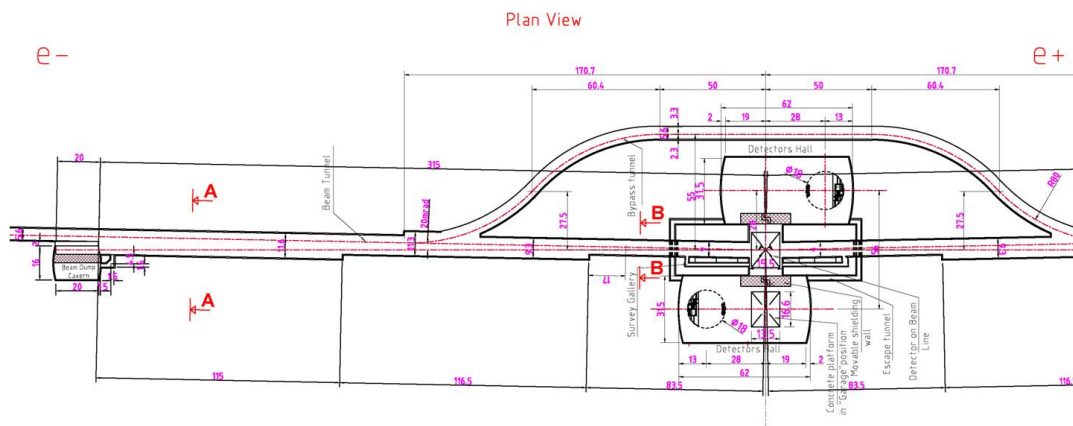


Fig. 6.17: Location and geometry of Main Beam dumps

and the bypass tunnel. The detector caverns will host the detectors during their installation underground and when they are in the ‘garage position’. The transfer tunnel links the two detector caverns and allows the sliding of each detector into ‘beam position’. The ‘push–pull’ system, used to move the detectors in and out of the beamline, is described in §5.12.4. The Interaction Region is illustrated in Fig. 6.19.

Each detector cavern is connected by an escape tunnel to a safety shelter located in the other detector cavern. In addition, a survey gallery will allow the alignment of the magnets located in the beam tunnels on both sides of the IR with respect to each other and to the detectors.

Space has been reserved for a 2-m-thick movable shielding wall at the interface between the detector cavern and the transfer tunnel to prevent the radiation produced in the transfer tunnel from propagating into the detector caverns.

Section A-A

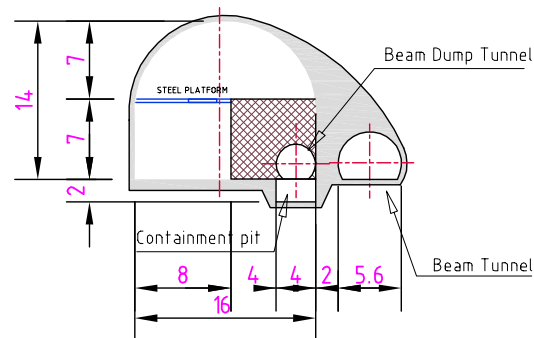


Fig. 6.18: Structure of Main Beam dump tunnel and cavern

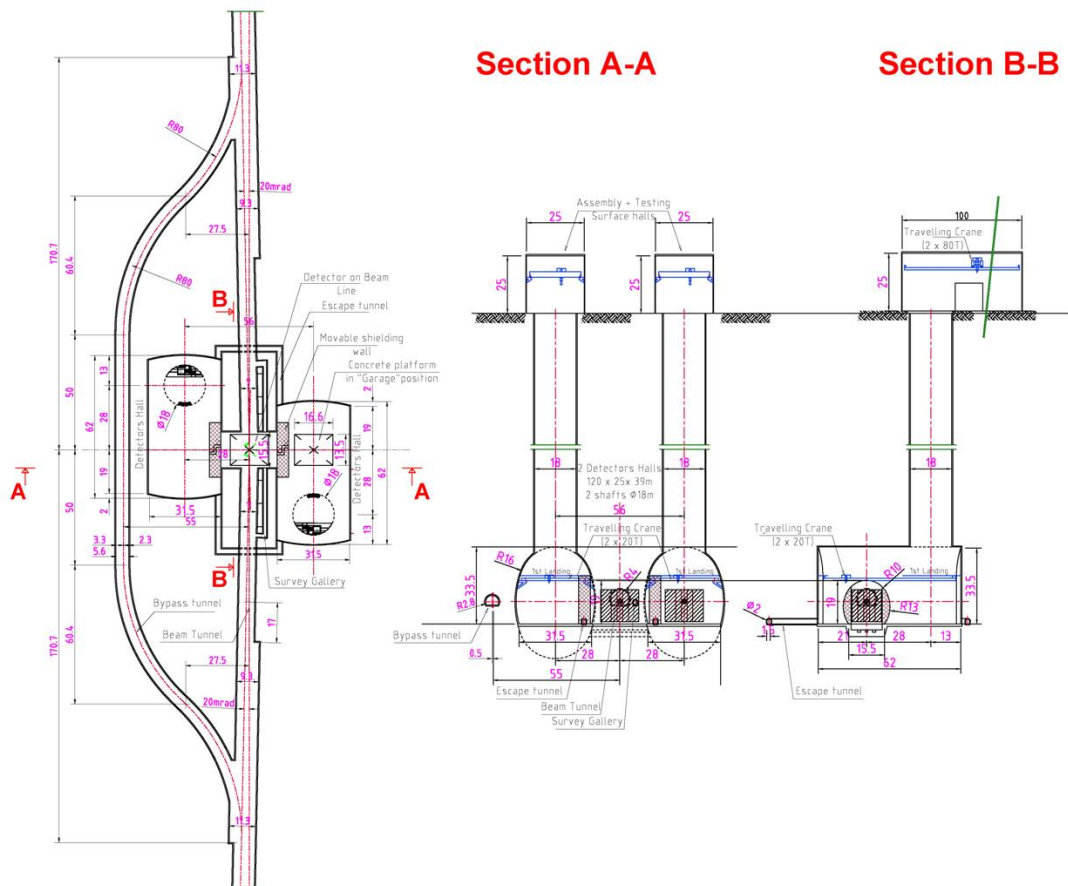


Fig. 6.19: Interaction Region

Two 18 m diameter shafts connect the detector caverns with corresponding surface halls where the detectors will be assembled and tested before being lowered underground. In order to assemble and service the detectors, travelling cranes have to be installed. Each surface hall is equipped with two 80 t cranes. The detector caverns are each equipped with one 20 t crane.

6.2.11 Cost considerations

The cost estimates for the 500 GeV and for the 3 TeV machine will be prepared based on the layouts presented here and the approved Project Breakdown Structure (PBS). The estimate will include all aspects of construction, final engineering designs, and construction management. Many of the inputs used to formulate this estimate will be based on real construction costs from the LHC (1998–2005). In order to allow cost comparison with the ILC Project, the same basic methodology will be adopted wherever possible [2].

6.2.11.1 Scheduling considerations

Detailed information on the CES scheduling can be found in §9.5.

6.3 Electricity supply

6.3.1 Overview

Electrical power is categorized by three major systems:

- RF power (modulators);
- conventional power (normal-conducting magnet power supplies, electronic racks, cooling and ventilation systems, and infrastructure components);
- emergency power provided by back-up generators (emergency lighting, sump pumps and ventilation systems for sub-surface enclosures).

Power requirements are dominated by the RF system (modulators) located in the central campus area. Table 6.1 gives the estimated nominal power for 500 GeV and 3 TeV center-of-mass operations.

Table 6.1: Estimated nominal power loads for 500 GeV and 3 TeV centre-of-mass operations

Location	500 GeV Operation			3 TeV Operation		
	Total losses [MW]	Total reactive power [Mvar]	Total apparent power [MVA]	Total losses (MW)	Total reactive power [Mvar]	Total apparent power [MVA]
Central campus	222	65	231	467	122	482
Main tunnel	23	12	26	98	53	111
Total	245	77	256	565	175	591

6.3.2 System configuration

The connection to the 400 kV utility network is in the main substation located in the central campus area. The selected voltage for the medium-voltage (MV) power distribution system is 36 kV. This choice provides maximum utilization of the standard MV equipment (dry transformers, switchgear, cables, etc.), and minimizes power distribution losses and voltage drop over long distances. Power from the main substation is routed at the 36 kV level to the individual substations (injectors, damping rings, beam transport, frequency multiplication) for further transformation and utilization. Existing and new cable galleries are used for 36 kV cable lines. Each individual substation is provided with a backup generator used for emergency lighting, sump pumps and ventilation systems for sub-surface enclosures, fire alarms, smoke detectors, etc. The low-voltage (LV) distribution system nominal voltage is 400 V allowing for utilization of standardized equipment. The HV and MV protection, monitoring, and communication systems are based on state-of-the-art relays fully utilizing the IEC 61850 substation automation standard.

6.3.3 Distribution for the main tunnel

Power for the main tunnel comes from the main substation and constitutes approximately 10% of the total power consumption for 500 GeV and approximately 15% for 3 TeV operations. The following 36 kV cable lines are routed along the main tunnel:

1. Cable lines providing power to conventional loads (power supplies, electronic racks, cooling and ventilation systems and infrastructure components) in each cavern along the tunnel. For redundancy a return line is added forming a loop.
2. Cable lines providing emergency power backed up by generators (emergency lighting, sump pumps and ventilation systems for sub-surface enclosures, fire alarms, smoke detectors, etc.).

Electrical equipment used in the main tunnel power distribution system is suitable for underground installations. This includes class F1 (self-extinguishing when exposed to fire) dry transformers, halogen-free and fire-resistant cables, and arc-proof switching equipment.

Figure 6.20 shows the power distribution concept for the main tunnel.

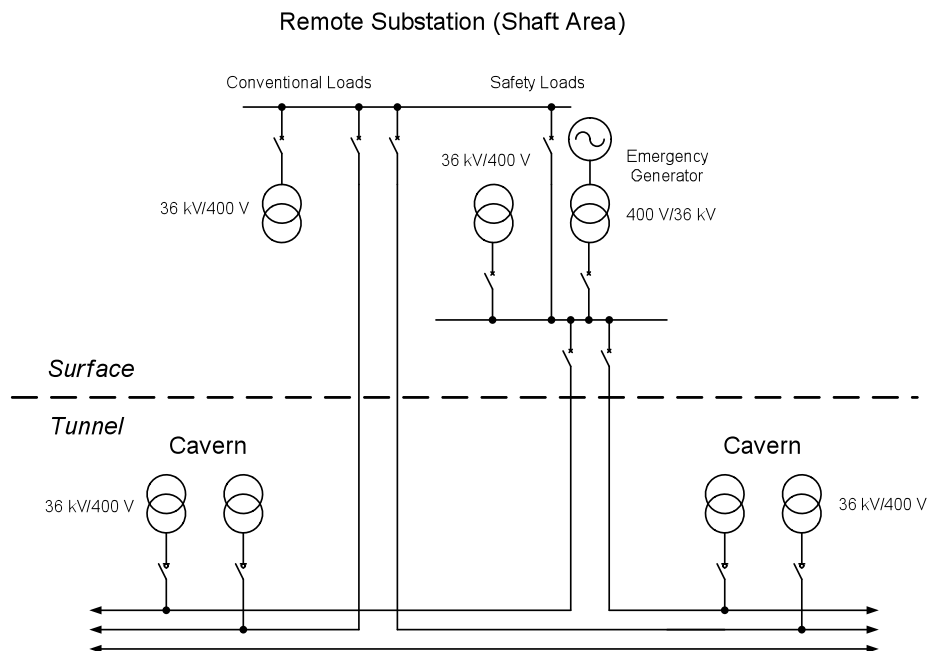


Fig. 6.20: Simplified concept of the power distribution for the main tunnel

6.3.4 Distribution for the main campus

Power for the Drive Beam and Main Beam production, beam transport, frequency multiplication, etc. also comes from the main substation, which houses 400/36 kV power transformers, switching equipment, power system protection, and automation equipment. A hot-spare power transformer and substation configuration ensures high availability.

The power distribution concept is presented in Fig. 6.21.

6.3.5 Emergency supplies

The emergency supply system is based on stand-by diesel generators. Each generator set supplies a protected substation, which is normally supplied by the utility power. During a utility power interruption,

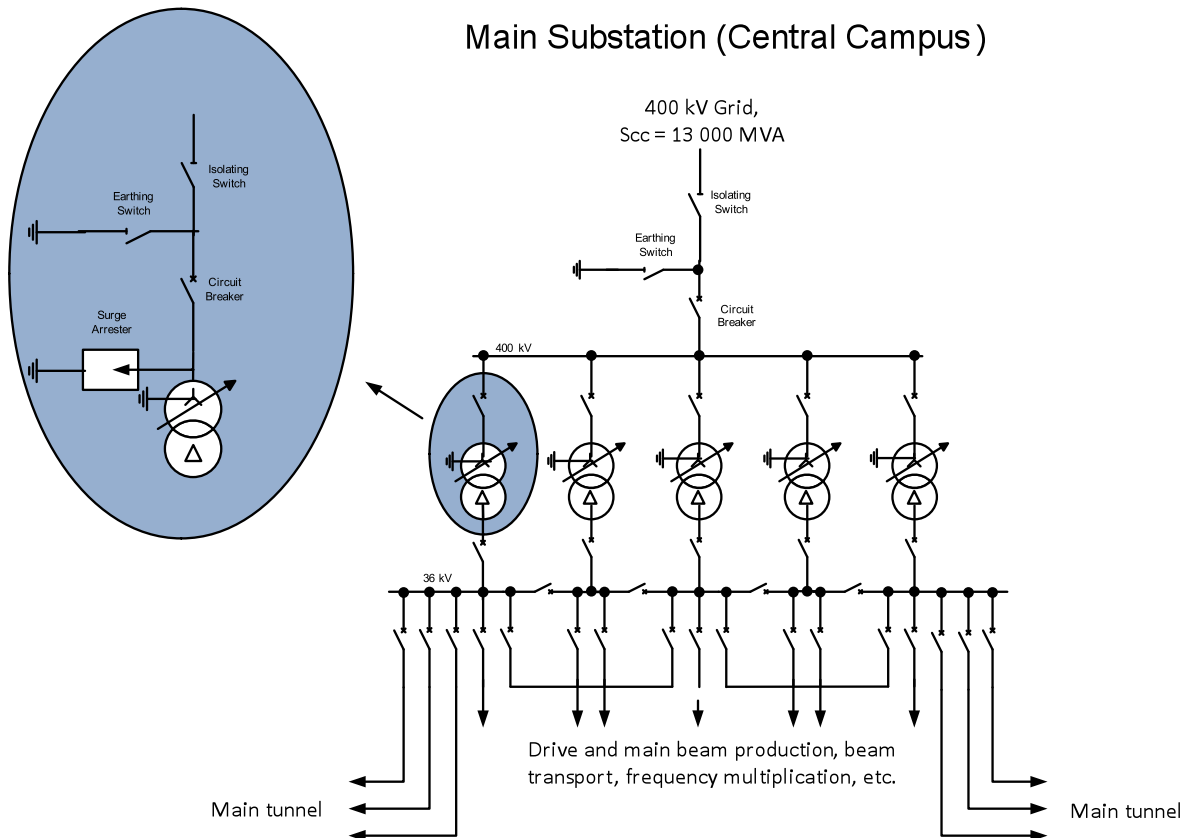


Fig. 6.21: Simplified concept of the power distribution for the central campus

the diesel engines start automatically and transfer the critical load when ready. Any critical system which cannot accept any power interruption is provided with an Un-interruptible Power Supply (UPS) system.

6.3.6 Cost considerations

The cost estimate for electricity supply is based on the following assumptions:

- The existing 400 kV connection is utilized,
- A new main substation will be located in the existing BE substation area near the CERN Control Centre (CCC),
- The existing cable galleries are re-utilized,
- The existing and new accelerator complexes are not operating at the same time,
- The cost estimate will be optimized after the design of the power distribution system is finalized.

6.4 Cooling and ventilation

6.4.1 Overview

Cooling and ventilation (CV) installations for CLIC have been sectorized in order to properly handle the thermal loads and to optimize the dimensions of the facilities and of the related CV plants. Each plant dedicated to a sector has been designed with elements that can be commonly found in industry in order to avoid, as much as possible, the use of custom-made parts. Several working parameters of some plants present very high values that require the installation in parallel of pumps and other equipment; this leads

6.4 COOLING AND VENTILATION

to a more complex operation and to a strong environmental impact; at a later stage, when more details are available, these circuits could be split into smaller ones, thus simplifying operation. Several elements of the present conceptual study will be reviewed in the next phase of the design process in order to solve the pending issues and to comply with more detailed requirements in particular with respect to radiation protection.

The following sections present the main principles for the ventilation and the cooling of CLIC and detail the most important working parameters as well as the different operation scenarios.

6.4.2 Ventilation

6.4.2.1 Design

The air handling installations are designed to

- supply fresh air for people,
- provide heating and ventilation,
- ensure destratification and maintain a suitable temperature at the surface of the equipment,
- dehumidify the supplied air to prevent condensation,
- allow smoke extraction from some areas (cold smokes only in some cases),
- purge the air of the tunnel before access,
- filter the exhaust air,
- provide sound attenuation measures at the exhaust air.

6.4.2.2 Indoor conditions

The indoor conditions that will be ensured by the ventilation system are given in Table 6.2.

Table 6.2: Indoor conditions

Location	Summer temperature [°C]	Winter temperature [°C]
Tunnels, underground caverns (at equipment level)	21±1	21±1
Surface buildings with controlled temperature	25±1	18±1

The values indicated are mean values at the heights where people and equipment are foreseen; according to the ventilation scheme, the temperature gradients along the supply and extraction louvers are different. The highest temperature gradients are expected in the main tunnels, dump areas and loops.

The relative humidity will not be regulated. Some specific areas (Faraday cages, clean rooms or other laboratories) might require a humidity regulation system. The dew point will however be kept below 12°C to avoid condensation. The outdoor conditions for the Geneva region, shown in Table 6.3, are used for dimensioning the air-handling equipment:

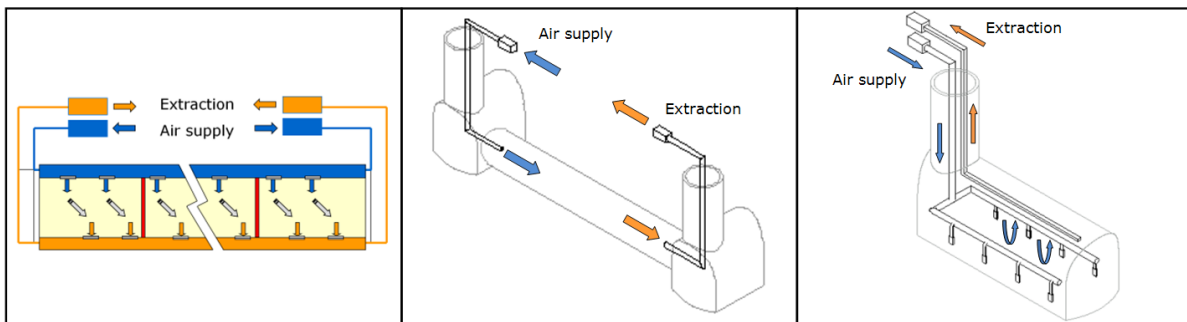
6.4.2.3 Ventilation schemes

Each tunnel is ventilated by air-handling units (AHUs) located on the surface and therefore accessible at any time; redundant units have been foreseen everywhere in order to avoid impacting the operation of the accelerator in case of breakdown. Because of the different needs for thermal stability, the geometric constraints (tunnel dimensions vs. duct size) and the thermal load to evacuate, three different ventilation schemes have been foreseen (Fig. 6.22):

Table 6.3: Outdoor conditions in the Geneva region.

Period	Dry bulb temperature [°C]	Relative humidity [%]
Summer	32	40
Winter	12	90

1. Semi-transversal ventilation: the air is supplied via a dedicated duct running all along the tunnel length and is extracted via a parallel duct,
2. Longitudinal ventilation: the air is blown via dedicated ducts at the entrance of the tunnel and then extracted at the opposite end,
3. Ventilation of caverns, premises other than the tunnels, and surface buildings: the air is blown via diffusers on each floor level and extracted via one or more ducts located on the ceiling.

**Fig. 6.22:** Ventilation schemes: (left) semi-transversal, (centre) longitudinal and (right) ventilation for caverns

In the semi-transversal ventilation scheme, inlet and extraction dampers are offset with respect to each other in order to ensure a better distribution of the air in the tunnel and avoid shortcuts between supply and extraction. Supply and extraction units for one sector are located at both ends; fire-resistant dampers will be installed every 500 m on all the ducts in the tunnels: in case of fire this will allow the isolation of a specific sector of the tunnel, from the ventilation point of view, while ensuring a proper ventilation of all the adjacent fire sectors for the safe evacuation of personnel in the tunnel.

The semi-transversal ventilation is used in tunnels with beamlines to achieve the required temperature stability; the longitudinal ventilation is used for passageways or with premises containing equipment other than the accelerators.

In particular the solutions described in Table 6.4 have been foreseen.

All other premises have a more standard configuration consisting of one dedicated unit per facility.

As a general principle, smoke extraction is foreseen in all the facilities presenting an important risk because of the fire loads or safety of people; for these, adequate space must be available for smoke extraction ducts. In case of fire, the fire brigade will be able to switch off or reconfigure manually the ventilation control system.

6.4.2.4 Ventilation of underground premises

6.4.2.5 Operational modes

Different modes are foreseen for the ventilation systems depending on the operating conditions, as shown in Table 6.5.

Table 6.4: Solutions for ventilation problems

Location	Solution
Main beam tunnel	Air-handling units for supply and extraction are located at each surface point, each sector is ventilated from both points.
UTRC, UTRA, roundabouts, dumps	Dedicated air-handling units are installed in the UTRA or the UTRC caverns to remove heat from these caverns and in the roundabouts; these units have coils cooled by chilled water produced in the surface points in order not to increase the thermal load of the tunnel.
Damping rings, delay loops, frequency multiplication, transfer lines	Due to the smaller length of these tunnels one-air handling unit for supply and one for extraction is foreseen for each ring or sector instead of two as in the main tunnels. In the damping ring area, the dead-end tunnels are equipped with relay fans in order to ensure a proper air circulation throughout their length.
Drive beam injectors tunnel	Four air-handling units for supply and four for extraction, located on the surface, each ventilate a part of the tunnel.

Table 6.5: Operational modes for different operating conditions

Operating condition	Modes
Run	No access, accelerators running and equipment powered.
Shutdown	Open access, accelerator stopped, maintenance interventions.
Purge	If needed before allowing access to personnel, accelerator stopped.

All motors for ventilators are foreseen to be equipped with variable-speed drives in order to adjust flow rates, to adapt the working conditions to the operational needs, and to achieve the requested dynamic confinement.

6.4.2.6 Working parameters

The main parameters of the ventilation units are listed in Table 6.6. The number of units indicated in the second column refers to the supply units used in each facility to ensure the removal of the heat loads; it therefore does not take into account the redundant units and the extraction units; the latter will present similar characteristics. The flow rates in Table 6.6 represent the flow rate in each of these units.

The longitudinal air speed in the tunnel will be kept below 1.4 ms^{-1} in order to safely evacuate personnel in case of fire. The filtering level of the exhaust air before release to the atmosphere will be decided according to the radiation protection constraints. The level of redundancy is set to N+1; the redundant units dedicated to air extraction will not be equipped with filters since these units might be used to extract smoke which could clog the filters. All units dedicated to safe areas and tunnels will be powered via the secure electrical network.

Figure 6.23 shows a schematic diagram of the ventilation system of the central area of the tunnel, including the detector caverns.

Table 6.6: Working parameters for AHUs dedicated to underground premises.

Underground premises	Total number of units	Flow rate run mode [m ³ /h]	Flow rate shutdown mode [m ³ /h]	Flow rate purge [m ³ /h]	Equipment heat load [kW]
Tunnel Drive Beam injector	4	63 000	63 000	120 000	1760
Tunnel Main Beam injector	1	55 000	55 000	80 000	380
Damping rings	5	30 000	15 000	30 000	950
Tunnel booster LINAC	1	15 000	6000	20 000	100
Transfer line to JP, SP	1	65 000	40 000	100 000	450
Loop	1	35 000	20 000	60 000	230
Transfer line e ⁻	1	30 000	16 000	50 000	0
Transfer line e ⁺	1	50 000	25 000	75 000	0
Frequency multiplication	4	15 000	10 000	30 000	405
Main tunnel* e ⁺	10	45 000	45 000	90 000	528
Main tunnel* e ⁻	10	45 000	45 000	90 000	528
Turnaround e ⁻ - end tunnel	1	30 000	30 000	60 000	35
Bunch compressor e ⁻	1	15 000	15 000	30 000	35
Turnaround e ⁺	1	30 000	30 000	60 000	35
Bunch compressor e ⁺	1	15 000	15 000	30 000	35
UTRC	10	16 000	32 000	60 000	95
UTRA	40	16 000	32 000	60 000	95
Drive Beam dump caverns/ post decelerators	48	1000	2000	3000	5
Loop	48	2000	2000	4000	10
BDS - intersection point	4	60 000	35 000	120 000	1560
Detector halls	2	45 000	45 000	9000	650
Main beam dump cavern	2	20 000	10 000	20 000	140
Service halls cavern (pt 2.2 and 3.2)	1	22 000	22 000	45 000	150
BC2 caverns	4	3000	10 000	10 000	20
Bypass tunnel	1	25 000	25 000	50 000	0
Escape tunnel	2	2500	5000	5000	0
Pressurized area shaft	2	15 000	45 000	45 000	0

* per sector, between two surface points

6.4.2.7 Ventilation of surface buildings

Each surface building will be ventilated with a dedicated air-handling unit. Where the building length requires it, several units in the same building are foreseen, each of them for a part of the building. Details of the most important installations are given in Table 6.7.

At present, no redundant units are considered necessary in these buildings; should this be needed, redundancy can easily be implemented. All surface buildings will be equipped with a mechanical system on the roof to extract smoke at 400°C for 2 hours providing an external counter pressure of 30 Pa.

6.4.2.8 Safety

All the supply air-handling units are equipped with smoke detection sensors downstream of the ventilator in order to avoid injection of smoke into the underground areas. Exhaust air ducts will have branches to connect the air monitoring equipment for radiation protection monitoring before release into the atmosphere.

6.4 COOLING AND VENTILATION

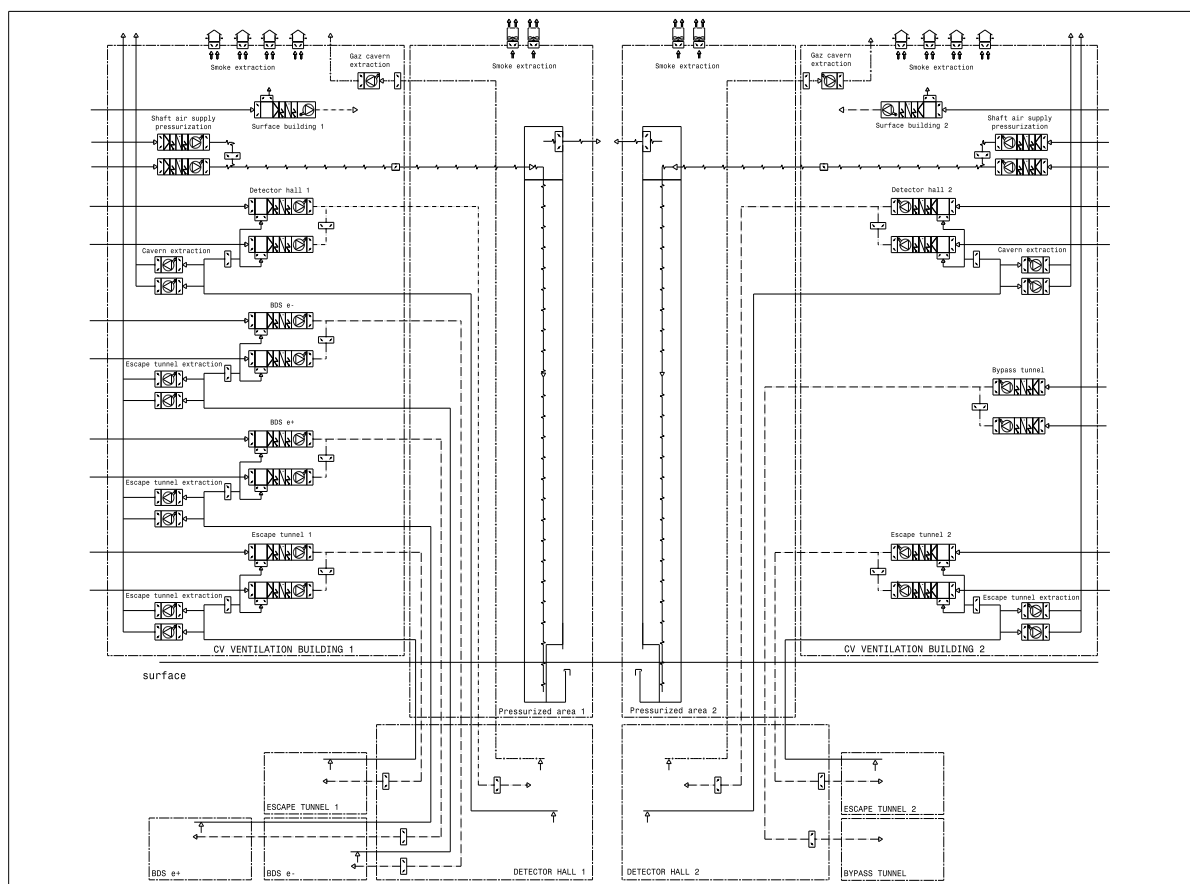


Fig. 6.23: Diagram of ventilation plants for the central area and halls for the detectors

Table 6.7: Working parameters for AHUs dedicated to surface buildings

Surface building	Number of units	Flow rate per unit [m ³ /h]	Equipment heat load [kW]
Drive beam Linac	50	70 000	15 840
Main Beam Linac Hall	9	10 000	608
Linac 1 and 2 target halls	2	5000	0
Compton ring	1	22 500	0
Damping rings area (5 buildings)	5	22 500	0
Booster linac	5	10 000	0
Injection hall	1	34 000	170
Combiner ring 1 & 2	2	55 000	380
Cryo building	1	12 000	n.a.
Gas building	1	8000	n.a.

6.4.2.9 Further considerations

The ventilation concept described above is based on the current CLIC design; it will be completed when all detailed requirements and constraints are finalized. In particular, the present study was based on the issues related to the extraction of the thermal loads, while the aspects related to radiation protection (and

consequent dynamic confinement) and fire safety will be dealt with in further studies. It is considered useful to make a thermo-fluid-dynamics simulation once detailed information on the equipment and the layout becomes available in order to validate the temperature profile in the tunnel. Given the very high temperature difference between inlet and outlet the eventual presence of hot spots will be highlighted.

Another relevant issue which remains to be optimized is the possibility of heat recovery and air recycling from the different plants. This is dependent on the exact location of the facilities and access points to the underground premises.

6.4.3 Cooling

6.4.3.1 General layout

The hydraulic installations are designed to handle

- industrial water and demineralized water: cooling of technical equipment (accelerators, detectors, cavities, electronic racks, cryogenic equipment etc.);
- chilled water: ventilation systems (air handling units);
- drinking water: sanitary purposes and make up of circuits;
- raw industrial water: fire fighting systems;
- waste water: reject and drain of waste water from underground and surface premises.

6.4.3.2 Cooling plants

The cooling plants will remove most of the heat generated in the accelerator areas by the accelerator and the technical equipment. In order to minimize the water consumption for economic and environmental reasons, a configuration in closed loops has been chosen. Therefore, primary circuits are cooled by evaporative cooling towers; a dedicated set of pumps on the primary and secondary side of the heat exchangers provides the necessary pressure head for each circuit. For accessibility reasons during operation and for simplicity of maintenance, the water-cooling stations including the heat exchangers and the pumps in the secondary circuits, are located in surface buildings. Cooling towers will be installed only on the central site (Prévessin); all cooling stations are subsequently centralized in that area; the environmental impact in the Surface Points is therefore minimized. The pipelines connecting the surface and the underground sites will be installed in the shafts closest to the cooling stations.

Primary circuits will use raw industrial water with a make-up of drinking water to compensate for evaporation losses and deconcentration; continuous water treatment against scaling and the proliferation of algae will also be included. The drinking water make-up is supposed to be provided by the local water supplier from facilities located outside CERN.

Secondary circuits mainly use demineralized water with a maximum conductivity of $0.1 \mu\text{S}/\text{cm}$; make-up to compensate losses will be provided by an independent central station producing demineralized water with a maximum capacity of $600 \text{ m}^3/\text{day}$. Given the volumes of each circuit, a connection with the existing demineralized water network of CERN is foreseen in order to allow faster filling at the time of commissioning of the circuits or in case of refilling of some sectors. Each secondary circuit will be equipped with demineralisation cartridges in order to locally adjust the conductivity.

In cooling towers and pumping stations, the redundancy level is defined to ensure continuous operation in case of breakdown of one single element (cell or pump), whereas no specific redundancy at present is considered necessary for plate heat exchangers, control and electrical cubicles. In case of a general power failure, all the cooling systems will stop as no further cooling capacity will be needed until the restart of the accelerator and the related equipment.

6.4.3.3 Working parameters

The working parameters, assuming siting in the Geneva region, are indicated in Table 6.8.

Table 6.8: Working parameters for primary and secondary circuits

Location	Temperature at inlet [°C]	Temperature at outlet [°C]
Primary circuit: cooling towers	45	25
Secondary circuit: heat exchanger	27	47

The temperature difference between inlet and outlet is 20°C. Tolerances on temperature are foreseen to be in the order of $\pm 0.5^\circ\text{C}$. If more stringent requirements on the temperature stability are expressed, the demineralized water in the network will be under-cooled and then heated to the required value by heaters installed immediately before the connection tap.

The cooling circuits have been divided into sectors as indicated in Table 6.9; each of these sectors will be connected to an independent set of cooling towers. Depending on the resulting dimensions and flow rates, some of these circuits could be split into smaller ones; this will become possible when details of the equipment to be cooled become available.

For the main tunnel, since the operating conditions, the tolerances, and the flow rates needed are different, two separate circuits have been foreseen: circuit A (currently foreseen to be embedded in the concrete slab) is dedicated to the cooling of the accelerator modules while circuit B will be used for the cooling of all equipment in UTRAs, UTRCs, loops and beam dumps. Circuit B will work with slightly different temperatures, i.e., 27°C at the inlet and 52°C at the return, thus having a temperature difference of 25°C. Pressure drops in those circuits require the implementation of booster pumps every 4.4 km along the length of the tunnels; these pumps will be located in accessible areas (preferably in UTRCs or equivalent) and N+1 redundancy is foreseen. This will allow the use of pipes with a maximum nominal pressure of 25 bar.

Table 6.10 shows the main characteristic of the pumps and heat exchanger per circuit; to achieve the requested overall power, the plate heat exchanger might be composed of two or three heat exchangers in series.

Figures 6.24 and 6.25 show the schematic layout of some of the future cooling stations.

6.4.3.4 Further considerations

For ventilation the architecture and the principles adopted have been selected on the basis of present knowledge and could therefore evolve.

One of the most important problems to tackle will be the exact location in the tunnel of all accessories and components to ensure proper operation of the plant while keeping an acceptable level of flexibility and maintainability. In particular, detailed studies should be made to define the location of the bypass valves between the inlet and return of each circuit, as well as of the drain valves to partially empty a circuit, and of manifolds and their connections to the main water pipes. The implementation of booster pumps must also be evaluated. Special care must be given to the choice of the best regulation principles.

Further studies will also optimize the location of pumping stations and routing of pipelines through shafts in the tunnels, as well as the detailed layout of the cooling plants.

6.4.4 Chilled water

The cooling of the ventilation plants is achieved with chilled-water circuits, located at each surface point. The main working parameters are the inside and outside temperatures, 6°C, and 12°C, respectively.

Table 6.9: Working parameters for AHUs dedicated to underground premises

Circuit	Cooling power [kW]	Q [m ³ /h]	Nominal diameter [mm]	Cooling towers		
				Power/cell [MW]	Number of cells N+1	Dimensions by cell [m]
Drive Beam injector – surface	155 000	6670	900	20	12	15×10
Drive Beam injector – tunnel	17 000	730	400			
Frequency multiplication	17 000	730	400			
Transfer lines	9000	390	300			
Chilled water production	19 000	2043	500			
<i>Total sector 1</i>	217 000	13 360	1300			
Main Beam injector – surface	16 000	690	300	20	5	15×10
Main Beam injector – tunnel	1700	70	150			
Damping rings – surface	24 000	1030	350			
Damping rings – tunnel	19 000	820	350			
Booster LINAC – tunnel	1180	50	100			
Booster LINAC – surface	5900	250	200			
Chilled water production	3000	325	250			
<i>Total sector 2</i>	70 780	3235	650			
Main tunnel e ⁻ - circuit A	69 000	3000	600	20	14	15×10
Main tunnel e ⁺ - circuit A	69 000	3000	600			
<i>Total sector 3</i>	138 000	6000	900			
Main tunnel e ⁻ - circuit B	56 500	2450	500	20	14	15×10
Main tunnel e ⁺ - circuit B	56 500	2450	500			
<i>Total sector 4</i>	113 000	4900	800			
Detector areas	18 700	800	350	10	9	10×10
BDS	46 000	1980	500			
Chilled water production	7500	800	350			
<i>Total sector 5</i>	72 200	3580	700			

In the central area, chilled water is produced by chiller units whose compressor is cooled by raw industrial water coming from the cooling towers. In the surface points, chillers are cooled by air in order to reduce the visual impact on the environment and adapting at the same time proper sound attenuation devices. For all the chillers cooled by water the chilled-water production plants will be located in buildings close to the cooling towers and raw water-cooling stations.

The cooling power needed and main characteristics of the chilled-water circuits are listed in Table 6.11.

For the cooling circuit the redundancy level is defined to ensure continuous operation in case of breakdown of one single element (chiller or distribution pump); in case of a general power failure, a buffer tank in each production circuit will ensure sufficient autonomy of part of the plant but the distribution pumps must be connected to the secure electrical network. If some equipment requires a continuous cooling, dedicated UPSs will have to be foreseen and the chillers connected to the secure network.

Table 6.10: Characteristics of main equipment per circuit.

Circuit	Pumps primary circuit			Plate heat exchangers		Pumps secondary circuit		
	Number	Flow rate [m ³ /h]	H [bar]	Number	Power per unit [MW]	Number	Flow rate [m ³ /h]	H [bar]
Drive beam injector – surface	8	1000	5	15	10	8	1000	10
Drive beam injector – tunnel	3	400		3	6	3	400	
Frequency multiplication	3	400	5	3	6	3	400	10
Transfer lines	3	200	5	3	3	3	200	10
Chilled water production	3	1000	5	See Table 6.11				
Main beam injector – surface	3	350	5	3	5.5	3	350	10
Main beam injector – tunnel	2	70	5	2	8.5	2	70	10
Damping rings – surface	3	500	5	4	6	3	500	10
Damping rings – tunnel	3	400	5	4	5	3	400	10
Booster Linac – tunnel	2	50	5	2	0.6	2	50	10
Booster Linac – surface	3	120	5	3	2	3	120	10
Chilled water production	3	160	5	See Table 6.11				
Main tunnel e ⁺ – circuit A	4	1000	5	6	10	4	1000	10
Main tunnel e [−] – circuit B	4	800	5	6	10	4	800	10
Main tunnel e ⁺ – circuit B	4	800	5	6	10	4	800	10
Detector areas	3	400	5	3	6,5	3	400	10
BDS	3	900	5	4	11	3	900	10
Chilled water production	3	450	5	See Table 6.11				

Table 6.11: Main characteristics of chilled water circuits

Location	Cooling power [kW]	Flow rate [m ³ /h]	Number of chillers	Cooling power/chiller [kW]	Chiller type
Drive Beam complex	19 000	2043	11	2000	Water-cooled
Main Beam complex	3000	323	3	1500	Water-cooled
Surface points	2900	315	4	1000	Air-cooled
Detector and BDS complex	7500	800	5	2000	Water-cooled

6.4.5 Other systems

6.4.5.1 Fire-fighting equipment

Fire-extinction means are planned on the surface and in underground sites; at present, it is foreseen to use only water for extinguishing fires. Since the central area is located on the Prévessin site, the water network for fire-extinction will be an extension of the existing one; the fire-fighting equipment in the tunnel must be supplied by dedicated stations at each surface point. Pumps connected to the fire-fighting network must be powered via the secure electrical supply.

6.4.5.2 Compressed air

A compressed-air distribution network is foreseen in the accelerator areas and in the workshops for all relevant equipment including the actuators for the control systems. Currently it looks preferable to plan

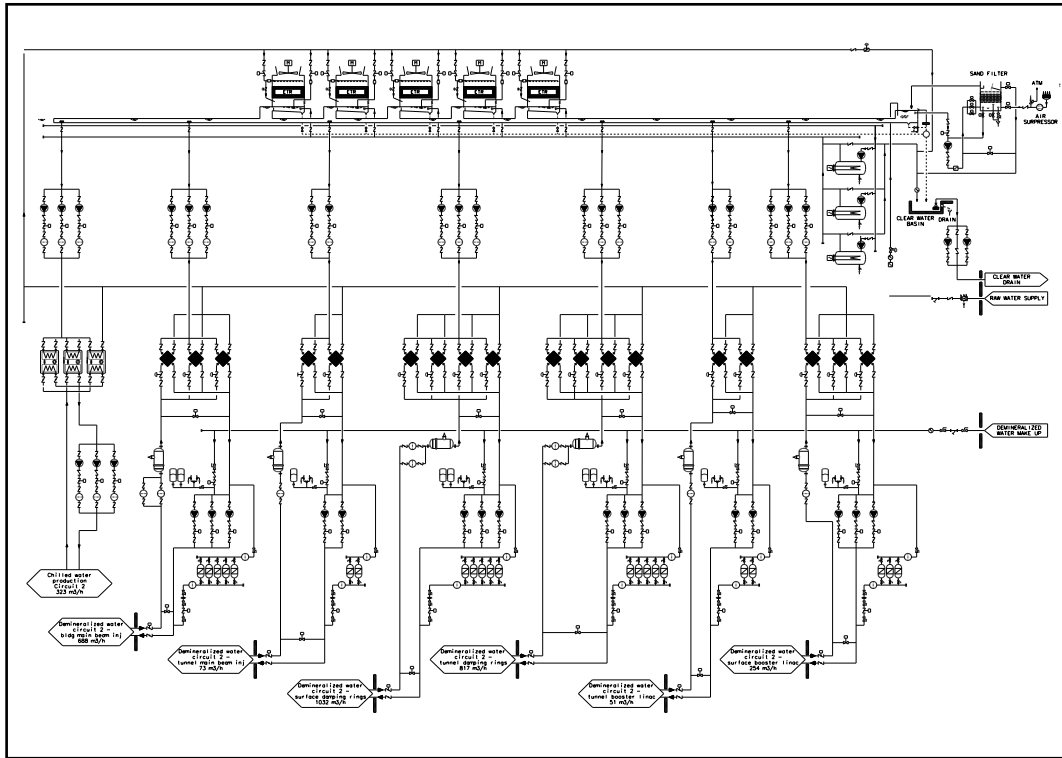


Fig. 6.24: Cooling scheme for sector 2.

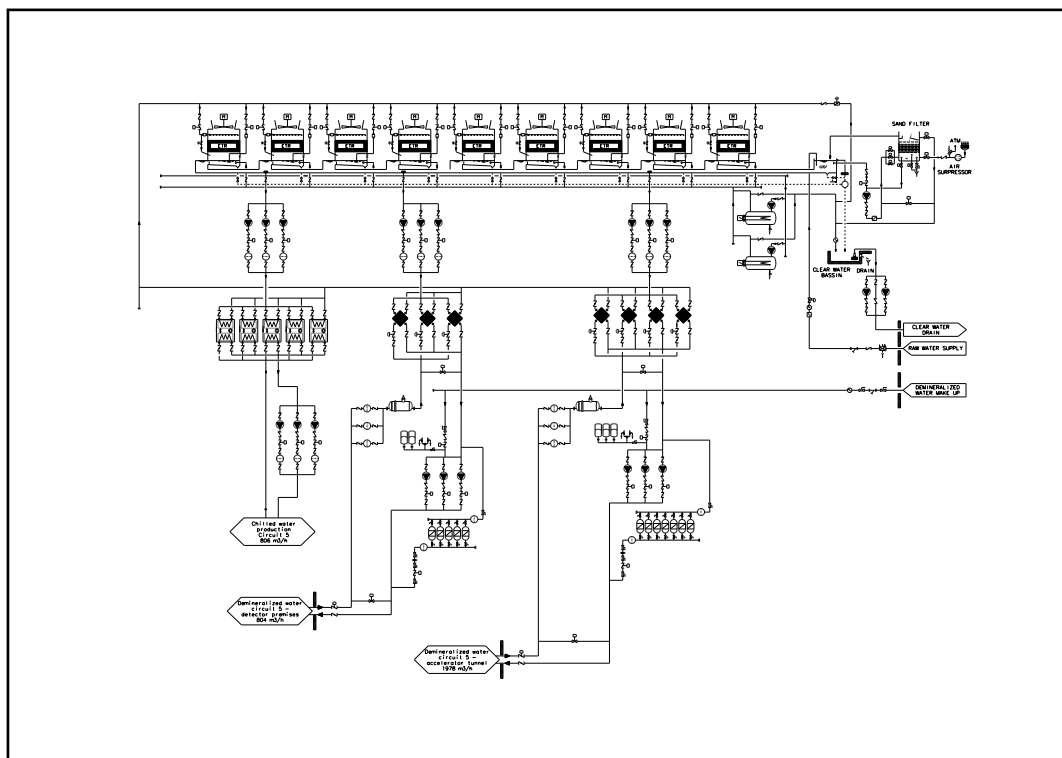


Fig. 6.25: Cooling scheme for sector 5

compressors at each Surface Point rather than in a centralized plant to cover the whole complex.

6.4.5.3 *Reject water*

Two systems of raising pumps for clear water and for sewage will be installed at each point and connected to the local drainage network; any equipment located underground (tunnel or caverns) must be redundant in order to avoid affecting operation in case of breakdown. The main parameters (temperature, pH) of the rejected water will be monitored. Proper alarms for high level and too high level will be implemented in all basins. Retention basins will be planned if reject water does not comply with legislation, presents a risk for pollution of the environment, or are required by flow rates.

6.4.6 **Cost considerations**

The present design of hydraulic and ventilation plants is aimed at minimizing their cost by using, as far as possible, existing industrial equipment and avoiding manufacture of special components; this includes the dimensions of units and pipes as well as the operation conditions of pumps, chillers, cooling towers, air handling units etc. However, it should be noted that some of this equipment is at the limit of standard industrial production and therefore the possibility of finding it on the market is limited to a few manufacturers.

Another factor that will have a major impact on the final cost of the works is the geographical location of the cooling and ventilation plants and their distance to the equipment and installations to be cooled; in addition, costs will depend strongly on which shafts will be used for routing the services in the underground premises.

6.5 **Transport and installation**

6.5.1 **Overview**

The transport and installation activities for the construction of the CLIC accelerator start from the unloading of components when they arrive at the CERN site. Transport and installation information for the experimental area, including overhead travelling cranes and lifts, is not covered here, but in §6.5.4.

The underground transport and installation of modules has been identified as the main transport and handling issue to be addressed at an early stage because of its influence on the 3D tunnel integration studies and also because of the large number of modules (more than 20 000) to be installed over the length of the machine. In order to keep the tunnel cross-section as small as possible, and also to be able to install modules rapidly, it is apparent that special equipment will be needed for their installation. Although the modules can be considered the most demanding items from an installation point of view, it is necessary to consider all the items to be transported.

6.5.2 **Items to be transported**

The quantity and variety of equipment to be installed for CLIC is huge. For the underground areas it includes:

- modules and their supports,
- magnets,
- vacuum pipes,
- beam dumps,
- cooling and ventilation equipment,
- electrical cables and cable trays,
- racks.

Transport and handling solutions will need to be defined in detail for all of the above types of equipment. For racks, cooling and ventilation equipment, electrical cables, and cable trays it is foreseen

to use industrial standard handling equipment. For modules and their supports, magnets, beam dumps and vacuum pipes it will be necessary develop special handling equipment.

The transport and installation operations include

- unloading, transfer within and between buildings on the surface for the purposes of assembly, test and storage;
- transport to the access sites along the length of the accelerator where items will either be installed in surface buildings or lowered to the underground areas;
- transport along the tunnel(s) and final installation.

6.5.3 Surface and shafts

6.5.3.1 Transport to the CERN site

Transport to the CERN site will be covered by the supply contracts of each item of equipment. This will include transport to assembly halls, storage areas, or tunnel access points as appropriate.

6.5.3.2 Surface transport and handling at CERN

Surface transport operations will include transfers inside and between buildings on the main laboratory site as well as transfers between the main laboratory site and the tunnel access points. This will be carried out using a fleet of road transport vehicles. Any specific requirements for these vehicles will be determined during the component design and development phases. Vehicle unloading and handling within buildings will be carried out as appropriate by mobile cranes, industrial lift trucks or overhead travelling cranes installed in surface buildings. The capacities of overhead travelling cranes are listed in Table 6.12 below.

Table 6.12: Overhead travelling cranes in CLIC surface buildings

Building Type	Crane load capacity (tonnes)	Comments
Detector assembly	80	Also permits lowering to underground area via shafts
Cooling tower and pump station	3.2	
Cooling and ventilation	20	For lowering to underground area via shafts
Cryogenic warm compressor	20	
Cryogenic surface cold box	20	
Workshop	10	
Central area machine cooling towers	5	
Shaft access	20	

Remote handling techniques will need to be incorporated into the positron target facility design to allow maintenance once the machine is operational.

6.5.3.3 Transfer between surface and underground

Access for equipment to be lowered to the tunnel is via 10 shafts and two inclined tunnels; inclined tunnels are used only when shafts are not feasible for geographical or environmental reasons.

The surface buildings above these access shafts are equipped with overhead travelling cranes with sufficient lift heights to lower equipment to the caverns at the base of the shafts via handling openings

6.5 TRANSPORT AND INSTALLATION

reserved in the shaft cross-section. In addition 3-tonne capacity goods/personnel lifts allow personnel access and will also be used to lower equipment. Emergency access stairwells will be installed next to the lifts. The cross-section of a machine access shaft with crane handling opening and lift shaft is shown in Fig. 6.26.

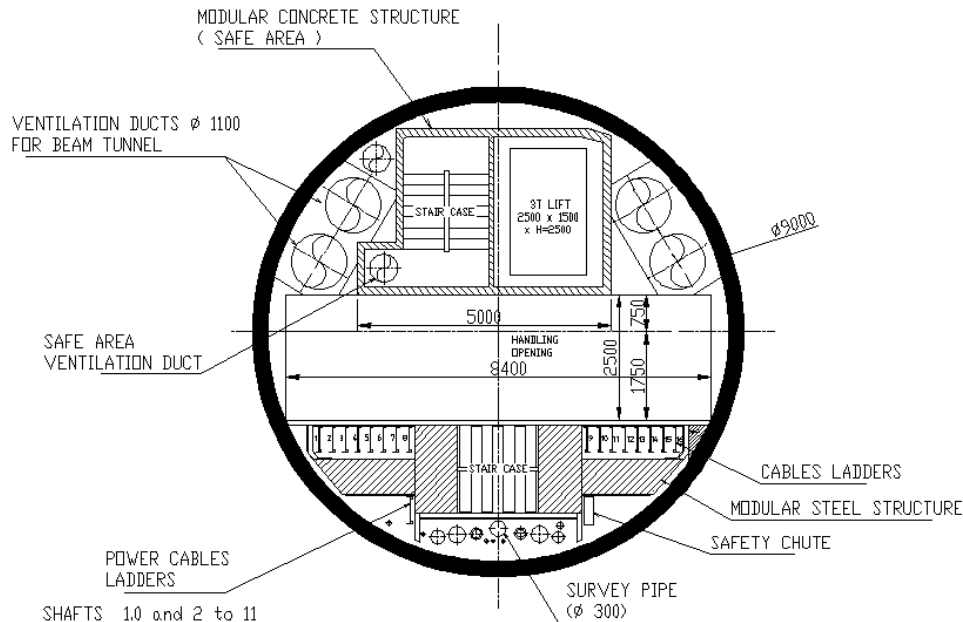


Fig. 6.26: Cross-section of access shaft

For the sloping access tunnels, a vehicle-based system will be developed for personnel and goods transit between the surface and underground areas. The system will be designed to ensure adequate throughput as required by the installation schedule and also to ensure safe exit for personnel working underground in the event of fire or accident.

6.5.4 Underground

Initially the full width of the tunnel will be available for installation of services, allowing the use of standard industrial tractors and trailers. The available space for transport will narrow once the modules and their supports start to be installed. For cost reasons the transport passage will be kept to a minimum. This means that module transport vehicles will not be able to pass each other in the tunnel.

Special equipment will be developed for the transport and installation of modules and magnets in order to achieve the highest rates of installation compatible with the space, precision, interconnection, and fragility constraints. Personnel transport in the tunnel will be mainly by means of small electrical tractors or bicycles.

6.5.4.1 Module transport and installation

The space required for module transport and installation has a major influence on the tunnel cross-section. Studies were therefore carried out to identify how the modules could be transported and installed in the tunnel. These studies had a secondary goal of feeding some design requirements related to transport and installation into the module design.

The large number of modules means that it is important to optimize the whole sequence to allow rapid transport and installation. Table 6.13 shows the number of modules.

Table 6.13: Module and supports – transport study input data

Item	Quantity (3 TeV)		Quantity (500 GeV)		Dimensions [mm]	Mass [kg]
	Per sector	Total	Per sector	Total		
Module	436	20 922	436	4248	2010×1550×1200	~1500
Module support	436	20 922	436	4248		

Before a module arrives at its installation point its supports will be installed and aligned using geodesic survey equipment. This order of installation means that the module has to be transferred laterally over the survey stretched wire equipment before being lowered into place on its supports. This means that the module will have to be supported from above during the transfer from the tunnel transport vehicle onto its supports. A conceptual design (Fig. 6.27) of the vehicle with its own on-board lifting equipment was produced in order to reserve the necessary space in the tunnel design. By using lifting devices installed on the vehicles, the unloading and installation operation time can be minimized.

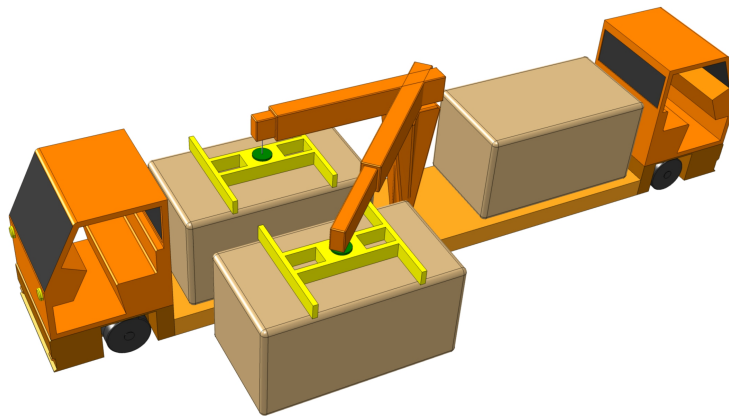


Fig. 6.27: Conceptual design of module transport vehicle. The module is shown as a rectangular block in transport and unloading positions

Figure 6.28 shows the module transport vehicle unloading a module onto its supports in the tunnel. Note the I section monorail above the vehicle to be used for electrical power supply to the vehicles and also the safety barriers at the module side of the transport passage.

In view of the narrow transport passage and the distances to travel, the module transport vehicles will be equipped with an automated guidance system. The operator of the vehicle will be required to ensure that the floor is clear of personnel and equipment.

Although module installation logistics should aim for sequential installation, the installation process must allow for installation of modules between two previously installed modules in the event of supply delays. In addition, the system must allow for the removal of previously installed modules if major repairs are needed.

A key requirement for module design is the need for a clear interconnection plane between them so that they can be lowered into their final position without interference with the adjacent module(s). As the clearance between adjacent modules will be minimized (10 mm or less), they will need to be carefully guided during the installation process.

In addition to the clear interconnection plane, adapting the module design for transport requires

6.5 TRANSPORT AND INSTALLATION

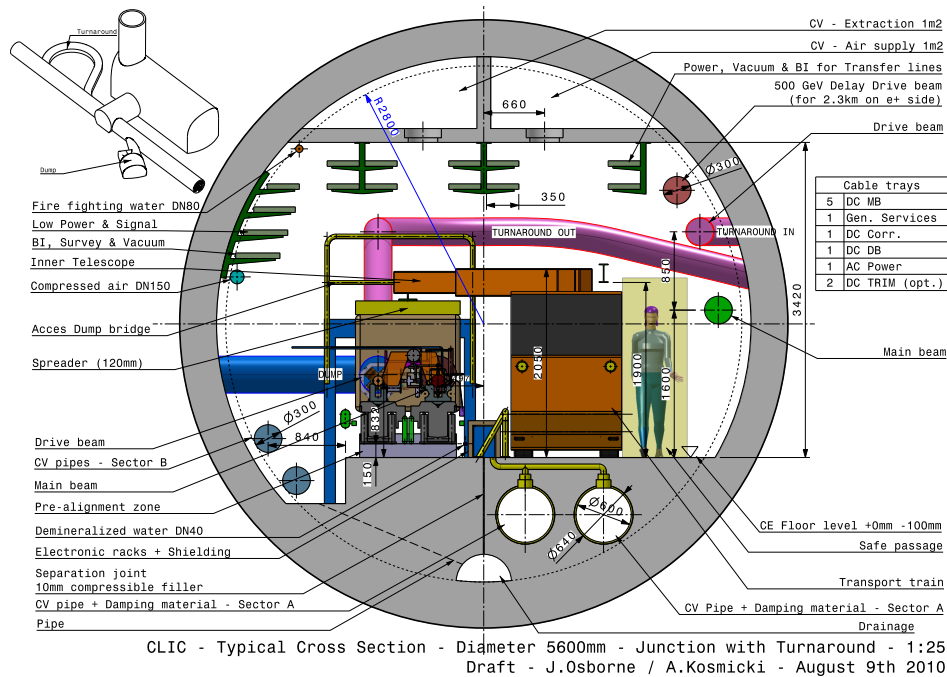


Fig. 6.28: Cross-section of CLIC tunnel showing vehicle installing a module.

the inclusion of lifting points and support points to allow the whole sequence of transport and handling operations. The module design effort includes transport restraints and special lifting beams to be used when handling fully assembled modules during the installation process.

6.5.4.2 *Underground transport infrastructure design*

In addition to the transport along the tunnel it is also necessary to design the infrastructure for the transfer from the surface, taking into account the need to minimize the time taken because of the large number of items to be installed. Lowering of modules from the surface will be carried out using the personnel/goods lifts as this is faster and requires less operator skill and vigilance than using overhead travelling cranes. The modules will be fitted to custom-made pallets in order to allow handling by powered pallet trucks.

At the tunnel level the UTRC caverns (Fig. 6.29) are designed so that the modules and other equipment can be taken from the lift and moved to a position close to the waiting transport and installation vehicles. They are then loaded onto the vehicle. It is planned that each vehicle will be able to simultaneously transport two modules for logistics reasons. Loading of modules onto the vehicle can be carried out by the vehicle's own lifting equipment or by the travelling crane installed in the UTRC service cavern.

Items outside the capacity of the lift will be lowered down the handling opening in the shaft and transferred to vehicles waiting in the UTRC cavern.

Once the vehicles are loaded they will be driven into the tunnel. If necessary, owing to co-activity constraints (for example interconnection shifts alternating with transport shifts), several vehicles can be parked along the tunnel in the area between the two junction galleries where the liaison galleries from the service cavern join the main tunnel.

During the module installation phase it is planned to use the whole UTRC gallery floor for transport activities such as a buffer parking space for loaded vehicles and for vehicle maintenance. The UTRC caverns will be equipped with 10 tonne travelling cranes to transfer equipment onto vehicles after lowering it down the shaft. These cranes will also be used for transporting maintenance equipment. Additional cranes may be required for beam dump handling for example.

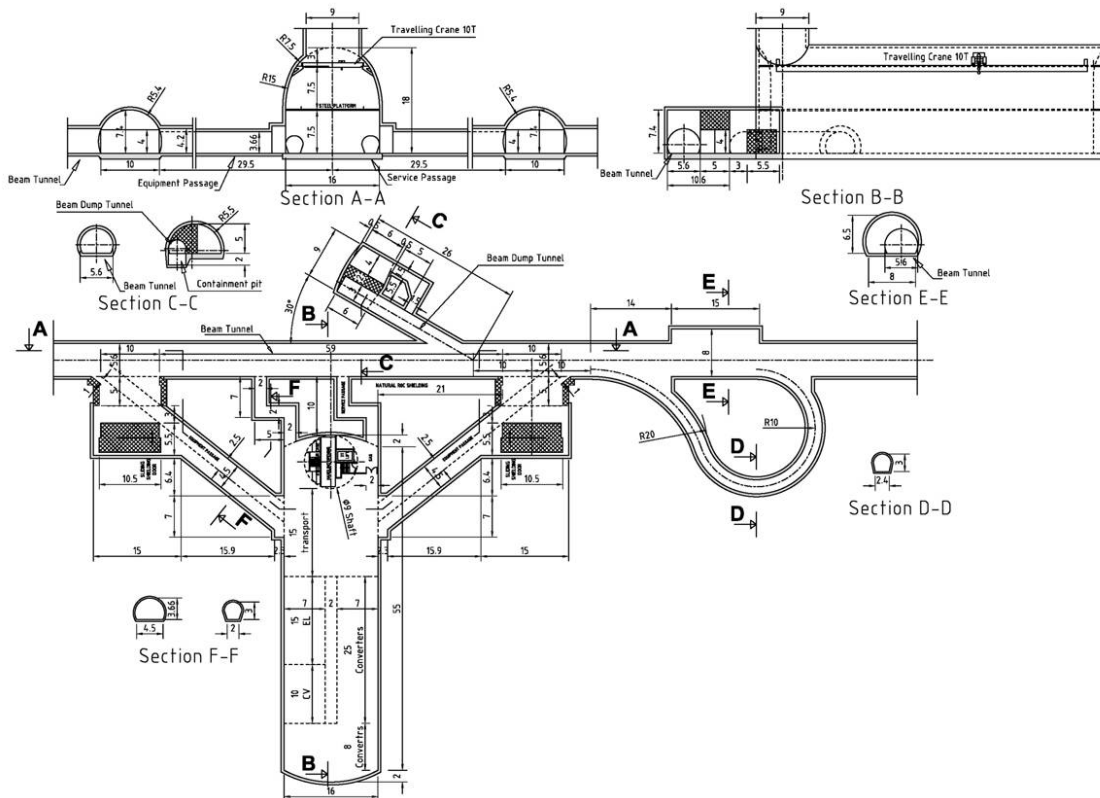


Fig. 6.29: UTRC cavern

6.5.4.3 Magnet transport and installation

The tunnel integration design includes beam lines attached to the tunnel vault, including in positions above the modules. Specially designed vehicles with integrated lift and transfer devices will be developed to allow safe and rapid installation of the magnets for these beam lines. The magnets to be installed are listed in Table 6.14.

The number of types of magnet transport vehicles for tunnel transport and installation will depend on the dimension and weight of the magnets as well as their final installation positions in the tunnel.

6.5.4.4 Transport and installation of other accelerator equipment

Further studies covering the transport, handling, and installation of other accelerator equipment will be carried out as more detailed information is generated by the machine design process.

6.5.4.5 Cost considerations

To keep handling equipment procurement costs down, standard transport and handling equipment will be used where possible. For items where space constraints mean that specialized handling equipment is needed, all requirements will be coordinated at an early stage so that the amount of equipment and procedures to be developed is minimized.

Experience from the LHC installation indicates that manpower costs will be of the same order as equipment costs; to reduce manpower costs during installation, logistics will need to be considered at the start of the design phase. Accelerator equipment and infrastructure integration will be optimized where possible for handling and transport.

Transport issues and requirements have been included in the inputs to the test module design

Table 6.14: Transport data – magnets

Item	Quantity (3 TeV)		Quantity (500 GeV)		Mass [kg]	Notes
	Per sector	Total	Per sector	Total		
Main Beam transfer line						
Magnet	4	200	4	42		
Main Beam Turnaround						
Magnet		1640		1640		
Drive Beam transfer line						
Quadrupole	16	768	16	160	320	Estimated length 1–2 m. Outer diameter ~200 mm 10 m long elements
Beampipe	88	4224	88	880		
Drive Beam turnaround loop						
Quadrupole	39	1872	39	390	500	
Dipole	24	1152	24	240	500	
Dipole CO	39	1872	39	390	300	
Sextupole	24	1152	24	240	300	
Drive Beam dump						
Quadrupoles, dipoles	20	960	20	200	5000	Rough estimate

process in order to allow installation issues to be considered and trials to be carried out when the test modules are installed on their supports in the test facility.

Early use of a short section of a full-scale tunnel mock-up to test installation equipment and procedures will allow problems to be ironed out and thus save time and money during tunnel installation.

6.6 Safety systems

6.6.1 Access control and personnel safety system

The access control and personnel safety system is used to protect people against exposure to various hazards related to the operation of the equipment in the accelerator complex, with and without beam.

6.6.1.1 Beam zones

To manage the access control and personnel safety in the underground accelerator structures, the CLIC accelerator complex is subdivided into 10 distinct beam zones. Each beam zone has its own independent access conditions and its own token system (access keys) for personnel access. The absence of beam in each zone is guaranteed by three or more beam-safety elements, with at least one passive element (e.g., a movable stopper) and one active element (e.g., magnet power converter interlock). These safety measures are activated and interlocked by the safety system if the access status makes a zone unsafe for operation with beam. Machine access cannot be given if the status of a safety element is unsafe.

The list of independent beam zones is given in Table 6.15. A further subdivision of some beam zones could be envisaged to ease commissioning. However, a too detailed subdivision is not favoured on account of cost (beam safety elements, access control systems) and operational considerations (inter zone

movement restriction of personnel). Moreover, partial beam commissioning may be further restricted by the available beam disposal systems.

Table 6.15: CLIC Beam zones

Beam zone	Designation
1	Drive Beam linac
2	Combiner complex
3	Main Beam source and linac
4	Damping ring complex e^+
5	Damping ring complex e^-
6	Booster Linac
7	Surface to main tunnel transfer
8	Two-beam accelerator e^+
9	Two-beam accelerator e^-
10	Experimental region

6.6.1.2 Access to beam zones

Dedicated access points provide the main personnel access to the underground structures. Each access point is equipped with one or more personnel access doors (a SAS with biometric control and dosimeter reader) and a personnel access token distribution system. An access point can further be equipped with a passage for small material and special doors for bulk material.

The passage of very large or heavy material will be possible through the pit heads of the material shafts and, around the interaction region, through movable shielding walls. The access control equipment will monitor the status of these passage ways.

6.6.1.3 Patrol sectors

The beam zones themselves are further subdivided into patrol sectors to simplify a search patrol after an intrusion event. An intrusion event occurs whenever the possibility exists that a person could have entered any of the beam areas in an unsupervised way. In this case the patrol-valid status for the corresponding sector is dropped. An intrusion event occurs when an access door is forced between a zone that has a patrol-valid status and a zone that does not, i.e., either a door of the external envelope of the machine or a door adjacent to a zone where the patrol-valid status is already dropped.

It should be noted that interbeam zone doors, separating different beam zones (i.e., zones with their own independent access control) are considered as doors to the external envelope. Forcing such a door will cause the search-valid status to be dropped on both sides. Hence, movement of people between different beam zones is restricted and sector doors between two different beam zones are to be used for emergencies only. The placement of the sector doors should be such that each sector can be scrutinized by a single person in linear progression. For practical purposes, the sectors in busy (complex) areas are also delimited to a reasonable length (500 m) and in a way that exposure to radiation hazard is limited. Where applicable, the sector doors will be combined with the fire containment doors.

To enforce a valid patrol, each sector will be equipped with patrol boxes (at least one box at the extremities of a sector) that have to be rearmed by the search patrol using a special search key. Figure 6.30 shows the defined sectors at the end of the Main Linac.

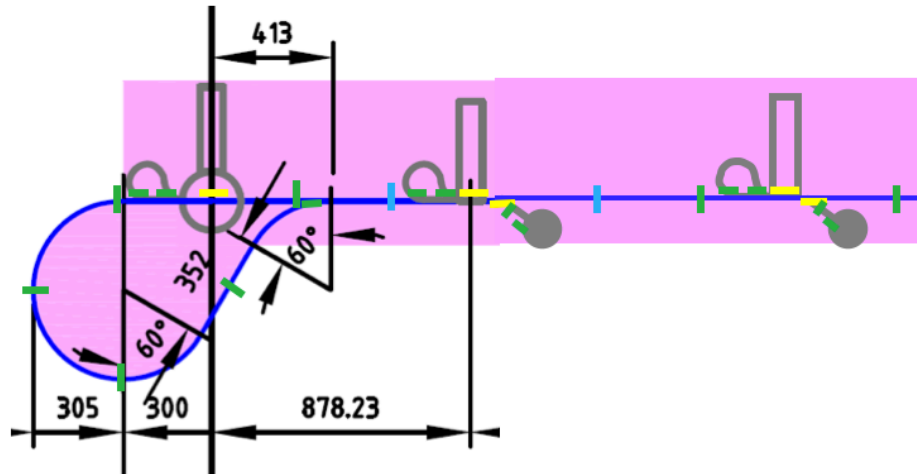


Fig. 6.30: Defined sectors at the extreme end of the two-beam tunnel and Main Beam turnaround.

6.6.2 Personnel safety systems

The access control system works in tight conjunction with the personnel safety system. The key elements of the personnel safety system are the beam and equipment interlocks. Access to the machine will only be allowed when the conditions are safe. When access is granted, the personnel safety system will interlock a number of safety elements for the duration of the access period. In case of an intrusion event while the machine is in an unsafe state, the personnel protection system will activate the interlocks.

The personnel safety system is further complemented with a public address system, a 'beam imminent' warning system, and an oxygen deficiency detection system.

6.6.3 Cost considerations

Table 6.16 summarizes the number of access control elements for the various beam zones. This data was gathered for the cost study of the access control and personnel safety systems and is based on present day technology and the requirements that were used in a 2010 tender for an LHC and PS access control system upgrade. In terms of the number of components, the system for the CLIC 3 TeV machine is of the same order of magnitude as the full access control and personnel safety system of the current CERN accelerator complex. With the advent of future new technologies and higher integration in controls and communication for safety systems, further cost optimization may be possible.

6.6.4 Radiation safety and radiation protection

6.6.4.1 Beam loss

The intensity of ionizing radiation in an accelerator and thus the magnitude of the observed effects are proportional to the rate of beam loss. Conservative estimates of beam loss in CLIC are derived from considerations of beam dynamics. In the Drive Beam decelerator (approximately 875 m in length), a loss of more than a fraction of 10^{-3} of the injected beam current would modify the parameters of the beam in such a way that the Drive Beam energy can no longer be efficiently absorbed in the PET structures. In the Main Beam, a fractional beam intensity loss of 10^{-3} over the whole of one Main Beam (20 km length) would lead to significant changes in luminosity and would be unacceptable from the viewpoint of a physics detector. These two observations define a conservative upper limit of fractional beam loss. Table 6.17 shows the planned beam intensity in CLIC and the resulting rate of beam loss per metre in the Drive and Main Beams.

The CLIC beam parameters and estimated maximum beam loss rate are based on a fractional

Table 6.16: Summary of access control elements.

Total	Access element count											Comments	
	Site Access	Surface building access	Access points	Personnel access door with biometry control	Material doors	Sector doors	Restricted sector doors	End zone doors	Inter zone doors	patrol boxes	Ventilation and technical gallery		Movable shielding or pit head covers
Beam zone 1		23	6	6	6	23	1	7		37	24	3	2600 m cut & cover, 700 m average distance
Beam zone 2		5	6	6	6	25		1	1	32		3	2060 m cut & cover, 500 m typical distance
Beam zone 3		12	4	4	4	13	1	3		21	8	2	880 m cut & cover, 400 m typical distance
Beam zone 4		4	4	4	4	16	1	1	2	24		2	1750 m cut & cover, 500 m typical distance
Beam zone 5		4	4	4	4	18	1	2		28		2	1420 m cut & cover, 800 m typical distance
Beam zone 6		8	2	2	2	7		3	2	12	6	2	500 m cut & cover, 400 m typical distance
Beam zone 7		5	2	2	2	29		4	2	56		2	5200 m mixed, 1500 m average distance
Beam zone 8 (0.5 TeV)	3	5	4	4	2	56	12			97		2	8500 m mixed, 4300 m average distance
Beam zone 8 (3.0 TeV)	11	17	8	8	6	193	52			333		6	28 000 m mixed, 15 000 m average distance
Beam zone 9 (0.5 TeV)	3	5	4	4	2	51	12			91		2	8500 m mixed, 4300 m average distance
Beam zone 9 (3.0 TeV)	11	17	8	8	6	188	52			327		6	28 000 m mixed, 15 000 m average distance
Beam zone 10		4	2	10	2				4		4	4	Experimental hall, 300 m typical distance
Total 0.5 TeV	6	75	38	46	34	238	28	21	11	398	42	24	32 000 m
Total 3.0 TeV	22	99	46	54	42	512	108	21	11	870	42	32	70 000 m

loss of 10^{-3} over the length of the beam (Main Beam) or one Drive Beam station (Drive Beam). All estimations of radiation effects were performed at the maximal and minimal energies of the respective beam and with the fractional beam loss rate indicated in the last column of Table 6.17.

Table 6.17: CLIC beam parameters and estimated maximum beam loss rate.

Location	Max. energy [GeV]	Min. energy [GeV]	Particles per bunch train	Repetition rate [Hz]	Beam loss [m ⁻¹]
Main Beam	1500	9	1.16×10^{12}	50	5×10^{-8}
Drive beam	2.4	0.24	1.5×10^{14}	50	6.7×10^{-6}

6.6.4.2 Modelling the accelerator

Simulations of electron beam losses have been limited to the lowest and highest energies, i.e., 0.24 GeV and 2.4 GeV for the Drive Beam and 9 GeV and 1500 GeV for the Main Beam. Simulations were performed using version 2008.3.5 of the FLUKA code [3], [4]. For each of the four loss energies, the build-up and decay of radiation over an 11.5 year period, with cycles of 180 days continuous running followed by 185 days shutdown, was simulated. The residual ambient dose equivalent rates at various waiting times within the shutdown periods were calculated. In addition, quantities related to the potential damage to electronic devices, i.e., the prompt absorbed dose, the 1 MeV neutron equivalent fluence on silicon, and the fluence of hadrons with energies higher than 20 MeV were calculated.

The FLUKA geometry includes an air-filled concrete tunnel 5.7 m in diameter, tunnel floor, silicon carbide girders and beam line components. The FLUKA representation of the beam line components including quadrupole magnets, PETs, acceleration structures, and beam position monitors (BPMs) is shown in Fig. 6.31. The quadrupoles consist of iron poles and yokes with copper blocks surrounding the poles. The type and sequence of the modules used in Main Beam simulations were consistent with design specifications [5]. In the model used for 1500 GeV, the Main Beam quadrupoles are 193.5 cm in length and in the model for 9 GeV, they are 42 cm in length. The Drive Beam quadrupoles are 27 cm in length. The span of the Main Beam quadrupole is 25 cm and the Drive Beam quadrupoles 31 cm. The PETs are modelled as hollow copper cylinders, of outer radii 6.5 cm with a vacuum chamber of radius 1.15 cm running through the centre. The accelerating structures are modelled as hollow copper cylinders with outer radii 4 cm with a vacuum chamber of radius 0.5 cm running through the centre. The accelerating structures are modelled with a central ‘cross’ of reduced density (4.5 g cm^{-3}) to represent void regions along the accelerating structure. The Drive Beam BPMs are modeled as cylinders 1.2 cm in diameter and 6.5 cm in length of a half-iron and half-copper mix with reduced density (4.0 g cm^{-3}) to represent void regions. All concrete shielding components have a density of 2.3 g cm^{-3} with the following chemical composition: oxygen (52.9%), silicon (33.7%), calcium (4.4%), aluminium (3.4%), iron (1.4%), hydrogen (1.0%), carbon (0.1%), magnesium (0.2%), sodium (1.6%) and potassium (1.3%).

Figure 6.31 shows a view of the simplified geometry of the accelerators implemented within FLUKA. Two CLIC modules are shown each of which has two Drive Beam quadrupoles. For the Main Beam one is equipped with eight accelerating sections (left) and one with a four-unit long quadrupole. This configuration is found in the high-energy part ($E > 750 \text{ GeV}$) of CLIC. Figure 6.32 shows cuts in a plane orthogonal to the beam.

6.6.4.3 Radiation damage

The generic term ‘radiation damage’ incorporates material damage, as well as total dose displacement damage in semiconductors, based on neutron (or more precisely, non-ionizing particle) fluence, and an unacceptably high rate of single-event effects (SEE), based on the high-energy hadron fluence. At very high neutron fluence (as in a nuclear reactor), displacement damage would also induce material damage (brittleness), but neutron fluences in CLIC are not high enough for this to occur.

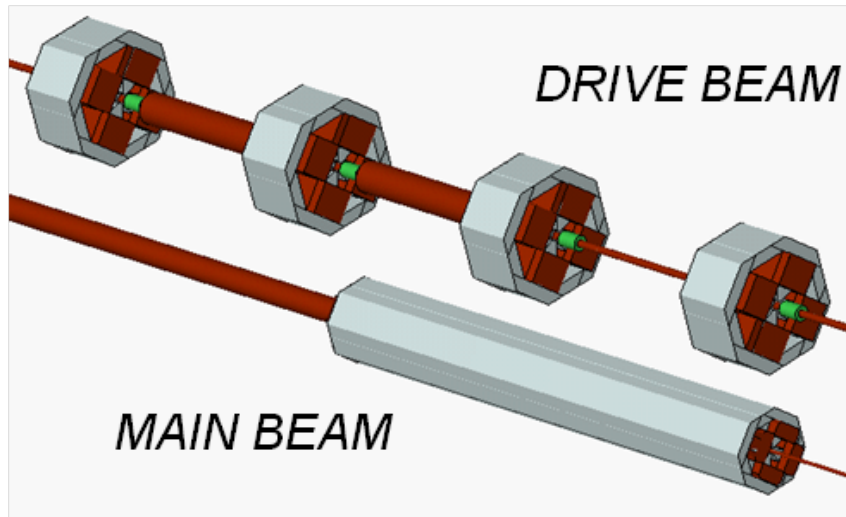


Fig. 6.31: View of the simplified accelerator geometry implemented in FLUKA.

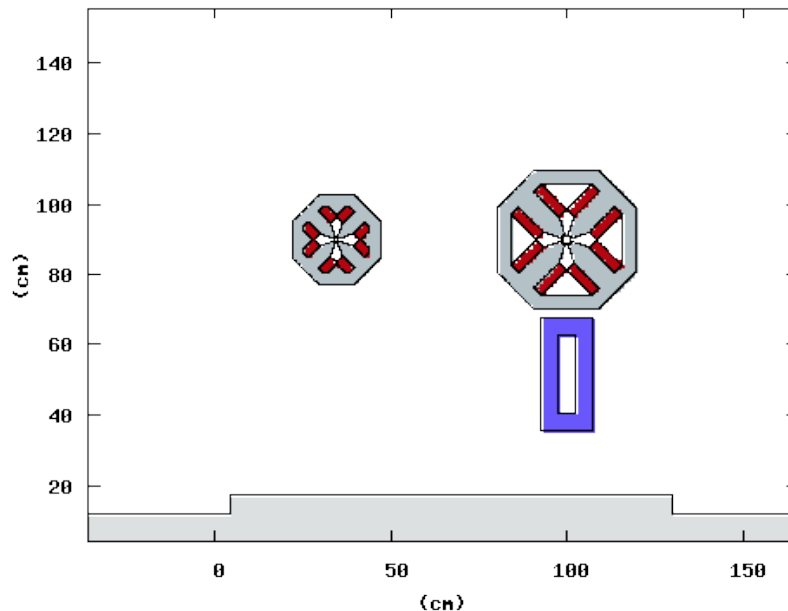


Fig. 6.32: Cuts in a plane orthogonal to the beam through the simulation models of the Main Beam quadrupole (left) and the Drive Beam quadrupole (right). Red: copper coils, grey: iron yokes, white: air or vacuum.

Table 6.18 lists acceptable radiation damage effects in an accelerator environment.

Based on the beam loss estimates given in the previous section, FLUKA 2008.3.5 [3], [4] was used to model the development of the secondary radiation cascade. The absorbed dose and fluence of neutrons or energetic hadrons provided by the code allow one to estimate the magnitude of the three types of radiation damage.

The absorbed dose has been estimated in the coils of the quadrupole magnets of the Drive Beam and the Main Beam accelerators. Table 6.19 lists the maximum permissible fractional beam loss in the low- and high-energy ends of each accelerator. At this loss rate, an absorbed dose of 1 MGy would be accumulated in one year, possibly inducing magnet failure after 10 years of operation. For the Drive Beam and the 9 GeV Main Beam, the loss required to reach $1 \text{ MGy} \cdot \text{y}^{-1}$ is greater than the assumed beam

Table 6.18: Radiation damage mechanisms and tolerable levels leading to negligible damage of accelerator components or electronics.

Damage Mechanism	Relevant estimator	Tolerable levels
Material damage	Total ionizing dose (absorbed dose)	<1 Gy/year (COTs) <1 MGy/year (epoxy resin, QP coils)
Lattice displacement	Non-ionizing energy loss scaled to '1 MeV neutron equivalent fluence' ^a	<1 × 10 ⁸ cm ⁻² /year (COTs)
SEEs	>20 MeV Hadron Fluence	<1 × 10 ⁷ cm ⁻² /year (COTs) ^b

^a Non-ionizing energy loss (NIEL) is usually scaled for convenience to the NIEL of 1 MeV neutrons where any particle fluence with a specific energy distribution is expressed in terms of the '1 MeV neutron-equivalent fluence' producing the same bulk damage in a specific semiconductor.

^b For SEEs only the probability of failures can be determined; at CNGS electronics started to fail due to SEE's at high-energy hadron fluences of 1 × 10⁷ cm⁻²

losses listed in §6.6.4.1, whereas for the 1500 GeV Main Beam, it is lower.

However, an estimate of the actual loss distribution along each beam is currently unknown. Therefore the losses were simulated immediately before, or close to, the quadrupole. It is possible this would lead to conservative results, particularly for the case of Main Beam at high energy, where the quadrupole spacing is approximately 18 m. The normalisation is per quadrupole or per metre, assuming two DB quadrupoles per CLIC module or one MB quadrupole per two modules at 9 GeV, and one MB quadrupole per nine modules at 1500 GeV.

Table 6.19: Estimated fractional beam loss required to accumulate an absorbed dose of 1 MGy in quadrupole magnet coils.

Loss Point		Fractional beam loss per QP for 1 MGy/yr in coils (m ⁻¹)	Fractional beam loss for 1 MGy/yr in coils (m ⁻¹)
DB – 240 MeV	End of PET (before QP)	2.1 × 10 ⁻⁶	2.1 × 10 ⁻⁶
DB - 2.4 GeV	End of PET (before QP)	2.0 × 10 ⁻⁵	2.0 × 10 ⁻⁵
MB – 9 GeV	End of AS (before QP)	4.8 × 10 ⁻⁵	1.2 × 10 ⁻⁵
MB – 1500 GeV	Continuous in AS (1 m before QP)	4.3 × 10 ⁻⁷	2.4 × 10 ⁻¹⁰

The 1 MeV neutron equivalent fluence and the fluence of hadrons with an energy above 20 MeV were scored in the whole tunnel volume for the four beam-loss conditions listed in Table 6.19. As an example, Fig. 6.33(a) shows the distribution of the energetic hadron fluence and Fig. 6.33(b) the 1 MeV neutron equivalent fluence in the tunnel cross-section for beam loss in the Main Beam at the maximal energy. In both cases one can see that the estimated fluences exceed the range of fluences leading to an acceptable lifetime of highly integrated semiconductor devices by several orders of magnitude.

Table 6.20 lists the annual 1 MeV neutron-equivalent fluence, and Table 6.21 the energetic-hadron fluence, for losses at maximal and minimal energy from the Drive and Main Beams. In each case, the

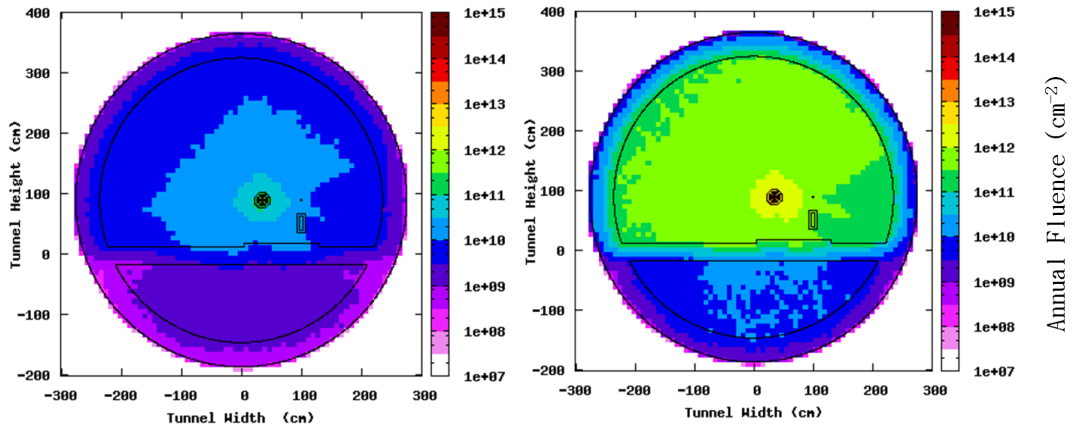


Fig. 6.33: Distribution of (a) the 1 MeV neutron-equivalent fluence and (b) the energetic hadron fluence in the tunnel cross-section for beam loss in the Main Beam at 1500 GeV.

fluence is estimated in volumes at two places within the tunnel: one near to the inside wall of the tunnel and one near the accelerator, as shown in Fig. 6.34. The volumes are cuboids of length 600 cm parallel to the beamline and of sides 24 cm in the plane orthogonal to the beamline.

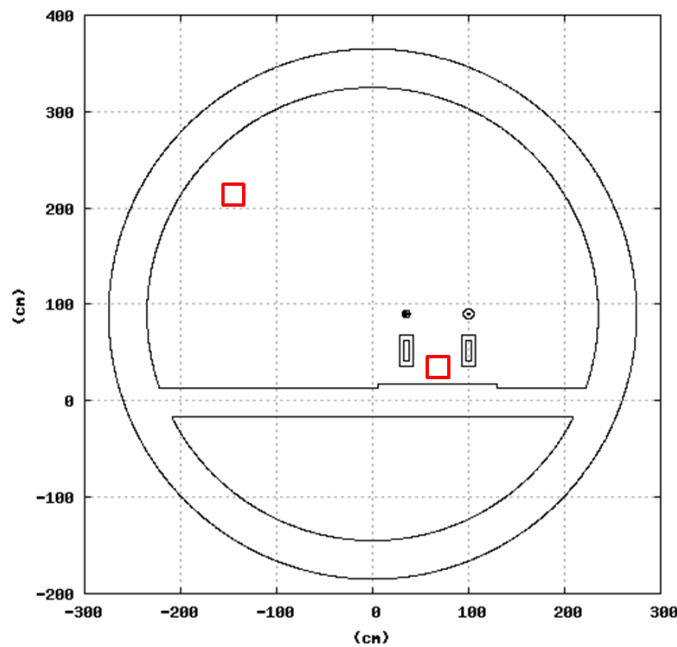


Fig. 6.34: Location of scoring volumes (in red) for the values estimated in Tables 6.20 and 6.21. Estimates of the 1 MeV neutron-equivalent fluence and high-energy hadron fluence were made near to the tunnel wall and near to the accelerator

Table 6.20: Estimated 1 MeV neutron-equivalent fluence in two tunnel locations for losses from the Drive Beam (DB) and Main Beam (MB)

	1 MeV neutron equiv. fluence close to accelerator [cm ⁻² year ⁻¹]	1 MeV neutron equiv. fluence close to tunnel wall [cm ⁻² year ⁻¹]
DB – 240 MeV	3.4×10^{11}	1.2×10^{11}
DB – 2.4 GeV	3.2×10^{12}	1.3×10^{12}
MB – 9 GeV	1.0×10^{10}	4.0×10^9
MB – 1500 GeV	8.5×10^{11}	3.1×10^{11}

Table 6.21: Estimated hadron fluence in two tunnel locations for losses from the Drive Beam (DB) and Main Beam (MB) assuming maximum losses permitted by beam dynamics considerations

	>20 MeV hadron fluence close to accelerator [cm ⁻² year ⁻¹]	>20 MeV hadron fluence close to tunnel wall [cm ⁻² year ⁻¹]
DB – 240 MeV	1.0×10^9	2.3×10^8
DB – 2.4 GeV	6.5×10^{10}	1.6×10^{10}
MB – 9 GeV	2.3×10^8	6.1×10^7
MB – 1500 GeV	2.4×10^{10}	7.01×10^9

6.6.4.4 Radiation protection

Radiation protection is concerned with the protection of workers and the public against the detrimental effects of ionizing radiation. For the conceptual study, the activation of accelerator materials and the subsequent irradiation of workers have been studied with the help of radiation transport and activation simulations. FLUKA 2008.3.5 has been used in these studies. It combines radiation transport algorithms with a nuclear interaction model. It is in principle able to predict the distribution of activation products in material irradiated with energetic particles. The follow-up of radioactive decay of the activation products then permits an estimation of the dose and dose equivalent after an arbitrary decay time.

These algorithms have been validated for short lived-products (up to $t_{1/2} = 3$ years) after proton irradiation [6]. A similar validation for primary electron beams is currently in process, [7], [8], [9].

In this study, the focus is on a scenario where all short-lived ($t_{1/2} < 1$ year) and some important other radionuclides (^{60}Co) are near their equilibrium concentration. Dose-equivalent rates are given for different waiting times in a shutdown after one year of CLIC operation with beam loss assumed to be equal to that in the previous section.

Figure 6.35 shows the two-dimensional distribution of ambient dose equivalent rate, $H^*(10)$ in the high-energy part of the CLIC tunnel after different delays (‘waiting time’) after turning off the accelerator running at nominal intensity and the associated rate of beam loss.

Table 6.22 gives the ambient dose equivalent rates at a location close to the accelerator for the delay times used in Fig. 6.35. For each beam, the dose rate is estimated in a volume near to the beamline, as shown in Fig. 6.36. The volumes are cuboids with a length 600 cm parallel to the beamline, and sides of 40 cm in the plane orthogonal to the beam.

In the optimization process required for interventions in radiation areas, one would have to combine the dose rates with time estimates for interventions. Without a more precise knowledge of these,

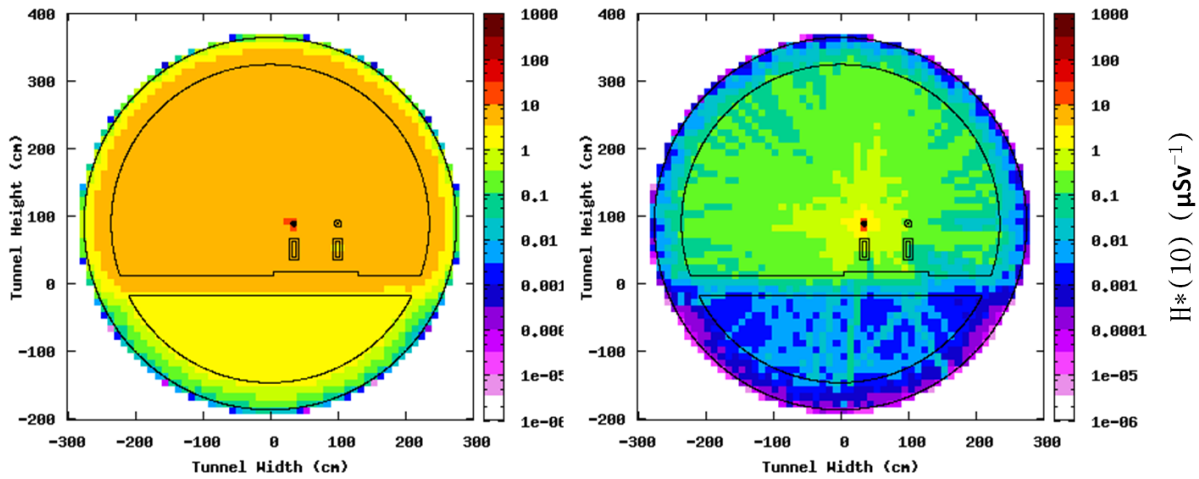


Fig. 6.35: Ambient dose rate map in a plane orthogonal to the beam at the high-energy end of CLIC ($E = 1.5$ TeV) after 1 year of operation at nominal beam intensity and an average beam loss of $5 \times 10^{-8} \text{ m}^{-1}$. Ambient dose rate is evaluated after turning off the accelerator for four hours (left) and one week (right)

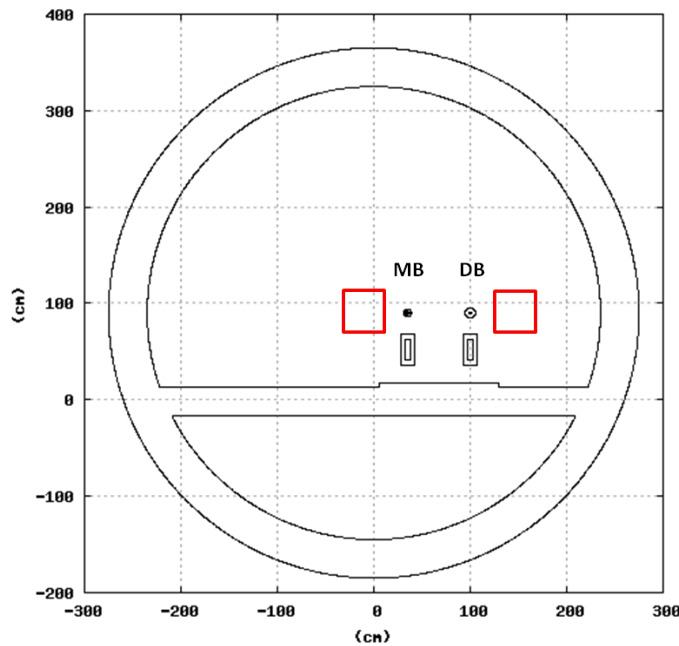


Fig. 6.36: Location of scoring volumes for the values estimated in Table 6.22. Estimates of the residual ambient dose equivalent rates were made in the left-hand red box for losses from the Main Beam and in the right-hand one for losses from the Drive Beam.

only general statements can be made. According to the presented estimations, justified urgent and non-recurrent interventions not taking longer than 1 hour would be possible after 4 hours of waiting time after turning off the accelerator. Personnel would receive a dose of up to 1 mSv during such an intervention. Work requiring longer access times can be undertaken after about one week delay time, at which point the ambient dose equivalent rate in the passageway is between 10 and 100 mSv h⁻¹. Dose rates close to the accelerators will be higher, but a discussion of the local distribution of activation and dose rate is beyond the scope of this study, which is based on a coarse approximation of beam loss.

Table 6.22: Estimated residual ambient dose equivalent rates for three different waiting times, assuming 180 days continuous running with maximum losses from the Drive Beam (DB) and Main Beam (MB).

	Ambient dose equivalent after 4 hours ($\mu\text{Sv h}^{-1}$)	Ambient dose equivalent after 1 week ($\mu\text{Sv h}^{-1}$)	Ambient dose equivalent after 4 months ($\mu\text{Sv h}^{-1}$)
DB – 240 MeV	2.5	0.11	0.03
DB – 2.4 GeV	40.0	1.5	0.3
MB – 9 GeV	0.09	0.007	0.001
MB – 1500 GeV	9.5	0.5	0.1

6.6.5 Fire safety

The goal of fire safety is to protect occupants, rescuers, external population/environment, facility, and continuity of mission. The problem is extended to the whole facility, including the underground premises and the surface buildings.

Once information is available on the layouts, and the way in which they are interconnected by means of the ventilation systems, detailed fire risk assessments and scenarios will have to be made for all areas of the CLIC complex, i.e., tunnels, experiment caverns, equipment alcoves, and linking galleries.

The most efficient protection strategy is one of enforcing a set of multi-level ‘safety barriers’, with a bottom-up structure, so as to trap most of the fire events at stages with no or few consequences, and thus limiting considerably the probability and impact of the largest events.

In order to ensure that large adverse events are possible only in very unlikely cases of failure of many barriers, measures at every possible level of functional design need to be implemented:

- in the conception of every piece of equipment (i.e., materials used in electrical components, circuit breakers, etc.);
- in the grouping of equipment in racks or boxes (i.e., generous cooling of racks, use of fire retardant cables, and fire detection with power cut within each rack, etc.);
- in the creation and organization of internal rooms (i.e., fire detection, power cut and fire suppression inside a room with equipment);
- In the definition of fire compartments;
- In the definition of firefighting measures;

It is impossible to describe in detail all of these measures, but the basic concepts, including most of the more severe constraints for the conceptual design are described in the following sections. The measures proposed here may require revisions to track the evolution of the CLIC design.

6.6.5.1 Legal constraints

Given the legitimate right to know which level of risk a National State is assuming by allowing CLIC onto its territory, the project will probably require approval by the territorial Authorities Having Jurisdiction (AHJ) before construction. The AHJ will typically apply the existing legislation for well identified cases (as, for instance, surface buildings), and typically will ask the CLIC design group to elaborate fire risk analyses for the more complex premises, such as the underground accelerator complex. This process has become, in the last decade, more and more based on fire scenario predictive calculation methods, and it is to be expected that this trend will continue in the future. Further constraints or modifications, can therefore be legitimately required by the AHJ.

6.6.5.2 *Measures limiting probability of onset of fire*

The following measures are examples of the principles to be followed in the design of the equipment for the facilities.

- put flammable equipment and materials on the surface, in a balanced approach (i.e., considering that also cables linking equipment to devices inside the tunnel are one of the variables);
- avoid, in underground spaces, equipment with flammable liquids (oil condensers, oil transformers, oil pumps, oil-based hydraulic actuators, etc.);
- segregate, in compartmentalized spaces (racks, huts, rooms), flammable equipment, and protect them by means of fire detection, automatic shut-off and fire suppression;
- seal, in metallic or other non-flammable boxes and containers, the flammable parts of equipment or cables trays;
- study all possible cooling aspects of dissipated power, including those connected with cable laying and ‘ampacity’ limits;
- avoid flammable gases as far as possible;
- Mix gas mixtures on the surface to concentrations below flash point;
- give preference to less dangerous materials in place of dangerous ones (e.g., use fire-retardant zero-halogen cables, fire retarding non halogenated printed circuit board cards, and borated polyethylene in place of normal ones, etc.);
- implement on-board local fire detection on flammable equipment, linked to automatic shut-off devices and/or fire suppression devices;
- use, where technically possible, equipment, devices and items with alabel of quality from certification authorities (CE labelled equipment equivalent).

6.6.5.3 *Measures aimed at allowing early detection and intervention*

A factor that is of help in allowing people to escape from fire and to limit damage is the readiness of reaction to the initial onset of fire. The main role of a fire detection and alarm system is precisely that of giving an early warning (normally located on the ceiling or at the ventilation outlets and surveying the whole room where equipment is installed). Detection and intervention measures are:

- fire detection shall be located in all areas with concentrations of equipment and all areas critical for evacuation;
- fire detection units shall be shielded from radiation, and protected areas should be considered in the early design;
- fire detection shall be properly designed in order to protect specific critical equipment and offer a general protection of the whole hall;
- selective power cuts triggered by automatic fire detection should be considered;
- fire detection shall trigger general warning system (evacuation alarm) and trigger immediate intervention of fire safety teams;
- public address systems shall be considered to broadcast specific emergency messages to workers underground;
- fire detection and evacuation system shall preserve their function in case of fire for at least two hours.

6.6.5.4 Measures aimed at safe evacuation of personnel

Evacuation pathways in area exposed to smoke

For caverns, the distance from any point to the nearest protected exit path should be limited to some 10 m to 30 m depending on the availability or not of a secondary exit path. This requirement is still reasonably applicable in underground halls, where smoke protected stairwells with access at every level can be implemented in the design.

Accelerator tunnels, in certain respects similar to road and railway tunnels, require more detailed analysis and a solid concept in order to make the evacuation of the structure feasible. Even with all the possible mitigating factors, distances should not go beyond limits that have been defined for road and railway tunnels. This limit is fixed between 200 m and 600 m, with a value of 500 m in the EU directive 2004/54. Several options are possible to attain this goal: splitting the long tunnel into compartments with solid doors and fire walls and parallelling the gallery with internal longitudinal passages (conceptually similar to side galleries). This appears to be the simplest and most reliable. An example of a firewall is shown in Fig. 6.37.

The ventilation system should be capable of creating a lower pressure in the compartment affected by the fire, and an over pressure in the areas at the sides. Figure 6.38 shows a schematic representation of the pressurization of the sector adjacent to a sector on fire. Related safety measures are:

- travel distance in tunnels should allow reaching a safe zone in a reasonable distance and time (600 m between safe havens). Several options are possible:
 - direct exits shafts to surface;
 - cross-links with another area not affected by the smoke, like a parallel tunnel;
 - splitting each tunnel into transverse compartments with a fire door and proper ventilation system.
- travel distances in halls and other areas with relatively high probability of being occupied by a large number of people shall be limited to a distance ranging from 10 m (blind corridors) to 30 m (2 exits). This can be done by providing access to pressurized areas at each level of the gangways;
- evacuation flow should proceed from higher to lower areas of radiation hazards both for the main and the secondary exit
- design should avoid the need for people to have to pass near to high-radiation areas to evacuate (e.g., targets, collimators, or similar);
- in tunnels ensure adequate clearance for emergency vehicles, allowing for the passage of slow bulk transportation and obstacles;
- compartments should be fire resistant for a reasonable time (two hours or more depending on the fire load).

Evacuation pathways in areas protected from smoke

Owing to the deep underground location of the accelerators, the only possible way to separate occupants from the source of fire is that of providing them a safe escape path.

The governing idea is that these ‘protected’ refuges shall be close enough, be reached quickly, and once a person is inside, they shall give all the time needed to proceed calmly and safely to the outside. ‘Protected’ in this case means protection from smoke, gases, heat, and all other possible effect of a fire (e.g., structural collapse). The measures that should be taken are:

- refuge areas shall be area large enough for the temporary accomodation of workers (the reference density is of 3 pp/m²);



Fig. 6.37: Conceptual representation of a fire wall transversal to the tunnel orientation

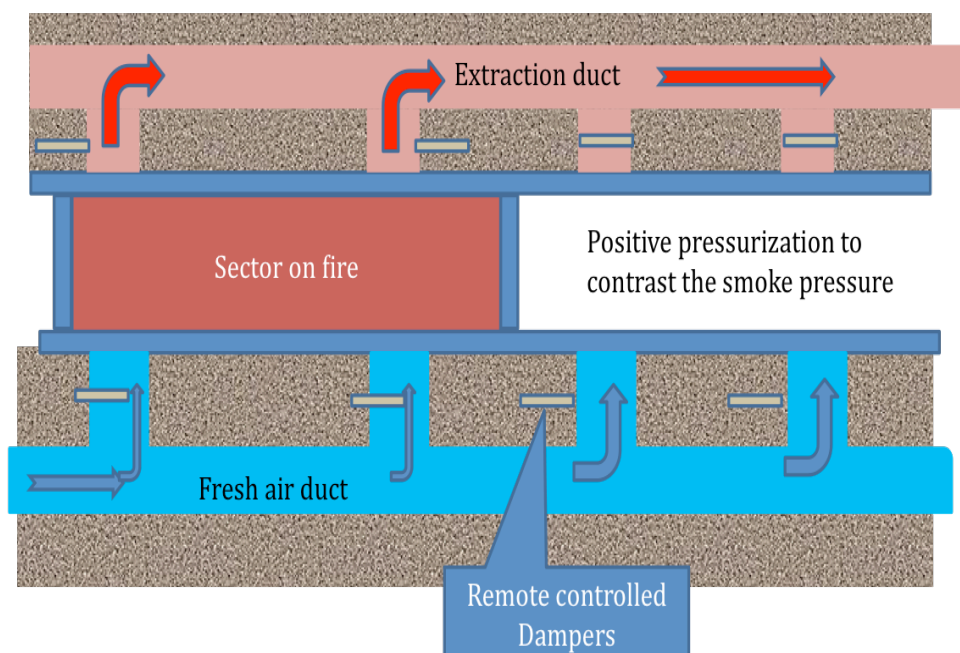


Fig. 6.38: Schematic representation of the pressurization of a sector adjacent to the sector on fire

- refuge areas shall be connected to the outside via a protected walking passage;
- refuges (and their lifts) shall ensure evacuation capability in case of fire events and or power cuts;
- pressurization shall prevent smoke and gases from entering;
- no electrical, gas, or any technical installation is allowed inside except those required to protect the refuge itself;
- no combustible materials are allowed inside;
- refuges and their structures shall be fire resistant for at least 2 hours.

6.6 SAFETY SYSTEMS

6.6.5.5 Measures aimed at limiting the propagation of fire along the facility

Fire propagation is to be limited by creating fire compartments. Typically, fire resistance will be at least two hours or more, depending on the fire load. The measures to protect the areas are:

- each large hall shall be a fire compartment;
- rooms with a considerable amount of electric equipment or gas handling equipment shall be fire compartments;
- Safe protected exit paths shall be fire compartments;
- sectors of tunnels, still to be identified, shall be fire compartments;
- all crossings for services shall be sealed with the same level of fire resistance as for the compartments;
- all ventilation ducts shall be properly sealed by dampers located at the walls;
- for surface buildings, technical galleries shall be isolated from the rest of the buildings and be separate fire compartments.

6.6.5.6 Measures aimed at limiting the propagation of smoke

The action of splitting the facility into compartments needs to be accompanied by a coherent design of the ventilation and smoke handling systems. Smoke coming from a fire has to be controlled for a number of reasons:

- it is toxic to bystanders;
- it can create damage within the compartments depending on its composition and concentration;
- it is essentially made by hot, partially combusted flammable species, that could reignite and spread the fire far from the origin.

Smoke control shall aim to accomplish the following goals:

- prevent propagation of the smoke from one compartment to another, by defining sectors of ventilation and smoke extraction, and by dynamic configuration capability, associated to smoke detection;
- in high-ceiling multi-floor caverns, ensure a slow descent of the smoke layer to allow evacuation. Specific fire scenarios can be evaluated to calculate the needed flow rates;
- overpressurize the areas on fire and reduce the pressure in the areas affected by fire by means of dynamic control of motorized fire dampers and regulation of the flow rates. This shall also take into account the volume of hot gases and the pressure field typical of fire;
- build to the appropriate specification to withstand the thermal impact of fire and ensure continuity of function;
- the normal ventilation system must be capable of being shut off or reconfigured to avoid the spreading of fire;
- in the case of an activated fire hazard, special filters shall be developed to prevent activated smoke from being rejected outside.

6.6.5.7 Fire-fighting measures

Measures to allow fire fighting and rescue on the premises include:

- allow rapid circulation for the rescuers in long tunnels by means of electric vehicles;

- allow local control and override of smoke extraction and ventilation system;
- allow communication underground via radio systems, mobile phones, fixed phones;
- all systems must remain efficient for the time required for fire-fighting operations and for not less than four hours;
- a fire-fighting water network shall be installed in all the tunnels and underground facilities;
- fire-fighting hoses shall be installed in the main caverns and all areas with important fire loads;
- additional fire-fighting means shall be installed in all areas with a relevant fire load and difficulty of access during a fire;
- all work areas shall have passages large enough for passage of a stretcher in the horizontal position;
- lifts shall be large enough to allow a stretcher to be laid down horizontally.

6.7 Survey and alignment

6.7.1 Geodesy and networks

A coordinate system, CERN Coordinate System (CCS) and a reference system, CERN Geodetic Reference Frame (CGRF) must be associated to the project as soon as possible as they provide a 3D framework. CCS is a right-handed 3D Cartesian coordinate system used to define the relative position of all the detectors and accelerators at CERN. CGRF defines the coordinates in latitude, longitude, as well as height coordinate measured along a normal to the surface. This ellipsoidal surface is not accurate enough for the measurement of heights as it does not take into account the direction of the gravity field, which must be determined locally. A geodetic model has been built from a combination of astro-zenithal, Global Positioning System (GPS), and gravimetric measurements [10].

For optimal stability of the machine, the linacs will be set up in a tunnel located in the most appropriate underground structure. The tunnel will be linked to the surface by shafts. Survey boreholes, with a diameter of 1.5 m, will be added between two machine shafts, in order to have a survey distance between shafts below 2.5 km. Reference is transferred through these shafts into the tunnel, from the surface geodetic network to the tunnel geodetic network, within ± 1 mm r.m.s. [11], as shown in Fig. 6.39.

The geodetic surface network will consist of pillars located close to the shafts whose positions will be determined by means of GPS. In parallel, measurements of vertical deflection will be performed on these same points. The transfer of the reference into the tunnel through the shafts will be carried out using the methods developed for the previous CERN accelerators: a combination of optical and mechanical measurements (3D triangulation and trilateration coupled with vertical wires acting as plumb lines between surface and tunnel). When possible (diameter of shaft large enough), astro-zenithal measurements from the bottom shaft will be added. The points located at the bottom of the shafts will be the backbone of the underground geodetic network. This underground network consists of reference points sealed in the ground, in the transport area, every 50 m, defined in CCS and CGRF. These points will be determined by angle, distance, wire-offset, direct optical levelling and gyroscopic measurements with respect to the pillars located at the bottom of the shafts, considered as fixed for the computation of data. This geodetic network is necessary for the implantation of all the general services (cable trays, cabling, piping, lighting) and the marking of all the components (beam, jacks) in the tunnels. It must be determined before any installation of general services.

In the case of the Main Linac and BDS, additional steps are needed: gravimetric measurements will be performed all along the tunnel, and an additional network will be installed from the underground geodetic network, the Metrological Reference Network (MRN). MRN consists of parallel stretched wires, metrological plates equipped with Wire Positioning Systems (WPS) sensors, and Hydrostatic Levelling Systems (HLS) sensors, defined in CCS and CGRF. This metrological network will be implemented and computed as early as possible, in order to allow an 'absolute' positioning of all the modules within ± 2 mm maximum pit-to-pit.

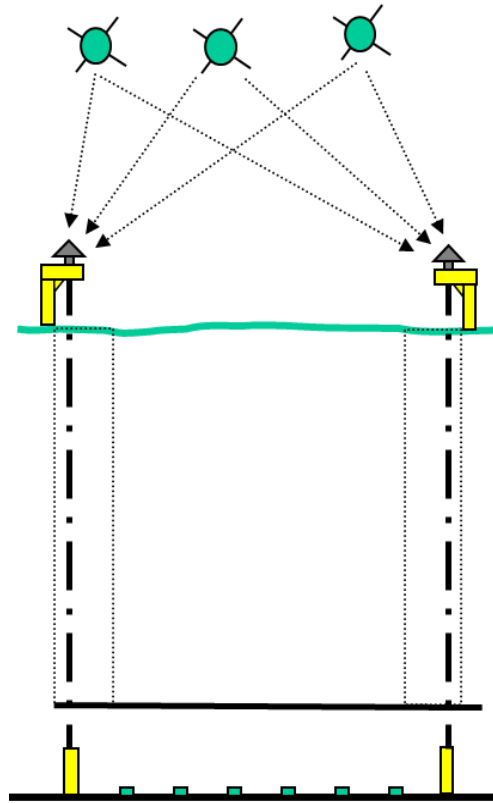


Fig. 6.39: Transfer of reference into the tunnel.

6.7.2 Machine installation and alignment

6.7.2.1 Measurements for installation

Special long rods will be sealed deep underground, in contact with solid stable rocks, in order to provide a stable reference, considered as fixed for all levelings. These special deep levelling references will be located around each shaft or specific areas, e.g., the damping rings.

As-built measurements will be performed at different stages of installation in specific ‘crowded’ areas, in order to prevent interference between services and components. These measurements are carried out with a laser scanner; 3D models are then re-constructed and can be integrated into the theoretical CAD models.

6.7.2.2 Fiducialization

Before installation in the tunnel, all the components to be aligned (or the supports on which they have been pre-aligned) must be fiducialized. This fiducialization step is the determination of the external alignment references (fiducials) of the components (or their supports), with respect to the beam axis. The uncertainty in measurement coming from fiducialization ranges from a few microns (Main Linac and BDS supports) to a few tenths of a millimetre. Several methods will be used depending on the accuracy needed (precision and accuracy of the machining, assembly jigs, laser tracker measurements, or Coordinate Measuring Machine). Some additional measurements can take place at that stage, e.g., the shape of the vacuum pipe inside a magnet or the mechanical position of the BPM with respect to the magnet. A reference will then be associated to each component (or support) to be fiducialized [12].

6.7.2.3 *Preparatory work*

The preparatory work is composed of the following steps in all tunnels (except the Main Linac and BDS).

- Marking on the floor
The vertical projection of the beamline and of the components (or their supports) will be marked on the floor. This work must be performed before the installation of services as it provides clear positioning for anybody working in the tunnels. The accuracy of the marks is ± 2 mm r.m.s.
- Positioning of the jacks
Jacks need to have an adjustment range of ± 10 mm (radial) and ± 20 mm (vertical): the errors of the floor, the errors in their own positioning, the mechanical interface error, and ground motion during the life of the tunnel must be taken into account. The heads of jacks are positioned within ± 2 mm with respect to the underground geodetic network before the installation of the components (or their supports), using displacement screws of the mechanical plate on which jacks are pre-positioned, or by shimming or grinding if no interface with ground settlement is foreseen. During that operation, adjustment screws of the jacks remain in their middle position. Once in position, jacks are sealed on the floor.

The Main Linac and BDS marking phase will take place with the installation of each module. Plates meant for initial mechanical alignment will then be positioned with respect to the MRN network.

6.7.2.4 *Alignment of components (or supports)*

The alignment of the standard components (or their supports) consists of two steps:

- First positioning
Each component (or its support) is aligned independently with respect to the underground geodetic network, within ± 0.3 mm r.m.s. At the same time, small local smoothing will take place between adjacent components (or supports) in order to validate the initial alignment (within ± 0.2 mm). This first positioning will be performed by direct optical levelling (vertical), and tachometer/laser tracker measurements coupled with wire offsets (radial). Adjustment is performed by acting on the jack screws.
- Smoothing
This step takes place once components (or their supports) are inter-connected, and/or under vacuum, so that all mechanical forces are taken into account. This final positioning step no longer refers to the geodetic network and concerns all components (or their supports) between two shafts. The relative position between components (or their supports) is measured using direct optical levelling (vertical), and wire offsets (radial) over a distance of 150 m, with a radial and vertical accuracy of ± 0.15 mm r.m.s. Components (or their supports) are then adjusted on the best-fit curve calculated after a global least-mean-square adjustment of the measurements. Adjustment (if needed) is performed by acting on the jack screws.

For the Main Linac and the BDS, the first positioning of the modules will take place with respect to the MRN. Once all the modules (shaft to shaft) are equipped with sensors and there is no more co-activity in the area, the active pre-alignment can take place, using the sensor readings, and re-adjusting with actuators.

REFERENCES

References

1. Enomoto, A., Kuchler, V. & Osborne, J. in *International Workshop on Linear Colliders 2010 (ECFA-CLIC-ILC Joint Meeting), 18-22 October 2010, Geneva, Switzerland* (2010). <<http://ilcagenda.linearcollider.org/getFile.py/access?contribId=601&sessionId=10&resId=1&materialId=slides&confId=4507>>.
2. Phinney, N., Toge, N. & Walker, N. *ILC Reference Design Report Vol. 3 - Accelerator* (SLAC, Stanford, CA, USA, 2007). <http://ilcdoc.linearcollider.org/record/6321/files/ILC_RDR_Volume_3-Accelerator.pdf?version=4>.
3. Ferrari, A., Sala, P. R., Fassò, A. & Ranft, J. *FLUKA: A multi-particle transport code* SLAC-R-773. CERN-2005-010. INFN-TC-2005-11 (SLAC, Stanford, CA, USA, 2005). <<http://www.slac.stanford.edu/cgi-wrap/getdoc/slac-r-773.pdf>>.
4. Battistoni, G. *et al.* in *AIP Conf. Proc. 896. Proc. Hadronic Shower Simulation Workshop 2006, 6-8 September 2006, Fermilab* (eds Albrow, M & Raja, R) **896** (2007), 31–49. <<http://scitation.aip.org/getpdf/servlet/GetPDFServlet?filetype=pdf&id=APCPCS000896000001000031000001&idtype=cvips&prog=normal>>.
5. Riddone, G. *et al.* in *Proc. 11th European Particle Accelerator Conf., 23-27 June 2008, Genoa, Italy* (2008). <<http://accelconf.web.cern.ch/AccelConf/e08/papers/mopp028.pdf>>.
6. Brugger, M., Ferrari, A., Roesler, S. & Ulrici, L. Validation of the FLUKA Monte Carlo for Predicting Induced Radioactivity at High-Energy Accelerators. *Nucl. Instr. and Meth. A* **562**, 814–818 (2006).
7. Bauer, J. *et al.* in *Proc. 1st Workshop on Accelerator Radiation Induced Activation, 3-7 October, 2008, Villigen, Switzerland* (2008), 96–106. <http://aria.web.psi.ch/Program/Papers/A15_Vincke.pdf>.
8. Bauer, J. *et al.* in *Proc. 1st Workshop on Accelerator Radiation Induced Activation, 3-7 October, 2008, Villigen, Switzerland* (2008), 107–111. <http://aria.web.psi.ch/Program/Papers/A16_Mallows.pdf>.
9. Mallows, S. & Otto, T. in *Proc. 1st Workshop on Accelerator Radiation Induced Activation, 3-7 October, 2008, Villigen, Switzerland* (2008), 128–132. <http://aria.web.psi.ch/Program/Papers/A17_Mallows.pdf>.
10. Jones, M. & Podevin, C. *Qualité de la chaîne des données Survey et système de coordonnées* CERN CERN-TS-Note-2005-034. TS-Note-2005-034 (CERN, 2005). <[https://edms.cern.ch/file/590567/1.0/TS-Note-2005-034 \(Jones\) .pdf](https://edms.cern.ch/file/590567/1.0/TS-Note-2005-034%20(Jones).pdf)>.
11. Hugon, P. *Etudes des méthodes optiques et mécaniques pour le transfert du réseau géodésique en surface au réseau souterrain, dans le cadre du projet CLIC au CERN* Mémoire de soutenance de Diplôme d'Ingénieur INSA Spécialité TOPOGRAPHIE. Institut National des Sciences Appliquées de Strasbourg. 2010. <<https://edms.cern.ch/file/1113075/1/memoire.pdf>>.
12. Quesnel, J.-P. in *Proc. 8th International Workshop on Accelerator Alignment, 4-7 October 2004, CERN, Geneva, Switzerland* (2004). <http://iwaa2004.web.cern.ch/IWAA2004/subsite/PDF/20041004_TS01-1_Jean-Pierre-Quesnel.pdf>.

Chapter 7

CLIC technologies demonstrated at CTF3



7.1 Objectives of CTF3

The aim of CTF3 (see Fig. 7.1), built at CERN by the CLIC/CTF3 international collaboration, is to prove the main feasibility issues of the CLIC two-beam acceleration technology. The two main points which CTF3 should demonstrate are:

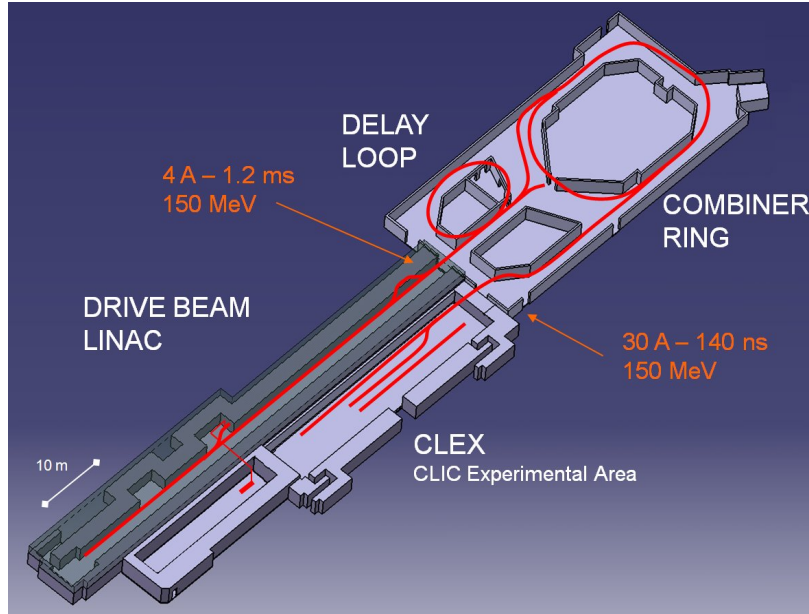


Fig. 7.1: CTF3 overall layout

1. Drive Beam Generation. Efficient generation of a high-current electron beam with the time structure needed to generate 12 GHz RF power (see Table 7.1). CLIC relies on a novel scheme of fully loaded acceleration in normal conducting travelling wave structures, followed by beam current and bunch frequency multiplication by funneling techniques in a series of delay lines and rings, using injection by RF deflectors. CTF3 is meant to use such a technique to produce a 30 A Drive Beam with 12 GHz bunch repetition frequency. The Drive Beam can be sent to an experimental area (CLEX) to be used for deceleration and two-beam experiments.
2. RF power production and two-beam issues. In CLIC the needed 12 GHz high power RF is obtained by decelerating the high-current Drive Beam in travelling wave resonant structures called PETS (Power Extraction and Transfer Structures). Such power is transferred efficiently to high gradient accelerating structures, operated at 100 MV/m. In the CTF3 experimental area (CLEX) one line (Test Beam Line, TBL) is used to decelerate the Drive Beam in a string of PETS. The Drive Beam can alternatively be sent to another beam line (Two-Beam Test Stand, TBTS), where a PETS is used to power one or more structures, used to further accelerate a 200 MeV electron beam provided by a dedicated injector.

CTF3 consists of a 150 MeV electron linac followed by a 42 m long Delay Loop and a 84 m Combiner Ring. To demonstrate the first point, the beam current is first doubled in the delay loop and then multiplied again by a factor of four in the combiner ring by interleaving bunches using transverse RF deflecting cavities. The power generation and transfer and the high gradient acceleration are instead demonstrated in the CLIC experimental area (CLEX), where the Drive Beam can be transported to lose its energy and produce RF power. In the same area a 200 MeV injector (CALIFES) generates a Probe Beam for two-beam experiments.

CTF3 has been installed and commissioned in stages since 2003. Delay loop running-in was basically completed in 2006. The Combiner Ring and the connecting transfer line were installed and put in operation in 2007, while the transfer line to CLEX was installed in 2008.

In 2009 this last beam-line and the various Drive Beam lines in CLEX were commissioned, together with the CALIFES Drive Beam injector. During the autumn of 2009, recombination with the DL and CR together was achieved, yielding up to 28 A of beam current. In 2010 the nominal power production from the PETS was obtained, and the first two-beam test was performed, reaching a measured gradient of 100 MV/m. In 2011, the Drive Beam stability was improved, a gradient of 145 MV/m was reached in two-beam tests, the PETS ON/OFF mechanism was successfully tested and a 20 A Drive Beam was decelerated by 26% of its initial energy in a string of 9 PETS structures.

Summary of the performances achieved in CTF3:

1. Drive Beam Generation:

- Full beam loading (94% transfer), high current operation (up to 5 A) of Drive Beam linac.
- Isochronous operation of ring ($\alpha_p < 10^{-4}$), in order to avoid bunch lengthening.
- Sub-Harmonic bunching, phase coding (~ 7 % residual charge in satellites).
- Fast phase coding switch (~ 6 ns switch time).
- Bunch train recombination factor of 2 in Delay Loop (from 3.5 to 7 A).
- Bunch train recombination factor of 4 in Combiner Ring (from 3.5 to 14 A).
- Bunch train recombination factor of 8, DL plus CR (from 3.5 to 28 A).
- Transverse r.m.s. emittance < 100 mm mrad (end of linac).
- Transverse r.m.s. emittance 150 mm mrad (combined beam factor of 4, vertical plane only).
- Bunch length control to < 1 mm r.m.s.
- Control of ring length to better than 0.2 mm.
- Beam current stability ~ 0.05 % end-of-linac, ~ 0.1 % combiner ring (combination factor 4).

Table 7.1: CLIC nominal parameters compared to the state of the art (CLIC Test Facility CTF3) and to future goals

Parameter [Units]	CLIC nominal	Present state of the art	Objective 2012	Objective 2013
I_{initial} [A]	4.2	7	–	–
I_{final} [A]	100	28	30	–
Q_b [nC]	8.4	4 (2.3 nom.)	–	–
Norm. emitt. r.m.s. [mm]	≤ 150	150	≤ 150	–
Norm. emitt. r.m.s. [mm]		(factor 4 comb. beam, vertical)	(factor 8 comb. beam, both planes)	
Norm. emitt. r.m.s. [mm]		≤ 1 (linac)	≤ 1 (CLEX)	–
Bunch length [mm]	≤ 1	≤ 2 (CLEX)		
E [GeV]	2.4	0.12	–	0.15
$T_{\text{pulse initial}}$ [μ s]	140	1.4	–	–
$T_{\text{pulse final}}$ [ns]	240	140 (240)	140 (240)	140 (240)
Beam load. eff. [%]	97	95	–	–
Deceleration [%]	90	26	35	50 or more
Phase stability @ 12 GHz [$^\circ$]	0.2	–	1	0.5
Intensity stability	0.75×10^{-3}	0.5×10^{-3} (linac) 1×10^{-3} (comb. 4)	2×10^{-3} (comb. 8)	$\leq 1 \times 10^{-3}$ (comb. 8)

7.2 ACHIEVEMENTS

2. RF power production and two-beam issues:

- RF power and pulse length in PETS > 200 MW, > 240 ns, well above CLIC nominal (135 MW, 240 ns).
- RF power delivered to accelerating structure > 100 MW (CLIC nominal 65 MW).
- Accelerating gradient measured in two-beam experiment 145 MV/m, above CLIC nominal (100 MV/m)
- Deceleration of the Drive Beam in a string of 9 PETS, by 26 % (from 115 MeV to 84 MeV), total 12 GHz power produced > 500 MW.

Performances to be reached in 2012:

Combined current 30 A, low-loss transport to CLEX, transverse emittance = 150π mm mrad in both planes, current stability $\sim 2 \times 10^{-3}$ for fully combined beam. Initial measurements of Drive Beam phase stability. Deceleration by 35% in the Test Beam Line (TBL) of CLEX, 13 Power Extraction Structures (PETS). Breakdown kicks are also planned as well as RF pulse shape control experiments in CLEX.

7.2 Achievements

7.2.1 Beam current, bunch structure, injector issues

The CTF3 Drive Beam injector consists of a high current thermionic gun [1], three 1.5 GHz sub-harmonic bunchers, and a 3 GHz system composed of a pre-buncher, a buncher and the first two accelerating structures in the linac, as shown in Fig. 7.2.

The sub-harmonic bunchers are used to give the first energy-time modulation to the beam and to perform the phase coding by means of fast 180° RF phase switches. The most important specifications common to all the sub-harmonic bunchers are summarized in Table 7.2. To compensate the different beam loading in the structures, they are tuned in a different way, as also listed in the table.

Downstream of this system, a 3 GHz pre-buncher and buncher are installed to create the final bucket structure and to accelerate the beam up to about 6 MeV. The most important specifications of these elements are shown in Table 7.3.

The first two accelerating cavities follow this system to bring the beam to an energy of about 20 MeV. These cavities are of the same type as those installed in the rest of the linac.

Exhaustive simulations have been performed using PARMELA to optimize the bunch length, the satellite population and the transverse emittance [2, 3]. The magnetic field distribution indicated

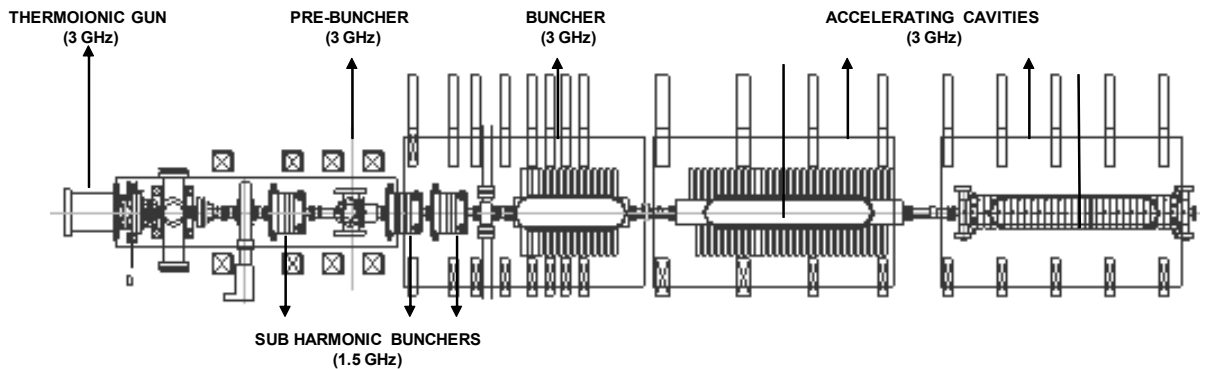


Fig. 7.2: Layout of the CTF3 pre-buncher and buncher

in Fig. 7.3 has been optimized to keep the emittance at the exit of the injector below 50π mm mrad. Measurements in the CTF3 linac gave emittances in agreement with the predicted ones [4].

A bunch length of 1 mm at the end of the linac and less than 2 mm has been measured in the combiner ring [5] by means of streak camera measurements.

As with the CLIC Drive Beam injector, the sub-harmonic bunchers perform 180° phase jumps to create the correct bunch train structure. The measured time for one phase switch in CTF3 is less than 6 ns which corresponds to eight 1.5 GHz periods, compared to the target time of 10 ns. Some particles captured by the 3 GHz system form satellites in between the 1.5 GHz buckets. The measured fraction of the satellites is about 8% to be compared with the 7% of the design. In Fig. 7.4 the image taken with a streak camera in the delay loop shows the typical distribution of the main buckets used in the recombination and the satellites in between.

7.2.2 Full beam loading, stability, linac issues

7.2.2.1 Full beam loading operation

As the overall efficiency is paramount for a linear collider, a very efficient energy transfer to the Drive Beam is crucial. For this purpose, the drive linac will be operated in the ‘full beam loading’ condition,

Table 7.2: Parameters of the CTF3 sub-harmonic bunchers, common parameters in the left, individual parameters in the right table.

Common parameter	Value		
Frequency [GHz]	1.49928		
Number of cells	6		
Cell length [cm]	2.6		
Iris diameter [cm]	6.6		
Input power [kW]	40		

Parameter	SHB1	SHB2	SHB3
Phase advance/cell [$^\circ$]	74.82	70.21	68.23
Phase velocity [c]	0.63	0.67	0.69
Group velocity [c]	0.048	0.050	0.051
R/Q [Ω /structure]	10.7	12.4	13.4
Fill time [ns]	11	10	10

Table 7.3: Parameters of the CTF3 pre-buncher and buncher

Parameter	Pre-buncher	Buncher
Frequency [GHz]	2.99855	2.99855
Number of cells	1	17
Cell length [cm]	2	[1.183, 3.333]
Phase advance/cell [rad]		$2\pi/3$
Phase velocity [c]		[0.7, 1]
Group velocity [c]		[0.047, 0.024]
R/Q [Ω /structure]		1.4
Input power [MW]	0.1	42

7.2 ACHIEVEMENTS

where the beam extracts almost entirely the power from the structures (see Fig. 7.5). In this condition, an overall transfer efficiency of about 98% is expected for CLIC. One of the main goals of CTF3 is the validation of the CLIC Drive Beam generation scheme with fully loaded linac operation.

The 3 GHz travelling wave accelerating structures designed and built for CTF3 [6] work in the

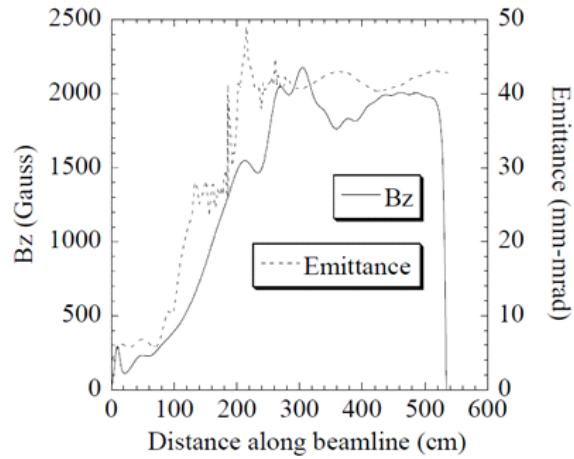


Fig. 7.3: Simulated magnetic field and transverse emittances along the injector

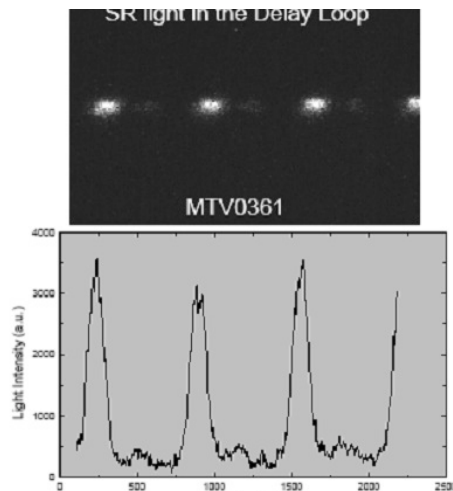


Fig. 7.4: Longitudinal distribution of the bunches (synchrotron light and correspondent spectrum) in the delay loop

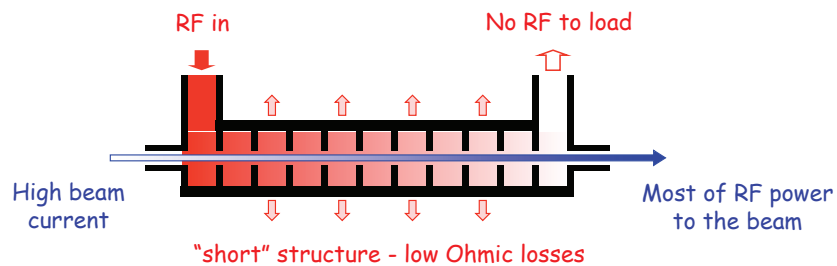


Fig. 7.5: Principle of full loaded acceleration

$2\pi/3$ mode, have a total length of 1.22 m and operate at a loaded gradient (nominal current) of 6.5 MV/m. In order to suppress the transverse Higher Order Modes (HOMs) the structures (called SICA, for Slotted Iris Constant Aperture) use four radial slots in the iris to couple out the HOMs to SiC loads. Simulations have shown that the beam emittance is conserved during acceleration despite the high beam current and the long beam pulse.

The RF power is supplied by klystrons with power ranging from 35 MW to 45 MW and compressed by a factor of two to provide $1.3 \mu\text{s}$ pulses with over 30 MW at each structure input. The pulse compression system uses a programmed phase ramp to produce a rectangular pulse.

Beam commissioning started in June 2003. The design beam current and pulse length were rapidly reached, successfully demonstrating the operation under nominal working conditions of the structures with their novel damping scheme [7]. The main result obtained was the first proof of stable operation under full beam loading. The beam was remarkably stable and no sign of beam break-up was observed at high current. The measured normalized emittance at the end of the CTF3 linac was routinely about $\epsilon_{x,y} \approx 50 \mu\text{m}$. This confirms that the Drive Beam accelerator wakefield effect are small, as predicted by simulations.

The energy spread during the initial beam transient (about 100 ns) could be reduced to a few per cent by partial RF filling of the structures at beam injection. The observation of the RF signals at the structures' output coupler was particularly useful. It allowed one to easily adjust the beam-to-RF phase by maximizing the beam loading and to determine the phase errors between structures.

The efficiency of the acceleration was demonstrated in a dedicated experiment [8]. After careful calibration of beam current and RF power measurements, the energy gain of the beam was calculated and compared to spectrometer energy measurements. Figure 7.6 shows an example of the RF power measured with and without beam, showing that the RF power is almost fully absorbed by the beam. The measurements were in excellent agreement with the theoretical energy gain. Including the ohmic losses, the obtained RF-to-beam transfer efficiency yielded 95.3%.

In summary, CTF3 has been stably operated over several years with fully loaded structures. The highly efficient acceleration of the Drive Beam has been successfully demonstrated.

7.2.2.2 Beam current stability

The stable operation relies crucially on the current stability of the Drive Beam. Due to the fully loaded acceleration, any current variation will result in an energy variation of about the same relative amplitude. Nevertheless, any high frequency variations will be averaged over the fill time of the Drive Beam accelerating structure.

The pulse-to-pulse current variations in the CTF3 linac were measured using the current measure-

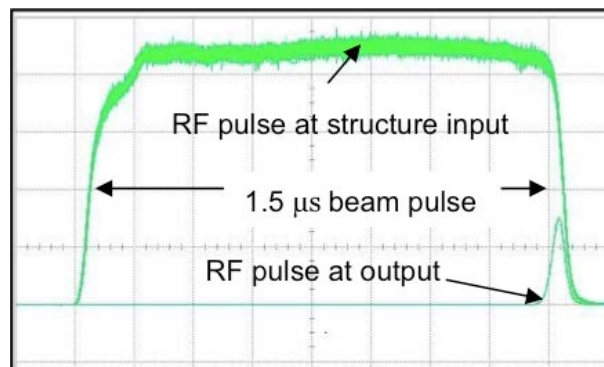


Fig. 7.6: RF power measured at the accelerating structure output with and without beam

7.2 ACHIEVEMENTS

ments of the beam position monitors. Initially, the stability was only of the order of $\Delta I/I = 2 \cdot 10^{-3}$ but it could be improved by replacing the gun heater power supply with a more stable one. A slow drift was still present that could be reduced by a feedback. Finally, a variation on a single BPM as low as $\Delta I/I = 0.6 \cdot 10^{-3}$ was measured (see Fig. 7.7). This is already better than the required current stability for CLIC of $\Delta I/I = 0.75 \times 10^{-3}$. A correlation analysis of different BPMs showed that the BPM noise level was of the order of $\Delta I/I = 0.3 \cdot 10^{-3}$, indicating that the real current variation is well below the CLIC target.

7.2.2.3 Other linac issues

CLIC has very tight requirements for the phase and amplitude stability of the Drive Beam. The RF r.m.s. phase jitter tolerance is 0.05° for a constant error along the whole Drive Beam train and 0.2% for the RF amplitude.

A CTF3 klystron was used to measure the short-term RF stability over 500 consecutive RF pulses (≈ 10 min). The mean pulse-to-pulse phase jitter measured with respect to the external reference is 0.035° . The pulse-to-pulse phase jitter for a fixed 10 ns time slice is 0.07° (3 GHz). The relative pulse-to-pulse power jitter has been 0.21% [9] (see Fig. 7.8). The measurements show that the RF stability of the klystron is very close to the CLIC requirements.

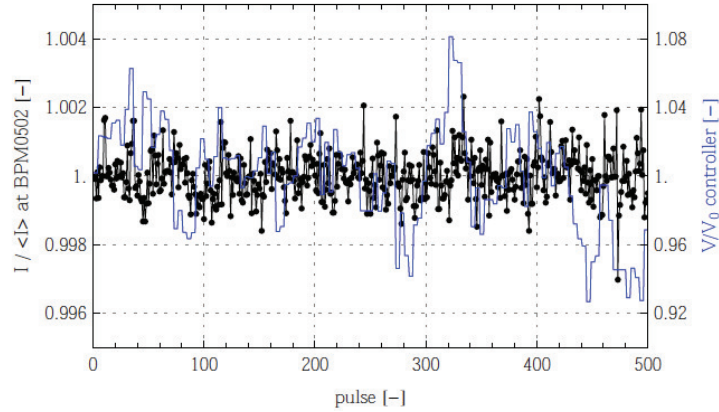


Fig. 7.7: Beam current variation measured in the CTF3 linac

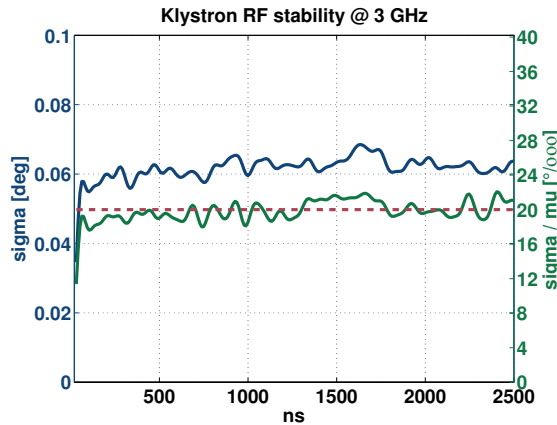


Fig. 7.8: Pulse-to-pulse RF phase (blue) and power (green) jitter measured on a CTF3 klystron

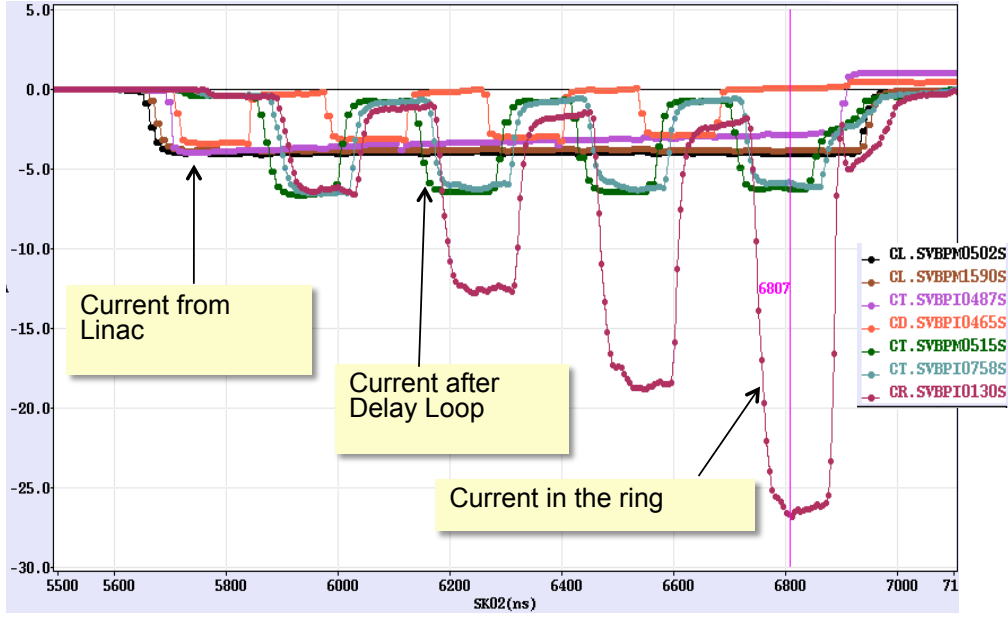


Fig. 7.9: Beam current multiplication in CTF3

7.2.3 Combination process, isochronicity requirements, measurement procedures

Beam recombination is done in two stages. First, using the Delay Loop (DL) a 1120 ns long bunch train with a current of 4 A is converted into 4 pulses of 140 ns and 7.5 A (taking into account the satellite bunches content). Later, the pulses are interleaved in the Combiner Ring (CR) to produce a single 140 ns long pulse with a current of 30 A. The first RF deflector, operating at 1.5 GHz, sends odd and even phase-coded sub-pulses either straight to the CR or into the DL, whose length is equal to the sub-pulse length. The sub-pulses circulating in the DL come back in the deflector at half a wavelength distance, and their orbits are merged with the following ones to obtain 140 ns long pulses with twice the initial current and twice the bunch repetition frequency. The pulses are combined again in the CR. In each ring a couple of RF deflectors is employed to create a time-dependent closed bump at injection, which can be used to interleave the bunches. The combination process must preserve transverse and longitudinal beam emittances: isochronous lattices, smooth linear optics, low impedance vacuum chambers and diagnostics, HOM free RF active elements are all needed to accomplish this task. CTF3 routinely provides a recombined beam of 28 A, slightly lower than the expected value (see Fig. 7.9). Initially, the recombined current was limited by losses. In 2011, several improvements reduced drastically the losses, but the satellite content increased due to the unavailability of one of the three 1.5 GHz RF sources used in the bunching system, such that the DL recombined beam had a current of 7.2 A. It is expected to obtain the recombined beam intensity of 30 A in 2012 after repair of the RF source.

7.2.3.1 Isochronicity and other lattice requirements

Together with the delivered beam current, the bunch length is fundamental for efficient RF power production in the PETS. Bunch length preservation requires the use of isochronous optics (which implies $R_{56}=0$) in the DL, the CR and the transfer line connecting them. The DL and CR arcs are based on the use of three-dipole isochronous cells. The isochronicity requirement is $|R_{56}| \leq \pm 1$ cm. The range of tunability of such a cell with three independent quadrupole families fits well the requirements (see Fig. 7.10). It is envisaged, but not yet implemented, to correct with sextupoles also the second order matrix term R_{566} . Bunch length control to < 1 mm r.m.s. was shown in the past after the linac. No time was then dedicated to get such a bunch length in CLEX as well, since the present value (< 2 mm r.m.s.),

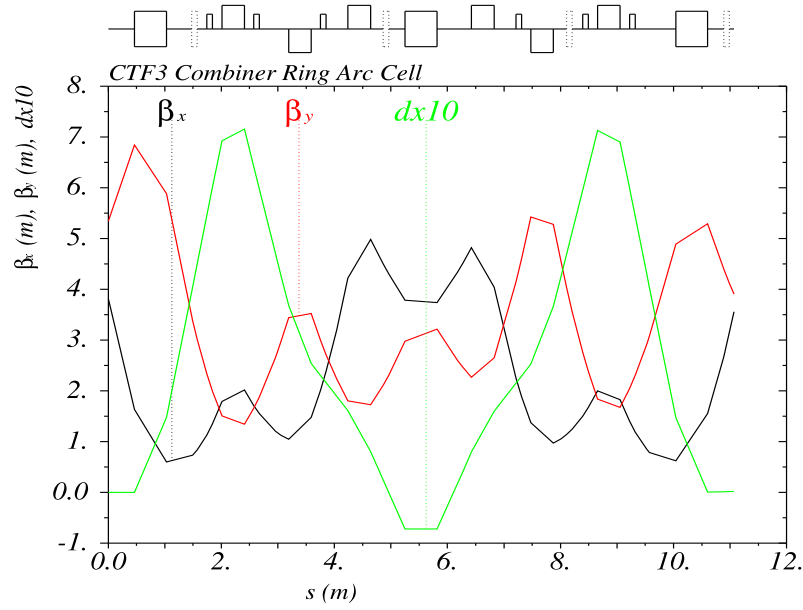


Fig. 7.10: Isochronous cell used in the CTF3 Combiner Ring

estimated from RF power production in CLEX and by direct streak camera measurements in the ring is entirely sufficient for CTF3 operation and in agreement with expectations. Nonetheless, it is planned to tune the machine for shorter bunches during the 2012 run.

Emittance preservation requires good control of the optics, a very good closure of the DL and CR orbits and that the beam from the linac is properly matched. The RF bump in the combiner ring must not introduce any distortion. Therefore the phase advance between the RF deflectors in the horizontal plane must be 180° , so that any distortion introduced by the first RF deflector is corrected by the second one. CTF3 has not yet reached the target emittances for the Drive Beam after combination, 150 mm in both planes. Although 50 mm is routinely obtained in the linac, measurements on the fully recombined beam typically give values two to four times greater than the target. Better results are obtained for the 4-beam combination, where the goal has been reached in the vertical plane. The main source of emittance growth was identified as orbit mismatch between delay loop and combiner ring, and non-perfect orbit closure in the ring itself. Several correcting measures are being put in place, and in 2012 we expect to reach the target.

Damping and detuning is used in the CR RF deflectors in order to minimize wakefields in the vertical plane, which are not extracted from the output coupler (reference needed). The lowest order horizontal dipole mode is the operational one, therefore it cannot be damped or detuned. However, the fill-time of the travelling wave deflectors is short enough to avoid turn-by-turn direct build-up. In order to avoid any residual amplification of the orbit errors from RF deflector induced wakefields, the tune of the Combiner Ring is set to be about 0.6 in both planes. Also, the β function in the deflectors should be as small as possible.

7.2.3.2 Recombination process and setting-up

Besides demonstrating the feasibility of the CLIC bunch combination principle, CTF3 has allowed us to develop an optimized setting-up procedure of such a process (see below), validating also the special diagnostics needed. Initially, the 1.5 GHz RF deflector is not used and magnetic correctors are employed to inject the beam on the DL design orbit. The design injection orbit is established, septa and main bend current are then adjusted. The injected beam must be matched to the DL closed solution. Hence,

the Twiss parameters of the beam are measured using the quadrupole-scan technique, in two Optical Transition Radiation (OTR) screens, located upstream and downstream of the DL injection. The optics in the linac is re-adjusted based on the results obtained, and the procedure is repeated a few times if needed.

In order to define the proper phase and amplitude in the RF deflector, the beam is sent straight past the DL into a dump. The RF deflector is powered, and its phase adjusted at zero crossing so it does not affect the beam trajectory. Afterwards, the phase is moved by 90° and the magnetic correctors used for injection are disabled. If the RF deflector amplitude is correct the bunches, sitting at the crest of the RF wave, would follow the reference orbit. If this is not the case the amplitude needs to be adjusted, and the procedure is repeated. When the RF deflector amplitude is finally determined, the phase is shifted by 180° , and beam is injected into the DL.

The recombination with RF deflectors requires the length of the DL and the CR to be precisely adjusted such that the bunches return at the proper RF phase with an accuracy of a few degrees. The lengths can be tuned in a maximum range of 3 cm using 4-pole wigglers. The length is precisely measured with 3 GHz phase monitors (BPRs), which compare the bunch phase with a 3 GHz reference signal. In case of the DL, the current of the wiggler is adjusted such that both the incoming and the outgoing beams gives no signal, i.e., the phase advance is 180° . After finding the required setting for the wiggler current, the optics of the loop must be corrected since this element introduces non negligible focusing in the vertical plane.

Another iteration may be needed to fine tune the DL orbit such that the circulating beam and the by-passing beams follow the same orbit after the DL. In the last step, phase switching is introduced in the sub-harmonic bunching system, and the sub-pulses are recombined.

The Combiner Ring setup also starts with RF deflectors disabled. A static magnetic corrector is used to inject the beam on a good orbit through the first half of the ring. As in the DL case, we need to find precisely the correct amplitude and phase of the RF deflectors. The pulse is shortened to less than the CR circumference (280 ns) and only the first RF deflector after injection is powered. The zero-crossing phase is determined as the phase that leaves the beam orbit unchanged. This is done for different RF amplitude values, thus measuring the phase dependence on the amplitude. In the next step the RF deflector phase is moved by 90° so bunches arrive at the crest and the corrector is disabled. The amplitude is adjusted in order to inject on the reference orbit, with the phase following according to the dependence found in the previous step. The timing of the klystron that feeds the deflectors is adjusted such that it stops just after the last bunch is injected. Since the RF deflectors are travelling wave structures with very short filling time, the train can thus make tens of thousands of turns in the ring. At this stage the orbit in the whole ring is corrected, as well as the ring length. The ring length must be $(N \pm 1/4)\lambda_{\text{RF}}$, where N is an integer number and λ_{RF} is the wavelength of the 3 GHz RF field. The fractional part λ_{RF}/N_f , can be determined precisely from Fourier transform of the BPR phase monitor of the coasting beam. To adjust the ring length the 4-pole wiggler is used.

In the next step the phase and amplitude of the second RF deflector are adjusted. The RF pulse for the deflectors is extended by 280 ns such that the field is present when the train makes the second turn. This should not change the orbit since the ring length was adjusted before. Attenuation of the second deflector is removed and phase adjusted such that the orbit stays unchanged. The RF pulse is extended by another 280 ns and the amplitude of the second deflector is fine tuned to keep beam position unaltered. If all is done properly, extending the RF pulse to the 4th turn will not affect the orbit. Putting back the beam pulse to the nominal value gives the recombined beam.

7.2.3.3 *Measurement procedures*

Several measurement procedures are used in order to determine the machine optics, compare it to the model and to measure the beam characteristics in the transverse and longitudinal phase space. The infor-

7.2 ACHIEVEMENTS

mation is eventually used to apply corrections and improve the performance. It is especially important to identify any discrepancy between the machine model and the reality.

7.2.3.4 *Response matrix*

The machine optics are measured and compared to the model using a direct measurement of the response matrix elements in all BPM locations, relating the position change in any BPM to a kick induced by a corrector. In this way it is possible to identify a local discrepancy with the model, usually originating from a hardware error. The modeling of some critical elements (e.g., the combined function main dipoles used in the ring) was also improved by using this method.

7.2.3.5 *Quadrupole scans with OTR screens*

During the machine setup the Twiss parameters are measured with the help of OTR screens using the quadrupole-scan technique. Such screens are installed at ten different positions along the machine and give access to the beam profile at these locations. The beam size is measured for several settings of the two or three upstream quadrupoles, in order to reconstruct, by a fit, the Twiss parameters of the beam at a reference point (in general at the entrance of the first quadrupole). The beam can be then rematched on the nominal optics, using the model predictions, and verified again. The emittance is also measured this way in different parts of the machine. Disagreement of the measured parameters with the model predictions indicates an error.

7.2.3.6 *Dispersion*

Dispersion is routinely checked along the machine by changing the beam energy and measuring the differential orbit in the BPMs. Alternatively, the magnetic strength of all elements in a region of the machine is changed and the differential orbit is taken. Both methods give similar results for incoming zero dispersion. Recently, a method using an energy step along the electron pulse was used with very good results.

7.2.4 Beam transport, losses and stability

7.2.4.1 *Combined beam current stability*

The current stability after the recombination process is not as good as in the linac. The main source of variations and jitter are the klystrons and RF pulse compression, which leads to a changing beam energy. Through dispersion, this leads to fractional losses of the beam current. After a factor of four combination in the Combiner Ring, a current stability of 1×10^{-3} was measured (see Fig. 7.11). While the apparent increase of the jitter in TL1 is dominated by the measurement noise, the beam current variation increases after extraction from the Combiner Ring. This increase is probably due to an emittance increase during the combination together with the aperture limitation for the extraction channel. For the factor eight combination with Delay Loop and Combiner Ring, a stability of 1% was reached.

7.2.4.2 *Feedback*

As the operation for the full factor 8 recombination is more complex, the beam becomes more sensitive to deviations from the nominal parameters. The biggest variations at CTF3 come from changes in the accelerating RF power and phase. This effect originates from temperature variations of the RF pulse compression cavities used to increase the instantaneous RF power. This is specific to CTF3 and will not be used in CLIC.

In order to counteract these variations, a feedback has been developed that takes into account the ambient temperature around the compression cavities, as the thermal isolation of these cavities is not perfect. The set point of the temperature stabilization system is corrected according to the variations in

the ambient temperature. This systems works well and significantly suppresses the RF variations [10]. A further feedback acts in addition to this on the setup of the RF pulse compression and keeps the RF power constant along the beam pulse.

Another feedback stabilizes the input RF phase of the different linac accelerating structures at a given phase reference by adjusting the low-level RF phase.

7.2.5 Power production, PETS issues

7.2.5.1 The Power Extraction and Transfer Structure

The RF power for the Main Beams is produced when the Drive Beam interacts with the impedance of a periodically loaded constant impedance power extraction structure (PETS), exciting preferentially the synchronous mode with frequency $\omega_{rf} = 2\pi \times 11.994$ GHz. Extensive studies have been performed to arrive at the current CLIC PETS design, including studies of high-power behavior [11–13] and higher-order mode behavior [11, 14, 15]. The RF power generated by a bunched beam in a constant impedance periodic structure in general can be expressed as [11, 14]

$$P = \frac{1}{4} (R'/Q) \frac{\omega_{rf}}{v_g} L^2 I^2 F^2 \eta_{\Omega}^2 \quad (7.1)$$

where R'/Q is the PETS impedance per metre (2290 linac- Ω /m), v_g the group velocity ($0.45c$), L the PETS length (0.21 m), I the Drive Beam current (101 A), F the beam form factor (0.97) and η_{Ω}^2 the ohmic loss efficiency (0.99); the CLIC baseline values are given in parenthesis. In CLIC each of the 140 000 PETS will generate 240 ns RF pulses of 135 MW.

High-power testing of the PETS using a klystron has been performed at the ASTA test stand at SLAC [16] demonstrating satisfactory high-power performance with a breakdown rate less than 2.4×10^{-7} per pulse per metre at nominal PETS power and pulse length. In CTF3, PETS prototypes are tested

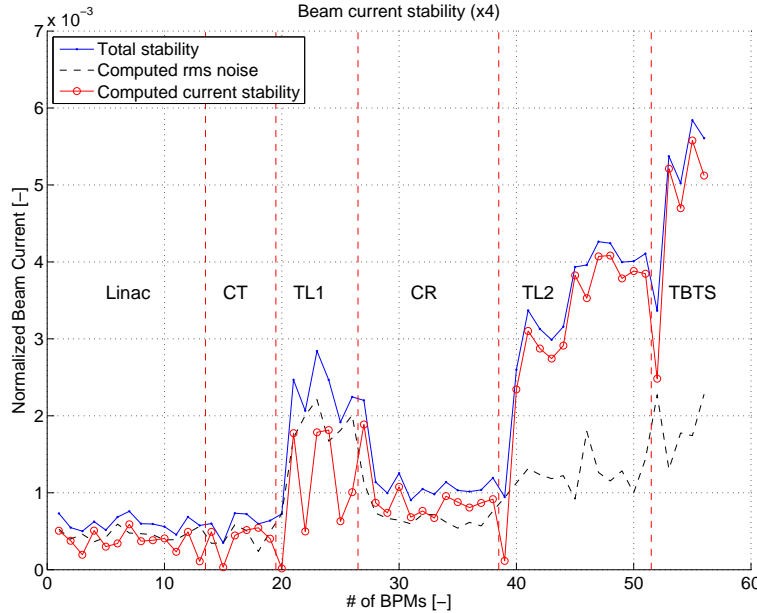


Fig. 7.11: Beam current variation measured in different parts of the CTF3 accelerator for a factor of four recombination. The dashed line shows the computed noise, the circles show the computed current stability after subtraction of the measured noise.

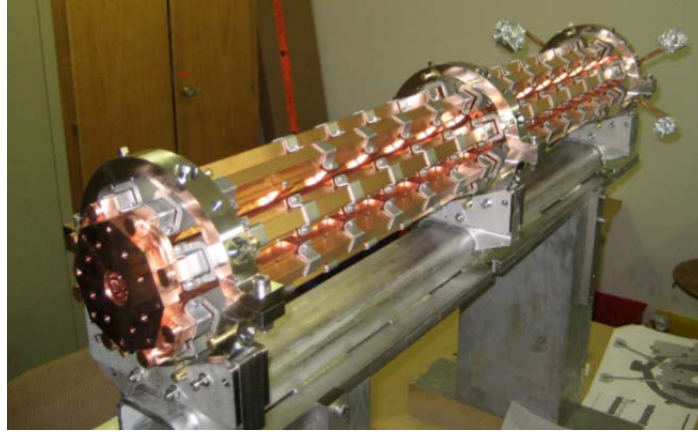


Fig. 7.12: The first 12 GHz PETS prototype, currently installed in the Two-Beam Test Stand experiment. The PETS prototype is based on the CLIC baseline design. The length is one metre as opposed to 0.21 m for CLIC, to be able to extract CLIC level power from the CTF3 Drive Beam (CTF3 has a maximum current of 30 A as opposed to the 100 A CLIC Drive Beam).

with beam in the Test Beam Line and the Two-Beam Test Stand. Figure 7.12 depicts the first 12 GHz PETS prototype, currently installed in the Two-Beam Test Stand experiment.

7.2.5.2 Test Beam Line power production

Up to sixteen 80 cm long PETS will be installed in the Decelerator Test Beam Line (TBL) [17]. The TBL itself is discussed in more detail in §7.2.7. Here we discuss power production studies in the first TBL PETS, installed in Fall 2009. The 80 cm long TBL PETS can produce CLIC PETS power levels of 135 MW with a 30 A CTF3 current (compared to the 100 A in CLIC). The first TBL PETS was successfully commissioned [18] in November and December 2009, with RF power levels of up to 20 MW produced. The beam line was commissioned with gradually higher Drive Beam current, with the PETS producing up to 70 MW of RF power. The power of this PETS is coupled out by a symmetric coupler into two WG90 waveguides, each equipped with directional couplers for measurements. The power is then dumped into high power loads. The measured TBL PETS power production has been consistent with theoretical predictions, and no particular issues with the PETS power production has been found to date. Figure 7.13 [19] illustrates the measurements for each coupler arm (15 MW total power), as well as the RF power as predicted from the measured beam current passing through the PETS. The agreement between measured and predicted RF power is very good, except towards the end of the pulse where the discrepancy could be explained by non-ideal bunch train combination in the combiner ring due to longitudinal dispersion.

7.2.5.3 Two-Beam Test Stand power production

In the Two-Beam Test Stand (TBTS) [20] a 1 m long PETS extracts RF power from the Drive Beam which is then transferred to an accelerating structure in the Probe Beam line. Figure 7.14 shows a sketch of the TBTS Drive Beam line. The TBTS PETS is equipped with a power recirculator which allows for the resonant build up of RF power. The recycling loop is equipped with a variable power splitter and RF phase shifter. With recirculator feedback coupling above zero the PETS will operate in the amplification mode, similar to the classical resonant rings, with the novelty that we now have a beam as an internal source of the RF power [12]. Depending on the recirculator parameter settings (namely the feedback coupling and recirculation circuit integrated phase advance) the PETS output peak power can reach levels more than 10 times higher compared to the case without recirculation. The extracted RF power can reach about factor of four in amplification. This gives greater flexibility in handling the

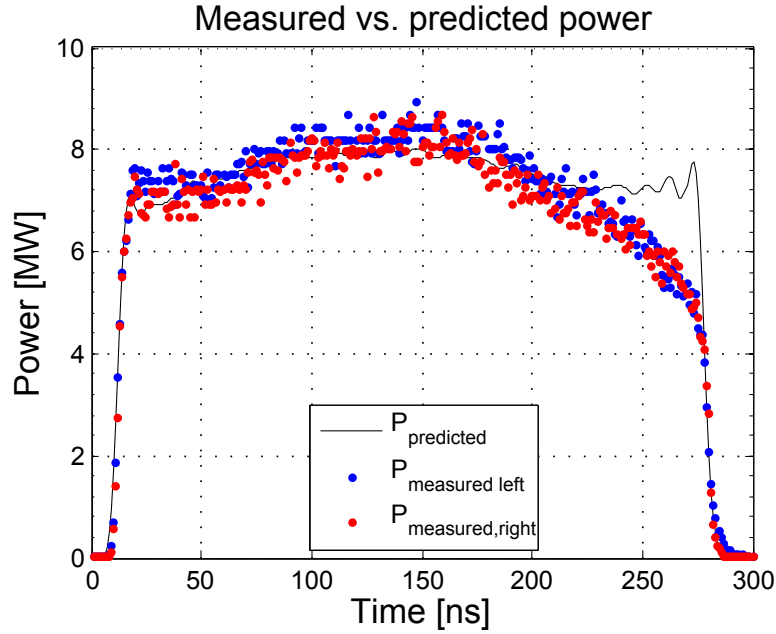


Fig. 7.13: Example of TBL PETS power measurements for each coupler arm (dotted), as well as the RF power as predicted from the measured beam current passing through the PETS (line). The agreement between measured and predicted RF power is very good, except towards the end of the pulse where the discrepancy could be explained by non-ideal bunch train combination in the combiner ring due to longitudinal dispersion.

RF power level delivered to the accelerating structure. In particular it gives the possibility to generate a CLIC parameter PETS RF pulse (135 MW, 240 ns) from the CTF3 Drive Beam [12]. Figure 7.15 depicts the TBTS PETS tank with the power recirculator installed, including the power splitter and phase shifter. The combined system, PETS plus recirculation loop, has been modeled in [14, 21] allowing for predictions of power production and deceleration with recirculation. Applications of this model to TBTS measurements can be found in [14, 21–24]. Figure 7.16 shows theoretical curves of PETS output power and extracted power for a Drive Beam of 9.5 A and a power split of 50%. These settings allow for both PETS high-power testing at the nominal power of 135 MW and powering of one accelerating structure at the nominal input power of 64 MW. Figure 7.17 shows measurements of power and deceleration for an 8 A current pulse together with the predicted power and deceleration using the recirculation model. The PETS output power is about 80 MW, while in comparison, the PETS output power without recirculation would be of the order of 15 MW.

The commissioning of the TBTS PETS with recirculation started in November 2008 with power levels up to 30 MW. The power level produced in the PETS was then increased according to the Drive Beam current and the experimental needs. Using a Drive Beam current of more than 15 A the PETS power routinely reached levels of more than 300 MW in the recirculation loop, twice the nominal PETS power. Figure 7.18 summarizes a total of 5×10^5 pulses from PETS operation during autumn 2010. Power levels above 300 MW are shown (for part of the run the RF signals were saturated). Highlighted in the figure is a period where the structure was operating with power levels about the nominal CLIC power, showing very small vacuum activity indicating a low breakdown rate at this power level. The analysis of the structure of the RF pulses during breakdown events showed evidence that in most of the cases, the activity was associated with waveguide components in the recirculation loop and not the PETS itself.

7.2 ACHIEVEMENTS

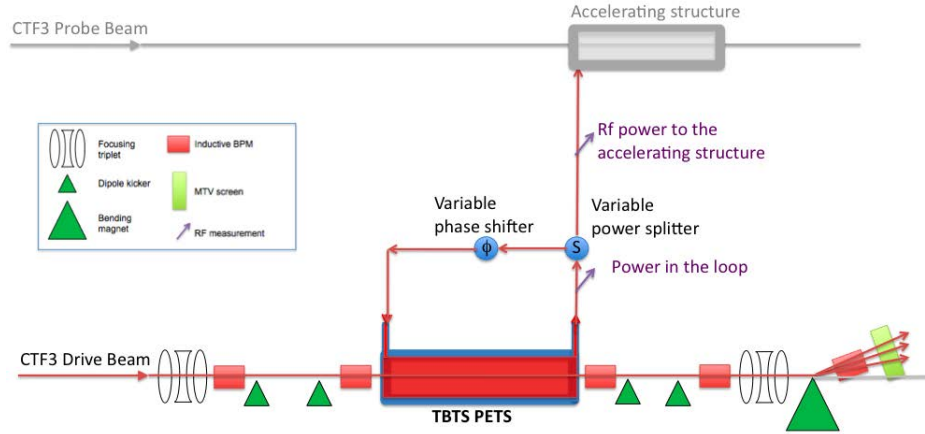


Fig. 7.14: Sketch of the TBTS Drive Beam line. The TBTS PETS is equipped with a power recirculator allowing for resonant build up of the RF power.



Fig. 7.15: The TBTS PETS tank with the power recirculator installed, including the variable power splitter and phase shifter

7.2.5.4 PETS ON/OFF high RF power demonstration with beam in CTF3

The PETS ON/OFF mechanism is required in CLIC in order to be able to switch on and off individual PETS whenever localized breakdowns threaten the normal machine operation. The system should also provide a gradual ramp-up of the generated power in order to reprocess either the main accelerating structure and/or the PETS itself. Therefore a suitable mechanism has been developed, based on an external high-power variable RF reflector [25], as illustrated in Fig. 7.19.

The reflector can be tuned to stop any power transfer to the accelerating structures, effectively preventing any further break-down in the structures. The reflected RF power is sent back to the PETS, where internal power recirculation is established by another (fixed) reflector placed at the PETS upstream end. The reflector positions are chosen such that the back-propagating power is in anti-phase with the forward one, achieving partial cancellation of the beam generated power inside the PETS as well. For the CLIC case, the RF power extracted from the Drive Beam in the PETS is suppressed down to 25% of its original value, which is expected to be enough to prevent or to reduce dramatically the probability of

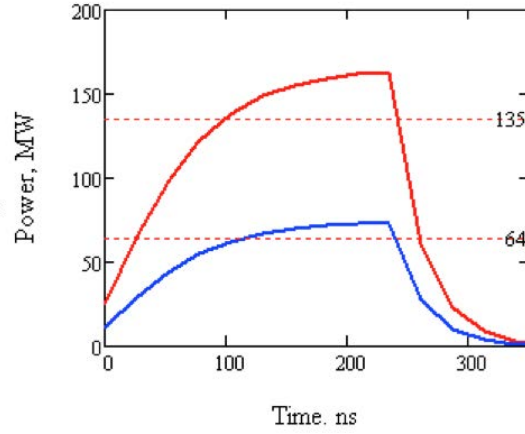


Fig. 7.16: Theoretical PETS power with a 9.5 A Drive Beam and 50% power split into the recirculating loop. The power circulating in the PETS (shown in red) builds up to above the nominal CLIC power of 135 MW, allowing for PETS high-power testing. A power levels above 64 MW, corresponding to the nominal accelerating structure power, can be extracted out of the loop (shown in blue).

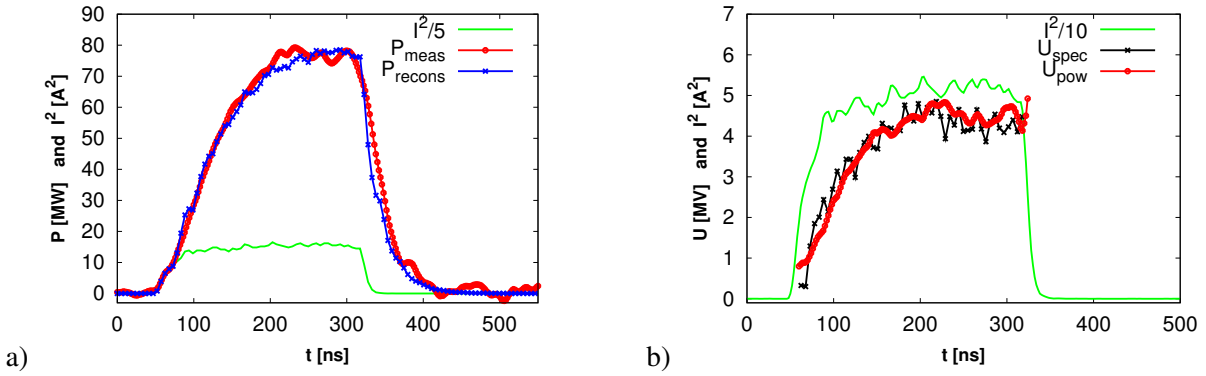


Fig. 7.17: Power (a) and deceleration (b) measurements for an 8 A current pulse together with the predicted power and deceleration using the recirculation model. The PETS output power is about 80 MW, while in comparison, the PETS output power without recirculation would be of the order of 15 MW.

RF breakdown in the PETS itself. The operational principle, layout and RF components developed for the local termination of the RF power production in a single PETS using the ON/OFF mechanism are described in detail in §5.5.2.3.

To do the test with beam in CTF3, we fabricated high-power prototypes of the variable RF reflector and variable RF short circuit. These components were installed on the TBTS PETS tank (see Fig. 7.20) in order to establish an internal recirculation RF circuit with the capability to control the coupling and RF phase advance in the loop.

At the very beginning the variable short circuit was set at the position that provided destructive phase advance in the loop for the case of full reflection in variable reflector. During experiments with beam, the variable reflector settings were changed gradually from full reflection to full transmission. The PR power signals produced by PETS and delivered to the accelerating structure were measured at different intermediate positions. The results are summarized in Fig. 7.21.

These experiments successfully demonstrated the PETS ON/OFF operational principle. They were in good agreement with computer simulations based on the low RF power measurements of all the RF

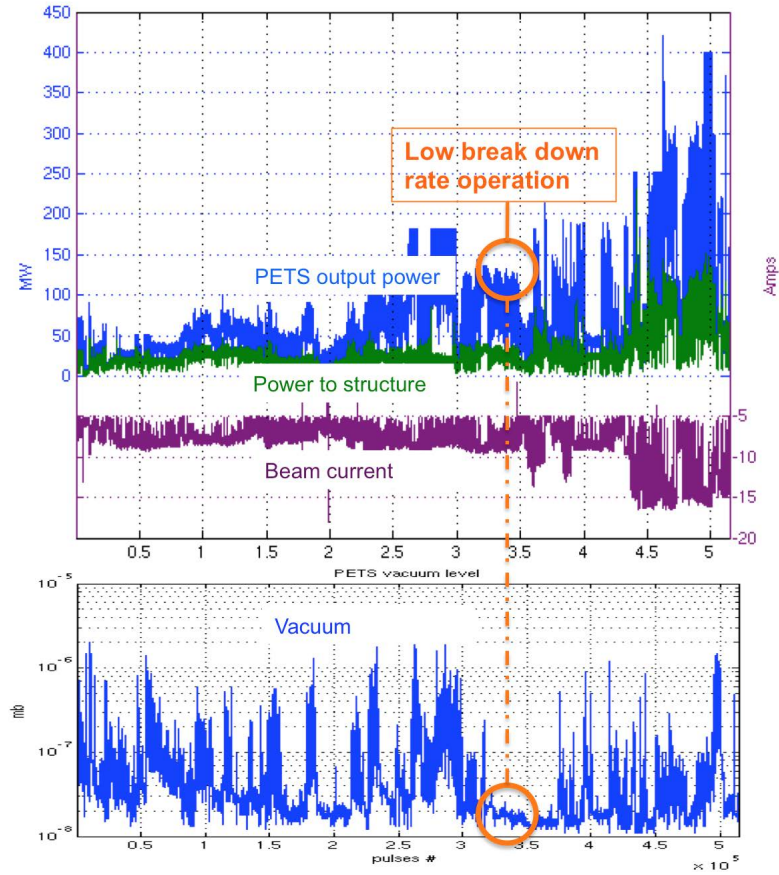


Fig. 7.18: Summary of power levels, Drive Beam current and vacuum levels for a total of 5×10^5 pulses from PETS operation during autumn 2010. Power levels above 300 MW are shown (for part of the run the RF signals were saturated). Highlighted in the figure is a period where the structure was operating with power levels about the nominal CLIC power, showing very small vacuum activity indicating a low breakdown rate at this power level.

components and the measured Drive Beam current pulse shape (see Fig. 7.22). However, the Drive Beam current limitation in CTF3 made it impossible for us to run the system at nominal CLIC RF power level. To demonstrate the power capability of the new RF components used in the ON/OFF RF circuit, we set recirculation parameters to their amplification mode, similar to the setup that was routinely used in TBTS PETS with external recirculation before [26]. Due to the system complexity we used the vacuum level measurements in the PETS tank to qualify the RF breakdown activity. The processing of the PETS with the ON/OFF circuit went rather fast. In about five days (2×10^5 pulses) the system was conditioned up to $130 \text{ MW} \times 200 \text{ ns}$. The processing history is summarized in Fig. 7.23 and Fig. 7.24.

To conclude, the PETS ON/OFF capability was successfully demonstrated in experiments with the Drive Beam in CTF3. Currently it is used to provide RF power for the two-beam experiments in the TBTS.

7.2.6 Two-beam operation and experiments

One of the key purposes of CTF3 is to demonstrate the CLIC two-beam acceleration scheme, in which RF power is produced efficiently from the Drive Beam and then transferred to high-gradient accelerating structures to accelerate the Main Beam (referred to as the Probe Beam in CTF3). For this purpose, the CTF3 facility contains the Two-Beam Test Stand (TBTS) and the injector linac CALIFES (Concept d'Accélérateur Linéaire pour Faisceaux d'Electrons Sondes), which provides the Probe Beam. The

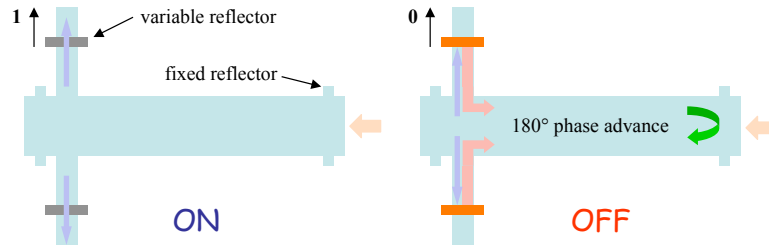


Fig. 7.19: Layout of the PETS ON/OFF mechanism

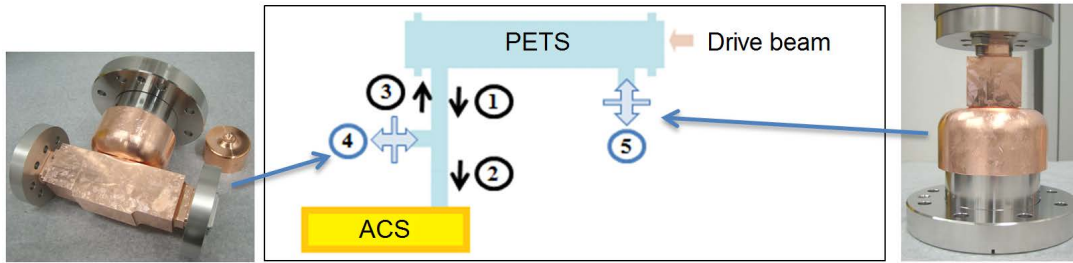


Fig. 7.20: Layout of the PETS ON/OFF setup in TBTS. The black arrows show RF power flows in the system: 1) RF power extracted from the PETS; 2) RF power transmitted to the accelerating structure; 3) RF power reflected back into the PETS. The new components are: 4) variable RF reflector; 5) variable RF short circuit.

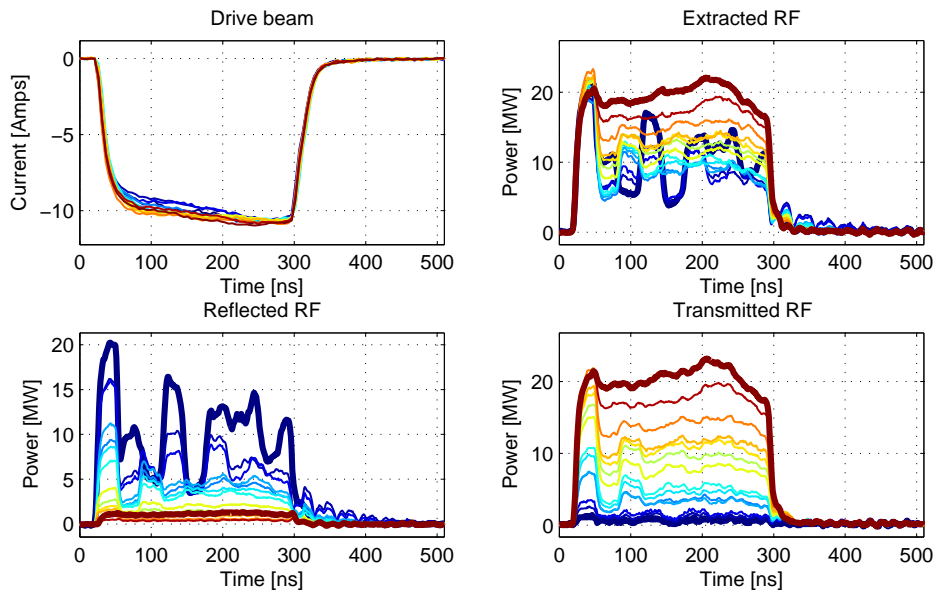


Fig. 7.21: TBTS PETS ON/OFF demonstration with beam. Here the coloured lines correspond to different setting of variable reflection. The colours are gradually changed from red (ON) to blue (OFF).

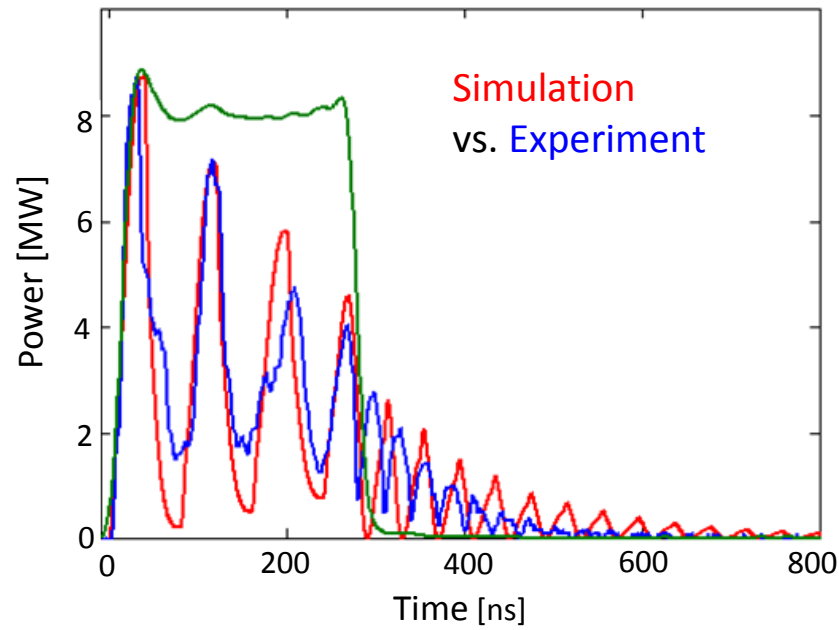


Fig. 7.22: The simulated (red) and measured (blue) RF pulses generated by PETS in the OFF state. The direct power production (ON state) is shown in green.

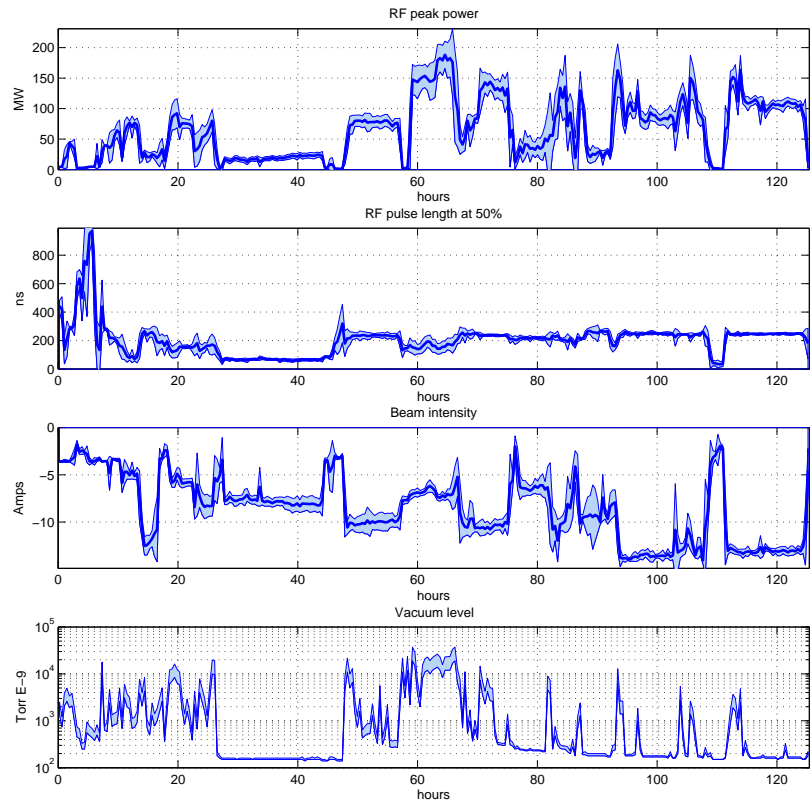


Fig. 7.23: The PETS ON/OFF processing history

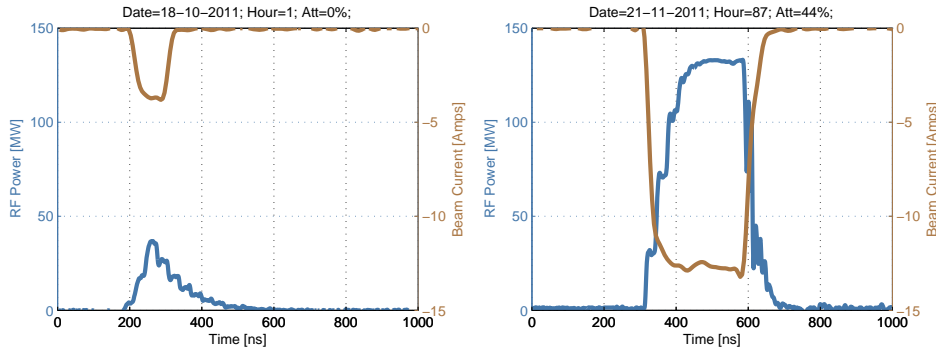


Fig. 7.24: Typical beam current and RF pulses shapes at the different stages of processing

Table 7.4: Main Parameters of the drive and Probe Beam in the TBTS

	Unit	Drive beam	Probe beam
Energy	MeV	120	200
Energy spread (r.m.s.)	%	2	1
Pulse length	ns	140–1100	0.6–150
Bunch frequency	GHz	1.5–15	1.5
Bunch charge	nC	up to 3	0.05–0.6
Intensity			
- short pulse	A	28	1
- long pulse	A	4	0.13
Repetition rate	Hz	0.8–5	0.8–5

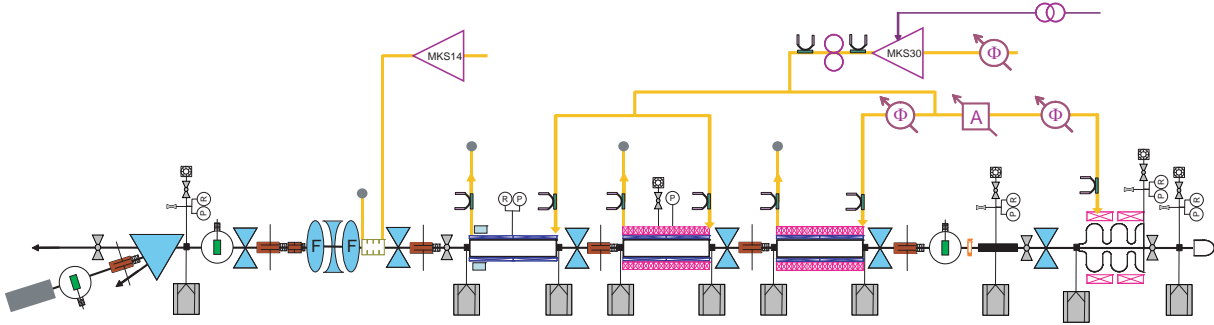


Fig. 7.25: Layout of the CALIFES Probe Beam linac and its RF power generation and distribution network

TBTS is the only facility available where CLIC type structures can be tested with beam. It is used for an extensive program to investigate both the PETS power production structures and high gradient accelerating structures. In the near future the TBTS will be adapted for testing up to three complete 2 m long CLIC test modules.

7.2.6.1 CALIFES Probe Beam Linac

The Probe Beam is generated in the 24 m long CALIFES injector linac, situated in CLEX like the TBTS. It has been developed by CEA Saclay, LAL Orsay and CERN to deliver single bunches and bunch trains at 1.5 GHz bunch repetition rate and energies up to 200 MeV (see Table 7.4). The layout of CALIFES is shown in Fig. 7.25 and its physical implementation in Fig. 7.26. CALIFES is based on three LEP In-



Fig. 7.26: Photo of the CALIFES Probe Beam linac installation in the CLEX hall [27]

jector Linac (LIL) 3 GHz accelerating structures one of which can be used as buncher [28]. The beam is generated in a photoinjector [29]. The Nd:YLF laser produces 1047 nm infra-red pulses at 1.5 GHz repetition rate, which are converted to green and then to ultra-violet before impinging on the photocathode [30]. The three LIL accelerating structures and the photoinjector are powered by a single 3 GHz klystron which delivers 45 MW RF pulses during $5.5 \mu\text{s}$ to an RF pulse compression cavity followed by an RF distribution network including high power splitters, two high power phase shifters and one attenuator.

Excellent beam quality is required for the high gradient acceleration tests in the TBTS. Therefore, just upstream of the TBTS, the end of the linac has been equipped with a diagnostics section to measure bunch train charge, energy, pulse length and beam emittance [31]. Six re-entrant cavity BPMs [32] are used together with three beam profile monitors and a beam current monitor. A 3 GHz traveling wave transverse deflecting cavity is used for bunch length measurements. A spectrometer line is available for beam energy measurements. The beam characteristics have been continuously improved since the first CALIFES run in December 2008.

The nominal bunch charge produced by the photo-injector is 0.6 nC, however for trains longer than 32 bunches the total beam charge is limited to 19.2 nC due to the beam loading in the LIL structures. CALIFES is usually operated with bunch charges of around 0.1 nC which can also be used for long bunch trains [33]. An new laser system is being developed to provide UV pulses with energy over $1 \mu\text{J}$, far beyond the present 220 nJ, to ease operation at higher charges.

Bunch lengths of the order of 1.4 ps have been measured, when using the first LIL structure in bunching mode, to be compared to the 6 ps laser pulse length on the cathode. When the first LIL structure is used in bunching mode, the Probe Beam energy is limited to 140 MeV. In full acceleration mode up to 200 MeV are obtained, albeit with longer bunch lengths. The energy spread can be tuned to less than 1% r.m.s.. A normalized beam emittance of 10 mm.mrad has been achieved [33].

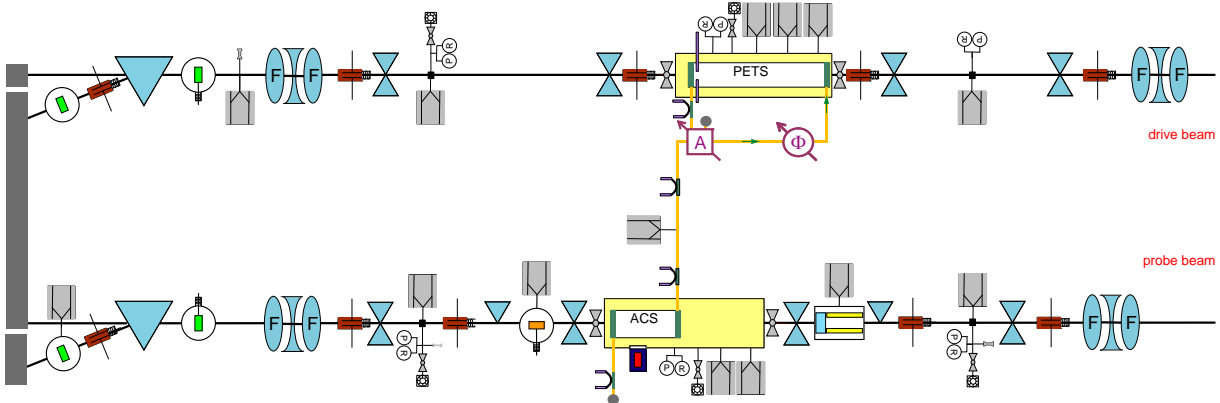


Fig. 7.27: Two-beam Test Stand layout including instrumentation, PETS, accelerating structure and RF network

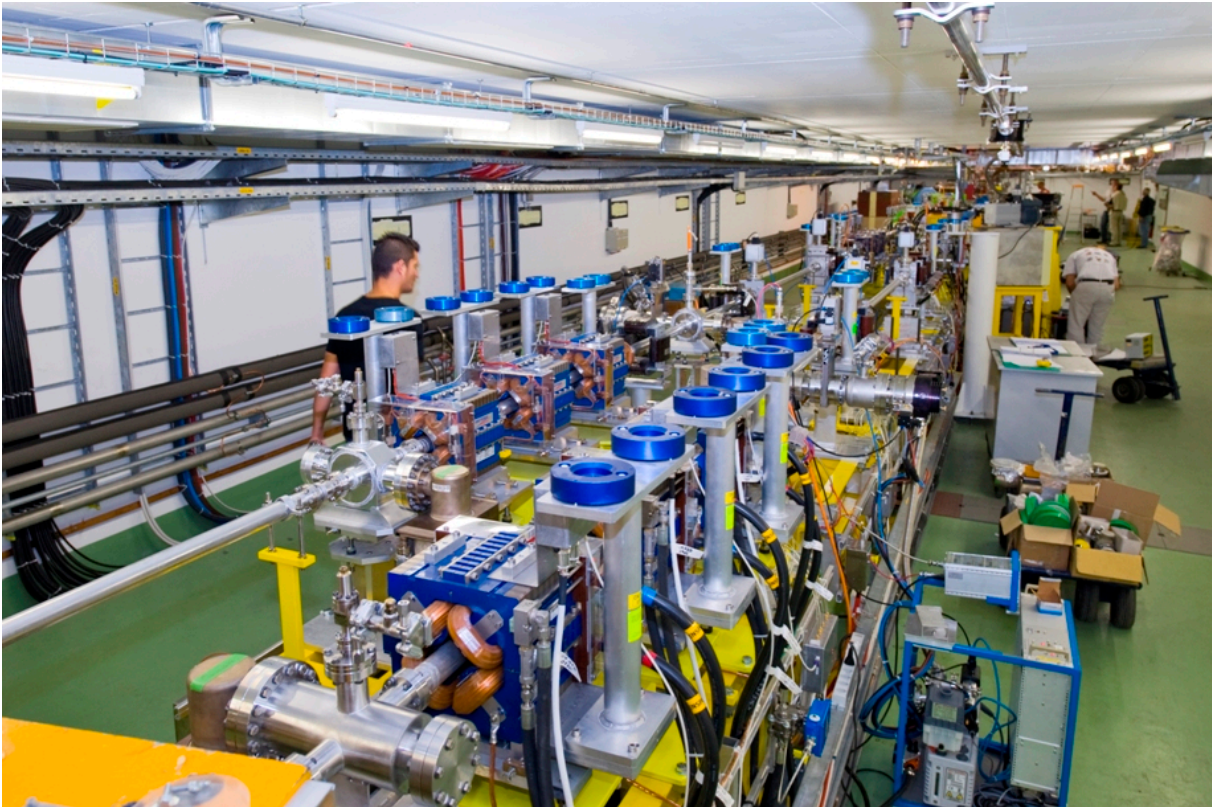


Fig. 7.28: Photo of the Two-beam Test Stand with the Drive Beam line (left) and Probe Beam line (right) [34]

7.2.6.2 Two-beam Test Stand (TBTS)

The TBTS was devised to demonstrate the feasibility of the two-beam acceleration concept and its key components [35]. It consists of two parallel beam lines as shown schematically in Fig. 7.27, fed respectively with the drive and the Probe Beam. The actual installation is shown in Fig. 7.28. In the central

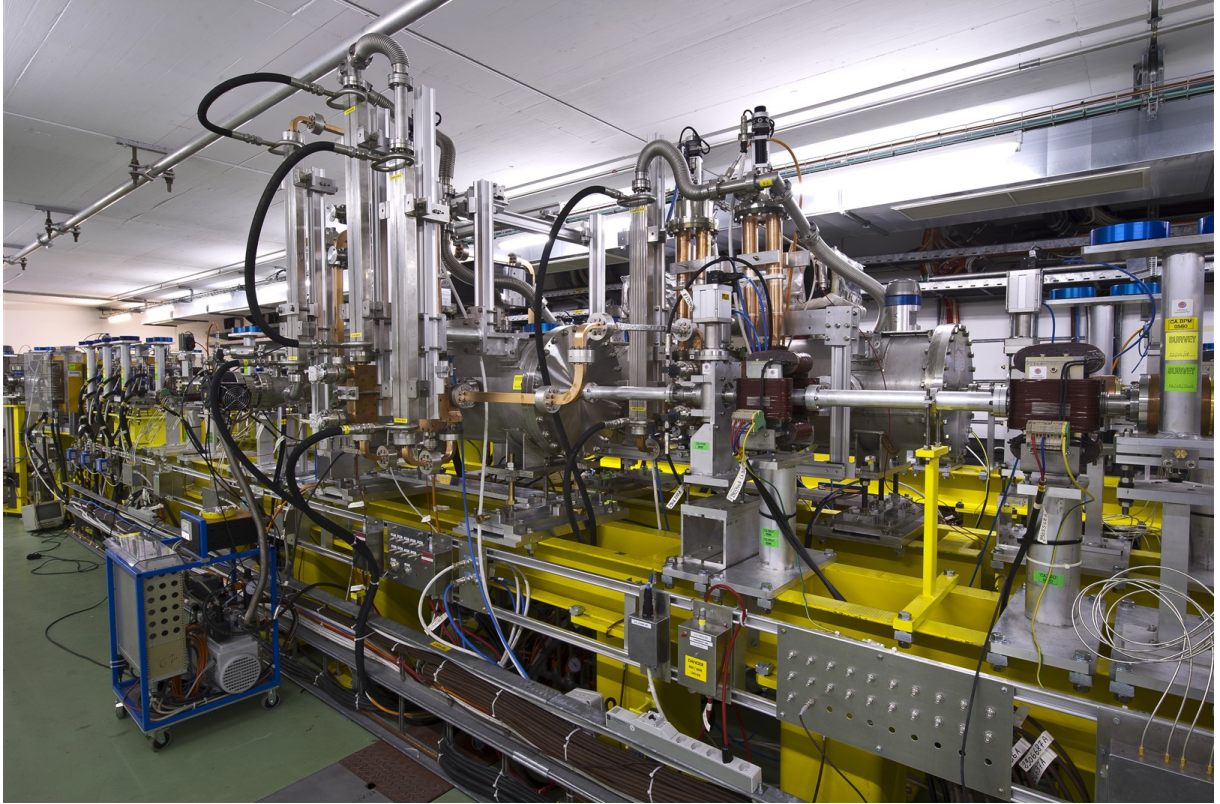


Fig. 7.29: Photo of the TBTS test area with vacuum tanks for the PETS (to the right) and accelerating structure (at the left) [27]

part of the TBTS, see Fig. 7.29, large vacuum tanks installed in the drive and Probe Beam lines contain a PETS and an accelerating structure respectively. The PETS decelerate the Drive Beam pulses providing RF power to the accelerating structure in the Probe Beam line. Instrumentation is available to investigate acceleration, wakefields and breakdown phenomena.

The TBTS PETS is a 1 m long 12 GHz RF structure in eight octants separated by damping slots in order to provide strong damping of transverse modes [12]. Two of the damping slots at 90° angle are equipped with a pick-up antenna to detect direct RF signals from the beam. The downstream end of the PETS is equipped with an output coupler. The initial configuration had an external waveguide loop, allowing for recirculation of the RF power in order to amplify it. Towards the end of the 2011 run the external recirculation circuit was replaced by an ON/OFF mechanism including external RF reflectors at both ends of the PETS [36].

During the 2010 and 2011 runs, the accelerating structure installed in the TBTS Probe Beam line was of the type TD24_vg1.8, a 24 cell detuned and damped design with a $2\pi/3$ phase advance and an active length of 20 cm. In addition, it has two matching cells and input/output couplers. It is designed to operate with nominal frequency $\nu_0 = 11.994$ GHz at a temperature of 30°C in vacuum to reach an accelerating gradient of 100 MV/m at an input power of approximately 45 MW (unloaded) [37].

7.2.6.3 Two-beam operation

During the 2009 run, the PETS produced over 170 MW peak in full RF re-circulation mode, well above the nominal 135 MW foreseen in CLIC, but in the presence of pulse shortening. The performance was limited by this effect, linked to RF breakdown in recirculation components such as a high power splitter and phase shifter. These parts were repaired and improved for the 2010 run, when RF power levels in

the 300 MW range were reached at the nominal pulse length. During the 2010 run the first two-beam acceleration of the Probe Beam was achieved. Figure 7.30 shows the Probe Beam energy while scanning its phase relative to the Drive Beam. The Probe Beam energy is measured in the spectrometer line as a

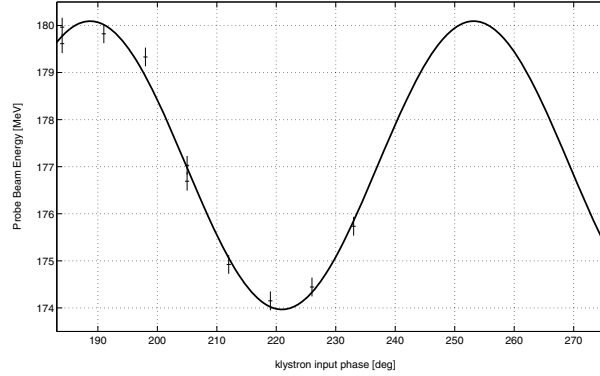


Fig. 7.30:

Probe beam energy after passing the accelerating structure as function of the CALIFES klystron phase input. During this experiment, the Probe Beam energy without acceleration was measured as 177 MeV. A relatively low RF power was used, corresponding to approximately 3 MeV of acceleration/deceleration.

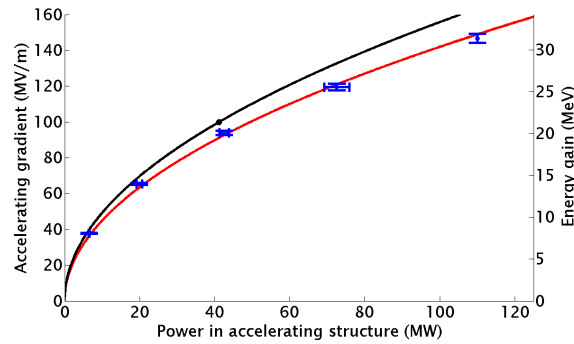


Fig. 7.31: Measured and nominal (black line) accelerating gradient as function of the RF input power for accelerating structure 12WSDVG1.8 (2011 run). The corresponding beam energy gain is given on the right hand axis.

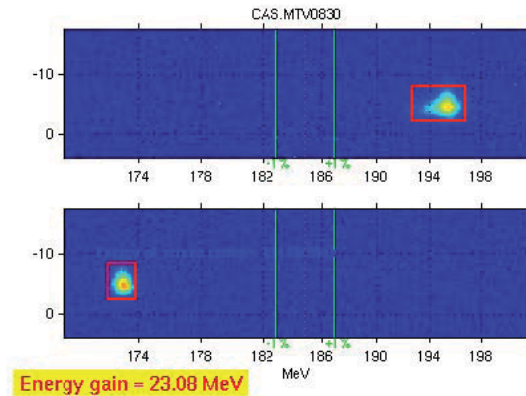


Fig. 7.32: Example Probe Beam acceleration in the TBTS with the 12 GHz RF power on (top) and off (bottom). The energy gain is 23.08 MeV which corresponds to a gradient of 106 MV/m in the accelerating structure.

7.2 ACHIEVEMENTS

function of the Probe Beam 3 GHz RF phase, which is phase-locked to the laser pulse timing. The phase scan is used to adjust the relative phase between Probe and Drive Beam for maximum acceleration.

The accelerating gradient and energy gain as function of the RF input power is shown in Fig. 7.31, and compared to the nominal specification of this structure (black line). The nominal CLIC accelerating gradient of 100 MV/m corresponds to a $\Delta E = 21.4$ MeV. The acceleration measurements were done using the spectrometer screen while running the Probe Beam at twice the repetition rate of the Drive Beam. Thus accelerated and non-accelerated beam energies can be measured alternatively. Figure 7.32 shows an example 23 MeV Probe Beam acceleration measured with the spectrometer screen, corresponding to an accelerating gradient of 106 MV/m. Note that due to screen size limitations it is only possible to monitor the accelerated and non-accelerated beam simultaneously when the energy gain is not more than ~ 27 MeV.

The RF input power is typically adjusted by extracting different turns in a factor 4 combined beam while for the highest accelerations PETS RF power recirculation (about 30%) was used, see Fig. 7.33. A

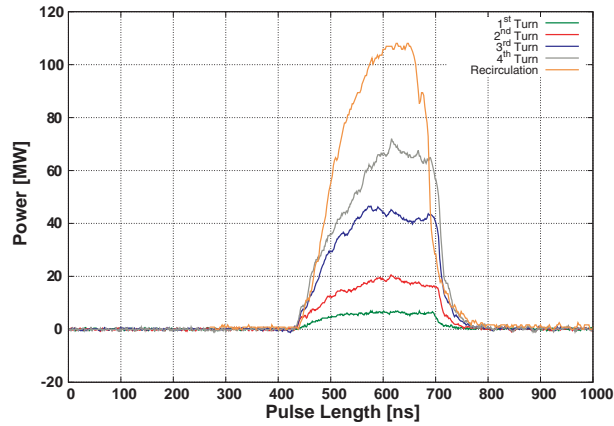


Fig. 7.33: RF input power signals for the different measurement points. The different power levels are produced by extraction of different turns from a 4 times recombined beam. In addition the highest power level was achieved by power recirculation in the PETS.

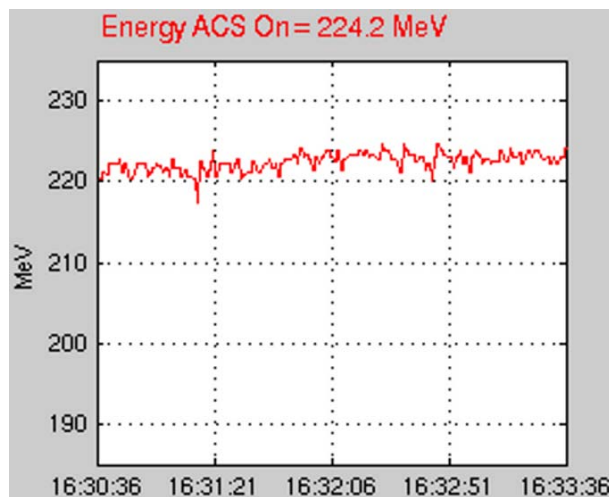


Fig. 7.34: Example of a high accelerating gradient operation with low breakdown rate. The image shows a set of 150 pulses during 3 minutes of operation. The non-accelerated beam energy was 192 MeV and the accelerated beam energy up to 224 MeV, i.e., an energy gain $\Delta E = 32$ MeV corresponding to an accelerating gradient of 147 MV/m.

difference of $\sim 20\%$ between the nominal and measured power-gradient curves is within the uncertainty of the calibration of the RF power measurement chain. Small phase and timing errors may also affect the result, even if during the measurements the phase and timing of the 20 ns long Probe Beam pulse were optimized for maximum acceleration.

Due to an extensive conditioning campaign during the 2011 run, energy gains of up to $\Delta E = 32$ MeV were achieved in the last month of operation with relatively low breakdown rate. Figure 7.34 shows an example run of three minutes with 150 pulses without breakdown. Accelerating gradients up to 165 MV/m were achieved during periods with higher breakdown rate.

7.2.6.4 RF Breakdown Studies

Due to the low pulse repetition rate of 0.8 Hz, very long run periods are required to condition the structure and acquire accurate RF breakdown statistics in the TBTS.

Figure 7.35 shows RF breakdown rates as measured during the 2011 run. The result of the conditioning process is clearly visible as the measured breakdown rates decreases over time as indicated

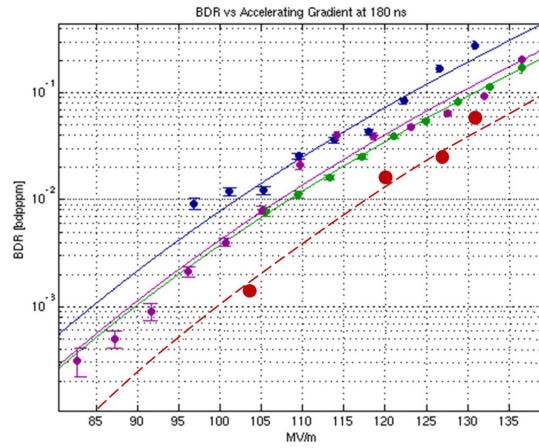


Fig. 7.35: RF breakdown rates as measured in the TBTS during the 2011 run. Different colours and lines linking data points indicate data sets taken at different periods in time. The large red dots represent the most recent data points.

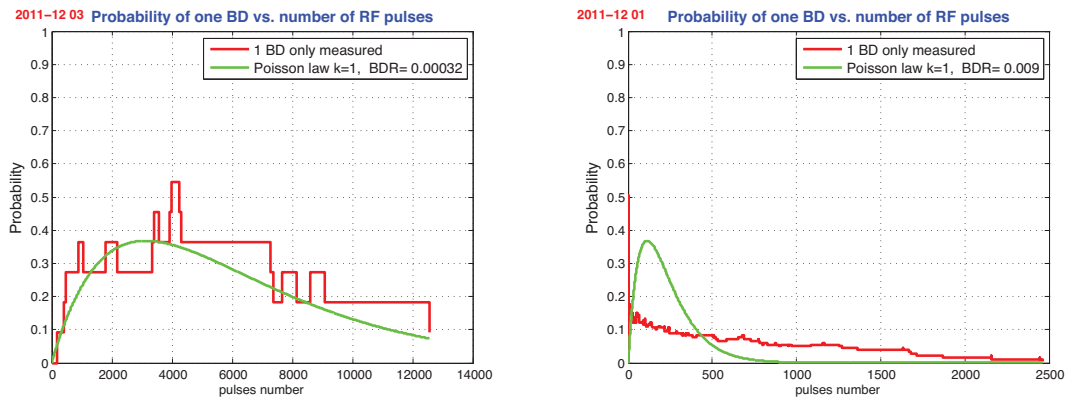


Fig. 7.36: Example of RF breakdown distribution from the 2011 run: Distribution of the number of pulses between breakdowns for a low and a high breakdown rate. The distribution follows a Poisson law (left). For a higher breakdown rate the distribution is dominated by the clustering of events and breakdowns are no longer independent. (right).

7.2 ACHIEVEMENTS

by the different lines linking the measurement data. It is difficult to compare this data with the one obtained from the klystron based measurements described in §5.5.1.3 because of the low repetition rate and amplitude stability of the beam based experiment. The data presented here corresponds to less than 24 hours of klystron-based RF conditioning and therefore reflects only the very beginning of the conditioning process. Note that for CLIC, breakdown rates in the order of 10^{-7} per metre per pulse are required. Most breakdowns were detected with the RF power signals measured with directional couplers in the waveguides before and after the accelerating structure by analyzing the waveforms of the forward, transmitted and reflected power. Pulse shortening and missing power can be detected like this. In addition, RF breakdown was detected with a photomultiplier sensitive to X-ray and visible light that was installed to view one of the cells in the accelerating structure. A Faraday cup, inserted at the outlet of the accelerating structure when the CALIFES Probe Beam was off, detected RF breakdown by means of measuring dark and breakdown currents.

It was noted that clusters of RF breakdowns appear at high breakdown rates, the RF breakdown probability is therefore increased after an RF breakdown. At lower breakdown rates, the distribution of RF breakdowns seems random, following a Poisson law, as shown in Fig. 7.36.

An RF breakdown is considered to stop the transmission of the RF wave in the travelling wave

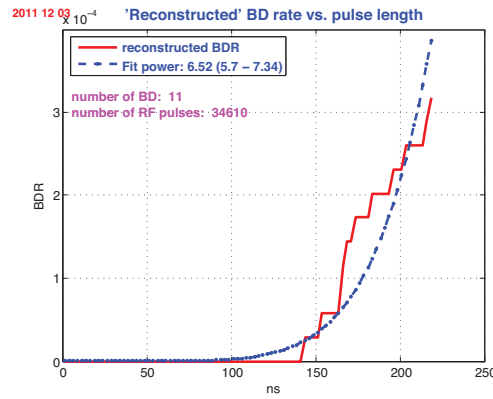


Fig. 7.37: RF breakdown rate versus exposure time. The data was fitted with a power law dependence.

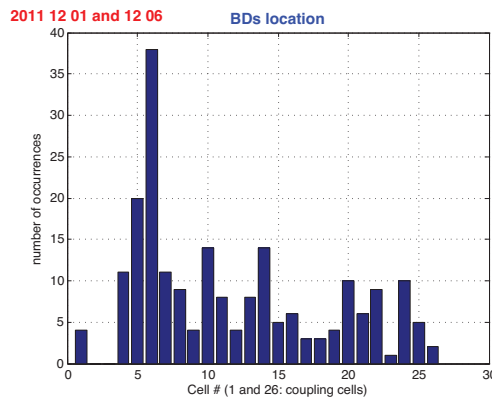


Fig. 7.38: Histogram of the breakdown location in the accelerating structure. The horizontal axis shows the time difference between the falling edge of the transmitted RF power pulse and the rising edge of the reflected RF power pulse. The red lines indicate the corresponding cell positions. The left hand histogram is based upon time difference between falling edge of transmitted RF pulse and rising edge of the reflected RF pulse. The right hand histogram is based upon time difference between the decay of the input RF signal and the reflected RF signal.

accelerating structure. The time and cell location of a breakdown can be determined from the RF signals. The time is given by the delay between the rising and falling edge of the RF output signal. Here we determine the rising edge as at half of the maximum value and the falling edge at 15% below the maximum value. Figure 7.37 shows the exposure time before a breakdown occurs and the RF breakdown rate as function of the exposure time with a power law fit. The breakdown rate dependence on RF pulse length found in klystron based experiments shows a similar exponent in the power law as discussed in §5.5.1.3. More details on the breakdown physics studies performed in the TBTS can be found in [38].

Various methods have been tried to determine the breakdown location within the structure. They are all based on the delay of signals indicating a breakdown to reach two different sensors preferably located at each side of the structure or signals propagating at different speeds. The signals indicating breakdown are: RF signals with their known group velocity along the structure and in the waveguides, the photomultiplier signal detecting X-rays and the emission of light, the Faraday cup signal detecting breakdown current (electrons) but which has uncertainties in the velocity. Among all possible pairs of these signals the most reliable seems to be the timing of the transmitted and reflected RF signals. The rising edge of the reflected RF power pulse associated with the falling edge of the transmitted RF power pulse allows the determination of the breakdown start location.

The breakdown location distribution as determined by this method is shown in Fig. 7.38 as a function of the cell number inside the accelerating structure. The peak in breakdown locations is at cell number five. This distribution is consistent with similar data measured at KEK on the same type of structure in a klystron based experiment. From the data taken so far it seems that the breakdown behavior in the two-beam situation is very similar to the klystron based experiments. The breakdown rate itself is not comparable because of the low repetition rate therefore an experiment using the CTF3 Drive Beam to load the structure with beam and RF at the same time with a high repetition rate klystron is in preparation to investigate this point in more detail.

7.2.6.5 Beam Orbit Kicks

Higher order modes and RF breakdowns in PETS and accelerating structures can affect the beam, modifying its orbit and energy. For the design of a stable two-beam accelerator it is important to understand these effects. The TBTS is equipped with beam position monitors before and after the PETS and accelerating structures. Thus transverse kicks in the beam orbit can be determined by using the beam position measurements as shown in Fig. 7.39. Five Beam Position Monitors (BPMs) [39] — two upstream and three downstream of the accelerator structure, the last one being in the spectrometer line — are used to measure beam orbit and energy, whereas a screen installed just before the spectrometer line is used to measure the beam spot. Any change in the beam trajectory on a single beam pulse during an RF breakdown in the accelerator structure is expected to show up as a step in the BPM traces, or as a modified (with respect to the unaffected beam) spot on the screen intercepting the beam.

The first measurements of the effects on the beam of RF breakdown in an accelerating structure are based on measurements of the beam spot with a YAG type beam screen situated just in front of

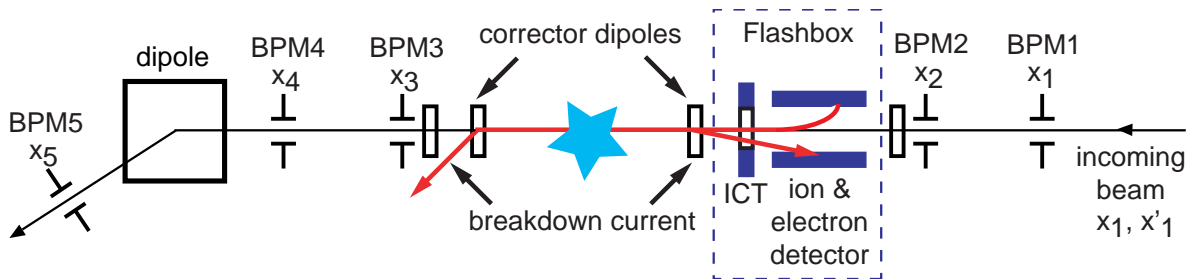


Fig. 7.39: Measurement set-up for RF breakdown and beam kick in the TBTS

7.2 ACHIEVEMENTS

the spectrometer line dipole. Double spots were occasionally measured as shown in (Fig. 7.40) on the same beam pulse which are explained as resulting from a change of the beam orbit during the pulse. In a preliminary analysis we consider the double spots that appeared on 35 breakdown events, recorded during 24 hours within a period of three days during Aug 2011. We plot the difference of the centre of gravity of the two spots which leads to the distribution shown in the compass plot in Fig. 7.41. The number of events is unfortunately too small to draw any firm conclusions. A more comprehensive analysis is ongoing. The magnitude of the measured kicks is about 0.13 mrad, which corresponds to a transverse momentum of about 25 keV/c in the accelerating structure. This estimation is consistent with previous measurements performed at SLAC [40].

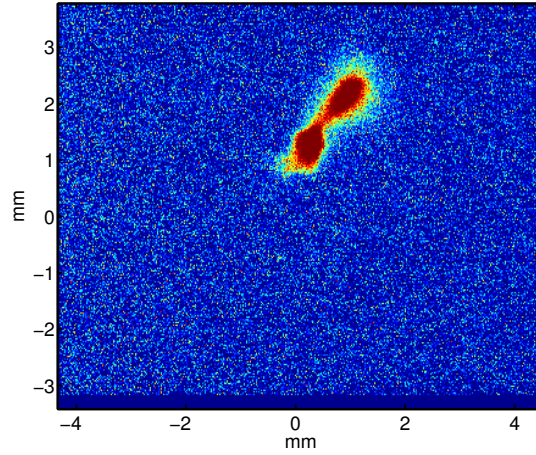


Fig. 7.40: Example of a double beam spot detected on a beam screen for the same Probe Beam pulse in correspondence with RF breakdown in the accelerating structure

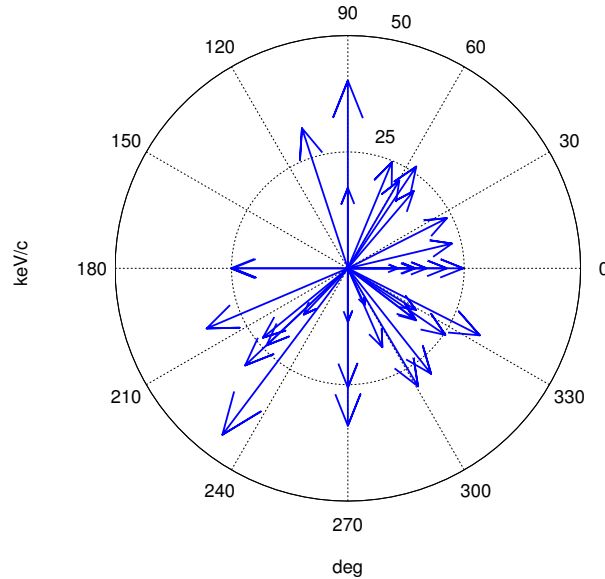


Fig. 7.41: Compass plot showing direction and transverse momentum of the kicks to the beam in correspondence of a breakdown in the accelerator structure. The transverse momentum is calculated considering the beam energy and the distance between the screen used for the measurement and the accelerator structure.

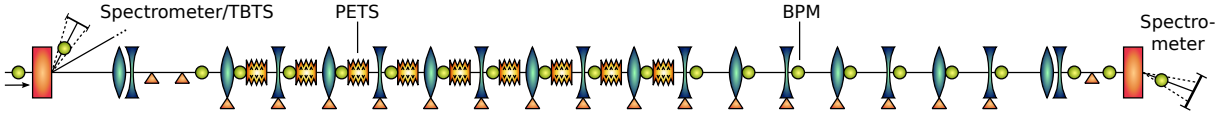


Fig. 7.42: Schematics of the test beam line showing the FODO-lattice with the PETS structures in the drift spaces and the diagnostic section before and after

7.2.6.6 Outlook for the near future

Future measurements based on the Beam Position Monitors will help to draw a more complete picture of the effects of RF breakdown, providing also temporal and energy information and a more accurate measurement of the kick. With a BPM resolution of $10\ \mu\text{s}$ it is expected to resolve transverse kick angles with $10\ \mu\text{rad}$ resolution [41]. The small steerer magnets before and after the structure can be used as a small chicane to remove the breakdown current from the Main Beam in order to minimize disturbance of the kick measurements in the BPMs.

Also higher order modes in the accelerating structures can cause transverse kicks of the beam orbit. Therefore several future accelerating structures will be installed with HOM monitors to study the possible relation between HOMs and beam kicks [42]. Diagnostics to measure the breakdown currents and their energy for emitted electrons and ions are in preparation. This is of special interest for the investigation of ions accompanying breakdown currents [43, 44].

During the 2012 run, the single accelerating structure will be replaced by two accelerating structures, each with a built-in wakefield monitor. Later on, the two-beam test area will be modified to install CLIC prototype two-beam modules for tests with beam.

7.2.7 Deceleration, Test Beam Line

The test beam line (TBL) was installed in the CLEX building of CTF3 to study the CLIC decelerator beam dynamics and 12 GHz power production. The beam line consists of a FODO lattice with high precision BPM's and quadrupoles on movers for precise beam alignment as shown in the schematic of Fig. 7.42.

A total of 16 Power Extraction and Transfer Structures (PETS) will be installed in between the quadrupoles to extract 12 GHz power from the Drive Beam provided by CTF3. The fully combined Drive Beam with a bunch-train length of 140 ns, 12 GHz bunch repetition frequency and an average current over the train of up to 28 A will be injected into the test beam line. Each PETS structure will produce 135 MW of 12 GHz power at nominal current corresponding to the nominal PETS output power in CLIC. The beam will have lost more than 50% of its initial energy of 150 MeV at the end of the beam line and will contain particles with energies between 65 MeV and 150 MeV. Table 7.5 compares beam parameters of TBL and CLIC.

The PETS in TBL have the same RF design as the CLIC PETS but their active length is a factor 4 longer compared to CLIC to compensate for the lower Drive Beam current. Therefore the end of the structure as well as the coupler will see the full nominal power of CLIC. The TBL lattice and the available diagnostics are comparable to the CLIC decelerator. The beam will fill 2/3 of the aperture after deceleration in TBL due to the much lower Drive Beam energy. Therefore the beam transport of the high energy spread beam is considered more challenging than in CLIC. On the other hand the effect of the wakefields will be smaller in TBL due to the much shorter decelerator. Due to the lower initial beam energy the maximum amount of beam energy which can be extracted in TBL is 54% compared to the 90% envisaged in CLIC.

The emphasis for the experimental program of TBL[17] will be on 12 GHz power production and the transport of the decelerated beam. It is essential for CLIC that the 12 GHz power production is

7.2 ACHIEVEMENTS

Table 7.5: Comparison of beam parameters for TBL and CLIC

Parameter [units]	Symbol	TBL	CLIC
Number of PETS	N_{PETS}	16	1492
Length of PETS [m]	L_{PETS}	0.80	0.21
Initial average current [A]	I_0	28	101
Power per PETS [MW]	P	~ 138	135
Initial energy [MeV]	E_0	150	2400
Mean energy extracted [%]	η_{extr}	~ 54	84
PETS sync. freq. [GHz]	f_{rf}	12	12
Number of FODO cells	N_{FODO}	8	524
Length of FODO cells [m]	L_{FODO}	2.82	2.01
Pulse length [ns]	t_{pulse}	140	240
Transient length [ns]	t_{fill}	3	1
Bunch length r.m.s. [mm]	σ_z	1.0	1.0
Init. norm. emittance [μm]	$\epsilon_N(x,y)$	150	150
Beampipe radius [mm]	a_0	11.5	11.5

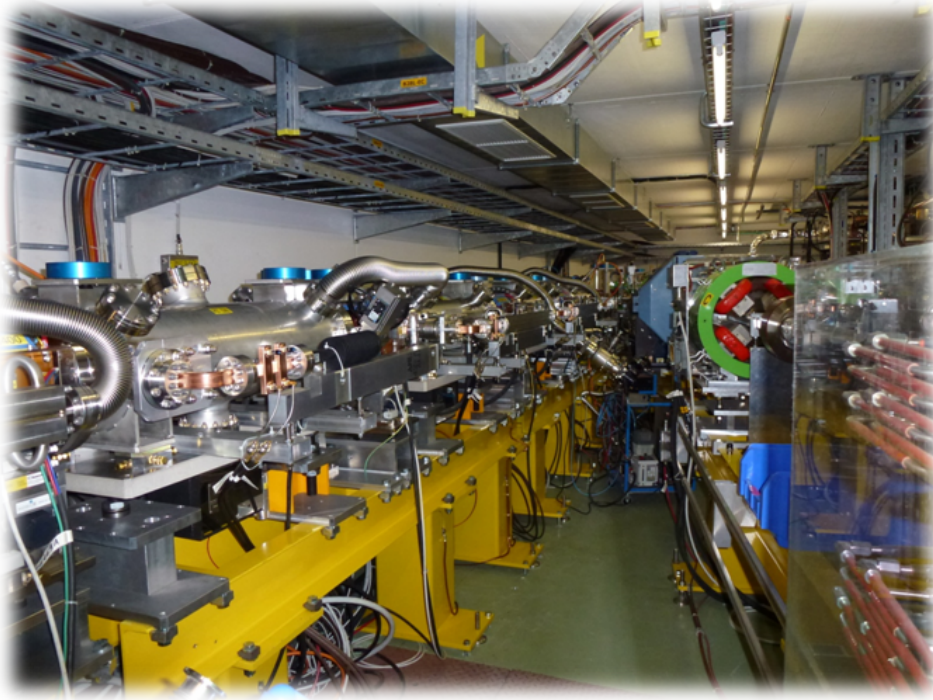


Fig. 7.43: Photo of the TBL beam line equipped with PETS tanks in the CLEX hall

efficient and stable. Therefore measurements of the energy balance of the produced RF power and the energy loss of the beam will be carried out. The stability of the produced power will be determined both in amplitude and phase. The quadrupoles have been installed on moving tables developed by CIEMAT [45] which allows positioning in the micrometer range. Beam based alignment studies are foreseen using the precision BPM's developed by IFIC Valencia and UPC Barcelona [46].

The beam line has been installed together with nine PETS tanks constructed by CIEMAT [47]

and CERN. Eight out of the nine PETS are equipped with HOM damping material. The commissioning of the beam line started at the end of 2009 [18]. Figure 7.43 shows a part of the beam line installed in the CLIC Test Facility at CERN. The maximum power produced so far was 70 MW per PETS or 630 MW total limited by the available beam current of 21 A. No sign of breakdown has been observed so far in the PETS. The beam was decelerated from 117 MeV by more than 30 MeV corresponding to about 26% of the beam energy extracted. The 12 GHz power produced by the beam agrees well with the theoretical predictions. To check the consistency of the power production and beam deceleration we can measure a time resolved beam spectrum at the end of the TBL line using a novel segmented dump [48]. Figure 7.44 shows a comparison of the time resolved energy measurement along the 140 ns long bunch train with the predicted energy profile from the 12 GHz power measurements and the beam current measurements. The three independent measurements are consistent assuming a bunch form factor of 0.95 for the prediction from the beam current and power measurements and a 10% calibration error in the 12 GHz power measurements. The form factor has been confirmed by bunch length measurements using a streak camera.

A first measurement of the BPM resolution measuring the trajectory of the beam in three consecutive BPMs to take out the effects of beam jitter has been performed. For a beam with 13 A average current, 9 μm resolution was measured corresponding well to the specified resolution of 5 μm for the nominal beam current of 28 A. The measured distribution of the residual error between the beam position measurements and the prediction from a set up with three consecutive BPM's is shown in Fig. 7.45. Beam based alignment studies have been started using the micrometric quadrupole movers. The beam could be aligned with a residual misalignment of 250 μm r.m.s. limited to date by beam jitter and residual dispersion coming from upstream of the beam line.

The test beam line is the ideal place to study the beam stability requirements for the CLIC Drive Beam. The current stability after Drive Beam generation as well as the stability of the 12 GHz power produced in terms of amplitude and phase can be measured directly. For a beam of 12 A obtained by a factor 4 combination in the combiner ring only, a current stability around 1% has been obtained regularly, the corresponding amplitude stability of the 12 GHz power scales roughly with the current squared. The phase stability along the pulse has been measured to be within 2° and the phase jitter pulse to pulse to

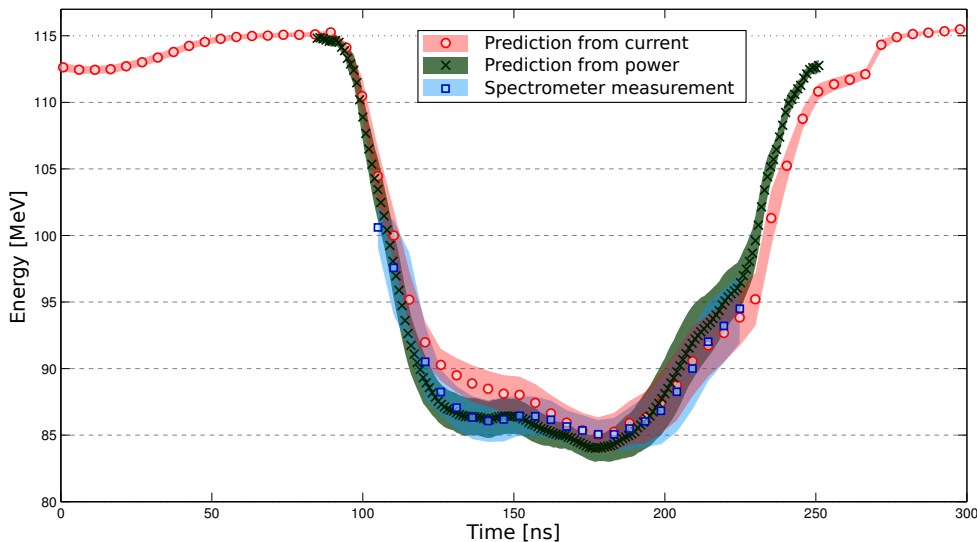


Fig. 7.44: Comparison between the measured time resolved energy profile of the beam along the pulse with a segmented beam dump and the predictions from beam current and power production measurements. The data points shown are the average of 48 consecutive pulse and the shaded areas indicate the standard deviation for the measurement over this pulses.

$\pm 5^\circ$. The pulse phase jitter likely comes from a timing jitter of the incoming beam in the ps range.

Four more PETS structures will be installed during the shutdown in March 2012 and the experiments will then be continued using a total of 13 consecutive deceleration structures.

7.2.8 CTF3 specific diagnostics

Diagnostics in the CTF3 complex have primarily been designed for CTF3 beam parameters and used to commission and optimize the performance of the CTF3 machine [49]. However, since the CTF3 Drive Beam is a small scale version of the proposed CLIC Drive Beam, it is natural that the CTF3 machine is also used as a test environment for CLIC-type beam diagnostics. A large fraction of the non-intercepting CTF3 instruments, such as the beam position monitors, beam loss monitors and longitudinal beam monitors, can be adapted for the CLIC Drive Beam parameters. However, because of the considerably higher bunch charge, higher beam energy and repetition rate in the CLIC Drive Beam, the CTF3 intercepting beam diagnostics, which are typically used for providing transverse beam size measurements (emittance and energy spread), would be of limited use for the CLIC Drive Beam (as discussed in §5.9.4).

7.2.8.1 Diagnostics for position measurements

There are 137 beam position monitors used in the CTF3 complex. The most abundant type, is the inductive pick-up that has been developed especially for CTF3 [39, 50]. The pickup detects the beam image current circulating on the vacuum chamber using eight electrodes. Several versions of this type of pick-up were designed, built and installed to match the size and shape of the vacuum chamber in the different parts of the CTF3 complex [46, 50, 51]. A 4 mm diameter aperture version of the pick-up [52] was built and tested at CTF3, with the aim of demonstrating the high-resolution needs of the Main Beam BPM. Although this technology has shown promising results on CTF3, it was not considered as the baseline solution for CLIC because it was estimated to be too expensive for the CLIC Drive Beam BPMs and not precise enough for CLIC Main Beam BPMs. More details on the beam position monitor for CLIC can be found in §5.9.2.

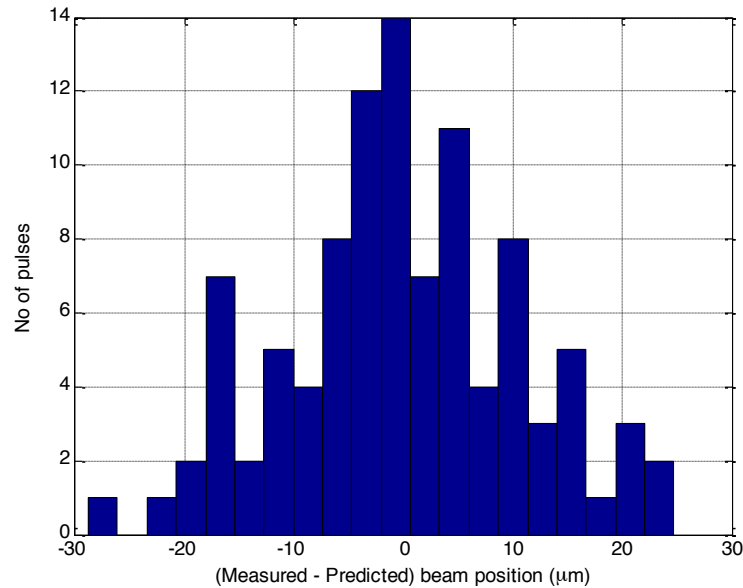


Fig. 7.45: Histogram of the residuals between the measured vertical beam position of the central BPM and the prediction from the two outer ones in a set up with three consecutive BPMs. The r.m.s. of the distribution is $9 \mu\text{m}$.

7.2.8.2 *Transverse profile measurements*

CTF3 has 21 operational optical transition radiation (OTR) based TV stations, in order to measure the transverse profile of the beam throughout the complex. These are used with the ‘quadrupole scan’ technique in regions of minimal dispersion to measure the average beam emittance and in spectrometer lines to measure the average energy spread. The imaging system can provide a resolution of up to $20\text{ }\mu\text{m}$, and when coupled to intensified gated cameras can provide time resolved transverse beam profiles. The latest OTR based TV stations installed in CTF3 are equipped with two screens for low and high charge operation respectively, a calibration target and a replacement chamber to ensure a continuity of the beam line, when the device is not in use, thus minimizing wakefield effects [49].

7.2.8.3 *Diagnostics for time resolved energy measurements*

In order to optimize the overall efficiency of the Drive Beam generation, the accelerating structures [6] are operated in a fully beam-loaded condition, meaning that all the RF power, except for ohmic losses, is transferred into beam energy. In this mode of operation, the resulting energy spectrum shows a strong time dependency, with higher energies in the first 10–50 ns of the pulse. Time-resolved spectrometry is therefore an essential beam diagnostic to correctly tune the timing of the RF pulses powering the accelerating structures in the linac. For this purpose segmented beam dumps [53] or multi-anode photomultipliers (MAPMT) [54] coupled to an OTR screen, were developed and are currently used for the daily optimization of the CTF3 Linac. A recently installed segmented beam dump for the CTF3 test beam line (TBL) has been designed to provide a time resolved measurement of the decelerated CTF3 Drive Beam [55]. A discussion on the possible applications of these segmented devices for CLIC with high beam power is presented in §5.9.8.

7.2.8.4 *Longitudinal beam diagnostics*

Longitudinal beam manipulation in the CTF3 and the CLIC Drive Beam are similar. Bunch length manipulation and bunch frequency multiplication has led to the development of adequate non-intercepting devices based on the detection of optical photons by a streak camera [56, 57] and on radio frequency pick-ups [58]. These devices are presented in detail in §5.9.5. Another technique for longitudinal beam profile measurements, which has already demonstrated extremely good time resolution (10 fs) [59], is based on RF deflecting cavities. As previously mentioned, such cavities are used in CTF3 for the RF injection in the Delay Loop and Combiner Ring. They can also serve for bunch length measurements [60]. However, in the present state of the CLIC beam instrumentation, RF deflectors have not been chosen as the baseline for bunch length measurements, because they are both costly and destructive to the beam passage.

REFERENCES

References

1. Bienvenu, G. *et al.* in *Proc. 8th European Particle Accelerator Conf.*, 3-7 June 2002, Paris, France (2002), 1753–1755. <<http://accelconf.web.cern.ch/accelconf/e02/PAPERS/TUPRI055.pdf>>.
2. Zhou, F. & Braun, H. *Optimisation of the CTF3 injector with 2 SHBs and 3SHBs* CTF3 Note 2000-01 (CERN, 2000). <<http://clic-study.web.cern.ch/CLIC-Study/CTF3/Notes/ctf3-001.pdf>>.
3. Thiery, Y., Gao, J. & LeDuff, J. in *Proc. XX Int.l Linac Conf.*, 21-25 August 2000, Monterey, CA, USA (2000), 95–97. <<http://epaper.kek.jp/l00/papers/MOB01.pdf>>.
4. Yeremian, A. *et al.* in *Proc. 8th European Particle Accelerator Conf.*, 3-7 June 2002, Paris, France (2002), 527–529. <<http://accelconf.web.cern.ch/accelconf/e02/PAPERS/MOPRI041.pdf>>.
5. Dabrowski, A. E. *et al.* in *Proc. 1st Int. Particle Accelerator Conf.*, 23-28 May 2010, Kyoto, Japan (2010), 1107–1109. <<http://accelconf.web.cern.ch/accelconf/IPAC10/papers/mope058.pdf>>.
6. Jensen, E. in *Proc. XXI Int. Linear Accelerator Conf.*, 19-23 August 2002, Gyeongju, Korea (2002), 34–36. <<http://accelconf.web.cern.ch/accelconf/l02/AUTINDEX/..%5CPAPERS%5CMO401.PDF>>.
7. Corsini, R. *et al.* in *Proc. 9th European Particle Accelerator Conf.*, 5-9 July 2004, Lucerne, Switzerland (2004), 39–41. <<http://accelconf.web.cern.ch/accelconf/e04/PAPERS/MOOCH02.PDF>>.
8. Braun, H. *et al.* in *Proc. 2006 Linear Accelerator Conf.*, 20-25 August 2006, Knoxville, Tennessee, USA (2006), 31–33. <<http://accelconf.web.cern.ch/accelconf/l06/PAPERS/MOP002.PDF>>.
9. Schulte, D. *et al.* in *Proc. XXV Linear Accelerator Conf.*, 12-17 September 2010, Tsukuba, Japan (2010), 103–105. <<http://accelconf.web.cern.ch/accelconf/LINAC2010/papers/mop024.pdf>>.
10. Dubrovskiy, A. & Tecker, F. in *Proc. 1st Int. Particle Accelerator Conf.*, 23-28 May 2010, Kyoto, Japan (2010), 3774–3776. <<http://accelconf.web.cern.ch/AccelConf/IPAC10/papers/thpea043.pdf>>.
11. Syratcev, I., Adli, E., Schulte, D. & Taborelli, M. in *Proc. 22nd Particle Accelerator Conf.*, 25-29 June 2007, Albuquerque, New Mexico, USA (2007), 2194–2196. <<http://accelconf.web.cern.ch/accelconf/p07/PAPERS/WEPMN071.PDF>>.
12. Syratcev, I., Riddone, G. & Tantawi, S. in *Proc. 11th European Particle Accelerator Conf.*, 23-27 June 2008, Genoa, Italy (2008), 1909–1911. <<http://accelconf.web.cern.ch/accelconf/e08/papers/weobg01.pdf>>.
13. Syratcev, I. *et al.* in *Proc. 23rd IEEE Particle Accelerator Conf.*, 4-8 May 2009, Vancouver, British Columbia, Canada (2009), 1873–1875. <<http://accelconf.web.cern.ch/accelconf/PAC2009/papers/we3rac02.pdf>>.
14. Adli, E. *A Study of the Beam Physics in the CLIC Drive Beam Decelerator* (University of Oslo, 2009). <<http://cdsweb.cern.ch/record/1239173/files/CERN-THESIS-2010-024.pdf>>.
15. Schulte, D. & Syratcev, I. in *Proc. 21st IEEE Particle Accelerator Conf.*, 16-20 May 2005, Knoxville, Tennessee, USA (2005), 1177–1179. <<http://accelconf.web.cern.ch/accelconf/p05/PAPERS/RPPP010.PDF>>.

16. Syratcev, I. *et al.* in *Proc. 23rd IEEE Particle Accelerator Conf., 4-8 May 2009, Vancouver, British Columbia, Canada* (2009), 1873–1875. <<http://accelconf.web.cern.ch/accelconf/PAC2009/papers/we3rac02.pdf>>.
17. Adli, E. *et al.* in *Proc. 1st Int. Particle Accelerator Conf., 23-28 May 2010, Kyoto, Japan* (2010), 4410–4412. <<http://accelconf.web.cern.ch/accelconf/IPAC10/papers/thpd056.pdf>>.
18. Doebert, S. *et al.* in *Proc. XXV Linear Accelerator Conf., 12-17 September 2010, Tsukuba, Japan* (2010), 85–87. <<http://accelconf.web.cern.ch/accelconf/LINAC2010/papers/mop018.pdf>>.
19. Lillestoel, R. *Power production experiments at the Test Beam Line in the CLIC Test Facility 3* CERN-THESIS-2010-246 (Norwegian University of Science and Technology, Trondheim, Norway, 2009). <<http://cdsweb.cern.ch/record/1392630/files/CERN-THESIS-2010-246.pdf>>.
20. Ruber, R. J. M. Y., Ziemann, G. V., Ekeloef, T., Johnson, M. & *et al.* in *Proc. 11th European Particle Accelerator Conf., 23-27 June 2008, Genoa, Italy* (2008), 2821–2823. <<http://accelconf.web.cern.ch/accelconf/e08/papers/wepp139.pdf>>.
21. Ruber, R. & Ziemann, V. *An Analytical Model for PETS Recirculation* CTF3-Note-092 (CERN, 2009). <<http://ctf3-tbts.web.cern.ch/ctf3-tbts/reports/recirculation4.pdf>>.
22. Adli, E. *et al.* in *Proc. 9th European Workshop on Beam Diagnostics and Instrumentation for Particle Accelerators, 25-27 May, 2009, Basel, Switzerland* (2009), 113–115. <<http://accelconf.web.cern.ch/accelconf/d09/papers/mopd29.pdf>>.
23. Adli, E. *Analysis of the first 12 GHz PETS tests with beam using a constant parameter recirculation model* CTF3-Note-096 (CERN, Geneva, 2009). <<http://clic-study.web.cern.ch/CLIC-Study/CTF3/Notes/CTF3Note096.pdf>>.
24. Hellenthal, C. *PETS Conditioning and RF Breakdown Analysis* CERN-OPEN-2010-010. CLIC-Note-811 (CERN, Geneva, 2010). <<http://cdsweb.cern.ch/record/1248704/files/CERN-OPEN-2010-010.pdf>>.
25. Syratcev, I. & Cappelletti, A. in *Proc. 1st Int. Particle Accelerator Conf., 23-28 May 2010, Kyoto, Japan* (2010), 3407–3409. <<http://accelconf.web.cern.ch/accelconf/IPAC10/papers/wepe026.pdf>>.
26. Adli, E. *et al.* X-band rf power production and deceleration in the two-beam test stand of the Compact Linear Collider test facility. *Phys. Rev. ST Accel. Beams* **14**, 081001 (2011).
27. Brice, M. *The CLIC Test Facility* CERN. <<http://cdsweb.cern.ch/record/1269610?ln=ru>> (2010).
28. Mosnier, A. *et al.* in *Proc. 10th European Particle Accelerator Conf., 26-30 June 2006, Edinburgh, Scotland, UK* (2006), 679–681. <<http://accelconf.web.cern.ch/accelconf/e06/PAPERS/MOPLS059.PDF>>.
29. Brossard, J., Desmons, M., Mercier, B. M., Prevost, C. P. & Roux, R. in *Proc. 10th European Particle Accelerator Conf., 26-30 June 2006, Edinburgh, Scotland, UK* (2006), 828–830. <<http://accelconf.web.cern.ch/accelconf/e06/PAPERS/MOPLS114.PDF>>.
30. Peauger, F., Bogard, d., Cheymol, G., Contrepois, P. & *et al.* in *Proc. XXIV Linear Accelerator Conf., 29 September - 3 October 2008, Victoria, British Columbia, Canada* (2008), 389–391. <<http://accelconf.web.cern.ch/accelconf/LINAC08/papers/tup004.pdf>>.

REFERENCES

31. Farabolini, W., Bogard, D., Brabant, A., Curtoni, A. & et al. in *Proc. 8th European Workshop on Beam Diagnostics and Instrumentation for Particle Accelerators*, 20-23 May 2007, Venice, Italy (2007), 99–101. <<http://accelconf.web.cern.ch/accelconf/d07/papers/tupb17.pdf>>.
32. Simon, C. S., Bogard, D. & Luong, M. in *Proc. 23rd IEEE Particle Accelerator Conf.*, 4-8 May 2009, Vancouver, British Columbia, Canada (2009), 3479–3481. <<http://accelconf.web.cern.ch/accelconf/PAC2009/papers/th5rfp024.pdf>>.
33. Ruber, R. et al. in *Proc. XXV Linear Accelerator Conf.*, 12-17 September 2010, Tsukuba, Japan (2010), 46–48. <<http://accelconf.web.cern.ch/accelconf/LINAC2010/papers/mop001.pdf>>.
34. Marcelloni, C. *The Two-beam Test Stand CERN*. <<http://ctf3-tbts.web.cern.ch/ctf3-tbts/photos/20080724/>> (2008).
35. Ruber, R. J. M. Y., Ziemann, G. V., Ekeloef, T., Johnson, M. & et al. in *Proc. 11th European Particle Accelerator Conf.*, 23-27 June 2008, Genoa, Italy (2008), 2821–2823. <<http://accelconf.web.cern.ch/accelconf/e08/papers/wepp139.pdf>>.
36. Syrathev, I. & Cappelletti, A. in *Proc. 1st Int. Particle Accelerator Conf.*, 23-28 May 2010, Kyoto, Japan (2010), 3407–3409. <<http://accelconf.web.cern.ch/accelconf/IPAC10/papers/wepe026.pdf>>.
37. Grudiev, A. *RF design and parameters of 12 GHz TD24-vgl.8-disk* EDMS 1070498 v.1 (CERN, Geneva, 2010). <https://edms.cern.ch/file/1070498/1/TD24_vglp8_disk.pdf>.
38. Farabolini, W. *Breakdown analysis of the TD24 accelerating structure installed in the CTF3/TBTS high gradient test stand* CLIC-Note-941 (CERN, 2012).
39. Gasior, M. in *Proc. 6th European Workshop on Beam Diagnostics and Instrumentation for Particle Accelerators*, 5-7 May 2003, Mainz, Germany (2003), 53–55. <<http://accelconf.web.cern.ch/accelconf/d03/papers/CT01.pdf>>.
40. Dolgashev, V. A. & Raubenheimer, T. in *Proc. XXII International Linear Accelerator Conf.*, 6-20 August, 2004, Lubeck, Germany (2004), 396–398. <<http://accelconf.web.cern.ch/accelconf/l04/PAPERS/TUP56.PDF>>.
41. Johnson, M., Ekeloef, T., Ruber, R., Ziemann, V. G. & Braun, H. in *Proc. 11th European Particle Accelerator Conf.*, 23-27 June 2008, Genoa, Italy (2008), 2800–2802. <<http://accelconf.web.cern.ch/accelconf/e08/papers/wepp131.pdf>>.
42. Peauger, F., Farabolini, W., Girardot, P. & et al. in *Proc. XXV Linear Accelerator Conf.*, 12-17 September 2010, Tsukuba, Japan (2010), 641–643. <<http://accelconf.web.cern.ch/accelconf/LINAC2010/papers/tup098.pdf>>.
43. Ziemann, V. The arrival-time spectrum of hot Coulomb explosions. *Nucl. Instr. and Meth. A* **575**, 539–541 (2007).
44. Johnson, M., Ruber, R., Ziemann, V. & Braun, H. Arrival time measurements of ions accompanying RF breakdown. *Nucl. Instr. and Meth. A* **595**, 568–571 (2008).
45. Toral, F. et al. in *Proc. 11th European Particle Accelerator Conf.*, 23-27 June 2008, Genoa, Italy (2008), 1517–1519. <<http://accelconf.web.cern.ch/accelconf/e08/papers/tupd040.pdf>>.
46. Garcia Garrigos, J. J. *Design and Construction of a Beam Position Monitor Prototype for the Test Beam Line of the CTF3* CLIC-Note-769 (Universitat Politècnica de Valencia, Valencia, Spain, 2008). <<http://cdsweb.cern.ch/record/1164156/files/CERN-OPEN-2009-002.pdf>>.

47. Toral, F. *et al.* in *Proc. 1st Int. Particle Accelerator Conf., 23-28 May 2010, Kyoto, Japan* (2010), 3768–3770. <<http://accelconf.web.cern.ch/accelconf/IPAC10/papers/thpea041.pdf>>.
48. Olvegaard, M. & *et al.* *Beam Profile Monitoring at the Test Beam Line at CTF3 (to be published in Phys. Rev. ST- AB)*
49. Lefevre, T. in *Beam Instrumentation Workshop, 4-8 May, 2008, Lake Tahoe, California, USA* (2008), 323–325. <<http://accelconf.web.cern.ch/accelconf/BIW2008/papers/weiotio02.pdf>>.
50. Gasior, M. in *Proc. 7th European Workshop on Beam Diagnostics and Instrumentation for Particle Accelerators, 6-8 June 2005, Lyon, France* (2005), 175–177. <<http://accelconf.web.cern.ch/accelconf/d05/PAPERS/POT014.PDF>>.
51. Stella, A., Ghigo, A., Marcellini, F. & Zolla, A. *Design of a Beam Position Monitor for the CTF3 Combiner Ring CTFF3-008* (INFN-LNF, Frascati, 2002). <<http://www.lnf.infn.it/acceleratori/ctf3/ctff3notes/CTFF3-008.pdf>>.
52. Soby, L., Guillot-Vignot, F. & Podadera, I. in *Proc. 23rd IEEE Particle Accelerator Conf., 4-8 May 2009, Vancouver, British Columbia, Canada* (2009), 3534–3536. <<http://accelconf.web.cern.ch/accelconf/PAC2009/papers/th5rfp039.pdf>>.
53. Lefevre, T., Braun, H., Bravin, E., Dutriat, C. & Welsch, C. P. in *Proc. 8th European Workshop on Beam Diagnostics and Instrumentation for Particle Accelerators, 20-23 May 2007, Venice, Italy* (2007), 340–342. <<http://accelconf.web.cern.ch/accelconf/d07/papers/wepc14.pdf>>.
54. Lefevre, T. *et al.* in *Proc. 10th European Particle Accelerator Conf., 26-30 June 2006, Edinburgh, Scotland, UK* (2006), 1205–1207. <<http://accelconf.web.cern.ch/accelconf/e06/PAPERS/TUPCH083.PDF>>.
55. Olvegaard, M. *et al.* in *Proc. 1st Int. Particle Accelerator Conf., 23-28 May 2010, Kyoto, Japan* (2010), 1113–1115. <<http://accelconf.web.cern.ch/accelconf/IPAC10/papers/mope060.pdf>>.
56. Welsch, C. P. *et al.* Longitudinal beam profile measurements at CTF3 using a streak camera. *J. Instrum.* **1**, 09002 (2006).
57. Welsch, C., Bravin, E. & Lefevre, T. *Layout of the Long Optical Lines in CTF3* CTF3 Note 072 (CERN, 2006). <<http://clic-study.web.cern.ch/CLIC-Study/CTF3/Notes/CTF3Note072.pdf>>.
58. Dabrowski, A. E., Adli, E., Bettoni, S., Corsini, R. & *et al.* in *Proc. XXV Linear Accelerator Conf., 12-17 September 2010, Tsukuba, Japan* (2010), 647–649. <<http://accelconf.web.cern.ch/accelconf/LINAC2010/papers/tup100.pdf>>.
59. Emma, P., Frisch, J. & Krejcik, P. *A Transverse RF Deflecting Structure for Bunch Length and Phase Space Diagnostics* LCLS-TN-00-12. SLAC-PUB-8864 (SLAC, Stanford, CA, USA, 2000). <<http://www-ssrl.slac.stanford.edu/lcls/technotes/lcls-tn-00-12.pdf>>.
60. Ghigo, A. *et al.* in *Proc. 21st IEEE Particle Accelerator Conf., 16-20 May 2005, Knoxville, Tennessee, USA* (2005), 785–787. <<http://accelconf.web.cern.ch/accelconf/p05/PAPERS/RPPP001.PDF>>.

Chapter 8

Energy Scanning



A. Yeats

8.1 Overview: CLIC operation at low energies

To access the full range of physics results, CLIC must be able to operate at different centre-of-mass energies, although the detailed requirements will depend on physics. In particular, CLIC must first be operated at full energy to discover new particles and then at lower energies to perform threshold scans to further study the properties of these particles. The possibility to operate at lower energy is thus a requirement on the design from the very beginning. The following presents the current baseline solution for CLIC, which is taken from Ref. [1].

This discussion is focused on significant changes in energy to new operating points. Small changes of a few percent during a threshold scan are performed by simply adjusting the accelerating gradient (by adjusting the Drive Beam current), while the other Main Beam parameters remain unchanged.

8.2 Parameter choice

8.2.1 General considerations

With any energy change, the beam energy remains at the nominal values throughout the whole complex up to the main linac. The final energy is changed only in the main linac. Three scenarios have been considered:

- **Gradient reduction (baseline):** The gradient is reduced along the main linac in order to deliver a lower final energy. This requires no additional hardware but the bunch charge has to be reduced linearly with the gradient in order to keep the same beam stability.
- **Early extraction (alternative):** The beam is accelerated in the first part of the main linac and then extracted. This solution requires multiple extraction lines at different positions along the main linac. Space for these lines requires additional length in the linac and the extracted beam emittance increases. An additional transport line is also required in the already densely populated tunnel. The bunch charge could remain the same as at full beam energy. This option is not considered as baseline as it would require significant changes in the tunnel layout and the main linac design. It is however an interesting alternative.
- **Introduction of a gradient profile (alternative):** The beam is accelerated in the first part of the main linac and then transported through the rest of the linac with no further acceleration. In this case, the bunch charge also needs to be reduced to keep the same beam stability. In the extreme case, the beam could be even accelerated above the target energy and then decelerated. This option requires less hardware modifications than early extraction, but it is not compatible with the luminosity recovery scheme described below.

As a baseline, we have chosen to use gradient reduction. The strength of the main linac magnets is reduced to keep the same normalized focusing as at 3 TeV. The beam delivery system layout is unchanged but the magnet strengths are adjusted to the beam energy with the same normalized strengths as at 3 TeV.

The Main Beam parameters remain unchanged except for the bunch charge and the number of bunches per beam pulse. In order to maintain the beam stability in the main linac and beam delivery system, the bunch charge is scaled according to $N/N_0 = E_{\text{cm}}/E_{\text{cm},0}$. At lower energies, the RF pulse length is increased and consequently more bunches per pulse used with the same bunch-to-bunch spacing, see below.

8.2.2 Choice of bunch charge

The bunch charge N scales proportionally to the linac gradient G , which is almost proportional to the centre-of-mass energy, hence $N/N_0 \approx E_{\text{cm}}/E_{\text{cm},0}$. The bunch length σ_z remains unaltered. The relative beam energy spread δ induced in the main linac is then almost independent of the final energy. The exception is at the beginning of the linac where, with lower gradients, the incoming energy spread is

reduced more slowly in proportion to the beam energy. The lattice strength is maintained since all magnet currents are simply adjusted to the beam energy.

With this scaling, the impact of wakefields on a jittering beam remains the same at all gradients. The relative correlated energy spread required for BNS damping remains unchanged:

$$\delta_{\text{BNS}}(s) \approx \beta_1^2(s) \frac{Ne^2 W_{\perp}(2\sigma_z)}{E(s)}. \quad (8.1)$$

where:

$W_{\perp}(2\sigma_z)$ is the wake function at a distance of twice the RMS bunch length,

$\beta(s)$ is the local beta-function,

$E(s)$ is the local energy,

e is the electron charge.

Again, after the beam has passed through some fraction of the main linac its energy is $E(s) \approx E_0(s)E_{\text{cm}}/E_{\text{cm},0} \approx E_0(s)N/N_0$, hence $\delta_{\text{BNS}} \approx \delta_{\text{BNS},0}$.

The emittance growth due to static imperfections is a concern in CLIC. The two main contributions are due to dispersive effects and wakefields. The spurious dispersion due to imperfections is independent of the gradient. Hence the constant energy spread results in a constant emittance growth at all energies. Only the incoming energy spread is somewhat more important at lower gradients. Wakefield induced emittance growth is reduced at lower energy. Full simulations for 1 TeV show an emittance growth somewhat below the 3 TeV case [2], see below.

8.2.3 Single bunch luminosity

The total and peak luminosity (i.e., the fraction within 1% of the nominal energy) per bunch crossing are shown in Fig. 8.1 normalized to the luminosity at full energy. The two scenarios are 1) the bunch charge remains constant and 2) the charge scales linearly with the centre-of-mass energy. These plots show the following:

- For constant bunch charge, the total luminosity does not follow the $\mathcal{L} \propto E_{\text{cm}}$ scaling that would be expected from the geometric emittance. The luminosity first remains nearly flat, then decreases faster than linearly.
- The quality of the spectrum improves at lower energies. This implies that the peak luminosity decreases less rapidly than total luminosity.
- If the charge scales with the energy, the luminosity per bunch crossing drops rapidly. However, the luminosity spectrum is even better at lower energies than for constant bunch charge.

8.2.4 Drive Beam configuration

The main linac gradient can be reduced by reducing the Drive Beam current $I \propto G$, i.e., by reducing the bunch charge or the number of bunches per unit time or both. The baseline is to change the bunch charge to adjust the gradient but at certain currents the number of bunches per unit time can be reduced and the bunch charge be brought back up to the nominal value for 3 TeV. This reduction of the number of bunches per unit time can be exploited to increase the pulse length. While the breakdown rate in the Main Beam accelerating structures and the PETS increases with pulse length, this is more than compensated by the reduction in breakdown rate at lower gradient.

The Drive Beam is generated in a central complex as a long stream of bunches, which is later split into ≈ 240 ns-long pulses that are then merged to form pulses of higher intensity. These short, high

8.2 PARAMETER CHOICE

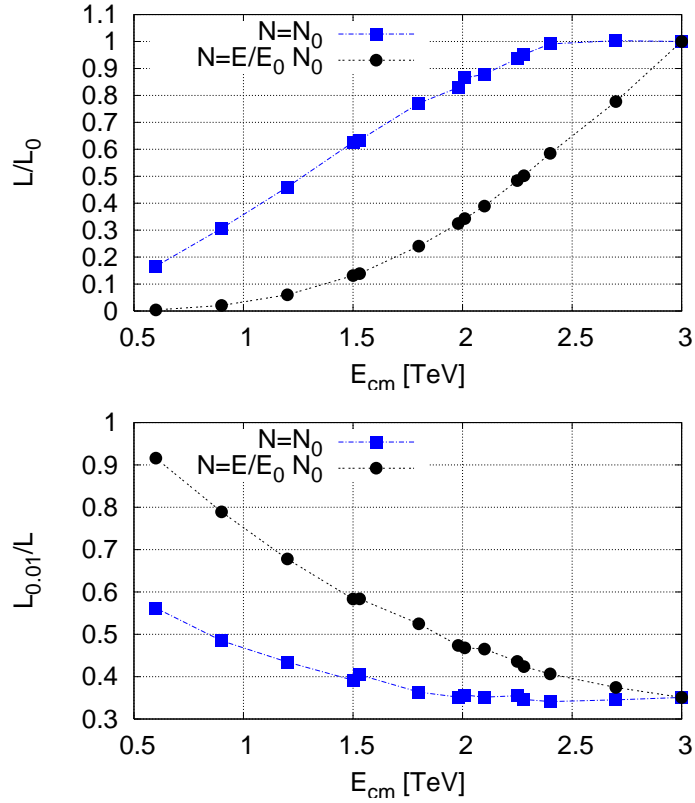


Fig. 8.1: The relative total (upper plot) and peak (lower plot) luminosity per single bunch crossing as a function of the beam energy. The two curves show dependence with constant bunch charge and with the bunch charge scaled proportional to the beam energy.

intensity pulses are sent into the main linac tunnel to produce the RF power needed to accelerate the Main Beam. More details can be found in §2.4.

To change the pulse length, the length of the delay loop must be changed and the pattern of switching between filling odd and even buckets must be adjusted. The delay loop is a relatively straightforward and inexpensive beam line, and therefore there could be several lines with different lengths, potentially integrated into a single design. This makes possible a number of different pulse lengths with different beam currents [3]. The combination scheme for nominal operation is illustrated in Fig. 8.2. Figure 8.3 shows the combination scheme for a pulse that is $4/3$ times longer and has only $3/4$ of the nominal current. For pulses of $3/2$ times the nominal length, three different switching patterns are needed, see Fig. 8.4. Pulses of twice the nominal length can be obtained by simply using a delay loop of twice the nominal length and by combining one pulse in the first combiner ring instead of two in parallel. In summary, we consider patterns with Drive Beam currents of $3/4$, $2/3$, $1/2$ and $3/8$ of the nominal value and pulse lengths of $4/3$, $3/2$, 2 and $8/3$ of the nominal value, respectively. This allows acceleration of 472, 552, 792 and 1112 Main Beam bunches per pulse.

In this scheme, the requirements on the Drive Beam source remain unaltered but the Main Beam systems need to be able to handle longer pulses and larger charges per pulse. The resulting design modifications appear to be minor but detailed studies remain to be performed. The damping rings have a large enough circumference to allow an increase of the Main Beam pulse length from 156 to 556 ns without difficulty. In this scheme not every bucket of the flat top of the Drive Beam pulse is filled in the decelerator. Simulations show that the impact is negligible.

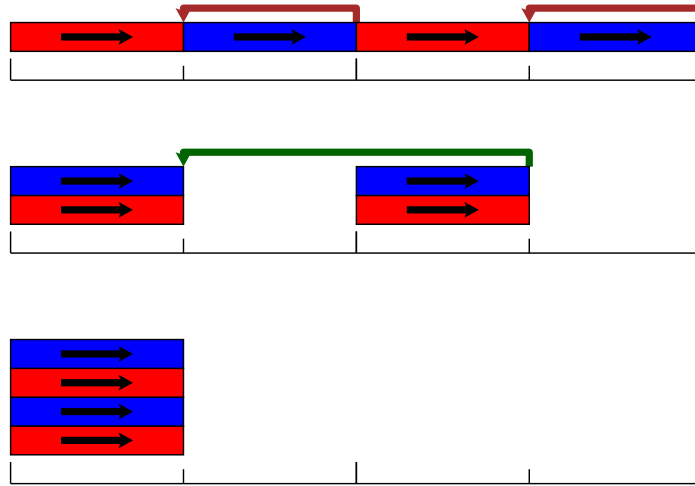


Fig. 8.2: Principle of the nominal combination scheme. In the first line, the blue bunches fill the odd buckets and are delayed with the delay loop for a time indicated by the arrow. The second line shows the timing of the bunches after the delay loop. The third line indicates the schematically the overlay of two of the pulses from the delay loop in the combiner rings. In reality 12 pulses are combined.

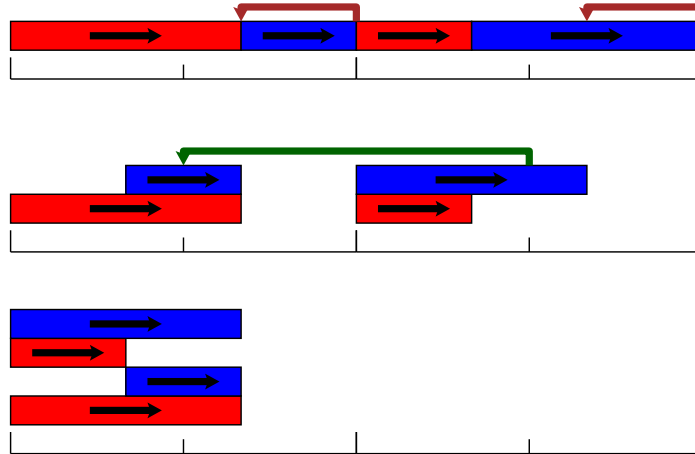


Fig. 8.3: Principle of the pulse stretching for an increase in pulse length to $4/3$ and a current reduction to $3/4$ of the nominal values. In the first line one can see that the switching from odd to even buckets is performed at different times than in the nominal scheme. In addition, the delay is reduced to $2/3$ of the nominal value. With the first switch pattern one can generate a pulse after the delay loop that is $4/3$ times longer than nominal and has the nominal current in the first half and only half the nominal current in the second half (see second line). With the second switch pattern, one can generate a pulse of the same length but with the nominal current in the second half. It should be noted that the ends of the pulses are aligned to the ends of the nominal pulses. Combining the two pulses, as indicated in the third line, one achieves a pulse that indeed has $3/4$ of the nominal current along the full length and is $4/3$ times longer than nominal.

8.3 Baseline design and luminosity

The different baseline operation modes are listed in Table 8.1 and the achievable luminosity is shown in Fig. 8.5. Another possibility for future study is to increase the repetition rate, which would increase

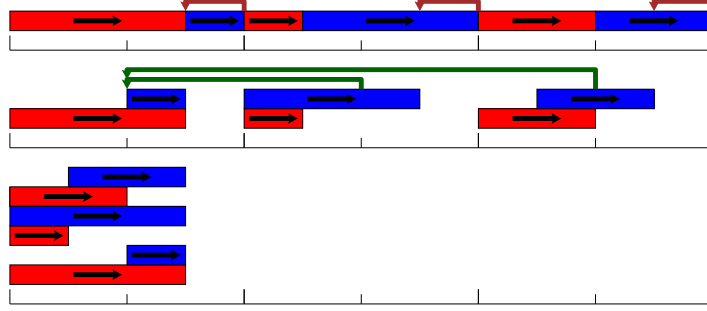


Fig. 8.4: Principle of the three switch patterns in order to achieve pulses of 3/2 times the nominal length.

the luminosity performance [1]. It is also possible that the beam delivery system can be re-designed to achieve a higher specific luminosity at lower energies.

Table 8.1: The operation modes and luminosities of the energy scan. E/E_0 indicates the maximum relative centre-of-mass energy to which the operation mode is valid. n_b is the number of bunches, N the number of particles per bunch, $n_{\mathcal{L}}$ is the relative increase in luminosity due to higher number of bunches, $Q_p/Q_{p,0}$ is the maximum Main Beam charge per pulse normalized to the nominal value, I/I_0 is the average Main Beam current normalized to the nominal value and P/P_0 is the beam power in the beam delivery system normalized to the nominal value. The repetition rate f_r remains unchanged.

E/E_0	f_r	n_b	$N[10^9]$	$n_{\mathcal{L}}$	$Q_p/Q_{p,0}$	I/I_0	P/P_0
1.0	50	312	3.72	1.0	1.0	1.0	1.0
0.75	50	472	2.79	1.5	1.125	1.125	0.84
0.667	50	552	2.48	1.77	1.18	1.18	0.79
0.5	50	792	1.86	2.54	1.27	1.27	0.63
0.375	50	1112	1.395	3.56	1.34	1.34	0.5

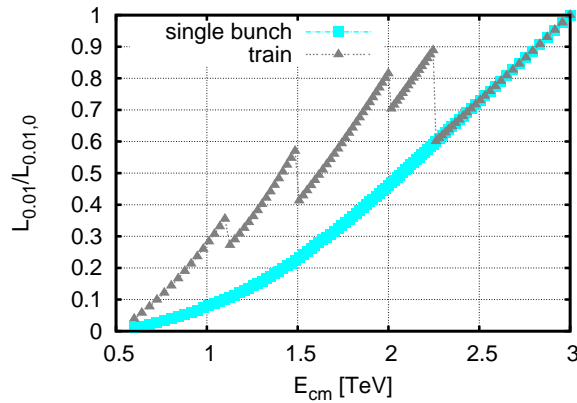


Fig. 8.5: Luminosity ($\mathcal{L}_{0.01}$) for operation below the nominal centre-of-mass energy, normalized to the luminosity at 3 TeV. The luminosity per bunch is shown together with the total value.

8.4 Impact on accelerator systems

8.4.1 Main Beam injectors

The main change for the Main Beam injectors are the pulse length and the charge per bunch. The other beam parameters remain constant. The different operation parameters are summarized in Table 8.1.

The charge per bunch is reduced while the pulse length increases. The maximum total charge per pulse is about 30% above the nominal pulse charge at 3 TeV. These parameter changes present no challenge for the particle sources. The impact on the electron source is very small and the positron target has enough margin to absorb 30% more charge per pulse.

The main impact is on the RF system which has to be flexible enough to accommodate the different pulse lengths and provide beam loading compensation for different bunch charges. The 200 MeV injector linacs for positron and electrons are separate and use pulse compression. The klystron pulse length of $8\mu s$ is long enough to cover the full range of pulse lengths, and the increased power required is partly compensated by the lower bunch charge. The booster linac and positron drive linac, however, need sufficient overhead to accelerate the long pulses.

8.4.2 Damping rings

The pre-damping ring (PDR) circumference of around 400 m sets a limit on the length of the train that can be injected into the main damping rings. With two trains stored in the ring, the maximum length for each train is 550 ns, leaving about 50 ns between the trains for the rise time of the kickers.

The single bunch collective effects scale with bunch charge, so they decrease with lower charge. In particular, the intra-beam scattering effect on the horizontal emittance scales roughly as the square root of the bunch charge, so at the lowest energy (around 1 TeV) the blow-up is negligible. In principle, this makes it possible to achieve a smaller emittance at lower energy and recover part of the luminosity loss. The space-charge tune-shift drops even more dramatically. It is linear with the beam energy and becomes almost a factor of three smaller (around 0.04) for the lowest energy. Multi-bunch effects remain constant as the total bunch train current is almost unchanged. The beam power increases slightly so the beam absorption system must be able to handle about 20% higher beam power, assuming that the wigglers run at full field. Finally, the low level RF system becomes less demanding with longer trains and smaller transient beam loading.

8.4.3 Ring to Main Linac Transport (RTML)

The impact of the low energy scenarios on the ring to main linac transport (RTML) is minor as this beamline has the same energy, serves the same functions and delivers bunches with the same properties. The most significant impact is on the compensation for the timing shift between electrons and positrons (see §3.3). The path length difference must be large enough to fit the longest bunch trains required during low energy running.

Single bunch effects, e.g., single bunch wakefields or coherent synchrotron radiation, are reduced for lower bunch charge, as are multi-bunch wakefields. However, the longer bunch trains do require a longer klystron pulse length.

8.4.4 Main Linac

8.4.4.1 Beam-based Alignment and Emittance Preservation

Studies of emittance growth at lower centre-of-mass energies due to static imperfections indicate that the effects of wakefields and of correlated beam energy spread are reduced. On the other hand, the initial energy spread decreases more slowly in the main linac and the emittance growth due to dispersive effects is somewhat larger. The table below shows results for 1 TeV centre-of-mass energy with reduced gradient and charge, assuming the same static errors as for 3 TeV.

Table 8.2: List of individual imperfections and resulting vertical emittance growth for the different steps of the BBA alignment method.

Imperfection	Value	$\Delta\epsilon_y RF$ [nm]	$\Delta\epsilon_y DFS$ [nm]	$\Delta\epsilon_y$ 1-2-1 [nm]
Girder end point	5 μm	0.02	0.62	0.62
Roll	100 μrad	0.11	0.11	0.11
BPM offset	14 μm	0.18	12.26	12.50
Cavity offset	14 μm	0.03	2.65	2.67
Cavity tilt	141 μrad	0.36	0.43	0.16
BPM resolution	0.1 μm	0.04	0.88	0.02
Wake monitor	3.5 μm	0.32	0.02	0.02
Quad offset	17 μm	0.02	0.02	0.02
All		1.22	16.50	501.85

Table 8.2 shows the vertical emittance growth at the end of the 1 TeV linac for each imperfection individually and for their sum. The results are for three steps of beam-based alignment (BBA) as described in [4]. The main sources of residual emittance growth after beam-based alignment are the BPM offsets, the quadrupole roll, the cavity tilt and the residual alignment of the wake monitors with respect to the structures. The residual vertical emittance growth when all the imperfections are considered together is about half of the growth at 3 TeV.

8.4.4.2 Main Linac vacuum

The fast beam-ion instability becomes more important at lower energy, and studies show that the vacuum needs to be about a factor of 2.5 lower at 1 TeV. This requirement has been integrated into the vacuum specifications.

8.4.5 Beam Delivery System (BDS)

The Beam Delivery system (BDS) has the same functions at all energies, as described in §3.5. The minimal approach is to assume the same BDS layout for all energies, where the strength of all magnetic elements (except final quadrupole QD0) simply scales with the beam energy. This leaves the optics and beam trajectories unchanged. The collimation is more problematic. To fully shield downstream components, the collimator gaps are kept the same for all energies. Since the beam size increases at lower energy, this means the collimators are cutting further into the beam. At 3 TeV, the collimation depths are $10\sigma_x$ and $55\sigma_y$, while at 1 TeV these are $5.8\sigma_x$ and $31.7\sigma_y$. The wakefields do not become stronger at lower energies since the bunch charge decreases with energy. Since the total energy of a bunch train is always lower at lower energies collimator survival is not an issue.

There are two possible ways to improve the luminosity at lower energies:

1. Adding non-linear correctors in the FFS to better cancel the geometrical aberrations arising for the larger transverse emittances.
2. Increasing the bending angle of the BDS dipoles to require weaker sextupoles for the chromaticity correction.

The first option is the least invasive but potentially has a lower luminosity gain. However, the second option requires a full re-positioning of all the BDS elements. The study and comparison of these two options is left for the technical design phase.

8.4.6 MDI and post-collision line

The power in the beam dumps is never larger than at 3 TeV so the average power in the beam dump does not pose a problem, but the charge per pulse increases by up to 34%. This could be a problem in the window of the dump, since the energy deposition is largely dependent on the beam current and not on the beam power. The power density in the window decreases at lower energies since the beam size increases faster than the pulse charge due to the increase in geometric emittance. The somewhat higher total power deposition in the windows seems not to be prohibitive but more detailed studies have to be performed.

8.4.7 Drive Beam injector and accelerator

No changes are required for the Drive Beam injector and accelerator.

8.4.8 Drive Beam delay lines

As described above, the odd and even bunch sequences are programmed differently at the source for each Main Beam energy band. The corresponding path differences are then built in different delay loops. The delays are given in Table 8.3. The combination of beam lines used for a given case is either a straight path for even bunches and a loop for odd bunches, or two different loops. A loop is made of four identical arcs, parameterized with a radius R and an angular span ϕ . Every arc is achromatic and isochronous up to second order in a momentum band of $\delta_p \leq 2\%$ in order to preserve the quality of the beam. To achieve this, the radius is close to $R \simeq 40$ m, similar to the first combiner ring from which the loop optics is adapted. The arc design may well evolve with more refined tracking studies. With four arcs the distance traversed along a loop is $L_{\text{loop}} = 4R\phi$ and along a straight path $L_s = 4R\sin\phi$. The delay is then either $c\tau = 4R(\phi - \sin\phi)$ or $c\tau = 4(R_1\phi_1 - R_2\phi_2)$. The arrangement proposed is shown in Fig. 8.6 and the parameters of the lines are given in Table 8.4. By fitting some of the parameters we reduce the number of loops to four, as indicated in Table 8.3. In every case the two beamlines have common start and end points, i.e., $A - D$ or $B - C$. This allows the use of one of a single pair of RF deflectors and simplifies the switch-yards which are located either before or after the deflectors. At present, the design does not include the short wiggler section in each loop which allows dynamic and precise adjustment of the loop length. These sections are identical to those in the combiner rings. The switchyards are also not included as they are dependent on the eventual details of the overall scheme.

Table 8.3: Delays needed for the different Main Beam energy bands. The time delay between odd and even bunches τ is given relatively to the nominal value $\tau_0 = 244$ ns at 3 TeV. Path 1 and 2 are the lines followed respectively by odd and even bunches. They are defined in Table 8.4 and shown in Fig. 8.6

E/E_0	τ/τ_0	$c\tau$ [m]	Path 1	Path 2
1.0	1	73.2	BC	DL1
0.75	2/3	48.8	DL4	DL2
0.667	1/2	36.6	BC/DL3	DL3/DL1
0.5	2	146.4	AD	DL2
0.375	4/3	97.6	AD	DL4

8.4.9 Beam trains in the combiner rings

The beam pulses from the delay loop are combined in the combiner rings in the same way as for nominal operation. However, as the pulse is lengthened, the number of pulses stored in a given ring has to be reduced. For a double length pulse, only a single pulse can be accumulated in the first combiner ring,

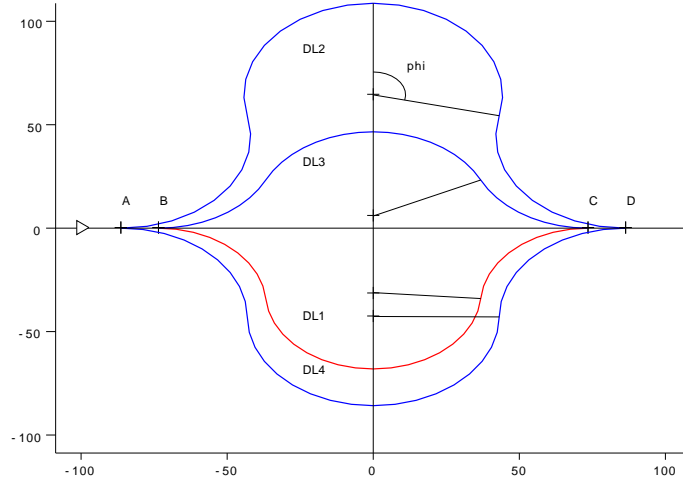


Fig. 8.6: The delay loop complex for energy scans. The beam produced in the Drive Beam linac enters upstream of point A from the left. The aspect ratio of the picture is not unity.

Table 8.4: The parameters of the beamlines in the delay line complex. The lines are shown in Fig. 8.6. The length L_s applies to straight lines, while R and ϕ are respectively the radius and the angular span of each of the four arcs which make a loop. The length of the loop is L_{loop} .

Path	L_s [m]	R [m]	ϕ [°]	L_{loop} [m]
AD	172.47	—	—	—
BC	147.15	—	—	—
DL1	-	36.90	85.54	220.35
DL2	-	44.28	103.15	318.87
DL3	-	40.70	64.67	183.75
DL4	-	43.12	89.72	270.07

and this pulse is stored for only three turns. The second combiner ring also contains only two pulses, not four as in normal operation.

8.4.10 Drive Beam in the decelerator

The plan described for CLIC energy scans has lower average beam current for the Drive Beam pulses than for 3 TeV. The lower Drive Beam charge is achieved by varying the fill patterns for the trains, which in turn leads to a varying energy profile along the bunch train during deceleration, see Fig. 8.7. The Drive Beam stability in the decelerators has been shown to be satisfactory for 3 TeV [5]. A potential concern is that the variation in charge patterns and energy could interact with the PETS dipole modes to cause instabilities and beam envelope growth. Simulations of the suggested patterns have found no significant extra envelope growth, implying that the Drive Beam stability in the decelerator is also satisfactory for the energy scans.

8.5 ALTERNATIVE APPROACH

The Drive Beam complex can be operated at the same magnet strengths as in the nominal conditions. The only exception is the Drive Beam decelerators and the Drive Beam dump extraction lines since the Drive Beam is decelerated less on average. The magnets in these areas are designed to be tuneable over a wide range of gradients.

8.4.12 Impact on the CLIC beam instrumentation

In general, there is no change to the required performance of the beam diagnostics.

8.4.12.1 Impact on the Main Beam instrumentation

All of the Main Beam instrumentation for the 3 TeV machine can operate during energy scans. The lower bunch charge and longer pulse length are included in the specifications of each instrument and have almost no impact on their design.

8.4.12.2 Impact on the Drive Beam instrumentation

The Drive Beam operation is adjusted to produce lower beam current and a longer pulse train but these parameters are part of the specifications and do not imply any crucial modifications. The increase in pulse length implies the use of new delay loops, which only differ from the one for the 3 TeV machine by their overall length. These additional beam lines contain more copies of the same instrumentation.

8.4.13 Operation

The lower beam energy has little impact on CLIC operation. The Main Beam has at most 34% larger total energy and charge per beam pulse, which has minor implications for machine protection. The energy per pulse at the end of the main linac is always less than at 3 TeV. The total energy and charge of the Drive Beam pulse is always less than nominal.

8.5 Alternative approach

An alternative approach for the energy scans would be to reduce the Drive Beam bunch charge $N \propto I$ and leave the number of Drive Beam bunches per unit time constant. This also reduces the deceleration of the Drive Beam in the decelerator, and allows a lower initial Drive Beam energy $E_D \propto I$. The RF power in the Drive Beam accelerator decreases as $P \propto I^2$, while maintaining full beam loading. In principle, this would make it possible to increase the repetition rate of CLIC, preferably only in multiples of 50 Hz, to remain coupled to the frequency of the mains power. At 70 % of the current only 70% of the beam energy is required, and the RF power required from each Drive Beam accelerator klystron is halved. This could allow for a doubled repetition frequency of 100 Hz, operating at the same average klystron and total power. However, klystrons that are operated below their nominal power usually have somewhat lower efficiency.

8.5.1 Expected klystron efficiency

If a klystron has been optimized for a particular operating point, lowering the RF drive power takes the tube out of saturation and significantly reduces the efficiency. Since the DC power remains the same, the efficiency scales roughly with output power P_{out} , i.e., reducing the power to 50% one would also halve the efficiency. This is primarily because the bunching at the output cavity is optimized for the nominal RF drive, and is therefore sub-optimal at other drive voltages.

To run a klystron at lower power without losing efficiency, the following procedure is more promising:

- The voltage V should be reduced,

- Since the DC current is proportional $V^{3/2}$, the DC input power follows $\propto V^{5/2}$.
- With these changed settings, the tube is no longer running at nominal setting, and the RF drive power must be adjusted to re-optimize the bunching in the output cavity. The RF drive is reduced until the bunching reaches the same $I_{\text{RF}}/I_{\text{DC}}$; this essentially reduces the input power proportional to the DC power. Once established, the output power varies as $P_{\text{out}} \propto I^2 \propto V^3$, and the efficiency varies as

$$\frac{P_{\text{out}}}{P_{\text{DC}}} \propto \frac{V^3}{V^{5/2}} = \sqrt{V} \propto P_{\text{out}}^{1/6} \quad (8.2)$$

- This results in a relatively modest reduction of the efficiency when operating the klystron at reduced power. At half power, the efficiency is reduced by 11%.

8.5.2 Conclusion on 100 Hz operation

With further R&D, it should be possible to double the repetition rate at lower energy and further enhance the luminosity.

8.6 Conclusion

There is a design for operation of CLIC at energies down to 1 TeV, without excessively reduced luminosity. Further optimisation of the low energy running is possible and requires further R&D.

REFERENCES

References

1. Schulte, D. *et al.* in *Proc. 1st Int. Particle Accelerator Conf.*, 23-28 May 2010, Kyoto, Japan (2010), 3395–3397. <<http://accelconf.web.cern.ch/AccelConf/IPAC10/papers/wepe022.pdf>>.
2. Dalena, B. *To be published*
3. Schulte, D. *To be published*
4. Schulte, D. in *Proc. 23rd IEEE Particle Accelerator Conf.*, 4-8 May 2009, Vancouver, British Columbia, Canada (2009), 4664–4666. <<http://accelconf.web.cern.ch/accelconf/PAC2009/papers/fr5rfp055.pdf>>.
5. Adli, E. *A Study of the Beam Physics in the CLIC Drive Beam Decelerator* (University of Oslo, 2009). <<http://cdsweb.cern.ch/record/1239173/files/CERN-THESIS-2010-024.pdf>>.

Chapter 9

Staged construction



T. Cerboni
[Signature]

9.1 Motivation and possible scenarios for staged construction

As discussed in earlier chapters, the feasibility of building the CLIC multi-TeV electron–positron linear collider is now well demonstrated by numerous studies and measurements. There are, however, several reasons to consider constructing it in stages. Initial implementation studies for CLIC have focused on three groups of issues: physics requirements, machine performance considerations, and practical implementation issues. The consequences of a staged implementation are briefly discussed below for these three groups of issues.

9.1.1 Physics considerations

The CLIC machine implementation must be guided by physics results. The LHC is currently exploring the TeV region and will most likely be able to set limits or discover a Standard Model (SM) Higgs, or a Higgs with properties close to the SM parameters, during the 2011–2012 runs. The results so far indicate the most probable energy range for the Higgs boson is likely to be in the region of 114–140 GeV [1], and the prospects for more precise statements at the end of 2012 look good. The implications of this for CLIC are that a future machine must be able to run with a reasonable luminosity at the production threshold of associated ZH production, i.e., somewhat above 220 GeV.

Beyond Standard Model (BSM) physics, for example supersymmetric (SUSY) models, is being addressed by a large number of theoretical studies and analyses, and impressive limits are set both by ATLAS and CMS [2] for various new physics processes. As one example, the Minimal Supersymmetric Standard Model (MSSM) limits for first and second generation squarks and gluino production have passed 1 TeV. The supersymmetry searches are nevertheless still at an early stage. As the LHC will increase its energy to 8 TeV in 2012, and 13–14 TeV in 2014–2015 these limits and the discovery potential for SUSY will improve dramatically. Furthermore, the current limits are also much harder to interpret in SUSY models that are less constrained, for example where the sparticle spectrum is such that even if sparticles are produced at the LHC their decays fail to trigger, or are not identified by current analyses, or mimic SM background too well. Many SUSY models also predict that the neutralinos, sleptons and charginos as well as the third generation squarks are lighter than the first and second generation squarks and gluinos. As a result it is currently difficult to interpret the LHC results in terms of implementation goals for CLIC, beyond that the machine needs to be able to run at a range of energies from the Higgs production threshold to as high as possible, with reasonable luminosities throughout. Other models for BSM physics, with their limits from the LHC [3], give a similar message; it is important to maintain the multi-TeV capabilities of CLIC.

To understand better how to explore the physics landscape within the reach of a future linear collider, it is a useful exercise to consider one specific physics model containing a SUSY spectrum, and extract the consequences for the linear collider operational parameters. As an example, the production cross-sections for SUSY point I [4] are shown in Fig. 9.1 below. By considering such a model, where only a limited set of parameters can be expected to be measured at the LHC, conclusions can be drawn that a linear collider should be able to run from the ZH threshold up to the highest possible energy. The LHC has the possibility to provide information about the high-energy part of such a model through measurements of squarks and gluinos as well as other possible states. To be able to disentangle the various SUSY particles in such a scenario it will be important to have the capability to run at different energies and also to perform fine scans whenever needed. The integrated luminosities needed are in most cases significant such that, as the energy of the machine is changed, the instantaneous luminosity must remain above $10^{34} \text{ cm}^{-2}\text{s}^{-1}$ (within 1% of the peak).

9.1.2 Machine performance considerations

The CLIC machine’s constraints and limitations in energy flexibility are discussed in Chapter 8. In general, unless other measures are taken, the luminosity of a given machine will drop proportionally to the

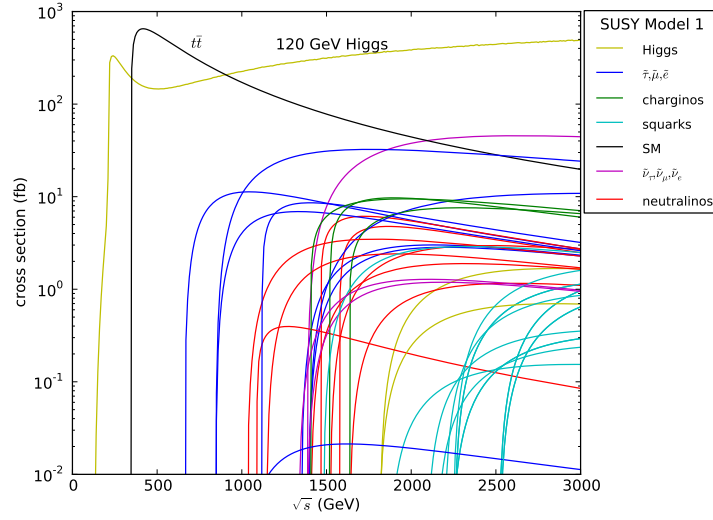


Fig. 9.1: Production cross-sections for various processes as a function of the E_{cm} for one specific SUSY model (point I, [4])

energy as the energy is decreased. For CLIC, optimized for a given energy, beam stability considerations impose further limitations and the bunch charge has to be reduced with decreasing energy as discussed in §8.1. This can partly be compensated for by lengthening the Drive-Beam pulse-length allowing more bunches per pulse, and maintaining the pulse repetition rate at 50 Hz. This scheme allows an energy flexibility of a factor around 3–4, within which the luminosity will scale as shown in Fig. 9.2 for a 3 TeV starting point. Furthermore, during a threshold scan small changes of a few per cent can be performed

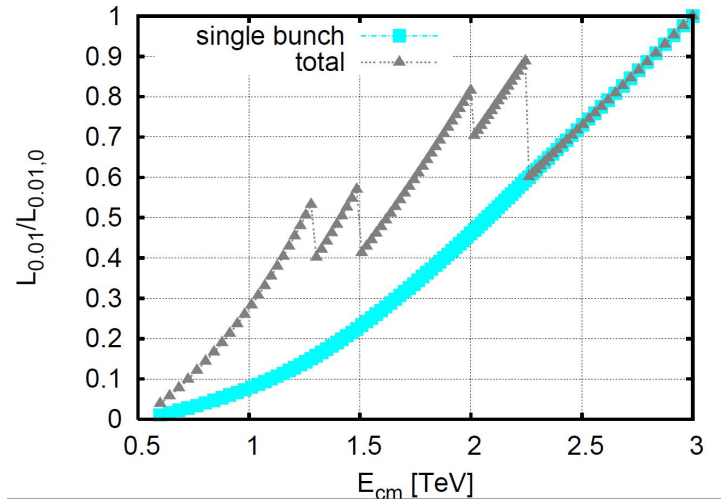


Fig. 9.2: Single-bunch luminosity scaling as function of energy, normalized to the single-bunch luminosity at 3 TeV, in blue. The compensation possible by increasing the number of bunches is shown in black. In both cases the peak luminosities are used (within 1%).

by simply adjusting the accelerating gradient.

The immediate conclusion is that, in order to be able to run from around 220 GeV–3 TeV, with luminosities $\geq 10^{34} \text{ cm}^{-2} \text{ s}^{-1}$ (within 1% of the peak), two or, more optimally, three stages will be needed. It is premature to conclude what the correct energy stages are but for the purpose of the discussion in this chapter three stages at 500 GeV, 1.5 TeV, and 3 TeV are considered. The parameters for the machine

at the two first stages are discussed in the following two sections, while the parameters for the 3 TeV machine are summarized in Appendix A. The parameters for the lower energy implementations are both preliminary and non-optimized in several cases. During the next phase of the project it is foreseen to develop optimal parameter sets for each chosen energy stage, to become part of the project implementation plan currently foreseen for 2016.

9.1.3 Implementation considerations

The possibility of constructing the machine in stages has advantages and imposes constraints, most of which have not yet been studied in detail. Some of the topics for detailed investigations over the coming years will be:

- scope and schedule for each stage, based on the best knowledge of the physics potential of the machine;
- fast and resource-optimized access to the initial physics goals;
- approval and construction planning for civil engineering and key technology components;
- re-use of parts going from one stage to another;
- risk reduction, flexibility and use of operational experience;
- power and energy consumption as function of energy and luminosity taking into account optimized yearly and daily operation scenarios.

To have large machines running at increasing energies and luminosities is of course nothing new in particle physics. Recent examples are the Tevatron, LEP, and the LHC, extending significantly the overall scientific program for each of these facilities in scope and duration with respect to their initial machine configurations. Gradually unlocking the full potential of an accelerator can be very beneficial scientifically and increase substantially the value of the facility for the user community. In addition to the scientific results coming from the first stages, there is also significant construction and operational experience that can be transferred from one stage to another. The gradual investment of resources building on earlier investment is also a well-proven path forward for scientific projects of this size, and a staged implementation of CLIC will naturally follow this tradition.

9.1.4 Brief summary and prospects

Generally there is a multitude of questions to be answered before being able to propose an optimized construction scenario for a machine like CLIC, but for several important reasons a staged implementation is being considered and studied. Some of the key elements for such an approach are discussed in this chapter, namely, intermediate energy parameter sets, energy and power consumption parameters, as well as scheduling. A staged implementation will be further discussed in the ‘Executive Summary’ to be published in autumn 2012, benefiting from the latest physics information from the LHC by summer 2012. However, these considerations are likely to remain preliminary until the LHC experiments have collected significantly more data. At this point significant data at full LHC energy seems to be needed before a final implementation proposal can be advanced. A comprehensive project implementation plan for CLIC is foreseen for 2016 [5].

9.2 Preliminary design of a 500 GeV accelerator

9.2.1 Overview

The design parameters for a 500 GeV CLIC machine have been investigated and are based on the 3 TeV design, respecting a number of basic boundary conditions in order to facilitate the upgrade from 500 GeV to 3 TeV. However, a full integration of a 500 GeV machine as a first stage of a 3 TeV machine remains to be done. Key parameters of the 500 GeV design are shown in Table 9.1, with the 3 TeV parameters given for comparison.

Table 9.1: Key parameters of the 500 GeV and 3 TeV designs.

Description [units]	Parameter	500 GeV	3 TeV
Centre-of-mass energy [TeV]	E_{cms}	0.5	3.0
Repetition frequency [Hz]	f_{rep}	50	50
Number of bunches per train	n_{b}	354	312
Bunch separation [ns]	Δt	0.5	0.5
Accelerating gradient [MV/m]	G	80	100
Total luminosity [$10^{34}\text{cm}^{-2}\text{s}^{-1}$]	L_{total}	2.3	5.9
Luminosity within 1% of E_{cms} [$10^{34}\text{cm}^{-2}\text{s}^{-1}$]	$L_{0.01}$	1.4	2.0
No. of photons per electron	n_{γ}	1.3	2.1
Average energy loss due to beamstrahlung	$\Delta E/E$	0.07	0.28
No. of coherent pairs per bunch crossing	N_{coh}	200	6.8×10^8
Energy of coherent pairs per bunch crossing [TeV]	E_{coh}	15	2.1×10^8
No. of incoherent pairs per bunch crossing	n_{incoh}	8×10^4	0.3×10^6
Energy of incoherent pairs per bunch crossing [GeV]	E_{incoh}	3.6×10^6	2.3×10^7
Hadronic events per crossing	n_{had}	0.3	3.2

The constraints used for the 500 GeV design are the following:

- The spacing of the Main Beam bunches is the same as for 3 TeV. This allows the same Main Beam generation complex to be used. Only limited modifications will be necessary to adjust for different bunch charges and emittances, and the slightly different number of bunches per pulse.
- The main linac accelerating structure has the same length at 500 GeV as at 3 TeV. This allows the same girders and main linac quadrupole designs to be used. An option was studied but not retained where the 500 GeV structure had a length of two 3 TeV structures.
- The module layouts are the same as for 3 TeV, i.e., with the same PETS.
- The RF pulse length has to be the same as for 3 TeV. This allows a similar Drive-Beam generation complex to be used, with limited modifications from the 3 TeV design. The delay loop and combiner rings can be the same as for 3 TeV. The spacing between the final turn-around loops of the Drive Beam in the main linac tunnel is also the same. This allows the same turn-arounds for 500 GeV and 3 TeV to be used. Since the BDS is shorter at 500 GeV, the final decelerator fits into the beginning of the tunnel for the 3 TeV BDS; the associated Drive-Beam turn-around at 500 GeV is the only component that cannot be re-used at 3 TeV. For the accelerating structures with length twice that of the 3 TeV structure, a doubled RF pulse length was considered.
- The input power per RF structure was kept similar to that for 3 TeV. This implies that the Drive-Beam energy and current also stay similar at both energies. It should be noted that the Drive-Beam current and beam energy is slightly higher at 500 GeV than at 3 TeV.
- The Drive-Beam at 500 GeV will be generated by a single complex producing the Drive-Beam

9.2 PRELIMINARY DESIGN OF A 500 GeV ACCELERATOR

pulses for both linacs, whereas at 3 TeV a separate Drive-Beam complex will be required for each linac.

- The horizontal emittance of the Main Beam is larger for 500 GeV (at the interaction point 2400 nm vs. 660 nm) in order to relax the requirements for the damping rings.

It should be noted that the normalized vertical emittance at the end of the linac is the same at 500 GeV and 3 TeV, i.e., 20 nm. For the 500 GeV parameters the emittance target at the interaction point is 25 nm. In contrast, no target emittance at the interaction point is defined for the 3 TeV parameters, since the beams develop tails that make the values of the emittances definition dependent. Instead the luminosity target at 3 TeV has been set to 83% of the luminosity that could be achieved if the beam delivery systems had no imperfections.

9.2.2 Parameter choice

The beam parameters for CLIC at 500 GeV centre-of-mass energy have been optimized in a way similar to that for 3 TeV [6].

9.2.2.1 Beam dynamics

The basic parameters at the collision point are determined by the different accelerator systems:

- The bunch charge N and length σ_z are mainly a function of the linac design. The longitudinal single bunch wakefield makes the bunch length a function of the charge $\sigma_z(N)$ in order to limit the final beam energy spread. The transverse wakefield effects then limit N , via the wakefield kick which is proportional to $NW_{\perp}(2\sigma_z)$.
- The horizontal emittance is mainly a function of the damping ring performance, with some contributions from other systems.
- The vertical emittance depends on the damping ring and the transport from the damping ring to the interaction point.
- The effective vertical and horizontal beta functions are a function of the final focus system and have lower limits $\beta_x \geq 8\text{ mm}$ and $\beta_y \geq 0.1\text{ mm}$, due to synchrotron radiation and non-linear effects.

Some parameters were chosen to be more relaxed than at 3 TeV:

- A larger horizontal emittance at the interaction point of $2.4\text{ }\mu\text{m}$ instead of $0.66\text{ }\mu\text{m}$ has been assumed to relax the damping ring design requirements.
- Somewhat larger beta-functions have been assumed at the collision point to relax the beam delivery system requirements.

The bunch charge in the main linac has been chosen in the same way as for the 3 TeV case, but taking into account that the machine is significantly shorter. This has two main consequences. Firstly, this allows the same transverse single bunch wakefield kick to be tolerated, even at lower gradients; in the case of the 3 TeV design the wakefield kick had to be reduced with the gradient since the length of the machine increased. Secondly, it allows the multi-bunch wakefield kick on the second bunch to be twice as large as at 3 TeV; the integrated effect will remain the same as at 3 TeV. In addition, the requirement on the quality of the luminosity spectrum at the interaction point has been made more stringent, in order to make the degradation of the spectrum quality due to beam-beam effects and the unavoidable initial-state radiation comparable to that at 3 TeV. As a figure of merit the luminosity delivered within a band of $\pm 1\%$ around the nominal centre-of-mass energy is used. In order to illustrate the difference between the two cases at 3 TeV and 500 GeV, the luminosity per bunch crossing in 1% energy spectrum divided by the bunch population L_{bx}/N versus the average aperture to the wavelength ratio $\langle a \rangle/\lambda$ is plotted in

Fig. 9.3 for three difference cases: 3 TeV, $\langle G \rangle = 100$ MV/m; 500 GeV, $\langle G \rangle = 100$ MV/m; and 500 GeV, $\langle G \rangle = 50$ MV/m.

Using the nominal structures optimized for 3 TeV in the 500 GeV main linac would result in a luminosity loss of about factor six from 0.3 to 0.05. This loss can be partially compensated by using an accelerating structure with larger aperture since for 500 GeV the optimum $\langle a \rangle / \lambda$ is close to 0.16. In addition, Fig. 9.3 shows the difference in the L_{bx}/N for 500 GeV between 100 MV/m and 50 MV/m accelerating gradients coming mainly from the linac length.

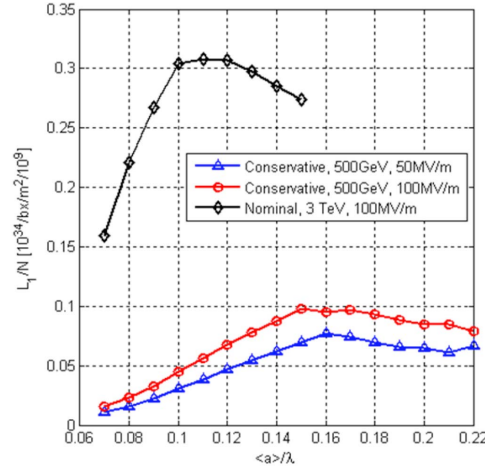


Fig. 9.3: The luminosity normalized to the beam current as a function of a/λ for the main linac accelerating structures. Two different gradients as well as 500 GeV and 3 TeV are shown. The black diamond curve represents the nominal 3 TeV case where the optimum $\langle a \rangle / \lambda$ is 0.11. The red circles and blue triangles show the luminosity at 500 GeV for a gradient of 100 MV/m and 50 MV/m, respectively.

9.2.2.2 RF constraints

The following three RF constraints have been used in the optimization:

- Surface electric field: $E_{\text{surfmax}} < 260$ MV/m
- Pulsed surface heating: $\Delta T_{\text{max}} < 56$ K
- Power: $P_{\text{in}}/C\tau_p^{1/3}f < 156$ MW/mm/ns^{2/3}

Here E_{surfmax} and ΔT_{max} refer to maximum surface electric field and maximum pulsed surface heating temperature rise in the structure respectively. P_{in} , τ_p and f denote input power, pulse length and frequency respectively. C is the circumference of the first regular iris. These constraints are the same as those used in the optimization of the 3 TeV CLIC main linac accelerating structure [7, 8]. This means that the structure high gradient performance is as challenging to achieve as that for the 3 TeV case. In addition, two values for the RF phase advance per cell in the structure have been investigated: $2\pi/3$ and $5\pi/6$.

9.2.2.3 3 TeV design constraints

As mentioned above, a number of additional constraints have been considered for the 500 GeV design in order to facilitate an upgrade to 3 TeV. The relevant parameters fixed by the 3 TeV design are: bunch separation N_s of six RF cycles, RF pulse length t_p of 242 ns and the structure active length L_s of 230 mm. The latter two parameters could be increased by a factor two.

Hence the different options studied were:

9.2 PRELIMINARY DESIGN OF A 500 GeV ACCELERATOR

- $N_s = \text{free}$; $L_s > 200 \text{ mm}$; $t_p = \text{free}$
- $N_s = 6$; $L_s = 230 \text{ mm}$; $t_p = 242 \text{ ns}$
- $N_s = 6$; $L_s = 480 \text{ mm}$; $t_p = 242 \text{ ns}$
- $N_s = 6$; $L_s = 480 \text{ mm}$; $t_p = 483 \text{ ns}$

where the first case represents the 500 GeV CLIC optimum without taking into account the 3 TeV design constraints. It is therefore a reference to indicate how much the performance is reduced due to the 3 TeV design constraints.

9.2.2.4 Optimization results

The 500 GeV CLIC main linac accelerating structure optimization was performed through a range of gradient $\langle G \rangle$ from 50 to 100 MV/m, always at 12 GHz. The figure of merit (FoM) $\eta L_b/N$ was maximized as in Refs. [7, 9], where η is the RF-to-beam efficiency. For fixed centre-of-mass collision energy this quantity is proportional to the average luminosity divided by the average RF power that has to be provided for acceleration. No cost model was available for 500 GeV CLIC optimization.

The results are presented in Fig. 9.4 for the four combinations mentioned above, each at two different values of the RF phase advance per cell. In addition, two cases are included that correspond to the use of the 3 TeV structure (CLIC_G in [8]) at nominal and double pulse lengths. Figure 9.4 clearly indicates that a reduction of the gradient allows one to design a structure that achieves more luminosity per power, since the apertures can be larger. The three most interesting cases are indicated in Fig. 9.4 by arrows:

- 1 The CLIC 3 TeV structure operated at 80 MV/m and a doubled pulse length. This would require some layout changes. The luminosity would be significantly smaller than for the best 500 GeV design at the same gradient.
- 2 An optimized structure of nominal length and nominal pulse length. The layout would not have to be changed in this case. At 80 MV/m the luminosity per power would be very close to the optimum.
- 3 An optimized structure of double length and double pulse length. This would require some changes in the layout. The luminosity per power would be close to the optimum and slightly higher than in the previous case but the gradient would be significantly lower at 50 MV/m.

The case [1] was chosen. The 3 TeV CLIC would provide significantly less luminosity and the case [3] structure would lead to a significantly longer linac, increasing the cost, while not significantly increasing the luminosity per beam power. Detailed parameters of the baseline structure can be found in Table 9.2.

9.2.3 Main Beam sources

9.2.3.1 Polarized electron source

The polarized electron source for CLIC uses a DC photo-cathode source followed by a 1 GHz bunching system to create the time structure as described in §5.1.2.1. The 500 GeV version requires a slightly longer bunch train of 354 bunches as opposed to 312 and the charge per bunch is almost doubled (see Table 9.3). The injector has to provide 1.6 nC per bunch compared to the 0.96 nC for the 3 TeV version. In an initial test at SLAC to demonstrate the CLIC polarized electron gun requirements the charge per pulse obtained was roughly a factor three higher than needed for CLIC 500 GeV. The higher bunch charge should be well within the capabilities of the CLIC electron source.

9.2.3.2 Positron source

As for the electron source, the main difference is the significantly increased charge per bunch. This has several consequences for the positron source. The total energy deposited onto the positron production

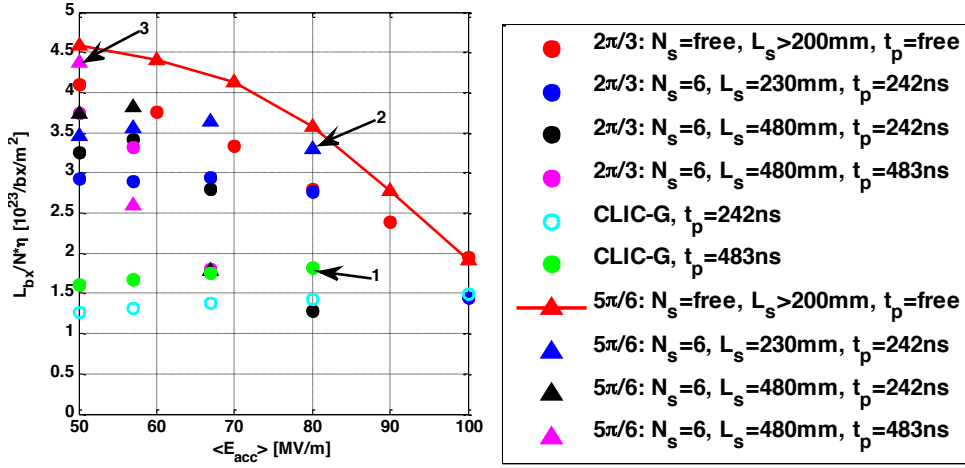


Fig. 9.4: Figure of Merit for 10 different sets of constraints described in the text

Table 9.2: 500 GeV CLIC accelerating structure parameters

Average loaded accelerating gradient	80 MV/m
Frequency	12 GHz
RF phase advance per cell	$5\pi/6$ rad
Average iris radius to wavelength ratio	0.145
Input, output iris radii	3.97, 3.28 mm
Input, output iris thickness	2.08, 1.67 mm
Input, output group velocity	1.88, 1.13 % of c
Number of regular cells	19
Structure length including couplers	230 mm (active)
Bunch spacing	0.5 ns
Bunch population	6.8×10^9
Number of bunches in the train	354
Filling time, rise time	50.3, 15.3 ns
Total pulse length	242 ns
Peak input power	74.2 MW
RF-to-beam efficiency	39.6%
Maximum surface electric field	250 MV/m
Maximum pulsed surface heating temperature rise	56 K

Table 9.3: CLIC electron source parameters

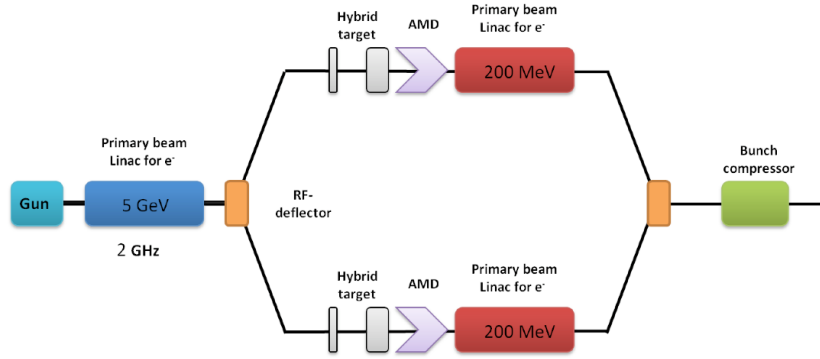
Parameter	Symbol	0.5 TeV	3 TeV
Electrons per microbunch	N_e	7.8×10^9	4.3×10^9
Number of microbunches	n_b	354	312
Time between microbunches	Δt_b	1 ns	1 ns
Width of macropulse	T_B	2×177 ns	2×156 ns
Macropulse repetition rate	f_b	50 Hz	50 Hz

target then exceeds the tolerable value for a single target, therefore a two-target station is required. This design has already been adopted for the 3 TeV baseline, where it will provide additional margin. The electron bunches arriving from the 5 GeV drive linac will be switched with a 500 MHz deflector between

Table 9.4: Characteristics of the primary e^- beam impinging the e^+ target for 500 GeV

Parameter	Units	Value
Energy	GeV	5
No. e^- /bunch	10^9	20
No. bunches / pulse	–	354
Pulse length	ns	2×177
Repetition frequency	Hz	50
Beam power	kW	283
Beam radius (r.m.s.)	mm	2.5
Bunch length (r.m.s.)	mm	0.3

the two target stations and the positrons will be recombined at an energy of 200 MeV after the capture linacs into a single train (see Fig. 9.5). The same kind of deflector is used for the delay loop in the Drive-Beam complex. The drive linac has to deliver the higher bunch charge onto the positron target, which will roughly double its beam loading. The accelerating structures designed for the injector linacs can cope with the higher charge, however sufficient RF power has to be installed for this linac to provide the energy needed to accelerate this beam. The bunch charge of 3.2 nC per bunch can be delivered by a thermionic gun or a photo injector as shown at the CTF3 facility.

**Fig. 9.5:** CLIC double-positron target station for 500 GeV

9.2.4 Damping Rings

The Damping Ring (DR) layout for CLIC at 500 GeV remains the same as the nominal 3 TeV case with two pre-damping rings (PDR), two main DRs, and a single delay loop for both species of particles. The pre-damping ring parameters remain frozen with respect to 3 TeV, as their role is to provide a first stage damping and capture of the wide energy spread beam, especially for positrons. As the DR lattice design does not aim for a very small emittance, the arc cell optics can be relaxed, and the dynamic aperture in the main DR can be significantly increased. Further studies should clearly indicate if the use of an electron PDR becomes obsolete.

The parameters for the nominal versus the 500 GeV case are displayed in Table 9.5. The main difference in the DRs is the almost 4-fold increase of the horizontal emittance, which puts the beam in a regime where intra beam scattering becomes a small perturbation (a few per cent) with respect to the zero current emittance, even if there is a 2-fold increase of the bunch charge. To achieve this emittance, apart from the above-mentioned arc cell optics modification, the number of damping wigglers can be reduced to 20 for each ring. This is the minimum number for keeping the damping time to around 4 ms, which is necessary for the beam to reach steady state within the 50 Hz repetition rate. Removing more damping

wigglers would necessitate the storing of staggered trains, which by itself creates difficulties due to the high average current.

The smaller number of wigglers reduces the energy loss per turn by more than a factor of two, which evens out the 2-fold increase of beam current (350 versus 170 mA), with respect to the average beam power. This means that the total power capacity of the absorbers remains the same, although the peak power per wiggler is increased by a factor of two. The wiggler radiation absorption scheme for preventing wiggler quenches has to be revised but seems straightforward by interleaving the full and empty wiggler FODO cells.

The vertical emittance target remains the same but owing to the increased emittance ratio the challenges of alignment, orbit control, vertical dispersion, and coupling correction to be achieved for reaching this emittance are somewhat higher. In any case, they remain close to modern X-ray storage ring performances.

The longitudinal emittance target remains unchanged, which implies that the bunch should be kept short, with an r.m.s. bunch length of around 1.8 mm. Owing to the arc optics relaxation, the momentum compaction factor is increased and the only variable available to keep the bunch length short is to increase the RF voltage by around 50%. This, in turn, may necessitate the installation of a larger number of RF cavities which can occupy the space of empty wiggler cells.

The horizontal beam size increase in the arc cells equilibrates the bunch charge increase and the vertical space-charge tune-shift remains at the same level of around 0.1. All other collective instabilities increase with the bunch charge but there is a significant reduction due to the increased emittance, as the charge density is reduced. At the same time the total impedance is expected to be lower due to the reduced number of wigglers and absorbers.

Finally, and considering the same performance in the pre-damping rings, the 500 GeV design relaxes the kicker stability requirements by more than a factor of two, putting the relative kick jitter to around 10^{-3} .

Table 9.5: Damping Ring performance parameters for CLIC at 500 GeV and 3 TeV

Parameters	CLIC@3 TeV	CLIC@500 GeV
Energy [GeV]	2.86	2.86
Circumference [m]	427.5	427.5
Energy loss/turn [MeV]	4.0	1.9
RF voltage [MV]	5.1	7.5
Stationary phase [°]	51	20
Momentum compaction factor	1.3×10^{-4}	3.3×10^{-4}
Damping time x/s [ms]	2/1	4.1/2.1
Number of dipoles/wigglers	100/52	100/16
Dipole/wiggler field [T]	1.0/2.5	1.0/2.5
Bend gradient [$1/m^2$]	-1.1	-1.1
Bunch population [10^9]	4.1	7.5
Horizontal normalized emittance [nm]	456	1800
Vertical normalized emittance [nm]	4.8	4.8
Bunch length [mm]	1.8	1.8
Longitudinal normalized emittance [keVm]	6.0	6.0

9.2.5 Ring to Main Linac transport

The functions which the ring to main linac transport (RTML) have to fulfill are the same as at the nominal 3 TeV (see §3.3). But the beam properties which are delivered by the damping rings and beam properties

which have to be delivered by the RTML to the main linac are different (Tables 9.6 and 9.7). The RTML and especially the bunch compression stages are sufficiently flexible to adapt for the different parameters without changes in layout, i.e., just by tuning. But a few layout changes might be beneficial to fit the RTML better into the overall CLIC layout.

Table 9.6: Beam properties at the start of the RTML.

Property [Units]		Value 3 TeV	Value 500 GeV
Particle energy [GeV]	E_0	2.86	2.86
Bunch charge [nC]	q_0	0.65	1.2
Bunch length [μm]	σ_s	1600	1600
r.m.s. energy spread [%]	σ_E	0.13	0.13
Normalized emittance [nm]	$\epsilon_{n,x}$	500	1800
	$\epsilon_{n,y}$	5	5

A potentially major impact on beam dynamics can be expected from the higher bunch charge which is needed for 500 GeV. This leads to stronger collective effects. In particular coherent synchrotron radiation (CSR) effects in the loops, arcs, and bunch compressor chicanes will be more important as well as wakefield effects in the bunch compressor RF and the booster linac. CSR will have an impact only in the horizontal plane since this is the bend plane, whereas wakefields will have an impact in the horizontal and vertical planes.

Since in the arcs and loops the bunches are rather long, i.e., $300\mu\text{m}$, CSR along these beam lines is negligible for the 3 TeV case. For the 500 GeV case with its larger bunch charge CSR will still be very small. In contrast, CSR in the chicanes of the two bunch compression stages (BC1 and BC2) already induces a non-negligible, though acceptable, emittance growth for 3 TeV parameters. CSR will certainly become stronger for 500 GeV parameters due to the larger charge since $P_{\text{csr}} \propto q^2$. Only in the last chicane does the longer final bunch length have some benefit, $P_{\text{csr}} \propto \sigma_s^{-4/3}$. In any case, the larger horizontal emittance and the larger horizontal emittance budget allow for stronger emittance dilution.

More important are short and long range wakefields in the cavities of BC1, BC2 and the booster linac since they also influence the vertical emittance. On the one hand, wakefields will get stronger due to the larger bunch charge. On the other hand, vertical emittance and emittance budget remain unchanged. This means that the alignment tolerances will be tightened. To improve long range wakefields in the booster linac stronger focusing and stronger HOM damping might be required.

The RTML layout can remain almost unchanged compared to the nominal layout. Only the long transfer lines need to be shortened to shift the turn-around loops closer to the shorter main linac. Owing to the larger horizontal emittance budget it might also be possible to shorten the turn-around loops to

Table 9.7: Beam properties at the end of the RTML

Property [Units]		Value 3 TeV	Value 500 GeV
Particle energy [GeV]	E_0	9	9
Bunch charge [nC]	q_0	> 0.6	> 1.1
Bunch length [μm]	σ_s	44	72
r.m.s. energy spread [%]	σ_E	< 1.7	< 1.7
Normalized emittance [nm]	$\epsilon_{n,x}$	< 600	< 2100
	$\epsilon_{n,y}$	< 10	< 10

reduce cost. Use of their tunnels will be discontinued in any case once CLIC is upgraded to 3 TeV.

9.2.6 Main Linac

9.2.6.1 Overview

The two main linacs accelerate the electron and positron beams from 9 GeV to 250 GeV, using normal conducting structures with a frequency of 12 GHz and a gradient of 80 MV/m. The two linacs are about 4.5 km long and consist of a sequence of modules. The designs of these modules are identical to those of the main linac at 3 TeV, except that the accelerating structures are different but with the same external dimensions.

9.2.6.2 Beam parameters

Table 9.8 shows the key beam parameters for the two main linacs.

Table 9.8: Beam parameters in the CLIC main linac at 500 GeV

Particles per bunch	6.8×10^9
Bunches per train	354
Bunch spacing	15 cm
Bunch length	$72 \mu\text{m}$
Initial r.m.s. energy spread	$\leq 1.7\%$
Final r.m.s. energy spread	$\leq 0.35\%$
Initial horizontal emittance	$\leq 2100 \text{ nm}$
Final horizontal emittance	$\leq 2300 \text{ nm}$
Initial vertical emittance	$\leq 10 \text{ nm}$
Final vertical emittance	$\leq 20 \text{ nm}$

9.2.6.3 System description

The RF power is provided by five Drive-Beam decelerators. The total number of accelerating structures per linac is 14 580. Only three out of the five different 3 TeV-module designs are used in the 500 GeV linacs.

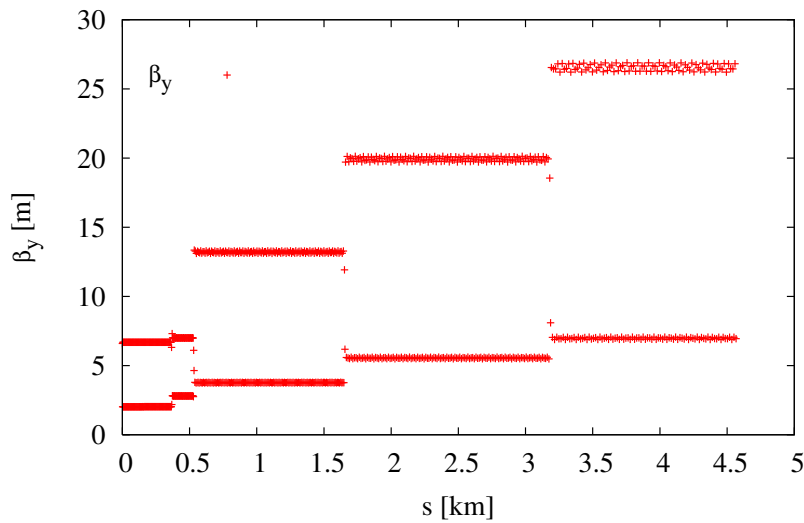


Fig. 9.6: Main linac lattice function.

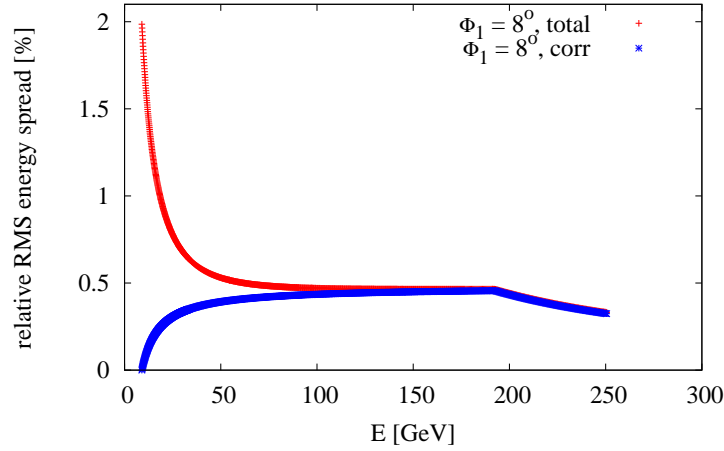


Fig. 9.7: Total energy spread and correlated energy spread along the linacs

The main linac optics is shown in Fig. 9.6. It is divided into five sectors using a simple FODO lattice similar to the 3 TeV design. The resulting correlated and total energy spread for nominal beam parameters along the linac are shown in Fig. 9.7. The main features of the five sectors are listed in Table 9.9.

Table 9.9: The main parameters of the different lattice sectors

Sector number	1	2	3	4	5
Quadrupole number	184	82	280	254	172
Quadrupole length [cm]	35	85	85	85	85
Quadrupole spacing [m]	2.01	2.01	4.02	6.03	8.04

9.2.6.4 Beam dynamics

The pre-alignment and Beam-Based-Alignment (BBA) alignment methods foreseen for the 500 GeV linacs are the same as those for the 3 TeV linacs. Simulations show that the emittance growth after BBA is well below the budget considering the same static imperfections as for the 3 TeV case.

Table 9.10 shows the emittance growth at the end of the 500 GeV linacs. The most important contributions, after the RF alignment, arise from the tilt of the structures, the limited accuracy of the wakefield monitors, and the quadrupole rolls. For each error source the emittance growth is smaller than for the 3 TeV design while the overall budget is the same. Hence the tolerances could be slightly relaxed.

9.2.6.5 Vacuum requirement

The vacuum in the main linac has to be good enough to avoid the fast beam-ion instability, see §3.8. Simulations of this instability have been performed and it is concluded that the requirements are the same or slightly relaxed with respect to the 3 TeV case, depending on the vacuum composition.

Table 9.10: List of individual imperfections and resulting vertical emittance growth for the different steps of the BBA alignment method. First one-to-one steering is applied (1-2-1) then, dispersion free steering (DFS) and finally the structures are aligned using the wakefield monitors (RF).

Imperfection	With respect to	Value	$\Delta\epsilon_y$ 1-2-1[nm]	$\Delta\epsilon_y$ DFS[nm]	$\Delta\epsilon_y$ RF[nm]
Girder end point	Articulation point	$5\ \mu\text{m}$	0.62	0.62	0.02
Roll	Longitudinal axis	$100\ \mu\text{rad}$	0.23	0.23	0.23
BPM offset	Wire reference	$14\ \mu\text{m}$	340	7.11	0.08
Cavity offset	Girder axis	$14\ \mu\text{m}$	3	3.19	0.01
Cavity tilt	Girder axis	$141\ \mu\text{rad}$	0.10	0.43	0.41
BPM resolution		$0.1\ \mu\text{m}$	0.00	0.51	0.01
Wake monitor	Structure centre	$3.5\ \mu\text{m}$	0.00	0.00	0.21
All			343.95	16.27	0.95

9.2.7 Beam Delivery Systems

9.2.7.1 Overview

The design of the CLIC BDS at 500 GeV follows the same philosophy and criteria as for the nominal design at 3 TeV, see §3.5. Therefore both designs consist of the same sections and fulfil the same functions. The following constraints arise from the 500 GeV design:

- The IP must be at the same location at 500 GeV and at 3 TeV. The crossing angle can vary slightly.
- The linac location and orientation must remain unchanged at both energies.
- The two BDS designs must fit in the same tunnel of 5.3 m diameter.
- The BDS at 500 GeV can be shorter to reduce the cost of the first stage. The length difference should correspond to the length of one Drive-Beam decelerator in order to be able to use the same turn-arounds at 3 TeV as at 500 GeV.

9.2.7.2 Beam parameters

Table 9.11 shows the key BDS and IP parameters at 500 GeV.

9.2.7.3 Systems

The diagnostics and collimation sections of the 500 GeV BDS have been scaled down from the 3 TeV design. Since the geometric emittances are larger the beta functions can be lower and still meet the $1\ \mu\text{m}$ beam size at the laser wire and guarantee survival of the first collimator. The bending angles at 500 GeV need to be larger in order to increase dispersion and better cancel the chromatic aberrations. The final layout is obtained by slightly varying the IP crossing angle and the collimation bending angles until the above constraints are satisfied. The resulting optics and layout are displayed in Fig. 9.8. The maximum deviation between the 500 GeV and the 3 TeV layout is 40 cm. This is consistent with a common tunnel of 5.3 m diameter. The IP crossing angle is 18.6 mrad instead of the 20 mrad at 3 TeV. This variation is considered acceptable for the detector and the post-collision line, see below.

9.2.8 Machine Detector Interface and post collision line

At 500 GeV the crossing angle is different from the 3 TeV case, 18.6 mrad instead of 20 mrad. Hence the position of the QD0 is different than at 3 TeV. The magnet itself follows the same design philosophy as the 3 TeV design, but a larger aperture is needed while the field gradient can be lower.

9.2 PRELIMINARY DESIGN OF A 500 GeV ACCELERATOR

Table 9.11: Key parameters of the BDS at 500 GeV. Effective values are given for the IP parameters.

Parameter [Units]	Value
Length (linac exit to IP distance)/side [m]	1750
Maximum energy/beam [TeV]	0.25
Distance from IP to first quad, L^* [m]	4.3
Crossing angle at the IP [mrad]	18.6
Nominal core beam size at IP, σ^* , x/y [nm]	202/2.3
Nominal beam divergence at IP, θ^* , x/y [μ rad]	25/23
Nominal beta-function at IP, β^* , x/y [mm]	8/0.1
Nominal bunch length, σ_z [μ m]	72
Nominal disruption parameters, D , x/y	0.1/12
Nominal bunch population, N	6.8×10^9
Beam power in each beam [MW]	4.9
Preferred entrance train to train jitter [σ]	< 0.2
Typical nominal collimation aperture, x/y [σ_x/σ_y]	10/55
Vacuum pressure level, near/far from IP [10^{-9} mbar]	100/10

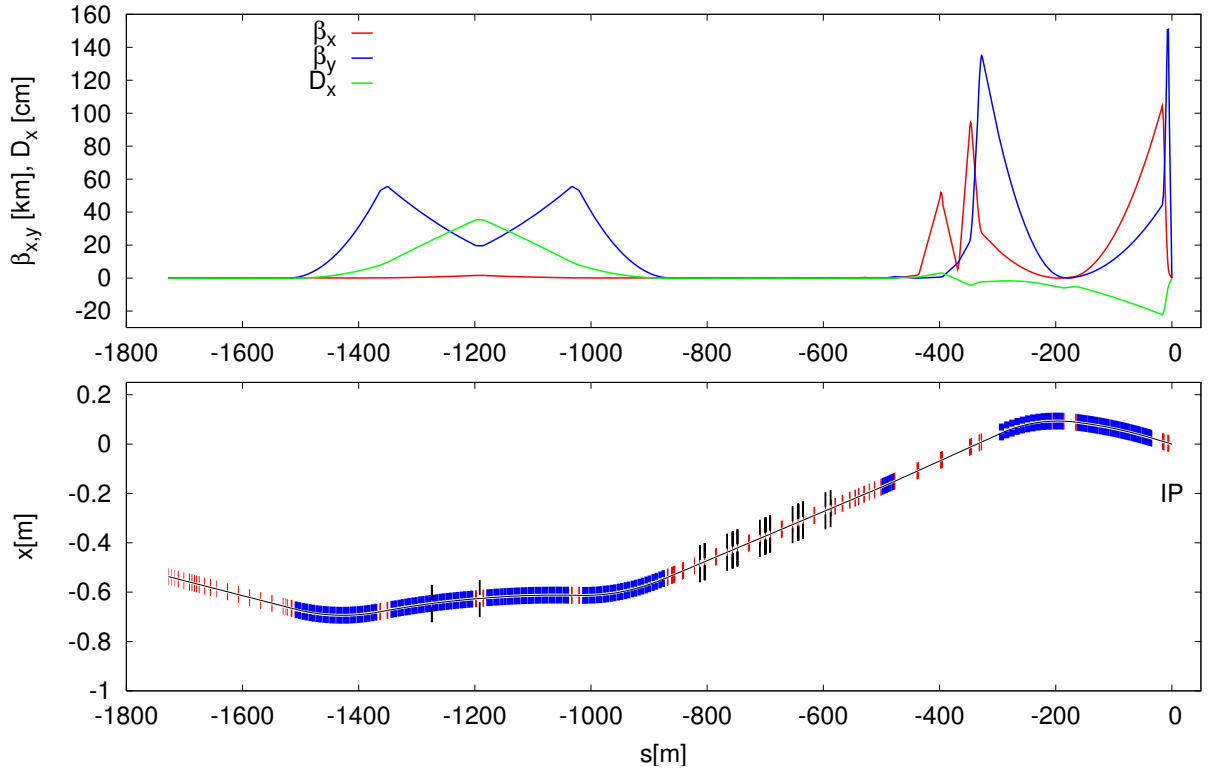


Fig. 9.8: CLIC 500 GeV optics (top) and layout (bottom). Dipoles, quadrupoles, and collimators are shown in blue, red, and black, respectively on the layout plot.

As the outgoing beam follows the direction of the incoming beam, its path will also be different from the 3 TeV case, by 0.7 mrad. Therefore the photons and e^+/e^- will hit the final beam dumps at an

offset of 19 cm with respect to the nominal case. As the divergence of the disrupted outgoing beam is much smaller than at 3 TeV, the impact is still fully contained within the spot at 3 TeV. This has been verified by simulation as shown in Fig. 9.9. The charged outgoing beam can be centred with an optional horizontal dipole magnet.

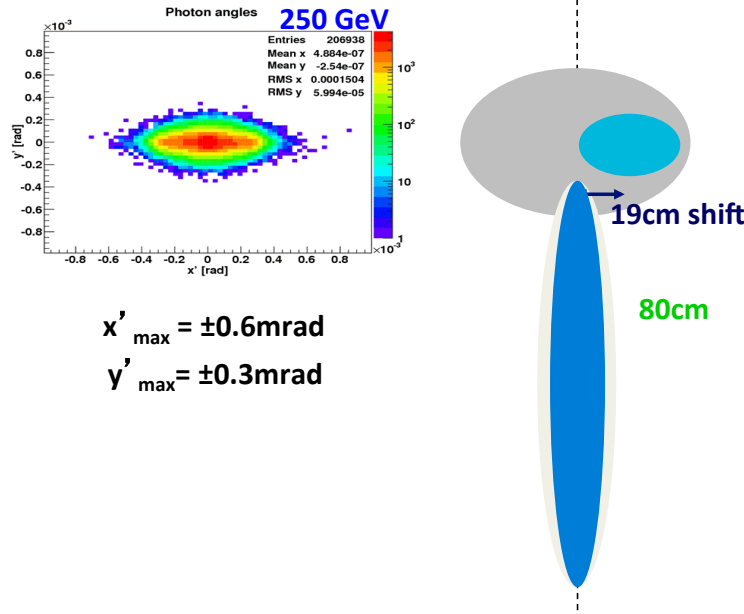


Fig. 9.9: The beam impact on the final beam dump at 500 GeV, overlaid with the 3 TeV case.

9.2.9 Drive-Beam

The main differences between the 500 GeV and the 3 TeV cases are

- At 500 GeV, the Main Beam accelerating RF structures will be different and must be fed with 16% more power, i.e., 74.2 MW compared to 63.9 MW at 3 TeV. The PETS will be identical in both cases. Therefore, the power extracted from the Drive-Beam in the decelerators will be 16% larger in an otherwise identical beamline as seen by the beam. The nominal beam current and the nominal beam momentum must both increase by 8%, i.e., respectively to 109 A compared with the 101 A, and to 2.56 GeV compared with 2.37 GeV. The train length which enters every decelerator will be identical.
- A single Drive-Beam generation complex is considered. The Drive-Beam trains for the two main linacs will be produced with a single drive linac and the frequency multiplication made in a single complex.
- The main linacs will each be made of five sectors as compared to twenty-four at 3 TeV. The full Drive-Beam train accelerated by the Drive-Beam linac will be shorter compared to the 3 TeV case. The single Drive-Beam linac will feed $2 \times 5 = 10$ decelerators in the main linac at 500 GeV, as compared to 24 per Drive-Beam linac at 3 TeV.

An implicit reference is made throughout this section to §4 on the Drive-Beam Complex in this volume and to Appendix A which lists the detailed CLIC parameters.

9.2.9.1 Linac structure and radio-frequency

The increase of power may be obtained either by using the same 15 MW klystrons and by making the linac 16% longer, or by considering more powerful klystrons (17.4 MW) thus maintaining the linac length. If 15 MW klystrons are used, the structures would be slightly overloaded due to the higher beam current, but the RF to beam efficiency remains almost unchanged. However, a longer linac would complicate the extension to higher energy and the additional civil engineering would be redundant. Hence we rather consider the more straightforward second case. Depending on the choices made for a future extension, and with the experience gained at 500 GeV, the larger klystron power might also appear to be a good investment. With the shorter overall Drive-Beam linac pulse length (10/24 of the 3 TeV case), the average power delivered by the RF system will be smaller thus making the operation easier compared to the 3 TeV case.

9.2.9.2 Frequency multiplication

The frequency multiplication system will be identical to that at 3 TeV. The beam loading in the RF-deflectors will be larger by 8%. Their design must be adapted accordingly. Collective effects will be slightly larger as well, but the frequency multiplication system contributes little to the overall picture from the gun to the decelerator. The energy deposition associated to synchrotron radiation will be smaller by $1.08^5 \times 10/24 = 0.61$.

9.2.9.3 Beam transport to the decelerators

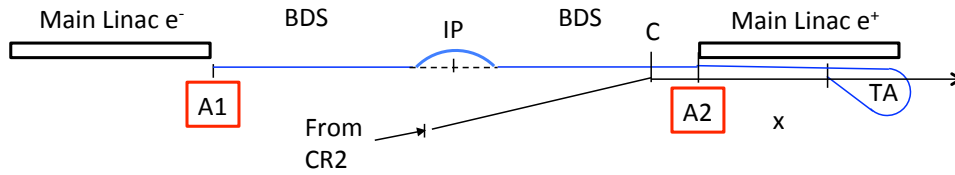


Fig. 9.10: The long delay loop

With a single Drive-Beam linac, the trains which feed the the e^- linac (loosely called e^- trains below) are formed and transported first, followed by those feeding the e^+ linac (e^+ trains below). All the trains are transported through the same channel down to the main tunnel next to the extremity of the e^+ linac, see Fig. 9.10. The time needed to produce the Drive-Beam for five sectors is $\Delta t = 5 \times 24 \times 240 \text{ ns} = 28\,800 \text{ ns}$. The corresponding length is $\Delta L = c\Delta t = 8640 \text{ m}$. The e^- trains are produced first and must follow a delay line of length ΔL following the injection point C of Fig. 9.10 such that the head of the first train reaches the end of the e^- linac (A1 in Fig. 9.10) at the same time as the first e^+ train reaches A2. The e^- trains travel in the Long Transfer Line of the e^+ trains across a distance x where a dedicated turn-around loop is located. The e^- trains then travel back across the Beam Delivery System, with an isochronous by-pass loop around the experimental cavern. The distance x is equal to $x = (\Delta L - 2L_{\text{BDS}} - L_{\text{TA}} - \delta_{\text{by-pass}}) = 2360 \text{ m}$, with $L_{\text{TA}} = 146 \text{ m}$, $L_{\text{BDS}} = 1870 \text{ m}$, and $\delta_{\text{by-pass}} = 32 \text{ m}$ is the difference in length between the by-pass and the corresponding straight distance. The turn-around loop is identical to the ones that drive the Drive-Beam trains in their respective decelerators. Schematically displayed in Fig. 9.11, the by-pass line is made of four isochronous arcs and a straight segment.

The optic of the arcs is derived from the arcs of the combiner rings of the frequency multiplication system. The magnets and the vacuum system are similar as well. The aperture of the vacuum system is identical with a radius of 40 mm.

The optics, the magnets, and the vacuum system of the additional long straight line for the e^- trains will be identical to the long transfer line which allows for the transport of the Drive-Beam along the main tunnel, i.e., weak quadrupole magnets and a vacuum chamber radius of 200 mm. The beam path-length on surface and down to the tunnel up to the point C of Fig. 9.10 is identical to the 3 TeV case. From C on, the first e^+ train travels across five sectors as compared to 24 in the 3 TeV case. The first e^- train travels across the equivalent of 15 sectors (10 along the long delay loop then 5 along its Main Linac). Therefore, as far as collective effects and optical aberrations are concerned, the 500 GeV case is less demanding.

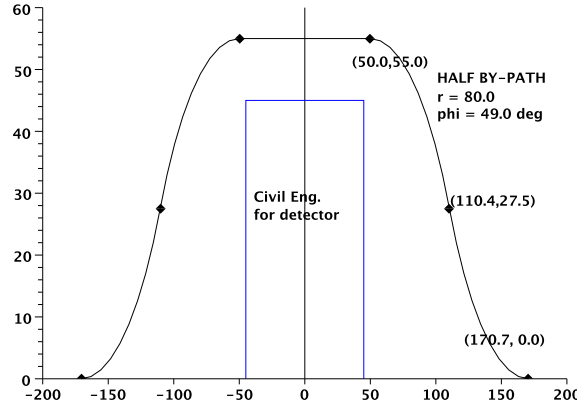


Fig. 9.11: The by-pass around the experimental cavern. It is made of four isochronous arcs of radius $R = 80\text{ m}$ each covering an angle $\phi = 49^\circ$ and of a drift space of 100 m. The blue rectangle contains both the experimental cavern around the interaction point and one 'garage' cavern. The aspect ratio of the picture is not unity.

9.2.9.4 Collective effects

Multi-bunch resistive wall instabilities induce beam offsets $\Delta y \propto N_{b,\text{dec}}^{1/2} Q_{b,\text{dec}} / E_{\text{in,dec}}$ [10]. The number of bunches $N_{b,\text{dec}}$ is 10/24 smaller at 500 GeV as compared to 3 TeV, while Q/E remains constant. As for ion effects, beam de-tuning and instability rise-times are both proportional to $N_{b,\text{dec}} Q_{b,\text{dec}}$, so they are smaller at 500 GeV. Depending on the beam line (linac or fixed-energy beam lines, bunch spacing), the dependence on Q or E varies but never exceeds the factor 10/24. Therefore collective effects are always smaller at 500 GeV.

9.3 Parameter space for other intermediate energies

9.3.1 Parameter choice at individual energies

The potential parameters at different energies can be based on existing CLIC designs. They have been established in detail at 3 TeV centre-of-mass energy and in less detail for 500 GeV. Designs at lower energies can be derived by shortening the main linac and re-designing the beam delivery system for the lower beam energy. All the Main Beam parameters, except for the final energy, remain unchanged. Consequently the Main Beam injection complex also remains unchanged. The length of the linac, and hence the collision energy, is most conveniently constructed from a specific number of complete decelerator sectors. The Drive Beam complex will require some slight modifications. These are discussed below.

Parameters for different energies between 1 TeV and 3 TeV are shown in Table 9.12. These are based on the same structure as the 3 TeV baseline design. Similarly Table 9.13 shows parameter sets below 500 GeV, based on the same structures as at 500 GeV. The luminosities have been calculated using the same beam delivery system design as at 3 TeV and 500 GeV respectively. This is a slightly conservative approach, as it might be possible to optimize the system design for a specific energy.

Table 9.12: Potential parameters of CLIC at different centre-of-mass energies. The design is based on the same structure design as CLIC at 3 TeV.

$E_{c.m.}$	[TeV]	1.0	1.5	2.0	2.4	3.0
n_{DB}		8	12	16	19	24
n_b		312	312	312	312	312
N	$[10^9]$	3.72	3.72	3.72	3.72	3.72
L	$[10^{34} \text{cm}^{-2} \text{s}^{-1}]$	2.2	3.75	5.0	5.7	5.9
$L_{0.01}$	$[10^{34} \text{cm}^{-2} \text{s}^{-1}]$	1.0	1.45	1.8	1.98	2.0
n_γ		1.7	1.95	2.1	2.1	2.1
$\Delta E/E$	%	17	22	26	27	28
N_{coh}		1.73×10^7	1.39×10^8	3.61×10^8	5.33×10^8	6.8×10^8
E_{coh}		2.51×10^9	2.81×10^{10}	9.10×10^{10}	1.56×10^{11}	2.1×10^{11}
N_{incoh}		1.2×10^5	2.2×10^5	3.0×10^5	3.4×10^5	3.0×10^5
E_{incoh}		2.21×10^6	7.01×10^6	1.40×10^7	1.98×10^7	2.3×10^7
n_{had}		0.7	1.5	2.5	3.1	3.2

9.3.2 Impact on system design

9.3.2.1 Sources, damping rings and Ring to Main Linac Transport

As mentioned above, the performance requirements of the Main Beam complex up to the main linac remain unchanged.

9.3.2.2 Main Linac

Above 500 GeV, the main linac will be the first part of the 3 TeV design. Hence, the beam conditions in the main linac remain either unchanged — e.g., the energy spread required for BNS damping — or improved — e.g., the emittance growth along the main linac due to static imperfections will be reduced, since the linac is shorter.

Below 500 GeV, the linac will correspond to the first part of the 500 GeV design, except that some of the accelerating structures are not installed (see below). However, the beam conditions will be the

Table 9.13: Potential parameters of CLIC at different centre-of-mass energies. The design is based on the same structure design as CLIC at 500 GeV.

$E_{\text{c.m.}}$	[GeV]	250	350	500
n_{DB}		3	4	5
n_{b}		354	354	354
N	$[10^9]$	6.8	6.8	6.8
L	$[10^{34} \text{ cm}^{-2}\text{s}^{-1}]$	1.2	1.69	2.3
$L_{0.01}$	$[10^{34} \text{ cm}^{-2}\text{s}^{-1}]$	0.9	1.13	1.4
n_{γ}		1.0	1.2	1.3
$\Delta E/E$	%	2.7	4.3	7
N_{incoh}		3.7×10^4	5.4×10^4	8×10^4
E_{incoh}		4.8×10^4	1.29×10^5	3.6×10^5
n_{had}		0.065	0.14	0.3

same or better than at 500 GeV.

9.3.2.3 Beam delivery system

In the beam delivery system (BDS), the reduced beam energy will allow the magnet apertures to be increased, in particular the aperture of the final doublet. This will allow relaxation of the collimation requirement.

For simplicity the BDS design at 3 TeV has been used for energies above 1 TeV. That is, all magnets are scaled to the lower beam energy, so that the gradient is reduced linearly with the centre-of-mass energy. A very small correction to this scaling is applied to take account of the non-linearity of the the synchrotron-radiation-induced energy loss in the bends of the BDS with energy. It should be noted that the performance of a fully re-optimized system would be slightly improved. Owing to the smaller gradient requirements, the magnet apertures can be opened up proportionally to $1/E$, while the beam sizes and divergences increase only as $1/\sqrt{E}$. The increase in magnet aperture allows the transverse collimation aperture to be increased accordingly, so that the collimation aperture normalized to the beam size can be relaxed as \sqrt{E} . The energy collimation system will remain unchanged.

9.3.2.4 Drive Beam complex

Some modifications will be needed to the Drive Beam complex. For the designs based on the 3 TeV structure, the linac energy has been chosen to be consistent with a number of complete decelerator sections. Consequently the changes are rather simple:

- For energies above 1.5 TeV, the pulse length in the Drive Beam accelerator can be reduced, since fewer Drive Beam decelerators are required along the main linac.
- For energies up to 1.5 TeV, only one Drive Beam generation complex is needed, feeding both linacs. This is similar to the 500 GeV machine described in §9.2. The pulse length is again given by the total number of Drive Beam decelerators that need to be fed.

The number of Drive Beam decelerators n_{DB} per linac is listed in Table 9.12. For the designs based on the 500 GeV structure, natural centre-of-mass energies would be about 300 GeV and 400 GeV corresponding to three or four Drive Beam decelerators. However, centre-of-mass energies of 250 GeV and 350 GeV have been used. In these cases the energy gain per decelerator can be lower than at 500 GeV. This

9.3 PARAMETER SPACE FOR OTHER INTERMEDIATE ENERGIES

uses fewer accelerating structures per decelerator. However, the length of the decelerator has to remain unchanged, since it is directly linked to the RF pulse length. For example, in the case of 250 GeV, the acceleration required per sector is about 84% of the value needed for 500 GeV. As a consequence, the linac will have 60% of the length at 500 GeV (three compared to five decelerators) but each sector contains only 84% of the accelerating structures. This allows the Drive Beam energy to be reduced by about 16%.

9.4 Power consumption with staged construction

9.4.1 Overview

The total electrical power is evaluated as a function of the centre-of-mass energy E_{CM} between 500 GeV and 3 TeV with a detailed power map at these two limits and at an intermediate value of 1.5 TeV. The power needs of these three reference cases are evaluated by considering for each one a stage of construction for which the hardware built allows one to reach the corresponding E_{CM} energy. The power at any other intermediate energy can be obtained by interpolating between the two adjacent reference cases. Energy scanning below the nominal energy is not considered here. The case $E_{\text{CM}} = 3$ TeV is discussed in detail in §2.9. The evaluation of the other two cases is derived in the next sections. Detailed data are found in Table 9.18. The nominal luminosity of the three reference cases is given in Table 9.14 together with the total electrical power, the Main Beam power (two beams), and the indicative power yield.

Table 9.14: The nominal luminosity and the total electrical power for the three reference cases.

Centre-of-mass energy	Luminosity	Electrical power	Main Beam power (2 beams)	Overall efficiency
E_{CM} [TeV]	$\mathcal{L}_{1\%}$ [cm ⁻² s ⁻¹]	P [MW]	P_{MB} [MW]	$\eta = P_{\text{MB}}/P$ [%]
0.5	1.40×10^{34}	271	9.4	3.5
1.5	1.45×10^{34}	361	14	3.9
3	2.00×10^{34}	582	28	4.8

9.4.1.1 Centre-of-mass energy 500 GeV

CLIC at 500 GeV is discussed in §9.2. The main linacs will each be made of five sectors instead of 24 at 3 TeV. The PETS will be identical, but the accelerating structures are optimized for the doubled intensity of the Main Beam bunches thus resulting in a lower operating gradient. The current and the momentum of the Drive Beam are both increased by 8%. The Drive Beam trains will therefore be 5/24 times shorter but with a power which is proportionally 16% larger. The power needed by the Drive Beam linac is $P_{500\text{GeV}} = 1.16 \times 5/24 \times P_{3\text{TeV}}$ to which the constant offset of the rise-time of the modulators is added, see Table 9.18. The shorter pulse allows a single drive-beam formation complex to be used. Only one drive-beam linac is built, followed by a single frequency-multiplication complex, see Fig. 9.12 and the corresponding figure for the 3 TeV case in §2.9. The five trains for the e^- main linac are produced first. They are transported down to the main tunnel through the e^+ line. In order to maintain the synchronization between the two main linacs, these trains follow a ‘delay line’ along the e^+ main linac and go through a turn-around similar to the Drive Beam return loops of the main tunnel. They then travel back towards the e^- linac, with a by-pass around the experimental area. The associated electrical power is quoted as item 12 in Table 9.18. The double Main-Beam intensity w.r.t. to the 3 TeV cases requires 8 MW in order to produce twice as many positrons, and the damping ring requires slightly more power, see items 2 and 4 in Table 9.18. The beam delivery system requires slightly less power.

9.4.1.2 Centre-of-mass energy 1.5 TeV

In order to reach a centre-of-mass energy of $E_{\text{CM}} = 1.5$ TeV, the main linacs are made of 12 sectors. The structure of the Main Beam and the Drive Beam trains are identical to those at 3 TeV. Similar to the 500 GeV case, a single drive-beam complex is sufficient to produce all the trains for both the e^+ and e^- decelerators. A longer ‘delay line’ allows the two main linacs to be synchronized. All the main positions in Table 9.18 are either identical or halved as compared to the 3 TeV case.

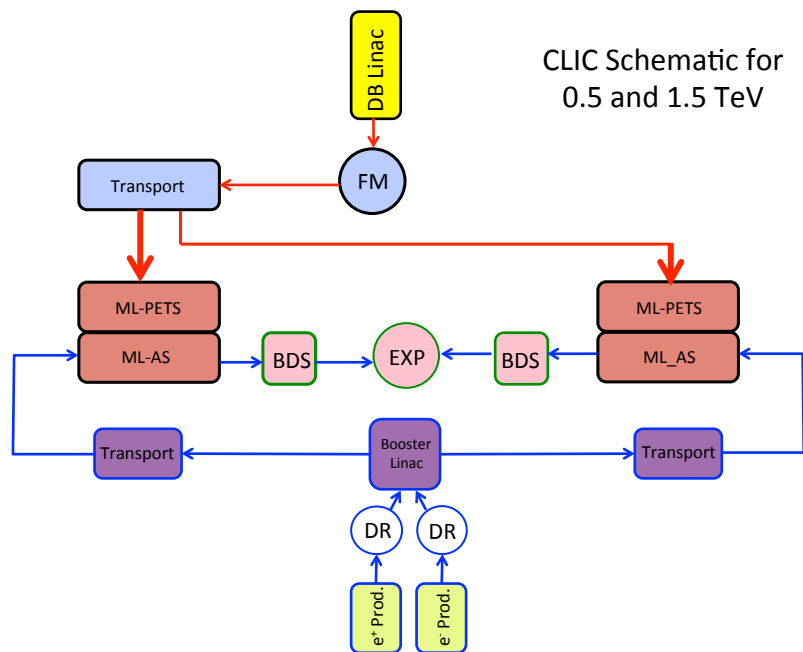


Fig. 9.12: The block diagram of the CLIC complex at 0.5 and 1.5 TeV. The Drive-Beam complex is made of one system. It consists of a source and a 1 GHz linac, followed by the frequency multiplication system (FM: delay loop and combiner rings) and the transport to the main tunnel down to each decelerator (PETS). The Main Beam production is made of two sources (electrons and positrons), each followed by a damping ring (DR), and a transport down to the head of the Main Linac (ML). The Main Linac is made of two-beam modules, with PETS structures to decelerate the Drive Beam and feed the RF power to the Accelerating Structures (AS). The beam delivery system (BDS) prepares the Main Beam for high-luminosity collisions in the experimental area.

9.4.1.3 Power maps

A detailed map is given in Table 9.18. The data for 3 TeV are discussed in §2.9. The reduction to 500 GeV and 3 TeV is discussed above. A summary by major systems is given in Table 9.15 and shown in the upper part of Fig. 9.13. The total power does not scale with the centre-of-mass energy. While the Drive-Beam power scales almost linearly with E_{CM} , there is an important overhead due to the nearly constant power needed to produce and transport the low-emittance Main Beams. The overhead of the frequency multiplication of the Drive Beam is mitigated by the use of a single Drive-Beam complex at 500 GeV and 1.5 TeV. The power maps, split by technical components, are shown in the lower part of Fig. 9.13. While the yield of the Drive-Beam RF system is already much optimized, see §2.9, the important contributions of the magnets and of the cooling and ventilation system deserve further consideration, see §9.4.2 below.

9.4.2 Potential for power and energy savings

A reduction of the power consumption at 500 GeV and 1.5 TeV can be considered with the same options discussed in more detail in §2.9 for the 3 TeV case. The power of the magnet system can be reduced by a factor two by using either permanent or super-ferric superconducting magnets. The power needed for ventilation and the cooling or heating of air can be reduced by one third. The water cooling is slightly reduced because of the improved magnet power map. The total power can thus be decreased by 42 MW (magnets: 27 MW; air: 13.5 MW; and water: 1.5 MW) at 500 GeV and by 55 MW (magnets: 37.5 MW; air: 15 MW; water: 2.5 MW) at 1.5 TeV. At 3 TeV the total economy is 86 MW. These potential savings require further study. No explicit studies were performed on either magnets or cooling and ventilation. A

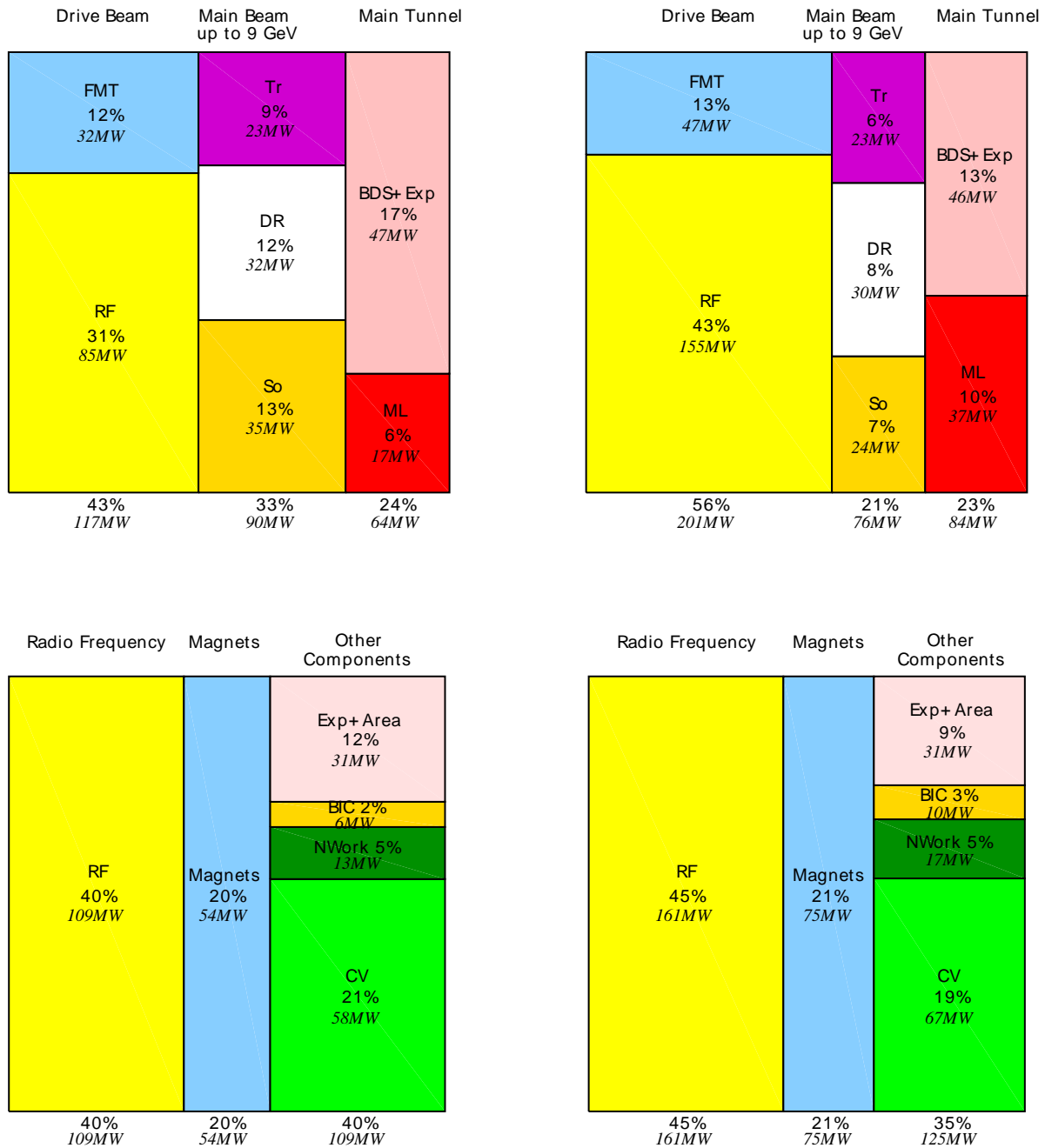


Fig. 9.13: Top: the power consumption for CLIC at 500 GeV (left), 1.5 TeV (right) by main systems, see text and Table 9.15. The contribution of each system is made of its own consumption to which a proportional fraction of contributions from cooling, ventilation, network losses, beam instrumentation, and controls are added. Bottom: the power consumption for CLIC at 500 GeV (left), 1.5 TeV (right) by technical components. The total power for each case is respectively 271 MW and 361 MW. These figures can be compared to corresponding ones at 3 TeV, see Figs. 2.34 and 2.35. The total power consumption at 3 TeV is 582 MW.

9.4 POWER CONSUMPTION WITH STAGED CONSTRUCTION

Table 9.15: Electrical power consumption split by major systems for the nominal CLIC at 500 GeV, 1.5 TeV and 3 TeV for respective luminosities $\mathcal{L}_{1\%} = 1.4 \times 10^{34} \text{ cm}^{-2}\text{s}^{-1}$, $\mathcal{L}_{1\%} = 1.45 \times 10^{34} \text{ cm}^{-2}\text{s}^{-1}$ and $\mathcal{L}_{1\%} = 2 \times 10^{34} \text{ cm}^{-2}\text{s}^{-1}$. Each value is the sum of the intrinsic power of a system and a proportional contribution to the power of auxiliary systems (instrumentation, controls, cooling, ventilation, and electrical network).

System	Sub-system	Power [MW]			Fractional power [%]		
		500 GeV	1.5 TeV	3 TeV	500 GeV	1.5 TeV	3 TeV
Drive Beam production							
	Linacs	85	155	305	31	43	52
	FM and Transport	32	47	88	12	13	15
Main Beam production							
	Sources	35	24	23	13	7	4
	Damping Rings	32	30	29	12	8	5
	Transport	23	22	22	9	6	4
Main Linac (TBM)		17	37	67	6	10	12
Beam delivery & experiment		47	46	47	17	13	8
Total		271	361	582	100	100	100

Table 9.16: Yearly energy and power consumption for the nominal case (upper part), see § 9.4.3, and with some power saving modifications (lower part), see § 9.4.2.

Nominal	Days	Power [MW]			Energy [TWh]		
		500 GeV	1.5 TeV	3.0 TeV	500 GeV	1.5 TeV	3.0 TeV
Nominal operation	177	271	361	582	1.15	1.53	2.47
Fault-induced down-time	44	40	45	60	0.04	0.05	0.06
Programmed stops	144	40	45	60	0.14	0.16	0.21
Energy consumption per year					1.33	1.74	2.74
Economy	Days	Power [MW]			Energy [TWh]		
		500 GeV	1.5 TeV	3.0 TeV	500 GeV	1.5 TeV	3.0 TeV
Nominal operation	177	229	306	496	0.97	1.30	2.11
Fault-induced down-time	44	28	30	40	0.03	0.03	0.04
Programmed stops	144	28	30	40	0.10	0.10	0.14
Energy consumption per year					1.10	1.43	2.29

balance between investment costs must be worked out and the usual construction standards for industrial buildings must be reconsidered for specific cases.

9.4.3 Energy consumption

The total power will be used under nominal beam conditions for only a fraction of the year. The machine will be stopped for a long shutdown of approximately 90 days per year. Considering that there will be a short technical stop of two days every two weeks (reset of faulty equipment) and a longer one of seven days every two months (maintenance), the machine will be stopped for a further 54 days per year. Therefore programmed stops amount to 144 days leaving 221 days for production. Additional stops associated with faults can be estimated using LHC data, where 20% of beam time is lost. With ten times more active elements, CLIC cannot be expected to do any better. Using the LHC figure gives an additional down-time of 44 days, leaving 177 days of production at nominal power. During stops there is a minimal

residual power consumption, mostly in order to maintain ventilation and cooling or heating in buildings and tunnels and some control systems. The yearly energy consumption in Table 9.16 integrates both the production and the non-production days. The data in the upper part of the table are related to the nominal power maps and in the lower part to the reduced power scheme discussed in §9.4.2.

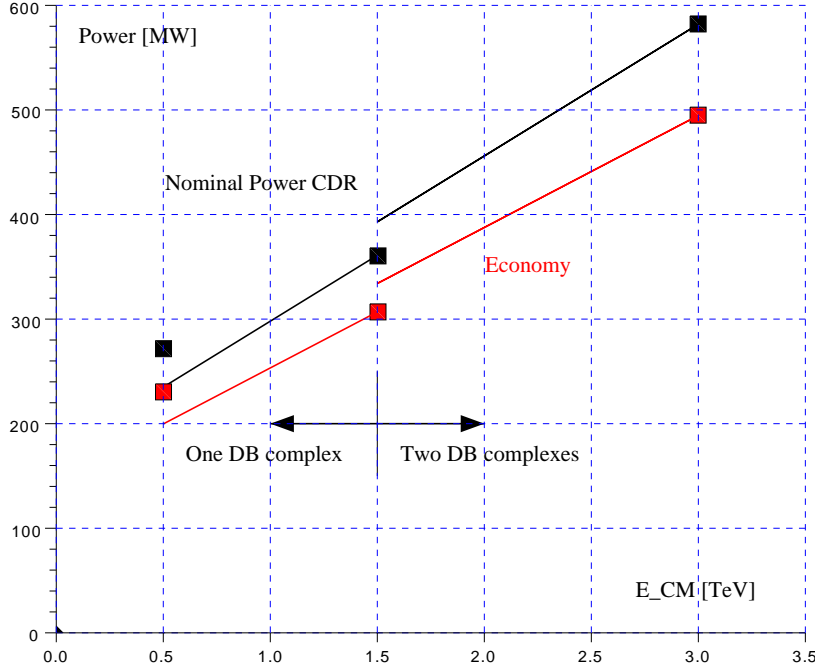


Fig. 9.14: The nominal power map of CLIC between the centre-of mass energies 0.5 TeV and 3 TeV. The three reference points (black squares) and the steps above 1.5 TeV are discussed in §9.4.4. The upper black curves correspond to the nominal CDR case and the lower red curves to the case with some power savings, see §9.4.2.

9.4.4 Nominal power over the range of centre-mass-energies

A continuous variation of electrical power with the centre-of-mass E_{CM} is shown in Fig. 9.14. The total power of the three reference cases is worked-out in §9.4.1. As discussed above, a single Drive-Beam formation complex is sufficient at 0.5 TeV and 1.5 TeV, while two are needed at 3.0 TeV. Detailed studies showed that a full Drive-Beam train feeding 24 sectors of the main linac is stable across the Drive-Beam linac and the frequency multiplication system in the 3 TeV case. With a single complex feeding the two main linacs at 1.5 TeV, the case is identical. The territory corresponding to a center-of-mass $E_{CM} > 1.5$ TeV with a single Drive-Beam linac, which shall then be made longer with ratio $L/L_0 = E_{CM}/1.5$ has not been studied. We therefore consider that a second Drive-Beam linac is needed immediately above 1.5 TeV. This requires the installation of a second frequency multiplication system and additional transport lines, including the additional need of auxiliary systems, mostly cooling and ventilation. The step of the curves in Fig. 9.14 corresponds to the power consumption of these additional systems. At 500 GeV, specific more intense beams are considered for better luminosity, see §9.2, thus requiring additional power. In order to interpolate between 500 GeV and 1.5 TeV, we consider the power needs of the case of nominal beam intensities at 500 GeV, which is discussed as 'Staged Scenario B' in the CLIC CDR Executive Summary. Between two reference points a simple linear interpolation is used.

9.4 POWER CONSUMPTION WITH STAGED CONSTRUCTION

A less power-demanding case is presented with red marks in Fig. 9.14, according to the data presented in §9.4.2.

9.4.5 Power and energy consumption for staged construction and operation scenario

Construction in three steps is considered, with each step corresponding to the reference E_{CM} energies discussed above. At each step, the operational scenario is an increase in luminosity over a few years (four years at 500 GeV, three years at 1.5 TeV and two years at 3 TeV) until the nominal value is reached, see Table 9.17. The maximum power reached during the luminosity ramping is lower than the nominal maximum power, but is only partially correlated to the luminosity, see Table 9.17.

At 500 GeV, a single positron target is used for the first three years (–10 MW compared to the full nominal mode). At the three stages and during the first year, the 177 days of operation are divided into three periods of 59 days. During the first period, a single train is formed in order to commission the Drive Beam generation complex. Then, each decelerator is commissioned, one after the other (–106 MW, –160 MW, and –230 MW at each construction stage compared to their respective full nominal mode). In the second period, the Main Linacs are commissioned. Nominal operation occurs during the third period at nominal power. The initial low-luminosity operation is related to the learning process with dynamic alignment, optical adjustment of the BDS and of the final focus, which have little or no impact on the power consumption. The power quoted in Table 9.17 is the average value over the three periods. The energy is the power integrated over time including the periods without beam. During operation with beam, a down-time of 50% is considered in addition to the down-time due to faults as discussed in §9.4.3. The beam time in the second year is divided into two periods of 88 days. During the first period, only one Main Linac is powered and the additional down-time is estimated at 30%. Nominal conditions are considered in the second period. The third year is nominal in all three stages.

The data of Table 9.17 are shown in Fig. 9.15 for luminosity and in Fig. 9.16 for power and energy. These values are quite optimistic. Unexpected operational difficulties may mitigate these values. Both total luminosities and luminosities limited to a 1% momentum window are shown. The nominal CDR power and energy maps of the CDR reference case are shown (black curves) together with the more economical option discussed in §9.4.2 (blue curves).

Table 9.17: Luminosity, power and energy with time for three reference centre-of-mass energies E_{CM} .

Years	E_{CM} [TeV]	$\mathcal{L}_{1\%}$ [cm ⁻² s ⁻¹]	\mathcal{L} [cm ⁻² s ⁻¹]	$\mathcal{L}_{1\%}\text{t/year}$ [fb ⁻¹]	$\mathcal{L}\text{t/year}$ [fb ⁻¹]	Power & Energy	
						[MW]	[TWh/Year]
1	0.5	1.00×10^{33}	1.60×10^{33}	12	20	207	0.62
2	0.5	3.50×10^{33}	5.60×10^{33}	43	69	230	0.76
3	0.5	7.00×10^{33}	1.12×10^{34}	86	137	261	0.95
4–5	0.5	1.40×10^{34}	2.24×10^{34}	171	274	271	1.33
6	1.5	3.75×10^{33}	9.40×10^{33}	46	115	275	0.79
7	1.5	7.50×10^{33}	1.88×10^{34}	92	229	317	1.13
8–12	1.5	1.50×10^{34}	3.75×10^{34}	184	459	361	1.74
13	3.0	5.00×10^{33}	1.50×10^{34}	61	184	427	1.18
14	3.0	1.00×10^{34}	3.00×10^{34}	122	367	582	1.74
15–20	3.0	2.00×10^{34}	6.00×10^{34}	245	734	582	2.74

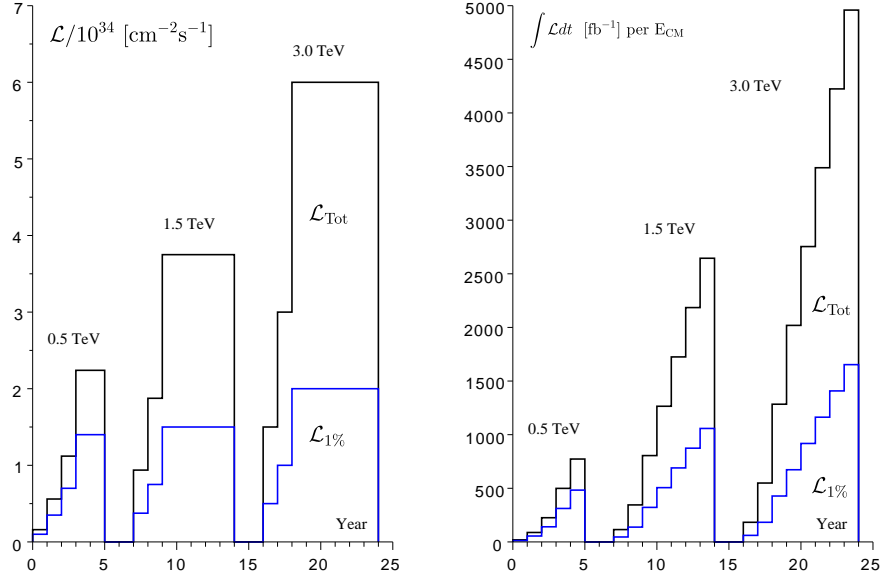


Fig. 9.15: The luminosity map of CLIC at the stages of construction corresponding to the three reference E_{CM} energies. An indicative gap of two years is considered between each stage. The uppermost black curve corresponds to the nominal case and the lower blue curve to the case with some power savings. Left: luminosity; Right: integrated luminosities per E_{CM} case. Black curve: total luminosity. Blue curve: luminosity in the 1% energy band around E_{CM} .

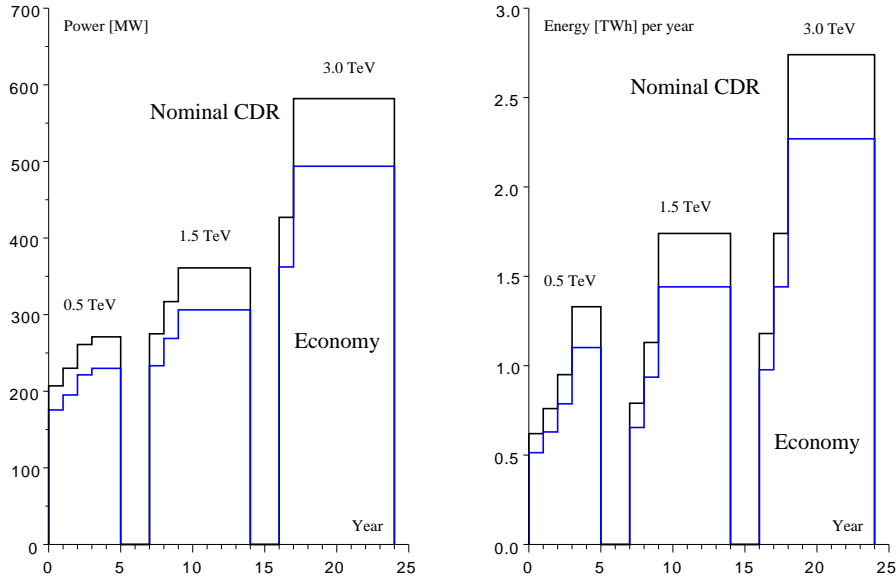


Fig. 9.16: The nominal power map of CLIC at the stage of construction corresponding to the three reference E_{CM} energies. An indicative gap of two years is considered between each stage. The uppermost black curve corresponds to the nominal case and the lower blue curve to the case with some power savings.

Table 9.18: Detailed direct electrical power consumption at 500 GeV, 1.5 TeV, and 3 TeV for luminosities $\mathcal{L}_{1\%} = 1.4 \times 10^{34} \text{ cm}^{-2} \text{ s}^{-1}$, $\mathcal{L}_{1\%} = 1.45 \times 10^{34} \text{ cm}^{-2} \text{ s}^{-1}$, and $\mathcal{L}_{1\%} = 2 \times 10^{34} \text{ cm}^{-2} \text{ s}^{-1}$ respectively.

Item no.	System	Power [MW]		
		500 GeV	1.5 TeV	3 TeV
1	MB injector magnets	1.0	1.0	1.0
2	MB injector RF	24.3	16.5	16.5
3	MB pre and damping ring magnets	5.1	5.1	5.1
4	MB pre and damping ring RF	17.6	17.2	17.2
5	MB transport	16.5	16.5	16.5
6	MB long transport line	0.1	0.3	0.5
7	DB injector solenoids and magnets	3.4	3.4	6.8
8	DB injector RF	66.8	127.6	255.2
9	DB frequency multiplication	9.3	9.3	18.5
10	DB transport to tunnel	0.1	0.1	3.0
11	DB transport in tunnel	8.1	19.6	39.1
12	DB long delay line	2.0	2.3	0.0
13	2-beam module MB	1.0	2.5	4.9
14	2-beam module DB	2.8	6.7	13.3
15	Post decelerator	2.2	5.3	10.6
16	BDS	0.9	1.2	1.6
17	Interaction area	16.3	16.3	16.3
18	Dump line	1.1	1.7	3.3
19	Instrumentation (main tunnel)	2.1	5.0	10.0
20	Instrumentation (other)	3.0	3.0	4.0
21	Controls (main tunnel)	0.4	1.0	2.0
22	Controls (other)	0.8	0.8	1.0
23	Experiments	15.0	15.0	15.0
Sub total		200	277	462
24	Cooling and ventilation	58	67	93
25	Network losses	13	17	28
Total [MW]		271	361	582
Total [MVA]		284	379	609

9.5 Construction schedules

9.5.1 Introduction

A preliminary scheduling exercise has been conducted for the construction of the CLIC complex (Main Linacs, injectors, experimental areas, and infrastructures), based on the experience acquired during the construction of large accelerator and experimental facilities for particle physics, particularly the LHC machine, the CMS detector, and several linac projects at CERN. As an example, Table 9.19 shows a number of similarities between the experimental areas of CLIC and CMS, justifying the proposed method for the schedule study.

Table 9.19: Similarities between the CLIC and CMS experimental areas

CLIC	CMS
2 experimental caverns	1 experimental cavern & 1 service cavern
2 access shafts	1 access shaft & 1 experimental shaft
2 surface assembly halls	1 surface assembly hall
1 by-pass tunnel	1 by-pass tunnel
2 evacuation galleries	2 evacuation galleries
2 survey galleries	2 survey galleries
2 modular detectors (ILD, SiD-like) – 7 elements	1 modular detector – 13 elements

Two goals were set for the CLIC schedule exercise, within the constraints and boundary conditions stemming from the experience acquired with past CERN projects: 1) to construct, install, and commission as fast as possible a 3 TeV centre-of-mass machine, and 2) to include a first intermediate stage at 500 GeV centre of mass, the commissioning and operation of which should not bring additional delay to the 3 TeV centre-of-mass program.

The scheduling exercise and its results are presented in the following: the total time required for the construction, installation, and commissioning of CLIC at 500 GeV is 7.25 years, while the 3 TeV machine can be built in about 10 years. The sequencing of the various installation activities has been studied in some detail, in order to minimize interference and consequently the amount of time lost. The scheduling exercise includes the preparatory phases, e.g., environmental impact study, invitations to tender, launching of industrial procurement.

9.5.2 Preparation

9.5.2.1 *Environmental impact study*

In view of the size of the project, and of the applicable legislation and regulations in many countries, the project will require an environmental impact study and corresponding public enquiry as a prerequisite to authorization. As an example, for an implantation in the vicinity of the CERN site, the application of the French procedure, previously experienced for the LEP and LHC projects, has been considered. Establishing the environmental impact study documents and conducting the public enquiry would take around one year, after which a delay of six months is needed to obtain agreement from the central French authorities ('Conseil d'Etat'). An equivalent amount of time is considered necessary for acquiring land, negotiating rights of way with the local owners, and obtaining work permits.

9.5.2.2 *Procurement of series components*

The construction schedule takes into consideration the time required to produce the main components, especially those with very large numbers such as the accelerating structures. For the 3 TeV centre-of-mass machine, meeting the schedule requirement of not unduly delaying installation requires the complete

9.5 CONSTRUCTION SCHEDULES

production of the 142 760 accelerating structures within 65 months of contract adjudication. Assuming that the total procurement is split among three companies, and taking account of the overcapacity needed for imperfect production yield and times for set-up and ramp-up of production, the cruise production rate is 925 accelerating structures per month and per company (Fig. 9.17).

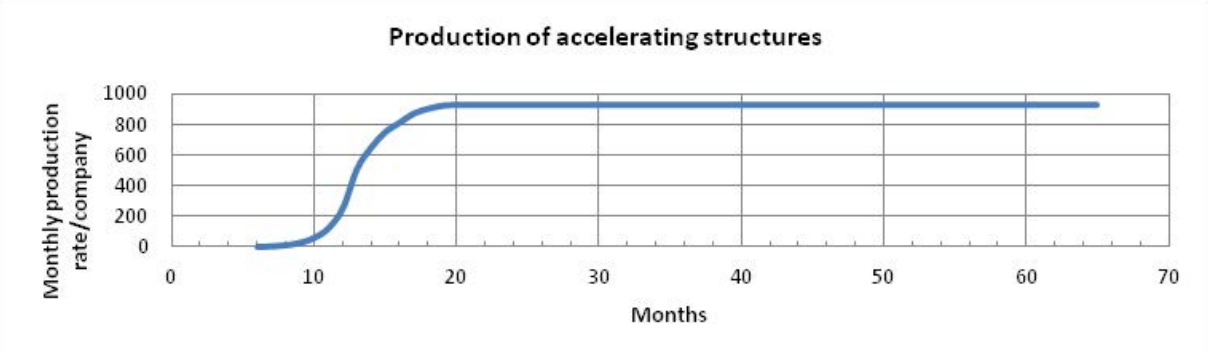


Fig. 9.17: Production of accelerating structures by each of the three suppliers

9.5.3 Main linacs

The general schedule for the Main Linacs is presented in Fig. 9.18.

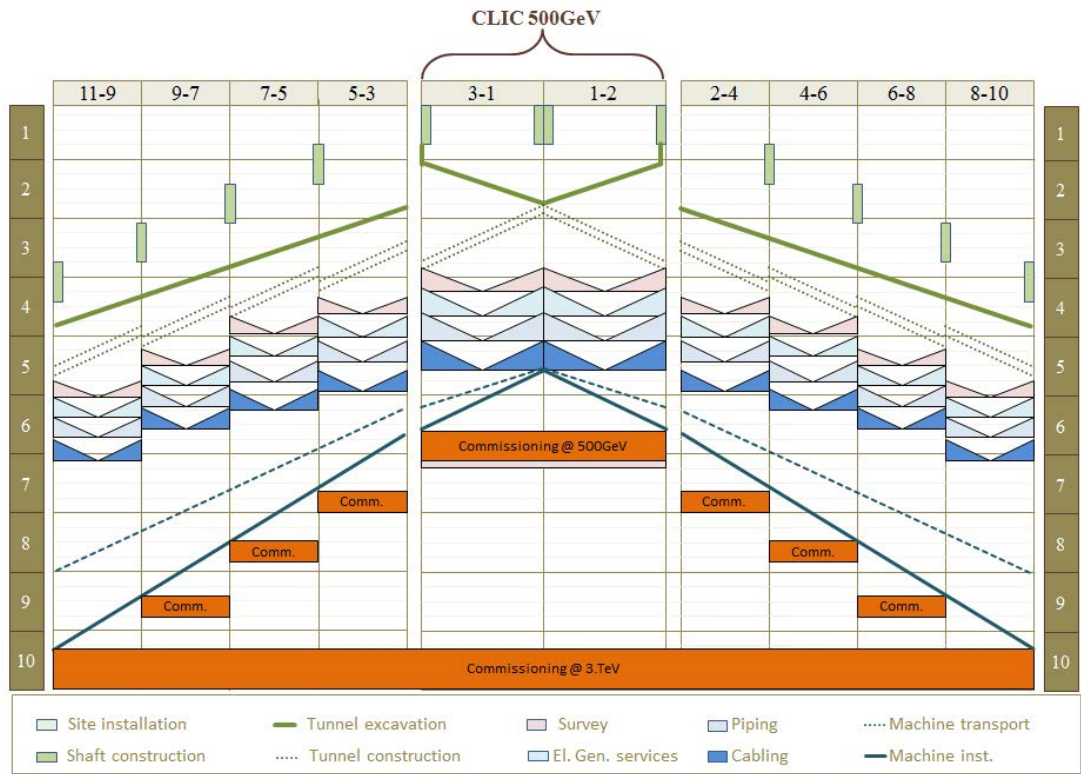


Fig. 9.18: General 'railway schedule' for the Main Linacs

9.5.3.1 *Rates of progress and logistic constraints*

Civil engineering

The civil engineering works schedule is based on a study performed by an external consultant (Amberg Engineering) in 2008. The following progress rates are retained for the CLIC complex construction:

- site installation: 15 weeks
- shaft excavation and concrete:
 - 180 m deep: 30 weeks
 - 150 m deep: 26 weeks
 - 100 m deep: 15 weeks
- service caverns: 35 weeks
- excavation by tunnel-boring machine (TBM): 150 m/week.

In order to ease logistics and preserve personnel safety, the construction of the main linacs, injectors, and experimental area constitute separate civil engineering work packages. A few weeks before civil engineering handover, geodesic measurements will be performed. These are crucial in view of the large geographical extent of the machine and its tight requirements in matters of alignment.

Installation of general services

The general services in the main linacs consist essentially of the following:

- survey: marking the position on the floor (one point every 2 m) – 9 weeks/km/front;
- electrical general services: lights, cable trays, and power boxes – 8 weeks/km/front;
- cooling & ventilation: ventilation ducts and pipes – 8 weeks/km/front;
- cabling: both AC and DC - 8 weeks/km/front.

Installation of two-beam modules

The modules will be transported to their final locations in the tunnel at a maximal rate of 550 modules per month.

The interconnections will follow, starting at a maximal rate of 300 modules per month (for the intermediate stage at 500 GeV centre of mass) and reaching a maximal rate of 400 modules interconnected per month (Fig. 9.19).

9.5.3.2 *Schedule*

The CLIC complex will be built in four main phases:

- **Civil engineering phase:** after almost four months of site installation, excavation of the main shafts will start. The two tunnel-boring machines will be mounted on site and will start the excavation of the right and left tunnels. As soon as one shaft is no longer needed for earth removal, the concrete work will start followed by installation of the ventilation ducts and finishing.
- **General services phase:** the handover by civil engineering of the different areas will be followed by the determination of the tunnel geodetic network and the marking of fiducial positions on the floor; this will be followed immediately by the installation of the general electrical services, piping, and cabling. The work sites will develop sequentially (with a small overlap) in order to ease logistics and avoid risky co-activities. At any given time, each general service activity will proceed along four fronts, in parallel in two sectors (right and left).

9.5 CONSTRUCTION SCHEDULES

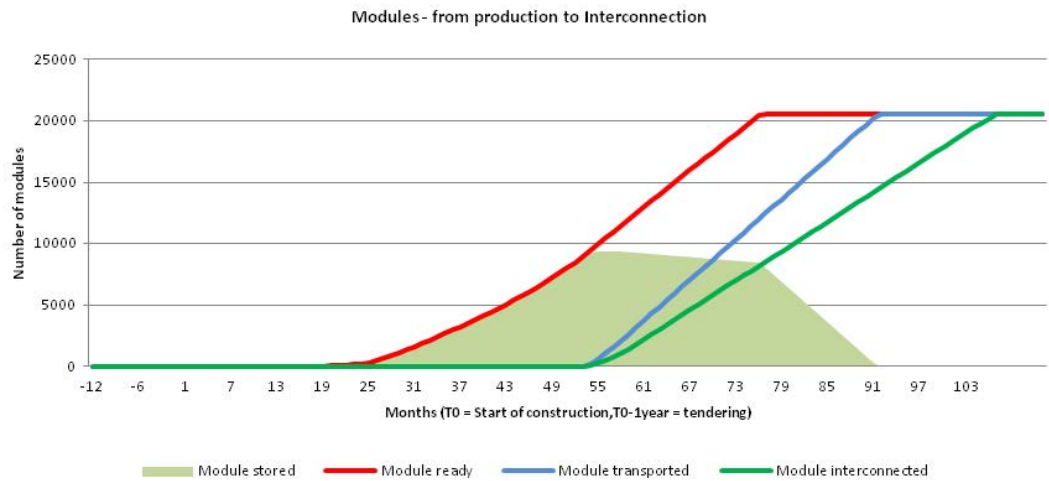


Fig. 9.19: Two-beam modules for the Main Linacs: from production to interconnection

- **Machine installation:** once most of the cabling work is completed, installation of the ground supports will start. The two-beam modules will then be transported, pre-aligned, and interconnected, working on two fronts in each sector.
- **Commissioning phase:** this phase involves commissioning of the accelerator systems without beam; it will take about one year and will be followed by a final alignment of the machine.

9.5.4 Injectors

Construction, installation, and commissioning of the injectors will take about six years. Detailed schedules have been drawn up based on the studies performed for smaller accelerator projects at CERN.

9.5.4.1 Pre-damping and damping rings

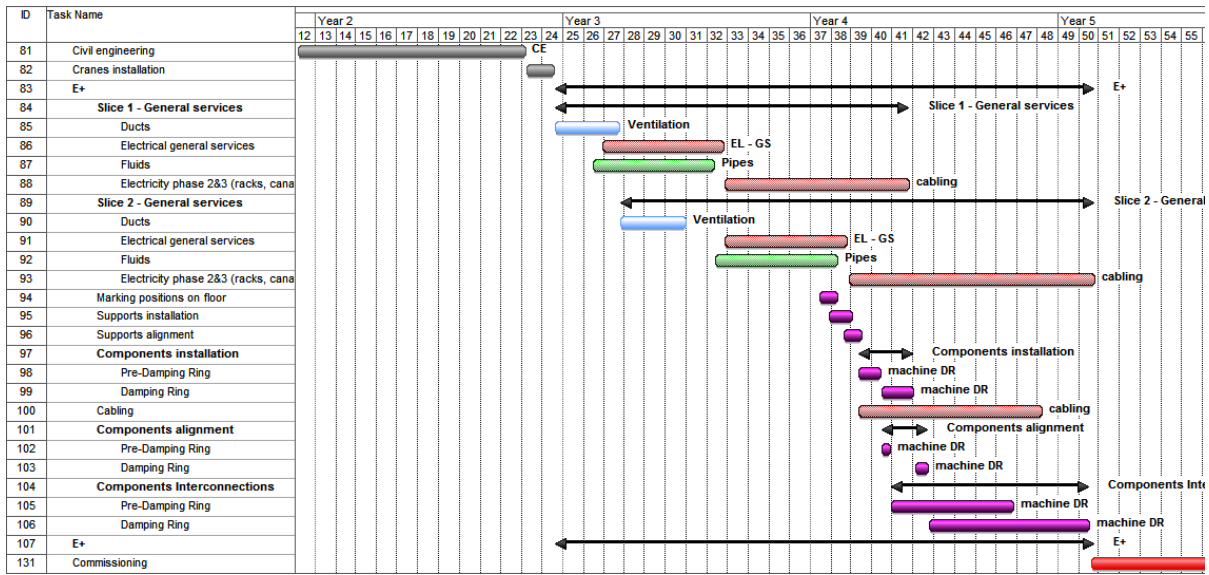


Fig. 9.20: Gantt generic schedule for the pre-damping and damping rings

The construction and installation of the pre-damping and damping ring complex will take four years and will be followed by commissioning (Fig. 9.20).

9.5.4.2 Main Beam injectors

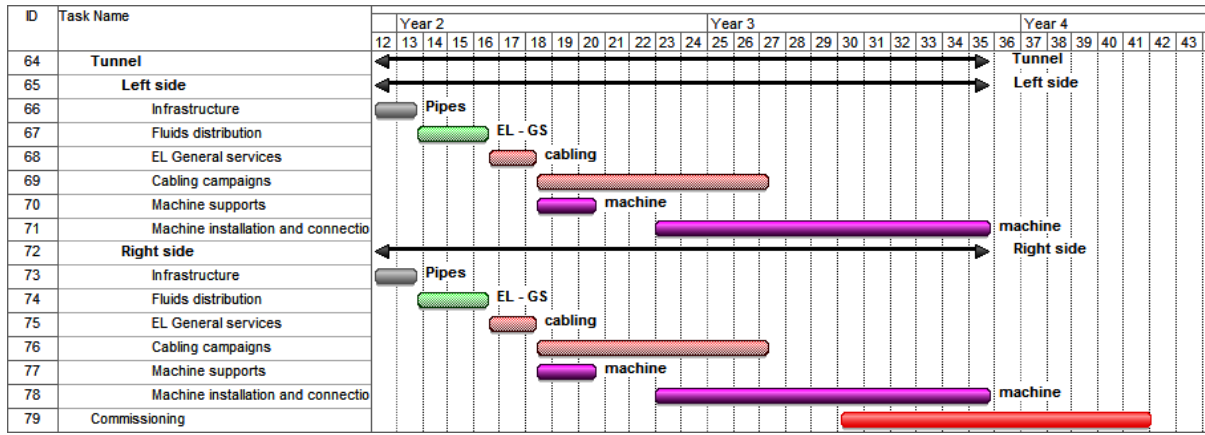


Fig. 9.21: Gantt generic schedule for the Main Beam injector complex

The construction and installation of the Main Beam injectors will take three and a half years and will be followed by commissioning (Fig. 9.21).

9.5.4.3 Drive Beam injectors

The same strategy will be applied for the construction and installation of the Drive Beam facilities (Fig. 9.22).

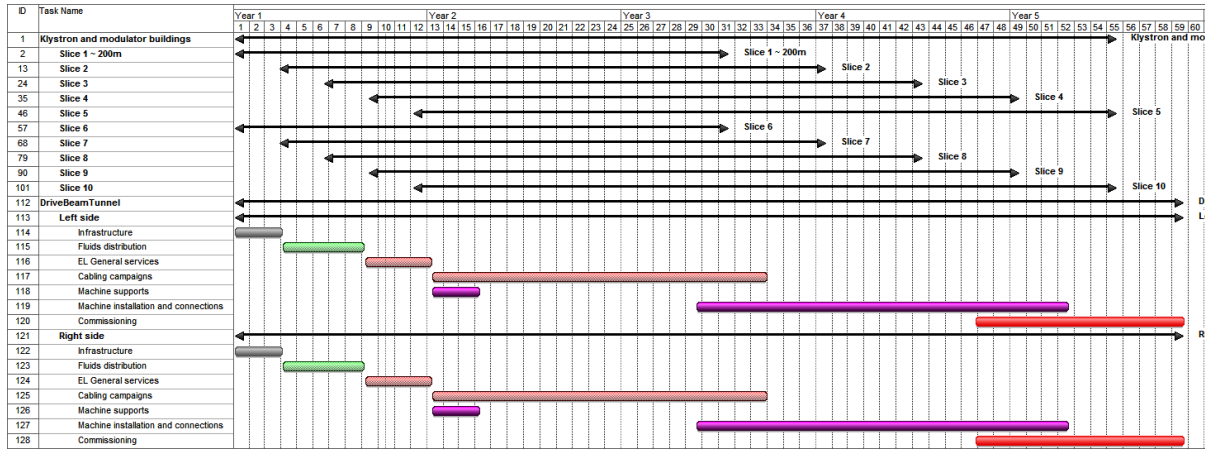


Fig. 9.22: Gantt schedule for the Drive Beam injector linacs

9.5.4.4 Summary schedule for the injectors

The injector schedule is presented in Fig. 9.23. The start of construction of each complex has been adapted in order to even out the required resources, while remaining compliant with the Main Linac schedule. It must be noted that for coherence of the civil engineering work, construction of the long descending transfer lines (black arrow in Fig. 9.23) must be completed in the time window between the end of excavation of the main tunnels and their handover for installation of infrastructure.

9.5 CONSTRUCTION SCHEDULES

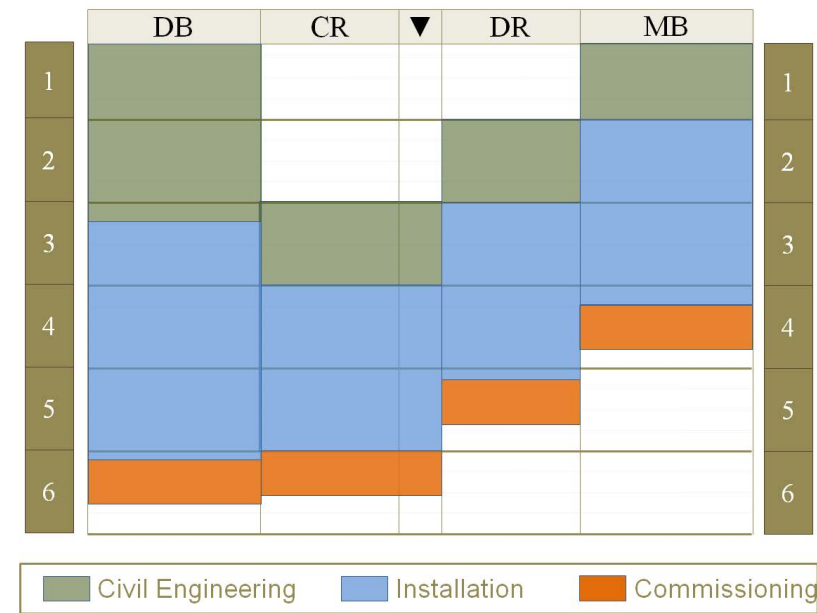


Fig. 9.23: Summary schedule for the injector complex. The central column (black arrow) refers to the long descending transfer lines from the injector complex at ground level, to the main tunnels underground

9.5.5 Experimental areas

A seven-year program has been established and is presented in Table 9.20.

In the course of year 4, the work in the shaft area of the assembly halls will have to be interrupted for 12 weeks to allow for the installation of important parts of the shaft technical infrastructure such as prefabricated concrete modules for lift and stairway, ventilation ducts, cooling pipes, cable trays, and metallic staircases for the shaft technical area. Figure 9.24 shows a Gantt chart form of the schedule for this period.



Fig. 9.24: Details of interaction region schedule in year 4

A lot more work is needed to fill in the details of this schedule but the current sequence seems to be compatible with the goal of being ready for beam at 500 GeV centre-of-mass seven years after the start of construction.

9.5.6 Overall schedule

The overall ‘railway schedule’ combining construction of the Main Linacs, injector complex, and Interaction Region is given in Fig. 9.25. Beam commissioning and operation of the 500 GeV stage could start in year 8 and continue in year 9, in parallel with further installation occurring in the left and right

Table 9.20: Construction and installation of CLIC Interaction Region (IR)

Year	Underground work	Surface work
1	Excavate two experimental shafts in parallel.	Construction of part (2/3) of two detector assembly halls in parallel, including services.
2	Excavate and carry out finishing of experimental caverns and transfer tunnel (2.5 years).	Assemble two detectors in their dedicated assembly halls (1 st of 4 years). Construct service buildings (cooling & ventilation, electrics, gas, counting rooms, etc.).
3	Proceed with finishing of the two experimental Caverns and transfer tunnel.	Assemble two detectors in assembly halls (2 nd of 4 years).
4	Finish the two experimental caverns and transfer tunnel. Install infrastructure and services in two experimental caverns and transfer tunnel (1.5 years). See details in Fig. 9.24.	Assemble two detectors in assembly halls (3 rd of 4 years). Complete construction of last third of two assembly halls.
5	Complete installation of infrastructure and services in two experimental caverns and transfer tunnel.	Complete assembly of two detectors in assembly halls. Installation of heavy-load gantry crane for lowering detectors.
6	Connect two detectors to the caverns' on-detector services and cable chains (6 months).	Lower two detectors (6 months).
7	Perform magnet tests. Trial run with cosmic rays. Commission safety systems. Test push-pull system including forward shielding.	

extensions of the Main Linac tunnels. However, the requirement to reach 3 TeV centre of mass as soon as possible would then interrupt the operation of the machine at 500 GeV centre-of-mass.

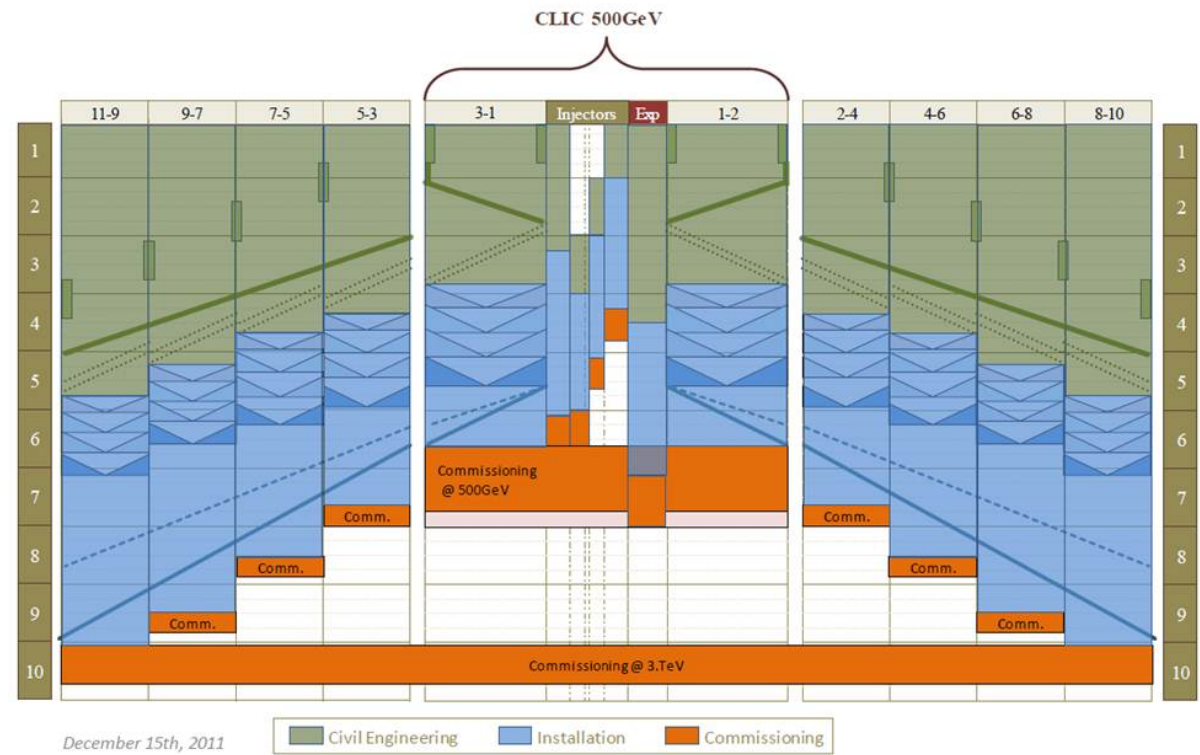


Fig. 9.25: Overall ‘railway’ schedule

References

1. Gianotti, F. & Tonelli, G. *Status of the Standard Model Higgs searches for the ATLAS and CMS experiments* <<https://indico.cern.ch/conferenceDisplay.py?confId=164890>> (2011).
2. Adams, D. L. in *47th Rencontres de Moriond on Electroweak Interactions and Unified Theories, 3-10 Mar 2012, La Thuile, Italy* (2012). <<http://indico.in2p3.fr/getFile.py/access?contribId=104&sessionId=8&resId=0&materialId=slides&confId=6001>>.
3. *Short-Term Outlook and Experimental Summary* <<http://indico.in2p3.fr/materialDisplay.py?contribId=70&sessionId=20&materialId=slides&confId=6004>> (2011).
4. Thomson, M. A. *The physics benchmark processes for the detector performance studies of the CLIC CDR LCD-Note-2011-016* (CERN, 2011).
5. *CERN Medium Term Plan 2012-2016* <<http://indico.cern.ch/materialDisplay.py?contribId=14&sessionId=0&materialId=0&confId=141021>> (2011).
6. Grudiev, A., Schulte, D. & Wuensch, W. in *Proc. 10th European Particle Accelerator Conf., 26-30 June 2006, Edinburgh, Scotland, UK* (2006). <<http://accelconf.web.cern.ch/accelconf/e06/PAPERS/WEOAPA02.PDF>>.
7. Grudiev, A., Braun, H.-H., Schulte, D. & Wuensch, W. in *Proc. XXIV Linear Accelerator Conf., 29 September - 3 October 2008, Victoria, British Columbia, Canada* (2008). <<http://trshare.triumf.ca/~linac08proc/Proceedings/LINAC08/papers/tup055.pdf>>.
8. Grudiev, A. & Wuensch, W. in *Proc. XXIV Linear Accelerator Conf., 29 September - 3 October 2008, Victoria, British Columbia, Canada* (2008). <<http://trshare.triumf.ca/~linac08proc/Proceedings/LINAC08/papers/thp062.pdf>>.
9. Braun, H., Corsini, R., Delahaye, J.-P. & Tecker, F. *CLIC 2008 Parameters CERN-OPEN-2008-021. CLIC-Note-764* (CERN, 2008). <<http://cdsweb.cern.ch/record/1132079/files/CERN-OPEN-2008-021.pdf>>.
10. Jeanneret, J. B. *et al.* in *Proc. 11th European Particle Accelerator Conf., 23-27 June 2008, Genoa, Italy* (2008), 3017–3019. <<http://accelconf.web.cern.ch/AccelConf/e08/papers/thpc018.pdf>>.

Appendices



Appendix A

CLIC parameters

Table A.1: Overall parameters

Parameter	Symbol	Value	Unit
Overall Parameters			
Centre-of-mass energy	E_{CMS}	3000	GeV
Main Linac RF frequency	f_{rf}	11.994	GHz
Luminosity	L	5.9	$10^{34} \text{cm}^{-2} \text{s}^{-1}$
Luminosity (in 1% of energy)	$L_{99\%}$	2	$10^{34} \text{cm}^{-2} \text{s}^{-1}$
Linac repetition rate	f_{rep}	50	Hz
No. of particles / bunch	N	3.72	10^9
No. of bunches / pulse	N_b	312	
Bunch separation	Δt_b	0.5 (6 periods)	ns
Bunch train length	τ_{train}	156	ns
Beam power / beam	P_b	14	MW
Unloaded / loaded gradient	$G_{\text{unl/l}}$	120 / 100	MV/m
Overall two linac length	l_{linac}	42.16	km
Total beam delivery length	l_{BD}	2 x 2.75	km
Proposed site length	l_{tot}	48.4	km
Total site AC power	P_{tot}	582	MW
Wall-plug-to-Main-Beam-power efficiency	η_{tot}	4.8	%

Table A.2: Main Linac and accelerating structure parameters

Parameter	Symbol	Value	Unit
Main Linac			
Fill factor	F	78.6	%
Overhead for energy fdbk & repair	ovh_{rep}	5	%
Overhead for off-crest operation	$\text{ovh}_{\text{off-crest}}$	5	%
Acceleration structure length (active)	l_{struct}	0.23	m
Average $\langle a/\lambda \rangle$	a/λ	0.11	
Group velocity	v_g/c	1.65 - 0.83	%
Filling time / rise time	τ_f, τ_r	67 / 21	ns
Unloaded quality factor	Q	5536 - 5738	
Shunt impedance (first/last cell)	r_s	81 / 103	(Linac)MΩ/m
Accelerator structure input power	P_{acc}	61.3	MW
RF → Main Beam efficiency	$\eta_{b,\text{RF}}$	28	%

Table A.3: Damping Ring and Main Beam parameters

Parameter	Symbol	Value	Unit
Electron / positron damping ring			
Ring circumference	C_{DR}	427.5	m
RF frequency	f_{DR}	1	GHz
Number of trains stored	n_{train}	2	
Number of bunches / train	N_b	156	
Bunch separation	$\Delta t_{b,\text{DR}}$	1	ns
Total wiggler length	l_{wig}	104	m
Damping times	$\tau_x / \tau_y / \tau_z$	2.0 / 2.0 / 1.0	ms
Tunes	Q_x / Q_y	48.38 / 10.39	
Main Beam in damping ring before extraction			
Energy	$E_{b,\text{DR}}$	2.86	GeV
No. of particles / bunch	N_b	4.07	10^9
Bunch length	$\sigma_{s,\text{DR}}$	1.8	mm
Energy spread	σ_E / E_{DR}	0.118	%
Transverse horizontal emittance	$\gamma \epsilon_{x,\text{DR}}$	456	nm rad
Transverse vertical emittance	$\gamma \epsilon_{y,\text{DR}}$	4.8	nm rad
Longitudinal emittance (normalized)		6.1	keV m
Main Beam at linac injection			
Energy	$E_{b,\text{inj}}$	9	GeV
No. of particles / bunch	N_b	3.72	10^9
Bunch length	$\sigma_{s,\text{inj}}$	44	μm
Energy spread	$\Delta E / E_{\text{inj}}$	1.3	%
Transverse horizontal emittance	$\gamma \epsilon_{x,\text{inj}}$	600	nm rad
Transverse vertical emittance	$\gamma \epsilon_{y,\text{inj}}$	10	nm rad

Table A.4: Beam Delivery System, IP and background parameters

Parameter	Symbol	Value	Unit
Beam Delivery System + IP			
Total diagnostic section length	l_{coll}	2x 0.37	km
Total collimation system length	l_{coll}	2x 1.92	km
Total final focus system length	l_{FF}	2x 0.46	km
Input transverse horizontal emittance	ϵ_x	660	nm rad
Input transverse vertical emittance	ϵ_y	20	nm rad
Nominal horizontal IP beta function	β_x^*	6.9	mm
Nominal vertical IP beta function	β_y^*	0.068	mm
Horizontal IP core beam size	σ_x^*	~ 45	nm
Vertical IP core beam size	σ_y^*	~ 0.9	nm
Bunch length	$\sigma_{s,\text{inj}}$	44	μm
Initial r.m.s. energy spread	$\sigma_{\Delta E/E}^*$	0.34	%
Total energy spread		1	%
Crossing angle at IP	θ_C	20	mrاد
Beamstrahlung energy loss	δ_B	28	%
No. of photons / electron	n_γ	2.1	
No. of coherent pairs / bunch crossing	N_{coh}	68	10^7
No. of incoherent pairs / bunch crossing	N_{incoh}	0.03	10^7
Hadronic events / crossing	N_{hadron}	3.2	
Total luminosity	L_{pk}	5.9	$10^{34}\text{cm}^{-2}\text{s}^{-1}$
Luminosity (in 1% of energy)	$L_{99\%}$	2.0	$10^{34}\text{cm}^{-2}\text{s}^{-1}$

Table A.5: Decelerator and PETS parameters

Parameter	Symbol	Value	Unit
Decelerator			
No. of Drive Beam sectors / linac	N_S	24	
Average decelerator length (total)	L_{dec}	878	m
No. of PETS / sector	$N_{\text{PETS,unit}}$	1492	
Length of PETS (active)	l_{PETS}	0.213	m
Nominal output RF Power / PETS	P_{out}	134	MW
Transfer efficiency PETS \rightarrow AS		93.8	%
Number of accelerating structures / PETS		2	
Main Beam energy gain / sector	ΔE_{main}	62.125	GeV
Drive Beam \rightarrow RF efficiency (AS input)	η_{decRF}	65	%

Table A.6: Drive Beam parameters

Parameter	Symbol	Value	Unit
Drive Beam basic parameters			
Energy (decelerator injection)	$E_{\text{in,dec}}$	2.37	GeV
Energy (final, minimum)	$E_{\text{fin,dec}}$	0.24	GeV
Average current in pulse	I_{dec}	101	A
Train duration	τ_{train}	244	ns
No. bunches / train	$N_{b,\text{dec}}$	2928	
Bunch charge	$Q_{b,\text{dec}}$	8.4	nC
Bunch separation	$\Delta_{b,\text{dec}}$	0.083	ns
Bunch length, r.m.s.	$\sigma_{s,\text{dec}}$	1	mm
Normalized emittance, r.m.s.	$\gamma\epsilon_{\text{dec}}$	150	$\mu\text{m rad}$
Drive Beam linac			
RF frequency	f_{RF}	999.5	MHz
Total number of klystrons	N_{kly}	2 * 819	
Klystron peak power	P_{kly}	15	MW
Repetition frequency	f_{rep}	50	Hz
Pulse length (total train)	τ_{pulse}	142	μs
Beam current per pulse	I_{DB}	4.2	A
Charge per pulse	Q_{pulse}	0.6	mC
Number of bunches / pulse	$N_{b,\text{pulse}}$	7.1	10^4
Bunch length (r.m.s.)	σ_s	4	mm
Normalized emittance (at injection)	$\gamma\epsilon_i$	100	$\mu\text{m rad}$
Total energy spread (at injection)	$\Delta E/E$	1	%
RF \rightarrow Drive Beam efficiency	$\eta_{b,\text{RF}}$	89	%

Table A.7: Delay Line and Combiner Ring parameter

Parameter	Symbol	Value	Unit
Delay Line			
Length	L_D	73.2	m
RF deflector frequency	f_D	499.8	MHz
Combination factor	$F_{C,D}$	2	
Bunch length (r.m.s.)	σ_s	2	mm
Combiner Ring 1			
Length	L_{R1}	292.6	m
RF deflector frequency	f_{R1}	999.5	MHz
Combination factor	$F_{C,R1}$	3	
Bunch length (r.m.s.)	σ_s	2	mm
Combiner Ring 2			
Length	L_{R2}	439.1	m
RF deflector frequency	f_{R2}	2998.6	MHz
Combination factor	$F_{C,R2}$	4	
Bunch length (r.m.s.)	σ_s	2	mm

Appendix B

Artwork in this CDR

The images at the beginning of each chapter in this CDR are the result of a successful collaboration between CERN and the Art Department at La Chataigneraie International School in Founex (near Geneva). Following a visit to the school campus in 2010, where the CLIC project was presented, students, aged from 15 to 17 years were invited to come up with their own visions of CLIC. In total, some 40 students took part in the project and submitted their artwork. The editorial team selected amongst these contributions ten samples and inserted those at the beginning of each chapter. Since not all contributions could become part of the CDR, below we show small thumbnails of all the contributions.

As recognition of the effort put in by the students, and also to expose their work a larger audience, an exhibition was held in CERN's Main Building on the evening of Monday 6th December 2010. Most of the students who had produced artworks were able to attend the event where they met and explained their work to the many CLIC collaborators who came along.

Here we include the personal account of three students who took part:

CLIC EXHIBITION AT CERN

“After a long day of school, and a rather short car ride we made it to CERN. We collected our access badges, and followed a black line along the floor. It went on for a long time, and eventually became like a never ending ‘yellow brick road.’

Once we finally found our way through the labyrinth of offices and formula-covered blackboards, a large white room opened before us. It was Monday evening (the 6th of December 2010) and we had finally arrived at the CLIC (Compact Linear Collider) exhibition.

We were all very excited to see our artwork (more like masterpieces!) created by IGCSE and some IB students at the start of this school year, following a presentation at school by CERN physicists about a new linear collider project called CLIC. All of the students’ artwork was presented on their own individual board. We all felt like we were part of something special, as we were standing on such a well-known and respected place.

We got to meet a lot of important, and influential people who were in charge of the CLIC project, or involved with CERN in one way or another. These scientists were from all over the world. They were nothing like the stereotypical scientists wearing white labs coats with mad hair like Einstein!

It was a bit scary at first when they approached us to ask us about our artwork, as they are such important people, but we eventually got the hang of it. We got to explain to them the whole idea behind our final piece, and what it means to us. They gave us feedback and praised us for our good work. Being acknowledged for our work was worth all the time we had dedicated to the project. We learned that three winning pieces would probably be chosen as cover pages for the volumes of the CLIC conceptual design report, but also that all the artwork will probably appear in the report as chapter dividers. What an exciting opportunity for the school and us students!

Monday the 6th of December was more than a pat on the back. It was a day we will never forget, and hopefully we will get to meet them again. Now we can only wait in suspense for their selection of the winner(s).”

Fiona Teeling, Marissa Nordentoft, Edna Dualeh (Year 11 students at the time)

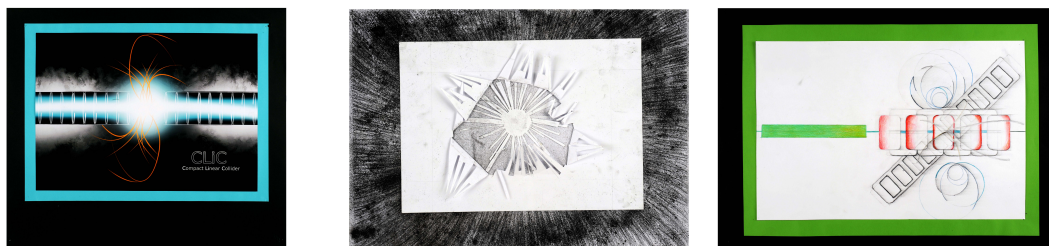


Fig. B.1: left: Alexander Duncan, centre: Alexander Iatsenia and right: Alexander Moloney



Fig. B.2: left: Alexandra Risberg, centre: Alexandra Roux and right: Alice Yeates



Fig. B.3: left: Ana Potter Lesage, centre: Asami Igarashi and right: Chiara Cerboni

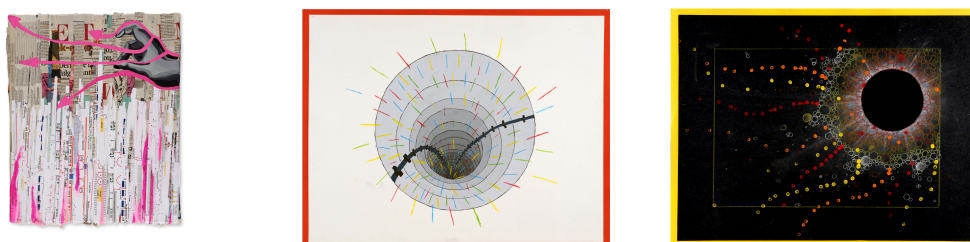


Fig. B.4: left: Claire Caillaux, centre: David Tyner and right: Edna Dualeh



Fig. B.5: left: Eleonora Bosman, centre: Fiona Teeling and right: Gregory Bossert

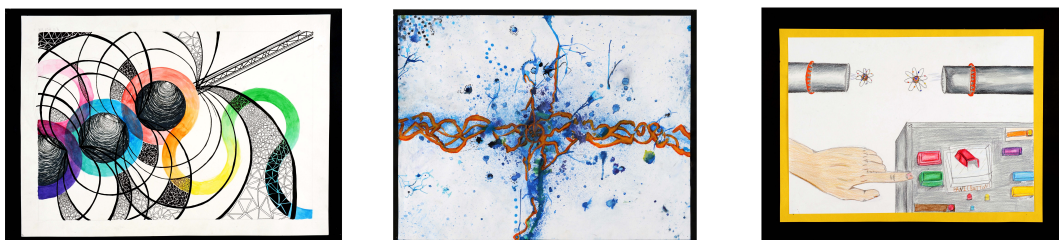


Fig. B.6: left: Iris van der Haagen, centre: Isabelle Edwards and right: Jacob Hanni



Fig. B.7: left: Jessica Flesher, centre: Joanna Jump and right: Johnathan Granger

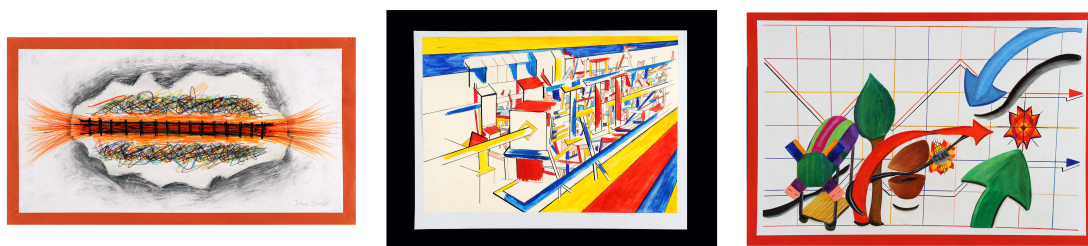


Fig. B.8: left: Joshua Johnson, centre: Julia Ericson and right: Karim Albekov

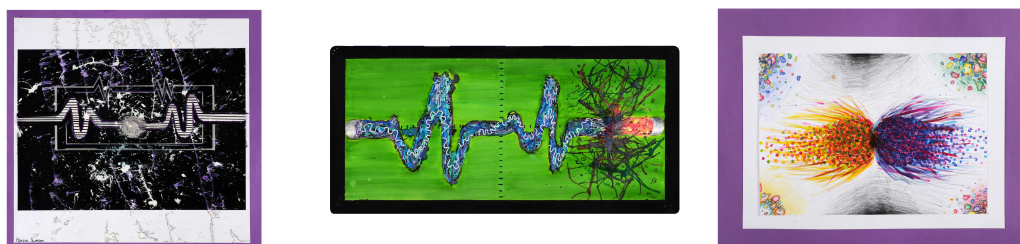


Fig. B.9: left: Karina Swinson, centre: Kelly Anderson and right: Kevin Doyle



Fig. B.10: left: Kyinat Motla, centre: Lukas Molkentin and right: Marco Delgado Schwartz



Fig. B.11: left: Marielle van Helvoort, centre: Marissa Nordentoft and right: Mélanie Church



Fig. B.12: left: Natasha De Heney, centre: Nathalie Martin and right: Neelson Beesley



Fig. B.13: left: Neila Fraiha, centre: Paola Tenconi and right: Samantha Kirk



Fig. B.14: left: Sarenne Wallbridge, centre: Sean Steed and right: Signe Kossmann

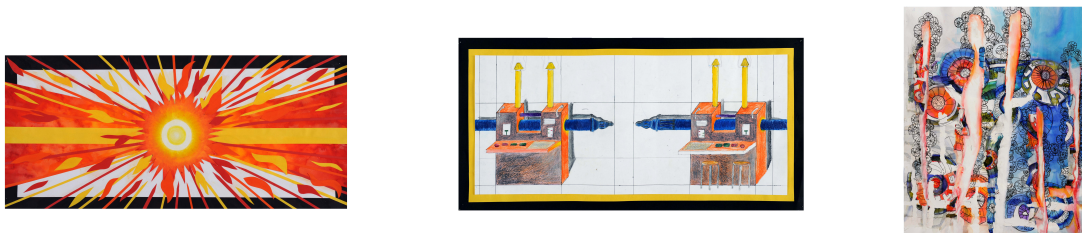


Fig. B.15: left: Spencer Kimball, centre: Stefan Hall and right: Stephanie Hultin



Fig. B.16: left: Tatjana Cerboni, centre: Vilma Heiskanen and right: Walma Willmann

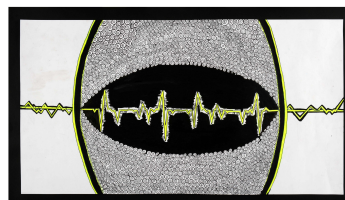


Fig. B.17: Zoe Williamson